

**International Ocean Discovery Program
Expedition 349 Preliminary Report**

South China Sea Tectonics

**Opening of the South China Sea and its implications for
southeast Asian tectonics, climates, and deep mantle
processes since the late Mesozoic**

26 January–30 March 2014

Expedition 349 Scientists



Published by
International Ocean Discovery Program

Publisher's notes

Material in this publication may be copied without restraint for library, abstract service, educational, or personal research purposes; however, this source should be appropriately acknowledged. Core samples and the wider set of data from the science program covered in this report are under moratorium and accessible only to Science Party members until 30 March 2015.

This publication was prepared by the International Ocean Discovery Program U.S. Implementing Organization (IODP-USIO): Consortium for Ocean Leadership, Lamont-Doherty Earth Observatory of Columbia University, and Texas A&M University, as an account of work performed under the International Ocean Discovery Program. Funding for the program is provided by the following agencies:

National Science Foundation (NSF), United States

Ministry of Education, Culture, Sports, Science and Technology (MEXT), Japan

European Consortium for Ocean Research Drilling (ECORD)

Ministry of Science and Technology (MOST), People's Republic of China

Korea Institute of Geoscience and Mineral Resources (KIGAM)

Australian Research Council (ARC) and GNS Science (New Zealand), Australian/New Zealand Consortium

Ministry of Earth Sciences (MoES), India

Coordination for Improvement of Higher Education Personnel, Brazil

Disclaimer

Any opinions, findings, and conclusions or recommendations expressed in this publication are those of the author(s) and do not necessarily reflect the views of the participating agencies, Consortium for Ocean Leadership, Lamont-Doherty Earth Observatory of Columbia University, Texas A&M University, or Texas A&M Research Foundation.

Portions of this work may have been published in whole or in part in other International Ocean Discovery Program documents or publications.

Copyright

Except where otherwise noted, this work is licensed under a [Creative Commons Attribution License](#). Unrestricted use, distribution, and reproduction is permitted, provided the original author and source are credited.

Citation:

Expedition 349 Scientists, 2014. South China Sea tectonics: opening of the South China Sea and its implications for southeast Asian tectonics, climates, and deep mantle processes since the late Mesozoic. *International Ocean Discovery Program Preliminary Report*, 349. <http://dx.doi.org/10.14379/iodp.pr.349.2014>

ISSN

World Wide Web: 2372-9562

Expedition 349 participants

Expedition 349 scientists

Chun-Feng Li
Co-chief Scientist
State Key Laboratory of Marine Geology
Tongji University
1239 Siping Road
200092 Shanghai
China
cfl@tongji.edu.cn

Jian Lin
Co-chief Scientist
Department of Geology and Geophysics
Woods Hole Oceanographic Institution
360 Woods Hole Road
Woods Hole MA 02543
USA
jlin@whoi.edu

Denise K. Kulhanek
Expedition Project Manager/Staff Scientist
International Ocean Discovery Program
Texas A&M University
1000 Discovery Drive
College Station TX 77845-9547
USA
kulhanek@iodp.tamu.edu

Trevor Williams
Logging Staff Scientist
Borehole Research Group
Lamont-Doherty Earth Observatory
of Columbia University
PO Box 1000, 61 Route 9W
Palisades NY 10964
USA
trevor@ldeo.columbia.edu

Rui Bao
Organic Geochemist
Geologisches Institut
Swiss Federal Institute of Technology (ETH
Zürich)
Sonneggstrasse 5, NO E57
8092 Zürich
Switzerland
ruibao@erdw.ethz.ch

Anne Briaïs
Physical Properties Specialist
Géosciences Environnement Toulouse
Centre National de la Recherche Scientifique
(CNRS)
Observatoire Midi-Pyrénées, University
of Toulouse
14 Avenue Edouard Belin
31400 Toulouse
France
anne.briaïs@get.obs-mip.fr

Elizabeth A. Brown
Paleontologist (foraminifers)
College of Marine Science
University of South Florida
140 7th Avenue South
St. Petersburg FL 33701
USA
eabrown@mail.usf.edu

Yifeng Chen
Inorganic Geochemist
Key Laboratory of Marginal Sea Geology
Guangzhou Institute of Geochemistry,
Chinese Academy of Sciences
511 Kehua Street, Tianhe District
510640 Guangzhou
China
yfchen@gig.ac.cn

Peter D. Clift
Sedimentologist
Department of Geology and Geophysics
Louisiana State University
E253 Howe-Russell-Kniffen Geoscience
Complex
Baton Rouge LA 70803
USA
pclift@lsu.edu

Frederick S. Colwell
Microbiologist
College of Earth, Ocean and Atmospheric
Sciences
Oregon State University
104 CEOAS Administration Building
Corvallis OR 97331-5503
USA
rcolwell@coas.oregonstate.edu

Kelsie A. Dadd
Sedimentologist
Department of Earth and Planetary Sciences
Macquarie University
Sydney NSW 2109
Australia
kelsie.dadd@mq.edu.au

Weiwei Ding
Structural Geologist
Key Laboratory of Submarine Geoscience
Second Institute of Oceanography,
State Oceanic Administration
36 Baochubei Road
310012 Hangzhou
China
wwding@gmail.com

Iván Hernández Almeida
Paleontologist (radiolarians)
Institute of Geography/Oeschger Centre
for Climate Change Research
University of Bern
Erlachstrasse 9a
3012 Bern
Switzerland
ivan.hernandez@giub.unibe.ch

Xiao-Long Huang
Inorganic Geochemist
State Key Laboratory of Isotope Geochemistry
Guangzhou Institute of Geochemistry,
Chinese Academy of Sciences
511 Kehua Street, Tianhe District
510640 Guangzhou
China
xlhuang@gig.ac.cn

Sangmin Hyun
Sedimentologist
Marine Environment and Conservation
Research Division
Korea Institute of Ocean Science and
Technology (KIOST)
787 Haeanlo
Ansan426-744
Republic of Korea
smhyun@kiost.ac

Tao Jiang
Sedimentologist
Department of Marine Science and
Engineering
Faculty of Earth Resources
China University of Geosciences
388 Lumo Road
Wuhan 430074
P.R. China
taojiang@cug.edu.cn
Secondary address:
Kochi Institute for Core Sample Research
Japan Agency for Marine-Earth Science and
Technology (JAMSTEC)
200 Monobe-Otsu
Nanko-ku, Kochi
783-8502
Japan
jiangtao@jamstec.go.jp

Anthony A.P. Koppers
Petrologist
College of Earth, Ocean and Atmospheric
Sciences
Oregon State University
104 CEOAS Administration Building
Corvallis OR 97331
USA
akoppers@coas.oregonstate.edu

Qianyu Li
Paleontologist (foraminifers)
School of Ocean and Earth Sciences
Tongji University
1239 Siping Road
200092 Shanghai
China
qli01@tongji.edu.cn

Chuanlian Liu
Paleontologist (nannofossils)
School of Ocean and Earth Sciences
Tongji University
1239 Siping Road
200092 Shanghai
China
liucl@tongji.edu.cn

Qingsong Liu
Paleomagnetist
State Key Laboratory of Lithospheric
Evolution
Institute of Geology and Geophysics,
Chinese Academy of Sciences
19 Beitucheng Western Road
Chaoyang District
100029 Beijing
China
qslu@mail.iggcas.ac.cn

Zhifei Liu
Sedimentologist
State Key Laboratory of Marine Geology
Tongji University
1239 Siping Road
200092 Shanghai
China
lzhifei@tongji.edu.cn

Renata H. Nagai
Paleontologist (foraminifers)
Department of Physical, Chemical and
Geological Oceanography
Instituto Oceanográfico
Universidade de São Paulo
191 sala 171 Praça do Oceanográfico
05508-120 São Paulo-SP
Brazil
renatanagai@usp.br

Alyssa Peleo-Alampay
Observer/Paleontologist (nannofossils)
National Institute of Geological Sciences
University of the Philippines
Diliman
1101 Quezon City
Philippines
ampanigs@yahoo.com

Xin Su
Paleontologist (nannofossils)
School of Marine Geosciences
China University of Geosciences
29 Xueyuan Road
100083 Beijing
China
xsu@cugb.edu.cn

Zhen Sun
Structural Geologist
Department of Marine Geology
South China Sea Institute of Oceanology
164 Xingangxi Road
510301 Guangzhou
China
zhensun@scsio.ac.cn

Maria Luisa (Marissa) G. Tejada
Petrologist
Japan Agency for Marine-Earth Science and
Technology (JAMSTEC)
2-15 Natsushima-cho, Yokosuka-shi
Kanagawa
237-0061
Japan
mtejada@jamstec.go.jp

Hai Son Trinh
Observer/Physical Properties Specialist
Department of Science and Technology
Ministry of Natural Resources and
Environment (MONRE)
10 Ton That Thuyet Street
Hanoi
Vietnam
thaison@monre.gov.vn

Yi-Ching Yeh
Observer/Physical Properties Specialist
Taiwan Ocean Research Institute
219 Dongfang Road, Section 1
Kaohsiung City 852
Taiwan
ycyeh@narlabs.org.tw

Chuanlun Zhang
Organic Geochemist
School of Ocean and Earth Sciences
Tongji University
1239 Siping Road
200092 Shanghai
China
archaea.zhang@gmail.com

Fan Zhang
Physical Properties Specialist
Department of Geology and Geophysics
Woods Hole Oceanographic Institution
243 Clark Laboratory
266 Woods Hole Road
Woods Hole MA 02543
USA
fzhang@whoi.edu

Guo-Liang Zhang
Petrologist
Key Laboratory of Marine Geology and
Environment
Institute of Oceanology, Chinese Academy
of Sciences
7 Nanhai Road
266071 Qingdao
China
zhangguoliang@qdio.ac.cn

Xixi Zhao
Paleomagnetist
Department of Earth and Planetary Sciences
University of California, Santa Cruz
1156 High Street
Santa Cruz CA 95064
USA
xzhao@ucsc.edu

Education and outreach

Haopeng Tang
Reporter
TV News Center, Shanghai Media Group
298 Weihai Road
200041 Shanghai
China

Abstract

The South China Sea (SCS) provides an outstanding opportunity to better understand complex patterns of continental margin breakup and basin formation. The sea is situated at the junction of the Eurasian, Pacific, and Indo-Australian plates and is a critical site linking some of the major western Pacific tectonic units. Despite extensive studies, sampling of basement rock and directly overlying basal sediment in the deep basin is lacking. This leaves a large margin of error in estimated ages of the SCS opening and closing, rendering various hypotheses regarding its opening mechanism and history untested. This also hampers understanding of East Asian tectonic and paleo-environmental evolution.

We drilled five sites in the deep basin of the SCS. Three of these sites (U1431, U1433, and U1434) cored into oceanic basement near the fossil spreading center. The two remaining sites (U1432 and U1435) are located proximal to the northern continent/ocean boundary. We recovered a total of 1524 m of sediment/sedimentary rock and 78 m of oceanic basalt and also carried out downhole geophysical logging (triple combination and Formation MicroScanner-sonic tool strings) at the two deepest sites (U1431 and U1433). These materials and data were extensively examined and discussed during the expedition and allowed us to draw the following principal conclusions on the opening of the SCS:

1. Based on shipboard dating of microfossils in the sediment immediately above the basaltic basement and between the lava flow units, the preliminary cessation age of spreading in both the East and Southwest Subbasins is around early Miocene (16–20 Ma). Further postcruise radiometric dating of basement basalt from these sites plus additional calibration of magnetic anomaly models and paleomagnetic measurements will further refine the age range. Overall, a large difference is not apparent in the terminal ages of seafloor spreading between the two subbasins.
2. At Site U1435, we were able to drill into a structural high standing along the continent/ocean boundary. Coring at this site recovered a sharp unconformity at ~33 Ma, above which is marine sediment and below which are poorly sorted sandstone and black mudstone, interpreted as littoral deposits. Environmental interpretation will require further shore-based studies because the sequence is almost entirely barren of marine microfossils. Nevertheless, we interpret this unconformity to be likely directly related to the continental break-up during the

initial opening of the SCS. The onset of seafloor spreading is therefore estimated to be at ~33 Ma.

3. All sites contain deep marine deposits but show significant areal variations in postspreading sedimentary environment and provenance. Site U1431 records evidence for deep-marine turbidite deposition from terrestrial sources. The observed coarser silt turbidites may have a source in Taiwan or other surrounding blocks, whereas interbedded calcareous turbidites at this site could be transported from local sources, such as nearby seamounts topped by carbonate platforms. In contrast, the source for upper Miocene clay and silt turbidites at Site U1433 could be from Borneo or mainland Southeast Asia, with the source of the interbedded carbonate turbidites likely from the Dangerous Grounds or Reed Bank area located south of the site.
4. Sites U1431 and U1434 are close to seamounts developed along the relict spreading center. Occurrences of basaltic clasts and mineral fragments in the volcanoclastic sandstone and breccia may reveal the magmatic history and mantle source of the seamounts and potentially their relationship with the terminal processes of spreading. The volcanoclastic breccia and sandstone at Site U1431 are dated as late middle Miocene to early late Miocene (~8–13 Ma), suggesting a 5 m.y. duration of seamount volcanism starting a few million years after the cessation of seafloor spreading. At Site U1434, volcanoclastic breccia and sandstone are most likely sourced from the adjacent seamount ~15 km to the north. The age of this recovered unit is late Miocene (younger than 9 Ma). Further postcruise sedimentological and geochemical studies, as well as radiometric dating of potassium-bearing mineral fragments, will refine the ages and timing of these seamount activities and reveal how magma sources at the dying spreading center evolved through time.
5. We successfully cored into ocean basement in the SCS for the first time and recovered basalt at three sites (U1431, U1433, and U1434). The cored basalt has variable phase assemblages of plagioclase, olivine, and clinopyroxene and is concluded to be typical mid-ocean-ridge basalt based on petrological and geochemical evidence. Postcruise radiometric dating will determine the absolute ages of the basaltic basement units. Postcruise petrological and geochemical analyses on the basalts will provide information on the mantle sources, melting, and crystallization history of the youngest ocean crust.

Introduction

Since the late Mesozoic, the South China Sea (SCS) area (Figs. F1, F2) has been at the center of many first-order tectonic and paleoclimatic events. Mesozoic subduction of the paleo-Pacific plate under the Eurasian plate partially occurred along the present-day northeastern SCS continental margin (Jahn et al., 1976; Hilde et al., 1977; Hamilton, 1979; Holloway, 1982; Taylor and Hayes, 1983; Hayes et al., 1995; Zhou and Li, 2000; Yang and Feng, 2003; Xiao and Zheng, 2004; Zhou et al., 2008; Li et al., 2008a). This subduction resulted in the emplacement of igneous rocks and the formation of a wide orogenic belt in Southeast Asia (Zhou and Li, 2000; Shi and Li, 2012). Subduction is thought to have ceased in the mid-Cretaceous, with a transition to regional extension during the Late Cretaceous. Opening of the SCS began in the Cenozoic through continental breakup and subsequent seafloor spreading. The Ailao Shan-Red River strike-slip fault also displaced the Indochina block by hundreds of kilometers during the Oligocene and Miocene (Tapponnier et al., 1986, 1990; Lacassin et al., 1997; Leloup et al., 2001; Gilley et al., 2003). The early work of Taylor and Hayes (1980, 1983) and Briais et al. (1993) suggested that the SCS opened from ~32 to ~16 Ma during the Oligocene and early Miocene. Recently, Barckhausen and Roeser (2004) and Barckhausen et al. (2014) argued that seafloor spreading was faster in the later stages than at the beginning of the opening and ceased at 20.5 Ma (Anomaly 6a1) over the entire SCS, ~4 m.y. earlier than interpreted in previous studies.

Ages of the oceanic crust in the SCS Basin are only constrained from magnetic anomaly correlations and empirical relationships between ages and bathymetry and/or heat flow. The uncertainties in the timing and episodes of the Cenozoic opening of the SCS hamper understanding of other key geological processes in Southeast Asia, including the geodynamic transition from Mesozoic subduction to Cenozoic rifting, the relationship between the motion on the large strike-slip faults and the extension (extrusion), the Cenozoic opening mechanism, oceanic crustal accretion and mantle evolution, and paleoceanographic and sedimentary responses. In order to address regional questions related to East Asian geology and fundamental issues regarding continental breakup and the mechanism through which the SCS Basin opened, it is essential to determine when seafloor spreading initiated and when it ceased. To do this, during Expedition 349 we drilled into the oceanic basement and retrieved both sedimentary and basaltic rocks from two subbasins of the SCS. Drilling and coring into igneous basement is the only means of validating various opening mechanisms.

Expedition 349 was based on Integrated Ocean Drilling Program Proposal 735-CPP2, developed in part from results of an international workshop held at Tongji University in Shanghai, China, in early 2012 (Li et al., 2012). The primary objectives of the expedition fall under four major categories and address the Earth Connections and Climate and Ocean Change themes in the science plan for the International Ocean Discovery Program (IODP) (available at www.iodp.org/science-plan-for-2013-2023):

1. To examine the mechanisms, timing, and sequences of Cenozoic seafloor spreading; to establish the complex opening history of different subbasins and styles of oceanic crustal accretion in the SCS; and to constrain the tectonic controls (such as spreading rate) on distinct magnetic contrasts among the subbasins;
2. To examine oceanic crustal accretion and mantle evolution and reveal the crustal nature and affinities of different subbasins in order to understand oceanic crustal and deep mantle processes associated with tectonic extrusion, magmatism, and magnetization;
3. To examine paleoceanographic and sedimentary responses to tectonic evolution of the SCS through development of a more complete 3-D sedimentation and subsidence model and linking it to regional climatic processes in response to various tectonic events; and
4. To examine driving forces leading to continental breakup and seafloor spreading and constrain whether the forces were far-field (triggered by the tectonic extrusion of the Indochina block), near-field (due to back-arc spreading or slab pull), or in situ (mantle plume and magmatism driven) in order to deepen our general understanding of the geodynamic interplay of mantle and lithosphere processes that led to the development of continental margin basins in the geological past and today.

Background

Geological setting

The SCS is a western Pacific marginal sea situated at the junction of the Eurasian, Pacific, and Indo-Australian plates. It developed from Cenozoic continental margin rifting, and its central portion is floored with oceanic crust. Despite its relatively small size and short evolutionary history, the SCS has undergone nearly a complete Wilson cycle from continental breakup to seafloor spreading to subduction and is well suited for studying various plate boundary activities, such as continental margin rifting

(e.g., Hayes and Nissen, 2005), seafloor subduction (the Manila Trench; e.g., Li et al., 2007a), strike-slip faulting (the Ailao Shan-Red River fault; e.g., Leloup et al., 2001; Clift and Sun, 2006), and active orogenic processes (Taiwan; e.g., Huang et al., 2001) (Fig. **F1**).

Hypotheses for the opening mechanism of the SCS differ markedly (Fig. **F3**) and include

1. India-Eurasia collision and the consequent tectonic extrusion mainly along the Ailao Shan-Red River fault (Fig. **F3A**) (Tapponnier et al., 1982; Lallemand and Jolivet, 1986; Schärer et al., 1990; Briaies et al., 1993; Flower et al., 2001; Leloup et al., 2001),
2. Slab pull and subduction of the proto-SCS under Sabah/Borneo (Fig. **F3B**) (Taylor and Hayes, 1980, 1983; Holloway, 1982; Hall, 2002),
3. Extension related to an upwelling mantle plume (Fig. **F3C**) (e.g., Fan and Menzies, 1992; Xu et al., 2012), and
4. Regional extension related to subduction and retreat of the Pacific plate along the western Pacific margin (Fig. **F3D**) (Taylor and Hayes, 1980, 1983; Shi and Li, 2012).

In addition to these end-member models, hybrid models have been proposed (e.g., Cullen et al., 2010).

The original SCS Basin before its subduction along the Manila Trench may have been twice the size that it is today (Sibuet et al., 2002), so geodynamic models must be able to explain the formation of this larger ocean basin. The Ailao Shan-Red River fault was active from 35 to 15 Ma, with displacement of as much as several hundred kilometers (e.g., Leloup et al., 2001; Gilley et al., 2003). Ages obtained from sites drilled during Expedition 349 will aid in testing the hypothesis that the motion on the Ailao Shan-Red River fault is coeval to and may have driven part of the extension and spreading in the SCS. Others suggested that only a minor amount of extension associated with the SCS spreading center may have been transferred to the Ailao Shan-Red River fault (Rangin et al., 1995; Morley, 2002; Clift et al., 2008). The initiation of regional rifting in East Asia during the Mesozoic occurred before the India-Eurasia collision (Fig. **F3D**) and is thought to be associated with subduction of the paleo-Pacific plate (Taylor and Hayes, 1980, 1983; Shi and Li, 2012).

Some hypotheses require the existence of a proto-SCS oceanic basin (Haile, 1973; Madon et al., 2000) that was once connected to the Pacific plate and began to close

around 44 Ma (e.g., Hall, 1996, 2002) in order to drive and accommodate the opening of the SCS (Fig. F3B). A large part of this proto-SCS may have been subducted into or uplifted as island arcs formed to the south in Borneo/Sabah and Palawan (Hall, 2002; Hutchinson, 1996, 2004), where remnants of the proto-SCS oceanic crust may be present (Hutchinson, 2005) and are one possible origin of the ophiolites of South Palawan (Rangin et al., 1990; Tu et al., 1992; Schlüter et al., 1996; Pubellier et al., 2004; Cullen, 2010). Slab-pull force from this subducting proto-SCS plate and a hypothesized in situ mantle plume may also have triggered or contributed to the opening of the SCS.

The opening of the SCS reveals complex patterns of continental breakup and seafloor spreading. Magnetic and seismic data suggest that the SCS Basin can be divided into five magnetically distinct zones (Li et al., 2008b) (Zones A–E in Fig. F4). In particular, magnetic amplitudes and orientations in the Southwest Subbasin (Zone E) differ markedly from those in the East Subbasin (Zone D). These two subbasins are divided by a complex set of transform faults forming the Zhongnan fault zone (Figs. F2, F4) (Yao, 1995; Jin et al., 2002; Li et al., 2007b, 2008b). This magnetic contrast may support an episodic seafloor-spreading model (Ru and Pigott, 1986) or may be attributed to the different tectonic contexts within which the two subbasins evolved. Pautot et al. (1986) suggested that the youngest part of the East Subbasin in Zone D developed within an older, preexisting oceanic crust, whereas the Southwest Subbasin in Zone E resulted from continental rifting. Within the East Subbasin, two distinct conjugate magnetic anomalies (M1 and M2 in Fig. F4) are thought to be the same age (anomaly 8 in Taylor and Hayes [1983] and Briais et al. [1993] models) and further divide the subbasin into a central part with high magnetic amplitudes and two separated parts with slightly weaker magnetization (Zones C1 and C1') near the two conjugate continental margins. The magnetic pattern of the Northwest Subbasin also differs from its adjacent segment in the East Subbasin.

Additional important contrasts exist between the East and Southwest Subbasins. For example, the greater average water depths of the Southwest Subbasin compared to the East Subbasin have been interpreted to imply relatively older crustal ages (Ru and Pigott, 1986; Yao et al., 1994; Li et al., 2008b), which conflict with younger ages inferred from the higher heat flow and shallower Curie-point depths of the Southwest Subbasin (Ru and Pigott, 1986; Li et al., 2010). Recent heating from magmatic activity could have contributed to the high heat flow in the Southwest Subbasin (Ru and Pigott, 1986; Li and Song, 2012), but this hypothesis needs to be tested through drilling.

A number of Cenozoic tectonic models have been proposed, but it remains uncertain as to whether the SCS Basin experienced a single episode or multiple episodes of extension and seafloor spreading and, if multiple episodes, in what sequence the subbasins evolved (e.g., Taylor and Hayes, 1980; Pautot et al., 1986; Ru and Pigott, 1986; Briais et al., 1993; Yao et al., 1994; Hayes and Nissen, 2005; Li et al., 2007b, 2008b). For example, the opening of the East and Northwest Subbasins may have predated or been synchronous with that of the Southwest Subbasin (Fig. F5A) (Taylor and Hayes, 1983; Briais et al., 1993; Lee and Lawver, 1995; Tongkul, 1994; Honza, 1995; Zhou et al., 1995; Schlüter et al., 1996; Hall, 2002; Hall and Morley, 2004; Hayes and Nissen, 2005; Braitenberg et al., 2006; Sun et al., 2009). This model contrasts with others in which an earlier opening of the Southwest Subbasin is preferred (Fig. F5B) (e.g., Ru and Pigott, 1986; Yao et al., 1994; Li et al., 2007b). This latter group of models considers the sharp contrasts between the East and Southwest Subbasins and the important role of the Zhongnan fault (Figs. F2, F4). There are also two models of slow propagation of the SCS spreading center, one with opening gradually propagating toward the northeast and the Taiwan Strait (Chung et al., 1994) and the other toward the Southwest Subbasin (Zhou et al., 1995).

Previous drilling

Five sites were drilled in the peripheral continental slope of the SCS during Ocean Drilling Program (ODP) Leg 184 (Feb–April 1999; Wang, Prell, Blum, et al., 2000). The major objectives of Leg 184 were to study the variability of East Asian monsoonal climates (including millennial- to possibly centennial-, orbital-, and tectonic-scale variability) from cored late Cenozoic hemipelagic sediment. All Leg 184 sites are located on the continental slope, and none penetrated into igneous basement rock. The deepest hole cored during the leg reached 861 meters below seafloor (mbsf) at Site 1148 in 3294 m of water (Figs. F2, F4), with the oldest sediment recovered of early Oligocene age. The records from both Leg 184 and Expedition 349 will be used to establish links between the East Asian and Indian monsoons and to evaluate mechanisms of internal (climate system feedbacks) and external (orbital and tectonic) climate forcing.

Seismic studies and site survey data

Figure F2 shows the sites drilled during Expedition 349 and available multichannel seismic (MCS) lines crossing those sites. Most drill sites are located at the intersection of two MCS lines; however, Sites U1434 and U1435 are not located on crossing points

but were interpreted to have only thin sedimentary cover above the igneous basement.

A dense 2-D MCS grid exists in the northern SCS continental margin and the northern part of the central SCS Basin. The Chinese National Offshore Oil Corporation (CNOOC) recently acquired most of these high-quality data. The northeastern part of the SCS has also been well studied and imaged with numerous geophysical surveys during Cruises SCSIO87, 973GMGS, ACT, TAICRUST, ORI645, and ORI689. More recent geophysical studies include the Taiwan Integrated Geodynamics Research (TAIGER) project (McIntosh et al., 2012) and surveys for gas hydrates.

Guangzhou Marine Geological Survey (GMGS) has undertaken extensive geophysical and geological mapping of a large portion of the central SCS Basin in recent years. As a result, MCS data and shallow sediment cores are regularly added to our existing site survey database. This mapping activity has already started producing 2-D seismic grids around our drill sites. Other MCS and magnetic data were collected near the drill sites by the R/Vs *Vema*, *Conrad*, and *Haiyang IV* (Taylor and Hayes, 1980, 1983; Yao et al., 1994; Hayes et al., 1995) (Fig. F2). Two stages of Sino-US cooperation in the early 1980s added more dense geophysical data coverage, which includes sonobuoy measurements, two-ship expanding spread profiles, and piston cores (Taylor and Hayes, 1983; Yao et al., 1994; Hayes et al., 1995). The German R/V *Sonne* carried out five cruises in 1987 (SO-49 and SO-50B), 1990 (SO-72A), 1994 (SO-95), and 2008 (SO-197) (Franke et al., 2011), and collected >10,000 km of MCS data and high-resolution echograms (Lüdmann and Wong, 1999; Lüdmann et al., 2001).

Swath bathymetry data are available for the entire SCS Basin from GMGS and the 2nd Institute of Oceanography of the State Oceanic Administration of China (Li et al., 2011). Magnetic anomalies covering all proposed drill sites were compiled by the Geological Survey of Japan and Coordinating Committee for Coastal and Offshore Geoscience Programs in East and Southeast Asia (CCOP) in 1996 (Ishihara and Kishimoto, 1996) (Fig. F4). This compilation offers remarkable coverage and accuracy and yields new insights into the dynamic opening process of the SCS (Li et al., 2008b, 2010; Li and Song, 2012).

A number of ocean bottom seismometer (OBS) studies have been carried out since 2000 (e.g., Yan et al., 2001; Zhang et al., 2013). The South China Sea Deep (SCSD) major research program of the National Science Foundation of China has funded coincident seismic refraction/reflection surveys, local active source 3-D OBS surveys, the

first regional passive source OBS survey, and the first deep-tow magnetic survey (Wang, 2012). Both deep-towed and surface-towed magnetic survey lines were designed to traverse the primary sites, allowing the establishment of the best possible magnetic anomaly model and calibrated age model of the ocean crust of the entire basin. The supporting site survey data for Expedition 349 are archived at the [Integrated Ocean Drilling Program Site Survey Data Bank](#).

Scientific objectives

Expedition 349 focuses on coring into igneous basement at multiple sites in the SCS Basin to better understand seafloor spreading, ocean crust accretion, and mantle evolution. In addition, coring the sedimentary sections above basement will allow examination of the sedimentary and paleoceanographic responses to basin opening and eventual subduction along the Manila Trench.

- 1. Date the timing of the opening of different subbasins of the SCS and correlate the ages from magnetic anomalies to biostratigraphic, magnetostratigraphic, and radiometric ages.*

Magnetostratigraphy, biostratigraphy, and radiometric dating are the three principal techniques that will be used for chronostratigraphic analysis of the recovered sequences. Age control in the sedimentary section will be made from routine microfossil analyses, paleomagnetism, and isotope analysis. The age sequences can also be constrained by correlating seismic reflections to different drill sites. Because drilling at all expedition sites intends to recover the oldest sediment deposited directly on the top of oceanic basement, paleontological analyses will provide a minimum age constraint for the basement. Except for the upper ~900 m at Site U1432 in the primary operations plan, we plan to core all intervals within the three primary sites, with micropaleontological analyses conducted on all core catcher material and additional samples from split-core sections to refine the biostratigraphy, as time permits. Calcareous microfossils, including nannofossils and foraminifers, should be abundant in the carbonate successions at all sites. Within some intervals, particularly in the Neogene, we expect to find well-preserved and abundant siliceous microfossils (biogenic silica dominated by diatoms and radiolarians) that can provide additional biostratigraphic control.

Basement volcanic rock will be dated with $^{40}\text{Ar}/^{39}\text{Ar}$ (Koppers et al., 2011) and possibly other high-resolution zircon dating techniques with uranium-series isotopes (Goldstein et al., 1991, 1994; Goldstein, 1995; Schwartz et al., 2005). Ocean crust rock

typically is very low in K concentrations and therefore more vulnerable to disturbances by submarine alteration. To ensure high-quality $^{40}\text{Ar}/^{39}\text{Ar}$ dating on basement samples collected in the SCS, we will (1) carefully select fresh highly crystalline groundmass and plagioclase phenocrysts, which are the most suitable for $^{40}\text{Ar}/^{39}\text{Ar}$ dating and (2) apply extended acid leaching procedures to remove altered portions of the groundmass or mineral separates (Koppers et al., 2011).

The half-spreading rates of the SCS are slow to intermediate, between 20 and 40 mm/y (Briais et al., 1993; Song and Li, 2012). Near the continent/ocean boundary, where Sites U1432 and U1435 are located, hyperextended crust exhuming possible lower crust and upper mantle could exist (Franke et al., 2011). If so, gabbro with late-stage minerals or felsic lithologies could be available for uranium-lead zircon dating using sensitive high-resolution ion microprobe reverse geometry (SHRIMP-RG), as well as for $^{40}\text{Ar}/^{39}\text{Ar}$ dating of plagioclase, biotite, and/or hornblende mineral separates. A newly developed method that detects tiny amounts of uranium-bearing minerals, such as zircon, in rocks could reliably date the age of ocean crust (Schwartz et al., 2005; Grimes et al., 2007).

2. Measure the magnetization, mineralization, and geochemical compositions of basement rocks to understand the causes of the sharp magnetic contrast between different subbasins.

Magnetic susceptibilities of extrusive basalt normally decrease with increasing degree of alteration, which reduces their titanomagnetite content (e.g., Bleil and Petersen, 1983). Serpentinization of peridotite at deeper depths is also known to smear surface magnetic anomalies (e.g., Dymant et al., 1997). Detailed mineralogical studies are essential to understand these processes that may cause the magnetic contrast between the East and the Southwest Subbasins. Because of the complex patterns of magnetic anomalies in the SCS, careful measurements of magnetic susceptibility are needed to constrain models of, for example, tectonic settings or spreading rates (Dymant and Arkani-Hamed, 1995) that can explain the distinct differences in magnetic patterns between different subbasins, as well as their crustal affinities. Magnetization measurements from cores are also vital for creation of an initial model for predicting magnetic anomaly strength, in order to better understand the observed magnetic anomalies.

3. Evaluate the origin and source evolution of SCS basement rock to understand the formation of SCS oceanic crust and the deep mantle processes driving crustal formation.

Trace element chemical analyses and measurement of Sr, Nd, and Pb isotopic ratios will provide insights into the material influx and deep crustal and mantle processes

(Castillo et al., 1991; Tejada et al., 2004). The opening mechanism of the SCS can be constrained by investigating the variation in these geochemical tracers in the igneous basement rock. The basaltic rock cored during this expedition could have three potential mantle sources: (1) Indian Ocean/Eurasian lithospheric mantle, (2) Pacific mantle, or (3) a putative mantle plume.

All of these sources have distinctive geochemical characteristics in their incompatible trace element and long-lived radiogenic isotope ratios, which are not affected by variations in degree of partial melting of the mantle and fractional crystallization of the resultant melt. Therefore, based on the Expedition 349 drilling transect, we should be able to test several geochemical evolution scenarios corresponding to the rifting and spreading models of the SCS, including (1) continental rifting leading to seafloor spreading (due to Indochina extrusion tectonism or slab pull with southward subduction under Borneo), (2) subduction-induced back-arc spreading, and (3) plume-initiated rifting.

4. Evaluate the paleoceanographic and climatic responses to the opening of the SCS and develop a 3-D sedimentation and subsidence model.

Because our drill sites are located in different parts of the SCS, we can build a detailed 3-D postspreading model of seismic stratigraphy that will offer invaluable insights into deepwater sedimentary processes and how they evolved through time. This sedimentary model will be coupled with paleoenvironmental and paleoceanographic data from analyses of sediment cores to detect major geological events. Information on sedimentation rates, provenance, water depths, tectonic subsidence, and facies changes will be determined and will be correlated to known tectonic and climatic events. By core-log-seismic integration, we can build detailed 3-D sedimentation models. Major unconformities and boundaries found in the different subbasins will be correlated with those in the continental slopes and rifting basins to trace the dynamic transitional process from rifting to spreading, and also constrain critical paleoceanographic and tectonic changes during opening of the SCS.

Mineralogical and geochemical analyses will help identify sediment provenance in the SCS and how it has evolved through time. Analyses of detrital zircon in the sediment, for example, can (1) determine the maximum age of stratigraphic successions and lead to a better understanding of the source-to-sink processes, (2) determine provenance characteristics such as age and composition, (3) test regional paleogeographic models via provenance analysis, and (4) unravel facets of geological history locked in the mineral chemistry of detrital zircon (Fedo et al., 2003).

Structural analyses of core samples will focus on deformation features such as fractures, faults, veins, deformation bands, etc. Postcruise statistical analyses on these structural features will help reveal the regional stress field and its changes through time. Together with geophysical downhole logging and other data, the structural features recorded in cores could reveal regional SCS magmatic and tectonic events, as well as local rock deformation and stress heterogeneities.

5. Obtain downhole geophysical logs to reveal physical properties of the sediments and the top oceanic basement and to provide a record of unrecovered intervals.

Our proposed deployment of a minimum of two wireline logging tool strings (the standard triple combination [triple combo] and the Formation MicroScanner [FMS]-sonic) will measure a wide spectrum of geophysical properties and will provide structural, mineralogical, and geochemical information of the penetrated sequences. These data will be particularly important for unrecovered intervals that typically occur when using the extended core barrel (XCB) and rotary core barrel (RCB).

The triple combo tool string records geophysical signals of the penetrated sediment and basement rock by measuring the total and spectral natural gamma radiation (NGR), density, porosity, and resistivity of the formation. Gamma ray data will be used to infer lithology and provenance. Porosity, sonic, and density logs will be critical for decompaction and backstripping analyses and for constraining tectonic subsidence. The subsidence and rifting parameters so obtained can offer new insights on the episodic opening history of the SCS and reveal mantle properties.

Wireline logs will provide a continuous record to aid in the detection of lava flow boundaries, interlayered sediment, and alteration zones in the basement to evaluate the dip of lava flows. The number of lava flow units penetrated has implications for how well geomagnetic secular variation has been sampled and hence the extent to which paleolatitudes can be most precisely constrained.

With FMS-sonic logging, we will obtain high-resolution quasi-2-D images (electrofacies) of the borehole wall to reveal the structure and orientation of the rock. These data will provide constraints on volcanostratigraphy and crustal accretion processes (e.g., Tominaga et al., 2009). The high-resolution FMS images will help to detect small-scale fractures and lithologic variations, evaluate the dips of lava flows, and reorient core pieces. The General Purpose Inclinator Tool, which includes both a three-axis inclinometer and a three-axis magnetometer, will be used to measure changes in magnetic properties of lithologies and in paleomagnetic direction.

Drilling and coring strategy

Our proposed operations plan for this expedition consisted of drilling three sites into basement (proposed Sites SCS-3G [U1431], SCS-6A [U1432], and SCS-4B [U1433]). Because of the predicted depth to basement at these sites (865–1830 mbsf) and to maximize our operational time, we requested and received approval from the Environmental Protection and Safety Panel and the Texas A&M Safety Panel to drill down through the uppermost ~900 m at the second site (U1432), provided that we encountered nothing unexpected at the first site (U1431), which was tied seismically to the second one. Even with this drill-down approval, it was unlikely that we would have sufficient time in the schedule to reach basement at all three of our primary sites unless operations proceeded better than predicted in the operations plan. With these issues in mind, we identified 10 alternate sites in the vicinity of our primary sites that required shallower penetration depths to reach basement. Three additional alternate sites in other locations targeted secondary objectives that could be addressed if for any reason we were unable to drill in the vicinity of one of our primary sites (Li et al., 2013).

Alternate sites with shallower penetration depths to basement were also important because coring at deeper depths is challenging. Hole stability is always a risk during coring and logging operations, and the longer the open-hole section, the higher the risk. Hole cleaning is also more difficult in deeper sections, particularly when coring dense basement material. We planned a reentry system to 900 mbsf for the deepest site (U1432; predicted total depth of 1930 mbsf) to help mitigate these issues. Given the relatively shallower total depths planned at the other two primary sites (U1431 and U1433), we felt that we could achieve the objectives without the aid of a reentry system. The reentry system at the deep site would serve two main purposes. First it would stabilize the upper portion of the hole, where unconsolidated sediment is more likely to cause hole stability problems. It also would provide a smaller annulus for hole cleaning, which increases annular velocity without having to significantly increase pump rates to remove dense basement cuttings from the hole. Higher flow rates generally result in washed-out sections in parts of the hole and can lead to stability issues. For the other primary sites, we planned to deploy a free-fall funnel to decrease the amount of time required to reach the basement objective.

This strategy of having multiple alternate sites approved for drilling prior to the start of the expedition proved to be valuable during this expedition. While installing the reentry system in Hole U1432B, we discovered that two of the three fiber optic cables

within the subsea camera wireline had failed. During a subsequent deployment, the camera system failed and we initially suspected that the final fiber optic cable had broken. Fortunately, the failure was related to the pan and tilt unit of the camera, so that after the problematic unit was removed the system worked again. This failure prompted discussions of alternate plans to meet the expedition objectives without the ability to perform reentries. During cementing of the final (10³/₄ inch) casing string in Hole U1432B, the pipe became stuck in the cement and ultimately forced us to abandon the hole. There was not enough time left in the expedition schedule to try another approach to reach the basement objective at that site; however, we were able to use the remaining time to reach basement at our primary site in the Southwest Subbasin (Site U1433). Additionally we were able to core at two alternate sites, proposed Sites SCS-4E (U1434) and SCS-6C (U1435). The latter site was thought to be a basement high very near the continent/ocean boundary (Fig. F6) with very thin (~10 m) sediment cover, whereas Site U1434 formed a short sampling transect with Site U1433, with Site U1434 located closer to the relict spreading center and also adjacent to a large seamount (Fig. F7).

Site summaries

Site U1431

Background and objectives

Site U1431 (proposed Site SCS-3G) is located near the relict spreading ridge where the youngest crustal magnetic anomalies are observed in the East Subbasin of the SCS (Figs. F4, F8). A positive magnetic anomaly that runs through this site allows regional correlation of crustal ages. This site is also surrounded by abyssal highs in the ocean crust, as well as younger seamounts (Figs. F6, F8B) whose volcanic and/or redepositional events may be recorded by sediments recovered from this site.

The primary objective at Site U1431 was to core into the oceanic basement to determine the age at which seafloor spreading ceased in the East Subbasin. The ~900 m thick package of sediment overlying basement also provides important constraints on the evolution of the ridge and associated late-stage magmatism, deep-marine sedimentary processes, and the paleoceanographic history following the termination of spreading in the SCS. Additionally, coring at this site will allow correlation of biostratigraphic, magnetostratigraphic, and radiometric ages to the observed crustal magnetic anomalies. Physical property and paleomagnetism measurements of base-

ment rock will help to elucidate the cause of the distinct contrasts in the nature of oceanic crust magnetic anomalies of the East and Southwest Subbasins. Furthermore, this site will provide constraints on mantle source, melting, and magmatic processes in the latest stages of basin formation. Physical property measurements of core samples and wireline logging measurements will provide stratigraphic information for correlation with regional seismic profiles. Microbiological sampling will explore the deep biosphere in the SCS to examine how sharp changes in lithology (interfaces) may affect subsurface community structure and function, as well as how posteruption processes might have influenced past ecosystems in the SCS.

Operations

After a 463 nmi transit from Hong Kong averaging 11.0 kt, the vessel stabilized over Site U1431 at 0640 h (UTC + 8 h) on 31 January 2014. We cored five holes at Site U1431 (Table T1). The original operations plan called for one hole to a depth of ~1061 mbsf, which included ~100 m of basement. The plan was modified during transit to include two additional short holes for high-resolution sampling of the upper ~20 m of section. Hole U1431A was successfully cored to 28.4 mbsf and Hole U1431B to 17.0 mbsf. After the first core from Hole U1431C retrieved a split core liner and no mudline, we opted to abandon the hole, which was completed to a depth of 14.2 mbsf, and spudded Hole U1431D. Hole U1431D was cored to 617.0 mbsf when the XCB failed, leaving the cutting shoe, core catcher sub assembly, and breakoff sub in the hole. We abandoned Hole U1431D and switched to the RCB to spud Hole U1431E, which was drilled to 507.0 mbsf, spot cored, and then cored continuously from 575.0 mbsf to total depth at 1008.8 mbsf in igneous basement. After conditioning the hole for logging, two logging runs were performed. The triple combo tool string was run to 463.0 m wireline depth below seafloor (WSF), and the FMS-sonic tool string was run to 444 m WSF with two passes. Total time spent at Site U1431 was 385.7 h (16.1 days).

A total of 122 cores were collected at this site. The advanced piston corer (APC) was deployed 26 times, recovering 225.61 m of core over 228.50 m of penetration (98.7% recovery). The XCB was deployed 48 times, recovering 236.50 m of core over 448.10 m (52.8% recovery). The RCB was deployed 48 times, recovering 243.00 m of core over 443.5 m of penetration (54.8% recovery).

Principal results

The cored section at Site U1431 is divided into 11 lithostratigraphic units, 9 sedimentary and 2 igneous, based mainly on a combination of data from Holes U1431D and U1431E (Fig. F9). Lithostratigraphic Unit I is a 101.16 m thick Pleistocene sequence of dark greenish gray clay and silty clay. Graded silt intervals are abundant and interpreted as turbidites. Discrete volcanic ash layers that are either mafic or felsic in composition and 0.5–5 cm thick occur throughout the unit. This unit is underlain by Unit II (Pliocene–Pleistocene age), which is divided into Subunits IIA (101.16–194.95 mbsf) and IIB (194.95–267.82 mbsf). The 166.66 m of Unit II is dominated by dark greenish gray clay with fewer volcanic tephra layers than Unit I. Subunit IIA is characterized by the presence of clay with nannofossils and calcareous turbidites, which are not found in Subunit IIB. Rare, thin silt turbidites are largely limited to Subunit IIB. Unit III (267.82–326.12 mbsf) is a 58.30 m thick upper Miocene to Pliocene sequence of dark greenish gray clay with modest amounts of interbedded calcareous turbidites. These graded turbidites typically have sandy foraminifer-rich intervals at the base and are interpreted to represent mass wasting events from neighboring seamounts. Unit IV (326.12–412.42 mbsf) is an upper Miocene unit comprising 86.30 m of dark greenish gray clay and silty clay with minor amounts of silt and fine sand interbeds interpreted as turbidites. This unit is much reduced in carbonate content compared to overlying Unit III. Unit V (412.42–603.42 mbsf) is a 191 m thick sequence of upper Miocene dark greenish gray silty sand and interbedded clay with nannofossil ooze. Recovery is low throughout the section, but sandy core catcher samples suggest that many of the unrecovered intervals may consist of sand.

Unit VI (603.42–797.30 mbsf) is readily distinguished from the overlying units by the abundance of greenish black volcanoclastic breccia and sandstone interbedded with minor amounts of claystone. This unit is 193.88 m thick and dated to the late Miocene. The clasts in this breccia are primarily composed of highly vesicular aphanitic basalt and scoria, nonvesicular to sparsely vesicular basalt, basaltic glass shards, and lesser amounts of pumice and mudstone. Major element data indicate that these clasts are characteristic of ocean island basalt (OIB). The breccia beds are typically massive and have erosive bases, indicative of deposition by mass wasting either as debris or grain flows. Based on the composition of the clasts and abundant magmatic mineral fragments, these deposits are likely sourced from the nearby seamounts. Unit VII (797.30–885.25 mbsf), 87.95 m thick and middle to late Miocene in age, is composed of interbedded dark greenish gray sandstone with lesser amounts of siltstone and claystone in a turbidite sequence. It is essentially a less coarse grained equivalent

to Unit VI and coarsens uphole through the unit. Unit VIII (885.25–889.88 mbsf) is a 4.63 m thick middle Miocene sequence of massive, dark olive-brown claystone that directly overlies the basalt of Unit IX (889.88–962.51 mbsf). The mudstone represents deep-marine sedimentation. Unit X (962.51–972.00 mbsf) is a 9.49 m thick sequence of lower Miocene yellowish brown claystone and claystone breccia that lies within the volcanic sequence. This unit is underlain by the basalt of Unit XI (972.00–1007.89 mbsf).

Calcareous nannofossils, planktonic foraminifers, and radiolarians recovered at Site U1431 are typical of low-latitude assemblages, characterized by species widely found in the tropical western Pacific region. Calcareous nannofossils are generally poorly preserved and frequent or common in Units I–IV but rare or absent downhole. Planktonic foraminifers are also poorly preserved and vary from frequent to rare in Units I–IV but are absent more frequently in samples from deeper units. Radiolarians are common and well preserved in samples from the uppermost 30 m, absent from 30 to 870 mbsf, and present but poorly preserved in Units VIII and X.

The biostratigraphy of Site U1431 is based on analysis of calcareous nannofossil, planktonic foraminifer, and radiolarian assemblages in all core catcher samples and additional samples from within cores from Holes U1431D and U1431E. The sedimentary succession recovered at Site U1431 spans the lower Miocene through Pleistocene (Fig. F10). Sediment from Units I–VIII is assigned to middle Miocene to Pleistocene calcareous nannofossil Zones NN6–NN21 and planktonic foraminifer Zones M9–Pt1, with no obvious hiatuses. The Pliocene/Pleistocene boundary is located between Cores 349-U1431D-15H and 18H, and the Miocene/Pliocene boundary is located between Cores 31X and 33X. Biostratigraphic control for the upper Miocene section is hampered by a paucity of nannofossils and planktonic foraminifers and poor core recovery in Units IV and V, which are dominated by turbidites. Nevertheless, the middle/late Miocene boundary is placed between Cores 349-U1431E-27R and 33R. In situ calcareous microfossils are absent from the claystones of Unit X; however, radiolarian biostratigraphy indicates that the rock is early Miocene in age (~16.7–17.5 Ma), corresponding to radiolarian Zone RN4. Sedimentation rates varied from ~8 cm/k.y. in the middle to early late Miocene, ~14 cm/k.y. for the remainder of the late Miocene, to ~5 cm/k.y. in the Pliocene–Pleistocene. Extremely low sedimentation rates (<2 cm/k.y.) occurred in the early to earliest middle Miocene during deposition of the claystones of Units VIII and X (Fig. F10).

The basalt of Unit IX was encountered at ~890 mbsf in Hole U1431E. Coring continued to ~1008 mbsf, recovering basement basalt separated by an interflow claystone between 3.7 and 9.5 m thick at 962.3 mbsf. In total, 46.2 m of basalt was recovered over a cored interval of 108.4 m, yielding an average recovery of 42.6%. The basalt is divided into 13 igneous lithologic units (Fig. F11) and is mainly composed of massive lava flows (six in Unit IX and two in Unit XI) as thick as ~26.7 m, with limited evidence for pillow basalt flows in between. Because no contacts between flow units were recovered, boundary locations and unit thickness estimates are approximate. The interpretation of igneous lithologic Units 1, 7–10, and 12 as pillow basalts is uncertain and is based on scarce evidence, such as the presence of glassy (curved) chilled margins, ropy flow structure, and a single occurrence of a hyaloclastite breccia.

Most basalt at Site U1431 is aphyric and ranges in grain size from microcrystalline to fine grained, with the groundmass grain size getting coarser (0.7–1 mm) in the cores of the thickest massive lava flows. All basalt has a phase assemblage of plagioclase and clinopyroxene (\pm olivine) in its groundmass, with 0.1–0.5 mm subhedral-euhedral olivine microphenocrysts present in some igneous lithologic units, resembling a typical mid-ocean-ridge basalt (MORB) crystallization history and, in conjunction with geochemical evidence, indicates that basalt recovered at Site U1431 is representative of typical MORB.

The alteration style of basalt at Site U1431 is typical of MORB. Alteration color is dominated by gray to dark gray-green and yellow to red-brown. Typical secondary minerals include saponite, Fe oxides, carbonate, and celadonite, which represent alteration assemblages at low temperature. Alteration intensity varies from slight to complete, but the majority of the recovered basement rock is moderately altered. There is no systematic change in the alteration nature (e.g., alteration color) with depth that might indicate a transition from more oxidizing to reducing conditions. The strongest alteration occurs in halos flanking veins, which overprints the background pervasive alteration, indicating that the overall distribution of alteration was controlled by fractures and vein structures. Most lithologic basement units include intervals with slight alteration, preserving remarkably fresh olivine crystals that show only limited alteration along their rims and “maschen” fractures.

Fractures and veins occur throughout the basalt in Hole U1431E. These features are randomly oriented, with no obvious offset or thickness variation. A fracture with ~1 cm of normal offset occurs in the interflow claystone of Unit X. The basalt fractures likely formed during cooling of the lava, whereas the fractures in the interflow clay-

stone may suggest slight movement as the lava of Unit IX flowed over it. The major veins are white or reddish brown and filled with carbonate and iron oxides. Arched veins generally occur in sets, often in combination with linear veins, forming a vein network consistent with fractures formed during cooling.

Geochemistry measurements at Site U1431 aimed to characterize the interstitial water chemistry, total organic carbon (TOC), bulk carbonate content, and igneous basement rock. The depth profiles of major elements and nutrients indicate that organic matter diagenesis, biogenic carbonate dissolution and recrystallization, and volcanic ash alteration occurred in the sediment. The interstitial water never reaches complete sulfate reduction in Hole U1431D, with minimum concentrations of ~2.3 mM occurring from ~170 to 260 mbsf. This is consistent with the very low methane concentrations, which range from 1.6 to 4.8 ppmv. Sulfate concentrations gradually increase below 260 mbsf, reaching 24.0 mM at the bottom of Hole U1431D (~600 mbsf). Shore-based isotopic analysis of these interstitial water samples should constrain the source of the sulfate-bearing fluid in Hole U1431D.

Bulk carbonate content varies with depth, ranging from 0 to 47 wt% in Hole U1431D and from 0 to 57 wt% in Hole U1431E. The discrete intervals with higher carbonate content in Hole U1431D correspond to nannofossil ooze beds, whereas in Hole U1431E higher carbonate content is associated with diagenetic carbonate concretions visible in the cores. TOC varies from 0 to 4.7 wt% in Hole U1431D, whereas in Hole U1431E, TOC is lower and ranges from 0 to 0.74 wt%. The TOC to total nitrogen (C/N) ratio is generally <4 at Site U1431, indicating that TOC is derived from a marine source; however, C/N ratios range from 8 to 12 in some intervals of lithostratigraphic Units III and IV in Hole U1431D, which could indicate a mixture of marine and terrestrial organic matter sources.

Major and minor element concentrations measured by inductively coupled plasma-atomic emission spectroscopy (ICP-AES) on Hole U1431D sediment indicate that it is most likely derived from an intermediate igneous source. The basalt recovered from below ~890 mbsf in Hole U1431E has moderately high loss on ignition (LOI) values (0.46–2.85 wt%), but low K₂O (≤0.53 wt%) and TiO₂ (1.01–1.77 wt%). The basalt samples of Unit IX contain higher MgO, FeO, and Ni concentrations than those of Unit XI, likely because of olivine accumulation. The basalt major element composition is similar to that of mid-ocean-ridge tholeiite, whereas clasts from the volcanoclastic breccia are alkali basalt with high K₂O (1.08–2.67 wt%) and TiO₂ (2.10–3.13 wt%), probably sourced from the nearby seamounts (Figs. [F12](#), [F13](#)).

A total of 105 whole-round samples (5–10 cm long) were collected for microbiological studies from Site U1431. These samples were typically taken adjacent to interstitial water whole-round samples for comparison to interstitial water chemistry when possible. These samples will be analyzed for microbial content based on DNA and lipid properties of the cells present. Subsamples were prepared for fluorescent in situ hybridization and single cell genomics. DNA and lipid samples were preserved at -80°C , whereas fluorescent in situ hybridization samples were preserved at -20°C . Four basalt whole-round samples were selected for cultivation-based studies, with sampled material inoculated into a seawater-based medium containing olivine as a source of energy. An additional 76 samples were collected and prepared for investigation of the microbiology of interfaces using lipid and nucleic acid analyses. These samples were collected mostly in the upper 200 m of Hole U1431D from specific interfaces, including five ash/clay interfaces and ten turbidite/clay interfaces. Selection of these samples was dependent upon recognition of key intervals by the core description team and occurred through consultation between the microbiologists and sedimentologists or petrologists.

Microbiology contamination testing at Site U1431 included the use of perfluorocarbon tracers (PFTs), fluorescent microspheres, and fluid community tracers (FCTs). PFTs were added to the drilling fluid for all APC coring in Holes U1431B–U1431D, as well as for the first four XCB cores in Hole U1431D. Twelve samples were taken from six sediment cores collected over this interval to measure contamination with the PFTs. Microspheres were added to the core catcher before the core barrel was deployed in Hole U1431E over the interval from 651.8 to 952.6 mbsf. Two microsphere samples were collected from each core, one from scraping of the core surface and one as a subsample from the interior of each whole-round sample. In addition, FCT samples were collected from the drilling fluids on a daily basis (for a total of 14) to track the microbial communities typical of seawater and other drilling mud constituents. Microbial community DNA and lipids from these fluids will be compared to those measurements made on the core samples to determine if there are microbes that can be recognized as contaminant taxa.

Variations in the natural remanent magnetization (NRM) intensity at Site U1431 are generally correlated with lithology. Paleomagnetic measurements indicate that the silty clay and clayey silt in Unit I (0–101.16 mbsf) have a mean NRM intensity on the order of 3×10^{-2} A/m, whereas the clay with nannofossils in Unit II (101.16–267.82 mbsf) has somewhat higher NRM intensity ($\sim 6 \times 10^{-2}$ A/m). Many discrete peaks of higher NRM values that appear in some depth intervals in both Units I and II can be

tied directly to the presence of volcanic ash layers. Magnetic susceptibility data also show positive peaks at these intervals. Overall, magnetic susceptibility and NRM intensity variations through the sedimentary units are closely correlated.

Magnetostratigraphic records at Site U1431 indicate the presence of several relatively well defined polarity intervals in the cores. Based on inclination and declination data, the Brunhes/Matuyama Chron boundary (0.781 Ma) is placed at ~46 mbsf in Hole U1431D (Fig. F10). The Matuyama Chron is defined between ~46 and ~135 mbsf. Below ~170 mbsf, the XCB cores are strongly overprinted by a drilling-induced remagnetization that cannot be removed by shipboard thermal demagnetization. The magnetic record improved in the RCB cores of Hole U1431E, allowing tentative correlation of certain parts of the magnetic polarity interval with the geomagnetic polarity timescale in conjunction with biostratigraphic constraints. In particular, the polarity shift from normal to reversed at ~716 mbsf may correspond to the Chron C5n/C5r boundary (11.056 Ma) (Fig. F10).

For basement rock units, the observed paleomagnetic signals cannot be directly linked to the geomagnetic polarity timescale yet because the basalts in lithostratigraphic Units IX and XI were erupted intermittently, and the pelagic clay sediment in lithostratigraphic Units VIII and X may represent a significant time interval. Nevertheless, reliable normal and reversed polarities occur within this interval, which indicates that the eruption of the basalt units may have spanned a significant amount of time on the order of a few thousand to one million years.

Whole-round cores from Holes U1431A–U1431C were measured for *P*-wave velocity, bulk density, magnetic susceptibility, and NGR. For Holes U1431D and U1431E, measurements were also made on whole-round cores, with additional measurements on split cores and discrete samples, including thermal conductivity, porosity, and bulk, dry, and grain densities. In general, the physical properties correlate with lithology, composition, and induration. In Hole U1431D, bulk density, *P*-wave velocity, shear strength, NGR, and thermal conductivity increase gradually with depth over the uppermost 150 mbsf (Fig. F9), whereas porosity measured on discrete samples decreases from 84% to 50% over the same depth range. This indicates that sediment compaction dominates the physical property variations above 150 mbsf. Volcanic ash layers in Unit I (e.g., at 25 and 100 mbsf) show relatively high magnetic susceptibility (300–500 SI) values. Below 150 mbsf, a decrease in shear strength may be associated with higher clay content. NGR counts are relatively high from the seafloor to 500 mbsf, which is consistent with the dominance of clay and silt in Units I–V.

Most physical properties show a significant change at ~550–600 mbsf, near the boundary between Units V and VI (Fig. F9). *P*-wave velocity and porosity increase, whereas NGR values and thermal conductivity are relatively low, a pattern consistent with the dominance of volcanoclastic breccia and sandstone in Unit VI. Layers with higher NGR counts and high magnetic susceptibility values occur at ~660 and ~710 mbsf. These do not correlate with the breccia but correspond to a silt- and/or sandstone probably enriched in magnetic minerals such as magnetite. The basalt units below 889.88 mbsf (Units IX and XI) display the lowest NGR, highest magnetic susceptibility, and largest bulk density values (Fig. F9). The interflow clay (Unit X) between the two basaltic units shows NGR values ~20 times larger than those of the basalt, as well as much lower magnetic susceptibility. Lower magnetic susceptibility and NGR values at the top of the basalt are consistent with higher but still moderate alteration in these basement units.

Two downhole logging tool strings were run in Hole U1431E, the triple combo (NGR, porosity, density, electrical resistivity, and magnetic susceptibility) and the FMS-sonic (NGR, sonic velocity, and electrical resistivity images) tool strings (Fig. F9). The triple combo tool string reached 464 m WSF before a bridge prevented access to the lower part of the borehole. The hole was wider than 17 inches below ~300 m WSF and showed closely spaced variations in borehole width above that depth. These were not ideal conditions for borehole log quality; however, stratigraphic changes are apparent in the NGR and magnetic susceptibility logs. The FMS-sonic tool string reached 444 m WSF, with two passes made above that depth. Downhole temperature measurements of the borehole fluid are consistent with the low geothermal gradient (~15°C/km) established from the advanced piston corer temperature tool (APCT-3) measurements taken on Cores 349-U1431D-4H, 7H, 10H, and 13H (Fig. F14).

Site U1432

Background and objectives

Site U1432 (proposed Site SCS-6A) is located ~60 km south of ODP Site 1148 (Wang, Prell, Blum, et al., 2000; Li et al., 2006; Wang and Li, 2009), just south of the northern continent/ocean boundary on the Chinese continental margin (Figs. F6, F8). This part of the basin shows the deepest basement and is likely the oldest among the sub-basins based on magnetic anomalies (Taylor and Hayes, 1980, 1983; Pautot et al., 1986; Briais et al., 1993) (Fig. F4). This site was designed to recover the oldest oceanic crust and the oldest sedimentary rock in the East Subbasin to test the hypothesis that

the onset of seafloor spreading in the SCS occurred here first at ~32 Ma. Magnetic anomaly 11, the oldest anomaly interpreted by Taylor and Hayes (1980) and Briais et al. (1993), passes near this site and hence would allow key calibration between ages estimated from magnetic anomalies and those from biostratigraphy, radiometric dating, and magnetostratigraphy.

The true nature of the continent–ocean transition and oceanic basement at this site is still speculative; there could be volcanic extrusions associated with early continental breakup and the onset of seafloor spreading, exhumed lower crustal materials from preferential lower crust extension, exhumed mantle materials, or even Mesozoic rock. Coring at this site was intended to help pinpoint the exact location and tectonic nature of the continent–ocean transition and address key problems in the early tectonic transition from rifting to drifting and associated paleoenvironmental changes, including

1. The age of basement (presumably the oldest oceanic crust) near the continent/ocean boundary;
2. Petrology and geochemistry of basement rock and their bearing on continental breakup, incipient seafloor spreading, and mantle evolution;
3. Physical properties of basement rock and their implications for interpreting sharp magnetic contrasts between different subbasins; and
4. Sedimentary, paleoceanographic, and ecosystem responses to the opening of the SCS.

As a result of operational challenges (see [“Operations”](#)), the objectives of sampling basement and basal sediment at Site U1432 were not achieved.

Operations

After a 181 nmi transit from Site U1431 averaging 11.0 kt, the vessel stabilized over Site U1432 at 2337 h (UTC + 8 h) on 16 February 2014. Site U1432 consisted of three holes (Table [T1](#)). The first hole was a planned jet-in test to determine the correct casing depth for the 20 inch casing string. The second hole was to consist of a reentry system with three strings of casing to ~900 mbsf, followed by coring to ~1930 mbsf. Because of poor weather conditions, an additional hole was piston cored while waiting on suitable weather to continue the reentry installation.

Hole U1432A was successfully jetted to 62.0 mbsf. A reentry system was then successfully installed to 787.1 mbsf in Hole U1432B. The final cement job on the last casing

string compromised the reentry system when the drill string became stuck in the cement. The drill string had to be severed, forcing us to abandon Hole U1432B. Hole U1432C was successfully cored to 110.0 mbsf with the APC. Four downhole temperature measurements were taken in Hole U1432C with the APCT-3. A total of 12 APC cores were collected at this site, recovering 88.74 m of core over 110.0 m of penetration (81% recovery). The total time spent on Site U1432 was 492 h (17.9 days).

Principal results

Hole U1432C consists of 12 cores (Cores 349-U1432C-1H through 12H) that penetrated to 110.0 mbsf. The lithology is dominated by a sequence of dark greenish gray clay and clay with silt, assigned to lithostratigraphic Unit I (Fig. F15). Clay layers are interbedded with very thin bedded (centimeter scale) or laminated silty layers. These layers mostly fine upward and have sharp erosive bases. These graded sequences are generally 10–20 cm thick and are interpreted as distal turbidites. A 2.4 m thick unconsolidated sand layer occurs in the middle of the drilled section. The sand and silt layers represent <5% of the total recovered core and can usually be identified using magnetic susceptibility measurements, as they typically exhibit lower values than the clays. Thin volcanic ash layers (0.5–2.0 cm thick) occur occasionally in some cores.

The age of the sedimentary sequence recovered in Hole U1432C is <0.91 Ma (Middle–Late Pleistocene) based on planktonic foraminifer and calcareous nannofossil biostratigraphy (Fig. F16). Radiolarians are abundant and moderately to poorly preserved in the upper 15 m of the hole but become progressively rarer and more poorly preserved downhole and comprise a Pleistocene–Holocene assemblage. Nannofossil preservation is moderate to good throughout the hole, with considerable reworking of Pliocene and Miocene species above ~50 mbsf. Preservation of planktonic foraminifers is also moderate to good, with evidence of moderate dissolution, as indicated by frequent fragmentation. Planktonic foraminifers are more dominant in sandy intervals that also contain reworked Pliocene species and shallow-water benthic foraminifers.

A total of 16 whole-round samples (5 cm in length) were taken for interstitial water measurements in Hole U1432C. Geochemical analysis shows that sulfate is completely consumed at ~90 mbsf, coincident with maximum methane concentrations between 4650 and 4750 ppmv just below this depth. The absence of higher hydrocarbons suggests that the methane is primarily microbial in origin. TOC in the hole varies from 0.34 to 0.99 wt%, whereas CaCO₃ concentrations are generally low (<12 wt%).

Five whole-round samples and five interface samples were collected from Hole U1432C for DNA and lipid analysis. The five whole-round samples were also used to inoculate several types of microbiological media to test whether autotrophic and heterotrophic microbes can be grown. For heterotrophic culture enrichments, glucose, acetate, fumarate, and formate were used as sources of carbon and energy. For autotrophic culture enrichments, sodium bicarbonate and hydrogen were used as sources of carbon and energy, respectively. We also collected and preserved 200 mL of drilling fluid for FCT analysis. The microbial communities present in these samples will be compared to those present on the inside and outside of the cores to determine whether microbes in the drilling fluid behave as suitable contaminant tracers.

As seen at Site U1431, the NRM of samples from Hole U1432C contains a vertical component generated by the drilling process, which is easily removed by 5–10 mT alternating field (AF) demagnetization. A polarity reversal at ~105 mbsf is defined as the Brunhes/Matuyama Chron boundary (0.781 Ma) (Fig. F16). In the Brunhes Chron, there are two directional anomaly intervals at ~10 mbsf and between 50 and 70 mbsf. These anomalies could represent authentic magnetic excursions or could be caused by postdepositional disturbances. These magnetostratigraphic results, when combined with the biostratigraphy, indicate a higher sedimentation rate (~13.5 cm/k.y.) in Hole U1432C (Fig. F16) than for the same age interval in Hole U1431D (~5.8 cm/k.y.), which is consistent with its location closer to the continental margin.

Physical property measurements made on whole-round core sections were smoothed using a five-point (10 cm) moving average and combined with discrete sample measurements. Bulk density, *P*-wave velocity, magnetic susceptibility, NGR, thermal conductivity, and shear strength decrease with depth in the uppermost 50 m of Hole U1432C (Fig. F15), showing an inverse relationship with porosity. Variations in these records are lower below 50 mbsf. This indicates that the compaction effect dominates the physical properties in the uppermost part of Hole U1432C. The 2.5 m thick sand layer near 50 mbsf is clearly delineated by low NGR, low magnetic susceptibility, and higher *P*-wave velocity (Fig. F15).

Four APCT-3 downhole temperature measurements on Cores 349-U1432C-5H, 7H, 9H, and 11H indicate a geothermal gradient of 85°C/km (Fig. F14). Combining these temperatures with thermal conductivity measurements made on the sediment cores, the preliminary heat flow value at Hole U1432C is 94 mW/m². The geothermal gradient and heat flow values are similar to those at Site 1148, ~60 km to the north-northeast (Wang, Prell, Blum, et al., 2000) (Fig. F14).

Site U1433

Background and objectives

As a result of the marked contrast in magnetic anomaly amplitudes between the Southwest and East Subbasins of the South China Sea (Yao, 1995; Jin et al., 2002; Li et al., 2007, 2008), it is questionable whether rifting and drifting within these two subbasins occurred synchronously and how these subbasins evolved in comparison to the Northwest Subbasin. Site U1433 (proposed Site SCS-4B) is located in the Southwest Subbasin near the relict spreading center and magnetic anomaly C5d identified by Briais et al. (1993) (Figs. F4, F8). Together with Site U1431 in the East Subbasin, coring at Site U1433 should help to explain the sharp differences in magnetic amplitude between the East and Southwest Subbasins and test the hypothesis that in the Southwest Subbasin the breakup from continental rifting to seafloor spreading occurred more recently than in the East Subbasin (Pautot et al., 1986). Coring will help determine the age of this subbasin near the end of the spreading and correlate ages from magnetic anomalies with biostratigraphic, magnetostratigraphic, and radiometric ages. The apparent weak magnetization in basement rock (Li et al., 2008) will be examined through petrological and geochemical analyses and by measurements of magnetic susceptibility and remanent magnetization. The specific objectives at this site were to

1. Determine the termination age of spreading in the Southwest Subbasin and correlate it with ages of regional tectonic events;
2. Test the hypothesis that rifting and subsequent seafloor spreading in the Southwest Subbasin occurred later than that in the East Subbasin;
3. Measure magnetization, mineralization, and geochemical compositions of basement rocks to trace how the mantle evolved through time; and
4. Examine the paleoceanographic and sedimentary response to the opening of the South China Sea.

Operations

After a 334 nmi transit from Site U1432 averaging 11.2 kt, the vessel stabilized over Site U1433 at 0230 h (UTC + 8 h) on 8 March 2014. The original operations plan consisted of drilling one hole to a depth of ~965 mbsf, which included 100 m of basement. This plan was modified during transit in order to eliminate the use of a free-fall funnel and the XCB by coring two holes (Table T1). Hole U1433A was cored using the APC to refusal at 188.3 mbsf. Hole U1433B was drilled to 186.1 mbsf and then cored

using the RCB. The sediment/basement interface was encountered at ~798.5 mbsf, and we advanced the hole by rotary coring into basement to a final depth of 858.5 mbsf. After conditioning the hole for logging, we deployed the modified triple combo tool string and the FMS-sonic tool string to 840 m WSF, with multiple passes made in the basement section of the hole with the latter tool.

A total of 94 cores were collected at this site. The APC was deployed 20 times, recovering 168.79 m of core over 188.3 m of penetration (89.6% recovery). The RCB system drilled one 186.1 m interval and collected 74 cores, recovering 443.04 m of core over 672.4 m of penetration (65.9% recovery). The overall recovery at Site U1433 was 71.1%. The total time spent on Site U1433 was 284.5 h (11.85 days).

Principal results

The cored section at Site U1433 is divided into four lithostratigraphic units (three sedimentary and one igneous) based on a combination of data from Holes U1433A and U1433B (Fig. F17). Lithostratigraphic Unit I is a 244.15 m thick sequence of Pleistocene dark greenish gray clay, silty clay, and clay with nannofossils. The clay is interbedded with small volumes of generally thin, graded quartzose silt and nannofossil ooze, both interpreted to be turbidite deposits that comprise <5% of the unit. This unit is underlain by middle Miocene to Pleistocene Unit II (244.15–747.93 mbsf), which is divided into two subunits: IIA (244.15–551.32 mbsf) and IIB (551.32–747.93 mbsf). The entire unit is 503.78 m thick and dominated by dark greenish gray clay with frequent graded carbonate interbeds, largely comprising nannofossil ooze and chalk that are characterized by sharp, erosive bases and gradational, bioturbated tops. In Subunit IIB, carbonate beds are sometimes substantially thicker, up to several meters, rather than <1 m and usually <50 cm in Subunit IIA. The carbonates are turbidite deposits with evidence of re-sedimentation from shallow-water regions based on the occurrence of benthic foraminifers that dwell in the photic zone. The lowermost sedimentary sequence, Unit III (747.93–796.67 mbsf), is a 48.74 m thick lower to middle Miocene sequence of claystone and claystone with silt. Most of the unit is reddish brown or yellowish brown massive sediment with common burrowing stained black by diagenetic alteration. As in Units I and II, bioturbation of Unit III is consistent with sedimentation at lower bathyal to abyssal water depths (*Nereites* ichnofacies). Unit III contains sparse, relatively thin calcareous turbidites. There is no evidence for hydrothermal influence on sedimentation or diagenesis despite the fact that it lies directly above the basalt of Unit IV (796.67–857.48 mbsf). Unit III is the product of relatively slow sedimentation in a distal setting at the foot of a continental margin and is sim-

ilar to the basal sediment at Site U1431 and to “red clay” deposits from the central Pacific (Bryant and Bennett, 1988).

Analysis of calcareous nannofossils, planktonic foraminifers, and radiolarians in core catcher samples and additional samples from split cores indicates that the sedimentary succession recovered at Site U1433 spans the lower Miocene to the Pleistocene (Fig. F18). Age control for the lower to lower middle Miocene section is difficult because of very rare occurrences of microfossils in the brown claystone (Unit III) overlying the basement. Nannofossils in sediment preserved in and around basalt pillows are Oligocene to early Miocene in age, but additional postexpedition analyses are required to determine if these assemblages are reworked or in situ.

Calcareous nannofossils are generally common to abundant with good preservation in samples from the Pliocene–Pleistocene section but are rare and heavily overgrown or even barren in some upper Miocene and Pliocene samples, especially those from nannofossil ooze/chalk intervals. Planktonic foraminifers also show considerable variations in both abundance and preservation. They are abundant and well preserved in silty layers with numerous small (<150 μm) specimens but poorly preserved and very difficult to identify in lithified intervals. Radiolarians are abundant and well preserved in the Upper Pleistocene section in Hole U1433A, but rare or absent in older sediment sections downhole. In Hole U1433B, samples are barren of radiolarians until the brown claystone of Unit III, in which rare and poorly preserved but biostratigraphically significant specimens occur.

Integration of biohorizons and paleomagnetic datums indicates extremely low sedimentation rates (<0.5 cm/k.y.) during the early to middle Miocene. Sedimentation rates varied from ~5 to 9 cm/k.y. from the late Miocene to early Pleistocene, but then increased sharply to ~20 cm/k.y. since 1 Ma (Fig. F18).

We cored 60.81 m into igneous basement below 796.67 mbsf in Hole U1433B, recovering 29.02 m of basalt (47.7% recovery). This short basement succession was divided into 45 igneous lithologic units, which are grouped into lithostratigraphic Unit IV and are immediately overlain by hemipelagic dark reddish brown to yellowish brown claystone (Unit III) (Fig. F19). The basement at Site U1433 is composed of a 37.5 m thick succession of small pillow basalt lava flows in the top (Fig. F20), with a 23.3 m series of massive basalt lava flows toward the bottom.

The igneous basement begins with a sequence of sparsely to highly plagioclase-phyric pillow basalt with a trace of olivine microphenocrysts. Most of the pillow basalts are

nonvesicular to sparsely vesicular, range in grain size from crypto- to microcrystalline, and in many cases have well-preserved glassy chilled margins along both the upper and lower unit boundaries. A few larger lobate flows are present, with flow thicknesses varying from 0.1 to 1.1 m. In two intervals, interpillow hyaloclastite breccia was encountered, with remnants of baked limestone in which Oligocene to early Miocene nannofossils occur. In between these sequences of pillow basalt flows, one 5.2 m thick microcrystalline to fine-grained massive flow was encountered that is sparsely olivine-plagioclase-phyric but has a holocrystalline groundmass with abundant clinopyroxene present in the interstitial spaces. Downhole, the basement is characterized by more massive basalt lava flows as thick as ~12.8 m. These massive flows have similar petrologic characteristics and range from sparsely to highly plagioclase-phyric with minor microphenocrysts of olivine. Toward the interiors of the thickest lava flows the grain size increases to fine grained.

All basalts have a phenocryst phase assemblage of plagioclase \pm olivine, whereas the more massive flows also have clinopyroxene in their groundmass. This assemblage resembles a typical MORB crystallization assemblage and, in conjunction with geochemical evidence, we conclude that the basement basalt at Site U1433 is typical MORB.

Alteration is also typical of that of MORB. The basalt ranges from mostly fresh/less altered to moderately altered in intensity, typically as halos in association with cracks and veins, and from gray to dark gray-green and yellow to red-brown in color. Basalt glasses are most abundant near the quenched margin of lava flows and are commonly altered to greenish palagonite, which might indicate alteration from more reducing fluids than that of brownish palagonite. Alteration veins are abundant at the top of the basement cores and decrease with depth, indicating limited downwelling fluid flow, which is also consistent with fewer fractures that occur with increasing depth. Vein filling minerals include carbonate, celadonite, Fe oxide/hydroxides, saponite, smectite, quartz, and some blue minerals that are difficult to identify. Typical secondary minerals include saponite, Fe oxides, carbonate, and celadonite, which represent a low-temperature alteration assemblage.

We measured 240 fractures and veins in the basalt of Hole U1433B. Most of the fractures occur along existing veins without either obvious offset or striations on the surfaces, indicative of drilling-induced fractures, whereas natural fractures are quite rare. In general, veins can be separated into four types with different shapes: single linear, triple-junction, branched, and crosscutting. Arched, crosscutting, and triple-junction

veins are usually distributed in pillow basalt layers, whereas single linear, branched, or sinuous veins are usually confined to the massive flows. The highest frequency of veins occurs in the pillow basalts, whereas there are fewer veins within the massive flows. Alteration along fractures and veins produced 1–2 cm wide yellow to brown halos.

At Site U1433, interstitial water sulfate concentration decreases with depth and sulfate is almost completely consumed (<1 mM) below ~30 mbsf. Alkalinity increases with depth, reaching a maximum of 25.8 mM at ~30 mbsf, before gradually decreasing with depth. The depth at which sulfate is consumed and alkalinity reaches its peak corresponds to an increase in methane from ~3 to 1100 ppmv. Below this depth, methane varies between ~22,000 and 93,000 ppmv before it decreases significantly below ~590 mbsf. Ethane and other higher hydrocarbons are also present in low concentrations below ~60 mbsf. This indicates that anaerobic oxidation of methane coupled with sulfate reduction is ongoing in the sediment. Other interstitial water chemistry profiles reflect both lithologic changes and diagenetic processes. TOC varies from 0 to 1.0 wt%, with a general decrease downhole. CaCO₃ content ranges from 0.5 to 77.8 wt%, with the lowest values (generally <15 wt%) in the upper 300 m of the site. Intervals with higher CaCO₃ content below 300 mbsf correspond to carbonate turbidite layers in lithostratigraphic Unit II. Peaks in TOC (1–1.5 wt%) at ~450 mbsf and 540–590 mbsf could reflect an influx of terrestrial organic matter; however, additional shore-based work is needed to confirm this interpretation.

The basalt recovered in Hole U1433B has low LOI values (0.52–2.06 wt%), as well as low K₂O (0.11–0.29 wt%), moderate TiO₂ (1.01–1.77 wt%), and high SiO₂ (48.5–51.1 wt%). In general, concentrations of major elements vary within narrow ranges. When plotted on the alkali vs. silica diagram of volcanic rock types (Le Maitre et al., 1989) (Fig. F12), the data plot within the tholeiite field. As shown in Figure F13, the data from these rocks overlap with but define a much smaller range than those of Indian Ocean and Pacific MORB and are distinct from the Hainan Island OIB and other SCS seamount basalt data fields (Figs. F12, F13). Thus, the basalt samples from Hole U1433B are tholeiites and considered representative of SCS MORB.

At Site U1433, we collected a total of 50 routine 5 cm whole-round samples for microbiological analysis from the seafloor to 790 mbsf. When possible, these samples were collected adjacent to samples for interstitial water measurements. We also collected 164 samples from split cores to study the microbiology of interfaces or coring-induced disturbance. We obtained these samples between 4 and 154 mbsf in Hole

U1433A and between 187 and 854 mbsf in Hole U1433B. Most of the samples collected at Site U1433 were preserved for shore-based analysis of DNA, RNA, and lipids. Some portions of the whole-round samples were selected for cultivation-based studies designed to enrich for anaerobic autotrophs and heterotrophs.

We used three methods of contamination testing during coring at Site U1433: PFTs, microspheres, and FCTs. PFT samples were acquired from the outside and inside of 16 cores between 140 and 390 mbsf in Holes U1433A and U1433B. PFTs were not detected in most of the samples collected and analyzed for this tracer regardless of whether the samples were taken from the outside or the inside of the core. Microsphere tracers were used with the RCB coring system in Hole U1433B between 709 and 854 mbsf. Two microsphere samples were taken from each core collected between these depths: one from scrapings of the core surface and one as a subsample from the interior of each whole-round sample. Twenty-four FCT samples were collected either from the drilling fluids that drained from the core liners when cores arrived on the catwalk or from a sampling port near the mud pumps on the rig floor during active coring. The fluids collected for FCT samples correspond to cores obtained from depths ranging between 6 and 824 mbsf.

We conducted paleomagnetic studies at Site U1433 on both sediment and basement cores using pass-through magnetometer measurements on all archive-half sections and AF demagnetization on representative discrete samples. Magnetostratigraphic records at Site U1433 suggest the existence of eight short reversed polarity events within the Brunhes normal chron. These short-lived events most likely represent geomagnetic excursions, as both declination and inclination change. The polarity shifts at depths of ~12, 18, 28, 48, 53, 132, and 152 mbsf match well with known excursion events: Mono Lake (33 ka), Laschamp (41 ka), Blake (120 ka), Iceland Basin (180 ka), Pringle Falls (211 ka), Big Lost (560–580 ka), and marine isotope Stage 17 (670 ka). For two directional anomalies at ~78 and 88 mbsf, there are no counterparts from previous studies, and further shore-based work is needed to confirm the origin of these two anomalies. The Brunhes/Matuyama Chron boundary (0.781 Ma) is tentatively placed at ~188 mbsf in Core 349-U1433A-20H, which indicates a higher sedimentation rate (~23.7 cm/k.y.) for the Middle–Late Pleistocene compared to Sites U1431 and U1432 (Fig. F18). Such a high sedimentation rate facilitates preservation of the short-lived polarity excursions mentioned above.

In Hole U1433B, six major normal chrons are recognized and tied to the geomagnetic polarity timescale using constraints from biostratigraphy. The basal boundaries for

the Matuyama Chron (2.581 Ma), Gauss Chron (3.596), and Gilbert Chron (6.066 Ma) are placed at ~350, 420, and 550 mbsf, respectively. The basal age for sediment in Core 349-U1433B-60R is ~11 Ma. Paleomagnetic results for the basalt units show that the upper part of the basement (805–817 mbsf) is dominated by normal polarity. Between ~817 and 830 mbsf, a relatively well defined reversed polarity zone is observed. Below this depth range, the paleomagnetic inclinations display both normal and reversed polarities. Overall, the remanent magnetization of rocks below ~817 mbsf is dominated by reversed polarity. This pattern is similar to that found in the upper part of the basalt units at Site U1431.

Cores from Holes U1433A and U1433B were measured for physical properties on whole-round cores, split cores, and discrete samples. The physical properties correlate well with lithology, composition, and observed lithification. Bulk density, *P*-wave velocity, shear strength, NGR, and thermal conductivity increase gradually with depth over the uppermost 150 m (Fig. F17), whereas the porosity measured on discrete samples decreases from 90% to 50% over the same depth range. This indicates that sediment compaction dominates physical property variations above 150 mbsf. Below 240 mbsf, variability in porosity, magnetic susceptibility, and NGR values reflects interbedding of carbonate and clay layers (Fig. F17). An increase in *P*-wave velocity from ~1700 to ~2000 m/s near 550 mbsf coincides with stronger lithification in the deeper sediment. From 680 to 750 mbsf, *P*-wave velocities measured in the lithified carbonates reach ~2600 m/s, contrasting strongly with those measured in the clay (~2000 m/s) (Fig. F17). The strong reflectors observed in the seismic profile from this site probably result from this contrast in velocity. Magnetic susceptibility gradually increases and NGR decreases in the clays between 750 and 800 mbsf (Fig. F17). The basalts below 800 mbsf display very low NGR and porosity and variable magnetic susceptibility. Some of the fresh, phenocryst-rich basalt has very high magnetic susceptibility and *P*-wave velocities.

The modified triple combo and FMS-sonic tool strings were run in Hole U1433B. Both tool strings reached 840 m WSF, ~18 m short of the bottom of the hole (Fig. F17). Between 100 and 550 m WSF, there are rapid variations in borehole diameter from ~25 to >43 cm. Below 550 m WSF, the hole diameter is mostly in gauge, with fewer washed out zones. Density and sonic velocity increases from the top of the logs at 100 m WSF downhole to 750 m WSF, caused by compaction and cementation with depth. Superimposed on this trend, excursions to higher velocity and photoelectric factor (PEF) and to lower NGR mark the occurrence of carbonate beds (Fig. F17). This information was used to infer lithology in the unrecovered intervals of Hole U1433B. In the red

clay of Unit III, from ~750 to 800 m WSF, high values in the PEF log indicate that hematite and other oxides increase in concentration downhole toward the top of the basalt at ~800 m WSF. Pillow basalt, a massive basalt flow, fractures, and veins are seen in the FMS images in the basement.

Site U1434

Background and objectives

Site U1434 (proposed Site SCS-4E) is located about 40 km northwest of Site U1433 and is directly on the uplifted shoulder of the relict spreading center in the Southwest Subbasin (Figs. F7, F8). This site is also located just south of a large seamount that formed near the relict spreading center after the termination of seafloor spreading. During coring at Site U1433, we decided to use some of our remaining time to core at a second site in the Southwest Subbasin to obtain basement samples more proximal to the extinct spreading center. Site U1434 also offered the opportunity to sample volcaniclastic material from the nearby seamount, which can be compared to the seamounts located near Site U1431 in the East Subbasin.

Sites U1434 and U1433 form a short sampling transect in the Southwest Subbasin (Fig. F7), and with age controls from these two sites, the evolution of the Southwest Subbasin can be better understood. Coring at these sites should help to explain the sharp differences in magnetic amplitude between the East and Southwest Subbasins and test the existing opening models for the Southwest Subbasin (e.g., Pautot et al., 1986). Coring will help determine the age of this subbasin near the end of seafloor spreading and correlate ages from magnetic anomalies with biostratigraphic, magnetostratigraphic, and radiometric ages. The apparent weak magnetization in basement rocks (Li et al., 2008) will be examined through petrological and geochemical analyses and by measurements of magnetic susceptibility and remanent magnetization. Rock samples cored here will place constraints on mantle evolution and oceanic crustal accretion, the terminal processes of seafloor spreading, and the timing and episodes of postspreading seamount volcanism in the area of the relict spreading center.

Operations

After an 18 nmi transit from Site U1433 averaging 10.3 kt, the vessel stabilized over Site U1434 at 0048 h (UTC + 8 h) on 20 March 2014. This site was an alternate site that was originally planned to core from the seafloor with APC/XCB to refusal, drop a free-fall funnel, change to the RCB, and then core 100 m into basement. Because of

time considerations, the plan was modified so that we drilled to ~200 mbsf using the RCB and then cored into basement as deeply as time permitted. Logging would then be considered depending on hole depth and condition. Hole U1434A was drilled to 197.0 mbsf and then cored with the RCB (Table T1). Basement was encountered at ~280 mbsf, and the hole was advanced by rotary coring to a final depth of 312.5 mbsf. The hole was terminated because of poor hole conditions and poor recovery. At this site there was one drilled interval of 197.0 m. The RCB was deployed 14 times, recovering 26.43 m of core over 115.5 m of penetration (22.9% recovery).

Principal results

The cored section at Site U1434 is divided into four lithostratigraphic units, three sedimentary and one igneous (Fig. F21). Lithostratigraphic Unit I (197.00–235.10 mbsf) is a 38.1 m thick sequence of upper Miocene dark greenish gray claystone interbedded with black volcanoclastic sandstone and occasional breccia. The fine-grained sediment is mottled greenish and light buff brown, with the browner sediment preferentially found in burrows. This unit is marked by strong bioturbation within the claystone intervals that make up ~40% of the total sediment. The trace fossil assemblages seen within the claystone intervals are consistent with sedimentation in deep water (i.e., lower bathyal or abyssal depths; >2500 m), with assemblages dominated by *Chondrites* and *Zoophycos*, although more vertical burrows are also noted. Sandstone beds are typically dark gray or black in color and are composed of volcanoclastic fragments. The volcanoclastic sandstone and breccia are interpreted to be part of the sedimentary apron of a nearby seamount because they contain abundant volcanic glass fragments, scoria, and basalt clasts, as well as isolated crystals of plagioclase, olivine, and biotite.

Lithostratigraphic Unit II (235.10–254.59 mbsf) contains upper Miocene greenish gray nannofossil-rich claystone with very thin claystone with sand interbeds. The color of the sediment varies at the decimeter scale as a result of changes in the carbonate and clay content. The sediment is locally a light greenish gray color, reflecting higher biogenic carbonate content over those intervals. Unit III (254.59–278.27 mbsf) consists of dominantly massive yellowish brown claystone with nannofossil- or foraminifer-rich claystone of latest middle to late Miocene age. This unit is primarily distinguished from Unit II by its color, which tends to be more yellowish or reddish brown compared to the greenish gray tones associated with the overlying unit.

Analysis of calcareous nannofossils and planktonic foraminifers in core catcher samples and additional samples from split cores indicates that the sedimentary succession

recovered at Site U1434 spans the uppermost middle to upper Miocene, with the base of the sequence younger than 11.9 Ma (Fig. F22). Calcareous nannofossils are generally common to abundant but decrease in abundance downhole, and preservation is poor to moderate. Planktonic foraminifers vary from common to absent, with good to poor preservation, but are frequently fragmented. Radiolarians are present in only one sample. Although none of the species present are biostratigraphic index taxa, the radiolarian assemblage is consistent with the late Miocene age inferred from nannofossils and foraminifers. Correlation of microfossil biohorizons and paleomagnetism data suggest a sedimentation rate of ~1.6 cm/k.y. for the sediment sequence recovered at Site U1434 (Fig. F22).

We cored 30.28 m into igneous basement below 278.37 mbsf in Hole U1434A, recovering 3.05 m of basalt (10.1% recovery). This basement succession is divided into seven igneous lithologic units, which are grouped into lithostratigraphic Unit IV (Fig. F23). The basement at Site U1434 comprises a succession of small pillow basalt flows or a thicker autobrecciated pillow lava flow with three occurrences of hyaloclastite breccia. The igneous basement comprises angular to subangular basalt fragments that are aphyric and have glassy to aphanitic groundmasses. The only phenocrystic phase is olivine, which appears as sparse euhedral-subhedral microphenocrysts throughout the core. The groundmass contains abundant plagioclase microlites, growing in spherulitic and variolitic patterns, with the majority of the groundmass consisting of variably altered mesostasis. Clinopyroxene is only observed in a few thin sections, growing in patches and filling the interstitial spaces between plagioclase microlites. Most of the basalt is nonvesicular to sparsely vesicular. The hyaloclastite breccia contains abundant fresh volcanic glass shards in a mostly clay and/or carbonate matrix. All basalts have phase assemblages of olivine ± plagioclase, and some slightly coarser basalt pieces also have clinopyroxene in their groundmass. These resemble typical MORB crystallization assemblages.

Basalt alteration at Site U1434 is typical of that of MORB. The recovered basalt is slightly to moderately altered. Pillow basalt pieces are altered in zones, with alteration color ranging from dark gray in the interior to light yellow-brown in halos along the outer rims. Typical secondary minerals include saponite and other clay minerals, Fe oxides, carbonate, and celadonite, which constitute a low-temperature alteration assemblage. Fresh basalt glass exists near some of the pillow basalt margins and in the clasts of hyaloclastite breccia. Those basalt glasses are partially altered to orange and brown palagonite. Most of the vesicles are empty or only partially filled with Fe oxide,

saponite, celadonite, and/or carbonate. Only two alteration veins were observed in this short basement section.

Most fractures observed in the sedimentary sequence at Site U1434 are drilling induced. One fracture shows some offset that suggests it occurred prior to consolidation of the sediments. Fractures are rare in the small amount of basalt recovered at this site. Several linear veins are present and filled with carbonate or Fe oxide.

We measured alkalinity and pH on five interstitial water samples taken from 207.9–264.8 mbsf in Hole U1434A. Alkalinity increases from 0.5 at 208 mbsf to 3.5 at 257 mbsf and then decreases in the two samples below that depth. The pH decreases from 7.9 at 208 mbsf to 7.2 at 265 mbsf and then increases slightly just above basement. Methane was detected in very low concentrations (<3.1 ppmv) in the headspace gas samples taken at this site. CaCO₃ content is low (<10 wt%) in lithostratigraphic Units I and II. Samples from the base of Unit III are higher in CaCO₃ (15–30 wt%). TOC is also low (<0.5 wt%), with the highest values near the base of the sedimentary section. ICP-AES major and trace element results from Site U1434 indicate that the basalt has somewhat higher K₂O than those at Sites U1431 and U1433 but is still tholeiitic in composition and similar to MORB (Figs. [F12](#), [F13](#)).

We collected six routine 5 cm whole-round samples for microbiological analysis from depths of 208–275 mbsf in Hole U1434A. These samples were collected adjacent to samples for interstitial water measurements so that microbiological data and water chemistry data are proximal. We also collected and preserved 13 samples from either the split cores on the sampling table or from basement samples shortly after the samples were retrieved from the catwalk to investigate the microbiology of interfaces. The whole-round and split core samples were preserved for shore-based characterization of the microbial communities (i.e., DNA, RNA, lipids, and cultivation-based studies).

We also collected samples for measuring contamination testing tracers, including microspheres and FCTs. Microsphere tracers were used with the RCB coring system in Hole U1434A by adding them to the core catcher for cores collected between 208 and 303 mbsf. Two microsphere samples were collected from each of the cores collected between those depth intervals: one from scrapings of the core surface and one as a subsample from the interior of each whole-round sample. Microscopic counts of the microspheres in these samples will be performed in shore-based laboratories. Six FCT samples were collected from drilling fluids that drained from the core liners when cores arrived on the catwalk or from a sampling port near the mud pumps on the rig

floor during active coring. The fluids collected for FCT samples correspond to cores obtained from depths ranging between 208 and 293 mbsf. Microbial community DNA and lipids from FCT samples will be compared to the same measurements made on the core samples to determine if the drilling fluids contain microbes that can be regularly tracked as recognizable contaminant taxa.

We conducted paleomagnetic studies at Site U1434 on both sediment and basement cores using pass-through magnetometer measurements on archive-half sections. NRM intensity ranges from 0.001 to 0.1 A/m for the sediment units and increases to several A/m for the basalt units, suggesting that the basalt contains more iron oxides than the sediment. Because of the poor recovery at the site, only fragmentary patterns of magnetic polarity are observed. Available biostratigraphic data allow us to tentatively correlate certain parts of the magnetic polarity interval recorded in the sediments with the geomagnetic polarity timescale. Near the base of the sedimentary sequence, biostratigraphy indicates an age <11.9 Ma, which we use to correlate the negative inclinations at ~278 mbsf to Chron C5r (11.056–12.049 Ma). The long, dominantly positive inclinations between ~250 and 270 mbsf may represent the long normal Subchron C5n (9.984–11.06 Ma), the short normal polarity zone between ~235 and 240 mbsf appears to have recorded Chron C4An (8.771–9.015 Ma), and the normal polarity zone between 205 and 210 mbsf can be tentatively assigned to Chron C4n around 7.15 Ma (Fig. F22).

Cores from Hole U1434A were measured for physical properties on whole-round cores, split cores, and discrete samples. In general, the physical properties correlate well with lithology, composition, and the observed lithification. Because of the low recovery rate, measurements of physical properties show significant discontinuities between intervals. In Hole U1434A, the observed range of values for magnetic susceptibility (30×10^{-5} to 80×10^{-5} SI) and NGR (25–45 cps) in Units I–III are typical for clay material, which dominates the sediment layers (Fig. F21). The low NGR value in Unit IV corresponds to the basalt layer. The magnetic susceptibility values in the basalt ranges from 10×10^{-5} to 90×10^{-5} SI, which is much lower than what is typical for basalt (Fig. F21). The high grain densities in the claystone of Units II and III suggest the presence of heavy minerals, such as hematite. The porosity measured on discrete samples increases from 40% to 60% with depth, which may be correlated to the lithification and composition of the claystone.

Site U1435

Background and objectives

Coring at Site U1435 (proposed Site SCS-6C) became a high priority after failing to achieve our basement objectives at Site U1432 when the final cementing operations compromised the reentry system. This site was originally added as an alternate because of the high risk of being unable to reach basement at Site U1432. The site is located on the continental side of the continent/ocean boundary and is fundamentally different from Site U1432 but nonetheless does have the potential to provide information about the breakup process. Site U1435 is located on a structural high at the transition between the extended continental crust and the oceanic crust (Figs. F6, F8). Similar conspicuous structural high features can be found on the continent/ocean boundary in many other seismic profiles crossing the SCS northern margin and therefore appear to represent tectonic structures typical of the area. The formation mechanism and nature of this structural high was still speculative; it could have been a volcanic extrusion associated with continental extension at the onset of seafloor spreading, lower crust material emplaced from preferential lower crust extension, exhumed mantle material, or a structural high composed of older (Mesozoic) sedimentary rock. Coring at this location was designed to help pinpoint the exact nature of this structure and improve our understanding of early continental breakup, the rift-to-drift transition, and seafloor spreading processes.

Operations

After a 336 nmi transit from Site U1434 averaging 8.5 kt, the vessel stabilized over Site U1435 at 1524 h (UTC + 8 h) on 24 March 2014. Because we anticipated shallow sediment cover (~10 m), we conducted a 3.5 kHz sonar survey to select a location with maximum sediment thickness to help stabilize the drill string when trying to penetrate basement with thin sediment cover in rough weather. After reaching basement, the plan was to core as deeply into basement as time permitted. Sediment thickness was significantly greater than expected based on the seismic interpretation. Hole U1435A was cored with the RCB to a final depth of 300.0 mbsf when time allocated to the expedition expired, never reaching igneous basement (Table T1). The RCB was deployed 32 times, recovering 171.37 m of core over 300.0 m of penetration (57.1%).

Principal results

The cored section at Site U1435 is divided into three sedimentary lithostratigraphic units (Fig. F24). Unit I (0–77.65 mbsf) is a sequence of Oligocene–Pleistocene greenish

gray nannofossil-rich clay and clayey nannofossil ooze, together with manganese nodules. The unit is divided into Subunits IA and IB based on variations in the nannofossil content of the sediment. Subunit IA (0–36.04 mbsf) is Miocene to Pleistocene in age and consists of manganese nodules underlain by clayey nannofossil ooze. The manganese nodules have a lobate appearance and are typically associated with very low sedimentation rates. The massive clayey nannofossil ooze has a few *Planolites* trace fossils visible on the cut surface of the core. Subunit IB (36.04–77.65 mbsf) is Oligocene in age and consists of mostly greenish gray nannofossil-rich clay and lesser quantities of greenish gray clay. There are interbedded silty clay and clay with silt intervals, but deeper in the section the sediment becomes more calcareous, primarily through an increase in the proportion of nannofossils. The sediment is heavily bioturbated with trace fossils of the *Nereites* ichnofacies.

Unit II (77.65–275.54 mbsf) is a 197.89 m thick sequence of pre-Oligocene thick-bedded and mostly medium-grained dark gray silty sandstone, with very little carbonate and minor sandy siltstone and conglomerate. The sandstone is better cemented than the Unit I nannofossil-rich clay and increases in lithification downhole. Units I and II are separated by a hard carbonate rock that likely represents a hiatus. The sandstone is moderately well sorted and is characterized by dispersed carbon fragments, shell fragments, and current lamination that is largely disrupted by bioturbation, with burrows typical of the *Cruziana* ichnofacies indicative of shallow-marine conditions. Several whole bivalves and gastropods occur in the sandstone. Unit III (275.54–300.00 mbsf) is a 24.46 m thick sequence of dark gray silty sandstone, silty mudstone, and minor conglomerate. The unit is distinguished from Unit II by being generally finer grained.

We analyzed all core catcher samples and additional samples from split cores for calcareous nannofossils, foraminifers, and radiolarians at Site U1435. Based on nine nannofossil and four planktonic foraminifer bioevents, the sedimentary sequence above 77.65 mbsf is assigned an age spanning the early Oligocene (<33.43 Ma) to the Pleistocene (>0.12 Ma), with possible unconformities or condensed sections existing between the upper Oligocene and middle Miocene, between the upper Miocene and lower Pliocene, and between the upper Pliocene and Middle Pleistocene. Based on a limited number of bioevents, sedimentation rates during the Oligocene were ~0.5 cm/k.y. (Fig. F25).

Samples from 77.65 to 300 mbsf are barren of nannofossils, radiolarians, and planktonic foraminifers. A few long-ranging, shallow-water benthic foraminifers occur in

samples from ~200 to 250 mbsf. Although these specimens are not useful for age control, they indicate a depositional environment of brackish water to shallow marine for Unit II, consistent with the deltaic setting inferred from the sedimentology and trace fossil assemblage.

A small number of deformation structures are present in the sedimentary rock of Site U1435. Most of the fractures are drilling induced, and in the black mudstones near the base of the section, these induced fractures developed along the bedding. Two normal fault structures are found in the sandstone, each composed of several fractures that have little offset. No deformation or thickness changes occur in the rock of the hanging walls and footwalls, indicating that these faults occurred at a later stage and did not control sedimentation. One linear white carbonate vein was found in the sandstone. Bedding is generally horizontal or subhorizontal in Unit I, but toward the base of Units II and III the strata are inclined to a significant degree ($>25^\circ$). These dips are not depositional and are interpreted to reflect rotation caused by normal faulting, possibly during formation of the structural high on which the site is located.

Downhole interstitial water concentrations of chloride, bromide, and sodium are variable and slightly higher than modern seawater; however, the Na/Cl ratio is ~0.85 throughout the sampled interval, which indicates that the interstitial water is of typical marine origin. Only very low concentrations (<10 ppmv) of methane and ethane were detected in the headspace gas samples from Hole U1435A. CaCO_3 content in the upper part of the hole is higher than that of the lower part, which corresponds to the change from nannofossil ooze and nannofossil-rich clay in lithostratigraphic Unit I to sandstone in Unit II. Despite variable TOC with depth, the ratio of TOC to total nitrogen (C/N) suggests that TOC is dominated by a terrestrial organic matter source, with lower input from marine organic matter.

We collected 25 routine 5 cm whole-round samples for microbiological analyses from 37 to 299 mbsf in Hole U1435A. These samples were collected adjacent to samples for interstitial water measurements so that microbiological data and water chemistry data are proximal. The whole-round samples were preserved for shore-based characterization of microbial communities (i.e., DNA, RNA, lipids, and cultivation-based studies).

We also collected samples for measuring contamination testing tracers, including microspheres and FCTs. Microsphere tracers were used with the RCB in Hole U1435A by adding them to the core catcher for Cores 349-U1435-5R through 32R (37–299 mbsf).

Two microsphere samples were taken from each of the cores collected between those depth intervals: one from scrapings of the core surface and one as a subsample from the interior of each whole-round sample. Microscopic counts of the microspheres in these samples will be performed in shore-based laboratories. Five FCT samples were collected from drilling fluids that drained from the core liners when cores arrived on the catwalk or from a sampling port near the mud pumps on the rig floor during active coring. The fluid collected for FCT samples corresponds to cores obtained from between 90 and 273 mbsf. Microbial community DNA and lipids from FCT samples will be compared to the same measurements made on the core samples to determine if the drilling fluids contain microbes that can be regularly tracked as recognizable contaminant taxa.

We performed measurements of NRM on all archive-half cores from Hole U1435A. We subjected these cores to AF demagnetization up to 20 mT in order to establish a reliable magnetostratigraphy at the site and to observe the magnetic properties of the different lithologies recovered. Because of time constraints, we were unable to perform measurements and demagnetization on discrete samples taken from the working halves. Overall, paleomagnetic data at Site U1435 are reasonably robust and provide magnetic information about the recovered sediment. Several relatively well defined polarity intervals are identified in the downhole magnetostratigraphic records, despite some samples showing unstable and ambiguous magnetization. Based on biostratigraphic data, we were able to tentatively correlate certain parts of the magnetic polarity interval recorded in the sediment with the geomagnetic polarity timescale. Assuming no significant hiatus between the marine Oligocene nannofossil-rich clay (Subunit IB) and the sandstone of Unit II, the Chron C16n/C15r boundary (36.05 Ma) is tentatively placed at ~280 mbsf. This interpretation indicates relatively high sedimentation rates for the sandstone of Unit II (~5 cm/k.y.) (Fig. F25).

Cores from Hole U1435A were measured for physical properties on whole-round cores, split cores, and discrete samples. Thermal conductivity was measured with a needle probe in soft sediment and then with a contact probe in the sedimentary rock. The physical properties correlate with lithology and observed lithification. *P*-wave velocity increases gradually with depth over the uppermost 150 m (Fig. F24), whereas porosity measured on discrete samples decreases from 65% to 30% over the same depth range, reflecting sediment compaction. Bulk density, NGR, magnetic susceptibility, and thermal conductivity show a sharp increase near 78 mbsf at the lithostratigraphic Unit I/II boundary between the nannofossil-rich clay and sandstone (Fig. F24). A significant increase in *P*-wave velocity and thermal conductivity is observed

near 170 mbsf, which is associated with stronger lithification of the sandstone. Magnetic susceptibility and NGR values decrease with depth below 270 mbsf, which corresponds to the change from a dominance of sandstone in Unit II to mudstone in Unit III (Fig. F24).

Expedition synthesis

Operations during Expedition 349 (26 January–30 March 2014) drilled five sites in the central basin of the SCS (Figs. F1, F2, F8). Sites U1431, U1433, and U1434 were cored into the igneous basement near the fossil spreading center where seafloor spreading terminated, whereas Sites U1432 and U1435 are located proximal to the northern continent/ocean boundary where seafloor spreading started. In total, we recovered 1524 m of sediment and sedimentary rock and 78 m of igneous basement and carried out geophysical logging (triple combo and FMS-sonic tool strings) at Sites U1431 and U1433. The materials recovered and data collected were extensively examined and discussed and allow us to draw the following conclusions concerning the opening history of the SCS, the sedimentary and paleoceanographic responses to the formation of this ocean basin, the mantle source and magmatic processes forming the ocean crust basement, and the geodynamic implications for the tectonics of the region.

Opening history of the South China Sea

Determining the timing of the onset and cessation of seafloor spreading in the SCS were the primary objectives of Expedition 349. At all three sites near the fossil spreading center, we recovered deep-sea claystone near the sediment/igneous basement interface, with interflow claystone between lava flows recovered at Site U1431, and evidence from downhole measurements for an unrecovered interflow sedimentary layer at Site U1433 (Figs. F11, F19, F23). Microfossils within these claystone units provide preliminary age models for the sedimentation history, which in turn helps us to refine the oceanic crustal age models. Relatively unaltered basalt from the ocean crust near the relict spreading center was recovered and will be dated using $^{40}\text{Ar}/^{39}\text{Ar}$ methods.

The age at which seafloor spreading ceased in the East Subbasin is estimated at ~16.7–17.5 Ma based on microfossils in the interflow claystone (Fig. F10), or even slightly younger because Site U1431 is ~15 km off the ridge axis. At Site U1433, ~50 km away from the relict spreading center in the Southwest Subbasin, we recorded a biostrati-

graphic depositional age range from ~18 to 21 Ma for sediment directly above the basement (Fig. F18). Rare and poorly preserved Oligocene to earliest Miocene calcareous nannofossils were also observed in sediment attached to basalt pieces in the upper part of the basement at Site U1433, which could indicate a substantially older age for the basement; however, it is not clear if the nannofossil assemblages are reworked or in situ.

Located just 35 km north of Site U1433, Site U1434 is on the uplifted shoulder of the relict spreading center and is only ~15 km from the spreading axis in the Southwest Subbasin. Here, biostratigraphic age data indicate that the basal sedimentary sequence, lying just above the basaltic basement, is younger than 12 Ma. The uplifted shoulder forms a topographic high that may have contributed to a depositional hiatus or extremely low sedimentation rates between the emplacement of basalt and the earliest sedimentary deposits. We deduce that the cessation age of seafloor spreading in the Southwest Subbasin is somewhere between ~12 and ~21 Ma. Overall, there does not appear to be a large difference in the ages at which seafloor spreading finished between the two subbasins.

We note here that the recorded biostratigraphic age ranges are likely minimum estimates because evidence from paleomagnetic reversals in the basalt units point to prolonged eruption histories at these sites. Postcruise radiometric dating of basement basalt from these sites, plus calibration with magnetic anomalies and paleomagnetic measurements, will constrain the eruptive history of the igneous basement at these sites in the SCS.

Because of a technical error in cementing the final casing string in Hole U1432B, we were unable to reach the oceanic basement near the continent/ocean boundary at the deepest planned drill site. This prevented us from collecting basement samples to directly date the onset of seafloor spreading. However, we were able to drill into one of the most enigmatic structures in the area, a structural high standing along the continent/ocean boundary at Site U1435. Coring here recovered a sharp unconformity, with sediment above dated to ~33 Ma. The sediment above the unconformity records deep marine facies, with sediment below dominated by sandy lithologies of shallow-marine deltaic or coastal facies. The age of this deeper unit, which is composed mainly of poorly sorted sandstone and thin black silty mudstone that are both relatively rich in organic matter (~0.4–1.3 wt%), awaits further shore-based studies as it is nearly barren of calcareous and siliceous marine microfossils. Immediately above the unconformity, drilling recovered abundant recrystallized calcite and dolomite

grains, which may have been formed by extremely slow sedimentation or diagenesis. Nevertheless, we interpret this sharp unconformity as the break-up unconformity caused by the initial opening of the SCS, which places the onset of seafloor spreading at ~33 Ma.

Sedimentary and paleoceanographic responses

Silt and carbonate turbidites

All sites contain deep-marine deposits that likely formed at water depths deeper than 3 km but show significant spatial variations in postspreading sedimentary environment and provenance. Site U1431, in the East Subbasin, records the strongest evidence of hemipelagic, deep-marine gravity flow deposition of material eroded from various (distal) terrestrial sources. Both silt and nannofossil-rich/calcareous turbidites are present, with the former being much more dominant. Silt turbidites are speculated to have been triggered by volcanism and/or earthquake events associated with the Manila subduction zone and/or the Taiwan Orogeny, with sources located to the east and northeast, whereas calcareous turbidites at this site were likely transported from local sources, possibly nearby seamounts topped by carbonate platforms (Fig. F8).

In contrast, Site U1433 in the Southwest Subbasin has nannofossil-rich calcareous turbidites that are more frequent in the cores, with some beds over several meters thick. These turbidites date to the late Miocene. Here the relict spreading center, with well-developed uplifted shoulders and a relatively deep axial trough, likely acted as an effective barrier, preventing terrestrial material from being transported to this site from northerly landmasses such as southern China, the Philippines, or Taiwan. Other possible sources in Borneo or mainland Southeast Asia are more likely. The source of the carbonate turbidites is most likely within the southerly Dangerous Grounds or the Reed Bank area (Fig. F8). Local sources, such as isolated seamounts or abyssal highs, are less likely because they are quite far away from the site or in relatively deep water. Variations in carbonate flux to Site U1433 may reflect subsidence and drowning of the carbonate reefs in the Dangerous Grounds and/or sea level changes.

Variation in the character of the uppermost Pleistocene sediment between Sites U1431 and U1432 also support contrasting provenances in different parts of the basin at that time. The uppermost unit from Site U1431 is dominated by turbidite silt and sand and has frequent ash layers (Fig. F9), whereas the uppermost unit from Site U1432 is mostly clay and shows fewer ash layers over a similar age interval (Fig. F15).

At Site U1433, eight geomagnetic excursions have been identified within the Brunhes Chron due to an extremely high sedimentation rate. Based on our current knowledge, two of the excursions have not been reported in previous studies, and postcruise studies will help determine their origin. A sudden increase in sedimentation rates from 5–9 to ~20 cm/k.y. is recorded at ~1 Ma at Site U1433 (Fig. F18) and may reflect some coupling effects of enhanced terrestrial supply and intensified sea level fluctuations associated with the mid-Pleistocene climate transition.

Variations in carbonate compensation depth

Variations in the carbonate compensation depth (CCD) may have had an effect on the massive deepwater carbonate sediments recovered during the expedition, but the mechanisms are not clear. Sediment at Sites U1431 and U1433 was apparently deposited at depths greater than the modern CCD or, alternatively, may have been strongly diluted by variable clastic flux from the continents. However, at Site U1434, sediment shows much less influence from turbidity currents and is rich in calcareous nannofossils. Here, sediment was deposited at slightly shallower water depths on top of a rifted basement high (Fig. F7). The mid-ocean ridge itself was also likely shallower prior to the postspreading subsidence caused by thermal and isostatic processes, as well as the loading from emplacement of a younger seamount on top of the spreading center. Sediment recovered at Site U1434 must have been deposited above the CCD and its compositional changes may reflect CCD variations after tectonic subsidence corrections.

Pelagic brownish to reddish or yellowish brown claystone

At Sites U1431, U1433, and U1434, we recovered a series of reddish brown to yellowish brown claystone and claystone with silt directly above the basement basalt units. At Site U1431 in the East Subbasin, this lower middle Miocene (~12–14 Ma) unit is only ~5 m thick and is massive and homogeneous in the lower part and laminated with silty claystone in the upper part (Figs. F9, F11). Another similarly colored lower Miocene (~16–18 Ma) claystone ~10 m thick is interbedded within the basalt lava sequence but is less homogeneous, showing evidence for local mass wasting, and is characterized mostly by claystone with minor intraformational breccia or conglomerate containing rare basalt clasts that have well-developed reaction rims.

At Site U1433 (Figs. F17, F19) in the Southwest Subbasin, the yellowish brown claystone and claystone with silt is ~49 m thick and is dated to the middle to late Miocene (~10–18 Ma). Although mostly massive, there are intervals of graded and bioturbated

clayey siltstone and silty claystone. At both Sites U1431 and U1433, only siliceous microfossils (radiolarians) are found in this unit, most likely because calcareous microfossils have been dissolved because of deposition below the CCD. At Site U1434 (Figs. F21, F23), ~24 m of yellowish or reddish brown claystone with variable amounts of nannofossils and foraminifers lies immediately above the basaltic basement. This sequence is dated as latest middle to late Miocene in age (~10–12 Ma) and is massive and structureless, with very little evidence for current influence during sedimentation. In contrast to the other sites, this unit at Site U1434 is characterized by a lack of radiolarians, with abundant foraminifers clearly visible on the core surface.

The reddish brown to yellowish brown claystone units at Sites U1431, U1433, and U1434 were deposited at somewhat different time intervals and water depths but all immediately overlie the basaltic basement. The estimated sedimentation rates are quite low, varying from <0.5 cm/k.y. at Site U1433 (Fig. F18) to <2.0 cm/k.y. at Site U1431 (Fig. F10) and ~1.6 cm/k.y. at Site U1434 (Fig. F22). We interpret the claystone to be largely a product of deep-sea pelagic and hemipelagic sedimentation at very low sedimentation rates. The yellowish brown to dark brown color reflects enhanced oxidation of the clastic components of the sediment, which is a typical feature of regions of slow sedimentation and oxygenated bottom water, such as in many parts of the Pacific, where “red clays” are widespread (Bryant and Bennett, 1988).

Although lacking sedimentary evidence, there may have been some hydrothermal influence on the deposition or later alteration after sedimentation as a result of fluid flow and geochemical exchange. Logging in this unit at Site U1433 showed distinctly high NGR logs of potassium, uranium, and thorium over these intervals (Fig. F17). NGR values decrease slightly, whereas PEF increases with depth toward the claystone/basalt boundary and reaches peaks within the top of the basalt unit. This could reflect an increasing abundance of hematite and other oxides in the claystone. The increased concentration of such oxides could result from hydrothermal processes and fluid flow, as well as chemical exchange between the basalt and overlying sediment.

Mantle and crustal processes

Seamount volcanism and terminal processes of the extinct spreading center

Sites U1431 and U1434 are located very close to seamounts developed along and on top of the relict spreading center (Fig. F8). Well-recovered volcanoclastic sandstone and breccia may therefore reveal the history of seamount volcanism following the end of seafloor spreading in the SCS. At Site U1431, we recovered ~280 m of domi-

nantly greenish black volcanoclastic breccia and sandstone, interbedded with minor amounts of claystone (Fig. F9) dated to the late middle Miocene to early late Miocene (~8–13 Ma). This would indicate an approximately 5 m.y. period of extensive seamount volcanic activity that started nearly 4 m.y. after the cessation of seafloor spreading. Volcanoclastic breccia layers comprise much of the section, are generally thicker bedded in the upper parts of this unit, and have normal grading and erosive bases, indicative of deposition by mass wasting either as debris or grain flows.

At Site U1434, volcanoclastic sandstone and minor breccia encountered at the top of the cored interval of the hole show coarse grain sizes and poor sorting (Fig. F21) and are indicative of a relatively local provenance, most likely the adjacent seamount ~15 km to the north (Fig. F8). The age of this unit is late Miocene (younger than 9 Ma). Its upper boundary was not cored, but the penetration rates during drilling of the interval above suggest well-lithified volcanoclastic breccia and sandstone at shallower depths (<200 mbsf). Volcanoclastic material is absent from the sediment deposited between ~12 and 9 Ma in the yellowish brown claystone unit directly overlying the basement basalt. This indicates that this seamount volcanism was not active until ~9 Ma but then was active for at least 2 m.y. based on the cored section. This also puts a time period of ~7 m.y. between the cessation of the seafloor spreading and the initiation of seamount activities in the Southwest Subbasin. This is comparable to late Miocene and Pliocene seamount volcanism found in the extreme southwest of the oceanic basin (Li et al., 2013). Further postcruise sedimentological and geochemical studies will refine the ages and nature of these seamount activities and reveal how magma sources at the dying spreading center evolved through time.

Mantle evolution and magma processes revealed by oceanic basalt

We successfully cored into oceanic basement in the SCS for the first time and recovered basalt at Sites U1431, U1433, and U1434 (Figs. F11, F19, and F23). This allows for the study of the mantle evolution and magmatic processes in this young ocean basin. Despite their apparent differences in groundmass grain sizes, all basalts have variable phase assemblages of plagioclase, olivine, and clinopyroxene, typical of MORB. This interpretation is also supported by geochemical evidence (Figs. F12, F13). Coring at Site U1431 recovered massive basalt lava flows with limited evidence for pillow basalt fragments on top of the section (Fig. F11). Most basalt is aphyric and ranges in grain size from microcrystalline to fine grained, with some medium- to coarse-grained intervals occurring in the interiors of the thickest massive lava flows. These basalts were altered in a low-temperature and oxidative environment, with long in-

tervals only slight affected, providing ample material for postcruise radiometric age dating.

The Site U1433 basement section shows more abundant, small pillow basalt lava flows at the top and a few massive basalt lava flows toward the bottom of the hole (Fig. F19). This basalt ranges from sparsely to highly plagioclase-phyric. Alteration of the basalt at this site is low in intensity and typical secondary minerals represent a low-temperature and both oxidative and nonoxidative alteration assemblage. The contrast in alteration style is interpreted to indicate less active fluid activities at Site U1433 compared to the other sites, possibly caused by the cover of clayey sediment with low permeability.

The basement unit at Site U1434 is comprised of a succession of small pillow lava flows, or a thicker autobrecciated pillow lava flow, with three occurrences of hyaloclastite breccia (Fig. F23). The basalts are aphyric with glassy to microcrystalline groundmasses. The phenocrysts observed are olivine and plagioclase. The secondary mineral assemblage indicates slight to moderate alteration under low temperature, limited fluid flow, and oxidative conditions.

A total of 34 basement basalt samples were analyzed for concentrations of major and trace elements from the three sites. Almost all samples are tholeiitic basalt (Fig. F12) with extremely low K_2O (<0.3 wt%), in contrast to the much higher K_2O contents (>1.0 wt%) in the alkali basalt clasts in the younger volcanoclastic breccia. Overall, all concentrations of major elements in the basalt overlap with, but define a much smaller range than those known from compilations of Indian Ocean and Pacific Ocean MORB data, and are distinct from the OIB data fields from nearby Hainan Island and other seamounts in the SCS (Figs. F12, F13). Further postcruise geochemical studies will trace the mantle source and magmatic processes involved during and after opening of the SCS in detail.

Geophysical constraints and geodynamic implications

During the expedition, a suite of physical property measurements and color spectra scanning was completed on whole-round cores, split cores, and discrete samples. Downhole logging at the two deepest sites provided in situ constraints on the sediments and rocks, which is particularly important over unrecovered intervals. These data will aid in future geophysical interpretations of geophysical data from the SCS.

Compaction and consolidation are controlling factors for physical property variations in the sediment, as measured porosity often has good inverse correlation with other measurements, such as bulk density, *P*-wave velocity, shear strength, NGR, and thermal conductivity. Increased compaction and lithification also lead to sharp velocity contrasts and differentiate velocities of different lithologies that would otherwise be similar. These observations explain the strong seismic reflectivity of strata in the bottom unit of the sedimentary cover at Site U1433, where lithified carbonates show much higher velocities than interbedded claystone (Fig. F17).

NGR downhole logging in the igneous basement at Site U1433 helped define two interflow sedimentary layers between lava units through identification of high peaks in NGR (Fig. F17). This was particularly useful because coring did not fully recover these layers. Cores show only traces of sediment attached to basalt pieces. Gamma ray logging also helped constrain the alternating nature of carbonate with low NGR values and clay layers with high NGR values and is therefore valuable in delineating turbidites.

Magnetic susceptibility was measured on both whole-round cores and the split archive halves. In addition, remanent magnetization, which is proportional to the magnetic susceptibility, was measured with the pass-through magnetometer on all archive halves and on representative discrete samples from the working halves. We found that magnetic susceptibility of the basalt varies from $\sim 10 \times 10^{-5}$ to 2000×10^{-5} SI (Figs. F9, F17, F21). The values are much higher in relatively unaltered intervals within the more massive basalt flows compared to small lava flow units that are typically more prone to alteration. For now it remains uncertain how the entire basaltic layer of the oceanic crust behaves with respect to magnetic susceptibility, since we only recovered its very top. Overall, we did not observe major differences in the measured magnetic susceptibilities between the East and Southwest Subbasins, whereas differences in magnetic susceptibilities have been previously predicted or suspected by the contrast in surface magnetic anomalies (Li et al., 2008). Therefore, other mechanisms such as spreading rate, thermal disturbance, compositional variation, and posteruption alteration are needed to further explain the observed surface magnetic contrast.

Interplay between microbiology, fluid flow, geochemistry, and tectonics

A suite of samples collected at all of the Expedition 349 sites for microbiological analysis will allow examination of how microbial community features are linked to large-scale geological processes characteristic of the SCS that are representative of subsea-

floor settings worldwide. Samples were collected to examine the importance of ammonia-oxidizing archaea in the sediment in which archaeal biomarkers are preserved, what these archaea indicate about paleoceanographic conditions, and whether *Bdellovibrio* and similar organisms (bacterial predators) exist in the seafloor under contrasting fluid flow and heat flow conditions. These microbiological samples were collected proximal to samples for interstitial water chemistry analysis to help us reconstruct the environmental conditions where these cells are present.

We collected samples allowing us to test the hypothesis that the habitats at key interfaces, such as where volcanic ashes or turbidites overlie fine-grained sediment, provide optimum conditions for microbial colonization and survival. In addition to helping to explain the explicit conditions under which microbial life in the deep seafloor may thrive, these sites provide several different environments that link to large-scale processes such as volcanism, tectonism, and turbidity flows. There is the potential to assess how regional and continental scale events related to erosion, seafloor spreading, and subduction zones can dictate life at the smallest scale.

Samples from most sites drilled during Expedition 349 show low levels of hydrocarbon gases; however, at Sites U1432 and U1433, sediment samples showed evidence of moderately high concentrations of methane. Ethane and propane concentrations increased with depth at these sites. Evidence of higher hydrocarbon contents in this deep-sea sediment is worth additional study, and their presence suggests factors that should be considered regarding the biogeochemistry of these deep seafloor systems and how they respond to regional tectonics and depositional settings.

Preliminary scientific assessment

Expedition 349 achieved the vast majority of its scientific objectives as outlined in the *Scientific Prospectus* (Li et al., 2013). The expedition also obtained several unexpected findings that bear significant science implications. We set out with five broadly defined objectives, each of which has been addressed as follows at the five sites drilled, cored, and logged during this expedition:

1. Date the timing of the opening of different subbasins of the SCS and correlate the ages from magnetic anomalies to biostratigraphic, magnetostratigraphic, and radiometric ages.
 - a. All of the five drill sites were designed to address this objective, although only at Sites U1431, U1433, and U1434 we were able to penetrate into igneous

basement. Site U1432 was designed to determine the onset age of seafloor spreading in the East Subbasin through coring the lower half of sediment layers and the uppermost 100 m of igneous basement. Hole U1432B was drilled to 800 mbsf with casing successfully installed to address this objective; however, a technical error during the final cementing operation forced us to abandon Hole U1432B. This prevented us from coring the oldest sediment and oceanic crust to determine the initiation age of seafloor spreading in the SCS. We urge the science community to work together toward a future IODP expedition to return to Site U1432.

- b. To determine the age of termination of seafloor spreading in the East Subbasin, we drilled Site U1431 and successfully obtained continuous sediment records and relatively fresh basaltic samples in the basement. Preliminary results for the sediment ages were obtained during the expedition through biostratigraphic and paleomagnetic analyses. Radiometric dating of basalt samples will be conducted during shore-based investigation.
 - c. At Sites U1433 and U1434 we successfully obtained sediment and basalt cores that will allow us to determine the termination age of seafloor spreading in the Southwest Subbasin and compare it to the Site U1431 termination age in the East Subbasin. Preliminary biostratigraphic and paleomagnetic dating was conducted during the expedition, whereas shore-based analysis will provide radiometric ages for the basalts.
 - d. At Site U1435, which is on a structural high near the ocean/continent boundary at the northern edge of the East Subbasin, we successfully obtained cores of Oligocene sediment above and pre-Oligocene sandstone below an unconformity. The obtained samples will provide us an opportunity to investigate the transition from rifting to seafloor spreading in the SCS.
2. Measure the magnetization, mineralization, and geochemical compositions of basement rock to understand the causes of the sharp magnetic contrast between different subbasins.
- a. We successfully obtained igneous basement rock in the East Subbasin (Site U1431) and the Southwest Subbasin (Sites U1433 and U1434), allowing us to measure and fully characterize the magnetization, mineralization, and geochemical compositions of basement rock.
 - b. The results of shipboard physical property measurements and shore-based analyses of the rock samples, integrated with regional geophysical and geological studies, will advance our understanding of the causes of the sharp magnetic contrast between the two subbasins.

3. Evaluate the origin and source evolution of SCS basement rocks to better understand the formation of SCS oceanic crust and the deep mantle processes driving this formation.
 - a. We successfully obtained basalt samples near the relict seafloor spreading centers in the East Subbasin (Site U1431) and the Southwest Subbasin (Sites U1433 and U1434). Preliminary petrological and geochemical studies were made during the expedition, and shore-based geochemical and petrological studies have already been coordinated and will be carried out by multiple laboratories. These studies will help to characterize geochemical compositions of the basement rocks to evaluate the origin and source evolution of the SCS oceanic crust and mantle.
 - b. A surprising finding from the expedition is that we obtained abundant samples of volcanoclastic materials in sedimentary sections at sites near the relict spreading centers of the East and Southwest Subbasins. Shore-based analyses of these volcanoclastics will allow us to date both their eruption and sedimentation ages, as well as to characterize their geochemical compositions. Results will allow us to investigate the combined source evolution of the SCS spreading centers and the nearby seamounts, and how they interacted.
4. Evaluate the paleoceanographic and climatic responses to the opening of the SCS and develop a 3-D sedimentation and subsidence model.
 - a. We obtained several surprising results that were previously unknown to the SCS research community. For example, the sediments reveal abundant turbidite sequences at Sites U1431, U1432, and U1433, suggesting a history of turbulent sedimentary deposition events that were previously unknown.
 - b. Thick carbonate turbidites in the form of deepwater carbonates and chinks found in the Southwest Subbasin (Site U1433) are indicators of provenance, and changes in the supply of these sediments to the site has implications for the paleoceanographic and paleoclimatic evolution in that region.
 - c. We have obtained complete records of the sedimentary seamount aprons, which contain valuable information on the history of seamount eruption and associated volcanoclastic deposits in both the East Subbasin (Site U1431) and the Southwest Subbasin (Sites U1433 and U1434).
 - d. Reddish brown to yellowish brown deep-sea claystone sequences were encountered immediately above the basement at Sites U1431, U1433, and U1434. The scientific implications of these sediment layers were debated and will become clearer after shore-based investigation.

- e. Preliminary ages were obtained through biostratigraphic and paleomagnetic analyses during the expedition. The results revealed a surprisingly wide range of sedimentation rates within individual holes and between different sites. Shore-based investigation will further improve the sedimentation models, identify potential hiatuses in the sedimentary records, and determine the provenance sources of the sediments.
5. Obtain downhole geophysical logs to reveal physical properties of the sediment and the top oceanic basement and to provide a record of unrecovered intervals.
- a. We successfully conducted downhole geophysical logging in the East Subbasin (Hole U1431E) and the Southwest Subbasin (Hole U1433B). These were the first downhole geophysical data obtained in the deep basins of the SCS.
 - b. In the Southwest Subbasin, downhole logging at Hole U1433B was accomplished using the triple combo and FMS-sonic tool strings. We successfully logged a significant proportion of the basement, revealing pillow basalt flow sequences. The downhole logging results provide a record of unrecovered intervals in both the sediment and basement cores, including two possible interbedded sedimentary layers up to 1.5 m thick in the pillow basalt sequence of Hole U1433B.
 - c. In the East Subbasin, downhole logging at Hole U1431E was also accomplished using the triple combo and FMS-sonic tool strings. At this site, the downhole logging tools reached a significant depth of the sediment layers, also providing a record of unrecovered intervals in the sediment cores.

Operations

Port call

Expedition 349 began with the first line ashore in Hong Kong at China Merchants Wharf at 0848 h (UTC + 8 h) on 26 January 2014. The science party and technical staff boarded on the day of arrival. The majority of incoming cargo and off-going cargo was loaded and unloaded on 26 January. The following day, the Siem Offshore crew change was completed. All main port call activities, including preparation of the passage plan were completed. Public relation tours were given on all three days of the port call. After taking on 2200 metric tons of marine gas oil, the vessel was secured for sea with the final maintenance checks performed prior to departure.

On the morning of 29 January, two tugs and the harbor pilot arrived at our location. The last line was released from shore at 1238 h, beginning the 463 nmi voyage to Site U1431 (proposed site SCS-3G). The pilot departed the vessel at 1326 h, and the vessel began the sea passage to the first site.

Site U1431

After a 463 nmi transit from Hong Kong averaging 11.0 kt, the vessel arrived at the first expedition site. A prespud meeting was held prior to arrival to review operations at the first site. The vessel stabilized and switched from cruise mode to dynamic positioning over Site U1431 at 0640 h on 31 January 2014. The positioning beacon was then deployed at 0712 h.

The bottom-hole assembly (BHA) was picked up and assembled and then run in the hole with drill pipe to 4165.25 meters below rig floor (mbrf). All drill pipe was measured (strapped) and the internal diameter verified (drifted) during the pipe trip. There were no operational problems running the drill string into the hole. The top drive was picked up, the drill string circulated out, and a pig was pumped to remove any debris that might have accumulated in the string. The calculated precision depth recorder (PDR) depth for the site was 4252.1 mbrf, and after some consideration 4248 mbrf was selected as the shoot depth for the first core. The bit was spaced out to 4248 mbrf and the APC barrel was run in the hole with wireline and landed. Hole U1431A was spudded at 0040 h on 1 February. The mudline core recovered 9.45 m of sediment and the seafloor was calculated to be 4248.1 mbrf (4237.3 meters below sea level [mbsl]). Nonmagnetic core barrels were used for APC coring from Core 349-U1431A-1H through 3H. Hole U1431A was terminated by plan at a final depth of 4276.5 mbrf (28.4 mbsf). At the conclusion of coring, the drill string was pulled from the hole. The seafloor was cleared at 0345 h on 1 February, ending Hole U1431A. Three piston cores were taken over a 28.4 m interval, with a total recovery of 28.39 m of core. Overall core recovery for Hole U1431A was 100.0%. The total time spent on Hole U1431A was 21.0 h.

After the bit cleared the seafloor, the vessel was offset 20 m east of Hole U1431A. As part of the planned microbiological analyses, the PFT pump was turned on and the drill string displaced with contamination testing fluid. The pump remained on for the remainder of coring operations in Hole U1431B. The bit was spaced out to 4245.5 mbrf in an attempt to recover ~7.0 m on the mudline core. The mudline core recovery was 7.5 m. The seafloor depth was calculated to be 4247.5 mbrf (4236.7 mbsl). Hole

U1431B was spudded at 0420 h on 1 February. Nonmagnetic core barrels were used for APC coring from Core 349-U1431B-1H through 2H to a final depth of 17.0 mbsf. At the conclusion of coring, the drill string was pulled from the hole. The bit cleared the seafloor at 0620 h, ending Hole U1431B. Two piston cores were taken over a 17.0 m interval in Hole U1431B, with a total recovery of 17.16 m of core (100.9%). The total time spent on Hole U1431B was 2.58 h.

After the bit cleared the seafloor, the vessel was offset 20 m south of Hole U1431B. The bit was spaced out to 4245.5 mbrf. The mudline core recovery was 4.7 m, but the core liner was split. The seafloor depth was calculated to be 4250.3 mbrf (4239.5 mbsl). Hole U1431C was spudded at 0700 h on 1 February. Nonmagnetic core barrels were used for APC coring from Core 349-U1431C-1H through 2H to a final depth of 14.2 mbsf. The PFT pump remained running during coring in Hole U1431C. Hole U1431C was terminated when we determined that the mudline core would not meet sampling requirements. At the conclusion of coring, the drill string was pulled from the hole. The bit cleared the seafloor at 0852 h on 1 February, ending Hole U1431C. A total of two piston cores were taken over a 14.2 m interval in Hole U1431C, with a total recovery of 14.45 m of core (101.8%). The total time spent on Hole U1431C was 2.42 h.

After the bit cleared the seafloor, the vessel was offset 20 m west of Hole U1431C. The bit was spaced out to 4245.0 mbrf. The mudline core recovery was 3.22 m. The seafloor depth was calculated to be 4251.3 mbrf (4240.5 mbsl). Hole U1431D was spudded at 0925 h on 1 February. Nonmagnetic core barrels were used for APC coring from Core 349-U1431D-1H through 19H to a depth of 168.9 mbsf. Temperature measurements were taken with the APCT-3 on Cores 4H, 7H, 10H, and 13H with good results. After six partial strokes of the APC, the coring system was switched over to the XCB. XCB coring continued from Core 20X through 67X at a final depth of 4868.3 mbrf (617.0 mbsf). The PFT pumps remained on through Core 23X. While cutting Core 67X, the rate of penetration dropped severely and the core barrel was retrieved after a 2.7 m advance. While recovering the core barrel at the surface, we discovered that the cutting shoe, core catcher sub assembly, and the break off sub were missing from the XCB coring assembly. With ~1 m of junk metal remaining in the hole, we decided to pull out of the hole, offset, and begin a new hole with the RCB coring system. The top drive was then set back and the bit tripped from the hole, clearing the seafloor at 0355 h on 6 February. The bit was then tripped to the surface and cleared the rig floor at 1415 h, ending Hole U1431D. A total of 19 APC cores were taken over a 168.9 m interval in Hole U1431D, with a total recovery of 165.61 m of core. The XCB was used

48 times over an interval of 448.1 m, recovering 236.50 m of core. Overall core recovery for Hole U1431D was 402.11 m over an interval of 617.0 m (65.2%). The total time spent on Hole U1431D was 125.5 h.

After offsetting the vessel 20 m west of Hole U1431D, an RCB BHA was assembled with a new RCB C-4 bit. The BHA was run in the hole to 4163.22 mbrf, and the rig crew performed a slip and cut of 115 ft of drilling line. The remainder of the drill pipe was then run in the hole, and at 4221.46 mbrf, the top drive was picked up and then spaced out to spud Hole U1431E. A center bit was dropped and pumped to land out in the bit. Hole U1431E was spudded at 0650 h on 7 February. The seafloor depth for the hole was determined to be 4251.3 mbrf, calculated using an offset depth from Hole U1431D. Hole U1431E was advanced by drilling without coring from the seafloor to 507.0 mbsf. The center bit was pulled from the BHA by wireline and a core barrel was dropped to take a spot core (349-U1431E-2R) from 507.0 mbsf. After cutting the core without recovery, the center bit was dropped and drilling continued from 516.7 to 575.0 mbsf. The center bit was then retrieved by wireline, a core barrel dropped, and continuous coring started with Core 349-U1431E-4R from 575.0 mbsf. The next three cores (4R to 6R [575.0–603.3 mbsf]) did not recover any material. Coring continued with good recovery from Core 7R through 36R (603.3–894.3 mbsf). Core 36R was the first to recover basalt, with several small pieces present in the core catcher. Coring then continued into acoustic basement from Core 37R to 47R (894.3–991.4 mbsf). Penetration rates varied from 1.62 to 4.66 m/h over this interval, except for a sediment section in Core 45R that cored more quickly than the basalt. Microspheres were deployed in the RCB core catcher for Cores 12R through 43R.

With torque becoming higher and erratic, we decided to make a wiper trip to allow any debris collecting around the drill collars to fall into the hole. After pumping a sweep from the bottom of the hole, the drill string was pulled back to 862.95 mbsf. The bit was then run back to bottom, tagging fill material at 972.65 mbsf. With 18.75 m of fill in the bottom of the hole, a core barrel was dropped and the bit worked back to bottom with circulation and rotation without difficulty. The core barrel was retrieved with 0.65 m of material that was curated as ghost Core 48G. Another 50 bbl high-viscosity mud sweep was pumped after reaching 991.4 mbsf, and then another core barrel dropped. Coring continued from 991.4 mbsf to the final depth of 1008.8 mbsf (Cores 49R and 50R). Just prior to finishing coring, a 50 bbl high-viscosity mud sweep was pumped to clean and condition the hole for logging. The total depth of Hole U1431E was reached at 0740 h on 14 February. After reaching total depth, the final core was pulled to the surface and laid out. A total of 47 RCB cores were collected

in Hole U1431E over a 443.5 m interval, with a total recovery of 242.35 m of core (54.8% recovery, excluding the single 0.65 m long ghost core).

At the completion of coring, the rotary shifting tool (RST) was deployed to activate the mechanical bit release and the bit was dropped in the bottom of the hole. The RST was retrieved, and the other RST run in the hole to shift the sleeve back into the closed position. The end of the drill pipe was then raised to a depth of 4900.08 mbrf (648.78 mbsf) with the top drive in place. The hole was displaced from 648 mbsf to the seafloor with 11.4 ppg high-viscosity mud designed to improve logging conditions. The top drive was set back and the end of the pipe raised to 4400.9 mbrf (149.62 mbsf) for logging operations. After holding a logging safety meeting for rig floor personnel, the triple combo tool string was rigged up and run in the hole, reaching 463.7 m WSF on 15 February. The hole was then logged up, a short repeat pass recorded, and the tool string was then pulled to surface and rigged down. After rigging down the triple combo tool string, the FMS-sonic tool string was rigged up and deployed to 444 m WSF. Two full passes were made with the tool string, and then the tool string was pulled to the surface and rigged down at 1915 h on 15 February. The drill string was then tripped out of the hole from 4900.9 mbrf (149.6 mbsf) and cleared the seafloor at 2010 h. While pulling out of the hole with the drill string, the starboard conveyor on the pipe racker had a hydraulic failure. The hydraulic block in the derrickman's control booth was repaired, but 1.5 h was recorded as operational downtime. The rest of the trip out of the hole was uneventful and the bit cleared the rig floor at 0555 h. The rig floor was secured for transit at 0600 h on 16 February, ending operations at Site U1431. Total time spent in Hole U1431E was 231.75 h.

Site U1432

The vessel arrived at Site U1432 (proposed Site SCS-6A) at 2337 h on 16 February 2014 after a 181 nmi transit at an average speed of 10.3 kt. An acoustic positioning beacon was deployed at 2352 h.

The primary objectives at this site required deep penetration, so the plan was to install a reentry cone and casing system, with the first step in this process to conduct a jet-in test to determine the length of 20 inch casing that should be attached to the reentry cone. The BHA for the jet-in test was assembled with an 18½ inch tricore bit and run to just above the seafloor. The vessel was offset 20 m south of the original coordinates for Site U1432 when the acoustic beacon landed within 6 m of the coordinates. The subsea camera and frame (VIT) was deployed to observe the bit tag the

seafloor (3840.0 mbrf). After picking up the top drive and spacing out the bit, Hole U1432A was spudded at 1525 h on 17 February. The BHA with the 18½ inch tricone bit was jetted into the formation 62.0 m over a 3 h period. The drill string was then pulled clear of the seafloor and the top drive set back. The remainder of the drill string was tripped out of the hole and the bit cleared the rotary table at 0205 h on 18 February, ending Hole U1432A. The total time spent in Hole U1432A was 26.5 h.

Based on the results from the jet-in test, a five-joint, 57.12 m long 20 inch casing string was selected. The 20 inch casing shoe joint was cut off to length and a Texas Pattern casing shoe welded on the end of the shoe joint. The remainder of the reentry cone and base were put together, moved into the moonpool, and positioned underneath the rotary table. The casing was run through the rotary table and the reentry cone in the moonpool. Each casing connection was tack welded to prevent the casing from backing out. The third joint of casing had to be replaced because of a damaged thread on the pin. The casing hanger and casing pup joint were picked up and attached to the top of the casing string. The Dril-Quip CADA (casing) running tool was made up into the casing hanger on the rig floor. The casing was then lowered through the rig floor, into the moonpool, and through the reentry cone. The casing hanger was landed into the landing ring inside the reentry cone and snapped into place inside the cone. The landing joint was lowered to release the weight of the casing. The casing running tool was rotated 3.75 turns to the right and the casing released. A BHA (casing stinger) with an 18½ inch bit, bit sub, and six drill collars was lowered into the reentry cone and casing. The casing running tool was inserted into this BHA and latched into the casing hanger in the reentry cone and secured by rotating the upper BHA 3.75 turns to the left. The moonpool doors were opened and the reentry system with the 20 inch casing was lowered through the moonpool to 3819 mbrf. The top drive was picked up and spaced out to jet-in the 20 inch casing. Hole U1432B was spudded at 0635 h on 19 February. Jetting continued as the casing was slowly lowered. Seven hours later the reentry system landed on the seafloor. The subsea camera was lowered to assist in releasing the casing. After attempting to release the casing for 2.5 h, the casing tool finally released after the vessel was offset from the original position in order to get the casing running tool to rotate. The rotation required to release the tool was observed clearly on the new subsea camera system. The camera was then pulled back to the surface and secured. The drill sting was tripped back to the surface, and the BHA was set back in the derrick. During the trip out of the hole, the rig was secured to slip and cut 115 ft of drilling line as per the slip and cut program.

An HOC underreamer with an 11³/₄ inch closed diameter was made up to the 18¹/₂ inch tricone bit and bit sub. The underreamer was set to open up the 18¹/₂ inch hole to 22 inches in diameter. The underreamer and bit were lowered into the moonpool, the top drive picked up, and the underreamer function tested. The top drive was then set back, and the remainder of the BHA assembled and run in the hole to 3828.7 mbrf. During the trip, the subsea camera system was deployed. The bit was spaced out for reentry and the vessel was positioned using the subsea camera system. Hole U1432B was reentered at 2005 h on 20 February. After reentering the hole, the top drive was picked up and the drill string washed down to the casing shoe at 57.1 mbsf. After carefully washing down below the casing shoe so that the underreamer was below the base of the 20 inch casing, the pump rate and speed (rotations per minute [rpm]) were optimized for drilling a 22 inch hole below the 20 inch casing. Drilling continued to 4000.0 mbrf (160.0 mbsf). Drilling was suspended at 0610 h on 21 February when weather conditions worsened and the high heave of the vessel began to severely affect the weight on the bit and underreamer. The bit was tripped back inside the 20 inch casing and the top drive set back. The drill string was then tripped back to the surface, clearing the seafloor at 0835 h on 21 February, and finally clearing the rig floor at 1620 h. The underreamer and bit were inspected and laid out, and the BHA racked back into the derrick. While waiting on the weather to subside, the vessel offset 40 m south to be well away from the reentry cone for Hole U1432B. An APC hole (U1432C) was cored and, after coring to 110.0 mbsf, the weather appeared to have subsided sufficiently for another attempt at drilling out the 22 inch hole for the 16 inch casing.

After pulling out of Hole U1432B, the upper guide horn was picked up from the drill collar rack, lifted to the rig floor, and reinstalled below the rotary table. An APC/XCB BHA was made up while the vessel was offset 40 m south of Hole U1432B. The drill string was then tripped toward the seafloor. After completing the pipe trip to just above the seafloor, the top drive was picked up and spaced out, and Hole U1432C was spudded at 0555 h on 22 February. The first coring attempt with the bit at 3835 mbrf did not recover any core. The bit was then lowered to 3838.5 mbrf and the next coring attempt recovered a mudline core of 7.95 m of sediment. This core length was used to calculate the seafloor depth at 3840.1 mbrf (3829.1 mbsl). Nonmagnetic core barrels were used for the APC from Core 329-U1432C-1H through 12H to a final depth of 110.0 mbsf. PFT fluid was displaced into the drill string prior to spudding the hole and was pumped continuously during Hole U1432C. Temperature measurements were taken with the APCT-3 on Cores 5H, 7H, 9H, and 11H with good results. The hole was terminated when weather conditions improved sufficiently to return to Hole U1432B. The bit was tripped to the surface and cleared the rig floor at 0735 h, ending

Hole U1432C. A total of 12 APC cores were taken over a 110.0 m interval in Hole U1432C, recovering 88.74 m of core (80.7% recovery). The total time spent in Hole U1432C was 39.25 h.

After tripping out of Hole U1432C, the BHA was set back in the derrick and the upper guide horn removed and laid out on the drill collar racks. We then returned to Hole U1432B to continue drilling the 22 inch hole for the 16 inch casing. As before, an HOC underreamer with an 11¾ inch closed diameter was made up to the 18½ inch tricone bit and bit sub. The underreamer was set to open up the 18½ inch hole to a 22 inch diameter. The underreamer and bit were lowered into the moonpool, the top drive picked up, and the underreamer function tested. The top drive was set back, and the remainder of the BHA assembled and run in the hole to 3828.7 mbrf. During the trip, the subsea camera system was deployed. The bit was spaced out for reentry and Hole U1432B reentered at 1944 h on 23 February. The subsea camera system was pulled back to surface while the top drive was picked up. The bit and underreamer were run in the hole to 160.0 mbsf and drilling continued from 4000 to 4090.0 mbrf (160.0–250.0 mbsf). The depth of Hole U1432B reached 250 mbsf at 0640 h on 24 February. The hole was conditioned and displaced with 379 bbl of 10.5 ppg mud. The drill string was tripped back to the surface and cleared the rig floor at 2120 h. During the trip out of the hole, the rig was secured to slip and cut 115 ft of drilling line as per the slip and cut program.

The drill floor was rigged up to run 16 inch casing. We assembled 240.85 m of 16 inch casing, including a Dril-Quip casing hanger. The casing was landed on the moonpool doors with the casing running tool, which was then released and pulled back through the rig floor. The 240.77 m casing stinger was made up to the bottom of the casing hanger running tool and lowered through the 16 inch casing in the moonpool. The casing hanger running tool with the casing stinger below was latched into the 16 inch casing hanger, with two control length drill collars and a tapered drill collar above the casing running tool. The entire casing string plus running tools were lowered to 3827.4 mbrf while filling the drill pipe with water every 20 stands. The subsea camera system was installed and lowered to reenter Hole U1432B. After 15 min of maneuvering the vessel, we reentered Hole U1432B at 0500 h on 26 February. The camera system was pulled back to the surface while the top drive was picked up. The casing was lowered into the 22 inch hole and washed down to ~200 mbsf. The subsea camera system was again lowered to assist in releasing the casing running tool from the casing. As the camera system neared the seafloor, the video feed from the subsea camera was lost. The camera system was pulled back to the surface for repair (water had intruded

the pan and tilt unit, causing a power overload in the system). The casing was washed in to 240.9 mbsf and landed in the reentry cone. The casing running tool was rotated clockwise 3.75 turns and released from the casing hanger. The BHA, including the internal casing stinger, was pulled back ~11 m and the top drive set back. The cementing assembly was rigged up, the lines were pressure tested, and ~20 bbl of cement mixed to 15 ppg was pumped downhole. The cement was displaced with seawater and positioned to balance at the casing shoe to an estimated height of 17 m above the casing shoe (both inside and outside the casing). The cementing equipment was rigged down and the drill string pulled back to 161.9 mbsf. The circulating head was connected and the drill string flushed with twice the drill string capacity with seawater. The remainder of the drill string was pulled from the hole, clearing the seafloor at 2140 h on 26 February and finally clearing the rig floor at 0400 h on 27 February. The BHA components were secured and the running tool was detorqued.

A new 14 $\frac{3}{4}$ inch bit and four stands of drill collars were made up and run in the hole with drill pipe while filling with water at 20-stand intervals. When the bit was at 3823.3 mbrf, the subsea camera system was lowered to allow reentry. Hole U1432B was reentered at 1655 h on 27 February, and the camera pulled back to the surface. After securing the camera system, the drill string was run in the hole until the top of the cement was tagged at 4069.0 mbrf (229 mbsf). The cement was drilled out from 4069.0 to 4083.0 mbrf (229.0–243.0 mbsf). After washing down to total depth (250.0 mbsf), new 14 $\frac{3}{4}$ inch hole was drilled from 4090.0 to 4640.0 mbrf (250.0–800.0 mbsf). After reaching 800.0 mbsf, the hole was swept clean with high-viscosity mud. After setting back the top drive, the drill string was pulled back to the surface. The bit cleared the rotary table at 1120 h on 1 March. The 10 $\frac{3}{4}$ inch casing stinger components were made up and the underreamer arms were set to 12 $\frac{3}{4}$ inches. The top drive was then picked up and the mud motor and underreamer tested. After the test was successfully completed, they were racked back in the derrick. After assembling all the casing stinger components, a slip and cut of the drilling line was completed.

The rig floor was then prepared for running 10 $\frac{3}{4}$ inch casing, and 787.06 m of casing with a 10 $\frac{3}{4}$ inch casing hanger were made up. The casing was lowered into the moon-pool and secured with a casing elevator on the prepared landing platform. The buoyant weight of the casing string was 70,000 lb. The running tool was released from the casing and pulled back to the rig floor. It was then made up to the bottom of a drill collar stand and racked back in the derrick. The casing stinger with the bit, underreamer, and mud motor were then run inside the casing. Also included in the stinger were three stands of drill collars and 24 stands of drill pipe. The bit and underreamer

were positioned just below the bottom of the casing after the running tool was landed and made up to the casing. The casing was run to the seafloor with drill pipe and the subsea camera system deployed to assist with the reentry at the seafloor. Hole U1432B was reentered at 0242 h on 3 March. The camera system was pulled back to the surface and set back into the storage position on the moonpool doors. The casing was run in the hole with drill pipe to 223.5 mbsf. The top drive was picked up and the casing lowered to 244.0 mbsf. The casing was washed to the bottom while pumping 530 gpm. At 530 gpm, the mud motor was turning the bit at 80–85 rpm with the under-reamer arms extended to clear a 12¾ inch hole in front of the casing. The casing was steadily lowered until it was landed and released at 1745 h on 3 March. The top drive was set back and the drill string tripped from the hole, clearing the seafloor at 2045 h, and then clearing the rotary table at 0915 h on 4 March. The casing stinger components were flushed with freshwater and either laid out or, in the case of the drill collars, racked back in the derrick.

After successfully running the 10¾ inch casing, a cementing stinger was assembled. The stinger consisted of a reentry/cleanout bit, a bit sub, a stand of drill collars, 24 stands of 5 inch drill pipe, F-cup tester, another two drill collars, a tapered drill collar, and two stands of 5½ inch transition drill pipe. The entire assembly was made up and run in the hole with drill pipe to just above the seafloor while stopping every 20 stands to fill the drill pipe with water. The subsea camera system was deployed to just above the seafloor and Hole U1432B reentered at 0344 h on 5 March. The camera system was pulled back to the surface and secured. The bit was run in the hole to 767 mbsf, 20 m above the 10¾ inch casing shoe. The F-cup tester was spaced out so that it was at 42 mbsf, inside the 16 inch casing. The circulating head was made up to the top of the drill string and the mud pumps were brought up to 60 spm to verify circulation up the annulus between the hole and the casing. After establishing circulation, the cement pump was used to pump 10 bbl of freshwater ahead of the cement slurry. Fourteen barrels of 15.5 ppg cement were then mixed and pumped downhole, followed by another 10 bbl of freshwater. This was displaced down the drill string with 263 bbl of saltwater using the mud pumps. After displacing the cement, the circulating head was removed and the driller attempted to pull out of the hole. He immediately noticed a steadily increasing overpull as he tried to pull out of the hole. After pulling up enough to remove two singles of drill pipe, we were unable to raise the drill string any further. It now appears that the formation collapsed around the 10¾ inch casing string, preventing circulation up the open hole annulus and outside the casing. Instead, the circulation path was up through the 10¾ casing, bypassing the cup tester. The elevated temperatures at 700 mbsf (~65°–70°C) accelerated the hardening of the

cement. The drill string was worked for the next 9 h using combinations of overpull, torque, and pump pressure in an effort to free the drill string. At that point, we rigged up to sever the drill string. The drill string severing charge was lowered to just above the cup tester, which has a 1.5 inch internal diameter. The charge was detonated at 0430 h on 6 March 2014; however, there was no loss of overpull on the pipe. The wireline was pulled out of the hole and the severing tool cleared the rig floor at 0808 h. The drill pipe was worked with a maximum of 100,000 lb of overpull for ~1 h. The elevators were then lowered back to the elevator stool while the rig was offset 200 m. The top drive was picked up and the drill pipe was picked up slowly while moving the rig back to the original location. The pipe was worked free with a maximum of 400 A of torque and 40,000 lb of overpull. The end of pipe cleared the casing hanger at 1105 h. The top drive was set back and the drill string pulled from the hole. The end of pipe cleared the rotary table at 1830 h. The acoustic positioning beacon was recovered while tripping drill pipe. The upper guide horn was reinstalled, the rig floor secured for transit, and the thrusters raised. The vessel switched to transit mode at 2036 h on 6 March, ending Site U1432. The total time spent on Hole U1432B was 363.25 h (15.1 days).

Site U1433

After a 334 nmi transit lasting 29.9 h, the vessel arrived at Site U1433 (proposed Site SCS-4B) and switched into dynamic positioning mode at 0230 h on 8 March 2014. At 0255 h, an acoustic positioning beacon was deployed. An APC/XCB BHA was assembled and run in the hole to 800.4 mbrf. At 0520 h, a tool joint parted on the twenty-fourth stand of drill pipe, just after picking up the drill string and just prior to unlatching the lower set of elevators. The load cell weight at the time of the incident was recorded at ~200,000 lb. The entire weight of the drill string dropped ~18 inches and landed in the lower set of elevators, which were resting on top of the dual elevator stool. The pin on the top single of drill pipe had parted, leaving one single hanging from the upper set of elevators and two singles sticking up from on top of the lower set of elevators. The stand was then laid out to the V-door. The broken pipe was visually inspected and photographed. As a precaution, the twenty-third stand was also disassembled and laid out. The bottom set of elevators was removed from use and replaced with a reconditioned set of elevators. After clearing the rig floor, the trip in the hole resumed. When the bit was at 1147.8 mbrf, another tool joint failed when the driller was picking up the thirty-sixth stand from the pipe racker. This time, one single fell back into the trough of the pipe racker still attached to the skate, and a double

remained connected to the elevators on the bales connected to the main block. After the second tool joint failure, we decided to discontinue using any of the 5 inch drill pipe that had been used in the stuck pipe incident at the previous site. Investigations continue into the root cause of the pipe failure. Documentation of the stuck pipe event was collected for analysis. The failed tool joints were prepared with care for shipment to a laboratory for detailed metallurgical analysis and were shipped from Keelung, Taiwan, at the end of the expedition. The drill string was tripped back to the BHA and all suspect drill pipe was removed from use and stored in the port pipe racker. We picked up 201 joints of new 5 inch drill pipe from the riser hold. The new drill pipe was strapped and drifted as it was assembled and lowered toward the sea-floor. After completing assembly of the new pipe, the remaining 37 stands from the starboard 5 inch pipe racker were picked up and run in the hole. The total number of 5 inch pipe stands available was then 104 stands. The remaining 101 stands of suspect drill pipe in the port pipe racker need to be inspected before they can be put back in service.

After running in the hole with 104 stands of 5 inch drill pipe, the 5½ inch drill pipe was picked up until the bit reached 4372.9 mbrf. The trip in the hole was stopped at 3587.0 mbrf to perform a slip and cut of the drilling line. The PDR recorded an estimated depth of 4394.4 mbrf for the seafloor. The top drive was picked up and spaced out to 4390 mbrf. The nonmagnetic core barrels were dressed with liners, the FlexIT core orientation tool was inserted, and a core barrel run down and landed. Hole U1433A was spudded at 1000 h on 9 March. The mudline core recovered 8.9 m of sediment and the seafloor was calculated to be 4390.6 mbrf (4379.4 mbsl). Coring continued without issue through Core 349-U1433A-16H (151.4 mbsf). While running in the hole with a core barrel, the bridge informed the driller that a fishing boat was drifting toward the vessel's location. At 0540 h on 10 March, the Captain ordered the driller to suspend operations. The core barrel was retrieved, and the driller began tripping out of the hole with the top drive. At 99.1 mbsf, the driller was instructed to standby. After the threat disappeared, the drill string was tripped back to bottom and coring continued to Core 20H (188.3 mbsf). After four consecutive partial strokes of the APC, refusal was called at 188.3 mbsf. Orientation was measured on all APC cores. Temperature measurements were taken with the APCT-3 on Cores 4H, 7H, 10H, and 13H with good results. PFT fluid was used on Cores 18H through 20H. The bit was tripped to the surface and cleared the rig floor at 0325 h on 11 March, ending Hole U1433A. A total of 20 APC cores were taken over a 188.3 m interval in Hole U1433A, recovering 168.79 m of core (89.6%). The total time spent on Hole U1433A was 73.0 h.

After offsetting the vessel 20 m east of Hole U1433A, an RCB BHA was assembled with a new RCB C-4 bit. Three additional drill collars had to be picked up from the drill collar racks to replace the ones lost in Hole U1432B. The core barrels were spaced out at the surface and the 172.07 m BHA assembled and run in the hole to 4350.3 mbrf. The top drive was then picked up and spaced out to spud Hole U1433B. A center bit was dropped and pumped to land out in the bit. Hole U1433B was spudded at 1515 h on 11 March. The seafloor depth for the hole was 4390.6 mbrf (4379.4 mbsl), determined by using an offset depth from Hole U1433A. Hole U1433B was advanced by drilling without coring from the seafloor to 186.1 mbsf. The center bit was pulled from the BHA by wireline and a core barrel dropped to start continuous RCB coring from Core 349-U1433B-2R through 75R to a total depth of 5249.1 mbrf (858.5 mbsf). The PFT pumps were turned on during the drilldown period, and PFT fluid was pumped through Core 26R (426.9 mbsf). Microspheres were added to the RCB core catcher for Cores 56R to 75R. Core 65R encountered basalt at 786.3 mbsf. Coring continued into acoustic basement from Core 65R to Core 75R (858.5 mbsf), with half-cores collected from Core 67R to the total depth in an attempt to improve recovery. Penetration rates varied from 0.9 to 3.9 m/h over the basement interval. The total depth of Hole U1433B was reached at 2100 h on 17 March and the final core was pulled to the surface and laid out. At the completion of coring Hole U1433B, 74 RCB cores had been cut over a 672.4 m interval, recovering 443.04 m of core (65.9%).

After pumping a 50 bbl high-viscosity mud sweep, a short wiper trip was made from total depth to just above the basement contact (786.3 mbsf) with the top drive installed. While tripping back to bottom, the hole had to be reamed from 847.4 to 858.5 mbsf. We then pumped another 50 bbl mud sweep to further clean the hole. The RST was then picked up and run into the hole with a coring line to release the bit for logging. An attempt was made to engage the sleeve in the mechanical bit release. After being unable to engage the shifting sleeve, the RST was pulled back to surface. Examination at the surface revealed the RST did not come back with the core line sinker bars. An overshot (fishing tool) was made up and run in the hole to fish for the RST. After securing the RST, the mechanical bit release sleeve was engaged and the bit was dropped from the drill string. The RST also dropped off the fishing tool on release, leaving the RST in the bottom of the hole. The core line was pulled back to surface and the RST to shift the sleeve back into the original position was deployed. With the bit released, the drill string was raised to 5196.3 mbrf (805.7 mbsf) with the top drive. The top drive was then set back and the drill string raised to 5079.7 mbrf (689.1 mbsf). The circulating head was picked up and the hole displaced from 689.1 mbsf to the seafloor with 10.5 ppg high-viscosity mud designed to improve logging conditions. The

drill string was then raised up and spaced out so that the end of the pipe was at 4490.7 mbrf (100.1 mbsf) for logging operations.

After holding a logging safety meeting for rig floor personnel, the triple combo tool string was rigged up and deployed. The tool string reached a total depth of 845.4 m WSF on 18 March. The hole was then logged up and the tool string pulled to surface and rigged down. After rigging down the triple combo tool string, the FMS-sonic tool string was rigged up and deployed to a depth of 842.4 m WSF. The basement section of the hole was logged five times with three passes with the calipers open. On the last pass, the tool become stuck but was eventually worked free. The rest of the open hole was logged up to the end of the drill pipe and the tool string was then pulled to the surface and rigged down. All logging equipment was rigged down by 1300 h on 19 March. The drill string was pulled from the hole and the BHA set back and secured for transit at 2300 h on 19 March, ending Site U1433. Total time spent in Hole U1433B was 211.5 h.

Site U1434

After an 18 nmi transit lasting 2 h, the vessel arrived at Site U1434 (proposed Site SCS-4E) and switched into dynamic positioning mode at 0048 h on 20 March 2014. At 0110 h, an acoustic positioning beacon was deployed. An RCB BHA was assembled with a new RCB C-7 bit. The core barrels were spaced out at the surface and the 172.07 m BHA assembled. The BHA was lowered to 4000.9 mbrf and the top drive picked up and spaced out to 4020.0 mbrf to spud Hole U1434A. A center bit was dropped and pumped down the drill string to land out in the bit. Hole U1434A was spudded at 1215 h on 20 March. The estimated depth of the seafloor was determined to be 4020.4 mbrf using the PDR. The final seafloor depth for the hole was 4020.4 mbrf (4009.0 mbsl), which was determined by tagging the seafloor with the drill bit. Hole U1434A was advanced by drilling without coring from the seafloor to 4217.4 mbrf (197.0 mbsf) over a 10 h period. The center bit was pulled and a core barrel dropped to start continuous RCB coring from Core 349-U1434A-2R. Coring continued through Core 15R to a depth of 4332.9 mbrf (312.5 mbsf). Microspheres were deployed in each RCB core catcher for the duration of RCB coring. We encountered the sediment/basement interface in Core 10R, with the formation change at ~280 mbsf. Coring continued into acoustic basement from Core 10R through 15R to a total depth of 4332.9 mbrf (312.5 mbsf). Half cores were started with Core 12R and continued to total depth. Penetration rates varied from 1.57 to 5.76 m/h over the basement interval. Coring was finally halted because of poor core recovery coupled with high torque and poor

coring conditions. The total depth of Hole U1434A was reached at 0925 h on 22 March. After reaching total depth, the final core was pulled to the surface and laid out. At the completion of coring Hole U1434A, 14 RCB cores had been cut over a 115.5 m interval, recovering 26.43 m of core (22.9%).

After retrieving the final core, we attempted to pull the drill string from the hole; however, the high torque and high overpull made this impossible. After 1.5 h of working the pipe with a combination of high torque (900 A), overpull, and constant pumping action, the drill string came free and was pulled out of the hole with the top drive to 4117.4 mbrf (97.0 mbsf). The top drive was then set back and the drill string was tripped to the surface. The bit cleared the seafloor at 1500 h, and then cleared the rotary table at 2300 h. After securing the rig floor for transit and pulling the hydrophones and thrusters, the vessel switched to cruise mode and began the transit to Site U1435 at 2348 h on 22 March. Total time spent on Hole U1434A was 71.0 h.

Site U1435

After a 336 nmi transit lasting 39.65 h, the vessel arrived at Site U1435 (proposed Site SCS-6C) and switched into dynamic positioning mode at 1524 h on 24 March 2014. At 2045 h, an acoustic positioning beacon was deployed. An RCB BHA was assembled with a new RCB C-7 bit. The core barrels were spaced out at the surface and the 172.07 m BHA assembled. The BHA was then run in the hole to 3214.9 mbrf and the top drive picked up and spaced out to 3261.6 mbrf to spud Hole U1435A. While lowering the drill pipe, we conducted a sonar survey with the 3.5 kHz array sonar to select a hole location to maximize sediment thickness. Hole U1435A was spudded at 0035 h on 25 March. The estimated depth of the seafloor was 3261.6 mbrf using the PDR. The final seafloor depth for the hole was 3264.0 mbrf (3252.5 mbsl), which was determined by tagging the seafloor with the drill bit. We advanced Hole U1435A by coring from the seafloor to 3564.0 mbrf (300.0 mbsf). Microspheres were deployed in each RCB core catcher from Core 349-U1435A-5R to the total depth of the hole. Coring continued to Core 349-U1435A-32R (300 mbsf), when operational time for the expedition expired. Penetration rates varied from 2.8 to 58.2 m/h over the cored interval. The total depth of Hole U1435A was reached at 0730 h on 27 March. After reaching total depth, the final core was pulled to the surface and laid out. At the completion of coring Hole U1435A, 32 RCB cores had been cut over a 300.0 m interval, recovering 171.37 m of core (57.1%).

After reaching total depth and laying out the last core, the drill string was pulled out of the hole with the top drive to 3535.1 mbrf (271.1 mbsf). The drilling knobbies were laid out, the top drive set back, and the drill string tripped to the surface. The bit cleared the seafloor at 1020 h, and then cleared the rotary table at 1835 h. After securing the rig floor for transit and pulling the hydrophones and thrusters, the vessel switched to cruise mode and began the transit to Keelung, Taiwan, at 1900 h on 27 March. Total time spent on Hole U1435A was 75.5 h. Expedition 349 officially ended with the first line ashore in Keelung at 0710 h on 30 March.

References

- Barckhausen, U., Engels, M., Franke, D., Ladage, S., and Pubellier, M., in press. Evolution of the South China Sea: revised ages for breakup and seafloor spreading. *Marine and Petroleum Geology*. <http://dx.doi.org/10.1016/j.marpetgeo.2014.02.022>
- Barckhausen, U., and Roeser, H.A., 2004. Seafloor spreading anomalies in the South China Sea revisited. In Clift, P., Wang, P., Kuhnt, W., and Hayes, D. (Eds.), *Continent-Ocean Interactions within East Asian Marginal Seas*. Geophysical Monograph, 149:121–125. <http://dx.doi.org/10.1029/149GM07>
- Bleil, U., and Petersen, N., 1983. Variations in magnetization intensity and low-temperature titanomagnetite oxidation of ocean floor basalts. *Nature*, 301(5899):384–388. <http://dx.doi.org/10.1038/301384a0>
- Braitenberg, C., Wienecke, S., and Wang, Y., 2006. Basement structures from satellite-derived gravity field: South China Sea ridge. *Journal of Geophysical Research: Solid Earth*, 111(B5):B05407. <http://dx.doi.org/10.1029/2005JB003938>
- Brais, A., Patriat, P., and Tapponnier, P., 1993. Updated interpretation of magnetic anomalies and seafloor spreading stages in the South China Sea: implications for the Tertiary tectonics of Southeast Asia. *Journal of Geophysical Research: Solid Earth*, 98(B4):6299–6328. <http://dx.doi.org/10.1029/92JB02280>
- Bryant, W.R., and Bennett, R.H., 1988. Origin, physical, and mineralogical nature of red clays: the Pacific Ocean Basin as a model. *Geo-Marine Letters*, 8(4):189–249. [doi:10.1007/BF02281640](http://dx.doi.org/10.1007/BF02281640)
- Castillo, P.R., Carlson, R.W., and Batiza, R., 1991. Origin of Nauru Basin igneous complex: Sr, Nd, and Pb isotope and REE constraints. *Earth and Planetary Science Letters*, 103(1–4):200–213. [http://dx.doi.org/10.1016/0012-821X\(91\)90161-A](http://dx.doi.org/10.1016/0012-821X(91)90161-A)
- Chung, S.-L., Sun, S., Tu, K., Chen, C.-H., and Lee, C., 1994. Late Cenozoic basaltic volcanism around the Taiwan Strait, SE China: product of lithosphere-asthenosphere interaction during continental extension. *Chemical Geology*, 112(1–2):1–20. [http://dx.doi.org/10.1016/0009-2541\(94\)90101-5](http://dx.doi.org/10.1016/0009-2541(94)90101-5)
- Clift, P., Lee, G.H., Duc, N.A., Barckhausen, U., Long, H.V., and Zhen, S., 2008. Seismic reflection evidence for a Dangerous Grounds miniplate: no extrusion origin for the South China Sea. *Tectonics*, 27(3):TC3008. <http://dx.doi.org/10.1029/2007TC002216>
- Clift, P.D., and Sun, Z., 2006. The sedimentary and tectonic evolution of the Yinggehai-Song Hong Basin and the southern Hainan margin, South China Sea: implications for Tibetan

- uplift and monsoon intensification. *Journal of Geophysical Research: Solid Earth*, 111(B6):B06405. <http://dx.doi.org/10.1029/2005JB004048>
- Cullen, A., Reemst, P., Henstra, G., Gozzard, S., and Ray A., 2010. Rifting of the South China Sea: new perspectives. *Petroleum Geoscience*, 16(3):273–282. <http://dx.doi.org/10.1144/1354-079309-908>
- Cullen, A.B., 2010. Transverse segmentation of the Baram-Balabac Basin, NW Borneo: refining the model of Borneo's tectonic evolution. *Petroleum Geoscience*, 16(1):3–29. <http://dx.doi.org/10.1144/1354-079309-828>
- Dyment, J., and Arkani-Hamed, J., 1995. Spreading-rate-dependent magnetization of the oceanic lithosphere inferred from the anomalous skewness of marine magnetic anomalies. *Geophysical Journal International*, 121(3):789–804. <http://dx.doi.org/10.1111/j.1365-246X.1995.tb06439.x>
- Dyment, J., Arkani-Hamed, J., and Ghods, A., 1997. Contribution of serpentinized ultramafics to marine magnetic anomalies at slow and intermediate spreading centres: insights from the shape of the anomalies. *Geophysical Journal International*, 129(3):691–701. <http://dx.doi.org/10.1111/j.1365-246X.1997.tb04504.x>
- Fan, W., and Menzies, M., 1992. Destruction of aged lower lithosphere and accretion of asthenosphere mantle beneath eastern China. *Geotectonics and Metallogeny*, 16:171–180.
- Fedo, C.M., Sircombe, K.N., and Rainbird, R.H., 2003. Detrital zircon analysis of the sedimentary record. In Hanchar, J.M., and Hoskin, P.W.O. (Eds.), *Zircon*. Reviews in Mineralogy and Geochemistry, 53(1):277–303. <http://dx.doi.org/10.2113/0530277>
- Flower, M.F.J., Russo, R.M., Tamaki, K., and Hoang, N., 2001. Mantle contamination and the Izu-Bonin-Mariana (IBM) “high-tide mark”: evidence for mantle extrusion caused by Tethyan closure. *Tectonophysics*, 333(1–2):9–34. [http://dx.doi.org/10.1016/S0040-1951\(00\)00264-X](http://dx.doi.org/10.1016/S0040-1951(00)00264-X)
- Franke, D., Barckhausen, U., Baristead, N., Engels, M., Ladage, S., Lutz, R., Montano, J., Pellejera, N., Ramos, E.G., and Schnabel, M., 2011. The continent–ocean transition at the southeastern margin of the South China Sea. *Marine and Petroleum Geology*, 28(6):1187–1204. <http://dx.doi.org/10.1016/j.marpetgeo.2011.01.004>
- Gilley, L.D., Harrison, T.M., Leloup, P.H., Ryerson, F.J., Lovera, O.M., and Wang, J.-H., 2003. Direct dating of left-lateral deformation along the Red River shear zone, China and Vietnam. *Journal of Geophysical Research: Solid Earth*, 108(B2):2127. <http://dx.doi.org/10.1029/2001JB001726>
- Goldstein, S.J., 1995. Uranium-series chronology of subsurface basalts, 9°31'N East Pacific Rise. In Batiza, R., Storms, M.A., and Allan, J.F. (Eds.), 1995. *Proceedings of the Ocean Drilling Program, Scientific Results*, 142: College Station, TX (Ocean Drilling Program), 37–39. <http://dx.doi.org/10.2973/odp.proc.sr.142.115.1995>
- Goldstein, S.J., Murrell, M.T., Janecky, D.R., Delaney, J.R., and Clague, D.A., 1991. Geochronology and petrogenesis of MORB from the Juan de Fuca and Gorda Ridges by ²³⁸U–²³⁰Th disequilibrium. *Earth and Planetary Science Letters*, 107(1):25–41. [http://dx.doi.org/10.1016/0012-821X\(91\)90041-F](http://dx.doi.org/10.1016/0012-821X(91)90041-F)
- Goldstein, S.J., Perfit, M.R., Batiza, R., Fornari, D.J., and Murrell, M.T., 1994. Off-axis volcanism at the East Pacific Rise detected by uranium-series dating of basalts. *Nature*, 367(6459):157–159. <http://dx.doi.org/10.1038/367157a0>
- Grimes, C.B., John, B.E., Kelemen, P.B., Mazdab, F.K., Wooden, J.L., Cheadle, M.J., Hanghøj, K., and Schwartz, J.J., 2007. Trace element chemistry of zircons from oceanic crust: a method for distinguishing detrital zircon provenance. *Geology*, 35(7):643–646. <http://dx.doi.org/10.1130/G23603A.1>

- Haile, N.S., 1973. The recognition of former subduction zones in Southeast Asia. In Tarling, D.H., and Runcorn, S.K., (Eds.), *Implications of Continental Drift to the Earth Sciences*, Vol. 2: London (Academic Press), 885–892.
- Hall, R., 1996. Reconstructing Cenozoic SE Asia. In Hall, R., and Blundell, D.J. (Eds.), *Tectonic Evolution of Southeast Asia*. Geological Society Special Publication, 106(1):153–184. <http://dx.doi.org/10.1144/GSL.SP.1996.106.01.11>
- Hall, R., 2002. Cenozoic geological and plate tectonic evolution of SE Asia and the SW Pacific: computer-based reconstructions, model and animations. *Journal of Asian Earth Sciences*, 20(4):353–431. [http://dx.doi.org/10.1016/S1367-9120\(01\)00069-4](http://dx.doi.org/10.1016/S1367-9120(01)00069-4)
- Hall, R., and Morley, C.K., 2004. Sundaland basins. In Clift, P.D., Kuhnt, W., Wang, P., and Hayes, D. (Eds.), *Continent-Ocean Interactions with East Asian Marginal Seas*. Geophysical Monograph, 149:55–85. <http://dx.doi.org/10.1029/149GM04>
- Hamilton, W.B., 1979. Tectonics of the Indonesian Region. *U.S. Geol. Surv. Prof. Pap.*, 1078.
- Hayes, D.E., and Nissen, S.S., 2005. The South China Sea margins: implications for rifting contrasts. *Earth and Planetary Science Letters*, 237(3–4):601–616. <http://dx.doi.org/10.1016/j.epsl.2005.06.017>
- Hayes, D.E., Nissen, S.S., Buhl, P., Diebold, J., Bochu, Y., Weijun, Z., and Yongqin, C., 1995. Throughgoing crustal faults along the northern margin of the South China Sea and their role in crustal extension. *Journal of Geophysical Research: Solid Earth*, 100(B11):22435–22446. <http://dx.doi.org/10.1029/95JB01867>
- Hékinian, R., Bonté, P., Pautot, G., Jacques, D., Labeyrie, L.D., Mikkelsen, N., and Reyss, J.-L., 1989. Volcanics from the South China Sea ridge system. *Oceanologica Acta*, 12(2):101–115.
- Hilde, T., Uyeda, S., and Kroenke, L., 1977. Evolution of the western Pacific and its margin. *Tectonophysics*, 38(1–2):145–165. [http://dx.doi.org/10.1016/0040-1951\(77\)90205-0](http://dx.doi.org/10.1016/0040-1951(77)90205-0)
- Holloway, N.H., 1982. North Palawan Block, Philippines: its relation to the Asian mainland and role in evolution of South China Sea. *AAPG Bulletin*, 66(9):1355–1383. <http://aapg-bull.geoscienceworld.org/content/66/9/1355.abstract>
- Honza, E., 1995. Spreading mode of backarc basins in the western Pacific. *Tectonophysics*, 251(1–4):139–152. [http://dx.doi.org/10.1016/0040-1951\(95\)00054-2](http://dx.doi.org/10.1016/0040-1951(95)00054-2)
- Huang, C.-Y., Xia, K., Yuan, P.B., and Chen, P.-G., 2001. Structural evolution from Paleogene extension to latest Miocene–recent arc-continent collision offshore Taiwan: comparison with on land geology. *Journal of Asian Earth Sciences*, 19(5):619–639. [http://dx.doi.org/10.1016/S1367-9120\(00\)00065-1](http://dx.doi.org/10.1016/S1367-9120(00)00065-1)
- Hutchison, C.S., 1996. The “Rajang accretionary prism” and “Lupar Line” problem of Borneo. In Hall, R., and Blundell, D.J. (Eds.), *Tectonic Evolution of Southeast Asia*. Geological Society Special Publication, 106(1):247–261. <http://dx.doi.org/10.1144/GSL.SP.1996.106.01.16>
- Hutchison, C.S., 2004. Marginal basin evolution: the southern South China Sea. *Marine and Petroleum Geology*, 21(9):1129–1148. <http://dx.doi.org/10.1016/j.marpetgeo.2004.07.002>
- Hutchison, C.S., 2005. *Geology of North-West Borneo*: Amsterdam (Elsevier B.V.). <http://www.sciencedirect.com/science/book/9780444519986>
- Ishihara, T., and Kisimoto, K., 1996. Magnetic anomaly map of East Asia, 1:4,000,000 (CD-ROM version). Geological Survey of Japan, Coordinating Committee for Coastal and Off-shore Geoscience Programs in East and Southeast Asia (CCOP).
- Jahn, B.-M., Chen, P.Y., and Yen, T.P., 1976. Rb-Sr ages of granitic rocks in southeastern China and their tectonic significance. *Geological Society of America Bulletin*, 87(5):763–776. [http://dx.doi.org/10.1130/0016-7606\(1976\)87<763:RAOGRI>2.0.CO;2](http://dx.doi.org/10.1130/0016-7606(1976)87<763:RAOGRI>2.0.CO;2)

- Jin, Z., Xu, S., and Li, Z., 2002. Inversion of heterogeneous magnetism for seamounts in the South China Sea. *Journal of Ocean University of Qingdao* (English Edition), 32:926–934. (in Chinese)
- Koppers, A.A.P., Russell, J.A., Roberts, J., Jackson, M.G., Konter, J.G., Wright, D.J., Staudigel, H., and Hart, S.R., 2011. Age systematics of two young en echelon Samoan volcanic trails. *Geochemistry, Geophysics, Geosystems*, 12(7):Q07025. <http://dx.doi.org/10.1029/2010GC003438>
- Lacassin, R., Maluski, H., Leloup, P.H., Tapponnier, P., Hinthong, C., Siribhakdi, K., Chuaviroj, S., and Charoenravat, A., 1997. Tertiary diachronic extrusion and deformation of western Indochina: structural and $^{40}\text{Ar}/^{39}\text{Ar}$ evidence from NW Thailand. *Journal of Geophysical Research: Solid Earth*, 102(B5):10013–10037. <http://dx.doi.org/10.1029/96JB03831>
- Lallemand, S., and Jolivet, L., 1986. Japan Sea: a pull apart basin? *Earth and Planetary Science Letters*, 76(3–4):375–389. [http://dx.doi.org/10.1016/0012-821X\(86\)90088-9](http://dx.doi.org/10.1016/0012-821X(86)90088-9)
- Le Maitre, R.W., Bateman, P., Dudek, A., Keller, J., Lameyre, J., Le Bas, M.J., Sabine, P.A., Schmid, R., Sorensen, H., Streckeisen, A., Woolley, A.R., and Zanettin, B., 1989. *A Classification of Igneous Rocks and Glossary of Terms*: Oxford (Blackwell).
- Lee, T.-Y., and Lawver, L.A., 1995. Cenozoic plate reconstruction of Southeast Asia. *Tectonophysics*, 251(1–4): 85–138. [http://dx.doi.org/10.1016/0040-1951\(95\)00023-2](http://dx.doi.org/10.1016/0040-1951(95)00023-2)
- Leloup, P.H., Arnaud, N., Lacassin, R., Kienast, J.R., Harrison, T.M., Trong, T.T.P., Replumaz, A., and Tapponnier, P., 2001. New constraints on the structure, thermochronology, and timing of the Ailao Shan-Red River shear zone, SE Asia. *Journal of Geophysical Research: Solid Earth*, 106(B4):6683–6732. <http://dx.doi.org/10.1029/2000JB900322>
- Li, C.-F., Lin, J., and Kulhanek, D.K., 2013. South China Sea tectonics: opening of the South China Sea and its implications for southeast Asian tectonics, climates, and deep mantle processes since the late Mesozoic. *International Ocean Discovery Program Scientific Prospectus*, 349. <http://dx.doi.org/10.2204/iodp.sp.349.2013>
- Li, C.-F., Shi, X., Zhou, Z., Li, J., Geng, J., and Chen, B., 2010. Depths to the magnetic layer bottom in the South China Sea area and their tectonic implications. *Geophysical Journal International*, 182(3):1229–1247. <http://dx.doi.org/10.1111/j.1365-246X.2010.04702.x>
- Li, C.-F., and Song, T.R., 2012. Magnetic recording of the Cenozoic oceanic crustal accretion and evolution of the South China Sea Basin. *Chinese Science Bulletin*, 57(24):3165–3181. [doi:10.1007/s11434-012-5063-9](https://doi.org/10.1007/s11434-012-5063-9)
- Li, C.-F., Wang, P., Franke, D., Lin, J., and Tian, J., 2012. Unlocking the opening processes of the South China Sea. *Scientific Drilling*, 14:55–59. <http://dx.doi.org/10.2204/iodp.sd.14.07.2012>
- Li, C.-F., Zhou, Z., Hao, H., Chen, H., Wang, J., Chen, B., and Wu, J., 2008a. Late Mesozoic tectonic structure and evolution along the present-day northeastern South China Sea continental margin. *Journal of Asian Earth Sciences*, 31(4–6):546–561. <http://dx.doi.org/10.1016/j.jseaes.2007.09.004>
- Li, C.-F., Zhou, Z., Li, J., Chen, B., and Geng, J., 2008b. Magnetic zoning and seismic structure of the South China Sea ocean basin. *Marine Geophysical Researches*, 29(4):223–238. <http://dx.doi.org/10.1007/s11001-008-9059-4>
- Li, C.-F., Zhou, Z., Li, J., Hao, H., and Geng, J., 2007b. Structures of the northeasternmost South China Sea continental margin and ocean basin: geophysical constraints and tectonic implications. *Marine Geophysical Researches*, 28(1):59–79. <http://dx.doi.org/10.1007/s11001-007-9014-9>

- Li, C.-F., Zhou, Z.Y., Li, J.B., Chen, H.J., Geng, J.H., and Li, H., 2007. Precollisional tectonics and terrain amalgamation offshore southern Taiwan: characterizations from reflection seismic and potential field data. *Science in China, Series D: Earth Sciences*, 50(6):897–908. [doi:10.1007/s11430-007-0025-9](https://doi.org/10.1007/s11430-007-0025-9)
- Li, J.-B., Ding, W.-W., Gao, J.-Y., Wu, Z.-Y., and Zhang, J., 2011. Cenozoic evolution model of the sea-floor spreading in South China Sea: new constraints from high resolution geophysical data. *Chinese Journal of Geophysics*, 54(6):894–906. <http://www.agu.org/wps/ChineseJGeo/54/06/ljb2.pdf>
- Li, Q., Wang, P., Zhao, Q., Shao, L., Zhong, G., Tian, J., Cheng, X., Jian, Z., and Su, X., 2006. A 33 Ma lithostratigraphic record of tectonic and paleoceanographic evolution of the South China Sea. *Marine Geology*, 230(3–4):217–235. <http://dx.doi.org/10.1016/j.mar-geo.2006.05.006>
- Lüdmann, T., and Wong, H.K., 1999. Neotectonic regime on the passive continental margin of the northern South China Sea. *Tectonophysics*, 311(1–4):113–138 [http://dx.doi.org/10.1016/S0040-1951\(99\)00155-9](http://dx.doi.org/10.1016/S0040-1951(99)00155-9)
- Lüdmann, T., Wong, H.K., and Wang, P., 2001. Plio-Quaternary sedimentation processes and neotectonics of the northern continental margin of the South China Sea. *Marine Geology*, 172(3–4):331–358. [http://dx.doi.org/10.1016/S0025-3227\(00\)00129-8](http://dx.doi.org/10.1016/S0025-3227(00)00129-8)
- Macdonald, G.A., 1968. Composition and origin of Hawaiian lavas. In Coats, R.R., Hay, R.L., and Anderson, C.A. (Eds.), *Studies in Volcanology—A Memoir in Honor of Howel Williams*. Memoir - Geological Society of America, 116:477–522.
- Macdonald, G.A., and Katsura, T., 1964. Chemical composition of Hawaiian lavas. *Journal of Petrology*, 5(1):82–133. <http://petrology.oxfordjournals.org/content/5/1/82.abstract>
- Madon, M.B.H., Meng, L.K., and Anuar, A., 1999. Sabah Basin. In Marican, T.S.D.'M.H. (Ed.), *The Petroleum Geology and Resources of Malaysia*. Kuala Lumpur, Malaysia (Petroliam Nasional Berhad), 499–542.
- McIntosh, K.D., Liu, C.-S., and Lee, C.-S., 2012. Introduction to the TAIGER special issue of Marine Geophysical Research. *Marine Geophysical Researches*, 33(4):285–287. <http://dx.doi.org/10.1007/s11001-013-9170-z>
- Morley, C.K., 2002. A tectonic model for the Tertiary evolution of strike-slip faults and rift basins in SE Asia. *Tectonophysics*, 347(4):189–215. [http://dx.doi.org/10.1016/S0040-1951\(02\)00061-6](http://dx.doi.org/10.1016/S0040-1951(02)00061-6)
- Pautot, G., Rangin, C., Briaies, A., Tapponnier, P., Beuzart, P., Lericolais, G., Mathieu, X., Wu, J., Han, S., Li, H., Lu, Y., and Zhao, J., 1986. Spreading direction in the central South China Sea. *Nature*, 321(6066):150–154. <http://dx.doi.org/10.1038/321150a0>
- Pubellier, M., Monnier, C., Maury, R., and Tamayo, R., 2004. Plate kinematics, origin and tectonic emplacement of supra-subduction ophiolites in SE Asia. *Tectonophysics*, 392(1–4):9–36. <http://dx.doi.org/10.1016/j.tecto.2004.04.028>
- Rangin, C., Jolivet, L., and Pubellier, M., 1990. A simple model for the tectonic evolution of Southeast Asia and Indonesia regions for the past 43 m.y. *Bulletin de la Société Géologique de France*, 6(6):889–905.
- Rangin, C., Klein, M., Roques, D., Le Pichon, X., and Trong, L.V., 1995. The Red River fault system in the Tonkin Gulf, Vietnam. *Tectonophysics*, 243(3–4):209–222. [http://dx.doi.org/10.1016/0040-1951\(94\)00207-P](http://dx.doi.org/10.1016/0040-1951(94)00207-P)
- Ru, K., and Pigott, J.D., 1986. Episodic rifting and subsidence in the South China Sea. *AAPG Bulletin*, 70(9):1136–1155. <http://aapgbull.geoscienceworld.org/content/70/9/1136.short>

- Schärer, U., Tapponnier, P., Lacassin, R., Leloup, P.H., Dalai, Z., and Ji, S., 1990. Intraplate tectonics in Asia: a precise age for large-scale Miocene movement along the Ailao Shan-Red River shear zone, China. *Earth and Planetary Science Letters*, 97(1–2):65–77. [http://dx.doi.org/10.1016/0012-821X\(90\)90099-J](http://dx.doi.org/10.1016/0012-821X(90)90099-J)
- Schlüter, H.U., Hinz, K., and Block, M., 1996. Tectono-stratigraphic terranes and detachment faulting of the South China Sea and Sulu Sea. *Marine Geology*, 130(1–2):39–78. [http://dx.doi.org/10.1016/0025-3227\(95\)00137-9](http://dx.doi.org/10.1016/0025-3227(95)00137-9)
- Schwartz, J.J., John, B.E., Cheadle, M.J., Miranda, E.A., Grimes, C.B., Wooden, J.L., and Dick, H.J.B., 2005. Dating the growth of oceanic crust at a slow-spreading ridge. *Science*, 310(5748):654–657. <http://dx.doi.org/10.1126/science.1116349>
- Shi, H., and Li, C.-F., 2012. Mesozoic and early Cenozoic tectonic convergence-to-rifting transition prior to opening of the South China Sea. *International Geology Review*, 54(15):1801–1828. <http://dx.doi.org/10.1080/00206814.2012.677136>
- Sibuet, J.-C., Hsu, S.-K., Le Pichon, X., Le Formal, J.-P., Reed, D., Moore, G., and Liu, C.-S., 2002. East Asia plate tectonics since 15 Ma: constraints from the Taiwan region. *Tectonophysics*, 344(1–2):103–134. [http://dx.doi.org/10.1016/S0040-1951\(01\)00202-5](http://dx.doi.org/10.1016/S0040-1951(01)00202-5)
- Smith, W.H.F., and Sandwell, D.T., 1997. Global seafloor topography from satellite altimetry and ship depth soundings. *Science*, 277(5334):1956–1962. <http://dx.doi.org/10.1126/science.277.5334.1956>
- Song, T., and Li, C., 2012. The opening ages and mode of the South China Sea estimated from high-density magnetic tracks. *Progress in Geophysics*, 27(4):1432–1442. <http://dx.doi.org/10.6038/j.issn.1004-2903.2012.04.018>
- Sun, Z., Zhong, Z., Keep, M., Zhou, D., Cai, D., Li, X., Wu, S., and Jiang, J., 2009. 3D analogue modeling of the South China Sea: a discussion on breakup pattern. *Journal of Asian Earth Sciences*, 34(4):544–556. <http://dx.doi.org/10.1016/j.jseaes.2008.09.002>
- Tapponnier, P., Lacassin, R., Leloup, P.H., Shärer, U., Dalai, Z., Haiwei, W., Xiaohan, L., Shaocheng, J., Lianshang, Z., and Jiayou, Z., 1990. The Ailao Shan/Red River metamorphic belt: Tertiary left-lateral shear between Indochina and South China. *Nature*, 343(6257):431–437. <http://dx.doi.org/10.1038/343431a0>
- Tapponnier, P., Peltzer, G., and Armijo, R., 1986. On the mechanics of the collision between India and Asia. In Ramsey, J.G., Coward, M.P., and Ries, A. (Eds.), *Collision Tectonics*. Geological Society Special Publication, 19:115–157. <http://dx.doi.org/10.1144/GSL.SP.1986.019.01.07>
- Tapponnier, P., Peltzer, G., Le Dain, A.Y., Armijo, R., and Cobbold, P., 1982. Propagating extrusion tectonics in Asia: new insights from simple experiments with plasticine. *Geology*, 10(12):611–616. [http://dx.doi.org/10.1130/0091-7613\(1982\)10<611:PETIAN>2.0.CO;2](http://dx.doi.org/10.1130/0091-7613(1982)10<611:PETIAN>2.0.CO;2)
- Taylor, B., and Hayes, D.E., 1980. The tectonic evolution of the South China Basin. In Hayes, D.E. (Ed.), *The Tectonic and Geologic Evolution of Southeast Asian Seas and Islands*. Geophysical Monograph, 23:89–104. <http://dx.doi.org/10.1029/GM023p0089>
- Taylor, B., and Hayes, D.E., 1983. Origin and history of the South China Sea Basin. In Hayes, D.E. (Ed.), *The Tectonic and Geologic Evolution of Southeast Asian Seas and Islands* (Pt. 2). Geophysical Monograph, 27:23–56. <http://dx.doi.org/10.1029/GM027p0023>
- Tejada, M.L.G., Mahoney, J.J., Castillo, P.R., Ingle, S.P., Sheth, H.C., and Weis, D., 2004. Pinpricking the elephant: evidence on the origin of the Ontong Java Plateau from Pb-Sr-Hf-Nd isotopic characteristics of ODP Leg 192 basalts. In Fitton, J.G., Mahoney, J.J., Wallace, P.J., and Saunders, A.D. (Eds.), *Origin and Evolution of the Ontong Java Plateau*. Geological Society Special Publication, 229(1):133–150. <http://dx.doi.org/10.1144/GSL.SP.2004.229.01.09>

- Tominaga, M., Teagle, D.A.H., Alt, J.C., and Umino, S., 2009. Determination of the volcanostратigraphy of the oceanic crust formed at superfast spreading ridge: electrofacies analyses of ODP/IOPD Hole 1256D. *Geochemistry, Geophysics, Geosystems*, 10(1):Q01003. <http://dx.doi.org/10.1029/2008GC002143>
- Tongkul, F., 1994. The geology of northern Sabah, Malaysia: its relationship to the opening of the South China Sea basin. *Tectonophysics*, 235(1–2):131–147. [http://dx.doi.org/10.1016/0040-1951\(94\)90021-3](http://dx.doi.org/10.1016/0040-1951(94)90021-3)
- Tu, K., Flower, M.F.J., Carlson, R.W., Xie, G., Chen, C.-Y., and Zhang, M., 1992. Magmatism in the South China Basin: 1. Isotopic and trace-element evidence for an endogenous Dupal mantle component. *Chemical Geology*, 97(1–2):47–63. [http://dx.doi.org/10.1016/0009-2541\(92\)90135-R](http://dx.doi.org/10.1016/0009-2541(92)90135-R)
- Wang, P., 2012. Tracing the life history of a marginal sea—on “The South China Sea Deep” research program. *Chinese Science Bulletin*, 57(24):3093–3114. <http://dx.doi.org/10.1007/s11434-012-5087-1>
- Wang, P., and Li, Q. (Eds.), 2009. *Developments in Paleoenvironmental Research (Vol. 13): The South China Sea: Paleooceanography and Sedimentology*: Dordrecht (Springer). 13. <http://dx.doi.org/10.1007/978-1-4020-9745-4>
- Wang, P., Prell, W.L., Blum, P., et al., 2000. *Proceedings of the Ocean Drilling Program, Initial Reports*, 184: College Station, TX (Ocean Drilling Program). <http://dx.doi.org/10.2973/odp.proc.ir.184.2000>
- Wang, X.-C., Li, Z.-X., Li, X.-H., Li, J., Liu, Y., Long, W.-G., Zhou, J.-B., and Wang, F., 2012. Temperature, pressure, and composition of the mantle source region of late Cenozoic basalts in Hainan Island, SE Asia: a consequence of a young thermal mantle plume close to subduction zones? *Journal of Petrology*, 53(1):177–233. <http://dx.doi.org/10.1093/petrology/egr061>
- Xiao, G., and Zheng, J., 2004. New opinions about “residual Tethys” in northern South China Sea slope and southern East China Sea. *Geoscience*, 18(1):103–108. (in Chinese)
- Xu, Y., Wei, J., Qiu, H., Zhang, H., and Huang, X., 2012. Opening and evolution of the South China Sea constrained by studies on volcanic rocks: preliminary results and a research design. *Chinese Science Bulletin*, 57(24):3150–3164. <http://dx.doi.org/10.1007/s11434-011-4921-1>
- Yan, P., Zhou, D., and Liu, Z., 2001. A crustal structure profile across the northern continental margin of the South China Sea. *Tectonophysics*, 338(1):1–21. [doi:10.1016/S0040-1951\(01\)00062-2](http://dx.doi.org/10.1016/S0040-1951(01)00062-2)
- Yang, J.Y., and Feng, X.S., 2003. An analysis of middle–late Mesozoic tectonics, paleogeography, and petroleum potential in the northeastern South China Sea. *China Offshore Oil and Gas (Geology)*, 17:89–103. http://en.cnki.com.cn/Article_en/CJFDTOTAL-ZHSD200302002.htm
- Yao, B., 1995. Characteristics and tectonic significance of the Zhongnan-Lile fault. *Geological Research of South China Sea, Memoir*, 7:1–14. (in Chinese)
- Yao, B., Zeng, W., Hayes, D.E., and Spangler, S., 1994. *The Geological Memoir of South China Sea Surveyed Jointly by China and USA*: Wuhan (China Univ. Geosci. Press). (in Chinese)
- Zhang, G.-L., Chen, L.-H., and Li, S.-Z., 2013. Mantle dynamics and generation of a geochemical mantle boundary along the East Pacific Rise—Pacific/Antarctic Ridge. *Earth and Planetary Science Letters*, 383:153–163. [doi:10.1016/j.epsl.2013.09.045](http://dx.doi.org/10.1016/j.epsl.2013.09.045)
- Zhang, G., Smith-Duque, C., Tang, S., Li, H., Zarikian, C., D’Hondt, S., Inagaki, F., and IODP Expedition 329 Scientists, 2012a. Geochemistry of basalts from IODP Site U1365: impli-

- cations for magmatism and mantle source signatures of the mid-Cretaceous Osbourn Trough. *Lithos*, 144–145:73–87. doi:10.1016/j.lithos.2012.04.014
- Zhang, G., Zeng, Z., Yin, X., Wang, X., and Chen, D., 2009. Deep fractionation of clinopyroxene in the East Pacific Rise 13°N: evidence from high MgO MORB and melt inclusions. *Acta Geologica Sinica*, 83(2):266–277. <http://dx.doi.org/10.1111/j.1755-6724.2009.00030.x>
- Zhang, G.-L., Zong, C.-L., Yin, X.-B., and Li, H., 2012b. Geochemical constraints on a mixed pyroxenite–peridotite source for East Pacific Rise basalts. *Chemical Geology*, 330–331:176–187. <http://dx.doi.org/10.1016/j.chemgeo.2012.08.033>
- Zhang, L., Zhao, M.H., Wang, J., He, E.Y., Ao, W., Qiu, X.L., Xu, H.L., Wei, X.D., and Zhang, J.Z., 2013. The correction of OBS position and recent advances of 3D seismic exploration in the central sub-basin of South China Sea. *Earth Science—Journal of China University of Earth Geosciences*, 2013(1):33–42. (in Chinese)
- Zhou, D., Ru, K., and Chen, H., 1995. Kinematics of Cenozoic extension on the South China Sea continental margin and its implications for the tectonic evolution of the region. *Tectonophysics*, 251(1–4):161–177. [http://dx.doi.org/10.1016/0040-1951\(95\)00018-6](http://dx.doi.org/10.1016/0040-1951(95)00018-6)
- Zhou, D., Sun, Z., Chen, H., Xu, H., Wang, W., Pang, X., Cai, D., and Hu, D., 2008. Mesozoic paleogeography and tectonic evolution of South China Sea and adjacent areas in the context of Tethyan and Paleo-Pacific interconnections. *Island Arc*, 17(2):186–207. <http://dx.doi.org/10.1111/j.1440-1738.2008.00611.x>
- Zhou, X.M., and Li, W.X., 2000. Origin of late Mesozoic igneous rocks in southeastern China: implications for lithosphere subduction and underplating of mafic magmas. *Tectonophysics*, 326(3–4):269–287. [http://dx.doi.org/10.1016/S0040-1951\(00\)00120-7](http://dx.doi.org/10.1016/S0040-1951(00)00120-7)

Expedition 349 Preliminary Report

Table T1. Coring summary, Expedition 349.

Hole	Latitude	Longitude	Water depth (m)	Penetration DSF (m)	Cored interval (m)	Recovered length (m)	Recovery (%)	Drilled interval (m)	Drilled interval (N)	Total cores (N)	APC cores (N)	XCB cores (N)
U1431A	15°22.5491'N	117°00.0009'E	4237.3	28.4	28.4	28.39	100	—	0	3	3	0
U1431B	15°22.5480'N	117°00.0125'E	4236.7	17.0	17.0	17.16	101	—	0	2	2	0
U1431C	15°22.5371'N	117°00.0108'E	4239.5	14.2	14.2	14.45	102	—	0	2	2	0
U1431D	15°22.5379'N	117°00.0022'E	4240.5	617.0	617.0	402.11	65	—	0	67	19	48
U1431E	15°22.5380'N	116°59.9903'E	4240.3	1008.8	443.5	242.35	55	565.3	2	47	0	0
U1432A	18°21.1051'N	116°23.4504'E	3829.0	62.0	—	—	0	62	1	0	0	0
U1432B	18°21.1062'N	116°23.4512'E	3829.0	800.0	—	—	0	800	4	0	0	0
U1432C	18°21.0831'N	116°23.4504'E	3829.0	110.0	110.0	88.74	81	—	0	12	12	0
U1433A	12°55.1380'N	115°02.8345'E	4379.4	188.3	188.3	168.79	90	—	0	20	20	0
U1433B	12°55.1313'N	115°02.8484'E	4379.3	858.5	672.4	443.04	66	186.1	1	74	0	0
U1434A	13°11.5080'N	114°55.4005'E	4009.0	312.5	115.5	26.43	23	197	1	14	0	0
U1435A	18°33.3466'N	116°36.6174'E	3252.5	300.0	300.0	171.37	57	—	0	32	0	0
			Total:		2506.3	1602.83		1810.4	9	273	58	48

APC = advanced piston corer, XCB = extended core barrel, RCB = rotary core barrel. — = no data.

Hole	Latitude	Longitude	RCB cores (N)	Other cores (N)	Date started (UTC)	Date finished (UTC)	Time on hole (days)	Comments
U1431A	15°22.5491'N	117°00.0009'E	0	0	1/30/2014 22:40	1/31/2014 19:45	0.88	
U1431B	15°22.5480'N	117°00.0125'E	0	0	1/31/2014 19:45	1/31/2014 22:20	0.11	
U1431C	15°22.5371'N	117°00.0108'E	0	0	1/31/2014 22:20	2/1/2014 00:52	0.11	Split liner on mud line core
U1431D	15°22.5379'N	117°00.0022'E	0	0	2/1/2014 00:52	2/6/2014 06:15	5.22	
U1431E	15°22.5380'N	116°59.9903'E	47	1	2/6/2014 06:15	2/15/2014 22:00	9.66	
U1432A	18°21.1051'N	116°23.4504'E	0	0	2/16/2014 15:30	2/17/2014 18:05	1.11	Jet-in test
U1432B	18°21.1062'N	116°23.4512'E	0	0	2/17/2014 18:05	3/6/2014 12:36	16.77	Jet-in 20 inch casing
U1432C	18°21.0831'N	116°23.4504'E	0	0	2/21/2014 08:20	2/22/2014 23:35	1.64	APC/XCB coring
U1433A	12°55.1380'N	115°2.8345'E	0	0	3/7/2014 18:30	3/10/2014 07:25	2.54	
U1433B	12°55.1313'N	115°2.8484'E	74	0	3/10/2014 19:25	3/19/2014 15:00	8.82	
U1434A	13°11.5080'N	114°55.4005'E	14	0	3/19/2014 16:48	3/22/2014 15:48	2.96	
U1435A	18°33.3466'N	116°36.6174'E	32	0	3/24/2014 07:24	3/27/2014 11:00	3.15	
Total:			167	1				

Figure F1. Regional topography and geodynamic framework of Southeast Asia. Data based on Smith and Sandwell (1997). Solid red lines = regional faults. Red arrows show direction of plate movement and solid red circles mark sites drilled during Expedition 349.

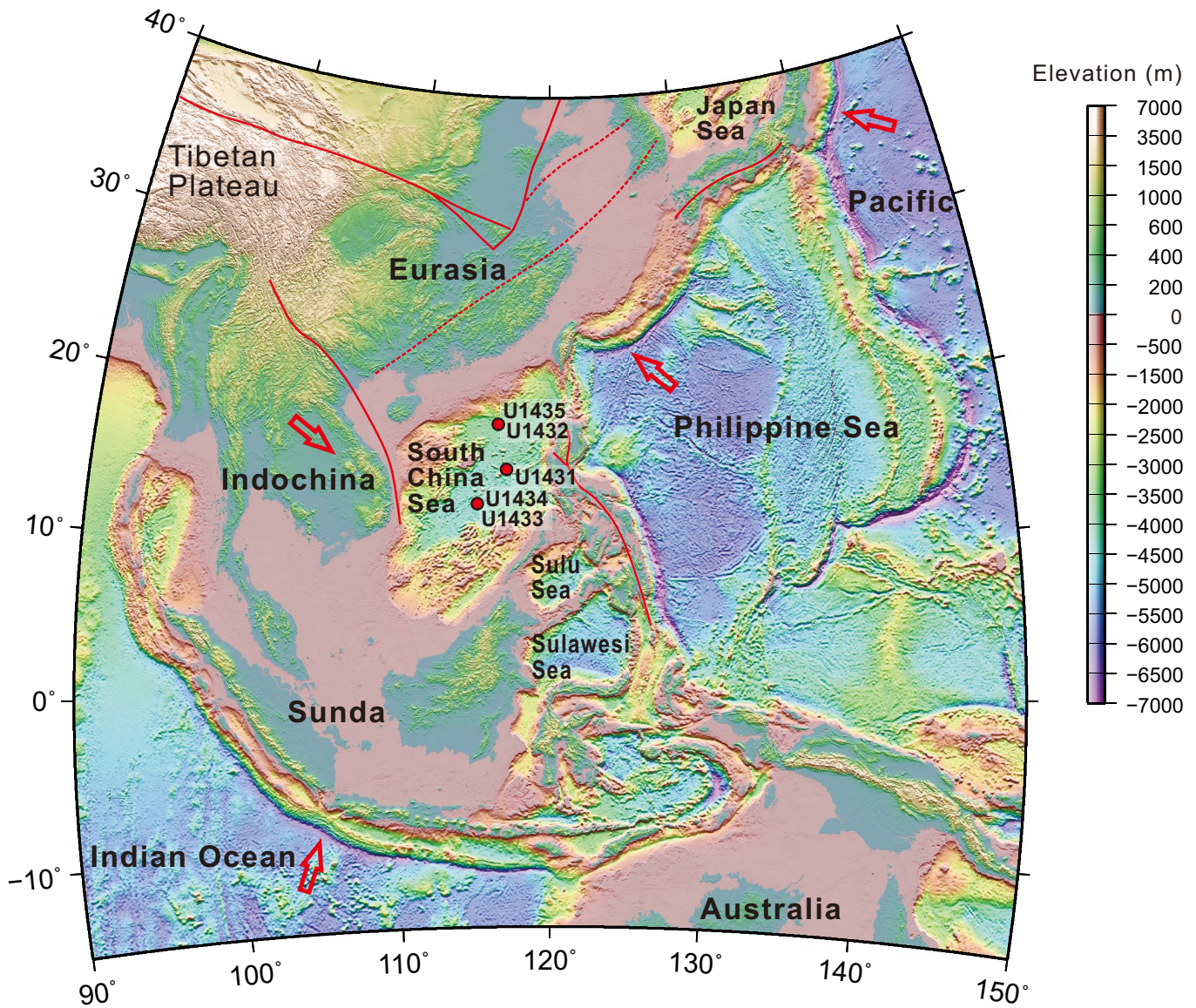


Figure F2. Topographic and bathymetric map of the South China Sea and surrounding region. Dashed red line = inferred Zhongnan fault. Solid red circles = sites drilled during Expedition 349. Solid white circle = location of Ocean Drilling Program (ODP) Site 1148. Pink lines = seismic surveys collected during Cruises SO49 (1987) and SO197 (2008) on the R/V *Sonne*. Blue, red, and black lines = seismic data collected by Chinese research institutes and oil companies. Turquoise lines = reflection seismic data acquired in the 1980s from Cruises V3607, V3608, V3613, V3614, and RC2006.

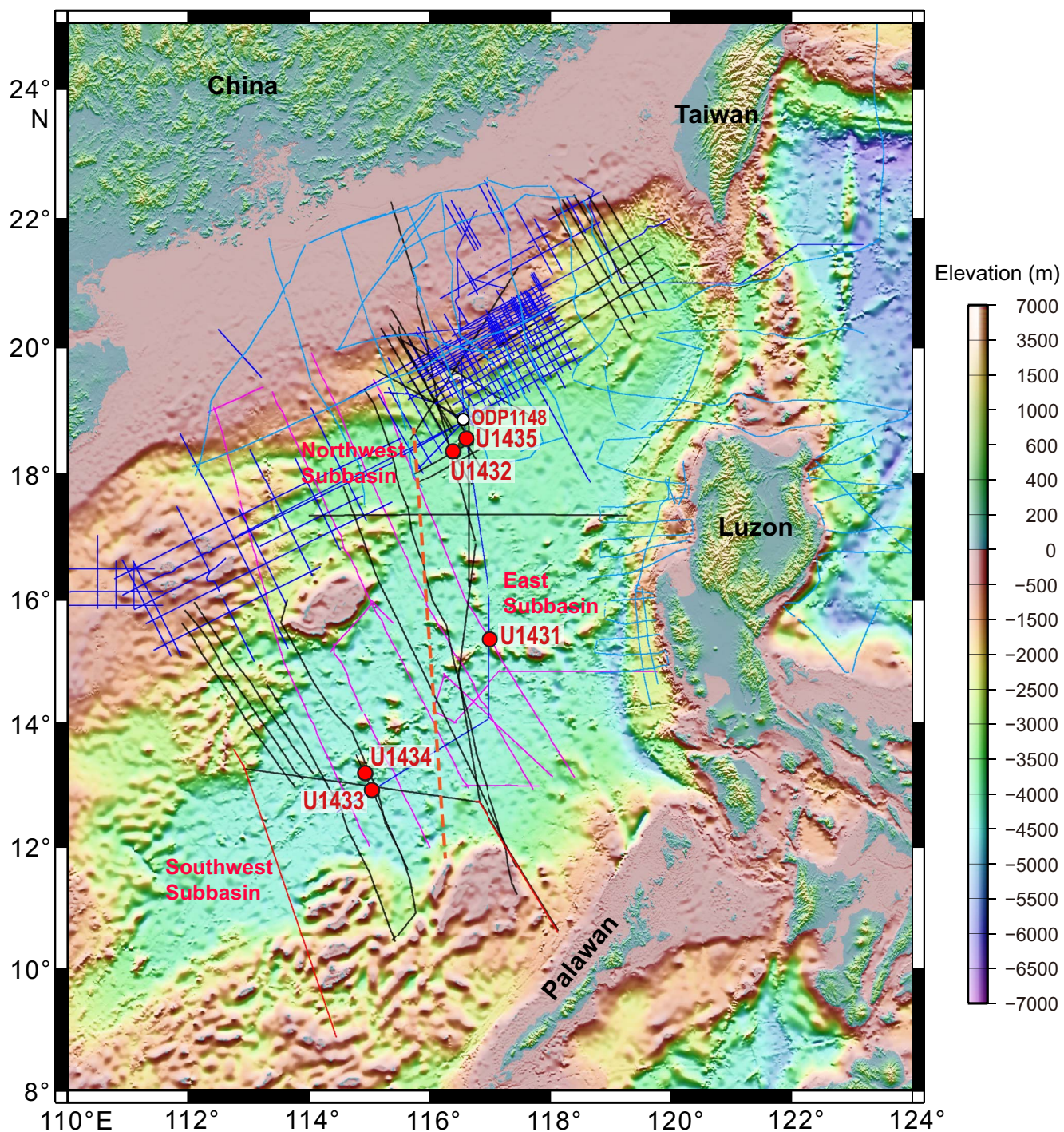


Figure F3. Different hypothetical models for the driving mechanisms of the opening of the South China Sea. **A.** Opening induced by India-Eurasia continental collision and consequent tectonic extrusion (Tapponnier et al., 1982, 1990; Briais et al., 1993; Leloup et al., 2001; Flower et al., 2001). **B.** Opening induced by slab pull and subduction of the proto-South China Sea (Taylor and Hayes, 1980, 1983; Holloway, 1982; Hall, 2002). **C.** Opening induced by an upwelling mantle plume (e.g., Fan and Menzies, 1992; Xu et al., 2012). **D.** Opening induced by regional extension related to subduction and retreat of the Pacific plate (Taylor and Hayes, 1980, 1983; Shi and Li, 2012).

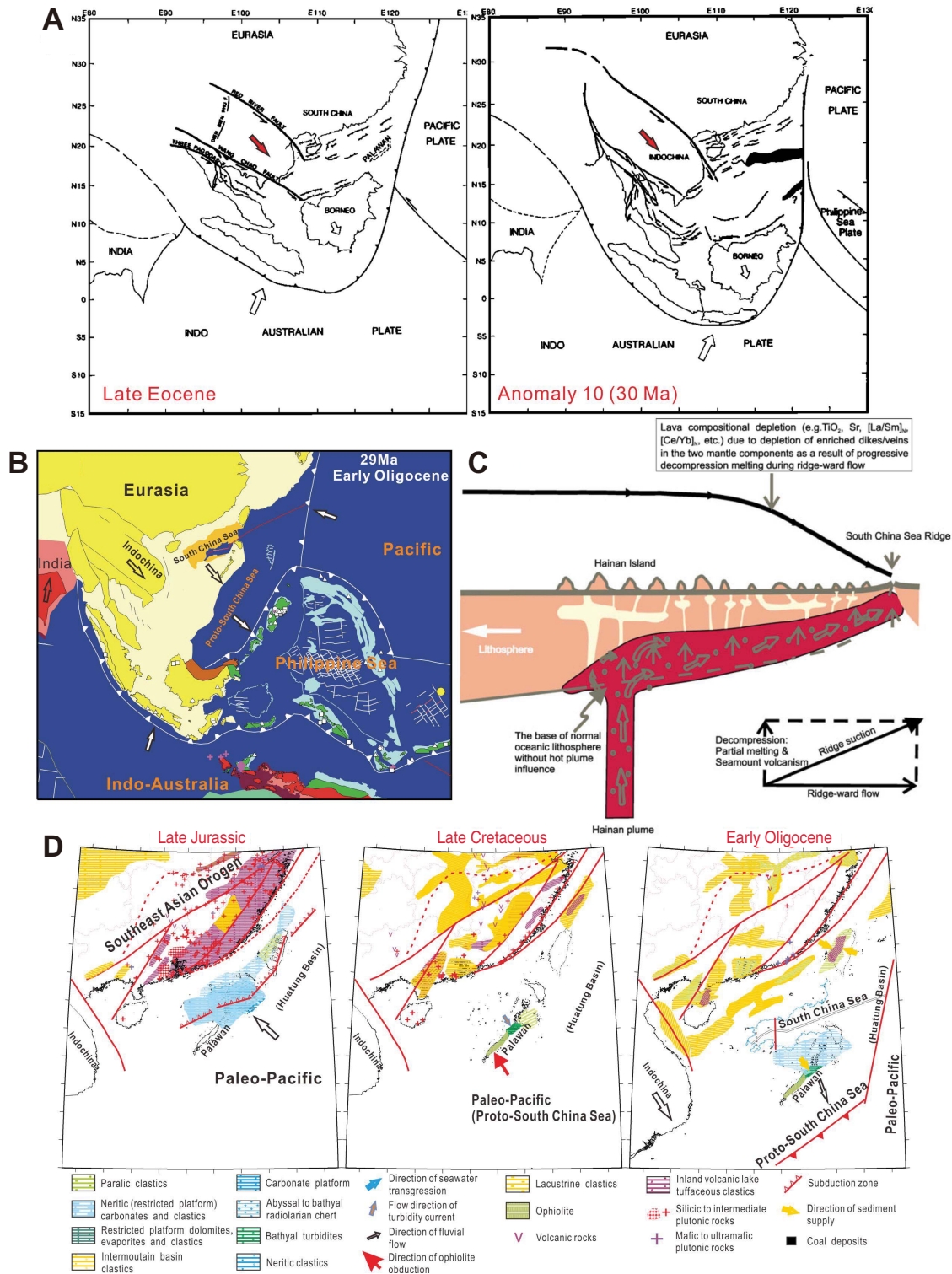


Figure F4. Total field magnetic map (based on [globalchange.nasa.gov/r/d/\[GCMD\]GSJ_EASTASIA_CDROM](http://globalchange.nasa.gov/r/d/[GCMD]GSJ_EASTASIA_CDROM)) showing major magnetic zones (A, B, C1, C1', C2, D, and E). M1 and M2 are two major magnetic anomalies in the East Subbasin. ZNF = Zhongnan fault, L RTPB = Luzon-Ryukyu transform plate boundary, DS = Dongsha Rise; SCMA = offshore south China magnetic anomaly, XS = Xisha, ZB = Macclesfield Bank, LB = Reed Bank, NM = Dangerous Grounds. Red lines = transform faults, solid yellow circles = sites drilled during Expedition 349, solid pink circle = location of Ocean Drilling Program (ODP) Site 1148. After Li et al. (2008b).

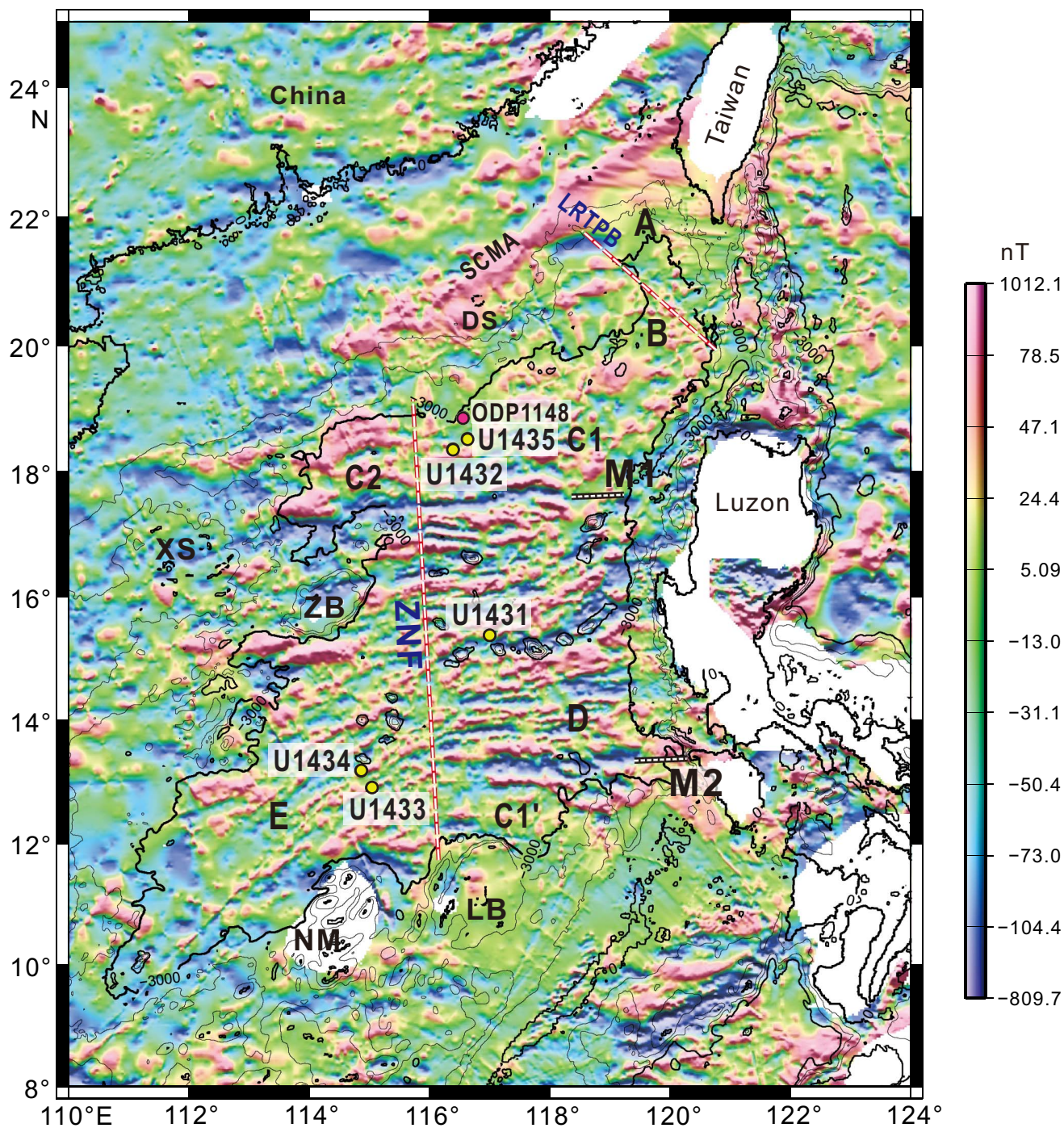


Figure F5. Examples of two groups of contrasting tectonic models for the opening phases of the South China Sea. **A.** Multiphase episodic rifting model in which the Southwest Subbasin is the first to open from continental rifting (after Ru and Pigott, 1986). N.P. = Northwest Palawan, S.P. = South Palawan, M.B. = Macclesfield Bank, R.B. = Reed Bank, P.I. = Paracel Islands, F1, F2, and F3 = faults. (Continued on next page.)

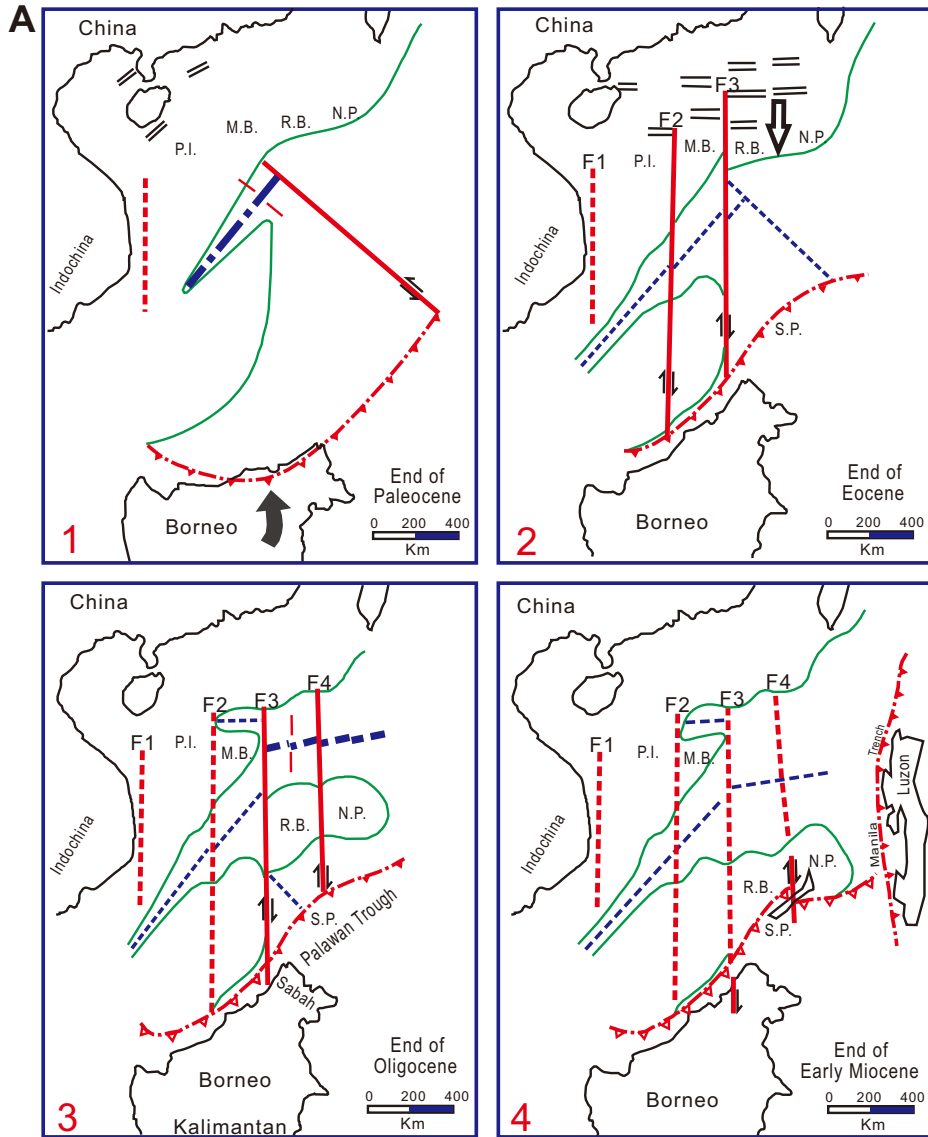


Figure F5 (continued). B. Southwestward continuous propagating model in which the Southwest Subbasin is coeval with the central East Subbasin (after Briais et al., 1993).

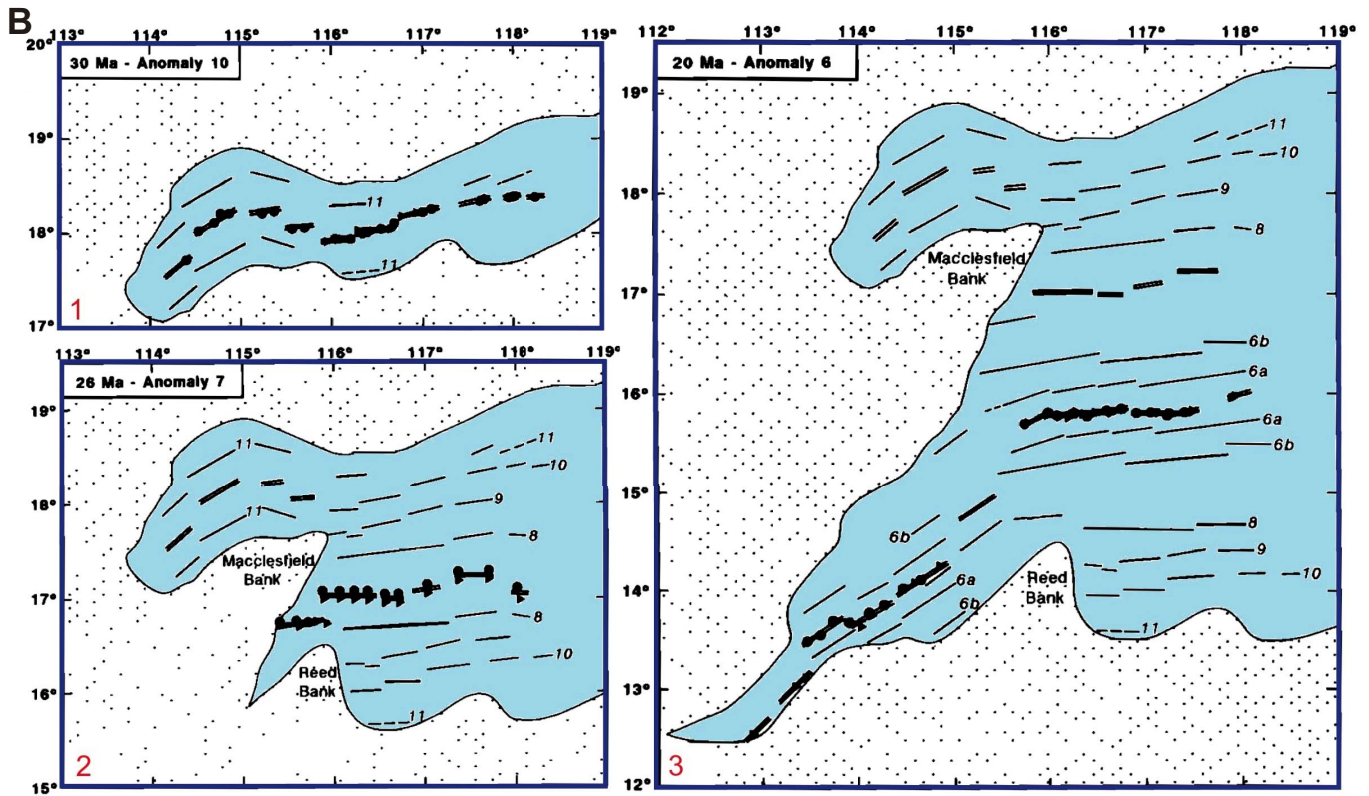


Figure F6. Proposed sampling transect in the East Subbasin (after Li et al., 2010). **A.** Total field magnetic anomaly and Bouguer anomaly along the seismic line shown in **B**. **B.** Sites U1431, U1432, and U1435 in the East Subbasin and Ocean Drilling Program (ODP) Site 1148 shown on a composite seismic line. Solid lines = sites that fall on the seismic profile, dashed lines = site locations projected onto the line. TWT = two-way traveltime, COT = continent-ocean transition zone, PRMB = Pearl River Mouth Basin, CDP = common depth point. **C.** Depths to the Moho and Curie point estimated from gravity and magnetic anomalies, respectively. w = width of moving windows.

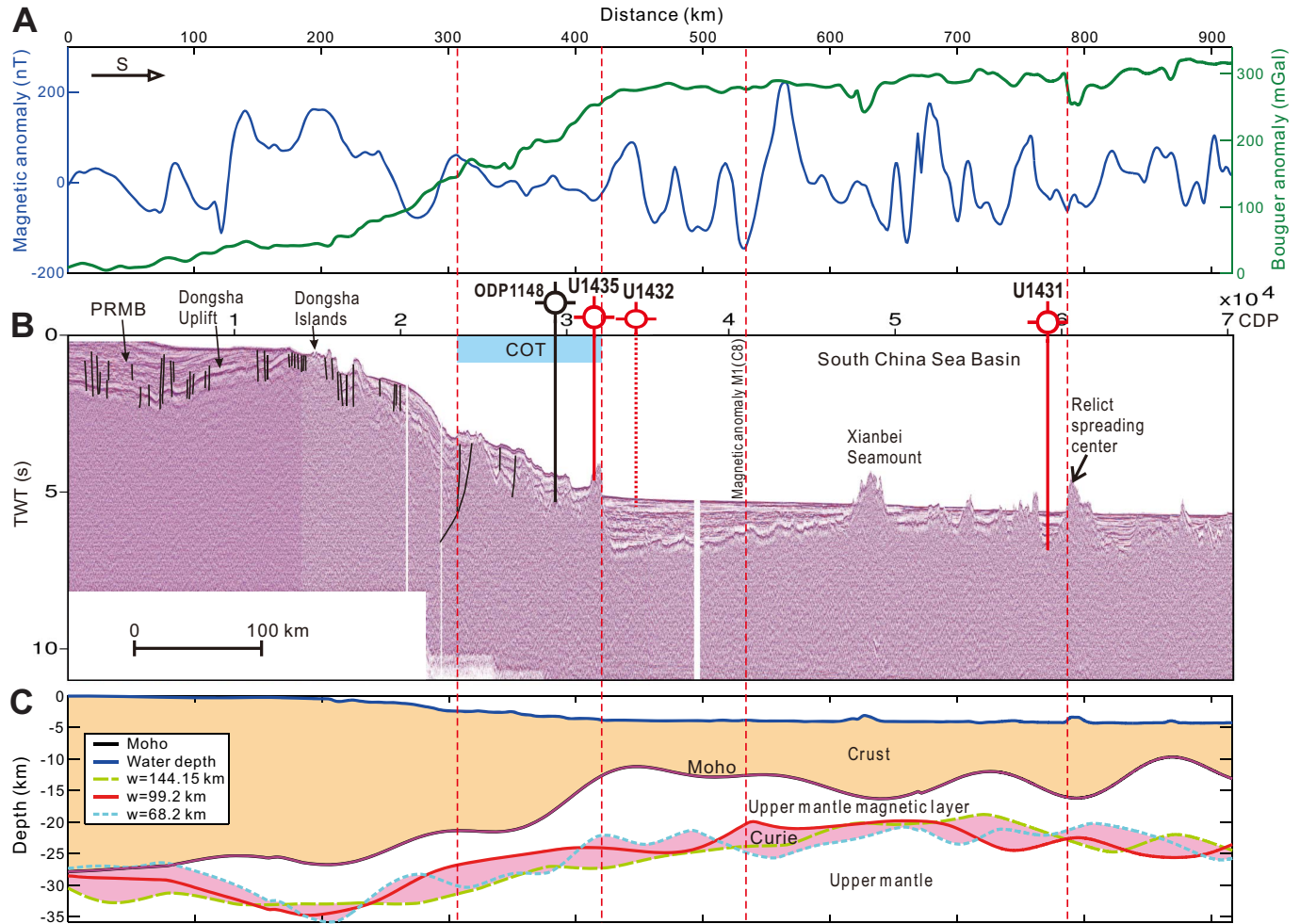


Figure F7. Seismic profile Line NDS3 showing the short sampling transect in the Southwest Subbasin and location of Sites U1433 and U1434. CDP = common depth point.

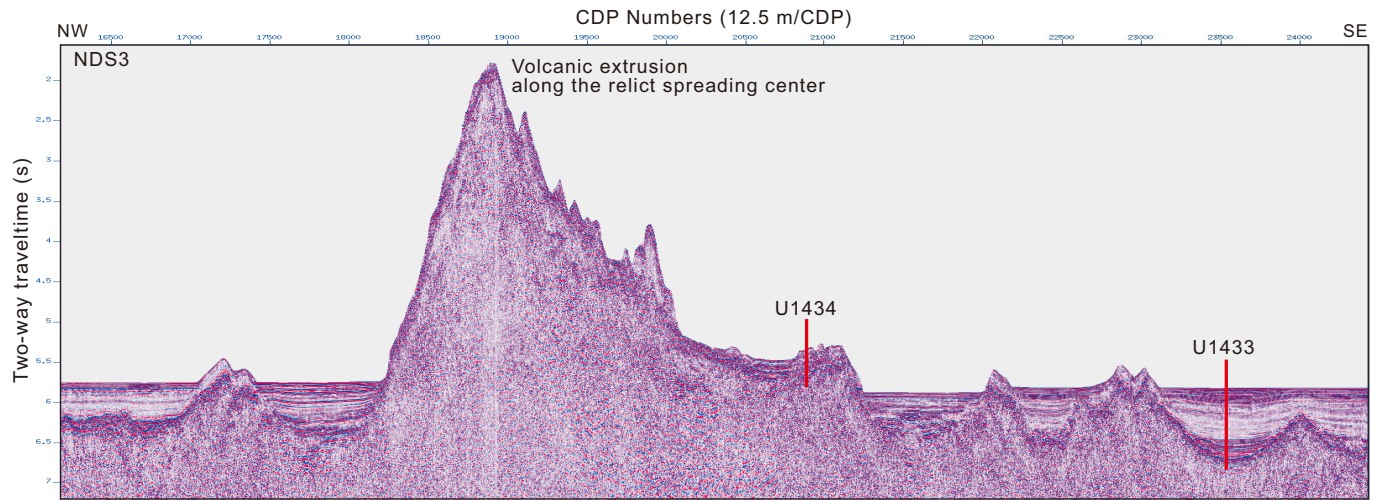


Figure F8. A. Bathymetric map of the South China Sea and surrounding region. Yellow circles denote sites drilled during International Ocean Discovery Program (IODP) Expedition 349. Solid pink circles are sites drilled during Ocean Drilling Program (ODP) Leg 184. Yellow dashed line = inferred continent/ocean boundary, blue lines = fossil South China Sea spreading center, white line with triangles = Manila Trench. **B.** Detailed bathymetry around Site U1431 (green box in A) showing nearby bathymetric highs and the Manila Trench. (Continued on next page.)

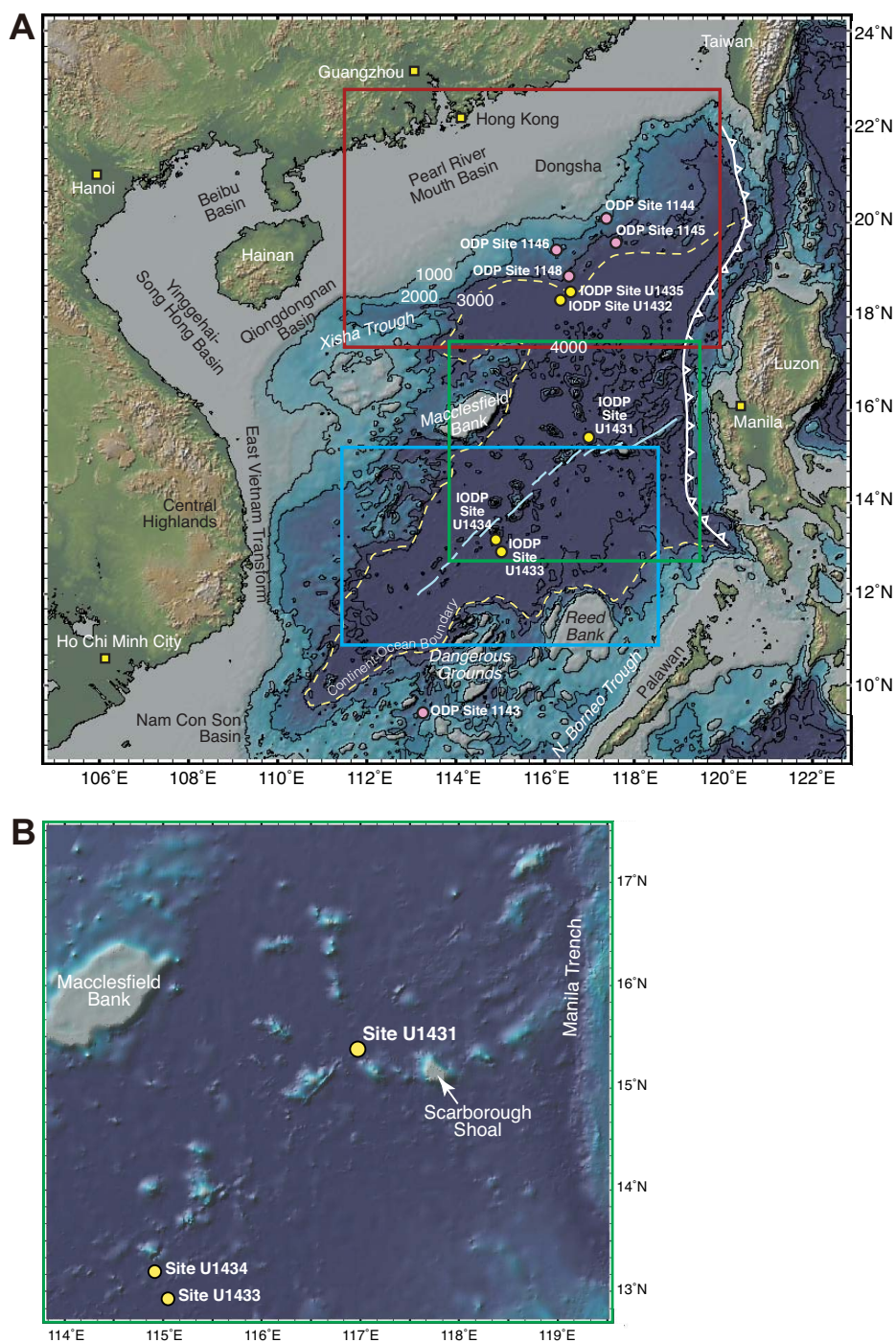


Figure F8 (continued). C. Detailed bathymetry around Sites U1432 and U1435 (red box in A) showing nearby continental shelf, the Manila Trench, and inferred continent/ocean boundary. D. Detailed bathymetry around Sites U1433 and U1434 (blue box in A) showing nearby seamount and Dangerous Grounds and Reed Bank to the south.

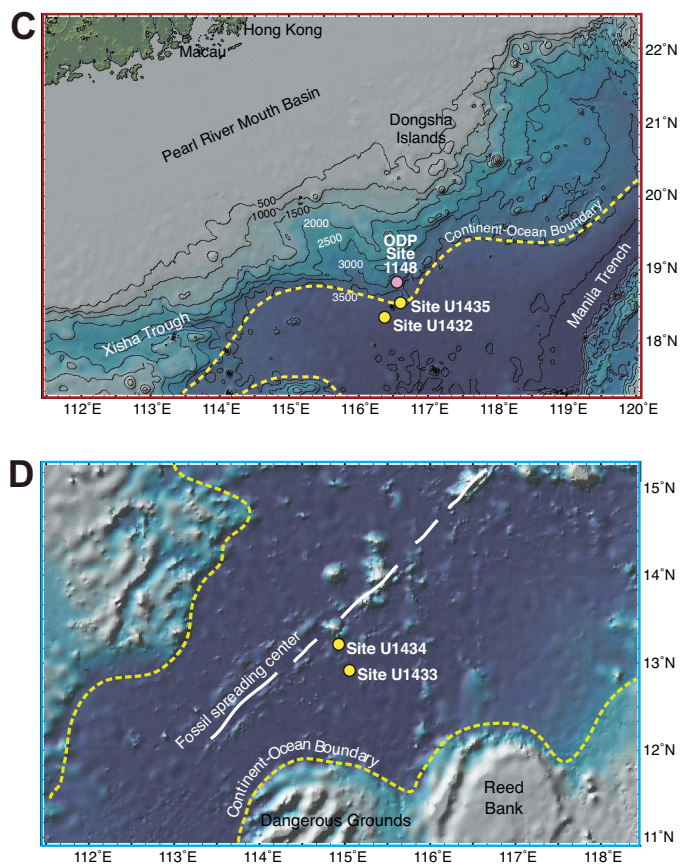


Figure F9. Lithostratigraphic and physical properties summary of Site U1431 based on a composite of Holes U1431D and U1431E. Core magnetic susceptibility and gamma-ray attenuation (GRA) density (filtered) were measured on the Section-Half Multisensor Logger, moisture and density (MAD) were measured on discrete samples, and *P*-wave velocities were measured on the Section Half Measurement Gantry. Downhole log data, magnetic susceptibility, and total natural gamma radiation are from the main pass of the triple combination tool string, and *P*-wave velocities are from Pass 2 of the Formation MicroScanner-sonic tool string. Downhole log depths have been shifted upwards by 5 m to correlate with the core physical property data.

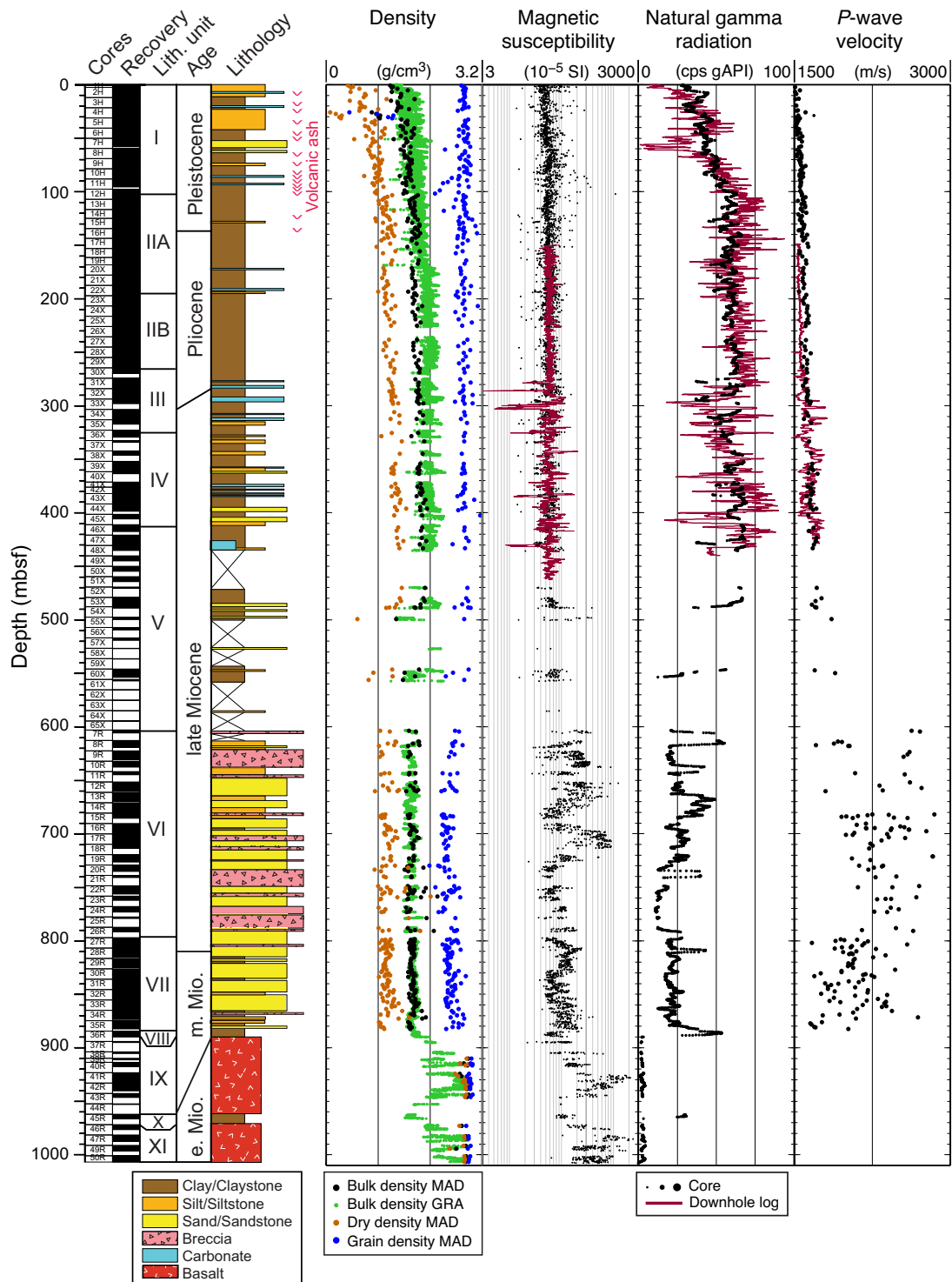


Figure F10. Age-depth model with estimated sedimentation rates for Site U1431 based on biostratigraphic and paleomagnetic datums. Dashed lines indicate an alternate or tentative interpretation.

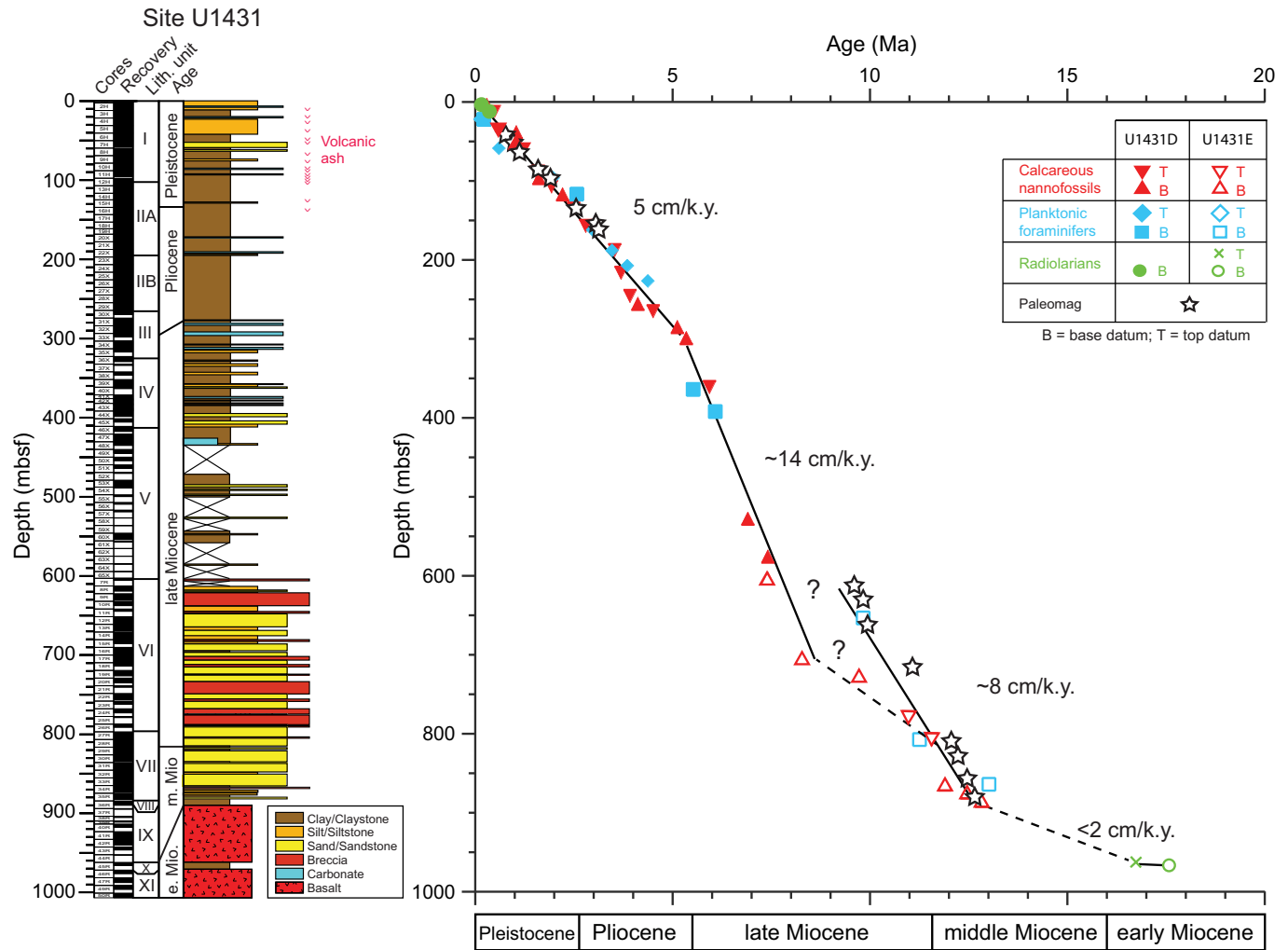


Figure F11. Lithostratigraphic summary of igneous rock and lithologic features, Hole U1431E. EOH = end of hole.

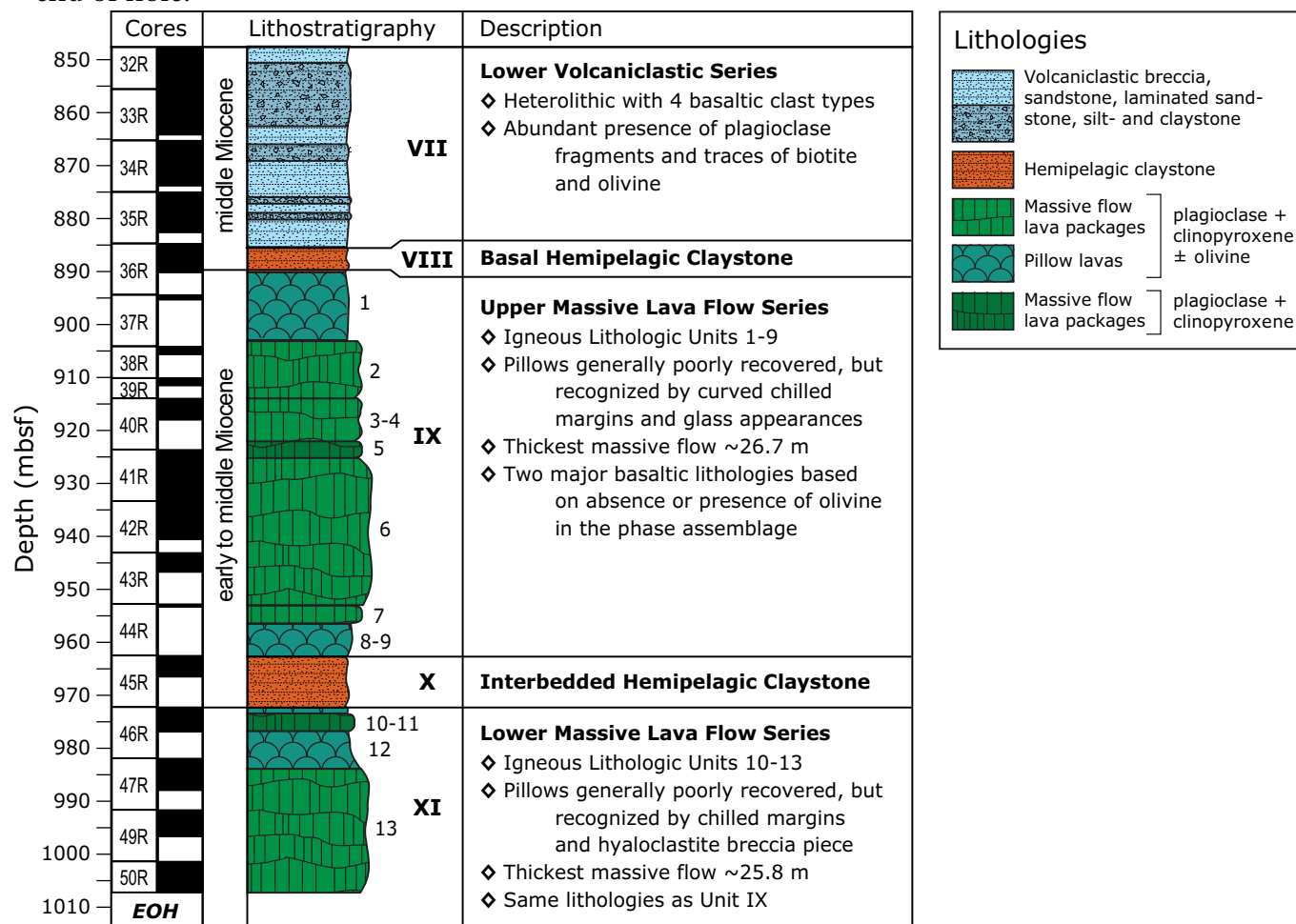


Figure F12. Total alkalis vs. silica, with classification of volcanic rock types of Le Maitre et al. (1989). The dashed blue line divides data between tholeiitic and alkalic lavas of Hawaii (Macdonald and Katsura, 1964; Macdonald, 1968). Shown for comparison are data for Indian Ocean mid-ocean-ridge basalt (MORB) from the Geochemical Rock Database (georoc.mpch-mainz.gwdg.de/), the seamount in the South China Sea (Tu et al., 1992; Hékinian et al., 1989), ocean island basalt of Hainan Island (Wang et al., 2012), and Pacific MORB (Zhang et al., 2009, 2012a, 2012b, 2013).

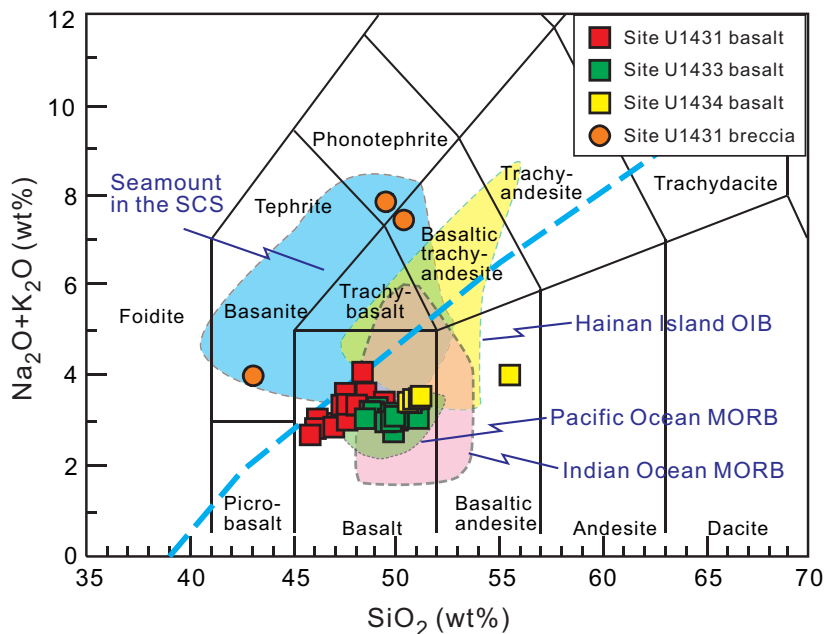


Figure F13. Plots of TiO_2 vs. (A) P_2O_5 , (B) V, (C) Sc, and (D) Sr. Shown for comparison are data for Indian Ocean mid-ocean-ridge basalt (MORB) from the Geochemical Rock Database (georoc.mpch-mainz.gwdg.de/), the seamount in the South China Sea (Tu et al., 1992; Hékinian et al., 1989), ocean island basalt of Hainan Island (Wang et al., 2012), and Pacific MORB (Zhang et al., 2009, 2012a, 2012b, 2013).

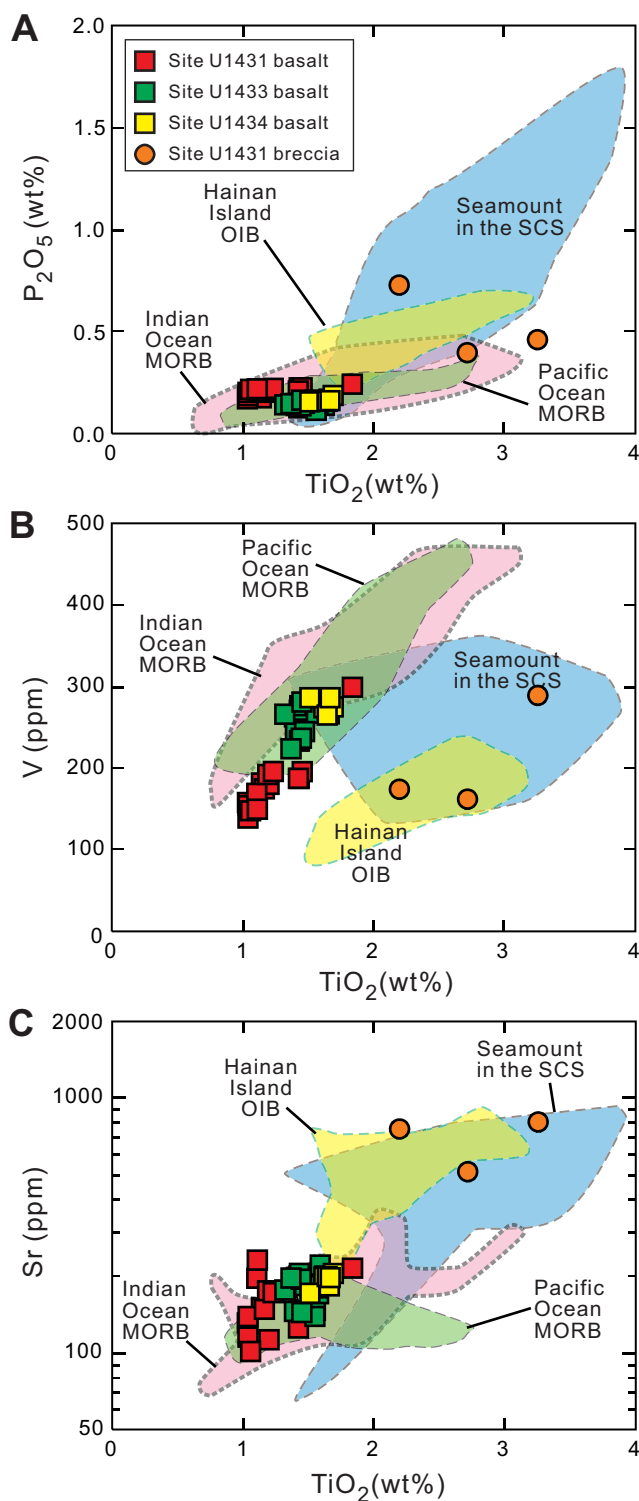


Figure F14. Map of heat flow values for Expedition 349 (large circles) and Ocean Drilling Program Leg 184 (large circles) and the compilation of heat flow data in Li et al., 2010 (small circles).

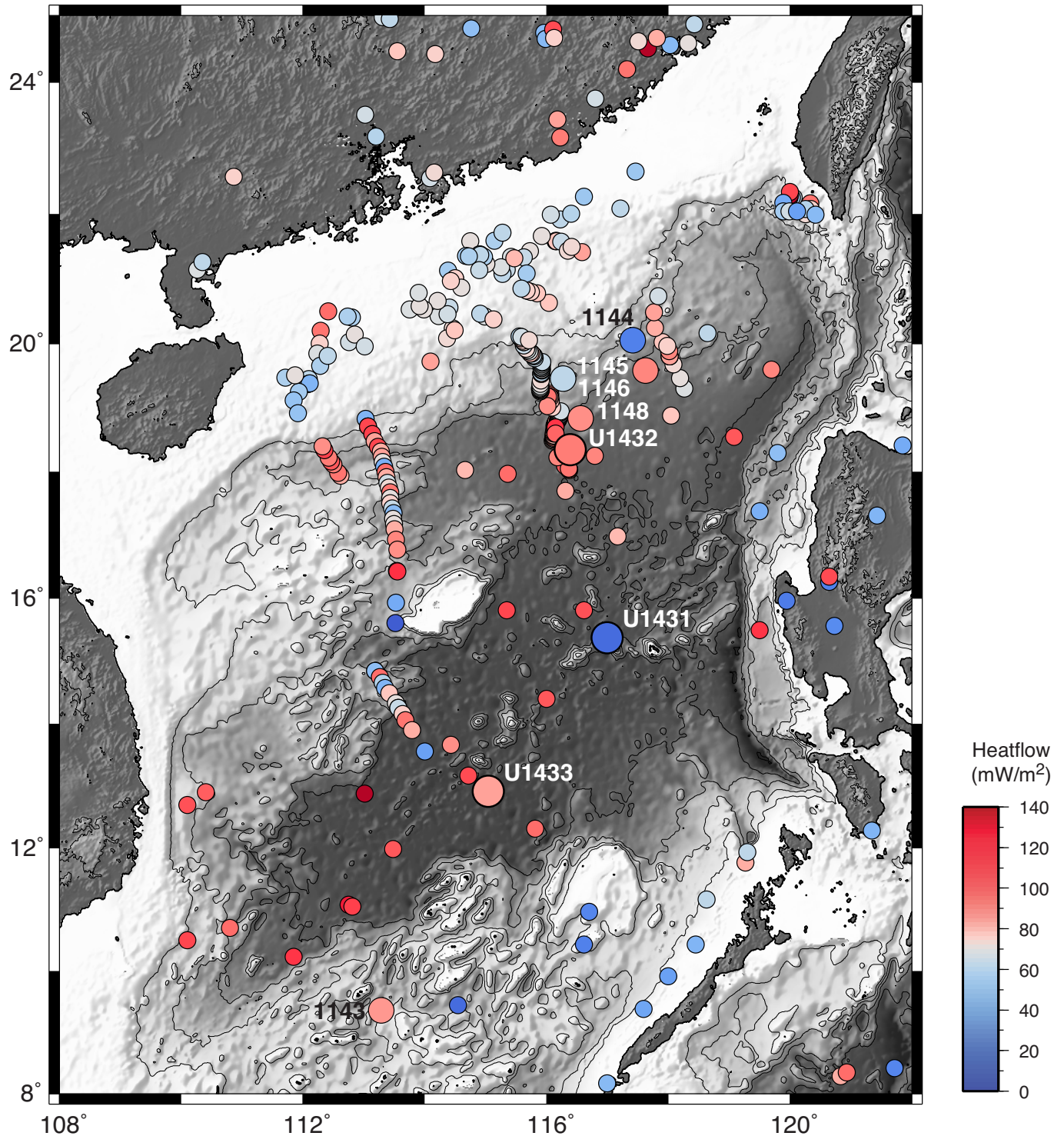


Figure F15. Lithostratigraphic and physical properties summary, Hole U1432C. Core magnetic susceptibility and gamma-ray attenuation (GRA) density (filtered) were measured on the Section-Half Multisensor Logger, moisture and density (MAD) were measured on discrete samples, and *P*-wave velocities were measured on the Section Half Measurement Gantry.

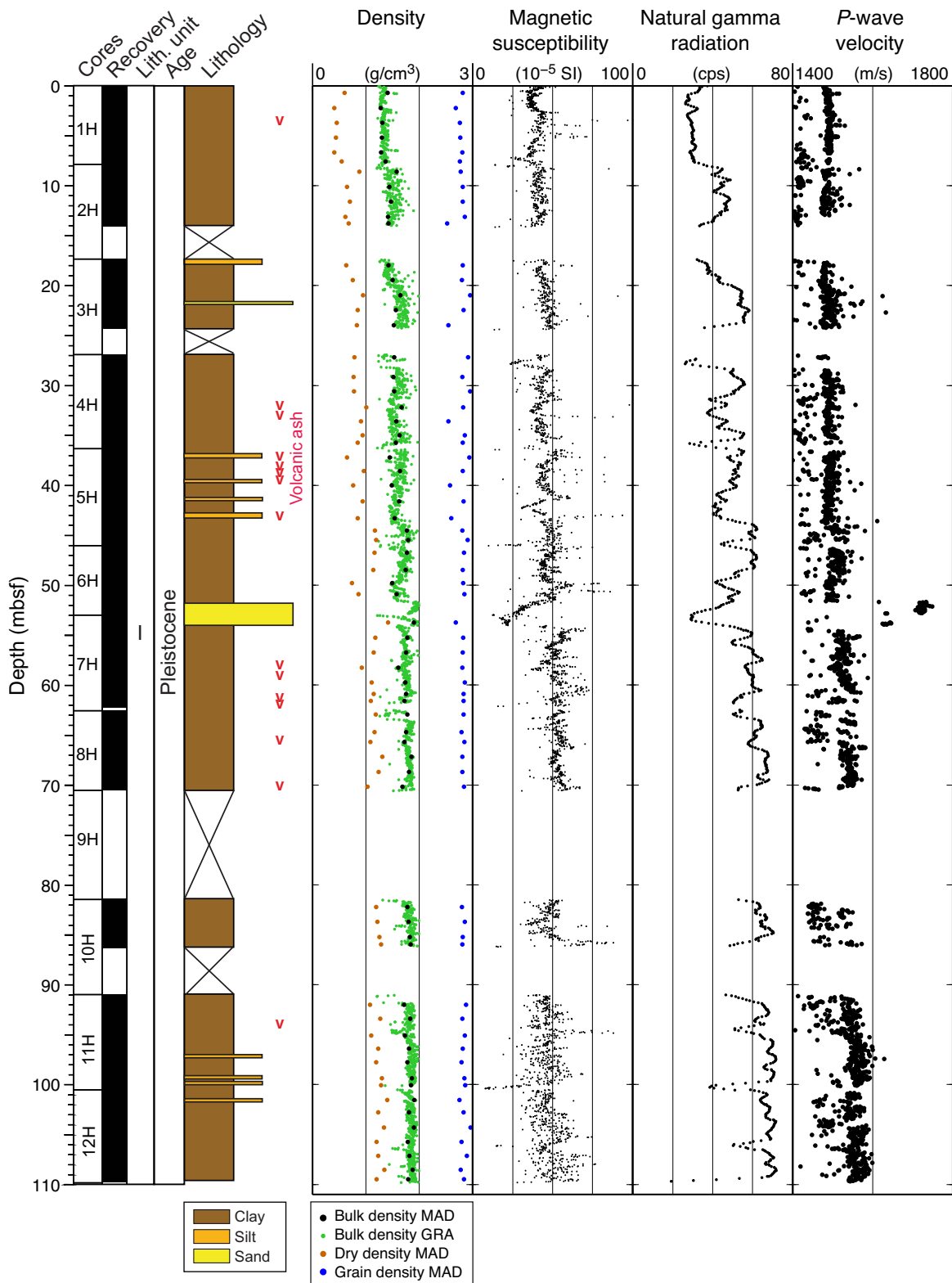


Figure F16. Age-depth model with estimated sedimentation rate for Hole U1432C based on biostratigraphic and paleomagnetic datums.

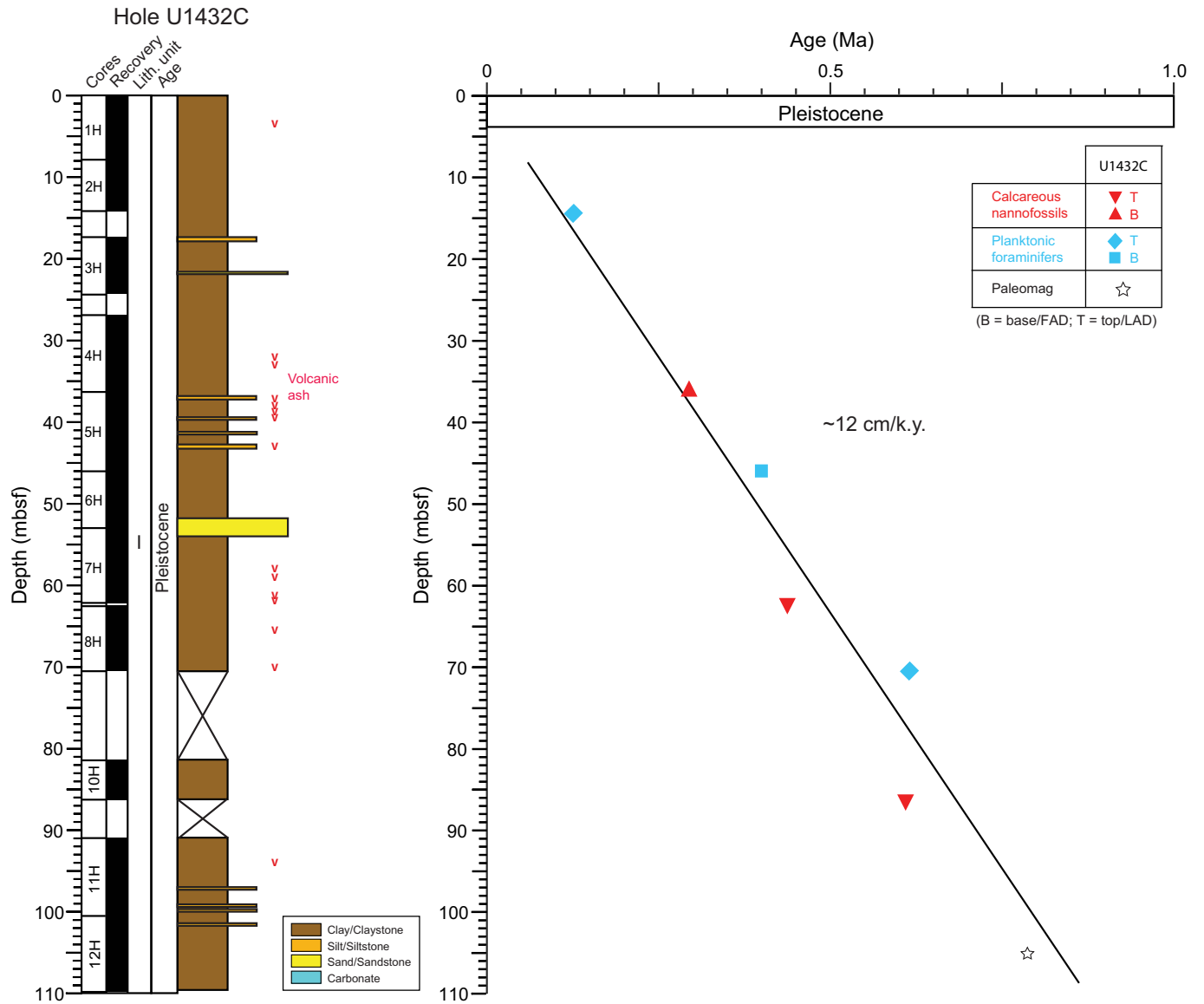


Figure F17. Lithostratigraphic and physical properties summary, Site U1433. Physical properties and downhole measurements are from Holes U1433A and U1433B. Core magnetic susceptibility and gamma-ray attenuation (GRA) density (filtered) were measured on the Section-Half Multisensor Logger, moisture and density (MAD) were measured on discrete samples, and *P*-wave velocities were measured on the Section Half Measurement Gantry. Downhole log data, magnetic susceptibility, and total natural gamma radiation are from the main pass of the triple combination tool string, and *P*-wave velocities are from the main pass of the Formation MicroScanner-sonic tool string. Downhole log depths have been shifted upward by ~2 m to correlate with the core physical property data.

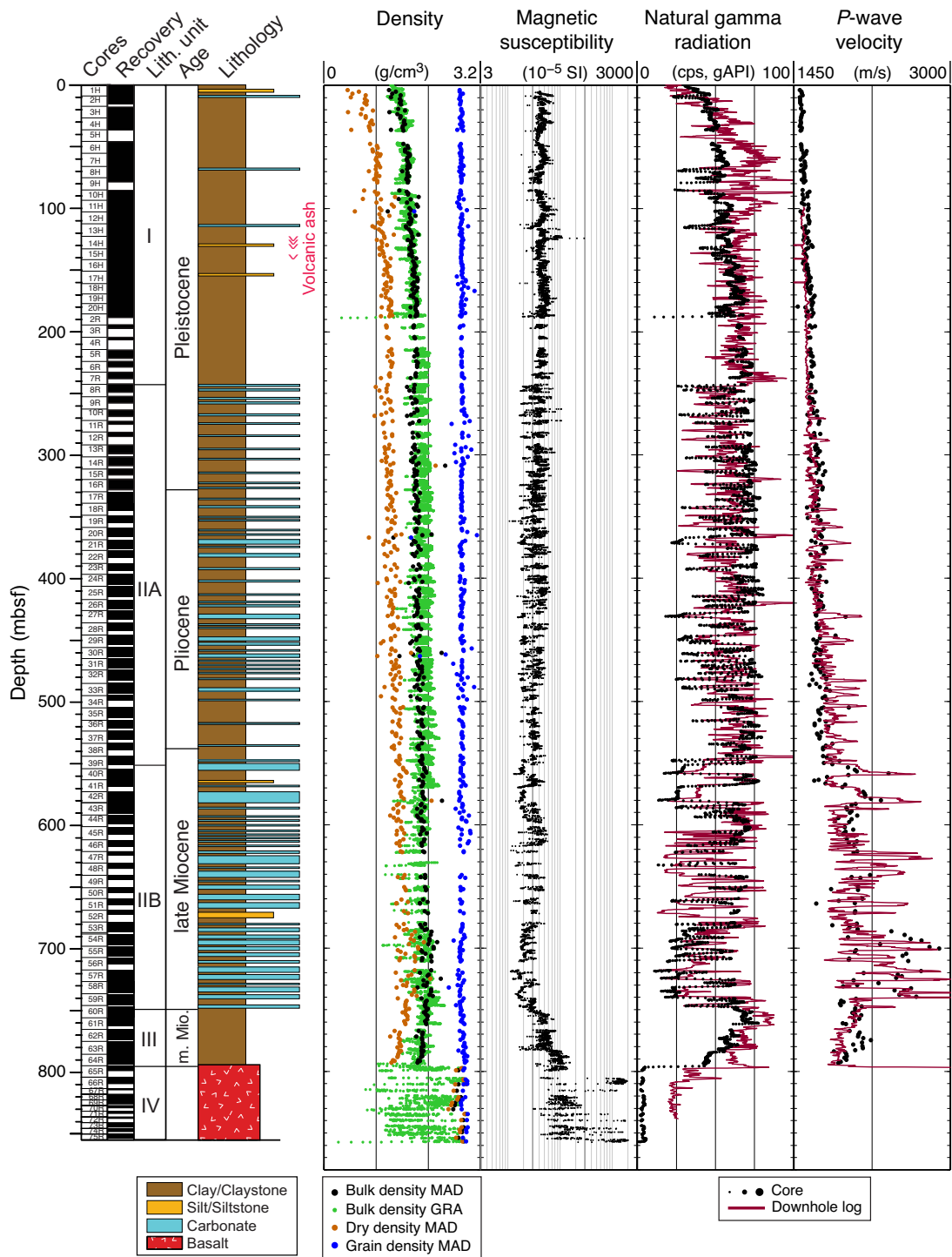


Figure F18. Age-depth model with estimated sedimentation rates for Site U1433 based on biostratigraphic and paleomagnetic datums. Dashed line indicates a tentative interpretation.

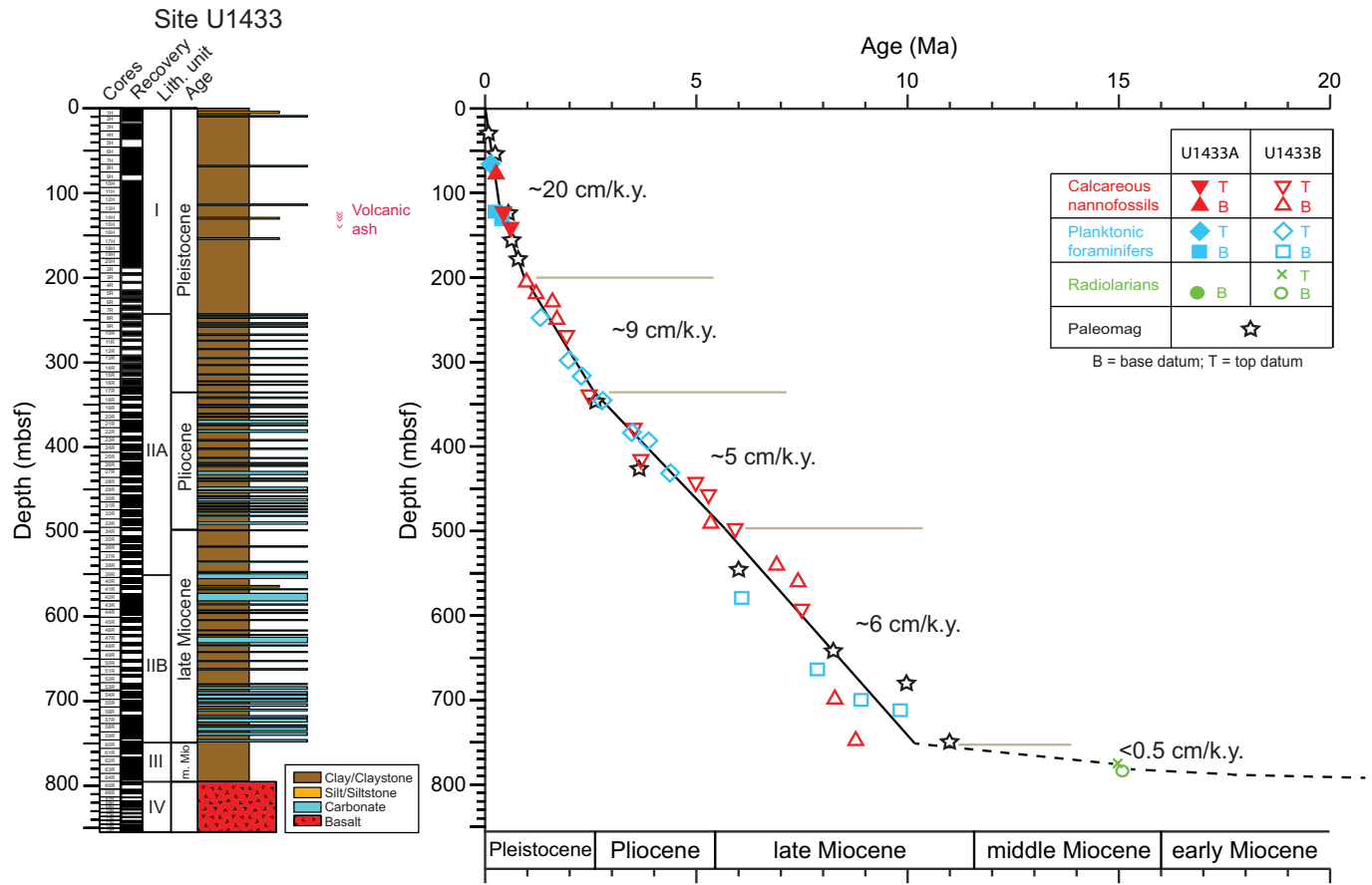


Figure F19. Lithostratigraphic summary of igneous rock and lithologic features, Hole U1433B. EOH = end of hole.

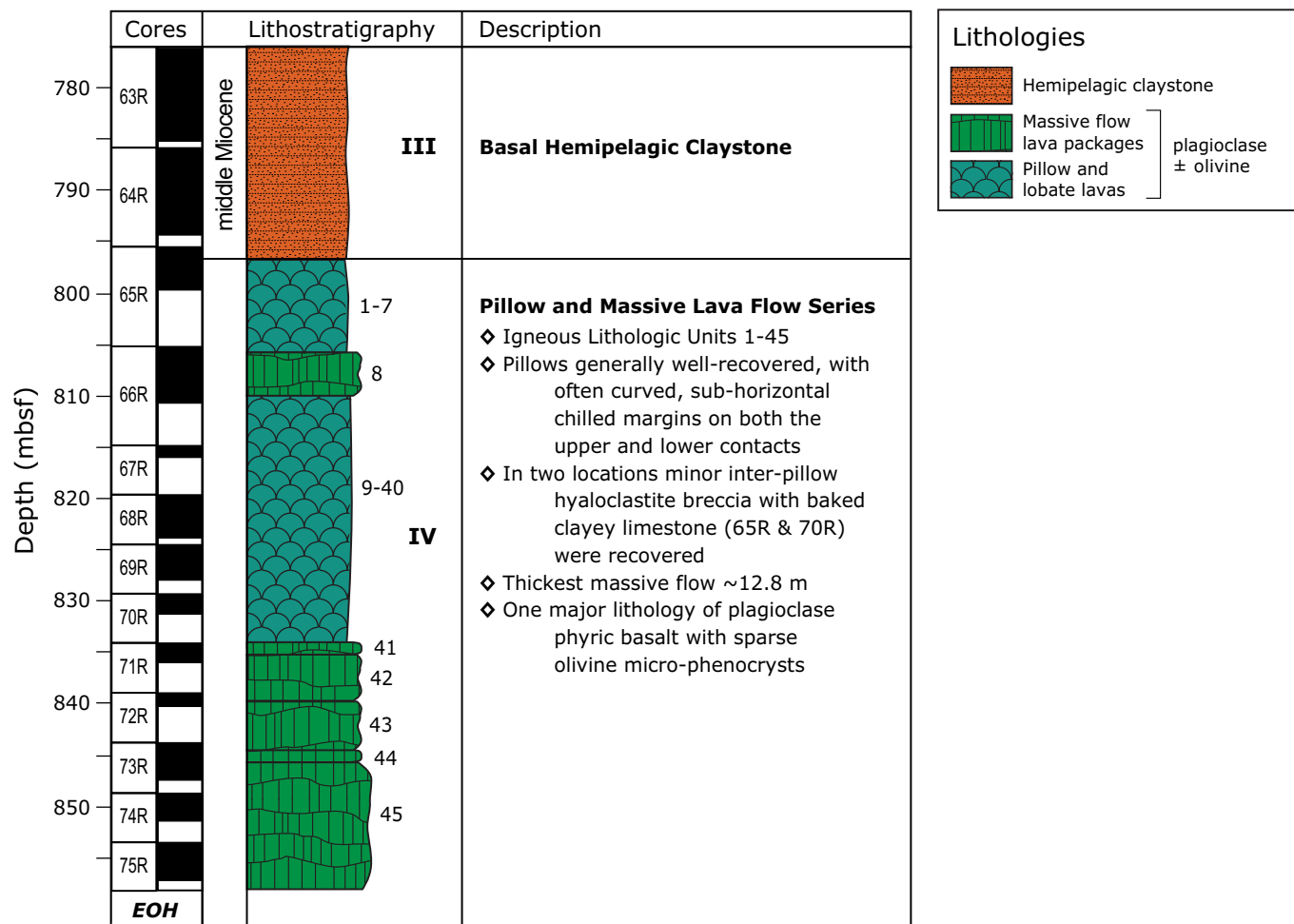


Figure F20. Downhole Formation MicroScanner (FMS) images showing basalt pillows in the 833–836 m WMSF interval, Hole U1433B.

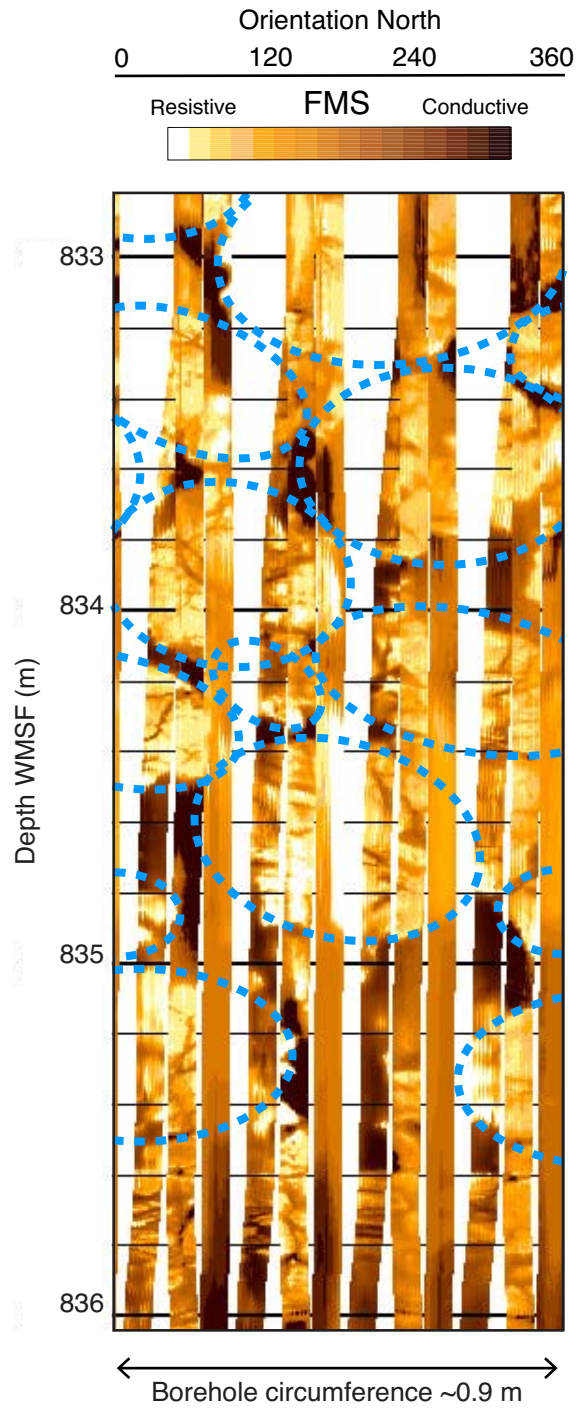


Figure F21. Lithostratigraphic and physical properties summary, Hole U1434A. Core magnetic susceptibility and gamma-ray attenuation (GRA) density (filtered) were measured on the Section-Half Multisensor Logger, moisture and density (MAD) were measured on discrete samples, and *P*-wave velocities were measured on the Section Half Measurement Gantry.

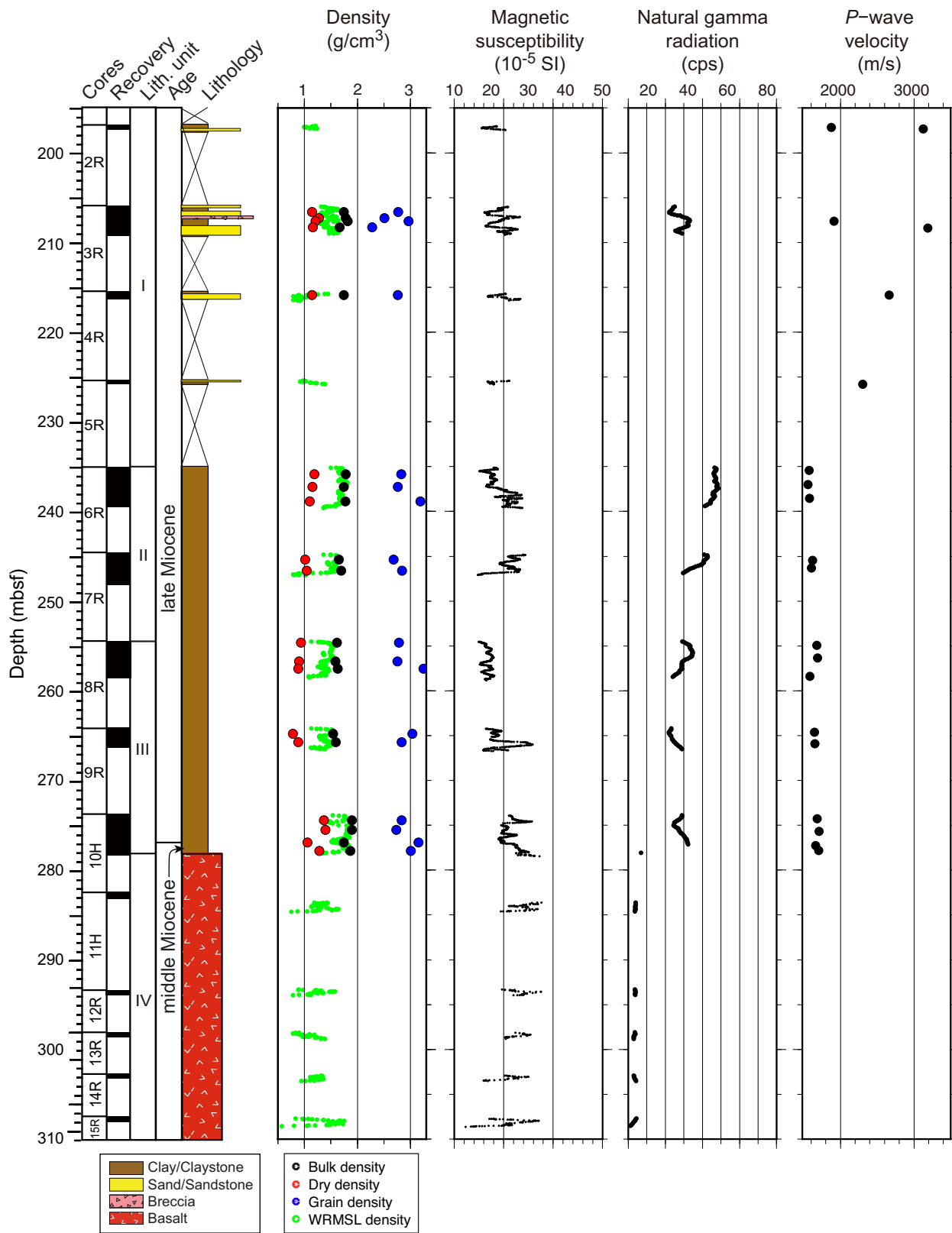


Figure F22. Age-depth model with estimated sedimentation rate for Site U1434 based on biostratigraphic and paleomagnetic datums.

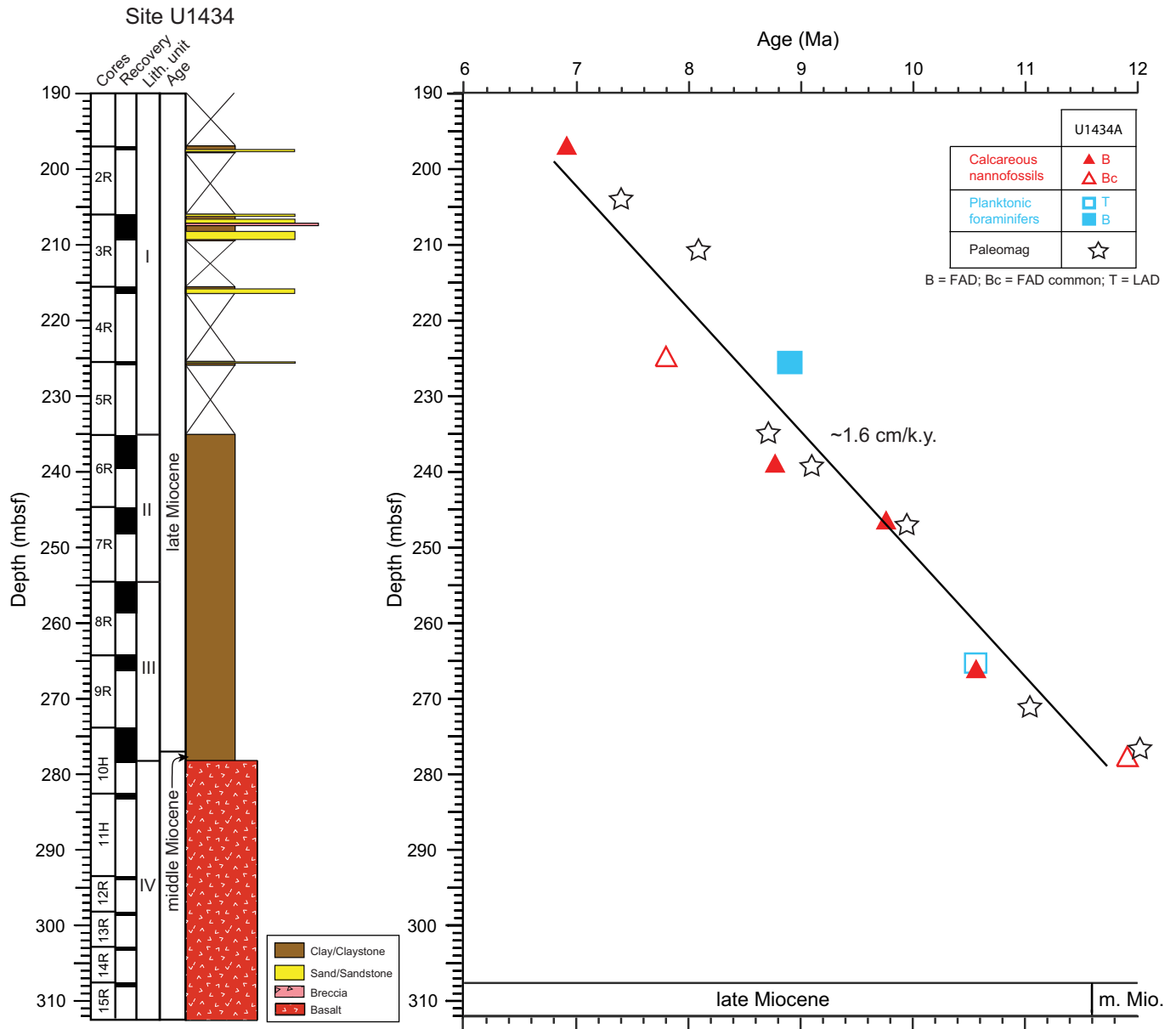


Figure F23. Lithostratigraphic summary of igneous rock and lithologic features, Hole U1434A. EOH = end of hole.

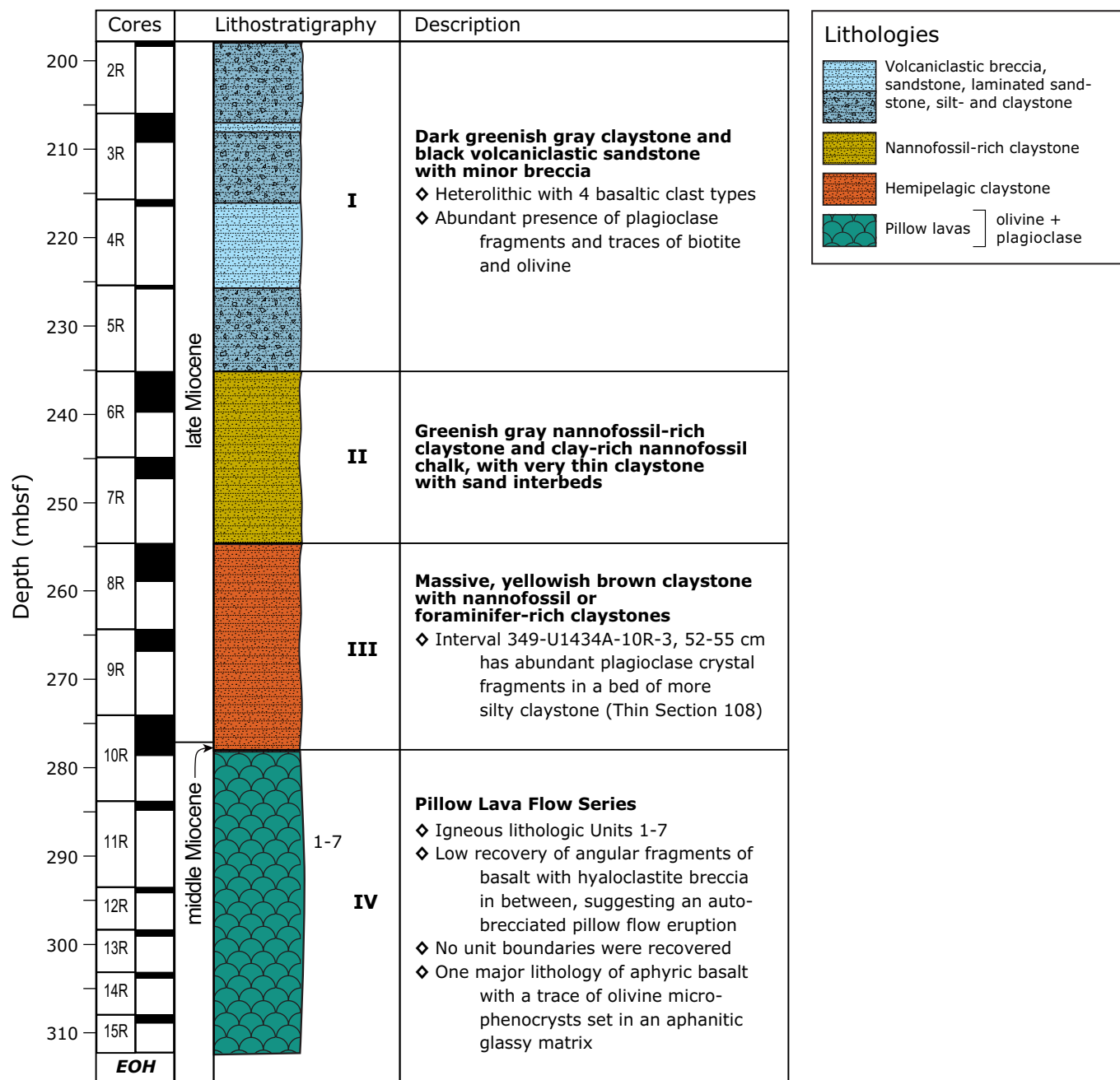


Figure F24. Lithostratigraphic and physical properties summary, Hole U1435A. Core magnetic susceptibility and gamma-ray attenuation (GRA) density (filtered) were measured on the Section-Half Multisensor Logger, moisture and density (MAD) were measured on discrete samples, and *P*-wave velocities were measured on the Section Half Measurement Gantry.

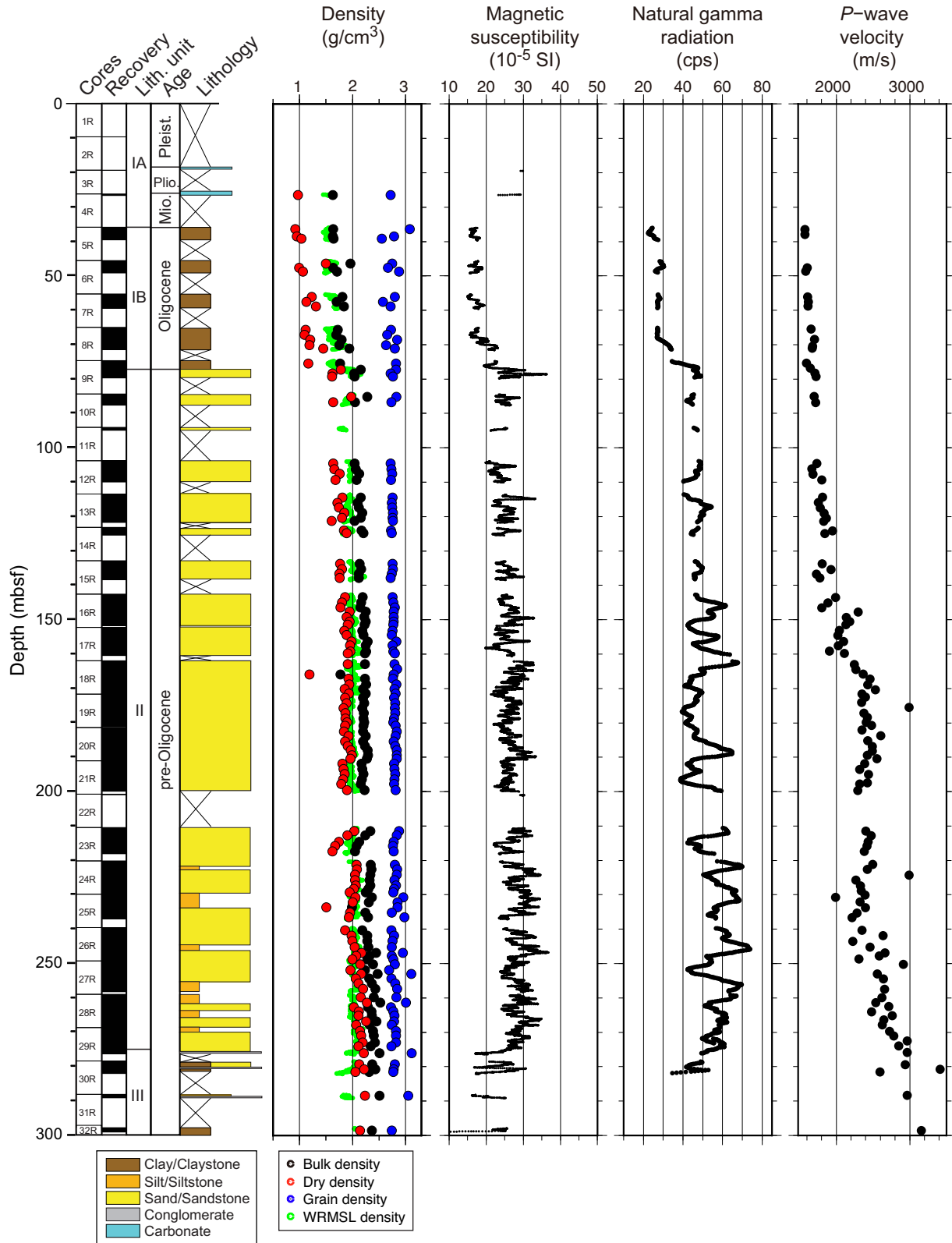
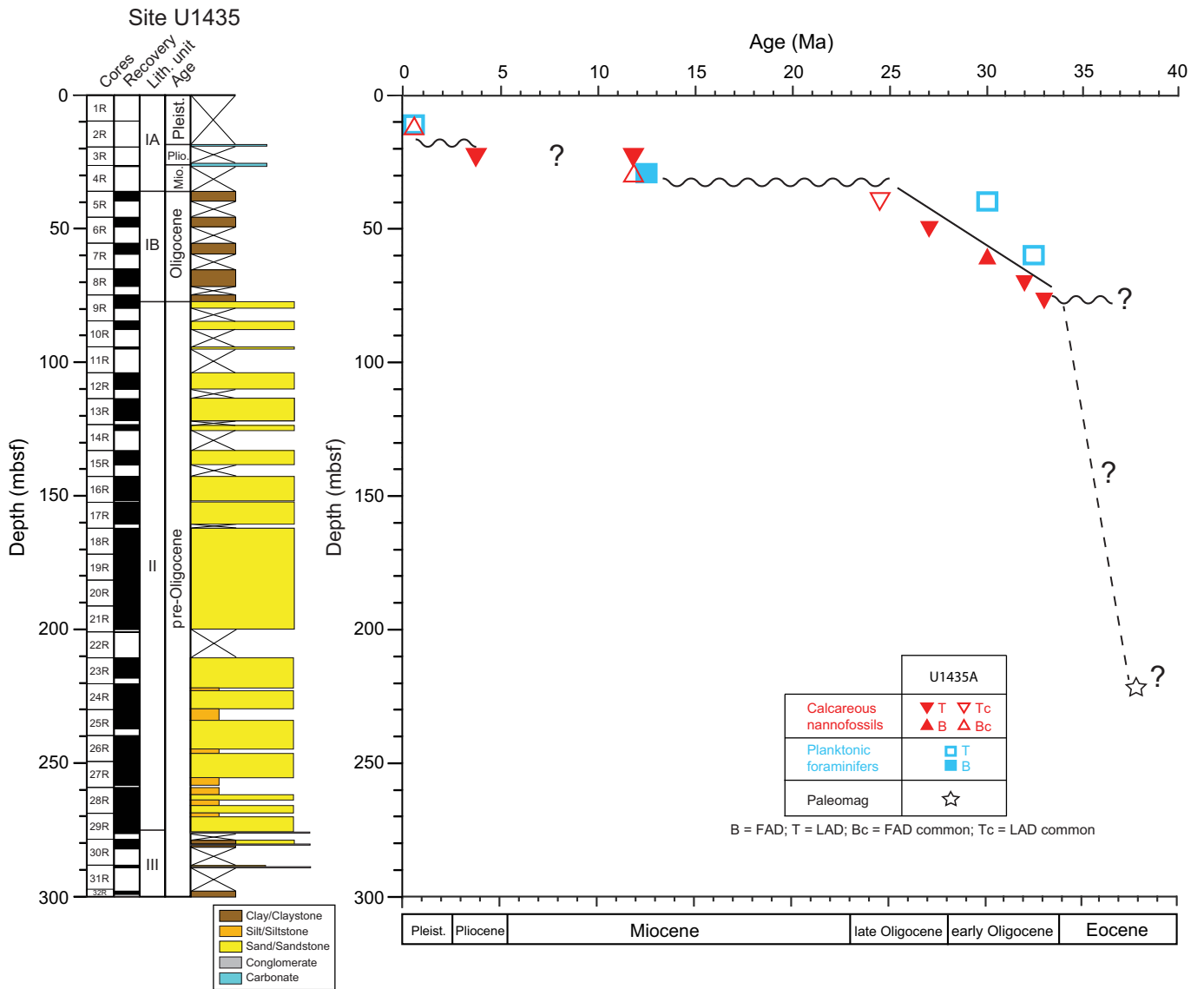


Figure F25. Age-depth model for Site U1435 based on biostratigraphic and paleomagnetic datums. Dashed line indicates a tentative interpretation. Wavy lines indicate possible hiatuses.



doi:10.14379/iodp.proc.349.101.2015

Expedition 349 summary¹



Contents

- 1 Abstract
- 2 Introduction
- 3 Background
- 6 Scientific objectives
- 10 Site summaries
- 30 Expedition synthesis
- 34 Preliminary scientific assessment
- 35 Operations
- 40 References

C.-F. Li, J. Lin, D.K. Kulhanek, T. Williams, R. Bao, A. Briais, E.A. Brown, Y. Chen, P.D. Clift, F.S. Colwell, K.A. Dadd, W.-W. Ding, I. Hernández-Almeida, X.-L. Huang, S. Hyun, T. Jiang, A.A.P. Koppers, Q. Li, C. Liu, Q. Liu, Z. Liu, R.H. Nagai, A. Peleo-Alampay, X. Su, Z. Sun, M.L.G. Tejada, H.S. Trinh, Y.-C. Yeh, C. Zhang, F. Zhang, G.-L. Zhang, and X. Zhao²

Keywords: International Ocean Discovery Program, IODP, *JOIDES Resolution*, Expedition 349, Site U1431, Site U1432, Site U1433, Site U1434, Site U1435, South China Sea, continent/ocean boundary, pelagic red clay, seamount volcanoclastics, interflow sediment, mid-ocean-ridge basalt, basement magnetization, carbonate turbidite, calcite compensation depth, microbiological community, magnetic susceptibility

Abstract

The South China Sea (SCS) provides an outstanding opportunity to better understand complex patterns of continental margin breakup and basin formation. The SCS is situated at the junction of the Eurasian, Pacific, and Indo-Australian plates and is a critical site linking some of the major western Pacific tectonic units. Despite extensive studies, sampling of basement rock and directly overlying basal sediment in the deep basin is lacking. This leaves a large margin of error in estimated ages of the SCS opening and closing, rendering various hypotheses regarding its opening mechanism and history untested. This also hampers understanding of East Asian tectonic and paleoenvironmental evolution.

We drilled five sites in the deep basin of the SCS. Three of these sites (U1431, U1433, and U1434) cored into oceanic basement near the fossil spreading center. The two remaining sites (U1432 and U1435) are located proximal to the northern continent/ocean boundary. We recovered a total of 1524 m of sediment/sedimentary rock and 78 m of oceanic basalt and also carried out downhole geophysical logging (triple combination and Formation MicroScanner-sonic tool strings) at the two deepest sites (U1431 and U1433). These materials and data were extensively examined and discussed during the expedition and allowed us to draw the following principal conclusions on the opening of the SCS:

1. Based on shipboard dating of microfossils in the sediment immediately above the basaltic basement and between the lava flow units, the preliminary cessation age of spreading in both the East and Southwest Subbasins is around early Miocene (16–20 Ma). Further postcruise radiometric dating of basement basalt from these sites plus additional calibration of magnetic anomaly models and paleomagnetic measurements will further refine the age range. Overall, a large difference is not apparent in

the terminal ages of seafloor spreading between the two subbasins.

2. At Site U1435, we were able to drill into a structural high standing along the continent/ocean boundary. Coring at this site recovered a sharp unconformity at ~33 Ma, above which is marine sediment and below which are poorly sorted sandstone and black mudstone, interpreted as littoral deposits. Environmental interpretation will require further shore-based studies because the sequence is almost entirely barren of marine microfossils. Nevertheless, we interpret this unconformity to be likely directly related to the continental breakup during the initial opening of the SCS. The onset of seafloor spreading is therefore estimated to be at ~33 Ma.
3. All sites contain deep marine deposits but show significant areal variations in postspreading sedimentary environment and provenance. Site U1431 records evidence for deep-marine turbidite deposition from terrestrial sources. The observed coarser silt turbidites may have a source in Taiwan or other surrounding blocks, whereas interbedded calcareous turbidites at this site could be transported from local sources, such as nearby seamounts topped by carbonate platforms. In contrast, the source for upper Miocene clay and silt turbidites at Site U1433 could be Borneo or mainland Southeast Asia, with the source of the interbedded carbonate turbidites likely the Dangerous Grounds or Reed Bank area located south of the site.
4. Sites U1431 and U1434 are close to seamounts developed along the relict spreading center. Occurrences of basaltic clasts and mineral fragments in the volcanoclastic sandstone and breccia may reveal the magmatic history and mantle source of the seamounts and potentially their relationship with the terminal processes of spreading. The volcanoclastic breccia and sandstone at Site U1431 are dated as late middle Miocene to early late Miocene (~8–13 Ma), suggesting a 5 million year duration of sea-

¹ Li, C.-F., Lin, J., Kulhanek, D.K., Williams, T., Bao, R., Briais, A., Brown, E.A., Chen, Y., Clift, P.D., Colwell, F.S., Dadd, K.A., Ding, W.-W., Hernández-Almeida, I., Huang, X.-L., Hyun, S., Jiang, T., Koppers, A.A.P., Li, Q., Liu, C., Liu, Q., Liu, Z., Nagai, R.H., Peleo-Alampay, A., Su, X., Sun, Z., Tejada, M.L.G., Trinh, H.S., Yeh, Y.-C., Zhang, C., Zhang, F., Zhang, G.-L., and Zhao, X., 2015. Expedition 349 summary. In Li, C.-F., Lin, J., Kulhanek, D.K., and the Expedition 349 Scientists, *Proceedings of the International Ocean Discovery Program, 349: South China Sea Tectonics*: College Station, TX (International Ocean Discovery Program). <http://dx.doi.org/10.14379/iodp.proc.349.101.2015>

² Expedition 349 Scientists' addresses.

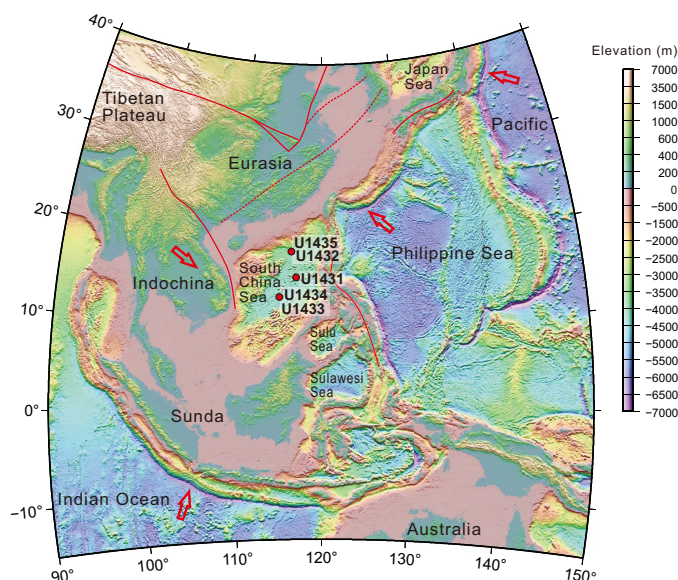
mount volcanism starting a few million years after the cessation of seafloor spreading. At Site U1434, volcanoclastic breccia and sandstone are most likely sourced from the adjacent seamount ~15 km to the north. The age of this recovered unit is late Miocene (younger than 9 Ma). Further postcruise sedimentological and geochemical studies, as well as radiometric dating of potassium-bearing mineral fragments, will refine the ages and timing of these seamount activities and reveal how magma sources at the dying spreading center evolved through time.

5. We successfully cored into ocean basement in the SCS for the first time and recovered basalt at three sites (U1431, U1433, and U1434). The cored basalt has variable phase assemblages of plagioclase, olivine, and clinopyroxene and is concluded to be typical mid-ocean-ridge basalt based on petrological and geochemical evidence. Postcruise radiometric dating will determine the absolute ages of the basaltic basement units. Postcruise petrological and geochemical analyses on the basalts will provide information on the mantle sources, melting, and crystallization history of the youngest ocean crust.

Introduction

Since the late Mesozoic, the South China Sea (SCS) area (Figures F1, F2) has been at the center of many first-order tectonic and paleoclimatic events. Mesozoic subduction of the paleo-Pacific plate under the Eurasian plate partially occurred along the present-day northeastern SCS continental margin (Jahn et al., 1976; Hilde et al., 1977; Hamilton, 1979; Holloway, 1982; Taylor and Hayes, 1983; Hayes et al., 1995; Zhou and Li, 2000; Yang and Feng, 2003; Xiao and Zheng, 2004; Zhou et al., 2008; Li et al., 2008a). This subduction resulted in the emplacement of igneous rocks and the formation of a wide orogenic belt in Southeast Asia (Zhou and Li, 2000; Shi and Li, 2012). Subduction is thought to have ceased in the mid-Cretaceous, with a transition to regional extension during the Late Cretaceous. Opening of the SCS began in the Cenozoic through continental breakup and subsequent seafloor spreading. The Red River strike-

Figure F1. Regional topography and geodynamic framework of Southeast Asia. Data based on Smith and Sandwell (1997). Solid red lines = regional faults. Red arrows show direction of plate movement and solid red circles mark sites drilled during Expedition 349.

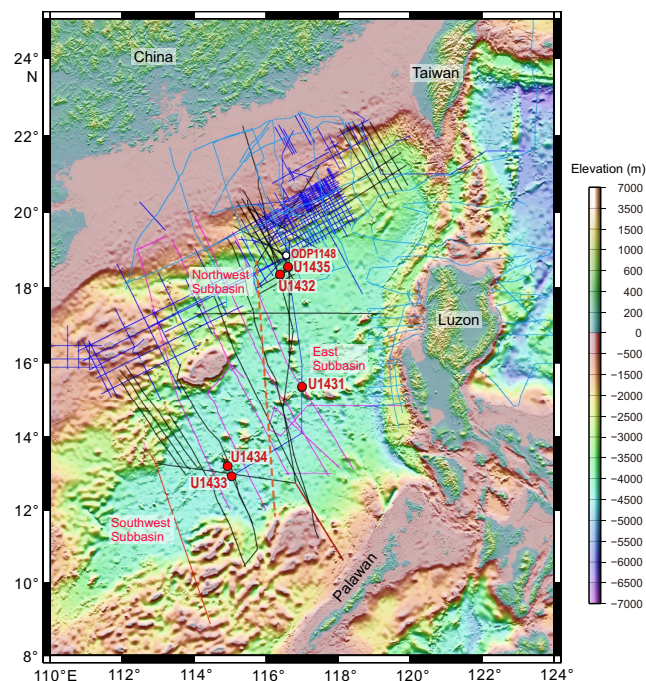


slip fault also displaced the Indochina block by hundreds of kilometers during the Oligocene and Miocene (Tapponnier et al., 1986, 1990; Lacassin et al., 1997; Leloup et al., 2001; Gilley et al., 2003). The early work of Taylor and Hayes (1980, 1983) and Briais et al. (1993) suggested that the SCS opened from ~32 to ~16 Ma during the Oligocene and early Miocene. Barckhausen and Roeser (2004) and Barckhausen et al. (2014) argued that seafloor spreading was faster in the later stages than at the beginning of the opening and ceased at 20.5 Ma (Anomaly 6a1) over the entire SCS, ~4 million years earlier than interpreted in previous studies.

Ages of the oceanic crust in the SCS basin were only constrained from magnetic anomaly correlations and empirical relationships between ages and bathymetry and/or heat flow. The uncertainties in the timing and episodes of the Cenozoic opening of the SCS hamper understanding of other key geological processes in Southeast Asia, including the geodynamic transition from Mesozoic subduction to Cenozoic rifting, the relationship between the motion on the large strike-slip faults and extension (extrusion), the Cenozoic opening mechanism, oceanic crustal accretion and mantle evolution, and paleoceanographic and sedimentary responses. In order to address regional questions related to East Asian geology and fundamental issues regarding continental breakup and the mechanism through which the SCS basin opened, it is essential to determine when seafloor spreading initiated and when it ceased. To do this, during Expedition 349 we drilled into the oceanic basement and retrieved both sedimentary and basaltic rocks from two subbasins of the SCS. Drilling and coring into igneous basement is the only means of validating various opening mechanisms.

Expedition 349 was based on Integrated Ocean Drilling Program Proposal 735-CPP2, developed in part from results of an in-

Figure F2. Topographic and bathymetric map of the SCS region. Dashed red line = inferred Zhongnan fault zone. Solid red circles = Expedition 349 sites. Solid white circle = ODP Site 1148. Pink lines = seismic surveys collected during Cruises SO49 (1987) and SO197 (2008) on the R/V *Sonne*. Blue, red, and black lines = seismic data collected by Chinese research institutes and oil companies. Turquoise lines = reflection seismic data acquired in the 1980s from Cruises V3607, V3608, V3613, V3614, and RC2006.



ternational workshop held at Tongji University in Shanghai, China, in early 2012 (Li et al., 2012). The primary objectives of the expedition fall under four major categories and address the Earth Connections and Climate and Ocean Change themes in the science plan for the International Ocean Discovery Program (IODP) (available at www.iodp.org/science-plan-for-2013-2023):

1. To examine the mechanisms, timing, and sequences of Cenozoic seafloor spreading; to establish the complex opening history of different subbasins and styles of oceanic crustal accretion in the SCS; and to constrain the tectonic controls (such as spreading rate) on distinct magnetic contrasts among the subbasins;
2. To examine oceanic crustal accretion and mantle evolution and reveal the crustal nature and affinities of different subbasins in order to understand oceanic crustal and deep mantle processes associated with tectonic extrusion, magmatism, and magnetization;
3. To examine paleoceanographic and sedimentary responses to tectonic evolution of the SCS through development of a more complete 3-D sedimentation and subsidence model and linking it to regional climatic processes in response to various tectonic events; and
4. To examine driving forces leading to continental breakup and seafloor spreading and constrain whether the forces were far-field (triggered by the tectonic extrusion of the Indochina block), near-field (due to back-arc spreading or slab pull), or in situ (mantle plume and magmatism driven) in order to deepen our general understanding of the geodynamic interplay of mantle and lithosphere processes that led to the development of continental margin basins in the geological past and today.

Background Geological setting

The SCS is a western Pacific marginal sea situated at the junction of the Eurasian, Pacific, and Indo-Australian plates. It developed from Cenozoic continental margin rifting, and its central portion is floored with oceanic crust. Despite its relatively small size and short evolutionary history, the SCS has undergone nearly a complete Wilson cycle from continental breakup to seafloor spreading to subduction and is well suited for studying various plate boundary activities, such as continental margin rifting (e.g., Hayes and Nissen, 2005), seafloor subduction (the Manila Trench; e.g., Li et al., 2007b), strike-slip faulting (the Red River fault; e.g., Leloup et al., 2001; Clift and Sun, 2006), and active orogenic processes (Taiwan; e.g., Huang et al., 2001) (Figure F1).

Hypotheses for the opening mechanism of the SCS differ markedly (Figure F3) and include

1. India-Eurasia collision and the consequent tectonic extrusion mainly along the Red River fault (Figure F3A) (Tapponnier et al., 1982; Lallemand and Jolivet, 1986; Schärer et al., 1990; Briais et al., 1993; Flower et al., 2001; Leloup et al., 2001),
2. Slab pull and subduction of the proto-SCS under Sabah/Borneo (Figure F3B) (Taylor and Hayes, 1980, 1983; Holloway, 1982; Hall, 2002),
3. Extension related to an upwelling mantle plume (Figure F3C) (e.g., Fan and Menzies, 1992; Xu et al., 2012), and
4. Regional extension related to subduction and retreat of the Pacific plate along the western Pacific margin (Figure F3D) (Taylor and Hayes, 1980, 1983; Shi and Li, 2012).

In addition to these end-member models, hybrid models have been proposed (e.g., Cullen et al., 2010).

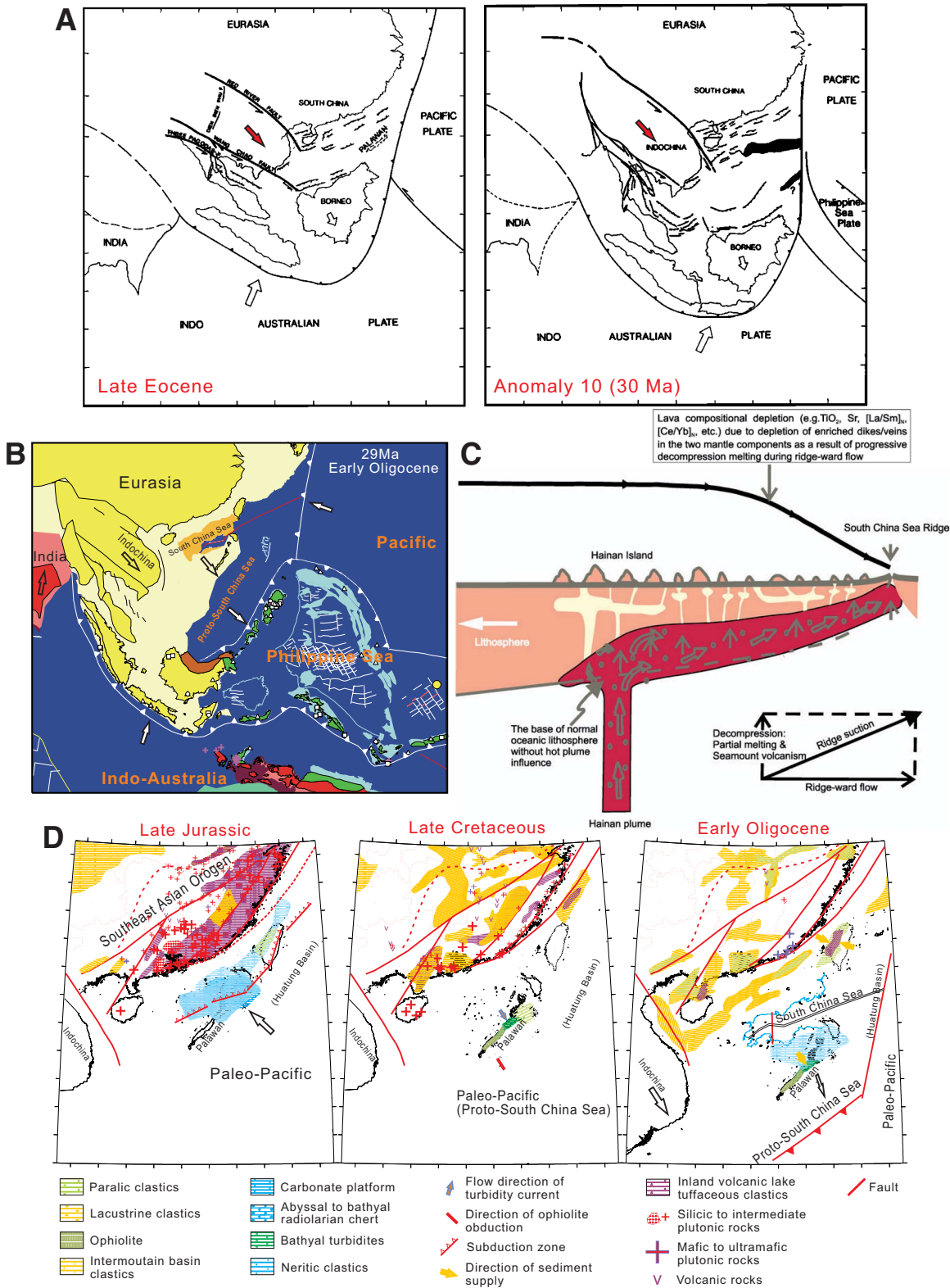
The original SCS basin before its subduction along the Manila Trench may have been twice the size that it is today (Sibuet et al., 2002), so geodynamic models must be able to explain the formation of this larger ocean basin. The Red River fault was active from 35 to 15 Ma, with displacement of as much as several hundred kilometers (e.g., Leloup et al., 2001; Gilley et al., 2003). Ages obtained from sites drilled during Expedition 349 will aid in testing the hypothesis that the motion on the Red River fault is coeval to and may have driven part of the extension and spreading in the SCS. Others suggested that only a minor amount of extension associated with the SCS spreading center may have been transferred to the Red River fault (Rangin et al., 1995; Morley, 2002; Clift et al., 2008). The initiation of regional rifting in East Asia during the Mesozoic occurred before the India-Eurasia collision (Figure F3D) and is thought to be associated with subduction of the paleo-Pacific plate (Taylor and Hayes, 1980, 1983; Shi and Li, 2012).

Some hypotheses require the existence of a proto-SCS oceanic basin (Haile, 1973; Madon et al., 1999) that was once connected to the Pacific plate and began to close around 44 Ma (e.g., Hall, 1996, 2002) in order to drive and accommodate the opening of the SCS (Figure F3B). A large part of this proto-SCS may have been subducted or uplifted as island arcs formed to the south in Borneo/Sabah and Palawan (Hall, 2002; Hutchinson, 1996, 2004), where remnants of the proto-SCS oceanic crust may be present (Hutchinson, 2005) and are one possible origin of the ophiolites of South Palawan (Rangin et al., 1990; Tu et al., 1992; Schlüter et al., 1996; Pubellier et al., 2004; Cullen, 2010). Slab-pull force from this subducting proto-SCS plate and a hypothesized in situ mantle plume may also have triggered or contributed to the opening of the SCS.

The opening of the SCS reveals complex patterns of continental breakup and seafloor spreading. Magnetic and seismic data suggest that the SCS basin can be divided into five magnetically distinct zones (Li et al., 2008b) (Zones A–E in Figure F4). In particular, magnetic amplitudes and orientations in the Southwest Subbasin (Zone E) differ markedly from those in the East Subbasin (Zone D). These two subbasins are divided by a complex set of transform faults forming the Zhongnan fault zone (Figures F2, F4) (Yao, 1995; Jin et al., 2002; Li et al., 2007a, 2008b). This magnetic contrast may support an episodic seafloor-spreading model (Ru and Pigott, 1986) or may be attributed to the different tectonic contexts within which the two subbasins evolved. Pautot et al. (1986) suggested that the youngest part of the East Subbasin in Zone D developed within an older, preexisting oceanic crust, whereas the Southwest Subbasin in Zone E resulted from continental rifting. Within the East Subbasin, two distinct conjugate magnetic anomalies (M1 and M2 in Figure F4) are thought to be the same age (anomaly 8 in Taylor and Hayes [1983] and Briais et al. [1993] models) and further divide the subbasin into a central part with high magnetic amplitudes and two separated parts with slightly weaker magnetization (Zones C1 and C1' in Figure F4) near the two conjugate continental margins. The magnetic pattern of the Northwest Subbasin also differs from its adjacent segment in the East Subbasin.

Additional important contrasts exist between the East and Southwest Subbasins. For example, the greater average water depths of the Southwest Subbasin compared to the East Subbasin have been interpreted to imply relatively older crustal ages (Ru and Pigott, 1986; Yao et al., 1994; Li et al., 2008b), which conflict with younger ages inferred from the higher heat flow and shallower Curie-point depths of the Southwest Subbasin (Ru and Pigott, 1986; Li

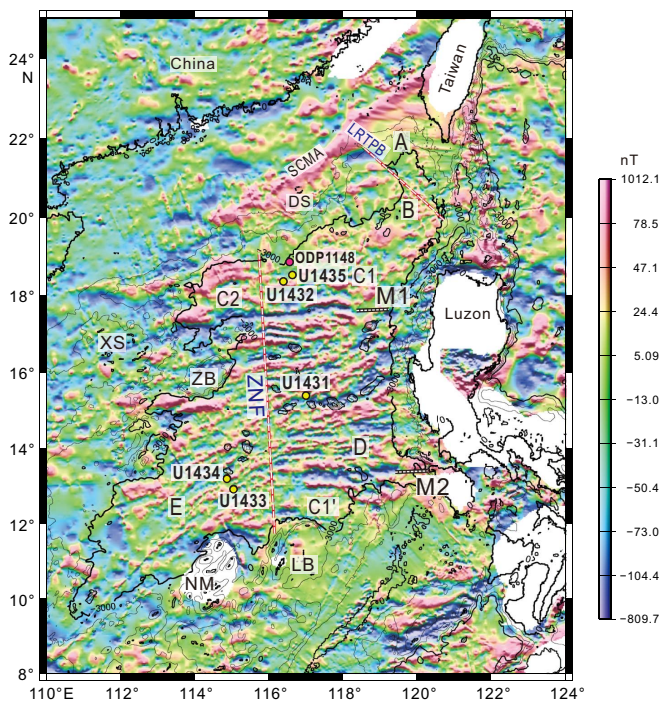
Figure F3. Hypothetical models for the driving mechanisms of the opening of the SCS. A. Opening induced by India-Eurasia continental collision and consequent tectonic extrusion (Tapponnier et al., 1982, 1990; Briais et al., 1993; Leloup et al., 2001; Flower et al., 2001). B. Opening induced by slab pull and subduction of the proto-SCS (Taylor and Hayes, 1980, 1983; Holloway, 1982; Hall, 2002). C. Opening induced by an upwelling mantle plume (e.g., Fan and Menzies, 1992; Xu et al., 2012). D. Opening induced by regional extension related to subduction and retreat of the Pacific plate (Taylor and Hayes, 1980, 1983; Shi and Li, 2012).



et al., 2010). Recent heating from magmatic activity could have contributed to the high heat flow in the Southwest Subbasin (Ru and Pigott, 1986; Li and Song, 2012), but this hypothesis needs to be tested through drilling.

A number of Cenozoic tectonic models have been proposed, but it remains uncertain as to whether the SCS basin experienced a single episode or multiple episodes of extension and seafloor spreading and, if multiple episodes, in what sequence the subbasins evolved (e.g., Taylor and Hayes, 1980; Pautot et al., 1986; Ru and Pigott, 1986; Briais et al., 1993; Yao et al., 1994; Hayes and Nissen, 2005; Li et al., 2007a, 2008b). For example, the opening of the East and Northwest Subbasins may have predated or been synchronous with that of the Southwest Subbasin (Figure F5A) (Taylor and Hayes, 1983; Briais et al., 1993; Lee and Lawver, 1995; Tongkul, 1994; Honza, 1995; Zhou et al., 1995; Schlüter et al., 1996; Hall, 2002; Hall and Morley, 2004; Hayes and Nissen, 2005; Braitenberg et al., 2006; Sun et al., 2009). This model contrasts with others in which earlier opening of the Southwest Subbasin is preferred (Figure F5B) (e.g., Ru and Pigott, 1986; Yao et al., 1994; Li et al., 2007a). This latter group of models considers the sharp contrasts between the East and Southwest Subbasins and the important role of the Zhongnan fault (Figures F2, F4). There are also two models of slow propagation of the SCS spreading center, one with opening gradually propagating toward the northeast and the Taiwan Strait (Chung et al., 1994) and the other toward the Southwest Subbasin (Zhou et al., 1995).

Figure F4. Total field magnetic map (based on [global-change.nasa.gov/r/d/\[GCMD\]GSJ_EASTASIA_CDROM](http://global-change.nasa.gov/r/d/[GCMD]GSJ_EASTASIA_CDROM)) showing major magnetic zones (A, B, C1, C1', C2, D, and E). M1 and M2 are two major magnetic anomalies in the East Subbasin. ZNF = Zhongnan fault zone, L RTPB = Luzon-Ryukyu transform plate boundary, DS = Dongsha Rise; SCMA = offshore south China magnetic anomaly, XS = Xisha, ZB = Macclesfield Bank, LB = Reed Bank, NM = Dangerous Grounds. Red lines = transform faults, solid yellow circles = Expedition 349 sites, solid pink circle = ODP Site 1148. After Li et al. (2008b).



Previous drilling

Five sites were drilled in the peripheral continental slope of the SCS during Ocean Drilling Program (ODP) Leg 184 (Feb–April 1999; Wang, Prell, Blum, et al., 2000). The major objectives of Leg 184 were to study the variability of East Asian monsoonal climates (including millennial- to possibly centennial-, orbital-, and tectonic-scale variability) from cored late Cenozoic hemipelagic sediment. All Leg 184 sites are located on the continental slope, and none penetrated into igneous basement rock. The deepest hole cored during the leg reached 861 meters below seafloor (mbsf) at Site 1148 in 3294 m of water (Figures F2, F4), with the oldest sediment recovered of early Oligocene age. The records from both Leg 184 and Expedition 349 will be used to establish links between the East Asian and Indian monsoons and to evaluate mechanisms of internal (climate system feedbacks) and external (orbital and tectonic) climate forcing.

Seismic studies and site survey data

Figure F2 shows the sites drilled during Expedition 349 and available multichannel seismic (MCS) lines crossing those sites. Most drill sites are located at the intersection of two MCS lines; however, Sites U1434 and U1435 are not located on crossing points but were interpreted to have only thin sedimentary cover above the igneous basement.

Figure F5. Examples of two groups of contrasting tectonic models for the opening phases of the SCS. A. Multiphase episodic rifting model in which the Southwest Subbasin is the first to open from continental rifting (after Ru and Pigott, 1986). N.P. = Northwest Palawan, S.P. = South Palawan, M.B. = Macclesfield Bank, R.B. = Reed Bank, P.I. = Parcel Islands; F1, F2, and F3 = faults. (Continued on next page.)

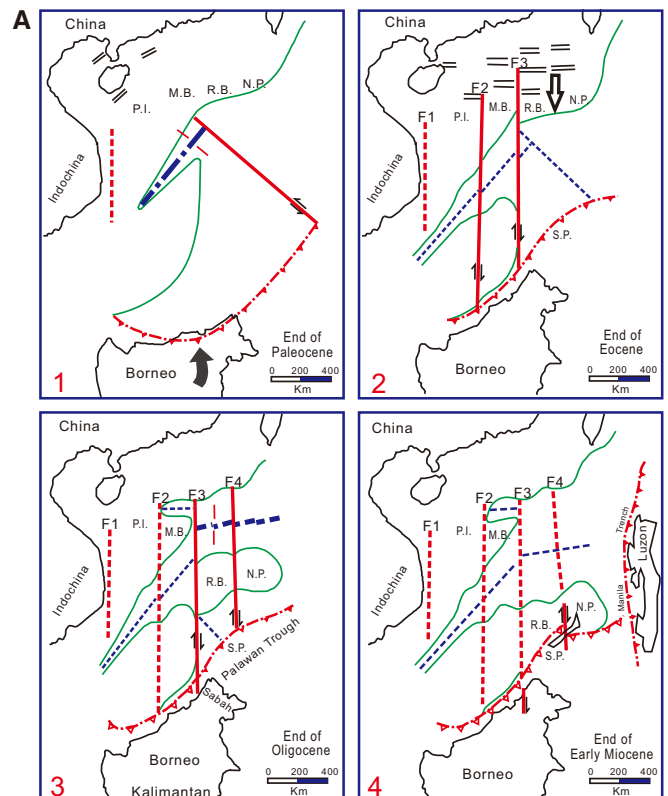
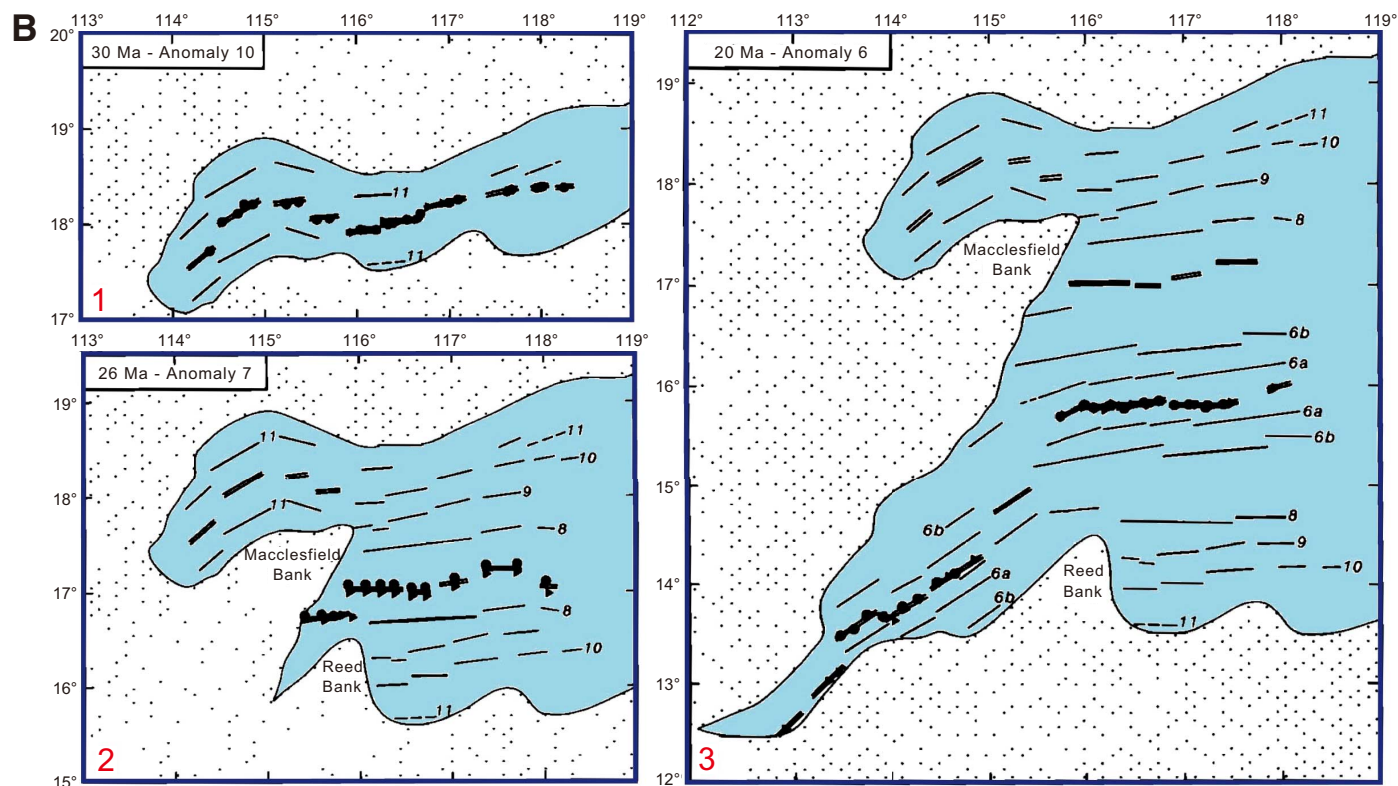


Figure F5 (continued). B. Southwestward continuous propagating model in which the Southwest Subbasin is coeval with the central East Subbasin (after Briaix et al., 1993).



A dense 2-D MCS grid exists in the northern SCS continental margin and the northern part of the central SCS basin. The Chinese National Offshore Oil Corporation (CNOOC) recently acquired most of these high-quality data. The northeastern part of the SCS has also been well studied and imaged with numerous geophysical surveys during Cruises SC51087, 973GMGS, ACT, TAICRUST, ORI645, and ORI689. More recent geophysical studies include the Taiwan Integrated Geodynamics Research (TAIGER) project (McIntosh et al., 2012) and surveys for gas hydrates.

Guangzhou Marine Geological Survey (GMGS) has undertaken extensive geophysical and geological mapping of a large portion of the central SCS basin in recent years. As a result, MCS data and shallow sediment cores are regularly added to our existing site survey database. This mapping activity has already started producing 2-D seismic grids around our drill sites. Other MCS and magnetic data were collected near the drill sites by the R/Vs *Vema*, *Conrad*, and *Haiyang IV* (Taylor and Hayes, 1980, 1983; Yao et al., 1994; Hayes et al., 1995) (Figure F2). Two stages of Sino-US cooperation in the early 1980s added more dense geophysical data coverage, which includes sonobuoy measurements, two-ship expanding spread profiles, and piston cores (Taylor and Hayes, 1983; Yao et al., 1994; Hayes et al., 1995). The German R/V *Sonne* carried out five cruises in 1987 (SO-49 and SO-50B), 1990 (SO-72A), 1994 (SO-95), and 2008 (SO-197) (Franke et al., 2011) and collected >10,000 km of MCS data and high-resolution echograms (Lüdmann and Wong, 1999; Lüdmann et al., 2001).

Swath bathymetry data are available for the entire SCS basin from GMGS and the 2nd Institute of Oceanography of the State Oceanic Administration of China (Li et al., 2011). Magnetic anomaly

maps covering all proposed drill sites were compiled by the Geological Survey of Japan and Coordinating Committee for Coastal and Offshore Geoscience Programs in East and Southeast Asia (CCOP) in 1996 (Ishihara and Kisimoto, 1996) (Figure F4). This compilation offers remarkable coverage and accuracy and yields new insights into the dynamic opening process of the SCS (Li et al., 2008b, 2010; Li and Song, 2012).

A number of ocean bottom seismometer (OBS) studies have been carried out since 2000 (e.g., Yan et al., 2001; Zhang et al., 2013). The South China Sea Deep (SCSD) major research program of the National Science Foundation of China has funded coincident seismic refraction/reflection surveys, local active source 3-D OBS surveys, the first regional passive source OBS survey, and the first deep-tow magnetic survey (Wang, 2012). Both deep-towed and surface-towed magnetic survey lines were designed to traverse the primary sites, allowing establishment of the best possible magnetic anomaly model and calibrated age model for the ocean crust for the entire basin. The supporting site survey data for Expedition 349 are archived at the [Integrated Ocean Drilling Program Site Survey Data Bank](#).

Scientific objectives

Expedition 349 focuses on coring into igneous basement at multiple sites in the SCS basin to better understand seafloor spreading, ocean crust accretion, and mantle evolution. In addition, coring the sedimentary sections above basement will allow examination of the sedimentary and paleoceanographic responses to basin opening and eventual subduction along the Manila Trench.

1. Date the timing of the opening of different subbasins of the SCS and correlate the ages from magnetic anomalies to biostratigraphic, magnetostratigraphic, and radiometric ages.

Magnetostratigraphy, biostratigraphy, and radiometric dating are the three principal techniques that will be used for chronostratigraphic analysis of the recovered sequences. Age control in the sedimentary section will be made from routine microfossil analyses, paleomagnetism, and isotope analysis. The age sequences can also be constrained by correlating seismic reflections to different drill sites. Because drilling at all expedition sites intends to recover the oldest sediment deposited directly on the top of oceanic basement, paleontological analyses will provide a minimum age constraint for the basement. Except for the upper ~900 m at Site U1432 in the primary operations plan, we planned to core all intervals within the three primary sites, with micropaleontological analyses conducted on all core catcher material and additional samples from split-core sections to refine the biostratigraphy, as time permitted. Calcareous microfossils, including nannofossils and foraminifers, should be abundant in the carbonate successions at all sites. Within some intervals, particularly in the Neogene, we expected to find well-preserved and abundant siliceous microfossils (biogenic silica dominated by diatoms and radiolarians) that can provide additional biostratigraphic control.

Basement volcanic rock will be dated with $^{40}\text{Ar}/^{39}\text{Ar}$ (Koppers et al., 2011) and possibly other high-resolution zircon dating techniques with uranium-series isotopes (Goldstein et al., 1991, 1994; Goldstein, 1995; Schwartz et al., 2005). Ocean crust rock typically is very low in K concentrations and therefore more vulnerable to disturbances by submarine alteration. To ensure high-quality $^{40}\text{Ar}/^{39}\text{Ar}$ dating on basement samples collected in the SCS, we will (1) carefully select fresh highly crystalline groundmass and plagioclase phenocrysts, which are the most suitable for $^{40}\text{Ar}/^{39}\text{Ar}$ dating, and (2) apply extended acid leaching procedures to remove altered portions of the groundmass or mineral separates (Koppers et al., 2011).

The half-spreading rates of the SCS are slow to intermediate, between 20 and 40 mm/y (Briaies et al., 1993; Song and Li, 2012). Near the continent/ocean boundary, where Sites U1432 and U1435 are located, hyperextended crust exhuming possible lower crust and upper mantle could exist (Franke et al., 2011). If so, gabbro with late-stage minerals or felsic lithologies could be available for uranium-lead zircon dating using sensitive high-resolution ion microprobe reverse geometry (SHRIMP-RG), as well as for $^{40}\text{Ar}/^{39}\text{Ar}$ dating of plagioclase, biotite, and/or hornblende mineral separates. A newly developed method that detects tiny amounts of uranium-bearing minerals, such as zircon, in rocks could reliably date the age of ocean crust (Schwartz et al., 2005; Grimes et al., 2007).

2. Measure the magnetization, mineralization, and geochemical compositions of basement rocks to understand the causes of the sharp magnetic contrast between different subbasins.

Magnetic susceptibilities of extrusive basalt normally decrease with increasing degree of alteration, which reduces their titanomagnetite content (e.g., Bleil and Petersen, 1983). Serpentinization of peridotite at deeper depths is also known to smear surface magnetic anomalies (e.g., Dyment et al., 1997). Detailed mineralogical studies are essential to understand these processes that may cause the magnetic contrast between the East and the Southwest Subbasins. Because of the complex patterns of magnetic anomalies in the SCS, careful measurements of magnetic susceptibility are needed to con-

strain models of, for example, tectonic settings or spreading rates (Dyment and Arkani-Hamed, 1995) that can explain the distinct differences in magnetic patterns between different subbasins, as well as their crustal affinities. Magnetization measurements from cores are also vital for creation of an initial model for predicting magnetic anomaly strength, in order to better understand the observed magnetic anomalies.

3. Evaluate the origin and source evolution of SCS basement rock to understand the formation of SCS oceanic crust and the deep mantle processes driving crustal formation.

Trace element chemical analyses and measurement of Sr, Nd, and Pb isotopic ratios will provide insights into the material influx and deep crustal and mantle processes (Castillo et al., 1991; Tejada et al., 2004). The opening mechanism of the SCS can be constrained by investigating the variation in these geochemical tracers in the igneous basement rock. The basaltic rock cored during this expedition could have three potential mantle sources: (1) Indian Ocean/Eurasian lithospheric mantle, (2) Pacific mantle, or (3) a putative mantle plume.

All of these sources have distinctive geochemical characteristics in their incompatible trace element and long-lived radiogenic isotope ratios, which are not affected by variations in degree of partial melting of the mantle and fractional crystallization of the resultant melt. Therefore, based on the Expedition 349 drilling transect, we should be able to test several geochemical evolution scenarios corresponding to the rifting and spreading models of the SCS, including (1) continental rifting leading to seafloor spreading (due to Indochina extrusion tectonism or slab pull with southward subduction under Borneo), (2) subduction-induced back-arc spreading, and (3) plume-initiated rifting.

4. Evaluate the paleoceanographic and climatic responses to the opening of the SCS and develop a 3-D sedimentation and subsidence model.

Because our drill sites are located in different parts of the SCS, we can build a detailed 3-D postspreading model of seismic stratigraphy that will offer invaluable insights into deepwater sedimentary processes and how they evolved through time. This sedimentary model will be coupled with paleoenvironmental and paleoceanographic data from analyses of sediment cores to detect major geological events. Information on sedimentation rates, provenance, water depths, tectonic subsidence, and facies changes will be determined and correlated to known tectonic and climatic events. By core-log-seismic integration, we can build detailed 3-D sedimentation models. Major unconformities and boundaries found in the different subbasins will be correlated with those in the continental slopes and rifting basins to trace the dynamic transitional process from rifting to spreading, and also constrain critical paleoceanographic and tectonic changes during opening of the SCS.

Mineralogical and geochemical analyses will help identify sediment provenance in the SCS and how it has evolved through time. Analyses of detrital zircon in the sediment, for example, can (1) determine the maximum age of stratigraphic successions and lead to a better understanding of the source-to-sink processes, (2) determine provenance characteristics such as age and composition, (3) test regional paleogeographic models via provenance analysis, and (4) unravel facets of geological history locked in the mineral chemistry of detrital zircon (Fedo et al., 2003).

Structural analyses of core samples will focus on deformation features such as fractures, faults, veins, deformation bands, and so on. Postcruise statistical analyses on these structural features will help reveal the regional stress field and its changes through time. Together with geophysical downhole logging and other data, the structural features recorded in cores could reveal regional SCS magmatic and tectonic events, as well as local rock deformation and stress heterogeneities.

5. *Obtain downhole geophysical logs to reveal physical properties of the sediments and the top oceanic basement and to provide a record of unrecovered intervals.*

Deployment of a minimum of two wireline logging tool strings (the standard triple combination [triple combo] and the Formation MicroScanner [FMS]-sonic) will measure a wide spectrum of geophysical properties and will provide structural, mineralogical, and geochemical information of the penetrated sequences. These data will be particularly important for unrecovered intervals that typically occur when using the extended core barrel (XCB) and rotary core barrel (RCB).

The triple combo tool string records geophysical signals of the penetrated sediment and basement rock by measuring the total and spectral natural gamma radiation (NGR), density, porosity, and resistivity of the formation. Gamma ray data will be used to infer lithology and provenance. Porosity, sonic, and density logs will be critical for decompaction and backstripping analyses and for constraining tectonic subsidence. The subsidence and rifting parameters so obtained can offer new insights on the episodic opening history of the SCS and reveal mantle properties.

Wireline logs will provide a continuous record to aid in the detection of lava flow boundaries, interlayered sediment, and alteration zones in the basement to evaluate the dip of lava flows. The number of lava flow units penetrated has implications for how well geomagnetic secular variation has been sampled and hence the extent to which paleolatitudes can be most precisely constrained.

FMS-sonic logging will obtain high-resolution quasi-2-D images (electrofacies) of the borehole wall to reveal the structure and orientation of the rock. These data will provide constraints on volcanostratigraphy and crustal accretion processes (e.g., Tominaga et al., 2009). The high-resolution FMS images will help to detect small-scale fractures and lithologic variations, evaluate the dips of lava flows, and reorient core pieces. The General Purpose Inclinator Tool, which includes both a three-axis inclinometer and a three-axis magnetometer, will be deployed to measure changes in magnetic properties of lithologies and in paleomagnetic direction.

Drilling and coring strategy

Our proposed operations plan for this expedition consisted of drilling three sites into basement (proposed Sites SCS-3G [U1431], SCS-6A [U1432], and SCS-4B [U1433]). Because of the predicted depth to basement at these sites (865–1830 mbsf) and to maximize our operational time, we requested and received approval from the Environmental Protection and Safety Panel and the Texas A&M Safety Panel to drill down through the uppermost ~900 m at the

second site (U1432), provided that we encountered nothing unexpected at the first site (U1431), which was tied seismically to the second one. Even with this drilldown approval, it was unlikely that we would have sufficient time in the schedule to reach basement at all three of our primary sites unless operations proceeded better than predicted in the operations plan. With these issues in mind, we identified 10 alternate sites in the vicinity of our primary sites that required shallower penetration depths to reach basement. Three additional alternate sites in other locations targeted secondary objectives that could be addressed if for any reason we were unable to drill in the vicinity of one of our primary sites (Li et al., 2013a).

Alternate sites with shallower penetration depths to basement were also important because coring at deeper depths is challenging. Hole stability is always a risk during coring and logging operations, and the longer the open-hole section, the higher the risk. Hole cleaning is also more difficult in deeper sections, particularly when coring dense basement material. We planned a reentry system to 900 mbsf for the deepest site (U1432; predicted total depth of 1930 mbsf) to help mitigate these issues. Given the relatively shallower total depths planned at the other two primary sites (U1431 and U1433), we felt that we could achieve the objectives without the aid of a reentry system. The reentry system at the deep site would serve two main purposes. First it would stabilize the upper portion of the hole, where unconsolidated sediment is more likely to cause hole stability problems. It also would provide a smaller annulus for hole cleaning, which increases annular velocity without having to significantly increase pump rates to remove dense basement cuttings from the hole. Higher flow rates generally result in washed-out sections in parts of the hole and can lead to stability issues. For the other primary sites, we planned to deploy a free-fall funnel to decrease the amount of time required to reach the basement objective.

This strategy of having multiple alternate sites approved for drilling prior to the start of the expedition proved to be valuable during this expedition. While installing the reentry system in Hole U1432B, we discovered that two of the three fiber optic cables within the subsea camera wireline had failed. During a subsequent deployment, the camera system failed and we initially suspected that the final fiber optic cable had broken. Fortunately, the failure was related to the pan and tilt unit of the camera, so that after the problematic unit was removed the system worked again. This failure prompted discussions of alternate plans to meet the expedition objectives without the ability to perform reentries. During cementing of the final (10 $\frac{3}{4}$ inch) casing string in Hole U1432B, the pipe became stuck in the cement and ultimately forced us to abandon the hole. There was not enough time left in the expedition schedule to try another approach to reach the basement objective at that site; however, we were able to use the remaining time to reach basement at our primary site in the Southwest Subbasin (Site U1433). Additionally we were able to core at two alternate sites, proposed Sites SCS-4E (U1434) and SCS-6C (U1435). The latter site was thought to be a basement high very near the continent/ocean boundary (Figure F6) with very thin (~10 m) sediment cover, whereas Site U1434 formed a short sampling transect with Site U1433, with Site U1434 located closer to the relict spreading center and also adjacent to a large seamount (Figure F7).

Figure F6. Proposed sampling transect in the East Subbasin (after Li et al., 2010). A. Total field magnetic anomaly and Bouguer anomaly along the seismic line shown in B. B. Sites U1431, U1432, and U1435 in the East Subbasin and ODP Site 1148 shown on a composite seismic line. Solid lines = sites that fall on the seismic profile, dashed lines = site locations projected onto the line. TWT = two-way traveltimes, COT = continent-ocean transition zone, PRMB = Pearl River Mouth Basin, CDP = common depth point. C. Depths to the Moho and Curie point estimated from gravity and magnetic anomalies, respectively. w = width of moving windows.

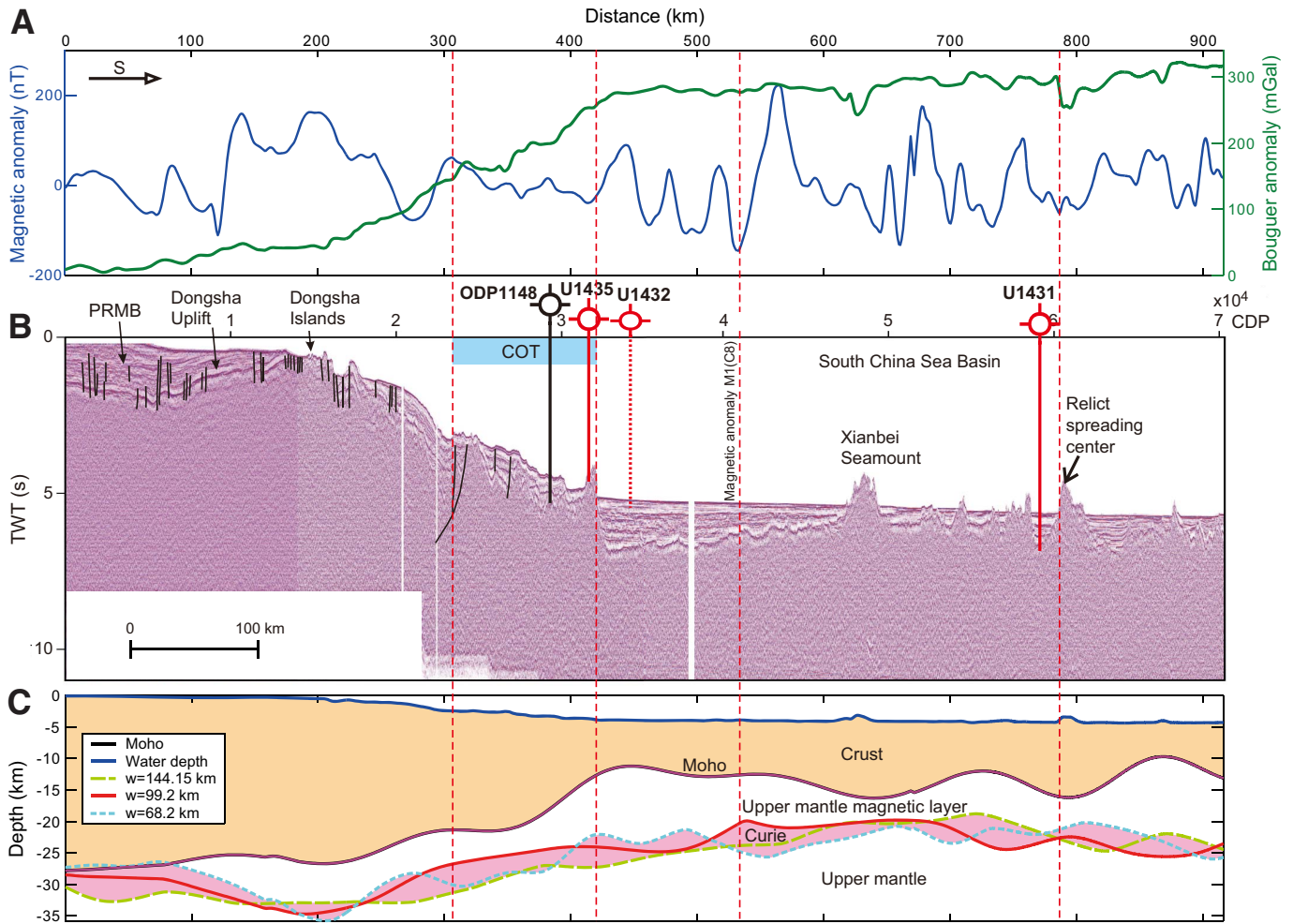
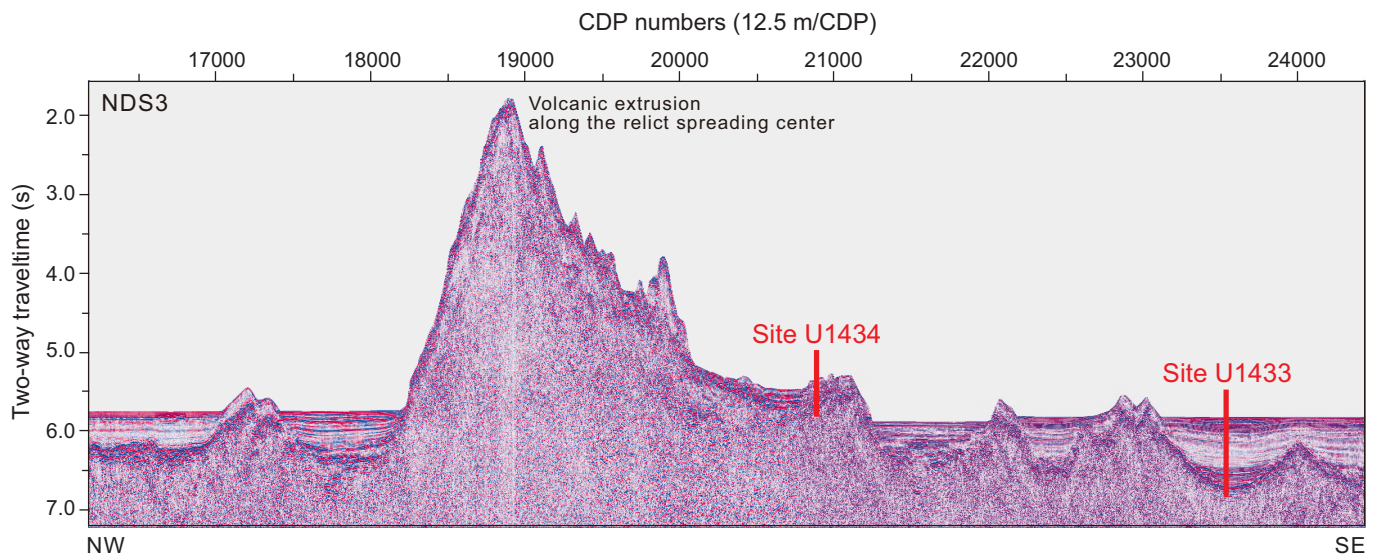


Figure F7. Seismic profile Line NDS3 showing the short sampling transect in the Southwest Subbasin and location of Sites U1433 and U1434. CDP = common depth point.



Site summaries

Site U1431

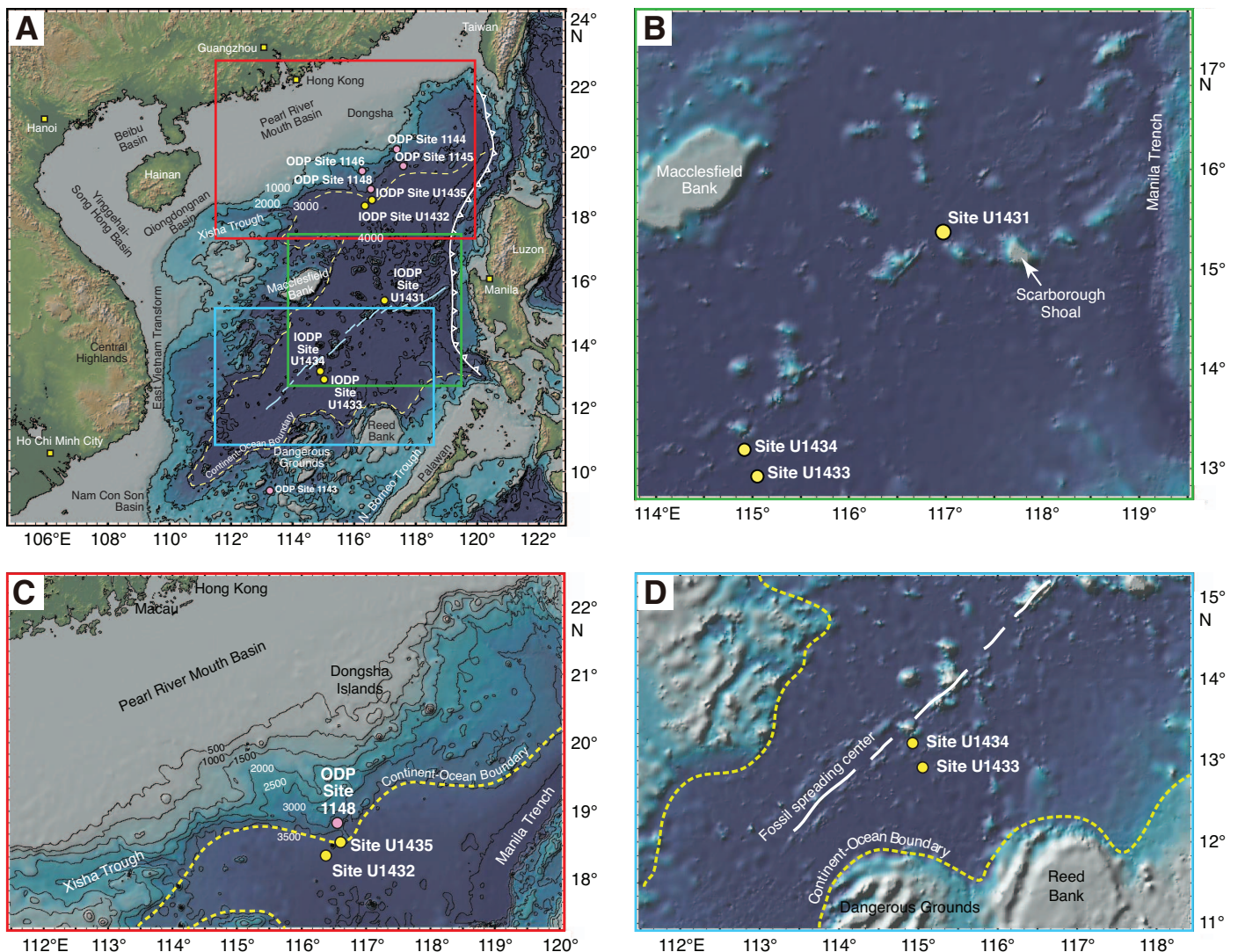
Background and objectives

Site U1431 is located near the relict spreading ridge where the youngest crustal magnetic anomalies are observed in the East Sub-basin of the SCS (Figures F4, F8). A positive magnetic anomaly that runs through this site allows regional correlation of crustal ages. This site is also surrounded by abyssal highs in the ocean crust, as well as younger seamounts (Figures F6, F8B) whose volcanic and/or redepositional events may be recorded by sediments recovered from this site.

The primary objective at Site U1431 was to core into the oceanic basement to determine the age at which seafloor spreading ceased in the East Subbasin. The ~900 m thick package of sediment overlying basement also provides important constraints on the evolution of the ridge and associated late-stage magmatism, deep-marine sed-

imentary processes, and the paleoceanographic history following the termination of spreading in the SCS. Additionally, coring at this site will allow correlation of biostratigraphic, magnetostratigraphic, and radiometric ages to the observed crustal magnetic anomalies. Physical property and paleomagnetism measurements of basement rock will help to elucidate the cause of the distinct contrasts in the nature of oceanic crust magnetic anomalies of the East and Southwest Subbasins. Furthermore, this site will provide constraints on mantle source, melting, and magmatic processes in the latest stages of basin formation. Physical property measurements of core samples and wireline logging measurements will provide stratigraphic information for correlation with regional seismic profiles. Microbiological sampling will explore the deep biosphere in the SCS to examine how sharp changes in lithology (interfaces) may affect subsurface community structure and function, as well as how post-eruption processes might have influenced past ecosystems in the SCS.

Figure F8. A. Bathymetric map of the SCS and surrounding region. Yellow circles = Expedition 349 sites. Solid pink circles = ODP Leg 184 sites. Yellow dashed line = inferred continent/ocean boundary, blue lines = fossil SCS spreading center, white-flagged line = Manila Trench. B. Detailed bathymetry around Site U1431 (green box in A) showing nearby bathymetric highs and the Manila Trench. C. Detailed bathymetry around Sites U1432 and U1435 (red box in A) showing nearby continental shelf, the Manila Trench, and inferred continent/ocean boundary. D. Detailed bathymetry around Sites U1433 and U1434 (blue box in A) showing nearby seamount and Dangerous Grounds and Reed Bank to the south.



Operations

After a 463 nmi transit from Hong Kong averaging 11.0 kt, the vessel stabilized over Site U1431 at 0640 h (UTC + 8 h) on 31 January 2014. We cored five holes at Site U1431 (Table T1). The original operations plan called for one hole to a depth of ~1061 mbsf, which included ~100 m of basement. The plan was modified during transit to include two additional short holes for high-resolution sampling of the upper ~20 m of section. Hole U1431A was successfully cored to 28.4 mbsf and Hole U1431B to 17.0 mbsf. After the first core from Hole U1431C retrieved a split core liner and no mudline, we opted to abandon the hole, which was completed to a depth of 14.2 mbsf, and spudded Hole U1431D. Hole U1431D was cored to 617.0 mbsf when the XCB failed, leaving the cutting shoe, core catcher sub assembly, and breakoff sub in the hole. We abandoned Hole U1431D and switched to the RCB to spud Hole U1431E, which was drilled to 507.0 mbsf, spot cored, and then cored continuously from 575.0 mbsf to total depth at 1008.8 mbsf in igneous basement. After conditioning the hole for logging, two logging runs were performed. The triple combo tool string was run to 463.0 m wireline depth below seafloor (WSF), and the FMS-sonic tool string was run to 444 m WSF with two passes. Total time spent at Site U1431 was 385.7 h (16.1 days).

A total of 122 cores were collected at this site. The advanced piston corer (APC) was deployed 26 times, recovering 225.61 m of core over 228.50 m of penetration (98.7% recovery). The XCB was deployed 48 times, recovering 236.50 m of core over 448.10 m (52.8%

recovery). The RCB was deployed 48 times, recovering 243.00 m of core over 443.50 m of penetration (54.8% recovery).

Principal results

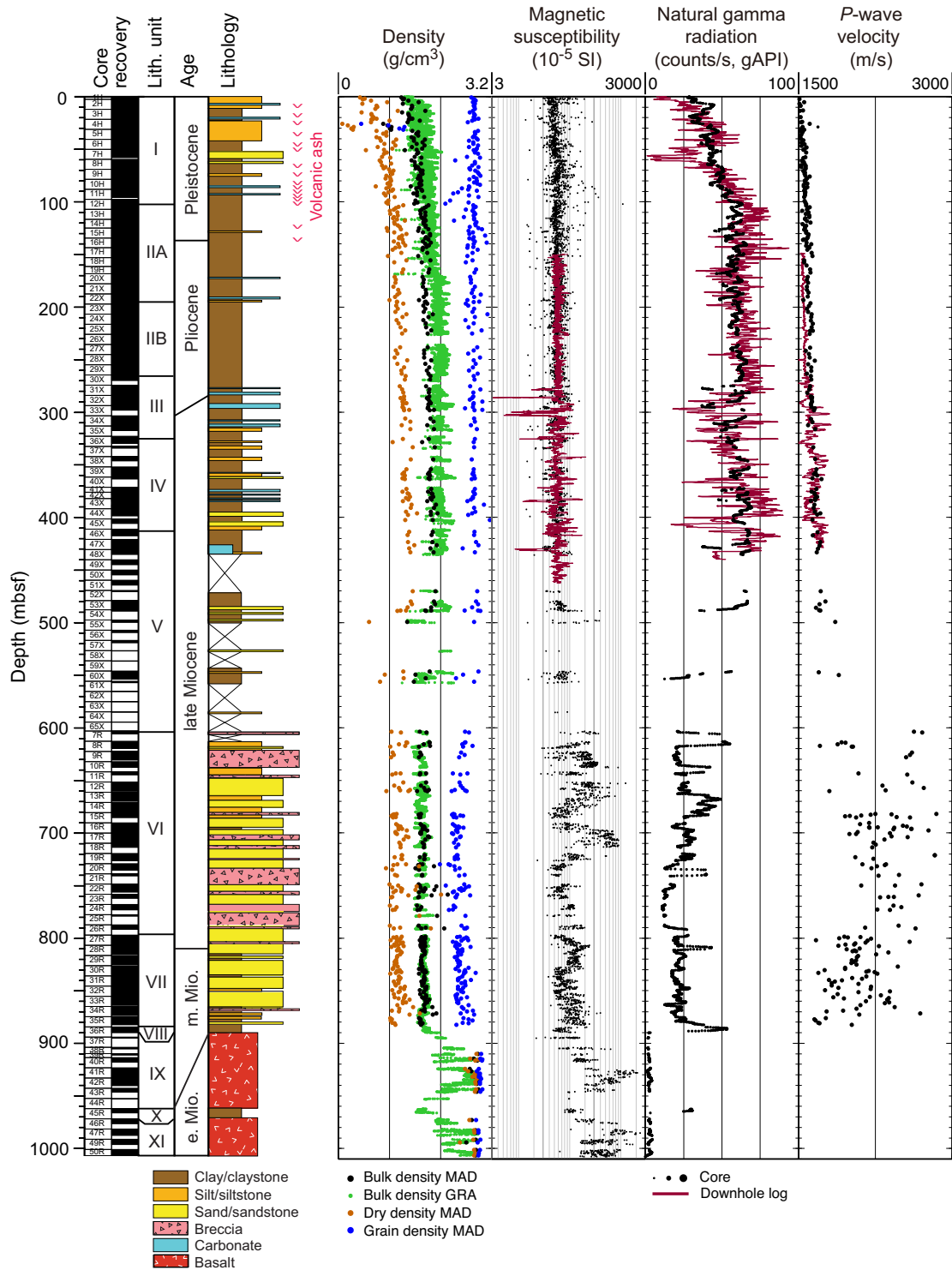
The cored section at Site U1431 is divided into 11 lithostratigraphic units, 9 sedimentary and 2 igneous, based mainly on a combination of data from Holes U1431D and U1431E (Figure F9). Lithostratigraphic Unit I is a 101.16 m thick Pleistocene sequence of dark greenish gray clay and silty clay. Graded silt intervals are abundant and interpreted as turbidites. Discrete volcanic ash layers that are either mafic or felsic in composition and 0.5–5 cm thick occur throughout the unit. This unit is underlain by Unit II (Pliocene–Pleistocene age), which is divided into Subunits IIA (101.16–194.95 mbsf) and IIB (194.95–267.82 mbsf). The 166.66 m of Unit II is dominated by dark greenish gray clay with fewer volcanic tephra layers than Unit I. Subunit IIA is characterized by the presence of clay with nannofossils and calcareous turbidites, which are not found in Subunit IIB. Rare, thin silt turbidites are largely limited to Subunit IIB. Unit III (267.82–326.12 mbsf) is a 58.30 m thick upper Miocene to Pliocene sequence of dark greenish gray clay with modest amounts of interbedded calcareous turbidites. These graded turbidites typically have sandy foraminifer-rich intervals at the base and are interpreted to represent mass wasting events from neighboring seamounts. Unit IV (326.12–412.42 mbsf) is an upper Miocene unit comprising 86.30 m of dark greenish gray clay and silty clay with minor amounts of silt and fine sand interbeds interpreted

Table T1. Coring summary, Expedition 349. APC = advanced piston corer, XCB = extended core barrel, RCB = rotary core barrel. [Download table in .csv format.](#)

Hole	Latitude	Longitude	Water depth (m)	Penetration DSF (m)	Cored interval (m)	Recovered length (m)	Recovery (%)	Drilled interval (m)	Drilled interval (N)	Total cores (N)	APC cores (N)	XCB cores (N)	
U1431A	15°22.5491'N	117°00.0009'E	4237.3	28.4	28.4	28.39	100	—	0	3	3	0	
U1431B	15°22.5480'N	117°00.0125'E	4236.7	17.0	17.0	17.16	101	—	0	2	2	0	
U1431C	15°22.5371'N	117°00.0108'E	4239.5	14.2	14.2	14.45	102	—	0	2	2	0	
U1431D	15°22.5379'N	117°00.0022'E	4240.5	617.0	617.0	402.11	65	—	0	67	19	48	
U1431E	15°22.5380'N	116°59.9903'E	4240.3	1008.8	443.5	242.35	55	565.3	2	47	0	0	
U1432A	18°21.1051'N	116°23.4504'E	3829.0	62.0	—	—	0	62.0	1	0	0	0	
U1432B	18°21.1062'N	116°23.4512'E	3829.0	800.0	—	—	0	800.0	4	0	0	0	
U1432C	18°21.0831'N	116°23.4504'E	3829.0	110.0	110.0	88.74	81	—	0	12	12	0	
U1433A	12°55.1380'N	115°02.8345'E	4379.4	188.3	188.3	168.79	90	—	0	20	20	0	
U1433B	12°55.1313'N	115°02.8484'E	4379.3	858.5	672.4	443.04	66	186.1	1	74	0	0	
U1434A	13°11.5080'N	114°55.4005'E	4009.0	312.5	115.5	26.43	23	197.0	1	14	0	0	
U1435A	18°33.3466'N	116°36.6174'E	3252.5	300.0	300.0	171.37	57	—	0	32	0	0	
Total:					2506.3	1602.83			1810.4	9	273	58	48

Hole	Latitude	Longitude	RCB cores (N)	Other cores (N)	Date started (UTC)	Date finished (UTC)	Time on hole (days)	Comments
U1431A	15°22.5491'N	117°00.0009'E	0	0	1/30/2014 22:40	1/31/2014 19:45	0.88	
U1431B	15°22.5480'N	117°00.0125'E	0	0	1/31/2014 19:45	1/31/2014 22:20	0.11	
U1431C	15°22.5371'N	117°00.0108'E	0	0	1/31/2014 22:20	2/1/2014 00:52	0.11	Split liner on mud line core
U1431D	15°22.5379'N	117°00.0022'E	0	0	2/1/2014 00:52	2/6/2014 06:15	5.22	
U1431E	15°22.5380'N	116°59.9903'E	47	1	2/6/2014 06:15	2/15/2014 22:00	9.66	
U1432A	18°21.1051'N	116°23.4504'E	0	0	2/16/2014 15:30	2/17/2014 18:05	1.11	Jet-in test
U1432B	18°21.1062'N	116°23.4512'E	0	0	2/17/2014 18:05	3/6/2014 12:36	16.77	Jet-in 20 inch casing
U1432C	18°21.0831'N	116°23.4504'E	0	0	2/21/2014 08:20	2/22/2014 23:35	1.64	APC/XCB coring
U1433A	12°55.1380'N	115°2.8345'E	0	0	3/7/2014 18:30	3/10/2014 07:25	2.54	
U1433B	12°55.1313'N	115°2.8484'E	74	0	3/10/2014 19:25	3/19/2014 15:00	8.82	
U1434A	13°11.5080'N	114°55.4005'E	14	0	3/19/2014 16:48	3/22/2014 15:48	2.96	
U1435A	18°33.3466'N	116°36.6174'E	32	0	3/24/2014 07:24	3/27/2014 11:00	3.15	
Total:			167	1				

Figure F9. Lithostratigraphic and physical properties summary of Site U1431 based on a composite of Holes U1431D and U1431E. Core magnetic susceptibility and gamma ray attenuation (GRA) density (filtered) were measured on the Section Half Multisensor Logger (SHMSL), moisture and density (MAD) measured on discrete samples, and *P*-wave velocities were measured on the Section Half Measurement Gantry (SHMG). Downhole log data, magnetic susceptibility, and total natural gamma radiation (NGR) are from the main pass of the triple combo tool string, and *P*-wave velocities are from Pass 2 of the Formation MicroScanner (FMS)-sonic tool string. Downhole log depths have been shifted upwards by 5 m to correlate with the core physical property data.



as turbidites. This unit is much reduced in carbonate content compared to overlying Unit III. Unit V (412.42–603.42 mbsf) is a 191 m thick sequence of upper Miocene dark greenish gray silty sand and interbedded clay with nanofossil ooze. Recovery is low throughout

the section, but sandy core catcher samples suggest that many of the unrecovered intervals may consist of sand.

Unit VI (603.42–797.30 mbsf) is readily distinguished from the overlying units by the abundance of greenish black volcanoclastic

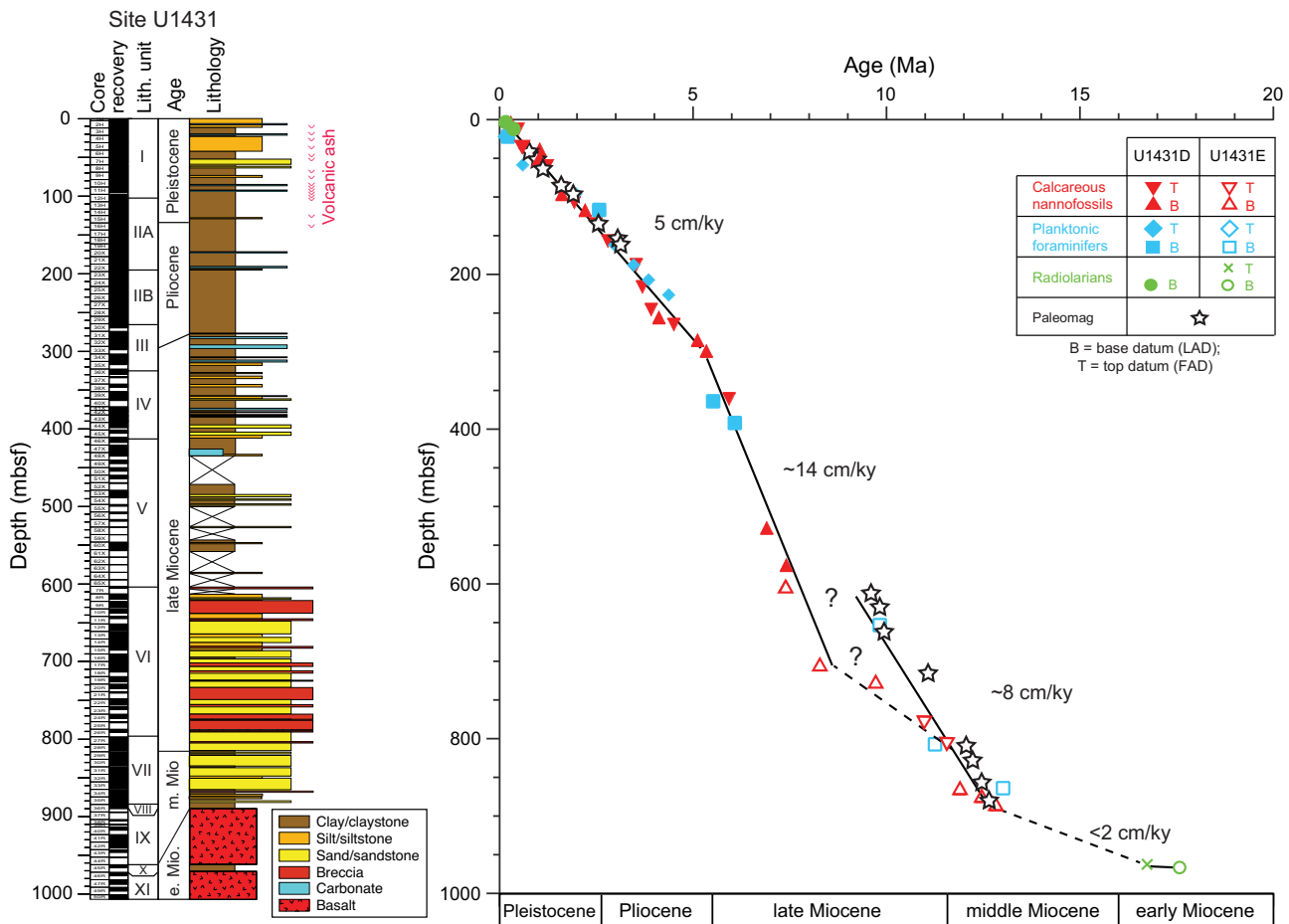
breccia and sandstone interbedded with minor amounts of claystone. This unit is 193.88 m thick and dated to the late Miocene. The clasts in this breccia are primarily composed of highly vesicular aphanitic basalt and scoria, nonvesicular to sparsely vesicular basalt, basaltic glass shards, and lesser amounts of pumice and mudstone. Major element data indicate that these clasts are characteristic of ocean island basalt (OIB). The breccia beds are typically massive and have erosive bases, indicative of deposition by mass wasting either as debris or grain flows. Based on the composition of the clasts and abundant magmatic mineral fragments, these deposits are likely sourced from the nearby seamounts. Unit VII (797.30–885.25 mbsf), 87.95 m thick and middle to late Miocene in age, is composed of interbedded dark greenish gray sandstone with lesser amounts of siltstone and claystone in a turbidite sequence. It is essentially a less coarse grained equivalent to Unit VI and coarsens uphole through the unit. Unit VIII (885.25–889.88 mbsf) is a 4.63 m thick middle Miocene sequence of massive, dark olive-brown claystone that directly overlies the basalt of Unit IX (889.88–962.51 mbsf). The mudstone represents deep-marine sedimentation. Unit X (962.51–972.00 mbsf) is a 9.49 m thick sequence of lower Miocene yellowish brown claystone and claystone breccia that lies within the volcanic sequence. This unit is underlain by the basalt of Unit XI (972.00–1007.89 mbsf).

Calcareous nanofossils, planktonic foraminifers, and radiolarians recovered at Site U1431 are typical of low-latitude assemblages, characterized by species widely found in the tropical western Pacific region. Calcareous nanofossils are generally poorly preserved and

frequent or common in Units I–IV but rare or absent downhole. Planktonic foraminifers are also poorly preserved and vary from frequent to rare in Units I–IV but are absent more frequently in samples from deeper units. Radiolarians are common and well preserved in samples from the uppermost 30 m, absent from 30 to 870 mbsf, and present but poorly preserved in Units VIII and X.

The biostratigraphy of Site U1431 is based on analysis of calcareous nanofossil, planktonic foraminifer, and radiolarian assemblages in all core catcher samples and additional samples from within cores from Holes U1431D and U1431E. The sedimentary succession recovered at Site U1431 spans the lower Miocene through Pleistocene (Figure F10). Sediment from Units I–VIII is assigned to middle Miocene to Pleistocene calcareous nanofossil Zones NN6–NN21 and planktonic foraminifer Zones M9–Pt1, with no obvious hiatuses. The Pliocene/Pleistocene boundary is located between Cores 349-U1431D-15H and 18H, and the Miocene/Pliocene boundary is located between Cores 31X and 33X. Biostratigraphic control for the upper Miocene section is hampered by a paucity of nanofossils and planktonic foraminifers and poor core recovery in Units IV and V, which are dominated by turbidites. Nevertheless, the middle/late Miocene boundary is placed between Cores 349-U1431E-27R and 33R. In situ calcareous microfossils are absent from the claystone of Unit X; however, radiolarian biostratigraphy indicates that the rock is early Miocene in age (~16.7–17.5 Ma), corresponding to radiolarian Zone RN4. Sedimentation rates varied from ~8 cm/ky in the middle to early late Miocene, ~14 cm/ky for the remainder of the late Miocene, to ~5 cm/ky in

Figure F10. Age-depth model, Site U1431. FAD = first appearance datum, LAD = last appearance datum.

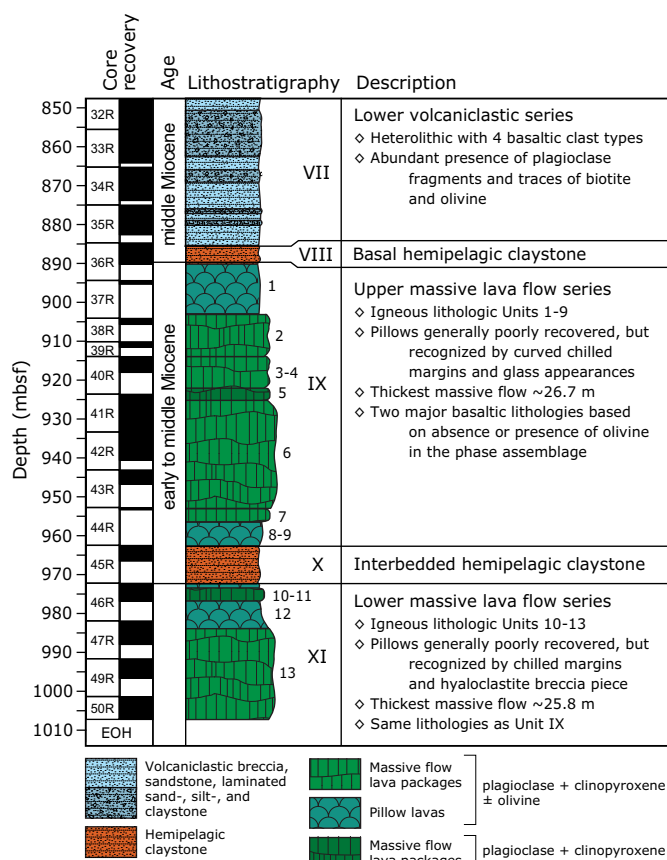


the Pliocene–Pleistocene. Extremely low sedimentation rates (<2 cm/ky) occurred in the early to earliest middle Miocene during deposition of the claystone of Units VIII and X (Figure F10).

The basalt of Unit IX was encountered at ~890 mbsf in Hole U1431E. Coring continued to ~1008 mbsf, recovering basement basalt separated by an interflow claystone between 3.7 and 9.5 m thick at 962.3 mbsf. In total, 46.2 m of basalt was recovered over a cored interval of 108.4 m, yielding an average recovery of 42.6%. The basalt is divided into 13 igneous lithologic units (Figure F11) and is mainly composed of massive lava flows (6 in Unit IX and 2 in Unit XI) as thick as ~26.7 m, with limited evidence for pillow basalt flows in between. Because no contacts between flow units were recovered, boundary locations and unit thickness estimates are approximate. The interpretation of igneous lithologic Units 1, 7–10, and 12 as pillow basalts is uncertain and is based on scarce evidence, such as the presence of glassy (curved) chilled margins, ropy flow structure, and a single occurrence of a hyaloclastite breccia.

Most basalt at Site U1431 is aphyric and ranges in grain size from microcrystalline to fine grained, with the groundmass grain size getting coarser (0.7–1 mm) in the cores of the thickest massive lava flows. All basalt has a phase assemblage of plagioclase and clinopyroxene (\pm olivine) in its groundmass, with 0.1–0.5 mm subhedral-euhedral olivine microphenocrysts present in some igneous lithologic units, resembling a typical mid-ocean-ridge basalt (MORB) crystallization history and, in conjunction with geochemical evidence, indicates that basalt recovered at Site U1431 is representative of typical MORB.

Figure F11. Lithostratigraphic summary of igneous rocks and their lithologic features, Hole U1431E. Lithostratigraphy column includes lithology, igneous lithologic units (1–13), and lithostratigraphic units (VII–XI). EOH = end of hole.



The alteration style of basalt at Site U1431 is typical of MORB. Alteration color is dominated by gray to dark gray-green and yellow to red-brown. Typical secondary minerals include saponite, Fe oxide, carbonate, and celadonite, which represent alteration assemblages at low temperature. Alteration intensity varies from slight to complete, but the majority of the recovered basement rock is moderately altered. There is no systematic change in the alteration nature (e.g., alteration color) with depth that might indicate a transition from more oxidizing to reducing conditions. The strongest alteration occurs in halos flanking veins, which overprints the background pervasive alteration, indicating that the overall distribution of alteration was controlled by fractures and vein structures. Most lithologic basement units include intervals with slight alteration, preserving remarkably fresh olivine crystals that show only limited alteration along their rims and “maschen” fractures.

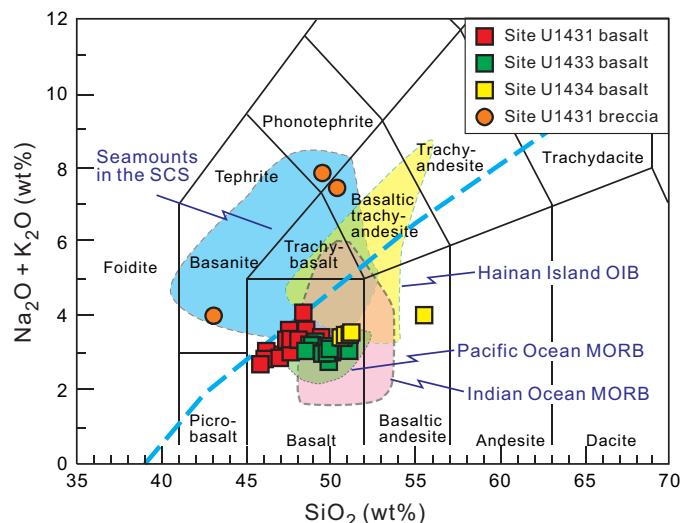
Fractures and veins occur throughout the basalt in Hole U1431E. These features are randomly oriented, with no obvious offset or thickness variation. A fracture with ~1 cm of normal offset occurs in the interflow claystone of Unit X. The basalt fractures likely formed during cooling of the lava, whereas the fractures in the interflow claystone may suggest slight movement as the lava of Unit IX flowed over it. The major veins are white or reddish brown and filled with carbonate and Fe oxide. Curved veins generally occur in sets, often in combination with straight veins, forming a vein network consistent with fractures formed during cooling.

Geochemistry measurements at Site U1431 aimed to characterize the interstitial water chemistry, total organic carbon (TOC), bulk carbonate content, and igneous basement rock. The depth profiles of major elements and nutrients indicate that organic matter diagenesis, biogenic carbonate dissolution and recrystallization, and volcanic ash alteration occurred in the sediment. The interstitial water never reaches complete sulfate reduction in Hole U1431D, with minimum concentrations of ~2.3 mM occurring from ~170 to 260 mbsf. This is consistent with the very low methane concentrations, which range from 1.6 to 4.8 ppmv. Sulfate concentrations gradually increase below 260 mbsf, reaching 24.0 mM at the bottom of Hole U1431D (~600 mbsf). Shore-based isotopic analysis of these interstitial water samples should constrain the source of the sulfate-bearing fluid in Hole U1431D.

Bulk carbonate content varies with depth, ranging from 0 to 47 wt% in Hole U1431D and from 0 to 57 wt% in Hole U1431E. The discrete intervals with higher carbonate content in Hole U1431D correspond to nannofossil ooze beds, whereas in Hole U1431E higher carbonate content is associated with diagenetic carbonate concretions visible in the cores. TOC varies from 0 to 4.7 wt% in Hole U1431D, whereas in Hole U1431E, TOC is lower and ranges from 0 to 0.74 wt%. The TOC to total nitrogen (C/N) ratio is generally <4 at Site U1431, indicating that TOC is derived from a marine source; however, C/N ratios range from 8 to 12 in some intervals of lithostratigraphic Units III and IV in Hole U1431D, which could indicate a mixture of marine and terrestrial organic matter sources.

Major and minor element concentrations measured by inductively coupled plasma–atomic emission spectroscopy (ICP–AES) on Hole U1431D sediment indicate that it is most likely derived from an intermediate igneous source. The basalt recovered from below ~890 mbsf in Hole U1431E has moderately high loss on ignition (LOI) values (0.46–2.85 wt%) but low K₂O (<0.53 wt%) and TiO₂ (1.01–1.77 wt%). The basalt samples of Unit IX contain higher MgO, FeO, and Ni concentrations than those of Unit XI, likely because of olivine accumulation. The basalt major element composition is similar to that of mid-ocean-ridge tholeiite, whereas clasts from the volcaniclastic breccia are alkaline and comprise basanite,

Figure F12. Total alkalis vs. silica, with classification of volcanic rock types of Le Maitre et al. (1989). Dashed blue line divides fields for tholeiitic and alkalic lavas of Hawaii (Macdonald and Katsura, 1964; Macdonald, 1968). Shown for comparison are data for Indian Ocean MORB from the Geochemical Rock Database (georoc.mpch-mainz.gwdg.de), the seamounts in the SCS (Tu et al., 1992; Hékinian et al., 1989), OIB of Hainan Island (Wang et al., 2012), and Pacific MORB (Zhang et al., 2009, 2012a, 2012b, 2013).

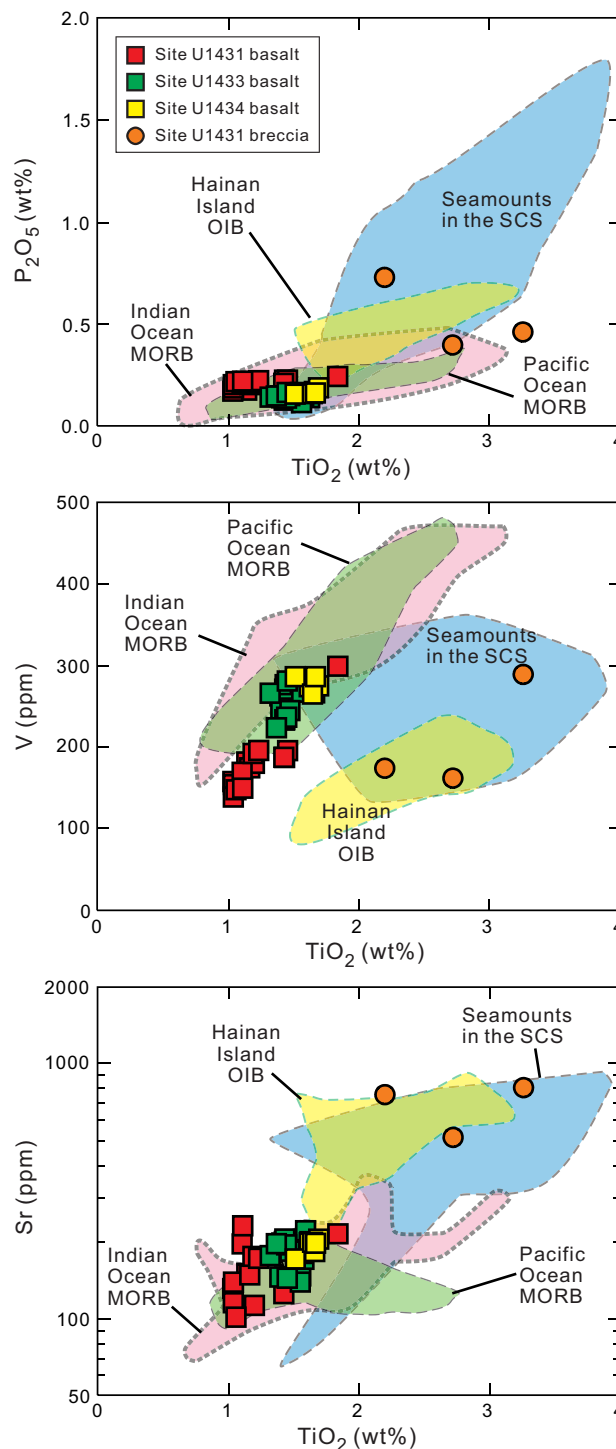


phonotephrite, and basaltic trachyandesite, with high K₂O (1.08–2.67 wt%) and TiO₂ (2.10–3.13 wt%), probably sourced from the nearby seamounts (Figures F12, F13).

A total of 105 whole-round samples (5–10 cm long) were collected for microbiological studies from Site U1431. These samples were typically taken adjacent to interstitial water whole-round samples for comparison to interstitial water chemistry when possible. These samples will be analyzed for microbial content based on DNA and lipid properties of the cells present. Subsamples were prepared for fluorescent in situ hybridization and single cell genomics. DNA and lipid samples were preserved at –80°C, whereas fluorescent in situ hybridization samples were preserved at –20°C. Four basalt whole-round samples were selected for cultivation-based studies, with sampled material inoculated into a seawater-based medium containing olivine as a source of energy. An additional 76 samples were collected and prepared for investigation of the microbiology of interfaces using lipid and nucleic acid analyses. These samples were collected mostly in the upper 200 m of Hole U1431D from specific interfaces, including five ash/clay interfaces and ten turbidite/clay interfaces. Selection of these samples was dependent upon recognition of key intervals by the core description team and occurred through consultation between the microbiologists and sedimentologists or petrologists.

Microbiology contamination testing at Site U1431 included the use of perfluorocarbon tracers (PFTs), fluorescent microspheres, and fluid community tracers (FCTs). PFTs were added to the drilling fluid for all APC coring in Holes U1431B–U1431D, as well as for the first four XCB cores in Hole U1431D. Twelve samples were taken from six sediment cores collected over this interval to measure contamination with the PFTs. Microspheres were added to the core catcher sub before the core barrel was deployed in Hole U1431E over the interval from 651.8 to 952.6 mbsf. Two microsphere samples were collected from each core, one from scraping of the core surface and one as a subsample from the interior of each

Figure F13. Titanium oxide vs. phosphate, vanadium, scandium, and strontium. Shown for comparison are data for Indian Ocean MORB from the Geochemical Rock Database (georoc.mpch-mainz.gwdg.de), the seamounts in the SCS (Tu et al., 1992; Hékinian et al., 1989), OIB of Hainan Island (Wang et al., 2012), and Pacific MORB (Zhang et al., 2009, 2012a, 2012b, 2013).



whole-round sample. In addition, FCT samples were collected from the drilling fluids on a daily basis (for a total of 14) to track the microbial communities typical of seawater and other drilling mud constituents. Microbial community DNA and lipids from these fluids

will be compared to those measurements made on the core samples to determine if there are microbes that can be recognized as contaminant taxa.

Variations in the natural remanent magnetization (NRM) intensity at Site U1431 generally correlate with lithology. Paleomagnetic measurements indicate that the silty clay and clayey silt in Unit I (0–101.16 mbsf) have a mean NRM intensity on the order of 3×10^{-2} A/m, whereas the clay with nanofossils in Unit II (101.16–267.82 mbsf) has somewhat higher NRM intensity ($\sim 6 \times 10^{-2}$ A/m). Many discrete peaks of higher NRM values that appear in some depth intervals in both Units I and II can be tied directly to the presence of volcanic ash layers. Magnetic susceptibility data also show positive peaks at these intervals. Overall, magnetic susceptibility and NRM intensity variations through the sedimentary units are closely correlated.

Magnetostratigraphic records at Site U1431 indicate the presence of several relatively well defined polarity intervals in the cores. Based on inclination and declination data, the Brunhes/Matuyama Chron boundary (0.781 Ma) is placed at ~ 46 mbsf in Hole U1431D (Figure F10). The Matuyama Chron is defined between ~ 46 and ~ 135 mbsf. Below ~ 170 mbsf, the XCB cores are strongly overprinted by a drilling-induced remagnetization that cannot be removed by shipboard thermal demagnetization. The magnetic record improved in the RCB cores of Hole U1431E, allowing tentative correlation of certain parts of the magnetic polarity interval with the geomagnetic polarity timescale in conjunction with biostratigraphic constraints. In particular, the polarity shift from normal to reversed at ~ 716 mbsf may correspond to the Chron C5n/C5r boundary (11.056 Ma) (Figure F10).

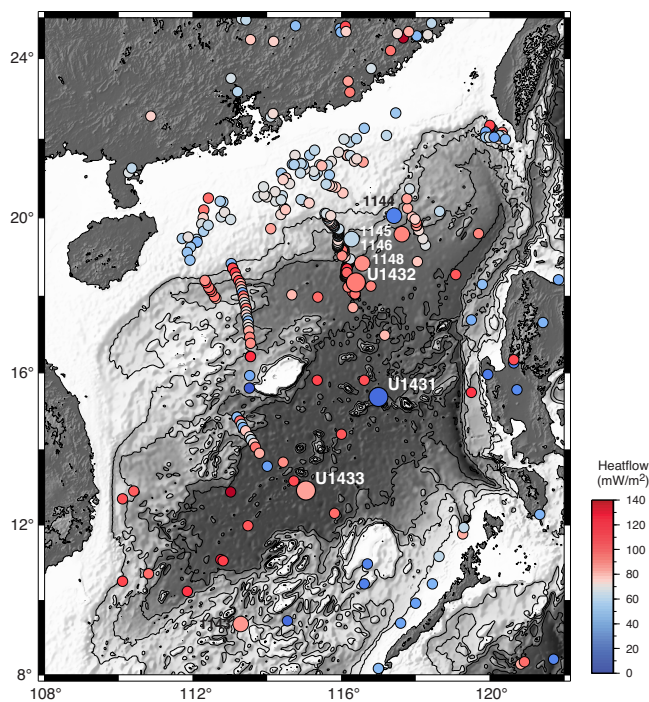
For basement rock units, the observed paleomagnetic signals cannot be directly linked to the geomagnetic polarity timescale yet because the basalt in lithostratigraphic Units IX and XI was erupted intermittently, and the pelagic clay sediment in lithostratigraphic Units VIII and X may represent a significant time interval. Nevertheless, reliable normal and reversed polarities occur within this interval, which indicates that the eruption of the basalt units may have spanned a significant amount of time on the order of a few thousand to one million years.

Whole-round cores from Holes U1431A–U1431C were measured for *P*-wave velocity, bulk density, magnetic susceptibility, and NGR. For Holes U1431D and U1431E, measurements were also made on whole-round cores, with additional measurements on split cores and discrete samples, including thermal conductivity, porosity, and bulk, dry, and grain densities. In general, the physical properties correlate with lithology, composition, and induration. In Hole U1431D, bulk density, *P*-wave velocity, shear strength, NGR, and thermal conductivity increase gradually with depth over the uppermost 150 mbsf (Figure F9), whereas porosity measured on discrete samples decreases from 84% to 50% over the same depth range. This indicates that sediment compaction dominates the physical property variations above 150 mbsf. Volcanic ash layers in Unit I (e.g., at 25 and 100 mbsf) show relatively high magnetic susceptibility (300–500 SI) values. Below 150 mbsf, a decrease in shear strength may be associated with higher clay content. NGR counts are relatively high from the seafloor to 500 mbsf, which is consistent with the dominance of clay and silt in Units I–V.

Most physical properties show a significant change at ~ 550 – 600 mbsf, near the boundary between Units V and VI (Figure F9). *P*-wave velocity and porosity increase, whereas NGR values and thermal conductivity are relatively low, a pattern consistent with the dominance of volcanoclastic breccia and sandstone in Unit VI. Layers with higher NGR counts and high magnetic susceptibility values occur at ~ 660 and ~ 710 mbsf. These do not correlate with the breccia but correspond to a silt- and/or sandstone probably enriched in magnetic minerals such as magnetite. The basalt units below 889.88 mbsf (Units IX and XI) display the lowest NGR, highest magnetic susceptibility, and largest bulk density values (Figure F9). The interflow clay (Unit X) between the 2 basaltic units shows NGR values ~ 20 times larger than those of the basalt, as well as much lower magnetic susceptibility. Lower magnetic susceptibility and NGR values at the top of the basalt are consistent with higher but still moderate alteration in these basement units.

Two downhole logging tool strings were run in Hole U1431E, the triple combo (NGR, porosity, density, electrical resistivity, and magnetic susceptibility) and the FMS-sonic (NGR, sonic velocity, and electrical resistivity images) tool strings (Figure F9). The triple combo tool string reached 464 m WSF before a bridge prevented access to the lower part of the borehole. The hole was wider than 17 inches below ~ 300 m WSF and showed closely spaced variations in borehole width above that depth. These were not ideal conditions for borehole log quality; however, stratigraphic changes are apparent in the NGR and magnetic susceptibility logs. The FMS-sonic tool string reached 444 m WSE, with two passes made above that depth. Downhole temperature measurements of the borehole fluid

Figure F14. Heat flow values for Expedition 349 (large circles) and ODP Leg 184 (medium circles) and the compilation of heat flow data in Li et al., 2010 (small circles).



are consistent with the low geothermal gradient ($\sim 15^{\circ}\text{C}/\text{km}$) established from the advanced piston corer temperature tool (APCT-3) measurements taken on Cores 349-U1431-D-4H, 7H, 10H, and 13H (Figure F14).

Site U1432

Background and objectives

Site U1432 is located ~ 60 km south of ODP Site 1148 (Wang, Prell, Blum, et al., 2000; Li et al., 2006; Wang and Li, 2009), just south of the northern continent/ocean boundary on the Chinese continental margin (Figures F6, F8). This part of the basin shows the deepest basement and is likely the oldest among the subbasins based on magnetic anomalies (Taylor and Hayes, 1980, 1983; Pautot et al., 1986; Briais et al., 1993) (Figure F4). This site was designed to recover the oldest oceanic crust and the oldest sedimentary rock in the East Subbasin to test the hypothesis that the onset of seafloor spreading in the SCS occurred here first at ~ 32 Ma. Magnetic Anomaly 11, the oldest anomaly interpreted by Taylor and Hayes (1980) and Briais et al. (1993), passes near this site and hence would allow key calibration between ages estimated from magnetic anomalies and those from biostratigraphy, radiometric dating, and magnetostratigraphy.

The true nature of the continent–ocean transition and oceanic basement at this site is still speculative; there could be volcanic extrusions associated with early continental breakup and the onset of seafloor spreading, exhumed lower crustal materials from preferential lower crust extension, exhumed mantle materials, or even Mesozoic rock. Coring at this site was intended to help pinpoint the exact location and tectonic nature of the continent–ocean transition and address key problems in the early tectonic transition from rifting to drifting and associated paleoenvironmental changes, including

1. The age of basement (presumably the oldest oceanic crust) near the continent/ocean boundary;
2. Petrology and geochemistry of basement rock and their bearing on continental breakup, incipient seafloor spreading, and mantle evolution;
3. Physical properties of basement rock and their implications for interpreting sharp magnetic contrasts between different subbasins; and
4. Sedimentary, paleoceanographic, and ecosystem responses to the opening of the SCS.

As a result of operational challenges (see **Operations**), the objectives of sampling basement and basal sediment at Site U1432 were not achieved.

Operations

After a 181 nmi transit from Site U1431 averaging 11.0 kt, the vessel stabilized over Site U1432 at 2337 h (UTC + 8 h) on 16 February 2014. Site U1432 consisted of three holes (Table T1). The first hole was a planned jet-in test to determine the correct casing depth for the 20 inch casing string. The second hole was to consist of a reentry system with three strings of casing to ~ 900 mbsf, followed by coring to ~ 1930 mbsf. Because of poor weather conditions, an additional hole was piston cored while waiting on suitable weather to continue the reentry installation.

Hole U1432A was successfully jetted to 62.0 mbsf. A reentry system was then successfully installed to 787.1 mbsf in Hole U1432B. The final cement job on the last casing string compromised the reentry system when the drill string became stuck in the

cement. The drill string had to be severed, forcing us to abandon Hole U1432B. Hole U1432C was successfully cored to 110.0 mbsf with the APC. Four downhole temperature measurements were taken in Hole U1432C with the APCT-3. A total of 12 APC cores were collected at this site, recovering 88.74 m of core over 110.0 m of penetration (81% recovery). The total time spent on Site U1432 was 492 h (17.9 days).

Principal results

Hole U1432C consists of 12 cores (Cores 349-U1432C-1H through 12H) that penetrated to 110.0 mbsf. The lithology is dominated by a sequence of dark greenish gray clay and clay with silt, assigned to lithostratigraphic Unit I (Figure F15). Clay layers are interbedded with very thin bedded (centimeter scale) or laminated silty layers. These layers mostly fine upward and have sharp erosive bases. These graded sequences are generally 10–20 cm thick and are interpreted as distal turbidites. A 2.4 m thick unconsolidated sand layer occurs in the middle of the drilled section. The sand and silt layers represent $<5\%$ of the total recovered core and can usually be identified using magnetic susceptibility measurements, as they typically exhibit lower values than the clays. Thin volcanic ash layers (0.5–2.0 cm thick) occur occasionally in some cores.

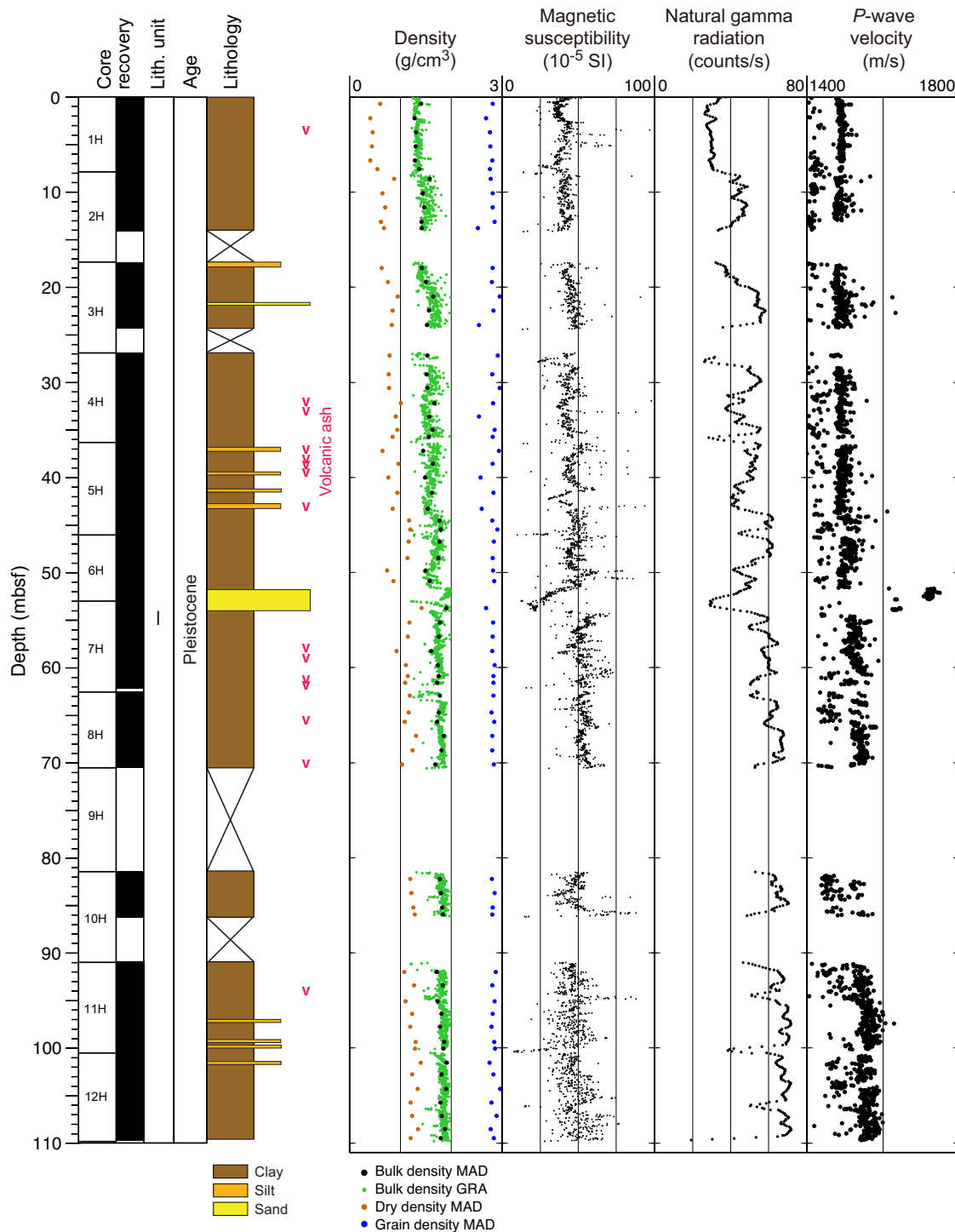
The age of the sedimentary sequence recovered in Hole U1432C is younger than 0.91 Ma (Middle–Late Pleistocene) based on planktonic foraminifer and calcareous nannofossil biostratigraphy (Figure F16). Radiolarians are abundant and moderately to poorly preserved in the upper 15 m of the hole but become progressively rarer and more poorly preserved downhole and comprise a Pleistocene–Holocene assemblage. Nannofossil preservation is moderate to good throughout the hole, with considerable reworking of Pliocene and Miocene species above ~ 50 mbsf. Preservation of planktonic foraminifers is also moderate to good, with evidence of moderate dissolution, as indicated by frequent fragmentation. Planktonic foraminifers are more dominant in sandy intervals that also contain reworked Pliocene species and shallow-water benthic foraminifers.

A total of 16 whole-round samples (5 cm in length) were taken for interstitial water measurements in Hole U1432C. Geochemical analysis shows that sulfate is completely consumed at ~ 90 mbsf, coincident with maximum methane concentrations between 4650 and 4750 ppmv just below this depth. The absence of higher hydrocarbons suggests that the methane is primarily microbial in origin. TOC in the hole varies from 0.34 to 0.99 wt%, and CaCO_3 concentrations are generally low (<12 wt%).

Five whole-round samples and five interface samples were collected from Hole U1432C for DNA and lipid analysis. The five whole-round samples were also used to inoculate several types of microbiological media to test whether autotrophic and heterotrophic microbes can be grown. For heterotrophic culture enrichments, glucose, acetate, fumarate, and formate were used as sources of carbon and energy. For autotrophic culture enrichments, sodium bicarbonate and hydrogen were used as sources of carbon and energy, respectively. We also collected and preserved 200 mL of drilling fluid for FCT analysis. The microbial communities present in these samples will be compared to those present on the inside and outside of the cores to determine whether microbes in the drilling fluid behave as suitable contaminant tracers.

As seen at Site U1431, the NRM of samples from Hole U1432C contains a vertical magnetic component generated by the drilling process, which is relatively easily removed by 5–10 mT alternating field (AF) demagnetization. A polarity reversal at ~ 105 mbsf is de-

Figure F15. Lithostratigraphic and physical properties summary, Hole U1432C. Core magnetic susceptibility and GRA density (filtered) were measured on the SHMSL, MAD was measured on discrete samples, and *P*-wave velocities were measured on the SHMG.

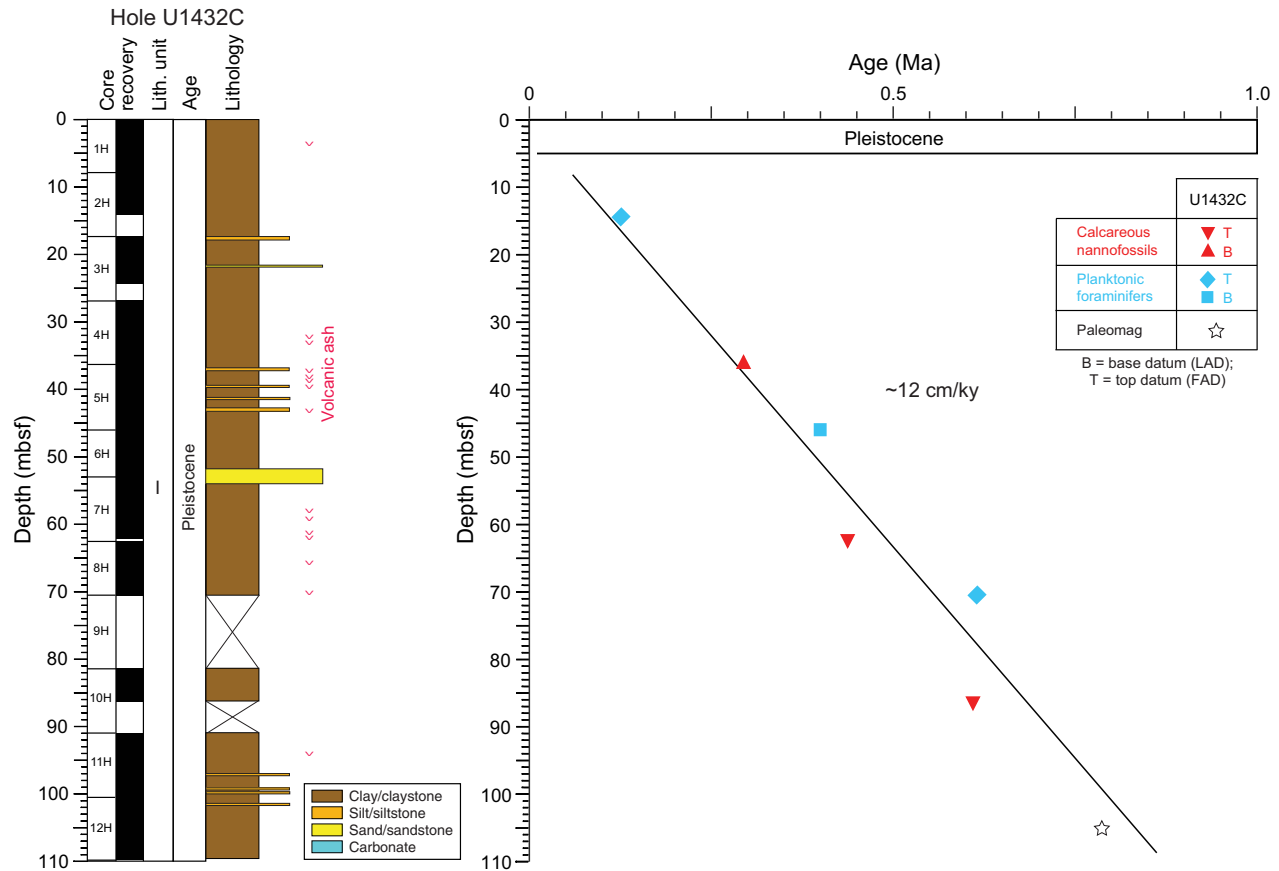


fined as the Brunhes/Matuyama Chron boundary (0.781 Ma) (Figure F16). Within the Brunhes Chron, there are two directional anomaly intervals at ~10 mbsf and between 50 and 70 mbsf, respectively. These anomalies could represent authentic magnetic excursions or could be caused by postdepositional disturbances. The preliminary magnetostratigraphic results, when combined with the biostratigraphy, indicate a higher sedimentation rate (~13.5 cm/ky)

in Hole U1432C (Figure F16) than for the same age interval in Hole U1431D (~5.8 cm/ky), which is consistent with its location being closer to the continental margin.

Physical property measurements made on whole-round core sections were smoothed using a 5-point (10 cm) moving average and combined with discrete sample measurements. Bulk density, *P*-wave velocity, magnetic susceptibility, NGR, thermal conductivity,

Figure F16. Age-depth model, Site U1432. FAD = first appearance datum, LAD = last appearance datum.



and shear strength decrease with depth in the uppermost 50 m of Hole U1432C (Figure F15), showing an inverse relationship with porosity. Variations in these records are lower below 50 mbsf. This indicates that the compaction effect dominates the physical properties in the uppermost part of Hole U1432C. The 2.5 m thick sand layer near 50 mbsf is clearly delineated by low NGR, low magnetic susceptibility, and higher P -wave velocity (Figure F15).

Four APCT-3 downhole temperature measurements on Cores 349-U1432C-5H, 7H, 9H, and 11H indicate a geothermal gradient of 85°C/km (Figure F14). Combining these temperatures with thermal conductivity measurements made on the sediment cores, the preliminary heat flow value at Hole U1432C is 94 mW/m². The geothermal gradient and heat flow values are similar to those at Site 1148, ~60 km to the north-northeast (Wang, Prell, Blum, et al., 2000) (Figure F14).

Site U1433

Background and objectives

As a result of the marked contrast in magnetic anomaly amplitudes between the Southwest and East Subbasins of the SCS (Yao, 1995; Jin et al., 2002; Li et al., 2007a, 2008b), it is questionable whether rifting and drifting within these two subbasins occurred synchronously and how these subbasins evolved in comparison to the Northwest Subbasin. Site U1433 is located in the Southwest Subbasin near the relict spreading center and magnetic Anomaly C5d identified by Briais et al. (1993) (Figures F4, F8). Together with Site U1431 in the East Subbasin, coring at Site U1433 should help to explain the sharp differences in magnetic amplitude between the

East and Southwest Subbasins and test the hypothesis that in the Southwest Subbasin the breakup from continental rifting to seafloor spreading occurred more recently than in the East Subbasin (Pautot et al., 1986). Coring will help determine the age of this subbasin near the end of spreading and correlate ages from magnetic anomalies with biostratigraphic, magnetostratigraphic, and radiometric ages. The apparent weak magnetization in basement rock (Li et al., 2008b) will be examined through petrological and geochemical analyses and by measurements of magnetic susceptibility and remanent magnetization. The specific objectives at this site were to

1. Determine the termination age of spreading in the Southwest Subbasin and correlate it with ages of regional tectonic events;
2. Test the hypothesis that rifting and subsequent seafloor spreading in the Southwest Subbasin occurred later than that in the East Subbasin;
3. Measure magnetization, mineralization, and geochemical compositions of basement rocks to trace how the mantle evolved through time; and
4. Examine the paleoceanographic and sedimentary response to the opening of the SCS.

Operations

After a 334 nmi transit from Site U1432 averaging 11.2 kt, the vessel stabilized over Site U1433 at 0230 h (UTC + 8 h) on 8 March 2014. The original operations plan consisted of drilling one hole to a depth of ~965 mbsf, which included 100 m of basement. This plan was modified during transit in order to eliminate the use of a free-

fall funnel and the XCB by coring two holes (Table T1). Hole U1433A was cored using the APC to refusal at 188.3 mbsf. Hole U1433B was drilled to 186.1 mbsf and then cored using the RCB. The sediment/basement interface was encountered at ~798.5 mbsf, and we advanced the hole by rotary coring into basement to a final depth of 858.5 mbsf. After conditioning the hole for logging, we deployed the modified triple combo tool string and the EMS-sonic tool string to 840 m WSF, with multiple passes made in the basement section of the hole with the latter tool.

A total of 94 cores were collected at this site. The APC was deployed 20 times, recovering 168.79 m of core over 188.3 m of penetration (89.6% recovery). The RCB system drilled one 186.1 m interval and collected 74 cores, recovering 443.04 m of core over 672.4 m of penetration (65.9% recovery). The overall recovery at Site U1433 was 71.1%. The total time spent on Site U1433 was 284.5 h (11.85 days).

Principal results

The cored section at Site U1433 is divided into 4 lithostratigraphic units (three sedimentary and one igneous) based on a combination of data from Holes U1433A and U1433B (Figure F17). Lithostratigraphic Unit I is a 244.15 m thick sequence of Pleistocene dark greenish gray clay, silty clay, and clay with nannofossils. The clay is interbedded with small volumes of generally thin, graded quartzose silt and nannofossil ooze, both interpreted to be turbidite deposits that comprise <5% of the unit. This unit is underlain by middle Miocene to Pleistocene Unit II (244.15–747.93 mbsf), which is divided into two subunits: IIA (244.15–551.32 mbsf) and IIB (551.32–747.93 mbsf). The entire unit is 503.78 m thick and dominated by dark greenish gray clay with frequent graded carbonate interbeds, largely comprising nannofossil ooze and chalk that are characterized by sharp, erosive bases and gradational, bioturbated tops. In Subunit IIB, carbonate beds are sometimes substantially thicker, up to several meters, rather than <1 m and usually <50 cm in Subunit IIA. The carbonates are turbidite deposits with evidence of resedimentation from shallow-water regions based on the occurrence of benthic foraminifers that dwell in the photic zone. The lowermost sedimentary sequence, Unit III (747.93–796.67 mbsf), is a 48.74 m thick lower to middle Miocene sequence of claystone and claystone with silt. Most of the unit is reddish brown or yellowish brown massive sediment with common burrowing stained black by diagenetic alteration. As in Units I and II, bioturbation of Unit III is consistent with sedimentation at lower bathyal to abyssal water depths (*Nereites* ichnofacies). Unit III contains sparse, relatively thin calcareous turbidites. There is no evidence for hydrothermal influence on sedimentation or diagenesis despite the fact that it lies directly above the basalt of Unit IV (796.67–857.48 mbsf). Unit III is the product of relatively slow sedimentation in a distal setting at the foot of a continental margin and is similar to the basal sediment at Site U1431 and to “red clay” deposits from the central Pacific (Bryant and Bennett, 1988).

Analysis of calcareous nannofossils, planktonic foraminifers, and radiolarians in core catcher samples and additional samples from split cores indicates that the sedimentary succession recovered at Site U1433 spans the lower Miocene to the Pleistocene (Figure F18). Age control for the lower to lower middle Miocene section is difficult because of very rare occurrences of microfossils in the brown claystone (Unit III) overlying the basement. Nannofossils in sediment preserved in and around basalt pillows are Oligocene to early Miocene in age, but additional postexpedition analyses are required to determine if these assemblages are reworked or in situ.

Calcareous nannofossils are generally common to abundant with good preservation in samples from the Pliocene–Pleistocene section but are rare and heavily overgrown or even barren in some upper Miocene and Pliocene samples, especially those from nannofossil ooze/chalk intervals. Planktonic foraminifers also show considerable variations in both abundance and preservation. They are abundant and well preserved in silty layers with numerous small (<150 μm) specimens but poorly preserved and very difficult to identify in lithified intervals. Radiolarians are abundant and well preserved in the Upper Pleistocene section in Hole U1433A but rare or absent in older sediment sections downhole. In Hole U1433B, samples are barren of radiolarians until the brown claystone of Unit III, in which rare and poorly preserved but biostratigraphically significant specimens occur.

Integration of biohorizons and paleomagnetic datums indicates extremely low sedimentation rates (<0.5 cm/ky) during the early to middle Miocene. Sedimentation rates varied from ~5 to 9 cm/ky from the late Miocene to early Pleistocene but then increased sharply to ~20 cm/ky since 1 Ma (Figure F18).

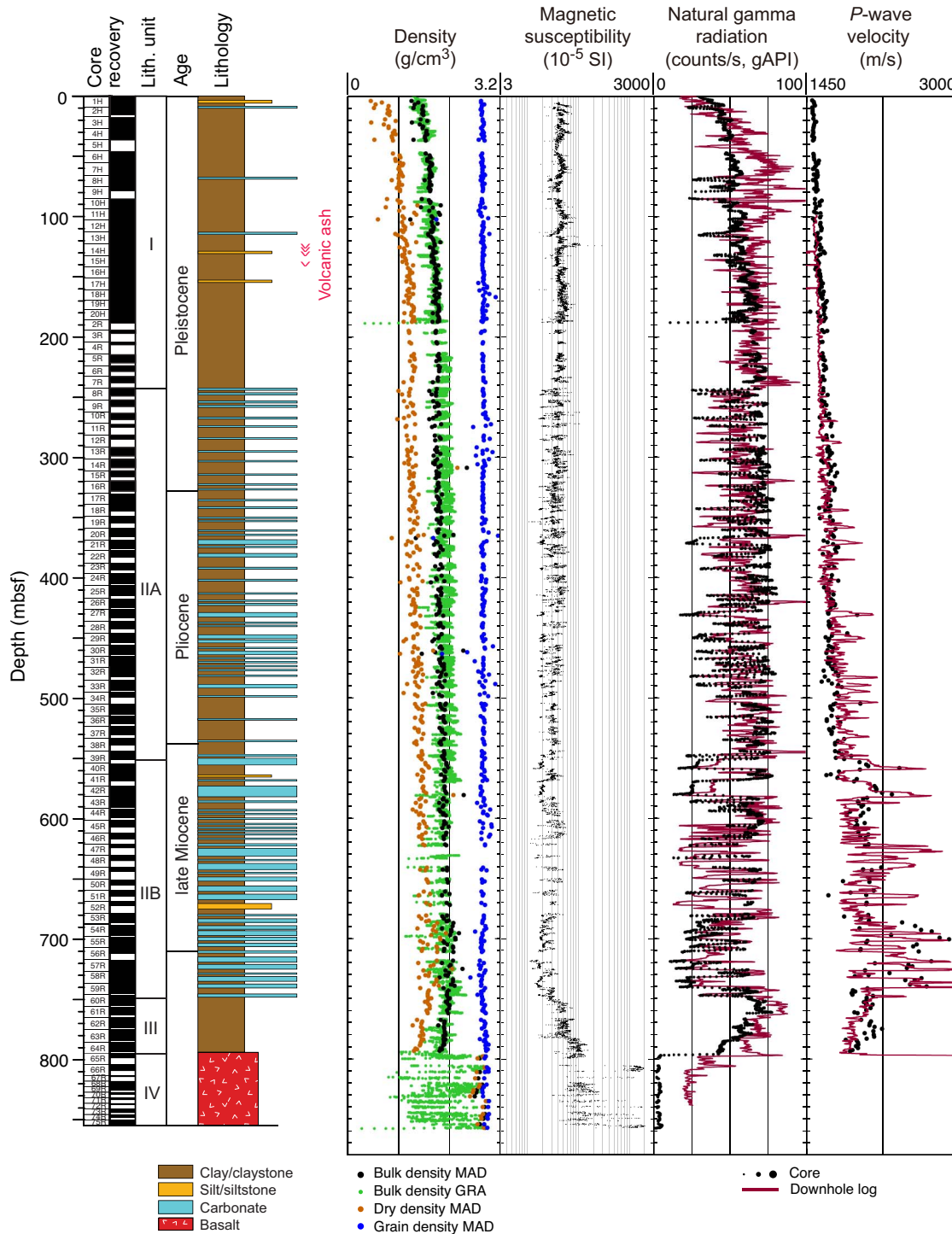
We cored 60.81 m into igneous basement below 796.67 mbsf in Hole U1433B, recovering 29.02 m of basalt (47.7% recovery). This short basement succession was divided into 45 igneous lithologic units, which are grouped into lithostratigraphic Unit IV and are immediately overlain by hemipelagic dark reddish brown to yellowish brown claystone (Unit III) (Figure F19). The basement at Site U1433 is composed of a 37.5 m thick succession of small pillow basalt lava flows in the top (Figure F20) with a 23.3 m series of massive basalt lava flows toward the bottom.

The igneous basement begins with a sequence of sparsely to highly plagioclase-phyric pillow basalt with a trace of olivine microphenocrysts. Most of the pillow basalts are nonvesicular to sparsely vesicular, range in grain size from crypto- to microcrystalline, and in many cases have well-preserved glassy chilled margins along both the upper and lower unit boundaries. A few larger lobate flows are present, with flow thicknesses varying from 0.1 to 1.1 m. In two intervals, interpillow hyaloclastite breccia was encountered, with remnants of baked limestone in which Oligocene to early Miocene nannofossils occur. In between these sequences of pillow basalt flows, one 5.2 m thick microcrystalline to fine-grained massive flow was encountered that is sparsely olivine-plagioclase-phyric but has holocrystalline groundmass with abundant clinopyroxene present in the interstitial spaces. Downhole, the basement is characterized by more massive basalt lava flows as thick as ~12.8 m. These massive flows have similar petrologic characteristics and range from sparsely to highly plagioclase-phyric with minor microphenocrysts of olivine. Toward the interiors of the thickest lava flows the grain size increases to fine grained.

All basalts have a phenocryst phase assemblage of plagioclase \pm olivine, whereas the more massive flows also have clinopyroxene in their groundmass. This assemblage resembles a typical MORB crystallization assemblage and, in conjunction with geochemical evidence, we conclude that the basement basalt at Site U1433 is typical MORB.

Alteration is also typical of that of MORB. The basalt ranges from mostly fresh/less altered to moderately altered in intensity, typically as halos in association with cracks and veins, and from gray to dark gray-green and yellow to red-brown in color. Basalt glasses are most abundant near the quenched margin of lava flows and are commonly altered to greenish palagonite, which might indicate alteration from more reducing fluids than that of brownish palagonite. Alteration veins are abundant at the top of the basement

Figure F17. Lithostratigraphic and physical properties summary, Site U1433. Physical properties and downhole measurements are from Holes U1433A and U1433B. Core magnetic susceptibility and GRA density (filtered) were measured on the SHMSL, MAD was measured on discrete samples, and *P*-wave velocities were measured on the SHMG. Downhole log data, magnetic susceptibility, and total NGR are from the main pass of the triple combo tool string, and *P*-wave velocities are from the main pass of the FMS-sonic tool string. Downhole log depths have been shifted upward by ~2 m to correlate with the core physical property data.

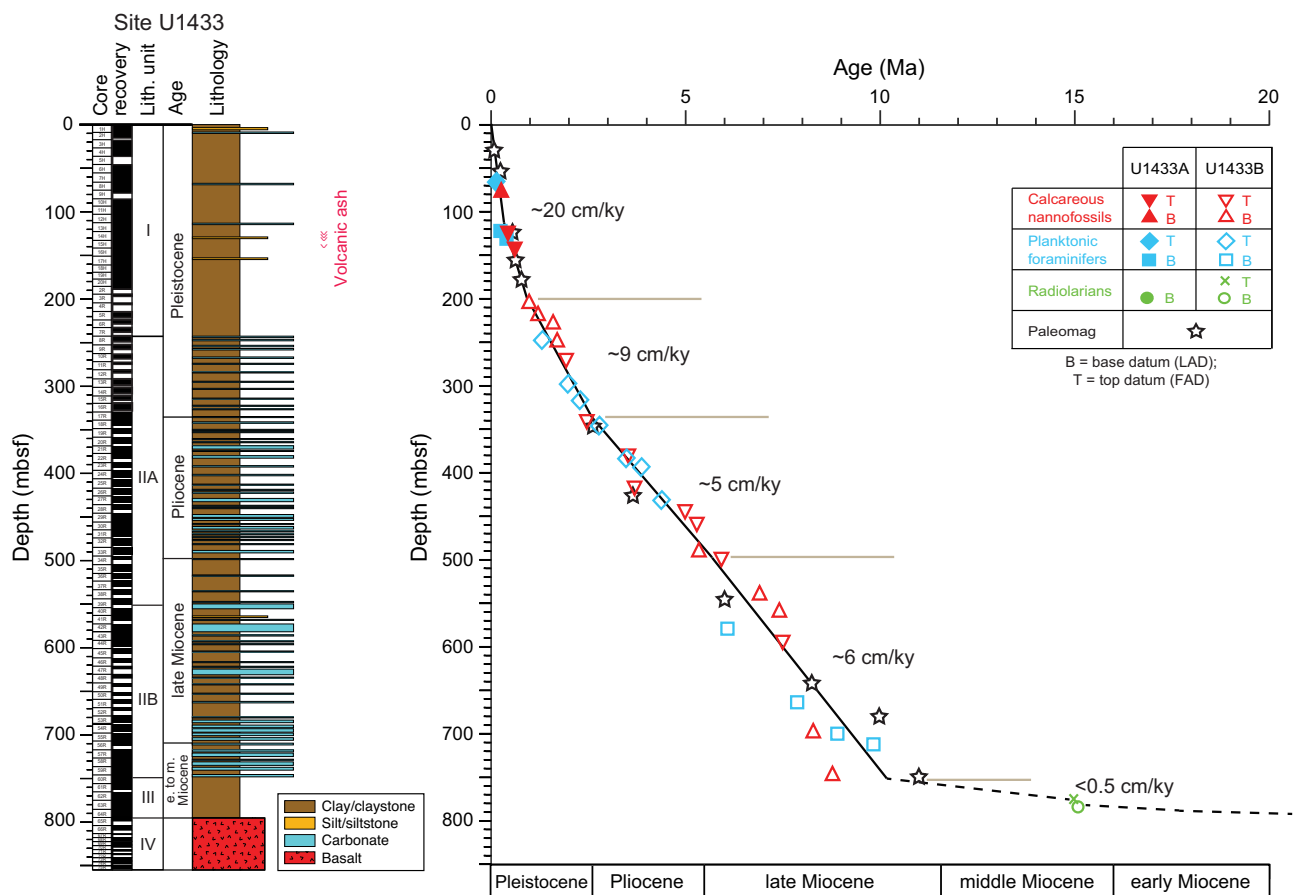


cores and decrease with depth, indicating limited downwelling fluid flow, which is also consistent with fewer fractures that occur with increasing depth. Vein filling minerals include carbonate, celadonite, Fe oxide/hydroxide, saponite, smectite, quartz, and some blue minerals that are difficult to identify. Typical secondary minerals in-

clude saponite, Fe oxide, carbonate, and celadonite, which represent a low-temperature alteration assemblage.

We measured 240 fractures and veins in the basalt of Hole U1433B. Most of the fractures occur along existing veins without either obvious offset or striations on the surfaces, indicative of drill-

Figure F18. Age-depth model, Site U1433. FAD = first appearance datum, LAD = last appearance datum.



ing-induced fractures, whereas natural fractures are quite rare. In general, veins can be separated into four types with different shapes: single straight, triple-junction, branched, and crosscutting. Curved, crosscutting, and triple-junction veins are usually distributed in pillow basalt layers, whereas single straight, branched, or sinuous veins are usually confined to the massive flows. The highest frequency of veins occurs in the pillow basalt, whereas there are fewer veins within the massive flows. Alteration along fractures and veins produced 1–2 cm wide yellow to brown halos.

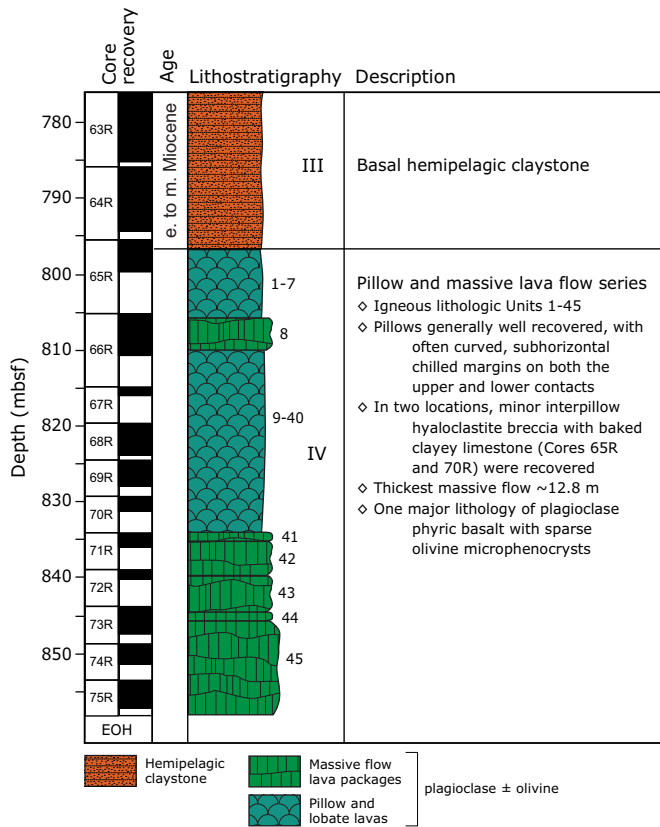
At Site U1433, interstitial water sulfate concentration decreases with depth, and sulfate is almost completely consumed (<1 mM) below ~30 mbsf. Alkalinity increases with depth, reaching a maximum of 25.8 mM at ~30 mbsf, before gradually decreasing with depth. The depth at which sulfate is consumed and alkalinity reaches its peak corresponds to an increase in methane from ~3 to 1100 ppmv. Below this depth, methane varies between ~22,000 and 93,000 ppmv before it decreases significantly below ~590 mbsf. Ethane and other higher hydrocarbons are also present in low concentrations below ~60 mbsf. This indicates that anaerobic oxidation of methane coupled with sulfate reduction is ongoing in the sediment. Other interstitial water chemistry profiles reflect both lithologic changes and diagenetic processes. TOC varies from 0 to 1.0 wt%, with a general decrease downhole. CaCO₃ content ranges from 0.5 to 77.8 wt%, with the lowest values (generally <15 wt%) in the upper 300 m of the site. Intervals with higher CaCO₃ content below 300 mbsf correspond to carbonate turbidite layers in lithostratigraphic Unit II. Peaks in TOC (1–1.5 wt%) at ~450 mbsf and 540–

590 mbsf could reflect an influx of terrestrial organic matter; however, additional shore-based work is needed to confirm this interpretation.

The basalt recovered in Hole U1433B has low LOI values (0.52–2.06 wt%), as well as low K₂O (0.11–0.29 wt%) and moderate TiO₂ (1.01–1.77 wt%) and SiO₂ (48.5–51.1 wt%) compared to an average basalt. In general, concentrations of major elements vary within narrow ranges. When plotted on the alkali vs. silica diagram of volcanic rock types (Le Maitre et al., 1989) (Figure F12), the data plot within the tholeiitic basalt field. As shown in Figure F13, the data from these rocks overlap with but define a much smaller range than those of Indian Ocean and Pacific MORB and are distinct from the Hainan Island OIB and other SCS seamount basalt data fields (Figures F12, F13). Thus, the basalt samples from Hole U1433B are tholeiites and considered representative of SCS MORB.

At Site U1433, we collected a total of 50 routine 5 cm whole-round samples for microbiological analysis from the seafloor to 790 mbsf. When possible, these samples were collected adjacent to samples for interstitial water measurements. We also collected 164 samples from split cores to study the microbiology of interfaces or coring-induced disturbance. We obtained these samples between 4 and 154 mbsf in Hole U1433A and between 187 and 854 mbsf in Hole U1433B. Most of the samples collected at Site U1433 were preserved for shore-based analysis of DNA, RNA, and lipids. Some portions of the whole-round samples were selected for cultivation-based studies designed to enrich for anaerobic autotrophs and heterotrophs.

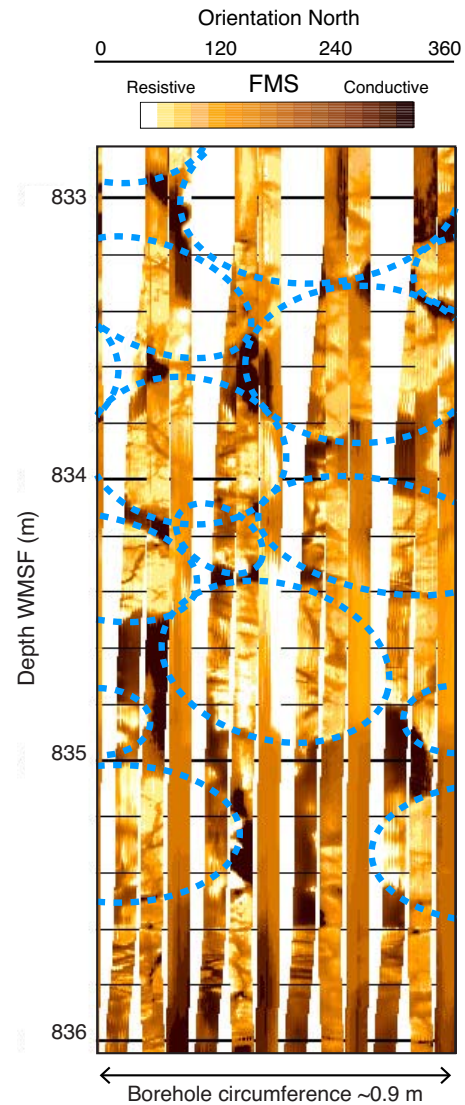
Figure F19. Lithostratigraphic summary of igneous rocks and their lithologic features with integrated downhole logging observations, Hole U1433B. Lithostratigraphy column includes lithology, igneous lithologic units (1–45), and lithostratigraphic units (III and IV). EOH = end of hole.



We used three methods of contamination testing during coring at Site U1433: PFTs, microspheres, and FCTs. PFT samples were acquired from the outside and inside of 16 cores between 140 and 390 mbsf in Holes U1433A and U1433B. PFTs were not detected in most of the samples collected and analyzed for this tracer regardless of whether the samples were taken from the outside or the inside of the core. Microsphere tracers were used with the RCB coring system in Hole U1433B between 709 and 854 mbsf. Two microsphere samples were taken from each core collected between these depths: one from scrapings of the core surface and one as a subsample from the interior of each whole-round sample. Twenty-four FCT samples were collected either from the drilling fluids that drained from the core liners when cores arrived on the catwalk or from a sampling port near the mud pumps on the rig floor during active coring. The fluids collected for FCT samples correspond to cores obtained from depths ranging between 6 and 824 mbsf.

We conducted paleomagnetic studies at Site U1433 on both sediment and basement cores using pass-through magnetometer measurements on all archive-half sections and AF demagnetization on representative discrete samples. Magnetostratigraphic records at Site U1433 suggest the existence of eight short reversed polarity events within the Brunhes normal chron. These short-lived events most likely represent geomagnetic excursions, as both declination and inclination change. The polarity shifts at depths of ~12, 18, 28, 48, 53, 132, and 152 mbsf match well with known excursion events: Mono Lake (33 ka), Laschamp (41 ka), Blake (120 ka), Iceland Basin (180 ka), Pringle Falls (211 ka), Big Lost (560–580 ka), and marine

Figure F20. Downhole FMS images showing basalt pillows in the 833–836 m wireline matched depth below seafloor (WMSF) interval, Hole U1433B.



isotope Stage 17 (670 ka). For two directional anomalies at ~78 and 88 mbsf, there are no counterparts from previous studies, and further shore-based work is needed to confirm the origin of these two anomalies. The Brunhes/Matuyama Chron boundary (0.781 Ma) is tentatively placed at ~188 mbsf in Core 349-U1433A-20H, which indicates a higher sedimentation rate (~23.7 cm/ky) for the Middle–Late Pleistocene compared to Sites U1431 and U1432 (Figure F18). Such a high sedimentation rate facilitates preservation of the short-lived polarity excursions mentioned above.

In Hole U1433B, six major normal chrons are recognized and tied to the geomagnetic polarity timescale using constraints from biostratigraphy. The basal boundaries for the Matuyama Chron (2.581 Ma), Gauss Chron (3.596), and Gilbert Chron (6.066 Ma) are placed at ~350, 420, and 550 mbsf, respectively. The basal age for sediment in Core 349-U1433B-60R is ~11 Ma. Paleomagnetic results for the basalt units show that the upper part of the basement (805–817 mbsf) is dominated by normal polarity. Between ~817 and 830 mbsf, a relatively well defined reversed polarity zone is observed. Below this depth range, the paleomagnetic inclinations dis-

play both normal and reversed polarities. Overall, the remanent magnetization of rocks below ~817 mbsf is dominated by reversed polarity. This pattern is similar to that found in the upper part of the basalt units at Site U1431.

Cores from Holes U1433A and U1433B were measured for physical properties on whole-round cores, split cores, and discrete samples. The physical properties correlate well with lithology, composition, and observed lithification. Bulk density, *P*-wave velocity, shear strength, NGR, and thermal conductivity increase gradually with depth over the uppermost 150 m (Figure F17), whereas the porosity measured on discrete samples decreases from 90% to 50% over the same depth range. This indicates that sediment compaction dominates physical property variations shallower than 150 mbsf. Deeper than 240 mbsf, variability in porosity, magnetic susceptibility, and NGR values reflects interbedding of carbonate and clay layers (Figure F17). An increase in *P*-wave velocity from ~1700 to ~2000 m/s near 550 mbsf coincides with stronger lithification in the deeper sediment. From 680 to 750 mbsf, *P*-wave velocities measured in the lithified carbonates reach ~2600 m/s, contrasting strongly with those measured in the clay (~2000 m/s) (Figure F17). The strong reflectors observed in the seismic profile from this site probably result from this contrast in velocity. Magnetic susceptibility gradually increases and NGR decreases in the clays between 750 and 800 mbsf (Figure F17). The basalt below 800 mbsf displays very low NGR and porosity and variable magnetic susceptibility. Some of the fresh, phenocryst-rich basalt has very high magnetic susceptibility and *P*-wave velocities.

The modified triple combo and FMS-sonic tool strings were run in Hole U1433B. Both tool strings reached 840 m WSF, ~18 m short of the bottom of the hole (Figure F17). Between 100 and 550 m WSF, there are rapid variations in borehole diameter from ~25 to >43 cm. Below 550 m WSF, the hole diameter is mostly in gauge, with fewer washed out zones. Density and sonic velocity increases from the top of the logs at 100 m WSF downhole to 750 m WSF, caused by compaction and cementation with depth. Superimposed on this trend, excursions to higher velocity and photoelectric factor (PEF) and to lower NGR mark the occurrence of carbonate beds (Figure F17). This information was used to infer lithology in the unrecovered intervals of Hole U1433B. In the red clay of Unit III, from ~750 to 800 m WSF, high values in the PEF log indicate that hematite and other oxides increase in concentration downhole toward the top of the basalt at ~800 m WSF. Pillow basalt, a massive basalt flow, fractures, and veins are seen in the FMS images in the basement.

Site U1434

Background and objectives

Site U1434 is located about 40 km northwest of Site U1433 and is directly on the uplifted shoulder of the relict spreading center in the Southwest Subbasin (Figures F7, F8). This site is also located just south of a large seamount that formed near the relict spreading center after the termination of seafloor spreading. During coring at Site U1433, we decided to use some of our remaining time to core at a second site in the Southwest Subbasin to obtain basement samples more proximal to the extinct spreading center. Site U1434 also offered the opportunity to sample volcanoclastic material from the nearby seamount, which can be compared to the seamounts located near Site U1431 in the East Subbasin.

Sites U1434 and U1433 form a short sampling transect in the Southwest Subbasin (Figure F7), and with age controls from these two sites, the evolution of the Southwest Subbasin can be better un-

derstood. Coring at these sites should help to explain the sharp differences in magnetic amplitude between the East and Southwest Subbasins and test the existing opening models for the Southwest Subbasin (e.g., Pautot et al., 1986). Coring will help determine the age of this subbasin near the end of seafloor spreading and correlate ages from magnetic anomalies with biostratigraphic, magnetostratigraphic, and radiometric ages. The apparent weak magnetization in basement rocks (Li et al., 2008b) will be examined through petrological and geochemical analyses and by measurements of magnetic susceptibility and remanent magnetization. Rock samples cored here will place constraints on mantle evolution and oceanic crustal accretion, the terminal processes of seafloor spreading, and the timing and episodes of postspreading seamount volcanism in the area of the relict spreading center.

Operations

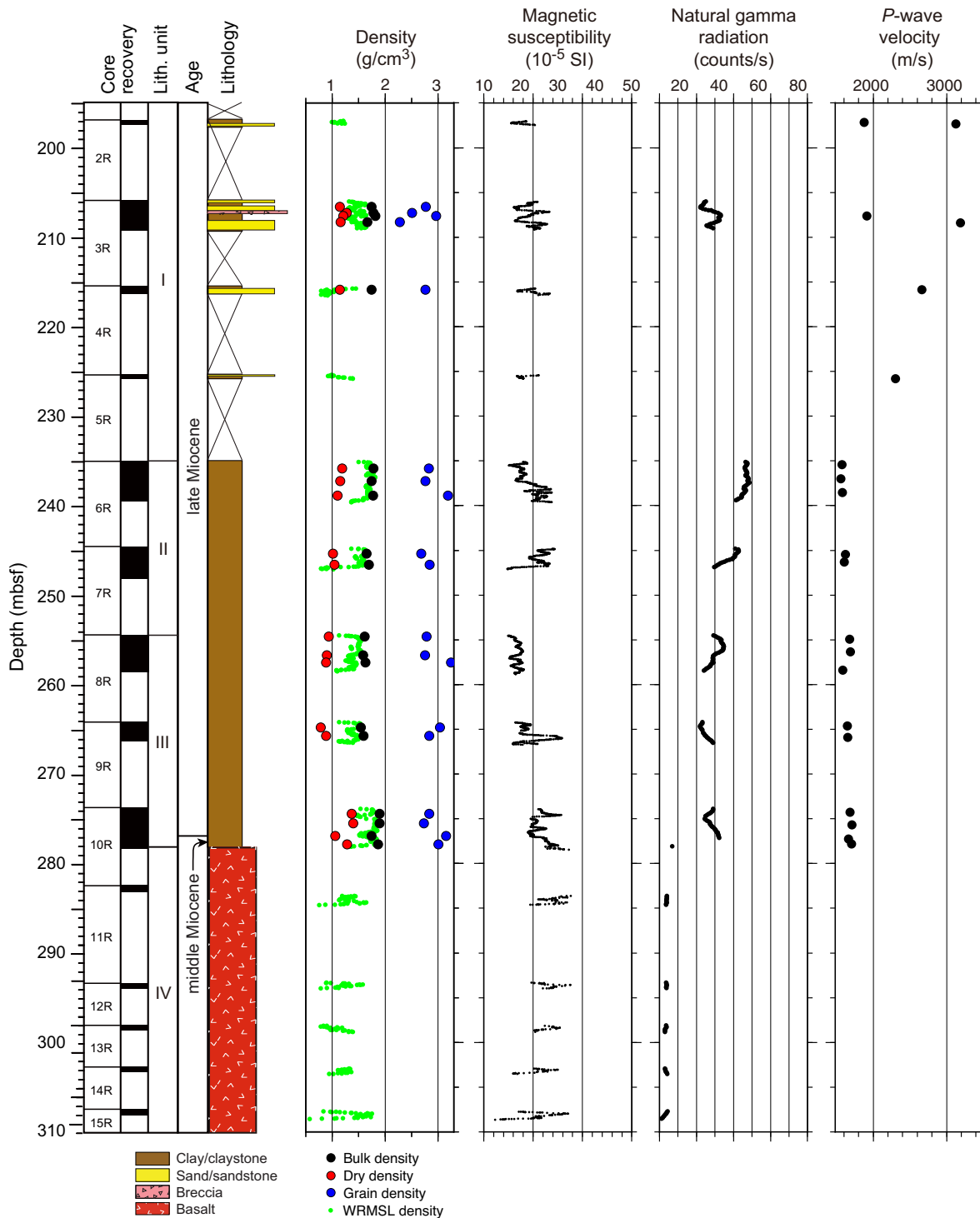
After an 18 nmi transit from Site U1433 averaging 10.3 kt, the vessel stabilized over Site U1434 at 0048 h (UTC + 8 h) on 20 March 2014. This site was an alternate site that was originally planned to core from the seafloor with APC/XCB to refusal, drop a free-fall funnel, change to the RCB, and then core 100 m into basement. Because of time considerations, the plan was modified so that we drilled to ~200 mbsf using the RCB and then cored into basement as deeply as time permitted. Logging would then be considered depending on hole depth and condition. Hole U1434A was drilled to 197.0 mbsf and then cored with the RCB (Table T1). Basement was encountered at ~280 mbsf, and the hole was advanced by rotary coring to a final depth of 312.5 mbsf. The hole was terminated because of poor hole conditions and poor recovery. At this site there was one drilled interval of 197.0 m. The RCB was deployed 14 times, recovering 26.43 m of core over 115.5 m of penetration (22.9% recovery).

Principal results

The cored section at Site U1434 is divided into four lithostratigraphic units, three sedimentary and one igneous (Figure F21). Lithostratigraphic Unit I (197.00–235.10 mbsf) is a 38.1 m thick sequence of upper Miocene dark greenish gray claystone interbedded with black volcanoclastic sandstone and occasional breccia. The fine-grained sediment is mottled greenish and light buff brown, with the browner sediment preferentially found in burrows. This unit is marked by strong bioturbation within the claystone intervals that make up ~40% of the total sediment. The trace fossil assemblages in the claystone intervals are consistent with sedimentation in deep water (i.e., lower bathyal or abyssal depths; >2500 m), with assemblages dominated by *Chondrites* and *Zoophycos*, although more vertical burrows are also noted. Sandstone beds are typically dark gray or black in color and are composed of volcanoclastic fragments. The volcanoclastic sandstone and breccia are interpreted to be part of the sedimentary apron of a nearby seamount because they contain abundant volcanic glass fragments, scoria, and basalt clasts, as well as isolated crystals of plagioclase, olivine, and biotite.

Lithostratigraphic Unit II (235.10–254.59 mbsf) contains upper Miocene greenish gray nannofossil-rich claystone with very thin claystone with sand interbeds. The color of the sediment varies at the decimeter scale as a result of changes in the carbonate and clay content. The sediment is locally a light greenish gray color, reflecting higher biogenic carbonate content over those intervals. Unit III (254.59–278.27 mbsf) consists of dominantly massive yellowish brown claystone with nannofossil- or foraminifer-rich claystone of latest middle to late Miocene age. This unit is primarily distinguished from Unit II by its color, which tends to be more yellowish

Figure F21. Lithostratigraphic and physical properties summary, Hole U1434A. Core magnetic susceptibility and GRA density (filtered) were measured on the SHMSL, MAD was measured on discrete samples, and P-wave velocities were measured on the SHMG.

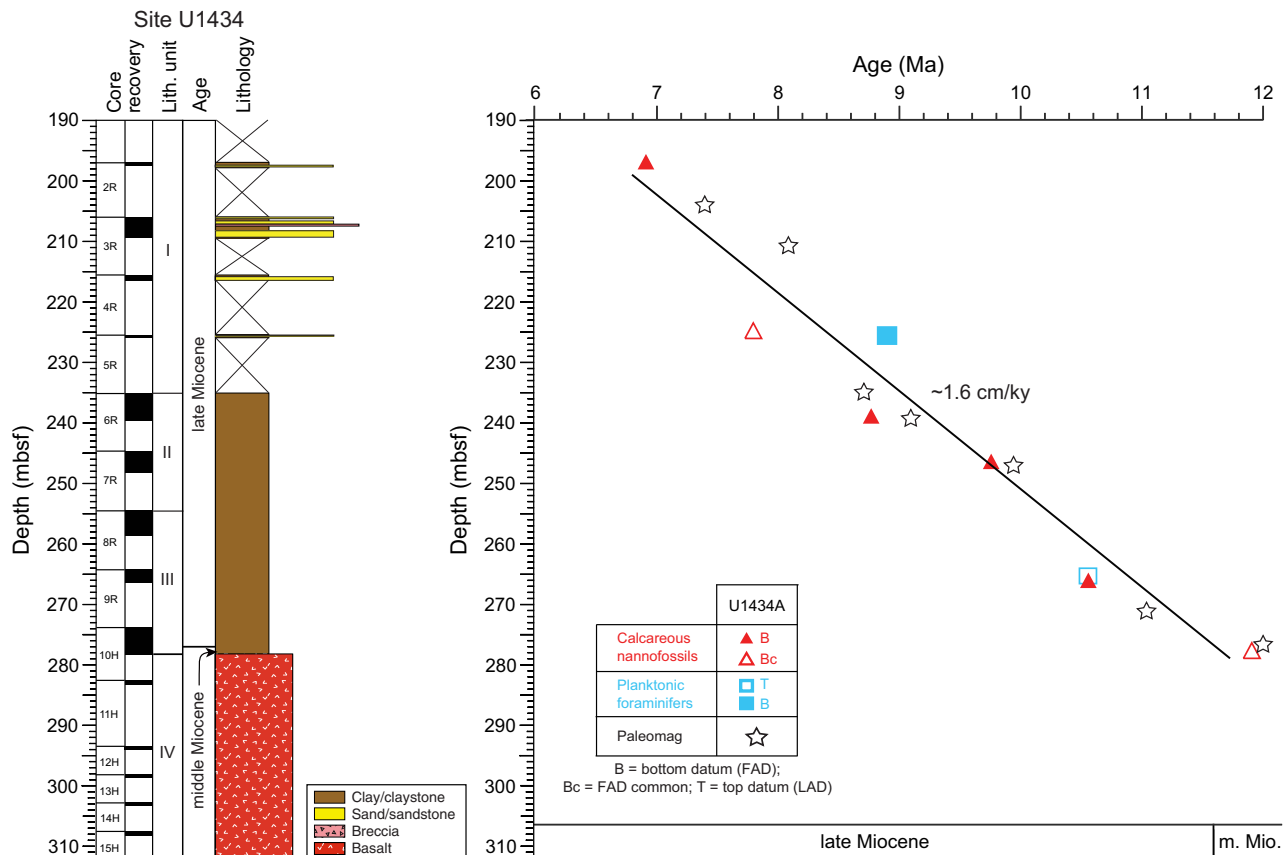


or reddish brown compared to the greenish gray tones associated with the overlying unit.

Analysis of calcareous nannofossils and planktonic foraminifers in core catcher samples and additional samples from split cores indicates that the sedimentary succession recovered at Site U1434 spans the uppermost middle to upper Miocene, with the base of the sequence younger than 11.9 Ma (Figure F22). Calcareous nannofos-

sils are generally common to abundant but decrease in abundance downhole, and preservation is poor to moderate. Planktonic foraminifers vary from common to absent, with good to poor preservation, but are frequently fragmented. Radiolarians are present in only one sample. Although none of the species present are biostratigraphic index taxa, the radiolarian assemblage is consistent with the late Miocene age inferred from nannofossils and foraminifers. Cor-

Figure F22. Age-depth model, Site U1434. FAD = first appearance datum, LAD = last appearance datum.



relation of microfossil biohorizons and paleomagnetic data suggests a sedimentation rate of ~ 1.6 cm/ky for the sediment sequence recovered at Site U1434 (Figure F22).

We cored 30.28 m into igneous basement below 278.37 mbsf in Hole U1434A, recovering 3.05 m of basalt (10.1% recovery). This basement succession is divided into seven igneous lithologic units, which are grouped into lithostratigraphic Unit IV (Figure F23). The basement at Site U1434 comprises a succession of small pillow basalt flows or a thicker autobrecciated pillow lava flow with three occurrences of hyaloclastite breccia. The igneous basement comprises angular to subangular basalt fragments that are aphyric and have glassy to aphanitic groundmasses. The only phenocrystic phase is olivine, which appears as sparse euhedral-subhedral microphenocrysts throughout the core. The groundmass contains abundant plagioclase microlites, growing in spherulitic and variolitic patterns, with the majority of the groundmass consisting of variably altered mesostasis. Clinopyroxene is only observed in a few thin sections, growing in patches and filling the interstitial spaces between plagioclase microlites. Most of the basalt is nonvesicular to sparsely vesicular. The hyaloclastite breccia contains abundant fresh volcanic glass shards in a mostly clay and/or carbonate matrix. All basalts have phase assemblages of olivine \pm plagioclase, and some slightly coarser basalt pieces also have clinopyroxene in their groundmass. These resemble typical MORB crystallization assemblages.

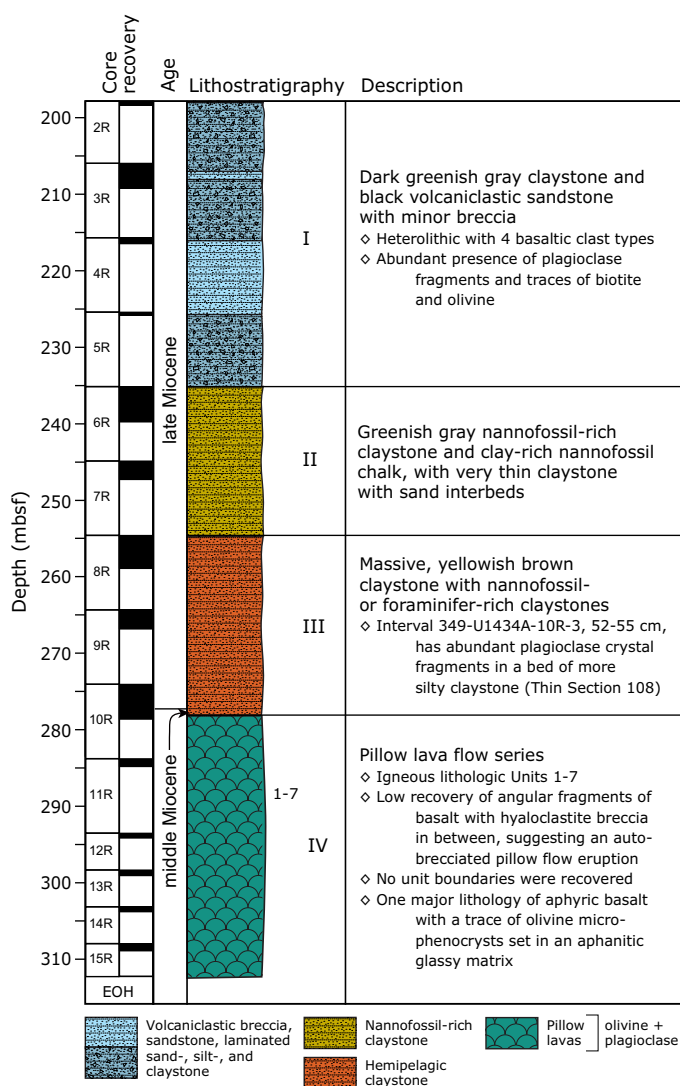
Basalt alteration at Site U1434 is typical of that of MORB. The recovered basalt is slightly to moderately altered. Pillow basalt pieces are altered in zones, with alteration color ranging from dark

gray in the interior to light yellow-brown in halos along the outer rims. Typical secondary minerals include saponite and other clay minerals, Fe oxide, carbonate, and celadonite, which constitute a low-temperature alteration assemblage. Fresh basalt glass exists near some of the pillow basalt margins and in the clasts in the hyaloclastite breccia. Those basalt glasses are partially altered to orange and brown palagonite. Most of the vesicles are empty or only partially filled with Fe oxide, saponite, celadonite, and/or carbonate. Only two alteration veins were observed in this short basement section.

Most fractures observed in the sedimentary sequence at Site U1434 are drilling induced. One fracture shows some offset that suggests it occurred prior to consolidation of the sediments. Fractures are rare in the small amount of basalt recovered at this site. Several straight veins are present and filled with carbonate or Fe oxide.

We measured alkalinity and pH on five interstitial water samples taken from 207.9–264.8 mbsf in Hole U1434A. Alkalinity increases from 0.5 mM at 208 mbsf to 3.5 mM at 257 mbsf and then decreases in the two samples below that depth. The pH decreases from 7.9 at 208 mbsf to 7.2 at 265 mbsf and then increases slightly just above basement. Methane was detected in very low concentrations (<3.1 ppmv) in the headspace gas samples taken at this site. CaCO_3 content is low (<10 wt%) in lithostratigraphic Units I and II. Samples from the base of Unit III are higher in CaCO_3 (15–30 wt%). TOC is also low (<0.5 wt%), with the highest values near the base of the sedimentary section. ICP-AES major and trace element results

Figure F23. Lithostratigraphic summary of igneous rocks and lithologic features, Hole U1434A. Lithostratigraphy column includes lithology, igneous lithologic units (1–7), and lithostratigraphic units (I–IV). EOH = end of hole.



from Site U1434 indicate that the basalt has somewhat higher K_2O than those at Sites U1431 and U1433 but is still tholeiitic in composition and similar to MORB (Figures F12, F13).

We collected six routine 5 cm whole-round samples for microbiological analysis from depths of 208–275 mbsf in Hole U1434A. These samples were collected adjacent to samples for interstitial water measurements so that microbiological data and water chemistry data are proximal. We also collected and preserved 13 samples from either the split cores on the sampling table or from basement samples shortly after the samples were retrieved from the catwalk to investigate the microbiology of interfaces. The whole-round and split core samples were preserved for shore-based characterization of the microbial communities (i.e., DNA, RNA, lipids, and cultivation-based studies).

We also collected samples for measuring contamination testing tracers, including microspheres and FCTs. Microsphere tracers were used with the RCB coring system in Hole U1434A by adding them to the core catcher sub for cores collected between 208 and 303 mbsf. Two microsphere samples were collected from each of

the cores collected between those depth intervals: one from scrapings of the core surface and one as a subsample from the interior of each whole-round sample. Microscopic counts of the microspheres in these samples will be performed in shore-based laboratories. Six FCT samples were collected from drilling fluids that drained from the core liners when cores arrived on the catwalk or from a sampling port near the mud pumps on the rig floor during active coring. The fluids collected for FCT samples correspond to cores obtained from depths ranging between 208 and 293 mbsf. Microbial community DNA and lipids from FCT samples will be compared to the same measurements made on the core samples to determine if the drilling fluids contain microbes that can be regularly tracked as recognizable contaminant taxa.

We conducted paleomagnetic studies at Site U1434 on both sediment and basement cores using pass-through magnetometer measurements on archive-half sections. NRM intensity ranges from 0.001 to 0.1 A/m for the sediment units and increases to several A/m for the basalt units, suggesting that the basalt contains more Fe oxide than the sediment. Because of the poor recovery at the site, only fragmentary patterns of magnetic polarity are observed. Available biostratigraphic data allow us to tentatively correlate certain parts of the magnetic polarity interval recorded in the sediment with the geomagnetic polarity timescale. Near the base of the sedimentary sequence, biostratigraphy indicates an age <11.9 Ma, which we use to correlate the negative inclinations at ~278 mbsf to Chron C5r (11.056–12.049 Ma). The long, dominantly positive inclinations between ~250 and 270 mbsf may represent the long normal Subchron C5n (9.984–11.06 Ma), the short normal polarity zone between ~235 and 240 mbsf appears to have recorded Chron C4An (8.771–9.015 Ma), and the normal polarity zone between 205 and 210 mbsf can be tentatively assigned to Chron C4n around 7.15 Ma (Figure F22).

Cores from Hole U1434A were measured for physical properties on whole-round cores, split cores, and discrete samples. In general, the physical properties correlate well with lithology, composition, and the observed lithification. Because of the low recovery rate, measurements of physical properties show significant discontinuities between intervals. In Hole U1434A, the observed range of values for magnetic susceptibility (30×10^{-5} to 80×10^{-5} SI) and NGR (25–45 counts/s) in Units I–III are typical for clay material, which dominates the sediment layers (Figure F21). The low NGR value in Unit IV corresponds to the basalt layer. The magnetic susceptibility values in the basalt range from 10×10^{-5} to 90×10^{-5} SI, which is much lower than what is typical for basalt (Figure F21). The high grain densities in the claystone of Units II and III suggest the presence of heavy minerals, such as hematite. The porosity measured on discrete samples increases from 40% to 60% with depth, which may be correlated to the lithification and composition of the claystone.

Site U1435

Background and objectives

Coring at Site U1435 became a high priority after failing to achieve our basement objectives at Site U1432 when the final cementing operations compromised the reentry system. This site was originally added as an alternate because of the high risk of being unable to reach basement at Site U1432. The site is located on the continental side of the continent/ocean boundary and is fundamentally different from Site U1432 but nonetheless does have the potential to provide information about the breakup process. Site U1435 is located on a structural high at the transition between the extended

continental crust and the oceanic crust (Figures F6, F8). Similar conspicuous structural high features can be found on the continent/ocean boundary in many other seismic profiles crossing the SCS northern margin and therefore they appear to represent tectonic structures typical of the area. The formation mechanism and nature of this structural high was still speculative; it could have been a volcanic extrusion associated with continental extension at the onset of seafloor spreading, lower crust material emplaced from preferential lower crust extension, exhumed mantle material, or a structural high composed of older (Mesozoic) sedimentary rock. Coring at this location was designed to help pinpoint the exact nature of this structure and improve our understanding of early continental breakup, the rift-to-drift transition, and seafloor spreading processes.

Operations

After a 336 nmi transit from Site U1434 averaging 8.5 kt, the vessel stabilized over Site U1435 at 1524 h (UTC + 8 h) on 24 March 2014. Because we anticipated shallow sediment cover (~10 m), we conducted a 3.5 kHz sonar survey to select a location with maximum sediment thickness to help stabilize the drill string when trying to penetrate basement with thin sediment cover in rough weather. After reaching basement, the plan was to core as deeply into basement as time permitted. Sediment thickness was significantly greater than expected based on the seismic interpretation. Hole U1435A was cored with the RCB to a final depth of 300.0 mbsf when time allocated to the expedition expired (Table T1). The RCB was deployed 32 times, recovering 171.37 m of core over 300.0 m of penetration (57.1%).

Principal results

The cored section at Site U1435 is divided into three sedimentary lithostratigraphic units (Figure F24). Unit I (0–77.65 mbsf) is a sequence of Oligocene–Pleistocene greenish gray nannofossil-rich clay and clayey nannofossil ooze, together with manganese nodules. The unit is divided into Subunits IA and IB based on variations in the nannofossil content of the sediment. Subunit IA (0–36.04 mbsf) is Miocene to Pleistocene in age and consists of manganese nodules underlain by clayey nannofossil ooze. The manganese nodules have a lobate appearance and are typically associated with very low sedimentation rates. The massive clayey nannofossil ooze has a few *Planolites* trace fossils visible on the cut surface of the core. Subunit IB (36.04–77.65 mbsf) is Oligocene in age and consists of mostly greenish gray nannofossil-rich clay and lesser quantities of greenish gray clay. There are interbedded silty clay and clay with silt intervals, but deeper in the section the sediment becomes more calcareous, primarily through an increase in the proportion of nannofossils. The sediment is heavily bioturbated with trace fossils of the *Nereites* ichnofacies.

Unit II (77.65–275.54 mbsf) is a 197.89 m thick sequence of pre-Oligocene thick-bedded and mostly medium-grained dark gray silty sandstone, with very little carbonate and minor sandy siltstone and conglomerate. The sandstone is better cemented than the Unit I nannofossil-rich clay and increases in lithification downhole. Units I and II are separated by a hard carbonate rock that likely represents a hiatus. The sandstone is moderately well sorted and is characterized by dispersed carbon fragments, shell fragments, and current lamination that is largely disrupted by bioturbation, with burrows typical of the *Cruziana* ichnofacies indicative of shallow-marine conditions. Several whole bivalves and gastropods occur in the sandstone. Unit III (275.54–300.00 mbsf) is a 24.46 m thick sequence of dark gray silty sandstone, silty mudstone, and minor con-

glomerate. The unit is distinguished from Unit II by being generally finer grained.

We analyzed all core catcher samples and additional samples from split cores for calcareous nannofossils, foraminifers, and radiolarians at Site U1435. Based on nine nannofossil and four planktonic foraminifer bioevents, the sedimentary sequence above 77.65 mbsf is assigned an age spanning the early Oligocene (<33.43 Ma) to the Pleistocene (>0.12 Ma), with possible unconformities or condensed sections existing between the upper Oligocene and middle Miocene, between the upper Miocene and lower Pliocene, and between the upper Pliocene and Middle Pleistocene. Based on a limited number of bioevents, sedimentation rates during the Oligocene were ~0.5 cm/ky (Figure F25).

Samples from 77.65 to 300 mbsf are barren of nannofossils, radiolarians, and planktonic foraminifers. A few long-ranging, shallow-water benthic foraminifers occur in samples from ~200 to 250 mbsf. Although these specimens are not useful for age control, they indicate a depositional environment of brackish water to shallow marine for Unit II, consistent with the deltaic setting inferred from the sedimentology and trace fossil assemblage.

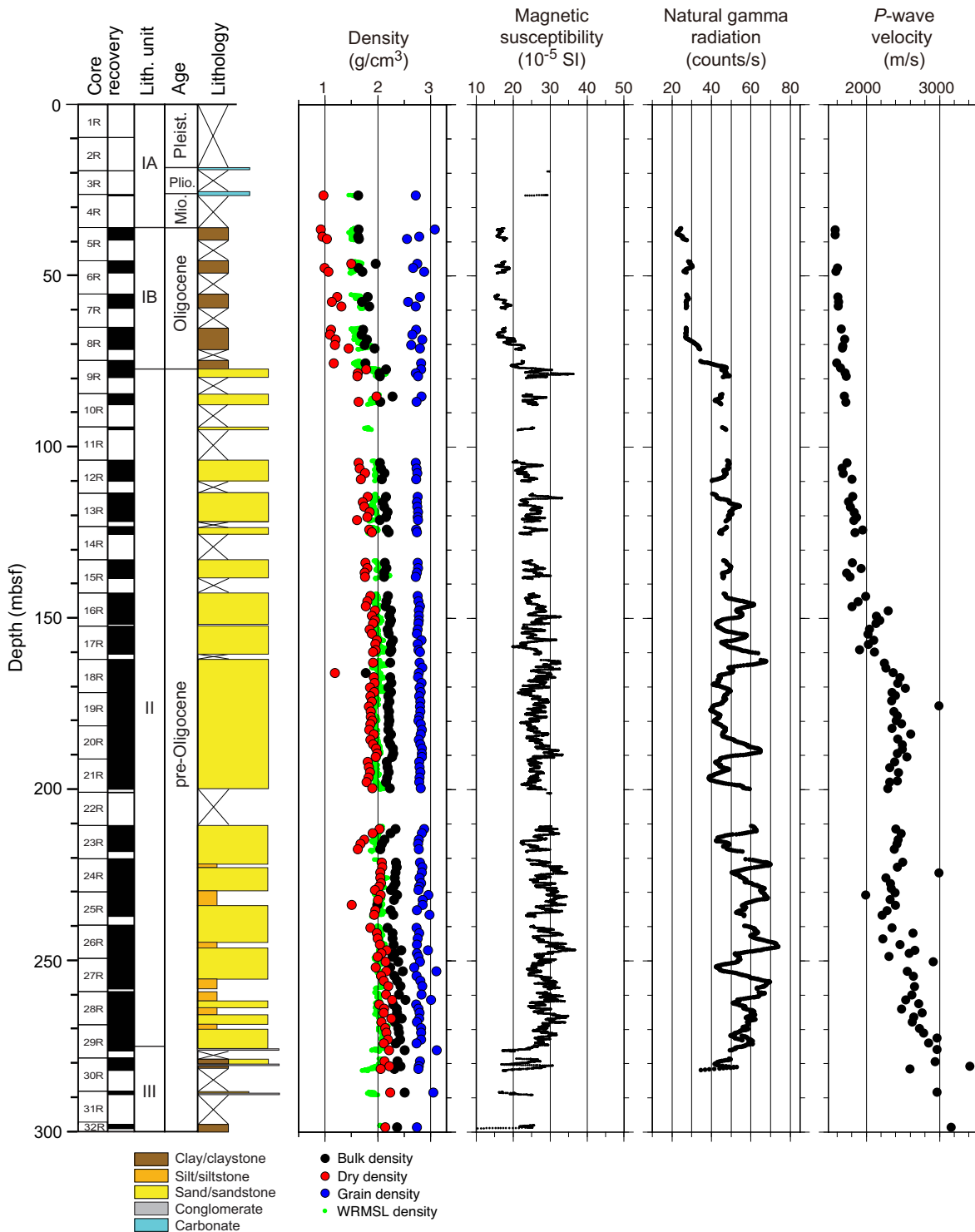
A small number of deformation structures are present in the sedimentary rock of Site U1435. Most of the fractures are drilling induced, and in the dark gray mudstone near the base of the section, these induced fractures developed along the bedding. Two normal fault structures are found in the sandstone, each composed of several fractures that have little offset. No deformation or thickness changes occur in the rock of the hanging walls and footwalls, indicating that these faults occurred at a later stage and did not control sedimentation. One straight white carbonate vein was found in the sandstone. Bedding is generally horizontal or subhorizontal in Unit I, but toward the base of Units II and III the strata are inclined to a significant degree (>25°). These dips are not depositional and are interpreted to reflect rotation caused by normal faulting, possibly during formation of the structural high on which the site is located.

Downhole interstitial water concentrations of chloride, bromide, and sodium are variable and slightly higher than modern seawater; however, the Na/Cl ratio is ~0.85 throughout the sampled interval, which indicates that the interstitial water is of typical marine origin. Only very low concentrations (<10 ppmv) of methane and ethane were detected in the headspace gas samples from Hole U1435A. CaCO₃ content in the upper part of the hole is higher than that of the lower part, which corresponds to the change from nannofossil ooze and nannofossil-rich clay in lithostratigraphic Unit I to sandstone in Unit II. Despite variable TOC with depth, the ratio of TOC to total nitrogen (C/N) suggests that TOC is dominated by a terrestrial organic matter source, with lower input from marine organic matter.

We collected 25 routine 5 cm whole-round samples for microbiological analyses from 37 to 299 mbsf in Hole U1435A. These samples were collected adjacent to samples for interstitial water measurements so that microbiological data and water chemistry data are proximal. The whole-round samples were preserved for shore-based characterization of microbial communities (i.e., DNA, RNA, lipids, and cultivation-based studies).

We also collected samples for measuring contamination testing tracers, including microspheres and FCTs. Microsphere tracers were used with the RCB in Hole U1435A by adding them to the core catcher sub for Cores 349-U1435-5R through 32R (37–299 mbsf). Two microsphere samples were taken from each of the cores collected between those depth intervals: one from scrapings of the core surface and one as a subsample from the interior of each whole-

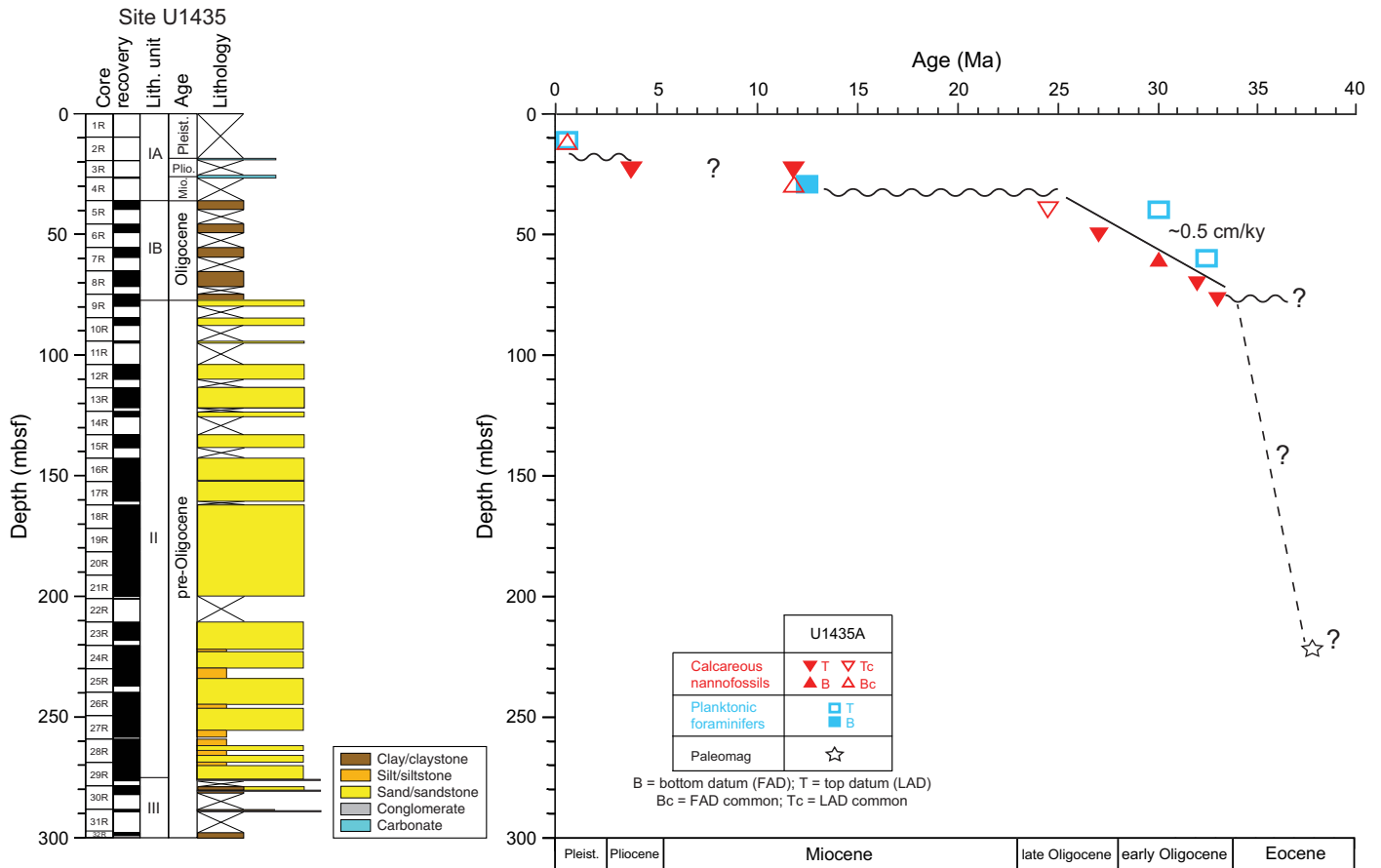
Figure F24. Lithostratigraphic and physical properties summary, Hole U1435A. Core magnetic susceptibility and GRA density (filtered) were measured on the SHMSL, MAD was measured on discrete samples, and P-wave velocities were measured on the SHMG.



round sample. Microscopic counts of the microspheres in these samples will be performed in shore-based laboratories. Five FCT samples were collected from drilling fluids that drained from the core liners when cores arrived on the catwalk or from a sampling port near the mud pumps on the rig floor during active coring. The fluid collected for FCT samples corresponds to cores obtained from

between 90 and 273 mbsf. Microbial community DNA and lipids from FCT samples will be compared to the same measurements made on the core samples to determine if the drilling fluids contain microbes that can be regularly tracked as recognizable contaminant taxa.

Figure F25. Age-depth model, Site U1435. FAD = first appearance datum, LAD = last appearance datum, wavy line = possible hiatus.



We performed measurements of NRM on all archive-half cores from Hole U1435A. We subjected these cores to AF demagnetization up to 20 mT in order to establish a reliable magnetostratigraphy at the site and to observe the magnetic properties of the different lithologies recovered. Because of time constraints, we were unable to perform measurements and demagnetization on discrete samples taken from the working halves. Overall, paleomagnetic data at Site U1435 are reasonably robust and provide magnetic information about the recovered sediment. Several relatively well defined polarity intervals are identified in the downhole magnetostratigraphic records, despite some samples showing unstable and ambiguous magnetization. Based on biostratigraphic data, we were able to tentatively correlate certain parts of the magnetic polarity interval recorded in the sediment with the geomagnetic polarity timescale. Assuming no significant hiatus between the marine Oligocene nanofossil-rich clay (Subunit IB) and the sandstone of Unit II, the Chron C16n/C15r boundary (36.05 Ma) is tentatively placed at ~280 mbsf. This interpretation indicates relatively high sedimentation rates for the sandstone of Unit II (~5 cm/ky) (Figure F25).

Cores from Hole U1435A were measured for physical properties on whole-round cores, split cores, and discrete samples. Thermal conductivity was measured with a needle probe in soft sediment and then with a contact probe in the sedimentary rock. The physical properties correlate with lithology and observed lithification. *P*-wave velocity increases gradually with depth over the uppermost

150 m (Figure F24), whereas porosity measured on discrete samples decreases from 65% to 30% over the same depth range, reflecting sediment compaction. Bulk density, NGR, magnetic susceptibility, and thermal conductivity show a sharp increase near 78 mbsf at the lithostratigraphic Unit I/II boundary between the nanofossil-rich clay and sandstone (Figure F24). A significant increase in *P*-wave velocity and thermal conductivity is observed near 170 mbsf, which is associated with stronger lithification of the sandstone. Magnetic susceptibility and NGR values decrease with depth below 270 mbsf, which corresponds to the change from a dominance of sandstone in Unit II to mudstone in Unit III (Figure F24).

Expedition synthesis

Operations during Expedition 349 (26 January–30 March 2014) drilled five sites in the central basin of the SCS (Figures F1, F2, F8). Sites U1431, U1433, and U1434 were cored into the igneous basement near the fossil spreading center where seafloor spreading terminated, whereas Sites U1432 and U1435 are located proximal to the northern continent/ocean boundary where seafloor spreading started. In total, we recovered 1524 m of sediment and sedimentary rock and 78 m of igneous basement and carried out geophysical logging (triple combo and FMS-sonic tool strings) at Sites U1431 and U1433. The materials recovered and data collected were extensively examined and discussed and allow us to draw the following conclu-

sions concerning the opening history of the SCS, the sedimentary and paleoceanographic responses to the formation of this ocean basin, the mantle source and magmatic processes forming the ocean crust basement, and the geodynamic implications for the tectonics of the region.

Opening history of the South China Sea

Determining the timing of the onset and cessation of seafloor spreading in the SCS were the primary objectives of Expedition 349. At all three sites near the fossil spreading center, we recovered deep-sea claystone near the sediment/igneous basement interface, with interflow claystone between lava flows recovered at Site U1431, and evidence from downhole measurements for an unrecovered interflow sedimentary layer at Site U1433 (Figures F11, F19, F23). Microfossils within these claystone units provide preliminary age models for the sedimentation history, which in turn helps us to refine the oceanic crustal age models. Relatively unaltered basalt from the ocean crust near the relict spreading center was recovered and will be dated using $^{40}\text{Ar}/^{39}\text{Ar}$ methods.

The age at which seafloor spreading ceased in the East Subbasin is estimated at ~16.7–17.5 Ma based on microfossils in the interflow claystone (Figure F10), or even slightly younger because Site U1431 is ~15 km off the ridge axis. At Site U1433, ~50 km away from the relict spreading center in the Southwest Subbasin, we recorded a biostratigraphic depositional age range from ~18 to 21 Ma for sediment directly above the basement (Figure F18). Rare and poorly preserved Oligocene to earliest Miocene calcareous nannofossils were also observed in sediment attached to basalt pieces in the upper part of the basement at Site U1433, which could indicate a substantially older age for the basement; however, it is not clear if the nannofossil assemblages are reworked or in situ.

Located just 35 km north of Site U1433, Site U1434 is on the uplifted shoulder of the relict spreading center and is only ~15 km from the spreading axis in the Southwest Subbasin. Here, biostratigraphic age data indicate that the basal sedimentary sequence, lying just above the basaltic basement, is younger than 12 Ma. The uplifted shoulder forms a topographic high that may have contributed to a depositional hiatus or extremely low sedimentation rates between the emplacement of basalt and the earliest sedimentary deposits. We deduce that the cessation age of seafloor spreading in the Southwest Subbasin is somewhere between ~12 and ~21 Ma. Overall, there does not appear to be a large difference in the ages at which seafloor spreading finished between the two subbasins.

We note here that the recorded biostratigraphic age ranges are likely minimum estimates because evidence from paleomagnetic reversals in the basalt units point to prolonged eruption histories at these sites. Postcruise radiometric dating of basement basalt from these sites, plus calibration with magnetic anomalies and paleomagnetic measurements, will constrain the eruptive history of the igneous basement at these sites in the SCS.

Because of a technical error in cementing the final casing string in Hole U1432B, we were unable to reach the oceanic basement near the continent/ocean boundary at the deepest planned drill site. This prevented us from collecting basement samples to directly date the onset of seafloor spreading. However, we were able to drill into one of the most enigmatic structures in the area, a structural high standing along the continent/ocean boundary at Site U1435. Coring here recovered a sharp unconformity, with sediment above dated to ~33 Ma. The sediment above the unconformity records deep marine facies, with sediment below dominated by sandy lithologies of shallow-marine deltaic or coastal facies. The age of this deeper unit,

which is composed mainly of poorly sorted sandstone and thin dark gray silty mudstone that are both relatively rich in organic matter (~0.4–1.3 wt%), awaits further shore-based studies as it is nearly barren of calcareous and siliceous marine microfossils. Immediately above the unconformity, drilling recovered abundant recrystallized calcite and dolomite grains, which may have been formed by extremely slow sedimentation or diagenesis. Nevertheless, we interpret this sharp unconformity as the break-up unconformity caused by the initial opening of the SCS, which places the onset of seafloor spreading at ~33 Ma.

Sedimentary and paleoceanographic responses

Silt and carbonate turbidites

All sites contain deep-marine deposits that likely formed at water depths deeper than 3 km but show significant spatial variations in postspreading sedimentary environment and provenance. Site U1431, in the East Subbasin, records the strongest evidence of hemipelagic, deep-marine gravity flow deposition of material eroded from various (distal) terrestrial sources. Both silt and nannofossil-rich/calcareous turbidites are present, with the former being much more dominant. Silt turbidites are speculated to have been triggered by volcanism and/or earthquake events associated with the Manila subduction zone and/or the Taiwan Orogeny, with sources located to the east and northeast, whereas calcareous turbidites at this site were likely transported from local sources, possibly nearby seamounts topped by carbonate platforms (Figure F8).

In contrast, Site U1433 in the Southwest Subbasin has nannofossil-rich calcareous turbidites that are more frequent in the cores, with some beds more than several meters thick. These turbidites date to the late Miocene. Here, the relict spreading center, with well-developed uplifted shoulders and a relatively deep axial trough, likely acted as an effective barrier, preventing terrestrial material from being transported to this site from northerly landmasses such as southern China, the Philippines, or Taiwan. Other possible sources in Borneo or mainland Southeast Asia are more likely. The source of the carbonate turbidites is most likely within the southerly Dangerous Grounds or the Reed Bank area (Figure F8). Local sources, such as isolated seamounts or abyssal highs, are less likely because they are quite far away from the site or in relatively deep water. Variations in carbonate flux to Site U1433 may reflect subsidence and drowning of the carbonate reefs in the Dangerous Grounds and/or sea level changes.

Variation in the character of the uppermost Pleistocene sediment between Sites U1431 and U1432 also support contrasting provenances in different parts of the basin at that time. The uppermost unit from Site U1431 is dominated by turbidite silt and sand and has frequent ash layers (Figure F9), whereas the uppermost unit from Site U1432 is mostly clay and shows fewer ash layers over a similar age interval (Figure F15). At Site U1433, eight geomagnetic excursions have been identified within the Brunhes Chron due to an extremely high sedimentation rate. Based on our current knowledge, two of the excursions have not been reported in previous studies, and postcruise studies will help determine their origin. A sudden increase in sedimentation rates from 5–9 to ~20 cm/ky is recorded at ~1 Ma at Site U1433 (Figure F18) and may reflect some coupling effects of enhanced terrestrial supply and intensified sea level fluctuations associated with the mid-Pleistocene climate transition.

Variations in calcite compensation depth

Variations in the calcite compensation depth (CCD) may have had an effect on the massive deepwater carbonate sediments recovered during the expedition, but the mechanisms are not clear. Sediment at Sites U1431 and U1433 was apparently deposited at depths greater than the modern CCD or, alternatively, may have been strongly diluted by variable clastic flux from the continents. However, at Site U1434, sediment shows much less influence from turbidity currents and is rich in calcareous nannofossils. Here, sediment was deposited at slightly shallower water depths on top of a rifted basement high (Figure F7). The mid-ocean ridge itself was also likely shallower prior to the postspreading subsidence caused by thermal and isostatic processes, as well as the loading from emplacement of a younger seamount on top of the spreading center. Sediment recovered at Site U1434 must have been deposited above the CCD and its compositional changes may reflect CCD variations after tectonic subsidence corrections.

Pelagic brownish to reddish or yellowish brown claystone

At Sites U1431, U1433, and U1434, we recovered a series of reddish brown to yellowish brown claystone and claystone with silt directly above the basement basalt units. At Site U1431 in the East Subbasin, this lower middle Miocene (~12–14 Ma) unit is only ~5 m thick and is massive and homogeneous in the lower part and laminated with silty claystone in the upper part (Figures F9, F11). Another similarly colored lower Miocene (~16–18 Ma) claystone ~10 m thick is interbedded within the basalt lava sequence but is less homogeneous, showing evidence for local mass wasting, and is characterized mostly by claystone with minor intraformational breccia or conglomerate containing rare basalt clasts that have well-developed reaction rims.

At Site U1433 (Figures F17, F19) in the Southwest Subbasin, the yellowish brown claystone and claystone with silt is ~49 m thick and is dated to the middle to late Miocene (~10–18 Ma). Although mostly massive, there are intervals of graded and bioturbated clayey siltstone and silty claystone. At both Sites U1431 and U1433, only siliceous microfossils (radiolarians) are found in this unit, most likely because calcareous microfossils have been dissolved because of deposition below the CCD. At Site U1434 (Figures F21, F23), ~24 m of yellowish or reddish brown claystone with variable amounts of nannofossils and foraminifers lies immediately above the basaltic basement. This sequence is dated as latest middle to late Miocene in age (~10–12 Ma) and is massive and structureless, with very little evidence for current influence during sedimentation. In contrast to the other sites, this unit at Site U1434 is characterized by a lack of radiolarians, with abundant foraminifers clearly visible on the core surface.

The reddish brown to yellowish brown claystone units at Sites U1431, U1433, and U1434 were deposited at somewhat different time intervals and water depths but all immediately overlie the basaltic basement. The estimated sedimentation rates are quite low, varying from <0.5 cm/ky at Site U1433 (Figure F18) to <2.0 cm/ky at Site U1431 (Figure F10) and ~1.6 cm/ky at Site U1434 (Figure F22). We interpret the claystone to be largely a product of deep-sea pelagic and hemipelagic sedimentation at very low sedimentation rates. The yellowish brown to dark brown color reflects enhanced oxidation of the clastic components of the sediment, which is a typical feature of regions of slow sedimentation and oxygenated bottom water, such as in many parts of the Pacific, where “red clays” are widespread (Bryant and Bennett, 1988).

Although lacking sedimentary evidence, there may have been some hydrothermal influence on the deposition or later alteration

after sedimentation as a result of fluid flow and geochemical exchange. Logging in this unit at Site U1433 showed distinctly high NGR logs of potassium, uranium, and thorium over these intervals (Figure F17). NGR values decrease slightly, whereas PEF increases with depth toward the claystone/basalt boundary and reaches peaks within the top of the basalt unit. This could reflect an increasing abundance of hematite and other oxides in the claystone. The increased concentration of such oxides could result from hydrothermal processes and fluid flow, as well as chemical exchange between the basalt and overlying sediment.

Mantle and crustal processes

Seamount volcanism and terminal processes of the extinct spreading center

Sites U1431 and U1434 are located very close to seamounts developed along and on top of the relict spreading center (Figure F8). Well-recovered volcanoclastic sandstone and breccia may therefore reveal the history of seamount volcanism following the end of seafloor spreading in the SCS. At Site U1431, we recovered ~280 m of dominantly greenish black volcanoclastic breccia and sandstone, interbedded with minor amounts of claystone (Figure F9) dated to the late middle Miocene to early late Miocene (~8–13 Ma). This would indicate an approximately 5 million year period of extensive seamount volcanic activity that started nearly 4 million years after the cessation of seafloor spreading. Volcanoclastic breccia layers comprise much of the section, are generally thicker bedded in the upper parts of this unit, and have normal grading and erosive bases, indicative of deposition by mass wasting either as debris or grain flows.

At Site U1434, volcanoclastic sandstone and minor breccia encountered at the top of the cored interval of the hole show coarse grain sizes and poor sorting (Figure F21) and are indicative of a relatively local provenance, most likely the adjacent seamount ~15 km to the north (Figure F8). The age of this unit is late Miocene (younger than 9 Ma). Its upper boundary was not cored, but the penetration rates during drilling of the interval above suggest well-lithified volcanoclastic breccia and sandstone at shallower depths (<200 mbsf). Volcanoclastic material is absent from the sediment deposited between ~12 and 9 Ma in the yellowish brown claystone unit directly overlying the basement basalt. This indicates that this seamount volcanism was not active until ~9 Ma but then was active for at least 2 million years based on the cored section. This also puts a time period of ~7 million years between the cessation of seafloor spreading and the initiation of seamount activities in the Southwest Subbasin. This is comparable to late Miocene and Pliocene seamount volcanism found in the extreme southwest of the oceanic basin (Li et al., 2013b). Further postcruise sedimentological and geochemical studies will refine the ages and nature of these seamount activities and reveal how magma sources at the dying spreading center evolved through time.

Mantle evolution and magma processes revealed by oceanic basalt

We successfully cored into oceanic basement in the SCS for the first time and recovered basalt at Sites U1431, U1433, and U1434 (Figures F11, F19, F23). This allows for the study of the mantle evolution and magmatic processes in this young ocean basin. Despite their apparent differences in groundmass grain sizes, all basalts have variable phase assemblages of plagioclase, olivine, and clinopyroxene, typical of MORB. This interpretation is also supported by geochemical evidence (Figures F12, F13). Coring at Site U1431 recovered massive basalt lava flows with limited evidence for pillow basalt fragments on top of the section (Figure F11). Most basalt is

aphyric and ranges in grain size from microcrystalline to fine grained, with some medium- to coarse-grained intervals occurring in the interiors of the thickest massive lava flows. These basalts were altered in a low-temperature and oxidative environment, with long intervals only slightly affected, providing ample material for postcruise radiometric age dating.

The Site U1433 basement section shows more abundant, small pillow basalt lava flows at the top and a few massive basalt lava flows toward the bottom of the hole (Figure F19). This basalt ranges from sparsely to highly plagioclase-phyric. Alteration of the basalt at this site is low in intensity, and typical secondary minerals represent a low-temperature and both oxidative and nonoxidative alteration assemblage. The contrast in alteration style is interpreted to indicate less active fluid activities at Site U1433 compared to the other sites, possibly caused by the cover of clayey sediment with low permeability.

The basement unit at Site U1434 is composed of a succession of small pillow lava flows, or a thicker autobrecciated pillow lava flow, with three occurrences of hyaloclastite breccia (Figure F23). The basalt flows are mostly olivine- and plagioclase-phyric with a glassy to microcrystalline groundmass. The phenocrysts observed are olivine and plagioclase. The secondary mineral assemblage indicates slight to moderate alteration under low temperature, limited fluid flow, and oxidative conditions.

A total of 34 basement basalt samples were analyzed for concentrations of major and trace elements from the three sites. Almost all samples are tholeiitic basalt (Figure F12) with extremely low K_2O (<0.3 wt%), in contrast to the much higher K_2O contents (>1.0 wt%) in the alkali basalt clasts in the younger volcanoclastic breccia. Overall, all concentrations of major elements in the basalt overlap with but define a much smaller range than those known from compilations of Indian Ocean and Pacific Ocean MORB data, and are distinct from the OIB data fields from nearby Hainan Island and other seamounts in the SCS (Figures F12, F13). Further postcruise geochemical studies will trace the mantle source and magmatic processes involved during and after opening of the SCS in detail.

Geophysical constraints and geodynamic implications

During the expedition, a suite of physical property measurements and color spectra scanning was completed on whole-round cores, split cores, and discrete samples. Downhole logging at the two deepest sites provided in situ constraints on the sediment and rock, which is particularly important over unrecovered intervals. These data will aid in future geophysical interpretations of geophysical data from the SCS.

Compaction and consolidation are controlling factors for physical property variations in the sediment, as measured porosity often has good inverse correlation with other measurements, such as bulk density, P -wave velocity, shear strength, NGR, and thermal conductivity. Increased compaction and lithification also lead to sharp velocity contrasts and differentiate velocities of different lithologies that would otherwise be similar. These observations explain the strong seismic reflectivity of strata in the bottom unit of the sedimentary cover at Site U1433, where lithified carbonate shows a much higher velocity than interbedded claystone (Figure F17).

NGR downhole logging in the igneous basement at Site U1433 helped define two interflow sedimentary layers between lava units through identification of high peaks in NGR (Figure F17). This was

particularly useful because coring did not fully recover these layers. Cores show only traces of sediment attached to basalt pieces. Gamma ray logging also helped constrain the alternating nature of carbonate with low NGR values and clay layers with high NGR values and is therefore valuable in delineating turbidites.

Magnetic susceptibility was measured on both whole-round cores and the split archive halves. In addition, remanent magnetization, which is proportional to the magnetic susceptibility, was measured with the pass-through magnetometer on all archive halves and on representative discrete samples from the working halves. We found that magnetic susceptibility of the basalt varies from $\sim 10 \times 10^{-5}$ to 2000×10^{-5} SI (Figures F9, F17, F21). The values are much higher in relatively unaltered intervals within the more massive basalt flows compared to small lava flow units that are typically more prone to alteration. For now it remains uncertain how the entire basaltic layer of the oceanic crust behaves with respect to magnetic susceptibility, since we only recovered its very top. Overall, we did not observe major differences in the measured magnetic susceptibilities between the East and Southwest Subbasins, whereas differences in magnetic susceptibilities have been previously predicted or suspected by the contrast in surface magnetic anomalies (Li et al., 2008b). Therefore, evidence of other mechanisms such as spreading rate, thermal disturbance, compositional variation, and posteruption alteration are needed to further explain the observed surface magnetic contrast.

Interplay between microbiology, fluid flow, geochemistry, and tectonics

A suite of samples collected at all of the Expedition 349 sites for microbiological analysis will allow examination of how microbial community features are linked to large-scale geological processes characteristic of the SCS that are representative of subseafloor settings worldwide. Samples were collected to examine the importance of ammonia-oxidizing archaea in the sediment in which archaeal biomarkers are preserved, what these archaea indicate about paleoceanographic conditions, and whether *Bdellovibrio* and similar organisms (bacterial predators) exist in the seafloor under contrasting fluid flow and heat flow conditions. These microbiological samples were collected proximal to samples for interstitial water chemistry analysis to help us reconstruct the environmental conditions where these cells are present.

We collected samples allowing us to test the hypothesis that the habitats at key interfaces, such as where volcanic ash or turbidites overlie fine-grained sediment, provide optimum conditions for microbial colonization and survival. In addition to helping to explain the explicit conditions under which microbial life in the deep subseafloor may thrive, these sites provide several different environments that link to large-scale processes such as volcanism, tectonism, and turbidity flows. There is the potential to assess how regional- and continental-scale events related to erosion, seafloor spreading, and subduction zones can dictate life at the smallest scale.

Samples from most sites drilled during Expedition 349 show low levels of hydrocarbon gases; however, at Sites U1432 and U1433, sediment samples showed evidence of moderately high concentrations of methane. Ethane and propane concentrations increased with depth at these sites. Evidence of higher hydrocarbon contents in this deep-sea sediment is worth additional study, and their presence suggests factors that should be considered regarding the bio-

geochemistry of these deep seafloor systems and how they respond to regional tectonics and depositional settings.

Preliminary scientific assessment

Expedition 349 achieved the vast majority of its scientific objectives as outlined in the *Scientific Prospectus* (Li et al., 2013). The expedition also obtained several unexpected findings that bear significant science implications. We set out with five broadly defined objectives, each of which has been addressed as follows at the five sites drilled, cored, and logged during this expedition:

1. Date the timing of the opening of different subbasins of the SCS and correlate the ages from magnetic anomalies to biostratigraphic, magnetostratigraphic, and radiometric ages.

- a. All five drill sites were designed to address this objective, although only at Sites U1431, U1433, and U1434 were we able to penetrate into igneous basement. Site U1432 was designed to determine the onset age of seafloor spreading in the East Subbasin through coring the lower half of sediment layers and the uppermost 100 m of igneous basement. Hole U1432B was drilled to 800 mbsf with casing successfully installed to address this objective; however, a technical error during the final cementing operation forced us to abandon Hole U1432B. This prevented us from coring and directly dating the oldest sediment and oceanic crust; however, based on biostratigraphy we have dated the breakup unconformity penetrated at Site U1435, which provides key constraints on the timing of initial seafloor spreading on the northern SCS continental margin
- b. To determine the age of termination of seafloor spreading in the East Subbasin, we drilled Site U1431 and successfully obtained continuous sediment records and relatively fresh basaltic samples in the basement. Preliminary results for the sediment ages were obtained during the expedition through biostratigraphic and paleomagnetic analyses. Radiometric dating of basalt samples will be conducted during shore-based investigation.
- c. At Sites U1433 and U1434 we successfully obtained sediment and basalt cores that will allow us to determine the termination age of seafloor spreading in the Southwest Subbasin and compare it to the Site U1431 termination age in the East Subbasin. Preliminary biostratigraphic and paleomagnetic dating was conducted during the expedition, whereas shore-based analysis will provide radiometric ages for the basalts.
- d. At Site U1435, which is on a structural high near the ocean/continent boundary at the northern edge of the East Subbasin, we successfully obtained cores of Oligocene sediment above and pre-Oligocene sandstone below an unconformity. The obtained samples will provide us an opportunity to investigate the transition from rifting to seafloor spreading in the SCS.

2. Measure the magnetization, mineralization, and geochemical compositions of basement rock to understand the causes of the sharp magnetic contrast between different subbasins.

- a. We successfully obtained igneous basement rock in the East Subbasin (Site U1431) and the Southwest Subbasin (Sites U1433 and U1434), allowing us to measure and fully charac-

terize the magnetization, mineralization, and geochemical compositions of basement rock.

- b. The results of shipboard physical property measurements and shore-based analyses of the rock samples, integrated with regional geophysical and geological studies, will advance our understanding of the causes and formation mechanism of the sharp magnetic contrast between the two subbasins and their formation mechanism.

3. Evaluate the origin and source evolution of SCS basement rocks to better understand the formation of SCS oceanic crust and the deep mantle processes driving this formation.

- a. We successfully obtained basalt samples near the relict seafloor spreading centers in the East Subbasin (Site U1431) and the Southwest Subbasin (Sites U1433 and U1434). Preliminary petrological and geochemical studies were made during the expedition, and shore-based geochemical and petrological studies have already been coordinated and will be carried out by multiple laboratories. These studies will help to characterize geochemical composition of the basement rocks to evaluate the origin and source evolution of the SCS oceanic crust and mantle.
- b. A surprising finding from the expedition is that we obtained abundant samples of volcanoclastic materials in sedimentary sections at sites near the relict spreading centers of the East and Southwest Subbasins. Shore-based analyses of these volcanoclastic rocks will allow us to date both their sedimentation age and eruption age of the igneous clasts, as well as to characterize their geochemical composition. Results will allow us to investigate the combined source evolution of the SCS spreading centers and the nearby seamounts, and how they interacted.

4. Evaluate the paleoceanographic and climatic responses to the opening of the SCS and develop a 3-D sedimentation and subsidence model.

- a. The sediment reveals abundant turbidite sequences at Sites U1431, U1432, and U1433, suggesting a history of turbulent sedimentary deposition events at a scale that was previously unknown.
- b. Thick carbonate turbidites in the form of deepwater carbonates and chalks found in the Southwest Subbasin (Site U1433) are indicators of provenance, and changes in the supply of these sediments to the site has implications for the paleoceanographic, paleoclimatic, and tectonic evolution in that region.
- c. We obtained complete records through sedimentary seamount aprons, which contain valuable information on the history of seamount eruption and associated volcanoclastic deposits in both the East Subbasin (Site U1431) and the Southwest Subbasin (Sites U1433 and U1434).
- d. Reddish brown to yellowish brown deep-sea claystone sequences were encountered immediately above the basement at Sites U1431, U1433, and U1434. The scientific implications of these sediment layers are critical and will receive extensive shore-based investigation.
- e. Preliminary ages were obtained through biostratigraphic and paleomagnetic analyses during the expedition. The results revealed a surprisingly wide range of sedimentation rates within individual holes and between different sites. Shore-based investigation will further improve the sedimen-

tation models, identify potential hiatuses in the sedimentary records, and determine the provenance and tectonic implications of the sediment.

5. *Obtain downhole geophysical logs to reveal physical properties of the sediment and the top oceanic basement and to provide a record of unrecovered intervals.*

- a. We successfully conducted downhole geophysical logging in the East Subbasin (Hole U1431E) and the Southwest Subbasin (Hole U1433B). These were the first downhole geophysical data obtained in the deep basins of the SCS.
- b. In the Southwest Subbasin, downhole logging at Hole U1433B was accomplished using the triple combo and FMS-sonic tool strings. We successfully logged a significant proportion of the basement, revealing pillow basalt flow sequences. The downhole logging results provide a record of unrecovered intervals in both the sediment and basement cores, including two possible sedimentary layers up to 1.5 m thick in the pillow basalt sequence of Hole U1433B.
- c. In the East Subbasin, downhole logging at Hole U1431E was also accomplished using the triple combo and FMS-sonic tool strings. At this site, the downhole logging tools reached a significant depth in the sediment layers, also providing a record of unrecovered intervals in the sediment cores.

Operations

Port call

Expedition 349 began with the first line ashore in Hong Kong at China Merchants Wharf at 0848 h (UTC + 8 h) on 26 January 2014. The science party and technical staff boarded on the day of arrival. The majority of incoming cargo and off-going cargo was loaded and unloaded on 26 January. The following day, the Siem Offshore crew change was completed. All main port call activities, including preparation of the passage plan were completed. Public relation tours were given on all three days of the port call. After taking on 2200 metric tons of marine gas oil, the vessel was secured for sea with the final maintenance checks performed prior to departure.

On the morning of 29 January, two tugs and the harbor pilot arrived at our location. The last line was released from shore at 1238 h, beginning the 463 nmi voyage to Site U1431. The pilot departed the vessel at 1326 h, and the vessel began the sea passage to the first site.

Site U1431

After a 463 nmi transit from Hong Kong averaging 11.0 kt, the vessel arrived at the first expedition site. A prespud meeting was held prior to arrival to review operations at the first site. The vessel stabilized and switched from cruise mode to dynamic positioning over Site U1431 at 0640 h on 31 January 2014. The positioning beacon was then deployed at 0712 h.

Hole U1431A

The bottom-hole assembly (BHA) was picked up and assembled and then run in the hole with drill pipe to 4165.25 meters below rig floor (mbrf). All drill pipe was measured (strapped) and the internal diameter verified (drifted) during the pipe trip. There were no operational problems running the drill string into the hole. The top drive was picked up, the drill string circulated out, and a pig was pumped to remove any debris that might have accumulated in the string. The calculated precision depth recorder (PDR) depth for the site was

4252.1 mbrf, and after some consideration 4248 mbrf was selected as the shoot depth for the first core. The bit was spaced out to 4248 mbrf and the APC barrel was run in the hole with wireline and landed. Hole U1431A was spudded at 0040 h on 1 February. The mudline core recovered 9.45 m of sediment and the seafloor was calculated to be 4248.1 mbrf (4237.3 meters below sea level [mbsl]). Nonmagnetic core barrels were used for APC coring from Core 349-U1431A-1H through 3H. Hole U1431A was terminated by plan at a final depth of 4276.5 mbrf (28.4 mbsf). At the conclusion of coring, the drill string was pulled from the hole. The seafloor was cleared at 0345 h on 1 February, ending Hole U1431A. Three piston cores were taken over a 28.4 m interval, with a total recovery of 28.39 m of core. Overall core recovery for Hole U1431A was 100.0%. The total time spent on Hole U1431A was 21.0 h.

Hole U1431B

After the bit cleared the seafloor, the vessel was offset 20 m east of Hole U1431A. As part of the planned microbiological analyses, the PFT pump was turned on and the drill string displaced with contamination testing fluid. The pump remained on for the remainder of coring operations in Hole U1431B. The bit was spaced out to 4245.5 mbrf in an attempt to recover ~7.0 m on the mudline core. The mudline core recovery was 7.5 m. The seafloor depth was calculated to be 4247.5 mbrf (4236.7 mbsl). Hole U1431B was spudded at 0420 h on 1 February. Nonmagnetic core barrels were used for APC coring from Core 349-U1431B-1H through 2H to a final depth of 17.0 mbsf. At the conclusion of coring, the drill string was pulled from the hole. The bit cleared the seafloor at 0620 h, ending Hole U1431B. Two piston cores were taken over a 17.0 m interval in Hole U1431B, with a total recovery of 17.16 m of core (100.9%). The total time spent on Hole U1431B was 2.58 h.

Hole U1431C

After the bit cleared the seafloor, the vessel was offset 20 m south of Hole U1431B. The bit was spaced out to 4245.5 mbrf. The mudline core recovery was 4.7 m, but the core liner was split. The seafloor depth was calculated to be 4250.3 mbrf (4239.5 mbsl). Hole U1431C was spudded at 0700 h on 1 February. Nonmagnetic core barrels were used for APC coring from Core 349-U1431C-1H through 2H to a final depth of 14.2 mbsf. The PFT pump remained running during coring in Hole U1431C. Hole U1431C was terminated when we determined that the mudline core would not meet sampling requirements. At the conclusion of coring, the drill string was pulled from the hole. The bit cleared the seafloor at 0852 h on 1 February, ending Hole U1431C. A total of two piston cores were taken over a 14.2 m interval in Hole U1431C, with a total recovery of 14.45 m of core (101.8%). The total time spent on Hole U1431C was 2.42 h.

Hole U1431D

After the bit cleared the seafloor, the vessel was offset 20 m west of Hole U1431C. The bit was spaced out to 4245.0 mbrf. The mudline core recovery was 3.22 m. The seafloor depth was calculated to be 4251.3 mbrf (4240.5 mbsl). Hole U1431D was spudded at 0925 h on 1 February. Nonmagnetic core barrels were used for APC coring from Core 349-U1431D-1H through 19H to a depth of 168.9 mbsf. Temperature measurements were taken with the APCT-3 on Cores 4H, 7H, 10H, and 13H with good results. After six partial strokes of the APC, the coring system was switched over to the XCB. XCB coring continued from Core 20X through 67X at a final depth of 4868.3 mbrf (617.0 mbsf). The PFT pump remained on through Core 23X. While cutting Core 67X, the rate of penetration dropped

severely and the core barrel was retrieved after a 2.7 m advance. While recovering the core barrel at the surface, we discovered that the cutting shoe, core catcher sub assembly, and the breakoff sub were missing from the XCB coring assembly. With ~1 m of junk metal remaining in the hole, we decided to pull out of the hole, offset, and begin a new hole with the RCB coring system. The top drive was then set back and the bit tripped from the hole, clearing the seafloor at 0355 h on 6 February. The bit was then tripped to the surface and cleared the rig floor at 1415 h, ending Hole U1431D. A total of 19 APC cores were taken over a 168.9 m interval in Hole U1431D, with a total recovery of 165.61 m of core. The XCB was used 48 times over an interval of 448.1 m, recovering 236.50 m of core. Overall core recovery for Hole U1431D was 402.11 m over an interval of 617.0 m (65.2%). The total time spent on Hole U1431D was 125.5 h.

Hole U1431E

After offsetting the vessel 20 m west of Hole U1431D, an RCB BHA was assembled with a new RCB C-4 bit. The BHA was run in the hole to 4163.22 mbrf, and the rig crew performed a slip and cut of 115 ft of drilling line. The remainder of the drill pipe was then run in the hole, and at 4221.46 mbrf, the top drive was picked up and then spaced out to spud Hole U1431E. A center bit was dropped and pumped to land out in the bit. Hole U1431E was spudded at 0650 h on 7 February. The seafloor depth for the hole was determined to be 4251.3 mbrf, calculated using an offset depth from Hole U1431D. Hole U1431E was advanced by drilling without coring from the seafloor to 507.0 mbsf. The center bit was pulled from the BHA by wireline and a core barrel was dropped to take a spot core (349-U1431E-2R) from 507.0 mbsf. After cutting the core without recovery, the center bit was dropped and drilling continued from 516.7 to 575.0 mbsf. The center bit was then retrieved by wireline, a core barrel dropped, and continuous coring started with Core 349-U1431E-4R from 575.0 mbsf. The next three cores (4R to 6R [575.0–603.3 mbsf]) did not recover any material. Coring continued with good recovery from Core 7R through 36R (603.3–894.3 mbsf). Core 36R was the first to recover basalt, with several small pieces present in the core catcher. Coring then continued into acoustic basement from Core 37R to 47R (894.3–991.4 mbsf). Penetration rates varied from 1.62 to 4.66 m/h over this interval, except for a sediment section in Core 45R that cored more quickly than the basalt. Microspheres were deployed in the RCB core catcher for Cores 12R through 43R.

With torque becoming higher and erratic, we decided to make a wiper trip to allow any debris collecting around the drill collars to fall into the hole. After pumping a sweep from the bottom of the hole, the drill string was pulled back to 862.95 mbsf. The bit was then run back to bottom, tagging fill material at 972.65 mbsf. With 18.75 m of fill in the bottom of the hole, a core barrel was dropped and the bit worked back to bottom with circulation and rotation without difficulty. The core barrel was retrieved with 0.65 m of material that was curated as ghost Core 48G. Another 50 bbl high-viscosity mud sweep was pumped after reaching 991.4 mbsf, and then another core barrel dropped. Coring continued from 991.4 mbsf to the final depth of 1008.8 mbsf (Cores 49R and 50R). Just prior to finishing coring, a 50 bbl high-viscosity mud sweep was pumped to clean and condition the hole for logging. The total depth of Hole U1431E was reached at 0740 h on 14 February. After reaching total depth, the final core was pulled to the surface and laid out. A total of 47 RCB cores were collected in Hole U1431E over a 443.5 m inter-

val, with a total recovery of 242.35 m of core (54.8% recovery, excluding the single 0.65 m long ghost core).

At the completion of coring, the rotary shifting tool (RST) was deployed to activate the mechanical bit release and the bit was dropped in the bottom of the hole. The RST was retrieved, and the other RST run in the hole to shift the sleeve back into the closed position. The end of the drill pipe was then raised to a depth of 4900.08 mbrf (648.78 mbsf) with the top drive in place. The hole was displaced from 648 mbsf to the seafloor with 11.4 lb/gal high-viscosity mud designed to improve logging conditions. The top drive was set back and the end of the pipe raised to 4400.9 mbrf (149.62 mbsf) for logging operations. After holding a logging safety meeting for rig floor personnel, the triple combo tool string was rigged up and run in the hole, reaching 463.7 m WSF on 15 February. The hole was then logged up, a short repeat pass recorded, and the tool string was then pulled to surface and rigged down. After rigging down the triple combo tool string, the FMS-sonic tool string was rigged up and deployed to 444 m WSF. Two full passes were made with the tool string, and then the tool string was pulled to the surface and rigged down at 1915 h on 15 February. The drill string was then tripped out of the hole from 4900.9 mbrf (149.6 mbsf) and cleared the seafloor at 2010 h. While pulling out of the hole with the drill string, the starboard conveyor on the pipe racker had a hydraulic failure. The hydraulic block in the derrickman's control booth was repaired, but 1.5 h was recorded as operational downtime. The rest of the trip out of the hole was uneventful and the bit cleared the rig floor at 0555 h. The rig floor was secured for transit at 0600 h on 16 February, ending operations at Site U1431. Total time spent in Hole U1431E was 231.75 h.

Site U1432

The vessel arrived at Site U1432 at 2337 h on 16 February 2014 after a 181 nmi transit at an average speed of 10.3 kt. An acoustic positioning beacon was deployed at 2352 h. The primary objectives at this site required deep penetration, so the plan was to install a reentry cone and casing system, with the first step in this process to conduct a jet-in test to determine the length of 20 inch casing that should be attached to the reentry cone.

Hole U1432A

The BHA for the jet-in test was assembled with an 18½ inch tricone bit and run to just above the seafloor. The vessel was offset 20 m south of the original coordinates for Site U1432 when the acoustic beacon landed within 6 m of the coordinates. The subsea camera and frame (VIT) was deployed to observe the bit tag the seafloor (3840.0 mbrf). After picking up the top drive and spacing out the bit, Hole U1432A was spudded at 1525 h on 17 February. The BHA with the 18½ inch tricone bit was jetted into the seafloor 62.0 m over a 3 h period. The drill string was then pulled clear of the seafloor and the top drive set back. The remainder of the drill string was tripped out of the hole and the bit cleared the rotary table at 0205 h on 18 February, ending Hole U1432A. The total time spent in Hole U1432A was 26.5 h.

Hole U1432B

Based on the results from the jet-in test, a five-joint, 57.12 m long 20 inch casing string was selected. The 20 inch casing shoe joint was cut off to length and a Texas Pattern casing shoe welded on the end of the shoe joint. The remainder of the reentry cone and base were put together, moved into the moonpool, and positioned

underneath the rotary table. The casing was run through the rotary table and the reentry cone in the moonpool. Each casing connection was tack welded to prevent the casing from backing out. The third joint of casing had to be replaced because of a damaged thread on the pin. The casing hanger and casing pup joint were picked up and attached to the top of the casing string. The Dril-Quip CADA (casing) running tool was made up into the casing hanger on the rig floor. The casing was then lowered through the rig floor, into the moonpool, and through the reentry cone. The casing hanger was landed into the landing ring inside the reentry cone and snapped into place inside the cone. The landing joint was lowered to release the weight of the casing. The casing running tool was rotated 3.75 turns to the right and the casing released. A BHA (casing stinger) with an 18½ inch bit, bit sub, and six drill collars was lowered into the reentry cone and casing. The casing running tool was inserted into this BHA and latched into the casing hanger in the reentry cone and secured by rotating the upper BHA 3.75 turns to the left. The moonpool doors were opened and the reentry system with the 20 inch casing was lowered through the moonpool to 3819 mbrf. The top drive was picked up and spaced out to jet-in the 20 inch casing. Hole U1432B was spudded at 0635 h on 19 February. Jetting continued as the casing was slowly lowered. Seven hours later the reentry system landed on the seafloor. The subsea camera was lowered to assist in releasing the casing. After attempting to release the casing for 2.5 h, the casing tool finally released after the vessel was offset from the original position in order to get the casing running tool to rotate. The rotation required to release the tool was observed clearly on the new subsea camera system. The camera was then pulled back to the surface and secured. The drill sting was tripped back to the surface, and the BHA was set back in the derrick. During the trip out of the hole, the rig was secured to slip and cut 115 ft of drilling line as per the slip and cut program.

An HOC underreamer with an 11¼ inch closed diameter was made up to the 18½ inch tricone bit and bit sub. The underreamer was set to open up the 18½ inch hole to 22 inches in diameter. The underreamer and bit were lowered into the moonpool, the top drive picked up, and the underreamer function tested. The top drive was then set back, and the remainder of the BHA assembled and run in the hole to 3828.7 mbrf. During the trip, the subsea camera system was deployed. The bit was spaced out for reentry and the vessel was positioned using the subsea camera system. Hole U1432B was reentered at 2005 h on 20 February. After reentering the hole, the top drive was picked up and the drill string washed down to the casing shoe at 57.1 mbsf. After carefully washing down below the casing shoe so that the underreamer was below the base of the 20 inch casing, the pump rate and speed (rotations per minute [rpm]) were optimized for drilling a 22 inch hole below the 20 inch casing. Drilling continued to 4000.0 mbrf (160.0 mbsf). Drilling was suspended at 0610 h on 21 February when weather conditions worsened and the high heave of the vessel began to severely affect the weight on the bit and underreamer. The bit was tripped back inside the 20 inch casing and the top drive set back. The drill string was then tripped back to the surface, clearing the seafloor at 0835 h on 21 February, and finally clearing the rig floor at 1620 h. The underreamer and bit were inspected and laid out, and the BHA racked back into the derrick. While waiting on the weather to subside, the vessel offset 40 m south to be well away from the reentry cone for Hole U1432B. An APC hole (U1432C) was cored and, after coring to 110.0 mbsf, the weather appeared to have subsided sufficiently for another attempt at drilling out the 22 inch hole for the 16 inch casing.

Hole U1432C

After pulling out of Hole U1432B, the upper guide horn was picked up from the drill collar rack, lifted to the rig floor, and reinstalled below the rotary table. An APC/XCB BHA was made up while the vessel was offset 40 m south of Hole U1432B. The drill string was then tripped toward the seafloor. After completing the pipe trip to just above the seafloor, the top drive was picked up and spaced out, and Hole U1432C was spudded at 0555 h on 22 February. The first coring attempt with the bit at 3835 mbrf did not recover any core. The bit was then lowered to 3838.5 mbrf and the next coring attempt recovered a mudline core of 7.95 m of sediment. This core length was used to calculate the seafloor depth at 3840.1 mbrf (3829.1 mbsl). Nonmagnetic core barrels were used for the APC from Core 329-U1432C-1H through 12H to a final depth of 110.0 mbsf. PFT fluid was displaced into the drill string prior to spudding the hole and was pumped continuously during Hole U1432C. Temperature measurements were taken with the APCT-3 on Cores 5H, 7H, 9H, and 11H with good results. The hole was terminated when weather conditions improved sufficiently to return to Hole U1432B. The bit was tripped to the surface and cleared the rig floor at 0735 h, ending Hole U1432C. A total of 12 APC cores were taken over a 110.0 m interval in Hole U1432C, recovering 88.74 m of core (80.7% recovery). The total time spent in Hole U1432C was 39.25 h.

Return to Hole U132B

After tripping out of Hole U1432C, the BHA was set back in the derrick and the upper guide horn removed and laid out on the drill collar racks. We then returned to Hole U1432B to continue drilling the 22 inch hole for the 16 inch casing. As before, an HOC underreamer with an 11¼ inch closed diameter was made up to the 18½ inch tricone bit and bit sub. The underreamer was set to open up the 18½ inch hole to a 22 inch diameter. The underreamer and bit were lowered into the moonpool, the top drive picked up, and the underreamer function tested. The top drive was set back, and the remainder of the BHA assembled and run in the hole to 3828.7 mbrf. During the trip, the subsea camera system was deployed. The bit was spaced out for reentry and Hole U1432B reentered at 1944 h on 23 February. The subsea camera system was pulled back to surface while the top drive was picked up. The bit and underreamer were run in the hole to 160.0 mbsf and drilling continued from 4000 to 4090.0 mbrf (160.0–250.0 mbsf). The depth of Hole U1432B reached 250 mbsf at 0640 h on 24 February. The hole was conditioned and displaced with 379 bbl of 10.5 lb/gal mud. The drill string was tripped back to the surface and cleared the rig floor at 2120 h. During the trip out of the hole, the rig was secured to slip and cut 115 ft of drilling line as per the slip and cut program.

The drill floor was rigged up to run 16 inch casing. We assembled 240.85 m of 16 inch casing, including a Dril-Quip casing hanger. The casing was landed on the moonpool doors with the casing running tool, which was then released and pulled back through the rig floor. The 240.77 m casing stinger was made up to the bottom of the casing hanger running tool and lowered through the 16 inch casing in the moonpool. The casing hanger running tool with the casing stinger below was latched into the 16 inch casing hanger, with two control length drill collars and a tapered drill collar above the casing running tool. The entire casing string plus running tools were lowered to 3827.4 mbrf while filling the drill pipe with water every 20 stands. The subsea camera system was installed and lowered to reenter Hole U1432B. After 15 min of maneuvering the

vessel, we reentered Hole U1432B at 0500 h on 26 February. The camera system was pulled back to the surface while the top drive was picked up. The casing was lowered into the 22 inch hole and washed down to ~200 mbsf. The subsea camera system was again lowered to assist in releasing the casing running tool from the casing. As the camera system neared the seafloor, the video feed from the subsea camera was lost. The camera system was pulled back to the surface for repair (water had intruded the pan and tilt unit, causing a power overload in the system). The casing was washed in to 240.9 mbsf and landed in the reentry cone. The casing running tool was rotated clockwise 3.75 turns and released from the casing hanger. The BHA, including the internal casing stinger, was pulled back ~11 m and the top drive set back. The cementing assembly was rigged up, the lines were pressure tested, and ~20 bbl of cement mixed to 15 lb/gal was pumped downhole. The cement was displaced with seawater and positioned to balance at the casing shoe to an estimated height of 17 m above the casing shoe (both inside and outside the casing). The cementing equipment was rigged down and the drill string pulled back to 161.9 mbsf. The circulating head was connected and the drill string flushed with twice the drill string capacity with seawater. The remainder of the drill string was pulled from the hole, clearing the seafloor at 2140 h on 26 February and finally clearing the rig floor at 0400 h on 27 February. The BHA components were secured and the running tool was detorqued.

A new 14 $\frac{3}{4}$ inch bit and four stands of drill collars were made up and run in the hole with drill pipe while filling with water at 20-stand intervals. When the bit was at 3823.3 mbrf, the subsea camera system was lowered to allow reentry. Hole U1432B was reentered at 1655 h on 27 February and the camera pulled back to the surface. After securing the camera system, the drill string was run in the hole until the top of the cement was tagged at 4069.0 mbrf (229 mbsf). The cement was drilled out from 4069.0 to 4083.0 mbrf (229.0–243.0 mbsf). After washing down to total depth (250.0 mbsf), new 14 $\frac{3}{4}$ inch hole was drilled from 4090.0 to 4640.0 mbrf (250.0–800.0 mbsf). After reaching 800.0 mbsf, the hole was swept clean with high-viscosity mud. After setting back the top drive, the drill string was pulled back to the surface. The bit cleared the rotary table at 1120 h on 1 March. The 10 $\frac{3}{4}$ inch casing stinger components were made up and the underreamer arms were set to 12 $\frac{3}{4}$ inches. The top drive was then picked up and the mud motor and underreamer tested. After the test was successfully completed, they were racked back in the derrick. After assembling all the casing stinger components, a slip and cut of the drilling line was completed.

The rig floor was then prepared for running 10 $\frac{3}{4}$ inch casing, and 787.06 m of casing with a 10 $\frac{3}{4}$ inch casing hanger were made up. The casing was lowered into the moonpool and secured with a casing elevator on the prepared landing platform. The buoyant weight of the casing string was 70,000 lb. The running tool was released from the casing and pulled back to the rig floor. It was then made up to the bottom of a drill collar stand and racked back in the derrick. The casing stinger with the bit, underreamer, and mud motor were then run inside the casing. Also included in the stinger were three stands of drill collars and 24 stands of drill pipe. The bit and underreamer were positioned just below the bottom of the casing after the running tool was landed and made up to the casing. The casing was run to the seafloor with drill pipe and the subsea camera system deployed to assist with the reentry at the seafloor. Hole U1432B was reentered at 0242 h on 3 March. The camera system was pulled back to the surface and set back into the storage po-

sition on the moonpool doors. The casing was run in the hole with drill pipe to 223.5 mbsf. The top drive was picked up and the casing lowered to 244.0 mbsf. The casing was washed to the bottom while pumping 530 gal/min. At 530 gal/min, the mud motor was turning the bit at 80–85 rpm with the underreamer arms extended to clear a 12 $\frac{3}{4}$ inch hole in front of the casing. The casing was steadily lowered until it was landed and released at 1745 h on 3 March. The top drive was set back and the drill string tripped from the hole, clearing the seafloor at 2045 h, and then clearing the rotary table at 0915 h on 4 March. The casing stinger components were flushed with freshwater and either laid out or, in the case of the drill collars, racked back in the derrick.

After successfully running the 10 $\frac{3}{4}$ inch casing, a cementing stinger was assembled. The stinger consisted of a reentry/cleanout bit, a bit sub, a stand of drill collars, 24 stands of 5 inch drill pipe, F-cup tester, another two drill collars, a tapered drill collar, and two stands of 5 $\frac{1}{2}$ inch transition drill pipe. The entire assembly was made up and run in the hole with drill pipe to just above the seafloor while stopping every 20 stands to fill the drill pipe with water. The subsea camera system was deployed to just above the seafloor and Hole U1432B reentered at 0344 h on 5 March. The camera system was pulled back to the surface and secured. The bit was run in the hole to 767 mbsf, 20 m above the 10 $\frac{3}{4}$ inch casing shoe. The F-cup tester was spaced out so that it was at 42 mbsf, inside the 16 inch casing. The circulating head was made up to the top of the drill string and the mud pumps were brought up to 60 strokes/min to verify circulation up the annulus between the hole and the casing. After establishing circulation, the cement pump was used to pump 10 bbl of freshwater ahead of the cement slurry. Fourteen barrels of 15.5 lb/gal cement were then mixed and pumped downhole, followed by another 10 bbl of freshwater. This was displaced down the drill string with 263 bbl of saltwater using the mud pumps. After displacing the cement, the circulating head was removed and the driller attempted to pull out of the hole. He immediately noticed a steadily increasing overpull as he tried to pull out of the hole. After pulling up enough to remove two singles of drill pipe, we were unable to raise the drill string any further. It now appears that the formation collapsed around the 10 $\frac{3}{4}$ inch casing string, preventing circulation up the open hole annulus and outside the casing. Instead, the circulation path was up through the 10 $\frac{3}{4}$ inch casing, bypassing the cup tester. The elevated temperatures at 700 mbsf (~65°–70°C) accelerated the hardening of the cement. The drill string was worked for the next 9 h using combinations of overpull, torque, and pump pressure in an effort to free the drill string. At that point, we rigged up to sever the drill string. The drill string severing charge was lowered to just above the cup tester, which has a 1.5 inch internal diameter. The charge was detonated at 0430 h on 6 March 2014; however, there was no loss of overpull on the pipe. The wireline was pulled out of the hole and the severing tool cleared the rig floor at 0808 h. The drill pipe was worked with a maximum of 100,000 lb of overpull for ~1 h. The elevators were then lowered back to the elevator stool while the vessel was offset 200 m. The top drive was picked up and the drill pipe was picked up slowly while moving the vessel back to the original location. The pipe was worked free with a maximum of 400 A of torque and 40,000 lb of overpull. The end of pipe cleared the casing hanger at 1105 h. The top drive was set back and the drill string pulled from the hole. The end of pipe cleared the rotary table at 1830 h. The acoustic positioning beacon was recovered while tripping drill pipe. The upper guide horn was reinstalled, the rig floor secured for transit, and the

thrusters raised. The vessel switched to transit mode at 2036 h on 6 March, ending Site U1432. The total time spent on Hole U1432B was 363.25 h (15.1 days).

Site U1433

Hole U1433A

After a 334 nmi transit lasting 29.9 h, the vessel arrived at Site U1433 and switched into dynamic positioning mode at 0230 h on 8 March 2014. At 0255 h, an acoustic positioning beacon was deployed. An APC/XCB BHA was assembled and run in the hole to 800.4 mbrf. At 0520 h, a tool joint parted on the twenty-fourth stand of drill pipe, just after picking up the drill string and just prior to unlatching the lower set of elevators. The load cell weight at the time of the incident was recorded at ~200,000 lb. The entire weight of the drill string dropped ~18 inches and landed in the lower set of elevators, which were resting on top of the dual elevator stool. The pin on the top single of drill pipe had parted, leaving one single hanging from the upper set of elevators and two singles sticking up from on top of the lower set of elevators. The stand was then laid out to the V-door. The broken pipe was visually inspected and photographed. As a precaution, the twenty-third stand was also disassembled and laid out. The bottom set of elevators was removed from use and replaced with a reconditioned set of elevators. After clearing the rig floor, the trip in the hole resumed. When the bit was at 1147.8 mbrf, another tool joint failed when the driller was picking up the thirty-sixth stand from the pipe racker. This time, one single fell back into the trough of the pipe racker still attached to the skate, and a double remained connected to the elevators on the bales connected to the main block. After the second tool joint failure, we decided to discontinue using any of the 5 inch drill pipe that had been used in the stuck pipe incident at the previous site. Investigations continue into the root cause of the pipe failure. Documentation of the stuck pipe event was collected for analysis. The failed tool joints were prepared with care for shipment to a laboratory for detailed metallurgical analysis and were shipped from Keelung, Taiwan, at the end of the expedition. The drill string was tripped back to the BHA and all suspect drill pipe was removed from use and stored in the port pipe racker. We picked up 201 joints of new 5 inch drill pipe from the riser hold. The new drill pipe was strapped and drifted as it was assembled and lowered toward the seafloor. After completing assembly of the new pipe, the remaining 37 stands from the starboard 5 inch pipe racker were picked up and run in the hole. The total number of 5 inch pipe stands available was then 104 stands. The remaining 101 stands of suspect drill pipe in the port pipe racker need to be inspected before they can be put back in service.

After running in the hole with 104 stands of 5 inch drill pipe, the 5½ inch drill pipe was picked up until the bit reached 4372.9 mbrf. The trip in the hole was stopped at 3587.0 mbrf to perform a slip and cut of the drilling line. The PDR recorded an estimated depth of 4394.4 mbrf for the seafloor. The top drive was picked up and spaced out to 4390 mbrf. The nonmagnetic core barrels were dressed with liners, the FlexIT core orientation tool was inserted, and a core barrel run down and landed. Hole U1433A was spudded at 1000 h on 9 March. The mudline core recovered 8.9 m of sediment and the seafloor was calculated to be 4390.6 mbrf (4379.4 mbsl). Coring continued without issue through Core 349-U1433A-16H (151.4 mbsf). While running in the hole with a core barrel, the bridge informed the driller that a fishing boat was drifting toward the vessel's location. At 0540 h on 10 March, the Captain ordered the driller to suspend operations. The core barrel was retrieved, and the driller began tripping out of the hole with the top

drive. At 99.1 mbsf, the driller was instructed to standby. After the threat disappeared, the drill string was tripped back to bottom and coring continued to Core 20H (188.3 mbsf). After four consecutive partial strokes of the APC, refusal was called at 188.3 mbsf. Orientation was measured on all APC cores. Temperature measurements were taken with the APCT-3 on Cores 4H, 7H, 10H, and 13H with good results. PFT fluid was used on Cores 18H through 20H. The bit was tripped to the surface and cleared the rig floor at 0325 h on 11 March, ending Hole U1433A. A total of 20 APC cores were taken over a 188.3 m interval in Hole U1433A, recovering 168.79 m of core (89.6%). The total time spent on Hole U1433A was 73.0 h.

Hole U1433B

After offsetting the vessel 20 m east of Hole U1433A, an RCB BHA was assembled with a new RCB C-4 bit. Three additional drill collars had to be picked up from the drill collar racks to replace the ones lost in Hole U1432A. The core barrels were spaced out at the surface and the 172.07 m BHA assembled and run in the hole to 4350.3 mbrf. The top drive was then picked up and spaced out to spud Hole U1433B. A center bit was dropped and pumped to land out in the bit. Hole U1433B was spudded at 1515 h on 11 March. The seafloor depth for the hole was 4390.6 mbrf (4379.4 mbsl), determined by using an offset depth from Hole U1433A. Hole U1433B was advanced by drilling without coring from the seafloor to 186.1 mbsf. The center bit was pulled from the BHA by wireline and a core barrel dropped to start continuous RCB coring from Core 349-U1433B-2R through 75R to a total depth of 5249.1 mbrf (858.5 mbsf). The PFT pumps were turned on during the drilldown period, and PFT fluid was pumped through Core 26R (426.9 mbsf). Microspheres were added to the RCB core catcher sub for Cores 56R to 75R. Core 65R encountered basalt at 786.3 mbsf. Coring continued into acoustic basement from Core 65R to Core 75R (858.5 mbsf), with half-cores collected from Core 67R to the total depth in an attempt to improve recovery. Penetration rates varied from 0.9 to 3.9 m/h over the basement interval. The total depth of Hole U1433B was reached at 2100 h on 17 March and the final core was pulled to the surface and laid out. At the completion of coring Hole U1433B, 74 RCB cores had been cut over a 672.4 m interval, recovering 443.04 m of core (65.9%).

After pumping a 50 bbl high-viscosity mud sweep, a short wiper trip was made from total depth to just above the basement contact (786.3 mbsf) with the top drive installed. While tripping back to bottom, the hole had to be reamed from 847.4 to 858.5 mbsf. We then pumped another 50 bbl mud sweep to further clean the hole. The RST was then picked up and run into the hole with a coring line to release the bit for logging. An attempt was made to engage the sleeve in the mechanical bit release. After being unable to engage the shifting sleeve, the RST was pulled back to surface. Examination at the surface revealed the RST did not come back with the core line sinker bars. An overshot (fishing tool) was made up and run in the hole to fish for the RST. After securing the RST, the mechanical bit release sleeve was engaged and the bit was dropped from the drill string. The RST also dropped off the fishing tool on release, leaving the RST in the bottom of the hole. The core line was pulled back to surface, and the RST to shift the sleeve back into the original position was deployed. With the bit released, the drill string was raised to 5196.3 mbrf (805.7 mbsf) with the top drive. The top drive was then set back and the drill string raised to 5079.7 mbrf (689.1 mbsf). The circulating head was picked up and the hole displaced from 689.1 mbsf to the seafloor with 10.5 lb/gal high-viscosity mud designed to improve logging conditions. The drill string was then

raised up and spaced out so that the end of the pipe was at 4490.7 mbrf (100.1 mbsf) for logging operations.

After holding a logging safety meeting for rig floor personnel, the triple combo tool string was rigged up and deployed. The tool string reached a total depth of 845.4 m WSF on 18 March. The hole was then logged up and the tool string pulled to surface and rigged down. After rigging down the triple combo tool string, the FMS-sonic tool string was rigged up and deployed to a depth of 842.4 m WSF. The basement section of the hole was logged five times with three passes with the calipers open. On the last pass, the tool became stuck but was eventually worked free. The rest of the open hole was logged up to the end of the drill pipe and the tool string was then pulled to the surface and rigged down. All logging equipment was rigged down by 1300 h on 19 March. The drill string was pulled from the hole and the BHA set back and secured for transit at 2300 h on 19 March, ending Site U1433. Total time spent in Hole U1433B was 211.5 h.

Site U1434

After an 18 nmi transit lasting 2 h, the vessel arrived at Site U1434 and switched into dynamic positioning mode at 0048 h on 20 March 2014. At 0110 h, an acoustic positioning beacon was deployed. An RCB BHA was assembled with a new RCB C-7 bit. The core barrels were spaced out at the surface and the 172.07 m BHA assembled. The BHA was lowered to 4000.9 mbrf and the top drive picked up and spaced out to 4020.0 mbrf to spud Hole U1434A. A center bit was dropped and pumped down the drill string to land out in the bit. Hole U1434A was spudded at 1215 h on 20 March. The estimated depth of the seafloor was determined to be 4020.4 mbrf using the PDR. The final seafloor depth for the hole was 4020.4 mbrf (4009.0 mbsl), which was determined by tagging the seafloor with the drill bit. Hole U1434A was advanced by drilling without coring from the seafloor to 4217.4 mbrf (197.0 mbsf) over a 10 h period. The center bit was pulled and a core barrel dropped to start continuous RCB coring from Core 349-U1434A-2R. Coring continued through Core 15R to a depth of 4332.9 mbrf (312.5 mbsf). Microspheres were deployed in each RCB core catcher sub for the duration of RCB coring. We encountered the sediment/basement interface in Core 10R, with the formation change at ~280 mbsf. Coring continued into acoustic basement from Core 10R through 15R to a total depth of 4332.9 mbrf (312.5 mbsf). Half-cores were started with Core 12R and continued to total depth. Penetration rates varied from 1.57 to 5.76 m/h over the basement interval. Coring was finally halted because of poor core recovery coupled with high torque and poor coring conditions. The total depth of Hole U1434A was reached at 0925 h on 22 March. After reaching total depth, the final core was pulled to the surface and laid out. At the completion of coring Hole U1434A, 14 RCB cores had been cut over a 115.5 m interval, recovering 26.43 m of core (22.9%).

After retrieving the final core, we attempted to pull the drill string from the hole; however, the high torque and high overpull made this impossible. After 1.5 h of working the pipe with a combination of high torque (900 A), overpull, and constant pumping action, the drill string came free and was pulled out of the hole with the top drive to 4117.4 mbrf (97.0 mbsf). The top drive was then set back and the drill string was tripped to the surface. The bit cleared the seafloor at 1500 h and then cleared the rotary table at 2300 h.

After securing the rig floor for transit and pulling the hydrophones and thrusters, the vessel switched to cruise mode and began the transit to Site U1435 at 2348 h on 22 March. Total time spent on Hole U1434A was 71.0 h.

Site U1435

After a 336 nmi transit lasting 39.65 h, the vessel arrived at Site U1435 and switched into dynamic positioning mode at 1524 h on 24 March 2014. At 2045 h, an acoustic positioning beacon was deployed. An RCB BHA was assembled with a new RCB C-7 bit. The core barrels were spaced out at the surface and the 172.07 m BHA assembled. The BHA was then run in the hole to 3214.9 mbrf and the top drive picked up and spaced out to 3261.6 mbrf to spud Hole U1435A. While lowering the drill pipe, we conducted a sonar survey with the 3.5 kHz array sonar to select a hole location to maximize sediment thickness. Hole U1435A was spudded at 0035 h on 25 March. The estimated depth of the seafloor was 3261.6 mbrf using the PDR. The final seafloor depth for the hole was 3264.0 mbrf (3252.5 mbsl), which was determined by tagging the seafloor with the drill bit. We advanced Hole U1435A by coring from the seafloor to 3564.0 mbrf (300.0 mbsf). Microspheres were deployed in each RCB core catcher sub from Core 349-U1435A-5R to the total depth of the hole. Coring continued to Core 349-U1435A-32R (300 mbsf), when operational time for the expedition expired. Penetration rates varied from 2.8 to 58.2 m/h over the cored interval. The total depth of Hole U1435A was reached at 0730 h on 27 March. After reaching total depth, the final core was pulled to the surface and laid out. At the completion of coring Hole U1435A, 32 RCB cores had been cut over a 300.0 m interval, recovering 171.37 m of core (57.1%).

After reaching total depth and laying out the last core, the drill string was pulled out of the hole with the top drive to 3535.1 mbrf (271.1 mbsf). The drilling knobbies were laid out, the top drive set back, and the drill string tripped to the surface. The bit cleared the seafloor at 1020 h, and then cleared the rotary table at 1835 h. After securing the rig floor for transit and pulling the hydrophones and thrusters, the vessel switched to cruise mode and began the transit to Keelung, Taiwan, at 1900 h on 27 March. Total time spent on Hole U1435A was 75.5 h. Expedition 349 officially ended with the first line ashore in Keelung at 0710 h on 30 March.

References

- Barckhausen, U., Engels, M., Franke, D., Ladage, S., and Pubellier, M., 2014. Evolution of the South China Sea: revised ages for breakup and seafloor spreading. *Marine and Petroleum Geology*, 58(Part B):599–611. <http://dx.doi.org/10.1016/j.marpetgeo.2014.02.022>
- Barckhausen, U., and Roeser, H.A., 2004. Seafloor spreading anomalies in the South China Sea revisited. In Clift, P., Wang, P., Kuhnt, W., and Hayes, D. (Eds.), *Continent-Ocean Interactions within East Asian Marginal Seas*. Geophysical Monograph, 149:121–125. <http://dx.doi.org/10.1029/149GM07>
- Bleil, U., and Petersen, N., 1983. Variations in magnetization intensity and low-temperature titanomagnetite oxidation of ocean floor basalts. *Nature*, 301(5899):384–388. <http://dx.doi.org/10.1038/301384a0>
- Braitenberg, C., Wienecke, S., and Wang, Y., 2006. Basement structures from satellite-derived gravity field: South China Sea ridge. *Journal of Geophysical Research: Solid Earth*, 111(B5):B05407. <http://dx.doi.org/10.1029/2005JB003938>
- Briaux, A., Patriat, P., and Tapponnier, P., 1993. Updated interpretation of magnetic anomalies and seafloor spreading stages in the South China Sea:

- implications for the Tertiary tectonics of Southeast Asia. *Journal of Geophysical Research: Solid Earth*, 98(B4):6299–6328. <http://dx.doi.org/10.1029/92JB02280>
- Bryant, W.R., and Bennett, R.H., 1988. Origin, physical, and mineralogical nature of red clays: the Pacific Ocean Basin as a model. *Geo-Marine Letters*, 8(4):189–249. <http://dx.doi.org/10.1007/BF02281640>
- Castillo, P.R., Carlson, R.W., and Batiza, R., 1991. Origin of Nauru Basin igneous complex: Sr, Nd, and Pb isotope and REE constraints. *Earth and Planetary Science Letters*, 103(1–4):200–213. [http://dx.doi.org/10.1016/0012-821X\(91\)90161-A](http://dx.doi.org/10.1016/0012-821X(91)90161-A)
- Chung, S.-L., Sun, S., Tu, K., Chen, C.-H., and Lee, C., 1994. Late Cenozoic basaltic volcanism around the Taiwan Strait, SE China: product of lithosphere-asthenosphere interaction during continental extension. *Chemical Geology*, 112(1–2):1–20. [http://dx.doi.org/10.1016/0009-2541\(94\)90101-5](http://dx.doi.org/10.1016/0009-2541(94)90101-5)
- Clift, P., Lee, G.H., Duc, N.A., Barckhausen, U., Long, H.V., and Zhen, S., 2008. Seismic reflection evidence for a Dangerous Grounds miniplate: no extrusion origin for the South China Sea. *Tectonics*, 27(3):TC3008. <http://dx.doi.org/10.1029/2007TC002216>
- Clift, P.D., and Sun, Z., 2006. The sedimentary and tectonic evolution of the Yinggehai-Song Hong Basin and the southern Hainan margin, South China Sea: implications for Tibetan uplift and monsoon intensification. *Journal of Geophysical Research: Solid Earth*, 111(B6):B06405. <http://dx.doi.org/10.1029/2005JB004048>
- Cullen, A., Reemst, P., Henstra, G., Gozzard, S., and Ray, A., 2010. Rifting of the South China Sea: new perspectives. *Petroleum Geoscience*, 16(3):273–282. <http://dx.doi.org/10.1144/1354-079309-908>
- Cullen, A.B., 2010. Transverse segmentation of the Baram-Balabac Basin, NW Borneo: refining the model of Borneo's tectonic evolution. *Petroleum Geoscience*, 16(1):3–29. <http://dx.doi.org/10.1144/1354-079309-828>
- Dyment, J., and Arkani-Hamed, J., 1995. Spreading-rate-dependent magnetization of the oceanic lithosphere inferred from the anomalous skewness of marine magnetic anomalies. *Geophysical Journal International*, 121(3):789–804. <http://dx.doi.org/10.1111/j.1365-246X.1995.tb06439.x>
- Dyment, J., Arkani-Hamed, J., and Ghods, A., 1997. Contribution of serpentinized ultramafics to marine magnetic anomalies at slow and intermediate spreading centres: insights from the shape of the anomalies. *Geophysical Journal International*, 129(3):691–701. <http://dx.doi.org/10.1111/j.1365-246X.1997.tb04504.x>
- Fan, W., and Menzies, M., 1992. Destruction of aged lower lithosphere and accretion of asthenosphere mantle beneath eastern China. *Geotectonics and Metallogeny*, 16:171–180.
- Fedo, C.M., Sircombe, K.N., and Rainbird, R.H., 2003. Detrital zircon analysis of the sedimentary record. In Hanchar, J.M., and Hoskin, P.W.O. (Eds.), *Zircon. Reviews in Mineralogy and Geochemistry*, 53(1):277–303. <http://dx.doi.org/10.2113/0530277>
- Flower, M.F.J., Russo, R.M., Tamaki, K., and Hoang, N., 2001. Mantle contamination and the Izu-Bonin-Mariana (IBM) “high-tide mark”: evidence for mantle extrusion caused by Tethyan closure. *Tectonophysics*, 333(1–2):9–34. [http://dx.doi.org/10.1016/S0040-1951\(00\)00264-X](http://dx.doi.org/10.1016/S0040-1951(00)00264-X)
- Franke, D., Barckhausen, U., Baristean, N., Engels, M., Ladage, S., Lutz, R., Montano, J., Pellejera, N., Ramos, E.G., and Schnabel, M., 2011. The continent–ocean transition at the southeastern margin of the South China Sea. *Marine and Petroleum Geology*, 28(6):1187–1204. <http://dx.doi.org/10.1016/j.marpetgeo.2011.01.004>
- Gilley, L.D., Harrison, T.M., Leloup, P.H., Ryerson, F.J., Lovera, O.M., and Wang, J.-H., 2003. Direct dating of left-lateral deformation along the Red River shear zone, China and Vietnam. *Journal of Geophysical Research: Solid Earth*, 108(B2):2127. <http://dx.doi.org/10.1029/2001JB001726>
- Goldstein, S.J., 1995. Uranium-series chronology of subsurface basalts, 9°31' N East Pacific Rise. In Batiza, R., Storms, M.A., and Allan, J.F. (Eds.), 1995. *Proceedings of the Ocean Drilling Program, Scientific Results*, 142: College Station, TX (Ocean Drilling Program), 37–39. <http://dx.doi.org/10.2973/odp.proc.sr.142.115.1995>
- Goldstein, S.J., Murrell, M.T., Janeky, D.R., Delaney, J.R., and Clague, D.A., 1991. Geochronology and petrogenesis of MORB from the Juan de Fuca and Gorda Ridges by ²³⁸U–²³⁰Th disequilibrium. *Earth and Planetary Science Letters*, 107(1):25–41. [http://dx.doi.org/10.1016/0012-821X\(91\)90041-F](http://dx.doi.org/10.1016/0012-821X(91)90041-F)
- Goldstein, S.J., Perfit, M.R., Batiza, R., Fornari, D.J., and Murrell, M.T., 1994. Off-axis volcanism at the East Pacific Rise detected by uranium-series dating of basalts. *Nature*, 367(6459):157–159. <http://dx.doi.org/10.1038/367157a0>
- Grimes, C.B., John, B.E., Kelemen, P.B., Mazdab, F.K., Wooden, J.L., Cheadle, M.J., Hanghøj, K., and Schwartz, J.J., 2007. Trace element chemistry of zircons from oceanic crust: a method for distinguishing detrital zircon provenance. *Geology*, 35(7):643–646. <http://dx.doi.org/10.1130/G23603A.1>
- Haile, N.S., 1973. The recognition of former subduction zones in Southeast Asia. In Tarling, D.H., and Runcorn, S.K. (Eds.), *Implications of Continental Drift to the Earth Sciences*, Vol. 2: London (Academic Press), 885–892.
- Hall, R., 1996. Reconstructing Cenozoic SE Asia. In Hall, R., and Blundell, D.J. (Eds.), *Tectonic Evolution of Southeast Asia*. Geological Society Special Publication, 106(1):153–184. <http://dx.doi.org/10.1144/GSL.SP.1996.106.01.11>
- Hall, R., 2002. Cenozoic geological and plate tectonic evolution of SE Asia and the SW Pacific: computer-based reconstructions, model and animations. *Journal of Asian Earth Sciences*, 20(4):353–431. [http://dx.doi.org/10.1016/S1367-9120\(01\)00069-4](http://dx.doi.org/10.1016/S1367-9120(01)00069-4)
- Hall, R., and Morley, C.K., 2004. Sundaland basins. In Clift, P.D., Kuhnt, W., Wang, P., and Hayes, D. (Eds.), *Continental–Ocean Interactions with East Asian Marginal Seas*. Geophysical Monograph, 149:55–85. <http://dx.doi.org/10.1029/149GM04>
- Hamilton, W.B., 1979. Tectonics of the Indonesian Region. *U.S. Geological Survey Professional Paper*, 1078.
- Hayes, D.E., and Nissen, S.S., 2005. The South China Sea margins: implications for rifting contrasts. *Earth and Planetary Science Letters*, 237(3–4):601–616. <http://dx.doi.org/10.1016/j.epsl.2005.06.017>
- Hayes, D.E., Nissen, S.S., Buhl, P., Diebold, J., Bochu, Y., Weijun, Z., and Yongqin, C., 1995. Throughgoing crustal faults along the northern margin of the South China Sea and their role in crustal extension. *Journal of Geophysical Research: Solid Earth*, 100(B11):22435–22446. <http://dx.doi.org/10.1029/95JB01867>
- Hékinian, R., Bonté, P., Pautot, G., Jacques, D., Labeyrie, L.D., Mikkelsen, N., and Reyss, J.-L., 1989. Volcanics from the South China Sea ridge system. *Oceanologica Acta*, 12(2):101–115.
- Hilde, T., Uyeda, S., and Kroenke, L., 1977. Evolution of the western Pacific and its margin. *Tectonophysics*, 38(1–2):145–165. [http://dx.doi.org/10.1016/0040-1951\(77\)90205-0](http://dx.doi.org/10.1016/0040-1951(77)90205-0)
- Holloway, N.H., 1982. North Palawan Block, Philippines: its relation to the Asian mainland and role in evolution of South China Sea. *AAPG Bulletin*, 66(9):1355–1383. <http://aapgbull.geoscienceworld.org/content/66/9/1355.abstract>
- Honza, E., 1995. Spreading mode of backarc basins in the western Pacific. *Tectonophysics*, 251(1–4):139–152. [http://dx.doi.org/10.1016/0040-1951\(95\)00054-2](http://dx.doi.org/10.1016/0040-1951(95)00054-2)
- Huang, C.-Y., Xia, K., Yuan, P.B., and Chen, P.-G., 2001. Structural evolution from Paleogene extension to latest Miocene–recent arc-continent collision offshore Taiwan: comparison with on land geology. *Journal of Asian Earth Sciences*, 19(5):619–639. [http://dx.doi.org/10.1016/S1367-9120\(00\)00065-1](http://dx.doi.org/10.1016/S1367-9120(00)00065-1)
- Hutchison, C.S., 1996. The “Rajang accretionary prism” and “Lupar Line” problem of Borneo. In Hall, R., and Blundell, D.J. (Eds.), *Tectonic Evolution of Southeast Asia*. Geological Society Special Publication, 106(1):247–261. <http://dx.doi.org/10.1144/GSL.SP.1996.106.01.16>
- Hutchison, C.S., 2004. Marginal basin evolution: the southern South China Sea. *Marine and Petroleum Geology*, 21(9):1129–1148. <http://dx.doi.org/10.1016/j.marpetgeo.2004.07.002>
- Hutchison, C.S., 2005. *Geology of North-West Borneo*: Amsterdam (Elsevier B.V.). <http://www.sciencedirect.com/science/book/9780444519986>
- Ishihara, T., and Kisimoto, K., 1996. Magnetic anomaly map of East Asia, 1:4,000,000 (CD-ROM version). Geological Survey of Japan, Coordinating

- Committee for Coastal and Offshore Geoscience Programs in East and Southeast Asia (CCOP).
- Jahn, B.-M., Chen, P.Y., and Yen, T.P., 1976. Rb-Sr ages of granitic rocks in southeastern China and their tectonic significance. *Geological Society of America Bulletin*, 87(5):763–776. [http://dx.doi.org/10.1130/0016-7606\(1976\)87<763:RAOGRI>2.0.CO;2](http://dx.doi.org/10.1130/0016-7606(1976)87<763:RAOGRI>2.0.CO;2)
- Jin, Z., Xu, S., and Li, Z., 2002. Inversion of heterogeneous magnetism for sea-mounts in the South China Sea. *Journal of Ocean University of Qingdao* (English Edition), 32:926–934. (in Chinese)
- Koppers, A.A.P., Russell, J.A., Roberts, J., Jackson, M.G., Konter, J.G., Wright, D.J., Staudigel, H., and Hart, S.R., 2011. Age systematics of two young en echelon Samoan volcanic trails. *Geochemistry, Geophysics, Geosystems*, 12(7):Q07025. <http://dx.doi.org/10.1029/2010GC003438>
- Lacassin, R., Maluski, H., Leloup, P.H., Tapponnier, P., Hinthong, C., Siribhakdi, K., Chuaviroj, S., and Charoenravat, A., 1997. Tertiary diachronic extrusion and deformation of western Indochina: structural and $^{40}\text{Ar}/^{39}\text{Ar}$ evidence from NW Thailand. *Journal of Geophysical Research: Solid Earth*, 102(B5):10013–10037. <http://dx.doi.org/10.1029/96JB03831>
- Lallemand, S., and Jolivet, L., 1986. Japan Sea: a pull apart basin? *Earth and Planetary Science Letters*, 76(3–4):375–389. [http://dx.doi.org/10.1016/0012-821X\(86\)90088-9](http://dx.doi.org/10.1016/0012-821X(86)90088-9)
- Le Maitre, R.W., Bateman, P., Dudek, A., Keller, J., Lameyre, J., Le Bas, M.J., Sabine, P.A., Schmid, R., Sorensen, H., Streckeisen, A., Woolley, A.R., and Zanettin, B., 1989. *A Classification of Igneous Rocks and Glossary of Terms*: Oxford, UK (Blackwell Science Publishing).
- Lee, T.-Y., and Lawver, L.A., 1995. Cenozoic plate reconstruction of Southeast Asia. *Tectonophysics*, 251(1–4): 85–138. [http://dx.doi.org/10.1016/0040-1951\(95\)00023-2](http://dx.doi.org/10.1016/0040-1951(95)00023-2)
- Leloup, P.H., Arnaud, N., Lacassin, R., Kienast, J.R., Harrison, T.M., Trong, T.T.P., Replumaz, A., and Tapponnier, P., 2001. New constraints on the structure, thermochronology, and timing of the Ailao Shan-Red River shear zone, SE Asia. *Journal of Geophysical Research: Solid Earth*, 106(B4):6683–6732. <http://dx.doi.org/10.1029/2000JB900322>
- Li, C.-F., Lin, J., and Kulhanek, D.K., 2013a. South China Sea tectonics: opening of the South China Sea and its implications for southeast Asian tectonics, climates, and deep mantle processes since the late Mesozoic. *International Ocean Discovery Program Scientific Prospectus*, 349. <http://dx.doi.org/10.2204/iodp.sp.349.2013>
- Li, C.-F., Shi, X., Zhou, Z., Li, J., Geng, J., and Chen, B., 2010. Depths to the magnetic layer bottom in the South China Sea area and their tectonic implications. *Geophysical Journal International*, 182(3):1229–1247. <http://dx.doi.org/10.1111/j.1365-246X.2010.04702.x>
- Li, C.-F., and Song, T.R., 2012. Magnetic recording of the Cenozoic oceanic crustal accretion and evolution of the South China Sea basin. *Chinese Science Bulletin*, 57(24):3165–3181. <http://dx.doi.org/10.1007/s11434-012-5063-9>
- Li, C.-F., Wang, P., Franke, D., Lin, J., and Tian, J., 2012. Unlocking the opening processes of the South China Sea. *Scientific Drilling*, 14:55–59. <http://dx.doi.org/10.2204/iodp.sd.14.07.2012>
- Li, C.-F., Zhou, Z., Hao, H., Chen, H., Wang, J., Chen, B., and Wu, J., 2008a. Late Mesozoic tectonic structure and evolution along the present-day northeastern South China Sea continental margin. *Journal of Asian Earth Sciences*, 31(4–6):546–561. <http://dx.doi.org/10.1016/j.jseaes.2007.09.004>
- Li, C.-F., Zhou, Z., Li, J., Chen, B., and Geng, J., 2008b. Magnetic zoning and seismic structure of the South China Sea ocean basin. *Marine Geophysical Researches*, 29(4):223–238. <http://dx.doi.org/10.1007/s11001-008-9059-4>
- Li, C.-F., Zhou, Z., Li, J., Hao, H., and Geng, J., 2007a. Structures of the northeasternmost South China Sea continental margin and ocean basin: geophysical constraints and tectonic implications. *Marine Geophysical Researches*, 28(1):59–79. <http://dx.doi.org/10.1007/s11001-007-9014-9>
- Li, C.-F., Zhou, Z.Y., Li, J.B., Chen, H.J., Geng, J.H., and Li, H., 2007b. Precollisional tectonics and terrain amalgamation offshore southern Taiwan: characterizations from reflection seismic and potential field data. *Science in China, Series D: Earth Sciences*, 50(6):897–908. <http://dx.doi.org/10.1007/s11430-007-0025-9>
- Li, J.-B., Ding, W.-W., Gao, J.-Y., Wu, Z.-Y., and Zhang, J., 2011. Cenozoic evolution model of the sea-floor spreading in South China Sea: new constraints from high resolution geophysical data. *Chinese Journal of Geophysics*, 54(6):894–906. <http://www.agu.org/wps/ChineseJ-Geo/54/06/ljb2.pdf>
- Li, L., Clift, P.D., and Nguyen, H.T., 2013b. The sedimentary, magmatic and tectonic evolution of the southwestern South China Sea revealed by seismic stratigraphic analysis. *Marine and Geophysical Research*, 34(3–4):393–406. <http://dx.doi.org/10.1007/s11001-013-9171-y>
- Li, Q., Wang, P., Zhao, Q., Shao, L., Zhong, G., Tian, J., Cheng, X., Jian, Z., and Su, X., 2006. A 33 Ma lithostratigraphic record of tectonic and paleoceanographic evolution of the South China Sea. *Marine Geology*, 230(3–4):217–235. <http://dx.doi.org/10.1016/j.margeo.2006.05.006>
- Lüdmann, T., and Wong, H.K., 1999. Neotectonic regime on the passive continental margin of the northern South China Sea. *Tectonophysics*, 311(1–4):113–138. [http://dx.doi.org/10.1016/S0040-1951\(99\)00155-9](http://dx.doi.org/10.1016/S0040-1951(99)00155-9)
- Lüdmann, T., Wong, H.K., and Wang, P., 2001. Plio-Quaternary sedimentation processes and neotectonics of the northern continental margin of the South China Sea. *Marine Geology*, 172(3–4):331–358. [http://dx.doi.org/10.1016/S0025-3227\(00\)00129-8](http://dx.doi.org/10.1016/S0025-3227(00)00129-8)
- Macdonald, G.A., 1968. Composition and origin of Hawaiian lavas. In Coats, R.R., Hay, R.L., and Anderson, C.A. (Eds.), *Studies in Volcanology—A Memoir in Honor of Howel Williams*. Memoir - Geological Society of America, 116:477–522. <http://dx.doi.org/10.1130/MEM116-p477>
- Macdonald, G.A., and Katsura, T., 1964. Chemical composition of Hawaiian lavas. *Journal of Petrology*, 5(1):82–133. <http://petrology.oxfordjournals.org/content/5/1/82.abstract>
- Madon, M.B.H., Meng, L.K., and Anuar, A., 1999. Sabah Basin. In Marican, T.S.D.M.H. (Ed.), *The Petroleum Geology and Resources of Malaysia*. Kuala Lumpur, Malaysia (Petroleum Nasional Berhad), 499–542.
- McIntosh, K.D., Liu, C.-S., and Lee, C.-S., 2012. Introduction to the TAIGER special issue of Marine Geophysical Research. *Marine Geophysical Researches*, 33(4):285–287. <http://dx.doi.org/10.1007/s11001-013-9170-z>
- Morley, C.K., 2002. A tectonic model for the Tertiary evolution of strike-slip faults and rift basins in SE Asia. *Tectonophysics*, 347(4):189–215. [http://dx.doi.org/10.1016/S0040-1951\(02\)00061-6](http://dx.doi.org/10.1016/S0040-1951(02)00061-6)
- Pautot, G., Rangin, C., Briaies, A., Tapponnier, P., Beuzart, P., Lericolais, G., Mathieu, X., Wu, J., Han, S., Li, H., Lu, Y., and Zhao, J., 1986. Spreading direction in the central South China Sea. *Nature*, 321(6066):150–154. <http://dx.doi.org/10.1038/321150a0>
- Pubellier, M., Monnier, C., Maury, R., and Tamayo, R., 2004. Plate kinematics, origin and tectonic emplacement of supra-subduction ophiolites in SE Asia. *Tectonophysics*, 392(1–4):9–36. <http://dx.doi.org/10.1016/j.tecto.2004.04.028>
- Rangin, C., Jolivet, L., and Pubellier, M., 1990. A simple model for the tectonic evolution of Southeast Asia and Indonesia regions for the past 43 m.y. *Bulletin de la Société Géologique de France*, 6(6):889–905.
- Rangin, C., Klein, M., Roques, D., Le Pichon, X., and Trong, L.V., 1995. The Red River fault system in the Tonkin Gulf, Vietnam. *Tectonophysics*, 243(3–4):209–222. [http://dx.doi.org/10.1016/0040-1951\(94\)00207-P](http://dx.doi.org/10.1016/0040-1951(94)00207-P)
- Ru, K., and Pigott, J.D., 1986. Episodic rifting and subsidence in the South China Sea. *AAPG Bulletin*, 70(9):1136–1155. <http://aapgbull.geoscienceworld.org/content/70/9/1136.short>
- Schärer, U., Tapponnier, P., Lacassin, R., Leloup, P.H., Dalai, Z., and Ji, S., 1990. Intraplate tectonics in Asia: a precise age for large-scale Miocene movement along the Ailao Shan-Red River shear zone, China. *Earth and Planetary Science Letters*, 97(1–2):65–77. [http://dx.doi.org/10.1016/0012-821X\(90\)90099-J](http://dx.doi.org/10.1016/0012-821X(90)90099-J)
- Schlüter, H.U., Hinz, K., and Block, M., 1996. Tectono-stratigraphic terranes and detachment faulting of the South China Sea and Sulu Sea. *Marine Geology*, 130(1–2):39–78. [http://dx.doi.org/10.1016/0025-3227\(95\)00137-9](http://dx.doi.org/10.1016/0025-3227(95)00137-9)

- Schwartz, J.J., John, B.E., Cheadle, M.J., Miranda, E.A., Grimes, C.B., Wooden, J.L., and Dick, H.J.B., 2005. Dating the growth of oceanic crust at a slow-spreading ridge. *Science*, 310(5748):654–657. <http://dx.doi.org/10.1126/science.1116349>
- Shi, H., and Li, C.-F., 2012. Mesozoic and early Cenozoic tectonic convergence-to-rifting transition prior to opening of the South China Sea. *International Geology Review*, 54(15):1801–1828. <http://dx.doi.org/10.1080/00206814.2012.677136>
- Sibuet, J.-C., Hsu, S.-K., Le Pichon, X., Le Formal, J.-P., Reed, D., Moore, G., and Liu, C.-S., 2002. East Asia plate tectonics since 15 Ma: constraints from the Taiwan region. *Tectonophysics*, 344(1–2):103–134. [http://dx.doi.org/10.1016/S0040-1951\(01\)00202-5](http://dx.doi.org/10.1016/S0040-1951(01)00202-5)
- Smith, W.H.F., and Sandwell, D.T., 1997. Global seafloor topography from satellite altimetry and ship depth soundings. *Science*, 277(5334):1956–1962. <http://dx.doi.org/10.1126/science.277.5334.1956>
- Song, T., and Li, C., 2012. The opening ages and mode of the South China Sea estimated from high-density magnetic tracks. *Progress in Geophysics*, 27(4):1432–1442. <http://dx.doi.org/10.6038/j.issn.1004-2903.2012.04.018>
- Sun, Z., Zhong, Z., Keep, M., Zhou, D., Cai, D., Li, X., Wu, S., and Jiang, J., 2009. 3D analogue modeling of the South China Sea: a discussion on breakup pattern. *Journal of Asian Earth Sciences*, 34(4):544–556. <http://dx.doi.org/10.1016/j.jseaes.2008.09.002>
- Tapponnier, P., Lacassin, R., Leloup, P.H., Shärer, U., Dalai, Z., Haiwei, W., Xiaohan, L., Shaocheng, J., Liangshang, Z., and Jiayou, Z., 1990. The Ailao Shan/Red River metamorphic belt: Tertiary left-lateral shear between Indochina and South China. *Nature*, 343(6257):431–437. <http://dx.doi.org/10.1038/343431a0>
- Tapponnier, P., Peltzer, G., and Armijo, R., 1986. On the mechanics of the collision between India and Asia. In Ramsey, J.G., Coward, M.P., and Ries, A. (Eds.), *Collision Tectonics*. Geological Society Special Publication, 19:115–157. <http://dx.doi.org/10.1144/GSL.SP.1986.019.01.07>
- Taylor, B., and Hayes, D.E., 1980. The tectonic evolution of the South China Basin. In Hayes, D.E. (Ed.), *The Tectonic and Geologic Evolution of Southeast Asian Seas and Islands*. Geophysical Monograph, 23:89–104. <http://dx.doi.org/10.1029/GM023p0089>
- Taylor, B., and Hayes, D.E., 1983. Origin and history of the South China Sea basin. In Hayes, D.E. (Ed.), *The Tectonic and Geologic Evolution of Southeast Asian Seas and Islands* (Pt. 2). Geophysical Monograph, 27:23–56. <http://dx.doi.org/10.1029/GM027p0023>
- Tejada, M.L.G., Mahoney, J.J., Castillo, P.R., Ingle, S.P., Sheth, H.C., and Weis, D., 2004. Pin-pricking the elephant: evidence on the origin of the Ontong Java Plateau from Pb-Sr-Hf-Nd isotopic characteristics of ODP Leg 192 basalts. In Fitton, J.G., Mahoney, J.J., Wallace, P.J., and Saunders, A.D. (Eds.), *Origin and Evolution of the Ontong Java Plateau*. Geological Society Special Publication, 229(1):133–150. <http://dx.doi.org/10.1144/GSL.SP.2004.229.01.09>
- Tominaga, M., Teagle, D.A.H., Alt, J.C., and Umino, S., 2009. Determination of the volcanostratigraphy of the oceanic crust formed at superfast spreading ridge: electrofacies analyses of ODP/IOPD Hole 1256D. *Geochemistry, Geophysics, Geosystems*, 10(1):Q01003. <http://dx.doi.org/10.1029/2008GC002143>
- Tongkul, F., 1994. The geology of northern Sabah, Malaysia: its relationship to the opening of the South China Sea basin. *Tectonophysics*, 235(1–2):131–147. [http://dx.doi.org/10.1016/0040-1951\(94\)90021-3](http://dx.doi.org/10.1016/0040-1951(94)90021-3)
- Tu, K., Flower, M.F.J., Carlson, R.W., Xie, G., Chen, C.-Y., and Zhang, M., 1992. Magmatism in the South China Basin: 1. Isotopic and trace-element evidence for an endogenous Dupal mantle component. *Chemical Geology*, 97(1–2):47–63. [http://dx.doi.org/10.1016/0009-2541\(92\)90135-R](http://dx.doi.org/10.1016/0009-2541(92)90135-R)
- Wang, P., 2012. Tracing the life history of a marginal sea—on “The South China Sea Deep” research program. *Chinese Science Bulletin*, 57(24):3093–3114. <http://dx.doi.org/10.1007/s11434-012-5087-1>
- Wang, P., and Li, Q. (Eds.), 2009. *Developments in Paleoenvironmental Research* (Vol. 13): *The South China Sea: Paleogeography and Sedimentology*. Dordrecht (Springer). 13. <http://dx.doi.org/10.1007/978-1-4020-9745-4>
- Wang, P., Prell, W.L., Blum, P., et al., 2000. *Proceedings of the Ocean Drilling Program, Initial Reports*, 184: College Station, TX (Ocean Drilling Program). <http://dx.doi.org/10.2973/odp.proc.ir.184.2000>
- Wang, X.-C., Li, Z.-X., Li, X.-H., Li, J., Liu, Y., Long, W.-G., Zhou, J.-B., and Wang, F., 2012. Temperature, pressure, and composition of the mantle source region of late Cenozoic basalts in Hainan Island, SE Asia: a consequence of a young thermal mantle plume close to subduction zones? *Journal of Petrology*, 53(1):177–233. <http://dx.doi.org/10.1093/petrology/egr061>
- Xiao, G., and Zheng, J., 2004. New opinions about “residual Tethys” in northern South China Sea slope and southern East China Sea. *Geoscience*, 18(1):103–108. (in Chinese)
- Xu, Y., Wei, J., Qiu, H., Zhang, H., and Huang, X., 2012. Opening and evolution of the South China Sea constrained by studies on volcanic rocks: preliminary results and a research design. *Chinese Science Bulletin*, 57(24):3150–3164. <http://dx.doi.org/10.1007/s11434-011-4921-1>
- Yan, P., Zhou, D., and Liu, Z., 2001. A crustal structure profile across the northern continental margin of the South China Sea. *Tectonophysics*, 338(1):1–21. [http://dx.doi.org/10.1016/S0040-1951\(01\)00062-2](http://dx.doi.org/10.1016/S0040-1951(01)00062-2)
- Yang, J.Y., and Feng, X.S., 2003. An analysis of middle-late Mesozoic tectonics, paleogeography, and petroleum potential in the northeastern South China Sea. *China Offshore Oil and Gas (Geology)*, 17:89–103. http://en.cnki.com.cn/Article_en/CJFDTOTAL-ZHSD200302002.htm
- Yao, B., 1995. Characteristics and tectonic significance of the Zhongnan-Lile fault. *Geological Research of South China Sea, Memoir*, 7:1–14. (in Chinese)
- Yao, B., Zeng, W., Hayes, D.E., and Spangler, S., 1994. *The Geological Memoir of South China Sea Surveyed Jointly by China and USA*: Wuhan (China Univ. Geosci. Press). (in Chinese)
- Zhang, G., Smith-Duque, C., Tang, S., Li, H., Zarikian, C., D’Hondt, S., Inagaki, F., and IODP Expedition 329 Scientists, 2012. Geochemistry of basalts from IODP Site U1365: implications for magmatism and mantle source signatures of the mid-Cretaceous Osborn Trough. *Lithos*, 144–145:73–87. <http://dx.doi.org/10.1016/j.lithos.2012.04.014>
- Zhang, G., Zeng, Z., Yin, X., Wang, X., and Chen, D., 2009. Deep fractionation of clinopyroxene in the East Pacific Rise 13°N: evidence from high MgO MORB and melt inclusions. *Acta Geologica Sinica*, 83(2):266–277. <http://dx.doi.org/10.1111/j.1755-6724.2009.00030.x>
- Zhang, G.-L., Chen, L.-H., and Li, S.-Z., 2013. Mantle dynamics and generation of a geochemical mantle boundary along the East Pacific Rise—Pacific/Antarctic Ridge. *Earth and Planetary Science Letters*, 383:153–163. <http://dx.doi.org/10.1016/j.epsl.2013.09.045>
- Zhang, G.-L., Zong, C.-L., Yin, X.-B., and Li, H., 2012. Geochemical constraints on a mixed pyroxenite–peridotite source for East Pacific Rise basalts. *Chemical Geology*, 330–331:176–187. <http://dx.doi.org/10.1016/j.chemgeo.2012.08.033>
- Zhang, L., Zhao, M.H., Wang, J., He, E.Y., Ao, W., Qiu, X.L., Xu, H.L., Wei, X.D., and Zhang, J.Z., 2013. The correction of OBS position and recent advances of 3D seismic exploration in the central sub-basin of South China Sea. *Earth Science—Journal of China University of Earth Geosciences*, 2013(1):33–42. (in Chinese)
- Zhou, D., Ru, K., and Chen, H., 1995. Kinematics of Cenozoic extension on the South China Sea continental margin and its implications for the tectonic evolution of the region. *Tectonophysics*, 251(1–4):161–177. [http://dx.doi.org/10.1016/0040-1951\(95\)00018-6](http://dx.doi.org/10.1016/0040-1951(95)00018-6)
- Zhou, D., Sun, Z., Chen, H., Xu, H., Wang, W., Pang, X., Cai, D., and Hu, D., 2008. Mesozoic paleogeography and tectonic evolution of South China Sea and adjacent areas in the context of Tethyan and Paleo-Pacific interconnections. *Island Arc*, 17(2):186–207. <http://dx.doi.org/10.1111/j.1440-1738.2008.00611.x>
- Zhou, X.M., and Li, W.X., 2000. Origin of late Mesozoic igneous rocks in southeastern China: implications for lithosphere subduction and underplating of mafic magmas. *Tectonophysics*, 326(3–4):269–287. [http://dx.doi.org/10.1016/S0040-1951\(00\)00120-7](http://dx.doi.org/10.1016/S0040-1951(00)00120-7)

doi:10.14379/iodp.proc.349.102.2015

Methods¹



C.-F. Li, J. Lin, D.K. Kulhanek, T. Williams, R. Bao, A. Briais, E.A. Brown, Y. Chen, P.D. Clift, F.S. Colwell, K.A. Dadd, W.-W. Ding, I. Hernández Almeida, X.-L. Huang, S. Hyun, T. Jiang, A.A.P. Koppers, Q. Li, C. Liu, Q. Liu, Z. Liu, R.H. Nagai, A. Peleo-Alampay, X. Su, Z. Sun, M.L.G. Tejada, H.S. Trinh, Y.-C. Yeh, C. Zhang, F. Zhang, G.-L. Zhang, and X. Zhao²

Keywords: International Ocean Discovery Program, IODP, *JOIDES Resolution*, Expedition 349, Site U1431, Site U1432, Site U1433, Site U1434, Site U1435, South China Sea, structural analysis, paleomagnetism, thermal demagnetization, igneous petrology, alteration, core description, microbial contamination tracers, microbiology, organic geochemistry, inorganic chemistry, physical properties, visual core description, ICP measurement, biostratigraphy, downhole measurements

Contents

- 1 Introduction, background, and operations
- 5 Lithostratigraphy
- 11 Biostratigraphy
- 20 Igneous petrology and alteration
- 29 Structural geology
- 32 Geochemistry
- 35 Microbiology
- 38 Paleomagnetism
- 43 Physical properties
- 48 Downhole measurements
- 53 References

Introduction, background, and operations Site locations

GPS coordinates from pre-cruise site surveys were used to position the vessel at all International Ocean Discovery Program (IODP) Expedition 349 sites. A SyQuest Bathy 2010 CHIRP sub-bottom profiler was used to monitor seafloor depth on the approach to each site to reconfirm the depth profiles from pre-cruise surveys. Once the vessel was positioned at a site, the thrusters were lowered, and a positioning beacon was dropped to the seafloor. The dynamic positioning control of the vessel used navigational input from the GPS and triangulation to the seafloor beacon, weighted by the estimated positional accuracy. The final hole position was the mean position calculated from the GPS data collected over a significant time interval.

Coring and drilling operations

All three standard coring systems, the advanced piston corer (APC), extended core barrel (XCB), and rotary core barrel (RCB), were used during Expedition 349. The APC was used in the upper portion of each hole to obtain high-quality core. The APC cuts soft-sediment cores with minimal coring disturbance relative to other IODP coring systems. After the APC core barrel is lowered through the drill pipe and lands near the bit, the drill pipe is pressured up until the two shear pins that hold the inner barrel attached to the outer barrel fail. The inner barrel then advances into the formation and cuts the core (Figure F1). The driller can detect a successful cut, or “full stroke,” from the pressure gauge on the rig floor.

APC refusal is conventionally defined in two ways: (1) the piston fails to achieve a complete stroke (as determined from the pump pressure reading) because the formation is too hard or (2) excessive force (>60,000 lb; ~267 kN) is required to pull the core barrel out of the formation. When a full stroke cannot be achieved, additional attempts are typically made, and after each attempt the bit is advanced by the length of core recovered. The number of additional attempts is generally dictated by the length of recovery of the partial stroke core and the time available to advance the hole by piston coring. Note that this results in a nominal recovery of ~100% based on the assumption that the barrel penetrates the formation by the equivalent of the length of core recovered. When a full or partial stroke is achieved but excessive force cannot retrieve the barrel, the core barrel is sometimes “drilled over,” meaning after the inner core barrel is successfully shot into the formation, the drill bit is advanced to total depth to free the APC barrel.

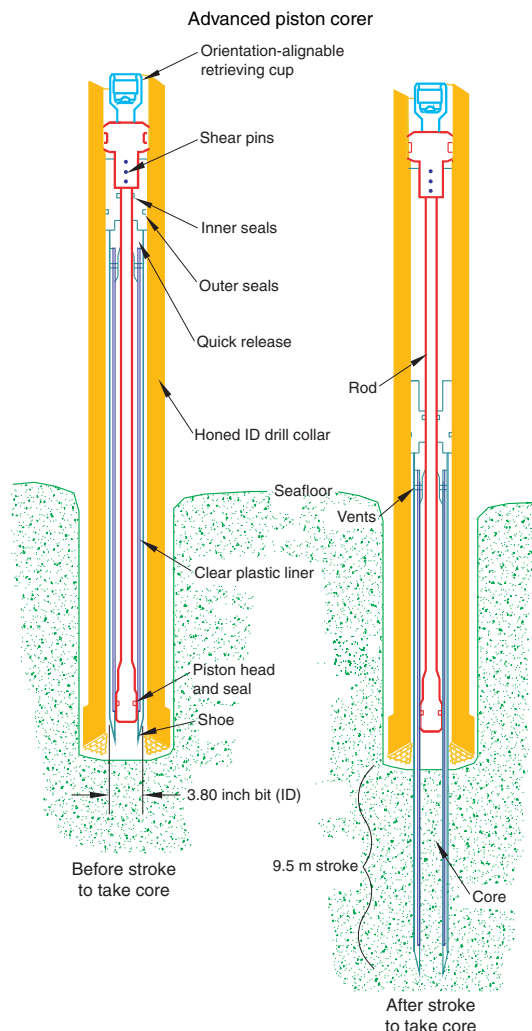
Nonmagnetic core barrels were used during all conventional APC coring to a pull force of ~40,000 lb. Except for cores taken in Hole U1432C, APC cores recovered during Expedition 349 were oriented using the FlexIT tool (see [Paleomagnetism](#)). Formation temperature measurements were made to obtain temperature gradients and heat flow estimates (see [Downhole measurements](#)) for all APC sections.

The XCB was used to advance the hole when APC refusal occurred before the target depth was reached or when the formation became either too stiff for APC coring or hard substrate was encountered. The XCB is a rotary system with a small cutting shoe (bit) that extends below the large APC/XCB bit. The smaller bit can cut a semi-indurated core with less torque and fluid circulation than the main bit, optimizing recovery. The XCB cutting shoe extends

¹ Li, C.-F., Lin, J., Kulhanek, D.K., Williams, T., Bao, R., Briais, A., Brown, E.A., Chen, Y., Clift, P.D., Colwell, F.S., Dadd, K.A., Ding, W., Hernández Almeida, I., Huang, X.-L., Hyun, S., Jiang, T., Koppers, A.A.P., Li, Q., Liu, C., Liu, Q., Liu, Z., Nagai, R.H., Peleo-Alampay, A., Su, X., Sun, Z., Tejada, M.L.G., Trinh, H.S., Yeh, Y.-C., Zhang, C., Zhang, F., Zhang, G.-L., and Zhao, X., 2015. Methods. In Li, C.-F., Lin, J., Kulhanek, D.K., and the Expedition 349 Scientists, *Proceedings of the Integrated Ocean Discovery Program, 349: South China Sea Tectonics*: College Station, TX (International Ocean Discovery Program). <http://dx.doi.org/10.14379/iodp.proc.349.102.2015>

² [Expedition 349 Scientists' addresses.](#)

Figure F1. Schematic of the APC system used during Expedition 349.

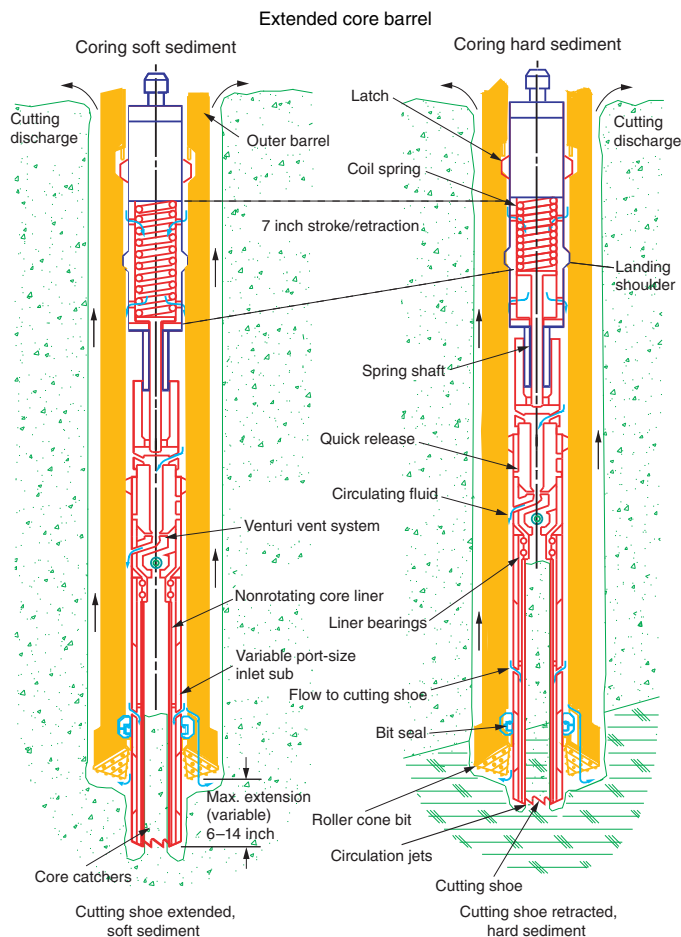


~30.5 cm ahead of the main bit in soft sediment but retracts into the main bit when hard formations are encountered (Figure F2). During Expedition 349, the XCB was only used at Site U1431. This system was not subsequently used because of poor core quality (the XCB cores collected at Site U1431 were highly biscuited) and the significant drilling-induced magnetic overprint resulting from the use of steel core barrels that are required for XCB coring. This overprint could not be removed by thermal demagnetization during ship-board analyses.

The bottom-hole assembly (BHA) is the lowermost part of the drill string. The exact configuration of the BHA is reported in the operations section of each site chapter. A typical APC/XCB BHA consisted of a drill bit (outer diameter = 11 7/16 inch), a bit sub, a seal bore drill collar, a landing saver sub, a modified top sub, a modified head sub, a nonmagnetic drill collar (for APC/XCB), a number of 8 inch (~20.32 cm) drill collars, a tapered drill collar, six joints (two stands) of 5 1/2 inch (~13.97 cm) drill pipe, and one crossover sub. A lockable float valve was used when downhole logging was planned so downhole logs could be collected through the bit.

The RCB was deployed when basement coring was expected (Figure F3). The RCB is the most conventional rotary drilling system and was used during Expedition 349 to drill and core into basement. The RCB requires a dedicated RCB BHA and a dedicated

Figure F2. Schematic of the XCB system used during Expedition 349.

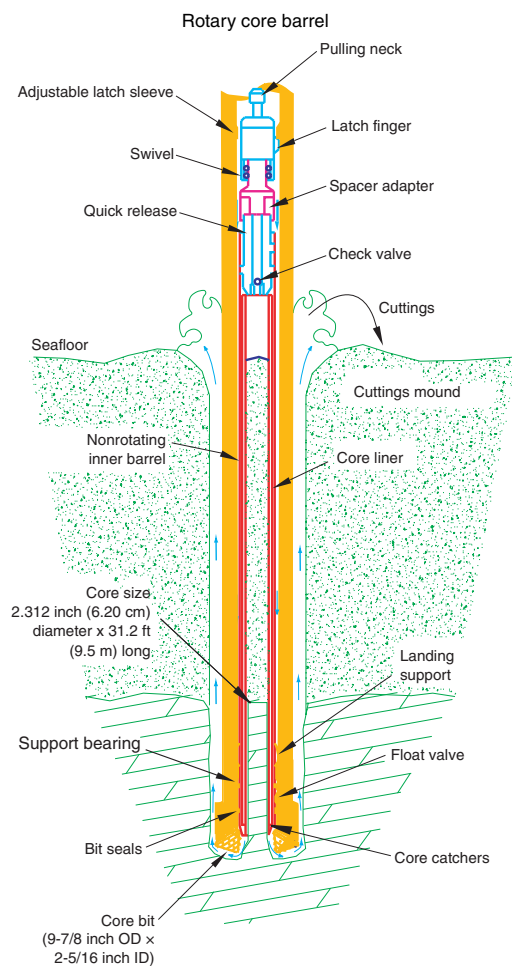


RCB drilling bit. The BHA used for RCB coring included a 9 5/8 inch RCB drill bit, a mechanical bit release (if logging was considered), a modified head sub, an outer core barrel, a modified top sub, a modified head sub, and 7 to 10 control-length drill collars followed by a tapered drill collar to the two stands of 5 1/2 inch drill pipe. Most cored intervals were ~9.7 m long, which is the length of a standard rotary core and approximately the length of a joint of drill pipe. In some cases, the drill string was drilled or “washed” ahead without recovering sediment to advance the drill bit to a target depth to resume core recovery. Such intervals were typically drilled using a center bit installed within the RCB bit. When coring basement, half-cores were sometimes collected to improve recovery and when rates of penetration decreased significantly.

IODP depth scales

Primary depth scale types are based on the measurement of drill string length (e.g., drilling depth below rig floor [DRF] and drilling depth below seafloor [DSF]), length of core recovered (e.g., core depth below seafloor [CSF]), and logging wireline (e.g., wireline log depth below rig floor [WRF] and wireline log depth below seafloor [WSF]). All units are in meters. The relationship between scales is defined either by protocol, such as the rules for computation of CSF from DSE, or by a combination of protocols with user-defined correlations. The distinction in nomenclature should keep the user aware that a nominal depth value at two different depth scales usually does not refer to exactly the same stratigraphic interval (see

Figure F3. Schematic of the RCB system used during Expedition 349.



Curatorial procedures and sample depth calculations. For editorial convenience, we use meters below seafloor (mbsf) for the CSF-A depth scale throughout this volume.

Core handling and analysis

The coring strategy for Expedition 349 consisted of APC coring in one hole (Hole A) at each site to refusal, except at Site U1431, where five holes were cored with the APC. Multiple holes at this site allowed high-resolution sampling for specific objectives (e.g., microbiology, interstitial water measurements, and optically stimulated luminescence dating). APC refusal was followed by XCB coring at Site U1431 to ~617 mbsf. RCB coring was employed to reach and core into basement at all sites except Site U1432.

Cores recovered during Expedition 349 were extracted from the core barrel in 67 mm diameter plastic liners. These liners were carried from the rig floor to the core processing area on the catwalk outside the Core Laboratory, where they were split into ~1.5 m sections. Liner caps (blue = top, colorless = bottom, and yellow = whole-round sample taken) were glued with acetone onto liner sections on the catwalk by the Marine Technicians. The length of each section was entered into the database as “created length” using the Sample Master application. This number was used to calculate core recovery. Sections were cut into smaller lengths on cores taken from Holes U1431A and U1431B to allow for interstitial water whole rounds, microbiological whole rounds, and optically stimulated lu-

minescence dating whole rounds to be taken at 50 cm resolution. A normal section length of 1.5 m was resumed following this high-resolution sampling in these two holes.

For sedimentary sections, as soon as cores arrived on deck, headspace samples were taken using a syringe for immediate hydrocarbon analysis as part of the shipboard safety and pollution prevention program. Core catcher samples were taken for biostratigraphic analysis. Whole-round samples were taken from some core sections for shipboard and postcruise interstitial water analyses. Rhizon interstitial water samples and syringe samples were taken from selected intervals in addition to whole rounds (see [Geochemistry](#)). In addition, whole-round and syringe samples were immediately taken from the ends of some cut sections for shore-based microbiological analysis.

Hard rock core pieces were slid out of the liners and placed in order in new, clean sections of core liner that had previously been split in half. Pieces having a vertical length greater than the internal (horizontal) diameter of the core liner are considered oriented pieces because they could have rotated only around their vertical axes. Those pieces were immediately marked on the bottom with a red wax pencil to preserve their vertical (upward) orientations. Pieces that were too small to be oriented with certainty were left unmarked. Adjacent but broken core pieces that could be fit together along fractures were curated as single pieces. The structural geologist or petrologist on shift confirmed the piece matches and corrected any errors. The structural geologist or petrologist also marked a split line on the pieces, which defined how the pieces should be cut into two equal halves. The aim was to maximize the expression of dipping structures on the cut face of the core while maintaining representative features in both archive and working halves. Whole-round microbiology samples were taken in the splitting room immediately after the core was slid from the liner. The petrologist on duty monitored the microbiology sampling to ensure that no critical petrographic interval was depleted. All microbiology whole-round samples were photographed and documented before being removed from the core. A foam spacer was used to mark where a microbiological sample was taken.

Core sections were then placed in core racks in the laboratory. When the cores reached equilibrium with laboratory temperature (typically after ~4 h), whole-round core sections were run through the Whole-Round Multisensor Logger (WRMSL; measuring *P*-wave velocity, density, and magnetic susceptibility) and the Natural Gamma Radiation Logger (NGRL). Thermal conductivity measurements were typically taken at a rate of one per core (see [Physical properties](#)). The core sections were then split lengthwise from bottom to top into working and archive halves. Investigators should note that older material may have been transported upward on the split face of each section during splitting. For hard rock sections, each piece of core was split with a diamond-impregnated saw into archive and working halves, with the positions of the plastic spacers between individual pieces maintained in both halves of the plastic liner. Pieces were numbered sequentially from the top of each section. Separate subpieces within a single piece were assigned the same number but were lettered consecutively (e.g., 1A, 1B, and 1C). Pieces were labeled only on the outer cylindrical surface of the core or on the core liner.

The working half of each sedimentary core was sampled for shipboard biostratigraphic, physical property, carbonate, paleomagnetic, and inductively coupled plasma–atomic emission spectroscopy (ICP-AES) analyses. The archive half of all cores was scanned on the Section Half Imaging Logger (SHIL) with a line scan camera

at 20 pixels/mm and measured for color reflectance and magnetic susceptibility on the Section Half Multisensor Logger (SHMSL). At the same time, the archive halves were described visually and by means of smear slides and thin sections. All observations were recorded in the Laboratory Information Management System (LIMS) database using DESClogik, a descriptive data capture application. After visual description, the archive halves were run through the cryogenic magnetometer. Finally, digital color close-up images were taken of particular features of the archive or working halves, as requested by individual scientists. For hard rock cores, a sampling meeting was held at 1200 h to select key sampling intervals for ship-board analyses. Discrete samples were taken from working halves for physical property, paleomagnetic, thin section, and ICP-AES analyses. Records of all samples taken are kept by the IODP curator. Sampling for personal postcruise research was conducted immediately after splitting for sedimentary sequences and during several sampling parties over the course of the expedition for hard rock.

Both halves of the core were put into labeled plastic tubes that were sealed and transferred to cold storage space aboard the ship. At the end of the expedition, the cores were transported from the ship to permanent cold storage at the Kochi Core Center (KCC) at Kochi University in Kochi, Japan. The KCC houses cores collected from the western Pacific Ocean, Indian Ocean, Kerguelen Plateau, and Bering Sea.

Drilling disturbance

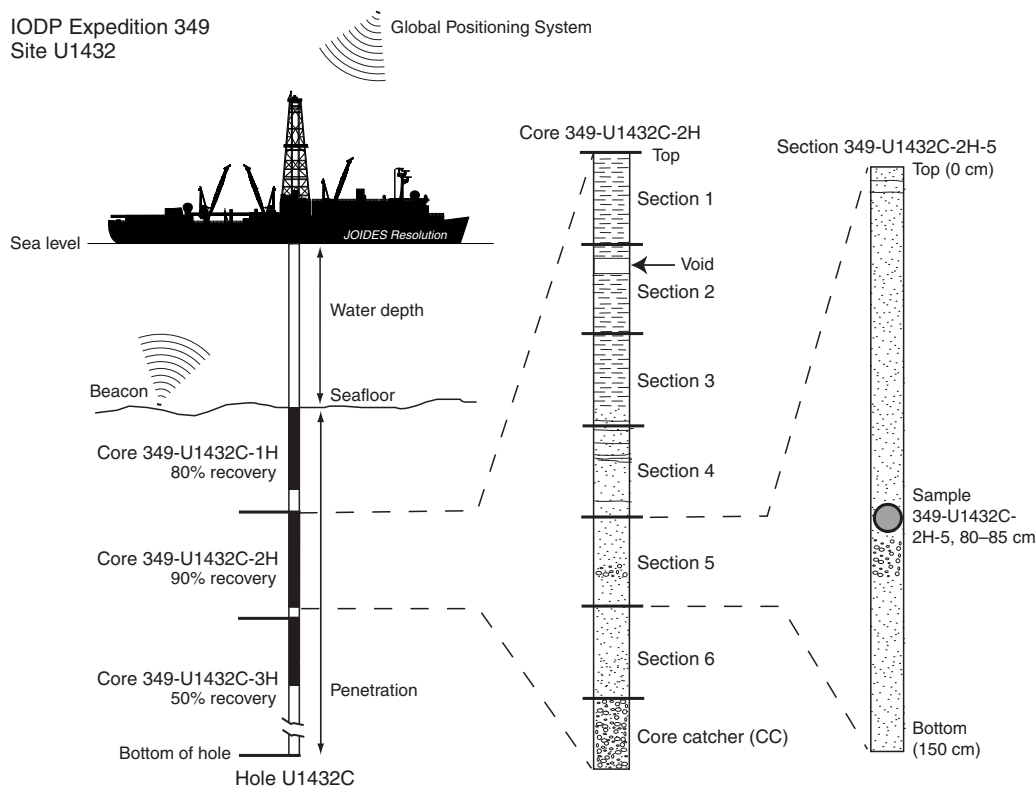
Cores may be significantly disturbed as a result of the drilling process and may contain extraneous material as a result of the coring and core handling process. In formations with loose sand layers, sand from intervals higher in the hole may be washed down by drilling circulation, accumulate at the bottom of the hole, and be sampled with the next core. The uppermost 10–50 cm of each core

must therefore be examined critically during description for potential “fall-in.” Common coring-induced deformation includes the concave-downward appearance of originally horizontal bedding. Piston action may result in fluidization (flow-in) at the bottom of APC cores. Retrieval from depth to the surface may result in elastic rebound. Gas that is in solution at depth may become free and drive core segments within the liner apart. Both elastic rebound and gas pressure can result in a total length for each core that is longer than the interval that was cored and thus a calculated recovery of >100%. If gas expansion or other coring disturbance results in a void in any particular core section, the void can be closed by moving material if very large, stabilized by a foam insert if moderately large, or left as is. When gas content is high, pressure must be relieved for safety reasons before the cores are cut into segments. This is accomplished by drilling holes into the liner, which forces some sediment as well as gas out of the liner. These disturbances are described in the Lithostratigraphy sections in each site chapter and are graphically indicated on the core summary graphic reports (visual core descriptions [VCDs]). In extreme instances core material can be ejected from the core barrel, sometimes violently, onto the rig floor by high pressure in the core or other coring problems. This core material is replaced in the plastic core liner by hand and should not be considered to be in stratigraphic order. Core sections so affected are marked by a yellow label marked “disturbed,” and the nature of the disturbance is noted in the coring log.

Curatorial procedures and sample depth calculations

Numbering of sites, holes, cores, and samples follows standard IODP procedure (Figure F4). Drilling sites are numbered consecutively from the first site drilled by the D/V *Glomar Challenger* in 1968. Integrated Ocean Drilling Program Expedition 301 began us-

Figure F4. IODP conventions for naming sites, holes, cores, and samples.



ing the prefix “U” to designate sites occupied by the United States Implementing Organization (USIO) platform, the R/V *JOIDES Resolution*. For all IODP drill sites, a letter suffix distinguishes each hole drilled at the same site. The first hole drilled is assigned the site number modified by the suffix “A,” the second hole the site number and the suffix “B,” and so on.

Cored intervals are defined by the core top depth in DSF and the distance the driller advanced the bit and/or core barrel in meters. The length of the core is defined by the sum of lengths of the core sections. The CSF depth of a sample is calculated by adding the offset of the sample below the section top and the lengths of all higher sections in the core to the core top depth measured with the drill string (DSF). During Expedition 349, all core depths below seafloor were calculated according to the CSF, Method A (CSF-A), depth scale (see IODP Depth Scales Terminology, v.2, at www.iodp.org/program-policies). To more easily communicate shipboard results, CSF-A depths are reported in this volume as mbsf unless otherwise noted.

Cores taken from a hole are numbered sequentially from the top of the hole downward. When an interval is drilled down, this interval is also numbered sequentially and the drill down designated by a “1” instead of a letter that designates the coring method used (e.g., 349-U1431E-11). Cores taken with the APC system are designated with “H,” “X” designates XCB cores, and “R” designates RCB cores. “G” designates “ghost” cores that are collected while washing down through a previously drilled portion of a hole with a core barrel in place. The core barrel is then retrieved prior to coring the next interval. Core numbers and their associated cored intervals are unique in a given hole. Generally, maximum recovery for a single core is 9.5 m of sediment (APC) or 9.7 m of rock or sediment (XCB/RCB) contained in a plastic liner (6.6 cm internal diameter) plus an additional ~0.2 m in the core catcher, which is a device at the bottom of the core barrel that prevents the core from sliding out when the barrel is retrieved from the hole. In certain situations, recovery may exceed the 9.5 or 9.7 m maximum. In soft sediment, this is normally caused by core expansion resulting from depressurization. In hard rock cores, this typically occurs when a pedestal of rock fails to break off and is grabbed by the core barrel of the subsequent core. High heave, tidal changes, and overdrilling can also result in an advance that differs from the planned 9.5/9.7 m.

Recovered cores are divided into 1.5 m sections that are numbered serially from the top downward (except for Holes U1431A and U1431B, which were cut into sections 0.5 m long to accommodate high-resolution whole-round sampling). When full recovery is obtained, the sections are numbered 1–7, with the last section usually being <1.5 m. Rarely, an unusually long core may require more than seven sections. When the recovered core is shorter than the cored interval, by convention the top of the core is deemed to be located at the top of the cored interval for the purpose of calculating (consistent) depths. When coring hard rock, all pieces recovered are placed immediately adjacent to each other in the core tray. Samples and descriptions of cores are designated by distance, measured in centimeters, from the top of the section to the top and bottom of each sample or interval. By convention, hard rock material recovered from the core catcher is placed below the last section. In sedimentary cores, the core catcher section is treated as a separate section (“CC”). When the only recovered material is in the core catcher, it is placed at the top of the cored interval.

A full curatorial sample identifier consists of the following information: expedition, site, hole, core number, core type, section number, and interval in centimeters measured from the top of the core

section. For example, a sample identification of “349-U1432C-2H-5, 80–85 cm,” represents a sample taken from the interval between 80 and 85 cm below the top of Section 5 of Core 2 (collected using the APC system) of Hole C of Site U1432 during Expedition 349 (Figure F4).

Authorship of site chapters

The separate sections of the site chapters and Methods chapter were written by the following shipboard scientists (authors are listed in alphabetical order; no seniority is implied):

Background and objectives: D.K. Kulhanek, C.-F. Li, J. Lin
 Operations: D.K. Kulhanek, S. Midgley
 Lithostratigraphy: P.D. Clift, K.A. Dadd, S. Hyun, T. Jiang, Z. Liu
 Biostratigraphy: E.A. Brown, I. Hernández-Almeida, Q. Li, C. Liu, R.H. Nagai, A. Peleo-Alampay, X. Su
 Igneous petrology and alteration: A.A.P. Koppers, M.L.G. Tejada, G.-L. Zhang
 Structural geology: W.-W. Ding, Z. Sun
 Geochemistry: R. Bao, Y. Chen, X.-L. Huang
 Microbiology: F.S. Colwell, C. Zhang
 Paleomagnetism: Q. Liu, X. Zhao
 Physical properties: A. Briaes, H.S. Trinh, Y.-C. Yeh, F. Zhang
 Downhole measurements: T. Williams

Lithostratigraphy

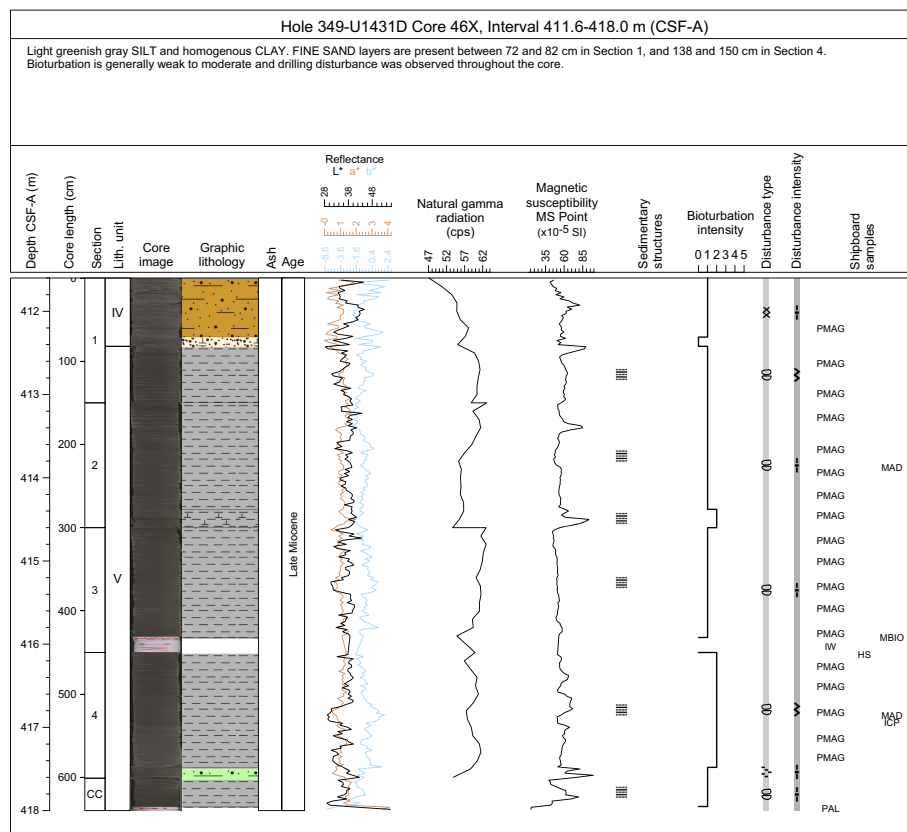
The lithology of sediment recovered during Expedition 349 was primarily determined using observations based on visual (macroscopic) core description, smear slides, and thin sections. In some cases, digital core imaging, color reflectance spectrophotometry, and magnetic susceptibility analysis provided complementary discriminative information. The methods employed during this expedition were similar to those used during Integrated Ocean Drilling Program Expeditions 330 and 339 (Expedition 330 Scientists, 2012; Expedition 339 Scientists, 2013). We used the DESClogik application to record and upload descriptive data into the LIMS database (see the DESClogik user guide at iodp.tamu.edu/labs/documentation). Spreadsheet templates were set up in DESClogik and customized for Expedition 349 before the first core on deck. The templates were used to record visual core descriptions as well as microscopic data from smear slides and thin sections, which were also used to quantify the texture and relative abundance of biogenic and nonbiogenic components. The locations of all smear slide and thin section samples taken from each core were recorded in the Sample Master application. Descriptive data uploaded to the LIMS database were also used to produce the VCD standard graphic reports.

Visual core descriptions

After descriptions of the cores were uploaded into the LIMS database, the data were used to produce VCDs, which include a simplified graphical representation of the core on a section-by-section basis with accompanying descriptions of the features observed (Figures F5, F6, F7). Depending on the type of material recovered, two VCDs were sometimes produced for the same section: one to describe sediments or sedimentary rocks and the other to describe igneous rocks.

Site, hole, and depth in meters below seafloor, calculated according to the CSF-A depth scale, are given at the top of each VCD, with depth of core sections indicated along the left margin. Observations of the physical description of the core correspond to entries in DESClogik, including bioturbation intensity, fossils, ash layers,

Figure F5. Example of the graphic description form (VCD), Expedition 349.



lithologic accessories, sedimentary structures, and drilling disturbance. Symbols used in the VCDs are given in Figures F6 and F7. Additionally, sedimentary VCDs display magnetic susceptibility, natural gamma radiation, color reflectance, and the locations of samples taken for shipboard measurements. Section summary text provides a generalized overview of the core section's lithology and features. This summary text and individual columns shown on the VCDs are described below in greater detail, followed by an outline of the lithostratigraphic classification system used during Expedition 349.

Section summary

A brief overview of major and minor lithologies present in the section, as well as notable features (e.g., sedimentary structures), is presented in the section summary text field at the top of the VCDs. The summary includes sediment color determined qualitatively using Munsell soil color charts. Because sediment color may evolve during drying and subsequent oxidization, color was described shortly after the cores were split and imaged or measured by the SHIL and SHMSL.

Section-half image

The flat faces of the archive halves were scanned with the SHIL as soon as possible after splitting and scraping to avoid color changes caused by sediment oxidation and drying. The SHIL uses three pairs of advanced illumination high-current-focused LED line lights to illuminate large cracks and blocks in the core surface and sidewalls. Each LED pair has a color temperature of 6,500 K and emits 90,000 lx at 3 inches. A line-scan camera images 10 lines/mm to create a high-resolution TIFF file. The camera height was adjusted so that each pixel imaged a 0.1 mm² section of the core. How-

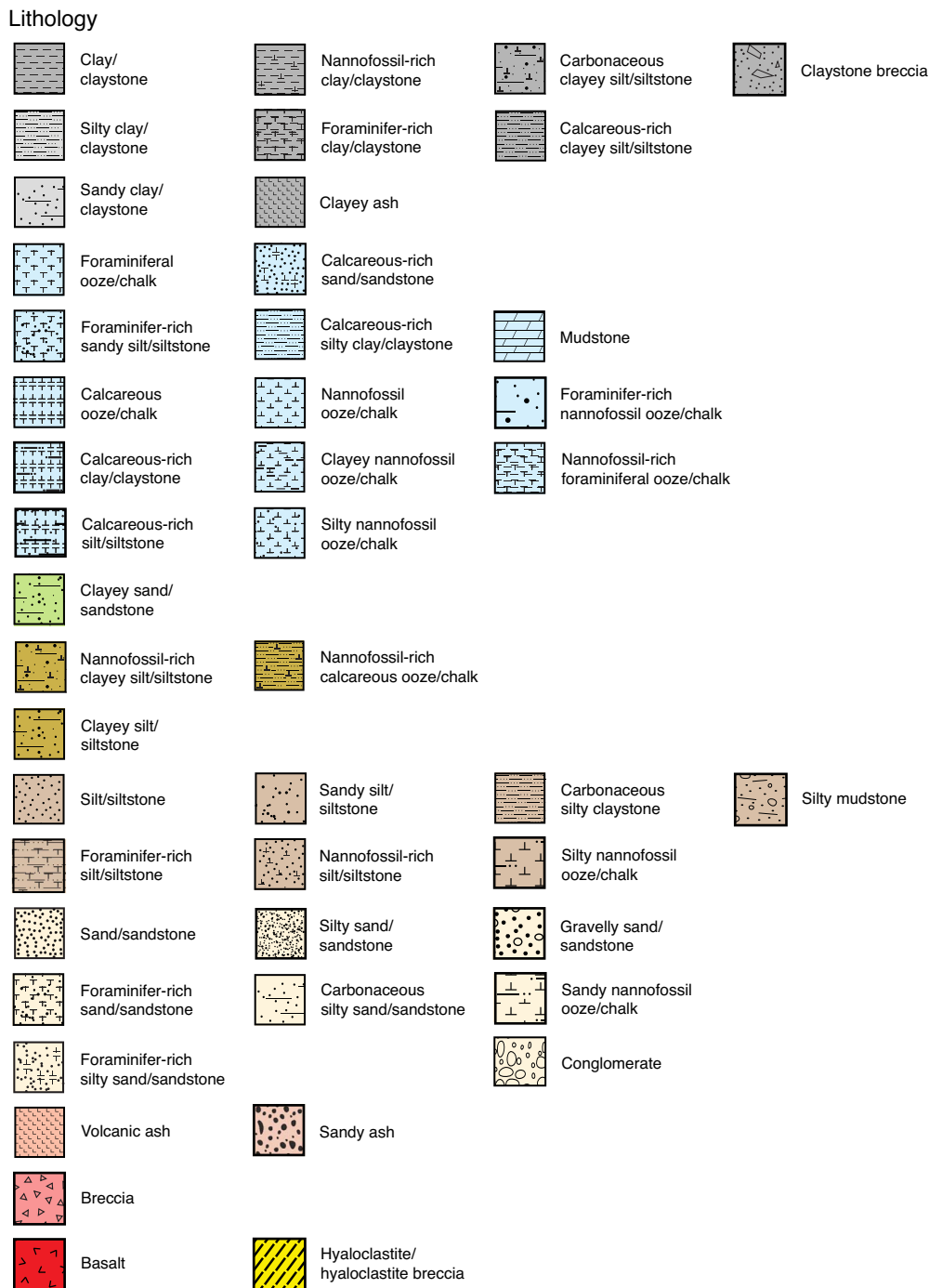
ever, actual core width per pixel varied because of differences in section-half surface height. High- and low-resolution JPEG files were subsequently created from the high-resolution TIFF file. All image files include a gray scale and ruler. Section-half depths were recorded so that these images could be used for core description and analysis.

Graphic lithology

Lithologies of the core intervals recovered are represented on the VCD sheets by graphic patterns in the Graphic lithology column, using the symbols illustrated in Figure F6. The Graphic lithology column on each VCD plots to scale all beds that are at least 2 cm thick. A maximum of two different lithologies (for interbedded sediment) are shown within the same core interval for interlayers <2 cm thick. The major modifier of a primary lithology is shown using a modified version of the primary lithology pattern. Lithologic abundances are rounded to the nearest 10%; lithologies that constitute <10% of the core are generally not shown but are listed in the Description section. However, some distinctive secondary lithologies, such as ash layers, are included graphically in the Graphic lithology column as the primary lithology for a thin stratigraphic interval. Relative abundances of lithologies reported in this way are useful for general characterization of the sediment but do not constitute precise, quantitative observations.

Spectrophotometry and magnetic susceptibility of the archive section halves were measured with the SHMSL. The SHMSL takes measurements in empty intervals and over intervals where the core surface is well below the level of the core liner, but it cannot recognize relatively small cracks, disturbed areas of core, or plastic section dividers. Thus, SHMSL data may contain spurious measurements that have to be edited out of the data set by the user.

Figure F6. Lithology symbols used for visual core description, Expedition 349.



Additional detailed information about measurement and interpretation of spectral data can be found in Balsam et al. (1997, 1998) and Balsam and Damuth (2000).

Spectrophotometry

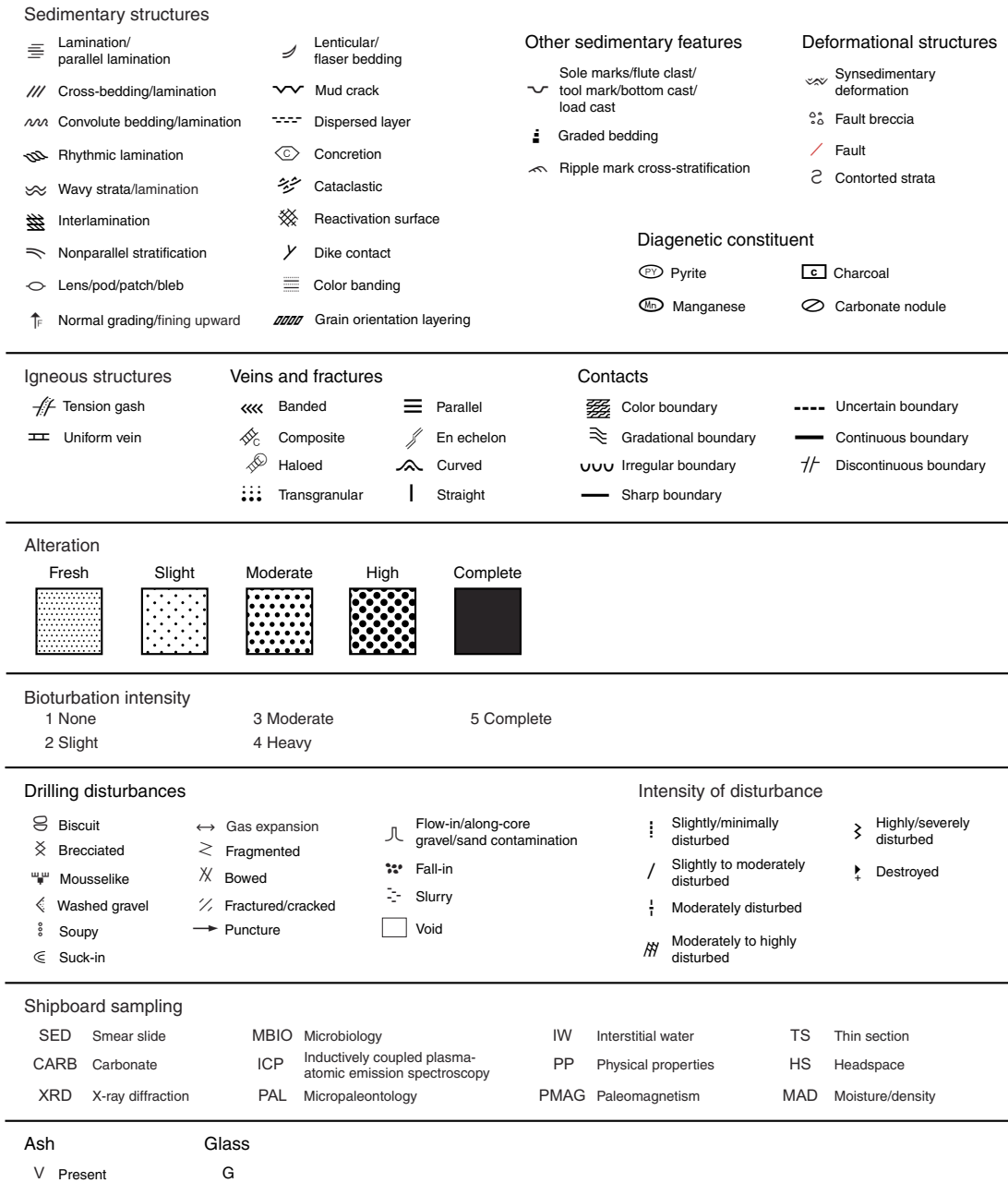
Reflectance of visible light from the archive halves of sediment cores was measured using an Ocean Optics USB4000 spectrophotometer mounted on the automated SHMSL. Freshly split soft cores were covered with clear plastic wrap and placed on the SHMSL. Measurements were taken at 1.0 or 2.0 cm spacings to provide a

high-resolution stratigraphic record of color variations for visible wavelengths. Each measurement was recorded in 2 nm wide spectral bands from 400 to 900 nm. Reflectance parameters of L*, a*, and b* were recorded.

Natural gamma radiation

Natural gamma radiation occurs primarily as a result of the decay of ²³⁸U, ²³²Th, and ⁴⁰K isotopes. This radiation is measured using the NGRL (see [Physical properties](#)). Data generated from this instrument are used to augment geologic interpretations.

Figure F7. Symbols and nomenclature used for visual core description, Expedition 349.



Magnetic susceptibility

Magnetic susceptibility was measured with a Bartington Instruments MS2E point sensor (high-resolution surface-scanning sensor) on the SHMSL. Because the SHMSL demands flush contact between the magnetic susceptibility point sensor and the split core, measurements were made on the archive halves of split cores that were covered with clear plastic wrap. Measurements were taken at 1.0 or 2.0 cm spacings. Measurement resolution was 1.0 SI, and each measurement integrated a volume of 10.5 mm × 3.8 mm × 4 mm, where 10.5 mm is the length perpendicular to the core axis, 3.8 mm is the width along the core axis, and 4 mm is the depth into the core. Only one measurement was taken at each measurement position.

Sedimentary structures

The locations and types of stratification and sedimentary structures visible on the prepared surfaces of the split cores are shown in the Sedimentary structures column of the VCD sheet. Symbols in this column indicate the locations and scales of interstratification, as well as the locations of individual bedding features and any other sedimentary features, such as sole marks, cross-lamination, and upward-fining intervals (Figure F7).

For Expedition 349, the following terminology (based on Stow, 2005) was used to describe the scale of stratification:

- Thin lamination = <3 mm thick.
- Medium lamination = 0.3–0.6 cm thick.
- Thick lamination = 0.6–1 cm thick.

Very thin bed = 1–3 cm thick.
 Thin bed = 3–10 cm thick.
 Medium bed = 10–30 cm thick.
 Thick bed = 30–100 cm thick.
 Very thick bed = >100 cm thick.

Lithologic accessories

Some postdepositional features (e.g., concretions) and grains of special interest (e.g., pumice and coated grains) are recorded in the Lithologic accessories column.

Bioturbation intensity

Five levels of bioturbation are recognized using a scheme similar to that of Droser and Bottjer (1986). These levels are illustrated with a numeric scale in the Bioturbation intensity column. Any identifiable trace fossils (ichnofossils) are identified in the bioturbation comments in the core description.

- 1 = no bioturbation.
- 2 = slight bioturbation (<10%–30%).
- 3 = moderate bioturbation (30%–60%).
- 4 = heavy bioturbation (60%–90%).
- 5 = complete bioturbation (>90%).

Sediment disturbance

Drilling-related sediment disturbance is recorded in the Disturbance type column using the symbols shown in Figure F7. The style of drilling disturbance is described for soft and firm sediments using the following terms:

- Fall-in: out-of-place material at the top of a core has fallen downhole onto the cored surface.
- Bowed: bedding contacts are slightly to moderately deformed but still subhorizontal and continuous.
- Flow-in, coring/drilling slurry, along-core gravel/sand contamination: soft-sediment stretching and/or compressional shearing structures are severe and are attributed to coring/drilling. The particular type of deformation may also be noted (e.g., flow-in, gas expansion, etc.).
- Soupy or mousse-like: intervals are water saturated and have lost all aspects of original bedding.
- Biscuit: sediments of intermediate stiffness show vertical variations in the degree of disturbance. Softer intervals are washed and/or soupy, whereas firmer intervals are relatively undisturbed.
- Cracked or fractured: firm sediments are broken but not displaced or rotated significantly.
- Fragmented or brecciated: firm sediments are pervasively broken and may be displaced or rotated.

The degree of fracturing within indurated sediments is described using the following categories:

- Slightly fractured: core pieces are in place and broken.
- Moderately fractured: core pieces are in place or partly displaced, but original orientation is preserved or recognizable.
- Highly fractured: core pieces are probably in correct stratigraphic sequence, but original orientation is lost.
- Drilling breccia: core is crushed and broken into many small and angular pieces, with original orientation and stratigraphic position lost.

Age

The subepoch that defines the age of the sediments was provided by the shipboard biostratigraphers (see [Biostratigraphy](#)) and is listed in the Age column.

Samples

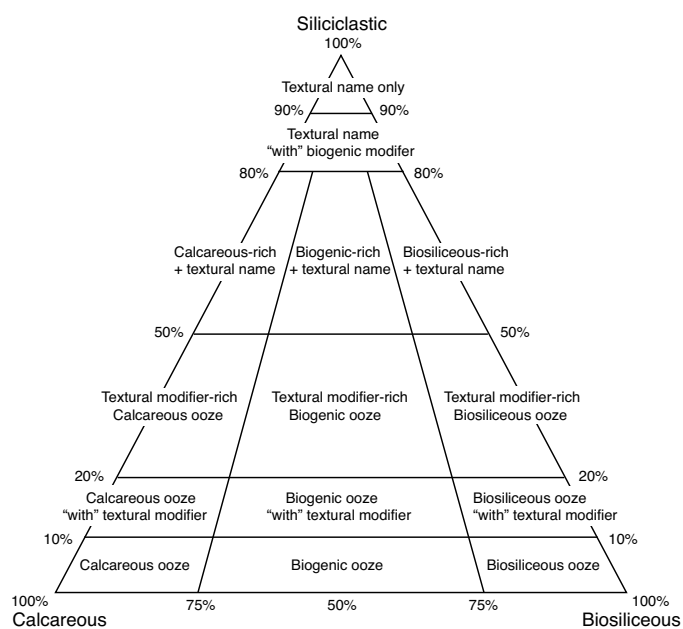
The exact positions of samples used for microscopic descriptions (i.e., smear slides and thin sections), biochronological determinations, and shipboard analysis of chemical and physical properties of sediment are recorded in the Shipboard samples column.

Sediment classification

The sediment recovered during Expedition 349 is composed of biogenic and siliciclastic components and is described using a classification scheme derived from Expedition 339 (Expedition 339 Scientists, 2013) and Stow (2005). The biogenic component is composed of the skeletal debris of open-marine calcareous and siliceous microfauna (e.g., foraminifers and radiolarians), microflora (e.g., calcareous nannofossils and diatoms), and macrofossil shell fragments. The siliciclastic component is composed of mineral and rock fragments derived from igneous, sedimentary, and metamorphic rocks. The relative proportion of these two components is used to define the major classes of sediment in this scheme (Figure F8).

Naming conventions for Expedition 349 follow the general guidelines of the Ocean Drilling Program (ODP) sediment classification scheme (Mazzullo et al., 1988), with the exception that a separate “mixed sediment” category was not distinguished during Expedition 349. As a result, biogenic sediment is that which contains >50% biogenic grains and <50% siliciclastic grains, whereas siliciclastic sediment is that which contains >50% siliciclastic grains and <50% biogenic grains. Sediment containing >50% silt- and sand-sized primary volcanic grains is classified as an ash layer. We follow

Figure F8. Siliciclastic-calcareous-biosiliceous ternary diagram used for sediment names of different compositions.



the naming scheme of Shepard (1954) for the classification of siliciclastic sediment and sedimentary rock depending on the relative proportion of sediment of different grain sizes (Figure F9). Sediment grain size divisions for both biogenic and siliciclastic components are based on Wentworth (1922), with eight major textural categories defined on the basis of the relative proportions of sand-, silt-, and clay-sized particles (Figure F10); however, distinguishing between some of these categories can be difficult (e.g., silty clay versus sandy clay) without accurate measurements of grain size abundances. The term “clay” is only used to describe particle size and is applied to both clay minerals and all other grains <4 μm in size.

The lithologic names assigned to sediment consists of a principal name and prefix based on composition and degree of lithification and/or texture as determined from visual description of the cores and from smear slide observations.

For a sediment that contains >90% of one component (either the siliciclastic or biogenic component), only the principal name is used. For sediments with >90% biogenic components, the name applied indicates the most common type of biogenic grain. For example, a sediment composed of >90% calcareous nannofossils is called a nannofossil ooze/chalk, and a sediment composed of 50% foraminifers and 45% calcareous nannofossils is called a calcareous ooze/chalk. For sediment with >90% siliciclastic grains, the principal name is based on the textural characteristics of all sediment particles (both siliciclastic and biogenic) (Figure F9).

For sediment that contains a significant mixture of siliciclastic and biogenic components (between 10% and 90% of both siliciclastic and biogenic components), the principal name is determined by the more abundant component. If the siliciclastic component is more abundant, the principal name is based on the textural characteristics of all sediment particles (both siliciclastic and biogenic) (Figure F9). If the biogenic component is more abundant, the principal name is based on the predominant biogenic component.

If a microfossil group composes 10%–50% of the sediment and this group is not included as part of the principal name, minor modifiers are used. When a microfossil group (e.g., diatom, nannofossil, or foraminifer) comprises 20%–50% of the sediment, a minor modifier consisting of the component name hyphenated with the suffix “-rich” (e.g., diatom-rich clay) is used.

If one component forms 80%–90% of the sediment, the principal name is followed by a minor modifier (e.g., “with diatoms”), with the minor modifier based on the most abundant component that forms 10%–20% of the sediment. If the minor component is biogenic, then the modifier describes the group of biogenic grains that exceeds the 10% abundance threshold. If the minor component is siliciclastic, the minor modifier is based on the texture of the siliciclastic fraction.

If the primary lithology for an interval of core has a major modifier, then that major modifier is indicated in the Graphic lithology column of the VCD sheets using a modified version of the lithologic pattern for the primary lithology (Figure F5). The modified lithologic patterns are shown in Figure F6. The minor modifiers of sediment lithologies are not included in the Graphic lithology column.

The following terms describe lithification that varies depending on the dominant composition:

Figure F9. Lithologic classification for textural names. A. Shepard ternary classification diagram (Shepard, 1954). B. Biogenic classification. D = diatom.

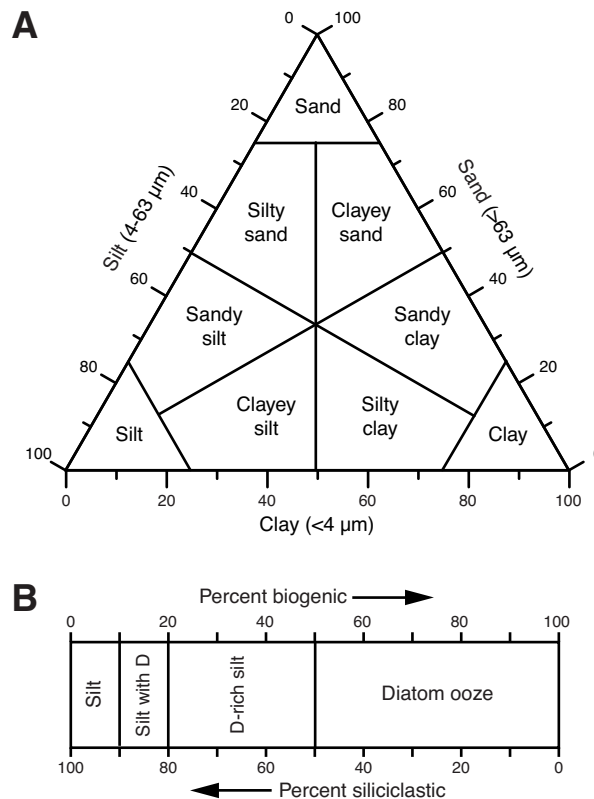


Figure F10. Udden-Wentworth grain-size classification of terrigenous sediment (Wentworth, 1922).

Millimeters (mm)	Micrometers (μm)	Phi (φ)	Wentworth size class
4096		-12.0	Boulder
256		-8.0	Cobble
64		-6.0	Pebble
4		-2.0	Granule
2.00		-1.0	Very coarse sand
1.00		0.0	Coarse sand
1/2	0.50	1.0	Medium sand
1/4	0.25	2.0	Fine sand
1/8	0.125	3.0	Very fine sand
1/16	0.0625	4.0	Coarse silt
1/32	0.031	5.0	Medium silt
1/64	0.0156	6.0	Fine silt
1/128	0.0078	7.0	Very fine silt
1/256	0.0039	8.0	Clay
0.00006	0.06	14.0	

- Sediment composed predominantly of calcareous, pelagic organisms (e.g., calcareous nannofossils and foraminifers): the lithification terms “ooze” and “chalk” reflect whether the sediment can be deformed with a finger (ooze) or can be scratched easily by a fingernail (chalk).
- Sediment composed predominantly of siliceous microfossils (diatoms, radiolarians, and siliceous sponge spicules): the lithification terms “ooze” and “radiolarite/diatomite” reflect whether the sediment can be deformed with a finger (ooze) or cannot be easily deformed manually (radiolarite/diatomite).
- Sediment composed of a mixture of calcareous pelagic organisms and siliceous microfossils and sediment composed of a mixture of siliceous microfossils: the lithification terms “ooze” and “indurated sediment” reflect whether the sediment can be deformed with a finger (ooze) or cannot be easily deformed manually (indurated sediment).
- Sediment composed predominantly of siliciclastic material: if the sediment can be deformed easily with a finger, no lithification term is added and the sediment is named for the dominant grain size (i.e., sand, silt, or clay). For more consolidated material, the lithification suffix “-stone” is appended to the dominant size classification (e.g., claystone), except for gravel-sized sediment, when the terms conglomerate or breccia are used.

The subclassification of volcanoclastic sediments followed here differs from the standard ODP classification (Mazzullo et al., 1988) in that we adopted a descriptive (nongenetic) terminology similar to that employed during ODP Leg 197 (Shipboard Scientific Party, 2002) and Integrated Ocean Drilling Program Expedition 324 (Expedition 324 Scientists, 2010). Unless an unequivocally pyroclastic origin for volcanogenic particles could be determined, we simply described these deposits as for siliciclastic sediment (i.e., sand, silt, etc.).

Where evidence for a pyroclastic origin was compelling, we adopted the classification scheme of Fisher and Schmincke (1984). In these instances, we used the grain size terms “volcanic blocks” (>64 mm), “lapilli/lapillistone” (2–64 mm), and “ash/tuff” (<2 mm). The term “hyaloclastite” was used for vitroclastic (i.e., glassy) materials produced by the interaction of water and hot magma or lava (Fisher and Schmincke, 1984).

Smear slide observation

Two or more smear slide samples of the main lithologies were collected from the archive half of each core when the sediment was not lithified. Additional samples were collected from areas of interest (e.g., laminations, ash layers, and nodules). A small amount of sediment was taken with a wooden toothpick and put on a 2.5 cm × 7.5 cm glass slide. The sediment sample was homogenized with a drop of deionized water and evenly spread across the slide to create a very thin (about <50 μm) uniform layer of sediment grains for quantification. The dispersed sample was dried on a hot plate. A drop of Norland optical adhesive was added as a mounting medium to a coverslip, which was carefully placed on the dried sample to prevent air bubbles from being trapped in the adhesive. The smear slide was then cured in an ultraviolet light box.

Smear slides were examined with a transmitted-light petrographic microscope equipped with a standard eyepiece micrometer. The texture of siliciclastic grains (relative abundance of sand-, silt-, and clay-sized grains) and the proportions and presence of biogenic and mineral components were recorded and entered into DESC-logik. Biogenic and mineral components were identified, and their percentage abundances were visually estimated using Rothwell

(1989). The mineralogy of clay-sized grains could not be determined from smear slides. Note that smear slide analyses tend to underestimate the amount of sand-sized and larger grains because these grains are difficult to incorporate onto the slide.

X-ray diffraction analyses

Since the shipboard X-ray diffractometer was unavailable during Expedition 349, samples for X-ray diffraction (XRD) were analyzed onshore following the expedition. Quantitative mineralogy of shipboard samples was analyzed using a PANalytical X'Pert PRO XRD at the State Key Laboratory of Marine Geology, Tongji University (China). About 3 g of sample (bulk sediment or sedimentary rock) was first dried in an oven at 60°C for 24 h. The sample was then powdered in an agate mortar. A sample holder with a hole 20 mm in diameter and 2.5 mm depth was filled with a random orientation of grains. The analysis was processed from 3° to 85°2θ at 0.0334°2θ step size, with CuKα radiation and Ni filter, under a voltage of 45 kV and an intensity of 40 mA. The sample holder was rotated at 60 rotations/min during scanning. The X'Pert HighScore Plus (version 2.2.5) software was used for identification and semi-quantitative calculation of individual minerals. The average accuracy error for most minerals using this method is ±5%. XRD data are available in XRD in [Supplementary material](#).

Biostratigraphy

During Expedition 349, calcareous nannofossils, radiolarians, and planktonic foraminifers in core catcher samples were studied at all sites. Samples from core sections were also examined when a more refined age determination was necessary and when time permitted. Biostratigraphic events, mainly the first appearance datum (FAD; or base) and last appearance datum (LAD; or top) of the diagnostic species, are tied to the geomagnetic polarity timescale (GPTS) of Gradstein et al. (2012) (Figures [F11](#), [F12](#), [F13](#)).

Calcareous nannofossils

Calcareous nannofossil zonation was based on the schemes of Okada and Bukry (1980) and Martini (1971). Calibrated ages for bioevents are from Gradstein et al. (2012) and given in Table [T1](#). The timescale of Gradstein et al. (2012) assigns the Pleistocene/Pliocene boundary between the Gelasian and Piacenzian stages (2.59 Ma), the Pliocene/Miocene boundary between the Zanclean and Messinian stages (5.33 Ma), and the late/middle Miocene boundary at 11.63 Ma. For calcareous nannofossil biostratigraphy, the Pleistocene/Pliocene boundary now falls within Zone NN16 (Martini, 1971), between the LADs of *Discoaster surculus* (2.49 Ma) and *Discoaster tamalis* (2.8 Ma). The Pliocene/Miocene boundary falls within Zone NN12, between the LAD of *Triquetrorhabdulus rugosus* (5.28 Ma) and the FAD of *Ceratolithus larrymayeri* (5.34 Ma); however, *C. larrymayeri* was not noted in our samples, so we use the FAD of *Ceratolithus acutus* (5.35 Ma) as an alternative event. The late/middle Miocene boundary is placed within Zone NN7, between the last common appearance of *Discoaster kugleri* (11.58 Ma) and the first common appearance of *D. kugleri* (11.90 Ma). In this study, the identification of these geological time boundaries was mostly based on recognition of these nannofossil bioevents.

Several species of the genus *Gephyrocapsa*, which are commonly used as Pleistocene biostratigraphic markers, often show a great range of variation in sizes and other morphological features, causing problems in identification (e.g., Samtleben, 1980; Su, 1996;

Figure F11. GPTS (Gradstein et al., 2012), biostratigraphic zonations, and microfossil events from 0 to 13 Ma used during Expedition 349. B = base, T = top, Bc = base common, Tc = top common, Ba = base acme, Ta = top acme, Br = base regular, Tr = top regular, X = crossover in abundance.

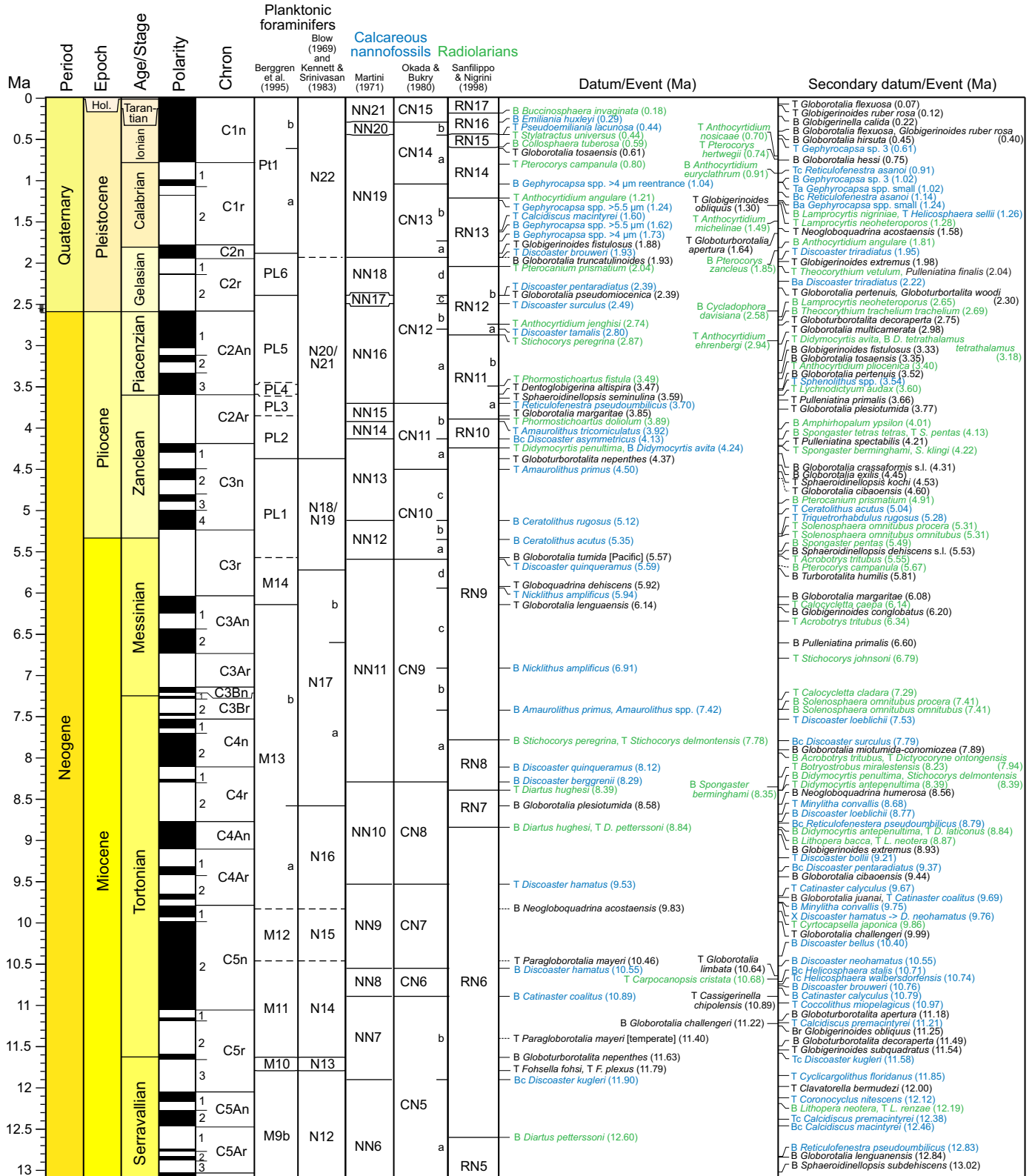


Figure F12. GPTS (Gradstein et al., 2012), biostratigraphic zonations, and microfossil events from 12.5 to 26.5 Ma used during Expedition 349. B = base, T = top, Bc = base common, Tc = top common, Ba = base acme, Ta = top acme, Br = base regular, Tr = top regular, X = crossover in abundance.

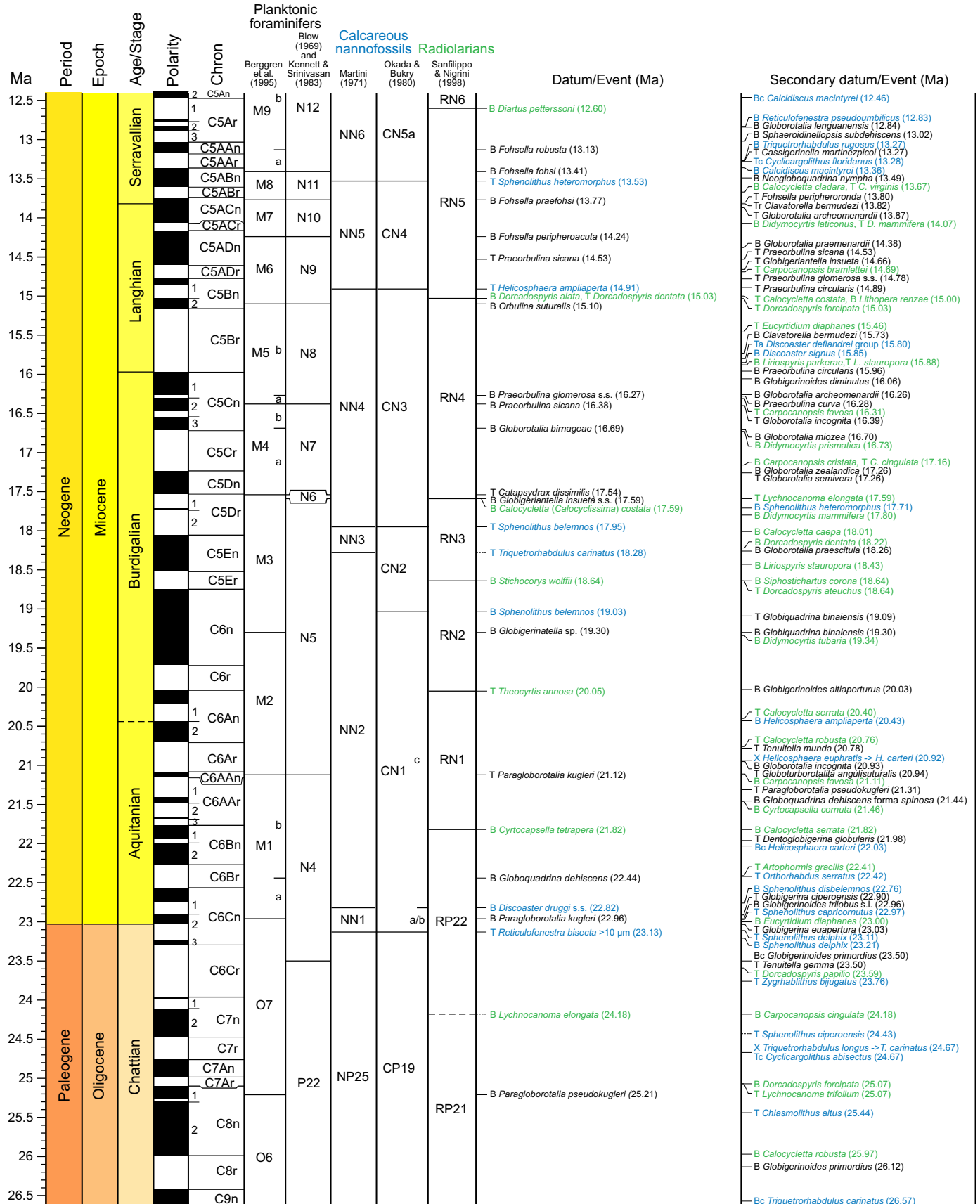


Figure F13. GPTS (Gradstein et al., 2012), biostratigraphic zonations, and microfossil events from 26 to 40 Ma used during Expedition 349. B = base, T= top, Bc = base common, Tc = top common, Ba = base acme, Ta = top acme, Br = base regular, Tr = top regular, X = crossover in abundance.

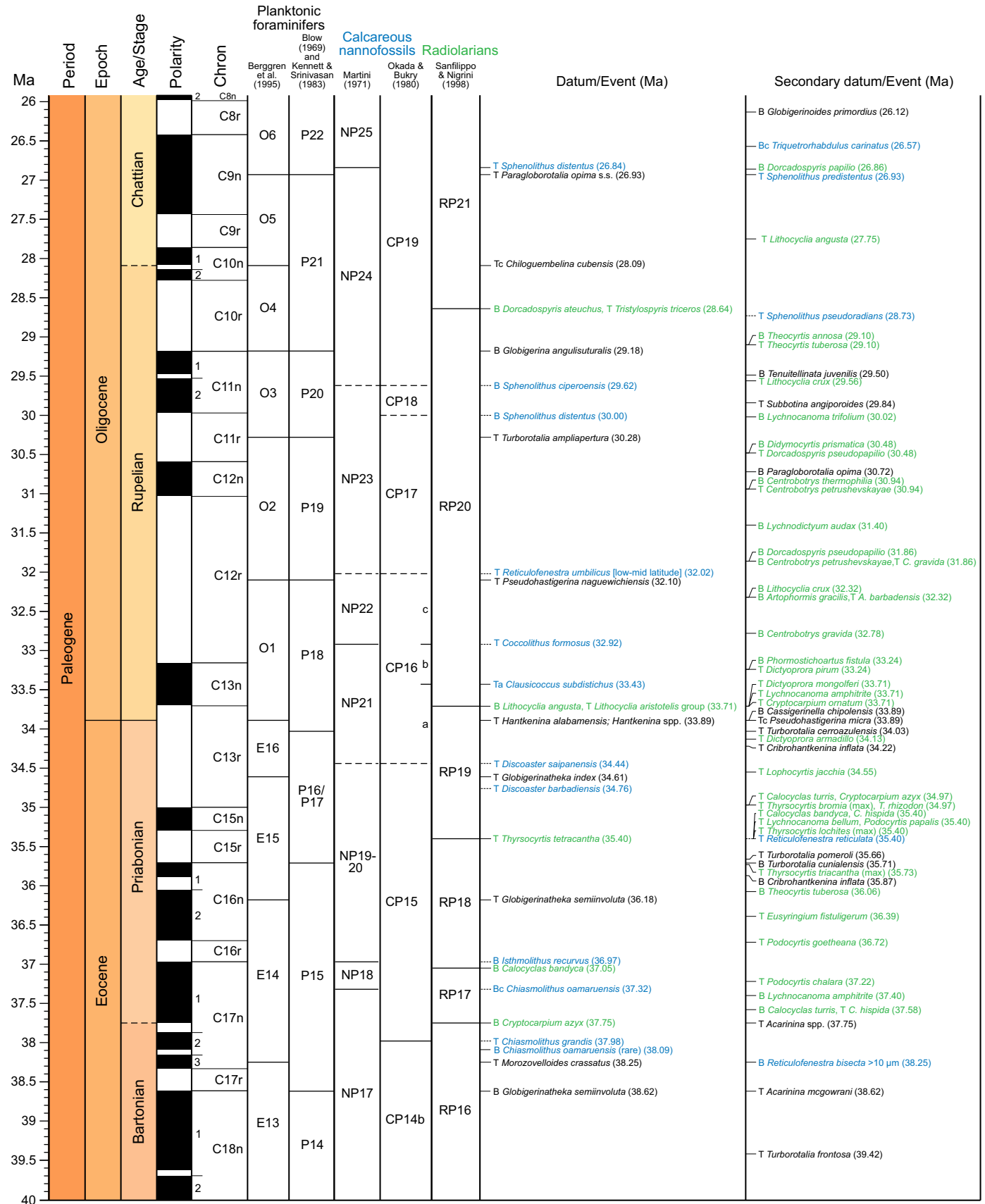


Table T1. Calcareous nannofossil events and ages (Gradstein et al., 2012 [GTS2012]) used during Expedition 349. T = top/last appearance datum, B = base/first appearance datum, Bc = base common, Tc = top common, Ba = base acme, Ta = top acme, X = crossover. Bold = zonal boundary definition. (Continued on next page.) [Download table in .csv format.](#)

GTS2012 chronostratigraphy (age)	Standard tropical–subtropical zonation		Datum/Event	GTS2012 age (Ma)
	Okada and Bukry (1980)	Martini (1971)		
0.126 Ma				
Ionian (M. Pleist.)	CN15/CN14b	NN21/NN20	B <i>Emiliania huxleyi</i>	0.29
	CN14b/CN14a	NN20/NN19	T <i>Pseudoemiliania lacunosa</i>	0.44
0.781 Ma	CN14a	NN19	T <i>Gephyrocapsa</i> sp. 3	0.61
Calabrian (e. Pleist.)			Tc <i>Reticulofenestra asanoi</i>	0.91
			B <i>Gephyrocapsa</i> sp. 3	1.02
			Ta <i>Gephyrocapsa</i> spp. small	1.02
	CN14a/CN13b		B <i>Gephyrocapsa</i> spp. >4 µm reentrance (reemG event)	1.04
	CN13b	NN19	Bc <i>Reticulofenestra asanoi</i>	1.14
			T <i>Gephyrocapsa</i> spp. >5.5 µm	1.24
			Ba <i>Gephyrocapsa</i> spp. small	1.24
			T <i>Helicosphaera sellii</i>	(1.26)
			T <i>Calcidiscus macintyreii</i>	1.60
			B <i>Gephyrocapsa</i> spp. >5.5 µm	1.62
	CN13b/CN13a		B <i>Gephyrocapsa</i> spp. >4 µm (= bmG event)	1.73
1.806 Ma	CN13a			
	CN13a/CN12d	NN19/NN18	T <i>Discoaster brouweri</i>	1.93
Gelasian (e. Pleist.)	CN12d	NN18	T <i>Discoaster triradiatus</i>	1.95
	CN12d/CN12c	NN18/NN17	Ba <i>Discoaster triradiatus</i>	2.22
	CN12c/CN12b	NN17/NN16	T <i>Discoaster pentaradiatus</i>	2.39
			T <i>Discoaster surculus</i>	2.49
2.588 Ma	CN12b	NN16		
Piacenzian (l. Pliocene)	CN12b/CN12a		T <i>Discoaster tamalis</i>	2.80
3.6 Ma	CN12a		T <i>Sphenolithus</i> spp.	3.54
	CN12a/CN11b	NN16/NN15	T <i>Reticulofenestra pseudumbilicus</i>	3.70
Zanclean (e. Pliocene)	CN11b	NN15/NN14	T <i>Amaurolithus tricorniculatus</i>	(3.92)
	CN11b/CN11a	NN14/NN13	Bc <i>Discoaster asymmetricus</i>	4.13
	CN11a/CN10c		T <i>Amaurolithus primus</i>	4.50
		NN13		
		CN10c/CN10b	NN13/NN12	T <i>Ceratolithus acutus</i>
			B <i>Ceratolithus rugosus</i>	5.12
5.333 Ma	CN10b	NN12	T <i>Triquetrorhabdulus rugosus</i>	5.28
	CN10b/CN10a			
Messinian (l. Miocene)	CN10a/CN9d	NN12/NN11	B <i>Ceratolithus acutus</i>	5.35
	CN9d/CN9c		T <i>Discoaster quinqueramus</i>	5.59
	CN9c/CN9b		T <i>Nicklithus amplificus</i>	5.94
7.246 Ma	CN9b	NN11	B <i>Nicklithus amplificus</i>	6.91
CN9b/CN9a			B <i>Amaurolithus primus</i> , <i>Amaurolithus</i> spp.	7.42
	CN9a		T <i>Discoaster loeblichii</i>	7.53
			Bc <i>Discoaster surculus</i>	7.79
			B <i>Discoaster quinqueramus</i>	(8.12)
	CN9a/CN8	NN11/NN10	B <i>Discoaster berggrenii</i>	8.29
Tortonian (l. Miocene)			T <i>Minylitha convallis</i>	8.68
			B <i>Discoaster loeblichii</i>	8.77
		CN8	Bc <i>Reticulofenestra pseudumbilicus</i>	8.79
			T <i>Discoaster bollii</i>	9.21
			Bc <i>Discoaster pentaradiatus</i>	9.37
		CN8/CN7	NN10/NN9	T <i>Discoaster hamatus</i>
			T <i>Catinaster calyculus</i>	9.67
			T <i>Catinaster coalitus</i>	9.69
			B <i>Minylitha convallis</i>	9.75
			X <i>Discoaster hamatus</i> → <i>D. neohamatus</i>	9.76
			B <i>Discoaster bellus</i>	10.40
			B <i>Discoaster neohamatus</i>	10.52
	CN7/CN6	NN9/NN8	B <i>Discoaster hamatus</i>	10.55
			Bc <i>Helicosphaera stalis</i>	10.71
			Tc <i>Helicosphaera walbersdorfensis</i>	10.74
			B <i>Discoaster brouweri</i>	10.76
			B <i>Catinaster calyculus</i>	10.79

Table T1 (continued).

GTS2012 chronostratigraphy (age)	Standard tropical–subtropical zonation		Datum/Event	GTS2012 age (Ma)	
	Okada and Bukry (1980)	Martini (1971)			
Tortonian (l. Miocene)	CN6/CN5b	NN8/NN7	B Catinaster coalitus	10.89	
	CN5b	NN7	T <i>Coccolithus miopelagicus</i> T <i>Calcidiscus premacintyre</i> Tc <i>Discoaster kugleri</i>	10.97 11.21 11.58	
11.608 Ma					
Serravallian (m. Miocene)	CN5b/CN5a	NN7/NN6	T <i>Cyclicargolithus floridanus</i>	11.85	
	CN5a	NN6	Bc Discoaster kugleri T <i>Coronocyclus nitescens</i> Tc <i>Calcidiscus premacintyre</i> Bc <i>Calcidiscus macintyre</i> B <i>Reticulofenestra pseudoumbilicus</i> B <i>Triquetrorhabdulus rugosus</i> Tc <i>Cyclicargolithus floridanus</i> B <i>Calcidiscus macintyre</i>	11.90 12.12 12.38 12.46 12.83 13.27 13.28 13.36	
	CN5a/CN4	NN6/NN5	T Sphenolithus heteromorphus	13.53	
	CN4	NN5			
13.82 Ma					
Langhian (m. Miocene)	CN4/CN3	NN5/NN4	T Helicosphaera ampliaperta	14.91	
	CN3	NN4	Ta <i>Discoaster deflandrei</i> group B <i>Discoaster signus</i>	15.80 15.85	
15.97 Ma					
Burdigalian (e. Miocene)	CN3/CN2	NN4/NN3	B <i>Sphenolithus heteromorphus</i>	17.71	
	CN2/CN1c	NN3/NN2	T Sphenolithus belemnus	17.95	
	CN1c	NN2	T Triquetrorhabdulus carinatus B <i>Sphenolithus belemnus</i> B <i>Helicosphaera ampliaperta</i> X <i>Helicosphaera euphratis</i> @ <i>H. carteri</i>	18.28 19.03 20.43 20.92	
(20.44) Ma					
Aquitanian (e. Miocene)	CN1c/CN1a-b	NN2/NN1	Bc <i>Helicosphaera carteri</i> T <i>Orthorhabdus serratus</i> B <i>Sphenolithus disbelemnus</i>	22.03 22.42 22.76	
	CN1a-b	NN1	B Discoaster druggi (sensu stricto) T <i>Sphenolithus capricornutus</i>	22.82 22.97	
	CN1a-b	NN1	T <i>Sphenolithus delphix</i>	23.11	
Chattian (l. Oligocene)	CN1a-b/CP19b	NN1/NP25	T Reticulofenestra bisecta (>10 μm)	23.13	
	CP19b	NP25	B <i>Sphenolithus delphix</i> T <i>Zygrhablithus bijugatus</i> T <i>Sphenolithus ciproensis</i> X <i>Triquetrorhabdulus longus</i> → <i>T. carinatus</i> Tc <i>Cyclicargolithus abisectus</i> T <i>Chiasmolithus altus</i> Bc <i>Triquetrorhabdulus carinatus</i>	23.21 23.76 24.43 ?? 24.67 25.44 26.57	
	CP19b/CP19a	NP25/NP24	T Sphenolithus distentus	26.84	
	CP19a	NP24	T <i>Sphenolithus predistentus</i>	26.93	
	(28.09) Ma				
	Rupelian (e. Oligocene)	CP19a/CP18	NP24/NP23	T <i>Sphenolithus pseudoradians</i>	28.73
		CP18/CP17	NP23	B Sphenolithus ciproensis	29.62
CP17/CP16c		NP23/NP22	B <i>Sphenolithus distentus</i>	30.00	
CP16c/CP16b		NP22/NP21	T Reticulofenestra umbilicus (low–mid latitude)	32.02	
CP16b/CP16a		NP21	T Coccolithus formosus	32.92	
33.89 Ma					
Priabonian (l. Eocene)	CP16a		Ta <i>Clausiococcus subdistichus</i>	33.43	
	CP16a/CP15	NP21/NP20-19	T Discoaster saipanensis	34.44	
	CP15	NP20-19	T <i>Discoaster barbadiensis</i> T <i>Reticulofenestra reticulata</i>	34.76 35.40	
		NP20-19/NP18	B Isthmolithus recurvus	36.97	
NP18/NP17		Bc Chiasmolithus oamaruensis	37.32		
(37.75) Ma					
Bartonian (m. Eocene)	CP15/CP14b	NP17	T <i>Chiasmolithus grandis</i>	37.98	
	CP14b		B <i>Chiasmolithus oamaruensis</i> (rare) B <i>Reticulofenestra bisecta</i> (>10 μm)	38.09 38.25	
	CP14b/CP14a		NP17/NP16	T Chiasmolithus solitus	40.40

Bollmann, 1997). Size-defined morphological groups of this genus (Young, 1998; Maiorano and Marino, 2004; Lourens et al., 2004; Raffi et al., 2006) were used as event markers during shipboard study, including the groups *Gephyrocapsa* sp. 3, medium *Gephyrocapsa* spp. ($\geq 4 \mu\text{m}$), large *Gephyrocapsa* spp. ($\geq 5.5 \mu\text{m}$), and small *Gephyrocapsa* spp. ($< 3.5 \mu\text{m}$).

Several *Reticulofenestra* species with different coccolith and central opening sizes have been used as Neogene and Quaternary biostratigraphic markers; however, these parameters show considerable variations within and between “species,” making species differentiation difficult (e.g., Young, 1998; Su, 1996). In this study, we followed the definition of *Reticulofenestra pseudoumbilicus* by Young (1998) as having a maximum coccolith length $> 7 \mu\text{m}$ (similar to the size of its holotype), especially for specimens from its uppermost range in the early Pliocene. We distinguished *Reticulofenestra asanoi* from the similarly sized *Pseudoemiliana lacunosa* by the absence of slits on the shield (Su, 1996).

The LAD of *Sphenolithus* spp. (3.54 Ma) in Pliocene Zone NN16 was based on the LAD of *Sphenolithus abies* and *Sphenolithus neobabies* according to Raffi et al. (2006). Species concepts for other taxa mainly follow those of Perch-Nielsen (1985) and Bown (1998).

Methods

Calcareous nannofossil samples were prepared using standard smear slide techniques. For sandy sediment, suspended aliquots of the raw sample were utilized for analysis. Samples were examined with a Zeiss microscope under cross-polarized and plane-transmitted or phase contrast light at 1000 \times to 2000 \times magnification. A Hitachi TM3000 tabletop scanning electron microscope (SEM) was used to confirm the presence of small forms. Preservation of nannofossils was noted as follows:

- VG = very good (no evidence of dissolution and/or overgrowth).
- G = good (slight dissolution and/or overgrowth; specimens identifiable to the species level).
- M = moderate (some etching and/or overgrowth; most specimens identifiable to the species level).
- P = poor (severely etched or with overgrowth; most specimens cannot be identified at the species and/or generic level).

The relative abundance of calcareous nannofossils within the sediment was visually estimated at 500 \times magnification by referring to the particle abundance charts in Rothwell (1989) and reported using the following abundance categories:

- D = dominant ($> 90\%$ of sediment particles).
- A = abundant ($> 50\%$ – 90% of sediment particles).
- C = common ($> 10\%$ – 50% of sediment particles).
- F = few (1% – 10% of sediment particles).
- R = rare ($< 1\%$ of sediment particles).
- B = barren (no nannofossils present in 100 fields of view [FOV]).

The relative abundance of individual calcareous nannofossil species or taxa groups was estimated at 1000 \times magnification:

- D = dominant ($> 50\%$, or 100 specimens per FOV).
- A = abundant (10% – 50% , or 10–100 specimens per FOV).
- C = common (10% – 10% , or 1–10 specimens per FOV).
- F = few (0.1% – 1% , or 1 specimen per 1–10 FOV).
- R = rare ($< 0.1\%$, or < 1 specimen per 10 FOV).

Planktonic foraminifers

The planktonic foraminiferal zonation schemes of Blow (1969, 1979) and Berggren et al. (1995), as modified by Wade et al. (2011),

were used in this study. Calibrated ages for bioevents are from Gradstein et al. (2012), as given in Table T2. We also adopted the use of the LAD (0.12 Ma; Thompson et al., 1979) and FAD (0.40 Ma; Li, 1997) of *Globigerinoides ruber* (pink) as biostratigraphic indicators.

Taxonomic concepts for Neogene and Paleogene taxa mainly follow those of Kennett and Srinivasan (1983) and Bolli and Saunders (1985).

Methods

Core catcher samples (plus one sample per section, as needed) were soaked in distilled water or in a weak hydrogen peroxide solution when necessary, warmed on a hot plate, and washed over a 63 μm mesh sieve. Lithified material was crushed to pea size, heated in a hydrogen peroxide solution, and then sieved as above. All samples were dried in a $< 60^\circ\text{C}$ oven. The dried samples were sieved over a 150 μm sieve, retaining the $< 150 \mu\text{m}$ size fraction for additional observation when necessary. The $> 150 \mu\text{m}$ size fraction specimens were examined under a Zeiss Discovery V8 microscope. The total abundance of planktonic foraminifers was defined as follows:

- A = abundant ($> 30\%$ planktonic foraminifer specimens in total residue).
- C = common (10% – 30% planktonic foraminifer specimens in total residue).
- R = rare (1% – 10% planktonic foraminifer specimens in total residue).
- P = present ($< 1\%$ planktonic foraminifer specimens in total residue).
- B = barren (no planktonic foraminifer specimens in total residue).

Individual planktonic foraminifers were recorded in qualitative terms based on an assessment of forms observed in a random sample of ~ 400 specimens from the $> 150 \mu\text{m}$ size fraction. Relative abundances were reported using the following categories:

- D = dominant ($> 30\%$ of the assemblage).
- A = abundant (10% – 30%).
- F = few (5% – 10%).
- R = rare (1% – 5%).
- P = present ($< 1\%$).

Planktonic foraminifer assemblage preservation was recorded as

- VG = very good (no evidence of breakage or dissolution).
- G = good ($> 80\%$ of specimens unbroken with only minor evidence of diagenetic alteration).
- M = moderate (30% – 80% of the specimens unbroken).
- P = poor (strongly recrystallized or dominated by fragments and broken or corroded specimens).

Radiolarians

Radiolarian biostratigraphy was mainly based on the zonation of Sanfilippo and Nigrini (1998), which uses the first and last appearances of key species. These datums are correlated to the timescale of Gradstein et al. (2012), as detailed in Figures F11, F12, and F13 and Table T3. For Pleistocene sections, we used the more specific radiolarian zonation for the South China Sea defined by Wang and Abelmann (1999). Taxonomic concepts for radiolarian species are mainly based on Moore (1995), Chen and Tan (1996), Sanfilippo and Nigrini (1998), Nigrini and Sanfilippo (2001), and Takahashi (1991).

Table T2. Planktonic foraminiferal events and ages (Gradstein et al., 2012 [GTS2012]) used during Expedition 349. T = top/last appearance datum, B = base/first appearance datum. Bc = base common, Tc = top common, Ba = base acme, Ta = top acme. Bold = zonal boundary definition. (Continued on next two pages.) [Download table in .csv format.](#)

GTS2012 chronostratigraphy (age)	Standard tropical–subtropical zonation		Datum/Event	GTS2012 age (Ma)		
	Blow (1969, 1979), Berggren et al. (1995); Indo-Pacific	Berggren et al. (1995), Wade et al. (2011); Indo-Pacific				
Tarantian (L. Pleist.)	N22	PT1b	T <i>Globorotalia flexuosa</i>	0.07		
0.126 Ma			T <i>Globigerinoides ruber rosa</i>	0.12		
Ionian (M. Pleist.)			B <i>Globigerinella calida</i>	0.22		
			B <i>Globigerinoides ruber rosa</i>	0.40		
			B <i>Globorotalia flexuosa</i>	0.40		
			B <i>Globorotalia hirsuta</i>	0.45		
0.781 Ma			PT1b/PT1a	T <i>Globorotalia tosaensis</i>	0.61	
Calabrian (e. Pleist.)			PT1a	B <i>Globorotalia hessi</i>	0.75	
				T <i>Globigerinoides obliquus</i>	1.3	±0.1
				T <i>Neogloboquadrina acostaensis</i>	1.58	±0.03
1.806 Ma		T <i>Globoturborotalita apertura</i>	1.64	±0.03		
Gelasian (e. Pleist.)	PT1a/PL6	T <i>Globigerinoides fistulosus</i>	1.88	±0.03		
		T <i>Globigerinoides extremus</i>	1.98	±0.03		
		B <i>Pulleniatina finalis</i>	2.04	±0.03		
		T <i>Globorotalia pertenuis</i>	2.30			
		T <i>Globoturborotalita woodi</i>	2.30	±0.02		
2.588 Ma	N22/N21	PL6/PL5	T <i>Globorotalia pseudomiocenica</i>	2.39		
Piacenzian (l. Pliocene)	N21		T <i>Globoturborotalita decoraperta</i>	2.75	±0.03	
			T <i>Globorotalia multicamerata</i>	2.98	±0.03	
	N21/N19-N20		B <i>Globigerinoides fistulosus</i>	3.33		
		PL5/PL4	B <i>Globorotalia tosaensis</i>	3.35		
		PL4	T <i>Dentoglobigerina altispira</i>	3.47		
3.6 Ma		B <i>Globorotalia pertenuis</i>	3.52	±0.03		
Zanclean (e. Pliocene)		PL4/PL3	T <i>Sphaeroidinellopsis seminulina</i>	3.59		
		PL3	T <i>Pulleniatina primalis</i>	3.66		
		PL3/PL2	T <i>Globorotalia plesiotumida</i>	3.77	±0.02	
			T <i>Globorotalia margaritae</i>	3.85	±0.03	
			T <i>Pulleniatina spectabilis</i>	4.21		
5.333 Ma		PL2/PL1	B <i>Globorotalia crassaformis</i> sensu lato	4.31	±0.04	
		PL1	T <i>Globoturborotalita nepenthes</i>	4.37	±0.01	
			B <i>Globorotalia exilis</i>	4.45	±0.04	
			T <i>Sphaeroidinellopsis kochi</i>	4.53	±0.17	
		T <i>Globorotalia cibaensis</i>	4.60			
Messinian (l. Miocene)	N19-20/N18		B <i>Sphaeroidinella dehiscens</i> sensu lato	5.53	±0.04	
	N18/N17b	PL1/M14	B <i>Globorotalia tumida</i>	5.57		
			B <i>Turborotalita humilis</i>	5.81	±0.17	
			T <i>Globoquadrina dehiscens</i>	5.92		
		M14/M13b	B <i>Globorotalia margaritae</i>	6.08	±0.03	
7.246 Ma	N17b/N17a		T <i>Globorotalia languensis</i>	6.14		
Tortonian (l. Miocene)		M13b	B <i>Globigerinoides conglobatus</i>	6.20	±0.41	
			B <i>Pulleniatina primalis</i>	6.60		
			B <i>Globorotalia miotumida</i> (conomiozea)	7.89		
		N17a/N16	B <i>Neogloboquadrina humerosa</i>	8.56		
			B <i>Globorotalia plesiotumida</i>	8.58	±0.03	
11.608 Ma		M13a	B <i>Globigerinoides extremus</i>	8.93	±0.03	
			B <i>Globorotalia cibaensis</i>	9.44	±0.05	
			B <i>Globorotalia juanai</i>	9.69	±0.26	
		N16/N15	B <i>Neogloboquadrina acostaensis</i>	9.83	±0.06	
			T <i>Globorotalia challengerii</i>	9.99		
		N15/N14	T <i>Paragloborotalia mayeri</i>	10.46	±0.02	
			B <i>Globorotalia limbata</i>	10.64	±0.26	
		T <i>Cassigerinella chipolensis</i>	10.89			
		B <i>Globoturborotalita apertura</i>	11.18	±0.13		
		B <i>Globorotalia challengerii</i>	11.22			
		Br <i>Globigerinoides obliquus</i>	11.25			
		B <i>Globoturborotalita decoraperta</i>	11.49	±0.04		
		T <i>Globigerinoides subquadratus</i>	11.54			

Table T2 (continued). (Continued on next page.)

GTS2012 chronostratigraphy (age)	Standard tropical–subtropical zonation		Datum/Event	GTS2012 age (Ma)		
	Blow (1969, 1979), Berggren et al. (1995); Indo-Pacific	Berggren et al. (1995), Wade et al. (2011); Indo-Pacific				
Serravallian (m. Miocene)	N14/N13	M11/M10	B Globoturborotalita nepenthes	11.63	±0.02	
	N13/N12	M10/M9b	T Fohsella fohsi, Fohsella plexus	11.79	±0.15	
			T Clavatorella bermudezi	12.00		
			B Globorotalia languanensis	12.84	±0.05	
			B Sphaeroidinellopsis subdehiscens	13.02		
		M9b/M9a	B Fohsella robusta	13.13	±0.02	
		M9a	T Cassigerinella martinezpicoi	13.27		
	N12/N11	M9a/M8	B Fohsella fohsi	13.41	±0.04	
Langhian (m. Miocene)	N11	M8	B Neogloboquadrina nympha	13.49		
	N11/N10	M8/M7	B Fohsella praefohsi	13.77		
	13.82 Ma		T Fohsella peripheroronda	13.80		
		N10	M7	Tr Clavatorella bermudezi	13.82	
				T Globorotalia archeomenardii	13.87	
				B Fohsella peripheroacuta	14.24	
		N10/N9	M7/M6	B Globorotalia praemenardii	14.38	
	N9	M6	T Praeorbulina sicana	14.53		
			T Globigeriantella insueta	14.66		
			T Praeorbulina glomerosa sensu stricto	14.78		
	N9/N8	M6/M5b	B Orbulina suturalis	15.10		
15.97 Ma			B Clavatorella bermudezi	15.73		
Burdigalian (e. Miocene)	N8	M5b	B Praeorbulina circularis	15.96		
			B Globigerinoides diminutus	16.06		
			B Globorotalia archeomenardii	16.26		
		M5b/M5a	B Praeorbulina glomerosa sensu stricto	16.27		
		M5a	B Praeorbulina curva	16.28		
		N8/N7	M5a/M4b	B Praeorbulina sicana	16.38	
	(20.44) Ma	N7	M4b	T Globorotalia incognita	16.39	
M4b/M4a				B Fohsella birnageae	16.69	
M4a				B Globorotalia miozea	16.70	
				B Globorotalia zealandica	17.26	
				T Globorotalia semivera	17.26	
		N7/N6	M4a/M3	T Catapsydrax dissimilis	17.54	
Aquitanian (e. Miocene)		N6-N5	M3	B Globigeriantella insueta sensu stricto	17.59	
	B Globorotalia praescitula			18.26		
	T Globiquadrina binaiensis			19.09		
		M3/M2	B Globigerinatella sp.	19.30		
				B Globiquadrina binaiensis	19.30	
				B Globigerinoides altiapertura	20.03	
	20.44 Ma		M2	T Tenuitella munda	20.78	
Aquitanian (e. Miocene)			B Globorotalia incognita	20.93		
			T Globoturborotalita angulisuturalis	20.94		
			T Paragloborotalia kugleri	21.12		
		N5/N4b	M2/M1b	T Paragloborotalia pseudokugleri	21.31	
		N4b	M1b	B Globoquadrina dehiscens forma spinosa	21.44	
				T Dentoglobigerina globularis	21.98	
				B Globoquadrina dehiscens	22.44	
	N4b/N4a	M1b/M1a	T Globigerina ciperoensis	22.90		
	N4a	M1a	B Globigerinoides trilobus sensu lato	22.96		
23.03 Ma	N4a/P22	M1a/O7	B Paragloborotalia kugleri	22.96		
Chattian (l. Oligocene)	P22 (N3)	O7	T Globigerina euapertura	23.03		
			Bc Globigerinoides primordius	23.50		
		O7/O6	T Tenuitella gemma	23.50		
		O6	B Paragloborotalia pseudokugleri	25.21		
	P22/P21	O6/O5	B Globigerinoides primordius	26.12		
			T Paragloborotalia opima sensu stricto	26.93		

Table T2 (continued).

GTS2012 chronostratigraphy (age)	Standard tropical–subtropical zonation		Datum/Event	GTS2012 age (Ma)
	Blow (1969, 1979), Berggren et al. (1995); Indo-Pacific	Berggren et al. (1995), Wade et al. (2011); Indo-Pacific		
(28.09) Ma	P21 (N2)	O5/O4		
Rupelian (e. Oligocene)	P21/P20	O4/O3	<i>Tc Chiloguembelina cubensis</i>	28.09
	P20	O3	B Globigerina angulisurens	29.18
	P20/P19	O3/O2	<i>B Tenuitellinata juvenilis</i>	29.50
	P19	O2	<i>T Subbotina angiporoides</i>	29.84
	P19/P18	O2/O1	T Turborotalia ampliapertura	30.28
		O1	<i>B Paragloborotalia opima</i>	30.72
33.89 Ma	P18	O1/E16	T Pseudohastigerina nagewichiensis	32.10
			<i>B Cassigerinella chipolensis</i>	33.89
Priabonian (l. Eocene)	P18/P17	E16	T Hantkenina spp.	33.89
			T Hantkenina alabamensis	33.89
	P17/P16	E15	<i>Tc Pseudohastigerina micra</i>	33.89
	P16		<i>T Turborotalia cerroazulensis</i>	34.03
	P16/P15	E14	<i>T Cribrohantkenina inflata</i>	34.22
	P15		T Globigerinatheka index	34.61
(37.75) Ma		E14	<i>T Turborotalia pomeroli</i>	35.66
Bartonian (m. Eocene)	P15/P14	E14/E13	<i>B Turborotalia cunialensis</i>	35.71
			<i>B Cribrohantkenina inflata</i>	35.87
			T Globigerinatheka semiinvoluta	36.18
			<i>T Acarinina spp.</i>	37.75
			T Morozovelloides crassatus	38.25
			B Globigerinatheka semiinvoluta	38.62
			<i>T Acarinina mcgowrani</i>	38.62
			<i>T Turborotalia frontosa</i>	39.42

Methods

Core catcher samples were prepared following the procedures described in Sanfilippo and Riedel (1985). A sediment sample of ~5 cm³ was placed in a beaker with a 20% solution of hydrogen peroxide to remove organic matter and 15% hydrochloric acid to dissolve all calcareous components from the sediment. The solution was washed and sieved through a 63 µm mesh screen. If the sample was found to contain clays adhering to the tests, it was treated for as long as 1 min in a concentrated solution of NaOH, immersed briefly in an ultrasonic bath, and then resieved. An aliquot of the residue was randomly settled with a pipette onto a slide and mounted with a coverslip using a few drops of Norland optical adhesive. Slides were examined under plane-transmitted light on a Zeiss Axioskop microscope. Additional samples from selected split cores were prepared using the method described above for planktonic foraminifers, and then radiolarians were picked from the >63 µm size fraction, mounted on a holder with double-sided tape, and observed using a Hitachi TM3000 tabletop SEM.

Overall radiolarian abundances were determined based on strewn slide evaluation at 200× magnification using the following categories:

- A = abundant (>100 specimens/slide traverse).
- C = common (51–100 specimens/slide traverse).
- F = few (11–50 specimens/slide traverse).
- R = rare (1–10 specimens/slide traverse).
- B = barren (no radiolarians in sample).

The abundance of individual species was recorded relative to the fraction of the total assemblage at 500× as follows:

- A = abundant (>30% of the total sample).

C = common (10%–30% of the total sample).

F = few (5%–10% of the total sample).

R = rare (<5% of the total sample).

Radiolarian preservation was defined as follows:

- G = good (majority of specimens complete, with minor dissolution, recrystallization, and/or breakage).
- M = moderate (minor but common dissolution, with a small amount of breakage).
- P = poor (strong dissolution, recrystallization, or breakage, many specimens unidentifiable).

Igneous petrology and alteration

The procedures for core description outlined here are adapted from Integrated Ocean Drilling Program Expedition 309/312 to the East Pacific Ridge flank (Expedition 309/312 Scientists, 2006), Expedition 324 to Shatsky Rise (Expedition 324 Scientists, 2010), Expedition 329 to the South Pacific Gyre (Expedition 329 Scientists, 2011), and Expedition 330 to the Louisville Seamount Trail (Expedition 330 Scientists, 2012). Our shipboard studies aimed to understand the nature of ocean crust in the South China Sea by systematically describing the petrology of the cored rocks and their alteration:

1. Igneous lithologic unit boundaries were defined by visual identification of actual lithologic contacts, or by inference, using observed changes in phenocryst assemblages or volcanic characteristics.
2. Lithology, phenocryst abundances and appearances, and characteristic igneous textures and vesicle distribution were described.

Table T3. Radiolarian events, mainly from Sanfilippo and Nigrini (1998) with additional Quaternary bioevents from Wang and Abelmann (1999), and ages (Gradstein et al., 2012 [GTS2012]) used during Expedition 349. * = GTS2012 ages applicable to the South China Sea. Bold type indicates marker taxa for the zone. T = top/last appearance datum, B = base/first appearance datum, X = crossover in abundance. (Continued on next two pages.) [Download table in .csv format.](#)

GTS2012 chronostratigraphy (age)	Standard tropical–subtropical zonation		Datum/Event	GTS2012 age (Ma)
	Sanfilippo and Nigrini (1998); low latitude	Wang and Abelmann (1999); South China Sea		
Tarantian (L. Pleist.)				
0.126				
Ionian (M. Pleist.)	RN16/RN17	NR2/NR1	B Buccinosphaera invaginata	0.18 (0.21)*
	RN15/RN16	NR3/NR2	T Stylatractus universus	0.44 (0.43–0.46)*
	RN14/RN15	NR3	B Collospira tuberosa	0.59 (0.42–0.46)*
0.781 Ma	RN14		T <i>Anthocyrtidium nosicae</i>	0.70
Calabrian (e. Pleist.)			B <i>Pterocorys hertwegii</i>	0.74
		NR4/NR3	T Pterocorys campanula	0.8 (0.72–0.73)*
		NR4	B <i>Anthocyrtidium euryclathrum</i>	0.91
1.806 Ma	RN13/RN14	NR5/NR4	T Anthocyrtidium angulare	1.21 (1.09)*
		NR5	B <i>Lamprocyrtis nigriniae</i>	1.26
			T <i>Lamprocyrtis neoheteroporos</i>	1.28
Gelasian (e. Pleist.)			B <i>Anthocyrtidium angulare</i>	1.81
	RN12/RN13	NR5 (base of zone)	B <i>Pterocorys zancleus</i>	1.85
	2.588 Ma	RN12b	T Pterocanium prismatium, Theocorythium ventulum	2.04
Piacenzian (l. Pliocene)			B <i>Cycladophora davisiana</i>	2.58
			B <i>Lamprocyrtis neoheteroporos</i>	2.65
		RN12a/RN12b	B <i>Theocorythium trachelium trachelium</i>	2.69
		RN11b/RN12a	T Anthocyrtidium jenghisi	2.74
		RN11b	T Stichocorys peregrina	2.87
		RN11a/RN11b	T <i>Anthocyrtidium ehrenbergi</i>	2.94
3.6 Ma			T <i>Didymocyrtis avita</i> , B <i>D. tetrathalamus tetrathalamus</i>	3.18
			T <i>Anthocyrtidium pliocenica</i>	3.40
			T Phormostichoartus fistula	3.49
Zanclean (e. Pliocene)			T <i>Lychnodictyum audax</i>	3.60
		RN10/RN11a	T Phormostichoartus doliolum	3.89
		RN10	B <i>Amphirhopalum ypsilon</i>	4.01
			T <i>Spongaster pentas</i> , B <i>Spongaster tetras tetras</i>	4.13
		RN9/RN10	T <i>Spongaster berminghami</i> , <i>Spongaster klingi</i>	4.22
5.333 Ma			T Didymocyrtis penultima , B <i>Didymocyrtis avita</i>	4.24
			B <i>Pterocanium prismatium</i>	4.91
			T <i>Solenosphaera omnitubus procera</i> , T <i>S. omnitubus omnitubus</i>	5.31
			B <i>Spongaster pentas</i>	5.49
			T <i>Acrobotrys tritubus</i>	5.55
Messinian (l. Miocene)			B <i>Pterocorys campanula</i> , T <i>Siphostichartus corona</i>	5.67
			T <i>Calocycletta caepa</i>	6.14
			T <i>Acrobotrys tritubus</i>	6.34
			T <i>Stichocorys johnsoni</i>	6.79
	7.246 Ma			
Tortonian (l. Miocene)			T <i>Calocycletta cladara</i>	7.29
			B <i>Solenosphaera omnitubus procera</i>	
			B <i>Solenosphaera omnitubus omnitubus</i>	7.41
		RN8/RN9	B Stichocorys delmontensis; T Stichocorys peregrina	7.78
			T <i>Dictyocoryne ontongensis</i>	7.94
			B <i>Acrobotrys tritubus</i>	7.94
			T <i>Botryostrobus miralestensis</i>	8.23
			B <i>Spongaster berminghami</i>	8.35
		RN7/RN8	B <i>Didymocyrtis penultima</i> , <i>Stichocorys delmontensis</i>	8.39
	RN7	T Diartus hughesi , <i>Didymocyrtis antepenultima</i>	8.39	
11.608 Ma		RN6/RN7	T <i>Didymocyrtis laticonus</i> , B <i>Didymocyrtis antepenultima</i>	8.84
			T Diartus petterssoni ; B <i>Diartus hughesi</i>	8.84
			T <i>Lithopera neotera</i> , B <i>Lithopera bacca</i>	8.87
			T <i>Cyrtocapsella japonica</i>	9.86
			T <i>Carpocanopsis cristata</i>	10.68

Table T3 (continued). (Continued on next page.)

GTS2012 chronostratigraphy (age)	Standard tropical–subtropical zonation		Datum/Event	GTS2102 age (Ma)
	Sanfilippo and Nigrini (1998); low latitude	Wang and Abelmann (1999); South China Sea		
Serravallian (m. Miocene)	RN5/RN6		T <i>Lithopera renzae</i> , B <i>Lithopera neotera</i>	12.19
			B <i>Diartus petterssoni</i>	12.60
13.82 Ma			T <i>Calocyclus virginis</i> , B <i>Calocyclus cladara</i>	13.67
Langhian (m. Miocene)	RN5		T <i>Didymocyrtis mammifera</i> , B <i>Didymocyrtis laticonus</i>	14.07
			T <i>Carpocanopsis bramlettei</i>	14.69
			T <i>Calocyclus costata</i> , B <i>Lithopera renzae</i>	15.00
	RN4/RN5		T <i>Dorcadospyris dentata</i> ; B <i>Dorcadospyris alata</i>	15.03
			T <i>Dorcadospyris dentata</i> , <i>Dorcadospyris forcipata</i>	15.03
			T <i>Eucyrtidium diaphanes</i>	15.46
15.97 Ma		RN4	T <i>Liriospyris stauropora</i> , B <i>Liriospyris parkerae</i>	15.88
Burdigalian (e. Miocene)	RN3		T <i>Carpocanopsis favosa</i>	16.31
			T <i>Didymocyrtis prismatica</i>	16.73
			T <i>Carpocanopsis cingulata</i> , B <i>Carpocanopsis cristata</i>	17.16
			B <i>Calocyclus costata</i> , T <i>Lychnocanoma elongata</i>	17.59
			B <i>Didymocyrtis mammifera</i>	17.80
			B <i>Calocyclus caepa</i>	18.01
			B <i>Dorcadospyris dentata</i>	18.22
			B <i>Liriospyris stauropora</i>	18.43
			B <i>Stichocorys wolffii</i>	18.64
			T <i>Dorcadospyris ateuchus</i> , B <i>Siphostichartus corona</i>	18.64
			B <i>Didymocyrtis tubaria</i>	19.34
			T <i>Theocyrtis annosa</i>	20.05
20.44 Ma			T <i>Calocyclus serrata</i>	20.40
Aquitanian (e. Miocene)	RP22/RN1		T <i>Calocyclus robusta</i>	20.76
			B <i>Carpocanopsis favosa</i>	21.11
			B <i>Cyrtocapsella cornuta</i>	21.46
			B <i>Cyrtocapsella tetrapera</i> , B <i>Calocyclus serrata</i>	21.82
			T <i>Artophormis gracilis</i>	22.41
23.03 Ma		RP22	B <i>Eucyrtidium diaphanes</i>	23.00
Chattian (l. Oligocene)	RP21/RP22		T <i>Dorcadospyris papilio</i>	23.59
			B <i>Lychnocanoma elongata</i> , <i>Carpocanopsis cingulata</i>	24.18
			T <i>Lychnocanoma trifolium</i> , B <i>Dorcadospyris forcipata</i>	25.07
			B <i>Calocyclus robusta</i>	25.97
			B <i>Dorcadospyris papilio</i>	26.86
28.09 Ma			T <i>Lithocyclia angusta</i>	27.75
Rupelian (e. Oligocene)	RP20		T <i>Tristylospyris tricerus</i> ; B <i>Dorcadospyris ateuchus</i>	28.64
			T <i>Tristylospyris tricerus</i>	28.64
			T <i>Theocyrtis tuberosa</i> , B <i>Theocyrtis annosa</i>	29.10
			T <i>Lithocyclia crux</i>	29.56
			B <i>Lychnocanoma trifolium</i>	30.02
			T <i>Dorcadospyris pseudopapilio</i> , B <i>Didymocyrtis prismatica</i>	30.48
			T <i>Centrobotrys petrushevskayae</i> , B <i>Centrobotrys thermophilla</i>	30.94
			B <i>Lychnodictyum audax</i>	31.40
			B <i>Centrobotrys petrushevskayae</i> , <i>Dorcadospyris pseudopapilio</i>	31.86
			T <i>Centrobotrys gravida</i>	31.86
			T <i>Artophormis barbadensis</i> , B <i>Lithocyclia crux</i> , <i>Artophormis gracilis</i>	32.32
			B <i>Centrobotrys gravida</i>	32.78
			T <i>Dictyoprora pirum</i> , B <i>Phormostichoartus fistula</i>	33.24
			T <i>Lithocyclia aristotelis</i> group; B <i>Lithocyclia angusta</i>	33.71
			T <i>Dictyoprora mongolferi</i>	33.71
			T <i>Cryptocarpium ornatum</i> , <i>Lychnocanoma amphitrite</i>	33.71
33.89 Ma		RP19	T <i>Dictyoprora armadillo</i>	34.13
Priabonian (l. Eocene)	RP18/RP19		T <i>Lophocyrtis (Lophocyrtis) jacchia</i>	34.55
			T <i>Calocyclus turris</i> , <i>Cryptocarpium azyx</i>	34.97
			T <i>Thyrsoyrtis bromia</i> (max), <i>Thyrsoyrtis rhizodon</i>	34.97
			T <i>Thyrsoyrtis tetracantha</i> , <i>Thyrsoyrtis lochites</i> (max)	35.40

Table T3 (continued).

GTS2012 chronostratigraphy (age)	Standard tropical–subtropical zonation		Datum/Event	GTS2102 age (Ma)
	Sanfilippo and Nigrini (1998); low latitude	Wang and Abelmann (1999); South China Sea		
Priabonian (l. Eocene)	RP18		T <i>Calocyclus bandyca</i> , <i>Calocyclus hispida</i>	35.40
			T <i>Lychnocanoma bellum</i> , <i>Podocyrtis papalis</i>	35.40
	T <i>Thyrsocyrtis triacantha</i> (max)		35.73	
	RP17/RP18		B <i>Theocyrtis tuberosa</i>	36.06
	RP17		T <i>Eusyringium fistuligerum</i>	36.39
			T <i>Podocyrtis goetheana</i>	36.72
37.75 Ma			B <i>Calocyclus bandyca</i>	37.05
Bartonian			T <i>Podocyrtis chalara</i>	37.22
			B <i>Lychnocanoma amphitrite</i>	37.40
			T <i>Calocyclus hispida</i> , B <i>Calocyclus turris</i>	37.58
	RP16/RP17		B <i>Cryptocarpium azyx</i>	37.75

- Alteration as well as vein and vesicle infillings and halos were recorded.
- These macroscopic observations were combined with detailed thin section petrographic studies of key igneous units and alteration intervals.

Core description workflow

Before splitting into working and archive halves, each hard rock piece was labeled individually with unique piece/subpiece numbers from the top to the bottom of each section. If the top and bottom of a piece of rock could be determined, an arrow was added to the label to indicate uphole. These hard rock pieces were split with a diamond-impregnated saw along lines chosen by a petrologist so that important compositional and structural features were preserved in both the archive and working halves. The archive halves were imaged using the SHIL, which also records red, green, and blue spectral colors along the centerline of the core. After imaging, the archive halves were analyzed for color reflectance and magnetic susceptibility at 1–2.5 cm intervals using the SHMSL (see [Physical properties](#)). The working halves were sampled for shipboard physical properties, paleomagnetic studies, thin sections, and ICP-AES analysis.

Each section of core was first macroscopically examined and described for petrologic and alteration characteristics, followed by description of structures (see [Structural geology](#)). All descriptions during Expedition 349 were made on the archive halves of the cores except for thin sections, which were sampled from the working halves. For macroscopic observations and descriptions, the DESClogik program was used to record the primary igneous characteristics (e.g., lithologic unit division, groundmass and phenocryst mineralogy, and vesicle abundance and type) and alteration (e.g., color, vesicle filling, secondary minerals, and vein/fracture fillings). The amount of individual mineral modes and the sizes were estimated by examining the archive halves under a binocular microscope or using hand lenses with graticules of 0.1 mm. For microscopic observation, as many as 12 thin sections were made daily, and the descriptions were entered in DESClogik. Macroscopic features observed in the cores are summarized and presented in the VCD (see [Macroscopic visual core description](#); Figures [F7](#), [F14](#)).

Igneous petrology

Igneous lithologic and lithostratigraphic unit classifications

The first step in visual core description is the classification of the igneous lithologic units and subunits. These of volcanic rock unit boundaries are generally chosen to reflect different volcanic cooling units. The definition of an igneous lithologic unit is usually based on the presence of lava flow contacts, typically marked by chilled or glassy margins on the upper and lower contact or by the presence of intercalated volcanoclastic or sedimentary horizons. If no such boundaries were recovered (e.g., because of low recovery), we defined the igneous lithologic unit boundaries according to changes in the primary mineral assemblage (based on abundances of visible phenocryst and groundmass mineral phases), grain size, color, and structure or texture. Igneous lithologic units are given consecutive downhole Arabic numerals (e.g., igneous lithologic Units 1, 2, 3, etc.) irrespective of whether they are pillows, lobate or massive flows, volcanoclastic deposits, or igneous intrusions. Igneous lithologic subunits were used in cases where mineralogy remains similar but frequent changes in texture take place (e.g., igneous lithologic Subunits 1a, 1b, 1c, etc.).

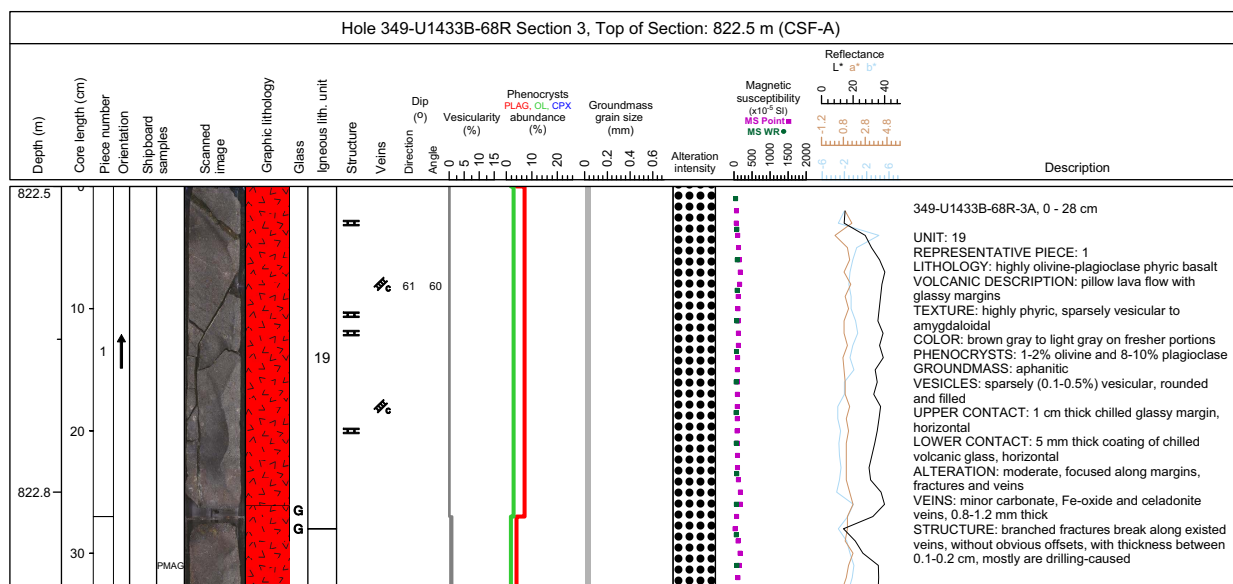
Lithostratigraphic units, on the other hand, were defined where successions of consecutive cooling or depositional units with similar volcanic characteristics could be identified, usually based on phenocryst assemblages. In effect, these lithostratigraphic units combine similar igneous lithologic units and subunits, providing a first step toward considering volcanic stratigraphy and eruptive units. These successions are given consecutive downhole Roman numerals (e.g., lithostratigraphic Units III, IV, and V) that follow directly from the overlying sedimentary units (lithostratigraphic Units I and II in this example).

Lava flow types

Pillow lava flows

Pillow lavas are characterized by curved chilled margins oblique to the vertical axis of the core. When these margins are absent, we can potentially identify those boundaries by the presence of variolitic textures, curved fractures, and microcrystalline or cryptocrystalline grain sizes. Pillow lava flows consist of discrete subrounded units (or lobes) of relatively small size (0.2–1.0 m in diameter).

Figure F14. Example of a standard graphic report (VCD) for igneous rocks, Expedition 349.



Their exteriors are entirely bounded by glassy rinds as a result of rapid cooling. The outer zones typically show bands of vesicles, whereas their interiors typically display internally radiating vesicle trains and joint patterns. Pillow lava flows result from subaqueous eruptions that allow separation of lava pods from point sources along the advancing front.

Lobate lava flows

Lobate flows (~1–2 m in diameter) can develop by the same inflation process as pillow lava flows. Although these extrusions resemble pillow lavas, they differ in that they have massive, coarser grained, and sparsely vesicular flow interiors, often with pipe vesicle domains. These inflation units are characterized by more effective degassing and vesicle formation than pillow lava flows. Typically, vesicle zoning is concentrated in the upper regions of the inflation unit and often occurs as a series of vesicle bands that develop as a result of the inward migration of the cooling front, whereas the lower part of the inflation unit typically contains either sparse, poorly defined vesicle banding or teardrop-shaped vesicles at or just above the basal chilled zone. Recognizing lobate flows and distinguishing those from pillows in drill core is often difficult.

Sheet and massive lava flows

Sheet lava flows are defined as igneous lithologic units <3 m thick of the same rock type, with grain sizes increasing toward the center of flows. Massive lava flows are defined for continuous intervals that are >3 m of a similar lithology. Where recovered, these units are significantly thicker than the normal (~0.2–2 m) dimensions of pillow or lobate lava flows. Characterized by sparse vesicle layering, sheet and massive flows often have texturally uniform cores, as thick as several meters, and can have vertical vesicle pipes containing late-stage melt segregation material. Sheet-like and massive flows may result from particularly high effusion rates and/or increased local slopes.

Primary igneous lithologies and features

Phenocryst-based lithology names

Porphyritic basaltic rocks were named according to major phenocryst phase(s) when the total abundance of phenocrysts was >1%.

The most abundant phenocryst appears last in the phenocryst-based lithology name. For example, olivine is the most abundant mineral in a plagioclase-olivine-phyric basalt. The term “phenocryst” was used for any crystal that was (1) significantly larger (typically at least five times) than the average size of the groundmass crystals, (2) >1 mm, and (3) euhedral or subhedral. The term “microphenocryst” was used for crystals larger than the modal groundmass grain size but smaller than 1 mm and is reported in the Microscopic (thin section) description template of DESClogik and in the lithologic unit summary under “Description” in the VCDs. A prefix was applied as a modifier to the primary lithology names to indicate the abundance of phenocrysts in the hand samples as follows:

- Aphyric (<1% phenocrysts),
- Sparsely phyric (1%–5% phenocrysts),
- Moderately phyric (5%–10% phenocrysts), and
- Highly phyric (>10% phenocrysts).

Aphyric rocks were not assigned any mineralogical modifier. Likewise, in coarser grained rocks with seriate to equigranular textures, we did not use modifiers unless there was a clear distinction in size between phenocrysts and groundmass crystals.

Groundmass

Groundmass is defined as the finer grained matrix (or the mesostasis) between the phenocryst phases, if the latter are present. Such groundmass is generally characterized by its texture (see below) and its grain size with the following standard notation:

- G = glassy.
- cx = cryptocrystalline (<0.1 mm).
- µx = microcrystalline (0.1–0.2 mm).
- fg = fine grained (>0.2–1 mm).
- mg = medium grained (>1–2 mm).
- cg = coarse grained (>2 mm).

An estimate of the average modal groundmass size (in millimeters) was included in the VCDs, whereas in the reports and description summaries we use descriptive terms (e.g., fine-grained or coarse-grained groundmass).

For volcanic rocks, the following terms were used to describe textures when microlites are present in the groundmass:

- Variolitic (fan-like arrangement of divergent microlites),
- Intergranular (olivine and pyroxene grains between plagioclase laths),
- Intersertal (glass between plagioclase laths),
- Subophitic (partial inclusion of plagioclase in clinopyroxene), and
- Ophitic (total inclusion of plagioclase in clinopyroxene).

Flow textures present in groundmass were described as follows:

- Trachytic (subparallel arrangement of plagioclase laths in the groundmass),
- Pilotaxitic (aligned plagioclase microlites embedded in a matrix of granular and usually smaller clinopyroxene grains), and
- Hyalopilitic (aligned plagioclase microlites with glassy matrix).

Description of habits for plagioclase and clinopyroxene groundmass crystals was adapted from those used during ODP Leg 206 (Shipboard Scientific Party, 2003) and Leg 148 (Shipboard Scientific Party, 1993). Four habit types were identified:

- Cryptocrystalline aggregates of fibrous crystals (fibrous),
- Comb-shaped or sheaf-like plumose crystals (fibrous),
- Granular-acicular subhedral to anhedral crystals, and
- Prismatic-stubby euhedral to subhedral crystals.

Rock color

Rock color was determined on a wet, cut surface of the archive half using Munsell color charts (Munsell Color Company, Inc., 1994) and converted to a more intuitive color name. Wetting of the rock was carried out using tap water and a sponge. Wetting was kept to a minimum because of adsorption of water by clay minerals (particularly saponite and celadonite) that are present throughout the core.

Volcanic textures and features

Various volcanic textures (e.g., glomerocrysts, coarser grained crystal aggregates, and xenoliths) were recorded, as were characteristic volcanic features such as chilled margins, baked contacts (with sediment), rubbly or brecciated flow tops, and so on. In particular, we noted the occurrence of vesicle banding, vesicle trains, pipe vesicles, and radiating cooling cracks.

Vesicles

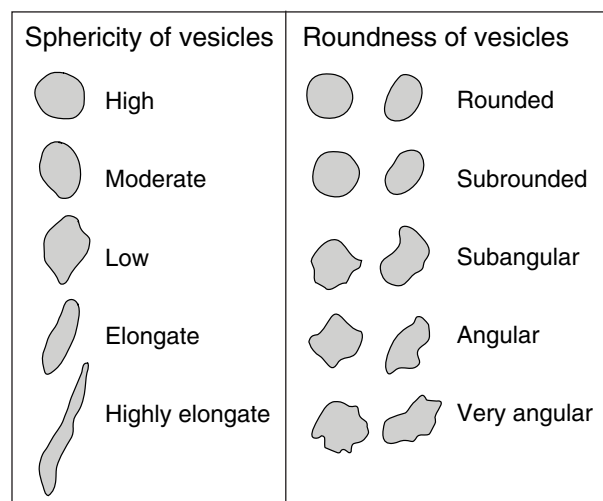
An estimate of the percentage of vesicles and their average size was included in the VCDs. Vesicularity is described according to the abundance, size, and shape (sphericity and angularity) of the vesicles (Figure F15). Vesicle abundance was recorded as follows:

- Nonvesicular = <1% vesicles.
- Sparsely vesicular = 1%–5% vesicles.
- Moderately vesicular = 5%–20% vesicles.
- Highly vesicular = >20% vesicles.

Alteration

Methods for describing alteration include hand sample descriptions and inspection of thin sections. These observations provided information on the alteration of primary igneous features, such as phenocrysts, groundmass minerals, and volcanic glass. In addition,

Figure F15. Comparison charts for describing the shape of vesicles in volcanic rocks. Modal shape and sphericity of vesicle populations were adapted from the Wentworth (1922) scheme for describing grain shape in sedimentary rocks.



the abundance of veins and vesicles and the succession of infilling materials were recorded to ascertain the order of mineral precipitation.

Alteration state and features

The alteration minerals were identified by color, habit and shape, association with primary minerals (if distinguishable), and hardness. Visual estimates of alteration degree, type, color, and textures (e.g., halos and patches) were recorded, as well as abundance (percentage) of minerals filling veins and vesicles, and the proportion of altered groundmass, volcanic glass, and all the different primary phenocryst phases. Complications arise in the identification of the secondary phases because many minerals produced during submarine alteration are visually similar, often being microcrystalline or amorphous, and are thus indistinguishable in the cores. Hence, identification of some alteration phases remains preliminary, pending detailed shore-based XRD studies and electron microprobe analyses.

Overall background alteration

The degree of the overall background alteration of groundmass and glass is defined and reported graphically on the VCDs according to various ranges of intensity in the alteration state. Different patterns are used to indicate slight, moderate, high, complete, or no (fresh) alteration (Figure F7) according to the following scale:

- Fresh = <2 vol%.
- Slight = 2–10 vol%.
- Moderate = 10–50 vol%.
- High = 50–95 vol%.
- Complete = >95 vol%.

Vesicle fillings

Vesicles were first recorded for their shape, percentage abundance, size, and density, after which the infilling minerals were identified. Voids were described in terms of size, abundance, and partial infilling minerals, often lining the walls of irregular open spaces.

Veins

During Expedition 349, petrologists first recorded the location of veins and the mineralogy of the infilling materials and the halos surrounding those veins; after that, the structural geologists measured and recorded the orientation and width of the same veins (see **Structural geology**). Description of the veins included location, shape, crosscutting nature, width, color, and the amount (percentage) and nature of filling minerals. All features were recorded in DESClogik using a series of codes (Figure F7 for vein shape (straight, sigmoidal, irregular, pull-apart, and fault), connectivity (isolated, single, branched, and network), texture (massive, cross fiber, slip fiber, vuggy, and polycrystalline), structure (simple, composite, banded, haloed, and intravenous), and geometry (en echelon, ribbon, and cross fractures).

Alteration halos

Alteration halos commonly form around hydrothermal veins that allow for fluid flow of varying chemical composition. They can be different from the overall background alteration and vesicle filling in color, secondary mineral composition, and abundance. Color, thickness, and secondary minerals of alteration halos are recorded in the Veins-Halo tab of the DESClogik program.

Alteration color

Alteration color was defined using Munsell Soil Color Charts (Munsell Color Company, Inc., 1994) and converted to a more intuitive color name (very dark gray, greenish gray, etc.).

Volcanic glass

The presence of both unaltered and variably altered volcanic glass was also recorded in terms of the percentage of fresh material by volume. In addition, the composition and extent of replacement by secondary minerals were described.

Macroscopic visual core description

We used DESClogik to document each section of the igneous cores and their alteration by uploading our descriptions into the central LIMS database. These uploaded data were then used to produce VCDs, which include a simplified graphical representation of the core (for each section) with accompanying descriptions of the features observed. An example VCD for igneous rocks is shown in Figure F14, and the symbols used in these VCDs are given in Figure F7. The VCDs display the following items:

- Depth in mbsf;
- Scale for core section length (0–150 cm);
- Sample piece number;
- Upward-pointing arrow indicating oriented pieces of core;
- Sample type and position of intervals selected for different types of shipboard analytical studies, such as thin sections (TS), ICP-AES (ICP), paleomagnetism (PMAG), and physical properties (PP);
- Scanned digital image of the archive half;
- Graphical representation of lithology;
- Next to the graphical lithology, the symbol “G” indicates the presence of volcanic glass, either in the glassy rind of chilled margins or when encountered in hyaloclastite breccia;
- Igneous lithologic unit number;
- Symbolized structural information;
- Structural measurements of dip direction and dip angle;

- Line chart displaying the percent vesicularity;
- Stacked line chart displaying phenocryst percentage for plagioclase (pl: red line), olivine (ol: green line), and clinopyroxene (cpx: blue line);
- A chart displaying variation in crystal size of modal groundmass (in millimeters)
- Column with variable patterns depicting alteration intensity;
- Chart displaying both point source and whole-round magnetic susceptibility measurements;
- Chart displaying color reflectance, with total reflectance (L^*), red (a^*), and blue (b^*) data arranged side by side; and
- Description summary for each igneous lithologic unit (see below for details).

The section summary text (displayed on the right side) provides a generalized overview of the core section’s lithology and features on a unit-by-unit basis. This summary includes the following:

- Expedition, site, hole, core and core type, section number, and the depth of the top of the core section in mbsf (measured according to the CSF-A depth scale) shown at the top of the VCD;
- Igneous lithologic unit or subunit number(s) (numbered consecutively downhole) and piece numbers belonging to unit (and on which piece, or pieces, the description was based);
- Lithology, rock description, and name;
- Volcanic description based on type of unit and igneous structure (e.g., pillow lava, massive flow);
- Texture based on total percentage of phenocrysts and microphenocrysts by volume: aphyric (<1%), sparsely phyric (1%–5%), moderately phyric (>5%–10%), or highly phyric (>10%);
- Color determined on wet rock surfaces;
- Phenocryst percentage and type based on minerals identifiable by eye, hand lens, or binocular microscope;
- Groundmass grain size and texture: glassy, aphanitic (crystalline but individual grains not discernible with a hand lens), fine grained (<1 mm), medium grained (1–2 mm), or coarse grained (>2 mm);
- Vesicle percentage by volume, including filled, partially filled, and open vesicles;
- Upper and lower unit contact relations and boundaries, based on physical changes observed in retrieved core material (e.g., presence of chilled margins, changes in vesicularity, and alteration), including information regarding their position within the section. The term “not recovered” was entered where no direct contact was recovered;
- Alteration of the rock material, veins, and vesicle infillings; and
- Structural features (see **Structural geology**).

Microscopic (thin section) description

Thin section analyses of sampled core intervals were used to complement and refine macroscopic core observations. Typically, one thin section was examined and logged per defined igneous lithologic unit. To maintain consistency, the same terminology and nomenclature are used for macroscopic and microscopic descriptions. Phenocryst assemblages (and their modal percentages, shapes, habits, and sizes), groundmass, and alteration phases were determined, and textural features were described. All observations were entered into the LIMS database with a special DESClogik thin section template. Downloaded tabular reports of all igneous thin section descriptions can be found in **Core descriptions**.

Thin section descriptions include both primary (igneous) and secondary (alteration) features, for example, textural features, grain size of phenocrysts and groundmass minerals, mineralogy, abundance (percentage), inclusions, alteration color, alteration extent (percentage) in the total rock, alteration veins (type and number), and vesicles (type and fillings). An example of a thin section description form is given in Figure F16.

Textural terms used are those defined by MacKenzie et al. (1982) and include

- Heterogranular (different crystal sizes),
- Equigranular (similar crystal sizes),
- Seriate (continuous range in grain size),
- Porphyritic (increasing presence of phenocrysts),
- Glomeroporphyritic (containing clusters of phenocrysts),
- Holohyaline (100% glass),
- Hypo- or holocrystalline (100% crystals),
- Variolitic (fine, radiating fibers of plagioclase or pyroxene),
- Intergranular (olivine and pyroxene grains between plagioclase laths),
- Intersertal (groundmass fills the interstices between unoriented feldspar laths),
- Ophitic (lath-shaped euhedral crystals of plagioclase, grouped radially or in an irregular mesh, completely surrounded with large anhedral crystals of pyroxene), and
- Subophitic (partial inclusion of plagioclase in pyroxene).

Glass in basalts with more glassy groundmass are defined as

- Fresh glass (amber in transmitted polarized light and isotropic in transmitted cross-polarized light),
- Dark glass (darkness is caused by abundant crystallites; interstitial volcanic glass of basaltic composition is termed trachylytic),
- Glass with spherulites (spheroid aggregates of acicular crystals forming a nucleus), and
- Altered glass (partially or completely altered to clay minerals).

For alteration description, thin sections were examined to

- Confirm macroscopic identification of secondary minerals;
- Determine their mode of occurrence in terms of vesicle and void fillings, vein composition, and primary mineral replacement;
- Determine the chronological relationships between different secondary minerals;
- Establish the distribution, occurrences, and abundance of secondary minerals downhole;
- Quantify the overall amount of alteration in the basaltic rocks;
- Identify mineralogies of vein and vesicle infillings, as well as cement and voids present in basaltic breccia; and
- Calculate the total alteration (percentage) using the modal proportions of phenocrysts and groundmass minerals and their respective percentages of alteration.



Individual thin sections in some cases contain multiple domains that require separate description. In DESClogik, the user can enter

multiple records for a single thin section, in the case where more than one domain can be recognized. We define the “domain” concept of DESClogik based on apparent observable differences in lithology, alteration, vesicle banding and grouping, and veining and when more than one clast type is present in volcanoclastic lithologies. Thin sections typically are taken so they represent a singular lithology, and thus by definition they encompass a single lithology domain (Figure F17A). In some cases, thin sections contain more than one lithology, with a sharp or diffuse boundary splitting the thin section into two lithology domains, whereby a diffuse (wider) boundary zone could be defined as a separate, third domain (Figure F17B). Alteration can result in many different domains in a rock, including the background alteration and various halos surrounding cracks and veins (Figure F17C). In pillow basalts, but also in thicker sheet and massive flows, different groupings or bands of vesicles may be apparent in thin section (Figure F17D). Multiple generations of veins with different filling patterns are often visible in thin section and should be assigned different domain names (Figure F17E). Heterolithic volcanoclastics often contain multiple clast types, as well as the matrix domain itself, that could be described separately (Figure F17F).

Finally, estimated volume percentages are required to quantify, for example, phenocryst and vesicle abundances. In DESClogik, the user is required to enter modal percentages of both whole-rock and groundmass constituents for extrusive and hypabyssal rocks. Using cartoons and example calculations, we define those modal percentages and explain how they add up to 100% in both cases. Figure F18A is a cartoon of an idealized porphyritic volcanic rock in a thin section with plagioclase and olivine phenocrysts, vesicles, and one crosscutting vein set in a finer grained groundmass matrix. The whole-rock constituents are the sum of all phenocrysts present, plus the vesicles and groundmass (Figure F18B). In this case, a total of 20% phenocrysts, 10% vesicles, and 70% groundmass matrix are present, equaling 100%. Veins and void spaces are ignored in this calculation. For the groundmass constituents, however, we examine the groundmass matrix as a whole (by ignoring the phenocrysts and vesicles), and we estimate the distribution of mineral phases, mesostasis, and fresh glass in it. In this case, the groundmass contains 40% plagioclase, 20% clinopyroxene, 10% olivine, 10% Fe-Ti oxides, and 20% mesostasis, equaling 100%. Fresh glass is not present in this example thin section, but if it were present, it would be considered a separate constituent from mesostasis. Mesostasis is the altered portion of the interstitial spaces between all the groundmass minerals present that originally often was volcanic glass. Figure F18C is a simplified view of a group of partially altered (replaced) olivine phenocrysts and partially filled vesicles. As explained above, in DESClogik the user at least records the percentage of the originally present phenocryst phases, groundmass mineral phases, and vesicles (Figure F18D). However, whenever possible, the user also should record how much of these constituents is still present (i.e., still fresh or not filled) and how much has been replaced (i.e., altered or filled) while taking into account that $\text{Original (\%)} = \text{Present (\%)} + \text{Replaced (\%)}$.

Figure F16. Example of thin section description for igneous rocks, Expedition 349.

THIN SECTION LABEL ID: 349-U1431E-43R-3-W 91/94-TSB(91-94)-TS54		Thin section no.: 54	
Unit/Subunit: IX	Piece no.: #12	Observer: MGTejada	
Thin section summary: Highly altered sparsely olivine-plagioclase-phyric basalt with intergranular texture containing a few vesicles that are partially filled with secondary minerals. A few microphenocrysts of olivine and plagioclase are present in the groundmass dominantly composed of variolitic plagioclase. The mesostasis is mostly composed of microcrystalline clinopyroxene and oxides.			

 <p>Plane-polarized: 24792191</p>	 <p>Cross-polarized: 24792211</p>
--	---

IGNEOUS ROCK - PRIMARY MINERALOGY			
Sample domain name: lithology	Domain rel. abundance (%): 100	Observer: G Zhang	
Lithology: sparsely olivine-plagioclase phyric basalt			
Texture:	Average grain size: fine grained	Grain size distribution:	
Domain comment: moderately altered microcrystalline basalt with alteration marked by brown patches and rusty stains at the corners. Contains minor microphenocrysts of olivine and plagioclase			

Vesicle	Original (%)	Empty (%)	Filled (%)	Size min. (mm)	Size max. (mm)	Size mode (mm)	Shape	Comments
Total (whole rock constituents):	5	3	2	0.2	0.4		rounded	

Phenocryst	Original (%)	Present (%)	Replaced (%)	Size min. (mm)	Size max. (mm)	Size mode (mm)	Shape	Habit	Special Features	Comments
Olivine	5	2	3	0.2	1.2	0.3	subhedral-anhedral	tabular		replaced along cracks and rims
Plagioclase	3	3	0	0.6	1.2	1	subhedral-anhedral	tabular		cut by saponite(?) veinlets
Total (whole rock constituents):	8	5	3							

Groundmass	Original (%)	Present (%)	Replaced (%)	Size min. (mm)	Size max. (mm)	Size mode (mm)	Shape	Habit	Comments
Plagioclase	45	35	10	0.05	1.5	0.8	subhedral	prismatic elongated	forms triangular arrangement of laths
Fe-Ti Oxide	12	12	0	0.01	0.08	0.04	subhedral		
Mesostasis	43	30	13						mostly composed of clinopyroxene microlites and oxides
Total (groundmass constituents):	100	77	23						
Total (whole rock constituents):	87	67	20						

IGNEOUS ROCK - SECONDARY MINERALOGY (ALTERATION)			
Observer: G Zhang			
Alteration intensity: highly altered	Total alteration (%): 65		
Alteration comments: Fe-oxide vein			

Alteration mineral:	Percent:
Carbonate	2

Vesicle filling:	Percent:
Carbonate	8
Saponite	24
Smectite	8
Total vesicle fill	40

Figure F17. A–F. Examples of thin section description types used in DESC-logik, Expedition 349.

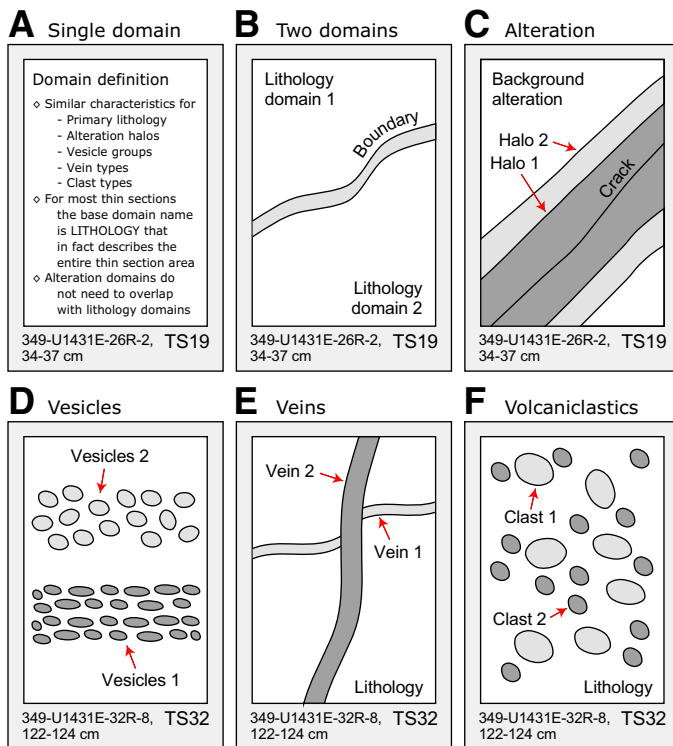
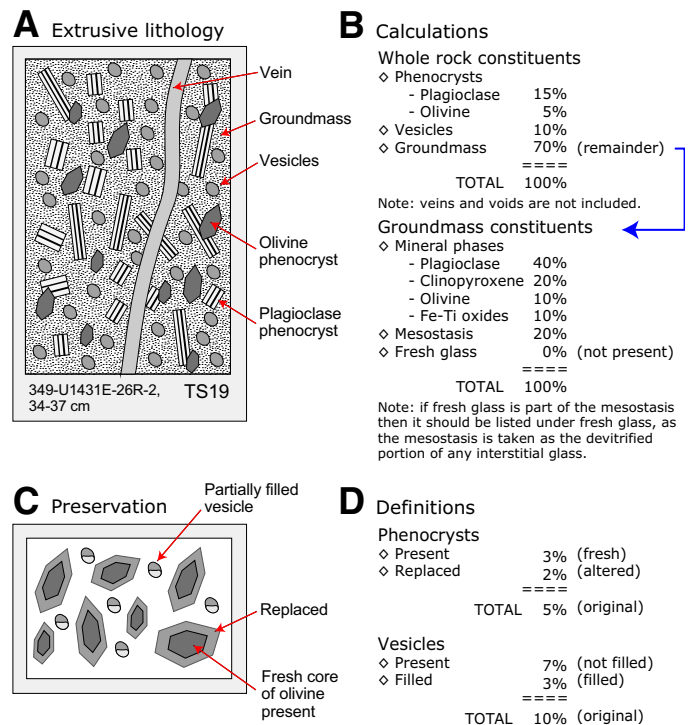


Figure F18. A–D. Examples of thin section modal calculations, Expedition 349.



Structural geology

This section outlines methods for documenting structural features observed in Expedition 349 cores, such as faults, fractures, breccia, and veins. After a core is split and described by sedimentologists or petrologists on shift, we documented structural features observed on the archive half by: (1) identifying structural features and classifying their structural types, (2) determining the top and bottom location of structural features in the core, (3) measuring the orientation of a structural feature where applicable, and (4) determining the sense of displacement on a structural feature where applicable. Our methods largely follow those used by structural geologists of Integrated Ocean Drilling Program Expedition 344 (Harris et al., 2013). The types of structural measurements and key parameters (either observed or calculated) are recorded on a spreadsheet (Figure F19). These data are then input into the LIMS database. Orientation data are corrected for rotation related to drilling using paleomagnetic declination and inclination information (see [Paleomagnetism](#)).

Graphic symbols and terminology

A predefined set of commonly observed structural features was used in the structural description of cores during Expedition 349. The terminology and graphic symbols used are presented in Figures F7 and F20. The major structural features identified include the following:

- Fractures: brittle failure with unknown displacement and with no secondary infill minerals; however, breaks clearly resulting from drilling were not logged as fractures;
- Veins: fractures filled with secondary minerals;

- Igneous contacts: material contacts of extrusive or intrusive igneous rocks; and
- Magmatic fabrics: magmatic foliations defined by the preferred orientations of primary minerals with no evidence of crystal-plastic deformation.

Structural observation and description

Structural features were described from the top to bottom of each section of the core. For fractures, we examined and measured the following parameters:

- Location: where a fracture occurs in a core, measured in centimeters from the top of the section;
- Morphology: morphological shape of a fracture, e.g., straight, curved, banded, irregular, composite, isolated, single or branched;
- Displacement: lateral offset and/or opening of a fracture measured in centimeters; a closed fracture with no lateral offset is recorded as 0 cm of displacement;
- Orientation: dip angle and dipping orientation of a fracture measured in degrees; where applicable, reorientation of a fracture to geographic coordinates (i.e., relative to true north) was done to determine the real dip direction (see [Orientation measurements and correction](#));
- Frequency: occurrence frequency of fractures per section; and
- Types: type of deformation of a fracture, e.g., normal, reverse, dextral, sinistral displacement, or a combination of the above.

For veins, we examined and measured several parameters:

- Location: where a vein occurs in a core, measured in centimeters from the top of the section;

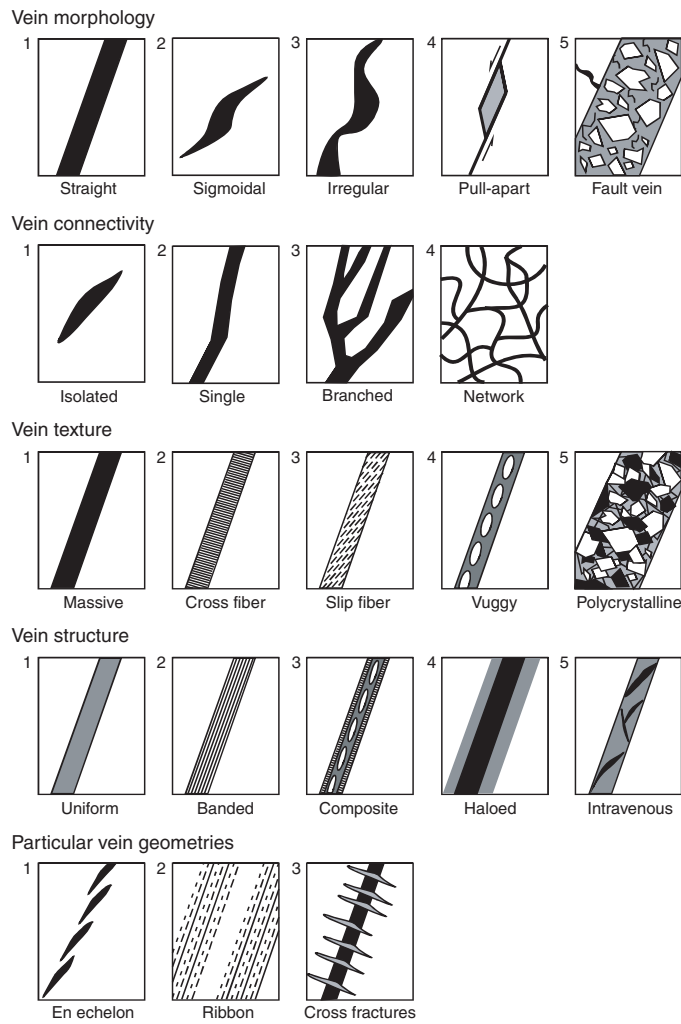
Figure F19. Example of the structural geology observation sheet used during Expedition 349.

Exp. 349 Structural Geology Observation Sheet

Site:U1431E

Core	Section	struct ID	top of struct	bottom of struct	Core face app.		2nd app. Dip		Calculated Orientation			P-mag pole		Corrected Orientation			note
					az	dip	az	dip	dip dir	strike	dip	Dec	Inc	dip dir	strike	dip	

Figure F20. Vein description scheme, modified after Expedition 324 Scientists (2010).



- Morphology: morphological shape of a vein;
- Orientation: dip angle and dipping direction of a vein;
- Frequency: occurrence frequency of veins per section; and
- Mineral infill and alteration: these features are recorded as described by petrologists.

For igneous contacts, we described the following parameters:

- Location: where an igneous contact occurs in a core, measured in centimeters from the top of the section;

- Type of contacts: type of igneous contact boundary;
- Orientation: dip angle and dipping direction of an igneous contact;
- Frequency: occurrence frequency of igneous contacts per section; and
- Mineral infill and alteration: these features are recorded as described by petrologists.

For magmatic fabrics, we measured the following parameters:

- Location: where a magmatic fabric feature occurs in a core, measured in centimeters from the top of the section;
- Morphology: morphological shape of a magmatic fabric feature;
- Orientation: dip angle and dipping direction of a magmatic fabric feature; and
- Frequency: occurrence frequency of magmatic fabrics per section.

Orientation measurements and correction

Orientation measurements

We used a plastic goniometer for orientation measurements (Figure F21). Orientations of planar and linear features in a core section were determined relative to the core reference frame (Figure F22). The vertical axis of the core reference frame is aligned with the upcore direction of the core section, whereas the double line marked on the archive half of the core liner is defined as 180° in the cross-sectional plane perpendicular to the core vertical axis.

To determine the orientation of a planar structural element (shaded plane in Figure F22), two apparent dips of the element were measured in the core reference frame. The first apparent dip measures the intersection angle between the planar structural element and the split face of the core (β_1 in Figure F22); it is determined by measuring the dip direction and angle of the planar structural element in the core reference frame. A planar structural element could

Figure F21. Goniometer used during Expedition 349 to measure dip and dip direction of planes in split cores.

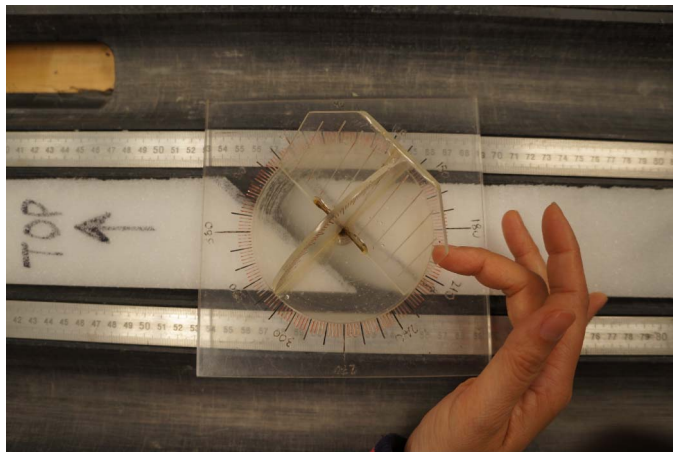
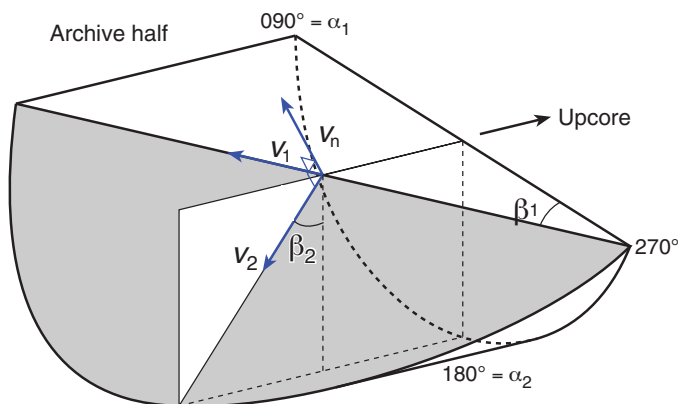


Figure F22. Diagram of core reference frame and coordinates used in orientation data calculation during Expedition 349.



have a trend of 90° or 270° and a plunge angle ranging from 0° to 90°. The second apparent dip measures the intersection angle between the central line of the planar structural element and the split face of the core (β_2 in Figure F22). In most cases, this was a plane either parallel or perpendicular to the core axis. In the former case, the apparent dip would trend 0° or 180° with plunge angle ranging from 0° to 90°; in the latter case, the trend would range from 0° to 360° with a plunge angle of 0°.

A linear feature observed in the surface of a split core is often associated with a planar structural element (e.g., a fault plane) in the core; the orientations of the planar structural element is determined by measuring either the rake (or pitch) of the associated plane or the trend and plunge of the planar element in the core reference frame. All measured data were manually typed into the log sheet together with the measured depths in the core section and descriptive information (Figure F19).

Plane orientation calculation

For a planar structural element (e.g., a bedding or fault plane), two apparent dips on two different surfaces (e.g., one being the split core surface, which is east–west vertical, and the other being horizontal or north–south vertical surface) were measured in the core reference frame. The two apparent dips are the azimuth (measured clockwise from north, looking down) and plunge. An x, y, z coordinate system was defined in such a way that the positive $x, y,$ and z directions coincide with north, east, and vertical downward, respectively. If the azimuths and plunges of the two apparent dips are given as (α_1, β_1) and (α_2, β_2) , respectively, as in Figure F22, the unit vectors representing these two lines, v_1 and v_2 , are given by the following expression:

$$v_1 = \begin{pmatrix} l_1 \\ m_1 \\ n_1 \end{pmatrix} = \begin{pmatrix} \cos \alpha_1 \cos \beta_1 \\ \sin \alpha_1 \cos \beta_1 \\ \sin \beta_1 \end{pmatrix} \text{ and}$$

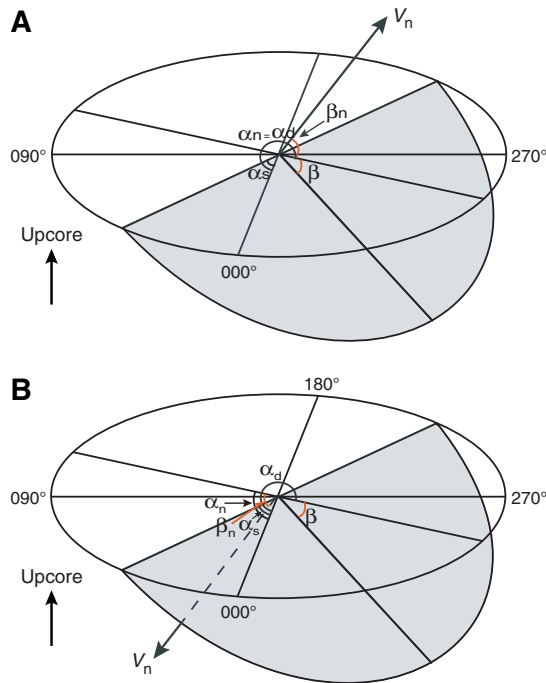
$$v_2 = \begin{pmatrix} l_2 \\ m_2 \\ n_2 \end{pmatrix} = \begin{pmatrix} \cos \alpha_2 \cos \beta_2 \\ \sin \alpha_2 \cos \beta_2 \\ \sin \beta_2 \end{pmatrix}.$$

The unit vector normal to the planar structural element v_n (Figure F23) is then defined as

$$v_n = \begin{pmatrix} l_n \\ m_n \\ n_n \end{pmatrix} = \frac{v_1 \times v_2}{|v_1 \times v_2|}, \text{ where}$$

$$v_1 \times v_2 = \begin{pmatrix} m_1 m_2 \\ n_1 n_2 \\ n_1 l_2 - n_2 l_1 \\ l_1 l_2 \\ m_1 m_2 \end{pmatrix} = \begin{pmatrix} m_1 n_2 - m_2 n_1 \\ n_1 l_2 - n_2 l_1 \\ l_1 m_2 - l_2 m_1 \end{pmatrix}.$$

Figure F23. Diagram of dip direction (α_d), right-hand rule strike (α_s), and dip (β) of a plane deduced from its normal azimuth (α_n) and dip (β_n). V_n denotes the unit vector normal to plane. A. $\beta_n < 0^\circ$. B. $\beta_n \geq 0^\circ$.



The azimuth α_n and plunge β_n of the vector v_n are given by

$$\alpha_n = \tan^{-1}\left(\frac{m_n}{l_n}\right) \text{ and}$$

$$\beta_n = \sin^{-1} n_n.$$

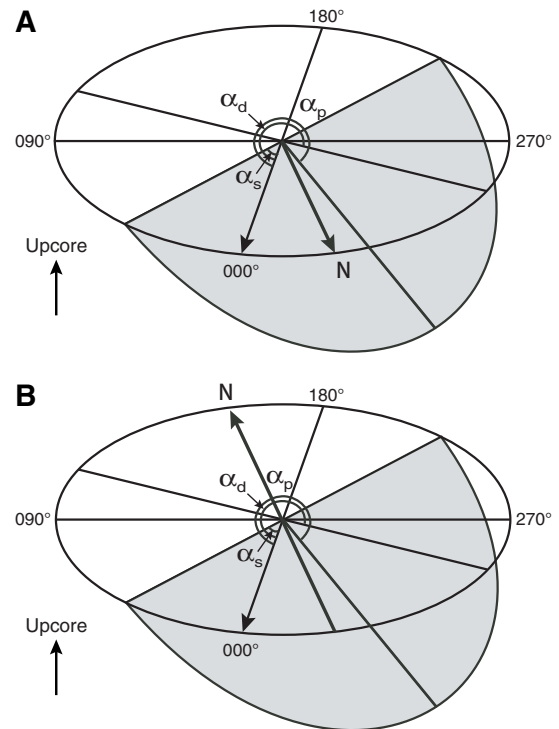
The dip direction α_d and dip angle β of this plane are $\alpha_d = \alpha_n$ and $\beta = 90^\circ + \beta_n$, respectively, when $\beta_n < 0^\circ$; and $\alpha_d = \alpha_n \pm 180^\circ$ and $\beta = 90^\circ - \beta_n$, respectively, when $\beta_n \geq 0^\circ$. The strike of this plane α_s according to the right-hand rule is then given by $\alpha_s = \alpha_d - 90^\circ$ (Figure F23).

Azimuth correction based on paleomagnetic data

Provided that a core is vertical, its magnetization is primary, and bedding is horizontal, its paleomagnetic declination α_p indicates the magnetic north direction when its inclination $\beta_p \geq 0^\circ$ (Figure F24); in contrast, the angle α_p indicates the magnetic south direction when $\beta_p < 0^\circ$. The dip direction and strike of a planar structural element in the geographic reference frame, α_d^* and α_s^* , are therefore $\alpha_d^* = \alpha_p - \alpha_d$ and $\alpha_s^* = \alpha_p - \alpha_s$ when $\beta_p \geq 0^\circ$; or $\alpha_d^* = 180^\circ + \alpha_p - \alpha_d$ and $\alpha_s^* = 180^\circ + \alpha_p - \alpha_s$ when $\beta_p < 0^\circ$.

If a core section was complete and continuous, one paleomagnetism sample per section (1.5 m) was deemed sufficient to determine the paleomagnetic orientation of the core section. If the core was discontinuous, one paleomagnetism sample for each subsection of the core that was continuous and structurally important was required. Paleomagnetism samples were taken as cubic or cylindrical samples close to a planar structural element of interest (usually

Figure F24. Diagrams of azimuth correction based on paleomagnetic data. α_p = paleomagnetic declination, α_d and α_s = dip direction and right-hand rule strike of a plane. A. $\beta_p \geq 0^\circ$. B. $\beta_p < 0^\circ$.



within 5 cm) and from a coherent core interval that included the structural element of interest. In general, we avoided core fragments that were so small that potential spinning during drilling might cause significant deviation from the core axis (e.g., fragments of brecciated segments).

Geochemistry

The shipboard geochemistry program for Expedition 349 included measurements for

- Headspace gas content;
- Interstitial water composition;
- Sedimentary geochemistry including total inorganic carbon, total carbon, total nitrogen, and major and minor element content; and
- Igneous rock geochemistry (major and minor element content).

These analyses were carried out to satisfy routine shipboard safety and pollution prevention requirements; characterize interstitial water, sediment, and rock geochemistry for shipboard interpretation; and provide a basis for sampling for shore-based research.

Interstitial water chemistry

Interstitial water collection

Routine interstitial water samples were obtained by squeezing whole-round sections cut from cores. Standard whole-round samples were 5 cm long, but as water content decreased downhole, the size of the whole-round samples was increased up to 15 cm to enable extraction of the ~30 mL of water needed for shipboard and shore-based analyses. Whole-round samples were cut and capped

as quickly as possible after the core arrived on deck and immediately moved to the chemistry laboratory for squeezing. Whole-round samples were typically collected at a frequency of up to 1 sample per section for the uppermost 20 m, 1–2 samples per core downhole to 100 mbsf, and then 1 sample per core until basement or until interstitial water extraction required a >15 cm whole-round section in order to preserve core for visual core description and other sampling. The exterior of the whole-round sample was carefully cleaned with a spatula to remove potential contamination from drilling fluid. For XCB cores, the intruded drilling mud between biscuits was also removed to eliminate contamination from drilling fluid. The cleaned sediment was placed into a 9 cm diameter titanium squeezer that was then placed in a Carver hydraulic press (Manheim and Sayles, 1974) and squeezed at pressures no higher than 25,000 lb (~17 MPa) to prevent the release of interlayer water from clay minerals during squeezing. The squeezed interstitial water was collected into a 60 mL deionized water-washed (18 M Ω /cm) high-density polyethylene syringe attached to the squeezing assembly and subsequently filtered through a 0.45 μ m polyethersulfone membrane filter into various sample containers.

For Hole U1431A, interstitial waters were collected by both squeezing whole-round samples and Rhizon samplers. The whole-round samples were taken every 50 cm in order to obtain high-resolution interstitial water depth profiles for the upper 20 m of sediment. Rhizon sampling collected interstitial water at 5, 10, 20, and 50 cm intervals for sediment at 0–3, 3–9, 9–17, and 17–28 mbsf intervals, respectively. Rhizon sampling for interstitial water lasted for ~2–4 h to obtain ~20 mL water samples for shore-based analyses.

Sample allocation was determined based on the pore fluid volume obtained and analytical priorities based on the objectives of the expedition. Aliquots for analysis by ICP-AES were acidified by adding ~10 μ L of trace metal-grade concentrated HNO₃ and placed in 4 mL cryovials. Aliquots for titration and ion chromatography analyses were put in 10 mL high-density polyethylene vials. Aliquots for dissolved inorganic carbon (DIC) and dissolved organic carbon (DOC) and their $\delta^{13}\text{C}$ were treated with 10 μ L of a saturated HgCl₂ solution and placed in 8 mL septum screw-lid glass vials. Aliquots for isotopic analyses of oxygen, hydrogen, and Sr ratios were also placed in 8 mL septum screw-lid glass vials. Aliquots for TH₂S were placed in 2 mL septum screw-lid glass vials with 0.5 mL of 20% zinc acetate solution. The samples were stored at 4°C after collection.

Alkalinity, pH, and salinity were analyzed immediately after interstitial water was obtained. Other shipboard analyses were carried out in batches. Dissolved sodium, calcium, magnesium, chloride, bromide, and sulfate were analyzed by ion chromatography. Ammonium and phosphate were analyzed by spectrophotometry. Major and minor element concentrations were analyzed by ICP-AES.

After interstitial water extraction was complete, sediment squeeze cakes were divided and sealed in plastic bags for shipboard and shore-based analyses. Squeeze cake samples for shore-based organic analysis were stored at –80°C. All other squeeze cake samples were refrigerated at 4°C.

Shipboard interstitial water analysis

Interstitial water samples were analyzed on board following the protocols in Gieskes et al. (1991), Murray et al. (2000), and the Integrated Ocean Drilling Program user manual for shipboard instrumentation, which was updated during Integrated Ocean Drilling Program Expedition 344 (Harris et al., 2013).

Salinity, alkalinity, and pH

Salinity, alkalinity, and pH were measured immediately after squeezing, following the procedures in Gieskes et al. (1991). Salinity was measured using a Fisher temperature-compensated handheld refractometer. The pH was measured with a combined glass electrode, and alkalinity was determined by Gran titration with an autotitrator (Metrohm 794 basic Titrino) using 0.1 M HCl at 25°C. International Association for the Physical Sciences of the Oceans (IAPSO) standard seawater was used for calibration and was analyzed at the beginning and end of a set of samples for each site and after every 10 samples. Alkalinity titrations had a precision within 2% based on repeated analysis of IAPSO standard seawater. For sample volumes of \leq 14 mL, alkalinity and pH were not measured because each alkalinity and pH analysis requires 3 mL of interstitial water.

Chloride by titration

High-precision chloride concentrations were acquired using a Metrohm 785 DMP autotitrator and silver nitrate (AgNO₃) solution calibrated against repeated titrations of IAPSO standard. A 0.5 mL aliquot of sample was diluted with 30 mL of an 80 mM HNO₃ solution and titrated with 0.1 N AgNO₃. Repeated analyses of an IAPSO standard yielded a precision better than 0.05%; however, the chloride concentrations yielded by titration includes not only dissolved chloride but also all of the other halide elements and bisulfide. The *JOIDES Resolution* is equipped with Metrohm 850 Professional ion chromatograph (IC), which can analyze anions and cations simultaneously. The chloride concentration was analyzed by both titration and ion chromatography for Holes U1431A and U1431D. Chloride concentrations analyzed by ion chromatography were not greater than those by titration, indicating that ion chromatography can mostly provide reliable chloride data. As a result, chloride concentration was analyzed only by ion chromatography for the remaining sites.

Sulfate, chloride, bromide, calcium, magnesium, and sodium

Sulfate, chloride, bromide, calcium, magnesium, and sodium concentrations were analyzed by ion chromatography (Metrohm 850 Professional IC) using aliquots of 100 μ L that were diluted 1:100 with deionized water (18 M Ω /cm). At the beginning and end of each run, different dilutions of IAPSO standard seawater were analyzed for quality control and to determine accuracy and precision. Analytical precision was within 0.9% for chloride, 4.0% for bromide, 1.0% for sulfate, 2.8% for calcium, 1.2% for magnesium, and 1.4% for sodium.

Ammonium and phosphate

Ammonium and phosphate concentrations were determined using an Agilent Technologies Cary Series 100 UV-Vis spectrophotometer with a sipper sample introduction system following the protocol in Gieskes et al. (1991). For ammonium concentration analysis, a 0.1 mL sample aliquot was diluted with 1 mL reagent water, to which 0.5 mL phenol ethanol, 0.5 mL sodium nitroprusside, and 1 mL oxidizing solution (trisodium citrate and sodium hydroxide) were added in a 5 mL capped glass vial (Gieskes et al., 1991). The solution was kept at room temperature for ~6.5 h to develop color. Ammonium concentrations were determined at an absorbance of 640 nm. Precision and accuracy of the ammonium analyses were within 2.5% and 3%, respectively.

For phosphate analysis, a 0.3 mL sample was diluted with 1 mL deionized water (18 M Ω /cm) in a 4 mL glass vial. Then 2 mL of mixed reagent (ammonium molybdate, sulfuric acid, ascorbic acid,

and potassium antimonyl tartrate) was added to the vial (Gieskes et al., 1991), which was capped and kept at room temperature for at least several minutes to develop color. The phosphate concentration was determined at an absorbance of 885 nm ~30 min after adding the mixed reagent solution. Precision and accuracy of the phosphate analyses were better than 2% and 2%, respectively.

Major and minor elements

Dissolved major and minor elements were determined by Leeman ICP-AES. For major cation (Na^+ , K^+ , Ca^{2+} , and Mg^{2+}) analyses, dilutions of IAPSO standard seawater were used as calibration standards. Standards and acidified samples were diluted 1:100 (v/v) with a 2% HNO_3 (by volume) solution (matrix) with Y at 10 ppm as an internal standard. Calibration for minor elements (Mn^{2+} , Fe^{2+} , B, Si, Sr^{2+} , Ba^{2+} , and Li^+) was done with dilutions of a multielement synthetic standard solution (composed of single-element standards). Acidified samples measured for minor elements on the ICP-AES were diluted 1:20 (v/v) with the same matrix used for the major element analysis. Drift correction was made for both major and minor elements using the factor from a drift monitor solution (100% IAPSO for majors and 100% stock solution for minors) that was analyzed every eight samples. The ICP-AES auto-sampler and analysis chamber were rinsed with a 3% (by volume) HNO_3 solution between samples. Major cations (Mg^{2+} , Ca^{2+} , K^+ , and Na^+) were also determined by IC at 1:100 dilutions; however, these results yielded poor quality K^+ data, whereas the ICP-AES yielded good quality data for K^+ .

Headspace gas geochemistry

One sediment sample (5 cm^3) from each core, collected immediately after retrieval on deck, was placed in a 20 cm^3 glass vial and sealed with a septum and a crimped metal cap. When consolidated or lithified samples were encountered, chips of material were placed in the vial and sealed. If an interstitial water sample was obtained, the headspace sample was taken from the top of the section immediately next to the interstitial water sample whenever possible. The vial was labeled with the core, section, and interval from which the sample was taken and then placed in an oven at 70°C for 30 min. A 5 cm^3 volume of gas extracted through the septum was then injected with a gas-tight glass syringe into a gas chromatograph (GC).

The GC (Agilent 6890 equipped with a flame ionization detector [FID]) was set at 250°C and used to accurately and rapidly measure the concentrations of methane (C_1), ethane (C_2), ethylene ($\text{C}_{2=}$), propane (C_3), and propylene ($\text{C}_{3=}$). A $2.4 \text{ m} \times 2.0 \text{ mm}$ stainless steel column packed with 80/100 mesh HayeSep "R" is installed in the oven. The injector consists of a $\frac{1}{16}$ inch Valco union with a $7 \mu\text{m}$ screen connected to a Valco-to-Luer lock syringe adaptor. This injector connects to a 10-port Valco valve that was switched pneumatically by a digital valve interface. The injector temperature was set at 120°C . Samples were introduced into the GC through a 0.25 cm^3 sample loop connected to the Valco valve. The valve can be switched automatically to backflush the column. The oven temperature was programmed to start at 80°C for 8.25 min and then increased to 150°C for 5 min at a rate of $40^\circ\text{C}/\text{min}$. Helium was used as the carrier gas. Initial helium flow in the column was $30 \text{ mL}/\text{min}$. Flow was then ramped to $60 \text{ mL}/\text{min}$ after 8.25 min to accelerate elution of C_3 and $\text{C}_{3=}$. The run time was 15 min. The GC was also equipped with an electronic pressure control module to control the overall flow into the GC.

Sediment geochemistry

Sedimentary inorganic and organic carbon content

Sediment samples were collected from the interstitial water squeeze cakes, with additional samples taken from intervals of distinct lithology. Samples were freeze-dried for ~24 h, crushed using an agate pestle and mortar, and then analyzed for total carbon, total inorganic carbon (TIC), and total nitrogen.

Total carbon and total nitrogen of the sediment samples were determined with a ThermoElectron Corporation FlashEA 1112 CHNS elemental analyzer equipped with a ThermoElectron packed column CHNS/NCS GC and a thermal conductivity detector (TCD). Approximately 10–15 mg of sediment was weighed into a tin cup and then combusted at 950°C in a stream of oxygen. The reaction gases were passed through a reduction chamber to reduce nitrogen oxides to nitrogen and were then separated by the GC before detection by TCD. All measurements were calibrated to a standard (Soil Reference Material NC [PN 33840025]), which was run every 10 samples. The peak areas from the TCD were calculated to determine the total carbon and total nitrogen of the samples.

TIC was determined using a Coulometrics 5015 CO_2 coulometer. Approximately 10 mg of sediment was weighed into a glass vial and acidified with 2 M HCl. The liberated CO_2 was titrated, and the corresponding change in light transmittance in the coulometric cell was monitored using a photodetection cell. The weight percent of calcium carbonate was calculated from the inorganic carbon content using the following equation:

$$\text{CaCO}_3 (\text{wt}\%) = \text{TIC} (\text{wt}\%) \times 100/12.$$

Standard CaCO_3 (standard reference material) was used to confirm accuracy. Total organic carbon content was calculated by subtraction of inorganic carbon from the total carbon.

Elemental analysis of bulk sediment/sedimentary rock by ICP-AES

Elemental composition of bulk sediment was determined using a Leeman ICP-AES. Our analytical approach followed the general procedure outlined by Murray et al. (2000) and the constraints indicated by Quintin et al. (2002). Analytical blanks were prepared using 400 mg of lithium metaborate (LiBO_2) flux to ensure matrix matching. Samples analyzed by ICP-AES were ignited before dissolution by heating 5 g of oven-dried (600°C for 12 h) ground sediment at 1025°C for 5 h to determine weight loss on ignition (LOI), to release volatile phases (H_2O , CO_2 , and S), and to fully oxidize all iron to ferric iron.

Aliquots of 100 mg of ignited sediment and standards were mixed with 400 mg of LiBO_2 flux. Subsequently, 10 μL of a wetting agent, 0.172 mM lithium bromide (LiBr), was added to the samples, standards, and blanks. This mixture was fused at 1050°C for 5 min in a Bead Sampler NT-4100 prior to dissolution in 50 mL of 10% HNO_3 . For complete dissolution, 1 h of shaking with a Burrell wrist-action shaker was required. Aliquots of 5 mL of the resulting solutions were filtered ($0.45 \mu\text{m}$) and diluted with 35 mL of 10% HNO_3 , resulting in a 4000 \times dilution of the original sediment.

A range of standards was selected to cover the entire range of expected sediment compositions, with their suitability monitored during the expedition. These standards were: STSD1, STSD2, STSD4, SO-1, SO-2, SO-3, SO-4, NBS-1c, JR-2, and BCR2. BHVO2 was also selected as both the drift and consistency standard. A range of major and trace elements was analyzed. Major elements

included Si, Al, Fe, Mg, Ca, Na, K, Ti, Mn, and P, and trace elements included Ba, V, Cr, Ni, Cu, Zn, Rb, Sr, Y, Zr, Li, and Sc. Major elements were expressed as weight percent oxide and trace elements as parts per million. LOI values were determined routinely. Samples were analyzed in duplicate. The procedures used to process the data are outlined in [Data reduction](#) below.

The elemental compositions of sediment/sedimentary rock were only analyzed at Site U1431 due to time constraints.

Igneous rock geochemistry

Sample preparation

Representative samples of igneous rocks were analyzed for major and trace element concentrations during Expedition 349 using the Leeman ICP-AES.

Samples ranging in size from ~2 to ~8 cm³ were cut from the core with a diamond saw blade. A thin section billet was taken from the same or adjacent interval for petrographic analysis and alteration determination (see [Igneous petrology and alteration](#)). All outer surfaces were ground on a diamond-impregnated disk to remove altered rinds and surface contamination derived from the drill or saw. Each sample was then placed in a beaker containing acetone and washed ultrasonically for 15 min. The acetone was decanted, and the samples were sonicated in deionized water (18 M Ω /cm) twice for 10 min. The cleaned pieces were dried for 10–12 h at 110°C.

The cleaned, dried samples were crushed to <1 cm chips between two disks of Delrin plastic in a hydraulic press. The rock chips were then ground to a fine powder in tungsten carbide in a SPEX 8515 Shatter box. After grinding, a 5.0 \pm 0.5 g aliquot of the sample powder was weighed on a Mettler Toledo balance and ignited at 1025°C for 4 h to determine LOI.

Murray et al. (2000) describes in detail the shipboard procedure for digestion of rocks and ICP-AES analysis of samples. The following protocol is an abbreviated form of this procedure with minor modifications. After determination of LOI, 100.0 \pm 0.2 mg splits of the ignited whole-rock powders were weighed and mixed with 400.0 \pm 0.5 mg of LiBO₂ flux that had been preweighed on shore. Standard rock powders and full procedural blanks were included with unknowns in each ICP-AES run (note that among the elements analyzed, contamination from the tungsten carbide mills is negligible; Shipboard Scientific Party, 2003). All samples and standards were weighed on a microbalance with weighing errors estimated to be \pm 0.05 mg under relatively smooth sea-surface conditions.

To prevent the cooled bead from sticking to the crucible, 10 mL of 0.172 mM aqueous LiBr solution was added to the mixture of flux and rock powder as a nonwetting agent. Samples were then fused individually in Pt-Au (95:5) crucibles for ~12 min at a maximum temperature of 1050°C in an internally rotating induction furnace (Bead Sampler NT-4100).

After cooling, beads were transferred to high-density polypropylene bottles and dissolved in 50 mL of 10% (by volume) HNO₃, aided by shaking with a Burrell wrist-action bottle shaker for 1 h. Following digestion of the bead, the solution was passed through a 0.45 μ m filter into a clean 60 mL wide-mouth high-density polypropylene bottle. Next, 1.25 mL of this solution was transferred to a plastic vial and diluted with 10% HNO₃ to a total volume of 10 mL. The final solution-to-sample dilution factor was ~4000 \times .

Analyses of igneous rocks

Major (Si, Ti, Al, Fe, Mn, Mg, Ca, Na, K, and P) and trace (Ba, Sr, Zr, Y, V, Sc, Zn, Co, Cr, Ni, Rb, and Nb) element concentrations of standards and samples were determined with a Leeman ICP-AES

instrument. The plasma was ignited at least 30 min before each run of samples to allow the instrument to warm up and stabilize.

The ICP-AES data presented in the Geochemistry section of each Expedition 349 site chapter were acquired using the Gaussian mode of the Prodigy software. This mode fits a curve to points across a peak and integrates the area under the curve for each element measured. Each sample was analyzed four times from the same dilute solution (i.e., in quadruplicate) within a given sample run. For elements measured at more than one wavelength, we either used the wavelength giving the best calibration line in a given run or, if the calibration lines for more than one wavelength were of similar quality, used the data from all wavelengths and reported the average concentration.

The ICP-AES run included

- Certified rock standards (including AGV-1, BCR-2, BHVO-2, BIR-1, JA-3, JGb-1, JP-1, JR-2) analyzed twice during each run;
- Samples (unknowns) analyzed in quadruplicate;
- A drift-correcting standard (BHVO-2) analyzed in every eighth sample position and at the beginning and end of each run;
- A blank solution analyzed near the beginning;
- Two or three “check” standards (BHVO-2 and BCR-2) run as unknowns, each also analyzed in quadruplicate; and
- A 10% HNO₃ wash solution run for 60 s between each analysis.

Data reduction

Following each run of the instrument, the measured raw-intensity values were transferred to a data file, corrected for instrument drift, and then corrected for the procedural blank. Drift correction was applied to each element by linear interpolation between the drift-monitoring solutions run in every eighth sample position.

After drift correction and blank subtraction, a calibration line for each element was calculated using the results for the certified rock standards. Element concentrations in the samples were then calculated from the relevant calibration lines.

Individual analyses of both standards and samples produced total volatile-free major element weight percentages that vary from 100 wt% by as much as several percent. Possible causes include some combination of errors in weighing the sample (particularly in rougher seas) and/or flux powders (although even when weighed on land, weighing errors are possible), variability in the dilutions (which were done volumetrically), and the duration and relatively low temperature of ignition. To facilitate comparison of Expedition 349 results with each other and with data from the literature, the measured major element values were normalized to 100 wt% totals.

Microbiology

During Expedition 349, samples for microbiological analysis collected from sediment and basement were preserved for determining the biomass, activity, and community structure of microbial communities. Relatively few analyses were performed shipboard because most measurements need to be made in shore-based laboratories. Accordingly, our effort was dedicated to collecting and preserving an adequate number of samples for subsequent shore-based studies. DNA and intact polar lipid analyses will be used to identify microbes in the samples. RNA determination will help to establish the activities of the communities. Single-cell genomics will provide detailed information about the functional potential of microbes in the samples, link those potentials to cellular identity, and provide clues related to the best ways to cultivate cells from the sediments. Fluorescence in situ hybridization (FISH) will allow key

community members to be viewed microscopically and provide data related to cellular activity. Enrichment for specific groups of organisms will identify the unique physiological properties of the organisms. A considerable amount of time during the expedition was dedicated to collecting samples for quality assurance and quality control to allow determination of the microbiological quality of the samples. Some limited analyses of the tracers were also conducted.

Core handling and sampling

Microbiological sampling depends on careful sample handling techniques and the use of contamination tracers. Microorganisms collected from the seafloor are expected to be sensitive to chemical and physical changes that they encounter when brought to the surface. Changes in oxygen concentration and temperature are two important factors to be considered when bringing cells from cold, anoxic settings to the surface. Accordingly, the following procedures were followed in order to minimize harm to subsurface microbes without compromising the other objectives of the expedition.

Contamination testing

When obtaining deep sediment or rock samples for microbiological research, considerable potential exists for contamination by microbes from the surface. Accordingly, it has become common practice to add tracers to the drilling fluids and core catcher sub so that the extent of contamination from the drilling fluids or core recovery methods can be evaluated. To check for potential intrusion of drilling fluids from the outside to the center of cores and to confirm the suitability of core material for microbiological research, the following tracers were used:

- Perfluorocarbon tracers (PFT) were used during coring of sediment with the APC and XCB;
- Cell-sized fluorescent microspheres were used during coring of lithified sedimentary rock and basalt with the RCB; and
- Periodic sampling of the drilling fluids, seawater (used to mix the drilling fluids), and outer surface of core was conducted in order to obtain community data based on extracted DNA or lipids. Comparison of microbial community profiles derived from likely sources of contamination with profiles from the interior of cores should yield notable differences; otherwise, there is reason to believe that the interior of the samples has been compromised.

Perfluorocarbon tracer

As a group, PFTs are nontoxic, inert, insoluble in water, and easily detected in a gas chromatograph with an electron capture detector (ECD). Perfluoromethylcyclohexane was used on the *JOIDES Resolution* during Expedition 349. PFTs were introduced into the drilling fluids with a high-pressure liquid chromatography pump at a constant concentration of 1 mg/L. This compound serves as an imperfect tracer for potential contamination of core material by nonindigenous microbes in the drilling fluids because it is much smaller than microbes; however, it is a useful guide for qualitative estimates of contamination. PFTs are volatile and samples must be collected quickly or they will show evidence of PFT contamination even though such contamination may not have occurred during drilling, but instead during processing of the core.

Based on prior reports from Expedition 329 (Expedition 329 Scientists, 2011) and difficulties associated with release of PFTs from core material, we did not attempt to develop the PFT as a

quantitative tracer. Instead, PFT samples were prepared according to previously established methods (Smith et al., 2000; Lever et al., 2006), slightly modified by taking 3 cm³ sediment samples on the catwalk immediately after core recovery (or soon thereafter) and placing them into GC vials. Each vial was quickly sealed and stored at 4°C for later analysis. The analyses were done on board using an Agilent 6890 GC with ECD. Samples for PFT characterization were obtained as shown in Figure F25.

Fluorescent microsphere tracers

Fluorescent microspheres, similar in size (0.5 µm in diameter) and charge to microorganisms, have been used in hydrology studies to determine dispersal and transport of microbe-sized objects (Harvey et al., 1989) and in drilling as tracers (Colwell et al., 1992). These microspheres (Fluoresbrite carboxylate microspheres; Polysciences, Inc.) appear bright green when observed by epifluorescence microscopy (458 nm excitation; 540 nm emission) and were used during Expedition 349 as a particulate tracer during coring of basalt and lithified sediment.

Microspheres were only deployed on cores acquired during RCB drilling when sampling was planned for microbiological cultivation and molecular biological analyses. The microspheres were deployed in plastic bags containing 40 mL of microsphere suspension in 18.2 MΩ water (10¹⁰ spheres/mL; 2 × 10¹¹ microspheres in a 40 mL bag according to Smith et al., 2000). The bag was then heat-sealed and placed into an additional plastic bag that was open at each end. By attaching the loose plastic ends with cord, the bag was wedged into a shim above the core catcher sub and stretched across the throat of the core barrel. The bags rupture and release the microspheres as the core enters the barrel. Samples for microsphere characterization were obtained as shown in Figure F26.

Preliminary estimates of concentrations of fluorescent microspheres in core samples were quantified on board using a Zeiss Axioptan 2 epifluorescence microscope fitted with CoolLED pE-100 LED light sources, a blue filter set, and a 40× Plan-NEOFLUAR oil-immersion objective, as performed during Expedition 330 (Expedition 330 Scientists, 2012). For hard rock samples, aliquots (0.5 g) of the crushed rock were suspended in 1 mL of 0.2 µm filtered NaCl-saturated solution and filtered onto black, 25 mm diameter polycarbonate filters (0.2 µm pore size) in a filtration tower. The filters were then mounted on microscope slides with a drop of nonfluorescent

Figure F25. Diagram of whole-round sample with subsample locations and perfluorocarbon tracer (PFT) sample locations on the outside of the core (Y) and on the inside of the core (Y*).

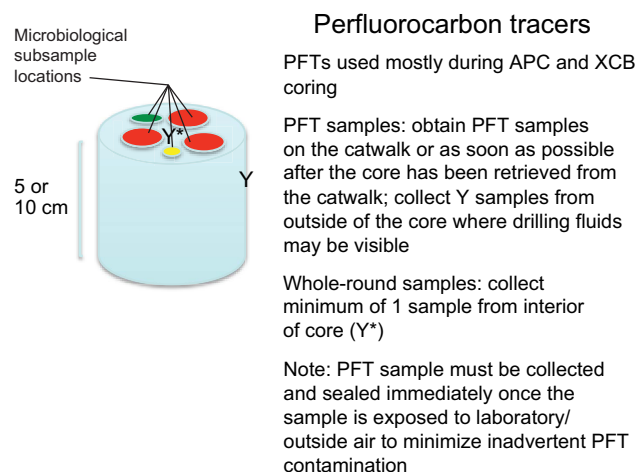
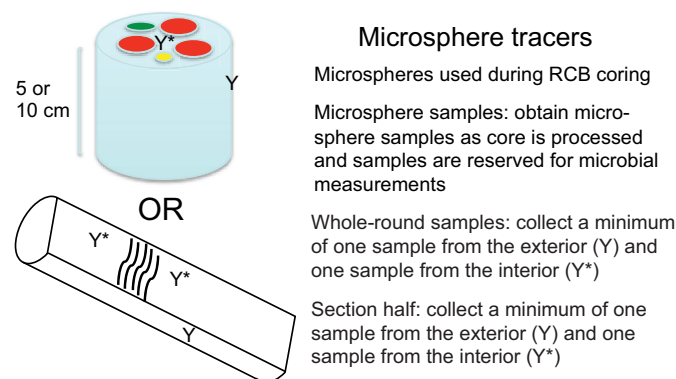


Figure F26. Diagram of whole-round sample and section half showing recommended microsphere sample locations on the outside of the core (Y) and on the inside of the core (Y*).



immersion oil and covered with a coverslip. Microsphere abundance on the filter was determined by averaging the total number seen in at least 20 randomly selected fields of view. Quantitative estimates of the number of fluorescent beads in samples are difficult to achieve because microspheres are released from the bag at the beginning of RCB coring and the levels of fluorescent beads decrease during the coring of each section, such that the last sections to be cored may not have received a substantial microsphere dose.

Fluid community tracers

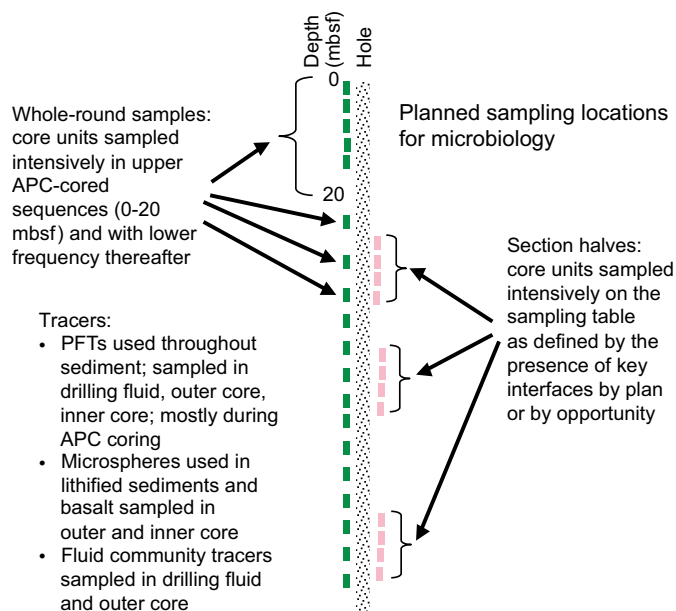
To further evaluate the extent to which contaminating cells may have penetrated a sample, contamination will be estimated by post-cruise comparison of the microbial community diversity in basalt and sediment samples with the respective drilling fluid collected at the time of coring. This technique was first performed with deep continental samples (Lehman et al., 1995) but is common for studies of subseafloor samples, in which contamination is ubiquitous and genomic signatures of the contaminating material are subtracted from those of the subseafloor samples. The method can be accomplished by obtaining and preserving an adequate number of samples from the different sources of contamination (seawater, drilling fluid) and from the interior of the cores and then carrying out high-throughput sequencing of the 16S rRNA genes in the respective samples. Subsequent comparison of the community signatures can help to identify samples that significantly overlap in community structure with the drilling fluids (deeming them contaminated), as well as samples that have unique community structure when compared to the fluids (deeming them unlikely to be contaminated). This approach is especially important during RCB drilling because this method requires large amounts of surface seawater to be pumped into the borehole. This water is a major source of microbial contamination to cores collected for microbiological analyses.

For fluid community tracers, microorganisms were collected on 0.2 μm pore filters by filtering seawater or drilling fluid collected from the core liner or from the rig floor before the water was pumped into the drill string. The filters were frozen (-80°C) and will be analyzed postcruise in order to compare the microbial community structures in the drilling fluids with those in the core samples.

Microbiological sampling

Two distinct sampling strategies were adopted for microbiological samples. The respective approaches, (1) routine sampling of

Figure F27. Generalized plan for microbiological sampling of whole-round sections and section halves, as well as planned tracer sampling points. PFT = perfluorocarbon tracer.



whole-round samples for microbiological measurements and (2) section half sampling for microbiological measurements across interfaces, are generally shown in Figure F27 and described in more detail below.

Whole-round samples

Once a core was retrieved, it was immediately transferred to the catwalk for labeling and cutting of sections. Cores were handled with care on the catwalk to prevent microbiological contamination. The core liner was cut by the standard IODP core cutter and with an ethanol-wiped spatula. Whole-round samples were provided to the microbiologist on duty as soon as possible on the catwalk. The core liner is not sterile, and the outer surface of the core is assumed to be contaminated during drilling. By subsampling the interior of the whole-round samples, the contaminated sediment or basalt that is next to the core liner can be avoided.

For routine microbiological sampling of whole-round samples, the upper sections close to the seafloor were sampled intensively, with whole-round samples taken as frequently as every 10 cm in the uppermost 1 mbsf. This sampling approach was followed when time permitted and when coring allowed a dedicated microbiology hole (e.g., Hole U1431B). Deeper than 1 mbsf, the sampling frequency decreased (see individual site reports), and the length of the whole-round samples collected was reduced to 5 cm. All whole-round samples were cut on the catwalk and capped on one end by an ethanol-rinsed plastic cap and by sterile foil on the other end. The whole-round samples were labeled and, with the foil covered ends held upright, transferred to the microbiology laboratory where they were stored in the cold room in an oxygen-free glove bag to minimize alteration of the microbial communities.

As soon as possible, the 5 or 10 cm long whole-round sample sections were subsampled into sterile 30 cm^3 tip-cut syringes and then transferred into sterile 50 mL centrifuge tubes. For indurated materials, a hammer and an aseptically cleaned chisel were used to remove outer portions of the whole-round sample to obtain the inner, less altered portion of the core, which was then transferred into

a sterile 50 mL centrifuge tube. In some cases, cores were hard enough that a SPEX 3624B X-Press hydraulic press was needed to crack the core to obtain material from the interior that was less likely to be contaminated by the drilling process. The pressure required to break the cores was usually <7 tons. Subsampling processes were carried out inside a N₂-sparged glove bag unless a hammer and chisel or the hydraulic press were required.

Samples were then either stored in an ultralow-temperature freezer (−80°C) for molecular analyses or in a refrigerator (4°C) for cultivation-based analyses. After one ultralow-temperature freezer stopped functioning, some lipid samples were transferred to −20°C storage. The outer portions of the cores that remained after microbiological subsampling were returned to the core laboratory. In cores collected by XCB coring, we examined the split core for signs of drilling disturbance (e.g., biscuiting) to determine whether contamination might have occurred. Therefore, some of the samples were flagged as possibly or clearly contaminated.

Section-half samples

For microbiological sampling at lithologic interfaces on the working half of the core, a different approach was required. Important interfaces (e.g., turbidites and volcanic ash) can only be detected following the initial physical property evaluations and after the core has been split for direct observation. We recognize that some properties of the microbial communities may change with extended storage prior to core splitting, but well-preserved samples were accounted for in the aforementioned routine microbiological sampling. Section-half sampling for microbiology occurred after observation of the working halves of the core and at the point when discrete geological features could be identified and used as a guide for intensive sampling for microbiological properties. This required that the microbiologist on shift observe the cores immediately after splitting so that samples could rapidly and carefully be taken from the working halves and preserved for subsequent molecular analyses or cultivations. This procedure was also applied to four samples from Site U1433 where section-half samples were acquired from locations in the core within 1 cm of where the whole-round sample for microbiology was acquired several hours before when the core arrived on the catwalk. This will allow a direct comparison of microbial properties in nearly identical geological material that only differ based on the elapsed time before sample preservation.

Direct visual examination of the cores was applied to identify where drilling fluid intrusion might be a problem. Using sterile scalpels and putty knives, the working half was scraped to remove exposed material on the cut surface and then the contrasting features and the associated interface was subsampled into sterile 50 cm³ centrifuge tubes. These tubes were then transferred to ultralow-temperature freezers (−80°C), the −20°C freezer, or refrigeration (4°C) as noted above for the whole-round samples.

Paleomagnetism

During Expedition 349, we conducted paleomagnetic studies primarily to determine directions of remanence components. Routine measurements were completed on all archive halves with stepwise alternating field (AF) demagnetization. Discrete cube and minicore samples were taken from selected working halves and were measured with stepwise AF and thermal demagnetization. These data were used for core reorientation, magnetostratigraphic dating, and paleolatitude determination.

Magnetic measurements

Remanent magnetization was measured using a 2G superconducting rock magnetometer (SRM) (2G Enterprises model 760R) equipped with direct-current superconducting quantum interference devices (SQUIDS) and an in-line, automated AF demagnetizer capable of reaching a peak field of 80 mT. Ocean drilling cores generally carry secondary remanence components (overprints), including natural viscous remanence and a steep downward-pointing component attributed to the drill string. To separate the overprints from the characteristic remanence (ChRM), stepwise demagnetization experiments were performed, as described below.

Archive-half sections

Measurements of archive halves were conducted using the software SRM for section (version 1.0) with a nominal sample-area parameter of 15.59 cm². The measurement interval and speed were 2.5 cm and 10 cm/s, respectively. The response functions of the pick-up coils of the SQUID sensors have a full width of 7–8 cm at half height (Parker and Gee, 2002). Therefore, data collected within ~4 cm of piece boundaries (or voids) are significantly affected by edge effects. Consequently, all data points within 4.5 cm of piece boundaries (as documented in the curatorial record) were filtered out prior to further processing. It should be noted that edge effects may also occur in a contiguous core piece if substantial heterogeneity (in intensity or direction) is present in the piece. It is more difficult to filter out such artifacts, but calculating the average direction (using Fisher statistics) for each core piece could provide a means of identifying these problems (Expedition 330 Scientists, 2012).

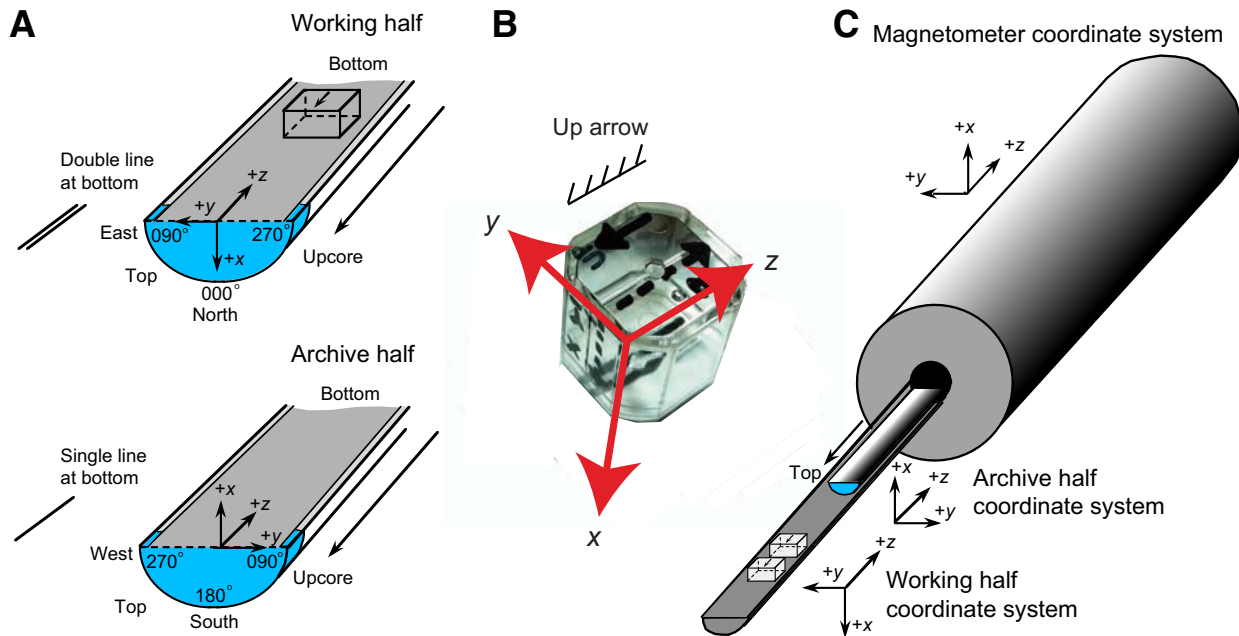
We performed successive AF demagnetization using the in-line AF demagnetizer of the SRM (2G Enterprises model 2G600) on all archive sections. The in-line AF demagnetizer applies a field to the *x*-, *y*-, and *z*-axes of the SRM in this fixed order. Previous reports suggest that higher AF demagnetization fields have produced significant anhysteretic remanent magnetization along the *z*-axis of the SRM. With this limitation, we used demagnetization steps up to 30 mT for demagnetizing sections. For most of the sediment sections, we performed steps from natural remanent magnetization to 30 mT demagnetization. The AF demagnetization results were plotted individually as vector plots (Zijderveld, 1967), as well as down-hole variations with depth. We inspected the plots visually to judge whether the remanence after demagnetization at the highest AF step reflects the ChRM and geomagnetic polarity sequence.

Discrete samples

Oriented discrete samples representative of the lithology were collected from working-half sections. In soft sediment, discrete samples were taken in plastic “Japanese” Natsuhara-Giken sampling cubes (7 cm³ sample volume; Figure F28). Cubes were pushed by hand into the working half of the core with the “up” arrow on the cube pointing upsection in the core. For indurated intervals, cubes were cut with a table saw and trimmed to fit in the plastic containers. In lithified sediment and hard rock, oriented minicores (~11 cm³) were taken. Measurements of discrete samples were conducted using the software SRM for discrete samples (version 1.0). Discrete samples were also measured using a spinner magnetometer (AGICO model JR-6A) when the cryogenic magnetometer was in use for long core pass-through measurements.

For discrete samples, we performed successive AF demagnetization with the DTech AF demagnetizer (model D-2000) for the spinner measurements to 120 mT (majority samples) and 200 mT (for

Figure F28. A. Coordinates of paleomagnetic samples (after Richter et al., 2007). B. Natsuhara-Giken sampling cubes (7 cm³ volume) shown with the sample coordinate system. Hatched arrow is parallel to the “up” arrow on the sample cube and points in the $-z$ sample direction. C. Coordinate system used for the superconducting rock magnetometer (SRM).



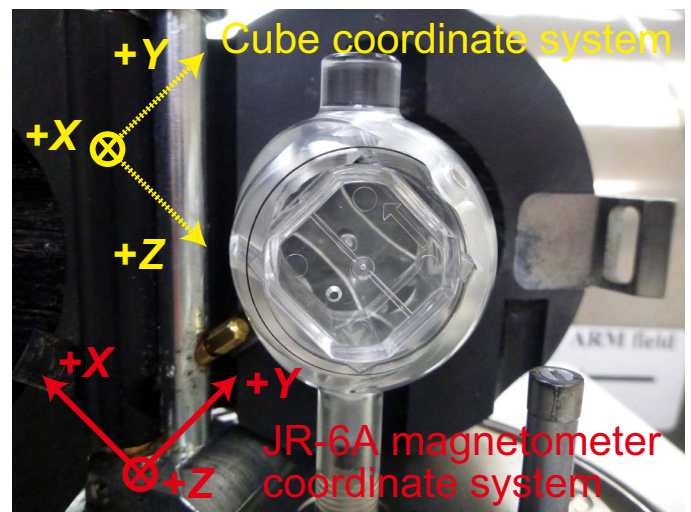
several high-coercivity samples). We also performed successive thermal demagnetization using a thermal specimen demagnetizer (ASC Scientific model TD-48SC) for several selected discrete samples up to 675°C. Temperature increments of 25–100°C were used depending on the unblocking temperature of each sample. We analyzed the stepwise demagnetization data of the discrete samples by principal component analysis to define the ChRM (Kirschvink, 1980). Section-half and discrete data collected on the pass-through SRM were uploaded to the LIMS database.

Low-field magnetic susceptibility of both whole rounds (see [Physical properties](#)) and split sections (see [Lithostratigraphy](#) and [Physical properties](#)) was routinely measured to roughly indicate the concentration of magnetic minerals. Anisotropy of magnetic susceptibility measurements were made on an AGICO KLY 4S Kappabridge instrument using the AMSSpin LabVIEW program designed by Gee et al. (2008) and adopted by the shipboard KLY 4S. The KLY 4S Kappabridge measures anisotropy of magnetic susceptibility by rotating the sample along three axes, stacking the data, and calculating the best-fit second-order tensor. It also measures the volume-normalized, calibrated bulk susceptibility (χ).

Coordinates

All magnetic data are reported relative to IODP orientation conventions: $+x$ is into the face of the working half, $+y$ points toward the left side of the face of the working half, and $+z$ points downsection. The relationship between the SRM coordinates (X , Y , and Z) and the data coordinates (x , y , and z) is $x = X$, $y = -Y$, and $z = Z$ for archive halves and $x = -X$, $y = Y$, and $z = Z$ for working halves (Figure F28). The coordinate system for the spinner magnetometer (AGICO model JR-6A) and Natsuhara-Giken sampling cubes are indicated in Figure F29.

Figure F29. Positioning of discrete samples in the “automatic holder” of the JR-6A magnetometer. The cube and JR-6A magnetometer coordinate systems are indicated by yellow and red, respectively.



Core orientation

Core orientation of the APC cores was achieved with an orientation tool (FlexIT) mounted on the core barrel. The tool consists of three mutually perpendicular fluxgate magnetic sensors and two perpendicular gravity sensors. The information from both sets of sensors allows the azimuth and dip of the hole to be measured, as well as the azimuth of the APC core orientation. The orientation information contributed to paleomagnetic polarity determinations and magnetostratigraphic interpretations.

ChRM also provides a reference frame to reorient cores (see **Structural geology**). Provided that the reference magnetic pole is known, the orientation of the paleomagnetic vector is then used to restore the azimuth of the core: the horizontal component of the mean ChRM makes an angle with the reference line, which specifies the rotation of the core relative to the geographic coordinates (e.g., Fuller, 1969). The other assumptions for reorientation include whether

1. The section has enough measurements to average out geomagnetic secular variation,
2. The original bedding is horizontal,
3. The core is vertical, and
4. The sedimentary unit has not experienced any vertical axis rotation.

Assumptions 2 and 3 were verified by shipboard structural geologists, seismic profiles of the drill sites, and drilling operational records. Confirmation of 1 and 4 will be conducted postexpedition.

For intervals of particular interest for structural geology, we report the ChRMs defined from discrete samples. More detailed demagnetization steps for the discrete samples allowed more accurate determination of ChRMs than those from the archive halves.

Magnetostratigraphy

Magnetostratigraphy for each site was constructed by correlating observed polarity sequences with the geomagnetic polarity timescale in combination with biostratigraphic datums (Figures **F11**, **F12**, **F13**). We adopted the geomagnetic polarity timescale of Gradstein et al. (2012) (Table **T4**), in which boundary ages for Chrons C1n–C13n and C24n.1n–C34n are orbitally tuned, whereas those for Chrons C13r–C23r are spline fitted.

Table T4. Geomagnetic polarity timescale (Gradstein et al., 2012) used during Expedition 349. (Continued on next two pages.) [Download table in .csv format.](#)

Geologic age	Base age (Ma)		Polarity chron	Top age (Ma)	Base age (Ma)	Duration (My)	Remarks
Neogene							
Holocene	11.5 ka						
Pleistocene		C1	C1n (Brunhes)	0	0.781	0.781	Base of Middle Pleistocene (Ionian) is base of Brunhes Chron.
late (Tarantian)	0.126		C1r.1r (Matuyama)	0.781	0.988	0.207	
middle (Ionian)	0.781		C1r.1n (Jaramillo)	0.988	1.072	0.084	
			C1r.2r	1.072	1.173	0.101	
			C1r.2n (Cobb Mountain)	1.173	1.185	0.012	Cobb Mountain Cryptochron is within early part of Matuyama (C1r) Chron.
			C1r.3r	1.185	1.778	0.593	
early (Calabrian)	1.806	C2	C2n (Olduvai)	1.778	1.945	0.167	Base of Calabrian is in lower part of Olduvai Chron.
			C2r.1r	1.945	2.128	0.183	
			C2r.1n (Reunion)	2.128	2.148	0.020	
			C2r.2r (Matuyama)	2.128	2.581	0.453	Base of Pleistocene is near base of Matuyama Chron.
(Gelasian)	2.588						
Pliocene		C2A	C2An.1n (Gauss)	0.000	3.032	3.032	"Gauss Normal Chron" (C2An) contains two reversed intervals, Kaena (2An.1r) and Mammoth (2An.2r).
			C2An.1r (Keana)	3.032	3.116	0.084	
			C2An.2n	3.116	3.207	0.091	
			C2An.2r (Mammoth)	3.207	3.330	0.123	
late (Piacenzian)	3.600		C2An.3n (Gauss)	3.330	3.596	0.266	Base of Piacenzian is base of Chron C2An.3n.
			C2Ar (Gilbert)	3.596	4.187	0.591	"Gilbert Reversed Chron" spans Chrons C2Ar through C3r.
		C3	C3n.1n (Cochiti)	4.187	4.300	0.113	
			C3n.1r	4.300	4.493	0.193	
			C3n.2n (Nunivak)	4.493	4.631	0.138	
			C3n.2r	4.631	4.799	0.168	
			C3n.3n (Sidufjall)	4.799	4.896	0.097	
			C3n.3r	4.896	4.997	0.101	
early (Zanclean)	5.332		C3n.4n (Thvera)	4.997	5.235	0.238	Base of Miocene is in uppermost Chron C3r.
Miocene			C3r (Gilbert)	5.235	6.033	0.798	
		C3A	C3An.1n	6.033	6.252	0.219	
			C3An.1r	6.252	6.436	0.184	
			C3An.2n	6.436	6.733	0.297	
			C3Ar	6.733	7.140	0.407	
		C3B	C3Bn	7.140	7.212	0.072	
late (Messinian)	7.246		C3Br.1r	7.212	7.251	0.039	Base of Messinian is in lowermost Chron C3Br.1r.
			C3Br.1n	7.251	7.285	0.034	
			C3Br.2r	7.285	7.454	0.169	
			C3Br.2n	7.454	7.489	0.035	
			C3Br.3r	7.489	7.528	0.039	
		C4	C4n.1n	7.528	7.642	0.114	
			C4n.1r	7.642	7.695	0.053	
			C4n.2n	7.695	8.108	0.413	

Table T4 (continued). (Continued on next page.)

Geologic age	Base age (Ma)	Polarity chron	Top age (Ma)	Base age (Ma)	Duration (My)	Remarks	
late (Tortonian)	11.63	C4r.1r	8.108	8.254	0.146	Cryptochron C4r.2r-1 is within C4r.2r (~8.661–8.699 Ma).	
		C4r.1n	8.254	8.300	0.046		
		C4r.2r	8.300	8.771	0.471		
		C4A	C4An	8.771	9.105		0.334
		C4Ar.1r	9.105	9.311	0.206		
		C4Ar.1n	9.311	9.426	0.115		
		C4Ar.2r	9.426	9.647	0.221		
		C4Ar.2n	9.647	9.721	0.074		
		C4Ar.3r	9.721	9.786	0.065		
		C5	C5n.1n	9.786	9.937		0.151
		C5n.1r	9.937	9.984	0.047		
		C5n.2n	9.984	11.056	1.072		
		C5r.1r	11.056	11.146	0.090		
		C5r.1n	11.146	11.188	0.042		
		C5r.2r	11.188	11.592	0.404	Subchron C5r.2r-1 is within C5r.2r (~11.263–11.308 Ma). Base of Tortonian is near base of Chron C5r.2n.	
		C5r.2n	11.592	11.657	0.065		
		C5r.3r	11.657	12.049	0.392		
		C5A	C5An.1n	12.049	12.174	0.125	
		C5An.1r	12.174	12.272	0.098		
		C5An.2n	12.272	12.474	0.202		
C5Ar.1r	12.474	12.735	0.261				
C5Ar.1n	12.735	12.770	0.035				
C5Ar.2r	12.770	12.829	0.059				
C5Ar.2n	12.829	12.887	0.058				
C5Ar.3r	12.887	13.032	0.145				
C5AA	C5AAAn	13.032	13.183	0.151			
C5AAr	13.183	13.363	0.180				
C5AB	C5ABn	13.363	13.608	0.245			
C5ABr	13.608	13.739	0.131				
C5AC	C5ACn	13.739	14.070	0.331		Base of Serravalian is upper Chron C5ACn.	
C5ACr	14.070	14.163	0.093				
C5AD	C5ADn	14.163	14.609	0.446			
C5ADr	14.609	14.775	0.166				
C5B	C5Bn.1n	14.775	14.870	0.095			
C5Bn.1r	14.870	15.032	0.162				
C5Bn.2n	15.032	15.160	0.128				
C5Br	15.160	15.974	0.814	Base of Langhian is base of Chron C5Br.			
C5C	C5Cn.1n	15.974	16.268	0.294			
C5Cn.1r	16.268	16.303	0.035				
C5Cn.2n	16.303	16.472	0.169				
C5Cn.2r	16.472	16.543	0.071				
C5Cn.3n	16.543	16.721	0.178				
C5Cr	16.721	17.235	0.514				
C5D	C5Dn	17.235	17.533	0.298	Cryptochron in C5Dr		
C5Dr.1r	17.533	17.717	0.184				
C5Dr.1n	17.717	17.740	0.023				
C5Dr.2r	17.740	18.056	0.316				
C5E	C5En	18.056	18.524	0.468			
C5Er	18.524	18.748	0.224				
C6	C6n	18.748	19.722	0.974	Cryptochron C6r-1		
C6r	19.722	20.040	0.318				
C6A	C6An.1n	20.040	20.213	0.173	Base of Burdigalian (working version) is approximate base of Chron C6An.1r (used here) or of Chron C6An.1n.		
C6An.1r	20.213	20.439	0.226				
C6An.2n	20.439	20.709	0.270				
C6Ar	20.709	21.083	0.374				
C6AA	C6AAAn	21.083	21.159	0.076			
C6AAr.1r	21.159	21.403	0.244				
C6AAr.1n	21.403	21.483	0.080				
C6AAr.2r	21.483	21.659	0.176				
C6AAr.2n	21.659	21.688	0.029				
C6AAr.3r	21.688	21.767	0.079				
early (Burdigalian)	20.44						

Table T4 (continued).

Geologic age	Base age (Ma)	Polarity chron	Top age (Ma)	Base age (Ma)	Duration (My)	Remarks			
early (Aquitanian) Paleogene Oligocene	23.03	C6B	C6Bn.1n	21.767	21.936	0.169	Base of Miocene is base of Chron C6Cn.2n.		
			C6Bn.1r	21.936	21.992	0.056			
			C6Bn.2n	21.992	22.268	0.276			
			C6Br	22.268	22.564	0.296			
		C6C	C6Cn.1n	22.564	22.754	0.190			
			C6Cn.1r	22.754	22.902	0.148			
			C6Cn.2n	22.902	23.030	0.128			
		C6Cr	C6Cn.2r	23.030	23.233	0.203			
			C6Cn.3n	23.233	23.295	0.062			
			C6Cr	23.295	23.962	0.667			
		C7	C7n.1n	23.962	24.000	0.038		Cryptochron C7r-1	
			C7n.1r	24.000	24.109	0.109			
			C7n.2n	24.109	24.474	0.365			
			C7r	24.474	24.761	0.287			
C7A	C7An	24.761	24.984	0.223					
	C7Ar	24.984	25.099	0.115					
C8	C8n.1n	25.099	25.264	0.165	Cryptochron C8n.2n-1				
	C8n.1r	25.264	25.304	0.040					
	C8n.2n	25.304	25.987	0.683					
	C8r	25.987	26.420	0.433					
C9	C9n	26.420	27.439	1.019	Cryptochrons C9n-1, 2				
	C9r	27.439	27.859	0.420	Cryptochron C9r-1				
late (Chattian)	28.09	C10	C10n.1n	27.859	28.087	0.228	Base of Chattian (working version) is base of Chron C10n.1n. Note: base is potentially at ~70% up in "undifferentiated Chron C10n" in candidate GSSP in Italy (Coccioni et al., 2008), which would project as equivalent to C10n.1n.4.		
			C10n.1r	28.087	28.141	0.054			
			C10n.2n	28.141	28.278	0.137			
			C10r	28.278	29.183	0.905			
C11	C11n.1n	29.183	29.477	0.294	Cryptochron C11r-1				
	C11n.1r	29.477	29.527	0.050					
	C11n.2n	29.527	29.970	0.443					
	C11r	29.970	30.591	0.621					
C12	C12n	30.591	31.034	0.443	Cryptochrons C12r-1 through 8				
	C12r	31.034	33.157	2.123					
early (Rupelian) Eocene	33.89	C13	C13n	33.157	33.705	0.548	Cryptochron C13n-1 Base of Rupellian is at Chron C13r.86. Cryptochrons C13r-1 through 4		
			C13r	33.705	34.999	1.294			
C15	35.294	C15n C15r	34.999	35.294	0.295	"C14" does not exist.			
			35.294	35.706	0.411				
			C16	C16n.1n	35.706		35.892	0.186	
				C16n.1r	35.892		36.051	0.159	
C16n.2n	36.051	36.700		0.649					
C16r	36.700	36.969		0.269					
late (Priabonian)	37.75	C17	C17n.1n	36.969	37.753	0.784	Base of Priabonian (working version) assigned as base of Chron C17n.1n.		
			C17n.1r	37.753	37.872	0.119			
			C17n.2n	37.872	38.093	0.221			
			C17n.2r	38.093	38.159	0.065			
			C17n.3n	38.159	38.333	0.174			
			C17r	38.333	38.615	0.283			
			C18	C18n.1n	38.615	39.627		1.012	Cryptochron C18n.1n-1
				C18n.1r	39.627	39.698		0.070	
				C18n.2n	39.698	40.145		0.447	
				C18r	40.145	41.154		1.010	
middle (Bartonian)	41.15					Base of Bartonian (working version) assigned as base of Chron C18r.			

For azimuthally unoriented samples from sedimentary rock deposited at low latitudes, determining the polarity of sedimentary units may be difficult. The polarity ambiguity arises when the samples are azimuthally unoriented and the inclination is shallow near the Equator (the angular distance between reversed and normal polarity inclinations is small). Because paleomagnetic inclinations from any samples will have some degree of dispersion on their mean inclination, it is likely that when the mean inclination is shallow, the sign of the inclination will not be indicative of the polarity (e.g., McFadden and Reid, 1982; Cox and Gordon, 1984) and should be used with caution as a definitive estimate of magnetic polarity.

Whenever possible, we offer an interpretation of the magnetic polarity following the naming convention of correlative anomaly numbers prefaced by the letter C (Tauxe et al., 1984). Normal polarity subchrons are referred to by adding suffixes (n1, n2, etc.) that increase with age. For the younger part of the timescale (Pliocene–Pleistocene), we use traditional names to refer to the various chrons and subchrons (e.g., Brunhes, Jaramillo, Olduvai, etc.). In general, polarity reversals occurring at core section ends have been treated with extreme caution.

Physical properties

High-resolution physical property measurements were made during Expedition 349 mainly to aid lithostratigraphic characterization and to tie core descriptions to borehole data and seismic profiles. In particular, physical property data play a major role in hole-to-hole and site-to-site stratigraphic correlation, detection of discontinuities and inhomogeneities, obtaining information about differences in the composition and texture of sediment, identification of major seismic reflectors, and construction of synthetic seismic profiles. A variety of techniques and methods were used to characterize Expedition 349 cores on whole-round, split section-half, and discrete samples. Core sections are generally 1.5 m in length, so a typical coring length (stroke) of 9.5 m yields 6 sections plus a shorter seventh section. Procedures for measuring sediment or hard rock cores differ slightly.

Sedimentary cores

Recovered whole-round sections were first allowed to equilibrate to ambient room temperature ($\sim 20^{\circ}\text{C}$) and pressure for ~ 4 h. After thermally equilibrating, core sections were run through the WRMSL for measurement of density by gamma ray attenuation (GRA), magnetic susceptibility, and compressional wave velocity on the *P*-wave logger (PWL). Cores recovered with the XCB or the RCB are slightly smaller in diameter than those cored with the APC. As a result, sections cored with the XCB or RCB typically have gaps between the liner and the core, so *P*-wave velocity was not measured with WRMSL. Sections were then measured with the spectral NGRL. Thermal conductivity was measured on one whole-round section per sediment core (typically Section 3) by a needle probe inserted into the section through a small hole drilled through the plastic core liner close to the middle of the section. After that, cores were split longitudinally, with one half designated as archive and one as working half for sampling and analysis. The archive half of the core was passed through the SHMSL for measurement of point magnetic susceptibility and color reflectance. Compressional *P*-wave velocity measurements on split cores were typically made on the working halves that had been sampled for moisture and density (MAD), employing the transducers oriented in *x*-axis and *z*-axis directions. Discrete samples were collected from the working halves

(every section for the first 15 cores and then every second section) to measure wet bulk density, dry bulk density, water content, porosity, and grain density with MAD procedures. For Hole U1431A, interstitial water was extracted by Rhizon samplers every 5, 10, or 20 cm before physical property measurements. *P*-wave velocity was expected to be higher in this hole compared to the others due to the extraction of water from the sediment, but the logs showed lower *P*-wave velocity, suggesting that the water in the liners was replaced by air.

Hard rock cores

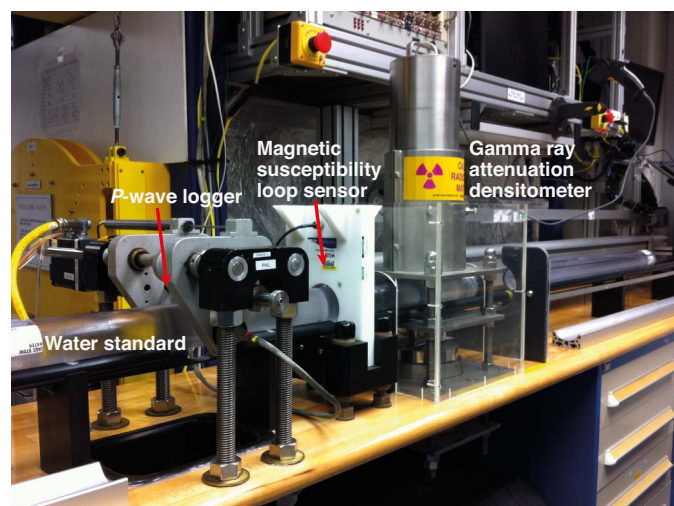
Recovered hard rock sections were shaken onto sterile liners in the core splitting room for examination by a petrologist, who decided where the pieces should be split between working and archive halves. The pieces were then put back into liners and run through the WRMSL and NGRL. *P*-wave velocity was not measured, as the spaces between the liner and the rock core pieces make these measurements meaningless. After physical property measurements on whole-round cores, the core sections were split into working and archive halves and all rock pieces labeled. The archive half of the core was passed through the SHMSL for measurement of point magnetic susceptibility and color reflectance. Thermal conductivity was measured once per core using a contact probe on a piece of section half in a bath of seawater. Samples were taken from the working half of the core at a sampling interval of ~ 1 m depending on lithologic variability. Some of these samples were shared for both paleomagnetic and MAD measurements. Compressional *P*-wave velocity measurements were made on these discrete samples.

A full discussion of all methodologies and calculations used aboard the *JOIDES Resolution* in the Physical Properties Laboratory is available in Blum (1997). Details and procedures for each physical property measurement are described below.

WRMSL measurements

GRA-derived bulk density, *P*-wave velocity, and magnetic susceptibility were measured nondestructively with the WRMSL (Figure F30). To optimize the measurement process, sampling intervals and measurement integration times were the same for all sensors.

Figure F30. WRMSL, which measures GRA bulk density, magnetic susceptibility, and *P*-wave velocity. A water standard is measured at the end of each core for QA/QC purposes.



Sampling intervals were set at 2.5 cm with an integration time of 5 s for each measurement. These sampling intervals are common denominators of the distances between the sensors installed on the WRMSL (30–50 cm), which allows sequential and simultaneous measurements. After every core, quality control and quality assurance (QC/QA) were monitored by passing a single core liner filled with deionized water through the WRMSL.

Gamma ray attenuation bulk density

Bulk density can be used to estimate the pore volume in sediment and evaluate the consolidation state of sediment. GRA density is an estimate of bulk density based on the attenuation of a gamma ray beam. The beam is produced by a ^{137}Cs gamma ray source at a radiation level of 370 MBq within a lead shield with a 5 mm collimator, which is directed through the whole-round core. The gamma ray detector on the opposite side of the core from the source includes a scintillator and an integral photomultiplier tube to record the gamma radiation that passes through the core. The attenuation of gamma rays occurs primarily by Compton scattering, in which gamma rays are scattered by electrons in the formation; the degree of scattering is related to the material bulk density. Therefore, for a known thickness of sample, the density (ρ) is proportional to the intensity of the attenuated gamma rays and can be expressed as

$$\rho = \ln(I/I_0)/(\mu d),$$

where

I = the measured intensity of gamma rays passing through the sample,

I_0 = gamma ray source intensity,

μ = Compton attenuation coefficient, and

d = sample diameter.

The μ and I_0 are treated as constants, such that ρ can be calculated from I .

In general, WRMSL measurements are most accurate when taken on a completely filled core liner with minimal drilling disturbance; otherwise, measurements tend to underestimate true values. By default, the instrument reports measurements using the internal diameter of the core liner (66 mm) as the assumed sample diameter. This assumption is suitable for most sediment cores obtained by the APC; however, for sediment and/or hard rock cored by the XCB or RCB, core diameter is usually about 58 mm or less. Following Jarard and Kerneklian (2007), the density measurements of cores obtained by XCB or RCB were corrected by multiplying the density values by $66/58 = 1.138$ to account for this bias. The spatial resolution of the GRA densitometer is less than ± 1 cm. The gamma ray detector is calibrated with sealed calibration cores (one standard core liner filled with distilled water and aluminum cylinders of various diameters). To establish the calibration curves, gamma ray counts were taken through each aluminum cylinder for 60 s. Each aluminum cylinder has a density of 2.7 g/cm^3 , and d is 1, 2, 3, 4, 5, or 6 cm. The relationship between I and μd is

$$\ln(I) = A(\mu d)^2 + B(\mu d) + C,$$

where A, B, and C are coefficients determined from the calibration.

Recalibration was performed as needed when the deionized water QA/QC standard deviated significantly (more than a few percent) from 1 g/cm^3 .

Magnetic susceptibility

Magnetic susceptibility (χ) is a dimensionless measure of the degree to which a material can be magnetized by an external magnetic field:

$$\chi = M/H,$$

where M is the magnetization induced in the material by an external field of strength H . Magnetic susceptibility is primarily sensitive to the concentration of ferrimagnetic minerals (e.g., magnetite and maghemite). It is also sensitive to magnetic mineralogy and can be related to the origin of the materials in the core and their subsequent diagenesis. Igneous materials typically have magnetic susceptibility a couple of orders of magnitude greater than their alteration products, such as clay.

The measurements were made using a Bartington MS2C loop sensor with a 9 cm diameter. An oscillator circuit in the sensor, which operates at a frequency of 0.565 kHz and an alternating field of $\sim 140 \text{ A/m}$, produces a low-intensity, nonsaturating alternating magnetic field. Sediment or hard rock core sections going through the influence of this field cause a change in oscillator frequency. Frequency information returned in pulse form to the susceptometer is converted into magnetic susceptibility. The loop sensor has a spatial resolution of 23–27 mm, and it is accurate to within 2%.

P-wave velocity

P -wave velocity data can be used to evaluate small-strain moduli, correlate between downhole logging and core data, and evaluate porosity and cementation. P -wave (compressional) velocity (V_p) is defined by the time required for a compressional wave to travel a specific distance

$$V_p = d/t_{\text{core}},$$

where d is the path length of the wave across the core and t_{core} is the traveltime through the core.

The PWL measures the traveltime of 500 kHz ultrasonic waves horizontally across the core at 2.5 cm intervals while it remains in the core liner. Waves are transmitted to the core by plastic transducer contacts connected to linear actuators. Pressure is applied to the actuators to ensure coupling between the transducers and the core liner. P -wave velocity transducers measure total traveltime of the compressional wave between transducers. The wave travels horizontally across the whole core and core liner. The total observed traveltime t_{core} is composed of

t_{delay} = time delay related to transducer faces and electronic circuitry,

t_{pulse} = delay related to the peak detection procedure,

t_{liner} = transit time through the core liner, and

t_{core} = traveltime through the sediment.

The system is calibrated using a core liner filled with distilled water, which provides control for t_{delay} , t_{pulse} , and t_{liner} . From these calibrations, V_p can be calculated for the whole-round specimens in core liners as

$$V_p = (d_{cl} - 2d_{liner}) / (t_o - t_{pulse} - t_{delay} - 2t_{liner}),$$

where

- d_{cl} = measured diameter of core and liner,
- d_{liner} = liner wall thickness, and
- t_o = measured total travelttime.

The above equation assumes that the core completely fills the core liner. The *P*-wave logger of the WRMSL was turned off for cores recovered with the XCB or RCB, which often do not fill the core liner.

NGRL measurements

Gamma radiation is emitted from the decay of mineral-hosted ²³⁸U, ²³²Th, and ⁴⁰K. The NGRL measures this natural emission on whole-round cores using a system designed and built at the Integrated Ocean Drilling Program-US Implementing Organization (USIO) (Texas A&M University) (Vasiliev et al., 2011; Dunlea et al., 2013) (Figure F31). When ²³⁸U, ²³²Th, and ⁴⁰K radioisotopes decay, they and their daughter products emit gamma radiation at specific energy levels unique to each isotope. NGR spectroscopy measures a wide energy spectrum that can be used to estimate the abundance of each isotope based on the strength of the signal at characteristic energies (Blum et al., 1997; Gilmore, 2008). Spectral data were collected and can be used for postcruise processing for U, Th, and K abundance but were not processed on board. Total counts were used on board, with high counts usually identifying fine-grained deposits containing K-rich clay minerals and their absorbed U and Th isotopes. NGR data thus reveal stratigraphic details that aid in core-to-core correlations. The system was installed on the renovated *JOIDES Resolution* in 2009 and has been used on every Integrated Ocean Drilling Program-USIO expedition starting with Expedition 320. The main NGR detector unit consists of 8 sodium iodide (NaI) detectors arranged along the core measurement axis at 20 cm intervals surrounding the lower half of the section (Figure F32). The detector array has passive (layers of lead) and active (plastic scintillators) shielding to reduce the background environmental and cosmic radiation. The overlying plastic scintillators detect incoming high-energy gamma and muon cosmic radiation and cancel this signal from the total counted by the NaI detectors.

A measurement run consisted of two sample positions, 10 cm apart, for a total of 16 measurements per 150 cm section. The qual-

Figure F31. NGRL for whole-round cores, which conducts 8 measurements at a time in 2 positions, resulting in 16 measurements per core.



ity of the energy spectrum measured in a core depends on the concentration of radionuclides in the sample but also on the counting time, with higher times yielding better spectra. Counting times were chosen as 5 min per position, or ~10 min per core, yielding statistically significant energy spectra (Vasiliev et al., 2011).

Thermal conductivity measurements

After NGR measurements were completed, thermal conductivity was measured with the TK04 (Teka Bolin) system using a needle-probe method in full-space configuration for whole-round sediment cores (Von Herzen and Maxwell, 1959) or a contact-probe method in half-space configuration on split cores for hard rock. The probes contain a heater wire and calibrated thermistor.

For soft sediment, the needle probe was inserted into a 2 mm diameter hole drilled through the liner along one of the lines that later guided core splitting. To avoid interference from air flow in the laboratory, the core was placed into an enclosed box outfitted with foam.

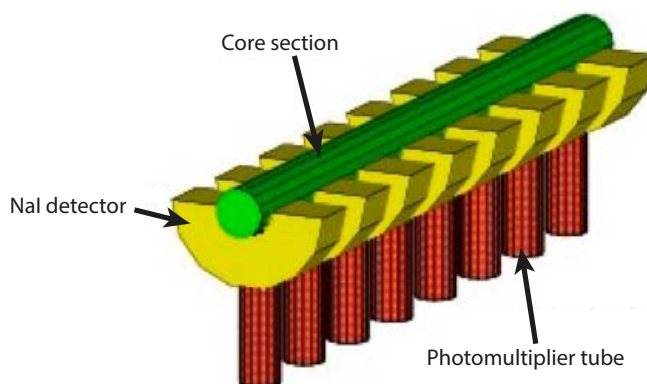
For hard rock cores, samples were selected from the working half and returned unaltered to the core liner upon completion of the tests. The contact probe embedded in the surface of an epoxy block with a low thermal conductivity (Vacquier, 1985) was maintained in contact with the sample and both were equilibrated together in a bath of seawater at room temperature in a cooler insulated with extruded polystyrene foam. The calibrated heat source of the probe was then turned on and the increase in temperature was recorded over 80 s. A heating power of 1.7 W/m was typically used in soft sediment and 1.9 W/m for indurated material. The solution to the heat conduction equation with a line source of heat was then fit to the temperature measurements to obtain the thermal conductivity. Because the probe is much more conductive than sediment or hard rock, the probe is assumed to be a perfect conductor. Under this assumption, the temperature of the superconductive probe has a linear relationship with the natural logarithm of the time after the initiation of the heat,

$$T(t) = (q/4\pi k) \times \ln(t) + C,$$

where

- T = temperature (K),
- q = heat input per unit length per unit time (J/m/s),
- k = thermal conductivity (W/[m·K]),
- t = time after the initiation of the heat (s), and
- C = instrumental constant.

Figure F32. Main elements of the NGRL (from IODP NGR User Guide, 2014).



Three measuring cycles were automatically performed to calculate average conductivity. A self-test, which included a drift study, was conducted at the beginning of each measurement cycle. Once the probe temperature stabilized, the heater circuit was closed and the temperature rise in the probe was recorded. Thermal conductivity was calculated from the rate of temperature rise while the heater current was flowing. Temperatures measured during the first 80 s of the heating cycle were fitted to an approximate solution of a constantly heated line source (for details, see Kristiansen, 1982; Blum, 1997). Measurement errors were 5%–10%. Thermal conductivity measurements were routinely taken in one section per core. Some cores retrieved by XCB yielded no results for thermal conductivity because cracks in the hard sediment caused bad coupling of the needle probe to the sediment.

SHMSL measurements

We measured color reflectance and magnetic susceptibility on archive section halves using the SHMSL. The archive half of the split core was placed on the core track, above which an electronic platform moves along a track, recording the height of the split-core surface with a laser sensor. The laser establishes the location of the bottom of the section, and then the platform reverses the direction of movement, moving from bottom to top making measurements of point magnetic susceptibility and color reflectance. All foam inserts were removed from the section-half cores before measurement, so the measured range of values represent that of the core material only. During Expedition 349, point magnetic susceptibility and color reflectance data were collected at constant intervals for each core but varied between 1 and 2.5 cm for different cores, depending on the available times for processing. These measurements have a sufficient resolution for comparing with the results obtained from the magnetic susceptibility loop of the WRMSL.

Color reflectance spectrometry

The color reflectance spectrometer uses an Ocean Optics 30 mm integrating sphere and both halogen and LED light source, which covers wavelengths from ultraviolet through visible to near infrared. The measurements were taken from 380 to 900 nm wavelengths at 2 nm intervals. The approximate 3 s data acquisition offset was applied for the entire scan of the archive section half. The data are reported using the $L^*a^*b^*$ color system, in which L^* is lightness, a^* is redness (positive) versus greenness (negative), and b^* is yellowness (positive) versus blueness (negative) of the rock. The color reflectance spectrometer calibrates on two spectra, pure white (reference) and pure black (dark). Color calibration was conducted approximately once every 6 h (twice per shift).

Point magnetic susceptibility

Point magnetic susceptibility was measured with a Bartington MS2 meter and an MS2K contact probe with a flat 15 mm diameter round sensor with a field of influence of 25 mm and an operation frequency of 930 Hz. The instrument averages three measurements from the sensor for each offset, leading to an accuracy of ~5%. The spatial resolution of the point magnetic susceptibility instrument is ~3.8 mm, higher than that of the whole-round magnetic susceptibility for sections containing broken pieces <4 cm in length (the spatial resolution of whole-round magnetic susceptibility). As with whole-round measurements, the output displayed by the point magnetic susceptibility sensor must be converted to dimensionless SI units by multiplying by 10^{-5} . The probe is zeroed in air before each measurement location to avoid influence from the metal track.

The point magnetic susceptibility meter was calibrated by the manufacturer before installation on the ship and is quality checked every ~6 h at the same time as color reflectance sensor calibration.

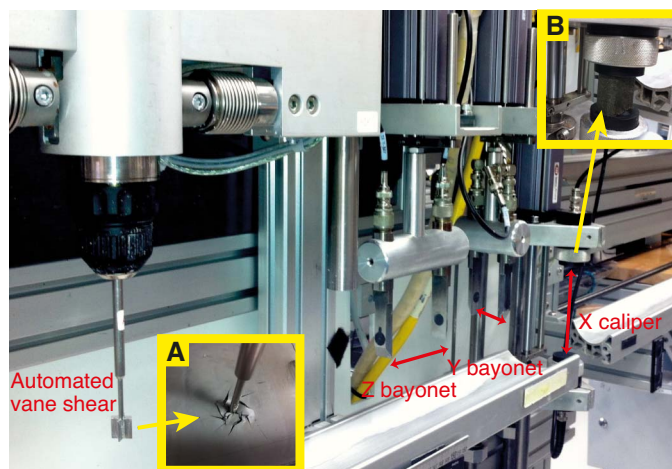
SHMG measurements

For soft-sediment cores, P -wave velocity and shear strength measurements were performed on the working half of split cores before any samples were taken. P -wave velocity measurements used the x -axis caliper and z -axis bayonet contact probe transducers on the Section Half Measurement Gantry (SHMG) (Figure F33), with one analysis per section. Measurements were usually taken at ~75 cm in the section; however, if this interval provided no good sediment/transducer coupling (e.g., caused by high amounts of sand or cracks), different positions were chosen to generate viable data. Cores drilled with the XCB generally did not provide usable data because of bad sediment/liner contact and disturbed sediment. For hard rock cores, P -wave velocity was measured on the discrete samples chosen for both physical property and paleomagnetic measurements.

P -wave velocity

The P -wave velocity system uses Panametrics-NDT Microscan delay line transducers, which transmit at 0.5 MHz. The signal received through the section half or the discrete sample was recorded by the computer attached to the system, with the peak (P -wave arrival) usually chosen by autopicking software. In case of a weak signal, the first arrival was manually picked. During Expedition 349, we often manually picked the very base of the first arrival peak, leaving out the automatically picked points that usually fell along the ascending curve. The distance between transducers was measured with a built-in linear voltage displacement transformer. Calibration was performed with a series of acrylic cylinders of differing thicknesses and a known P -wave velocity of 2750 ± 20 m/s. The determined system time delay from calibration was subtracted from the picked arrival time to give a traveltime of the P -wave through the sample. The thickness of the sample (calculated by the linear voltage

Figure F33. SHMG showing the x -axis caliper and y - and z -axis bayonets to measure P -wave velocity on split-core sections of soft sediment or discrete samples of indurated sediment or hard rock. AVS is used to measure shear strength. A. Deformation in the sediment after rotation of the vane. B. Measurement of P -wave velocity on a hard rock discrete sample using the x -axis caliper.



displacement transformer, in meters) was divided by the traveltime (in seconds) to calculate P -wave velocity in meters per second.

Shear strength

Shear strength is the resistance of a material to failure in shear. Shear stress in unconsolidated materials is resisted only by the network of solid particles. Shear strength (τ_f) can be expressed as a function of the effective normal stress at failure (σ'), the effective cohesion (c'), and friction angle (ϕ'),

$$\tau_f = c_2 + \sigma_2 \tan(\phi_2),$$

where c_2 and ϕ_2 are the shear strength parameters that define a linear relationship between τ_f and ϕ_2 , according to the Mohr-Coulomb failure criterion.

Shear strength parameters can be determined by means of multiple laboratory tests. The c_2 and ϕ_2 are relevant in situations where field drainage conditions correspond to test conditions. The shear strength of a soil under undrained conditions (interstitial water drainage does not occur during failure) is different from that under drained conditions (interstitial water drainage occurs).

Undrained shear strength can be expressed in terms of total stress in the case of fully saturated materials of low permeability (e.g., clays), denoted by S_u . The most common strength tests in shipboard laboratories are the vane shear and penetrometer tests, which provide measurement of undrained shear strength (S_u) (Blum, 1997).

During Expedition 349, S_u was measured in undisturbed fine-grained sediment using the automated vane shear (AVS) system in working-half cores (Figure F33). Using the AVS, undrained shear strength was determined by inserting a four-bladed vane into the split core and rotating it at a constant 90°/min to determine the torque required to cause a cylindrical surface to be sheared by the vane, which provides a measurement of the peak shear strength. The difference in rotational strain between the top and the bottom of a linear spring is measured using digital shaft encoders. Measurements were made with the vane rotation axis perpendicular to the split surface. The residual shear strength was taken to be the constant and lowest measured shear strength after reaching the peak value during the test cycle. Sampling rates were one per core unless the sediment was too firm for instrument penetration or was disturbed during coring.

Vane shear strength $S_{u(v)}$ (kPa) is calculated as

$$S_{u(v)} = T/K_v = (\Delta/B)/K_v,$$

where

- T = torque required to induce material failure (N·m),
- K_v = constant, depending on vane dimensions (m³),
- Δ = maximum torque angle (°) at failure, and
- B = spring constant that relates the deflection angle to the torque (°/N·m) (Blum, 1997).

All measurements used a vane with a height and diameter of 12.7 mm. Failure torque (T) was determined by measuring the degrees of rotation of one of four torsional springs. A linear calibration equation (specified by the manufacturer) relates the rotation angle to the torque for the particular spring being used. Selection of the appropriate spring was based on the anticipated shear strength of the material. Vane shear results were generally considered reliable

for shear strength values less than ~150–200 kPa, above which excessive cracking and separation of the core material occurred.

Discrete sample MAD measurements

Discrete samples were collected from the working halves to determine wet and dry bulk density, grain density, water content, and porosity. In soft sediment, ~10 cm³ samples were collected with a plastic syringe, the diameter of which fit that of the glass vials. An attempt was made to sample every section for the first 15 cores and every second section for deeper cores, depending on lithologic variability. In indurated sediment and hard rock, minicores were extracted from the working halves for physical property measurements, with some also shared for paleomagnetic measurements.

Sample preparation

Soft-sediment samples were placed in numbered, preweighed ~16 mL Wheaton glass vials for wet and dry sediment weighing, drying, and dry volume measurements. Determination of an accurate wet mass of the minicore samples of indurated sediment and hard rock first required that the pore space of the samples be completely saturated with seawater. To do this, we placed the samples in individual plastic vials filled with seawater and used a vacuum chamber. A vacuum pump removed the air from the chamber to a pressure of ~40–50 kPa below the atmospheric pressure, forcing seawater into the samples. The samples were kept under saturation for at least 24 h, with the vacuum maintained in the chamber by turning the pump on for 30 min every 5 h. After removal from the saturator, the minicores were patted dry with a paper towel and wet mass immediately determined using the dual balance system. P -wave velocities were then measured on the wet samples. Following the velocity measurements, the samples were dried in a convection oven for at least 24 h at 105° ± 5°C. Dried samples were then cooled in a desiccator for at least 60 min before the dry mass and the volume were measured.

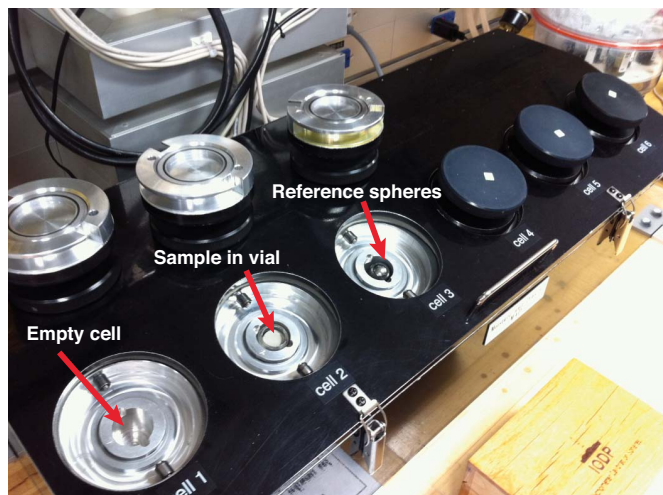
Dual balance mass measurement

The weights of wet and dry sample masses were determined to a precision of 0.005 g using two Mettler Toledo electronic balances, with one acting as a reference. A standard weight of similar value to the sample was placed upon the reference balance to increase accuracy. A computer averaging system was used to compensate for the ship's motion. The default setting of the balances is 300 measurements (taking ~1.5 min).

Pycnometer volume measurement

Dry sample volume was determined using a hexapycnometer system of a six-celled, custom-configured Micrometrics AccuPyc 1330TC helium-displacement pycnometer (Figure F34). The precision of each cell is 1% of the full-scale volume. Volume measurement was preceded by three purges of the sample chamber with helium warmed to ~28°C. Three measurement cycles were run for each sample. A reference volume (set of two calibration spheres) was placed sequentially in one of the chambers to check for instrument drift and systematic error. The volumes occupied by the numbered Wheaton vials were calculated before the cruise by multiplying each vial's weight against the average density of the vial glass. Dry mass and volume were measured after samples were heated in an oven at 105° ± 5°C for 24 h and allowed to cool in a desiccator. The procedures for the determination of these physical properties comply with the American Society for Testing and Mate-

Figure F34. Pycnometer used to measure the volume of dry samples, either in small vials for soft sediment or as discrete samples.



rials (ASTM) designation (D) 2216 (ASTM International, 1990). The fundamental relation and assumptions for the calculations of all physical property parameters are discussed by Blum (1997) and summarized below.

Mass and volume calculation

We measured wet mass (M_{wet}), dry mass (M_{dry}), and dry volume (V_{dry}). The ratio of mass (rm) is a computational constant of 0.965 (i.e., 0.965 g of freshwater per 1 g of seawater). Salt precipitated in sediment pores during the drying process is included in the M_{dry} and V_{dry} values. The mass of the evaporated water (M_{water}) and salt (M_{salt}) in the sample are given by

$$M_{water} = M_{wet} - M_{dry}, \text{ and}$$

$$M_{salt} = M_{water}[s/(1 - s)],$$

where s is the assumed saltwater salinity (0.035%) corresponding to a pore water density (ρ_{pw}) of 1.024 g/cm³ and a salt density (ρ_{salt}) of 2.22 g/cm³. The corrected mass of pore water (M_{pw}), volume of pore water (V_{pw}), mass of solids excluding salt (M_{solid}), volume of salt (V_{salt}), volume of solids excluding salt (V_{solid}), and wet volume (V_{wet}) are

$$M_{pw} = (M_{wet} - M_{dry})/rm,$$

$$V_{pw} = M_{pw}/\rho_{pw}$$

$$M_{solid} = M_{wet} - M_{pw}$$

$$M_{salt} = M_{pw} - (M_{wet} - M_{dry}),$$

$$V_{salt} = M_{salt}/\rho_{salt}$$

$$V_{wet} = V_{dry} - V_{salt} + V_{pw} \text{ and}$$

$$V_{solid} = V_{wet} - V_{pw}$$

Calculation of bulk properties

For all sediment samples, water content (w) is expressed as the ratio of mass of pore water to wet sediment (total) mass,

$$w = M_{pw}/M_{wet}.$$

Wet bulk density (ρ_{wet}), dry bulk density (ρ_{dry}), sediment grain density (ρ_{solid}), porosity (ϕ), and void ratio (VR) are calculated as:

$$\rho_{wet} = M_{wet}/V_{wet}$$

$$\rho_{dry} = M_{solid}/V_{wet}$$

$$\rho_{solid} = M_{solid}/V_{solid}$$

$$\phi = V_{pw}/V_{wet} \text{ and}$$

$$VR = V_{pw}/V_{solid}.$$

Moisture and density properties reported and plotted in the Physical properties sections of all site chapters were calculated with the MADMax shipboard program, set with "method C" calculation process.

Downhole measurements

Downhole logs are used to determine physical, chemical, and structural properties of the formation penetrated by a borehole. The data are rapidly collected, continuous with depth, and measured in situ; they can be interpreted in terms of the stratigraphy, lithology, mineralogy, magnetic characteristics, and geochemical composition of the penetrated formation. Where core recovery is incomplete or disturbed, log data may provide the only way to characterize the borehole section. Where core recovery is good, log and core data complement one another and may be interpreted jointly.

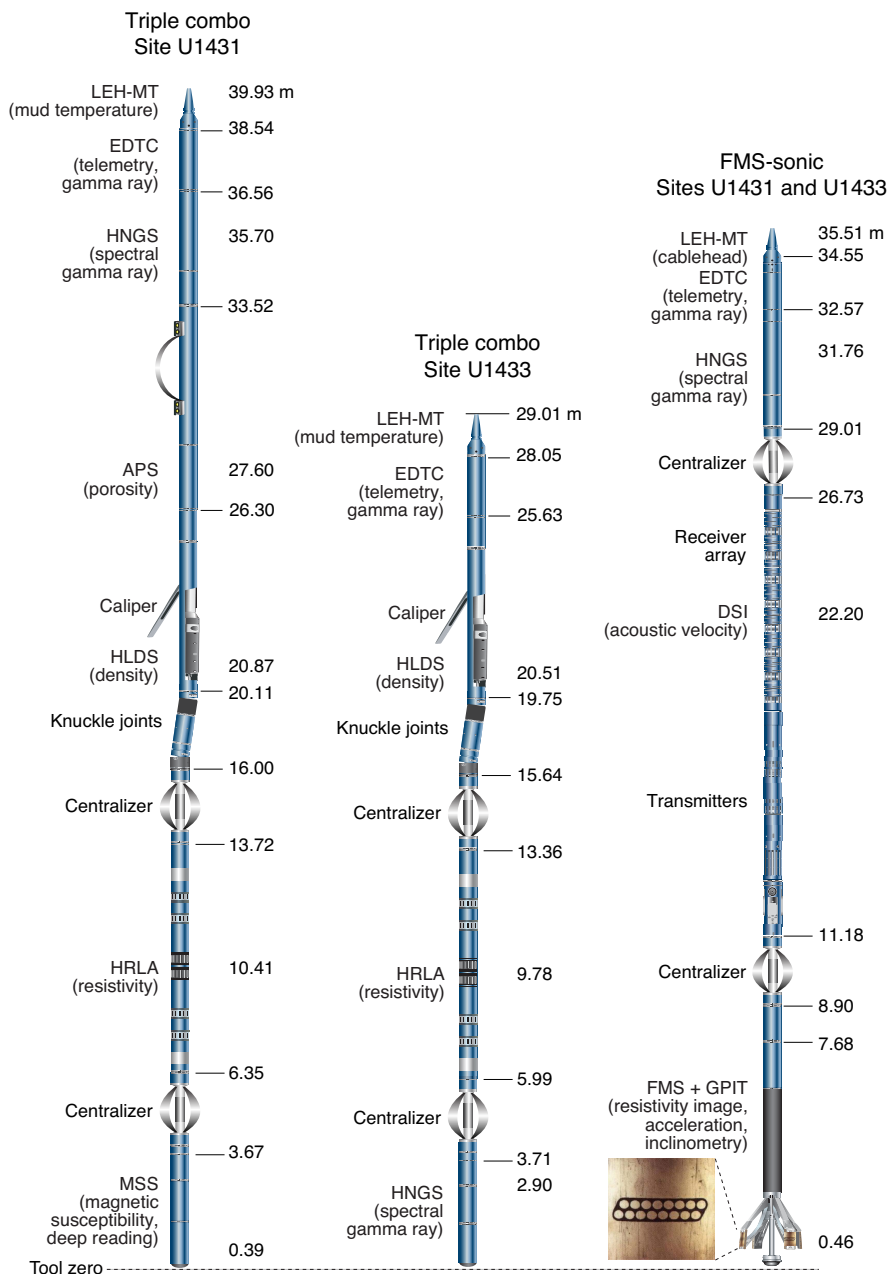
Downhole logs measure formation properties on a scale that is intermediate between those obtained from laboratory measurements on core samples and those from geophysical surveys. They are useful in calibrating the interpretation of geophysical survey data (e.g., through the use of synthetic seismograms) and provide a necessary link for the integrated understanding of physical and chemical properties on different scales.

During Expedition 349, downhole logging measurements were taken in Holes U1431E and U1433B. In addition, downhole temperature measurements were acquired using the advanced piston corer temperature tool (APCT-3) in Holes U1431D, U1432C, and U1433A.

Wireline logging

During wireline logging operations, logs are recorded with Schlumberger logging tools combined into several tool strings, which are lowered into the hole after completion of coring operations. Two main tool strings were used during Expedition 349. The first is a variant of the triple combination (triple combo) tool string, which measures, from top to bottom, borehole fluid temperature, NGR, porosity, density, electrical resistivity, and magnetic susceptibility. The second tool string is the Formation MicroScanner (FMS)-sonic, which measures NGR, sonic velocities, and FMS resistivity images of the borehole wall (Figure F35; Table T5). Each tool string also contains an Enhanced Digital Telemetry Cartridge

Figure F35. Wireline tool strings used during Expedition 349. Numbers next to tool strings mark the height of the tool joints and sensors above the bottom of the tool string. For definitions of tool acronyms, see Table T6. LEH-QT = Logging Equipment Head (model QT).



(EDTC) for communicating through the wireline to the Schlumberger data acquisition system (MAXIS unit) on the drillship.

In preparation for logging, the boreholes were reamed in their lower sections, flushed of debris by circulating drilling fluid, and filled with seawater-based logging gel (sepiolite mud mixed with seawater and weighted with barite; approximate density = 10.5 lb/gal) to help stabilize the borehole walls in sections where instability was expected from drilling and coring results. The BHA was pulled up to ~150 m wireline depth below seafloor (WSF) to cover the unstable upper part of Hole U1431E and to 100 m WSF in Hole U1433B. The tool strings were then lowered downhole on a seven-conductor wireline cable before being pulled up at constant

speed, typically ~300 m/h for the triple combo and 600 m/h for the FMS-sonic, to provide continuous log measurements of several properties simultaneously.

Each tool string deployment is termed a logging “run.” During each run, tool strings can be lowered and pulled up in the hole several times to check repeatability and to increase coverage of the FMS borehole images. Each lowering or hauling-up of the tool string while collecting data constitutes a “pass.” Incoming data were recorded and monitored in real time on the MCM MAXIS logging computer. A wireline heave compensator (WHC) was used to minimize the effect of ship’s heave on the tool position in the borehole (see below).

Table T5. Downhole measurements made by wireline tool strings during Expedition 349. For definitions of tool acronyms, see Table T6. All tool and tool string names except the MSS are trademarks of Schlumberger. [Download table in .csv format.](#)

Tool string	Tool	Measurement	Sampling interval (cm)	Approximate vertical resolution (cm)
Triple combo	EDTC	Total gamma ray	5 and 15	30
	HNGS	Spectral gamma ray	15	20–30
	APS	Porosity	15	38
	HLDS	Bulk density and caliper	2.5 and 15	38
	HRLA	Resistivity	15	30
Formation MicroScanner (FMS)-sonic	MSS	Magnetic susceptibility	4	12–36
	EDTC	Total gamma ray	5 and 15	30
	GPIT	Tool orientation and acceleration	3.8	15
	DSI	Acoustic velocity	15	107
	FMS	Microresistivity and caliper	0.25	1

Logged sediment properties and tool measurement principles

The logged properties and the principles used in the tools that measure them are briefly described below. The main logs are listed in Table T6. More detailed information on individual tools and their geological applications may be found in Serra (1984, 1986, 1989), Schlumberger (1989, 1994), Rider (1996), Goldberg (1997), Lovell et al. (1998), and Ellis and Singer (2007). A complete online list of acronyms for the Schlumberger tools and measurement curves is at www.apps.slb.com/cmd.

Natural gamma radiation

The Hostile Environment Natural Gamma Ray Sonde (HNGS) was used on both the triple combo and FMS-sonic tool strings to measure NGR in the formation. The HNGS uses two bismuth germanate scintillation detectors and five-window spectroscopy to determine concentrations of potassium (in weight percent), thorium (in parts per million), and uranium (in parts per million) from the characteristic gamma ray energies of isotopes in the ^{40}K , ^{232}Th , and ^{238}U radioactive decay series, which dominate the natural radiation spectrum. The computation of the elemental abundances uses a least-squares method of extracting U, Th, and K elemental concentrations from the spectral measurements. The HNGS filters out gamma ray energies below 500 keV, eliminating sensitivity to bentonite or KCl in the drilling mud and improving measurement accuracy. The HNGS also provides a measure of the total gamma ray emission (HSGR) and uranium-free or computed gamma ray emission (HCGR) that are measured in American Petroleum Institute units (gAPI). The HNGS response is influenced by the borehole diameter, and therefore the HNGS data are corrected for borehole diameter variations during acquisition.

An additional NGR sensor was housed in the EDTC, which was used primarily to communicate data to the surface. The sensor includes a sodium iodide scintillation detector that also measures the total NGR emission of the formation. It is not a spectral tool (does not provide U, Th, and K concentrations), but it provides total gamma radiation for each pass.

The inclusion of the HNGS in every tool string allows use of the gamma ray data for precise depth match processing between logging strings and passes and for core-log integration.

Density and photoelectric factor

Formation density was measured with the Hostile Environment Litho-Density Sonde (HLDS). The sonde contains a radioactive cesium (^{137}Cs) gamma ray source (622 keV) and far and near gamma ray detectors mounted on a shielded skid, which is pressed against the borehole wall by a hydraulically activated decentralizing arm. Gamma radiation emitted by the source undergoes Compton scattering, in which gamma rays are scattered by electrons in the formation. The number of scattered gamma rays that reach the detectors is proportional to the density of electrons in the formation, which is in turn related to bulk density. Porosity may also be derived from this bulk density if the matrix (grain) density is known.

The HLDS also measures the photoelectric effect factor (PEF), a measure of the photoelectric absorption of low-energy gamma radiation. Photoelectric absorption occurs when their energy falls below 150 keV as a result of being repeatedly scattered by electrons in the formation. PEF is determined by comparing the counts from the far detector in the high-energy region, where only Compton scattering occurs, with those in the low-energy region, where count rates depend on both reactions. Because PEF depends on the atomic number of the elements in the formation (heavier elements have higher PEF), it also varies according to the chemical composition of the minerals present and can be used for the identification of the overall mineral make-up of the formation. For example, the PEF of calcite is 5.08 barn/e⁻, illite is 3.03 barn/e⁻, quartz is 1.81 barn/e⁻, and hematite is 21 barn/e⁻. Good contact between the tool and borehole wall is essential for good HLDS logs; poor contact results in underestimation of density values. Both the density correction and caliper measurement of the hole are used to check the contact quality. In the deeper parts of the hole, the PEF log should be used with caution, especially in washouts, because barium in the logging mud swamps the signal, despite correction for mud effect.

Electrical resistivity

The High-Resolution Laterolog Array (HRLA) tool provides six resistivity measurements with different depths of investigation (including the borehole, or mud, resistivity and five measurements of formation resistivity with increasing penetration into the formation). The tool sends a focused current into the formation and measures the intensity necessary to maintain a constant drop in voltage across a fixed interval, providing direct resistivity measurements.

Table T6. Acronyms and units used for downhole wireline tools and measurements during Expedition 349. For the complete list of acronyms used in IODP and for additional information about tool physics, consult IODP-USIO Science Services, LDEO, at iodp.ideo.columbia.edu/TOOLS_LABS/tools.html. [Download table in .csv format.](#)

Tool	Output	Description	Unit
EDTC		Enhanced Digital Telemetry Cartridge	
	GR	Total gamma ray	gAPI
	ECGR	Environmentally corrected gamma ray	gAPI
	EHGR	High-resolution environmentally corrected gamma ray	gAPI
HNGS		Hostile Environment Gamma Ray Sonde	
	HSGR	Standard (total) gamma ray	gAPI
	HCGR	Computed gamma ray (HSGR minus uranium contribution)	gAPI
	HFK	Potassium	wt%
	HTHO	Thorium	ppm
	HURA	Uranium	ppm
APS		Accelerator Porosity Sonde	
	APLC	Near/array limestone corrected porosity	Dec. fraction
	STOF	Computed standoff	Inches
	SIGF	Formation capture cross section	Capture units
HLDS		Hostile Environment Litho-Density Sonde	
	RHOM	Bulk density	g/cm ³
	PEFL	Photoelectric effect	barn/e ⁻
	LCAL	Caliper (measure of borehole diameter)	Inches
	DRH	Bulk density correction	g/cm ³
HRLA		High Resolution Laterolog Array Tool	
	RLA1-5	Apparent resistivity from computed focusing Mode 1–5	Ωm
	RT	True resistivity	Ωm
	MRES	Borehole fluid resistivity	Ωm
MSS		Magnetic Susceptibility Sonde	
	LSUS	Magnetic susceptibility, deep reading	Uncalibrated units
FMS		Formation MicroScanner	
	C1, C2	Orthogonal hole diameters	Inches
	P1AZ	Pad 1 azimuth	Degrees
		Spatially oriented resistivity images of borehole wall	
GPIT		General Purpose Inclinator Tool	
	DEVI	Hole deviation	Degrees
	HAZI	Hole azimuth	Degrees
	Fx, Fy, Fz	Earth's magnetic field (three orthogonal components)	Degrees
	Ax, Ay, Az	Acceleration (three orthogonal components)	m/s ²
DSI		Dipole Sonic Imager	
	DTCO	Compressional wave slowness	μs/ft
	DTSM	Shear wave slowness	μs/ft
	DT1	Shear wave slowness, lower dipole	μs/ft
	DT2	Shear wave slowness, upper dipole	μs/ft

The array has one central (source) electrode and six electrodes above and below it, which serve alternatively as focusing and returning current electrodes. By rapidly changing the role of these electrodes, a simultaneous resistivity measurement at six penetration depths is achieved. The tool is designed to ensure that all signals are measured at exactly the same time and tool position and to reduce the sensitivity to “shoulder bed” effects when crossing sharp beds thinner than the electrode spacing. The design of the HRLA, which eliminates the need for a surface reference electrode, improves formation resistivity evaluation compared to traditional dual induction and allows the full range of resistivity to be measured, from low (e.g., in high-porosity sediments) to high (e.g., in basalt). The HRLA needs to be run centralized in the borehole for optimal results, so knuckle joints were used to centralize the HRLA while allowing the density and porosity tools to maintain good contact with the borehole wall (Figure F35).

Calcite, silica, and hydrocarbons are electrical insulators, whereas ionic solutions like interstitial water are conductors. Elec-

trical resistivity, therefore, can be used to evaluate porosity for a given salinity and resistivity of the interstitial water. Clay surface conduction also contributes to the resistivity values, but at high porosities, this is a relatively minor effect.

Acoustic velocity

The Dipole Shear Sonic Imager (DSI) measures the transit times between sonic transmitters and an array of eight receivers. It combines replicate measurements, thus providing a direct measurement of sound velocity through formations that is relatively free from the effects of formation damage and an enlarged borehole (Schlumberger, 1989). Along with the monopole transmitters found on most sonic tools, it also has two crossed-dipole transmitters that allow the measurement of shear wave velocity in addition to compressional wave velocity. Dipole measurements are necessary to measure shear velocities in slow formations with shear velocity less than the velocity of sound in the borehole fluid. Such slow formations are typically encountered in deep-ocean drilling.

Formation MicroScanner

The FMS provides high-resolution electrical resistivity-based images of borehole walls. The tool has four orthogonal arms and pads, each containing 16 button electrodes that are pressed against the borehole wall during logging. The electrodes are arranged in two diagonally offset rows of 8 electrodes each. A focused current is emitted from the button electrodes into the formation, with a return electrode near the top of the tool. Resistivity of the formation at the button electrodes is derived from the intensity of current passing through the button electrodes.

Processing transforms the resistivity measurements into oriented high-resolution images that reveal geologic structures of the borehole wall. Features such as bedding, stratification, fracturing, slump folding, and bioturbation can be resolved (Luthi, 1990; Salimullah and Stow, 1992; Lovell et al., 1998). Because the images are oriented to magnetic north, further analysis can provide measurement of the dip and direction (azimuth) of planar features in the formation. In addition, when the corresponding planar features can be identified in the recovered core samples, individual core pieces can be reoriented with respect to true north.

Approximately 30% of a borehole with a diameter of 25 cm is imaged during a single pass. Standard procedure is to make two full uphole passes with the FMS to maximize the chance of getting full borehole coverage with the pads. The maximum extension of the caliper arms is 40.6 cm (16 inches). In holes with a diameter greater than this maximum, the pad contact at the end of the caliper arms will be inconsistent, and the FMS images may appear out of focus and too conductive. Irregular (rough) borehole walls will also adversely affect the images if contact with the wall is poor.

Magnetic Susceptibility Sonde

The Magnetic Susceptibility Sonde (MSS) is a nonstandard wireline tool designed by Lamont-Doherty Earth Observatory (LDEO). It measures the ease with which formations are magnetized when subjected to a magnetic field. The ease of magnetization is ultimately related to the concentration and composition (size, shape, and mineralogy) of magnetic minerals (principally magnetite) in the formation. These measurements provide one of the best methods for investigating stratigraphic changes in mineralogy and lithology because the measurement is quick, repeatable, and nondestructive and because different lithologies often have strongly contrasting susceptibilities.

The MSS dual-coil sensor provides ~40 cm resolution measurements, with ~20 cm depth of horizontal investigation. The MSS was run as the lowermost tool in the triple combo tool string, using a specially developed data translation cartridge to enable the MSS to be run in combination with the Schlumberger tools. The MSS also has an optional single-coil sensor to provide high-resolution measurements (~10 cm), but this was not used during Expedition 349 because it has a large bowspring that would require the MSS to be run higher up in the tool string and because it is very sensitive to separation from the borehole wall.

Magnetic susceptibility data from both the high-resolution and deep-reading sensors are plotted as uncalibrated units. The MSS reading responses are affected by temperature and borehole size (higher temperatures lead to higher susceptibility measurements). Preliminary processing was performed offshore to remove the temperature drift by calculating a least-squares polynomial fit to the data and subtracting the calculated trend from the data set. When the magnetic susceptibility signal in sediment is very low, the detection limits of the tool may be reached. For quality control and envi-

ronmental correction, the MSS also measures internal tool temperature, z-axis acceleration, and low-resolution borehole conductivity.

Acceleration and inclinometry

The General Purpose Inclinometer Tool (GPIT) was included in the FMS-sonic tool string to calculate tool acceleration and orientation during logging. Tool orientation is defined by three parameters: tool deviation, tool azimuth, and relative bearing. The GPIT utilizes a three-axis inclinometer and a three-axis fluxgate magnetometer to record the orientation of the FMS as the magnetometer records the magnetic field components (F_x , F_y , and F_z). Thus, the FMS images can be corrected for irregular tool motion, and the dip and direction (azimuth) of features in the FMS image can be determined.

Log data quality

The main influence on log data quality is the condition of the borehole wall. Where the borehole diameter varies over short intervals because of washouts of softer material or ledges of harder material, the logs from tools that require good contact with the borehole wall (i.e., FMS, density, and porosity) may be degraded. Deep investigation measurements such as gamma radiation, resistivity, and sonic velocity, which do not require contact with the borehole wall, are generally less sensitive to borehole conditions. "Bridged" sections, where borehole diameter is much below the bit size, will also cause irregular log results. The quality of the borehole is improved by minimizing the circulation of drilling fluid while drilling, flushing the borehole to remove debris, and logging as soon as possible after drilling and conditioning are completed. During this expedition, the necessity of flushing dense basement rocks up and out of the borehole required heavy circulation.

The quality of the wireline depth determination depends on several factors. The depth of the logging measurements is determined from the length of the cable payed out from the winch on the ship. The seafloor is identified on the NGR log by the abrupt reduction in gamma ray count at the water/sediment interface (mudline). Discrepancies between the drilling depth and the wireline log depth may occur. For the case of drilling depth, discrepancies are due to core expansion, incomplete core recovery, or incomplete heave compensation. In the case of log depth, discrepancies between successive runs occur because of incomplete heave compensation, incomplete correction for cable stretch, and cable slip. Tidal changes in sea level affect both drilling and logging depths, although these were <1 m in the South China Sea.

Wireline heave compensator

During wireline logging operations, the up-and-down motion of the ship (heave) causes a similar motion of the downhole logging tools. If the amplitude of this motion is large, depth discrepancies can be introduced into the logging data. The risk of damaging downhole instruments is also increased. A WHC system was thus designed to compensate for the vertical motion of the ship and maintain a steady motion of the logging tools to ensure high-quality logging data acquisition (Liu et al., 2012; Iturrino et al., 2013). The WHC uses a vertical accelerometer (motion reference unit [MRU]) positioned under the rig floor near the ship's center of gravity to calculate the vertical motion of the ship with respect to the seafloor. It then adjusts the length of the wireline by varying the distance between two sets of pulleys through which the cable passes in order to minimize downhole tool motion. Real-time measurements of uphole (surface) and downhole acceleration are made simultaneously

by the MRU and the EDTC, respectively. An LDEO-developed software package allows these data to be analyzed and compared in real time, displaying the actual motion of the logging tool string and enabling monitoring of the efficiency of the compensator. The WHC was used for logging Hole U1431E but not for Hole U1433B because heave conditions were calm.

Logging data flow and log depth scales

Data for each wireline logging run were monitored in real time and recorded using the Schlumberger MAXIS 500 system. Initial logging data were referenced to the rig floor (wireline depth below rig floor [WRF]). After logging was completed, the data were shifted to a seafloor reference (WSF), which was based on the step in gamma radiation at the sediment/water interface.

Data were transferred onshore to LDEO, where standardized data processing took place. The main part of the processing is depth matching to remove depth offsets between logs from different logging runs, which results in a new depth scale: wireline log matched depth below seafloor (WMSF). Also, corrections are made to certain tools and logs (e.g., FMS imagery is corrected for tool acceleration, including “stick and slip”), documentation for the logs (with an assessment of log quality) is prepared, and the data are converted to ASCII for the conventional logs and GIF for the FMS images. The Schlumberger Geo-Quest’s GeoFrame software package is used for most of the processing of the collected wireline logging data. The data were transferred back to the ship within a few days of logging, and this processed data set was made available to the science party (in ASCII and DLIS formats) through the shipboard IODP logging database and shipboard servers.

In situ temperature measurements

During Expedition 349, in situ temperature measurements were made with the APCT-3 in Hole A at each site when the APC was deployed, except at Site U1431, where 4 in situ temperature measurements were made in Hole U1431D. The APCT-3 fits directly into the coring shoe of the APC and consists of a battery pack, data logger, and a platinum resistance-temperature device calibrated over a temperature range from 0° to 30°C. Before entering the borehole, the tool is first stopped at the mudline for 5 min to thermally equilibrate with bottom water. However, the lowest temperature recorded during the run was occasionally used instead of the average temperature at the mudline as an estimate of the bottom water temperature because (1) it was more repeatable and (2) the bottom water is expected to have the lowest temperature in the profile. When the APC is plunged into the formation, there is an instantaneous temperature rise from frictional heating. This heat gradually dissipates into the surrounding sediment as the temperature at the APCT-3 equilibrates toward the temperature of the sediment. After the APC penetrated the sediment, it was held in place for 5 min while the APCT-3 recorded the temperature of the cutting shoe every second.

The equilibrium temperature of the sediment was estimated by applying a mathematical heat-conduction model to the temperature decay record (Horai and Von Herzen, 1985). The synthetic thermal decay curve for the APCT-3 is a function of the geometry and thermal properties of the probe and the sediment (Bullard, 1954; Horai and Von Herzen, 1985). Equilibrium temperature was estimated by applying a fitting procedure (Pribnow et al., 2000). However, where the APC did not achieve a full stroke or where ship heave pulled the APC up from full penetration, the temperature equilibration curve

is disturbed and temperature determination is less accurate. The nominal accuracy of the APCT-3 temperature measurements is $\pm 0.05^\circ\text{C}$.

APCT-3 temperature data were combined with measurements of thermal conductivity (see **Physical properties**) obtained from whole-round core sections to obtain heat flow values. Heat flow was calculated according to the Bullard method, to be consistent with the synthesis of ODP heat flow data by Pribnow et al. (2000).

References

- ASTM International, 1990. Standard method for laboratory determination of water (moisture) content of soil and rock (Standard D2216–90). In *Annual Book of ASTM Standards for Soil and Rock* (Vol. 04.08): Philadelphia (American Society for Testing Materials). [revision of D2216-63, D2216-80]
- Balsam, W.L., and Damuth, J.E., 2000. Further investigations of shipboard vs. shore-based spectral data: implications for interpreting Leg 164 sediment composition. In Paull, C.K., Matsumoto, R., Wallace, P., and Dillon, W.P. (Eds.), *Proceedings of the Ocean Drilling Program, Scientific Results*, 164: College Station, TX (Ocean Drilling Program), 313–324. <http://dx.doi.org/10.2973/odp.proc.sr.164.222.2000>
- Balsam, W.L., Damuth, J.E., and Schneider, R.R., 1997. Comparison of shipboard vs. shore-based spectral data from Amazon Fan cores: implications for interpreting sediment composition. *Proceedings of the Ocean Drilling Program, Scientific Results*, 155: College Station, TX (Ocean Drilling Program), 193–215. <http://dx.doi.org/10.2973/odp.proc.sr.155.210.1997>
- Balsam, W.L., Deaton, B.C., and Damuth, J.E., 1998. The effects of water content on diffuse reflectance spectrophotometry studies of deep-sea sediment cores. *Marine Geology*, 149(1–4):177–189. [http://dx.doi.org/10.1016/S0025-3227\(98\)00033-4](http://dx.doi.org/10.1016/S0025-3227(98)00033-4)
- Berggren, W.A., Kent, D.V., Swisher, C.C., III, and Aubry, M.-P., 1995. A revised Cenozoic geochronology and chronostratigraphy. In Berggren, W.A., Kent, D.V., Aubry, M.-P., and Hardenbol, J. (Eds.), *Geochronology, Time Scales and Global Stratigraphic Correlation*. Special Publication - SEPM (Society for Sedimentary Geology), 54:129–212. <http://dx.doi.org/10.2110/pec.95.04.0129>
- Blow, W.H., 1969. Late middle Eocene to Recent planktonic foraminiferal biostratigraphy. *Proceedings of the International Conference on Planktonic Microfossils*, 1:199–422.
- Blow, W.H., 1979. *The Cainozoic Foraminifera* (Vols. 1–3): Leiden, The Netherlands (E. J. Brill).
- Blum, P., 1997. Physical properties handbook: a guide to the shipboard measurement of physical properties of deep-sea cores. *Ocean Drilling Program Technical Note*, 26. <http://dx.doi.org/10.2973/odp.tn.26.1997>
- Bolli, H.M., and Saunders, J.B., 1985. Oligocene to Holocene low latitude planktic foraminifera. In Bolli, H.M., Saunders, J.B., and Perch-Nielsen, K. (Eds.), *Plankton Stratigraphy* (Vol. 1): *Planktic Foraminifera, Calcareous Nannofossils and Calpionellids*: Cambridge, UK (Cambridge University Press), 155–262.
- Bollmann, J., 1997. Morphology and biogeography of *Gephyrocapsa* coccoliths in Holocene sediments. *Marine Micropaleontology*, 29(3–4):319–350. [http://dx.doi.org/10.1016/S0377-8398\(96\)00028-X](http://dx.doi.org/10.1016/S0377-8398(96)00028-X)
- Bown, P.R. (Ed.), 1998. *Calcareous Nannofossil Biostratigraphy*: Dordrecht, The Netherlands (Kluwer Academic Publishing).
- Bullard, E.C., 1954. The flow of heat through the floor of the Atlantic Ocean. *Proceedings of the Royal Society of London, Series A: Mathematical, Physical and Engineering Sciences*, 222(1150):408–429. <http://dx.doi.org/10.1098/rspa.1954.0085>
- Chen, M.H., and Tan, Z.Y., 1996. *Radiolaria from Surface Sediments of the Central and Northern South China Sea*: Beijing (Science Press). (in Chinese with English summary)
- Colwell, F.S., Stormberg, G.J., Phelps, T.J., Birnbaum, S.A., McKinley, J., Rawson, S.A., Veverka, C., Goodwin, S., Long, P.E., Russell, B.F., Garland, T., Thompson, D., Skinner, P., and Grover, S., 1992. Innovative techniques for

- collection of saturated and unsaturated subsurface basalts and sediments for microbiological characterization. *Journal of Microbiological Methods*, 15(4):279–292. [http://dx.doi.org/10.1016/0167-7012\(92\)90047-8](http://dx.doi.org/10.1016/0167-7012(92)90047-8)
- Cox, A., and Gordon, R.G., 1984. Paleolatitudes determined from paleomagnetic data from vertical cores. *Reviews of Geophysics and Space Physics*, 22(1):47–71. <http://dx.doi.org/10.1029/RG022i001p00047>
- Droser, M.L., and Bottjer, D.J., 1986. A semiquantitative field classification of ichnofabric. *Journal of Sedimentary Research*, 56(4):558–559. <http://dx.doi.org/10.1306/212F89C2-2B24-11D7-8648000102C1865D>
- Dunlea, A.G., Murray, R.W., Harris, R.N., Vasiliev, M.A., Evans, H., Spivack, A.J., and D'Hondt, S., 2013. Assessment and use of NGR instrumentation on the JOIDES Resolution to quantify U, Th, and K concentrations in marine sediment. *Scientific Drilling*, 15:57–63. <http://dx.doi.org/10.2204/iodp.sd.15.05.2013>
- Ellis, D.V., and Singer, J.M., 2007. *Well Logging for Earth Scientists* (2nd ed.): New York (Elsevier).
- Expedition 309/312 Scientists, 2006. Methods. In Teagle, D.A.H., Alt, J.C., Umino, S., Miyashita, S., Banerjee, N.R., Wilson, D.S., and the Expedition 309/312 Scientists. *Proceedings of the Integrated Ocean Drilling Program*, 309/312: Washington, DC (Integrated Ocean Drilling Program Management International, Inc.). <http://dx.doi.org/10.2204/iodp.proc.309312.102.2006>
- Expedition 324 Scientists, 2010. Methods. In Sager, W.W., Sano, T., Geldmacher, J., and the Expedition 324 Scientists, *Proceedings of the Integrated Ocean Drilling Program*, 324: Tokyo (Integrated Ocean Drilling Program Management International, Inc.). <http://dx.doi.org/10.2204/iodp.proc.324.102.2010>
- Expedition 329 Scientists, 2011. Methods. In D'Hondt, S., Inagaki, F., Alvarez Zarikian, C.A., and the Expedition 329 Scientists, *Proceedings of the Integrated Ocean Drilling Program*, 329: Tokyo (Integrated Ocean Drilling Program Management International, Inc.). <http://dx.doi.org/10.2204/iodp.proc.329.102.2011>
- Expedition 330 Scientists, 2012. Methods. In Koppers, A.A.P., Yamazaki, T., Geldmacher, J., and the Expedition 330 Scientists, *Proceedings of the Integrated Ocean Drilling Program*, 330: Tokyo (Integrated Ocean Drilling Program Management International, Inc.). <http://dx.doi.org/10.2204/iodp.proc.330.102.2012>
- Expedition 339 Scientists, 2013. Methods. In Stow, D.A.V., Hernández-Molina, F.J., Alvarez Zarikian, C.A., and the Expedition 339 Scientists, *Proceedings of the Integrated Ocean Drilling Program*, 339: Tokyo (Integrated Ocean Drilling Program Management International, Inc.). <http://dx.doi.org/10.2204/iodp.proc.339.102.2013>
- Fisher, R.V., and Schmincke, H.-U., 1984. *Pyroclastic Rocks*: Berlin (Springer-Verlag). <http://dx.doi.org/10.1007/978-3-642-74864-6>
- Fuller, M., 1969. Magnetic orientation of borehole cores. *Geophysics*, 34(5):772–774. <http://dx.doi.org/10.1190/1.1440047>
- Gee, J.S., Tauxe, L., and Constable, C., 2008. AMSSpin: a LabVIEW program for measuring the anisotropy of magnetic susceptibility with the Kappa-bridge KLY-4S. *Geochemistry, Geophysics, Geosystems*, 9(8):Q08Y02. <http://dx.doi.org/10.1029/2008GC001976>
- Gieskes, J.M., Gamo, T., and Brumsack, H., 1991. Chemical methods for interstitial water analysis aboard JOIDES Resolution. *Ocean Drilling Program Technical Note*, 15. <http://dx.doi.org/10.2973/odp.tn.15.1991>
- Gilmore, G.R., 2008. *Practical Gamma-ray Spectrometry* (2nd ed.): Hoboken, NJ (John Wiley & Sons). <http://dx.doi.org/10.1002/9780470861981>
- Goldberg, D., 1997. The role of downhole measurements in marine geology and geophysics. *Reviews of Geophysics*, 35(3):315–342. <http://dx.doi.org/10.1029/97RG00221>
- Gradstein, F.M., Ogg, J.G., Schmitz, M.D., and Ogg, G.M. (Eds.), 2012. *The Geological Time Scale 2012*: Amsterdam (Elsevier).
- Harris, R.N., Sakaguchi, A., Petronotis, K., Baxter, A.T., Berg, R., Burkett, A., Charpentier, D., Choi, J., Diz Ferreiro, P., Hamahashi, M., Hashimoto, Y., Heydolph, K., Jovane, L., Kastner, M., Kurz, W., Kutterolf, S.O., Li, Y., Malinverno, A., Martin, K.M., Millan, C., Nascimento, D.B., Saito, S., Sandoval Gutierrez, M.I., Scream, E.J., Smith-Duque, C.E., Solomon, E.A., Straub, S.M., Tanikawa, W., Torres, M.E., Uchimura, H., Vannucchi, P., Yamamoto, Y., Yan, Q., and Zhao, X., 2013. Methods. In Harris, R.N., Sakaguchi, A., Petronotis, K., and the Expedition 344 Scientists, *Proceedings of the Integrated Ocean Drilling Program*, 344: College Station, TX (Integrated Ocean Drilling Program). <http://dx.doi.org/10.2204/iodp.proc.344.102.2013>
- Harvey, R.W., George, L.H., Smith, R.L., and LeBlanc, D.R., 1989. Transport of microspores and indigenous bacteria through a sandy aquifer: results of natural- and forced-gradient tracer experiments. *Environmental Science & Technology*, 23(1):51–56. <http://dx.doi.org/10.1021/es00178a005>
- Horai, K., and Von Herzen, R.P., 1985. Measurement of heat flow on Leg 86 of the Deep Sea Drilling Project. In Heath, G.R., Burckle, L.H., et al., *Initial Reports of the Deep Sea Drilling Project*, 86: Washington, DC (U.S. Government Printing Office), 759–777. <http://dx.doi.org/10.2973/dsdp.proc.86.135.1985>
- Iturrino, G., Liu, T., Goldberg, D., Anderson, L., Evans, H., Fehr, A., Guerin, G., Inwood, J., Lofi, J., Malinverno, A., Morgan, S., Mrozowski, S., Slagle, A., and Williams, T., 2013. Performance of the wireline heave compensation system onboard D/V JOIDES Resolution. *Scientific Drilling*, 15:46–50. <http://dx.doi.org/10.2204/iodp.sd.15.08.2013>
- Jarrard, R.D., and Kernekian, M.J., 2007. Data report: physical properties of the upper oceanic crust of ODP Site 1256: multisensor track and moisture and density measurements. In Teagle, D.A.H., Wilson, D.S., Acton, G.D., and Vanko, D.A. (Eds.), *Proceedings of the Ocean Drilling Program, Scientific Results*, 206: College Station, TX (Ocean Drilling Program), 1–11. <http://dx.doi.org/10.2973/odp.proc.sr.206.011.2007>
- Kennett, J.P., and Srinivasan, M.S., 1983. *Neogene Planktonic Foraminifera: A Phylogenetic Atlas*: Stroudsburg, PA (Hutchinson Ross).
- Kirschvink, J.L., 1980. The least-squares line and plane and the analysis of palaeomagnetic data. *Geophysical Journal of the Royal Astronomical Society*, 62(3):699–718. <http://dx.doi.org/10.1111/j.1365-246X.1980.tb02601.x>
- Kristiansen, J.I., 1982. The transient cylindrical probe method for determination of thermal parameters of earth materials [Ph.D. dissert.]. Århus Univ., Århus, Denmark.
- Lehman, R.M., Colwell, F.S., Ringelberg, D.B., and White, D.C., 1995. Combined microbial community-level analyses for quality assurance of terrestrial subsurface cores. *Journal of Microbiological Methods*, 22(3):263–281. [http://dx.doi.org/10.1016/0167-7012\(95\)00012-A](http://dx.doi.org/10.1016/0167-7012(95)00012-A)
- Lever, M.A., Alperin, M., Engelen, B., Inagaki, F., Nakagawa, S., Steinsbu, B.O., Teske, A., and IODP Expedition 301 Scientists, 2006. Trends in basalt and sediment core contamination during IODP Expedition 301. *Geomicrobiology Journal*, 23(7):517–530. <http://dx.doi.org/10.1080/01490450600897245>
- Li, B., 1997. Paleooceanography of the Nansha Area, southern South China Sea since the last 700,000 years [Ph.D. dissert.]. Nanjing Institute of Geology and Palaeontology, Academic Sinica, Nanjing, China. (in Chinese, with abstract in English)
- Liu, T., Iturrino, G., Goldberg, D., Meissner, E., Swain, K., Furman, C., Fitzgerald, P., Frisbee, N., Chlimoun, J., Van Hyfte, J., and Beyer, R., 2013. Performance evaluation of active wireline heave compensation systems in marine well logging environments. *Geo-Marine Letters*, 33(1):83–93. <http://dx.doi.org/10.1007/s00367-012-0309-8>
- Lourens, L.J., Hilgen, F.J., Laskar, J., Shackleton, N.J., and Wilson, D., 2004. The Neogene period. In Gradstein, F.M., Ogg, J., et al. (Eds.), *A Geological Time Scale 2004*: Cambridge, UK (Cambridge University Press), 409–440.
- Lovell, M.A., Harvey, P.K., Brewer, T.S., Williams, C., Jackson, P.D., and Williamson, G., 1998. Application of FMS images in the Ocean Drilling Program: an overview. In Cramp, A., MacLeod, C.J., Lee, S.V., and Jones, E.J.W. (Eds.), *Geological Evolution of Ocean Basins: Results from the Ocean Drilling Program*. Geological Society Special Publication, 131(1):287–303. <http://dx.doi.org/10.1144/GSL.SP.1998.131.01.18>
- Luthi, S.M., 1990. Sedimentary structures of clastic rocks identified from electrical borehole images. In Hurst, A., Lovell, M.A., and Morton, A.C. (Eds.), *Geological Applications of Wireline Logs*. Geological Society Special Publication, 48(1):3–10. <http://dx.doi.org/10.1144/GSL.SP.1990.048.01.02>

- MacKenzie, W.S., Donaldson, C.H., and Guilford, C., 1982. *Atlas of Igneous Rocks and Their Textures*: Essex, UK (Longman Group UK Limited).
- Maiorano, P., and Marino, M., 2004. Calcareous nannofossil bioevents and environmental control on temporal and spatial patterns at the early–middle Pleistocene. *Marine Micropaleontology*, 53(3–4):405–422. <http://dx.doi.org/10.1016/j.marmicro.2004.08.003>
- Manheim, F.T., and Sayles, F.L., 1974. Composition and origin of interstitial waters of marine sediments, based on deep sea drill cores. In Goldberg, E.D. (Ed.), *The Sea* (Vol. 5): *Marine Chemistry: The Sedimentary Cycle*: New York (Wiley), 527–568.
- Martini, E., 1971. Standard Tertiary and Quaternary calcareous nannoplankton zonation. In Farinacci, A. (Ed.), *Proceedings of the Second Planktonic Conference, Roma 1970*: Rome (Edizioni Tecnoscienza), 2:739–785.
- Mazzullo, J.M., Meyer, A., and Kidd, R.B., 1988. New sediment classification scheme for the Ocean Drilling Program. In Mazzullo, J., and Graham, A.G. (Eds.), *Handbook for shipboard sedimentologists*. Ocean Drilling Program Technical Note, 8:44–67. <http://dx.doi.org/10.2973/odp.tn.8.1988>
- McFadden, P.L., and Reid, A.B., 1982. Analysis of paleomagnetic inclination data. *Geophysical Journal of the Royal Astronomical Society*, 69(2):307–319. <http://dx.doi.org/10.1111/j.1365-246X.1982.tb04950.x>
- Moore, T.C., Jr., 1995. Radiolarian stratigraphy, Leg 138. In Pisias, N.G., Mayer, L.A., Janecek, T.R., Palmer-Julson, A., and van Andel, T.H. (Eds.), *Proceedings of the Ocean Drilling Program, Scientific Results*, 138: College Station, TX (Ocean Drilling Program), 191–232. <http://dx.doi.org/10.2973/odp.proc.sr.138.111.1995>
- Munsell Color Company, Inc., 1994. *Munsell Soil Color Chart* (Revised ed.): Newburgh, MD (Munsell Color).
- Murray, R.W., Miller, D.J., and Kryc, K.A., 2000. Analysis of major and trace elements in rocks, sediments, and interstitial waters by inductively coupled plasma–atomic emission spectrometry (ICP–AES). *Ocean Drilling Program Technical Note*, 29. <http://dx.doi.org/10.2973/odp.tn.29.2000>
- Nigrini, C., and Sanfilippo, A., 2001. Cenozoic radiolarian stratigraphy for low and middle latitudes with descriptions of biomarkers and stratigraphically useful species. *Ocean Drilling Program Technical Note*, 27. <http://dx.doi.org/10.2973/odp.tn.27.2001>
- Okada, H., and Bukry, D., 1980. Supplementary modification and introduction of code numbers to the low-latitude coccolith biostratigraphic zonation (Bukry, 1973; 1975). *Marine Micropaleontology*, 5:321–325. [http://dx.doi.org/10.1016/0377-8398\(80\)90016-X](http://dx.doi.org/10.1016/0377-8398(80)90016-X)
- Parker, R.L., and Gee, J.S., 2002. Calibration of the pass-through magnetometer—II. Application. *Geophysical Journal International*, 150:140–152. <http://dx.doi.org/10.1046/j.1365-246X.2002.01692.x>
- Perch-Nielsen, K., 1985. Cenozoic calcareous nannofossils. In Bolli, H.M., Saunders, J.B., and Perch-Nielsen, K. (Eds.), *Plankton Stratigraphy*: Cambridge, UK (Cambridge University Press), 427–554.
- Pribnow, D., Kinoshita, M., and Stein, C., 2000. *Thermal Data Collection and Heat Flow Recalculations for Ocean Drilling Program Legs 101–180*: Hanover, Germany (Institute for Joint Geoscientific Research, Institut für Geowissenschaftliche Gemeinschaftsaufgaben [GGA]). <http://www-odp.tamu.edu/publications/heatflow/ODPReprt.pdf>
- Quintin, L.L., Faul, K.L., Lear, C., Graham, D., Peng, C., Murray, R.W., and Shipboard Scientific Party, 2002. Geochemical analysis of bulk marine sediment by inductively coupled plasma–atomic emission spectroscopy on board the *JOIDES Resolution*. In Lyle, M., Wilson, P.A., Janecek, T.R., et al., *Proceedings of the Ocean Drilling Program, Initial Reports*, 199: College Station, TX (Ocean Drilling Program), 1–14. <http://dx.doi.org/10.2973/odp.proc.ir.199.107.2002>
- Raffi, I., Backman, J., Fornaciari, E., Pälke, H., Rio, D., Lourens, L., and Hilgen, F., 2006. A review of calcareous nannofossil astrochronology encompassing the past 25 million years. *Quaternary Science Reviews*, 25(23–24):3113–3137. <http://dx.doi.org/10.1016/j.quascirev.2006.07.007>
- Richter, C., Acton, G., Endris, C., and Radsted, M., 2007. Handbook for shipboard paleomagnetists. *Ocean Drilling Program Technical Note*, 34. <http://dx.doi.org/10.2973/odp.tn.34.2007>
- Rider, M.H., 1996. *The Geological Interpretation of Well Logs* (2nd ed.): Caithness (Whittles Publishing).
- Rothwell, R.G., 1989. *Minerals and Mineraloids in Marine Sediments: An Optical Identification Guide*: London (Elsevier).
- Salimullah, A.R.M., and Stow, D.A.V., 1992. Application of FMS images in poorly recovered coring intervals: examples from ODP Leg 129. In Hurst, A., Griffiths, C.M., and Worthington, P.F. (Eds.), *Geological Application of Wireline Logs II*. Geological Society Special Publication, 65(1):71–86. <http://dx.doi.org/10.1144/GSL.SP.1992.065.01.06>
- Samtleben, C., 1980. Die Evolution der Coccolithophoriden-Gattung *Gephyrocapsa* nach Befunden im Atlantik. *Paläontologische Zeitschrift*, 54(1–2):91–127. <http://dx.doi.org/10.1007/BF02985885>
- Sanfilippo, A., and Nigrini, C., 1998. Code numbers for Cenozoic low latitude radiolarian biostratigraphic zones and GPTS conversion tables. *Marine Micropaleontology*, 33(1–2):109–117, 121–156. [http://dx.doi.org/10.1016/S0377-8398\(97\)00030-3](http://dx.doi.org/10.1016/S0377-8398(97)00030-3)
- Sanfilippo, A., and Riedel, W.R., 1985. Cenozoic radiolaria. In Bolli, H.M., Saunders, J.B., and Perch-Nielsen, K. (Eds.), *Plankton Stratigraphy*: Cambridge, UK (Cambridge Univ. Press), 631–712.
- Schlumberger, 1989. *Log Interpretation Principles/Applications*: Houston (Schlumberger Education Services), SMP-7017.
- Schlumberger, 1994. *IPL Integrated Porosity Lithology*: Houston (Schlumberger Wireline Testing), SMP-9270.
- Serra, O., 1984. *Fundamentals of Well-Log Interpretation* (Vol. 1): *The Acquisition of Logging Data*: Amsterdam (Elsevier).
- Serra, O., 1986. *Fundamentals of Well-Log Interpretation* (Vol. 2): *The Interpretation of Logging Data*. Amsterdam (Elsevier).
- Serra, O., 1989. *Formation MicroScanner Image Interpretation*: Houston (Schlumberger Education Services), SMP-7028.
- Shepard, F.P., 1954. Nomenclature based on sand-silt-clay ratios. *Journal of Sedimentary Research*, 24(3):151–158. <http://dx.doi.org/10.1306/D4269774-2B26-11D7-8648000102C1865D>
- Shipboard Scientific Party, 1993. Explanatory notes. In Alt, J.C., Kinoshita, H., Stokking, L.B., et al., *Proceedings of the Ocean Drilling Program, Initial Reports*, 148: College Station, TX (Ocean Drilling Program), 5–24. <http://dx.doi.org/10.2973/odp.proc.ir.148.101.1993>
- Shipboard Scientific Party, 2002. Explanatory notes. In Tarduno, J.A., Duncan, R.A., Scholl, D.W., et al., *Proceedings of the Ocean Drilling Program, Initial Reports*, 197: College Station, TX (Ocean Drilling Program), 1–89. <http://dx.doi.org/10.2973/odp.proc.ir.197.102.2002>
- Shipboard Scientific Party, 2003. Explanatory notes. In Wilson, D.S., Teagle, D.A.H., Acton, G.D. et al., *Proceedings of the Ocean Drilling Program, Initial Reports*, 206: College Station, TX (Ocean Drilling Program), 1–94. <http://dx.doi.org/10.2973/odp.proc.ir.206.102.2003>
- Smith, D.C., Spivack, A.J., Fisk, M.R., Haveman, S.A., and Staudigel, H., 2000. Tracer-based estimates of drilling-induced microbial contamination of deep sea crust. *Geomicrobiology Journal*, 17(3):207–219. <http://dx.doi.org/10.1080/01490450050121170>
- Stow, D.A.V., 2005. *Sedimentary Rocks in the Field: A Colour Guide*: London (Manson Publishing).
- Su, X., 1996. Development of late Tertiary and Quaternary coccolith assemblages in the northeast Atlantic. *GEOMAR Report*, 48.
- Takahashi, K., 1991. *Radiolaria: Flux, Ecology, and Taxonomy in the Pacific and Atlantic*. Ocean Biocoenosis Series, 3. <http://hdl.handle.net/1912/408>
- Tauxe, L., Tucker, P., Peterson, N.P., and LaBrecque, J.L., 1984. Magnetostratigraphy of Leg 73 sediments. In Hsü, K.J., LaBrecque, J.L., et al., *Initial Reports of the Deep Sea Drilling Project*, 73: Washington, DC (U.S. Government Printing Office), 609–621. <http://dx.doi.org/10.2973/dsdp.proc.73.123.1984>
- Thompson, P.R., Bé, A.W.H., Duplessy, J.-C., and Shackleton, N.J., 1979. Disappearance of pink-pigmented *Globigerinoides ruber* at 120,000 yr BP in the Indian and Pacific oceans. *Nature*, 280(5723):554–558. <http://dx.doi.org/10.1038/280554a0>
- Vacquier, V., 1985. The measurement of thermal conductivity of solids with a transient linear heat source on the plane surface of a poorly conducting body. *Earth and Planetary Science Letters*, 74(2–3):275–279. [http://dx.doi.org/10.1016/0012-821X\(85\)90027-5](http://dx.doi.org/10.1016/0012-821X(85)90027-5)

- Vasiliev, M.A., Blum, P., Chubarian, G., Olsen, R., Bennight, C., Cobine, T., Fackler, D., Hastedt, M., Houpt, D., Mateo, Z., and Vasilieva, Y.B., 2011. A new natural gamma radiation measurement system for marine sediment and rock analysis. *Journal of Applied Geophysics*, 75:455–463. <http://dx.doi.org/10.1016/j.jappgeo.2011.08.008>
- Von Herzen, R., and Maxwell, A.E., 1959. The measurement of thermal conductivity of deep-sea sediments by a needle-probe method. *Journal of Geophysical Research*, 64(10):1557–1563. <http://dx.doi.org/10.1029/JZ064i010p01557>
- Wade, B.S., Pearson, P.N., Berggren, W.A., and Pälike, H., 2011. Review and revision of Cenozoic tropical planktonic foraminiferal biostratigraphy and calibration to the geomagnetic polarity and astronomical time scale. *Earth-Science Reviews*, 104(1–3):111–142. <http://dx.doi.org/10.1016/j.earscirev.2010.09.003>
- Wang, R., and Abelmann, A., 1999. Pleistocene radiolarian biostratigraphy in the South China Sea. *Science in China (Series D)*, 42(5):537–543.
- Wentworth, C.K., 1922. A scale of grade and class terms for clastic sediments. *Journal of Geology*, 30(5):377–392. <http://dx.doi.org/10.1086/622910>
- Young, J.R., 1998. Neogene. In Bown, P.R. (Ed.), *Calcareous Nannofossil Biostratigraphy*: Dordrecht, The Netherlands (Kluwer Academic Publishing), 225–265.
- Zijderveld, J.D.A., 1967. AC demagnetization of rocks: analysis of results. In Collinson, D.W., Creer, K.M., and Runcorn, S.K. (Eds.), *Methods in Palaeomagnetism*: Amsterdam (Elsevier), 254–286.

doi:10.14379/iodp.proc.349.103.2015

Site U1431¹



C.-F. Li, J. Lin, D.K. Kulhanek, T. Williams, R. Bao, A. Briais, E.A. Brown, Y. Chen, P.D. Clift, F.S. Colwell, K.A. Dadd, W.-W. Ding, I. Hernández-Almeida, X.-L. Huang, S. Hyun, T. Jiang, A.A.P. Koppers, Q. Li, C. Liu, Q. Liu, Z. Liu, R.H. Nagai, A. Peleo-Alampay, X. Su, Z. Sun, M.L.G. Tejada, H.S. Trinh, Y.-C. Yeh, C. Zhang, F. Zhang, G.-L. Zhang, and X. Zhao²

Keywords: International Ocean Discovery Program, IODP, *JOIDES Resolution*, Expedition 349, Site U1431, South China Sea, deep-marine turbidite, pelagic red clay, seamount volcanoclastics, Ar-Ar dating, interflow sediment, mid-ocean-ridge basalt, basement magnetization, basalt alteration, radiolarians, *Nereites* ichnofacies, debris flow

Contents

- 1 Background and objectives
- 1 Operations
- 7 Lithostratigraphy
- 17 Biostratigraphy
- 23 Igneous petrology and alteration
- 29 Structural geology
- 30 Geochemistry
- 35 Microbiology
- 38 Paleomagnetism
- 42 Physical properties
- 46 Downhole measurements
- 53 References

Background and objectives

International Ocean Discovery Program (IODP) Site U1431 is located near the relict spreading ridge where the youngest crustal magnetic anomalies are observed in the East Subbasin of the South China Sea (Figure **F1**). A positive magnetic anomaly lineation that runs through this site will possibly allow regional correlation of crustal age (Figure **F2**). This site is also surrounded by abyssal highs in the ocean crust and younger seamounts (Figure **F3**), whose volcanic and/or redepositional events are recorded in sediments recovered from this site.

The primary objective at Site U1431 is to core into the oceanic basement to determine the termination age of seafloor spreading in the East Subbasin. The thick package of sediment (~900 m) overlying basement will also provide important constraints on the evolution of the ridge and associated late-stage magmatism, deep-marine sedimentary processes, and the paleoceanographic history following the termination of seafloor spreading in the South China Sea. Additionally, this site will allow for correlation of biostratigraphic, magnetostratigraphic, and radiometric ages to the observed crustal magnetic anomalies. Physical property and paleomagnetism measurements of basement rocks will help elucidate the cause of the distinct magnetic contrasts between the East and Southwest Subbasins. Furthermore, this site will provide constraints on mantle source, melting, and magma crystallization processes in the latest stages of basin formation. Physical property measurements of core samples and wireline logging measurements will provide stratigraphic information for correlation with regional seismic profiles. Microbiological analyses will help explore the deep biosphere in the South China Sea to examine how sharp changes in lithology (interfaces) affect subsurface community structure and function, as well as how posteruption processes have influenced past ecosystems in the deep-sea basin.

Operations

The original operations plan for Site U1431 (proposed Site SCS-3G) called for one hole to a depth of ~1061 m below seafloor (mbsf), which included ~100 m of basement. The plan was modified during transit to include two additional short holes for high-resolution sampling of the upper ~20 m of section (Table **T1**). Hole U1431A was successfully cored using the advanced piston corer (APC) to 28.4 mbsf, and Hole U1431B was cored to 17.0 mbsf. After the first core from Hole U1431C retrieved a split core liner and no mudline, we opted to abandon the hole, which was completed to 14.2 mbsf, and spudded Hole U1431D. Hole U1431D was cored to 617.0 mbsf when the extended core barrel (XCB) failed, leaving the cutting shoe, core catcher sub assembly, and breakoff sub in the hole. We abandoned Hole U1431D and switched to the rotary core barrel (RCB) to spud Hole U1431E, which was drilled to 507.0 mbsf, spot cored, and then cored continuously from 575.0 mbsf to total depth at 1008.8 mbsf in igneous basement. After conditioning the hole for logging, two logging runs were performed. The triple combination (triple combo) tool string was run to 463.0 m wireline depth below seafloor (WSF), and the Formation MicroScanner (FMS)-sonic tool string was run to 444 m WSF with two passes. Total time spent at Site U1431 was 385.7 h (16.1 days).

A total of 122 cores were collected at this site. The APC was deployed 26 times, recovering 225.61 m of core over 228.50 m of penetration (98.7% recovery). The XCB was deployed 48 times, recovering 236.50 m of core over 448.10 m (52.8% recovery). The RCB was deployed 48 times, recovering 243.00 m of core over 443.5 m of penetration (54.8% recovery).

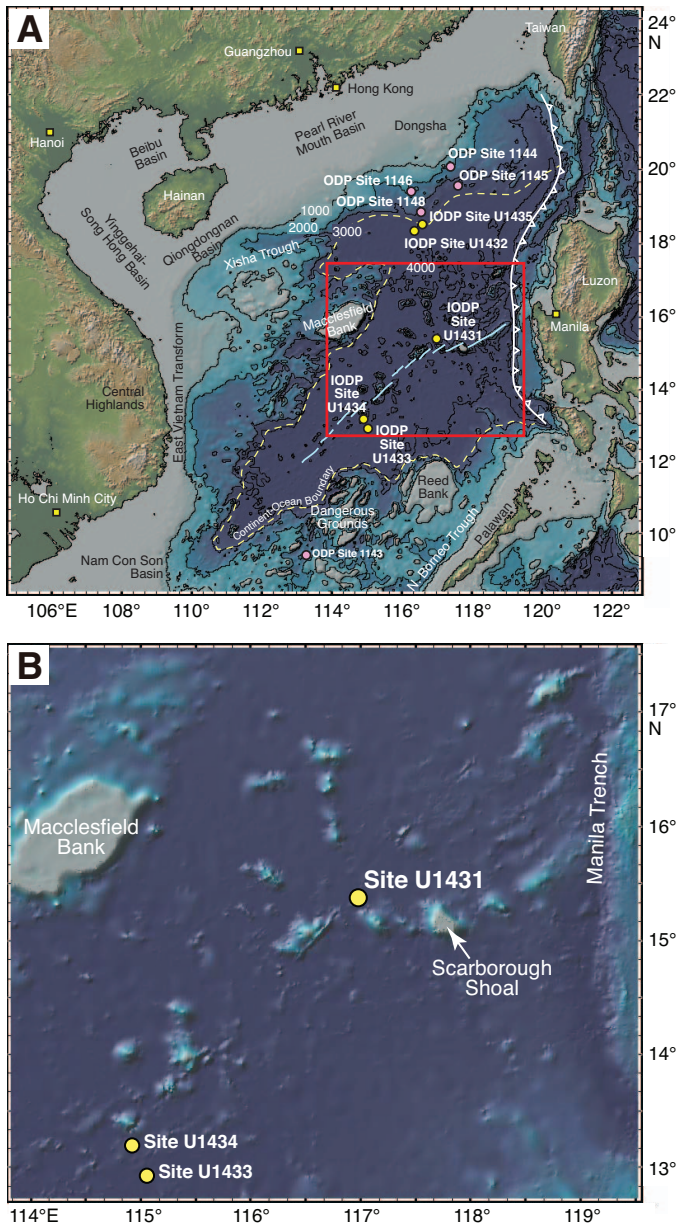
Transit to Site U1431

After a 463 nmi transit from Hong Kong averaging 11.0 kt, the vessel arrived at Site U1431. A prespud meeting was held prior to

¹ Li, C.-F., Lin, J., Kulhanek, D.K., Williams, T., Bao, R., Briais, A., Brown, E.A., Chen, Y., Clift, P.D., Colwell, F.S., Dadd, K.A., Ding, W., Hernández-Almeida, I., Huang, X.-L., Hyun, S., Jiang, T., Koppers, A.A.P., Li, Q., Liu, C., Liu, Q., Liu, Z., Nagai, R.H., Peleo-Alampay, A., Su, X., Sun, Z., Tejada, M.L.G., Trinh, H.S., Yeh, Y.-C., Zhang, C., Zhang, F., Zhang, G.-L., and Zhao, X., 2015. Site U1431. In Li, C.-F., Lin, J., Kulhanek, D.K., and the Expedition 349 Scientists, *Proceedings of the International Ocean Discovery Program, 349: South China Sea Tectonics*: College Station, TX (International Ocean Discovery Program). <http://dx.doi.org/10.14379/iodp.proc.349.103.2015>

² Expedition 349 Scientists' addresses.

Figure F1. A. Bathymetric map of South China Sea region. Solid yellow circles = Expedition 349 sites. Solid pink circles = ODP Leg 184 sites. Yellow dashed line = inferred continent/ocean boundary, blue lines = fossil South China Sea spreading center, white-flagged line = Manila Trench. B. Detailed bathymetry around Site U1431 (red box in A) showing nearby bathymetric highs and the Manila Trench.

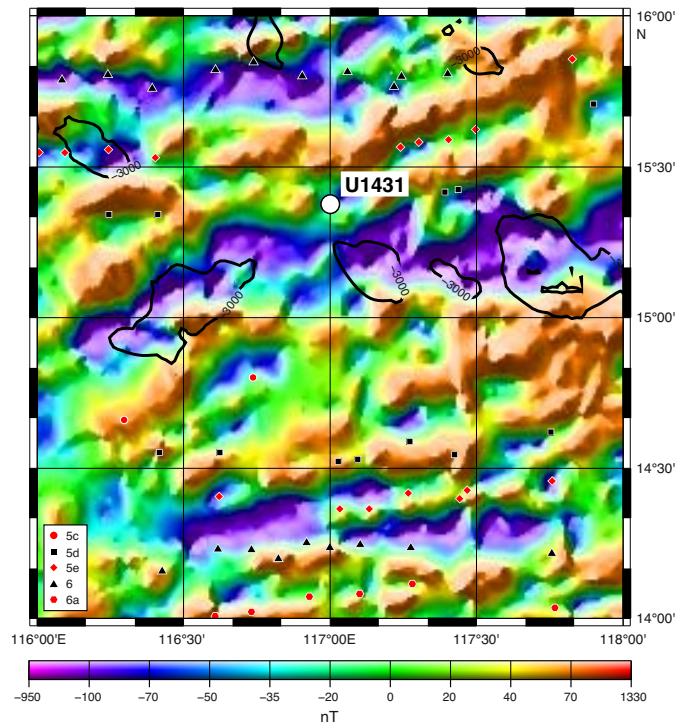


arrival to review operations at the first site. The vessel stabilized and switched from cruise mode to dynamic positioning over Site U1431 at 0640 h (UTC + 8 h) on 31 January 2014. The positioning beacon was then deployed at 0712 h. The position reference was a combination of GPS signals and a single acoustic beacon.

Hole U1431A

After arriving on site and deploying the acoustic positioning beacon, the bottom-hole assembly (BHA) was picked up and assembled and then run in the hole with drill pipe to 4165.25 meters below rig floor (mbrf). All drill pipe was measured (strapped) and the internal diameter verified (drifted) during the pipe trip. There were

Figure F2. Shaded map of magnetic anomalies near Site U1431 (data from Ishihara and Kisimoto, 1996). Black lines mark 3000 m isobaths outlining the seamounts. Symbols are magnetic anomaly picks from Briais et al. (1993).

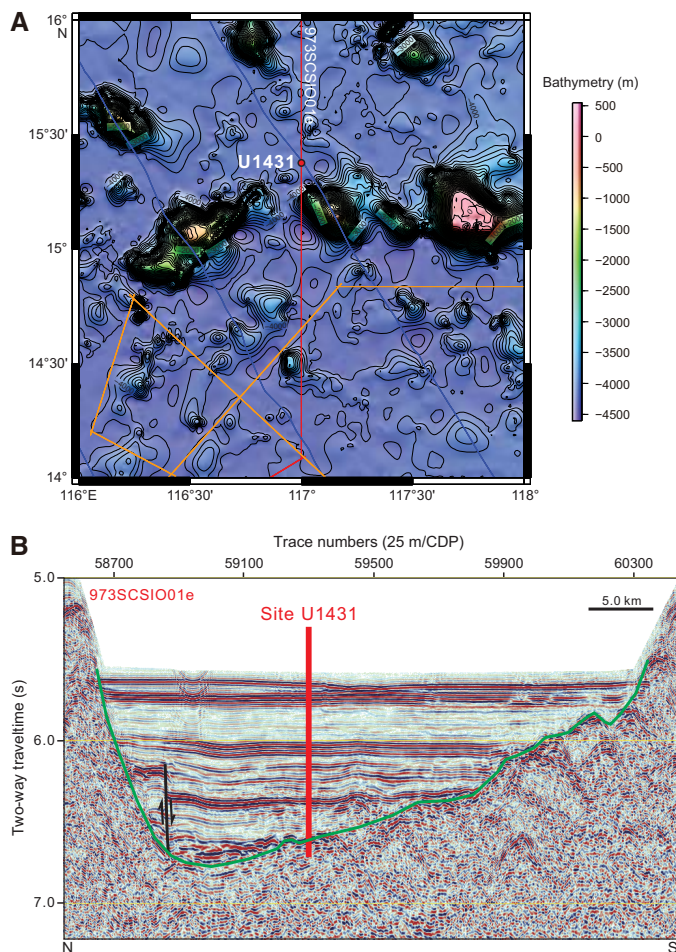


no operational problems running the drill string to near the seafloor. The top drive was picked up, the drill string circulated out, and a pig was pumped to remove any debris that might have accumulated in the string. The calculated precision depth recorder depth for the site was 4252.1 mbrf, and after some consideration, 4248 mbrf was selected as the shoot depth for the first core. The bit was spaced out to 4248 mbrf, and the APC core barrel was run in the hole by wireline and landed. Hole U1431A was spudded at 0040 h on 1 February 2014. The mudline core recovered 9.45 m of sediment, and the seafloor was calculated to be 4248.1 mbrf (4237.3 meters below sea level [mbsl]). Nonmagnetic core barrels were used for APC coring from Core 349-U1431A-1H through 3H. Hole U1431A was terminated by plan at a final depth of 4276.5 mbrf (28.4 mbsf). At the conclusion of coring, the drill string was pulled from the hole. The seafloor was cleared at 0345 h, ending Hole U1431A. Three piston cores were taken over a 28.4 m interval, with a total recovery of 28.39 m of core. Overall core recovery for Hole U1431A was 100.0%. The total time spent in Hole U1431A was 21.0 h (0.9 days).

Hole U1431B

After the bit cleared the seafloor, the vessel was offset 20 m east of Hole U1431A. As part of the planned microbiological analyses, the perfluorocarbon tracer (PFT) pump was turned on and the drill string displaced with contamination testing fluid. The pump remained on for the remainder of coring operations in Hole U1431B. The bit was spaced out to 4245.5 mbrf in an attempt to recover ~7.0 m in the mudline core. The mudline core recovery was 7.5 m. The seafloor depth was calculated to be 4247.5 mbrf (4236.7 mbsl). Hole U1431B was spudded at 0420 h on 1 February 2014. Nonmagnetic core barrels were used for APC coring from Core 349-U1431B-1H through 2H to a final depth of 17.0 mbsf. At the conclu-

Figure F3. A. Regional contoured bathymetric map showing seismic reflection profiles (orange, red, and blue lines) and the location of Site U1431. Contour interval = 100 m. B. Seismic profile Line 973SCSI001e with location of Site U1431. CDP = common depth point. Green line = interpreted top of basement, black line = interpreted fault with arrows indicating displacement direction.



sion of coring, the drill string was pulled from the hole. The bit cleared the seafloor at 0620 h, ending Hole U1431B. Two piston cores were taken over a 17.0 m interval in Hole U1431B, with a total recovery of 17.16 m of core (100.9% recovery). The total time spent on Hole U1431B was 2.58 h (0.1 days).

Hole U1431C

After the bit cleared the seafloor, the vessel was offset 20 m south of Hole U1431B. The bit was spaced out to 4245.5 mbrf. The mudline core recovery was 4.7 m, but the core liner was split. The seafloor depth was calculated to be 4250.3 mbrf (4239.5 mbsl). Hole U1431C was spudded at 0700 h on 1 February 2014. Nonmagnetic core barrels were used for APC coring from Core 349-U1431C-1H through 2H to a final depth of 14.2 mbsf. The PFT pump remained running during coring in Hole U1431C. Hole U1431C was terminated when we determined that the mudline core would not meet sampling requirements. At the conclusion of coring, the drill string was pulled from the hole. The bit cleared the seafloor at 0852 h, ending Hole U1431C. A total of 2 piston cores were taken over a 14.2 m interval in Hole U1431C, with a total recovery of 14.45 m of

core (101.8% recovery). The total time spent on Hole U1431C was 2.42 h (0.1 days).

Hole U1431D

After the bit cleared the seafloor, the vessel was offset 20 m west of Hole U1431C. The bit was spaced out to 4245.0 mbrf. The mudline core recovery was 3.22 m. The seafloor depth was calculated to be 4251.3 mbrf (4240.5 mbsl). Hole U1431D was spudded at 0925 h on 1 February 2014. Nonmagnetic core barrels were used for APC coring from Core 349-U1431D-1H through 19H to 168.9 mbsf. Temperature measurements were taken with the advanced piston corer temperature tool (APCT-3) on Cores 4H, 7H, 10H, and 13H with good results. After 6 partial strokes of the APC, the coring system was switched over to the XCB. XCB coring continued from Core 20X through 67X at a final depth of 4868.3 mbrf (617.0 mbsf). The PFT pumps remained on through Core 23X. While cutting Core 67X, the rate of penetration dropped severely, and the core barrel was retrieved after a 2.7 m advance. While recovering the core barrel at the surface, we discovered that the cutting shoe, core catcher sub assembly, and the breakoff sub were missing from the XCB coring assembly. With ~1 m of junk metal remaining in the hole, we decided to pull out of the hole, offset, and begin a new hole with the RCB coring system. The top drive was then set back and the bit tripped from the hole, clearing the seafloor at 0355 h on 6 February. The bit was then tripped to the surface and cleared the rig floor at 1415 h, ending Hole U1431D. A total of 19 APC cores were taken over a 168.9 m interval in Hole U1431D, with a total recovery of 165.61 m of core (98.1%). The XCB was used 48 times over an interval of 448.1 m, recovering 236.50 m of core (52.8%). Overall core recovery for Hole U1431D was 402.11 m over an interval of 617.0 m (65.2% recovery). The total time spent in Hole U1431D was 125.5 h (5.2 days).

Hole U1431E

After offsetting the vessel 20 m west of Hole U1431D, an RCB BHA was assembled with a new RCB C-4 bit. The BHA was run in the hole to 4163.22 mbrf, and the rig crew performed a slip and cut of 115 ft of drilling line. The remainder of the drill pipe was then run in the hole. At 4221.46 mbrf, the top drive was picked up and spaced out to spud Hole U1431E. A center bit was dropped and pumped to land out in the bit. Hole U1431E was spudded at 0650 h on 7 February 2014. The seafloor depth for the hole was determined to be 4251.3 mbrf, calculated using an offset depth from Hole U1431D. Hole U1431E was advanced by drilling without coring from the seafloor to 507.0 mbsf. The center bit was pulled from the BHA by wireline, and a core barrel was dropped to take a spot core (349-U1431E-2R) from 507.0 mbsf. After cutting the core without recovery, the center bit was dropped and drilling continued from 516.7 to 575.0 mbsf. The center bit was then retrieved by wireline, a core barrel dropped, and continuous coring started with Core 4R from 575.0 mbsf. The next three cores (4R through 6R; 575.0–603.3 mbsf) did not recover any material. Coring continued with good recovery from Core 7R through 36R (603.3–894.3 mbsf). Core 36R was the first to recover basalt, with several small pieces present in the core catcher. Coring then continued into acoustic basement from Core 37R through 47R (894.3–991.4 mbsf). Penetration rates varied from 1.62 to 4.66 m/h over this interval, except for a sediment section in Core 45R that cored more quickly than the basalt. Microspheres were deployed in the RCB core catcher sub for Cores 12R through 43R.

Table T1. Coring summary, Site U1431. CSF = core depth below seafloor, DRF = drilling depth below rig floor, DSF = drilling depth below seafloor. BHA = bottom hole assembly, APC = advanced piston corer, XCB = extended core barrel, RCB = rotary core barrel. H = advanced piston corer, X = extended core barrel, R = rotary core barrel, numeric core type = drilled interval. APCT-3 = advanced piston corer temperature tool, PFTs = perfluorocarbon tracers. (Continued on next three pages.) [Download table as .csv.](#)

Hole U1431A

Latitude: 15°22.5491'N
 Longitude: 117°00.0009'E
 Water depth (m): 4237.26
 Date started (UTC): 30 January 2014, 2240 h
 Date finished (UTC): 31 January 2014, 1945 h
 Time on hole (days): 0.9
 Seafloor depth (m DRF): 4248.1
 Seafloor depth calculation method: APC calculated depth
 Rig floor to sea level (m): 10.84
 Drilling system: 11-7/16 inch APC/XCB bit with 136.63 m long BHA
 Penetration depth (m DSF): 28.40
 Cored interval (m): 28.40
 Recovered length (m): 28.39
 Recovery (%): 100
 Total cores (no.): 3
 APC cores (no.): 3
 Age of oldest sediment cored: Middle Pleistocene

Hole U1431B

Latitude: 15°22.5480'N
 Longitude: 117°00.0125'E
 Water depth (m): 4236.66
 Date started (UTC): 31 January 2014, 1945 h
 Date finished (UTC): 31 January 2014, 2220 h
 Time on hole (days): 0.1
 Seafloor depth (m DRF): 4247.5
 Seafloor depth calculation method: APC calculated depth
 Rig floor to sea level (m): 10.84
 Drilling system: 11-7/16 inch APC/XCB bit with 136.63 m long BHA
 Penetration depth (m DSF): 17.0
 Cored interval (m): 17.00
 Recovered length (m): 17.16
 Recovery (%): 101
 Total cores (no.): 2
 APC cores (no.): 2
 Age of oldest sediment cored: Middle Pleistocene

Hole U1431C

Latitude: 15°22.5371'N
 Longitude: 117°00.0108'E
 Water depth (m): 4239.46
 Date started (UTC): 31 January 2014, 2220 h
 Date finished (UTC): 1 February 2014, 0052 h
 Time on hole (days): 0.1
 Seafloor depth (m DRF): 4250.3
 Seafloor depth calculation method: APC calculated depth
 Rig floor to sea level (m): 10.84
 Drilling system: 11-7/16 inch APC/XCB bit with 136.63 m long BHA
 Penetration depth (m DSF): 14.2
 Cored interval (m): 14.20
 Recovered length (m): 14.45
 Recovery (%): 102
 Total cores (no.): 2
 APC cores (no.): 2
 Age of oldest sediment cored: Middle Pleistocene

Hole U1431D

Latitude: 15°22.5379'N
 Longitude: 117°00.0022'E
 Water depth (m): 4240.46
 Date started (UTC): 1 February 2014, 0052 h
 Date finished (UTC): 6 February 2014, 0615 h
 Time on hole (days): 5.2
 Seafloor depth (m DRF): 4251.3
 Seafloor depth calculation method: APC calculated depth
 Rig floor to sea level (m): 10.84
 Drilling system: 11-7/16 inch APC/XCB bit with 136.63 m long BHA
 Penetration depth (m DSF): 617.0
 Cored interval (m): 617.0
 Recovered length (m): 402.11

Table T1 (continued). (Continued on next page.)

Recovery (%): 65
 Total cores (no.): 67
 APC cores (no.): 19
 XCB cores (no.): 48
 Age of oldest sediment cored: late Miocene

Hole U1431E
 Latitude: 15°22.5380'N
 Longitude: 116°59.9903'E
 Water depth (m): 4240.34
 Date started (UTC): 6 February 2014, 0615 h
 Date finished (UTC): 15 February 2014, 2200 h
 Time on hole (days): 9.7
 Seafloor depth (m DRF): 4251.3
 Seafloor depth calculation method: offset depth from Hole U1431D
 Rig floor to sea level (m): 10.96
 Drilling system: 9-7/8 inch RCB bit with 172.07 m long BHA
 Penetration depth (m DSF): 1008.8
 Cored interval (m): 443.50
 Recovered length (m): 243.00
 Recovery (%): 55
 Drilled interval (m): 565.3
 Drilled interval (no.): 2
 Total cores (no.): 48
 RCB cores (no.): 47
 Other cores (no.): 1
 Age of oldest sediment cored: early Miocene

Core	Date (2014)	Time UTC (h)	Depth DSF (m)			Depth CSF (m)		Length of core recovered (m)	Length of core curated (m)	Recovery (%)	Sections (no.)	Comments
			Top of interval	Bottom of interval	Interval advanced (m)	Top of cored interval	Bottom of cored interval					
349-U1431A-												
1H	31 Jan	1705	0	9.4	9.4	0	9.45	9.45	9.45	101	19	
2H	31 Jan	1825	9.4	18.9	9.5	9.40	19.18	9.78	9.78	103	20	
3H	31 Jan	1920	18.9	28.4	9.5	18.90	28.06	9.16	9.16	96	10	
					Totals:	28.4		28.39		100	49	
349-U1431B-												
1H	31 Jan	2045	0	7.5	7.5	0	7.63	7.63	7.63	102	15	PFTs
2H	31 Jan	2205	7.5	17.0	9.5	7.50	17.03	9.53	9.53	100	8	PFTs
					Totals:	17.0		17.16		101	23	PFTs
349-U1431C-												
1H	31 Jan	2330	0	4.7	4.7	0	4.79	4.79	4.79	102	5	FlexIT, PFTs
2H	1 Feb	0035	4.7	14.2	9.5	4.70	14.36	9.66	9.66	102	8	FlexIT, PFTs
					Totals:	14.2		14.45		102	13	
349-U1431D-												
1H	1 Feb	0205	0	3.2	3.2	0	3.22	3.22	3.22	101	4	FlexIT, PFTs
2H	1 Feb	0325	3.2	12.7	9.5	3.20	12.22	9.02	9.02	95	7	FlexIT, PFTs
3H	1 Feb	0450	12.7	22.2	9.5	12.70	22.14	9.44	9.44	99	8	FlexIT, PFTs
4H	1 Feb	0610	22.2	31.7	9.5	22.20	32.13	9.93	9.93	105	8	FlexIT, APCT-3, PFTs
5H	1 Feb	0720	31.7	41.2	9.5	31.70	41.52	9.82	9.82	103	8	FlexIT, PFTs
6H	1 Feb	0835	41.2	50.7	9.5	41.20	50.95	9.75	9.75	103	8	FlexIT, PFTs
7H	1 Feb	1000	50.7	60.2	9.5	50.70	58.58	7.88	7.88	83	7	FlexIT, APCT-3, PFTs
8H	1 Feb	1055	60.2	69.7	9.5	60.20	69.54	9.34	9.34	98	8	FlexIT, PFTs
9H	1 Feb	1200	69.7	79.2	9.5	69.70	78.91	9.21	9.21	97	8	FlexIT, PFTs
10H	1 Feb	1325	79.2	88.7	9.5	79.20	89.06	9.86	9.86	104	9	FlexIT, APCT-3, PFTs
11H	1 Feb	1425	88.7	98.2	9.5	88.70	96.15	7.45	7.45	78	5	FlexIT, PFTs
12H	1 Feb	1530	98.2	107.7	9.5	98.20	107.65	9.45	9.45	99	7	FlexIT, PFTs
13H	1 Feb	1655	107.7	117.2	9.5	107.70	116.93	9.23	9.23	97	8	FlexIT, APCT-3, PFTs
14H	1 Feb	1805	117.2	125.5	8.3	117.20	125.52	8.32	8.32	100	7	FlexIT, PFTs
15H	1 Feb	1925	125.5	135.0	9.5	125.50	135.26	9.76	9.76	103	8	FlexIT, PFTs
16H	1 Feb	2040	135.0	144.2	9.2	135.00	144.18	9.18	9.18	100	8	FlexIT, PFTs
17H	1 Feb	2200	144.2	153.6	9.4	144.20	153.61	9.41	9.41	100	8	FlexIT, PFTs
18H	1 Feb	2320	153.6	162.0	8.4	153.60	162.07	8.47	8.47	101	8	FlexIT, PFTs
19H	2 Feb	0055	162.0	168.9	6.9	162.00	168.87	6.87	6.87	100	6	FlexIT, PFTs
20X	2 Feb	0255	168.9	178.5	9.6	168.90	177.95	9.05	9.05	94	7	PFTs
21X	2 Feb	0530	178.5	188.1	9.6	178.50	188.35	9.85	9.85	103	8	PFTs
22X	2 Feb	0710	188.1	197.7	9.6	188.10	197.89	9.79	9.79	102	8	PFTs
23X	2 Feb	0845	197.7	207.3	9.6	197.70	207.61	9.91	9.91	103	9	PFTs
24X	2 Feb	1050	207.3	216.9	9.6	207.30	217.12	9.82	9.82	102	8	
25X	2 Feb	1300	216.9	226.5	9.6	216.90	226.62	9.72	9.72	101	8	

Table T1 (continued).

Core	Date (2014)	Time UTC (h)	Depth DSF (m)		Interval advanced (m)	Depth CSF (m)		Length of core recovered (m)	Length of core curated (m)	Recovery (%)	Sections (no.)	Comments
			Top of interval	Bottom of interval		Top of cored interval	Bottom of cored interval					
24R	9 Feb	1705	768.2	777.9	9.7	768.20	773.38	4.73	5.18	49	4	Microspheres
25R	9 Feb	1905	777.9	787.6	9.7	777.90	779.40	1.27	1.50	13	1	Microspheres
26R	9 Feb	2005	787.6	797.3	9.7	787.60	791.74	3.55	4.14	37	3	Microspheres
27R	9 Feb	2320	797.3	807.0	9.7	797.30	807.34	9.77	10.04	101	9	Microspheres
28R	10 Feb	0125	807.0	816.7	9.7	807.00	815.68	8.49	8.68	88	8	Microspheres
29R	10 Feb	0315	816.7	826.4	9.7	816.70	825.41	8.48	8.71	87	7	Microspheres
30R	10 Feb	0535	826.4	836.1	9.7	826.40	834.97	8.18	8.57	84	8	Microspheres
31R	10 Feb	0820	836.1	845.8	9.7	836.10	845.99	9.65	9.89	99	9	Microspheres
32R	10 Feb	1125	845.8	855.5	9.7	845.80	855.85	9.79	10.05	101	9	Microspheres
33R	10 Feb	1415	855.5	865.2	9.7	855.50	864.15	8.45	8.65	87	8	Microspheres
34R	10 Feb	1645	865.2	874.9	9.7	865.20	873.81	7.93	8.61	82	7	Microspheres
35R	10 Feb	1900	874.9	884.6	9.7	874.90	882.60	7.36	7.70	76	6	Microspheres
36R	10 Feb	2115	884.6	894.3	9.7	884.60	890.15	5.28	5.55	54	5	Microspheres
37R	11 Feb	0040	894.3	904.0	9.7	894.30	895.29	0.81	0.99	8	1	Microspheres
38R	11 Feb	0400	904.0	910.0	6.0	904.00	905.60	1.22	1.60	20	2	Microspheres
39R	11 Feb	0625	910.0	913.8	3.8	910.00	911.49	1.28	1.49	34	1	Microspheres
40R	11 Feb	1120	913.8	923.5	9.7	913.80	917.91	3.31	4.11	34	4	Microspheres
41R	11 Feb	1845	923.5	933.2	9.7	923.50	933.12	9.20	9.62	95	8	Microspheres
42R	12 Feb	0235	933.2	942.9	9.7	933.20	940.46	6.62	7.26	68	6	Microspheres
43R	12 Feb	0645	942.9	952.6	9.7	942.90	946.64	3.14	3.80	32	3	Microspheres
44R	12 Feb	1040	952.6	962.3	9.7	952.60	953.23	0.58	0.63	6	1	
45R	12 Feb	1325	962.3	972.0	9.7	962.30	966.36	3.72	4.06	38	4	
46R	12 Feb	1750	972.0	981.7	9.7	972.00	976.67	3.36	3.36	35	4	
47R	13 Feb	0120	981.7	991.4	9.7	981.70	987.79	5.35	6.09	55	5	
48G	13 Feb	0730	900.0	900.0	0.0	900.00	900.72	0.65	0.72	NA	1	
49R	13 Feb	1605	991.4	1001.1	9.7	991.40	996.44	4.33	5.04	45	4	
50R	14 Feb	0110	1001.1	1008.8	7.7	1001.10	1007.89	6.31	6.79	82	6	
				Total:	1008.8			243.00		54	220	

With torque becoming higher and erratic, we decided to make a wiper trip to allow any debris collecting around the drill collars to fall into the hole. After pumping a sweep from the bottom of the hole, the drill string was pulled back to 862.95 mbsf. The bit was then run back to bottom, tagging fill material at 972.65 mbsf. With 18.75 m of fill in the bottom of the hole, a core barrel was dropped and the bit worked back to bottom without difficulty using circulation and rotation. The core barrel was retrieved with 0.65 m of material that was curated as ghost Core 48G. Another 50 bbl high-viscosity mud sweep was pumped after reaching 991.4 mbsf, and then another core barrel was dropped. Coring continued from 991.4 mbsf to the final depth of 1008.8 mbsf (Cores 49R and 50R). Just prior to finishing coring, a 50 bbl high-viscosity mud sweep was pumped to clean and condition the hole for logging. The total depth of Hole U1431E was reached at 0740 h on 14 February. After reaching total depth, the final core was pulled to the surface and laid out. A total of 47 RCB cores were collected in Hole U1431E over a 443.5 m interval, with a total recovery of 242.35 m of core (54.8% recovery, excluding the single 0.65 m ghost core).

At the completion of coring, the rotary shifting tool (RST) was deployed to activate the mechanical bit release and the bit was dropped in the bottom of the hole. The RST was retrieved, and the other RST run in the hole to shift the sleeve back into the closed position. The end of the drill pipe was then raised to a depth of 4900.08 mbrf (648.78 mbsf) with the top drive in place. The hole was displaced from 648 mbsf to the seafloor with 11.4 lb/gal high-viscosity mud designed to improve logging conditions. The top drive was set back, and the end of the pipe was raised to 4400.9 mbrf (149.62 mbsf) for logging operations. After holding a logging safety meeting for rig floor personnel, the triple combo tool string was

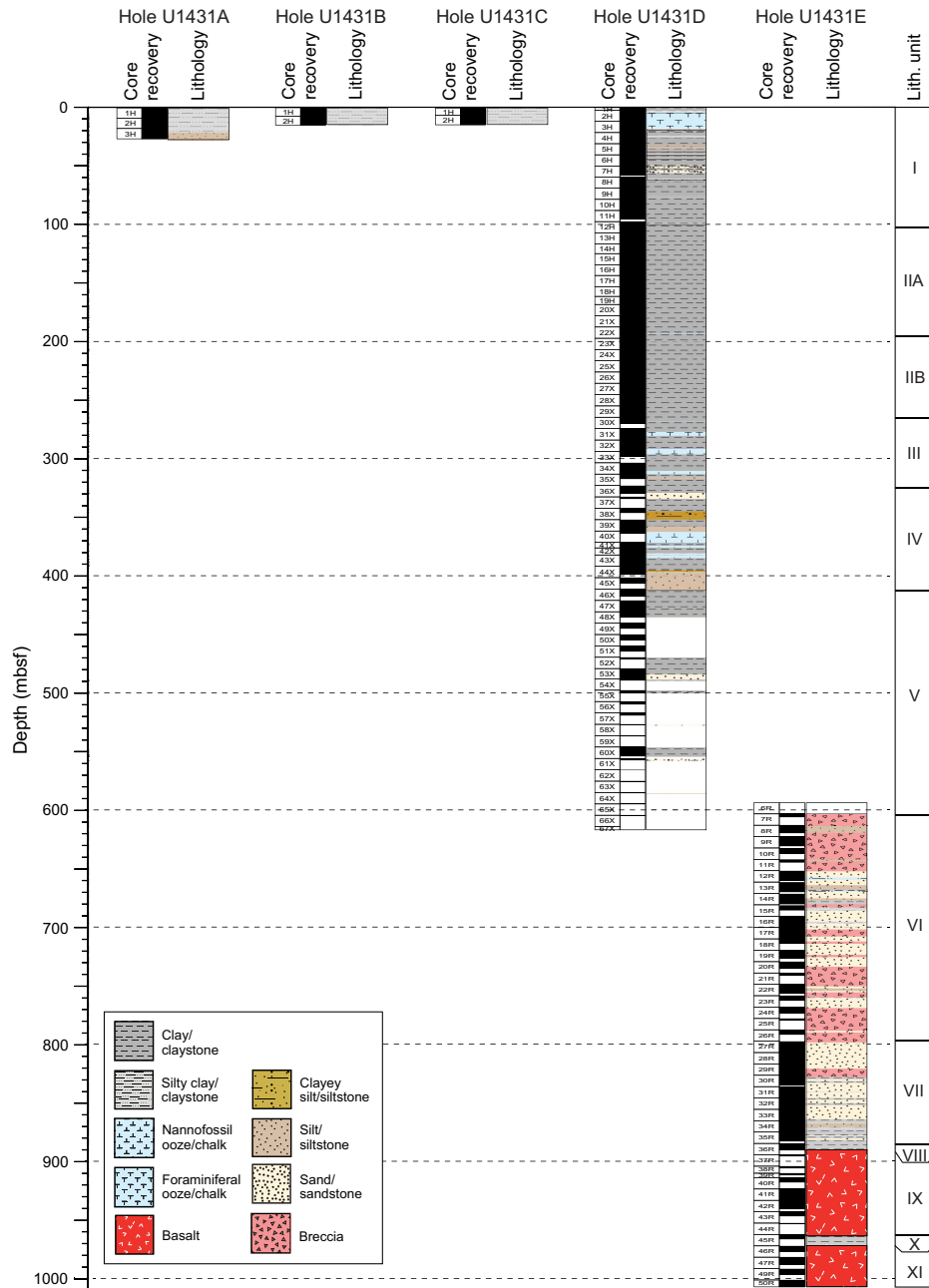
rigged up and run in the hole, reaching 463.7 m WSF on 15 February. The hole was then logged up, a short repeat pass was recorded, and the tool string was then pulled to the surface and rigged down. After rigging down the triple combo tool string, the FMS-sonic tool string was rigged up and deployed to 444 m WSF. Two full passes were made with the tool string, and then the tool string was pulled to the surface and rigged down at 1915 h on 15 February. The drill string was then tripped out of the hole from 4900.9 mbrf (149.6 mbsf) and cleared the seafloor at 2010 h. While pulling out of the hole with the drill string, the starboard conveyor on the pipe racker had a hydraulic failure. The hydraulic block in the derrickman's control booth was repaired, but 1.5 h was recorded as operational downtime. The rest of the trip out of the hole was uneventful, and the bit cleared the rig floor at 0555 h. The rig floor was secured for transit at 0600 h on 16 February, ending operations at Site U1431. Total time spent in Hole U1431E was 231.75 h (9.7 days).

Lithostratigraphy

Lithostratigraphic units

We defined 11 lithostratigraphic units (9 sedimentary and 2 igneous units) at Site U1431 based on visual core description, smear slide and thin section inspection, and scanning for an array of physical properties, including magnetic susceptibility and color spectra (see [Lithostratigraphy](#) and [Physical properties](#) in the Methods chapter [Li et al., 2015]). Although 5 holes were cored at this site, the lithostratigraphic units were determined mainly by a combination of Holes U1431D and U1431E because Holes U1431A–U1431C penetrated <30 mbsf (Figure F4). The lowermost sedimentary unit is interbedded with the basalt at the bottom of the cored strati-

Figure F4. Lithostratigraphy summary, Site U1431.

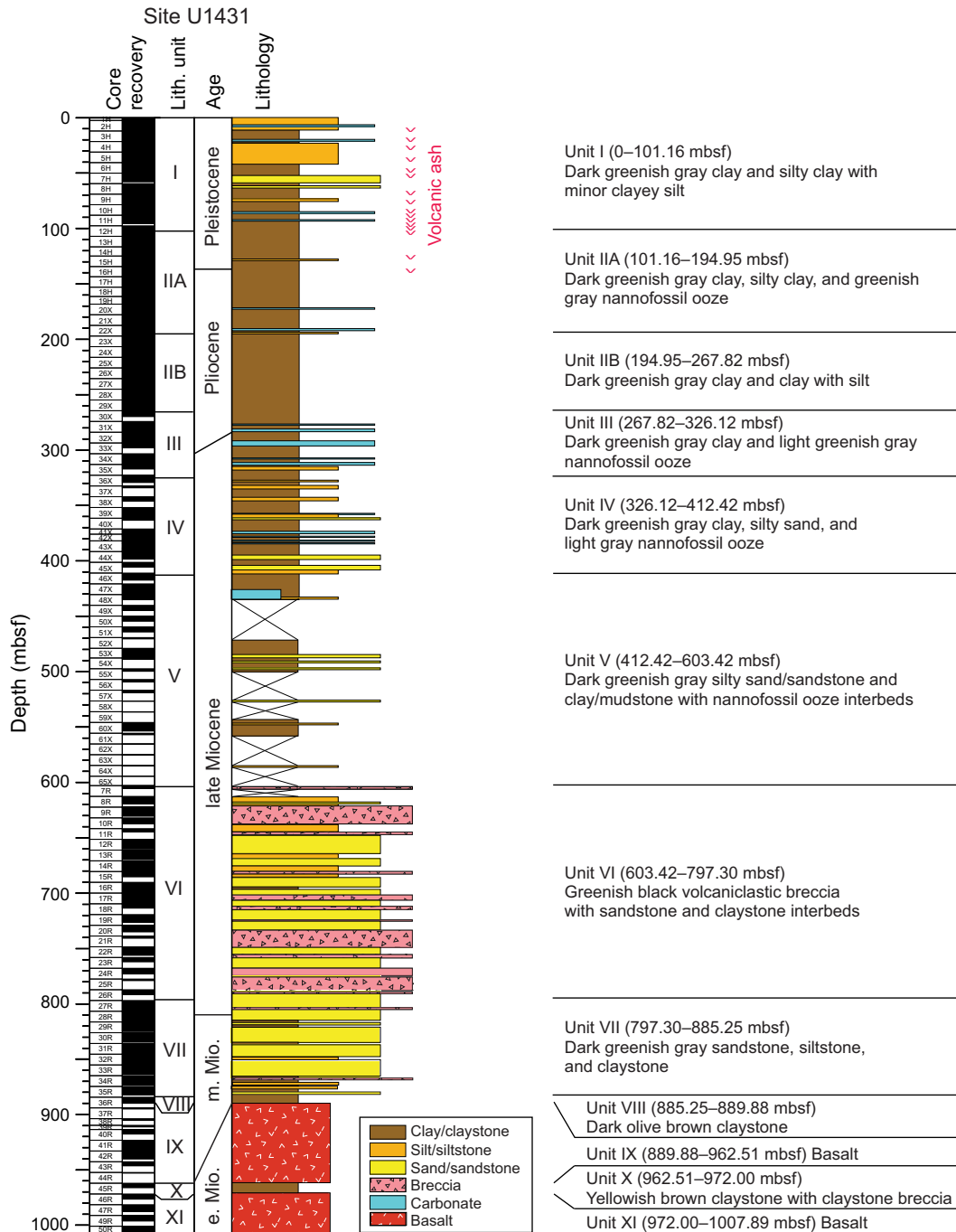


graphy. The dominant lithologies in the upper part of the stratigraphy (Units I–V) are clay, clayey silt, and silty sand with variable contents of nannofossil ooze and volcanic ash (Figures F4, F5). The lower part of the sedimentary stratigraphy (Units VI–VIII and X) consists mainly of volcaniclastic breccia and interbedded sandstone and claystone. The igneous lithologic units (IX and XI) mainly comprise massive basalt lava flows that are described in **Igneous petrology and alteration**.

Unit I is composed of dark greenish gray clay and silty clay with minor clayey silt. Unit II contains dark greenish gray clay (Subunit IIA) and silty clay with greenish gray nannofossil ooze intervals (Subunit IIB). Unit III contains dark greenish gray clay with volumetrically significant interbeds of light greenish gray nannofossil ooze. Unit IV is dominated by dark greenish gray clay and silty sand.

Unit V is composed of dark greenish gray silty sand/sandstone interbedded with clay with nannofossil ooze intervals. Consolidation increases sharply at and below Core 349-U1431D-54X (~490 mbsf) in Unit V. Recovery was low between ~430 and 620 mbsf, but core catcher samples suggest that the section is primarily composed of loose sand. Unit VI is characterized by greenish black volcaniclastic breccia with significant numbers of sandstone and claystone interbeds. Sediment is completely lithified below Core 349-U1431E-7R (~603 mbsf) in Unit VI. Unit VII is defined by abundant dark greenish gray sandstone, siltstone, and claystone with minor intervals of volcaniclastic breccia. Unit VIII is composed of dark olive-brown claystone that overlies the basalt basement of Unit IX (see **Igneous petrology and alteration**). Unit X between the two basalt Units IX and XI consists of brown and yellowish claystone and claystone

Figure F5. Synthesis sedimentary log of Site U1431 stratigraphy showing combined recovery in Holes U1431D and U1431E.



breccia. All unit boundaries are also recognized in both magnetic susceptibility and, to a lesser extent, color spectra (Figure F6).

Unit descriptions

Unit I (0–101.16 mbsf)

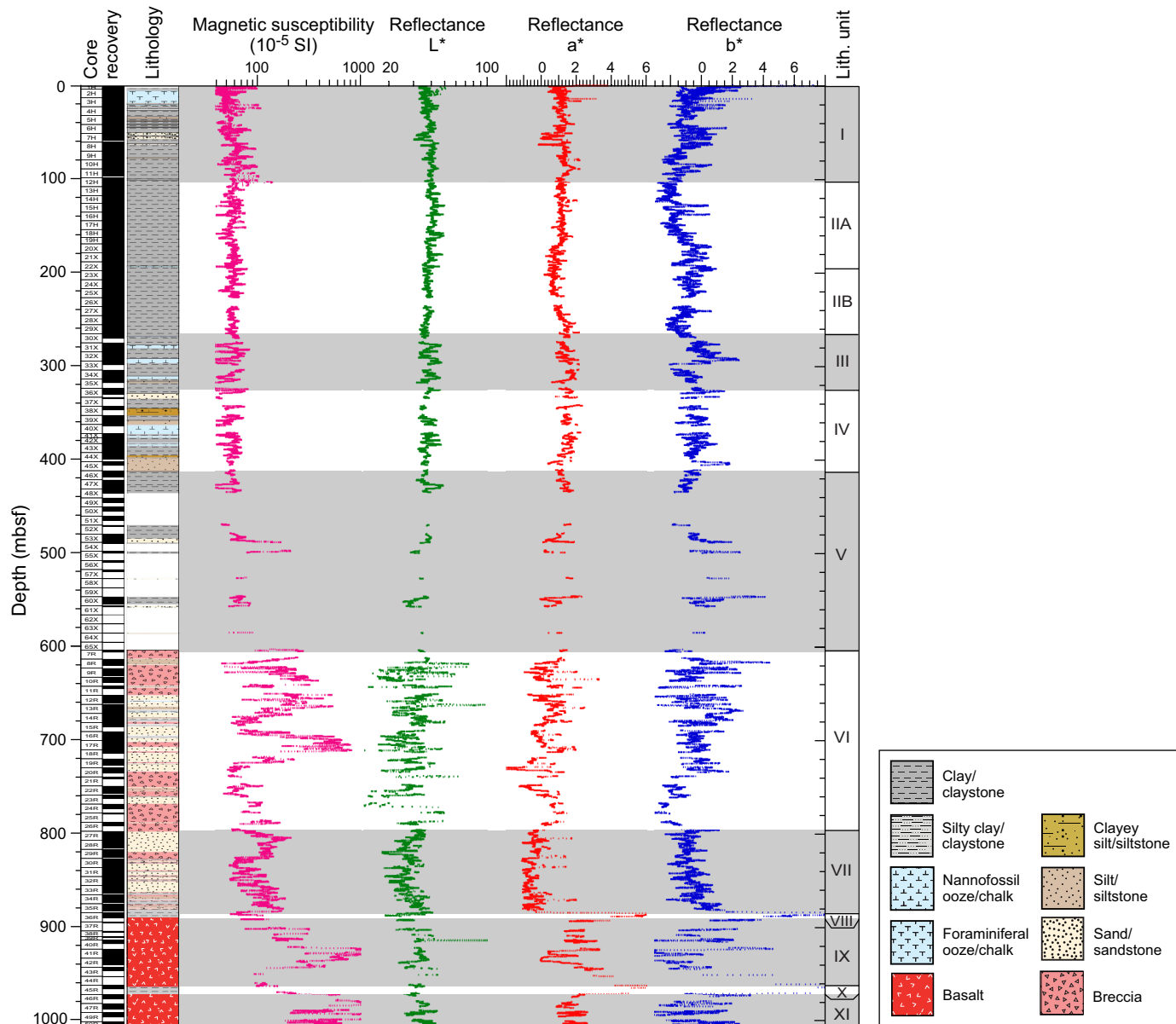
Intervals: 349-U1431A-1H through 3H; 349-U1431B-1H through 2H; 349-U1431C-1H through 2H; 349-U1431D-1H-1, 0 cm, through 349-U1431D-12H-2, 146 cm

Depths: Hole U1431A: 0–28.06 mbsf (total depth); Hole U1431B: 0–17.03 mbsf (total depth); Hole U1431C: 0–14.36 mbsf (total depth); Hole U1431D: 0–101.16 mbsf

Age: Pleistocene

Unit I spans the uppermost 101.16 m and is characterized by a sequence of clay, silty clay, and clayey silt. The more silty layers occur as dark greenish gray interbeds within a finer grained background and are typically marked by graded, fining-upward cycles that we interpret as turbidite sequences. Unit I is substantially more silty than the underlying Unit II. The redeposited silt-rich beds seen in this unit are usually 15–30 cm thick and are almost never thicker than 50 cm. At the base of each bed there is a sharp erosive contact between the overlying silty clay or clayey silt and the underlying clay layer. Microscopic inspection shows that the silt is composed of grains of quartz, feldspar, and smaller amounts of amphibole, mica, volcanic glass, and foraminifer shells (Figure F7). The clay layers are

Figure F6. Correlation of lithostratigraphic units with magnetic susceptibility and reflectance spectroscopy (after 40-point running average), Site U1431.



often massive and homogeneous but locally show the effects of bioturbation.

Greenish gray nanofossil-rich clay and clayey nanofossil ooze occur in low abundances within Unit I and also display a fining-upward character above an erosive base. We interpret these as turbidite deposits. The thickest clayey nanofossil ooze beds have a coarser layer of foraminifer ooze at the base often showing parallel lamination indicative of current sorting. Unit I is noteworthy in having a high abundance of volcanic ash layers compared to other units. Thin volcanic ash layers (0.5–5.0 cm thick) are observed throughout this unit (e.g., Figure F8) and comprise <1% of the entire sequence, with up to 3 layers per section. Most ash layers are dark

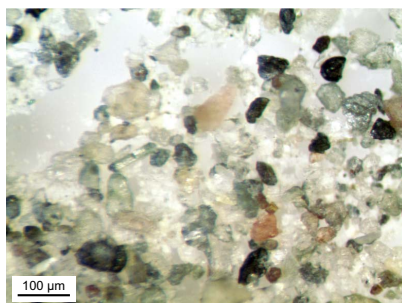
gray, blackish, or brown, suggestive of mafic to intermediate compositions.

Unit II (101.16–267.82 mbsf)

Interval: 349-U1431D-12H-2, 146 cm, through 30X-2, 122 m
 Depth: 101.16–267.82 mbsf
 Age: early Pleistocene–Pliocene

Unit II is composed of dark greenish gray clay and silty clay with greenish gray nanofossil ooze intervals and is divided into two sub-units on the basis of nanofossil content. Compared to Unit I, Unit II has very little silt, and we define the top of the unit at the base of the last major silt turbidite layer, below which silt is either admixed

Figure F7. Silty sand in Hole U1431D, Unit I, consisting mainly of quartz, feldspar, amphibole, mica, volcanic glass, and foraminifers (7H-2, 32 cm).



into the clay background or is present only as thin beds within a dominant clay section.

Subunit IIA (101.16–194.95 mbsf)

Interval: 349-U1431D-12H-2, 146 cm, through 22X-5, 85 cm

Depth: 101.16–194.95 mbsf

Age: early Pleistocene–Pliocene

Subunit IIA is dominated by clay, clay with nannofossils, and silty clay. The boundary between Subunit IIA and IIB is defined at the base of the deepest major nannofossil-rich calcareous ooze bed. The thick-bedded clay is dark greenish gray in color and is interbedded with greenish gray, medium- to thick-bedded clay with nannofossil ooze and dark greenish gray, thin- to medium-bedded clayey silt layers. The clayey silt deposits that do occur fine upward into clay and have planar, sharp bases, often erosive in character, and we interpret these layers as turbidite sequences. The overlying clay is heavily bioturbated and is often completely homogeneous. Nannofossil-rich layers usually show sharp, erosive bases and fine upward from fine sand–grade foraminifer ooze bases. These sequences are also interpreted as turbidite deposits. Deepwater trace fossil assemblages (*Nereites* ichnofacies) are seen in the color contrast between the lighter colored carbonate-rich sediment and the darker colored clay. Thin volcanic ash layers (0.5–2.0 cm thick) are occasionally observed in this unit but are limited to the top of the section and are much less common than in Unit I.

Subunit IIB (194.95–267.82 mbsf)

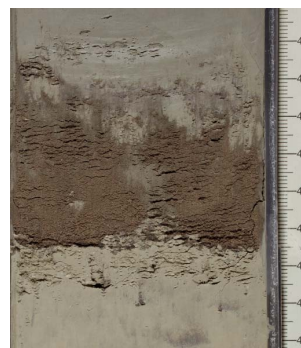
Interval: 349-U1431D-22X-5, 85 cm, through 30X-2, 122 cm

Depth: 194.95–267.82 mbsf

Age: Pliocene

Subunit IIB is composed mostly of dark greenish gray clay and clay with silt. The clay intervals dominate and are generally thick bedded (>30 cm). The clay is typically homogeneous with faint color banding. The clay layers are interbedded with moderate- to thin-bedded clay with silt layers that fine upward and are often parallel-laminated downsection to sharp, erosive contacts with underlying clay. Sequences of clay with silt and overlying clay are mostly interpreted as turbidite deposits. Interbeds of greenish gray, thin- to medium-bedded clay with nannofossils form a minor lithology within the subunit. These interbeds do not exceed 5% of the total section and are also interpreted as turbidite deposits based on sedimentary structures. The tops of the carbonate turbidites often contain the *Nereites* ichnofacies, especially *Chondrites*. Volcanic ash layers are entirely absent from this subunit.

Figure F8. Graded mafic to intermediate tephra, Hole U1431D, Unit I (10H-7A, 40–48 cm).



Unit III (267.82–326.12 mbsf)

Interval: 349-U1431D-30X-2, 122 cm, through 36X-2, 132 cm

Depth: 267.82–326.12 mbsf

Age: early Pliocene to late Miocene

Unit III comprises clay together with significant volumes of interbedded nannofossil ooze that distinguish it from Unit II. The top of the unit is defined by the first prominent nannofossil ooze with foraminifers. Clay, which still dominates the section, is dark greenish gray and is found in thick-bedded layers interbedded with light greenish gray, moderate- to thick-bedded nannofossil ooze. The clay in particular shows strong bioturbation. Thin-bedded silty clay layers occur frequently within the dominant clay but account for <5% of the section. In contrast, nannofossil ooze layers are the most frequently occurring secondary lithology, and the base of Unit III is placed at the base of a large, 90 cm thick nannofossil ooze bed in Core 349-U1431D-36X. The nannofossil ooze beds are interpreted as calcareous turbidite deposits because they usually have planar, erosive contacts with the underlying clay layers and fine upward. They also show well-developed deepwater trace fossil assemblages (Figure F9). The thick nannofossil ooze beds have thin, parallel-laminated, sand-grade foraminifer ooze sections at their base. The foraminifer ooze is dominated by unbroken or large fragments of planktonic species. Volcanic ash layers are absent.

Unit IV (326.12–412.42 mbsf)

Interval: 349-U1431D-36X-2, 132 cm, through 46X-1, 82 cm

Depth: 326.12–412.42 mbsf

Age: late Miocene

Unit IV comprises clay, nannofossil ooze, silt, and sandy silt mostly recovered in strongly biscuited cores from XCB coring. This unit is essentially different from Unit III in having a much greater proportion of coarser clastic beds, reaching sand grade in the thicker-bedded examples (Figure F5). The middle of the unit contains a significant number of nannofossil ooze layers, but the top and base of the unit are defined on the basis of the first and last appearance of sand and silty sand, respectively. The unit is nonetheless still dominated by dark greenish gray clay, which is thick-bedded and strongly bioturbated, with horizontal burrows of *Chondrites* and/or *Thalassionoides* type. No vertical burrows are observed. The clay layers are interbedded with silty sand layers that have planar, erosive contacts with the underlying clay layers. Silty sand beds are often tens of centimeters thick, usually fine upward, and are inter-

Figure F9. Deepwater trace fossil assemblage of the *Nereites* ichnofacies, Hole U1431D, Unit III (31X-4A, 12–26 cm).



Figure F10. Thin silt turbidite with prominent pyrite concretion, Hole U1431D, Unit IV (42X-3A, 32–37 cm).



Figure F11. Normally graded calcareous turbidite with foraminifer-rich sandy base grading upward into silt and nannofossil ooze, interbedded with bioturbated clays below and laminated quartzose silts above, Hole U1431D, Unit V (43X-4A, 43–59 cm).



puted as turbidite deposits. Smear slide analysis shows that the sand differs from the silt found in Units I and II by having much higher proportions of mostly mafic volcanic glass shards, although quartz grains are still commonly found in silt and sand layers. The nannofossil ooze beds in the middle of the unit are medium- (10–30 cm) and occasionally thick-bedded (>30 cm), reaching almost 2 m thick in Core 349-U1431D-41X. These beds are made up of light gray sediment above a sharp, erosive base and grade up into greenish gray clay. The lower parts of the beds are silty, or even sandy, and parallel laminated, indicative of high-energy laminar flow during sedimentation, likely from turbidity currents. Unit IV is the shallowest unit to show visible effects of diagenesis beyond consolidation. Most prominent is the occurrence of pyrite concretions, which are found in small volumes in all main lithologies of the unit (Figure F10).

Unit V (412.42–603.42 mbsf)

Intervals: 349-U1431D-46X-1, 82 cm, through 66X-CC, 31 cm; 349-U1431E-7R-1, 0–12 cm

Depths: Hole U1431D: 412.42–604.91 mbsf (total depth); Hole U1431E: 603.30–603.42 mbsf

Age: late Miocene

The description and definition of Unit V is hampered by low recovery starting from Core 349-U1431D-48X through the total depth of Hole U1431D. Unit V is defined as lying below the base of an erosive silty turbidite in Section 349-U1431D-46X-1 and above a volcanoclastic breccia whose top is at 349-U1431E-7R-1, 12 cm. Recovered intervals of the unit are characterized by dark greenish gray silty sand and clay with nannofossil ooze layers. Core catcher samples indicate that some of the unrecovered section is sand and silt. As in Unit IV, the carbonate-rich beds fine upward with erosive or sharp, planar bases that indicate sedimentation from turbidity currents (Figure F11). Two types of clastic interbeds are noted, both showing normal grading and erosive bases. One variety is composed of greenish gray silt or silty clay that is quartz rich with low proportions of volcanic ash shards. The other clastic interbeds are generally coarser, ranging from sand to gravel, and are dominated by vesicular, mafic ash shards with minor amounts of quartz. These

coarser-grained beds are generally dark green to black and less well sorted than the quartz-rich deposits. The volcanic shard-rich sands locally compose >40% of the section and are considered to be more proximal turbidite deposits than the quartz-bearing deposits. The tops of volcanoclastic turbidite beds show strong bioturbation, with prominent *Nereites* ichnofacies burrows that show a strong color contrast with the background sediment. Sediment becomes more lithified at and below Core 349-U1431D-54X (below ~490 mbsf) and is classified as silty sandstone and interbedded mudstone.

Unit VI (603.42–797.30 mbsf)

Interval: 349-U1431E-7R-1, 12 cm, through 27R-1, 0 cm

Depth: 603.42–797.30 mbsf

Age: late Miocene

Unit VI comprises greenish black or black volcanoclastic breccia with significant but subsidiary interbeds of sandstone and claystone. This unit is essentially different from all other units in having dominant thick-bedded volcanoclastic breccia (Figure F12). The breccia is typically massive, ungraded, and poorly sorted with angular to subangular basaltic clasts, as well as minor reworked subrounded calcareous mudstone, mudstone, and sandstone clasts. Thin- to medium-bedded breccia layers are occasionally found underlying sand-

Figure F12. Volcaniclastic breccia, Hole U1431E, Unit VI (7R-2A, 86–97 cm).

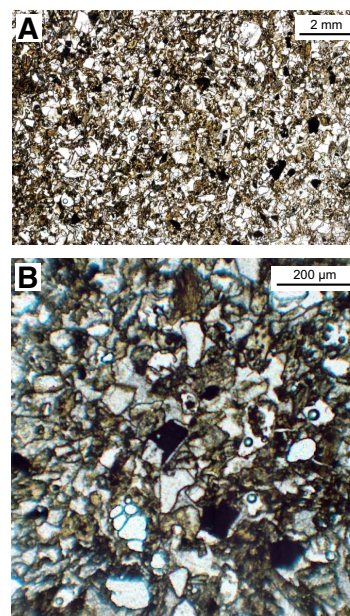


stone and silty claystone sequences in the middle part of the unit. Sandstone is classified into at least two types, some more greenish gray in color, whereas others are very dark, almost black on the split core face. This color difference reflects changes in the relative abundance of dark sand grains, mostly pieces of basalt and basaltic glass. Figure F13A shows the moderate sorting of a typical fine sandstone. Close inspection (Figure F13B) shows the presence of opaque minerals within a dominant volcanic lithic, glass, and quartz framework with a clay matrix. Figure F14 shows a parallel-laminated siltstone with larger sand-sized quartz grains at the base of a turbidite bed. The cross-polarized light (XPL) image (Figure F14B) emphasizes the relatively low proportion of quartz in these deposits and thus their generally volcanoclastic provenance.

Four types of basaltic clasts are observed in the breccia units, including nonvesicular aphyric basalt, sparsely vesicular aphyric basalt, highly vesicular aphyric basalt, and nonvesicular glassy basalt (Figure F15). Medium- to thick-bedded dark gray volcanoclastic sandstone and claystone cycles occur as interbeds between the breccia layers. These intervals have current ripples and parallel laminations indicative of high-energy flow conditions during sedimentation (Figure F16). Bases with load structures also indicate that coarse clastic sedimentation was likely rapid and induced dewatering of the underlying claystone. The middle of the unit contains common interbedded dark greenish gray sandstone, siltstone, and silty claystone intervals. Reworked beds usually fine upward from sandstone to silty claystone over tens of centimeters and have sharp and erosive bases. These deposits are interpreted as turbidites. Sandstone and siltstone are commonly laminated or cross-laminated. In places, but only over short lengths of the core (<1 m), the lamination is not horizontal but shows steep dips (>40°) (Figure F17). We interpret this as syndepositional folding, most likely slump folding linked to mass wasting rather than tectonically induced tilting of the whole sequence. Silty claystone and claystone intervals are usually heavily bioturbated with typical *Chondrites*-dominated trace fossil assemblages.

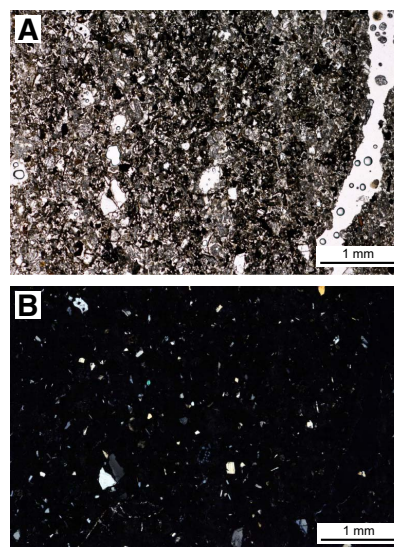
Carbonate beds are very rare in Unit VI, but carbonate is sometimes present as large pebble- and cobble-sized clasts in the breccia. In Section 349-U1431E-9R-5, there is a rare ~20 cm thick pelagic

Figure F13. Black volcanic sandstone within the breccia sequence, Hole U1431E, Unit VI (16R-2, 67–70 cm). A. Moderately well sorted texture showing scattered dark grains that give the sandstone its color. B. Magnified image showing opaque grains, some of which are basaltic glass fragments, within the overall framework of volcanic glass and lithic and quartz grains with a clay matrix.



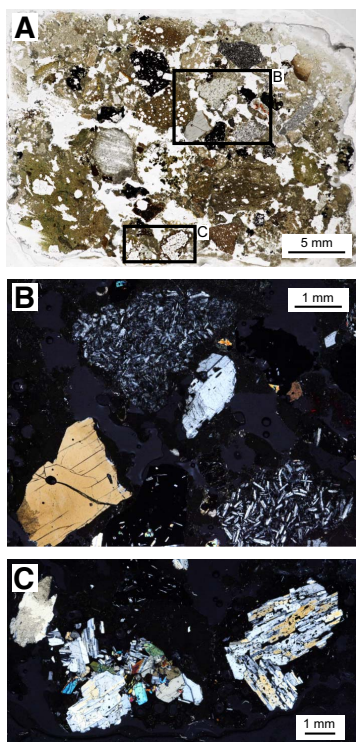
c

Figure F14. Base of a graded sandstone, Hole U1431E, Unit VI (14R-6, 45–48 cm). Sand is only moderately sorted and is rich in volcanic rock fragments and glass. Minor amounts of quartz are apparent in the cross-polarized image. A. Plane-polarized light (PPL). B. Cross-polarized light (XPL).



carbonate deposit. In thin section, this limestone is found to be micritic in texture, with minor amounts of opaque minerals and rare intact and broken planktonic foraminifers suspended in the background matrix (Figure F18). This bed is unusual in that it is clearly not redeposited and may reflect a period of quiet pelagic sedimentation.

Figure F15. Volcanic breccia, Hole U1431E, Unit VI (7R-2, 75–78 cm). A. Low-magnification view highlighting poor sorting and diverse clast assemblage (PPL). B. Close-up showing plagioclase-phyric volcanic rock clasts and a large feldspar grain (XPL). C. Clasts of volcanic rock with clusters of plagioclase and pyroxene (left) and plagioclase alone (right) (XPL).



Unit VII (797.30–885.25 mbsf)

Interval: 349-U1431E-27R-1, 0 cm, through 36R-1, 65 cm

Depth: 797.30–885.25 mbsf

Age: middle Miocene

The top of Unit VII is defined at the base of a thick-bedded volcanoclastic breccia that forms the lowest bed in overlying Unit VI. The unit is composed of dark greenish gray sandstone, siltstone, and claystone with minor intervals of volcanoclastic breccia. This unit is characterized by a sharp reduction in the volume of breccia compared to Unit VI. Sandstone is usually found interbedded with bioturbated and laminated siltstone and claystone. Together, these compose fining-upward, graded cycles that range from 10 cm to >1 m thick, all marked by erosive bases. These cycles are interpreted as turbidite sequences. The base of each graded unit is often composed of coarse sandstone with load casts and parallel lamination through the bottom half of the sandy interval. In the lower part of the unit, the interbedded siltstone and claystone cycles are mostly at centimeter scale with well-developed parallel and cross-lamination, especially in siltstone. Bioturbation is heavy in claystone and occasionally shows escape trace fossil structures penetrating from the underlying clay-rich siltstone into the overlying sandstone.

Unit VIII (885.25–889.88 mbsf)

Interval: 349-U1431E-36R-1, 65 cm, through 36R-5, 17 cm

Depth: 885.25–889.88 mbsf

Age: middle Miocene

Figure F16. Sand deposited in high-energy flow conditions, Hole U1431E, Unit VI (22R-4A, 59–71 cm). Note the cross-lamination and small-scale load structures on the base of the upper laminated turbidite sandstone. Lowermost claystone shows burrowing.

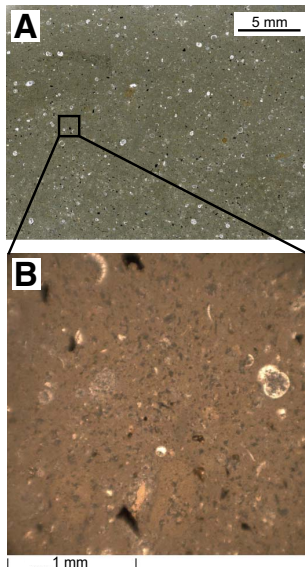


Figure F17. Greenish gray siltstone in Hole U1431E, Unit VI, showing lamination and steep dips as a result of soft-sediment deformation during slumping (14R-3A, 76–87 cm).



Unit VIII is characterized by thick-bedded, dark olive-brown to yellowish brown claystone that occurs only in Core 349-U1431E-36R. This claystone marks the base of the sedimentary sequence overlying the basement basalt. The 4.63 m thick claystone is massive and homogeneous in the lower part and laminated with silty claystone in the upper part. The core interval is variable in color and is light gray over limited sections. Figure F19 shows an example of the more homogeneous brown claystone with mottling, common small-scale burrows, and development of pyrite concretions. This sediment represents a very different sedimentary environment compared to the overlying lithostratigraphic units. We interpret it as a deep-sea pelagic deposit.

Figure F18. Carbonate interbed within volcanic breccia, Hole U1431E, Unit VI (9R-5, 30–32 cm). A. Fine-grained micritic matrix with planktonic foraminifers, together with occasional opaque minerals. B. Close-up showing fine-grained texture and both broken and whole planktonic foraminifer shells.



Unit X (962.51–972.00 mbsf)

Interval: 349-U1431E-45R-1, 21 cm, through 46R-1, 0 cm

Depth: 962.51–972.00 mbsf

Age: early Miocene

Unit X is a claystone deposit interbedded within the basalt lava sequence. The recovered claystone (3.83 m thick) in Core 349-U1431E-45R differs from that in Unit VIII above the basement in being less homogeneous and characterized mostly by claystone with intraformational breccia or conglomerate. The breccia/conglomerate has rare basalt clasts with well-developed reaction rims. In the more massive claystone intervals, microscopic inspection reveals significant dispersed volcanic fragments. The upper part of Core 45R is more clastic, mostly with fragments of reworked claystone but with a few intervals containing granule and pebble grade basalt clasts (Figure F20). Black-brown altered pyrite grains occur sparsely in some intervals with bands ranging from 1–8 cm wide that we interpret to reflect diagenesis.

Discussion

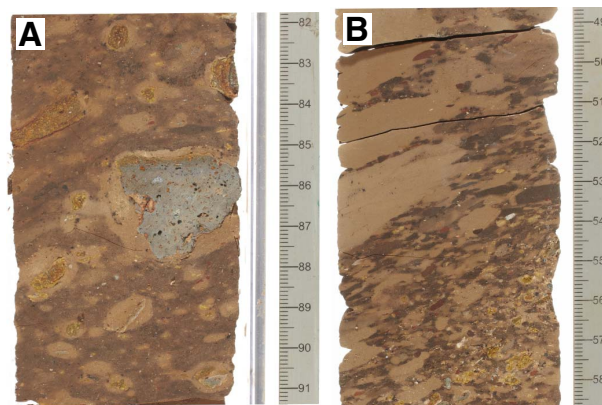
Gravity flow deposits

Gravity flow deposits are common throughout most units cored at Site U1431. They are divided into four types based on thickness, sedimentary structures, and clastic composition and are summarized here based on shipboard observations. In Unit I, gravity flow deposits occur as thin, fining-upward, silty clay and clayey silt turbidite beds. These turbidite sequences occur frequently, commonly 3–10 cycles per ~1.5 m. Silt-rich intervals at the base are usually 15–30 cm thick and generally thinner than 50 cm with irregular erosive contacts with the underlying clay layers. Considering their relatively young age (Pleistocene) and potential proximity to the Luzon arc, we speculate that their deposition might have been triggered by volcanism and/or earthquake events associated with the subduction tectonics.

Figure F19. Claystone (Unit VIII) immediately overlying the uppermost lava flows of Unit IX, Hole U1431E (36R-3A, 27–36 cm). These fine-grained sedimentary rocks contain common volcanic ash shards and are interbedded with reworked claystone breccia with variable but subsidiary amounts of basaltic lava clasts.



Figure F20. Unit X sediment, Hole U1431E. A. Clasts of angular basalt surrounded by reaction halos in claystone breccia (45R-2A, 82–91 cm). B. Breccia entirely dominated by intraformational clasts (45R-1A, 49–59 cm).



In Units II and III, gravity flow deposits are dominated by thick clayey silt beds and beds of nanofossil ooze with foraminifers, which are also interpreted as turbidites. They usually display horizontal, erosive basal contacts with the underlying clay layers. Foraminifer ooze intervals at the bottom of some turbidite sequences are generally dominated by unbroken or large fragments of planktonic species that fine upward and are sand sized. Based on the calcareous components and deepwater depositional environment, thought to be deeper than the calcite compensation depth at this site, we suggest that the turbidite sediments could be transported from local sources (e.g., nearby seamounts topped by carbonate-rich environments).

Gravity flow deposits in Units IV and V consist mainly of silty to coarse-grained sand layers that are interpreted as turbidites. They occur as medium- to very thick bedded deposits, usually fining upward, with horizontal, erosive contacts with the underlying clay layer. Upper Miocene Unit V contains many thick, unconsolidated sand layers. The basal section of these turbidite layers is coarser grained than those in the upper two units, suggesting a different and more proximal provenance.

Units VI and VII contain various types of gravity flow deposits, including turbidites, slump deposits, and debris flow deposits as volcanoclastic breccia, indicating high-energy sedimentary environments. Black volcanoclastic breccia (see [Breccia](#)) and dark greenish gray sandstone are common in Unit VI. Sequences with sharp, irregular erosive bases and parallel lamination that fines upward from sandstone to silty claystone are interpreted as turbidites. In contrast, debris flow deposits in the form of volcanoclastic breccia and sandstone with gravels are poorly sorted and/or not graded. Slumps are seen locally, especially in the form of soft-sediment deformation structures (Figure [F17](#)). We hypothesize that this type of gravity flow deposit may be linked to earthquake and/or volcanic activity associated with mid-ocean-ridge tectonics soon after the cessation of seafloor spreading.

Breccia

Thick, massive, poorly sorted breccia beds dominate Unit VI and occur occasionally in Unit VII. The breccia beds range in thickness from a few centimeters to >4.8 m (Cores 349-U1431E-23R and 24R). The bases of breccia beds are sharp and erosive (Figure [F21](#)), and the beds coarsen upward over a thin interval as thick as 5 cm. In some of the thicker beds, the breccia then fines upward over several meters. In Core 17R, a 4 m thick breccia bed has coarser and finer intervals, suggesting deposition of the bed in several continuous but overlapping pulses. The breccia is overlain by 1.5 m of pebbly sandstone of the same composition and clast type. Section 349-U1431E-18R-2 includes the top of a breccia layer that fines upward through coarse and medium sand to laminated fine sand to silt. This bed is then overlain by silty clay (Figure [F22](#)). There may be a sharp contact between the massive breccia and the overlying laminated breccia, but it is hard to identify. Breccia occurs from the top of Section 11R-1 to the top of Section 8R-5; this interval also contains mudstone intervals that may be either large clasts or interbeds with irregular contacts. If this is one 14.45 m thick continuous breccia bed, grain size variation within the interval suggests deposition in several pulses, similar to Core 17R.

Clasts in the breccia are angular to subrounded and are dominantly basaltic volcanic rock (Figure [F12](#)) with sparse single crystals of plagioclase and clinopyroxene, clasts of mudstone (sometimes calcareous), and mafic vitroclasts. Mudstone clasts are clay rich and contain foraminifer fossils. Some mudstone clasts are more rounded than others in the breccia and have thin altered rims, whereas some are laminated. Mudstone clasts are numerous in the breccia in Core 349-U1431E-9R, where one laminated mudstone clast appears to be ~60 cm in diameter. The large clasts extend over several pieces and are interpreted as clasts based on their upper and lower contacts with the breccia. The percentage of mudstone clasts decreases with depth in the hole.

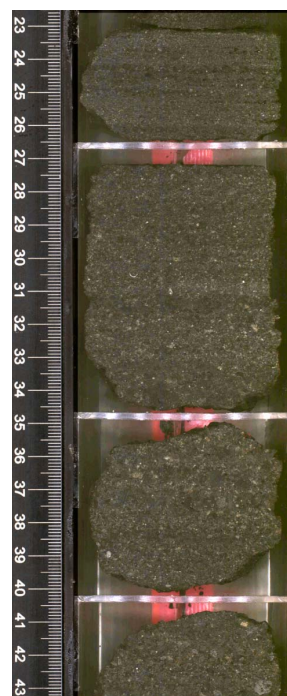
The basalt clasts vary in the percentage of vesicles (from nonvesicular to highly scoriaceous) and in both texture and phenocryst content. Some clasts have a pilotaxitic texture and few phenocrysts, whereas in contrast, others are plagioclase-phyric (Figure [F15](#)) or contain both plagioclase and clinopyroxene. There are rare altered olivine phenocrysts in some clasts. Some basalt clasts have alteration rims suggesting alteration of a glassy groundmass. The matrix percentage varies between breccia beds, from very little up to 40%. The matrix is a mix of clay, finer grained altered basalt clasts, and mafic vitroclasts. There are occasional foraminifer fossils in the matrix (Figure [F23](#)). Some layers have calcite cement between clasts.

The breccia beds were most likely deposited as a series of debris flows. This is supported by their massive structure, poor sorting, and reverse-graded bases (e.g., Middleton and Hampton, 1973;

Figure F21. Sharp, reverse-graded base of a breccia layer, Hole U1431E, Unit VII (27R-6A, 115.5–124 cm). The breccia layer overlies dark greenish gray clay with moderate to heavy bioturbation.

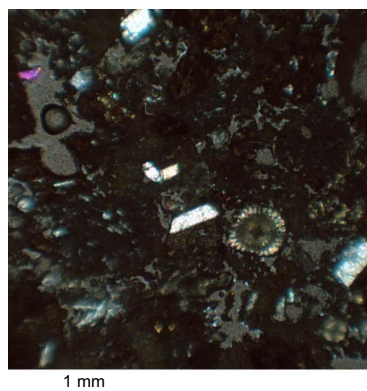


Figure F22. Top of a breccia layer and cryptic contact with overlying laminated sandstone, Hole U1431E (18R-2A, 23–43 cm). Both units have similar composition.



Lowe, 1982). Alternately, because they show similar features, they may have been deposited as grain flows that provide a mechanism for moving the gravel-sized clasts in breccia beds with little matrix. Grain flows are known to show reverse grading from base to top because larger clasts move toward the top as a result of high dispersive pressure (Saint-Ange et al., 2013); however, this is not apparent in the breccia beds at Site U1431. Variations in grain size in single breccia layers suggest pulsing in the flow. The finer grained and occasionally laminated upper parts of some layers suggest that the main debris flow was followed quickly by more dilute turbidity flows from the same source. The flow may have also transformed into a lower density turbidity current because of dilution and an increase in turbulence. At Site U1431, the subrounded shape of clasts and the mix of lithologies in the breccia, as well as the presence of foraminifer tests in the matrix, suggest that the clasts were reworked briefly in a shallow-water environment prior to being entrained in the debris flows, although clasts are not round enough for

Figure F23. Foraminifer test in the breccia matrix, Hole U1431E, Unit VI (18R-3A, 34–36 cm). The white crystals are plagioclase, and the gray areas are epoxy. The glassy basalt clasts are dark under XPL.



the deposits to have spent a significant length of time in a shallow-water, wave-influenced environment (e.g., Németh et al., 2009). The breccia units contain some large clasts. Although these clasts can be carried long distances through buoyancy by the matrix strength of a debris flow, studies of observed debris flows (e.g., Takahashi, 1991) show that such flows tend to deposit the largest blocks within the proximal fan or apron environment and that only the largest volume flows continue to deposit coarse debris outward to the distal environment. This supports a fairly local source for the clasts in the breccia, possibly from the nearby seamount volcanoes. Chemical analysis of the basalt clasts are described in [Geochemistry](#) and do indicate a “within-plate” seamount affiliation.

Ash layers

The combination of grading, sharp bases, and bioturbated tops (Figure F8) is typical of air fall ash deposited in deep-marine settings. The source of the darker colored, more mafic ash is likely to be proximal, whereas lighter colored, more felsic ashes that tend to be more explosive and spread farther from the source may be from either proximal or distal sources. The ash layers occur only in Unit I and at the top of Unit II (Figure F5), suggesting that either volcanism began abruptly at ~2.6 Ma or that the volcanic source moved closer to its current position at about that time. Prior to this, the source may have been too far for ash to travel to Site U1431. Alternately, the wind may have changed direction at ~2.6 Ma, shortly after the onset of Northern Hemisphere glaciation, when climatic conditions changed sharply on a global scale (Maslin et al., 1998).

Biostratigraphy

We analyzed core catcher samples and selected samples from within cores for calcareous nannofossils, planktonic foraminifers, and radiolarians in all holes at Site U1431. Biostratigraphic datums based on calcareous nannofossils, planktonic foraminifers, and radiolarians show that the sedimentary succession recovered at Site U1431 spans the lower Miocene to the Pleistocene (Figure F24; Tables T2, T3, T4). Age determination for the Miocene section is difficult because of very rare occurrences of calcareous nannofossils and planktonic foraminifers in the depositional sequences, which are dominated by turbidites (lithostratigraphic Units IV–VII; see [Lithostratigraphy](#)).

The biostratigraphic record is discontinuous in Hole U1431E due to the absence of calcareous nannofossils in most of the samples

from volcanoclastic breccia and sandstone of Units VI–VII and claystone of Units VIII and X and of planktonic foraminifers in Units VIII and X, as well as in parts of Units VI and VII. Very rare reworked Paleocene nannofossils occur in Unit X. Although absent in the upper part of the sequence, radiolarians become common in Units VIII and X. Two radiolarian events in the interflow claystone of Unit X (at 963.27 and 966.28 mbsf) are indicative of an early Miocene age (16.73–17.59 Ma) (Table T4).

Preservation of calcareous nannofossils and planktonic foraminifers is good to moderate, providing a robust biostratigraphic framework for the Pleistocene to Pliocene (Tables T2, T3). Some fragmentation of planktonic foraminifers is evident in most samples. The uppermost core catchers (Samples 349-U1431D-1H-CC through 3H-CC) also contain well-preserved, highly diverse assemblages of radiolarians typical of low latitudes and very low abundances of other siliceous microfossils, such as diatoms and sponge spicules. Radiolarians are not observed below Sample 349-U1431D-5H-CC (41.33 mbsf) except in the deep-sea claystone of Units VIII and X.

Calibrated biohorizons allow us to estimate extremely low sedimentation rates (<2 cm/ky) during the early Miocene to middle Miocene (lithostratigraphic Units VIII and X). The sedimentation rate increased to ~8 cm/ky toward the late middle Miocene (Unit VII). During the late Miocene, sedimentation rates increased to ~14 cm/ky, the highest observed for Site U1431, before decreasing to ~5 cm/ky during the Pliocene–Pleistocene (Figure F24). Resolution of the age discrepancy between bioevents and paleomagnetic datums (see [Paleomagnetism](#)) given for Unit VI (question marks in Figure F24) awaits further postexpedition studies.

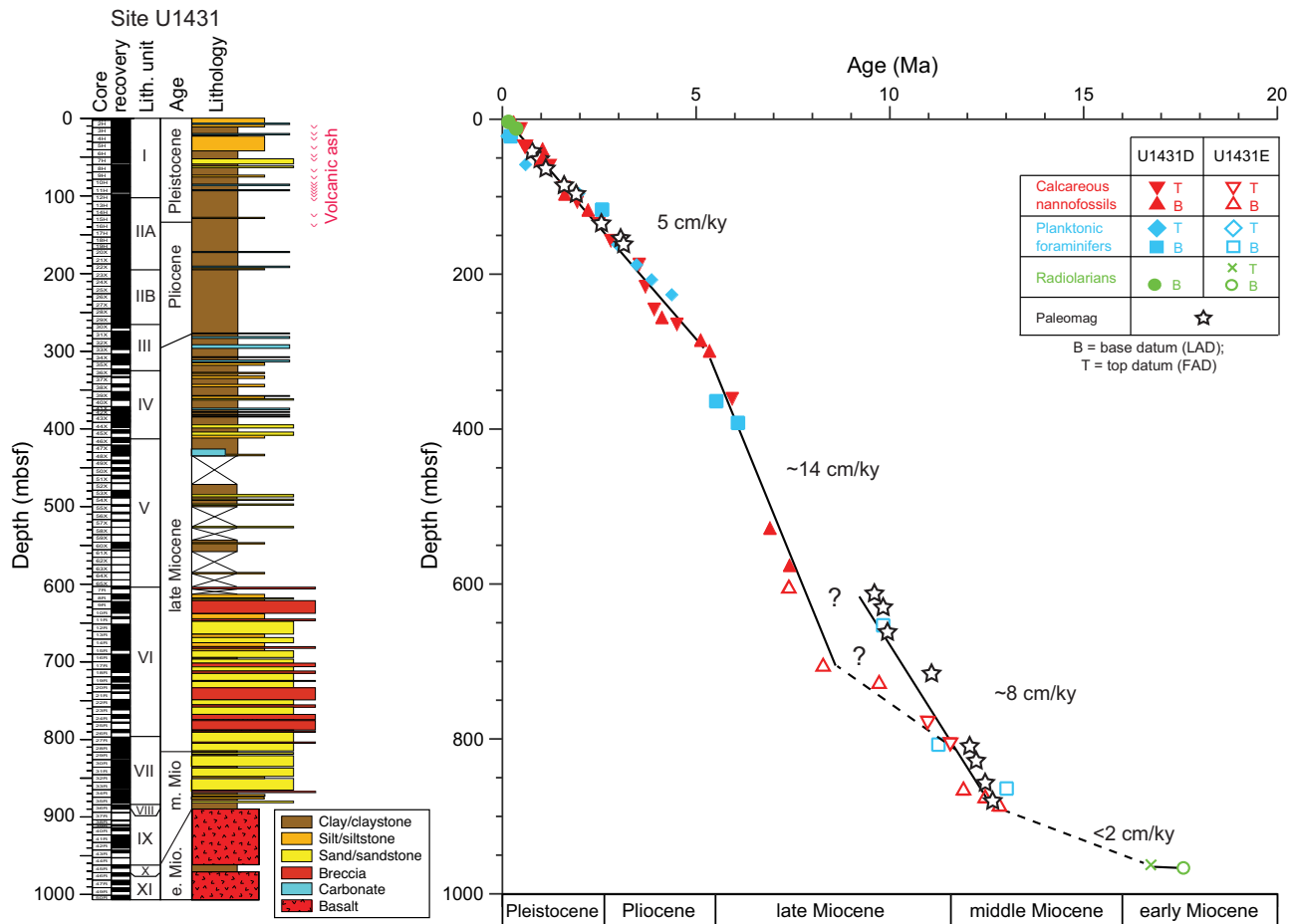
Calcareous nannofossils

Core catchers from all holes (U1431A–U1431E) were examined (Tables T5, T6, T7). Calcareous nannofossil biostratigraphy for Site U1431 is based mainly on analysis of all core catcher samples from Holes U1431D and U1431E. To better constrain biostratigraphic events, a number of samples from within cores were also analyzed.

Recovered sediment in Hole U1431D is dominated by varied cycles of turbidites. The recovered sections in Hole U1431E are composed of lithified volcanoclastic breccia interbedded with sandstone, siltstone, and claystone (see [Lithostratigraphy](#)). Calcareous nannofossil abundances are low in most of the upper part of the succession (Cores 349-U1431D-1H through 9H), generally becoming more abundant below Sample 349-U1431D-10H-CC (89.01 mbsf), but with intermittent low abundances to the bottom of Hole U1431D. In Hole U1431E, nannofossils are rare and poorly preserved in lithified claystone but are generally absent in volcanoclastic breccia or sandstone layers. Most samples exhibit some degree of reworking; this is more pronounced in the interval between 90 and 110 mbsf in Hole U1431D. Varying degrees of overgrowth on nannofossils as well as abundant broken fragments, especially among discoasters, are common in the sediment sequences of Hole U1431E (Figure F25). In general, the nannofossil assemblages preserved in sediment at Site U1431 are variably affected by turbidites and carbonate dissolution.

Twenty-nine nannofossil biostratigraphic datums are recognized in the middle Miocene to Pleistocene sediment sequence at Site U1431 (Table T2; Figure F24). The oldest nannofossil event identified is the first appearance datum (FAD) of *Reticulofenestra pseudoumbilicus*, which occurs at 884.60 mbsf, indicating an age <12.83 Ma for much of the sedimentary sequence at Site U1431.

Figure F24. Age-depth model, Site U1431. FAD = first appearance datum, LAD = last appearance datum.



Pleistocene

The top of Hole U1431D (Sample 349-U1431D-1H-CC; 3.15 mbsf) is dated as Late Pleistocene, based on the presence of *Emiliania huxleyi* (marker species for Zone NN21). Recognition of the last appearance datum (LAD) of *Pseudoemiliania lacunosa* in Sample 2H-CC (12.15 mbsf) defines the top of Zone NN19. Zone NN19 is further divided by six nannofossil events (Table T2):

1. The LAD of *Gephyrocapsa* sp. 3 in Sample 4H-CC (32.08 mbsf)
2. The FAD of *Gephyrocapsa* sp. 3 in Sample 5H-6, 47 cm (39.67 mbsf);
3. The FAD of medium *Gephyrocapsa* spp. ($>4 \mu\text{m}$) in Sample 6H-CC (50.9 mbsf);
4. The LAD of large *Gephyrocapsa* spp. ($>5.5 \mu\text{m}$) in Sample 8H-1, 50 cm (60.7 mbsf);
5. The LAD of *Calcidiscus macintyreii* in Sample 10H-CC (89.01 mbsf); and
6. The FAD of large *Gephyrocapsa* spp. ($>5.5 \mu\text{m}$) in Sample 11H-CC (96.10 mbsf).

The top of Zone NN18 is marked by the LAD of *Discoaster brouweri* in Sample 12H-CC (107.57 mbsf). The LAD of *Discoaster pentaradiatus* defines the top of Zone NN17; however, this event could not be identified because of reworking. This species occurs abundantly as reworked fossils in samples from Cores 349-U1431D-

10H through 13H (89.01–116.85 mbsf) in the upper part of Hole U1431D, where younger age-diagnostic fossils are present (e.g., *Gephyrocapsa* spp. [$>5.5 \mu\text{m}$] and *Discoaster triradiatus*). This makes it difficult to recognize Zone NN18 based on core catcher samples. The top of Zone NN16 is defined based on the LAD of *Discoaster surculus*, which occurs in Sample 15H-CC (135.20 mbsf).

Pliocene

Nannofossil Zones NN16–NN12 are recognized in the Pliocene section of Hole U1431D (Table T2). Two events occur in the lower part of Zone NN16: the LAD of *Discoaster tamalis* (2.8 Ma) and the LAD of *Sphenolithus* spp. (3.54 Ma) in Samples 349-U1431D-18H-4, 60–61 cm (157.4 mbsf), and 21X-CC (188.3 mbsf), respectively. The Zone NN16/NN15 boundary occurs in Sample 24X-CC (217.07 mbsf), based on the LAD of *R. pseudoumbilicus* (3.70 Ma). The LAD of *Amaurolithus tricorniculatus* (~ 3.92 Ma) in Sample 27X-CC (245.87 mbsf) marks the top of Zone NN14. The LAD of *Amaurolithus primus*, which marks the top of Zone NN13 (4.5 Ma), occurs in Sample 29X-CC (265.21 mbsf). The FAD of *Ceratolithus rugosus* (5.12 Ma), found in Sample 31X-CC (284.6 mbsf), marks the top of Zone NN12. We could not identify the LAD of *Triquetrorhabdulus rugosus* within Zone NN12, as this species occurs sporadically and is frequently reworked in the upper part of the Pliocene sequences. The Miocene/Pliocene boundary in Hole

Table T2. Depths and ages of calcareous nannofossil events, Holes U1431D and U1431E. * = end of hole. T = top/last appearance datum, B = base/first appearance datum, Ba = base acme, Tc = top common, Bc = base common. [Download table as .csv.](#)

Epoch	Zone (Martini, 1971)	Calcareous nannofossil event	Hole U1431D		Hole U1431E		Age (Ma)	
			Core, section, interval (cm)	Top depth (mbsf)	Core, section, interval (cm)	Top depth (mbsf)		
Pleistocene	NN21/NN20	B <i>Emiliana huxleyi</i>	1H-CC	3.15			0.29	
	NN20/NN19	T <i>Pseudoemiliana lacunosa</i>	2H-CC	12.15			0.44	
	NN19	T <i>Gephyrocapsa</i> sp. 3	4H-CC	32.08			0.61	
		B <i>Gephyrocapsa</i> sp. 3	5H-6, 47	39.67			1.02	
		B <i>Gephyrocapsa</i> spp. >4 µm (reemG event)	6H-CC	50.90			1.04	
		T <i>Gephyrocapsa</i> spp. >5.5 µm	8H-1, 50	60.70			1.24	
		T <i>Calcidiscus macintyre</i>	10H-CC	89.01			1.6	
	NN11	B <i>Gephyrocapsa</i> spp. >5.5 µm	11H-CC	96.10			1.62	
	NN19/NN18	T <i>Discoaster brouweri</i>	12H-CC	107.57			1.93	
	NN18	Ba <i>Discoaster triradiatus</i>	13H-CC	116.85			2.22	
	NN17/NN16	T <i>Discoaster surculus</i>	15H-CC	135.20			2.49	
Pliocene	NN16	T <i>Discoaster tamalis</i>	18H-4, 60	157.40			2.8	
		T <i>Sphenolithus</i> spp.	21X-CC	188.30			3.54	
	NN16/NN15	T <i>Reticulofenestra pseudoumbilicus</i>	24X-CC	217.07			3.7	
	NN15/NN14	T <i>Amaurolithus tricorniculatus</i>	27X-CC	245.87			3.92	
	NN14/NN13	Bc <i>Discoaster asymmetricus</i>	28X-CC	255.38			4.13	
	NN13	T <i>Amaurolithus primus</i>	29X-CC	265.21			4.5	
	NN13/NN12	B <i>Ceratolithus rugosus</i>	31X-CC	284.60			5.12	
late Miocene	NN12	B <i>Ceratolithus acutus</i>	33X-CC	298.56			5.35	
	NN11	T <i>Nicklithus amplificus</i>	39X-CC	361.67			5.94	
		B <i>Nicklithus amplificus</i>	58X-CC	527.31			6.91	
		B <i>Amaurolithus primus</i> , <i>Amaurolithus</i> spp.	63X-CC	575.50	7R-1, 2	603.32	7.42	
	NN11/NN10	B <i>Discoaster berggrenii</i>	66X-CC*	604.81	17R-7, 4–6	707.40	8.29	
		B <i>Minylitha convallis</i>			20R-1, 102–103	730.42	9.75	
	NN9	T <i>Coccolithus miopelagicus</i>			25R-1, 142–150	779.32	10.97	
		Tc <i>Discoaster kugleri</i>			27R-9, 99–100	807.28	11.58	
	middle Miocene	NN7/NN6	Bc <i>Discoaster kugleri</i>			33R-8, 0–5	864.10	11.9
		NN6	Bc <i>Calcidiscus macintyre</i>			34R-7, 0–5	873.74	12.46
B <i>Reticulofenestra pseudoumbilicus</i>					36R-1A, 7	884.60	<12.829	

Table T3. Depths and ages of planktonic foraminifer events, Holes U1431D and U1431E. T = top/last appearance datum, B = base/first appearance datum, Br = base regular. [Download table as .csv.](#)

Epoch	Zone (Berggren et al., 1995; Wade et al., 2011)	Planktonic foraminifer event	Hole U1431D		Hole U1431E		Age (Ma)
			Core, section, interval (cm)	Top depth (mbsf)	Core, section, interval (cm)	Top depth (mbsf)	
Pleistocene	PT1b	T <i>Globigerinoides ruber rosa</i>	3H-CC	22.11			0.12
		B <i>Globigerinella calida</i>	3H-CC	22.11			0.22
	PT1b/PT1a	T <i>Globorotalia tosaensis</i>	7H-CC	58.53			0.61
		T <i>Globigerinoides extremus</i>	11H-5, 140–145	96.10			1.98
Pliocene	PL5	B <i>Globorotalia truncatulinoides</i>	13H-CC	116.85			2.58
		T <i>Globorotalia multicamerata</i>	18H-CC	162.00			2.98
	PL5/PL4	T <i>Dentoglobigerina altispira</i>	21X-CC	188.30			3.47
	PL3/PL2	T <i>Globorotalia margaritae</i>	23X-CC	207.56			3.85
	PL2/PL1	T <i>Globoturborotalita nepenthes</i>	25X-CC	226.57			4.37
late Miocene	PL1	B <i>Sphaeroidinella dehiscentes</i> s.l.	40X-CC	363.92			5.53
	M14	B <i>Globorotalia margaritae</i>	43X-CC	392.30			6.08
	M13b	B <i>Globigerinoides extremus</i>	66X-CC	604.81			8.93
	M13a/M12	B <i>Neoglobobiquadrina acostaensis</i>			12R-1, 134–135	653.14	9.83
Br <i>Globigerinoides obliquus</i>				27R-9, 99–105	807.28	11.25	
middle Miocene	M9b	B <i>Sphaeroidinellopsis subdehiscentes</i>			33R-8, 89–94	864.10	13.02

U1431D is assigned between Samples 31X-CC (284.60 mbsf) and 33X-CC (298.56 mbsf), based on the FADs of *C. rugosus* (5.12 Ma) and *Ceratolithus acutus* (5.35 Ma), respectively.

Miocene

Ten events occur in the Miocene strata of Holes U1431D and U1431E (Table T2; Figure F24). The top of Zone NN11 is defined by the LAD of *Discoaster quinqueramus* (5.59 Ma); however, it is not

possible to identify this event in Hole U1431D, as this species frequently occurs in Pliocene and uppermost Miocene sediment because of reworking. Four events within Zone NN11 were identified. The LAD (5.94 Ma) and FAD (6.91 Ma) of *Nicklithus amplificus* occur in Samples 349-U1431D-39X-CC (361.67 mbsf) and 58X-CC (527.31 mbsf), respectively. The FADs of *A. primus* and *Amaurolithus* spp. (7.42 Ma) are found in Sample 63X-CC (575.50 mbsf) in Hole U1431D and in Sample 349-U1431E-7R-1, 0–2 cm

Table T4. Depths and ages of radiolarian events, Holes U1431D and U1431E. T = top/last appearance datum, B = base/first appearance datum. [Download table as .csv.](#)

Epoch	Zone (Wang and Abelmann, 1999; Sanfilippo and Nigrini, 1998)	Radiolarian event	Hole U1431D		Hole U1431E		Age (Ma)
			Core, section	Top depth (mbsf)	Core, section, interval (cm)	Top depth (mbsf)	
Pleistocene	NR1	B <i>Buccinosphaera invaginata</i>	1H-CC	3.16			0.21
	NR2	B <i>Collosphaera tuberosa</i>	2H-CC	12.15			0.42
early Miocene	RN4	T <i>Didymocyrtis prismatica</i>			45R-1, 49–51	962.79	16.73
		B <i>Calocycletta costata</i>			45R-4, 21–23	966.28	17.59

Table T5. Distribution of calcareous nannofossil species, Holes U1431A, U1431B, and U1431C. [Download table as .csv.](#)

Table T6. Distribution of calcareous nannofossil species, Hole U1431D. [Download table as .csv.](#)

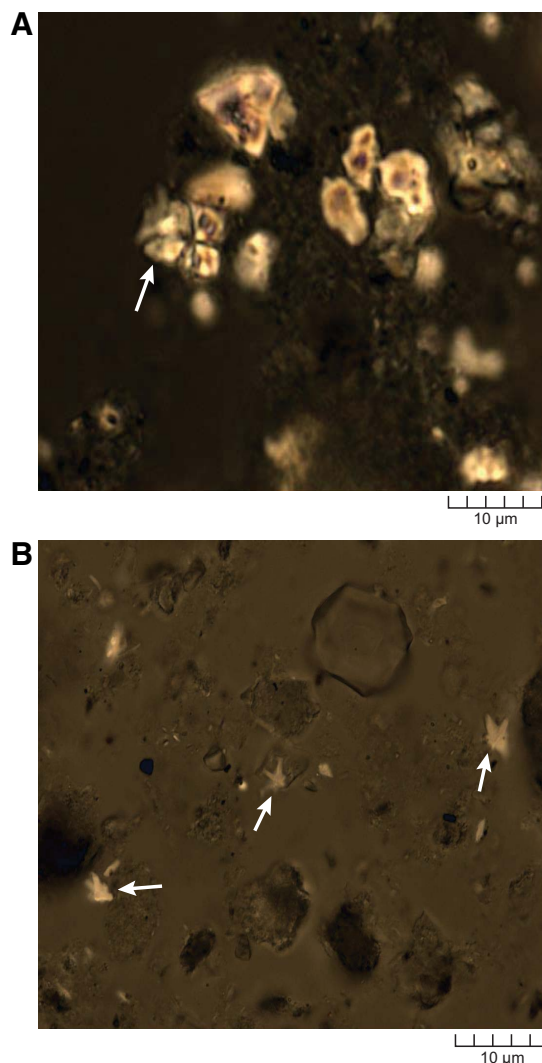
Table T7. Distribution of calcareous nannofossil species, Hole U1431E. [Download table as .csv.](#)

(603.32 mbsf). The FAD of *Discoaster berggrenii* (8.29 Ma) is found in Sample 349-U1431E-17R-7, 4–6 cm (707.40 mbsf). *D. berggrenii* occurs commonly in Sample 349-U1431D-66X-CC (604.81 mbsf), which is from the deepest core taken in Hole U1431D, suggesting an age of <8.29 Ma. This allows reliable biostratigraphic correlation between the deepest part of Hole U1431D and the uppermost section of Hole U1431E (Table T2).

Zones NN10–NN8 could not be reliably identified in samples from Cores 349-U1431E-18R through 24R (711.39–773.31 mbsf) due to poor preservation (Figure F25A) or the absence of nannofossils in several core catcher and split core samples. The FAD of *Minylitha convallis* is used to mark the base of Zone NN9 (9.75 Ma), but its occurrence in Sample 349-U1431E-20R-1, 102–103 cm (730.42 mbsf), may not represent its true FAD because several samples below this depth are barren of nannofossils. The LAD of *Coccolithus miopelagicus* (10.97 Ma) occurs in Sample 25R-1, 142–150 cm (779.32 mbsf), defining the top of Zone NN7. The last common appearance (LCA) of *Discoaster kugleri* (11.58 Ma) within Zone NN7 occurs in Sample 27R-9, 99–105 cm (807.28 mbsf). The top of Zone NN6 is marked by the first common appearance (FCA) of *D. kugleri* (11.9 Ma), found in Sample 33R-8, 0–5 cm (864.1 mbsf). The upper/middle Miocene boundary falls within Zone NN7, between these aforementioned datums (Gradstein et al., 2012). Two additional events within Zone NN6 are the FCA of *Calcidiscus macintyreii* (12.46 Ma) and the FAD of *R. pseudoumbilicus* (12.83 Ma). The FCA of *C. macintyreii* is found in Sample 34R-7, 0–5 cm (873.74 mbsf). The presence of *R. pseudoumbilicus* in Sample 349-U1431E-36R-1A, 7 cm (884.67 mbsf), at the base of lithostratigraphic Unit VII, indicates that the overlying sedimentary sequence in Hole U1431E is younger than 12.83 Ma.

A Paleocene nannofossil assemblage mainly composed of abundant *Fasciculithus* spp. and very rare *Sphenolithus primus* is found in Sample 349-U1431E-46R-4, 16–21 cm (976.62 mbsf), from the interflow claystone of lithostratigraphic Unit X. Species of *Fasciculithus* also occur sporadically in very low abundance in a few of the Miocene samples from Hole U1431E (e.g., Sample 349-U1431E-28R-CC; 815.62 mbsf) (Table T7). The occurrence of these species in these sections is attributed to reworking.

Figure F25. Calcareous nannofossils (XPL). A. Overgrown specimen of *Sphenolithus* (arrow) and several pieces of calcite debris (U1431E-22R-3, 0–2 cm; 750.90 mbsf). B. Broken fragments of *Discoaster* (arrows) (U1431D-60X-CC; 554.09 mbsf).



Planktonic foraminifers

All core catchers from Holes U1431A–U1431E were examined for planktonic foraminifers (Tables T8, T9, T10). In Holes U1431A–U1431C, planktonic foraminifers are well preserved and

rare to common in abundance. The assemblage is dominated by dissolution-resistant tropical species, including *Sphaeroidinella dehiscentes*, *Globigerinoides sacculifer*, *Globorotalia tumida*, and *Pulleniatina obliquiloculata* (Table T8). Their presence indicates a late Quaternary age for the sedimentary succession recovered in Holes U1431A–U1431C. In Hole U1431D, planktonic foraminifers are also well preserved and abundant through Core 349-U1431D-12H (107.57 mbsf) but decrease in abundance downhole, with moderate to poor preservation (Table T9). We distinguished in situ bioevents from reworked occurrences by relying more heavily on FADs rather than LADs. We also discounted bioevents that occurred out of order with the known biostratigraphic sequence. Because the lithology is dominated by turbidites (see **Lithostratigraphy**), the concurrence of several bioevents was most likely caused by redeposition rather than an indication of a hiatus. This filtering approach enabled us to locate 15 planktonic foraminiferal bioevents for the biostratigraphy of Hole U1431D (Table T3; Figure F24).

Our results indicate that the sediment sequence recovered in Hole U1431D spans the upper Miocene (Zone M13) through the Pleistocene (Zone Pt1b). The Pliocene/Pleistocene boundary lies between Samples 349-U1431D-13H-CC (116.5 mbsf) and 14H-CC (125 mbsf), as indicated by the FAD of *Globorotalia truncatulinoides* (2.58 Ma). The presence of *Globorotalia multicamerata* implies a Pliocene age for the interval between Samples 14H-CC and 31X-CC (125.45–284.60 mbsf). The boundary between the lower and upper Pliocene occurs in Sample 21X-CC (188.3 mbsf), as indicated by the LAD of *Dentoglobigerina altispira* (3.47 Ma), but differentiation of faunal Zones PL1–PL6 for the Pliocene is hampered by reworking of specimens due to the frequent occurrence of turbidites (see **Lithostratigraphy**). Although the Miocene/Pliocene boundary could not be determined due to the absence of diagnostic planktonic foraminifers, the abrupt occurrence of abundant warm-water species including *G. multicamerata* and *Pulleniatina* spp. in Sample 31X-CC (284.60 mbsf) implies deposition in the Pliocene. The upper Miocene includes Samples 40X-CC through 66X-CC (363.92–604.81 mbsf), with common *Globigerinoides extremus* and *Neogloboquadrina acostaensis*, but the Zone M13/M14 boundary could not be determined due to the absence of the zonal marker *Globorotalia linguaensis*. From the base of Hole U1431D, Sample 66X-CC (604.8 mbsf) contains *G. extremus*, indicating an age younger than 8.93 Ma (late Miocene).

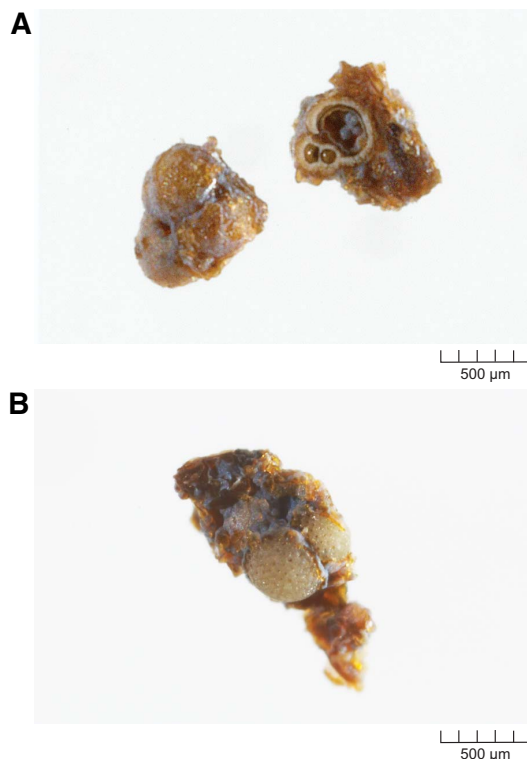
In Hole U1431E, we analyzed planktonic foraminifers in core catcher samples, as well as in samples from within selected cores. The abundance of planktonic foraminifers varies from absent to common, with poor preservation in samples from Cores 349-U1431E-7R through 33R (603.30–864.10 mbsf) (Table T10; Figure F26). Four bioevents distinguish Subzones M13b–M9b, indicating sediment deposition during the middle and late Miocene from ~13 to ~8 Ma (Table T3; Figure F24). Samples from lithostratigraphic Unit VI in Cores 7R through 12R are assigned to Miocene Subzone M13b through Zone M12 based on the presence of *Globigerinoides obliquus*, *Globoturbotalita nepenthes*, and *N. acostaensis* and the absence of *Globorotalia margaritae* and *Globigerinoides conglobatus*. The Subzone M13a/Zone M12 boundary occurs between Samples 349-U1431E-12R-1, 134–135 cm (653.14 mbsf), and 12R-4, 51–53 cm (656.61 mbsf), based on the FAD of *N. acostaensis* (9.83 Ma). Zones M12–M9 could not be differentiated due to the absence of zonal markers. Several bioevents are useful for biostratigraphic division of the interval from Cores 349-U1431E-13R through 34R (670–873.7 mbsf). These include datums found in

Table T8. Distribution of planktonic foraminifer species, Holes U1431A, U1431B, and U1431C. [Download table as .csv.](#)

Table T9. Distribution of planktonic foraminifer species, Hole U1431D. [Download table as .csv.](#)

Table T10. Distribution of planktonic foraminifer species, Hole U1431E. [Download table as .csv.](#)

Figure F26. Planktonic foraminifers, Hole U1431E (reflected light). A. Two poorly preserved or broken specimens of *Globigerinoides sacculifer* s.l. (24R-CC; 773.31 mbsf). B. Poorly preserved specimen of *Sphaeroidinellopsis seminulina* (25R-CC; 779.32 mbsf).



samples from Unit VII, including the FAD of *G. obliquus* (11.25 Ma) in Sample 27R-9, 99–105 cm (807.28 mbsf), indicating mid-Zone M11, and the FAD of *Sphaeroidinellopsis subdehiscentes* (13.02 Ma) in Sample 33R-8, 89–94 cm (864.1 mbsf), indicating Subzone M9b (upper middle Miocene). Samples from Units VIII (dark olive-brown claystone) and X (yellowish brown claystone) are completely barren of planktonic foraminifers.

Radiolarians

The siliceous fraction of biogenic sediment from Site U1431 is dominated by radiolarians with minor proportions of diatoms and sponge spicules. Radiolarians were analyzed in all core catcher samples from Hole U1431D but are only abundant and well preserved in Samples 349-U1431D-1H-CC through 3H-CC (3.15–22.09 mbsf). The overall radiolarian assemblage is composed of a modern and diverse South China Sea fauna (i.e., *Euchitonia furcata*, *Phorticium pylonium*, *Theocorythium trachelium*, *Anthocorytidium ophirensis*, *Ommatartus tetrathalmus tetrathalmus*, *Solenosphaera quadrata*, and *Tetrapyle octacantha*) (Chen and Tan, 1997) (Table T11). The radiolarian stratigraphy spans Zones NR1–NR2 (Late Pleistocene).

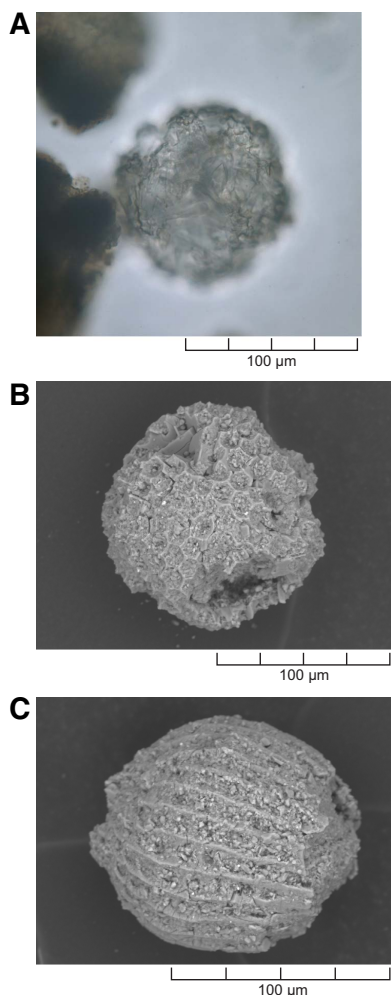
Sample 349-U1431D-1H-CC (3.15 mbsf) contains Late Pleistocene radiolarian *Buccinosphaera invaginata*, which is a marker for Zone NR1 (Table T4); however, it occurs in very low abundances because it is a relatively rare and delicate species (Bjørklund and Goll, 1979). Recognition of this species requires a well-preserved assemblage, which is often absent in drill cores (Knoll and Johnson, 1975).

Radiolarians are rare and preservation is poor in Samples 349-U1431D-4H-CC and 5H-CC (32.08–41.47 mbsf). Although the radiolarian assemblage represents a Pleistocene–Holocene sequence that corresponds to lithostratigraphic Unit I, the absence of any age-diagnostic species makes it impossible to assign the section to any biostratigraphic zone. Below Sample 5H-CC (41.47 mbsf) in Hole U1431D, samples are barren of radiolarians and diatoms and have high amounts of coarse siliciclastic sand and variable proportions of volcanic ash.

Table T11. Distribution of radiolarian species, Hole U1431D. [Download table as .csv.](#)

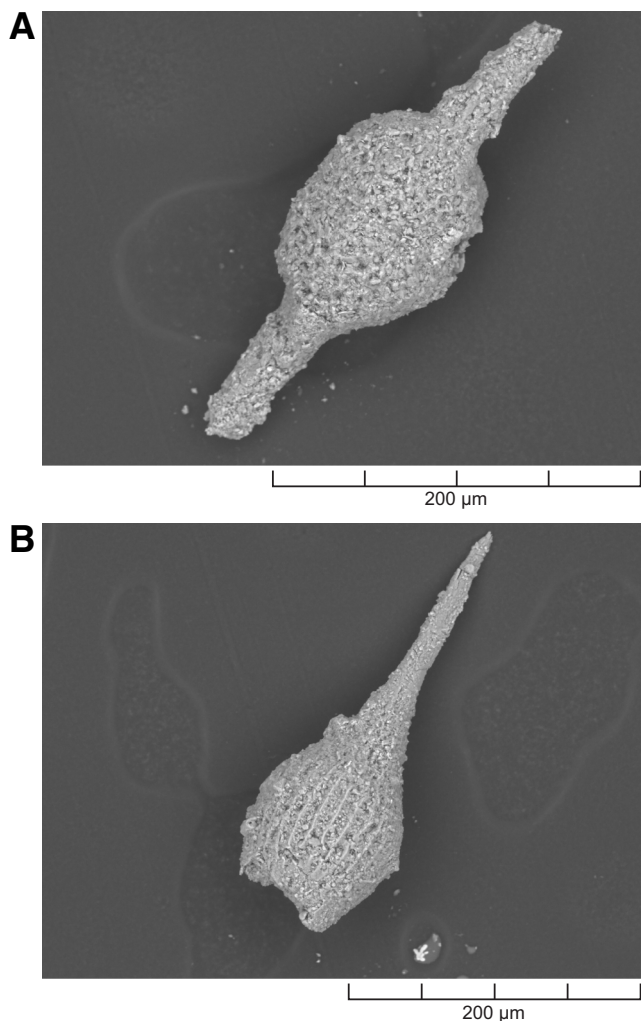
Table T12. Distribution of radiolarian species, Hole U1431E. [Download table as .csv.](#)

Figure F27. Broken and recrystallized radiolarian specimens, Hole U1431E. A. 36R-5, 12–16 cm (889.83 mbsf; PPL). B. 45R-4, 26–28 cm (966.33 mbsf; SEM). C. Broken and recrystallized specimen of *Calocycletta costata* in 45R-2, 128–130 cm (964.5 mbsf; SEM).



We analyzed radiolarians in core catchers and in samples from selected cores in Hole U1431E (Table T12). Radiolarians are barren in most of the samples from Cores 349-U1431E-7R through 33R (603.30–864.10 mbsf). Sample 349-U1431E-17R-7, 4–6 cm (707.40 mbsf), contains some radiolarians, but they are poorly preserved and recrystallized, and species identification was not possible. In Samples 34R-7, 25–32 cm (873.74 mbsf), 35R-6, 102–108 cm (882.54 mbsf), 36R-5, 12–16 cm (889.83 mbsf), and 45R-4, 21–23 cm (966.3 mbsf), radiolarians are more frequent but also show heavy dissolution, making them difficult to identify in the light microscope (Figure F27A). Therefore, radiolarians were picked from the 63 µm size fraction and prepared for observation using a scanning electron microscope (Figures F27B, F27C). Samples 45R-1, 49–51 cm, through 45R-4, 21–23 cm (962.79–966.28 mbsf), from Unit X are assigned to Zone RN4 (17.59–16.73 Ma; early Miocene) based on the presence of *Didymocyrtis prismatica* and *Calocycletta costata* (Sanfilippo and Nigrini, 1998) (Figure F28), providing age control for the bottom of the sedimentary sequence (Unit X) of Hole U1431E (Table T4; Figure F24).

Figure F28. Radiolarians (A) *Didymocyrtis prismatica* and (B) *Calocycletta costata* (U1431E-45R-3, 9–11 cm; 965.72 mbsf; SEM).

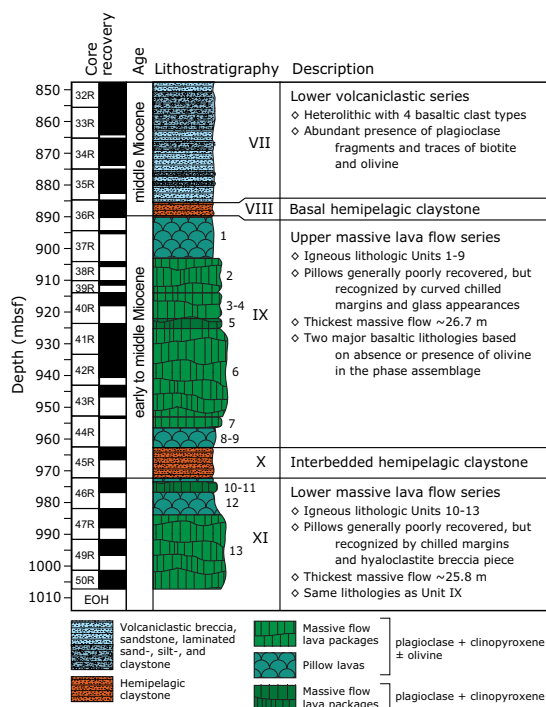


Igneous petrology and alteration

We cored 118.01 m into igneous basement below 889.88 mbsf in Hole U1431E and recovered 46.7 m of basalt (43% recovery). The basement succession was divided into 13 igneous lithologic units, which were then grouped into two lithostratigraphic units (Units IX and XI) separated by a hemipelagic yellowish brown claystone at least 3.7 m thick (Unit X; Figure F29). Both basement units comprise massive basalt lava flows with limited evidence for pillow basalt fragments on top of these flows. The igneous basement is overlain by another hemipelagic dark olive-brown claystone (Unit VIII) that grades upward into a 282 m thick volcanoclastic series (Units VII and VI). These volcanoclastic clay-, silt-, and sandstones and breccias are interpreted to form part of the sedimentary apron of one or more seamounts in the vicinity and contain abundant volcanic glass fragments, scoria, basalt clasts, and fewer mudstone clasts, as well as crystal fragments of plagioclase, olivine, clinopyroxene, and biotite.

The uppermost igneous basement begins with a sequence of mostly fine-grained aphyric basalt, followed downhole by a series of massive basalt lava flows as thick as ~26.7 m with thinner (rubbly) basalt, interpreted as pillow lava, at their tops. Most basaltic cores at Site U1431 are aphyric and range in grain size from microcrystalline to fine grained, with a few medium- to coarse-grained basalts occurring in the interiors of the thickest massive lava flows. All basalts have a phase assemblage of plagioclase and clinopyroxene (±olivine) in their groundmass, with subhedral to euhedral olivine (0.1–1.0 mm in size) present in some lithologic units as microphenocrysts. This resembles a typical mid-ocean-ridge basalt (MORB) crystallization assemblage, and in conjunction with geochemical evidence, we conclude that the basement basalt at Site U1431 is typical MORB (see [Geochemistry](#)). Alteration is also typical of that of MORB. The basalt ranges from mostly fresh to completely altered

Figure F29. Lithostratigraphic summary of igneous rocks and their lithologic features, Hole U1431E. Lithostratigraphy column includes lithology, igneous lithologic units (1–13), and lithostratigraphic units (VI–XI).



and from gray to dark gray-green and yellow to red-brown in color. Alteration color is predominately yellow to brown, especially when altered olivine is present. Typical secondary minerals include saponite, Fe oxides, carbonate, and celadonite, which represent low-temperature alteration assemblages.

Basaltic clasts in volcanoclastic Units VI and VII

Lithostratigraphic Units VI and VII represent an overall series of greenish black volcanoclastic breccia with sand- and claystone interbeds in the upper part (Figure F30A) and dark greenish gray sand-, silt-, and claystone in the lower part (Figure F30B). These units contain numerous well-preserved high-energy volcanoclastic sandy turbidites (Figure F30C) and can be interpreted to represent a seamount apron series (see [Lithostratigraphy](#)). Although calcareous components such as foraminifers, black to gray mudstone clasts, and interbedded micritic carbonate beds are present in the top of Unit VI, these components disappear toward the bottom and are absent in Unit VII. All volcanoclastic breccias and sandstones are heterolithic and contain as many as four basaltic clast types, as well as many (large) broken pieces of primary volcanic crystal phases containing mainly plagioclase but also clinopyroxene, olivine, and biotite. In Unit VI, most breccias are matrix supported, grading to clast supported toward the bottom of the sequence in Unit VII. The packing of the clasts in the breccias makes their identification often difficult. In this section, we describe the basaltic clasts and the crystal fragments within these volcanoclastic units based on their appearance in hand specimen and under the petrographic microscope. Each major basalt clast type and crystal fragment type (Figure F31) is described below from highest to lowest abundance in the section.

Type 1: nonvesicular to sparsely vesicular aphyric basalt

These clasts are angular to subangular, range in size up to 2 cm, are greenish gray to dark gray, have microcrystalline to glassy groundmass with traces of feldspar laths, and have few, typically unfilled, vesicles (Figure F31A). In many of the volcanoclastic breccias and sandstones, this clast type appears to be most common in the finer grain size fraction (Figure F31D), even though their identification is difficult because clasts smaller than 2 mm could also be glass shards broken off from the Type 2 highly vesicular aphyric basalt clasts and scoria.

Figure F30. Volcanoclastic rocks, Hole U1431E. A. Heterolithic volcanoclastic breccia overlying claystone with silt (12R-1A, 5–18 cm; Unit VI). B. Dark greenish gray to black sand- and siltstone showing cross-lamination (28R-5A, 0–13 cm; Unit VII). C. High-energy sandstone turbidite (faintly laminated) above claystone (22R-2A, 90–103 cm; Unit VI).

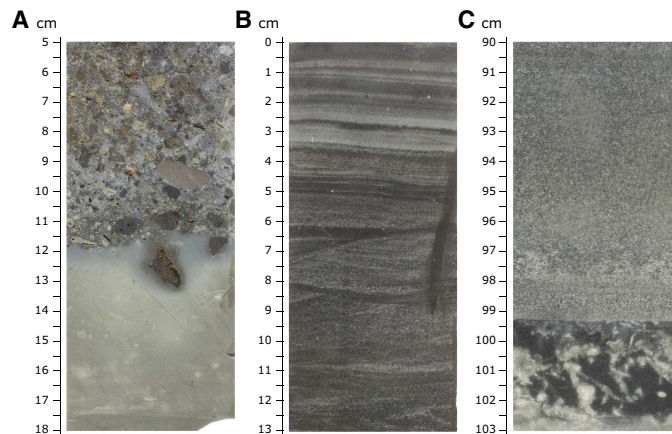
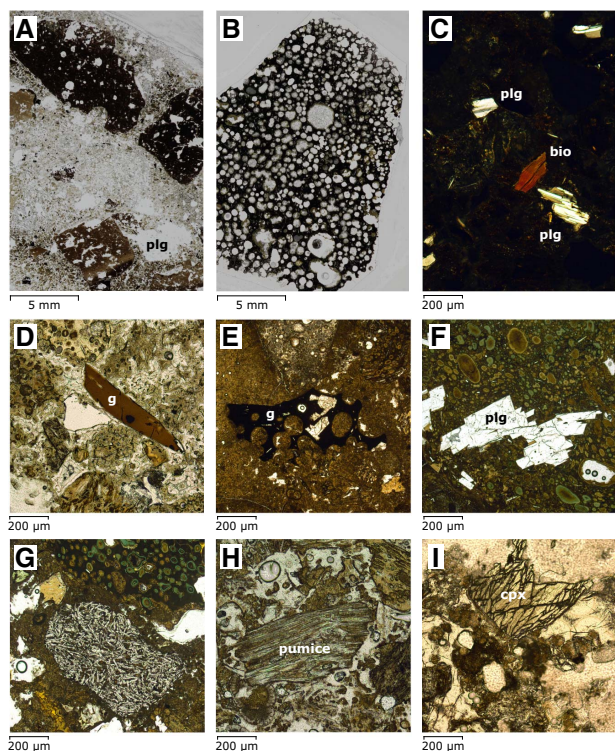


Figure F31. Clast types and crystal fragments in volcanoclastic breccia, Hole U1431E, Units VI and VII. plg = plagioclase, bio = biotite, g = glass, cpx = clinopyroxene. A. Type 1: non- to sparsely vesicular aphyric basalt clast, often microcrystalline or glassy in groundmass and angular to subangular (12R-3, 0–3 cm; TS15; PPL). B. Type 2: highly vesicular aphyric basalt clast, 3 cm × 2 cm, with unfilled to completely filled vesicles (21R-1, 12–14 cm; TS36; PPL). C. Types 3 and 6: plagioclase crystal fragments and biotite flakes as part of volcanic breccia matrix (27R-2, 98–100 cm; TS39; XPL). D. Type 1: fresh angular glass shard with 2 (faint) plagioclase microlites in volcanic breccia matrix (9R-2, 59–62 cm; TS6; PPL). E. Type 2: scoria clast with plagioclase phenocrysts showing sharp but intact vesicle-wall breakage points, indicating very limited transport from the volcanic source (30R-1, 91–94 cm; TS44; PPL). F. Type 2: plagioclase-phyric scoria clast with palagonite replacing glassy matrix and infilling vesicles (7R-2, 75–78 cm; TS2; PPL). G. Type 4: subangular basalt clast with trachytic texture (10R-4, 116–118 cm; TS12; PPL). H. Type 5: highly banded pumice clast (11R-2, 67–70 cm; TS13; PPL). I. Type 6: clinopyroxene crystal fragment (29R-5, 114–117 cm; TS43; PPL).



Type 2: highly vesicular aphyric to plagioclase-phyric basalt

These highly vesicular clasts are often scoriaceous, with well-preserved volcanic glass (fragments) occasionally present (Figures F31B, F31E). The clasts are angular to subangular, have a large range in size to 8 cm, and are dark gray and brown-gray to sometimes reddish when oxidized. Some clasts contain plagioclase glomerocrysts from 0.2 to 1 mm in size (Figure F31F). All clasts are typically glassy but sometimes show microcrystalline groundmass and have vesicle abundances of 10%–50%. These clasts are moderately to completely altered, often with characteristic palagonite rims around vesicles, which often are only partially filled with various alteration minerals.

Type 3: plagioclase crystal fragments

Throughout lithostratigraphic Units VI and VII, from 1% to 3% plagioclase fragments, up to 20 mm in size, are present (Figure F31C). These plagioclase fragments have generally sharp outlines.

Often they retain spiky corners as a result of fragmentation and are overall unaltered. It is likely that these plagioclase fragments are the broken pieces of the larger Type 2 and 4 plagioclase-phyric clasts that occasionally are found in the cores but must have been abundant in the volcanic source(s) of these volcanoclastic units.

Type 4: trachytic basalt and highly plagioclase-phyric basalt

This minor clast type is not easily observed macroscopically in the archive-half sections; however, it occurs frequently in thin sections (Figure F31G). The clasts are angular to subangular, small (up to 1 cm), light gray to dark gray often with a pinkish/brownish tint, and have fine-grained holocrystalline groundmass littered with many plagioclase laths. Some of the clasts are highly plagioclase-phyric with euhedral to subhedral phenocrysts up to 20 mm in size. These clasts are typically nonvesicular and slightly to moderately altered.

Type 5: pumice

This rare clast type is apparent because of its (dirty) white to light gray color and high vesicularity, often with stretched vesicles that make it appear fibrous in the archive halves. These clasts are soft to the saw blade. They are angular to subangular, up to 1 cm in size, and are moderately to highly altered. In thin section, this clast type is distinguished by its highly laminated or banded nature (Figure F31H).

Type 6: biotite, clinopyroxene, and olivine crystal fragments

Although plagioclase dominates the crystal fragments in Units VI and VII, flakes of well-preserved biotite (Figure F31C) and crystal fragments of relatively unaltered clinopyroxene and olivine (Figure F31I) occur in many thin sections. The combined presence of plagioclase, clinopyroxene, olivine, biotite, and trachytic basalt points to an intraplate volcanic source, potentially the neighboring seamounts near Site U1431.

Lithostratigraphic and igneous lithologic units

Unit IX (889.88–962.51 mbsf)

Interval: 349-U1431E-36R-5, 17 cm, to 45R-1, 21 cm

Depth: 889.88–962.51 mbsf

Thickness: 72.63 m (26.67 m at 36.7% recovery)

Lithology: massive basalt flows with possible pillow basalt interbeds

Igneous lithologic units: 1–9

The base of the dark olive-brown hemipelagic claystone (lithostratigraphic Unit XIII) and the first appearance of aphyric to sparsely olivine-phyric basalt fragments at 12 cm in Section 349-U1431E-36R-5 mark the upper boundary of lithostratigraphic Unit IX at 889.88 mbsf. Throughout Unit IX, most basaltic cores are aphyric and nonvesicular in nature, with minor occurrences of olivine-microphyric basalt and one amygdaloidal basalt unit (Figure F32). Overall, the degree of crystallinity in the basalt is high and increases to holocrystalline in medium- to coarse-grained varieties (Figure F33).

Igneous lithologic Units 1–4 (3.8–14.2 m thick) are poorly recovered, and flow boundaries are inferred from the occurrence of chilled margins on separate pieces, with occasional thin glassy rinds preserved, at the tops of Sections 349-U1431E-38R-1, 40R-1, 40R-4, and 41R-1. These first four units comprise aphyric to sparsely olivine-phyric basalt with aphanitic to microcrystalline groundmass (Figure F32A) at the top of each unit, significantly coarsening in

Figure F32. Basement basalt, Hole U1431E, Unit IX. A. Olivine-phyric basalt with glassy rim (37R-1A, 0–23 cm; Unit 1). B. Amygdaloidal microcrystalline basalt (41R-1A, 40–63 cm; Unit 5). C. Coarse-grained aphyric basalt (41R-8A, 20–43 cm; Unit 6).

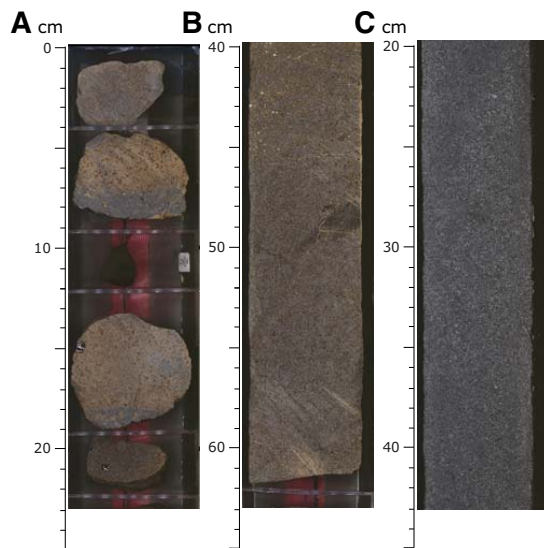
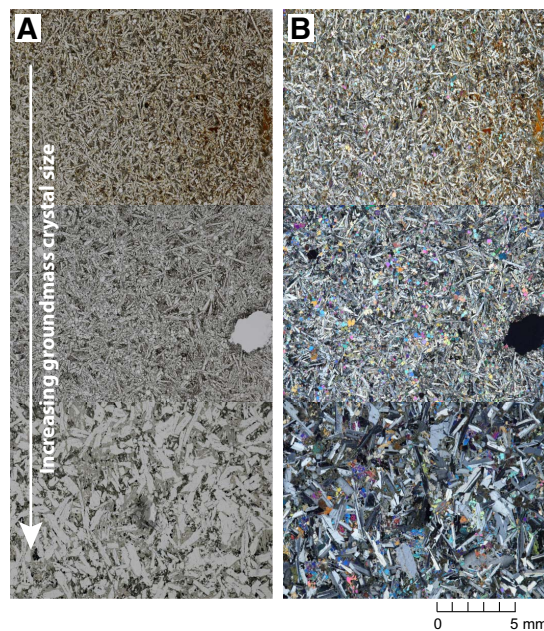


Figure F33. Groundmass grain size increasing from top to bottom in ~26.7 m thick massive basalt flow, Hole U1431E, Unit IX, Unit 6. Top: 37R-1, 5–7 cm; TS31. Middle: 38R-2, 19–21 cm; TS33. Bottom: 41R-8, 0–2 cm; TS51. A. PPL. B. XPL.



crystal size toward the cores of the thicker flows. These basalts are nonvesicular and fresh to moderately altered. Some units contain up to 10% fresh olivine microphenocrysts, as large as 0.5 mm, with distinctive equant habit (Figure F34A). Groundmass varies from cryptocrystalline intersertal in olivine-phyric basalts to intergranular, consisting of triangular networks of long-prismatic plagioclase sheaves with clinopyroxene growing interstitially, in some cases subophitically, with plagioclase (Figure F34B).

Figure F34. Basalt, Hole U1431E, Units IX and XI (XPL). A. Unaltered equant olivine microphenocrysts in groundmass containing plagioclase and clinopyroxene (38R-2, 19–21 cm; TS33). B. Anhedral clinopyroxene interstitial to long-prismatic sheaves of plagioclase (41R-8, 0–2 cm; TS51). C. Variolitic growth texture of plagioclase around a cluster of equant olivine microphenocrysts (46R-1, 60–62 cm; TS56). D. Long-prismatic plagioclase habit with a single row of (melt) inclusions in interior and parallel to x-axis, indicative of fast crystallization during relatively fast cooling of this basalt magma (46R-1, 60–62 cm; TS56).

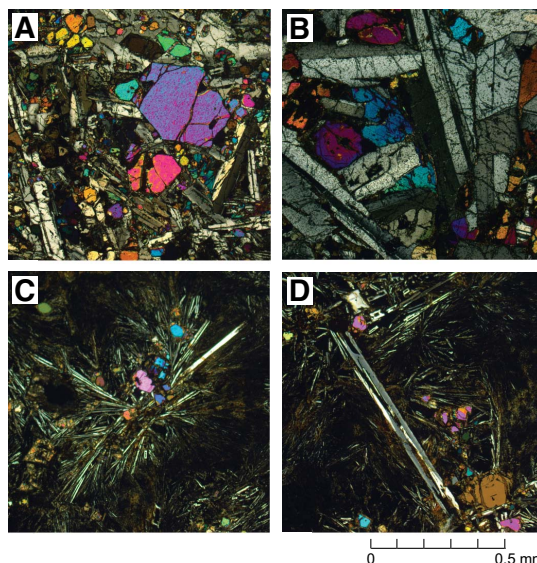
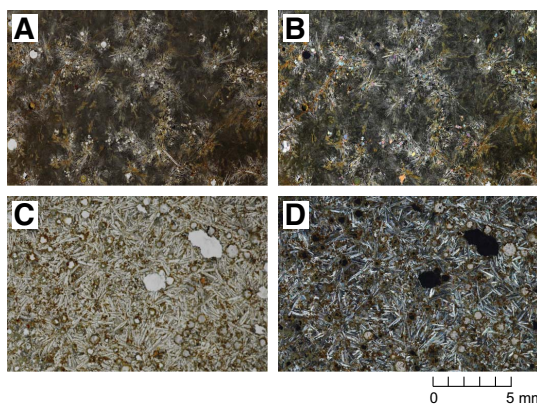


Figure F35. Basalt with variolitic textures and abundant plagioclase laths or needles, Hole U1431E. A, B. 46R-1, 60–62 cm (Unit XI); TS57. C, D. 41R-1, 37–40 cm (Unit IX); TS47. (A, C) PPL, (B, D) XPL.



Igneous lithologic Unit 5 (2.4 m thick) is an amygdaloidal aphyric basalt with up to 15% rounded vesicles, also distinguished from other basaltic units by the absence of olivine microphenocrysts (Figure F32B). This unit has markedly variolitic textures with plagioclase laths or needles forming subradial aggregates around vesicles (Figures F35C, F35D). This is the most altered unit in the basement sequence based on the presence of abundant filled vesicles and veins.

Igneous lithologic Unit 6 (26.7 m thick) is the thickest massive flow in Unit IX and, like Units 1–4, contains olivine microphenocrysts and is once again largely nonvesicular (Figure F32C). Grain size varies from microcrystalline to coarse grained in the core (Fig-

ure F33) of this massive flow, with the coarsest observed grain sizes in Section 349-U1431E-43R-3.

Igneous lithologic Units 7–9 include a thin basalt unit (Unit 7) of only 0.4 m thickness, which has a well-preserved ropy flow-top surface (Figure F36) with a (planar) chilled margin (<1 cm), probably indicating eruption on the seafloor in the form of a sheet lava flow. In addition, a single piece of hyaloclastite breccia was encountered in Unit 8 that is the best evidence of pillow basalt forming between the massive lava flows, where recovery typically was minimal. This breccia has well-preserved angular glass fragments up to 2 cm in size with distinctive yellow to brown palagonite rims and is set in a white carbonate matrix (Figure F37). The hemipelagic yellowish-brown claystone that follows at the base of Unit IX contains basaltic clasts up to 5 cm in diameter of similar lithology (Figure F20).

Unit XI (972.00–1007.89 mbsf)

Interval: 349-U1431E-46R-1, 0 cm, to 50R-6, 20 cm

Depth: 972.00–1007.89 mbsf

Thickness: 35.89 m (20.00 m at 55.7% recovery)

Lithology: massive basalt flows with possible pillow basalt interbeds
Igneous lithologic units: 10–13

The base of the yellowish brown hemipelagic claystone (Unit X) and the first appearance of aphyric to sparsely olivine-phyric basalt fragments at the top of Section 349-U1431E-46R-1 are taken as the upper boundary of lithostratigraphic Unit XI at 972.00 mbsf. Unit XI is very similar in character to Unit IX and is composed of two thick, fine- to medium-grained aphyric massive flow units that alternate with two thinner (possibly pillow basalt) flow units. In a similar fashion, the degree of crystallinity in these basalts is high and increases to holocrystalline in medium- to coarse-grained varieties in the cores of the massive flows.

Igneous lithologic Unit 10 is a sparsely vesicular and olivine-phyric aphanitic basalt directly below the yellowish-brown claystone and shows some characteristic variolitic textures (Figures F34C, F34D, F35A, F35B). Only ~1 m of core, comprising 17 loose basalt pieces, was recovered.

Igneous lithologic Unit 11 is an amygdaloidal aphyric basalt flow (8.6 m thick) that contains up to 10% vesicles, often completely filled with green clays and/or carbonate minerals. This amygdaloidal basalt resembles Unit 5 in lithostratigraphic Unit IX, as it does not contain olivine as part of its phase assemblage and ranges in grain size from fine to medium grained from top to bottom. Igneous lithologic Unit 12 is a thin, 42 cm thick interval of aphyric basalt to sparsely olivine-phyric basalt with one piece showing a thin (<0.5 cm) chilled margin. Igneous lithologic Unit 13 is a fine- to medium-grained massive basalt flow very similar in texture and mineralogy to Unit 6 in lithostratigraphic Unit IX. The basalts are nonvesicular and generally fresh to moderately altered and contain many very small (up to 0.5 mm in size) fresh olivine microcrysts. These equant euhedral olivines are typically dwarfed in size by groundmass plagioclase and clinopyroxene minerals that have grown into intricate crystal networks with long-prismatic habits and relatively large crystal sizes. Drilling at Site U1431 terminated at 1008.8 mbsf (with the base of the recovered section at 1007.89 mbsf) after coring 25.8 m into this last massive lava flow.

Figure F36. Ropy flow top, Hole U1431E, Unit IX (44R-1, 0–8 cm; Unit 7). A. Top view showing ropy surface morphology. B. Side view showing limited thickness (<5 mm) of the chilled margin.

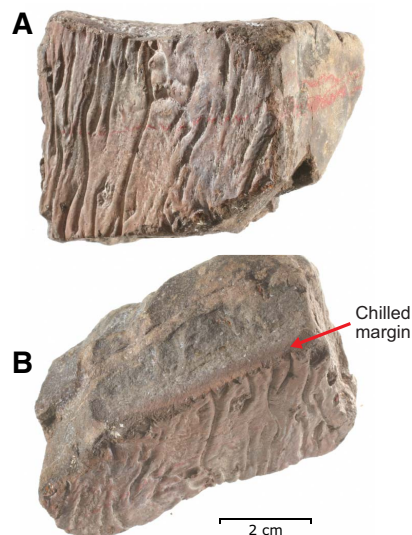


Figure F37. Hyaloclastite breccia, Hole U1431E, Unit IX (44R-1, 43–47 cm; Unit 8).



Interpretation of the igneous succession

The primary goal of Expedition 349 was to recover basement to help understand the opening history of the South China Sea. Site U1431 was positioned close to what is generally believed to be a relict spreading center in order to get an age estimate for the cessation of seafloor spreading in the East Subbasin. This site is also flanked by nearby seamounts. We recovered 46.7 m of basalt after penetrating 118.0 m into igneous basement at Site U1431 and identified 13 igneous lithologic units, all of which are consistent with MORB from a petrological point of view. Both lithostratigraphic Units IX and XI are devoid of seamount-derived volcanic products, but the

thick sequence of overlying volcanoclastic rocks of Units VI and VII probably originated from intraplate volcanism, as is evidenced by plagioclase and biotite crystal fragments and high abundances of highly vesicular scoria, plagioclase-phyric and trachytic basalt clasts, and finer grained (fresh) volcanic glass shards (Figure F36). Site U1431 evidently penetrated the volcanic apron of nearby seamounts active during the middle to late Miocene (see **Lithostratigraphy**).

The recovered basement basalts all have phase assemblages of plagioclase and clinopyroxene and, in some cases, olivine (typically as microphenocrysts). We used these different crystallization histories, as identified in thin section, as well as textural features, such as the presence of glassy (curved) chilled margins and a single occurrence of a hyaloclastite breccia, to define a total of 13 eruptive units (Figure F29). Eruption at Site U1431 temporarily halted with the deposition of the hemipelagic claystone of Unit X. Only 3.7 m of this sediment was recovered, yet it may be as thick as 9.5 m if we take the top of Section 349-U1431E-46R-1 as its lower boundary. Unit X was deposited at ~17.6 to 16.7 Ma based on the occurrence of Miocene radiolarians (see **Biostratigraphy**); however, the duration of volcanic quiescence cannot be resolved at this time, and shore-based radiometric dating of the basement samples is required to help constrain the eruption history of the igneous basement at Site U1431.

Because no well-defined contacts were recovered during coring and recovery was moderate to poor, our boundary locations and unit thickness estimates are approximate, particularly in the interpretation of the pillow basalt units (igneous lithologic Units 1, 7–10, and 12) based on scarce evidence mentioned above. We presume here that low-recovery intervals could be characteristically composed of pillow basalt units that do not core very well. The wash Core 349-U1431E-48G, which was recovered after picking the drill bit up to above the sediment/basement interface at ~890 mbsf to allow all the debris collecting around the drill collars to fall in, contained several pillow basalt fragments, providing further evidence for the presence of pillow lavas in the basement. Downhole logging was not able to reach the basement section, so the igneous lithologic unit boundaries remain poorly defined (see **Downhole measurements**).

Alteration

Basement rocks at Site U1431 primarily have been subjected to alteration by interaction with seawater. Alteration intensity varies from slight to complete, whereby the majority of the recovered basement rocks are moderately altered, yet in many units we identified (substantial) intervals of only slight alteration. In these intervals, olivine crystals are remarkably unaltered, chilled margins often have well-preserved glassy rinds, and the sole hyaloclastite breccia sample recovered still contains fresh volcanic glass. However, compared to other (typically older) ocean crust basement sites (e.g., Ocean Drilling Program Holes 801C and 735B and Integrated Ocean Drilling Program Holes U1365A and U1368A) (Alt et al., 1992; Bach et al., 2001; Expedition 329 Scientists, 2011), the background alteration at Site U1431 seems relatively high. The alteration assemblage of secondary minerals of saponite, Fe oxides, carbonate, and celadonite indicate low-temperature alteration dominated by interaction of basalt with oxidizing seawater (Kurnosov et al., 2008). There is no systematic change in the alteration nature or color with depth that might indicate a transition from more oxidizing to re-

ducing conditions. Based on macroscopic and thin section observations, the overall alteration style (Figures F38, F39) is characterized by the following categories:

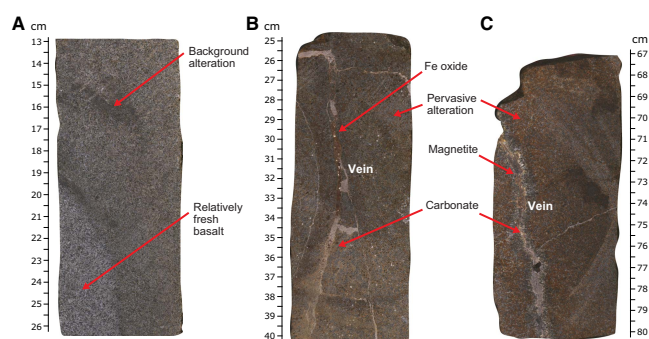
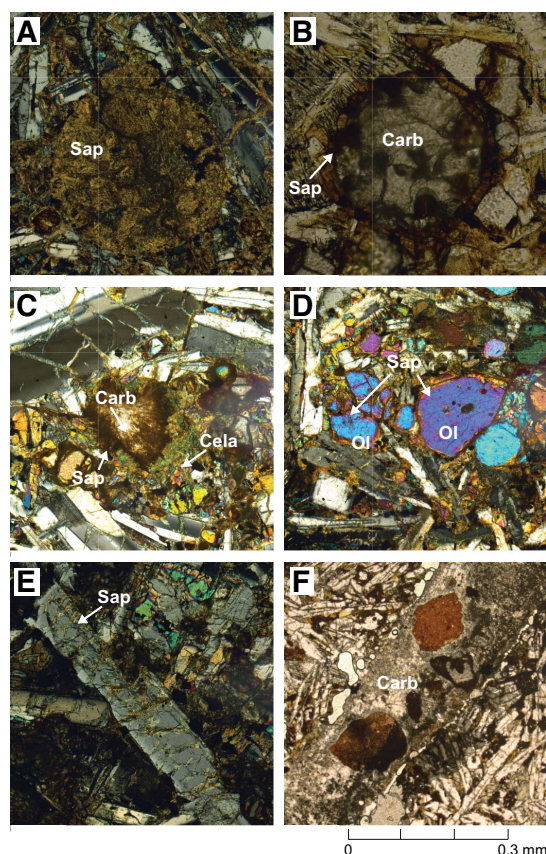


Figure F39. Basalt alteration, Hole U1431E (XPL). A. Vesicle filled with saponite (Sap) only (46R-3, 39–41 cm; TS57). B. Vesicle filled with saponite first, then carbonate (Carb) (43R-3, 91–94 cm; TS54). C. Vesicle filled with celadonite (Cela) first, then saponite and carbonate (50R-6, 0–3 cm; TS63). D. Olivine (Ol) replaced by saponite (37R-1, 5–7 cm; TS31). E. Plagioclase replaced by saponite (41R-2, 26–28 cm; TS48). F. Carbonate vein (41R-2, 26–28 cm; TS48).



- Background alteration with saponite and Fe oxide, occurring throughout the holocrystalline basalt groundmass and the less frequently observed mesostasis between the groundmass minerals, and (when present) olivine microphenocrysts;
- Alteration halos, typically associated with cracks and veins;
- Minor vein fillings by secondary minerals, mostly carbonate, Fe oxide, or both; and
- Partial to complete vesicle fillings by secondary minerals, typically carbonate and saponite, and less frequently celadonite.

Alteration phases

Alteration at this site includes mainly background and alteration halos. For both styles of alteration, oxidative alteration (dominated by Fe oxide and saponite) is the most widespread, whereas few parts of the core were altered at oxygen-starved conditions (dominated by saponite and celadonite). We distinguish four characteristic alteration minerals in Hole U1431E: saponite, Fe oxide, celadonite, and carbonate. Saponite is the most widespread alteration mineral at Site U1431 and, in macroscopic observation, its color ranges from yellow to orange to red-brown. Saponite is the major alteration mineral in the background alteration and in halos flanking the veins and filling the vesicles (Figure F39A). Formation of saponite results from alteration of olivine (when present) (Figure F39D) and groundmass mesostasis. Other clays have been recognized in thin section but are too fine grained to be positively identified.

Fe oxide is the second most abundant alteration mineral after saponite and occurs throughout the recovered cores. Fe oxide varies from yellow-brown to dark brown. The Fe oxide is often intermixed with saponite and is present in veins, vesicles, and halos. In addition, iron oxyhydroxide mixed with clay typically replaces olivine phenocrysts as iddingsite to form hyalophitic textures.

Celadonite is the third most abundant mineral in the background alteration, although it often is difficult to observe from macroscopic observation alone. Based on the available shipboard thin sections, celadonite is observed throughout Hole U1431E, especially in the background alteration. Celadonite is distinctively bright green, typically fills veins and vesicles, and replaces primary interstitial spaces in basaltic groundmass.

Carbonate appears throughout the recovered cores, mainly in vesicle and vein fillings (Figures F39B, F39C), typically replacing olivine (and plagioclase).

Finally, palagonite is present as a bright orange to red alteration product of volcanic glass, appearing in the chilled margins of pillow and sheet flow tops, as well in the volcanic glass clasts making up the singular hyaloclastite breccia (Figure F37) recovered in Hole U1431E.

Alteration of primary minerals

Olivine is the most strongly altered mineral throughout the basalt at Site U1431. It occurs as the only (micro)phenocrystic phase in the basement units and often is recognized by its pseudomorphic shape. Olivine is altered to some small extent even in the least altered basalts; entirely fresh olivine crystals are rare in Hole U1431E. Therefore, the replacement of olivine by various secondary mineral types ranges from minor to 100% based on thin section observation. Olivine usually is totally replaced by saponite, Fe oxide, carbonate, and celadonite. Clinopyroxene only occurs in the groundmass and often is replaced by saponite, other clays, and Fe oxide. Plagioclase is the most abundant mineral in the basement at Site U1431 and only occurs in the groundmass. It is the most resistant mineral to alteration, as fresh plagioclase is found in the most strongly altered

basalt. Plagioclase typically is replaced by saponite, other clays, and Fe oxide, and its alteration intensity ranges from negligible to 50% based on thin section observation.

Pervasive background alteration

Most of the background alteration in basement Units IX and XI is pervasive, in the sense that it affects all lithologies and all cores (Figure F38), as opposed to the minor alteration that occurs in halos surrounding fractures and veins. Pervasive replacement of groundmass minerals and phenocrysts, such as plagioclase and olivine, occurs in the cores of every massive flow. It is characterized by formation of Fe oxide, saponite, and in some cases celadonite and represents the early stage of alteration caused by oxidizing seawater before the later stages of alteration by veining (Figures F38B, F38C). This background alteration is most obvious in the top of flow units, as in Cores 349-U1431E-37R through 40R in the upper massive flow series (Unit IX) and Core 47R in the lower series (Unit XI). Background alteration decreases toward the interiors of the recovered sheet and massive lava flows.

Vein fillings and alteration halos

Based on macroscopic observation of archive sections, we identified 131 veins in the 46.7 m of recovered basement basalt, with an average vein density of 2.8 veins per meter. Vein thickness varies from <0.1 to 4 mm, with an average thickness of 0.7 mm. Veins observed in the basement at Site U1431 exhibit curved, planar, irregular, and (complex) anastomosing shapes; they are isolated, branched, or form a network. Vein fillings have colors varying from white to red-brown and white-yellow to white-green. Vein fillings consist of celadonite, Fe oxide, carbonate, magnetite, and accessory minerals (Figures F38B, F38C, F39F). Veins are typically 40%–100% filled by secondary minerals. Most veins exhibit uniform infillings, whereas composite veins have more than one infilling mineral, typically in banded arrangement. Veins filled with carbonate are most abundant (88%), followed by veins filled with Fe oxide (17%) and/or celadonite (10%). Only one magnetite-filled vein was identified. The distribution of vein filling minerals (from the vein walls inward) indicates their formation sequence from saponite, Fe oxide, to carbonate, which is usually the last mineral to precipitate. In some cases, celadonite appears before the carbonate infilling. A minor number of veins (10%) have halos that vary in width from 0.5 to 3 cm. The observed alteration minerals in halos are similar to the pervasive background alteration phases, except that alteration intensity in those halos is generally higher.

Vesicle filling

Vesicles make up <1% of the recovered basement basalt in Hole U1431E, although a few individual basalt units have vesicle abundances up to 30% (igneous lithologic Units 5 and 11). Based on thin section observations, vesicle fillings range from none to 100% and can include saponite, Fe oxide, carbonate, and celadonite. The filling minerals and filling order are similar to those of veins: first Fe oxide, then saponite (or celadonite), and finally carbonate (Figure F39C). Saponite typically is the most abundant vesicle-filling mineral, followed by carbonate and Fe oxide, and then by rare celadonite.

Basalt glass alteration

Basalt glass was recovered from Cores 349-U1431E-36R, 38R, and 44R. When present, glass may be well preserved and fresh; when altered, it is totally replaced by palagonite and/or clay. Fresh fractions of basaltic glass vary from 10% in Core 349-U1431E-36R

(~1.5 cm thick chilled margin) to 60%–70% in Cores 38R (~1.5 cm thick chilled margin) and 44R (~2 cm large hyaloclastite fragments).

Interpretation of alteration

Alteration of the basement basalt at Site U1431 in Units IX and XI is dominated by oxidative alteration, quite similar to the upper part of the ocean crust recovered in Holes 801C, 735B, U1365A, and U1368A (Alt et al., 1992; Bach et al., 2001; Expedition 329 Scientists, 2011). No mineral assemblage typical of high-temperature hydrothermal alteration occurs, indicating that principally low-temperature oxidative seawater interacted with basement at this site. Pervasive background alteration generally occurs near the top and bottom of (massive) lava flows, where fractures and veins are concentrated (see **Structural geology**). The strongest alteration occurs in halos surrounding those structures and merges into the background alteration, showing that the overall distribution of alteration was controlled by the location of fractures and veins. The observed sequence of vein and vesicle filling minerals shows the evolution of circulating fluids, which typically ends with the formation of carbonate. In only a few intervals, we encountered crosscutting veins, with a younger generation of Fe oxide veins cutting through older carbonate veins. This may indicate reopening of fractures, allowing later stage oxidative fluid flow, yet it remains unclear whether alteration at Site U1431 was continuous or episodic.

Structural geology

Site U1431 lies immediately north of the relict spreading ridge of the South China Sea. A north–south oriented seismic profile across this site shows a local depression with a volcanic seamount located to the south. Offsets on seismic reflectors reveal evidence for normal faulting structures on the north side of this depression (Figure F3). No obvious unconformity can be seen on the seismic profile, and the sediment sequence reflectors are generally horizontal and parallel to the seafloor.

Although five holes were cored at Site U1431, traces of deformation are only observed in the consolidated sediment and basement rock of Hole U1431E. We measured the dip orientation and dip angle of ~130 fractures and veins in Hole U1431E. The lithologies include claystone, siltstone, sandstone, and volcanoclastic breccia (lithostratigraphic Units VI and VII; see **Lithostratigraphy**), as well as basalt in Units IX and XI (see **Igneous petrology and alteration**). The structural information collected from these lithified rocks of Hole U1431E is relatively sparse.

Fractures

Most fractures are drilling induced, showing irregular fracture surfaces and densely distributed slickensides that are not expected in this tectonic setting. Natural fractures are quite rare and, when occurring, they often have neither offset nor striation on fracture surfaces. Fracture orientations in the basalt sequences (Units IX and XI) are randomly distributed (Figure F40), suggesting a lack of obvious extensional or compressional activities and that the fractures were formed mainly due to the cooling of hot magma or heterogeneous local stress perturbations. Some fractures reactivate along veins (Figure F41), making it difficult to tell if these reactivated fractures were caused by drilling or local stress perturbations. Most of the fractures identified in the claystone of Unit X, deposited between the igneous lithostratigraphic units (Units IX and XI), are similar to those in the basalt (i.e., showing neither offset nor stria-

Figure F40. Orientation distribution of structural features in Hole U1431E.

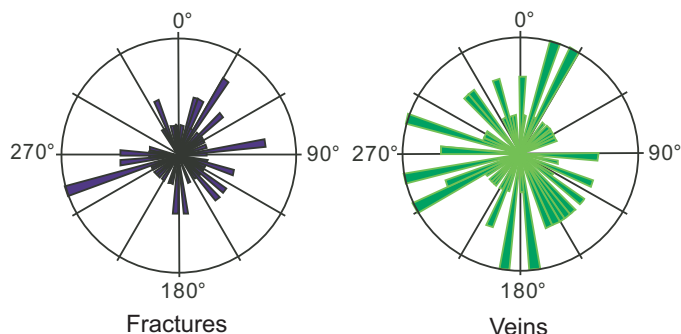


Figure F41. Straight vein infilled along preexisting fracture (top) and reactivated fracture along the vein (below) (U1431E-41R-5A). A. Core image. B. Interpretation.

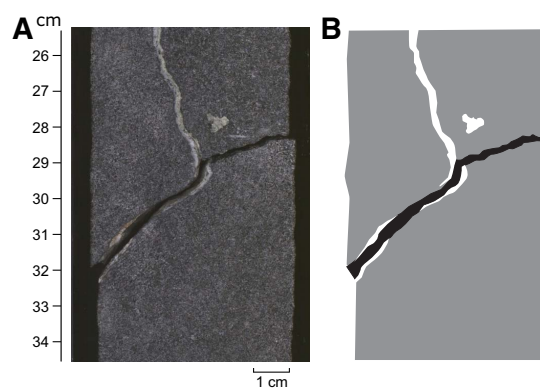
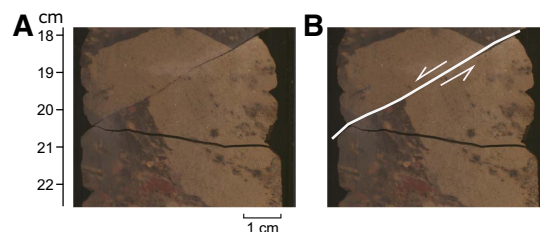


Figure F42. Fracture with ~1 cm offset in U1431E-45R-2A. A. Core image. B. Interpretation. White line is the fracture, and arrows indicate offset direction.

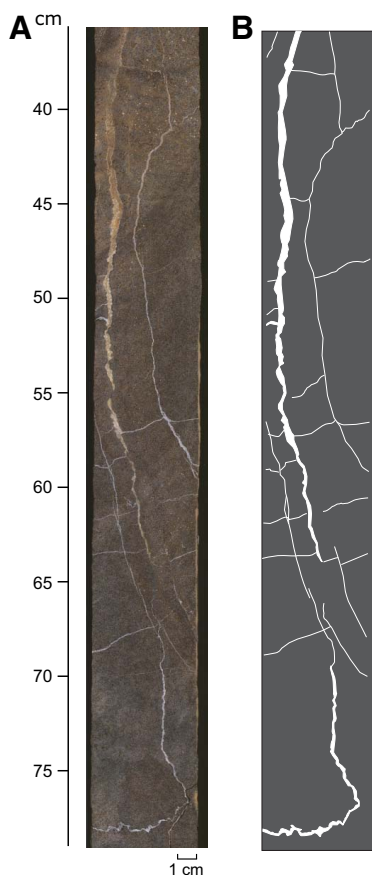


tion). Only 1 fracture observed in Section 349-U1431E-45R-2 shows ~1 cm of normal offset (Figure F42). We hypothesize that these fractures are related to weak movement as magma flowed above the sedimentary sequence.

Veins

Alteration veins are ubiquitous, but together they are volumetrically insignificant. The veins generally may reflect later stages of cracking, fluid circulation, and fluid-rock reaction. The major veins are either white or red-brown and filled with carbonate and/or with Fe oxide. The vein orientations are also random (Figure F40B). In general, there are two main types of veins that differ in shape: straight veins with different widths (Figure F41) and curved veins. As shown in Figure F43, three subparallel curved veins of different thicknesses combine with several straight radiative veins to sur-

Figure F43. A typical curved and radiating vein network showing the development of fractures during the magma cooling process and later calcite infilling (U1431E-41R-2A). A. Core image. B. Interpretation.



round the fresh basalt in the center. They form a network with primary orientations consistent with fractures that formed during the magma cooling process. Cross-cutting between veins is seldom seen.

Geochemistry

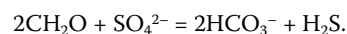
Interstitial water chemistry

We collected 38 whole-round samples (5 cm long) for interstitial water measurements at an interval of 0.5 m from 0 to 20.4 mbsf in Hole U1431A. In addition, interstitial water was collected by Rhizon samplers at intervals between 5 and 50 cm to the base of Hole U1431A (0–28.4 mbsf). In Hole U1431D, we collected 23 whole-round interstitial water samples (5–10 cm long) in the APC section (0–168.9 mbsf) and 20 interstitial water samples (10–15 cm long) in the XCB section (168.9–556.1 mbsf) at a frequency of 1 sample per core. Hole U1431A cored the uppermost 28.4 m of sediment and is ~20 m away from Hole U1431D. Interstitial water chemistry profiles of whole-round samples from Holes U1431A and U1431D are shown in Figures F44, F45, F46, and F47. Interstitial water chemistry data are given in Tables T13 and T14.

Sulfate, alkalinity, ammonium, and phosphate

The alkalinity and sulfate depth profiles are approximate mirror images of each other (Figure F44). The changes in the alkalinity and sulfate concentration are most likely caused by bacterially mediated

organic matter diagenesis coupled with sulfate reduction according to the simplified reaction,



Alkalinity reaches a maximum value of 7.9 mM at 64.7 mbsf, and sulfate reaches a minimum value of 2.3 mM at 241 mbsf; however, low sulfate values of <3.0 mM occur from 166 to 260 mbsf. In this interval, ammonium reaches a maximum value of 903 μM at 203 mbsf, indicative of organic matter diagenesis in the sediment. Alkalinity decreases downhole, from its maximum value at 64.7 mbsf to a minimum value of ~2.2 mM, which is close to the modern seawater value (~2.3 mM), near the base of Hole U1431D. Both ammonium and phosphate follow a similar trend, decreasing to ~0 μM near the base of Hole U1431D. In contrast, sulfate concentrations gradually increase to 24 mM near the base of Hole U1431D, which is close to the modern seawater value (28.9 mM).

Potential source of unusual sulfate concentrations in Hole U1431D

The interstitial water contains significant amounts of sulfate (3.3–24.0 mM) from 260 to 549.11 mbsf (Figure F44; Table T13). It is worth noting that sulfate is not completely consumed throughout Hole U1431D, with minimum sulfate concentrations of ~2.3 mM occurring from 166 to 260 mbsf. The presence of high sulfate concentrations could be evidence for contamination of the interstitial water by drilling fluids. If so, the observed interstitial water sulfate concentrations suggest 13%–88% contamination. The highest sulfate concentration in the interval from 260 to 549.11 mbsf was measured in Section 349-U1431D-60X-2. This sample was thoroughly cleaned by scraping prior to analysis, and intact, unfractured pieces were used for interstitial water extraction, so contamination is unlikely. Further evidence against contamination is that correcting for drilling fluid using the sulfate proxy results in negative magnesium and potassium concentrations for samples close to the bottom of Hole U1431D. Thus, no sulfate correction is applied, and the presence of dissolved sulfate is interpreted as evidence for sulfate-bearing fluid. Shore-based isotopic analyses of the interstitial water samples will help to constrain the source of the sulfate-bearing fluid in Hole U1431D.

Calcium, magnesium, and strontium

Downhole distributions of Ca^{2+} , Mg^{2+} , and Sr^{2+} are shown in Figure F45. Calcium concentrations are slightly higher than that of modern seawater (10.5 mM), ranging from 10.5 to 12.4 mM in the uppermost 46 m. Values then decrease to a minimum of 3.4 mM at 193 mbsf, before increasing downhole to 16.6 mM at 549 mbsf. Changes in calcium concentration are mostly caused by carbonate diagenesis (i.e., dissolution and recrystallization of biogenic carbonate). Magnesium concentrations are lower than the modern seawater value (54 mM) throughout Hole U1431D, decreasing from 51 mM close to the seafloor to 35 mM at 193 mbsf. Magnesium concentrations then fluctuate around 35 mM from 190 to 310 mbsf before increasing slightly to 38 mM near the bottom of the hole. Magnesium behaves differently from calcium, possibly due to diagenetic reactions occurring in the sediment, such as clay ion exchange and low-temperature ash alteration, rather than carbonate diagenesis. Sr^{2+} concentrations are constant at ~90 μM (same as the value of modern seawater) in the uppermost 180 m and then steadily increase with depth to 276 μM (three times modern seawater value) at 420 mbsf before decreasing to 178 μM near the bottom of the hole. The highest Sr^{+} concentrations are within lithostratigraphic Units

Figure F44. Interstitial water sulfate, alkalinity, ammonium, and phosphorous, Holes U1431A (red) and U1431D (black). Blue dashed line = modern seawater value.

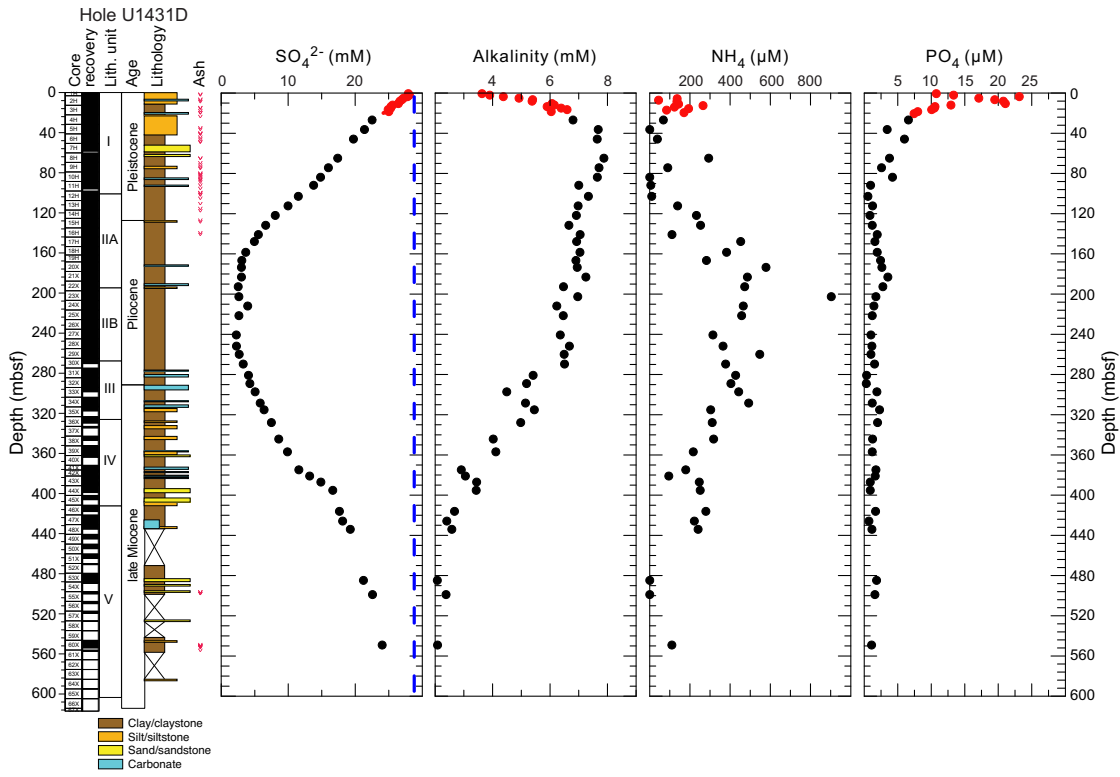


Figure F45. Interstitial water calcium, magnesium, strontium, and boron, Holes U1431A (red) and U1431D (black). Blue dashed lines = modern seawater values.

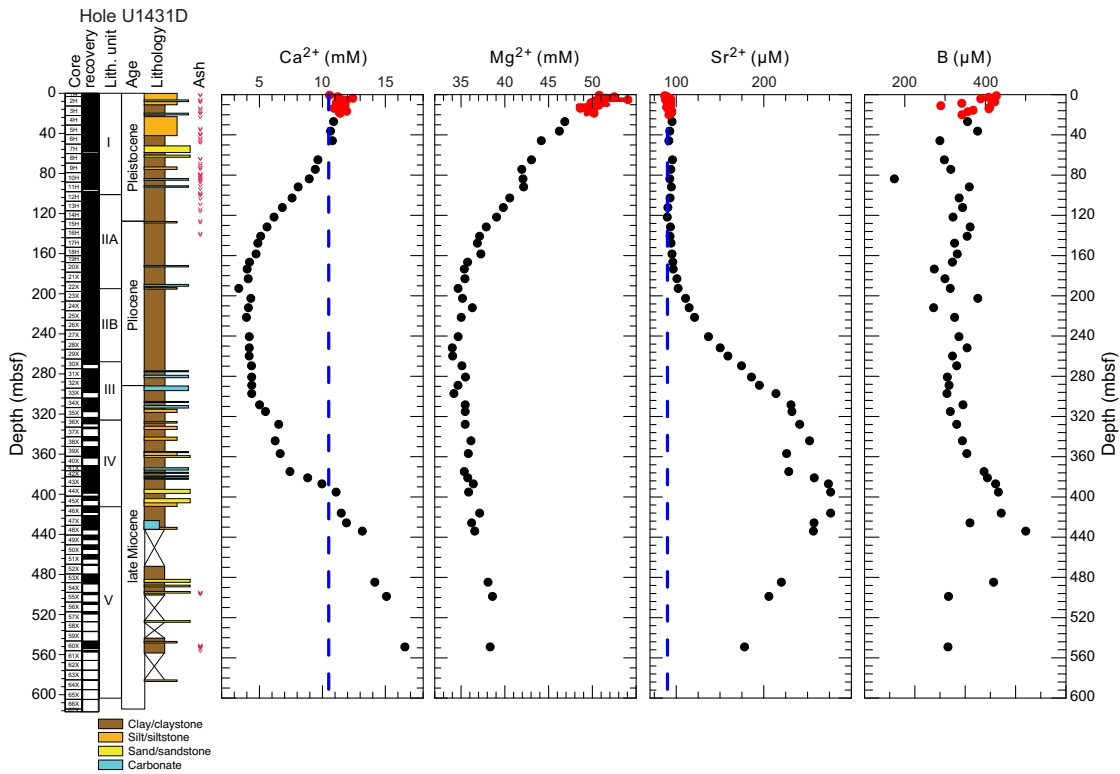


Figure F46. Interstitial water bromide, chloride, sodium, and potassium, Holes U1431A (red) and U1431D (black). Blue dashed lines = modern seawater values.

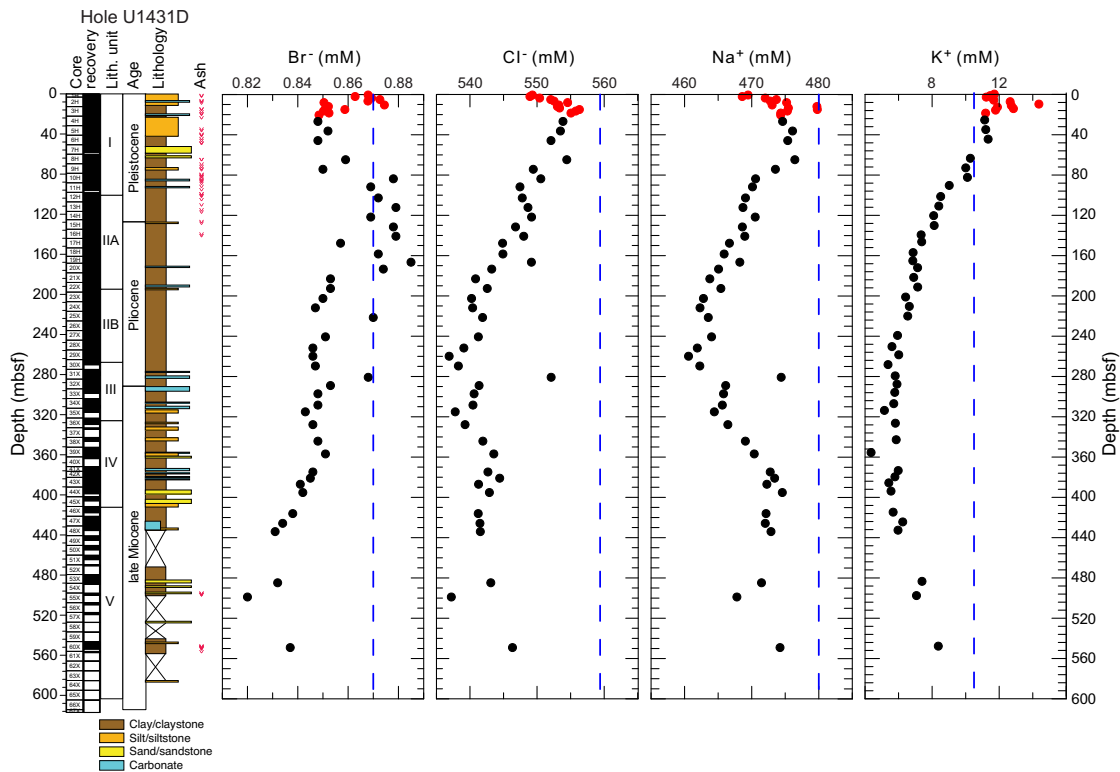


Figure F47. Interstitial water iron, manganese, lithium, and silica, Holes U1431A (red) and U1431D (black). Blue dashed line = modern seawater value.

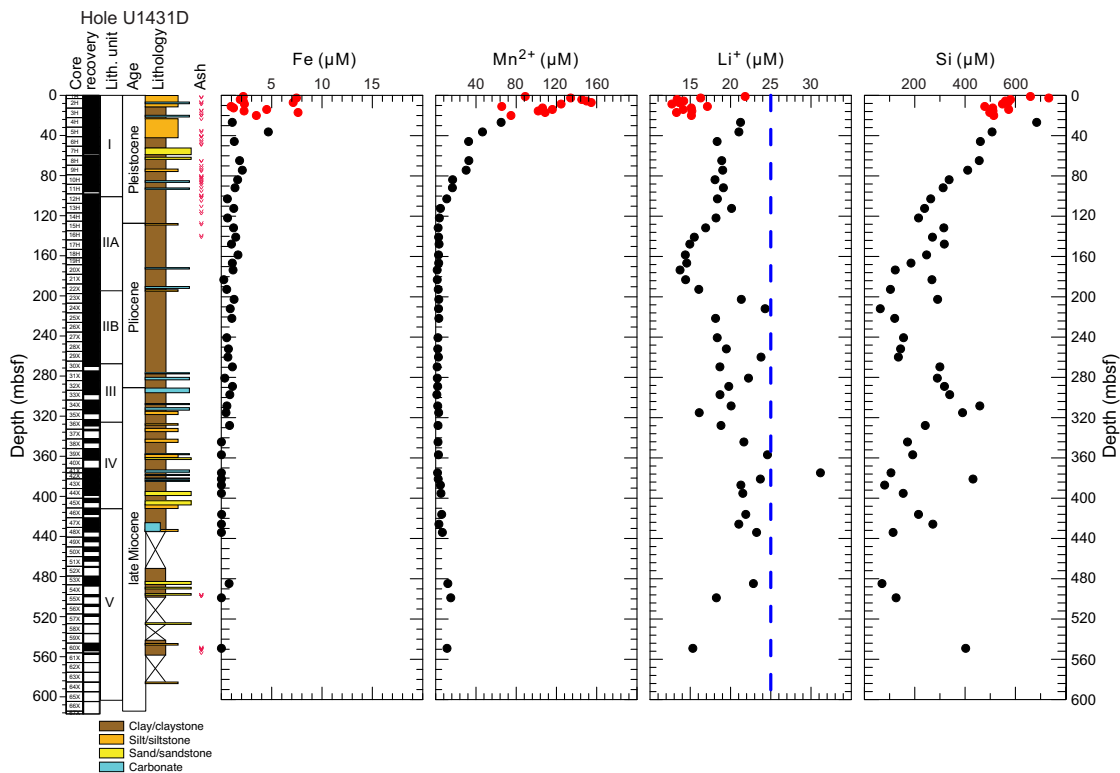


Table T13. Interstitial water major element concentrations, ammonium, alkalinity, bromide, calcium, chlorine, magnesium, pH, phosphate, potassium, salinity, sodium, and sulfate, Holes U1431A and U1431D. [Download table as .csv.](#)

Table T14. Interstitial water minor element concentrations, boron, barium, iron, lithium, manganese, strontium, and silica, Holes U1431A and U1431D. [Download table as .csv.](#)

IV–V, which contain nannofossil ooze interbeds, indicating that the increased values are mostly caused by carbonate recrystallization.

Bromide, chloride, and alkalis (sodium and potassium)

Downhole profiles of chloride, bromide, sodium, and potassium in Hole U1431D are shown in Figure F46. Chloride concentrations fluctuate slightly with depth, ranging between 537 and 554 mM (slightly lower than the modern seawater value of 559 mM) throughout the hole. The sodium profile mimics that of chloride, with concentrations of 461–476 mM, which are slightly lower than the modern seawater value (480.7 mM). Bromide concentrations range from 0.82 to 0.89 mM. Concentrations slightly higher than that of modern seawater (0.87 mM) occur close to the seafloor and also in an interval from 80 to 160 mbsf. Below 160 mbsf, bromide concentrations decrease downhole with a minimum value of 0.82 mM at 499 mbsf. The bromide depth profile is mostly controlled by seawater diffusion and organic matter diagenesis in the sediment.

K⁺ concentrations are higher than that of modern seawater (10.5 mM) in the uppermost 50 m. This phenomenon has been observed at numerous sites such as Integrated Ocean Drilling Program Sites U1381 and U1414 and has been attributed to ion exchange with clay minerals (Expedition 334 Scientists, 2012; Harris et al., 2013). Below 50 mbsf, K⁺ concentrations decrease with depth from the seawater value of 10.5 mM to a minimum value of 4 mM at 360 mbsf. Below 400 mbsf, K⁺ concentrations increase from 5.5 to 8.4 mM near the bottom of the hole.

Barium, boron, lithium, silica, iron, and manganese

Downhole distributions of boron, iron, manganese, lithium, and silica are shown in Figures F45 and F47, and concentrations of these elements, plus barium, are given in Table T14. Barium concentrations are elevated with respect to modern seawater (0.032–0.15 μM), ranging from 0.35 to 9.9 μM. In the uppermost 160 mbsf, Ba²⁺ concentrations are relatively constant, ranging from 0.35 to 2 μM. Below 160 mbsf, Ba²⁺ concentrations increase with depth, reaching a maximum value of ~9.9 μM between 210 and 220 mbsf and then decrease to 0.52 μM near the bottom of the hole. High Ba²⁺ concentrations occur at 160–280 mbsf, which corresponds to the minimum sulfate interval. Ba²⁺ concentrations are likely controlled by the stability of the mineral barite (BaSO₄). The Ba²⁺ increase may be the result of in situ barite dissolution due to sulfate reduction or the migration of Ba²⁺ in the low-sulfate fluid. Shore-based solid-phase barium analyses will be critical for determining the origin of the elevated barium and the history of fluid flow.

Boron concentrations vary from 170 to ~480 μM with a general decreasing trend with depth in the uppermost 80 mbsf. From 90 to 300 mbsf, boron concentrations vary slightly around 300 μM. Boron concentrations then increase from 310 to 500 μM over the interval from 320 to 440 mbsf, before decreasing with depth to 300 μM near the bottom of the hole.

Figure F48. Headspace methane, Hole U1431D.

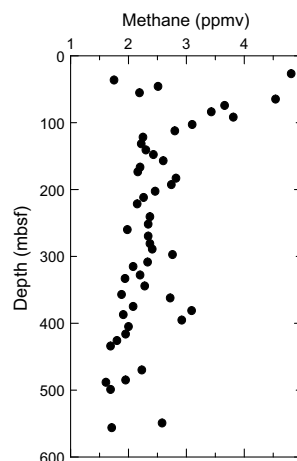


Table T15. Hydrocarbon concentrations of headspace gas, methane and ethane, Holes U1431A and U1431D. [Download table as .csv.](#)

In the uppermost 25 m, lithium concentrations range from 12 to 21.8 μM, lower than the modern seawater value (25 μM). Lithium concentrations then decrease from 21.2 μM at 27 mbsf to a minimum of 13.7 μM at 170 mbsf. Lithium concentrations in this interval are most likely controlled by secondary mineral precipitation and clay ion exchange reactions. Below 170 mbsf, lithium concentrations vary with depth and reach a maximum of 31.2 μM at 375 mbsf and then decrease with depth to 15.3 μM near the bottom of the hole.

The dissolved Si profile reflects lithology and silicate mineral diagenesis. In the upper 20 mbsf, silica concentrations range from 440 to 795 μM, much higher than the modern seawater value (0–180 μM). Below 30 mbsf, silica concentrations decrease to a minimum value of 62 μM at ~210 mbsf within an interval of dominantly clay-rich sediment. Silica concentrations increase with depth to ~460 μM at 320 mbsf and then vary significantly downhole, with values ranging from 80 to 400 μM near the bottom of the hole.

Dissolved iron concentrations range from 1.0 to 18.6 μM in the uppermost 20 mbsf. Below this, dissolved iron concentrations mostly vary between 0 and 2 μM with a maximum value of 4.7 μM at 36 mbsf.

Dissolved manganese concentrations increase slightly from 80 μM close to the seafloor to a maximum of 162 μM at 7.5 mbsf and then vary between 66 and 150 μM downhole to 20 mbsf. Below 20 mbsf, concentrations decrease with depth from 65 to 3.5 μM at 120 mbsf and then remain constant at ~2 μM to 390 mbsf, before increasing to >10 μM near the bottom of the hole.

Headspace gas geochemistry

Headspace gas was monitored according to the standard protocol required for shipboard safety and pollution prevention. We analyzed 53 headspace gas samples from Holes U1431A and U1431D for hydrocarbon compositions (Figure F48; Table T15). No samples were taken from Hole U1431E because of the indurated nature of the rocks. Methane (C₁) was the only hydrocarbon detected in Hole U1431A, ranging from 3 to 5 ppmv, all within background levels. Methane is also the predominant hydrocarbon present throughout Hole U1431D, varying from 1.75 to 4.81 ppmv. Ethane (C₂) was ob-

served only in Section 349-U1431D-44X-3 (395.2 mbsf), at 1.32 ppmv (Table T15).

Sediment geochemistry

Total organic carbon and calcium carbonate

The distribution of total organic carbon (TOC), calcium carbonate (CaCO₃), and the total organic carbon to total nitrogen ratio (C/N) at Site U1431 is illustrated in Figures F49 and F50 and listed in Table T16. Samples were selected to provide a measure of the carbon content in different lithologies. CaCO₃ content varies from 2 to ~50 wt% with maximum values in foraminifer ooze beds within lithostratigraphic Unit III in Hole U1431D (Figure F49). TOC content varies from ~0 to 4.1 wt% (average ~0.5 wt%) in Holes U1431A and U1431D. TOC reaches a maximum of 4.1 wt% within lithostratigraphic Unit IV. C/N ratios are often used as an indicator of the origin of organic matter. C/N values in Holes U1431A and U1431D vary with depth, ranging from ~0 to 17. C/N ratios >5 suggest a mixture of marine and terrestrial sources for organic matter in sediment. Values >5 occur in the uppermost 10 mbsf and in some intervals in Units II–V.

In Hole U1431E, CaCO₃ content ranges between 0.1 and ~60 wt% (Figure F50). Although the carbonate profile shows a wide range of values, higher carbonate content typically corresponds to mudstone or sandstone horizons. TOC content varies from below the detection limit to ~0.7 wt%. Unit VII shows consistently low TOC content (<0.1 wt%), whereas a couple of higher values (0.6–0.7 wt%) occur near the top of Unit VI.

Major and minor elements in bulk sediment

We analyzed 23 sediment samples from Core 349-U1431D-2H through 53X for major and minor element concentrations by inductively coupled plasma–atomic emission spectroscopy (ICP-AES) (Figure F51; Table T17).

Total weight percentages for the major element oxides vary from 66.19 to 91.85 wt%. Weight loss on ignition (LOI) values are generally high, ranging from 5.7 to 21.6 wt%. Samples from lithostratigraphic Unit I display the greatest variation in all measured elements, whereas samples from Subunit IIB and Unit III are nearly constant in element concentrations (Figure F51). Overall, Na₂O and Co show a decrease with depth, whereas Zn remains nearly constant downhole except for some anomalies within Units I, IV, and V.

In the discriminant function diagram of Roser and Korsch (1988) that highlights the provenance signatures of sandstone-mudstone suites, Hole U1431D samples plot mostly within the field of intermediate igneous provenance (Figure F52).

Igneous rock geochemistry

Fifteen igneous rock samples from Core 349-U1431E-37R through 50R and 3 igneous clasts from volcanoclastic breccia samples within lithostratigraphic Unit VI of Hole U1431E were analyzed for concentrations of major and trace elements by ICP-AES (Table T18).

Total weight percentages for the major element oxides vary from 97.5 to 105.5 wt%. LOI serves as a rough indicator of the overall level of alteration in these rocks. LOI values in the igneous samples

Figure F49. Calcium carbonate, TOC, and C/N ratios, Hole U1431D.

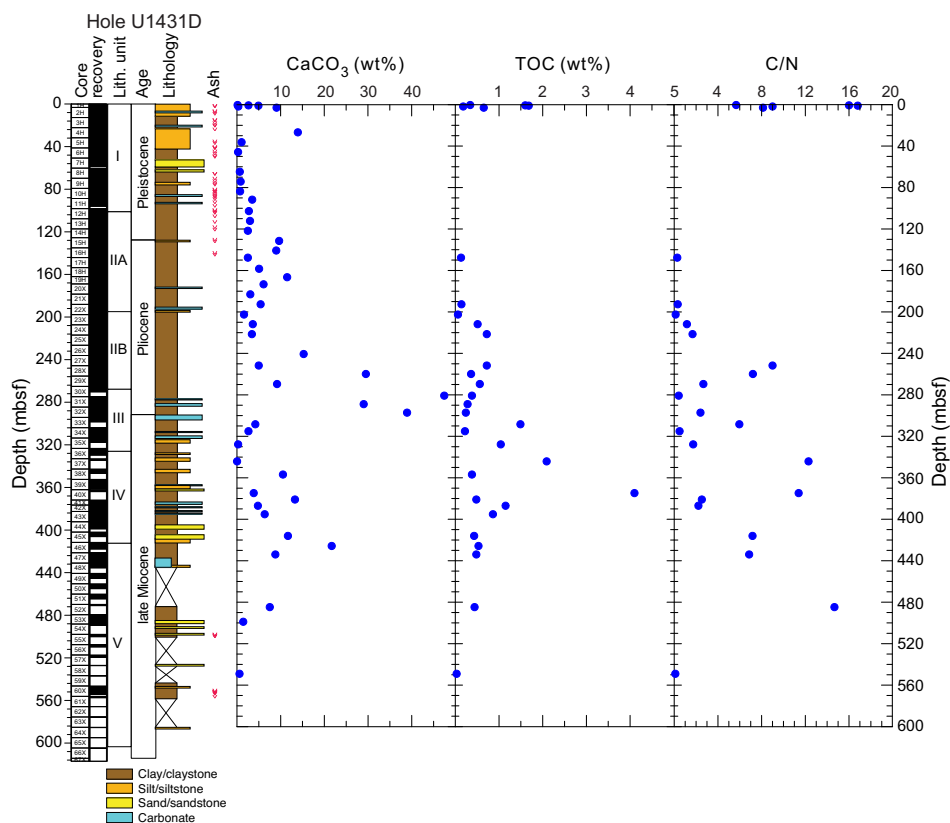


Figure F50. Calcium carbonate and TOC, Hole U1431E.

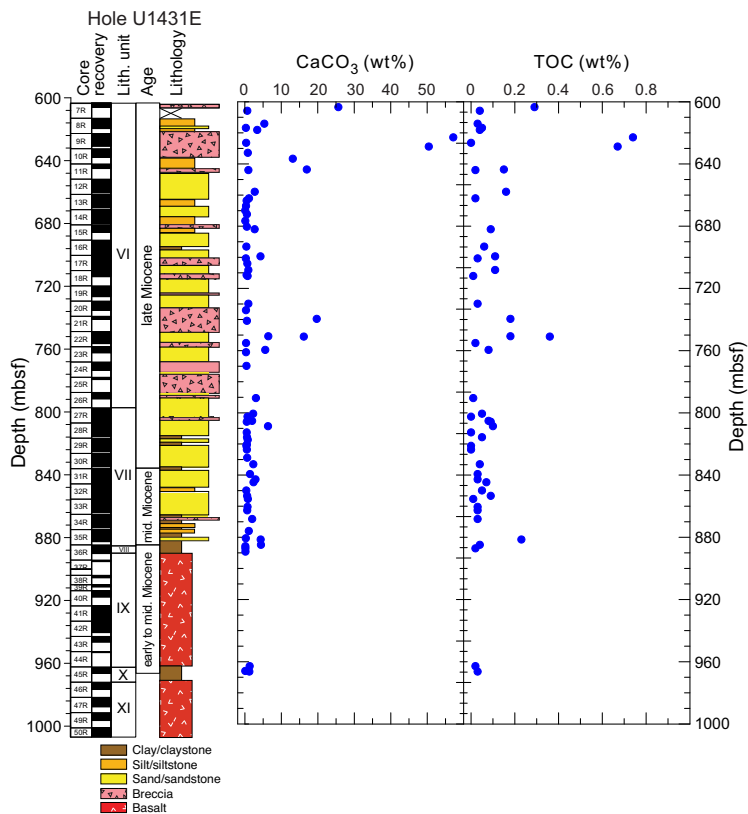


Table T16. Inorganic carbon, total carbon, TOC, carbonate, and total nitrogen concentrations and C/N ratios, Holes U1431A, U1431D, and U1431E.

[Download table as .csv.](#)

are high as a whole, ranging from 0.46 to 2.85 wt%, with five samples higher than 2.0 wt%. Three breccia clast samples have much higher LOI (2.87–8.74 wt%) than the basement igneous samples. K_2O in the igneous samples varies from below the detection limit to 0.53 wt%, but only one sample has a K_2O value higher than 0.30 wt%. The igneous samples have variable SiO_2 (44.0–51.9 wt%), Al_2O_3 (14.62–18.46 wt%), CaO (8.11–11.13 wt%), MgO (6.18–13.31 wt%), and Fe_2O_3 (8.93–12.52 wt%), whereas TiO_2 (1.01–1.77 wt%) and Na_2O (2.45–3.53 wt%) vary less. Three volcanoclastic breccia samples have much higher K_2O (1.08–2.67 wt%) and TiO_2 (2.10–3.13 wt%) than the igneous samples, although they have similar SiO_2 contents.

When plotted on the alkali versus silica diagram for volcanic rock types (Le Maitre et al., 1989) (Figure F53), the three breccia clast samples are clearly alkaline and plot in the basanite, phonotephrite, and basaltic trachyandesite fields, whereas the igneous samples are tholeiitic and all plot in the basalt field. As shown in Figure F54, the igneous samples from basement are similar to Indian Ocean MORB and Pacific Ocean MORB but are distinct from the Hainan Island ocean island basalt (OIB) and the seamount basalts in the South China Sea. Thus, igneous basalt samples from lithostratigraphic Units IX and XI are tholeiitic basalt, representative of South China Sea MORB, whereas mafic igneous clasts in the volcanoclastic breccia of Unit VI are alkaline and likely sourced from the nearby seamounts.

Microbiology

Our goal for microbiological research conducted at Site U1431 was to collect and preserve samples for shore-based characterization of the microbial communities. We collected samples on a routine basis throughout the cored intervals and on a case by case basis according to features in the cores that suggested the presence of important geological interfaces. We used a limited number of samples to start microbial cultivations aboard the ship. In addition, we also used a suite of contamination testing tracers including perfluorocarbons, microspheres, and fluid community tracers.

Specific depths sampled for microbiology at Site U1431 are shown in Figure F55. Coring at Site U1431 yielded 105 routine 5–10 cm whole-round samples to be used for microbiological analysis from the seafloor to 937 mbsf from Holes U1431B, U1431D, and U1431E. We acquired 29 whole-round samples from Hole U1431B (uppermost 17 m) and then, assuming ample core recovery, one whole-round sample per core in Holes U1431D (27–549 mbsf) and U1431E (604–937 mbsf). Whenever possible, we collected whole-round samples for microbiology adjacent to samples for interstitial water in order to understand proximal interstitial water chemistry.

We collected and preserved 76 samples for investigating the microbiology of interfaces using lipid and nucleic acid analyses. We obtained these samples mostly in the upper 200 m of Hole U1431D (Figure F55B). We sampled five ash/clay interfaces and 10 turbidite/clay interfaces. Five samples deeper than 200 mbsf were collected for interface sampling, the deepest at ~984 mbsf in Hole U1431E (Figure F55C). Fewer samples were collected at these deeper depths because of drilling-induced disturbance of the cores or the inability to easily collect interface samples because the core

Figure F51. Bulk sediment major and minor elements, Hole U1431D. Colored boxes denote lithostratigraphic units.

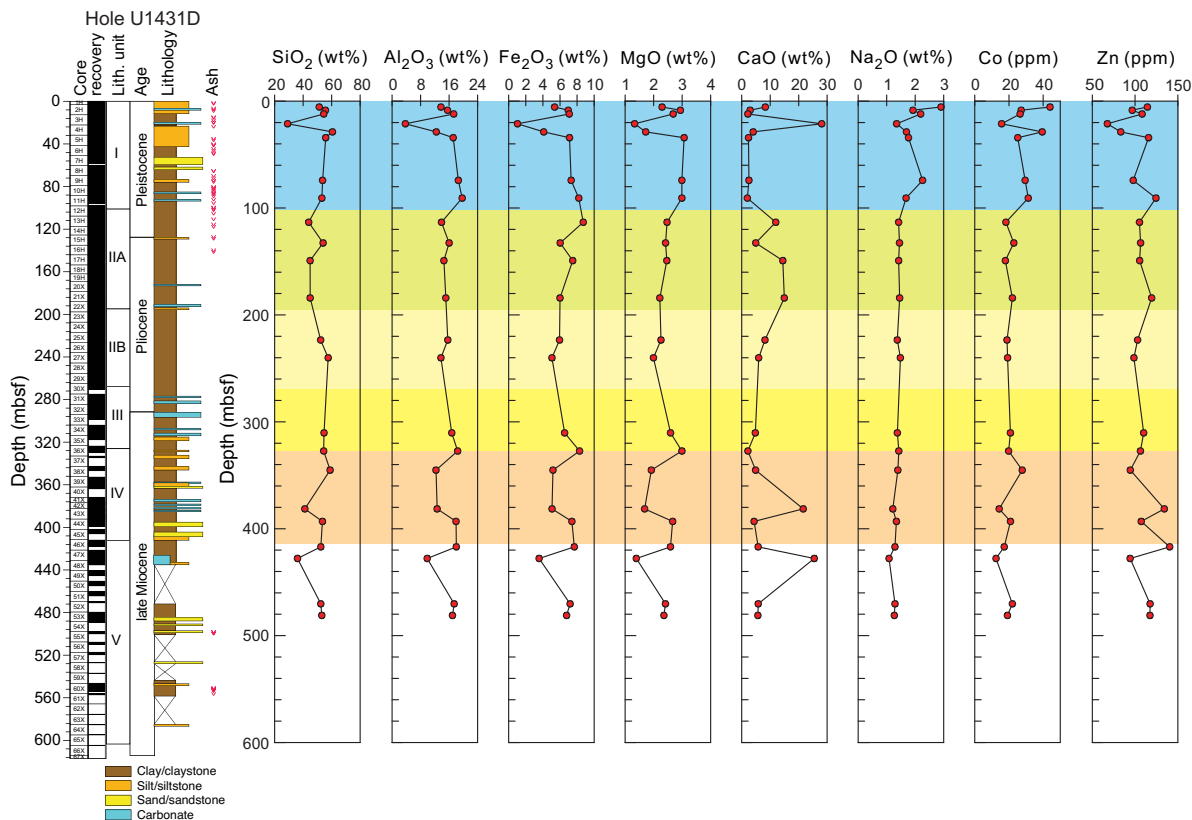
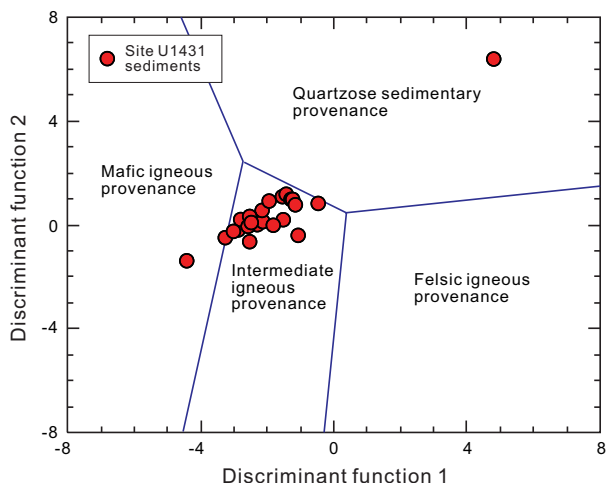


Table T17. Major element oxide (silica, titanium, aluminum, iron, magnesium, manganese, calcium, sodium, potassium, and phosphorus) and trace element (barium, cobalt, chromium, copper, scandium, strontium, vanadium, zinc, and zircon) composition and LOI of sedimentary samples, Hole U1431D. [Download table as .csv.](#)

Table T18. Major element oxide (silica, titanium, aluminum, iron, magnesium, manganese, calcium, sodium, potassium, and phosphorus) and trace element (barium, cobalt, chromium, copper, scandium, strontium, vanadium, zinc, and zircon) composition and LOI of igneous basement samples and clasts from the volcanoclastic breccia, Hole U1431E. [Download table as .csv.](#)

Figure F52. Discriminant function diagram for provenance signatures of sandstone-mudstone suites (after Roser and Korsch, 1988). Function 1 = $30.638 TiO_2/Al_2O_3 - 12.541 Fe_2O_3/Al_2O_3 + 7.329 MgO/Al_2O_3 + 12.031 Na_2O/Al_2O_3 + 35.402 K_2O/Al_2O_3 - 6.382$. Function 2 = $56.600 TiO_2/Al_2O_3 - 10.879 Fe_2O_3/Al_2O_3 + 30.875 MgO/Al_2O_3 - 5.404 Na_2O/Al_2O_3 + 11.112 K_2O/Al_2O_3 - 3.89$.



was indurated. We selected all interface samples depending on recognition of key intervals through consultation with shipboard sedimentologists or petrologists.

Microbiological analyses

Most of the samples collected at Site U1431 were preserved for shore-based analysis. Samples to be used for DNA and RNA extractions and sequencing were frozen at $-80^{\circ}C$, and samples to be used for lipid extraction and analysis were frozen at $-80^{\circ}C$. Subsamples of the whole-round samples were prepared for fluorescent in situ hybridization (67 subsamples preserved at $-20^{\circ}C$) and single cell genomics (74 subsamples preserved at $-80^{\circ}C$). Subsamples from four cores (349-U1431E-42R, 43R, 46R, and 47R) were selected for cultivation-based studies to enrich for iron-oxidizing microbes. We inoculated these samples into a seawater-based medium (described in Smith et al., 2011) containing olivine as a source of reduced iron. Minimal oxygen was provided, and the enrichments were incubated at room temperature in the dark. A negative control (olivine plus seawater-based medium but without core sample inoculation) was also prepared to screen for laboratory contaminants that may have been introduced during preparation of the enrichments.

Figure F53. Total alkalis vs. silica diagram, Hole U1431E. Classification of volcanic rock types from Le Maitre et al. (1989). Dashed line divides tholeiitic and alkalic lavas of Hawaii (Macdonald and Katsura, 1964; Macdonald, 1968). Shown for comparison are data for Indian Ocean MORB from the Geochemical Rock Database (geo.roc.mpch-mainz.gwdg.de), SCS seamounts (Tu et al., 1992; Hékinian et al., 1989), Hainan Island OIB (Wang et al., 2012), and Pacific Ocean MORB (Zhang et al., 2009, 2012a, 2012b, 2013).

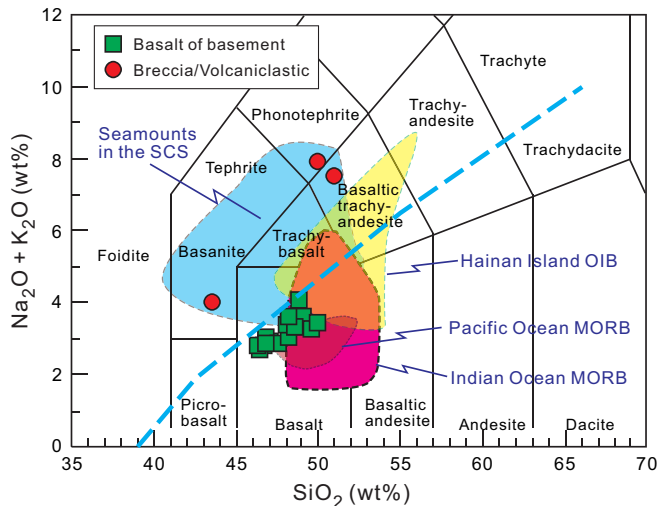
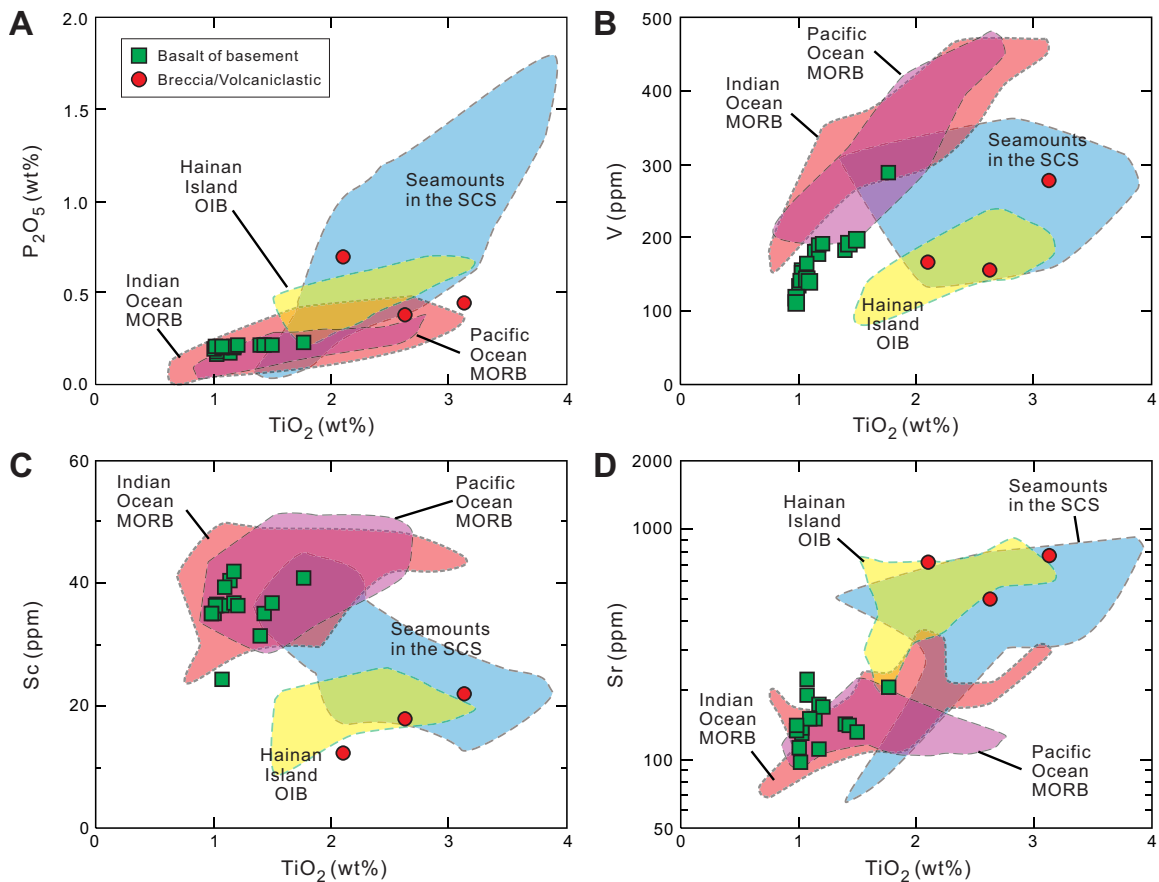


Figure F54. A–D. TiO_2 vs. P_2O_5 , V, Sc, and Sr, Hole U1431E. Shown for comparison are data for Indian Ocean MORB from the Geochemical Rock Database (geo.roc.mpch-mainz.gwdg.de), SCS seamounts (Tu et al., 1992; Hékinian et al., 1989), Hainan Island OIB (Wang et al., 2012), and Pacific Ocean MORB (Zhang et al., 2009, 2012a, 2012b, 2013).

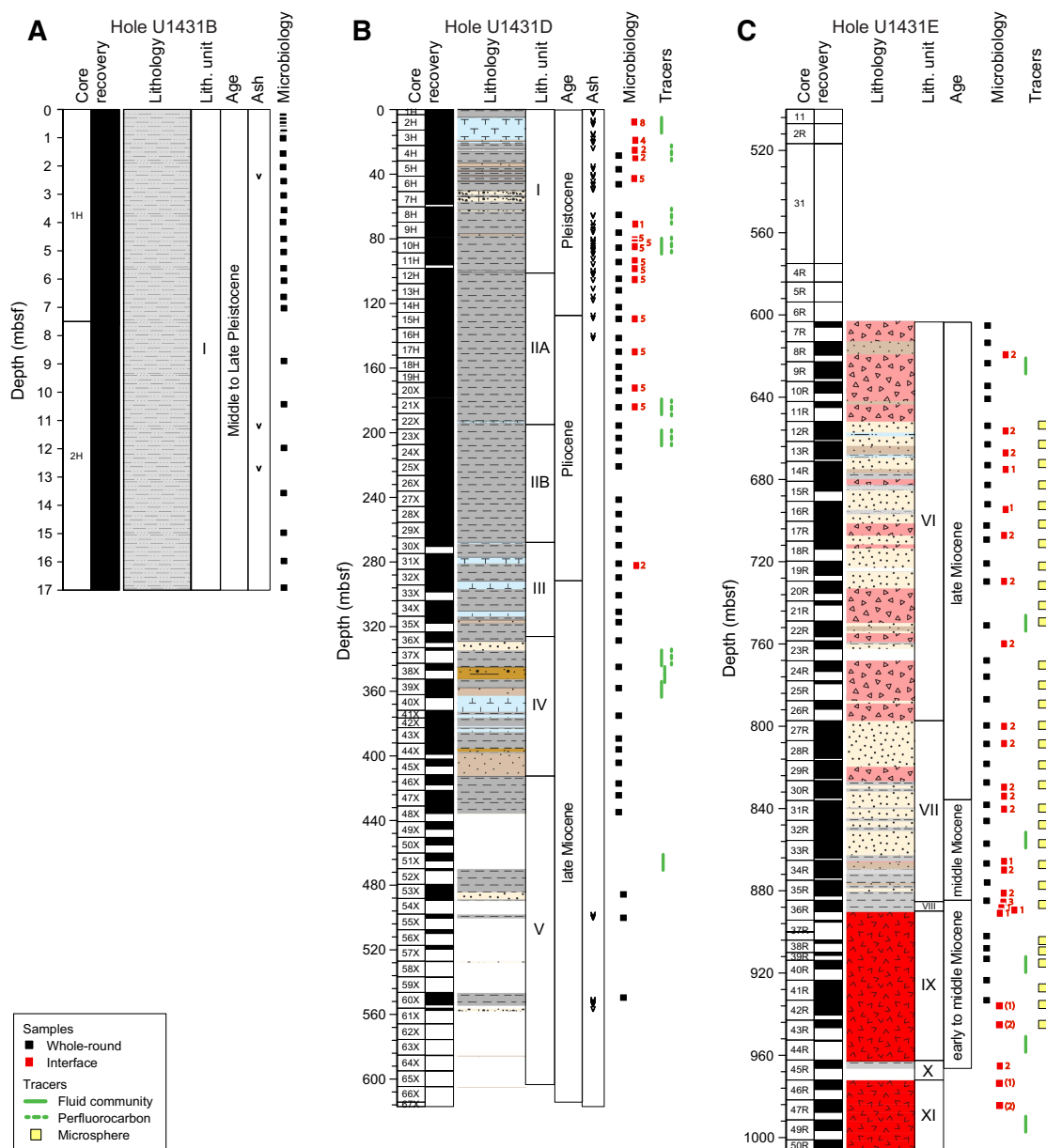


Contamination testing

We used three different methods of contamination testing during coring of Holes U1431B, U1431D, and U1431E. The PFT perfluoromethylcyclohexane was introduced into the drilling fluid during coring of Hole U1431D from 0 to 197.7 mbsf to trace potential drilling fluid contamination of the cores (Figure F55B). PFT samples were acquired from three APC and three XCB cores while coring the upper sections of Hole U1431D. PFT results are ambiguous. In some cases (e.g., Section 349-U1431D-4H-7), PFT concentrations measured on samples from the outside of the core are higher than those measured on the inside of the core; however, in other situations the inside of the core has higher levels (e.g., as occurred with the sample from Section 349-U1431D-8H-7). Given the small number of samples collected for analysis, we cannot conclude how effective the PFTs are as a tracer for contamination.

Microsphere tracers were used with the RCB coring system in Hole U1431E by adding them to the core catcher sub before cutting Cores 349-U1431E-12R through 44R (651.8–962.3 mbsf; Figure F55C). Two microsphere samples were collected from each of these cores: one from scrapings of the core surface and one as a subsample from the interior of each whole-round sample. We used the Procedure for Curation of DeepBIOS (www.kochi-core.jp/DeepBIOS) to conduct preliminary counting of the microspheres on the ship, but final counts will be performed in shore-based laboratories.

Figure F55. Microbiology whole-round and interface samples and contamination testing samples, Site U1431. Numbers next to red squares indicate number of samples taken from those depths.



Fourteen fluid community tracer (FCT) samples were collected from the drilling fluids to track the microbial communities typical of the seawater and other mud constituents (Figure F55). The FCTs were the most comprehensively sampled of the contamination testing tracers, as they were collected periodically throughout the coring of Holes U1431D and U1431E and correspond to cores obtained from depths between 5 and 1000 mbsf. Microbial community DNA and lipids from FCT samples will be compared to the same measurements made on the core samples to determine if the drilling fluids contain microbes that can be regularly tracked as recognizable contaminant taxa.

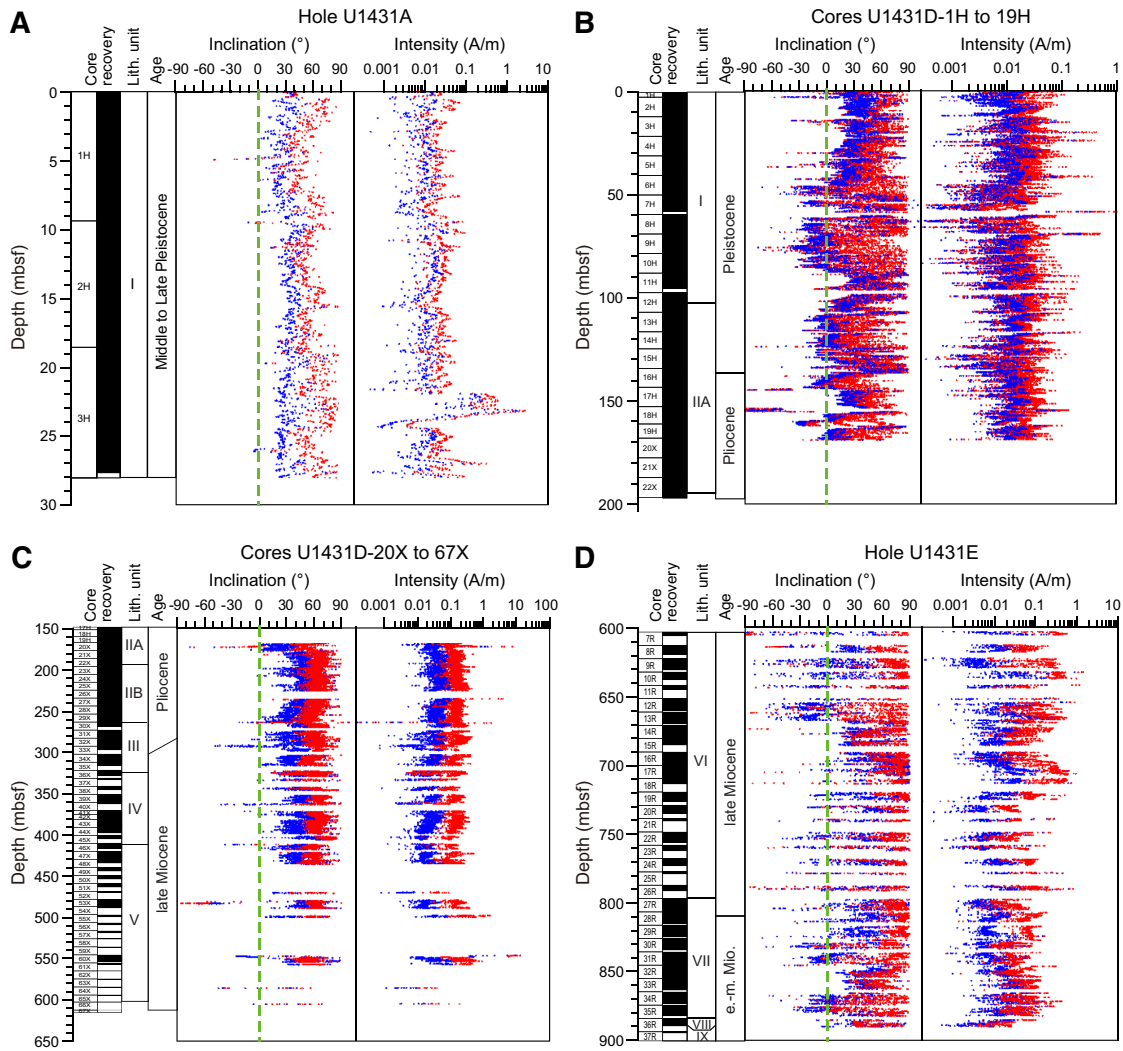
Paleomagnetism

At Site U1431, Cores 349-U1431A-1H through 3H and 349-U1431D-1H through 19H were cored with the APC using nonmag-

netic core barrels. Cores 349-U1431D-20X through 67X were cored with the XCB using a standard cutting shoe. Cores in Hole U1431E were cored using the RCB. Cores 349-U1431D-1H through 19H were oriented with the FlexIT orientation tool. Paleomagnetic directions can be used to construct magnetostratigraphy for dating sediment. Orientation data (i.e., corrected declinations) facilitate the magnetostratigraphy investigation for Site U1431.

We made pass-through magnetometer measurements on all archive-half cores and on representative discrete samples taken from the working halves. In order to isolate the characteristic remanent magnetization (ChRM), sedimentary archive-half cores were demagnetized in an alternating field (AF) using 5, 10, 15, and 20 mT steps and then were measured with the pass-through superconducting rock magnetometer (SRM) at 2.5 cm intervals. Selected discrete samples were first AF demagnetized to 20 mT using the 2G SRM and then with an ASC Scientific D-2000 AF demagnetizer using 30,

Figure F56. A–D. Paleomagnetic measurements of NRM inclination and intensity on archive sections after 0 mT (red) and 20 mT (blue) AF demagnetization.



40, 60, 80, and 100 mT steps. About 30 discrete samples were also subjected to stepwise thermal demagnetization up to 400°C with steps of 100°C, and then up to 600°C at 50°C steps. Remanence was measured using the SRM. We analyzed the results in Zijderveld diagrams (Zijderveld, 1967) and calculated the ChRM direction using principal component analysis (Kirschvink, 1980).

Natural remanent magnetization of sedimentary cores

To illustrate the overall demagnetization behavior, we show natural remanent magnetization (NRM) intensities and inclinations before and after 20 mT AF demagnetization for the recovered cores in Figure F56. Variations in NRM intensity are generally correlated with lithology. Paleomagnetic measurements indicate that the silty clay and clayey silt in lithostratigraphic Unit I (0–101.16 mbsf) have a mean NRM intensity on the order of 3×10^{-2} A/m, whereas the clay with nanofossils in Unit II (101.16–267.82 mbsf) has higher NRM intensity ($\sim 6 \times 10^{-2}$ A/m). Many discrete peaks of higher NRM and magnetic susceptibility values (see **Physical properties**) in both Units I and II can be tied directly to the presence of volcanic tephra layers (see **Lithostratigraphy**). To the first order, this indi-

cates that the magnetic moment is determined by the concentration of magnetic minerals.

As with many other ocean drilling expeditions, remagnetization imparted by the coring process was encountered at Site U1431. NRM inclinations are strongly biased toward vertical (mostly toward +90°) in a majority of cores. For the recovered sediment core sections, AF demagnetization to 10 mT seems to be effective in removing the drilling-induced overprinting magnetization for a high percentage of samples, as shown by inclinations shifted toward shallower values that are comparable to the expectation for the site ($\sim \pm 29^\circ$). Magnetization intensity also decreases by a factor of ~ 3 –4 after 5 mT demagnetization and by an order of magnitude after 20 mT demagnetization (Figure F56). For many core sections from lithostratigraphic Units II–V, AF demagnetization up to 20 mT was not effective in recovering primary remanence magnetization. Inclinations shifted toward shallower values but are still steeper than the expected value for the site, indicating the near-vertical drilling-induced remagnetization was not completely removed (Figure F56C). Therefore, the paleomagnetic results for this interval (cored by XCB) were not used to construct the magnetostratigraphy for Site U1431 at this time. Detailed postcruise study should help remedy the magnetostratigraphy for this interval.

Demagnetization properties

NRM declinations of Cores 349-U1431D-1H through 19H before orientation correction deviate significantly from the expected values for this site. After orientation correction using data from the orientation tool, declinations become close to magnetic north for normal polarity cores and magnetic south for most cores with negative inclinations, indicating that the primary sources of magnetization are remanent magnetization (Figure F57). ChRM declinations can be used to determine the orientation of deeper cores (see [Magnetostatigraphy](#)).

Magnetic properties observed in section halves were also confirmed through discrete sample measurements (Figure F57). The nearly vertical overprint was removed by AF demagnetization of 5–10 mT for nearly all samples. AF demagnetization was generally successful in isolating ChRM for most discrete samples. Most discrete samples in lithostratigraphic Unit I show straightforward demagnetization behavior and reveal ChRM (Figures F57B, F57C); however, several discrete samples display more complicated demagnetization paths that do not simply decay toward the origin (Figure F57D).

Thermal demagnetization results show that magnetite and hematite are the dominant magnetic carriers for ChRM (Figures F57E, F57F). The secondary overprints can be easily removed by 100°C thermal treatment. Because of the complexities of coercivity and unblocking spectra of the NRM, we suggest that sequential demagnetization by combining AF and thermal methods could be the best approach to fully isolate ChRM, specifically for Cores 349-U1431D-20X through 67X.

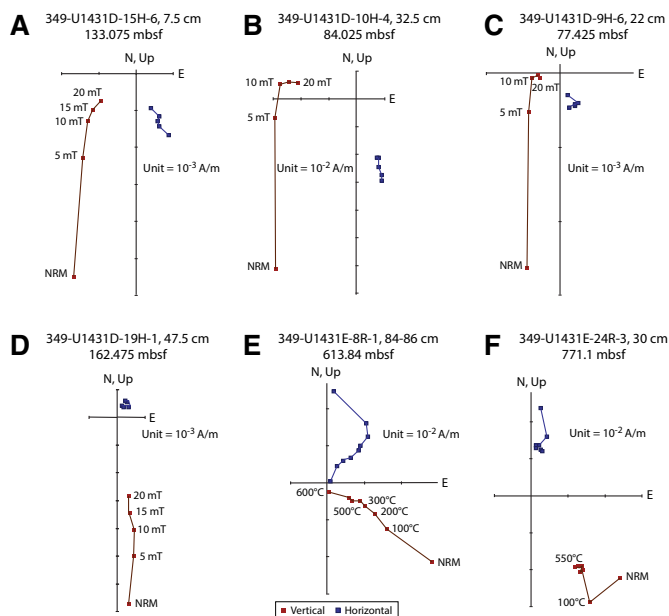
Inclinations after 20 mT AF demagnetization are illustrated in Figure F58. The similarity of results between Holes U1431A and U1431D for the upper 30 m strongly attests to the fidelity of the paleomagnetic records. In addition, this indicates that the chronology of Hole U1431D is strongly correlated to that of Hole U1431A. We note that steep inclinations (>50°) are present throughout the profile, most likely still affected by the drilling overprint or post-depositional disturbances.

Magnetostatigraphy

At the latitude of Site U1431 (~15°N), a near 180° shift in declination in the cores is a more reliable sign of a polarity transition than changing inclinations, considering that the vertical component of magnetization caused by the drilling process affects inclination more strongly than declination.

The construction of magnetostatigraphy is based on correlation between the measured polarity pattern and the geomagnetic polarity timescale (Gradstein et al., 2012), as well as on constraints from biostratigraphy. By comparing inclination and declination, we observed that declination exhibits much sharper subchron boundaries than inclination. As shown in Figure F58, several magnetic excursions may be discerned on the basis of changes in sign of both inclinations and declinations (e.g., at ~46 and ~87 mbsf). It has been recently documented that there are small magnetic polarity changes after the Brunhes/Matuyama Chron boundary (0.78 Ma) (e.g., Jovane et al., 2008; Saganuma et al., 2011). Some of the small inclination fluctuations in Hole U1431D (Figure F58) may correspond to such changes, but further evidence is needed to determine their true origin. We noticed that some of the directional swings just deeper than the Brunhes/Matuyama boundary correspond to sandy layers, possibly suggesting that these swings are associated with the loose material and disturbances.

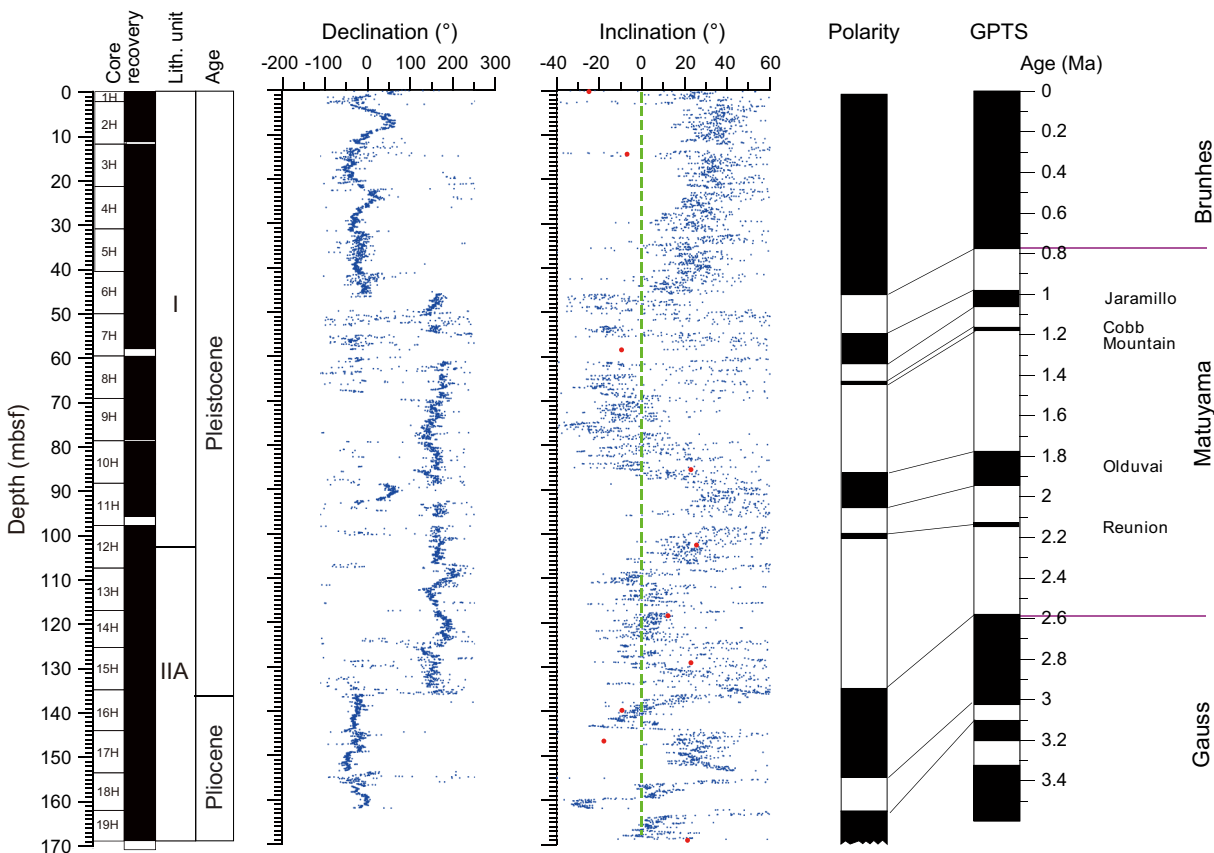
Figure F57. A–F. Representative vector endpoint diagrams (Zijderveld, 1967) for sediment samples through stepwise AF or thermal demagnetizations. All samples display a normal vertical component of drilling-induced magnetization that is reduced or removed after 5 mT demagnetization or by 100°C thermal demagnetization.



By integrating both inclination and declination data, the Brunhes/Matuyama Chron boundary (0.78 Ma) is confidently placed at ~46 mbsf and the Matuyama Chron is defined between ~46 and ~135 mbsf (Figure F58). The Jaramillo Subchron (0.98–1.072 Ma) was also identified between ~51.87 and 67.6 mbsf. The Olduvai (1.78–1.95 Ma) and Reunion (~2.128–2.148 Ma) Subchrons are defined between ~87 and ~94 mbsf and between ~99 and 100 mbsf, respectively. From 125 to ~170 mbsf, paleomagnetic records reveal three positive and two reversed subchrons. This pattern is highly consistent with the Gauss Chron. For cores not oriented with the FlexIT orientation tool, declinations cannot be used for constructing magnetostatigraphy. Thus, only inclinations are used to define the polarity reversal boundaries for the deeper sections. This tends to produce relatively wider subchrons, but the overall pattern of the magnetostatigraphy is still valid. More detailed postexpedition paleomagnetic studies are needed to resolve the polarity assignment and improve the magnetostatigraphy at Site U1431.

As mentioned above, strong magnetic overprinting from XCB coring on Cores 349-U1431D-20X through 67X precludes reliable identification of any polarity subchrons. In contrast, sections in Hole U1431E cored with the RCB reveal more reasonable polarity patterns from both section-half and discrete-sample measurements (blue and red circles in Figure F59, respectively). Preliminary micropaleontological studies suggest that sediment between 600 and 650 mbsf is late Miocene in age (<10 Ma). With this age constraint, we define the Chron C5n/C5r boundary (11.056 Ma) at ~716 mbsf (see [Biostratigraphy](#)). Between ~720 and ~785 mbsf is a series of short normal and reversed polarities. We tentatively correlate this interval to Chron C5r (~11.06–12.05 Ma) based on the overall similarity of the polarity pattern. However, the presence of calcareous nannofossil taxa with first appearance datums between ~8.3 and 8.7 Ma at this depth (Figure F24) is inconsistent with this

Figure F58. Magnetostratigraphic results, Hole U1431D. Paleomagnetic declination and inclination after 20 mT AF demagnetization. Red circles = discrete samples. For polarity and GPTS (Gradstein et al., 2012), black = normal and white = reversed polarity.



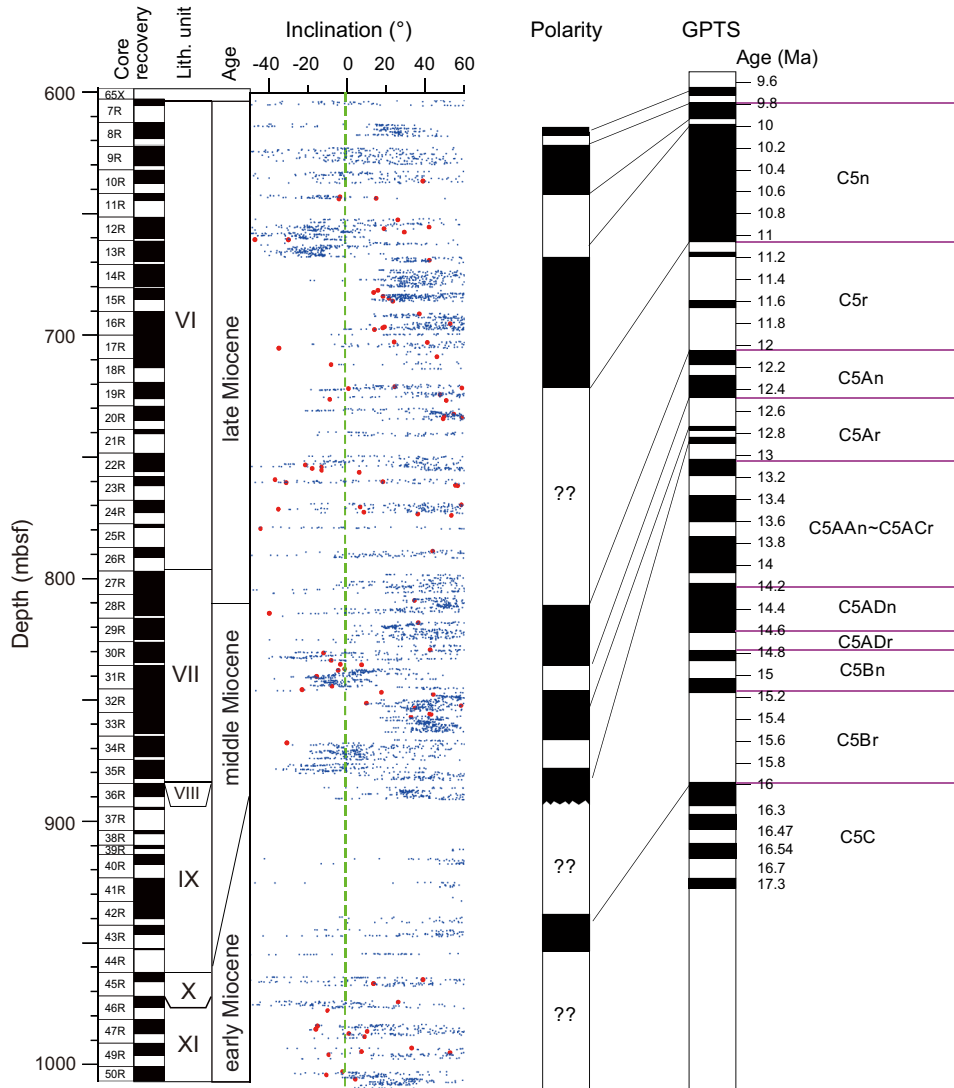
interpretation. Additional shore-based studies are needed to resolve this mismatch.

Between 785 and 890 mbsf, three normal and two reversed polarities can be tied to Chron C5An and the younger reversed sub-chron within C5Ar. Therefore, the age at ~890 mbsf is ~12.7 Ma. These paleomagnetically inferred ages are remarkably consistent with nannofossil and foraminifer biostratigraphy for this interval (Figure F24).

For basement rock, the observed paleomagnetic signals cannot be directly linked to the geomagnetic polarity timescale because of the intermittent nature of basalt eruptions and apparently extremely low sedimentation rate of the pelagic clay sediment in Cores 349-

U1431E-36R through 45R. Nevertheless, we observed normal and reversed polarities within the interval of basement rock, indicating that the eruption of the basalt units may have spanned a significant amount of time. In particular, core sections between 962.5 and 972.0 mbsf show dominantly normal polarity. Radiolarian biostratigraphy indicates an early Miocene age (~16.7–17.5 Ma) for this interval (Core 45R) (see **Biostratigraphy**), suggesting that the observed polarity zones should correlate with Chron C5c (16.2–17.3 Ma). Reversal rates during this time interval are typically ~2 times/million years, and it takes ~5000 y to complete a reversal. Therefore, we estimate that eruption of recovered basalt at this site spans at least 5000 y and up to ~1 million years.

Figure F59. Magnetostratigraphic results, Hole U1431E. Paleomagnetic inclination after 20 mT AF demagnetization. Red circles = discrete samples. For polarity and GPTS (Gradstein et al., 2012), black = normal and white = reversed polarity. ?? = uncertainty.



Physical properties

We measured physical properties on whole-round cores for all five holes (U1431A–U1431E) drilled at Site U1431. These measurements include *P*-wave velocity, bulk density (using gamma ray attenuation), magnetic susceptibility, and natural gamma radiation (NGR). No measurements were done on the split half sections of cores from Holes U1431A–U1431C. For cores from Holes U1431D and U1431E, physical property measurements were also performed on split cores (thermal conductivity and *P*-wave velocity measured with the *x*-caliper and *z*-bayonet), as well as on discrete samples (porosity, moisture, and density). These measurements were used to compare with lithostratigraphic description, to correlate core observations with downhole logging, and to compare stratigraphy between holes and with seismic profiles. The measurements of *P*-wave velocity, bulk density, and magnetic susceptibility using the Whole-Round Multisensor Logger (WRMSL) agree with those on split cores or on discrete samples for cores recovered with the APC in the uppermost 170 m (through Core 349-U1431D-19H). A small difference is usually observed in the magnetic susceptibility and *P*-wave velocity data between measurements on whole-round cores and on

section halves or samples from XCB or RCB coring because of the slightly smaller diameter of the cores causing water/air infill of the gap between the core and the liner (Figure F60).

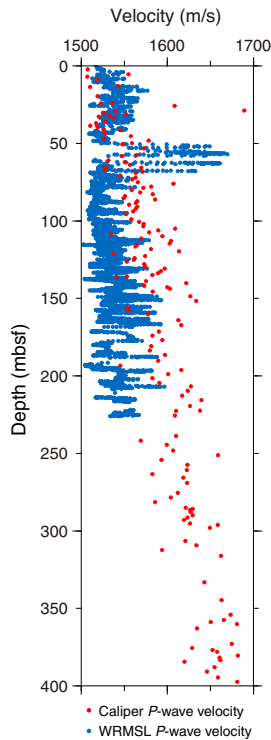
Whole-Round Multisensor Logger measurements

Measurement points that are clearly out of range were removed from the whole-round core data, which were then smoothed using a 5-point average moving window. The combined measurements of physical properties of Holes U1431D and U1431E are shown in Figure F61.

Gamma ray attenuation bulk density

Bulk density increases with depth from 1.6 to nearly 2 g/cm³ in the uppermost 150 m (Figure F61) and remains constant near 2 g/cm³ downhole to ~600 mbsf, which coincides with the dominant clay lithology of lithostratigraphic Units II–V. Density decreases to 1.5 g/cm³ in the coarser grained intervals of Units VI and VII and increases again, ranging from 2 to 2.8 g/cm³, in the basalt of Units IX and XI.

Figure F60. WRMSL *P*-wave velocity and *x*-caliper *P*-wave velocity. Below 63 mbsf, WRMSL *P*-wave velocities tend to be lower than caliper *P*-wave velocities. At ~50–63 mbsf, significantly higher WRMSL *P*-wave velocity values might be related either to sand/sandstone not measured with the caliper or to other unidentified factors.



Magnetic susceptibility

Magnetic susceptibility data are sensitive to magnetic mineral content and mineralogy of the formation. These data help identify specific lithologies, such as volcanic ash and igneous rock (Figure F61; Table T19). The background magnetic susceptibility value is about $<200 \times 10^{-5}$ SI for sedimentary units. Ash layers in Units I and II of Hole U1431D are characterized by magnetic susceptibility peaks (arrows in Figure F61). Two layers several meters thick near 670 and 710 mbsf show relatively high magnetic susceptibility, up to $\sim 1000 \times 10^{-5}$ SI (blue box in Figure F61). These layers do not correlate with volcanoclastic breccia but with siltstone/sandstone and are characterized by higher NGR counts compared to the volcanoclastic breccia (up to 50 counts/s).

Magnetic susceptibility values are very high (up to 1900×10^{-5} SI) in the basalt of lithostratigraphic Units IX and XI. The significant variability in these basement layers may result from multiple factors, such as core fragmentation, magnetite content, crystal size, and alteration (see **Basalt and basalt alteration**).

***P*-wave velocity**

P-wave velocity was measured on whole-round cores from the seafloor to ~200 mbsf (Figure F61). Cores collected with the XCB (Cores 349-U1431D-20X through 67X) or the RCB (all of Hole U1431E) have a diameter smaller than the core liner; therefore, poor coupling between the core and the liner prevented good measurements of compressive *P*-wave velocity on the WRMSL. Thus, we switched off the *P*-wave velocity measurement on the WRMSL for whole-round cores below Core 20X (168.9 mbsf) and for Hole U1431E. *P*-wave velocity near the seafloor is close to the velocity in water (~1500 m/s) for Holes U1431A–U1431D, reflecting the high porosity of near-surface sediment. Between about 50 and 63 mbsf,

Figure F61. Physical property summary, Holes U1431D and U1431E. Dashed lines A and B delineate major physical property boundaries. Blue bar marks high magnetic susceptibility zone in sand/sandstone. Arrows indicate magnetic susceptibility peaks associated with ash layers. PWV = *P*-wave velocity.

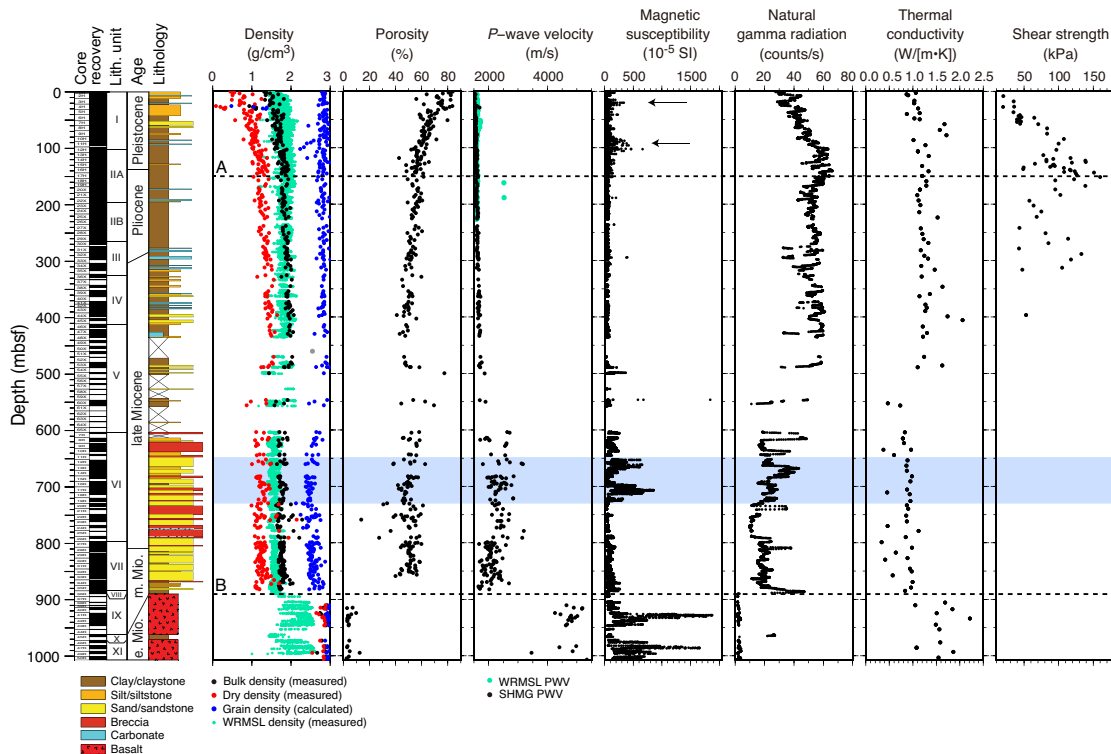


Table T19. Reference values for magnetic susceptibilities (Clark and Emerson, 1991) and natural gamma radiation (Russell, 1944) in different lithologies used during Expedition 349. [Download table as .csv.](#)

Lithology	Magnetic Susceptibility ($\times 10^{-5}$ SI)	Natural gamma radiation (counts/s)
Sandstone	0–2000	0–25
Clay	20–200	40–70
Basalt	20–17500	0–5

significantly higher values in WRMSL *P*-wave velocity might be related to sand/sandstone layers not measured with the caliper or due to other unidentified factors (Figure F60).

For Hole U1431A, interstitial water was extracted by Rhizon samplers every 5, 10, or 20 cm before physical property measurements. *P*-wave velocity was expected to be higher in this hole compared to the others at the same depth interval because of the extraction of water from the sediment, but the logs show lower *P*-wave velocity instead, suggesting that water in the liners was replaced by air.

Natural gamma radiation

NGR values display significant variations with rock type, with higher NGR counts for silt and mud (~40–70 counts/s), lower counts for sandstone (~0–20 counts/s), and even lower counts for basalt (~0–5 counts/s) (Table T19) (Russell, 1944). In Holes U1431D and U1431E, NGR counts are relatively high from the seafloor to 500 mbsf (~45 counts/s on average), consistent with the clay- and silt-dominated sediment of lithostratigraphic Units I–V (Figure F61). Between 500 and 900 mbsf, background NGR drops to 20 counts/s, which corresponds to the dominant breccia and sandstone lithologies of Units VI and VII. Layers with higher NGR counts and magnetic susceptibility are observed near 670 and 710 mbsf (blue box in Figure F61), which coincide with silt/sandstone layers. NGR counts are very low (<5 counts/s) in the basalt of Units IX and XI.

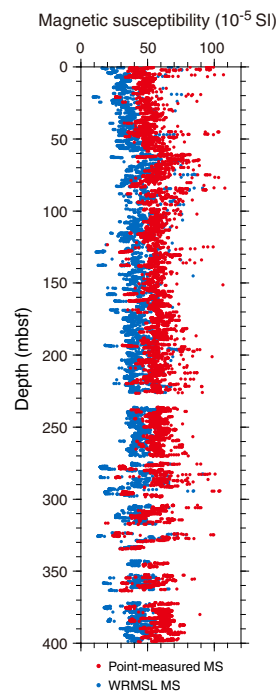
Thermal conductivity

Thermal conductivity increases from 1 to 1.2 W/(m·K) in the top 150 m and then remains relatively constant downhole to ~600 mbsf (lithostratigraphic Units I–V). It is slightly lower (near 0.85 W/(m·K)) in the breccia and sandstone layers of Units VI and VII and then increases drastically in the basalt (Units IX and XI) to values between 1.5 and 2.2 W/(m·K). The contact probe requires that measurements on hard rock cores be made on large pieces with a smooth splitting surface, so the values likely overestimate the average in situ thermal conductivity.

Point magnetic susceptibility

Point magnetic susceptibility measurements agree well with WRMSL results. A small offset observed between the two types of measurements results from the difference in instrument resolution (see [Physical properties](#) in the Methods chapter [Li et al., 2015]). On average, point magnetic susceptibility is 20×10^{-5} SI greater than WRMSL magnetic susceptibility (Figure F62). Point magnetic susceptibility peaks in lithostratigraphic Units I and II, reflecting the presence of ash layers. As described previously, layers with high magnetic susceptibility observed near 670 and 710 mbsf coincide with siltstone/sandstone formations. Magnetic susceptibility values for the basalt in Units IX and XI range between 200 and 1900×10^{-5} SI, with the highest values in the thick lava flows (Figure F63).

Figure F62. WRMSL magnetic susceptibility (MS) and point-measured MS. Point-measured MS is generally 20×10^{-5} SI higher than the WRMSL measurement.



Compressional wave (*P*-wave) velocity

P-wave velocity gradually increases from near seawater velocity (1500 m/s) to almost 1800 m/s in Hole U1431D; values are much higher in the indurated sediment of Hole U1431E (Figure F61). *P*-wave velocity varies between 2000 and 3000 m/s in the volcanoclastic layers of Unit VI, decreases to ~1800–2200 m/s in Unit VII, and increases to nearly 5000 m/s in the basalt of Units IX and XI.

Shear strength

Shear strength increases with depth from 20 to 150 kPa in the uppermost 150 m. Below 150 mbsf, shear strength drops to ~80 kPa, which may be associated with higher abundances of clay compared to the overlying sediment (Figure F61). Because of sediment compaction, vane shear strength was not measured below 400 mbsf, as large cracks started to develop during the measurements.

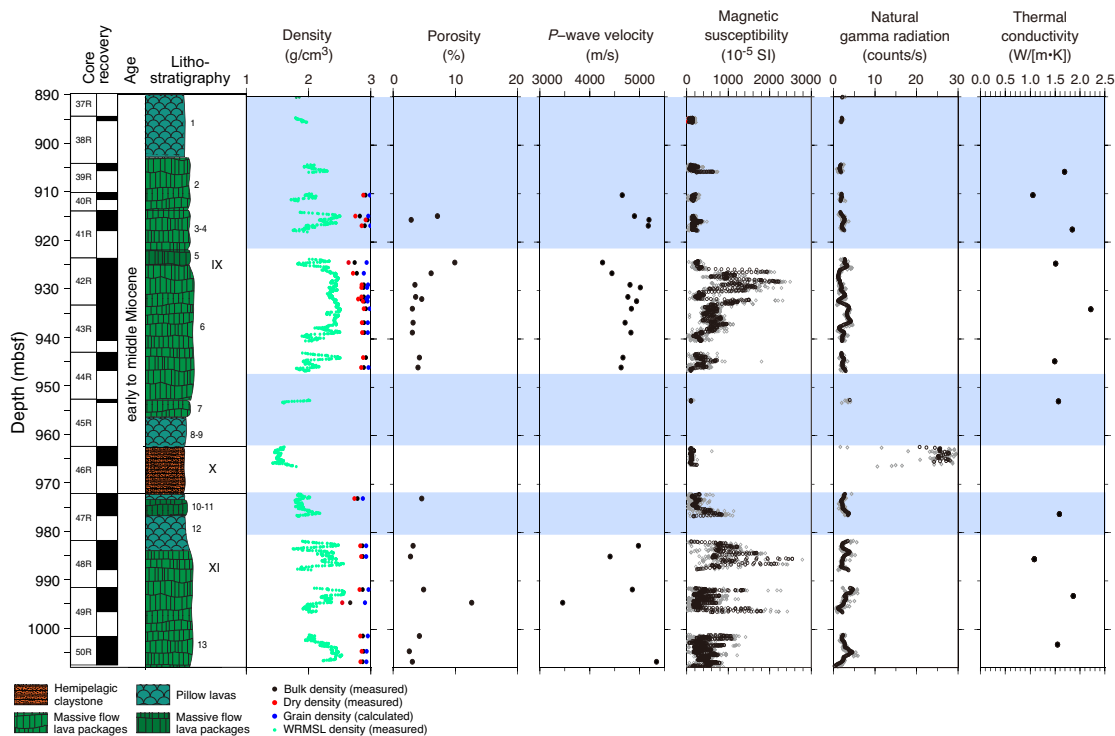
Moisture and density

Bulk and dry density measured on individual samples show the same variations as those measured on whole-round cores (Figure F61). Grain density is almost constant (~2.8 g/cm³) in clay-rich lithostratigraphic Units I–V and is lower in Unit VI, ~2.4 g/cm³ on average, which may be related to the composition of the sandstone. Basalt grain densities are close to 2.9 g/cm³. Porosity shows a large decrease with depth in the uppermost 150 m, from 80% to 50%, and remains relatively constant in the deeper sediment and sedimentary rocks. Density drops to 4%–6% in the basaltic layers.

Data interpretation and lithology correlation

In general, physical properties correlate with lithology, composition, and lithification. The variations of some of the physical properties near the seafloor reflect compaction of the sediment.

Figure F63. Physical properties of lithostratigraphic Units IX–XI. Note low magnetic susceptibility values in some basalt layers (blue shaded areas).



Surface sediment compaction

In Hole U1431D, bulk density, *P*-wave velocity, NGR, and thermal conductivity increase gradually with depth over the uppermost 150 m (dashed line A in Figure F61), whereas porosity measured on discrete samples decreases from 84% to 50% over the same depth range. A good inverse correlation exists between *P*-wave velocity and porosity as a second-order polynomial function (Figure F64A), and a linear inverse trend is observed between bulk density and porosity (Figure F64B). This indicates that sediment compaction dominates some of the physical property variations above 150 mbsf.

Ash layers

Ash layers are often marked by high magnetic susceptibility, although some layers are too thin to be detected at the resolution of the point magnetic susceptibility measurements. Relatively high magnetic susceptibility (300×10^{-5} to 500×10^{-5} SI) corresponds to volcanic ash layers at 25 and 100 mbsf (arrows in Figure F61).

Clay/silt/sand content

Relative clay/silt/sand content is often reflected by the combination of magnetic susceptibility and NGR values. For example, high magnetic susceptibility near 670 and 710 mbsf (blue box in Figure F61) does not correspond to volcanoclastic breccia layers but to siltstone/sandstone, as evidenced by high NGR (up to 50 counts/s). The siltstone/sandstone may contain magnetic minerals such as magnetite, possibly eroded from the nearby seamounts.

The 5 m thick layer of claystone (lithostratigraphic Unit X) between the two basalt units (Units IX and XI) clearly shows NGR values ~ 20 times greater than those of the basalt layers (Figure F63) and much lower magnetic susceptibility.

Volcaniclastics

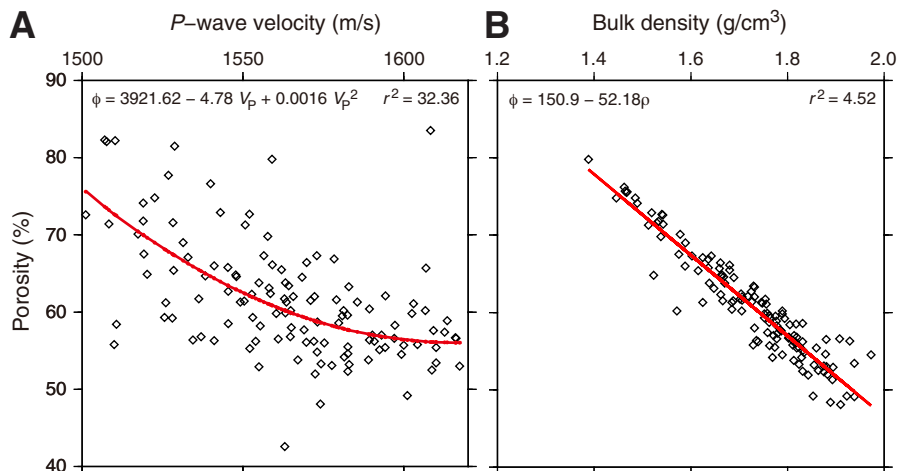
Most physical properties show significant change below 600 mbsf, at the boundary between lithostratigraphic Units V and VI, such as increased *P*-wave velocity (>2000 m/s), relatively low NGR, low average thermal conductivity (0.85 W/[m·K]), and higher porosity variations (50%–70%), which correspond to the presence of volcanoclastic breccia (Figure F61). The variation in these physical properties in Unit VI reflects the interbedding between sandstone layers, volcanoclastic breccias, and silt/claystones.

Basalt and basalt alteration

Drastic changes in physical properties near 890 mbsf correspond to the first occurrence of basalt layers. The basalt units below 890 mbsf (dashed line B in Figure F61) display the lowest NGR (~ 6 counts/s on average), highest point-measured magnetic susceptibility (2100×10^{-5} SI in Unit IX and 2300×10^{-5} SI in Unit XI), and bulk density of 2.5 – 2.8 g/cm³.

As shown in Figure F63, the basalt layers (Units IX and XI) show a very large range of magnetic susceptibility values ($\sim 30 \times 10^{-5}$ to 2300×10^{-5} SI). Variations in magnetic susceptibility in the basalt units may result from different factors. Lower magnetic susceptibility measurements might reflect the small length of some of the recovered basalt pieces and/or could be related to lower magnetite content due to the composition of the basalt. Crystal size also likely influences magnetic susceptibility values; larger crystals near the center of the basalt flows (see **Igneous petrology and alteration**), including larger magnetite crystals, may result from the slower cooling of the cores of massive basalt compared to their edges. Finally, alteration of basalt affects its mineralogy and therefore its physical properties. The low magnetic susceptibility and low NGR values at the top of the basalt layers likely result from a combination of all of these factors.

Figure F64. (A) P-wave velocity and (B) bulk density as a function of porosity above 150 mbsf in Hole U1431D. Red lines = best-fit correlation. Note the linear correlation in B, whereas the correlation in A is best represented by a polynomial.

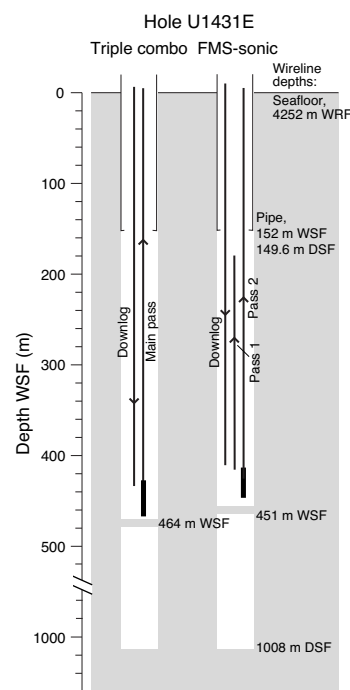


Downhole measurements Logging operations

Hole preparation for logging started before the last core from Hole U1431E arrived on deck. After coring to 991.4 mbsf, a wiper trip was made from 863 to 979 m drilling depth below seafloor (DSF) to allow debris that had been collecting around the drill collars to fall into the hole. Several 50 bbl sepiolite mud sweeps were also run at regular intervals to clear the hole. After the last core, the RCB drill bit was released near the bottom of the hole, and the hole was displaced from 648 m DSF upward with 240 bbl of heavy (11.4 lb/gal; barite weighted) mud. The pipe was raised to logging depth (4400.9 m drilling depth below rig floor [DRF]; 149.6 m DSF) (Figure F65). Rig-up for downhole logging started at 1820 h (local time; UTC +8 h) on 14 February 2014. Heave conditions were ~1 m for the triple combo tool string run and up to 2 m for the FMS-sonic tool string run. The wireline heave compensator was used for both runs. A brand new logging cable was used, which had to be detorqued and run no faster than ~1800 m/h. This slowed the trips through the water column compared to a seasoned cable.

The modified triple combo tool string started downhole at 2100 h on 14 February. The Hostile Environment Natural Gamma Ray Sonde (HNGS), Accelerator Porosity Sonde (APS), Hostile Environment Litho-Density Sonde (HLDS), High-Resolution Laterolog Array (HRLA), and Magnetic Susceptibility Sonde (MSS) were included. The centralized tools were run in the lower part of the tool string so that it would be easier to lower the tool string past ledges than an eccentricized tool (see [Downhole measurements](#) in the Methods chapter [Li et al., 2015] for tool diagrams). The tool string was prevented from moving further down the hole by an impassable bridge at 464 m WSF. The heavy mud, which might have stabilized the borehole walls, did not reach up to this point because of underestimation of the diameter of the borehole and the volume of heavy mud required to fill it. The absence of the barite-weighted heavy mud is apparent by the absence of photoelectric effect factor log values > 5 b/e⁻, which would have been an indicator of the presence of the heavy element barium, and the absence of viscous mud on the tools themselves after they were brought back up to the rig floor. The FMS-sonic tool string was run into the pipe at 0900 h on 15 February. Sonic logs were taken on the descent, and two upward

Figure F65. Logging operations summary, Hole U1431E.

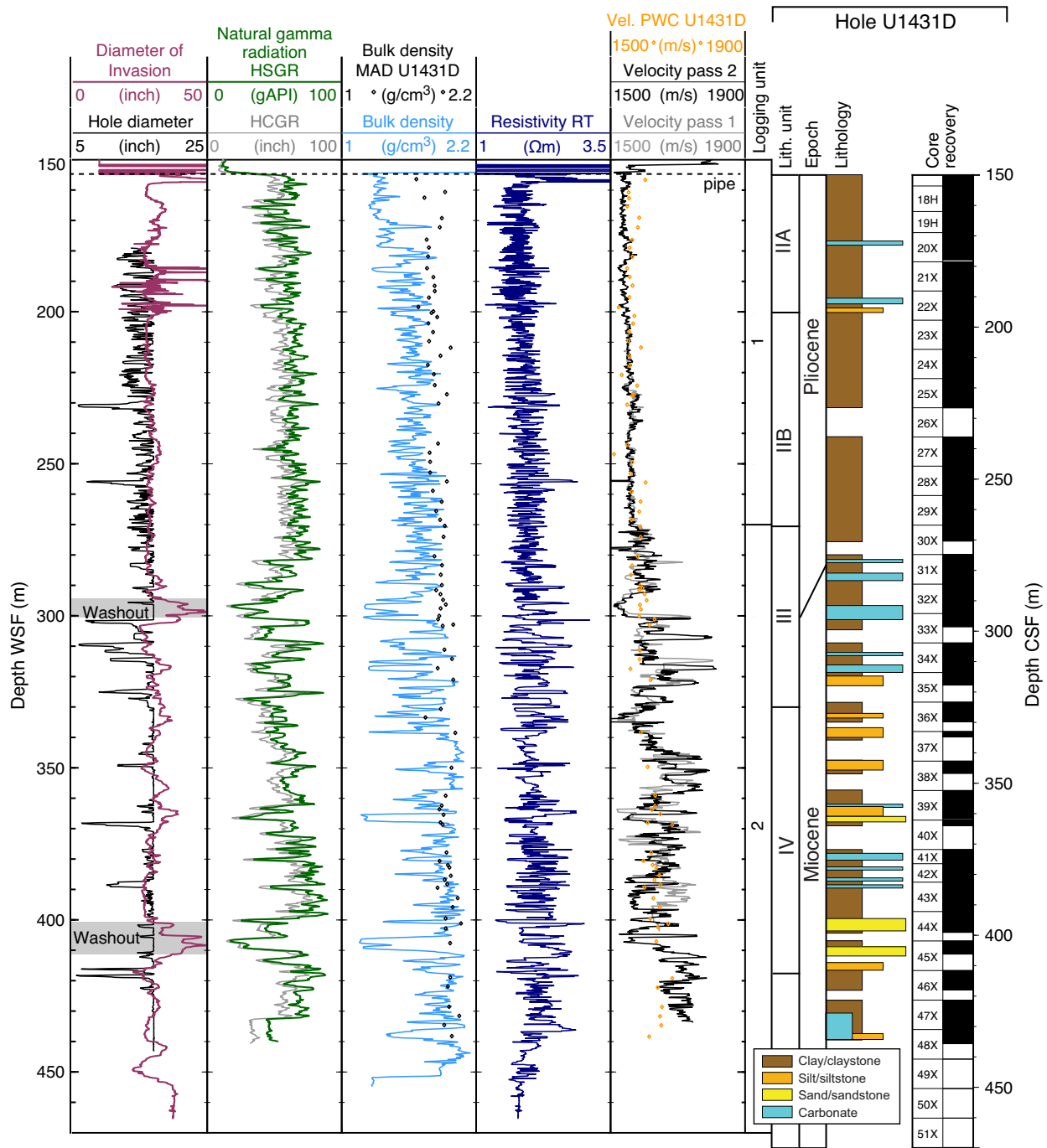


passes, including both FMS and sonic logs, were made from 410 (Pass 1) and 451 m WSF (Pass 2).

Log data quality

Log data quality was affected by the large borehole diameter, exceeding the 17 inch limit of the HLDS caliper arm in about half of the logged interval (Figure F66). Some particularly large caves were found, for example in the 296–301 and 405–411 m WSF intervals (labeled “Washout” on Figure F66), leading to uncertainty in most of the log values in such intervals. A lot of circulation of drilling fluid is generally required to keep deep holes open and prevent sand from building up around the drill pipe, which often results in washout of sand-rich sediment. Several thin, bridged (narrow diameter)

Figure F66. Hole U1431E downhole logs compared to Hole U1431D discrete sample MAD, P-wave caliper (PWC), lithology, and core recovery data. Equivalent features appear ~5 m shallower in Hole U1431D core data due to a depth shift between the holes. HSGR = standard (total) gamma radiation, HCGR = computed (U-free) gamma radiation, RT = "true" resistivity.



intervals also occur, for example at 231 and 310 m WSF. Despite the often wide and rapidly varying borehole width, interpretable features are seen in the FMS resistivity images. The triple combo main upward pass was taken as the depth reference, and the other logging runs were depth matched to it by means of the NGR log.

Logging units

Logging Unit 1: base of drill pipe to 270 m WSF

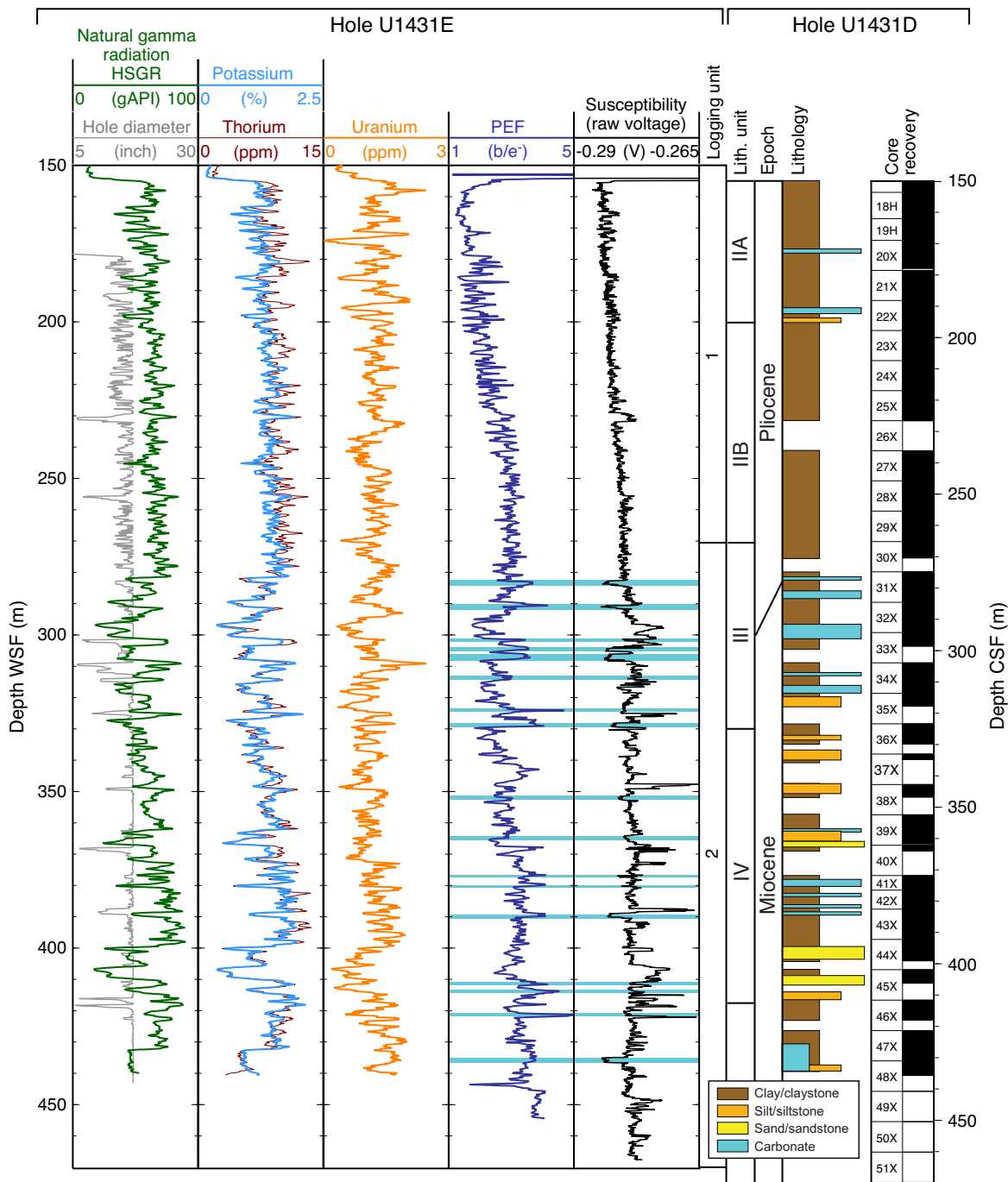
This logging unit is characterized by relative homogeneity in the logs without major excursions to higher or lower log values (e.g.,

sonic velocity and magnetic susceptibility logs) (Figures F66, F67). It is also characterized by submeter-scale layering, particularly evident in the caliper and resistivity logs and FMS images. This logging unit corresponds to lithostratigraphic Unit II (see Lithostratigraphy).

Logging Unit 2: 270–460 m WSF

This unit is characterized by higher variability in the logs compared to logging Unit 1. For example, NGR values vary from ~20 to 90 gAPI (Figure F66). Excursions to lower and higher values also

Figure F67. Hole U1431E downhole logs that are dependent on geochemistry and mineralogy of the formation. Hole U1431D lithology is shown for comparison. Blue bars = carbonate-rich sediment layers interpreted from log data (see text and Figure F68). Note that equivalent features appear ~5 m shallower in the Hole U1431D core data. HSGR = standard (total) gamma radiation, PEF = photoelectric effect.



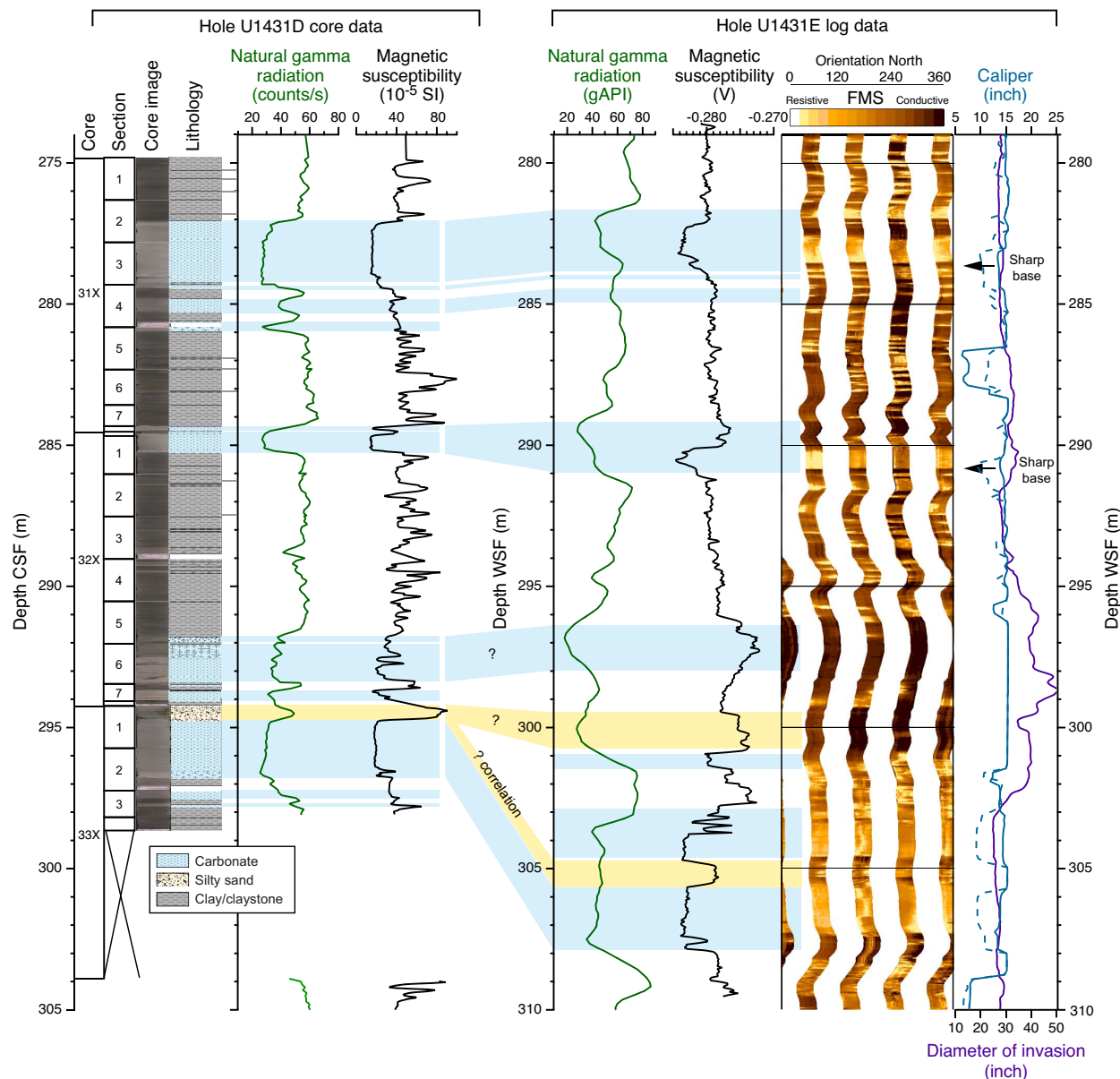
punctuate the magnetic susceptibility log (Figure F67). The sonic velocity log shows clear contrast to logging Unit 1, with velocities reaching 1800 m/s. This logging unit corresponds to lithostratigraphic Units III and IV and the upper part of Unit V (see Lithostratigraphy), which include thicker and coarser turbidites than Unit II.

Downhole logs and lithology

The downhole logs and FMS images reflect lithology at Site U1431. The lithology in the upper 460 m of the hole is clay domi-

nated and punctuated with centimeter- to meter-scale beds of coarser material, some of which is calcareous (see Lithostratigraphy). The clay-dominated sediment has high NGR because of K and Th in the clay minerals, whereas the calcareous sediment has lower NGR and magnetic susceptibility because of a relative lack of radioactive and magnetic minerals. The same NGR and magnetic susceptibility signatures are also seen in the physical property measurements made on cores from Hole U1431D (Figures F60, F68), which enables the downhole logs from Hole U1431E to be correlated to the core data from Hole U1431D. The same lithologic

Figure F68. Correlation of carbonate layers using Hole U1431D NGR and magnetic susceptibility to equivalent measurements in Hole U1431E downhole log data from 275 to 310 m WSF. Blue bars = correlation of carbonate layers, yellow bars = correlation of a loose silty sand layer.



features appear ~5 m lower in Hole U1431E log depth than they do in Hole U1431D. This depth offset can be caused by stratigraphic dip between the two holes, uncertainty in the seafloor depth, or uncertainty in the cable-stretch correction, among other reasons (see **Downhole measurements** in the Methods chapter [Li et al., 2015]).

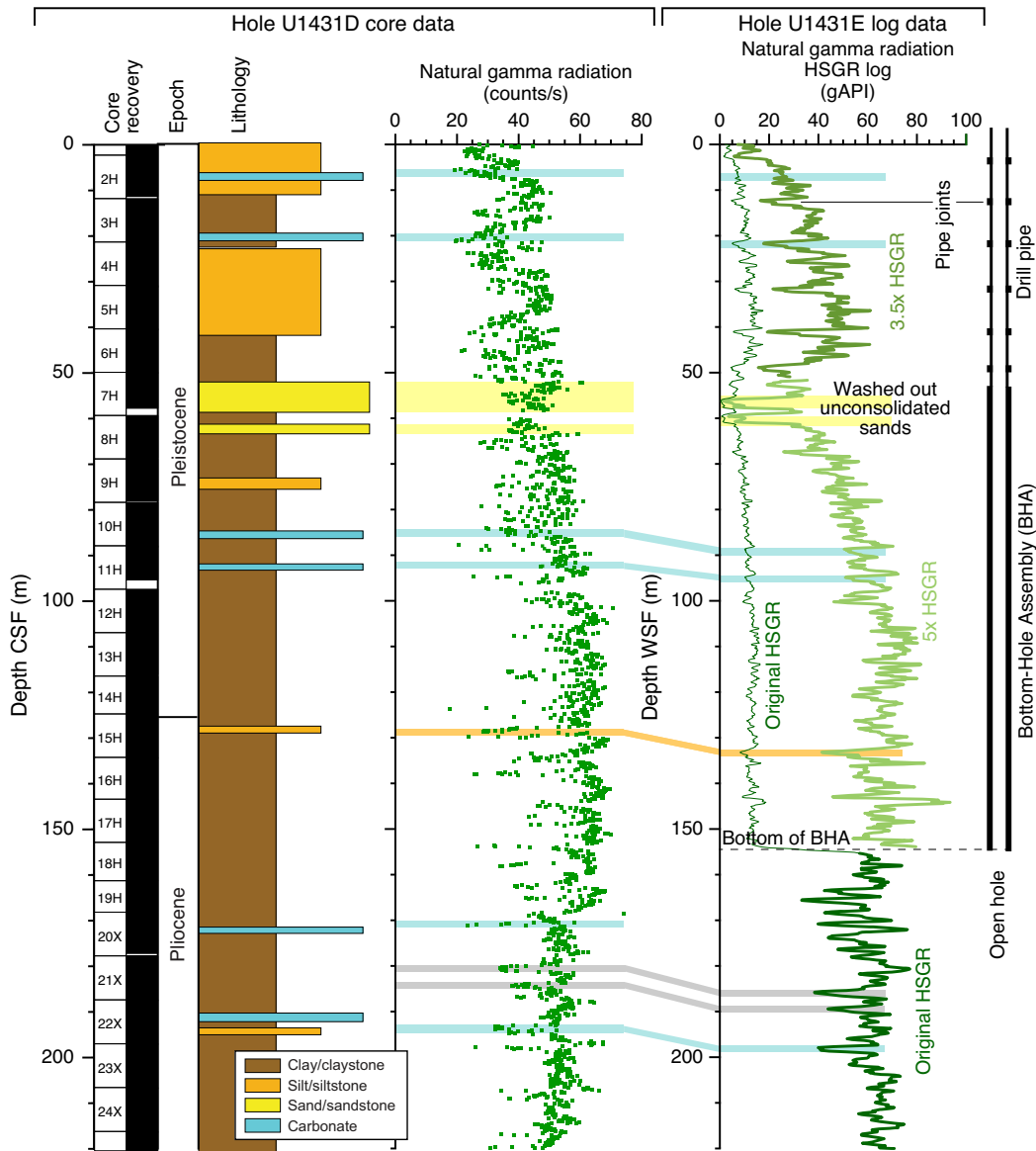
The contrasts in NGR and magnetic susceptibility can be seen both in the logs as a whole (Figure F67) and in a short section examined in more detail (Figure F68). In particular, the calcareous beds can be readily identified in the downhole logs, with low NGR and magnetic susceptibility and a resistive signature in the FMS images. The FMS images also show the sharp bases of the calcareous turbidites (e.g., at 283.5 and 291 m WSF; arrows in Figure F68). These calcareous beds appear to be washed out in their upper part but not so much in their lower part. These washouts are observed as having wide borehole diameter (Figure F66), more conductive FMS images, and higher logging magnetic susceptibility values. Somewhat counterintuitively, magnetic susceptibility as measured by the MSS

tool moves to anomalously higher values where the borehole is very wide, for example at 289–290 and 296–298 m WSF.

Sand-rich beds can be difficult to identify because they tend to be only partially recovered in the cores and because they become easily washed out in the borehole, resulting in anomalous log data values. In fact, the best indication of sand layers in the logs may be the diameter of the borehole (e.g., washed out sections at 296–301 and 405–411 m WSF). Such washouts also have very low NGR values (e.g., between 52 and 62 m WSF; yellow boxes in Figure F69).

The FMS images contain thin (submeter scale) alternations of high- and low-resistivity beds. These are clearly related to the short-scale variations in borehole diameter (Figure F68), but the question remains whether these submeter-scale washouts are themselves controlled by lithology or if the drilling process is responsible for their formation. In Figure F68, the calcareous beds can clearly be identified in the FMS image, but the thin resistive features do not appear to correlate very well with the thin silty beds identified in the

Figure F69. Correction of downhole NGR for attenuation through the pipe and the BHA. A multiplier of 5 is used to correct NGR in the BHA, and a multiplier of 3.5 is used for the drill pipe. Attenuation by the thicker drill pipe joints has not been corrected here. Correlation of features in Hole U1431D cores to equivalent features in Hole U1431E log data is also shown. HSGR = standard (total) gamma radiation.



visual core descriptions. The interpretation of the thin, apparently resistive features in the FMS images therefore remains unclear.

Sonic velocity and two-way traveltime

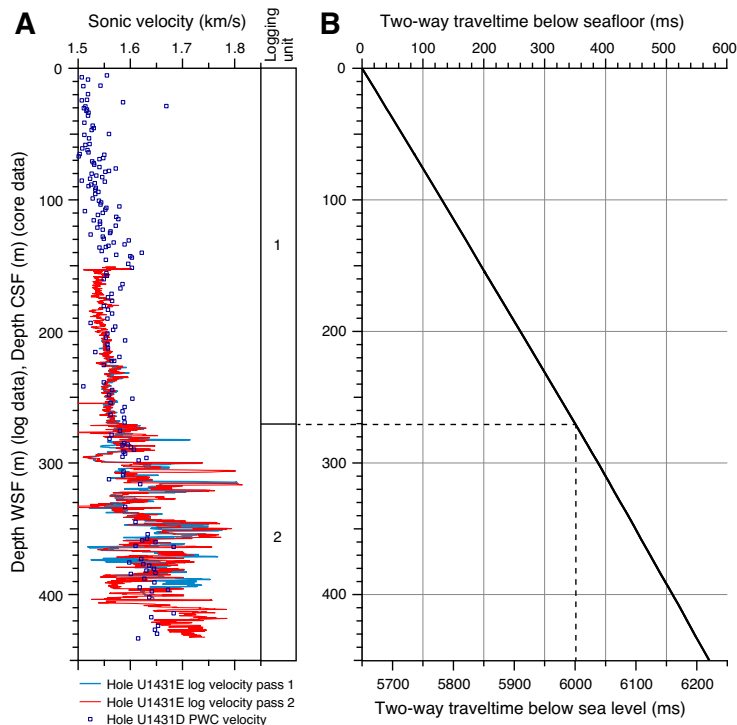
The sonic velocity log repeated reasonably well between the two passes of the logging tool, so the data are considered to be fairly robust, a conclusion that is supported by the general similarity to the *P*-wave velocities measured on core samples (Figure F70A). Sonic velocities remain at low values until ~270 mbsf and then become faster below this depth. These two data sets were used to calculate interval velocities between measurement points and then were summed and doubled to yield two-way traveltime for the uppermost 460 m at Site U1431 (Figure F70B). From these data, the boundary between logging Units 1 and 2 at 270 mbsf lies at the top

of the set of high-amplitude reflectors in the seismic section at ~6 s two-way traveltime (Figure F3).

Borehole cross-sectional shape and crustal stress

When the borehole is oval in cross-section, the two orthogonal pairs of FMS caliper arms tend to follow the semimajor and semiminor axes of the borehole oval. The cross-sectional shape of the borehole is controlled by the stress state of the crust in the area surrounding the borehole: the long axis follows the direction of minimum horizontal compressional stress (S_H) and the short axis follows the direction of maximum horizontal stress (S_H) (Moos and Zoback, 1990; Lin et al., 2010). The long axis often includes borehole breakouts. The FMS tool is oriented by magnetometry, so the azimuth of

Figure F70. (A) Sonic velocity and (B) two-way travelttime (TWT). TWT was calculated from Hole U1431D *P*-wave caliper (PWC) velocity between the seafloor and 155 m CSF and Hole U1431E sonic velocity log data (Pass 2) between 155 and 430 m WSF.



these directions can be determined. The borehole long axis in the interval where the caliper arms were open (194–443 m WSF) is consistently oriented NNW–SSE (Figure F71), indicating that S_H is oriented ENE–WSW in this part of the South China Sea.

Downhole temperature and heat flow

Four APCT-3 downhole temperature measurements in Hole U1431D ranged from 2.95°C at 31.7 m DSF to 4.22°C at 117.2 m DSF (Table T20; Figures F72, F73A), giving a geothermal gradient of 14.8°C/km. These measurements, together with the seafloor temperature of 2.5°C, indicate that the temperature increases linearly with depth.

Thermal conductivity under in situ conditions was estimated from laboratory-determined thermal conductivity from Hole U1431D using the method of Hyndman et al. (1974) (see **Physical properties** in the Methods chapter [Li et al., 2015]). The calculated in situ values average 1.1% higher than the measured laboratory values. Thermal resistance was then calculated by integrating the inverse of the in situ thermal conductivity over depth (Figure F73B). A heat flow of 17.2 mW/m² was obtained from the linear fit between temperature and thermal resistance (Figure F73C) (Pribnow et al., 2000). The geothermal gradient and heat flow at Site U1431 are relatively low for the South China Sea (Li et al., 2010), and we speculate that this might be caused by a downwelling limb of hydrothermal circulation in the area of Site U1431, which lies in a small basin adjacent to seamounts.

Figure F71. Rose diagram showing the NNW–SSE azimuth of the long axis of the borehole cross section, given by the direction of the wider of the 2 borehole diameters recorded by the FMS caliper arms, relative to magnetic north, at 193–443 m WSF, Hole U1431E. Only long axis data 0.5 inch or greater than the short axis are plotted. The short axis of the borehole oval (WSW–ENE) is interpreted to represent the direction of maximum horizontal stress (see text).

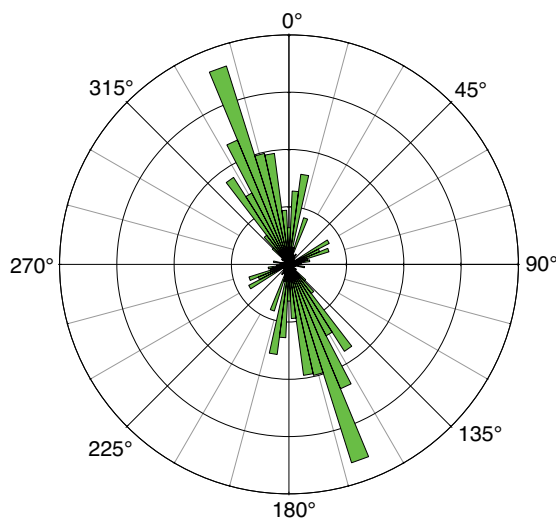


Table T20. Advanced piston corer temperature tool (APCT-3) measurements in Hole U1431D. [Download table as .csv.](#)

Core	Depth DSF (m)	Temperature (°C)
Seafloor	0.0	2.5
349-U1431D-4H	31.7	2.95
349-U1431D-7H	60.2	3.52
349-U1431D-10H	88.7	3.83
349-U1431D-13H	117.2	4.22

Figure F72. APCT-3 temperature-time series with extrapolated formation temperature estimates, Site U1431.

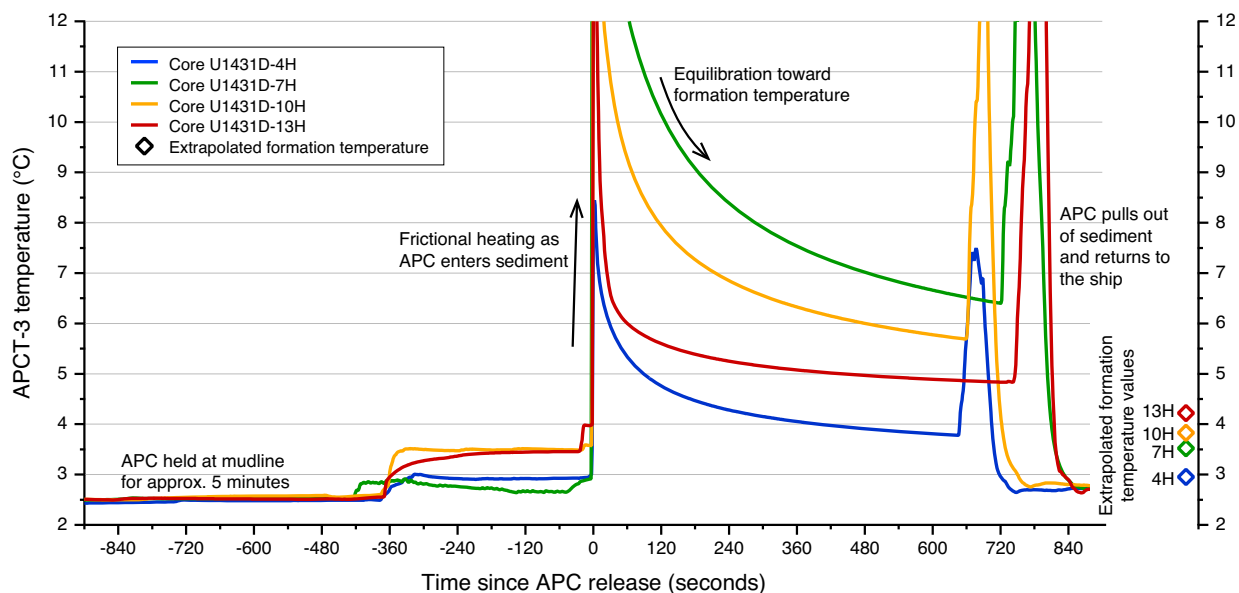
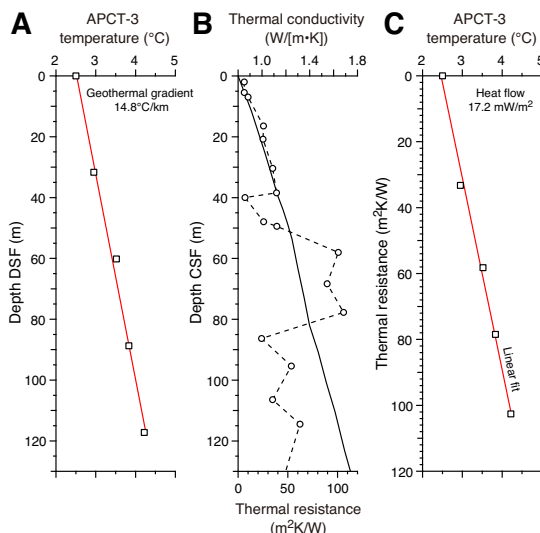


Figure F73. Heat flow calculations, Site U1431. A. APCT-3 sediment temperatures. B. Thermal conductivity data from Hole U1431D (circles and dashed line) with calculated thermal resistance (solid line). C. Bullard plot of heat flow calculated from a linear fit of the temperature data.



References

- Alt, J.C., France-Lanord, C., Floyd, P.A., Castillo, P., and Galy, A., 1992. Low-temperature hydrothermal alteration of Jurassic ocean crust, Site 801. In Larson, R.L., Lancelot, Y., et al., *Proceedings of the Ocean Drilling Program, Scientific Results*, 129: College Station, TX (Ocean Drilling Program), 415–427. <http://dx.doi.org/10.2973/odp.proc.sr.129.132.1992>
- Bach, W., Alt, J.C., Niu, Y., Humphris, S.E., Erzinger, J., and Dick, H.J.B., 2001. The geochemical consequences of late-stage low-grade alteration of lower ocean crust at the SW Indian Ridge: results from ODP Hole 735B (Leg 176). *Geochimica Cosmochimica Acta*, 65(19):3267–3287. [http://dx.doi.org/10.1016/S0016-7037\(01\)00677-9](http://dx.doi.org/10.1016/S0016-7037(01)00677-9)
- Berggren, W.A., Kent, D.V., Swisher, C.C., III, and Aubry, M.-P., 1995. A revised Cenozoic geochronology and chronostratigraphy. In Berggren, W.A., Kent, D.V., Aubry, M.-P., and Hardenbol, J. (Eds.), *Geochronology, Time Scales and Global Stratigraphic Correlation*. Special Publication - SEPM (Society for Sedimentary Geology), 54:129–212. <http://dx.doi.org/10.2110/pec.95.04.0129>
- Bjorklund, K.R., and Goll, R.M., 1979. Internal skeletal structures of *Collosphaera* and *Trisolenia*: a case of repetitive evolution in the Collosphaeriidae (Radiolaria). *Journal of Paleontology*, 53(6):1293–1326. <http://www.jstor.org/stable/1304135>
- Briais, A., Patriat, P., and Tapponnier, P., 1993. Updated interpretation of magnetic anomalies and seafloor spreading stages in the South China Sea: implications for the Tertiary tectonics of Southeast Asia. *Journal of Geophysical Research: Solid Earth*, 98(B4):6299–6328. <http://dx.doi.org/10.1029/92JB02280>
- Chen, M., and Tan Z., 1997. Radiolarian distribution in surface sediments of the northern and central South China Sea. *Marine Micropaleontology*, 32(1–2):173–194. [http://dx.doi.org/10.1016/S0377-8398\(97\)00019-4](http://dx.doi.org/10.1016/S0377-8398(97)00019-4)
- Clark, D.A., and Emerson, D.W., 1991. Notes on rock magnetization characteristics in applied geophysical studies. *Exploration Geophysics*, 22(3):547–555. <http://dx.doi.org/10.1071/EG991547>
- Expedition 329 Scientists, 2011. Site U1365. In D'Hondt, S., Inagaki, E., Alvarez Zarikian, C.A., and the Expedition 329 Scientists, *Proceedings of the Integrated Ocean Drilling Program*, 329: Tokyo (Integrated Ocean Drilling Program Management International, Inc.). <http://dx.doi.org/10.2204/iodp.proc.329.103.2011>
- Expedition 334 Scientists, 2012. Site U1381. In Vannucchi, P., Ujiie, K., Stroncik, N., Malinverno, A., and the Expedition 334 Scientists, *Proceedings of the Integrated Ocean Drilling Program*, 334: Tokyo (Integrated Ocean Drilling Program Management International, Inc.). <http://dx.doi.org/10.2204/iodp.proc.334.106.2012>
- Gradstein, F.M., Ogg, J.G., Schmitz, M.D., and Ogg, G.M. (Eds.), 2012. *The Geological Time Scale 2012*: Oxford, UK (Elsevier).
- Harris, R.N., Sakaguchi, A., Petronotis, K., Baxter, A.T., Berg, R., Burkett, A., Charpentier, D., Choi, J., Diz Ferreiro, P., Hamahashi, M., Hashimoto, Y., Heydolph, K., Jovane, L., Kastner, M., Kurz, W., Kutterolf, S.O., Li, Y., Malinverno, A., Martin, K.M., Millan, C., Nascimento, D.B., Saito, S., Sandoval Gutierrez, M.I., Sreaton, E.J., Smith-Duque, C.E., Solomon, E.A., Straub, S.M., Tanikawa, W., Torres, M.E., Uchimura, H., Vannucchi, P., Yamamoto, Y., Yan, Q., and Zhao, X., 2013. Input Site U1414. In Harris, R.N., Sakaguchi, A., Petronotis, K., and the Expedition 344 Scientists, *Proceedings of the Integrated Ocean Drilling Program*, 344: College Station, TX (Integrated Ocean Drilling Program). <http://dx.doi.org/10.2204/iodp.proc.344.104.2013>
- Hékinian, R., Bonté, P., Pautot, G., Jacques, D., Labeyrie, L.D., Mikkelsen, N., and Reys, J.-L., 1989. Volcanics from the South China Sea ridge system. *Oceanologica Acta*, 12(2):101–115.
- Hyndman, R.D., Erickson, A.J., and Von Herzen, R.P., 1974. Geothermal measurements on DSDP Leg 26. In Davies, T.A., Luyendyk, B.P., et al., *Initial Reports of the Deep Sea Drilling Project*, 26: Washington, DC (U.S. Government Printing Office), 451–463. <http://dx.doi.org/10.2973/dsdp.proc.26.113.1974>
- Ishihara, T., and Kisimoto, K., 1996. Magnetic anomaly map of East Asia, 1:4,000,000 (CD-ROM version). Geological Survey of Japan, Coordinating Committee for Coastal and Offshore Geoscience Programs in East and Southeast Asia (CCOP).
- Jovane, L., Acton, G., Florindo, F., and Verosub, K.L., 2008. Geomagnetic field behavior at high latitudes from a paleomagnetic record from Eltanin Core 27–21 in the Ross Sea sector, Antarctica. *Earth and Planetary Science Letters*, 267(3–4):435–443. <http://dx.doi.org/10.1016/j.epsl.2007.12.006>
- Kirschvink, J.L., 1980. The least-squares line and plane and the analysis of palaeomagnetic data. *Geophysical Journal of the Royal Astronomical Society*, 62(3):699–718. <http://dx.doi.org/10.1111/j.1365-246X.1980.tb02601.x>
- Knoll, A.H., and Johnson, D.A., 1975. Late Pleistocene evolution of the collosphaerid radiolarian *Buccinosphaera invaginata* Haeckel. *Micropaleontology*, 21(1):60–68. <http://dx.doi.org/10.2307/1485155>
- Kurnosov, V.B., Zolotarev, B.P., Artamonov, A.V., Lyapunov, S.M., Kashinzev, G.L., Chudae, O.V., Sokolova, A.L., and Garanina, S.A., 2008. Technical note: alteration effects in the upper oceanic crust—data and comments. *Transactions of the Geological Institute of the Russian Academy of Sciences*, 581.
- Le Maitre, R.W., Bateman, P., Dudek, A., Keller, J., Lameyre, J., Le Bas, M.J., Sabine, P.A., Schmid, R., Sorensen, H., Streckeisen, A., Woolley, A.R., and Zanettin, B., 1989. *A Classification of Igneous Rocks and Glossary of Terms*: Oxford, UK (Blackwell Science Publishing).
- Li, C.-F., Lin, J., Kulhanek, D.K., Williams, T., Bao, R., Briais, A., Brown, E.A., Chen, Y., Clift, P.D., Colwell, F.S., Dadd, K.A., Ding, W., Hernández-Almeida, I., Huang, X.-L., Hyun, S., Jiang, T., Koppers, A.A.P., Li, Q., Liu, C., Liu, Q., Liu, Z., Nagai, R.H., Peleo-Alampay, A., Su, X., Sun, Z., Tejada, M.L.G., Trinh, H.S., Yeh, Y.-C., Zhang, C., Zhang, F., Zhang, G.-L., and Zhao, X., 2015. Methods. In Li, C.-F., Lin, J., Kulhanek, D.K., and the Expedition 349 Scientists, *Proceedings of the Integrated Ocean Drilling Program*, 349: South China Sea Tectonics: College Station, TX (International Ocean Discovery Program). <http://dx.doi.org/10.14379/iodp.proc.349.102.2015>
- Li, C.-F., Shi, X., Zhou, Z., Li, J., Geng, J., and Chen, B., 2010. Depths to the magnetic layer bottom in the South China Sea area and their tectonic implications. *Geophysical Journal International*, 182(3):1229–1247. <http://dx.doi.org/10.1111/j.1365-246X.2010.04702.x>
- Lin, W., Doan, M.-L., Moore, J.C., McNeill, L., Byrne, T.B., Ito, T., Saffer, D., Conin, M., Kinoshita, M., Sanada, Y., Moe, K.T., Araki, E., Tobin, H., Boutt, D., Kano, Y., Hayman, N.W., Flemings, P., Huftile, G.J., Cukur, D., Buret, C., Schleicher, A.M., Efimenko, N., Kawabata, K., Buchs, D.M., Jiang, S., Kameo, K., Horiguchi, K., Wiersberg, T., Kopf, A., Kitada, K., Eguchi, N., Toczko, S., Takahashi, K., and Kido, Y., 2010. Present-day principal horizontal stress orientations in the Kumano forearc basin of the southwest Japan subduction zone determined from IODP NanTroSEIZE drilling Site C0009. *Geophysical Research Letters*, 37(13):L13303. <http://dx.doi.org/10.1029/2010GL043158>
- Lowe, D.R., 1982. Sediment gravity flows, II. Depositional models with special reference to the deposits of high-density turbidity currents. *Journal of Sedimentary Petrology*, 52(1):279–297. <http://jse.dres.sepmone-line.org/cgi/content/abstract/52/1/279>
- Macdonald, G.A., 1968. Composition and origin of Hawaiian lavas. In Coats, R.R., Hay, R.L., and Anderson, C.A. (Eds.), *Studies in Volcanology: A Memoir in Honor of Howel Williams*. Memoir—Geological Society of America, 116:477–522. <http://dx.doi.org/10.1130/MEM116-p477>
- Macdonald, G.A., and Katsura, T., 1964. Chemical composition of Hawaiian lavas. *Journal of Petrology*, 5(1):82–133. <http://petrology.oxfordjournals.org/content/5/1/82.abstract>
- Martini, E., 1971. Standard Tertiary and Quaternary calcareous nannoplankton zonation. In Farinacci, A. (Ed.), *Proceedings of the Second Planktonic Conference, Roma 1970*: Rome (Edizioni Tecnoscienza), 2:739–785.
- Maslin, M.A., Li, X.S., Loutre, M.-F., and Berger, A., 1998. The contribution of orbital forcing to the progressive intensification of Northern Hemisphere

- glaciation. *Quaternary Science Reviews*, 17(4–5):411–426. [http://dx.doi.org/10.1016/S0277-3791\(97\)00047-4](http://dx.doi.org/10.1016/S0277-3791(97)00047-4)
- Middleton, G.V., and Hampton, M.A., 1973. Sediment gravity flows: mechanics of flow and deposition. In Middleton, G.V., and Bouma, A.H. (Eds.), *Turbidites and Deep Water Sedimentation*. Short Course Notes, Society of Economic Paleontologists and Mineralogists, Pacific Section, 1–38. http://archives.data-pages.com/data/pac_sepm/015/015001/pdfs/1.pdf
- Moos, D., and Zoback, M.D., 1990. Utilization of observations of well bore failure to constrain the orientation and magnitude of crustal stresses: application to continental, Deep Sea Drilling Project, and Ocean Drilling Program boreholes. *Journal of Geophysical Research: Solid Earth*, 95(B6):9305–9325. <http://dx.doi.org/10.1029/JB095iB06p09305>
- Németh, K., Cronin, S.J., Stewart, R.B., and Charley, D., 2009. Intra- and extracaldera volcanoclastic facies and geomorphic characteristics of a frequently active mafic island-arc volcano, Ambrym Island, Vanuatu. *Sedimentary Geology*, 220(3–4):256–270. <http://dx.doi.org/10.1016/j.sedgeo.2009.04.019>
- Pribnow, D., Kinoshita, M., and Stein, C., 2000. *Thermal Data Collection and Heat Flow Recalculations for Ocean Drilling Program Legs 101–180*: Hanover, Germany (Institute for Joint Geoscientific Research, Institut für Geowissenschaftliche Gemeinschaftsaufgaben [GGA]). <http://www-odp.tamu.edu/publications/heatflow/ODPREpr.pdf>
- Roser, B.P., and Korsch, R.J., 1988. Provenance signatures of sandstone-mudstone suites determined using discriminant function analysis of major-element data. *Chemical Geology*, 67(1–2):119–139. [http://dx.doi.org/10.1016/0009-2541\(88\)90010-1](http://dx.doi.org/10.1016/0009-2541(88)90010-1)
- Russell, W.L., 1944. The total gamma ray activity of sedimentary rocks as indicated by Geiger counter determinations. *Geophysics*, 9(2):180–216. <http://dx.doi.org/10.1190/1.1445076>
- Saint-Ange, F., Bachèlery, P., Babonneau, N., Michon, L., and Jorry, S.J., 2013. Volcanoclastic sedimentation on the submarine slopes of a basaltic hotspot volcano: Piton de la Fournaise Volcano (La Réunion Island, Indian Ocean). *Marine Geology*, 337:35–52. <http://dx.doi.org/10.1016/j.margeo.2013.01.004>
- Sanfilippo, A., and Nigrini, C., 1998. Code numbers for Cenozoic low latitude radiolarian biostratigraphic zones and GPTS conversion tables. *Marine Micropaleontology*, 33(1–2):109–117, 121–156. [http://dx.doi.org/10.1016/S0377-8398\(97\)00030-3](http://dx.doi.org/10.1016/S0377-8398(97)00030-3)
- Smith, A., Popa, R., Fisk, M., Nielsen, M., Wheat, C.G., Jannasch, H.W., Fisher, A.T., Becker, K., Sievert, S.M., and Flores, G., 2011. In situ enrichment of ocean crust microbes on igneous minerals and glasses using an osmotic flow-through device. *Geochemistry, Geophysics, Geosystems*, 12(6):Q06007. <http://dx.doi.org/10.1029/2010GC003424>
- Suganuma, Y., Okuno, J., Heslop, D., Roberts, A.P., Yamazaki, T., and Yokoyama, Y., 2011. Post-depositional remanent magnetization lock-in for marine sediments deduced from ^{10}Be and paleomagnetic records through the Matuyama–Brunhes boundary. *Earth and Planetary Science Letters*, 311(1–2):39–52. <http://dx.doi.org/10.1016/j.epsl.2011.08.038>
- Takahashi, T., 1991. *Debris Flow: International Association for Hydraulic Research Monograph*: Rotterdam, The Netherlands (Balkema).
- Tu, K., Flower, M.F.J., Carlson, R.W., Xie, G., Chen, C.-Y., and Zhang, M., 1992. Magmatism in the South China Basin: 1. Isotopic and trace-element evidence for an endogenous Dupal mantle component. *Chemical Geology*, 97(1–2):47–63. [http://dx.doi.org/10.1016/0009-2541\(92\)90135-R](http://dx.doi.org/10.1016/0009-2541(92)90135-R)
- Wade, B.S., Pearson, P.N., Berggren, W.A., and Pälike, H., 2011. Review and revision of Cenozoic tropical planktonic foraminiferal biostratigraphy and calibration to the geomagnetic polarity and astronomical time scale. *Earth-Science Reviews*, 104(1–3):111–142. <http://dx.doi.org/10.1016/j.earscirev.2010.09.003>
- Wang, R., and Abelmann, A., 1999. Pleistocene radiolarian biostratigraphy in the South China Sea. *Science in China (Series D)*, 42(5):537–543.
- Wang, X.-C., Li, Z.-X., Li, X.-H., Li, J., Liu, Y., Long, W.-G., Zhou, J.-B., and Wang, F., 2012. Temperature, pressure, and composition of the mantle source region of late Cenozoic basalts in Hainan Island, SE Asia: a consequence of a young thermal mantle plume close to subduction zones? *Journal of Petrology*, 53(1):177–233. <http://dx.doi.org/10.1093/petrology/egr061>
- Zhang, G., Smith-Duque, C., Tang, S., Li, H., Zarikian, C., D'Hondt, S., Inagaki, F., and IODP Expedition 329 Scientists, 2012. Geochemistry of basalts from IODP Site U1365: implications for magmatism and mantle source signatures of the mid-Cretaceous Osborn Trough. *Lithos*, 144–145:73–87. <http://dx.doi.org/10.1016/j.lithos.2012.04.014>
- Zhang, G., Zeng, Z., Yin, X., Wang, X., and Chen, D., 2009. Deep fractionation of clinopyroxene in the East Pacific Rise 13°N: evidence from high MgO MORB and melt inclusions. *Acta Geologica Sinica*, 83(2):266–277. <http://dx.doi.org/10.1111/j.1755-6724.2009.00030.x>
- Zhang, G.-L., Chen, L.-H., and Li, S.-Z., 2013. Mantle dynamics and generation of a geochemical mantle boundary along the East Pacific Rise—Pacific/Antarctic Ridge. *Earth and Planetary Science Letters*, 383:153–163. <http://dx.doi.org/10.1016/j.epsl.2013.09.045>
- Zhang, G.-L., Zong, C.-L., Yin, X.-B., and Li, H., 2012. Geochemical constraints on a mixed pyroxenite–peridotite source for East Pacific Rise basalts. *Chemical Geology*, 330–331:176–187. <http://dx.doi.org/10.1016/j.chemgeo.2012.08.033>
- Zijderveld, J.D.A., 1967. AC demagnetization of rocks: analysis of results. In Collinson, D.W., Creer, K.M., and Runcorn, S.K. (Eds.), *Methods in Palaeomagnetism*: Amsterdam (Elsevier), 254–286.

doi:10.14379/iodp.proc.349.104.2015

Site U1432¹



C.-F. Li, J. Lin, D.K. Kulhanek, T. Williams, R. Bao, A. Briais, E.A. Brown, Y. Chen, P.D. Clift, F.S. Colwell, K.A. Dadd, W.-W. Ding, I. Hernández-Almeida, X.-L. Huang, S. Hyun, T. Jiang, A.A.P. Koppers, Q. Li, C. Liu, Q. Liu, Z. Liu, R.H. Nagai, A. Peleo-Alampay, X. Su, Z. Sun, M.L.G. Tejada, H.S. Trinh, Y.-C. Yeh, C. Zhang, F. Zhang, G.-L. Zhang, and X. Zhao²

Keywords: International Ocean Discovery Program, IODP, *JOIDES Resolution*, Expedition 349, Site U1432, South China Sea, continent/ocean boundary, deep-marine turbidite, nannofossils, deep biosphere, continental breakup, seafloor spreading, magnetic anomalies, sedimentation rate, pyrite nodule

Contents

- 1 Background and objectives
- 1 Operations
- 6 Lithostratigraphy
- 9 Biostratigraphy
- 10 Geochemistry
- 15 Microbiology
- 16 Paleomagnetism
- 17 Physical properties
- 19 Downhole measurements
- 20 References

Background and objectives

International Ocean Discovery Program (IODP) Site U1432 is located ~60 km south of Ocean Drilling Program (ODP) Site 1148 (Shipboard Scientific Party, 2000; Li et al., 2006; Wang and Li, 2009), just south of the northern continent/ocean boundary (Figure F1). This part of the basin has the deepest basement in the northern part of the South China Sea and is likely the oldest among the subbasins based on magnetic anomalies (Taylor and Hayes, 1980, 1983; Pautot et al., 1986; Briais et al., 1993). This site was chosen to recover the oldest oceanic crust and the oldest sedimentary rocks in the East Subbasin to test the hypothesis that the onset of seafloor spreading in the South China Sea occurred here first at ~32 Ma. Magnetic Anomaly 11, the oldest anomaly interpreted by Taylor and Hayes (1980) and Briais et al. (1993), passes near this site (Figure F2) and hence would allow key calibrations between ages estimated from magnetic anomalies and in situ ages from biostratigraphy, radiometric dating, and magnetostratigraphy.

The true nature of the continent–ocean transition and oceanic basement at this site is speculative (Figure F3); there could be volcanic extrusions associated with early continental breakup and the onset of seafloor spreading, exhumed lower crustal material from preferential lower crust extension, exhumed mantle material, or Mesozoic rocks. Coring at this site will help pinpoint the exact location and tectonic nature of the continent–ocean transition and address key problems in the early tectonic transition from rifting to drifting and associated paleoenvironmental changes, including the following:

1. The age of basement (presumably the oldest oceanic crust) near the continent/ocean boundary;
2. Petrological and geochemical characteristics of basement rocks and their bearings on continental breakup, incipient seafloor spreading, and mantle evolution;

3. Physical properties of basement rocks and their implications for interpreting sharp magnetic contrasts between different subbasins; and
4. Sedimentary, paleoceanographic, and ecosystem responses to the opening of the South China Sea.

Because of operational challenges (see **Operations**), the objectives of sampling basement and basal sediments at Site U1432 were not achieved.

Operations

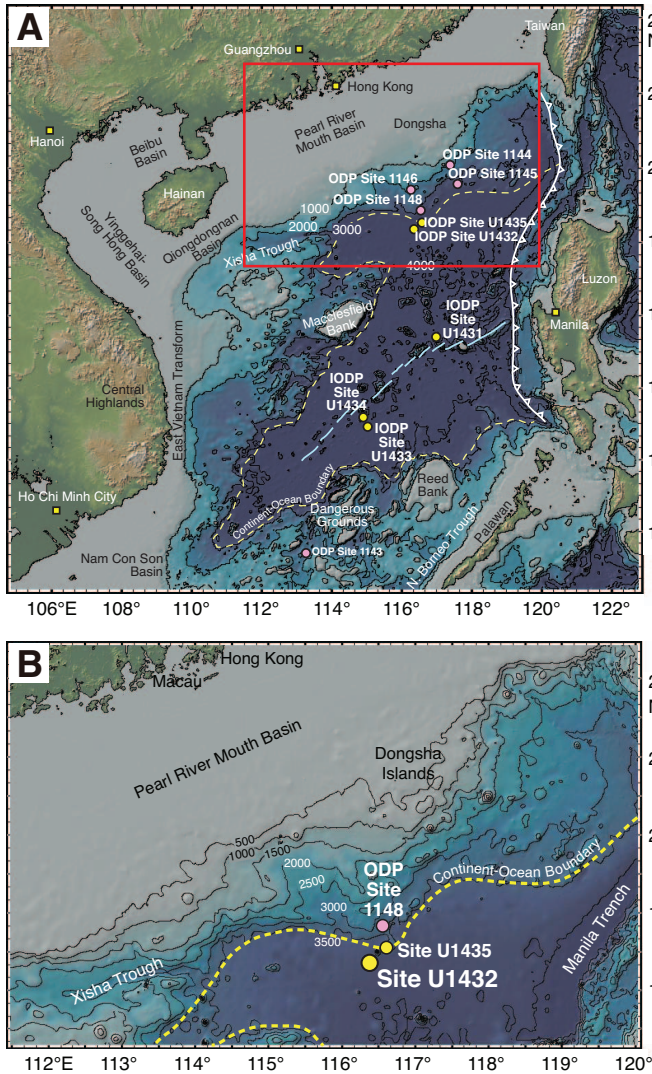
The primary objectives at this site required deep penetration, so the plan was to install a reentry cone and casing system. Site U1432 (proposed Site SCS-6A) consisted of three holes (Table T1). The first hole (U1432A) was a planned jet-in test to determine the correct casing depth for the 20 inch casing string. The second hole (U1432B) was to consist of a reentry system with three strings of casing to ~900 meters below seafloor (mbsf), followed by coring to ~1930 mbsf. Because of poor weather conditions, an additional hole (U1432C) was piston cored while waiting on suitable weather to continue the reentry installation.

Hole U1432A was successfully jetted-in to 62.0 mbsf. A reentry system was then successfully installed to 787.1 mbsf in Hole U1432B. The final cement job on the last casing string compromised the reentry system when the drill string became stuck in the cement. The drill string had to be severed, forcing us to abandon Hole U1432B. Hole U1432C was successfully cored to 110.0 mbsf with the advanced piston corer (APC). Four downhole temperature measurements were taken in Hole U1432C with the advanced piston corer temperature tool (APCT-3). A total of 12 APC cores were collected at this site, recovering 88.74 m of core over 110.0 m of penetration (81% recovery). The total time spent on Site U1432 was 492 h (17.9 days).

¹ Li, C.-F., Lin, J., Kulhanek, D.K., Williams, T., Bao, R., Briais, A., Brown, E.A., Chen, Y., Clift, P.D., Colwell, F.S., Dadd, K.A., Ding, W.-W., Hernández-Almeida, I., Huang, X.-L., Hyun, S., Jiang, T., Koppers, A.A.P., Li, Q., Liu, C., Liu, Q., Liu, Z., Nagai, R.H., Peleo-Alampay, A., Su, X., Sun, Z., Tejada, M.L.G., Trinh, H.S., Yeh, Y.-C., Zhang, C., Zhang, F., Zhang, G.-L., and Zhao, X., 2015. Site U1432. In Li, C.-F., Lin, J., Kulhanek, D.K., and the Expedition 349 Scientists, *Proceedings of the International Ocean Discovery Program, 349: South China Sea Tectonics*: College Station, TX (International Ocean Discovery Program). <http://dx.doi.org/10.14379/iodp.proc.349.104.2015>

² Expedition 349 Scientists' addresses.

Figure F1. A. Bathymetric map of South China Sea region. Solid yellow circles = Expedition 349 sites. Solid pink circles = ODP Leg 184 sites. Yellow dashed line = inferred continent/ocean boundary, blue lines = fossil South China Sea spreading center, white-flagged line = Manila Trench. B. Detailed bathymetry around Site U1432 (red box in A) showing nearby continental shelf, the Manila Trench, and inferred continent/ocean boundary.



Transit to Site U1432

The vessel arrived at Site U1432 at 2337 h (UTC + 8 h) on 16 February 2014 after a 181 nmi transit at an average speed of 10.3 kt. An acoustic positioning beacon was deployed at 2352 h. The position reference was a combination of GPS signals and a single acoustic beacon.

Hole U1432A

The bottom-hole assembly (BHA) for the jet-in test was assembled with an 18½ inch tricone bit and run to just above the seafloor. The vessel was offset 20 m south of the original coordinates for Site U1432 when the acoustic beacon landed within 6 m of the coordinates. The subsea camera and frame (VIT) was deployed to observe the bit tag the seafloor (3840.0 meters below rig floor [mbrf]). After

Figure F2. Shaded map of magnetic anomalies near Site U1432 (data from Ishihara and Kisimoto, 1996). Black lines mark 3000 m isobaths outlining the continental shelf and seamounts. Symbols are magnetic picks from Briais et al. (1993).

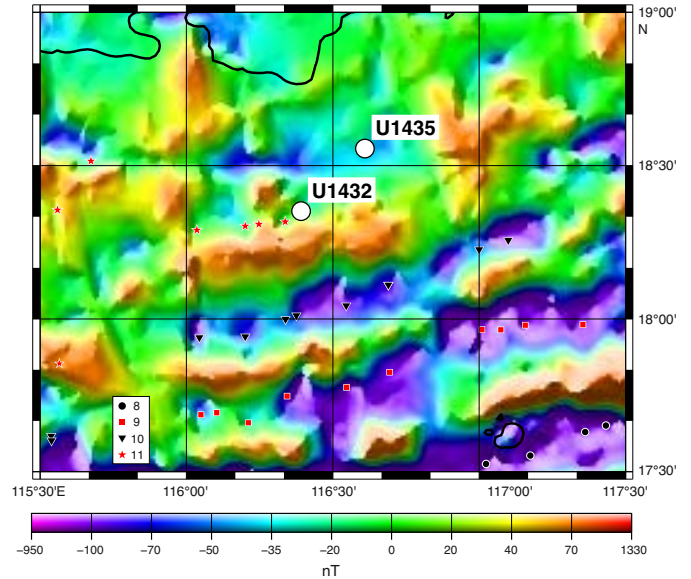


Figure F3. A. Regional contoured bathymetric map showing seismic reflection profiles (yellow and red lines) and the location of Sites U1432 and U1435 and ODP Site 1148. Contour interval = 100 m. B. Seismic profile Line 08ec1573 with location of Site U1432. SP = shotpoint. Green line = interpreted top of basement, blue line = interpreted Oligocene/Miocene boundary.

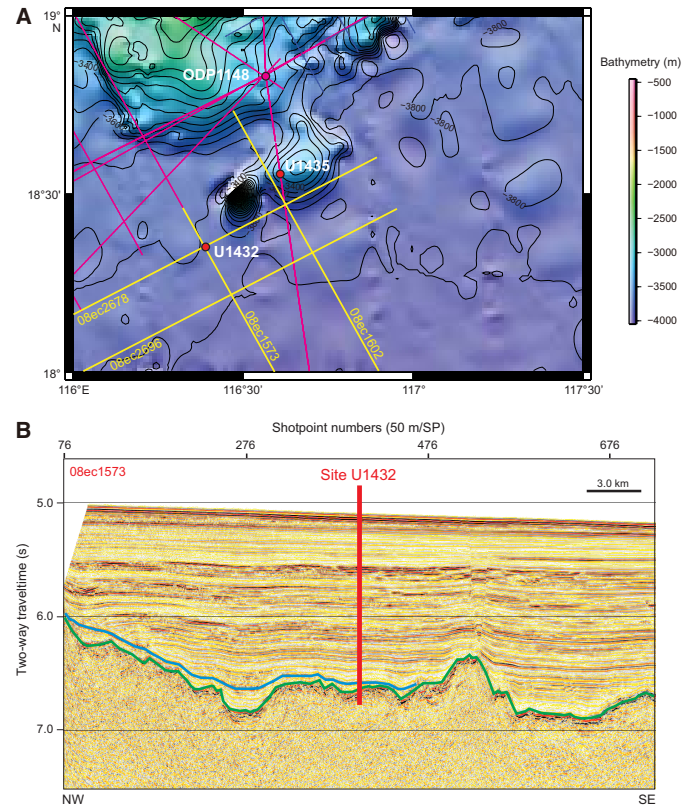


Table T1. Coring summary, Site U1432. CSF = core depth below seafloor, DRF = drilling depth below rig floor, DSF = drilling depth below seafloor. BHA = bottom hole assembly, APC = advanced piston corer. H = advanced piston corer, numeric core type = drilled interval. APCT-3 = advanced piston corer temperature tool, PFTs = perfluorocarbon tracers. (Continued on next page.) [Download table in .csv format.](#)

Hole U1432A

Latitude: 18°21.1051'N
 Longitude: 116°23.4504'E
 Water depth (m): 3829.0
 Date started (UTC): 16 February 2014, 1530 h
 Date finished (UTC): 17 February 2014, 1805 h
 Time on hole (days): 1.1
 Seafloor depth (m DRF): 3840.0
 Seafloor depth calculation method: Seafloor tag confirmed by subsea camera
 Rig floor to sea level (m): 11.00
 Drilling System: 18-1/2 inch tricone bit with 142.84 m BHA
 Penetration depth (m DSF): 62.0
 Cored interval (m): 0
 Drilled interval (m): 62.0
 Drilled interval (no.): 1

Hole U1432B

Latitude: 18°21.1062'N
 Longitude: 116°23.4512'E
 Water depth (m): 3828.98
 Date started (UTC): 17 February 2014, 1805 h
 Date finished (UTC): 6 March 2014, 1236 h
 Time on hole (days): 15.1
 Seafloor depth (m DRF): 3840.0
 Seafloor depth calculation method: Offset depth from Hole U1432A
 Rig floor to sea level (m): 11.20
 Drilling System: 18-1/2 inch, 14-3/4 inch, 9-7/8 inch tricone bits, various BHAs
 Penetration depth (m DSF): 800.0
 Cored interval (m): 0
 Drilled interval (m): 800.0
 Drilled interval (no.): 4

Hole U1432C

Latitude: 18°21.0831'N
 Longitude: 116°23.4504'E
 Water depth (m): 3829.04
 Date started (UTC): 21 February 2014, 0820 h
 Date finished (UTC): 22 February 2014, 2335 h
 Time on hole (days): 1.6
 Seafloor depth (m DRF): 3840.1
 Seafloor depth calculation method: Offset depth from Hole U1432A
 Rig floor to sea level (m): 11.60
 Drilling System: 11-7/16 inch APC/XCB bit with 127.36 m BHA
 Penetration depth (m DSF): 110.0
 Cored interval (m): 110.0
 Recovered length (m): 88.74
 Recovery (%): 81
 Total cores (no.): 12
 APC cores (no.): 12
 Age of oldest sediment cored: Middle Pleistocene

Core	Date (2014)	Time UTC (h)	Depth DSF (m)			Depth CSF (m)		Length of core recovered (m)	Recovery (%)	Sections (no.)	Comments
			Top of interval	Bottom of interval	Interval advanced (m)	Top of cored interval	Bottom of cored interval				
349-U1432A-											
11	17 Feb	0941	0	62.00	62.0						***Drilled from 0 to 62.0 m DSF without coring***
				Totals:	62.0						
349-U1432B-											
11	19 Feb	0500	0	57.10	57.1						***Drilled from 0 to 57.1 m DSF without coring***
12	20 Feb	2215	57.10	160.00	102.9						***Drilled from 57.1 to 160.0 m DSF without coring***
13	23 Feb	2245	160.00	250.00	90.0						***Drilled from 160.0 to 250.0 m DSF without coring***
14	28 Feb	1415	250.00	800.00	550.0						***Drilled from 250.0 to 800.0 m DSF without coring***
				Totals:	800.0						
349-U1432C-											
1H	21 Feb	2215	0	7.90	7.9	0	7.95	7.95	101	7	PFTs
2H	21 Feb	2315	7.90	17.40	9.5	7.90	14.15	6.25	66	6	PFTs

Table T1. (Continued).

Core	Date (2014)	Time UTC (h)	Depth DSF (m)			Depth CSF (m)		Length of core recovered (m)	Recovery (%)	Sections (no.)	Comments
			Top of interval	Bottom of interval	Interval advanced (m)	Top of cored interval	Bottom of cored interval				
3H	22 Feb	0010	17.40	26.90	9.5	17.40	24.44	7.04	74	6	PFTs
4H	22 Feb	0100	26.90	36.40	9.5	26.90	36.46	9.56	101	9	PFTs
5H	22 Feb	0200	36.40	45.90	9.5	36.40	46.06	9.66	102	8	APCT-3, PFTs
6H	22 Feb	0255	45.90	53.00	7.1	45.90	53.01	7.11	100	6	PFTs
7H	22 Feb	0415	53.00	62.50	9.5	53.00	62.16	9.16	96	8	APCT-3, PFTs
8H	22 Feb	0515	62.50	72.00	9.5	62.50	70.64	8.14	86	6	PFTs
9H	22 Feb	0625	72.00	81.50	9.5	72.00	72.16	0.16	2	1	APCT-3, PFTs
10H	22 Feb	0740	81.50	91.00	9.5	81.50	86.21	4.71	50	5	PFTs
11H	22 Feb	0840	91.00	100.50	9.5	91.00	100.57	9.57	101	8	APCT-3, PFTs
12H	22 Feb	0935	100.50	110.00	9.5	100.50	109.93	9.43	99	7	PFTs
Total:					110.0			88.74	81.5	77	

picking up the top drive and spacing out the bit, Hole U1432A was spudded at 1525 h on 17 February 2014. The BHA with the 18½ inch tricone bit was jetted into the formation 62.0 m over a 3 h period. The drill string was then pulled clear of the seafloor and the top drive set back. The remainder of the drill string was tripped out of the hole and the bit cleared the rotary table at 0205 h on 18 February, ending Hole U1432A. The total time spent in Hole U1432A was 26.5 h (1.1 days).

Hole U1432B

Based on the results from the jet-in test, a 5-joint, 57.12 m long 20 inch casing string was selected. The 20 inch casing shoe joint was cut off to length and a Texas-pattern casing shoe welded on the end of the shoe joint. The remainder of the reentry cone and base were put together, moved into the moonpool, and positioned underneath the rotary table. The casing was run through the rotary table and the reentry cone in the moonpool. Each casing connection was tack welded to prevent the casing from backing out. The third joint of casing had to be replaced because of a damaged thread on the pin. The casing hanger and casing pup joint were picked up and attached to the top of the casing string. The Dril-Quip CADA (casing) running tool was made up into the casing hanger on the rig floor. The casing was then lowered through the rig floor, into the moonpool, and through the reentry cone. The casing hanger was landed into the landing ring inside the reentry cone and snapped into place inside the cone. The landing joint was lowered to release the weight of the casing. The casing running tool was rotated 3.75 turns to the right and the casing released. A BHA (casing stinger) with an 18½ inch bit, bit sub, and 6 drill collars was lowered into the reentry cone and casing. The casing running tool was inserted into this BHA and latched into the casing hanger in the reentry cone and secured by rotating the upper BHA 3.75 turns to the left. The moonpool doors were opened and the reentry system with the 20 inch casing was lowered through the moonpool to 3819 mbrf. The top drive was picked up and spaced out to jet-in the 20 inch casing. Hole U1432B was spudded at 0635 h on 19 February 2014. Jetting continued as the casing was slowly lowered. Seven hours later, the reentry system landed on the seafloor. The subsea camera was lowered to assist in releasing the casing. After attempting to release the casing for 2.5 h, the casing tool finally released after the vessel was offset from the original position in order to get the casing running tool to rotate. The rotation required to release the tool was observed clearly on the new subsea camera system. The camera was

then pulled back to the surface and secured. The drill sting was tripped back to the surface, and the BHA was set back in the derrick. During the trip out of the hole, the rig was secured to slip and cut 115 ft of drilling line as per the slip and cut program.

An underreamer with an 11¼ inch closed diameter was made up to the 18½ inch tricone bit and bit sub. The underreamer was set to open up the 18½ inch hole to 22 inches in diameter. The underreamer and bit were lowered into the moonpool, the top drive was picked up, and the underreamer function was tested. The top drive was then set back, and the remainder of the BHA was assembled and run in the hole to 3828.7 mbrf. During the trip, the VIT was deployed. The bit was spaced out for reentry, and the vessel was positioned using the subsea camera system. Hole U1432B was reentered at 2005 h on 20 February. After reentering the hole, the top drive was picked up and the drill string washed down to the casing shoe at 57.1 mbsf. After carefully washing down below the casing shoe so that the underreamer was below the base of the 20 inch casing, the pump rate and speed were optimized for drilling a 22 inch hole below the 20 inch casing. Drilling continued to 4000.0 mbrf (160.0 mbsf). Drilling was suspended at 0610 h on 21 February when weather conditions worsened and the high heave of the vessel began to severely affect the weight on the bit and underreamer. The bit was tripped back inside the 20 inch casing, and the top drive was set back. The drill string was then tripped back to the surface, clearing the seafloor at 0835 h on 21 February, and finally clearing the rig floor at 1620 h. The underreamer and bit were inspected and laid out and the BHA racked back into the derrick. While waiting on the weather to subside, the vessel offset 40 m south to be well away from the reentry cone for Hole U1432B. An APC hole (U1432C) was cored and, after coring to 110.0 mbsf, the weather appeared to have subsided sufficiently for another attempt at drilling out the 22 inch hole for the 16 inch casing.

After tripping out of Hole U1432C, the BHA was set back in the derrick and the upper guide horn was removed and laid out on the drill collar racks. We then returned to Hole U1432B to continue drilling the 22 inch hole for the 16 inch casing. As before, an underreamer with an 11¼ inch closed diameter was made up to the 18½ inch tricone bit and bit sub. The underreamer was set to open up the 18½ inch hole to a 22 inch diameter. The underreamer and bit were lowered into the moonpool, the top drive picked up, and the underreamer function tested. The top drive was set back, and the remainder of the BHA was assembled and run in the hole to 3828.7 mbrf. During the trip, the VIT was deployed. The bit was

spaced out for reentry, and Hole U1432B was reentered at 1944 h on 23 February. The VIT was pulled back to the surface while the top drive was picked up. The bit and underreamer were run in the hole to 160.0 mbsf, and drilling continued from 4000 to 4090.0 mbrf (160.0–250.0 mbsf). The depth of Hole U1432B reached 250 mbsf at 0640 h on 24 February. The hole was conditioned and displaced with 379 bbl of 10.5 lb/gal mud. The drill string was tripped back to the surface and cleared the rig floor at 2120 h. During the trip out of the hole, the vessel was secured to slip and cut 115 ft of drilling line as per the slip and cut program.

The drill floor was rigged up to run 16 inch casing. We assembled 240.85 m of 16 inch casing, including a Drill-Quip casing hanger. The casing was landed on the moonpool doors with the casing running tool, which was then released and pulled back through the rig floor. The 240.77 m casing stinger was made up to the bottom of the casing hanger running tool and lowered through the 16 inch casing in the moonpool. The casing hanger running tool with the casing stinger below was latched into the 16 inch casing hanger, with two control length drill collars and a tapered drill collar above the casing running tool. The entire casing string plus running tools was lowered to 3827.4 mbrf while filling the drill pipe with water every 20 stands. The subsea camera system was installed and lowered to reenter Hole U1432B. After 15 min of maneuvering the vessel, we reentered Hole U1432B at 0500 h on 26 February. The camera system was pulled back to the surface while the top drive was picked up. The casing was lowered into the 22 inch hole and washed down to ~200 mbsf. The VIT was again lowered to assist in releasing the casing running tool from the casing. As the camera system neared the seafloor, the video feed from the subsea camera was lost. The camera system was pulled back to the surface for repair (water had intruded the pan and tilt unit, causing a power overload in the system). The casing was washed in to 240.9 mbsf and landed in the reentry cone. The casing running tool was rotated clockwise 3.75 turns and released from the casing hanger. The BHA, including the internal casing stinger, was pulled back ~11 m, and the top drive was set back. The cementing assembly was rigged up, the lines were pressure tested, and ~20 bbl of cement mixed to 15 lb/gal was pumped downhole. The cement was displaced with seawater and positioned to balance at the casing shoe to an estimated height of 17 m above the casing shoe (both inside and outside the casing). The cementing equipment was rigged down and the drill string pulled back to 161.9 mbsf. The circulating head was connected and the drill string flushed with twice the drill string capacity with seawater. The remainder of the drill string was pulled from the hole, clearing the seafloor at 2140 h on 26 February and finally clearing the rig floor at 0400 h on 27 February. The BHA components were secured, and the running tool was detorqued.

A new 14 $\frac{3}{4}$ inch bit and four stands of drill collars were made up and run in the hole with drill pipe while filling with water at 20-stand intervals. When the bit was at 3823.3 mbrf, the subsea camera system was lowered to view reentry. Hole U1432B was reentered at 1655 h on 27 February and the VIT pulled back to surface. After securing the camera system, the drill string was run in the hole until the top of the cement was tagged at 4069.0 mbrf (229 mbsf). The cement was drilled out from 4069.0 to 4083.0 mbrf (229.0–243.0 mbsf). After washing down to total depth (250.0 mbsf), new 14 $\frac{3}{4}$ inch hole was drilled from 4090.0 to 4640.0 mbrf (250.0–800.0 mbsf). After reaching 800.0 mbsf, the hole was swept clean with high-viscosity mud. After setting back the top drive, the drill string was pulled back to the surface. The bit cleared the rotary table at 1120 h on 1 March. The 10 $\frac{3}{4}$ inch casing stinger components

were made up, and the underreamer arms were set to 12 $\frac{3}{4}$ inches. The top drive was then picked up, and the mud motor and underreamer were tested. After the test was successfully completed, they were racked back in the derrick. After assembling all the casing stinger components, slip and cut of the drilling line was completed.

The rig floor was then prepared for running 10 $\frac{3}{4}$ inch casing, and 787.06 m of casing with a 10 $\frac{3}{4}$ inch casing hanger was made up. The casing was lowered into the moonpool and secured with a casing elevator on the prepared landing platform. The buoyant weight of the casing string was 70,000 lb. The running tool was released from the casing and pulled back to the rig floor and then made up to the bottom of a drill collar stand and racked back in the derrick. The casing stinger with the bit, underreamer, and mud motor were then run inside the casing. Also included in the stinger were three stands of drill collars and 24 stands of drill pipe. The bit and underreamer were positioned just below the bottom of the casing after the running tool was landed and made up to the casing. The casing was run to the seafloor with drill pipe and the subsea camera system deployed to assist with the reentry at the seafloor. Hole U1432B was reentered at 0242 h on 3 March. The camera system was pulled back to the surface and set back into the storage position on the moonpool doors. The casing was run in the hole with drill pipe to 223.5 mbsf. The top drive was picked up and the casing lowered to 244.0 mbsf. The casing was washed to the bottom while pumping 530 gal/min. At 530 gal/min, the mud motor was turning the bit at 80–85 rotations/min with the underreamer arms extended to clear a 12 $\frac{3}{4}$ inch hole in front of the casing. The casing was steadily lowered until it was landed and released at 1745 h on 3 March. The top drive was set back and the drill string tripped from the hole, clearing the seafloor at 2045 h and then clearing the rotary table at 0915 h on 4 March. The casing stinger components were flushed with freshwater and either laid out or, in the case of the drill collars, racked back in the derrick.

After successfully running the 10 $\frac{3}{4}$ inch casing, a cementing stinger was assembled. The stinger consisted of a reentry/cleanout bit, a bit sub, a stand of drill collars, 24 stands of 5 inch drill pipe, F-cup tester, another 2 drill collars, a tapered drill collar, and 2 stands of 5 $\frac{1}{2}$ inch transition drill pipe. The entire assembly was made up and run in the hole with drill pipe to just above the seafloor while stopping every 20 stands to fill the drill pipe with water. The VIT was deployed to just above the seafloor, and Hole U1432B was reentered at 0344 h on 5 March. The camera system was pulled back to the surface and secured. The bit was run in the hole to 767 mbsf, 20 m above the 10 $\frac{3}{4}$ inch casing shoe. The F-cup tester was spaced out so that it was at 42 mbsf, inside the 16 inch casing. The circulating head was made up to the top of the drill string, and the mud pumps were brought up to 60 strokes/min to verify circulation up the annulus between the hole and the casing. After establishing circulation, the cement pump was used to pump 10 bbl of freshwater ahead of the cement slurry. Fourteen barrels of 15.5 lb/gal cement were then mixed and pumped downhole, followed by another 10 bbl of freshwater. This was displaced down the drill string with 263 bbl of saltwater using the mud pumps. After displacing the cement, the circulating head was removed, and the driller attempted to pull out of the hole. He immediately noticed a steadily increasing overpull as he tried to pull out of the hole. After pulling up enough to remove 2 singles of drill pipe, we were unable to raise the drill string any further. It now appears that the formation collapsed around the 10 $\frac{3}{4}$ inch casing string, preventing circulation up the open hole annulus and outside the casing. Instead, the circulation path was up through the 10 $\frac{3}{4}$ casing, bypassing the cup tester. The elevated tem-

peratures at 700 mbsf (~65°–70°C) accelerated the hardening of the cement. The drill string was worked for the next 9 h using combinations of overpull, torque, and pump pressure in an effort to free the drill string. At that point, we rigged up to sever the drill string. The drill string severing charge was lowered to just above the cup tester, which has a 1.5 inch internal diameter. The charge was detonated at 0430 h on 6 March; however, there was no loss of overpull on the pipe. The wireline was pulled out of the hole, and the severing tool cleared the rig floor at 0808 h. The drill pipe was worked with a maximum of 100,000 lb of overpull for ~1 h. The elevators were then lowered back to the elevator stool while the vessel was offset 200 m. The top drive was picked up and the drill pipe was picked up slowly while moving the vessel back to the original location. The pipe was worked free with a maximum of 400 A of torque and 40,000 lb of overpull. The end of pipe cleared the casing hanger at 1105 h. The top drive was set back and the drill string pulled from the hole. The end of pipe cleared the rotary table at 1830 h. The acoustic positioning beacon was recovered while tripping drill pipe. The upper guide horn was reinstalled, the rig floor was secured for transit, and the thrusters were raised. The vessel switched to transit mode at 2036 h on 6 March, ending Site U1432. The total time spent on Hole U1432B was 363.25 h (15.1 days).

Hole U1432C

After pulling out of Hole U1432B to wait on weather, the upper guide horn was picked up from the drill collar rack, lifted to the rig floor, and reinstalled below the rotary table. An APC/extended core barrel (XCB) BHA was made up while the vessel was offset 40 m south of Hole U1432B. The drill string was then tripped toward the seafloor. After completing the pipe trip to just above the seafloor, the top drive was picked up and spaced out, and Hole U1432C was spudded at 0555 h on 22 February 2014. The first coring attempt with the bit at 3835 mbrf did not recover any core. The bit was then lowered to 3838.5 mbrf, and the next coring attempt recovered a mudline core of 7.95 m of sediment. This core length was used to calculate the seafloor depth at 3840.1 mbrf (3829.1 mbsl). Nonmagnetic core barrels were used with the APC for Cores 329-U1432C-1H through 12H to a final depth of 110.0 mbsf. Perfluorocarbon tracer (PFT) fluid was displaced into the drill string prior to spudding the hole and was pumped continuously during Hole U1432C. Temperature measurements were taken with the APCT-3 on Cores 5H, 7H, 9H, and 11H, with good results. The hole was terminated when weather conditions improved sufficiently to return to Hole U1432B. The bit was tripped to the surface and cleared the rig floor at 0735 h, ending Hole U1432C. A total of 12 APC cores were taken over a 110.0 m interval in Hole U1432C, recovering 88.74 m of core (80.7% recovery). The total time spent in Hole U1432C was 39.25 h (1.6 days).

Lithostratigraphy

Lithostratigraphic units

One lithostratigraphic unit was defined at Site U1432 based on visual core description, smear slide, and thin section inspection, together with scanning of an array of physical properties, especially magnetic susceptibility and color spectra, as described in [Lithostratigraphy](#) in the Methods chapter (Li et al., 2015a).

Unit description

Unit I (0–109.93 mbsf)

Interval: Cores 349-U1432C-1H through 12H

Depth: 0–109.93 mbsf (total depth)

Age: Pleistocene

Unit I (Figure F4) spans the uppermost 109.93 m (a minimum thickness limited by drilling depth in this hole) and is dominated by a sequence comprising dark greenish gray clay and clay with silt. The clay has faint color banding with color variation typically across 10–20 cm intervals. Some lighter colored intervals have higher nanofossil content, but otherwise there is little difference seen in microscopic examination of the clay. Patches and layers of more intense green color in the clay intervals are interpreted to contain glauconite. Most clay intervals have heavy bioturbation, resulting in a homogeneous appearance. No individual burrows are visible. Rare pyrite nodules occur in the clay intervals. There are three pyrite nodules in the interval from 54.5 to 56.0 mbsf (Section 349-U1432C-7H-2A). One nodule, ~2 cm in width, is rounded and slightly botryoidal in shape (Figure F5); another is elongate, ~4 cm long, and appears to be replacing a burrow.

The clay is interbedded with rare silty layers that vary from dark greenish gray silty clay to clayey silt with sand. These layers are usually only a few millimeters thick but are rarely as thick as 10 cm, fine

Figure F4. Lithostratigraphy summary.

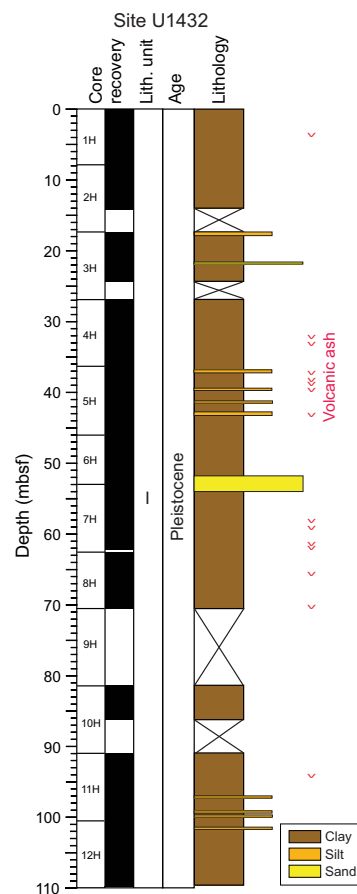


Figure F5. Pyrite nodule in a clay layer (349-U1432C-7H-2A). A. Close-up showing nodule shape. B. Reflected-light thin section showing microcrystals of pyrite and shapes of foraminifers (113–117 cm; TS64).

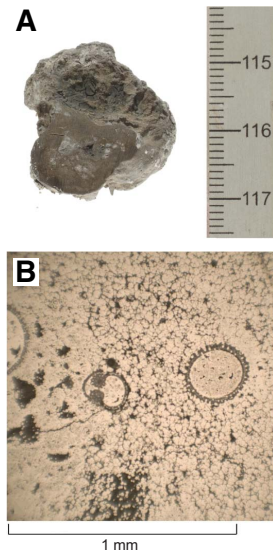
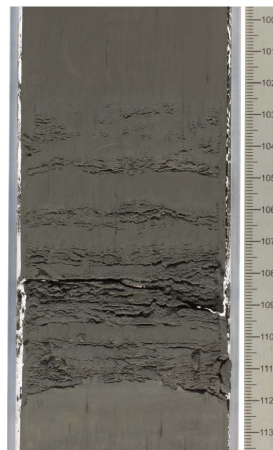


Figure F6. Very thin, upward-fining, sharp-based silt layers, Hole U1432C (12H-1A, 100–113 cm).



upward, and have sharp erosive bases (Figure F6). The number of silty layers varies between cores but is up to three or four per section. We interpret the silty layers as distal turbidites. Some silty intervals have multiple layers, up to six within an interval of <10 cm, indicating that at times multiple turbidites followed one another in quick succession.

Microscopic inspection of the silty layers shows that they contain subrounded to subangular grains of quartz, feldspar, and minor amounts of mica, volcanic glass, and foraminifer shells. The silty layers have low magnetic susceptibility compared to the clay-rich layers (Figures F7, F8), possibly due to greater abundance of non-magnetic minerals such as quartz and feldspar.

The base of Core 349-U1432C-6H and top of Core 7H contain a sand interval that is approximately 2.42 m thick. The sand is soupy, probably as a result of drilling disturbance, and no sedimentary structures are preserved. The sand is dominantly siliciclastic with

Figure F7. Magnetic susceptibility and reflectance spectroscopy profiles (after 10-point running average), Site U1432. The shaded area correlates with a prominent sand layer.

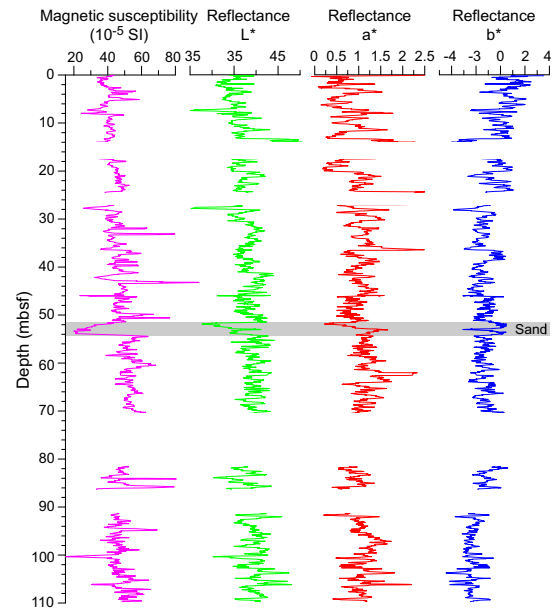
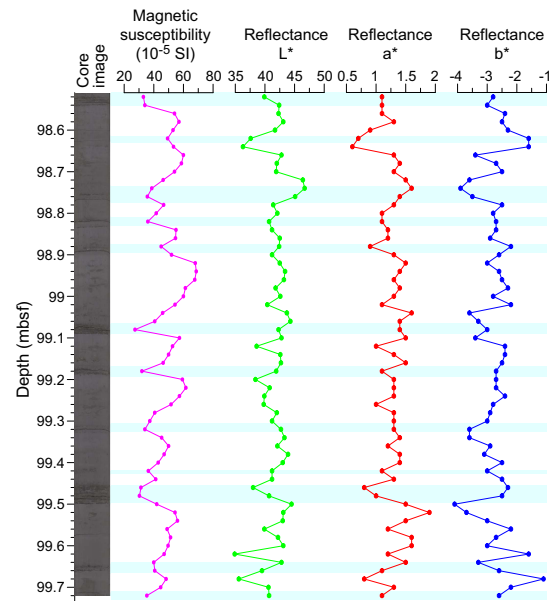


Figure F8. Correlation of lithology with magnetic susceptibility and reflectance spectroscopy (349-U1432C-11H-6A).



subangular to subrounded grains of quartz and rock fragments and with lesser feldspar and minor mica, amphibole, and mafic ash shards (Figure F9). There are abundant foraminifer grains. The sand has very low magnetic susceptibility (Figure F7).

Thin volcanic ash layers (0.5–2.0 cm thick) occur in many cores in this unit but overall comprise <1% by volume. They vary in color from light colored (Figure F10) and slightly pinkish to dark brown and black, indicating varying chemical composition of the ash particles. Most ash layers have a sharp base and fine upward; however,

Figure F9. Sand in Unit I of Hole U1432C consisting mainly of quartz, feldspar, volcanic glass, and foraminifer fragments (6H-5A, 90 cm).

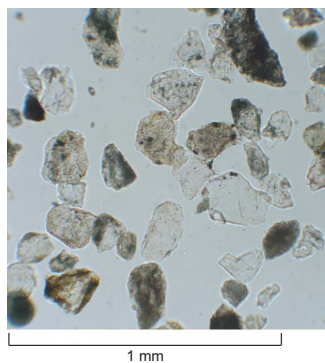


Figure F10. Light-colored ash layer, Hole U1432C (7H-5A, 23–32 cm).



others are bioturbated and occur as isolated pods within the clay or silt.

Discussion

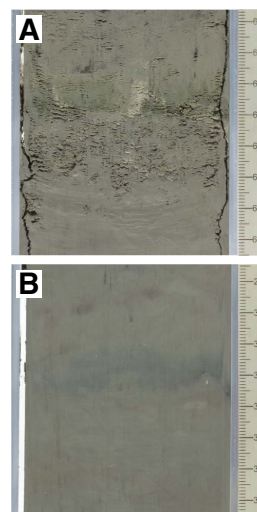
Unit I at Site U1432 can be correlated with Unit I at Site U1431; however, here the unit is much richer in clay and the silty turbidites are thinner and separated by greater thicknesses of strongly bioturbated clay. This unit also lacks the rare foraminifer sands of Site U1431 and has fewer ash layers, most likely because it is further away from the active volcanic arc and has no nearby seamount-derived sediment source.

The thin silt beds that fine upward and have erosive bases are interpreted as the distal deposits of turbidity currents. The silt has a similar grain composition to the silty intervals at Site U1431 (see Figure F7 in the Site U1431 chapter [Li et al., 2015b]), and probably has a similar source, with the siliciclastic grains coming from a continental region, likely South China or Taiwan (Figure F1).

Dark green and/or greenish sediment layers occur intermittently in the sediment at Sites U1431 and U1432 and form a distinctive characteristic of the sediment. These layers occur both within turbidite beds and separately (Figure F11).

Similar green sediment was encountered at Deep Sea Drilling Project (DSDP) Leg 90 Sites 588, 590, 591, 592, and 593 (Gardner et al., 1986), ODP Leg 130 Sites 803–807 (Lind et al., 1993), ODP Leg 162 Site 985 (Ikehara et al., 1999), and ODP Leg 184 Sites 1143 and 1148 (Tamburini et al., 2003), and discussions on their origins were included in their site reports. These investigations were based on a combination of smear slide and thin section observation, X-ray diffraction (XRD), grain size analysis, and sediment chemistry. During initial shipboard investigations on sediment from New Caledonia to

Figure F11. Two types of green layers, Hole U1432C. A. Graded silt layer with very thin bedded green layer (11H-3A, 60–67 cm). B. Green layer in mud layer with strong bioturbation (12H-4A, 29–36 cm).



the New Zealand region (Leg 90), the origin and formation mechanism of the green sediment were largely explained by external factors, such as the supply of volcanic ash, but it was revealed that there was no significant mineralogical variation between the green sediment and the host sediment (Lind et al., 1993).

More detailed investigation of similar greenish sediment layers was conducted during Leg 162 in the Gardar Drift of the North Atlantic (ODP Site 983; Ikehara et al., 1999) and during postcruise research in the northern South China Sea (Leg 184; Tamburini et al., 2003). The organic geochemistry of the greenish clay sediment sampled at Site 983 was analyzed and indicated that the sediment contained a large amount of organic matter and sulfur, reaching a maximum of 5.6 wt% total organic carbon (TOC) and 26 wt% sulfur. The sediment also contained large amounts of molecular *n*-alkanes, indicating a terrigenous source (Ikehara et al., 1999), as well as significant amounts of hopanoid hydrocarbons such as diploptene, suggesting that prokaryotes, such as methane-oxidizing bacteria or cyanobacteria, may have contributed to the formation of that organic-rich sediment.

Research following Leg 184 in the South China Sea included detailed grain size analysis, XRD, and inorganic and organic geochemistry. Tamburini et al. (2003) concluded that the green color in the sediment formed as a result of the initial process of glauconite formation. The sedimentary environment and active sedimentation processes may have favored a reducing environment at the sediment/water interface. This may have led to increased microbial activity and degradation of organic matter. Tamburini et al. (2003) found that the green layers had lower TOC than the surrounding sediment. The reducing conditions may have led to dissolution of carbonate and a subsequent increase in Ca, Ba, and Sr, as found in the green layers at Sites 1147 and 1148 of Leg 184. Examination of the relationship between TOC and the green layers at Sites U1431 and U1432 will be included in later research.

The sediment color can be expressed by three color components (L^* , a^* , and b^*). Based on previous work, the L^* (lightness) value appears to be mainly controlled by calcium carbonate content, such that the lightness of the sediment color increases with an increase in the calcium carbonate content, and more blackish colors indicate an

increase in the organic matter content (e.g., Nagao and Nakashima, 1992; Hyun et al., 1999; Ortiz et al., 1999); the a^* (psychometric red–green) value is controlled by iron for pelagic sediment and also by manganese carbonate; and the b^* value (psychometric yellow–blue) is thought to be a function of iron content in the form of hydroxides. Recently, Khim et al. (2009) and Helmke et al. (2002) have shown that these color changes, particularly L^* , in sediment provide valuable information on the depositional environment and can assist with chronostratigraphy and paleoceanographic interpretations. For example, L^* can be related to sediment that is deposited under anoxic conditions. Darker sediment generally has a laminated structure suggesting lack of bioturbation and oxygen.

The dark greenish sediment layers at Sites U1431 and U1432 are distinguished by visual core inspection and are not differentiated from the other sediment layers by color reflectance data. There may be a slight decrease in the a^* value for green layers, but this has not been determined on a systematic basis. Further study is needed to determine whether there is a correlation between the green color and sediment organic and inorganic geochemistry.

Biostratigraphy

We analyzed all core catcher samples for calcareous nannofossils, planktonic foraminifers, and radiolarians in Hole U1432C. Specimens of calcareous nannofossils, foraminifers, and radiolarians are present in all samples. Based on three planktonic foraminifer events and three calcareous nannofossil events, sediment recovered at Site U1432 spans the Middle to Late Pleistocene, with

the base of the sequence older than 0.61 Ma and younger than 0.91 Ma (Figure F12; Tables T2, T3). Radiolarian age control is based on the general assemblage because of the lack of biostratigraphic index species. A correlation of biohorizons with paleomagnetic data from the same hole suggests a sedimentation rate of ~12 cm/ky for the 108.83 m sequence of Hole U1432C.

Preservation of calcareous nannofossils is moderate to good, although some intervals appear to contain heavy reworking (Table T4). Preservation of planktonic foraminifer assemblages is poor to good, with frequent observation of test fragmentation; reworking is also evident in some samples (Table T5). Radiolarian preservation is poor to moderate (Table T6). Siliceous sponge spicules and diatoms are present but rare in abundance.

Calcareous nannofossils

Calcareous nannofossil biostratigraphy in Hole U1432C was established through analysis of core catcher and additional split-core samples. Nannofossil preservation is moderate to good, with some samples (e.g., Samples 349-U1432C-1H-CC and 4H-CC) containing reworked Miocene species (Table T4). Three Pleistocene nannofossil datums are identified in the recovered sedimentary sequence. The presence of *Emiliana huxleyi* in Samples 1H-CC through 4H-CC (7.90–36.41 mbsf) indicates a Middle to Late Pleistocene age (≤ 0.29 Ma) based on the first appearance datum (FAD) of *E. huxleyi* (Zone NN21). Zone NN20 is assigned to Sections 5H-CC and 6H-CC. The top of Zone NN19 is recognized in Sample 7H-CC (62.11 mbsf) based on the last appearance datum (LAD) of *Pseudoemiliana lacunosa* (0.44 Ma). The LAD of *Gephyrocapsa* sp. 3

Figure F12. Age-depth model.

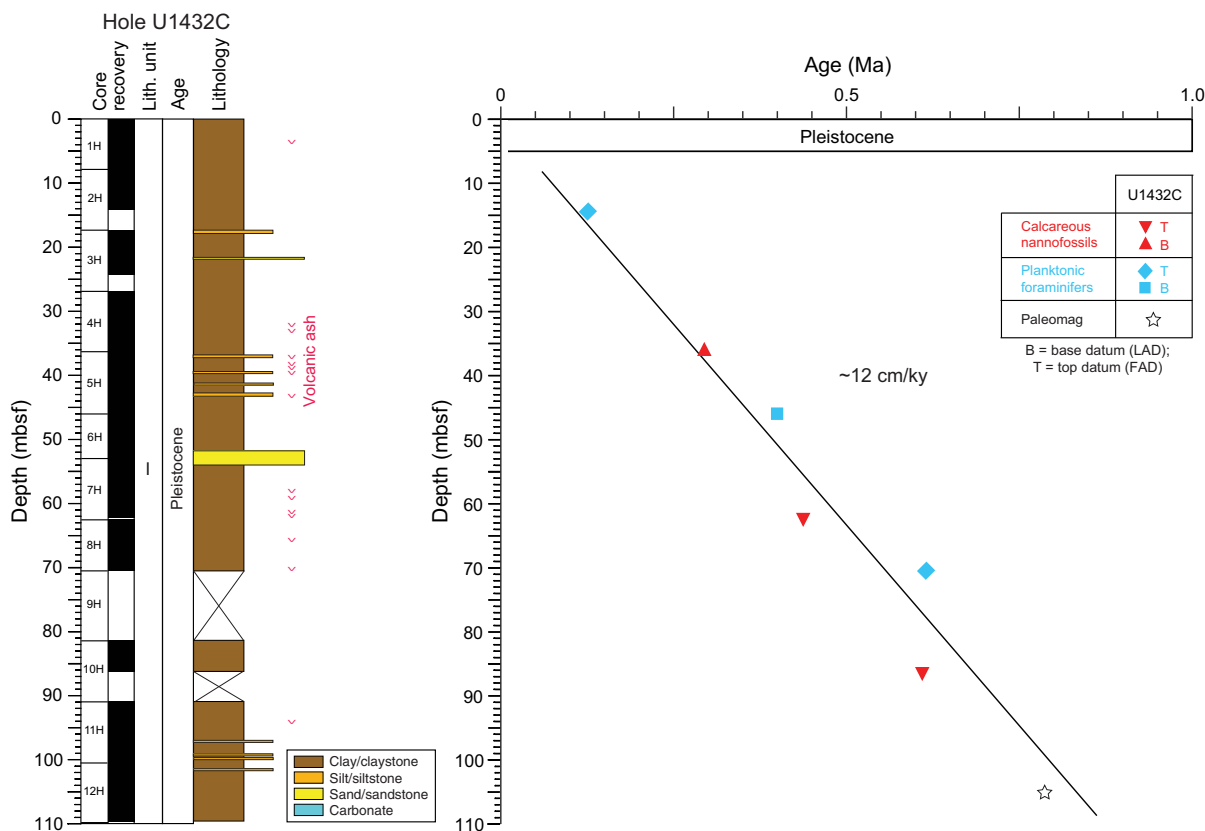


Table T2. Depths and ages of calcareous nannofossil events, Hole U1432C. T = top/last appearance datum, B = base/first appearance datum. [Download table in .csv format.](#)

Epoch	Zone (Martini, 1971)	Calcareous nannofossil event	Hole U1432C		
			Core, section	Top depth (mbsf)	Age (Ma)
Middle to Late Pleistocene	NN21/NN20	B <i>Emiliana huxleyi</i>	4H-CC	36.41	0.29
Middle Pleistocene	NN20/NN19	T <i>Pseudoemiliana lacunosa</i>	7H-CC	62.11	0.44
	NN19	T <i>Gephyrocapsa</i> sp. 3	10H-CC	86.15	0.61

Table T3. Depths and ages of planktonic foraminifer events, Hole U1432C. T = top/last appearance datum, B = base/first appearance datum. [Download table in .csv format.](#)

Epoch	Zone (Berggren et al., 1995; Wade et al., 2011)	Planktonic foraminifer event	Hole U1432C		
			Core, section	Top depth (mbsf)	Age (Ma)
Late Pleistocene	PT1b	T <i>Globigerinoides ruber rosa</i>	2H-CC	14.10	0.12
Middle Pleistocene	PT1a	B <i>Globigerinoides ruber rosa</i>	5H-CC	46.01	0.40
		T <i>Globorotalia tosaensis</i>	8H-CC	70.59	0.61

Table T4. Distribution of calcareous nannofossils, Hole U1432C. [Download table in .csv format.](#)Table T5. Distribution of planktonic foraminifer species, Hole U1432C. [Download table in .csv format.](#)Table T6. Distribution of radiolarian species, Hole U1432C. [Download table in .csv format.](#)

(0.61 Ma) occurs in Sample 10H-CC (86.15 mbsf), indicating that this sample is within Zone NN19. Based on these latter two datums (0.44 and 0.61 Ma; Gradstein et al., 2012), a Middle Pleistocene age can be assigned to Samples 5H-CC through 10H-CC. Rare specimens of *Reticulofenestra asanoi* occur in Samples 6H-CC and 7H-CC (52.96–62.11 mbsf); however, these specimens are considered reworked, as they co-occur with the LAD of *P. lacunosa* at the same depth. *R. asanoi* also occurs rarely in Sample 11H-CC (100.57 mbsf) but is absent in the bottommost sample (Sample 12H-CC; 109.83 mbsf), indicating an interval above its last common appearance datum at 0.91 Ma. Thus, an age of >0.61 and <0.91 Ma is estimated for the base of the sediment sequence recovered in Hole U1432C.

Planktonic foraminifers

We analyzed planktonic foraminifers in core catcher samples from Hole U1432C. The abundance of planktonic foraminifers varies from rare to abundant with poor to good preservation (Table T5). Fragmented planktonic foraminifer tests are common, reaching 70% or more in Sample 349-U1432C-7H-CC (62.11 mbsf).

The planktonic foraminifer assemblage is dominated by late Quaternary tropical to subtropical Indo-Pacific species, including *Globorotalia* spp., *Globigerinoides* spp., *Pulleniatina obliquiloculata*, *Sphaeroidinella dehiscens*, *Neogloboquadrina dutertrei*, and *Orbulina universa*. Together with three bioevents (Table T3), this planktonic foraminifer assemblage indicates that the sedimentary sequence recovered in Hole U1432C is from Pleistocene Zone Pt1. The LAD and FAD of *Globigerinoides ruber* (pink) occur in Samples

349-U1432C-2H-CC (14.5 mbsf) and 5H-CC (46.0 mbsf), respectively, indicating Subzone Pt1b. The LAD of *Globorotalia tosaensis* (0.61 Ma) in Sample 8H-CC (70.59 mbsf) is used to mark the Pleistocene Subzone Pt1b/Pt1a boundary.

The absence of *Globigerinoides obliquus* indicates an age younger than 1.3 Ma for the base of this sequence (see Table T3 in the Methods chapter [Li et al., 2015a]). The mixing of younger (Pleistocene) species such as *G. tosaensis* and older (Pliocene) species such as *Dentoglobigerina altispira* and *Globorotalia multicamerata* is interpreted as resulting from redeposition by turbidites (see [Lithostratigraphy](#)), especially in Sample 349-U1432C-6H-CC (53.01 mbsf) (Table T5), which contains abundant sand and some shallow-water benthic foraminifers.

Radiolarians

The radiolarian assemblage from Hole U1432C (Samples 349-U1432C-1H-CC through 12H-7, 63–73 cm) represents a Pleistocene sequence. Detailed biostratigraphic zonation could not be assigned to this assemblage because of the lack of biostratigraphically important species; however, the presence of *Collosphaera tuberosa* in Sample 1H-CC (7.95 mbsf) suggests an age no older than Zone NR2 (<0.42 Ma) (Wang and Abelmann, 1999). Radiolarians in Hole U1432C vary from abundant to few in Samples 1H-CC and 2H-CC (Table T6) to rare or barren downhole (14.15–109.93 mbsf). Preservation ranges from moderate to poor. Sponge spicules and diatoms are scarce.

Geochemistry Interstitial water chemistry

We collected 16 whole-round sediment samples (5 cm long) from 2.95 to 105 mbsf in Hole U1432C for interstitial water measurements. Interstitial water samples were taken at a frequency of 2 samples per core for the uppermost 35 mbsf and at a frequency of 1 sample per core below 40 mbsf. Interstitial water chemistry data are given in Tables T7 and T8 and shown in Figures F13, F14, F15, and F16.

Table T7. Interstitial water major element concentrations, salinity, pH, alkalinity, sulfate, ammonium, phosphate, chloride, bromide, calcium, magnesium, sodium, and potassium, Hole U1432C. [Download table in .csv format.](#)

Table T8. Interstitial water minor element concentrations, barium, iron, lithium, manganese, silicon, and strontium, Hole U1432C. [Download table in .csv format.](#)

Figure F13. Interstitial water chloride, bromide, sodium, and potassium. Blue dashed lines = modern seawater values.

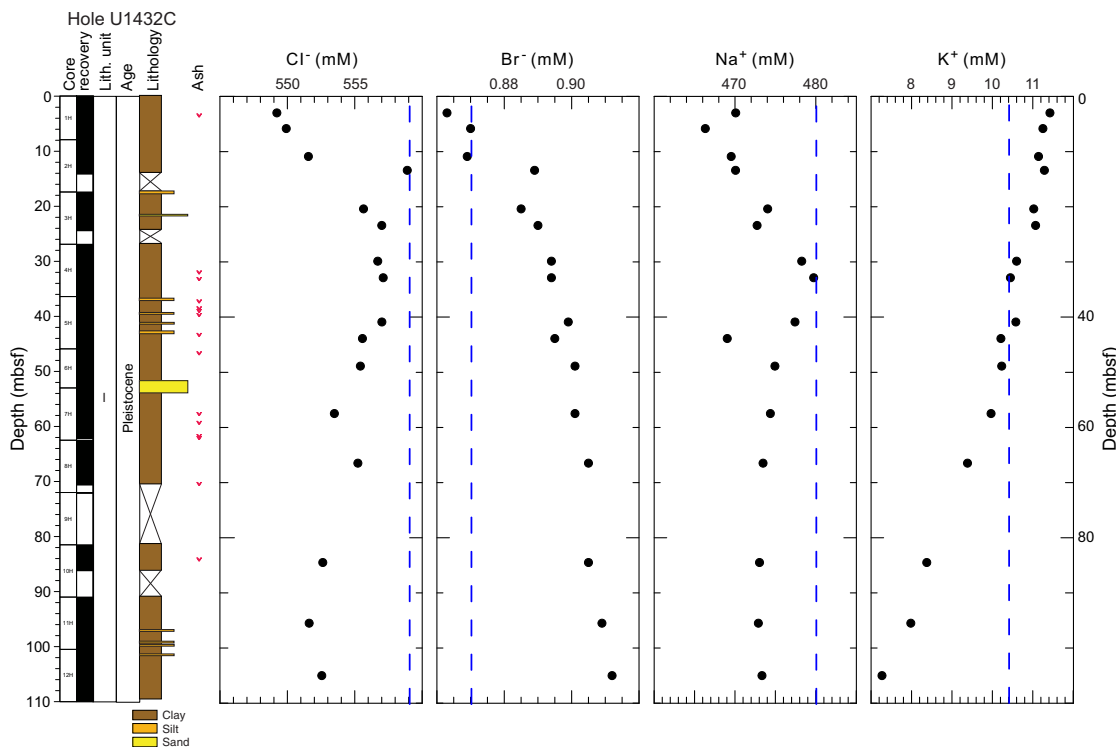


Figure F14. Interstitial water sulfate, alkalinity, ammonium, and phosphate. Blue dashed lines = modern seawater values.

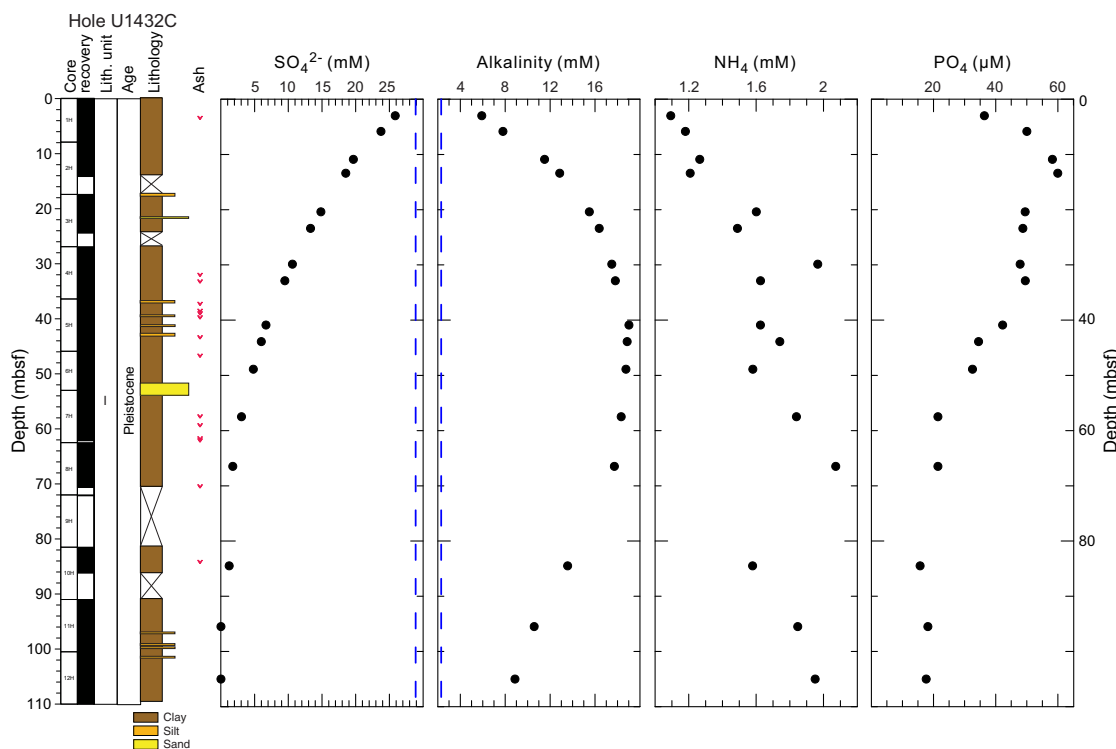


Figure F15. Interstitial water calcium, magnesium, strontium, and boron. Blue dashed lines = modern seawater value.

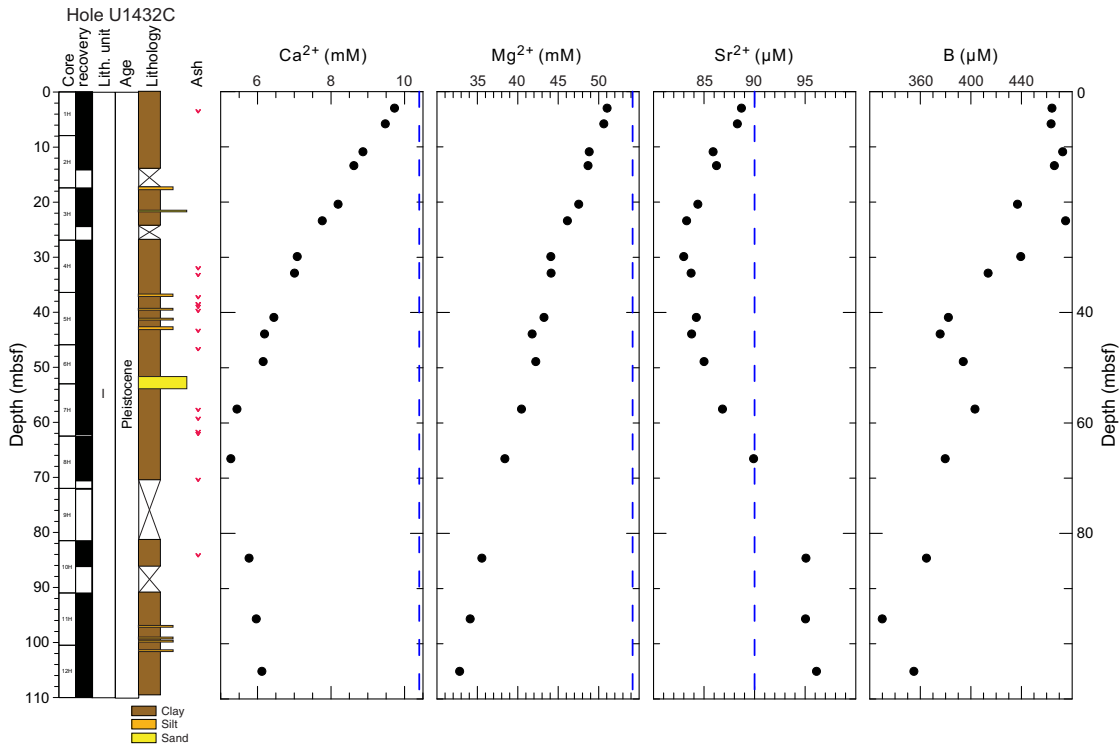
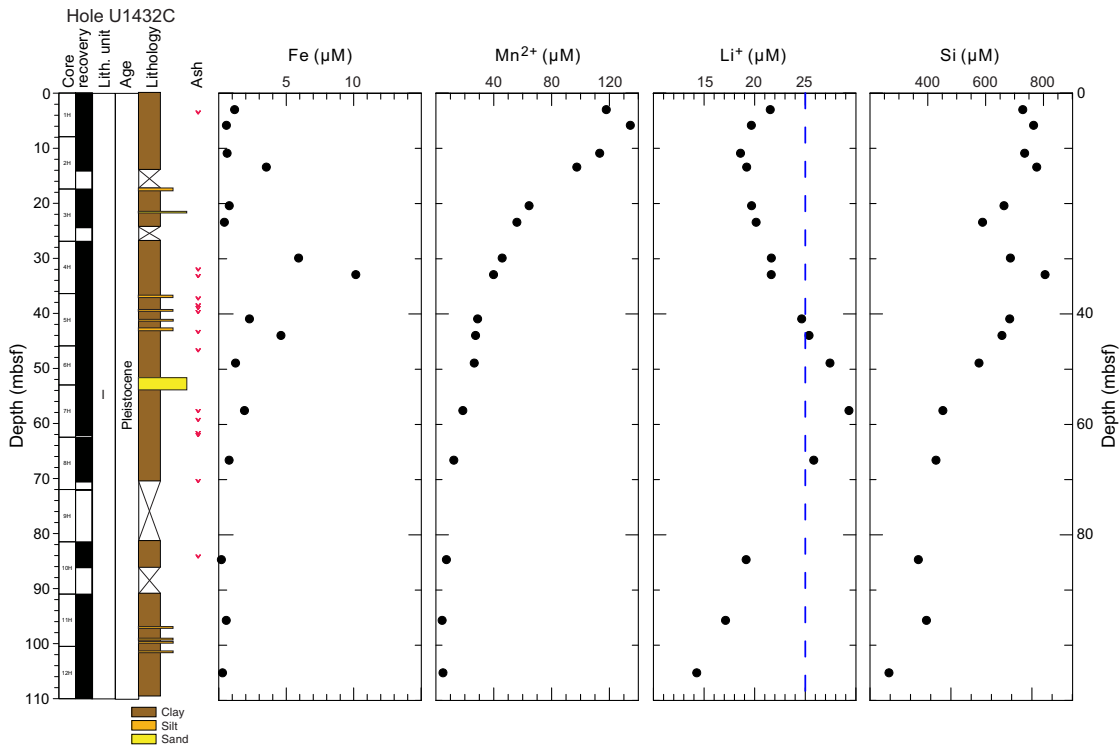


Figure F16. Interstitial water iron, manganese, lithium, and silica. Blue dashed line = modern seawater value.



Chloride, bromide, and alkalis (sodium and potassium)

Downhole profiles of chloride, bromide, sodium, and potassium in Hole U1432C are shown in Figure F13. Chloride concentrations fluctuate slightly with depth, ranging between 549 and 559 mM throughout the hole. Only one sample at ~13.4 mbsf has a modern seawater-like value (559 mM), whereas other chloride concentrations are slightly lower than the modern seawater value. Sodium concentrations vary from 466 to 479 mM in the uppermost 44 mbsf, with several samples close to modern seawater (480 mM) between 30 and 41 mbsf. Below 48 mbsf, sodium concentrations remain constant at ~473 mM. Bromide concentrations increase with depth, ranging from 0.86 mM close to the seafloor to 0.91 mM at the bottom of the hole. Most concentrations are higher than that of modern seawater (0.87 mM). The high bromide concentrations may be caused by organic matter diagenesis in the sediment as indicated by sulfate reduction and high methane concentrations (Figures F14, F17).

The K^+ concentrations decrease with depth throughout the hole, from 11.4 mM at the top to 7.3 mM (~70% that of seawater) at the bottom. Concentrations higher than modern seawater (10.4 mM) occur in the uppermost 40 mbsf. This phenomenon was also observed at Site U1431 and was attributed to ion exchange with clay minerals (see [Geochemistry](#) in the Site U1431 chapter [Li et al., 2015b]). The significant K^+ decrease below 40 mbsf is likely caused by K-rich and Si-rich mineral formation in the sediment, as silica concentrations also decrease with depth below 40 mbsf (Figure F16).

Sulfate, alkalinity, ammonium, and phosphate

Alkalinity, sulfate, ammonium, and phosphate profiles are shown in Figure F14. Alkalinity increases from ~6 mM close to the seafloor to a maximum of ~19 mM at ~41 mbsf, which is ~50 m

above the depth at which sulfate is completely consumed. Below 41 mbsf, alkalinity decreases with depth to ~9 mM at the bottom of the hole. The decrease in alkalinity is mainly caused by carbonate precipitation around the sulfate–methane transition zone (SMTZ), as suggested by the calcium depth profile (Figure F15).

Sulfate decreases with depth and is completely depleted at ~90 mbsf, where methane reaches a maximum ~4800 ppmv (Figure F17). Methane concentration increases from 4 to 50 ppmv at 66.5 mbsf, reaching concentrations between 2400 and 4800 ppmv below that depth. This is in good agreement with the decrease in sulfate concentrations to ~1.8 mM at 66.5 mbsf, reaching 0 mM below. Based on sulfate and methane concentrations, the SMTZ occurs between ~70 and 100 mbsf. Shore-based carbon isotope analysis of dissolved inorganic carbon will provide better understanding of the SMTZ.

Ammonium concentration shows a general increasing trend from ~1 mM near the seafloor to a maximum value of ~2 mM at 66.5 mbsf, corresponding to the depth where methane increases sharply and sulfate is depleted. This suggests ammonium production is mostly caused by organoclastic decomposition coupled to sulfate reduction. Phosphate behaves differently from ammonium; it increases from 36 μM at the top to a maximum of ~60 μM at 13.4 mbsf, followed by a decrease with depth to ~18 μM at the bottom of the hole.

Calcium, magnesium, and strontium

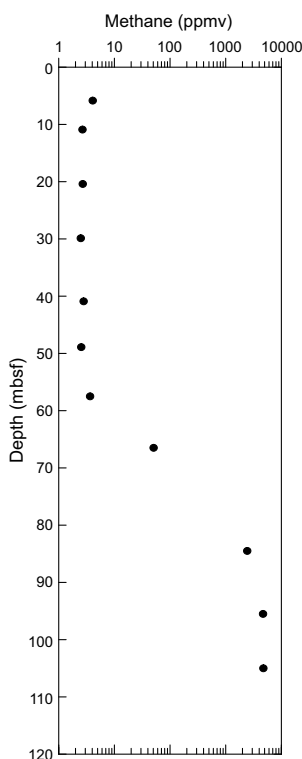
Downhole distributions of Ca^{2+} , Mg^{2+} , and Sr^{2+} are shown in Figure F15. Calcium concentration decreases from 10.2 mM near the seafloor to a minimum of 5.4 mM at 66.5 mbsf, where sulfate is almost completely consumed. Alkalinity reaches a maximum of ~19 mM at ~40 mbsf, which could trigger diagenetic carbonate precipitation, causing the uptake of Ca^{2+} and some of the other alkaline earth elements, particularly Mg^{2+} and Sr^{2+} . Calcium concentrations increase below this depth to 6.1 mM at the bottom of the hole. Magnesium concentrations are lower than the modern seawater value (54 mM) throughout Hole U1432C, decreasing from 51 mM near the seafloor to 33 mM at the bottom of the hole. Magnesium behaves differently from calcium, possibly because of other diagenetic reactions occurring in the sediment, such as clay ion exchange and low-temperature ash alteration. Sr^{2+} concentrations decrease from 89 μM near the seafloor to 83 μM at ~30 mbsf, followed by an increase with depth to 96 μM at the bottom of the hole.

Boron, barium, lithium, silica, iron, and manganese

Downhole distributions of boron, iron, manganese, lithium, and silica are given in Figures F15 and F16. Barium concentrations (Table T8) increase from a seawater-like value of ~0.02 μM close to the seafloor to a maximum of 55.1 μM at 84.5 mbsf, followed by a slight decrease with depth to ~42.4 μM at the bottom of the hole. The highest Ba^{2+} concentrations (42.4–55.1 μM) occur at 84–105 mbsf, corresponding to the SMTZ. The Ba^{2+} concentration is likely controlled by the stability of the mineral barite (BaSO_4). The Ba^{2+} concentration increase may result from in situ barite dissolution due to sulfate reduction or the migration of Ba^{2+} in the low-sulfate fluid. Shore-based solid-phase barium analyses will be critical for determining the origin of the elevated barium and the history of fluid flow.

Boron concentrations vary from 330 to ~475 μM , with the highest values of ~470 μM at 25 mbsf, followed by a decrease to ~360 μM at ~45 mbsf. Below 50 mbsf, boron shows a general decreasing trend to a minimum of 330 μM at ~100 mbsf).

Figure F17. Headspace methane, Hole U1432C.



Lithium concentrations decrease from 21.5 μM close to the seafloor, which is slightly lower than the modern seawater value (25 μM), to 18.6 μM at ~11 mbsf, followed by a gradual increase with depth to a maximum of 29.3 μM at ~60 mbsf, before decreasing with depth to a minimum of 14.3 μM at the bottom of the hole. The decrease in lithium concentration is likely caused by secondary mineral precipitation, probably related to clay ion exchange reactions in that interval.

Silica concentrations are elevated compared to modern seawater (0–180 μM), ranging from 266 to 806 μM . This is mostly controlled by lithology and silicate mineral diagenesis. In the upper 40 mbsf, silica concentrations are high, ranging from 550 to 806 μM , and vary with depth with an average around 650 μM . Below 40 mbsf, silica concentrations gradually decrease with depth, from ~650 to 350 μM at the bottom of the hole.

Dissolved iron concentrations vary with depth, ranging from 0.2 to 10.2 μM , with two peaks of 3.5 μM at 13.3 mbsf and 10.2 μM at 33 mbsf. The second iron peak corresponds to a volcanic ash layer, which may indicate that the higher iron concentrations are caused by volcanic ash alteration. Dissolved manganese concentrations increase from 117.8 μM at the top to a maximum of 134.5 μM at 5.8 mbsf, followed by a gradual decrease with depth to a minimum of ~4 μM at the bottom of the hole. The manganese peak is above

the iron peaks, reflecting a normal order for the redox sequence in marine sediments.

Headspace gas geochemistry

We analyzed 11 headspace gas samples as part of the shipboard safety and pollution prevention program (Figure F17; Table T9). Methane is the predominant hydrocarbon present in Hole U1432C, ranging from 2 to 4748 ppmv. Methane (C_1) concentrations abruptly increase by 2 orders of magnitude at 84 mbsf. Ethane (C_2) and ethene ($\text{C}_{2=}$) are observed only in one sample at 5.84 mbsf (Sample 349-U1432C-1H-5, 0–5 cm), with values of 1.61 and 1.02 ppmv, respectively.

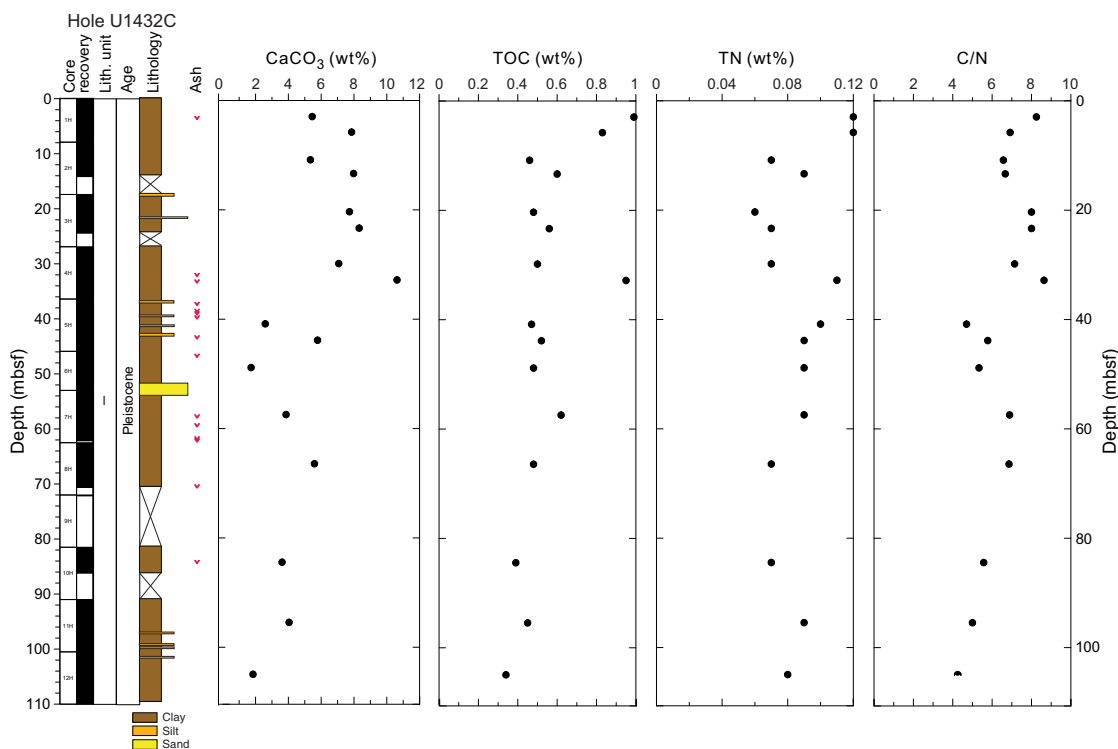
Bulk carbon and nitrogen analysis

The distributions of TOC, calcium carbonate (CaCO_3), total nitrogen, and the total organic carbon to total nitrogen ratio (C/N) at Site U1432 are illustrated in Figure F18 and listed in Table T10. TOC content decreases slightly with depth from ~1 to 0.5 wt% in the uppermost 11 mbsf, and then increases to ~1 wt% at 32 mbsf. Below 40 mbsf, TOC contents vary little between 0.4 and 0.6 wt% to the bottom of the hole. CaCO_3 content increases with depth from 5.5 wt% at the top to 10.6 wt% at 32 mbsf. Below 40 mbsf, CaCO_3 content is variable with depth ranging from 1.7 to 5.8 wt%. The C/N ratio ranges from 4.3 to 8.6.

Table T9. Headspace sample hydrocarbon concentrations, methane, ethene, and ethane, Hole U1432C. [Download table in .csv format.](#)

Table T10. Carbon and nitrogen content, TOC, CaCO_3 , TN, and C/N ratios, Hole U1432C. [Download table in .csv format.](#)

Figure F18. Calcium carbonate, TOC, TN, and C/N ratios.



Microbiology

Our goal for microbiological research conducted at Site U1432 was to collect and preserve samples for shore-based characterization of the microbial communities. We collected samples on a routine basis throughout the cored interval and on a case by case basis, according to features in the cores that suggested the presence of important geological interfaces. We used a limited number of samples to start microbial cultivations on board the ship. In addition, we collected samples for measuring contamination testing tracers including perfluorocarbons and fluid community tracers. Microspheres were not used at Site U1432.

Specific depths sampled for microbiology at Site U1432 are shown in Figure F19. Five routine, 5–10 cm whole-round samples were collected from 4.3 to 95.4 mbsf in Hole U1432C to be used for microbiological analysis. These whole-round samples for microbiology were collected adjacent to samples for interstitial water measurements in order to understand proximal interstitial water chemistry.

We collected and preserved 24 samples for investigating the microbiology of interfaces using lipid and nucleic acid analyses. We obtained these samples between 38.9 and 108.5 mbsf in Hole U1432C. Two sets of interface samples were obtained from volcanic ash/clay interfaces and three sets were obtained from turbidite sand (silt)/clay interfaces. We selected all interface samples based on recognition of key intervals and through consultation with shipboard sedimentologists.

Microbiological analyses

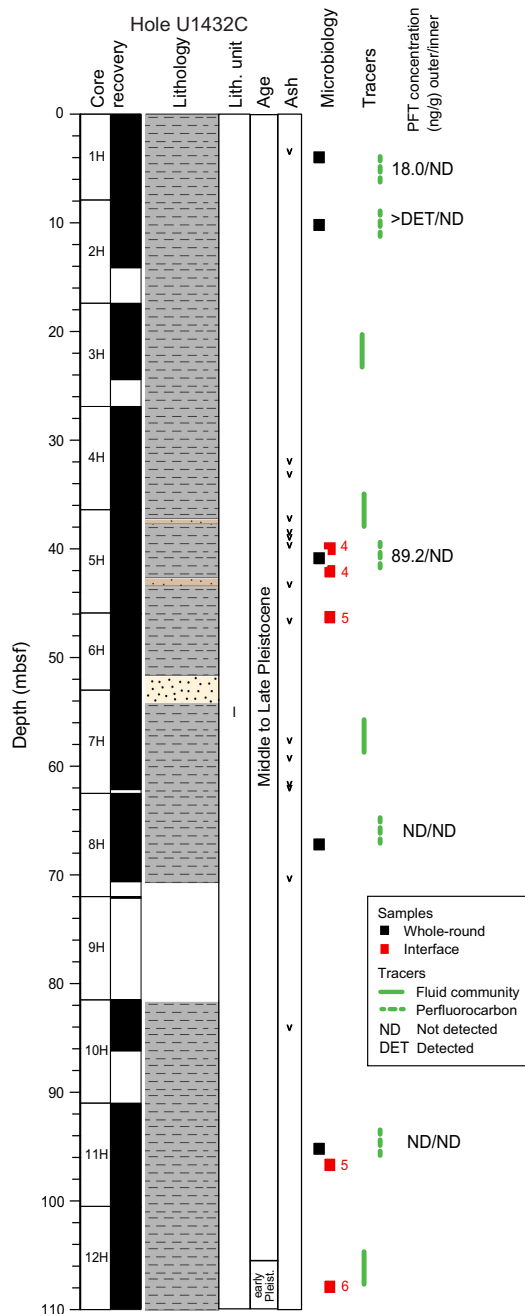
Most of the samples collected at Site U1432 were preserved for shore-based analysis. Samples for DNA and RNA extractions and sequencing were frozen at -80°C and samples for lipid extraction and analysis were frozen at either -80° or -20°C . Subsamples of the routinely collected whole-round samples were prepared for fluorescent in situ hybridization analysis (five subsamples preserved at -20°C). Portions of the whole-round samples were selected for cultivation-based studies to enrich anaerobic heterotrophs, sulfate reducers, and nitrate reducing microorganisms.

Contamination testing

We used two different methods of contamination testing during coring of Hole U1432C. The PFT perfluoromethylcyclohexane was introduced into the drilling fluid throughout coring of Hole U1432C to trace potential drilling fluid contamination of the cores. PFT samples were acquired from the outside and inside of five cores from Hole U1432C (Figure F19). PFT concentrations measured on samples from the outside of the core are higher than those measured on the inside of the core in 3 of the core sections measured (Sections 349-U1432C-1H-3, 2H-2, and 5H-4), which indicates no apparent drilling fluid contamination of the interiors of these cores. On the other hand, PFTs could not be detected in either the outer or inner samples from either of the 2 deeper sections of Hole U1432C that were used for PFT analysis (Sections 349-U1432C-8H-5 and 11H-3). The PFT pump was operating during these coring events, but it is possible that the lack of detectable PFTs in the outer samples of these 2 cores may be the result of insufficient mixing of the PFTs during circulation of the drilling fluid. For these deeper samples, we cannot conclude whether drilling fluid contamination occurred based on the PFT measurements.

Four fluid community tracer (FCT) samples were collected from the drilling fluids to track the microbial communities typical of the

Figure F19. Microbiology whole-round and interface samples and contamination testing samples.



seawater and other mud constituents. The fluids collected for FCT samples correspond to cores obtained from depths ranging between 22 and 106 mbsf. Microbial community DNA and lipids from FCT samples will be compared to the same measurements made on the core samples to determine if the drilling fluids contain microbes that can be regularly tracked as recognizable contaminant taxa. Shortly after coring Hole U1432C, we also collected samples of sepiolite mixed with seawater from the mud pits. These samples will be treated like other FCT samples in order to determine whether there are key microbial taxa that are introduced to the hole when sepiolite is used to remove cuttings from the hole (e.g., during coring in Holes U1431E and U1433B).

Paleomagnetism

At Site U1432, Cores 349-U1432C-1H through 12H were cored with the APC using nonmagnetic core barrels. Shipboard paleomagnetic studies for Hole U1432C consisted of continuous measurements of archive-half core sections and progressive demagnetization measurements of discrete samples. The pass-through magnetometer measurements on all archive-half cores were conducted using the 2G superconducting rock magnetometer (SRM), with demagnetization steps of 0, 5, 10, 15, and 20 mT. Selected discrete samples were alternating field (AF) demagnetized to 120 mT with an ASC Scientific D-2000 AF demagnetizer using 0, 5, 10, 15, 20, 30, 40, 60, 80, 100, and 120 mT steps. Remanences were measured using the SRM. We analyzed the results in Zijdeveld diagrams (Zijdeveld, 1967) and calculated the characteristic remanent magnetization (ChRM) direction using principal component analysis (Kirschvink, 1980).

Natural remanent magnetization of sedimentary cores

Downhole variation in natural remanent magnetization (NRM) properties is illustrated in Figure F20. NRM intensity of the archive halves from Hole U1432C is <0.06 A/m. NRM intensities peak at certain depth intervals, such as at ~ 32 mbsf (Section 349-U1432C-4H-5), ~ 46 mbsf (Section 5H-5), and ~ 84 mbsf (Section 10H-2), which correspond to thin ash layers (see [Lithostratigraphy](#)). At the base of Core 349-U1432C-6H and top of Core 7H, at ~ 52 – 54 mbsf, a 2.42 m thick loose sand layer has the lowest NRM intensity of the hole (Figure F20). Variations in NRM intensities are consistent with variations in magnetic susceptibility (see [Physical properties](#)).

Pervasive remagnetization imparted by the coring process is commonly encountered in cores from Hole U1432C, as shown by the significant decreases of NRM intensity after 20 mT AF demagnetization. NRM inclinations are biased toward vertical (mostly toward $+90^\circ$) in a majority of cores. Typically at the base of each core, NRM inclinations are $>80^\circ$, which suggests that a more complete remagnetization during coring occurs near the drill bit. Such strong magnetization contaminations cannot be removed even after 20 mT AF demagnetization. Nevertheless, average inclination after 20 mT AF demagnetization is consistent with the expected dipole inclination for the site (33.56° for normal polarity or -33.56° for reversed polarity).

Paleomagnetic demagnetization results

Representative vector plots (Zijdeveld, 1967) showing magnetism behavior of detailed AF demagnetization are given in Figure F21. For most samples, the nearly vertical overprints were removed by AF demagnetization of 5–10 mT. Assuming that the viscous remanent magnetization (VRM) of core samples was acquired during the entire Brunhes normal polarity chron, the horizontal orientation of the secondary magnetization points to geographic north on average. Thus, VRM direction could be used for reorientation of the drilled site. At Site U1432, VRM is not observed, mostly because VRM could share coercivity spectra similar to that of the induced remanent magnetization. For samples demagnetized using the ASC Scientific D-2000 AF demagnetizer up to 120 mT, ChRM can be clearly defined between 20 and 120 mT using principal component analysis (Kirschvink, 1980). Therefore, we use remanent magnetization after 20 mT AF demagnetization to represent ChRM for the pass-through magnetometer measurements on all archive-half cores of this site. Inclinations after 20 mT AF demagnetization are

illustrated in Figure F22. Clearly, the negative inclinations at ~ 52 – 54 mbsf correspond to the soupy sand layer. Moreover, the steep ChRM inclinations at the base of each core (e.g., green arrows in Figure F22) indicate that the overprints of the drilling-induced magnetization are not removed. Thus, these anomalous inclinations

Figure F20. Paleomagnetic measurements of NRM inclination and intensity on archive core sections after 0 mT (red) and 20 mT (blue) AF demagnetization for Hole U1432C.

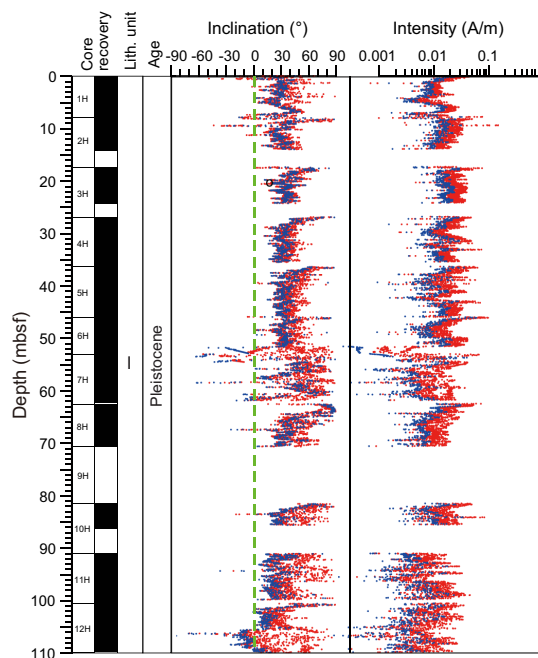


Figure F21. Representative vector endpoint diagrams (Zijdeveld, 1967) for sediment samples through stepwise AF demagnetization. A, C. Normal polarity. B, D. Reversed polarity. Most samples display a normal vertical component of drilling-induced magnetization that is removed after 10 mT AF demagnetization.

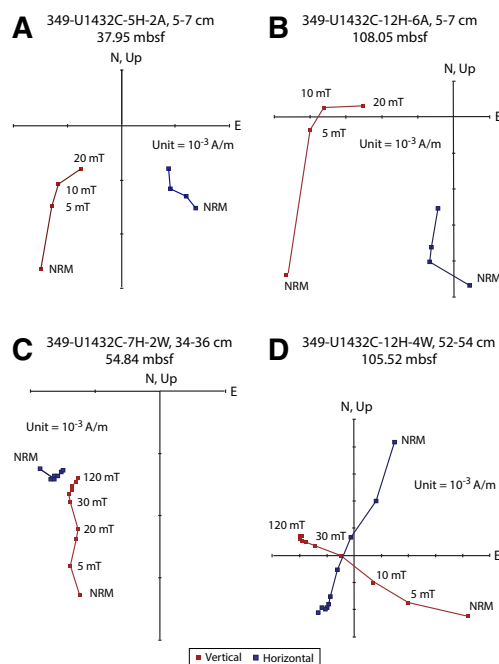
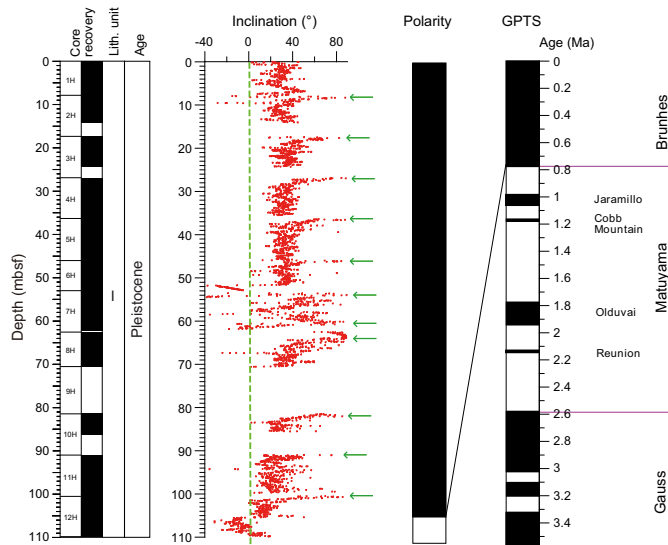


Figure F22. Magnetostratigraphic results, Hole U1432C. Paleomagnetic inclination after 20 mT AF demagnetization. Green arrows indicate steep characteristic remanent magnetization inclinations at the end of each core caused by overprints of drilling-induced magnetization. For polarity and GPTS (Gradstein et al., 2012), black = normal polarity and white = reversed polarity.



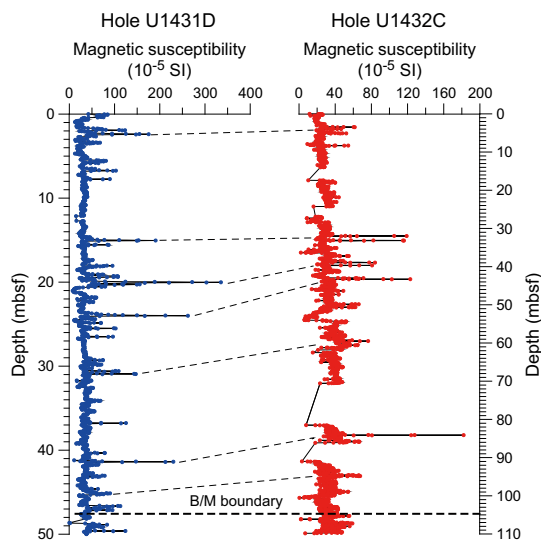
cannot be regarded as reliable paleomagnetic records. Interestingly, there are 2 short inclination shifts from positive to negative between ~62 and 67 mbsf that are not associated with core ends or loose sands. Shore-based studies on discrete samples at these intervals are needed to confirm these short polarity changes.

Magnetostratigraphy

Unlike cores from Site U1431, which were oriented with the FlexIT orientation tool (hence with magnetic declination correction available), only inclinations from cores in Hole U1432C can be used to construct magnetostratigraphy; weather prevented the use of the FlexIT orientation tool in Hole U1432C. Because the age of the bottom of Core 349-U1432C-12H is <0.91 Ma based on planktonic foraminifer and calcareous nannofossil biostratigraphy (see [Biostratigraphy](#)), we assign the first magnetic reversal at ~105 mbsf as the Brunhes/Matuyama Chron boundary (0.781 Ma) (Figure F22). Demagnetization of the corresponding core section also shows antipodal relative declinations. After AF demagnetization at 20 mT, the reversal indicated by the difference in polarity of inclination at ~105.4 mbsf is confirmed by a near 180° change in declination. This positive “antipodal test” is perhaps the most compelling evidence for isolating primary ChRM.

To further test our polarity pattern assignments, we compare the magnetic susceptibility curves of Holes U1431D and U1432C (Figure F23). The sharp magnetic susceptibility peaks (usually >50 SI) mark ash layers. The excellent correlation of magnetic susceptibility curves between these two holes demonstrates that (1) ash layers are coevally distributed across a relatively large area and (2) the assignment of the Brunhes/Matuyama Chron boundary in Hole U1432C is tenable. Therefore, it is possible that a composite age model can be constructed by integrating age controls from these two holes. The properties of ash layers from these two holes can be

Figure F23. Comparison of magnetic susceptibility curves. Thin dashed lines show interpreted correlation between ash layers in the 2 holes. Note the different depth scales in these 2 plots, indicating that the sedimentation rate for Site U1432 is ~2 times higher than that of Site U1431 for the same age interval.



compared in detail and their absolute ages assigned accordingly. For example, the ash layers at ~32 mbsf (Section 349-U1432C-4H-5), ~46 mbsf (Section 5H-5), and ~84 mbsf (Section 10H-2) are paleomagnetically dated to ~0.23, 0.54, and 0.62 Ma, respectively, which could be compared to ash layers in Hole U1431D.

Preliminary magnetic polarity stratigraphy (Figure F22) in Hole U1432C is used to estimate the sedimentation rate at this site at ~13.5 cm/ky, which is approximately two times higher than that of Site U1431 for the same age interval. These rates are generally in agreement with those inferred from shipboard biostratigraphic studies (see [Biostratigraphy](#)).

Physical properties

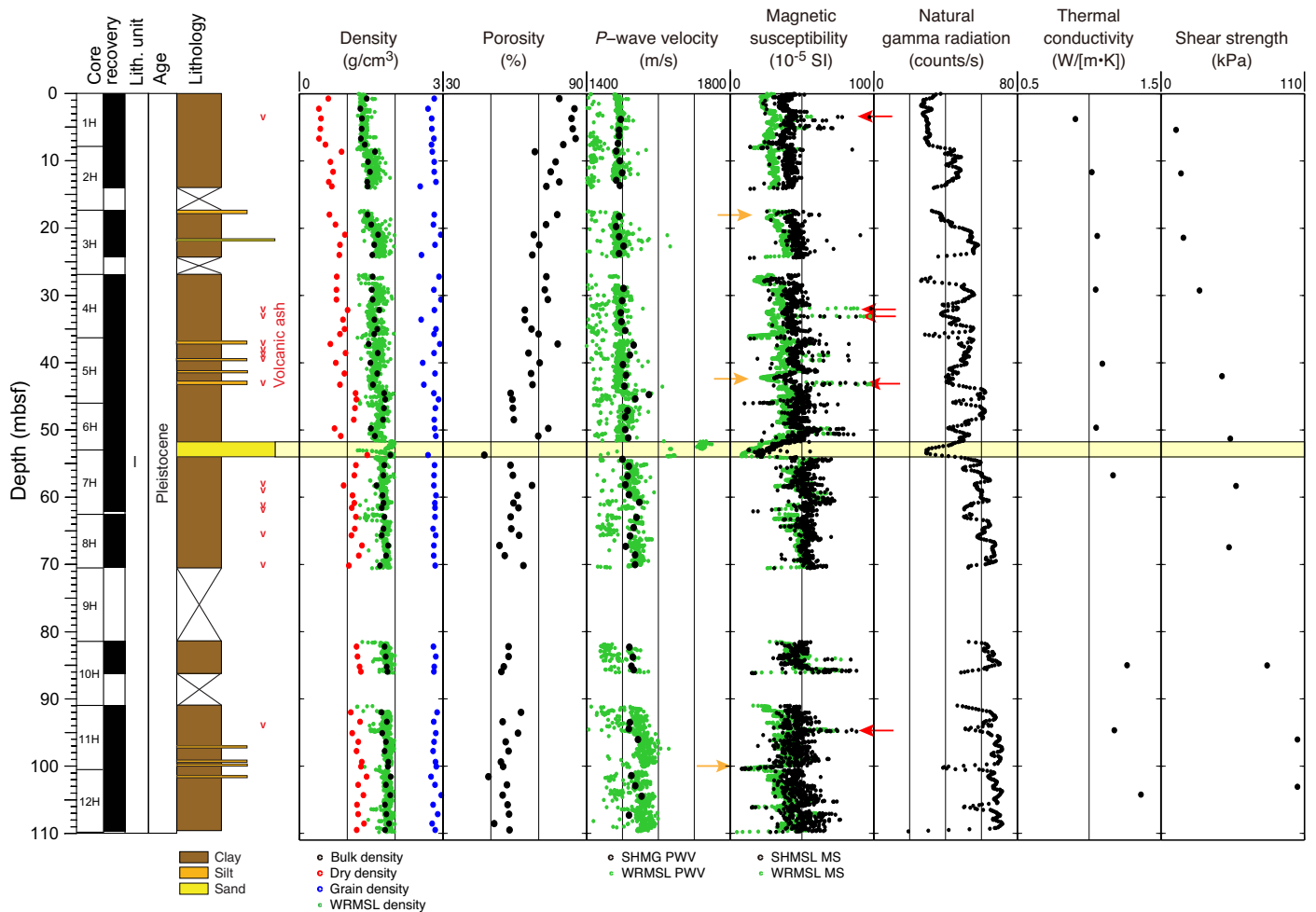
At Site U1432, we measured physical properties on whole-round cores (P -wave velocity, bulk density from gamma ray attenuation, magnetic susceptibility, and natural gamma radiation [NGR]), on split cores (thermal conductivity and x -caliper and z -bayonet P -wave velocities), and on discrete samples (porosity, moisture, and density). Only one discrete sample could be collected from the soupy sand layer between 52 and 54 mbsf, so its properties are better observed on the whole-round measurements.

Physical property measurements

Measurement points clearly out of range were removed from the whole-round core data, which were then smoothed using a 5-point average moving window. The compiled measurements of physical properties of Hole U1432C are shown in Figure F24. The measurements are mutually consistent and correspond to lithology.

Magnetic susceptibility values increase in Hole U1432C from ~30 × 10⁻⁵ to 50 × 10⁻⁵ SI in the uppermost 70 mbsf and then remain near 50 × 10⁻⁵ SI below 70 mbsf. Values approximately 20 × 10⁻⁵ to 40 × 10⁻⁵ SI lower than the background are observed in short

Figure F24. Physical property measurements, Hole U1432C. Red arrows = ash layers, yellow arrows = thin sand/silt layers. Shaded yellow bar corresponds to a sand layer between 52 and 54 mbsf with higher *P*-wave velocity, lower magnetic susceptibility, and lower NGR than the clay. Porosity was measured on discrete samples, and thermal conductivity was measured on whole-round sections.



intervals near 18, 47, 52–54, and 100 mbsf (yellow arrows in Figure F24). Narrow peaks up to 100×10^{-5} SI are observed near 4 mbsf, between 30 and 45 mbsf, and near 95 mbsf (red arrows in Figure F24). NGR values display a general increase from ~ 30 to ~ 70 counts/s in the uppermost 70 mbsf of Hole U1432C and then remain relatively constant near 70 counts/s. NGR values that are ~ 20 – 30 counts/s below the general trend typically coincide with either highs or lows in magnetic susceptibility values. *P*-wave velocity near the seafloor in Hole U1432C is close to the velocity in seawater (~ 1500 m/s), increases to ~ 1550 m/s in the uppermost 70 mbsf, and then remains approximately constant. The layer at 52–54 mbsf shows higher velocities ranging from 1600 to 1750 m/s (yellow box in Figure F24).

Bulk density increases with depth from ~ 1.2 to ~ 1.8 g/cm³ in the uppermost 70 mbsf and then remains constant near 1.8 g/cm³ to the bottom of the hole. Dry bulk density values are very low near the seafloor (~ 0.5 g/cm³), reflecting higher porosity. Dry bulk density increases with depth to ~ 1.2 g/cm³ near 110 mbsf. Grain density is almost constant at 2.9 g/cm³. Porosity is very high near the seafloor ($\sim 85\%$), decreases with depth to $\sim 60\%$ in the uppermost 70 mbsf, and then remains nearly constant below 70 mbsf.

Thermal conductivity increases gradually from 0.8 to 1.4 W/(m·K) in Hole U1432C. The increase in shear strength with depth from 10 to 110 kPa also spans the entire Hole U1432C.

Data interpretation and lithology correlation

In general, physical properties correlate with lithology, composition, and lithification. In Hole U1432C, the observed ranges of magnetic susceptibility (30×10^{-5} to 70×10^{-5} SI) and NGR (30–70 counts/s) are typical for clay, which dominates the lithology. Variations from these background values coincide with the compaction effect near the surface, as well as the observation of ash layers and silt/sand.

Bulk and dry densities, *P*-wave velocity, NGR, and thermal conductivity increase gradually with depth, whereas porosity measured on discrete samples decreases from 85% to 60% over the uppermost 70 mbsf (Figure F24). Variations of thermal conductivity and shear strength also mainly result from compaction.

Higher magnetic susceptibility and lower NGR values correspond to ash layers (red arrows in Figure F24). Volcanic material typically has lower NGR values and higher magnetic susceptibility, resulting from the presence of ferromagnetic minerals. Similar

physical properties of ash layers were also observed at Site U1431; however, because of the thicker and more abundant turbidites in the top of Hole U1431D, it is difficult to compare the stratigraphy between the holes based on observed physical properties.

Low magnetic susceptibility and low NGR values coincide with sand and silt (yellow arrows in Figure F24), which usually contain fewer magnetic minerals. Compared to clay, the sand layer from 52 to 54 mbsf shows a higher *P*-wave velocity measured on whole-round core sections (yellow box in Figure F24).

Downhole measurements

Downhole temperature and heat flow

Four APCT-3 downhole temperature measurements in Hole U1432C range from 6.6°C at 45.9 mbsf to 10.9°C at 100.5 mbsf (Table T11; Figure F25), giving a geothermal gradient of 85°C/km (Figure F26). These measurements, together with the seafloor temperature of 2.4°C, indicate that the temperature increases linearly with depth.

Thermal conductivity under in situ conditions was estimated from laboratory-determined thermal conductivity in Hole U1432C using the method of Hyndman et al. (1974) (see [Downhole mea-](#)

[surements](#) in the Methods chapter [Li et al., 2015a]). Calculated in situ values average 0.8% higher than measured laboratory values. Thermal resistance was then calculated by integrating the inverse of the in situ thermal conductivity over depth (Figure F26). A heat flow of 94 mW/m² was obtained from the linear fit between temperature and thermal resistance (Pribnow et al., 2000). This is a high heat flow, but it is similar to heat flow measurements at other sites within a few tens of kilometers of Site U1432, including at Site 1148 (Li et al., 2010).

Table T11. Advanced piston corer temperature tool (APCT-3) temperature measurements, Hole U1432C. [Download table in .csv format.](#)

Core	Depth DSF (m)	APCT-3 temperature (°C)
Seafloor	0	2.4
5H	45.9	6.6
7H	62.5	8
9H	81.5	9.6
11H	100.5	10.9

Figure F25. APCT-3 temperature-time series with extrapolated formation temperature estimates, Site U1432.

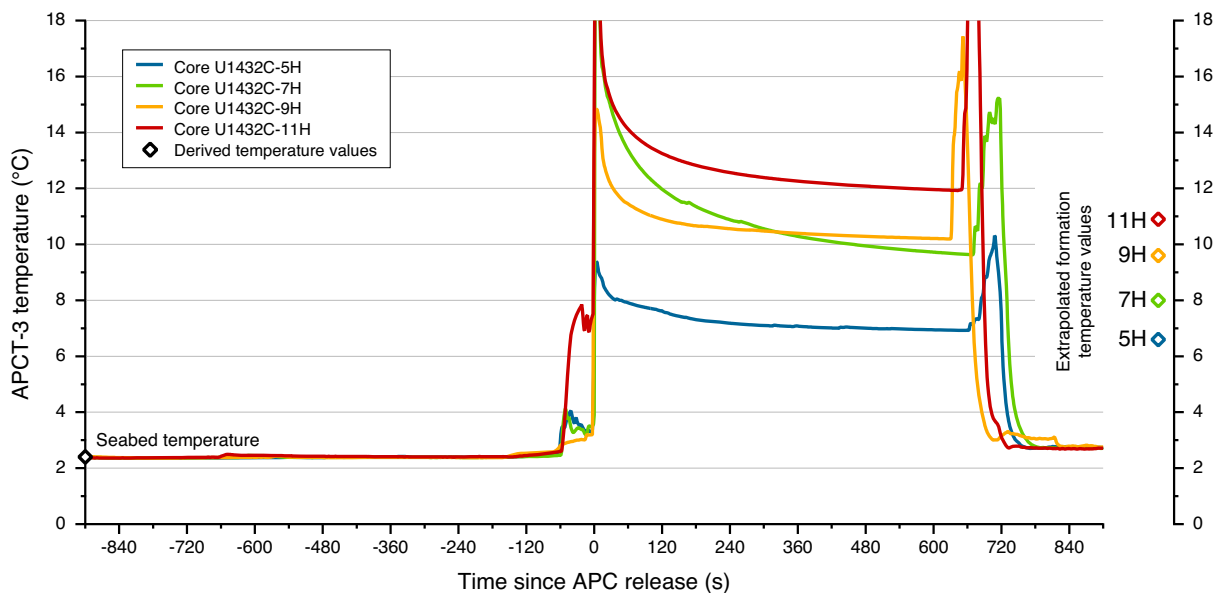
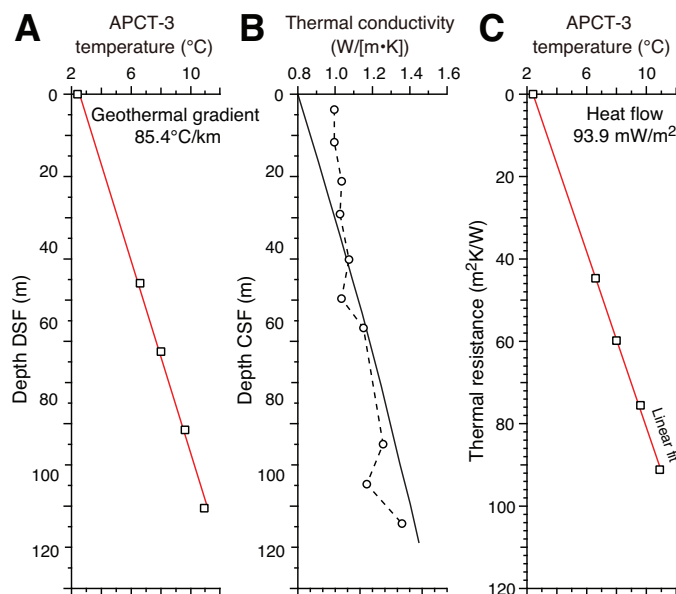


Figure F26. Heat flow calculations, Site U1432. A. APCT-3 sediment temperatures. B. Thermal conductivity data from Hole U1432C (circles and dashed line) with calculated thermal resistance (solid line). C. Bullard plot of heat flow calculated from a linear fit of the temperature data.



References

- Briaux, A., Patriat, P., and Tapponnier, P., 1993. Updated interpretation of magnetic anomalies and seafloor spreading stages in the South China Sea: implications for the Tertiary tectonics of Southeast Asia. *Journal of Geophysical Research: Solid Earth*, 98(B4):6299–6328. <http://dx.doi.org/10.1029/92JB02280>
- Gardner, J.V., Nelson, C.S., and Baker, P.A., 1986. Distribution and character of pale green laminae in sediment from Lord Howe Rise: a probable late Neogene and Quaternary tephrostratigraphic record. In Kennett, J.P., von der Borch, C.C., et al., *Initial Reports of the Deep Sea Drilling Project*, 90: Washington, DC (U.S. Government Printing Office), 1145–1159. <http://dx.doi.org/10.2973/dsdp.proc.90.125.1986>
- Gradstein, F.M., Ogg, J.G., Schmitz, M.D., and Ogg, G.M. (Eds.), 2012. *The Geological Time Scale 2012*: Oxford, UK (Elsevier).
- Helmke, J.P., Schulz, M., and Bauch, H.A., 2002. Sediment-color record from the northeast Atlantic reveals patterns of millennial-scale climate variability during the past 500,000 years. *Quaternary Research*, 57(1):49–57. <http://dx.doi.org/10.1006/qres.2001.2289>
- Hyndman, R.D., Erickson, A.J., and Von Herzen, R.P., 1974. Geothermal measurements on DSDP Leg 26. In Davies, T.A., Luyendyk, B.P., et al., *Initial Reports of the Deep Sea Drilling Project*, 26: Washington, DC (U.S. Government Printing Office), 451–463. <http://dx.doi.org/10.2973/dsdp.proc.26.113.1974>
- Hyun, S., Ortiz, J.D., Raymo, M.E., and Taira, A., 1999. Low-frequency oscillations in Site 983 sediments: relationships between carbonate and productivity proxies. In Raymo, M.E., Jansen, E., Blum, P., and Herbert, T.D. (Eds.), *Proceedings of the Ocean Drilling Program, Scientific Results*, 162: College Station, TX (Ocean Drilling Program), 197–207. <http://dx.doi.org/10.2973/odp.proc.sr.162.019.1999>
- Ikehara, M., Kawamura, K., Ohkouchi, N., and Taira, A., 1999. Organic geochemistry of greenish clay and organic-rich sediments since the early Miocene from Hole 985A, Norway Basin. In Raymo, M.E., Jansen, E., Blum, P., and Herbert, T.D. (Eds.), *Proceedings of the Ocean Drilling Program, Scientific Results*, 162: College Station, TX (Ocean Drilling Program), 209–216. <http://dx.doi.org/10.2973/odp.proc.sr.162.020.1999>
- Ishihara, T., and Kisimoto, K., 1996. Magnetic anomaly map of East Asia, 1:4,000,000 (CD-ROM version). Geological Survey of Japan, Coordinating Committee for Coastal and Offshore Geoscience Programs in East and Southeast Asia (CCOP).
- Khim, B.-K., Tada, R., Park, Y.H., Bahk, J.J., Kido, Y., Itaki, T., and Ikehara, K., 2009. Correlation of TL layers for the synchronous paleoceanographic events in the East Sea (Sea of Japan) during the late Quaternary. *Geosciences Journal*, 13(2):113–120. <http://dx.doi.org/10.1007/s12303-009-0010-8>
- Kirschvink, J.L., 1980. The least-squares line and plane and the analysis of palaeomagnetic data. *Geophysical Journal of the Royal Astronomical Society*, 62(3):699–718. <http://dx.doi.org/10.1111/j.1365-246X.1980.tb02601.x>
- Li, C.-F., Lin, J., Kulhanek, D.K., Williams, T., Bao, R., Briaux, A., Brown, E.A., Chen, Y., Clift, P.D., Colwell, F.S., Dadd, K.A., Ding, W., Almeida, I.H., Huang, X.-L., Hyun, S., Jiang, T., Koppers, A.A.P., Li, Q., Liu, C., Liu, Q., Liu, Z., Nagai, R.H., Peleo-Alampay, A., Su, X., Sun, Z., Tejada, M.L.G., Trinh, H.S., Yeh, Y.-C., Zhang, C., Zhang, F., Zhang, G.-L., and Zhao, X., 2015a. Methods. In Li, C.-F., Lin, J., Kulhanek, D.K., and the Expedition 349 Scientists, *Proceedings of the Integrated Ocean Drilling Program, 349: South China Sea Tectonics*: College Station, TX (International Ocean Discovery Program). <http://dx.doi.org/10.14379/iodp.proc.349.102.2015>
- Li, C.-F., Lin, J., Kulhanek, D.K., Williams, T., Bao, R., Briaux, A., Brown, E.A., Chen, Y., Clift, P.D., Colwell, F.S., Dadd, K.A., Ding, W., Almeida, I.H., Huang, X.-L., Hyun, S., Jiang, T., Koppers, A.A.P., Li, Q., Liu, C., Liu, Q., Liu, Z., Nagai, R.H., Peleo-Alampay, A., Su, X., Sun, Z., Tejada, M.L.G., Trinh, H.S., Yeh, Y.-C., Zhang, C., Zhang, F., Zhang, G.-L., and Zhao, X., 2015b. Site U1431. In Li, C.-F., Lin, J., Kulhanek, D.K., and the Expedition 349 Scientists, *Proceedings of the Integrated Ocean Drilling Program, 349: South China Sea Tectonics*: College Station, TX (International Ocean Discovery Program). <http://dx.doi.org/10.14379/iodp.proc.349.103.2015>
- Li, C.-F., Shi, X., Zhou, Z., Li, J., Geng, J., and Chen, B., 2010. Depths to the magnetic layer bottom in the South China Sea area and their tectonic implications. *Geophysical Journal International*, 182(3):1229–1247. <http://dx.doi.org/10.1111/j.1365-246X.2010.04702.x>
- Li, Q., Wang, P., Zhao, Q., Shao, L., Zhong, G., Tian, J., Cheng, X., Jian, Z., and Su, X., 2006. A 33 Ma lithostratigraphic record of tectonic and paleoceanographic evolution of the South China Sea. *Marine Geology*, 230(3–4):217–235. <http://dx.doi.org/10.1016/j.margeo.2006.05.006>
- Lind, I.L., Janecek, T.R., Kriisek, L.A., Prentice, M.L., and Stax, R., 1993. Color bands in Ontong Java Plateau carbonate oozes and chalks. In Berger, W.H., Kroenke, L.W., Mayer, L.A., et al., *Proceedings of the Ocean Drilling Program, Scientific Results*, 130: College Station, TX (Ocean Drilling Program), 453–470. <http://dx.doi.org/10.2973/odp.proc.sr.130.007.1993>
- Nagao, S., and Nakashima, S., 1992. The factors controlling vertical color variations of North Atlantic Madeira abyssal plain sediments. *Marine Geology*, 109(1–2):83–94. [http://dx.doi.org/10.1016/0025-3227\(92\)90222-4](http://dx.doi.org/10.1016/0025-3227(92)90222-4)
- Ortiz, J.D., O'Connell, S., and Mix, A., 1999. Data report: spectral reflectance observations from recovered sediments. In Raymo, M.E., Jansen, E., Blum, P., and Herbert, T.D. (Eds.), *Proceedings of the Ocean Drilling Program, Scientific Results*, 162: College Station, TX (Ocean Drilling Program), 259–264. <http://dx.doi.org/10.2973/odp.proc.sr.162.029.1999>
- Pautot, G., Rangin, C., Briaux, A., Tapponnier, P., Beuzart, P., Lericolais, G., Mathieu, X., Wu, J., Han, S., Li, H., Lu, Y., and Zhao, J., 1986. Spreading direction in the central South China Sea. *Nature*, 321(6066):150–154. <http://dx.doi.org/10.1038/321150a0>
- Pribnow, D., Kinoshita, M., and Stein, C., 2000. *Thermal Data Collection and Heat Flow Recalculations for Ocean Drilling Program Legs 101–180*: Hanover, Germany (Institute for Joint Geoscientific Research, Institut für Geowissenschaftliche Gemeinschaftsaufgaben [GGA]). <http://www-odp.tamu.edu/publications/heatflow/ODPreprt.pdf>
- Shipboard Scientific Party, 2000. Site 1148. In Wang, P., Prell, W.L., Blum, P., et al., *Proceedings of the Ocean Drilling Program, Initial Reports*, 184: College Station, TX (Ocean Drilling Program), 1–122. <http://dx.doi.org/10.2973/odp.proc.ir.184.109.2000>

- Tamburini, F., Adatte, T., and Föllmi, K.B., 2003. Origin and nature of green clay layers, ODP Leg 184, South China Sea. In Prell, W.L., Wang, P., Blum, P., Rea, D.K., and Clemens, S.C. (Eds.), *Proceedings of the Ocean Drilling Program, Scientific Results*, 184: College Station, TX (Ocean Drilling Program), 1–23. <http://dx.doi.org/10.2973/odp.proc.sr.184.206.2003>
- Taylor, B., and Hayes, D.E., 1980. The tectonic evolution of the South China Basin. In Hayes, D.E. (Ed.), *The Tectonic and Geologic Evolution of South-east Asian Seas and Islands*. Geophysical Monograph, 23:89–104. <http://dx.doi.org/10.1029/GM023p0089>
- Taylor, B., and Hayes, D.E., 1983. Origin and history of the South China Sea Basin. In Hayes, D.E. (Ed.), *The Tectonic and Geologic Evolution of South-east Asian Seas and Islands* (Pt. 2). Geophysical Monograph, 27:23–56. <http://dx.doi.org/10.1029/GM027p0023>
- Wang, P., and Li, Q. (Eds.), 2009. *Developments in Paleoenvironmental Research* (Vol. 13): *The South China Sea: Paleooceanography and Sedimentology*: Dordrecht (Springer). 13. <http://dx.doi.org/10.1007/978-1-4020-9745-4>
- Wang, R., and Abelmann, A., 1999. Pleistocene radiolarian biostratigraphy in the South China Sea. *Science in China (Series D)*, 42(5):537–543.
- Zijderveld, J.D.A., 1967. AC demagnetization of rocks: analysis of results. In Collinson, D.W., Creer, K.M., and Runcorn, S.K. (Eds.), *Methods in Palaeomagnetism*: Amsterdam (Elsevier), 254–286.

doi:10.14379/iodp.proc.349.105.2015

Site U1433¹



C.-F. Li, J. Lin, D.K. Kulhanek, T. Williams, R. Bao, A. Briais, E.A. Brown, Y. Chen, P.D. Clift, F.S. Colwell, K.A. Dadd, W.-W. Ding, I. Hernández-Almeida, X.-L. Huang, S. Hyun, T. Jiang, A.A.P. Koppers, Q. Li, C. Liu, Q. Liu, Z. Liu, R.H. Nagai, A. Peleo-Alampay, X. Su, Z. Sun, M.L.G. Tejada, H.S. Trinh, Y.-C. Yeh, C. Zhang, F. Zhang, G.-L. Zhang, and X. Zhao²

Keywords: International Ocean Discovery Program, IODP, *JOIDES Resolution*, Expedition 349, Site U1433, South China Sea, pelagic red clay, Ar-Ar dating, plagioclase phenocryst, deep biosphere, carbonate turbidite, calcite compensation depth, basalt alteration, magnetic susceptibility, cooling effect, magnetic anomalies, radiolarians, nannofossils, *Nereites* ichnofacies, Dangerous Grounds

Background and objectives

Because of the marked contrast in magnetic anomaly amplitude between the Southwest and East Subbasins of the South China Sea (SCS) (Yao, 1995; Jin et al., 2002; Li et al., 2007, 2008), it is justifiable to question whether rifting and drifting within these 2 subbasins were synchronous or diachronous and how these subbasins evolved in comparison to the Northwest Subbasin. Site U1433 is located in the Southwest Subbasin near the relict spreading center and magnetic Anomaly C5d identified by Briais et al. (1993) (Figures **F1**, **F2**, **F3**). Together with Site U1431 in the East Subbasin, coring at these sites will help to explain the sharp differences in magnetic amplitude between the East and Southwest Subbasins and test the hypothesis that in the Southwest Subbasin the transition from continental rifting to seafloor spreading occurred more recently than in the East Subbasin (Pautot et al., 1986). Coring will help determine the age of this subbasin near the end of the spreading and correlate ages from magnetic anomalies with biostratigraphic, magnetostratigraphic, and radiometric ages. The apparent weak magnetization in basement rocks suggested by the magnetic anomaly amplitudes will be examined by petrological analyses of chemical compositions and measurements of magnetic susceptibility. The specific objectives at this site are to

1. Determine the termination age of spreading in the Southwest Subbasin and correlate it to ages of regional tectonic events;
2. Test the rifting and subsequent seafloor spreading models of the Southwest Subbasin;
3. Measure magnetization, mineralization, and geochemical compositions of basement rocks to trace how the mantle evolved through time; and
4. Examine the paleoceanographic and sedimentary response to the opening of the SCS.

Contents

1	Background and objectives
1	Operations
6	Lithostratigraphy
13	Biostratigraphy
18	Igneous petrology and alteration
23	Structural geology
25	Geochemistry
32	Microbiology
34	Paleomagnetism
38	Physical properties
41	Downhole measurements
48	References

Operations

The original operations plan for Site U1433 (proposed Site SCS-4B) consisted of drilling one hole to a depth of ~965 m below seafloor (mbsf), which included 100 m of basement. This plan was modified during transit in order to eliminate the use of a free-fall funnel and the extended core barrel (XCB) by coring 2 holes (Table **T1**). Hole U1433A was cored using the advanced piston corer (APC) to refusal at 188.3 mbsf. Hole U1433B was drilled to 186.1 mbsf and then cored using the rotary core barrel (RCB). The sediment/basement interface was encountered at ~798.5 mbsf, and we advanced the hole by rotary coring into basement to a final depth of 858.5 mbsf. After conditioning the hole for logging, we deployed the modified triple combination (triple combo) tool string and the Formation MicroScanner (FMS)-sonic tool string to 840 m wireline depth below seafloor (WSF), with multiple passes made in the basement section of the hole with the latter tool.

A total of 94 cores were collected at this site. The APC was deployed 20 times, recovering 168.79 m of core over 188.3 m of penetration (89.6% recovery). The RCB system drilled one 186.1 m interval and collected 74 cores, recovering 443.04 m of core over 672.4 m of penetration (65.9% recovery). The overall recovery at Site U1433 was 71.1%. The total time spent on Site U1433 was 284.5 h (11.9 days).

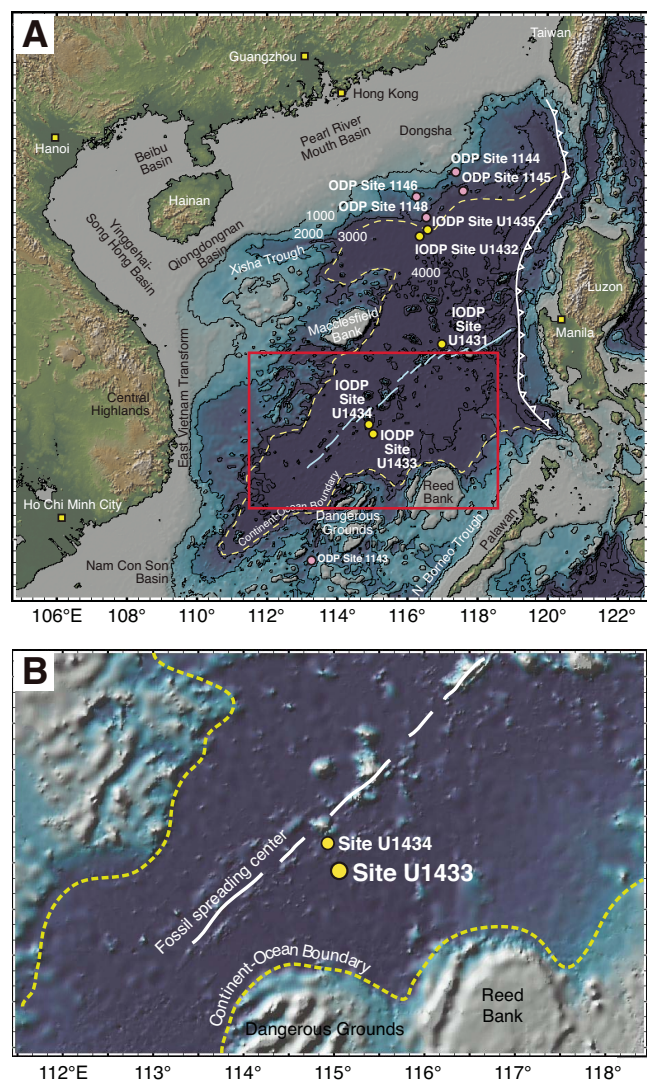
Transit to Site U1433

After a 334 nmi transit lasting 29.9 h, the vessel arrived at Site U1433 (proposed Site SCS-4B) and switched to dynamic positioning mode at 0230 h (UTC + 8 h) on 8 March 2014. At 0255 h, an acoustic positioning beacon was deployed. The position reference was a combination of GPS signals and a single acoustic beacon.

¹ Li, C.-F., Lin, J., Kulhanek, D.K., Williams, T., Bao, R., Briais, A., Brown, E.A., Chen, Y., Clift, P.D., Colwell, F.S., Dadd, K.A., Ding, W.-W., Hernández-Almeida, I., Huang, X.-L., Hyun, S., Jiang, T., Koppers, A.A.P., Li, Q., Liu, C., Liu, Q., Liu, Z., Nagai, R.H., Peleo-Alampay, A., Su, X., Sun, Z., Tejada, M.L.G., Trinh, H.S., Yeh, Y.-C., Zhang, C., Zhang, F., Zhang, G.-L., and Zhao, X., 2015. Site U1433. In Li, C.-F., Lin, J., Kulhanek, D.K., and the Expedition 349 Scientists, *Proceedings of the International Ocean Discovery Program, 349: South China Sea Tectonics*: College Station, TX (International Ocean Discovery Program). <http://dx.doi.org/10.14379/iodp.proc.349.105.2015>

² Expedition 349 Scientists' addresses.

Figure F1. A. Bathymetric map of the South China Sea region. Solid yellow circles = Expedition 349 sites. Solid pink circles = ODP Leg 184 sites. Yellow dashed line = inferred continent/ocean boundary, blue lines = fossil South China Sea spreading center, white-flagged line = Manila Trench. B. Detailed bathymetry around Sites U1433 and U1434 (red box in A) showing nearby seamounts and the Dangerous Grounds and Reed Bank to the south.



Hole U1433A

After arriving on site and deploying the acoustic positioning beacon, an APC/XCB bottom-hole assembly (BHA) was assembled and run to 800.4 m below rig floor (mbrf). At 0520 h, a tool joint parted on the twenty-fourth stand of drill pipe, just after picking up the drill string and just prior to unlatching the lower set of elevators. The load cell weight at the time of the incident was recorded at ~200,000 lb. The entire weight of the drill string dropped ~18 inches and landed in the lower set of elevators, which were resting on top of the dual elevator stool. The pin on the top single of drill pipe had parted, leaving one single hanging from the upper set of elevators and 2 singles sticking up from on top of the lower set of elevators. The stand was then laid out to the V-door. The broken pipe was visually inspected and photographed. As a precaution, the twenty-third stand was also disassembled and laid out. The bottom set of elevators was removed from use and replaced with a recondi-

Figure F2. Shaded map of magnetic anomalies near Sites U1433 and U1434 (data from Ishihara and Kisimoto, 1996). Bold black lines mark 3000 m isobaths outlining the seamounts. Symbols are magnetic anomaly picks from Brais et al. (1993).

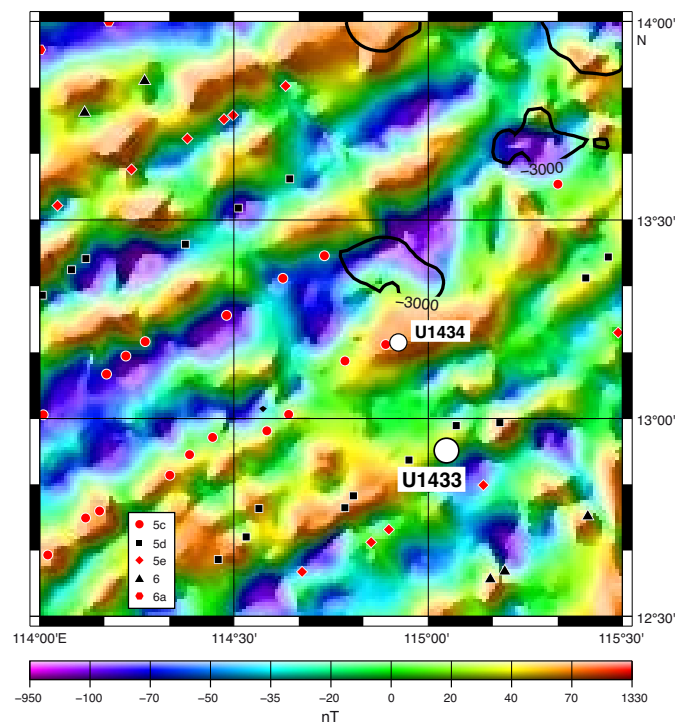


Figure F3. A. Regional contoured bathymetric map showing seismic reflection profiles (red lines) and the location of Sites U1433 and U1434. Contour interval = 100 m. B. Seismic profile Line 973SCSIO_2b with location of Site U1433. SP = shotpoint. Green line = interpreted top of basement, blue line = approximate uppermost Miocene sediment.

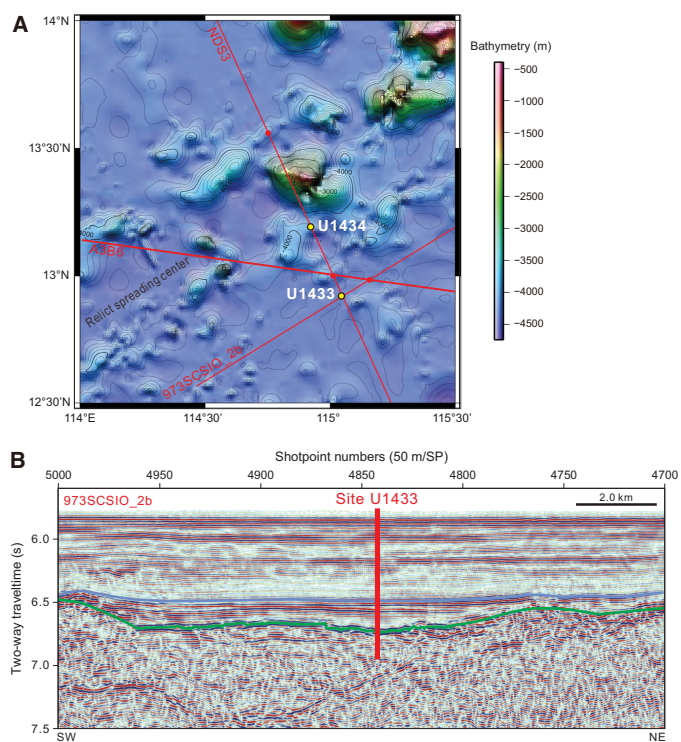


Table T1. Coring summary, Site U1433. CSF = core depth below seafloor, DRF = drilling depth below rig floor, DSF = drilling depth below seafloor. H = advanced piston corer, R = rotary core barrel, numeric core type = drilled interval. APCT-3 = advanced piston corer temperature tool, PFTs = perfluorocarbon tracers, APC = advanced piston corer, RCB = rotary core barrel. (Continued on next two pages.) [Download table in .csv format.](#)

Hole U1433A

Latitude: 12°55.1380'N
 Longitude: 115°2.8345'E
 Water depth (m): 4379.55
 Date started (UTC): 7 March 2014, 1830 h
 Date finished (UTC): 10 March 2014, 1925 h
 Time on hole (days): 3.0
 Seafloor depth (m DRF): 4390.6
 Seafloor depth calculation method: APC calculated depth
 Rig floor to sea level (m): 11.25
 Drilling System: 11-7/16 inch APC/XCB bit with 136.63 m BHA
 Penetration depth (m DSF): 188.30
 Cored interval (m): 188.30
 Recovered length (m): 168.79
 Recovery (%): 90
 Total cores (no.): 20
 APC cores (no.): 20
 Age of oldest sediment cored: Middle Pleistocene

Hole U1433B

Latitude: 12°55.1313'N
 Longitude: 115°2.8484'E
 Water depth (m): 4379.33
 Date started (UTC): 10 March 2014, 1925 h
 Date finished (UTC): 19 March 2014, 1500 h
 Time on hole (days): 8.8
 Seafloor depth (m DRF): 4390.6
 Seafloor depth calculation method: Offset depth from Hole U1433A
 Rig floor to sea level (m): 11.27
 Drilling System: 9-7/8 inch RCB bit with 172.07 m BHA
 Penetration depth (m DSF): 858.5
 Cored interval (m): 672.40
 Recovered length (m): 443.04
 Recovery (%): 66
 Drilled interval (m): 186.1
 Drilled interval (no.): 1
 Total cores (no.): 74
 RCB cores (no.): 74
 Age of oldest sediment cored: early Miocene

Core	Date (2014)	Time UTC (h)	Depth DSF (m)		Interval advanced (m)	Depth CSF (m)		Length of core recovered (m)	Length of core curated (m)	Recovery (%)	Sections (no.)	Comments
			Top of interval	Bottom of interval		Top of cored interval	Bottom of cored interval					
349-U1433A-												
1H	9 Mar	0305	0	8.90	8.9	0	8.90	8.90	8.90	100	7	FlexIT
2H	9 Mar	0435	8.90	18.40	9.5	8.90	16.26	7.36	7.36	77	6	FlexIT
3H	9 Mar	0535	18.40	27.90	9.5	18.40	27.57	9.17	9.17	97	7	FlexIT
4H	9 Mar	0705	27.90	37.40	9.5	27.90	37.25	9.35	9.35	98	8	FlexIT, APCT-3
5H	9 Mar	0805	37.40	46.90	9.5	37.40	37.42	0.02	0.02	0	1	FlexIT
6H	9 Mar	0910	46.90	56.40	9.5	46.90	56.40	9.50	9.50	100	8	FlexIT
7H	9 Mar	1030	56.40	65.90	9.5	56.40	66.40	10.00	10.00	105	8	FlexIT, APCT-3
8H	9 Mar	1135	65.90	75.40	9.5	65.90	75.30	9.40	9.40	99	7	FlexIT
9H	9 Mar	1245	75.40	84.90	9.5	75.40	79.60	4.20	4.20	44	4	FlexIT
10H	9 Mar	1355	84.90	94.40	9.5	84.90	93.20	8.30	8.30	87	8	FlexIT, APCT-3
11H	9 Mar	1505	94.40	103.90	9.5	94.40	102.54	8.11	8.14	85	6	FlexIT
12H	9 Mar	1605	103.90	113.40	9.5	103.90	113.27	9.37	9.37	99	8	FlexIT
13H	9 Mar	1730	113.40	122.90	9.5	113.40	122.91	9.51	9.51	100	7	FlexIT, APCT-3
14H	9 Mar	1850	122.90	132.40	9.5	122.90	132.36	9.46	9.46	100	7	FlexIT
15H	9 Mar	2000	132.40	141.90	9.5	132.40	141.74	9.34	9.34	98	8	FlexIT
16H	9 Mar	2105	141.90	151.40	9.5	141.90	151.26	9.36	9.36	99	7	FlexIT
17H	10 Mar	0050	151.40	160.70	9.3	151.40	160.75	9.35	9.35	101	8	FlexIT
18H	10 Mar	0230	160.70	169.70	9.0	160.70	169.68	8.98	8.98	100	7	FlexIT, PFTs
19H	10 Mar	0350	169.70	178.80	9.1	169.70	178.87	9.17	9.17	101	8	FlexIT, PFTs
20H	10 Mar	0530	178.80	188.30	9.5	178.80	188.74	9.94	9.94	105	8	FlexIT, PFTs
			Totals:		188.3			168.79		90	138	

Table T1 (continued).

Core	Date (2014)	Time UTC (h)	Depth DSF (m)		Interval advanced (m)	Depth CSF (m)		Length of core recovered (m)	Length of core curated (m)	Recovery (%)	Sections (no.)	Comments
			Top of interval	Bottom of interval		Top of cored interval	Bottom of cored interval					
67R	16 Mar	0340	814.90	819.70	4.8	814.90	816.12	1.00	1.22	21	1	Microspheres
68R	16 Mar	0930	819.70	824.60	4.9	819.70	823.94	3.81	4.24	78	3	Microspheres
69R	16 Mar	1450	824.60	829.40	4.8	824.60	828.08	3.05	3.48	64	3	Microspheres
70R	16 Mar	1755	829.40	834.20	4.8	829.40	831.38	1.57	1.98	33	2	Microspheres
71R	16 Mar	2045	834.20	839.10	4.9	834.20	836.18	1.61	1.98	33	2	Microspheres
72R	16 Mar	2325	839.10	844.00	4.9	839.10	840.38	1.05	1.28	21	1	Microspheres
73R	17 Mar	0240	844.00	848.90	4.9	844.00	847.67	3.04	3.67	62	3	Microspheres
74R	17 Mar	0650	848.90	853.70	4.8	848.90	851.65	2.46	2.75	51	2	Microspheres
75R	17 Mar	1345	853.70	858.50	4.8	853.70	857.48	3.62	3.78	75	4	Microspheres
			Total:		858.5			443.04		65	400	

tioned set of elevators. After clearing the rig floor, the trip to the seafloor resumed. When the bit was at 1147.8 mbrf, another tool joint failed when the driller was picking up the thirty-sixth stand from the pipe racker. This time, one single fell back into the trough of the pipe racker still attached to the skate, and a double remained connected to the elevators on the bales connected to the main block. After the second tool joint failure, we decided to discontinue using any of the 5 inch drill pipe that had been used in the stuck pipe incident at the previous site. Investigations continue into the root cause of the pipe failure. Documentation of the stuck pipe event was collected for analysis. The failed tool joints were prepared with care for shipment to a laboratory for detailed metallurgical analysis and were shipped from Keelung, Taiwan, at the end of the expedition. The drill string was tripped back to the BHA, and all suspect drill pipe was removed from use and stored in the port pipe racker. We picked up 201 joints of new 5 inch drill pipe from the riser hold. The new drill pipe was strapped and drifted as it was assembled and lowered toward the seafloor. After completing assembly of the new pipe, the remaining 37 stands from the starboard 5 inch pipe racker were picked up and run in the hole. The total number of 5 inch pipe stands available was then 104 stands. The remaining 101 stands of suspect drill pipe in the port pipe racker need to be inspected before they can be put back in service.

After tripping toward the seafloor with 104 stands of 5 inch drill pipe, the 5½ inch drill pipe was picked up until the bit reached 4372.9 mbrf. The trip was stopped at 3587.0 mbrf to perform a slip and cut of the drilling line. The precision depth recorder recorded an estimated depth of 4394.4 mbrf for the seafloor. The top drive was picked up and spaced out to 4390 mbrf. The nonmagnetic core barrels were dressed with liners, the FlexIT core orientation tool was inserted, and a core barrel was run down and landed. Hole U1433A was spudded at 1000 h on 9 March 2014. The mudline core recovered 8.9 m of sediment, and the seafloor was calculated to be 4390.6 mbrf (4379.4 m below sea level [mbsl]). Coring continued without issue through Core 349-U1433A-16H (151.4 mbsf). While running in the hole with a core barrel, the bridge informed the driller that a fishing boat was drifting toward the vessel's location. At 0540 h on 10 March, the Captain ordered the driller to suspend operations. The core barrel was retrieved, and the driller began tripping out of the hole with the top drive. At 99.1 mbsf, the driller was instructed to stand by. After the threat disappeared, the drill string was tripped back to bottom, and coring continued to Core 20H (188.3 mbsf). After 4 consecutive partial strokes of the APC, refusal was called at 188.3 mbsf. Orientation was measured on all APC cores. Temperature measurements were taken with the advanced

piston corer temperature tool on Cores 4H, 7H, 10H, and 13H, with good results. Perfluorocarbon tracer (PFT) fluid was used on Cores 18H through 20H. The bit was tripped to the surface and cleared the rig floor at 0325 h on 11 March, ending Hole U1433A. A total of 20 APC cores were taken over a 188.3 m interval in Hole U1433A, recovering 168.79 m of core (89.6% recovery). The total time spent on Hole U1433A was 73.0 h (3.0 days).

Hole U1433B

After offsetting the vessel 20 m east of Hole U1433A, an RCB BHA was assembled with a new RCB C-4 bit. Three additional drill collars had to be picked up from the drill collar racks to replace the ones lost in Hole U1432B. The core barrels were spaced out at the surface and the 172.07 m BHA assembled and run to 4350.3 mbrf. The top drive was then picked up and spaced out to spud Hole U1433B. A center bit was dropped and pumped to land out in the bit. Hole U1433B was spudded at 1515 h on 11 March 2014. The seafloor depth for the hole was 4390.6 mbrf (4379.4 mbsl), determined by using an offset depth from Hole U1433A. Hole U1433B was advanced by drilling without coring from the seafloor to 186.1 mbsf. The center bit was pulled from the BHA by wireline, and a core barrel was dropped to start continuous RCB coring of Cores 349-U1433B-2R through 75R to a total depth of 5249.1 mbrf (858.5 mbsf). The PFT pumps were turned on during the drilldown period, and PFT fluid was pumped through Core 26R (426.9 mbsf). Microspheres were added to the RCB core catcher sub for Cores 56R through 75R. Core 65R encountered basalt at 786.3 mbsf. Coring continued into acoustic basement from Core 65R to 75R (858.5 mbsf), with half-cores collected from Core 67R to the total depth in an attempt to improve recovery. Penetration rates varied from 0.9 to 3.9 m/h over the basement interval. The total depth of Hole U1433B was reached at 2100 h on 17 March, and the final core was pulled to the surface and laid out. At the completion of coring Hole U1433B, 74 RCB cores had been cut over a 672.4 m interval, recovering 443.04 m of core (65.9% recovery).

After pumping a 50 bbl high-viscosity mud sweep, a short wiper trip was made from total depth to just above the basement contact (786.3 mbsf) with the top drive installed. While tripping back to bottom, the hole had to be reamed from 847.4 to 858.5 mbsf. We then pumped another 50 bbl mud sweep to further clean the hole. The rotary shifting tool (RST) was then picked up and run into the hole with a coring line to release the bit for logging. An attempt was made to engage the sleeve in the mechanical bit release. After being unable to engage the shifting sleeve, the other RST was pulled back to the surface. Examination at the surface revealed the RST did not

come back with the core line sinker bars. An overshoot (fishing tool) was made up and run in the hole to fish for the RST. After securing the RST, the mechanical bit release sleeve was engaged and the bit was dropped from the drill string. The RST also dropped off the fishing tool on release, leaving the RST in the bottom of the hole. The core line was pulled back to surface, and the RST was deployed to shift the sleeve back into the original position. With the bit released, the drill string was raised to 5196.3 mbrf (805.7 mbsf) with the top drive. The top drive was then set back, and the drill string was raised to 5079.7 mbrf (689.1 mbsf). The circulating head was picked up, and the hole was displaced from 689.1 mbsf to the sea-floor with 10.5 lb/gal high-viscosity mud designed to improve logging conditions. The drill string was then raised up and spaced out so that the end of the pipe was at 4490.7 mbrf (100.1 mbsf) for logging operations.

After holding a logging safety meeting for rig floor personnel, the triple combo tool string was rigged up and deployed. The tool string reached a total depth of 845.4 m WSF on 18 March. The hole was then logged up, and the tool string was pulled to the surface and rigged down. After rigging down the triple combo tool string, the FMS-sonic tool string was rigged up and deployed to a depth of 842.4 m WSF. The basement section of the hole was logged five times with three passes with the calipers open. On the last pass, the tool became stuck but was eventually worked free. The rest of the open hole was logged up to the end of the drill pipe and the tool string was then pulled to the surface and rigged down. All logging equipment was rigged down by 1300 h on 19 March. The drill string was pulled from the hole and the BHA set back and secured for transit at 2300 h on 19 March, ending Site U1433. Total time spent in Hole U1433B was 211.5 h (8.8 days).

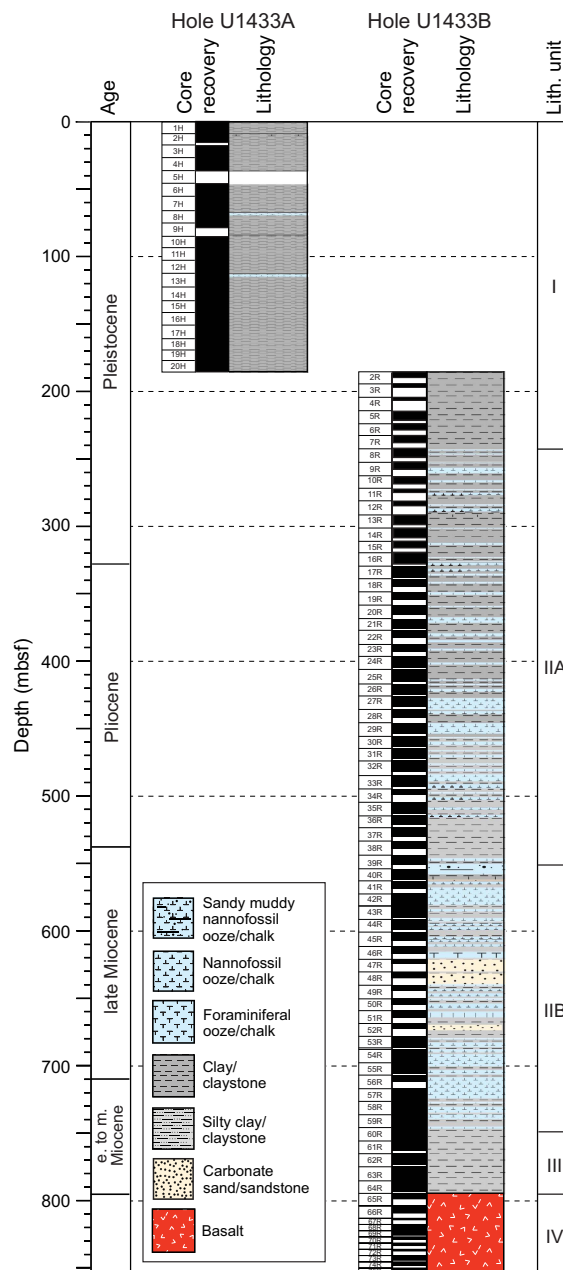
Lithostratigraphy

Lithostratigraphic units

Four lithostratigraphic units are defined at Site U1433 based on a combination of visual core description and smear slide and thin section inspection as well as scanning for an array of physical properties, including magnetic susceptibility and color spectra (see [Lithostratigraphy](#) and [Physical properties](#) in the Methods chapter [Li et al., 2015b]). A composite stratigraphy was derived through a combination of material from Holes U1433A and U1433B (Figure F4). Three major sedimentary units overlie a single lithostratigraphic unit that forms the crystalline, igneous basement (Figures F4, F5). This lower unit is dominantly composed of basaltic igneous rocks and is discussed in detail in [Igneous petrology and alteration](#). Very small volumes of thin-bedded (1.0–1.5 cm thick) sedimentary rock were found between pillow basalt and massive flows in Unit IV and are discussed along with the igneous rocks in [Igneous petrology and alteration](#), as well as in [Biostratigraphy](#).

Unit I is composed of dark greenish gray clay with interbedded very thin clayey silt. Unit II contains dark greenish gray clay and claystone with frequent medium to thick greenish gray nannofossil ooze and chalk interbeds. This unit is divided into upper and lower subunits based on the occurrence of thick to very thick (>1 m) greenish gray nannofossil chalk interbeds in Subunit IIB, compared to thinner beds in Subunit IIA. Unit III consists of dominantly massive reddish and yellowish brown claystone and claystone with silt, with little coarser material present, occasional thin silty turbidites, and common dark staining associated with bioturbation. This unit lies directly on the basaltic basement (Unit IV).

Figure F4. Lithostratigraphy summary, Site U1433.



Unit descriptions

Unit I (0–244.15 mbsf)

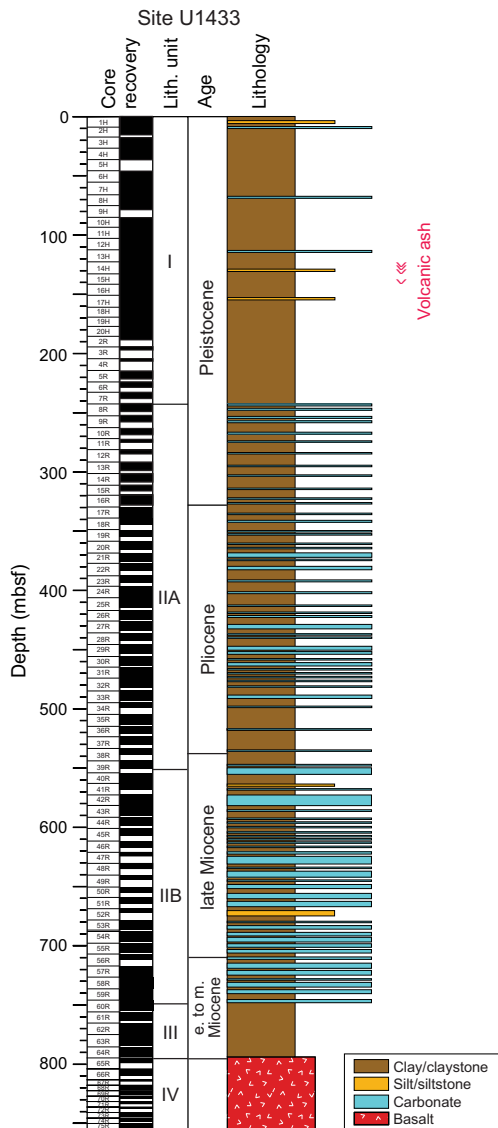
Intervals: 49-U1433A-1H through 20H; 349-U1433B-2R-1, 0 cm, through 8R-2, 5 cm

Depths: Hole U1433A: 0–188.30 mbsf (total depth); Hole U1433B: 186.10–244.15 mbsf

Age: Pleistocene

Unit I is composed of dark greenish gray clay with rare interbeds of thin and very thin (<5 mm) clayey silt beds. There are dark brownish clay layers in the upper parts of the unit, together with minor light greenish gray clay with nannofossils and nannofossil ooze layers throughout the section. The clay is generally massive and homogeneous, sometimes marked by faint color banding of more in-

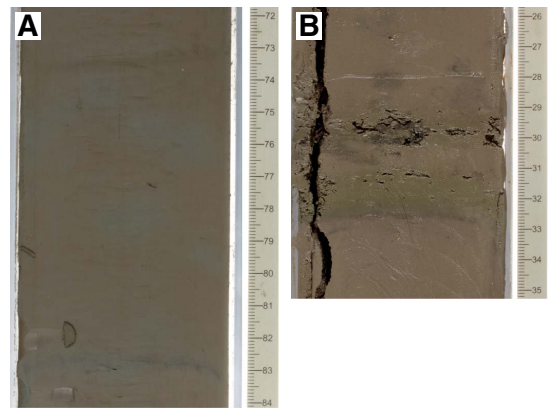
Figure F5. Synthesis sedimentary log for Site U1433 showing combined recovery in Holes U1433A and U1433B. Interpretation of poorly recovered areas was enhanced by reference to downhole logging results.



tense green against the background of greenish gray (Figure F6A). In some locations the green sediment is better defined and more intense in color, where it forms well-defined green bands rich in glauconite (Figure F6B). Thin clayey silt layers are usually graded and fine upward above sharp bases that at least locally show signs of erosion (Figure F7A). Silt beds in Unit I are mostly 1–2 cm thick (Figure F7B), occasionally up to 15 to 20 cm thick, but generally comprise <10% of the entire section.

We interpret both the carbonate and graded silt intervals as turbidites. In places several small turbidite silts are stacked on top of one another (Figure F7C), with up to four in succession. In these cases the lower silt is the thickest and is overlain by thinner beds, often <5 mm thick and separated by a similar thickness of clay from

Figure F6. Green layer development, Hole U1433A, Unit I. A. Massive clay with faintly developed green layering typical of the unit (14H-3A, 76–83 cm). B. Green layer in clay (2H-2A, 29–36 cm).



the next silt. Further evidence for seafloor erosion and reworking is found in some locations where 2 slightly differently colored clays are found juxtaposed with a sharp erosive contact between the two (Figure F8). These may represent areas of erosion and bypassing by turbidity currents, although very thin silts (<2 mm thick) are sometimes seen along these surfaces, which often show topography, indicating a slight angle during deposition, at least in the lee of seafloor topography.

At the microscopic level, the apparently homogeneous clay contains common quartz silt and volcanic glass shards. In lighter colored intervals, the proportion of biogenic and redeposited calcite can be significant. Figure F9A shows the abundance of radiolarians in parts of Unit I, together with other largely siliceous microfossils including diatoms and sponge spicules. In more calcareous intervals, we also identified foraminifers, nannofossils, and calcite shelly material of undetermined origin. Foraminifers are often broken and are also found in association with quartz and volcanic glass shards (Figure F9B).

Volcanic ash layers are rare at Site U1433, only found in Unit I from 120 to 140 mbsf (Figure F5). Figure F10 shows the thickest example of a dark-colored, graded tephra layer 6 cm thick within clay. More typically there are a number of thin (<2 cm thick) felsic ash layers in the middle part of the unit. These deposits are volumetrically insignificant, although very small amounts of volcanic glass shards are often found scattered through clay and silt beds. All identified tephras show sharp bases and normal grading from a silt-sized basal layer, typical of air fall deposits.

Rare nannofossil ooze layers are found in Unit I. The beds all fine upward and have erosive bases, consistent with a turbidite origin, but these intervals are volumetrically small, resulting in Unit I being dominated by clay.

Taken together, the evidence from Unit I supports sedimentation in a distal hemipelagic muddy setting with siliceous plankton-dominated pelagic deposition and limited influxes of calcareous material. Bioturbation is presumed to be intense because of the lack of lamination, but because most of the sediment is the same color there is little chance to see burrows highlighted with contrasting

Figure F7. Silt turbidites, Hole U1433A, Unit I. A. Rare thick-bedded silt turbidite (16H-2, 55–71 cm). B. More typical thin-bedded graded silt turbidite (7H-3A, 66–75 cm). C. Thin, stacked silt turbidites in clay (4H-4, 44–57 cm).

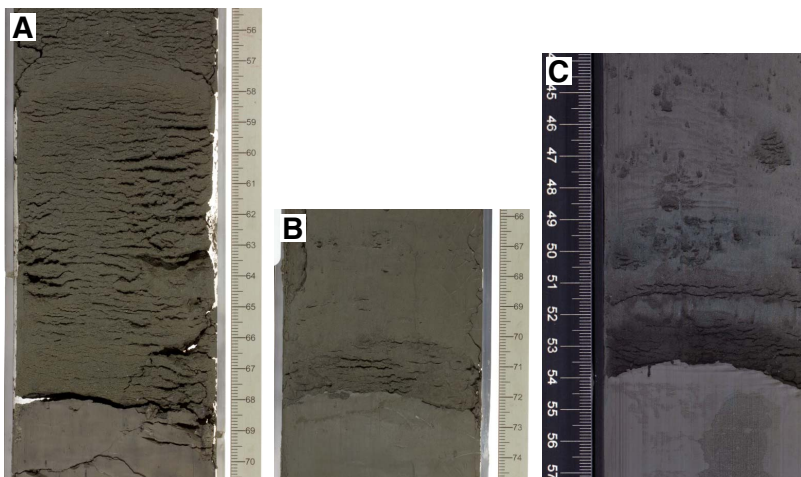


Figure F8. Erosion surface between 2 clay units, Hole U1433A, Unit I (16H-6A, 62–71 cm). Note the thin silt developed on the left side of the core along the contact.



Figure F9. Hole U1433A, Unit I (plane-polarized light [PPL]). (A) Radiolarians in clay (2H-1, 89 cm) and (B) clay with foraminifers, sponge spicules, and radiolarians, as well as quartz silt (6H-5, 73 cm).

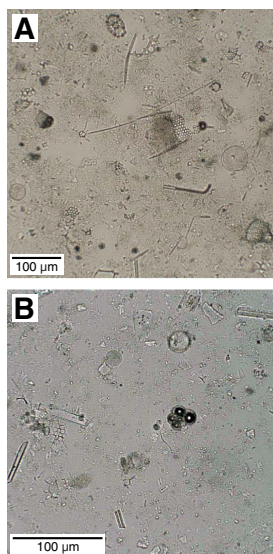


Figure F10. Dark-colored mafic tephra layer, Hole U1433A, Unit I (14H-1A, 117–130 cm).



lithologies. Figure F11A shows an exception to this, in which small horizontal burrows are found within a more nannofossil-rich interval. The burrows themselves are filled by coarse foraminiferal sand and are of relatively low abundance.

Unit II (244.15–747.93 mbsf)

Interval: 349-U1433B-8R-2, 5 cm, through 60R-1, 93 cm
 Depth: 244.15–747.93 mbsf
 Age: Pleistocene–middle Miocene

Unit II represents the majority of the sediment recovered at this site, and is readily distinguished from overlying deposits by the presence of common calcareous turbidite beds within a dominant clay and claystone background. The unit is also unique in its physical properties (Figure F12) because it shows low magnetic susceptibility values not seen in Unit I and has much more variable color spectral proxies, especially in L* and to a lesser extent b*. Lithification increases quickly downsection from the top of this unit. Because sediment at Site U1433 was deposited below the modern calcite compensation depth, a mechanism is needed to explain the

Figure F11. Burrows in sediment. A. Simple burrows (*Planolites*) in ooze infilled by foraminifer sands, Hole U1433A, Unit I (8H-3A, 117–125 cm). B. Horizontal burrows in ooze, likely *Scolicia*, Hole U1433B (29R-1A, 97–104 cm). C. Bioturbated top of a typical calcareous turbidite within Unit II, Hole U1433B. Burrows are dominated by *Planolites*, *Chondrites*, and *Zoophycos* (19R-1A, 83–94 cm).

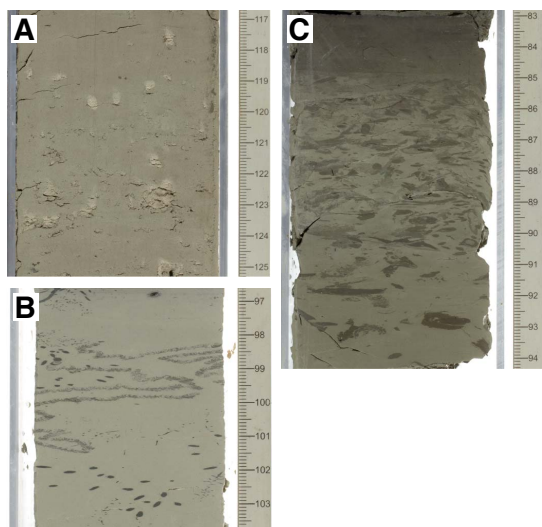
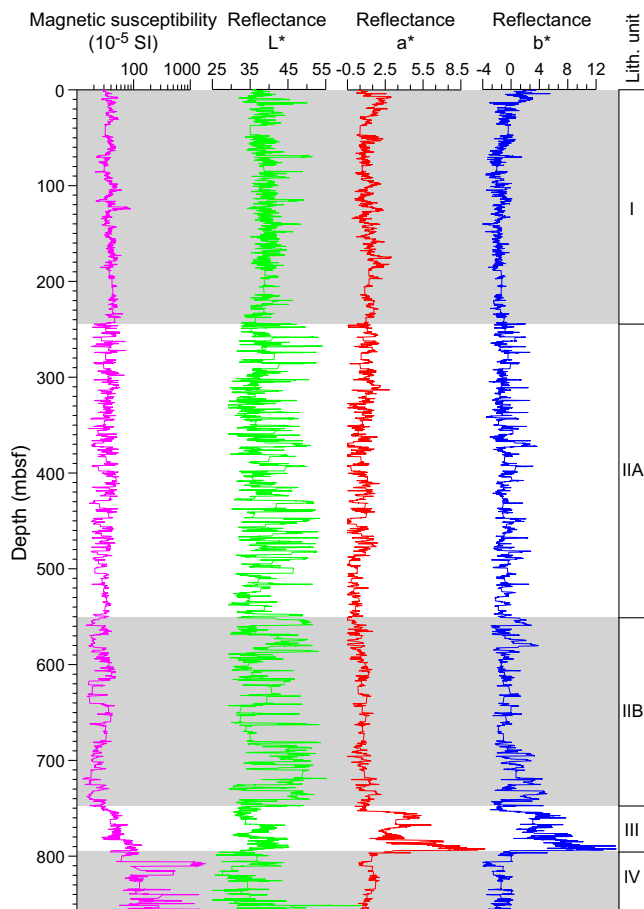


Figure F12. Correlation of lithostratigraphic units with magnetic susceptibility and reflectance spectroscopy (after 30-point running average), Site U1433.



significant amount of carbonate in the core. We propose rapid redeposition from shallower water settings into the deepwater basin by turbidity currents. Unit II is divided into 2 subunits, with the lower one distinguished by much thicker carbonate turbidites but otherwise basically of the same facies as the upper subunit. The boundary between the 2 subunits is at the top of the first multimeter-thick carbonate bed encountered downsection.

Subunit IIA (244.15–551.32 mbsf)

Interval: 349-U1433B-8R-2, 5 cm, through 39R-6, 100 cm
 Depth: 244.15–551.32 mbsf
 Age: Pleistocene–Pliocene

The sediments of Subunit IIA are typified by cycles of redeposited carbonate and a background of rapidly deposited, largely dark greenish gray claystone (Figure F13). The carbonate beds tend to be 15–50 cm thick and account for ~20% of the total section. Each bed is marked by a sharp, erosive base with color and grain-size gradation upward toward a more diffuse boundary with the overlying greenish gray clay. The basal few centimeters are often characterized by silt or fine sand-grade sediment with parallel laminations often observed over the basal 1–2 cm. The upper contact of each turbidite is often heavily bioturbated and contains a variety of deepwater traces of the *Nereites* ichnofacies. Figure F11C shows a close-up of the trace fossil assemblages in Subunit IIA. The smallest burrows are the *Chondrites* ichnospecies and are commonly also found in conjunction with the larger *Planolites* and *Zoophycos*. Horizontal *Scolicia* burrows are present but less commonly observed.

Figure F13. Typical calcareous turbidite cycle showing grading from the erosive base to the bioturbated top (349-U1433B-17R-3A, 32–66 cm).



This is the most typical trace fossil assemblage seen within the sub-unit. Typically, the intense burrowing exists in the uppermost 10 cm of the calcareous turbidite, leaving the rest of the bed undisturbed.

Figure F14 shows 2 turbidites stacked on top of one another. In this example the lower turbidite unit (interval 349-U1433B-48R-1A, 65–72 cm) is finer grained but still shows a sharp erosional base grading up into a bioturbated top. The burrows are filled with a more clay-rich, darker sediment that is in turn truncated by a second turbidite (interval 48R-1A, 57–65 cm) with parallel-laminated silt and fine sand–grade material that in turn passes up into dark bioturbated gray clay. This upper turbidite unit is also different in being bioturbated by large *Planolites*-type burrows, which have lower density than those in the lower turbidite unit. Turbidites within Subunit IIA are almost exclusively carbonate with very little siliciclastic material observed.

At the microscopic level, the clay lithologies are composed of not only clay minerals but significant quantities of opaque material and fine silt-sized quartz, as well as some lithic grains and feldspar. Occasional fragments of angular, mafic, volcanic glass are also observed in minute quantities. The amount of biogenic material is relatively small (Figure F15A). Deeper in the subunit, diagenesis results in these mud-rich units being affected by pyrite growth. Figure F15B shows an example of very fine-grained pyrite in its earliest stage of growth within a claystone interval. With continued growth, the pyrite forms nodules and in some cases replaces burrows, although the total volume of pyrite remains relatively low. The appearance of pyrite is interpreted to reflect pervasive reducing conditions within the claystone. Microscopic analysis of the redeposited carbonate units shows that they are formed from a variety of shelly material, although foraminifers are the dominant type of clast. Figure F16C shows one of these turbidite silts higher in the section, showing the whole, unbroken character of the foraminifers, as well as a variety of less recognizable fragments of shells, together with volcanic glass and fragments of larger foraminifers. In contrast, deeper within Subunit IIA the carbonate deposits are dominated

Figure F14. Two calcareous turbidites stacked on top of one another, Hole U1433B (48R-1A, 56–73 cm). The lower turbidite is finer grained claystone to siltstone with a *Chondrites*-burrowed top. The upper turbidite is silty and laminated with larger *Planolites* burrows, grading upward into claystone.



Figure F15. Typical clay/claystone lithologies, Hole U1433B (PPL). A. Clay with minor quartz silt and brown mafic volcanic glass shards (9R-3, 43 cm). B. Common pyrite crystals scattered through the matrix (15R-5, 52 cm).

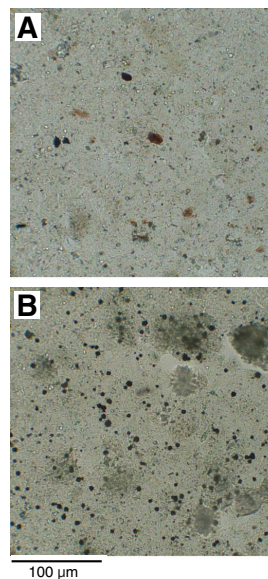
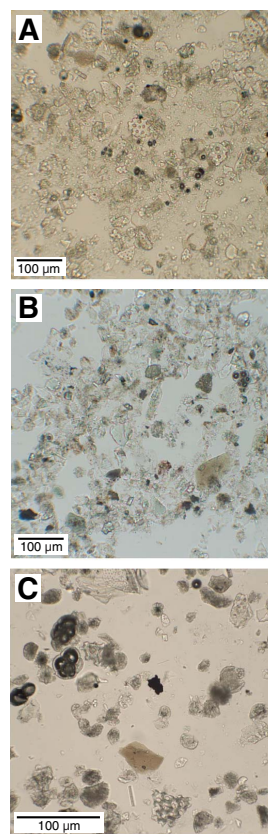


Figure F16. Coarser clastic material (PPL). A. Broken, mostly calcareous fine sand with foraminifer fragments (U1433B-25R-1, 41 cm). B. Siliciclastic silt with minor glass shards and foraminifers (U1433B-6R-4, 115 cm). C. Carbonate sand dominated by whole and fragmented foraminifers (U1433A-8H-3, 39 cm).



more by broken shell material (Figure F16A) and significant numbers of nannofossils. We interpret the shell breakage to have occurred during transport, not burial.

Both of these types of deposits contrast with quartz-rich silty turbidites that are mostly found within Unit I and to a lesser extent in Subunit IIA (Figure F16B). These deposits are moderately sorted and mostly composed of subangular to subrounded grains of quartz, feldspar, volcanic glass, and a lower proportion of biogenic carbonate material. Green grains of glauconite are also visible in some beds.

Subunit IIB (551.32–747.93 mbsf)

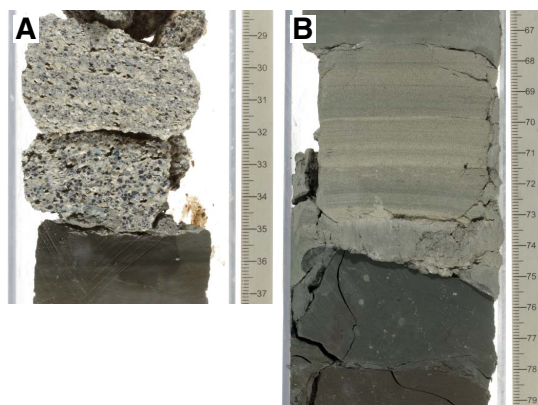
Interval: 349-U1433B-39R-6, 100 cm, through 60R-1, 93 cm

Depth: 551.32–747.93 mbsf

Age: middle–late Miocene

In many respects, Subunit IIB is like Subunit IIA but is mostly distinguished by being somewhat thicker bedded and with a higher proportion of carbonate, at least over moderate lengths of the core. The Subunit IIA/IIB boundary does not stand out in most physical properties measured (Figure F12), except *P*-wave velocity (see **Physical properties**). We defined the top of this subunit to be coincident with the top of the first carbonate turbidite that is several meters thick. One consequence of the appearance of thicker re-deposited carbonates is that the grain size also increases. Figure F17A shows an example in which the base of a turbidite, lying with an erosive contact on the underlying claystone, is marked by a massive to weakly laminated coarse sandstone that grades uphole over a distance of ~20 cm into medium sandstone. In this particular case, the sand consists mainly of shallow-water benthic foraminifer species, chert, feldspar, volcanic lithic fragments, and quartz grains (Figure F18), showing that the sediment is derived from a nearby shallow-water environment. In other examples, the carbonate sand is very well laminated (Figure F17B), demonstrating deposition under a high-energy laminar flow regime, which we interpret as being part of the Bouma B division (Bouma, 1962). Figure F19 shows abundant well-preserved planktonic foraminifers and occasional micro-authigenic pyrite grains within a laminated, light greenish gray foraminifer chalk from this facies. As before, these deposits are all interpreted to be the product of sedimentation from a turbidity current with a source on some of the shallow banks mostly lying to the south of the drilling site (Figure F1), although at this stage we can-

Figure F17. Erosive bases of calcareous turbidites, Hole U1433B. A. Coarse sand–grade base with carbonate and volcanic rock fragments (47R-1A, 28–37 cm). B. Laminated medium sand of foraminifer-rich carbonate material overlying claystone (26R-5A, 68–79 cm).



not rule out the influence of more localized sources on isolated sea-mounts, despite being less likely than at Site U1431.

In one unusual example (Figure F20), the coarse sand at the base of a turbidite deposit contains large amounts of fine-grained organic carbon material, which was preserved as a black substance, deformed in a plastic fashion between relatively rigid grains mostly of carbonate composition. This particular bed was quite unique in its appearance compared to the other sandstone beds within the subunit, suggesting that this was an atypical sedimentation event. As a general rule we saw little evidence for significant amounts of organic carbon in the sediment.

Figure F18. Coarse carbonate sandstone, Hole U1433B, Subunit IIB (47R-1, 30–32 cm). A. PPL. B. Well-preserved benthic foraminifers (a) *Lepidocyclus* and (b) *Amphistegina* that live in water depths shallower than 100 m. Sub-rounded to rounded (c) chert, feldspar, and quartz grains also occur (cross-polarized light [XPL]).

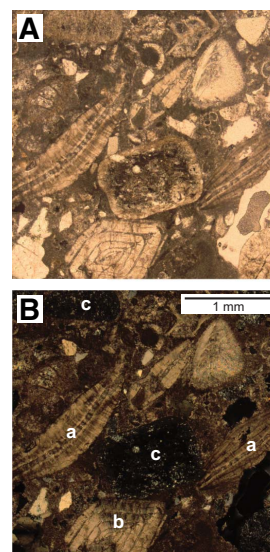
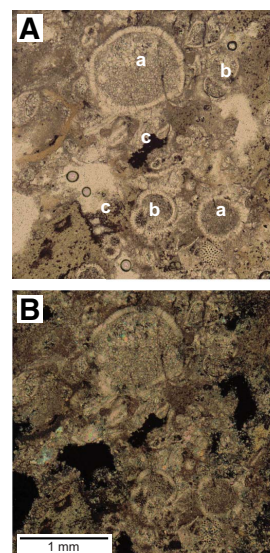


Figure F19. Parallel-laminated foraminifer chalk, Hole U1433B, Subunit IIB (40R-5, 38–40 cm). A. Planktonic foraminifers including (a) *Orbulina* and (b) *Globigerinoides* are major components of the chalk. Microauthigenic (c) pyrite grains occur as black spots or aggregates (PPL). B. XPL.



Bioturbation within Subunit IIB is generally similar to that seen in Subunit IIA with one or two exceptions in the thick carbonate beds. Figure F11B shows an example of a horizontal burrow of the *Scolicia* ichnospecies. This particular deposit is not heavily bioturbated but shows *Chondrites* and associated *Scolicia* burrows in the sediment immediately underlying. Sparse bioturbation within these carbonates likely reflects the relatively low amounts of organic material on which the borrowing infauna would have been able to feed.

Unit III (747.93–796.67 mbsf)

Interval: 349-U1433B-60R-1, 93 cm, through 65R-1, 117 cm

Depth: 747.93–796.67 mbsf

Age: early–middle Miocene

The third major unit overlying the igneous basement is much thinner than the other 2 units (~49 m thick) and is distinguished by being entirely composed of claystone and claystone with silt with only minimal millimeter-scale silt intervals. We defined the top of this unit as being the base of the lowest significant carbonate deposit within Subunit IIB. The claystone that directly underlies this carbonate bed is very similar to much of that seen within Subunit

IIB, being massive, well bioturbated, and dark greenish gray. This claystone then passes rapidly downsection through a color transition into a dominant reddish brown or yellowish brown claystone, which represents the bulk of this unit. Figure F21A shows an example of the massive-bedded reddish claystone. Sedimentary structures are not common within this unit, although there are intervals of graded, quite bioturbated clayey siltstone and silty claystone that show parallel lamination and normal grading over distances of 20–30 cm (Figure F21B). Some of the claystone intervals themselves show grading over similar distances, but more typically they are massive and occasionally bioturbated with the same type of assemblages seen in Unit II, albeit less densely developed. The unit is especially noteworthy for having a common black staining of the claystone that is sometimes, but not always, associated with burrowing (Figure F21C). In the absence of X-ray diffraction (XRD) constraints, we were unable to define causes of this black staining, although organic carbon seems the most likely, especially given the association with bioturbation.

We interpreted Unit III to be deposited as a distal pelagic mudstone overlying the basaltic basement. There is no lithologic evidence for any significant hydrothermal activity during the deposition of these clays or for significant alteration after sedimentation as a result of high-temperature fluid flow. In many ways, these sediments are reminiscent of the deepwater red clays in the Central Pacific (Bryant and Bennet, 1988) and other deep abyssal plain areas, including Site U1431. Microscopic analysis shows that many or all of the carbonate microfossils that would have been deposited have dissolved as a result of sedimentation below the calcite compensation depth, leaving only siliceous microfossils such as radiolarians. Sedimentation rates are much slower in this subunit compared to the rest of the stratigraphy (see **Biostratigraphy**), although they are faster than those seen in the Central Pacific, reflecting the fact that our drilling location is located much closer to continental sediment sources, which are inferred to supply the silty material seen within the claystone.

Figure F20. Organic carbon-bearing sandstone at the base of a turbidite, Hole U1433B (53R-1A, 65–72 cm).

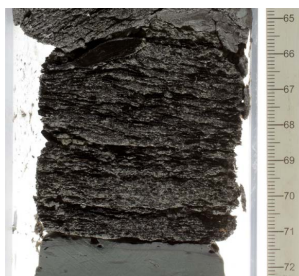
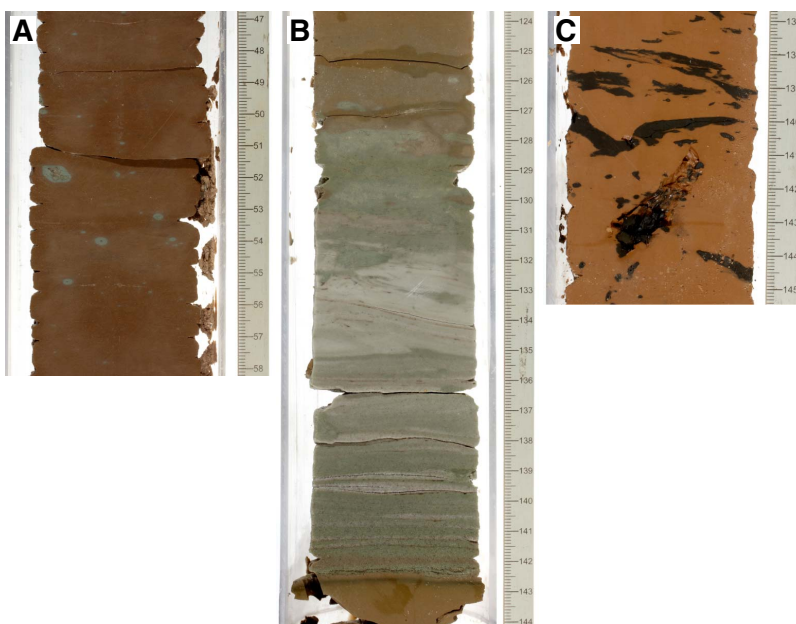


Figure F21. Claystone, Hole U1433B, Unit III. A. Massive reddish brown claystone typical of the deposits immediately overlying basement (61R-1A, 47–58 cm). B. Redeposited clayey siltstone and silty claystone beds within the dominant claystone (63R-3A, 124–144 cm). C. Black-stained burrows in claystone (64R-4A, 137–145 cm).



Discussion

Trace fossils

Trace fossils preserved in deep-sea sediments represent the last burrows that are imposed on a sediment beneath the mixed surface layer, which spans the uppermost 5–7 cm of the seafloor (Ekdale et al., 1984). The assemblages seen in our cores are typical of very deepwater sedimentary environments in distal clastic settings and correspond to the *Nereites* ichnofacies. This ichnofacies is typical of the uppermost 3–7 cm in the modern subseafloor sediment of the South China Sea, where water depths exceed 4000 m (Wetzel, 2002), although after correcting for the expected thermal subsidence we anticipate that these assemblages must have been formed at shallower water depths, albeit ones at least as deep as typical seafloor spreading ridges (~2500 m). Work on deep-sea cores from the Central Pacific suggests that *Zoophycos* is more common in sediments with slightly higher organic carbon content (Kemp, 1995), and because this particular trace is relatively rare in our cores, we deduce that the organic carbon content is never particularly high, an observation confirmed by shipboard analysis (see [Geochemistry](#)). Conversely, we note that vertical burrows such as *Skolithos* are almost absent from our cores. *Skolithos* burrows are commonly associated with particularly low sedimentation rate environments with extremely depleted organic content (Kemp, 1995). Thus, compared to the Central Pacific, the South China Sea does not experience the types of sediment starvation and low productivity associated with these deep-sea desert regions, which is perhaps not surprising given its relative proximity to landmasses in Southeast Asia and the continental runoff associated with them. It is noteworthy that *Zoophycos* is only sparsely developed in Unit II but was found at least in parts of Unit III despite the relatively low sedimentation rates inferred for this part of the stratigraphy.

Provenance

Several sources may have contributed sediment to Site U1433. The location of the drill site south of the fossil mid-ocean ridge suggests that derivation of material from southern China, the Philippines, or Taiwan is unlikely, especially since these landmasses are farther away than the other possible sources in Borneo or mainland Southeast Asia (Figure [F1](#)). Modern sediment transport routes between the Sunda shelf and the drill site would presently favor sediment transport from the Mekong River, which could be the source of the clay and silt. During sea level lowstands, sediment could also flow from peninsular Malaysia or even from Sumatra via the Molengraaff River (Hanebuth and Stattegger, 2004). Seismic reflection data from offshore the Mekong Delta suggest that this system has been particularly active only since ~5 Ma (Li et al., 2013), which means that prior to that time sediment flux from Indochina must have been only from smaller rivers, such as those draining directly from the mainland into the South China Sea. These in turn would have been rejuvenated and strengthened during the uplift of the Central Highlands of Vietnam following the emplacement of flood basalts there at ~8 Ma (late Miocene; Carter et al., 2000).

In theory, clastic material could flow to the region from mainland Borneo, but in order to do this the sediment would have to cross the tectonically generated bathymetry of the Dangerous Grounds (Figure [F1](#)), which is marked by many ridges and deep basins that would act as efficient sediment traps. Although the sediment could be transported as hyperpycnal plumes, there is little evidence from satellite imagery to suggest that this is a common process today, and the proliferation of active carbonate reefs dating back into the Miocene would also indicate that substantial transport

of clay across the Dangerous Grounds from Borneo is unlikely to have been significant on geological timescales (Hutchison and Vijayan, 2010). Surface currents in the South China Sea also do not favor transport from south to north across the Dangerous Grounds (Hu et al., 2000).

The source of the carbonate sediment, and the turbidites in particular, within Unit II is most likely within the Dangerous Grounds or the Reed Bank area. Local sources, such as isolated seamounts, seem less likely at Site U1433 compared to those at Site U1431 because there are fewer shallow seamounts in the region. The seismic reflection data that cross the seamount that sits on the fossil seafloor spreading axis to the north of Site U1433 do not show evidence for substantial carbonate buildup on top (see Figure [F7](#) in the Expedition 349 summary chapter [Li et al., 2015a]). We conclude that most of the carbonate material found in the turbidite sediments is derived from the south in the Dangerous Grounds, but it is worth asking why the flow of this material is suddenly truncated during the Pleistocene at the boundary between Units I and II after several million years of quite active sedimentation. This is particularly enigmatic given the fact that over longer periods of time sea level has been falling during the Pleistocene (Haq et al., 1987). We suggest that the reduction in carbonate flux to the drill site reflects the steady subsidence and drowning of the carbonate reefs in the Dangerous Grounds despite the overall sea level fall. Although several reefs still remain and give the region its name, much of the original carbonate buildup has been drowned as a result of postrift thermal subsidence reducing the extent of shallow water within this tectonic block (Hutchison, 2004; Hutchison and Vijayan, 2010; Steuer et al., 2013).

What triggers the emplacement of individual carbonate turbidites is not entirely apparent, although they could reflect variability in sea level, as falling sea level tends to result in erosion of shallow-water regions and resedimentation into basinal areas (e.g., Vail et al., 1977). We note that falling sea level would also affect the flux of clay and silt from the southwest and would not necessarily result in more carbonate turbidites. Some of the turbidite events may have been triggered by earthquakes, especially during the Miocene after the collision of the Dangerous Grounds with Borneo starting at ~16 Ma (Hutchison, 2004). Better age control and statistical analysis will be needed if we are to understand whether the frequency of carbonate turbidites reflects some larger controlling process.

Biostratigraphy

We analyzed core catcher samples and additional samples from split cores in Holes U1433A and U1433B. Biostratigraphic datums based on calcareous nannofossils, planktonic foraminifers, and radiolarians indicate that the sedimentary succession recovered at Site U1433 spans the lower Miocene to the Pleistocene (Figure [F22](#); Tables [T2](#), [T3](#), [T4](#)). Age control for the lower to middle Miocene section is difficult because of very rare occurrences of calcareous nannofossils and planktonic foraminifers in the depositional sequences, which are dominated by the reddish brown claystone of lithostratigraphic Unit III (see [Lithostratigraphy](#)). Radiolarian bioevents in Hole U1433B between 753.82 and 794.23 mbsf (Unit III) indicate sediment deposition during the early and middle Miocene (~20.6 to ~14.7 Ma). Nannofossils in carbonate infillings between basalt pillows appear to indicate an Oligocene to early Miocene age, but postexpedition studies are required to confirm this.

Calcareous nannofossils are generally common to abundant with good preservation in samples from the Pleistocene–Pliocene

Figure F22. Age-depth model, Site U1433. FAD = first appearance datum, LAD = last appearance datum.

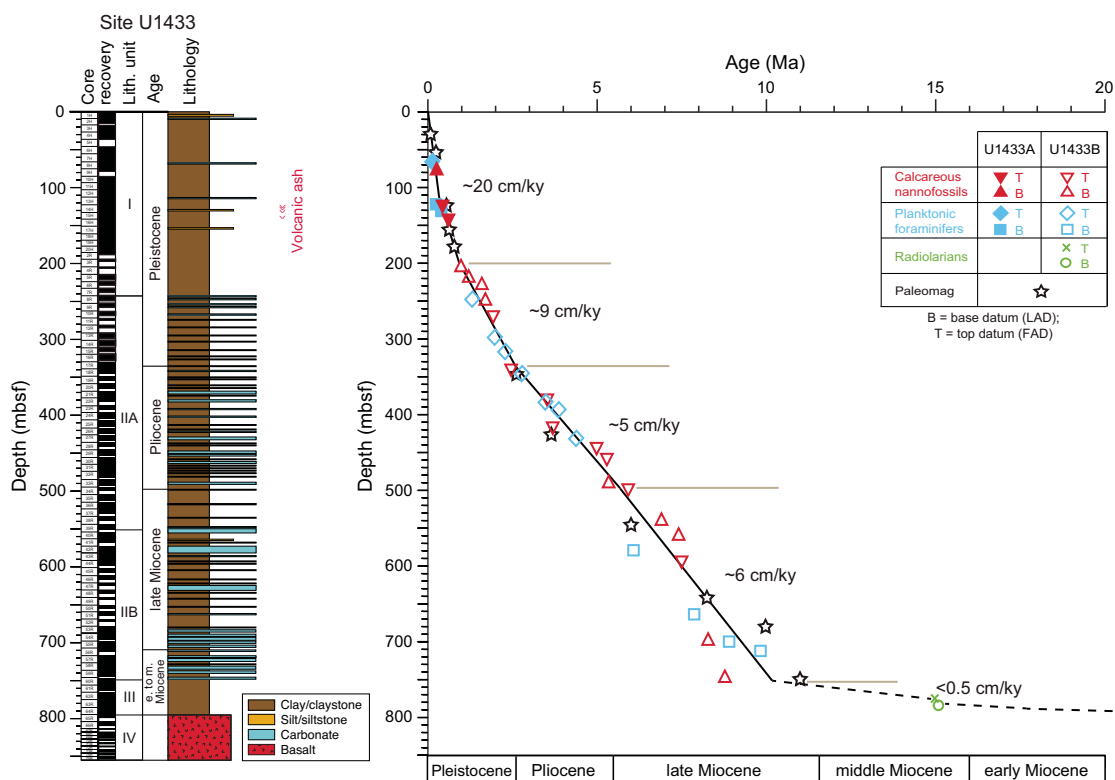


Table T2. Depths and ages of calcareous nannofossil events, Holes U1433A and U1433B. T = top/last appearance datum, B = base/first appearance datum, Ba = base acme. [Download table in .csv format.](#)

Epoch	Zone (Martini, 1971)	Calcareous nannofossil event	Hole U1433A		Hole U1433B		Age (Ma)
			Core, section	Top depth (mbsf)	Core, section	Top depth (mbsf)	
Middle to Late Pleistocene	NN21/NN20	B <i>Emiliana huxleyi</i>	9H-CC	79.55			0.29
Middle Pleistocene	NN20/NN19	T <i>Pseudoemiliana lacunosa</i>	13H-CC	122.78			0.44
		T <i>Gephyrocapsa</i> sp. 3	15H-CC	141.5			0.61
early Pleistocene	NN19	B <i>Gephyrocapsa</i> sp. 3			4R-CC	205.74	1.02
		Ba small <i>Gephyrocapsa</i> spp.			5R-CC	220.52	1.24
		B large <i>Gephyrocapsa</i> spp. >5.5 μm			6R-CC	229.07	1.62
		B medium (>4 μm) <i>Gephyrocapsa</i> spp. (=bmG event)			8R-CC	249.28	1.73
late Pliocene	NN18	T <i>Discoaster triradiatus</i>			10R-CC	268.89	1.95
	NN17/NN16	T <i>Discoaster surculus</i>			17R-CC	338.30	2.49
early Pliocene	NN16	T <i>Sphenolithus</i> spp.			21R-CC	377.54	3.54
	NN16/NN15	T <i>Reticulofenestra pseudumbilicus</i>			25R-CC	415.69	3.70
late Miocene	NN13	T <i>Ceratolithus acutus</i>			28R-CC	441.87	5.04
	NN12	T <i>Triquetrorhabdulus rugosus</i>			29R-CC	453.36	5.28
		B <i>Ceratolithus acutus</i>			33R-CC	491.59	5.35
late Miocene	NN11	T <i>Nicklithus amplificus</i>			34R-CC	499.30	5.94
		B <i>Nicklithus amplificus</i>			38R-CC	539.46	6.91
		B <i>Amaurolithus primus</i> , <i>Amaurolithus</i> spp.			40R-CC	561.73	7.42
		T <i>Discoaster loeblichii</i>			43R-CC	590.68	7.53
late Miocene	NN11/NN10	B <i>Discoaster berggrenii</i>			54R-CC	697.73	8.29
	NN10	B <i>Discoaster loeblichii</i>			59R-CC	747.11	8.77

section but are rare and heavily overgrown or even absent in some Pliocene and upper Miocene samples. Varying degrees of overgrowth on nannofossils, especially among discoasters, are common in nannofossil ooze and nannofossil chalk from the lower part of the sediment sequences in Hole U1433B. Planktonic foraminifers are rare to common with good to moderate preservation in most Pleis-

tocene–Pliocene samples but decrease in abundance in some Pliocene–upper Miocene samples. Planktonic foraminifers are abundant and well preserved in silty layers, with numerous small (<150 μm) specimens probably transported by turbidity currents, but are poorly preserved and very difficult to identify in upper Miocene lithified intervals. Radiolarians are abundant and well pre-

Table T3. Depths and ages of planktonic foraminifer events, Holes U1433A and U1433B. T = top/last appearance datum, B = base/first appearance datum. [Download table in .csv format.](#)

Epoch	Zone (Berggren et al., 1995; Wade et al., 2011)	Planktonic foraminifer event	Hole U1433A		Hole U1433B		Age (Ma)
			Core, section	Top depth (mbsf)	Core, section, interval (cm)	Top depth (mbsf)	
Pleistocene	PT1b	T <i>Globigerinoides ruber rosa</i>	7H-CC	66.35			0.12
		B <i>Globigerinella calida</i>	13H-CC	122.78			0.22
		B <i>Globigerinoides ruber rosa</i>	14H-CC	132.23			0.40
	PT1a	T <i>Globigerinoides obliquus</i>			8R-CC	249.28	1.30
Pliocene	PL6	T <i>Globigerinoides extremus</i>			13R-CC	299.20	1.98
		T <i>Globoturborotalita woodi</i>			15R-CC	317.66	2.30
	PL5	T <i>Globoturborotalita decoraperta</i>			18R-CC	345.76	2.75
	PL5/PL4	T <i>Dentoglobigerina altispira</i>			22R-CC	383.07	3.47
late Miocene	PL3/PL2	T <i>Globorotalia margaritae</i>			23R-4, 80–82	394.40	3.85
	PL2/PL1	T <i>Globoturborotalita nepenthes</i>			27R-CC	431.91	4.37
	M14	B <i>Globorotalia margaritae</i>			42R-CC	580.86	6.08
	M13b	B <i>Globorotalia miotumida</i>			51R-CC	664.30	7.89
late Miocene	M13a	B <i>Globigerinoides extremus</i>			54R-CC	697.73	8.93
	M13a/M12	B <i>Neogloboquadrina acostaensis</i>			56R-CC	710.98	9.83

Table T4. Depths and ages of radiolarian events, Hole U1433B. T = top/last appearance datum, B = base/first appearance datum. [Download table in .csv format.](#)

Epoch	Zone (Wang and Abelmann, 1999; Sanfilippo and Nigrini, 1998)	Radiolarian event	Hole U1433B		
			Core, section, interval (cm)	Top depth (mbsf)	Age (Ma)
middle Miocene	RN5	T <i>Calocycletta costata</i>	63R-3, 13–15	779.22	15.00
		B <i>Dorcadospyris alata</i>	63R-CC	785.09	15.03

served in the upper Pleistocene section in Hole U1433A, becoming rare or absent in older sediment sections downhole. In Hole U1433B, samples are barren of radiolarians until Sample 349-U1433B-60R-5, 92–94 cm (753.82 mbsf), which contains rare and poorly preserved specimens. Sponge spicules are present occasionally, whereas diatoms are absent.

The calibrated biohorizons and paleomagnetic datums indicate extremely low sedimentation rates (<0.5 cm/ky) during the early to middle Miocene when the reddish brown clay of lithostratigraphic Unit III was deposited. In the late Miocene to early Pleistocene (corresponding to lithostratigraphic Unit II), sedimentation rates varied between ~5–6 and ~9 cm/ky. The sedimentation rate during the Middle and Late Pleistocene reached ~20 cm/ky, the highest rate recorded during Expedition 349 (Figure F22).

Calcareous nannofossils

Calcareous nannofossil biostratigraphy at Site U1433 is based mainly on analysis of all core catcher samples from Holes U1433A and U1433B (Tables T5, T6). To better constrain biostratigraphic events, a number of samples from within cores were also analyzed.

Calcareous nannofossils are common to abundant with good preservation in samples from Hole U1433A. In Hole U1433B, nannofossils are generally common to abundant in samples from the Pleistocene–Pliocene section (shallower than 300 mbsf) but are rare to common in most Pliocene–upper Miocene samples (300–697 mbsf) and are absent in most samples from the reddish brown claystone of lithostratigraphic Unit III. Pleistocene nannofossils have good preservation, but nannofossils in most Pliocene to upper Miocene samples are moderately to poorly preserved. Varying degrees of overgrowth on nannofossils, especially among discoasters, are common in nannofossil ooze and nannofossil chalk from the lower part of the sediment sequences in Unit II of Hole U1433B.

Table T5. Distribution of calcareous nannofossils, Hole U1433A. [Download table in .csv format.](#)

Table T6. Distribution of calcareous nannofossils, Hole U1433B. [Download table in .csv format.](#)

Nineteen nannofossil biostratigraphic datums are recognized in the upper Miocene to Pleistocene sediment sequence at Site U1433 (Table T1; Figure F22). The oldest nannofossil event identified is the first appearance datum (FAD) of *Discoaster loeblichii*, which is found at 747.11 mbsf (Sample 349-U1433B-59R-CC), indicating an age younger than 8.77 Ma for much of the sedimentary sequence at Site U1433.

Pleistocene

The presence of *Emiliania huxleyi* in Samples 349-U1433A-1H-CC through 9H-CC (8.85–79.55 mbsf) indicates that this sediment is Middle to Upper Pleistocene (≤0.29 Ma) based on the FAD of *E. huxleyi* (Zone NN21). Samples 10H-CC through 12H-CC are assigned to Zone NN20 based on the absence of both *E. huxleyi* and *Pseudoemiliania lacunosa*. The top of Zone NN19 is recognized in Sample 13H-CC (122.78 mbsf), where the last appearance datum (LAD) of *P. lacunosa* (0.44 Ma) occurs. The LAD of *Gephyrocapsa* sp. 3 (0.61 Ma), which falls within Zone NN19, is found in Sample 15H-CC (141.5 mbsf). These latter 2 datums indicate a Middle Pleistocene age, which spans Samples 10H-CC through 15H-CC. The base of Hole U1433A (Sample 20H-CC; 188.69 mbsf) is assigned to mid-Zone NN19 (Middle Pleistocene).

The lower part of Zone NN19 is divided by 4 nannofossil events found in Hole U1433B:

1. The FAD of *Gephyrocapsa* sp. 3 in Sample 4R-CC (205.74 mbsf),

- The FAD of the acme of small *Gephyrocapsa* spp. in Sample 5R-CC (220.52 mbsf),
- The FAD of large *Gephyrocapsa* spp. (>5.5 µm) in Sample 6R-CC (229.07 mbsf), and
- The FAD of medium *Gephyrocapsa* spp. (>4 µm) in Sample 8R-CC (249.28 mbsf).

Zone NN18 can be recognized based on the LAD of *Discoaster triradiatus* in Sample 10R-CC (268.89 mbsf). Similar to Site U1431, Zone NN17 cannot be recognized due to reworking of *Discoaster pentaradiatus*. The top of Zone NN16 is defined by the LAD of *Discoaster surculus* in Sample 17R-CC (338.30 mbsf). These datums indicate an early Pleistocene age for the sedimentary sequence from Samples 4R-CC through 17R-CC (205.74–338.30 mbsf).

Pliocene

Pliocene nannofossil Zones NN16–NN12 are recognized in Hole U1433B. The LAD of *Sphenolithus* spp. (3.54 Ma) in Sample 21R-CC (377.54 mbsf) marks the lower part of Zone NN16. The top of Zone NN15 is defined by the LAD of *Reticulofenestra pseudumbilicus* (3.70 Ma), which occurs in Sample 25R-CC (415.69 mbsf). The LAD of *Ceratolithus acutus* (5.04 Ma) in Sample 28R-CC (441.87 mbsf) indicates lower Zone NN13. The LAD of *Triquetrorhabdulus rugosus*, which marks the top of Zone NN12 (5.28 Ma), occurs in Sample 29R-CC (453.36 mbsf). The Miocene/Pliocene boundary in Hole U1433B falls between Samples 29R-CC (453.36 mbsf) and 33R-CC (491.59 mbsf) based on the LAD of *T. rugosus* (5.28 Ma) and the FAD of *C. acutus* (5.35 Ma), respectively.

Miocene

Six nannofossil bioevents occur in the upper Miocene strata of Hole U1433B. The FAD of *C. acutus* (5.35 Ma), which marks the base of Zone NN12, occurs in Sample 33R-CC (491.59 mbsf). Three nannofossil events within Zone NN11 are identified. The FAD of *Nicklithus amplificus* (6.91 Ma) occurs in Sample 38R-CC (539.46 mbsf), the FADs of *Amaurolithus primus* and *Amaurolithus* spp. (7.42 Ma) occur in Sample 40R-CC (561.73 mbsf), and the LAD of *Discoaster loeblichii* (7.53 Ma) occurs in Sample 43R-CC (590.68 mbsf). The FAD of *Discoaster beggrenii* (8.29 Ma) occurs in

Sample 54R-CC (697.73 mbsf) and defines the Zone NN11/NN10 boundary. The FAD of *D. loeblichii*, which falls within Zone NN10, in Sample 59R-CC (747.11 mbsf), indicates that the overlying sedimentary sequence in Hole U1433B is younger than 8.77 Ma.

We also analyzed eight sediment samples from the uppermost surface of the igneous basement and intrapillow fillings. Six of these samples contain rare and poorly preserved calcareous nannofossils, whereas the other two (Samples 349-U1433B-65R-CC [799.62 mbsf] and 68R-2A, 8–10 cm [821.16 mbsf]) are completely barren (Table T6). Preliminary biostratigraphic ages were established based on diagnostic species found in four samples (Table T7). The presence of *Triquetrorhabdulus carinatus* (LAD at 18.28 Ma) and *Triquetrorhabdulus challengerii* (which has a very restricted geological range in the earliest Miocene spanning Zones NN1 and NN2) in Sample 65R-1A, 117 cm (796.66 mbsf), suggests an age range from 18.28 to ~23 Ma. Older species, including *Zygrhablithus bijugatus*, observed in this sample are considered reworked. Sample 65R-2A, 45–50 cm (797.12 mbsf), contains *Helicosphaera carteri* (first common appearance at 22.03 Ma) and *Sphenolithus conicus* (Zones NP25–NN3), which indicate an age range of ~18–22.03 Ma. Therefore, the 3 samples from the upper part of the pillow basalts in Core 349-U1433B-65R can be assigned an age range between 18.28 and 22.03 Ma. In Sample 70R-1, 88 cm (830.20 mbsf), nannofossils are poorly preserved and strongly overgrown, but some specimens of *Z. bijugatus* and *Sphenolithus distentus* can still be recognized and indicate an Oligocene age. The concurrence of *Z. bijugatus* (>23.74 Ma) and *S. distentus* (26.84–30.0 Ma), if not reworked, would indicate an age of ~27–30 Ma.

We note that the greenish clay and carbonate layers from the upper part of the sedimentary sequence at Site U1433 are turbidities of shallower-water origin (see **Lithostratigraphy**) and contain common to abundant reworked fossils of older ages. Generally, reworked microfossils are more abundant in nannofossil ooze or carbonate layers than in the greenish clay. Reworking can be distinguished when younger and older species co-occur, such as *Z. bijugatus* in Sample 65R-1A, 117 cm, described above; however, whether *Z. bijugatus* and *S. distentus* in Sample 70R-1, 88 cm (830.2 mbsf), from the intrapillow sediment represent an original or reworked assemblage is not clear. Postcruise studies, including

Table T7. Species composition and inferred ages of sediment found in and immediately overlying basalt, Hole U1433B. * = radiolarian. All others are calcareous nannofossils. [Download table in .csv format.](#)

Core, section, interval (cm)	Depth (mbsf)	Sample feature and location in basalt sequences
349-U1433B-		
65R-1, 79–91	796.29	Brownish claystone
65R-1A, 117	796.66	One piece of light yellow claystone (1 cm) between overlying red clay and underlying basalt
65R-2A, 45–50	797.12	Thin green clay layer (~1 mm) between basalt glass and white carbonate layer
65R-2A, 49–51	797.16	Green clasts within the white calcareous pebble found between pillow basalt samples
70R-1, 88	830.20	1 thin (~30 mm) yellow carbonate layer found on the bottom of one basalt piece

Core, section, interval (cm)	Depth (mbsf)	Important species	Age range (Ma)
349-U1433B-			
65R-1, 79–91	796.29	<i>Stichocorys delmontensis</i> *	<20.6
65R-1A, 117	796.66	<i>Triquetrorhabdulus carinatus</i> , <i>Triquetrorhabdulus challengerii</i> , <i>Zygrhablithus bijugatus</i>	18.28 to ~23
65R-2A, 45–50	797.12	<i>Helicosphaera carteri</i> , <i>Helicosphaera obliqua</i> , <i>Sphenolithus conicus</i> , <i>Sphenolithus dissimilis</i>	~18 to 22.03
65R-2A, 49–51	797.16	<i>Sphenolithus dissimilis</i>	
70R-1, 88	830.20	<i>Zygrhablithus bijugatus</i> , <i>Sphenolithus distentus</i> ?	26.84 to 30.0

micropaleontological, paleomagnetic, and $^{40}\text{Ar}/^{39}\text{Ar}$ dating of basalt sequences, may help to resolve this issue.

Planktonic foraminifers

We analyzed planktonic foraminifers in core catcher samples and selected split core samples from Holes U1433A and U1433B. In general, the abundance and preservation of planktonic foraminifers vary with lithology, which is dominated by turbidite deposits (see [Lithostratigraphy](#)). Planktonic foraminifers are rare or barren in clay-rich sediment and increase in abundance and are better preserved in coarser grained sediment. Samples from silt layers often contain abundant small (<150 μm) well-preserved planktonic foraminifers, whereas large, poorly preserved planktonic foraminifer specimens commonly occur in sandy and chalky intervals, indicating redeposition by turbidity currents.

In Hole U1433A, planktonic foraminifers vary from common to rare or absent, are poorly to well preserved, and decrease in abundance downhole (Table [T8](#)). The planktonic foraminifer assemblage is composed mainly of *Globorotalia menardii*, *Globorotalia tumida*, *Globigerinoides ruber*, *Globigerinoides sacculifer*, *Pulleniatina obliquiloculata*, *Neogloboquadrina dutertrei*, *Orbulina universa*, and other characteristic late Quaternary tropical Indo-Pacific species. The LAD (0.12 Ma) and FAD (0.40 Ma) of *G. ruber* (pink) occur in Samples 349-U1433A-7H-CC (66.3 mbsf) and 14H-CC (132.23 mbsf), respectively. Together with the FAD of *Globigerinella calida* (0.22 Ma) in Sample 13H-CC (122.7 mbsf), these bioevents indicate Pleistocene Subzone Pt1b (Table [T3](#)). The presence of *Globigerinoides obliquus* (≥ 1.30 Ma) and many large-sized Pleistocene species in Sample 13H-CC (122.7 mbsf), which is from within the range of *G. ruber* (pink) (0.40–0.12 Ma), is interpreted as a result of redeposition by turbidity currents. Planktonic foraminifers in Samples 15H-CC through 20H-CC (141.5–188.69 mbsf) from the lower part of Hole U1433A are very rare or absent, making age determination for this interval difficult; however, the absence of *Globorotalia tosaensis* and older species indicates that the sedimentary succession recovered in Hole U1433A represents deposition during the Middle and Late Pleistocene.

Planktonic foraminifers in Hole U1433B also vary from absent to abundant with variable preservation (Table [T9](#)). Our results indicate that the sediment sequence recovered in Hole U1433B spans the late Miocene (Zone M12) through the Pleistocene (Subzone Pt1a) (Table [T3](#); Figure [F22](#)). Samples 349-U1433B-2R-CC through 15R-CC (187.79–317.66 mbsf) are Pleistocene in age. The Pliocene/Pleistocene boundary is found between Samples 15R-CC (317.66 mbsf) and 18R-CC (345.76 mbsf), as defined by the LAD of *Globoturborotalita woodi* (2.30 Ma) and the LAD of *Globoturborotalita decoraperta* (2.75 Ma), respectively. The Pliocene comprises the interval encompassing Samples 18R-CC through 27R-CC (345.76–431.91 mbsf). Three bioevents help distinguish Pliocene Zones PL5–PL2. Because sediment from Cores 349-U1433B-3R through 5R (~197–220 mbsf) contains only a few small specimens of planktonic foraminifers redeposited by turbidity currents, the uppermost occurrence of *G. tosaensis* in Sample 6R-CC (229.07 mbsf) is not considered to represent its LAD (0.61 Ma). The LAD of *Dentoglobigerina altispira* (3.47 Ma) in Sample 22R-CC (383.07 mbsf) marks the Zone PL5/PL4 boundary, which corre-

sponds to the early/late Pliocene boundary. The Miocene/Pliocene boundary occurs between Samples 27R-CC (431.91 mbsf) and 42R-CC (580.95 mbsf), as indicated by the LAD of *Globoturborotalita nepenthes* (4.37 Ma) and the FAD of *Globorotalia margaritae* (6.08 Ma), respectively.

The upper Miocene includes Samples 42R-CC through 59R-CC (580.95–747.21 mbsf), with common occurrences of *Globigerinoides extremus*, *G. obliquus*, *Sphaeroidinellopsis seminulina*, and *Neogloboquadrina acostaensis*. Samples from lithostratigraphic Subunit IIB in Cores 43R through 56R are assigned to upper Miocene Zone M13 based on the presence of the FAD of *Globorotalia miotumida* (7.89 Ma) in Sample 51R-CC (664.3 mbsf) and the FAD of *G. extremus* (8.93 Ma) in Sample 54R-CC (697.73 mbsf). The Zone M13/M12 boundary occurs in Sample 56R-CC (710.98 mbsf) based on the FAD of *N. acostaensis* (9.83 Ma). The presence of *Globorotalia limbata* in Sample 59R-CC (710.98 mbsf) indicates an age younger than 10.64 Ma (late Miocene). Samples from Cores 60R through 65R (756.18–798.95 mbsf) from the reddish brown claystone of Unit III are mostly barren of planktonic foraminifers; however, sporadic specimens of *Globigerina praebulloides* in Sample 65R-1, 79–81 cm (796.29 mbsf), and *G. woodi* in Sample 65R-1, 110–112 cm (796.6 mbsf), indicate an early Miocene age (Kennett and Srinivasan, 1983; Bolli and Saunders, 1985).

Radiolarians

The radiolarians at Site U1433 vary from abundant and common with good preservation in the uppermost sections of Hole U1433A (Samples 349-U1433A-1H-CC through 3H-CC; 8.85–27.47 mbsf) to rare or absent at the bottom of Hole U1433A (Table [T10](#)). Hole U1433B is barren of radiolarians until Sample 349-U1433B-60R-5, 92–94 cm (753.82 mbsf). Radiolarians at the bottom of Hole U1433B are common to few in abundance, with moderate to poor preservation (Table [T11](#)). Sponge spicules and diatoms are only present occasionally.

The presence of *Buccinosphaera invaginata* in Samples 349-U1433A-1H-CC and 2H-CC (8.85 and 16.21 mbsf, respectively) indicates Zone NR1 (<0.21 Ma). Sample 3H-CC (27.47 mbsf) is estimated to be no older than Zone NR2 based on the presence of *Collosphaera tuberosa* (FAD at 0.42–0.46 Ma). For Samples 4H-CC through 20H-CC (37.19–188.69 mbsf), no marker species were found; therefore, age determination could not be made.

In Hole U1433B, *Stichocorys delmontensis* is the dominant species in all analyzed samples from below 753.82 mbsf. Two radiolarian bioevents found between 753.82 and 794.23 mbsf indicate deposition during the early to middle Miocene (~20.6 to ~14.7 Ma) (Table [T4](#); Figure [F22](#)). Radiolarian assemblages from Cores 349-U1433B-60R through 64R (lithostratigraphic Unit III) are indicative of the middle Miocene (Zones RN5–RN4). Sample 349-U1433B-60R-5, 92–94 cm (753.82 mbsf), is assigned to middle Miocene Zone RN5 based on the presence of *Carpocanopsis bramlettei*, *Liriospyris geniculosa*, and *Phormospyris stabilis scaphipes*. The LAD of *Calocycletta costata* (15 Ma) is placed between Samples 60R-5, 92–94 cm (753.82 mbsf), and 63R-3, 13–15 cm (779.22 mbsf). The Zone RN5/RN4 boundary occurs in Sample 63R-CC (785.09 mbsf), as indicated by the FAD of *Dorcadospyris alata* (15.03 Ma).

Table T8. Distribution of planktonic foraminifers, Hole U1433A. [Download table in .csv format.](#)

Table T9. Distribution of planktonic foraminifers, Hole U1433B. [Download table in .csv format.](#)

Table T10. Distribution of radiolarians, Hole U1433A. [Download table in .csv format.](#)

Table T11. Distribution of radiolarians, Hole U1433B. [Download table in .csv format.](#)

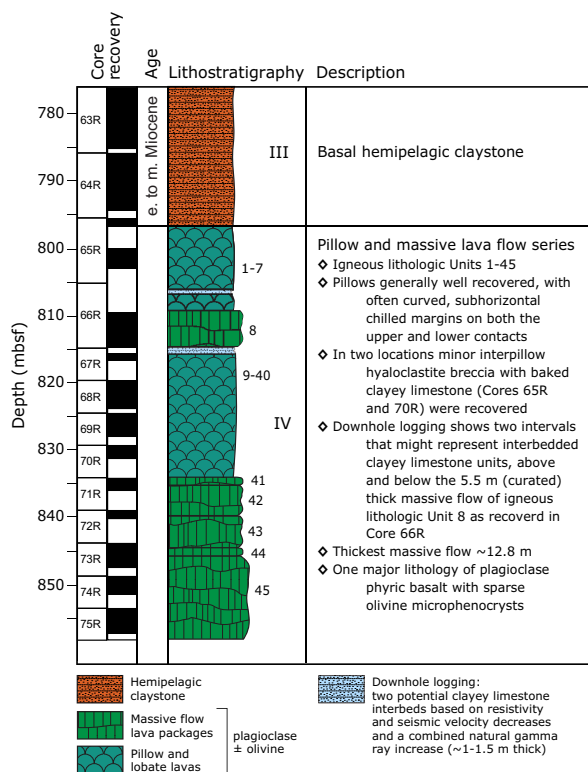
Sample 65R-1, 79–81 cm (796.29 mbsf), contains very few poorly preserved radiolarians. Although the early/middle Miocene boundary could not be determined because of the absence of diagnostic radiolarian species, the presence of *S. delmontensis* in this sample implies an age younger than 20.6 Ma (early Miocene) (Theyer et al., 1978) for the interval between Samples 64R-2, 41–45 cm, and 65R-1, 79–81 cm (787.45–796.29 mbsf).

Igneous petrology and alteration

We cored 60.81 m into igneous basement below 796.67 mbsf in Hole U1433B and recovered 29.02 m of basalt (47.7% recovery). This short basement succession is divided into 45 igneous lithologic units, which are grouped into lithostratigraphic Unit IV (Figure F23). The basement unit at Site U1433 is composed of a 37.5 m thick succession of small pillow basalt lava flows in the top followed by 23.3 m of massive basalt lava flows toward the bottom. The igneous basement is overlain by hemipelagic reddish to yellowish brown claystone (Unit III).

The igneous basement begins with a sequence of sparsely to highly plagioclase-phyric pillow basalt with a trace of olivine microphenocrysts. Most of the pillow basalts are nonvesicular to sparsely vesicular, range in grain size from crypto- to microcrystalline, and in many cases have well-preserved curved glassy chilled margins along the top and bottom unit boundaries. A few larger lobate flows are present, varying in curved thicknesses up to 1.1 m. In three intervals, interpillow hyaloclastite breccias were encountered, with remnants of baked clayey limestone in which early Miocene nannofossils are preserved (see [Biostratigraphy](#)). Downhole logging pro-

Figure F23. Lithostratigraphic summary of igneous rocks and their lithologic features with integrated downhole logging observations, Hole U1433B. Lithostratigraphy column includes lithology, igneous lithologic units (1–45), and lithostratigraphic units (III and IV).



vided further indications for 2 unrecovered ~1–1.5 m thick sediment (potentially clayey limestone) interbeds, based on combined increases in natural gamma radiation (NGR) measurements and decreases in the *P*-wave seismic velocity, electrical resistivity, and bulk density (see [Downhole measurements](#)). In between this stack of pillow basalt flows, microcrystalline to fine-grained massive flows up to 5.2 m thick were encountered that are sparsely olivine-plagioclase-phyric but have a holocrystalline groundmass with abundant plagioclase and clinopyroxene present in the interstitial spaces.

Downhole, the basement is characterized by more massive basalt lava flow units as thick as ~12.8 m. These massive flow units have similar petrologic characteristics and range from sparsely to highly plagioclase-phyric with only a trace of olivine microphenocrysts. Groundmass grain size increases to fine grained toward the interior of the thickest lava flow. All basalts have a phenocryst phase assemblage of plagioclase ± olivine, whereas the more massive lava flows have clinopyroxene in their groundmass. In conjunction with geochemical evidence, we conclude that the basement basalt at Site U1433 is typical mid-ocean-ridge basalt (MORB) (see [Geochemistry](#)).

Alteration is also typical of that of MORB and ranges from nearly absent or slightly altered to moderately altered in intensity and from gray to dark gray-green and yellow to rusty brown in color. Background alteration in the basement at Site U1433 is low, with most of it focused in halos surrounding fractures and veins. Typical secondary minerals include saponite, Fe oxide, carbonate, and celadonite, all of which represent a low-temperature alteration assemblage. Abundant basaltic glassy margins found near the quenched boundaries of pillow fragments are commonly altered to greenish palagonite, which may indicate alteration from nonoxidative fluids. Alteration veins are abundant at the top of the basement and decrease significantly downhole, indicating limited downwelling fluid flow. Vein-filling minerals include carbonate, celadonite, Fe oxide, saponite, smectite, quartz, and a blue mineral that is difficult to identify without XRD analysis, which was not available during this expedition.

Lithostratigraphic and igneous lithologic units Unit IV (796.67–857.48 mbsf)

Interval: 349-U1433B-65R-1, 117 cm, to 75R-4, 74 cm

Depth: 796.67–857.48 mbsf

Thickness: 60.81 m (29.02 m at 47.7% recovery)

Lithology: pillow and massive basalt flows

Igneous lithologic units: 1–45

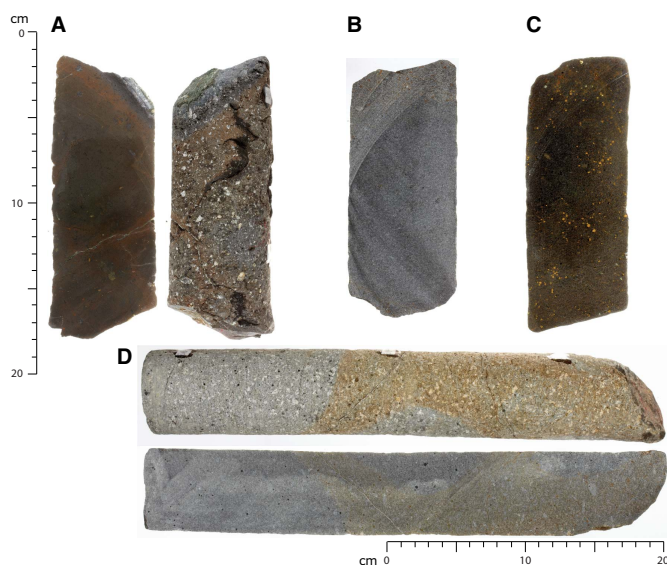
The base of the reddish to yellowish brown hemipelagic claystone (lithostratigraphic Unit III) and the first appearance of sparsely to highly olivine-plagioclase-phyric pillow basalt fragments at the top of Section 349-U1433B-65R-2 mark the upper boundary of lithostratigraphic Unit IV at 796.67 mbsf. Throughout Unit IV, most basalt cores are moderately to highly plagioclase-phyric with traces of (pseudomorph) olivine microphenocrysts and are sparsely vesicular, with only minor occurrences of amygdaloidal basalt (Figure F24). The plagioclase phenocrysts are as large as 10 mm, often occur in subhedral short prismatic habit, and vary between 1% and 15% (with an overall average of 7%) in modal abundance in both the pillow and the massive basalt flows (Figure F25). In addition, there is abundant presence of well-preserved curved glassy margins (Figures F26, F27, F28) at the top and bottom boundaries of the pillow basalt flows. Although most of the pillow basalts are aphanitic with

cryptocrystalline groundmass and contain a large proportion of mesostasis, the massive basalt flows have a high degree of groundmass crystallinity, increasing to holocrystalline in basalt varieties that are microcrystalline to fine grained (Figures F25G, F25H). Plagioclase shows a wide range of crystal habits and textures, including glomerocrysts, melt inclusions, zonation, and overgrowths (Figure F29).

Igneous lithologic Units 1–7 (0.24–1.14 m in curated thickness) are poorly recovered; therefore, flow boundaries are inferred from the occurrence of chilled margins on separate pieces, with abundant curved glassy rims preserved on the top or bottom of the pillows, typically 0.3–1.5 cm in thickness. These basement units are interpreted to represent pillow basalt flows composed of sparsely to highly phyric plagioclase basalt, with 0.5%–2% microphenocrysts of olivine, set in an aphanitic, cryptocrystalline groundmass (Figures F24A, F25A–F25D). These basalts are nonvesicular and are fresh to moderately altered, with most of the alteration present in halos along veins. Units with chilled margins almost all contain fresh glass showing gradations into devitrified cryptocrystalline groundmass (Figures F25A, F26A, F28A–F28C). Two occurrences of clayey limestone were recorded at Sections 349-U1433B-65R-1A, 117 cm, and 349-U1433B-65R-2A, 75 cm (Figure F23). In one case, the “baked” limestone is still attached to a glassy chilled margin. These intervals were interpreted to be interpillow hyaloclastite breccia (Figures F27, F28A, F28B). Nanofossils recovered from these intervals may indicate eruption of these pillow basalts during the early Miocene (see [Biostratigraphy](#)).

Igneous lithologic Unit 8 (5.2 m thick) is a sparsely olivine-plagioclase-phyric massive basalt flow with up to 2% plagioclase. It is also sparsely vesicular with up to 2% well-rounded, filled vesicles. Compared to the pillow basalt, the basalt in this unit has a holocrystalline groundmass ranging from microcrystalline to fine-grained and consisting of dense networks of long-prismatic plagioclase with clinopyroxene growing interstitially and, in many cases, subophitically with plagioclase. Alteration in this unit is very low and only occurs in thin halos surrounding a small number of existing veins.

Figure F24. Basement basalt types, Hole U1433B, Unit IV. A. Highly olivine-plagioclase phyric basalt with glassy rim (65R-2A, 0–19 cm; Unit 1). B. Amygdaloidal, sparsely olivine-plagioclase-phyric basalt (70R-2A, 16–33 cm; Unit 40). C. Fine-grained, sparsely olivine-plagioclase-phyric basalt (71R-1A, 59–71 cm; Unit 41). D. Highly plagioclase-phyric microcrystalline basalt with sparse olivine (73R-2A, 115–145 cm; Unit 45).



Igneous lithologic Units 9–40 (0.08–1.05 m in curated thickness) comprise a second stack of pillow lava flows. The flows are mostly moderately olivine-plagioclase-phyric basalt, but some are highly phyric with plagioclase abundances up to 15% (Figures F24B, F25E, F25F). As with the pillow lavas at the top of the basement in Hole U1433B, many pillows have well-preserved glassy chilled margins (Figures F26B, F28C). At Section 70R-1W, 88 cm, another nanofossil-bearing limestone was found in contact with a chilled margin (see [Biostratigraphy](#)). Most pillow basalts are sparsely vesicular with 0.5%–2% vesicles, typically completely filled with secondary minerals, but Units 12 and 40 are strongly amygdaloidal with 7% and 12% vesicles, respectively.

The lower half of the basement unit consists of massive basalt flows of igneous lithologic Units 41–45. The basalts are nonvesicular and generally slightly to moderately altered with only a trace of olivine microphenocrysts that range from fresh to completely replaced (Figures F25G, F25H). The few equant euhedral olivine phenocrysts observed are as large as 3.6 mm, but commonly they are

Figure F25. Basalt, Hole U1433B, Unit IV. A, B. Moderately olivine-plagioclase-phyric pillow flow with glassy margins and pseudomorphs of equant olivine and fresh plagioclase phenocrysts set in hypocrystalline groundmass (65R-3, 93–96 cm; TS71); (A) PPL, (B) XPL. C, D. Moderately olivine-plagioclase-phyric basalt containing olivine and plagioclase phenocrysts in cryptocrystalline groundmass with plagioclase microlites (65R-3, 104–107 cm; TS72); (C) PPL, (D) XPL. E, F. Moderately olivine-plagioclase-phyric fine-grained basalt with large euhedral to subhedral olivine and plagioclase phenocrysts in microcrystalline intersertal groundmass of plagioclase and clinopyroxene (70R-1, 55–58 cm; TS90); (E) PPL, (F) XPL. G, H. Moderately plagioclase-phyric basalt with a trace of olivine microphenocrysts in medium-grained groundmass showing variolitic growth texture of plagioclase around clinopyroxene (72R-1, 112–115 cm; TS93); (G) PPL, (H) XPL.

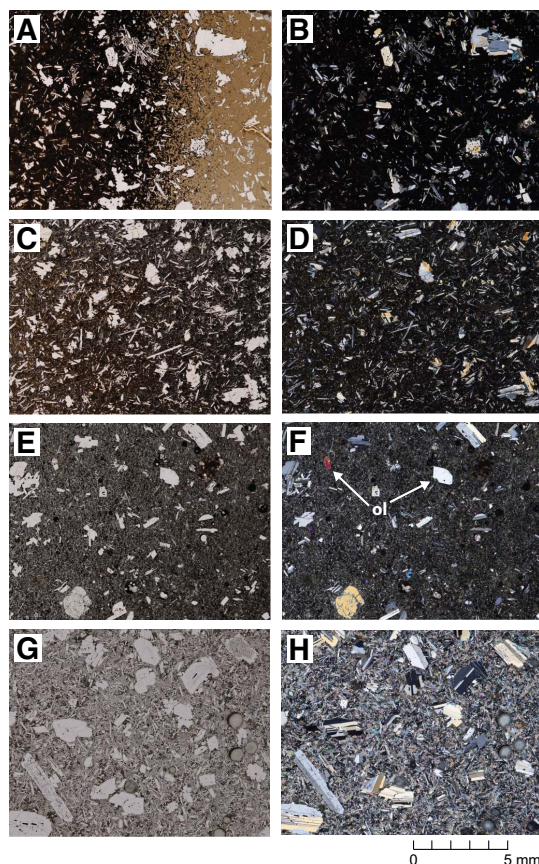


Figure F26. Pillow lava chilled margins, Hole U1433B, Unit IV. A. 2 cm wide glassy margin (65R-3, 93–109 cm). B. Top and side views of chert sandwiched between 2 chilled margins (68R-3, 133–135 cm).

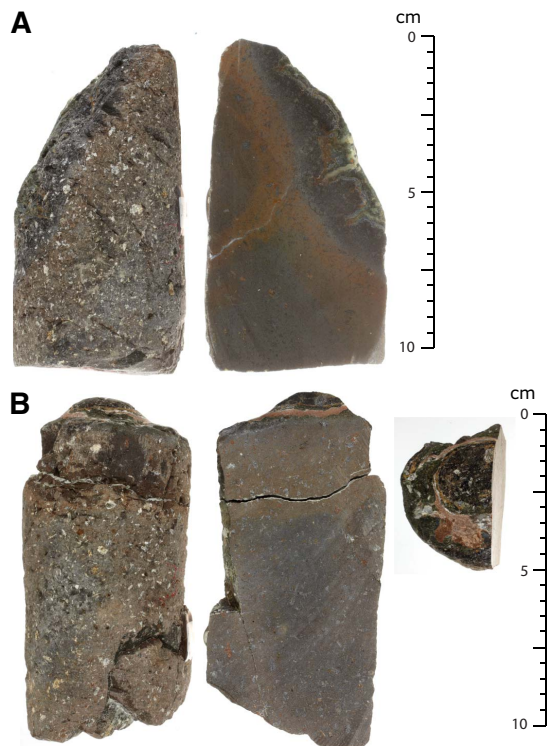
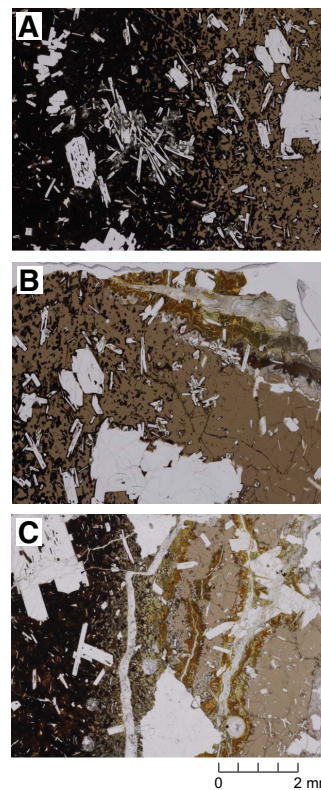


Figure F27. Interpillow hyaloclastite and baked clayey limestone containing inclusions of green claystone and chert fragments, Hole U1433B, Unit IV (65R-2, 40–55 cm).



1 mm or smaller, approaching the typical size of groundmass plagioclase and clinopyroxene minerals that have grown in crystal networks with long-prismatic habits and are of similar size. Groundmass grain size varies from microcrystalline to fine grained

Figure F28. Chilled margins in thin section, Hole U1433B, Unit IV (PPL). A. Fresh glass grading into palagonitized glass toward pillow interior (65R-3, 93–96 cm; TS71). B. Same as A showing contact with hyaloclastite containing a limestone fragment. C. Several layers of glassy margins showing palagonitized boundaries (70R-1, 88–90 cm; TS91).



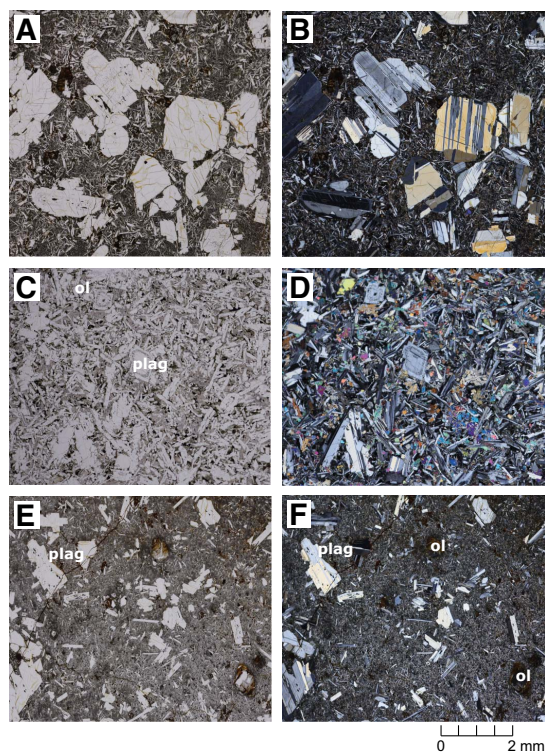
in the interiors (Figure F24D) of these massive flows, with the coarsest observed grain sizes in Core 349-U1433B-73R. Drilling at Site U1433 terminated at 857.48 mbsf after coring 12.8 m into this lowermost massive lava flow.

Interpretation of the igneous succession

The primary goal of Expedition 349 was to recover basement to help understand the opening history of the South China Sea. Site U1433 was positioned close to what is believed to be a relict spreading center (Figure F1) to obtain an age estimate for the cessation of seafloor spreading in the Southwest Subbasin. We recovered 29.02 m of basalt after penetrating 60.81 m into igneous basement at Site U1433 and identified 45 igneous lithologic units. The basement unit cored contains 2 sequences of pillow basalts alternating with 2 series of massive basalt lava flows. All basement lithologies have phase assemblages of predominantly plagioclase and sparse olivine (typically as microphenocrysts), with the coarser holocrystalline massive basalt flows also having clinopyroxene present in the groundmass. All of these phase assemblages are consistent with MORB from a petrological point of view.

In three intervals, we cored interpillow hyaloclastite breccias with remnants of clayey limestone in which early Miocene microfossils are present (see Biostratigraphy). This provides evidence for a possible prolonged eruption age from between ~19 and 22 Ma for the upper pillow lavas to >23 Ma for the lower pillow lava series. Shore-based radiometric dating of the basement samples is required to further constrain the eruption history of the igneous basement at Site U1433. Downhole logging measurements provide

Figure F29. Plagioclase (plag) textures and olivine (ol) phenocrysts, Hole U1433B, Unit IV. A, B. Overgrowth zoning and fractured and sieved texture in plagioclase with infill of melt along cleavage and cracks (74R-2, 6–8 cm; TS99); (A) PPL, (B) XPL. C, D. Melt inclusions along overgrowth boundaries in plagioclase and partially replaced euhedral olivine (66R-2, 104–107 cm; TS77); (C) PPL, (D) XPL. E, F. Euhedral to subhedral pseudomorphs of olivine (66R-4, 128–132 cm; TS78); (E) PPL, (F) XPL.



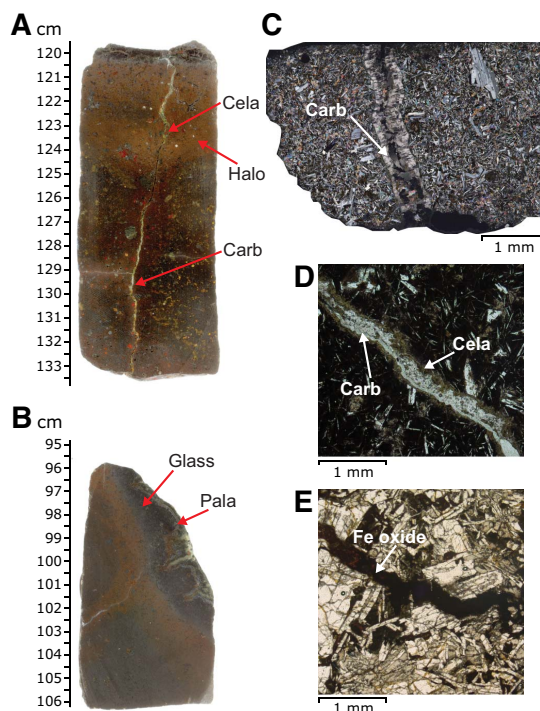
evidence for 2 potentially clayey limestone interbeds ~1 to 1.5 m thick that were not recovered in Cores 349-U1433B-66R and 67R (Figure F23). The combined increase in NGR and decreases in *P*-wave seismic velocity, electrical resistivity, and bulk density (see **Downhole measurements**) are indicative of lithologies that are not basaltic but rather a clay-rich, less-resistive sedimentary layer that is compatible with downhole FMS images. If present, these 2 sedimentary interbeds may indicate some hiatus between volcanic eruptions at Site U1433, just before and shortly after the emplacement of the massive lava flow of igneous lithologic Unit 8 (Figure F23).

Alteration

Alteration intensity of the igneous basement at Site U1433 is significantly lower than at Site U1431. In addition, compared to other Integrated Ocean Drilling Program ocean crust basement sites of similar age, such as Hole U1368F (Expedition 329 Scientists, 2011), the basalts at Site U1433 seem relatively unaltered. Alteration intensity varies from slight to complete, with the majority of the recovered Site U1433 basement basalt being unaltered to slightly altered only. The highest extent of alteration occurs in the halos flanking the veins (Figures F24D, F30A). According to our macroscopic shipboard description, background alteration accounts for ~71% of the recovered cores at Site U1433, whereas the highly altered halos and veins account for ~28% and ~1%, respectively.

Alteration veins and associated halos are abundant in the top of the basement cores and decrease downhole (Figure F31), indicating

Figure F30. Types of alteration halos, basalt glass alteration, and alteration veins, Hole U1433B. Images in A and B are of a wet surface with fill-in lightening to enhance alteration features. A. Alteration halo flanking a composite vein filled with carbonate (Carb) and celadonite (Cela) (69R-1A, 120–134 cm). B. Greenish palagonite (Pala) from altered basalt glass (65R-3A, 93–109 cm). C. Carbonate vein (~3 mm thick) across the fine-grained basalt groundmass (66R-1, 63–66 cm; TS76; XPL). D. Composite vein filled with celadonite and carbonate (69R-1, 111–114 cm; TS 88; XPL). E. Vein filled with Fe oxide (74R-1, 83–86 cm; TS97; PPL).



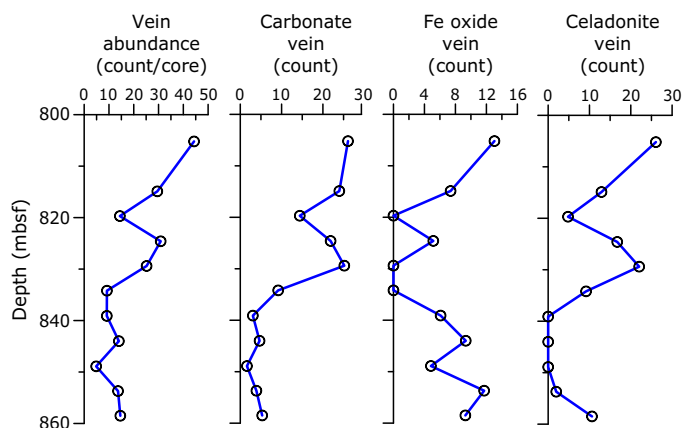
more limited interaction with seawater with depth. Background alteration colors in the basalt cores range from gray to gray-green and yellow-brown. Alteration halos vary in color from green to red-brown. In intervals away from veins and halos, plagioclase phenocrysts, olivine microphenocrysts, and the basaltic groundmass are all remarkably unaltered, and large proportions of well-preserved glassy rinds remain in the chilled margins. Based on macroscopic and thin section observations, the overall alteration style is characterized by the following categories:

- Green to red-brown alteration halos, typically associated with veins;
- Partial to complete vesicle fillings (Figure F32) by secondary minerals, typically celadonite, carbonate, Fe oxide, smectite, and saponite (in decreasing order);
- Minor vein fillings by celadonite, carbonate, Fe oxide, smectite, quartz, and some other (unidentifiable) secondary minerals; and
- Background alteration occurring in slightly altered basalt, typically represented by alteration of olivine, plagioclase, clinopyroxene, and mesostasis in the groundmass.

Alteration phases

Alteration in the Site U1433 basement is characterized by halo alteration caused by fluid/seawater flow through fractures and veins (Figures F24D, F30A). Oxidative and nonoxidative alteration appear to both exist in the basalt cores. Oxidative alteration is indi-

Figure F31. Downhole abundance (number of veins per 9.7 m length of core) variation of all veins, as well as individual plots for veins filled with carbonate, Fe oxide, and celadonite. The total abundance of veins and the abundance of specific veins were calculated and corrected for percent recovery in each core.



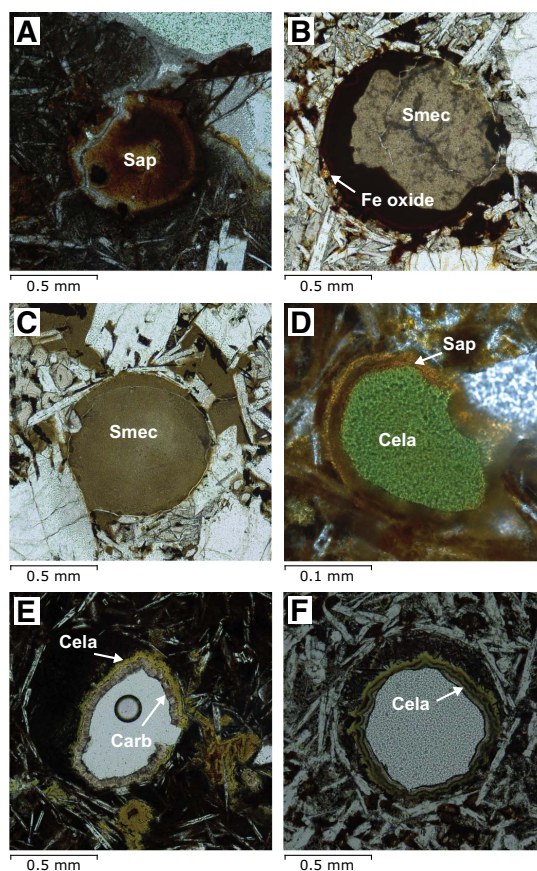
cated by the occurrence of abundant Fe oxide in veins and as mineral fillings in vesicles. Nonoxidative alteration is marked by the occurrence of greenish palagonite in volcanic glass rinds and smectite. The major alteration minerals include celadonite, saponite, carbonate, palagonite, and Fe oxide.

Celadonite is distinctively bright green and is observed throughout the basement cores in Hole U1433B. It is the most abundant secondary mineral in vein fillings, vein-surrounding halos, and vesicles. Saponite is also a widespread alteration mineral at Site U1433 and occurs as one of the major vesicle-filling minerals. It has a color that ranges from yellow to light brown. Carbonate appears throughout the recovered basement cores and in vein fillings (Figures F30A, F30C, F30D). In some places, it also replaces the groundmass mesostasis. Palagonite is present as a green alteration product of basaltic glass and typically is observed in the chilled margins of pillow basalt and thin sheet flows (Figure F30B). Fe oxide mainly exists as a vein-filling mineral (Figure F30E), but it also replaces primary minerals such as olivine. Colors of Fe oxide vary from yellow-brown to dark brown. Other alteration phases, such as quartz (in veins in Section 349-U1433B-71R-1) and unidentified light blue and red minerals, are also observed, particularly as minor vein-filling minerals.

Alteration of primary minerals

Olivine microphenocrysts are usually completely altered to secondary minerals in halos and highly altered basalt, where they can only be recognized by their pseudomorphs. They are mostly fresh (1%–10% alteration) in most of the unaltered and slightly altered basalt cores; entirely fresh olivine crystals are rare in Hole U1433B. Similar to Site U1431, replacement of olivine by various secondary mineral phases (e.g., saponite, Fe oxide, and celadonite) ranges from 1% to 100%. Clinopyroxene is only observed in the interstitial spaces in groundmass and is often replaced by saponite, smectite, and Fe oxide. Plagioclase accounts for the majority of the phenocrysts and groundmass minerals but is the least altered mineral. Unaltered plagioclase can be found even in the most strongly altered basalt cores, and its alteration intensities range from 0% to 20% only. Plagioclase

Figure F32. Vesicle fillings, Hole U1433B (PPL). A. Saponite (Sap) (66R-4, 128–132 cm; TS78). B. Fe oxide and smectite (Smec) (67R-1, 59–62 cm; TS81). C. Smectite (67R-1, 98–100 cm; TS82). D. Saponite and celadonite (Cela) (69R-1, 34–38 cm; TS87). E. Celadonite and carbonate (Carb) (69R-1, 111–114 cm; TS88). F. Celadonite (73R-1, 11–14 cm; TS94).



is replaced by clay minerals, such as saponite, smectite, and Fe oxide in these highly altered intervals.

Background alteration

The background alteration at Site U1433 has low intensity overall. The strongest background alteration occurs in the upper part of the basement section and in the upper (Section 349-U1433B-68R-1) and lower part of the massive flow of igneous lithologic Unit 8. The background alteration in these intervals is characterized by the formation of Fe oxide, saponite, and celadonite. Even in the least altered basalt, olivine is mostly altered.

Veins and alteration halos

Based on macroscopic observation of archive sections, we identified 106 veins in the 29.02 m of recovered basement basalt, with an average vein abundance of 3.7 per meter, which is higher than that at Site U1431 (2.8 veins per meter). Vein thickness varies from <0.2 to 2.5 mm, with an average thickness of 0.96 mm. Veins observed in the basement at Site U1433 exhibit curved, planar, irregular, and (complex) anastomosing shapes, and they are mostly isolated, with a few branched veins or vein networks. Vein fillings have colors varying from white to dirty white, light green to green, and in some

cases they are pink or light blue. Fillings consist of celadonite, saponite, Fe oxide, carbonate, quartz, and other secondary minerals (Figures F30C, F30D). Veins range from slightly to completely filled. Most have 1 mineral filling, but some have more than 1 mineral filling and are banded. Veins filled with carbonate are most abundant (63%), followed by veins filled with celadonite (55%), Fe oxide (31%), and quartz (3%). The distribution of vein-filling minerals, from the vein walls inward, indicates that their formation sequence progressed from Fe oxide to saponite to smectite to celadonite to carbonate. Quartz occurs only near the highly altered basaltic glass remnants. Most of the veins (85%) observed at Site U1433 have halos that vary in width from <0.1 to 3 cm.

Vesicle fillings

Vesicles make up (on average) only 1% of the recovered basement basalt in Hole U1433B, with individual core sections having vesicle abundances up to 12%. According to thin section observations, vesicle fillings range from none to 100% and include saponite, Fe oxide, carbonate, celadonite, and smectite. The general filling order is Fe oxide or saponite, smectite, celadonite, and carbonate (Figure F32).

Basalt glass alteration

Basaltic glass was recovered from most of the lobate flow and pillow lava flow boundaries. These glasses are partly altered to greenish palagonite (Figure F30B), but overall they are well preserved.

Interpretation of alteration

Evidence for both oxidative and nonoxidative alteration exists at Site U1433, which is typical of previous sites with a thick (clay-rich) sediment cover, such as Ocean Drilling Program (ODP) Holes 801C and 504B (Alt et al., 1992). The abundant basaltic glass altered to green palagonite indicates that alteration occurred in nonoxidative conditions, whereas the secondary mineral assemblage of Fe oxide and saponite suggests low-temperature and oxidative alteration. Alteration at Site U1433 is controlled by the formation of vein halos, where the background alteration is less intense compared to Site U1431 where it occurs pervasively throughout the cores. In fact, most of the basaltic cores at Site U1433 are quite fresh or only slightly altered. The strongest alteration occurs in halos flanking veins, which mostly are concentrated in the top part of the basement section.

The total abundance of veins at Site U1433 and the abundance of each specific vein type, such as Fe oxide- or celadonite-dominated veins, show downhole variations. The number of total veins, carbonate veins, and celadonite veins appears to be highest toward the top of the basement and decreases with depth (Figure F31). Such a vein distribution could be the result of a limited downwelling fluid flow and/or presence of fewer fractures with increasing depth. This vein distribution is consistent with the downhole decrease in overall alteration extent based on macroscopic observations.

Structural geology

Site U1433 is located in a seafloor depression bordered by 2 abyssal highs and is ~50 km southeast of the relict spreading ridge (Figure F1). Seismic reflectors show quite continuous sedimentation around the site with no obvious faulting activity at shallow depth (Figure F3). We cored ~60 m of basalt and successfully recov-

ered ~29 m of basement cores. The basalt sequence consists of 9.7 m of thick pillow basalts, ~5 m of thick massive flows, ~20 m of thick pillow basalts, and ~23 m of thick massive flow at the bottom (see **Igneous petrology and alteration**). Pieces of mudstone and limestone were also present above and below the 5 m thick massive flow.

Shape and connectivity of fractures and veins

We observed >300 fractures and veins at this site and measured roughly 240 of them. Many of the structural features are either irregular or in small branches and thus could not be measured easily. The veins generally reflect later stages of cracking, fluid circulation, and fluid-rock reaction, whereas many fractures are reactivated along existing veins during drilling or by local stress perturbation. Most of the fractures or veins observed have no obvious lateral offset or striations on the fractured surface. These structures can be used as an indicator of the degree of rock fragmentation.

Veins are filled with different minerals, including dark green celadonite, white smectite, white carbonate, and brownish Fe oxide. In general, the veins (including reactivated fractures along existing veins) can be categorized into six types of distinctive shapes:

1. Single straight or curved veins (Figure F33),
2. Irregular sinuous veins (Figure F34),
3. Triple-junction veins (Figure F35),
4. Branched veins (Figure F36),
5. Crosscutting veins (Figure F37), and
6. Radiate veins (Figure F38).

Curved, crosscutting, irregular sinuous, radiate, and triple-junction veins are usually distributed in pillow basalt units, whereas single straight and branched veins are usually found in the massive flow units. In many cases, curved veins appear subparallel to the chilled margins of pillow basalt units, whereas radiate veins point away from the flow center toward the chilled margins. Triple-

Figure F33. Single curved veins subparallel to the chilled margin in pillow basalt, Hole U1433B (68R-3A, 132–137 cm). A. Original photo. B. Interpretation.

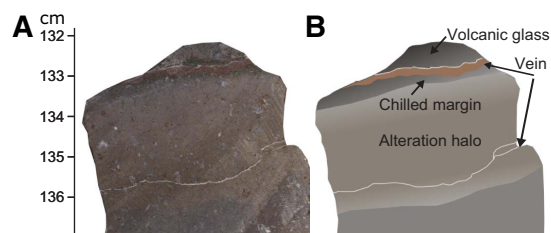


Figure F34. Irregular sinuous veins in pillow basalt, Hole U1433B (69R-3A, 78–89 cm). A. Original photo. B. Interpretation.

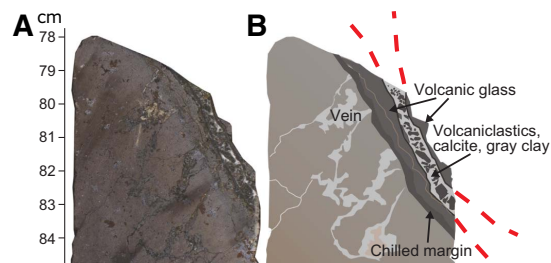


Figure F35. Triple-junction veins, Hole U1433B (69R-3A, 54–66 cm). A. Original photo. B. Interpretation.

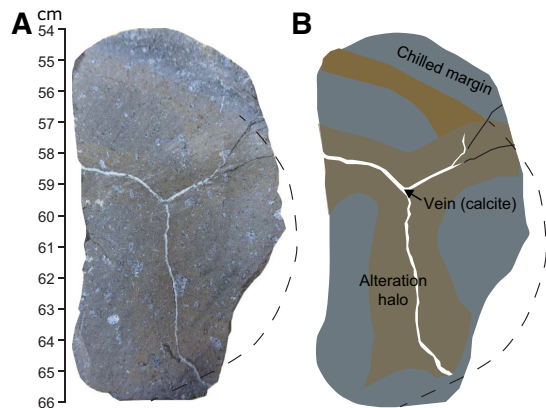


Figure F36. Branched veins, Hole U1433B (68R-3A, 7–26 cm). A. Original photo. B. Interpretation.

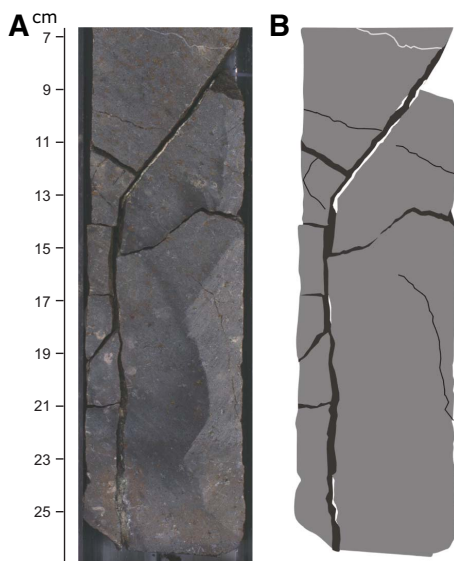
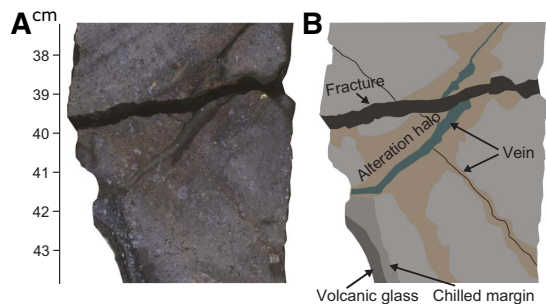
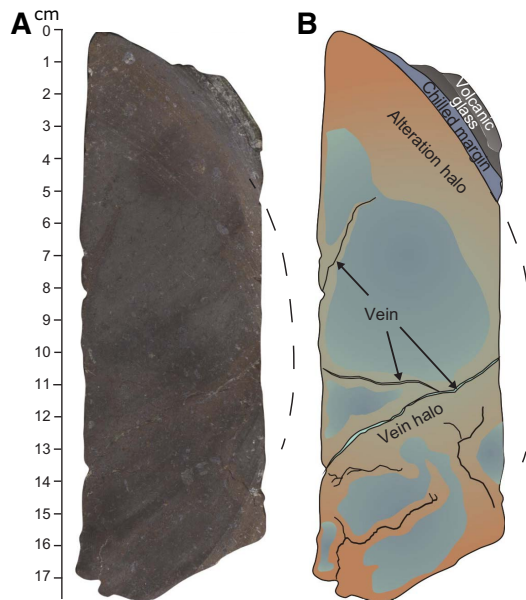


Figure F37. Cross-cutting veins, Hole U1433B (65R-2A, 37–44 cm). A. Original photo. B. Interpretation.



junction veins appear as a part of the radiate structure with three arms pointing to different directions toward the chilled margin. Alteration along the fractures or veins often generates 1–2 cm wide yellow to brown vein halos. These kinds of veins are either parallel or perpendicular to the chilled margin and are thought to form

Figure F38. Radiate veins developed in pillow basalt, Hole U1433B (65R-2A, 0–17 cm). A. Original photo. B. Interpretation.



during cooling of the pillow lava. Single straight or branched veins are sparse and usually observed in massive flow basalts with random orientations.

Frequency of fractures and veins

In order to evaluate the rock fragmentation, the frequency of fractures and veins was calculated (Figure F39). First, the total number of fractures and veins in each section was counted. Frequency was obtained by dividing the total number of fractures and veins by the length of the section. For pillow basalt units, the calculated frequency may underestimate the degree of fragmentation because the pillows were broken into small pieces that were not counted; however, the results remain informative.

The average frequency of fractures and veins in the basalt is ~10 per meter, which is about 57% of the average frequency of fractures and veins observed at the basalt units of Site U1431. The frequency of fractures and veins changes in different basalt segments. High frequencies occur in the pillow basalt units, whereas massive flow basalts have lower frequencies. During the magma cooling process, pillow basalts generally break much more easily along well-developed fractures and veins. Massive flow basalts are much thicker or larger, so most of the fractures or veins occur on the margins with their occurrence decreasing toward the center of the basalt flow unit.

Orientation statistics

In order to evaluate the causes of the fractures and veins, we created orientation rose diagrams (Figure F40). Usually, fractures align in particular dipping directions if they were caused by a relatively uniform regional stress field. The rose diagram for the total population of fractures and veins shows a very scattered dipping distribution. We hypothesize that the fractures and veins resulted mainly from cooling. The regional stress field might have a weak effect on fracture or vein formation, but this effect is difficult to evaluate because of the scattered orientations.

Figure F39. Frequency of fractures and veins in basalt, Site U1433. Lithostratigraphy column includes lithology, igneous lithologic units (1–45) and lithostratigraphic unit (IV).

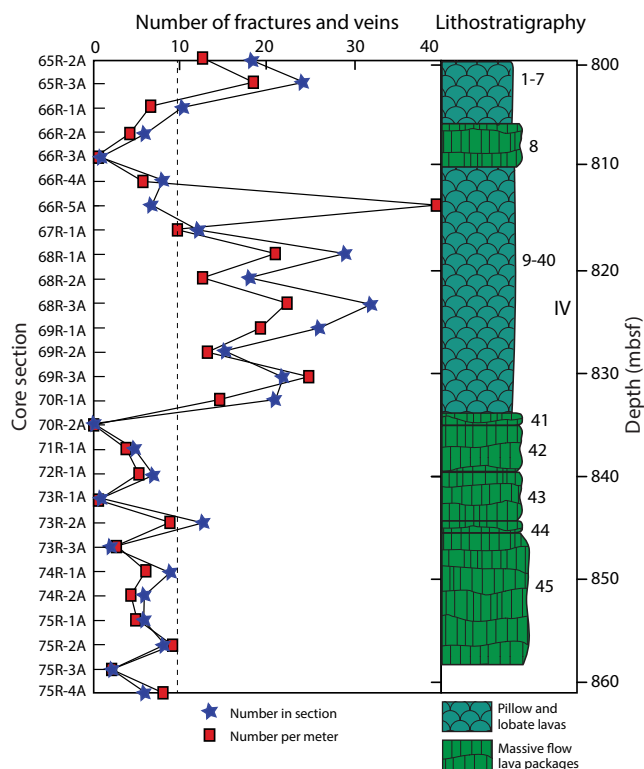
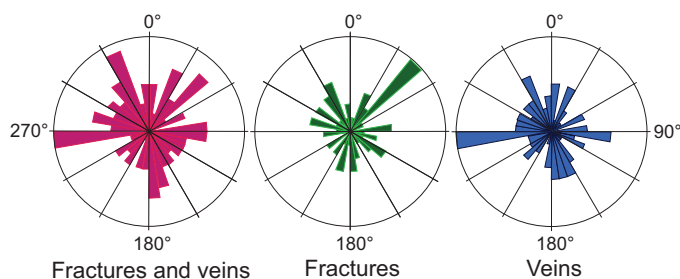


Figure F40. Rose diagrams showing dipping angles of total fractures and veins, fractures, and veins in basalt units, Site U1433.



Geochemistry

Interstitial water chemistry

We collected 25 whole-round samples (5 cm long) for interstitial water measurements between 0 and 186.8 mbsf in Hole U1433A at a frequency of 2 samples per core. In Hole U1433B, which is ~20 m away from Hole U1433A, 39 interstitial water samples were taken from 196 to 604.5 mbsf at a frequency of one sample per core. Interstitial water chemistry data are given in Tables T12 and T13 and shown in Figures F41, F42, F43, F44, and F45.

Chloride, bromide, sodium, and potassium

Downhole profiles of chloride, bromide, sodium, and potassium at Site U1433 are shown in Figure F41. Chloride, sodium, and bromide show similar profiles with depth. Chloride and sodium concentrations are relatively constant downhole to ~200 mbsf, ranging

Table T12. Interstitial water major element concentrations, salinity, pH, alkalinity, SO₄, NH₄, PO₄, Cl, Br, Ca, Mg, Na, and K, Holes U1433A and U1433B. [Download table in .csv format.](#)

Table T13. Interstitial water minor element concentrations, B, Ba, Fe, Li, Mn, Si, and Sr, Holes U1433A and U1433B. [Download table in .csv format.](#)

from 543 to 560 mM and from 468 to 485 mM, respectively. Bromide concentrations increase from 0.84 mM close to the seafloor to 0.94 mM at ~200 mbsf; however, chloride, bromide, and sodium vary significantly between 217 and 284 mbsf, which corresponds to the transition from the clay of lithostratigraphic Unit I to interbedded clay and carbonate turbidite deposits in Subunit IIA (see **Lithostratigraphy**). Shore-based oxygen and hydrogen isotopic analysis will delineate possible causes for interstitial water variations in this interval. Chloride and sodium concentrations from ~300 to 550 mbsf are similar to those in the uppermost 200 m of the site, whereas bromide concentrations are somewhat more variable over this interval but average ~0.95 mM. Concentrations of chloride, bromide, and sodium vary widely at the top of lithostratigraphic Subunit IIB (550–605 mbsf), which is characterized by thicker carbonate turbidite deposits (see **Lithostratigraphy**). Over this interval, chloride concentrations range from 550 mM (similar to seawater) to a hypersaline value of 801 mM, with other peaks of ~640 mM. Throughout the depth profile, most bromide concentrations are higher than that of modern seawater (0.87 mM), most likely caused by organic matter diagenesis in the sediment, as indicated by sulfate reduction and high methane concentrations (Figures F41, F42, F46).

Potassium concentrations increase from 10.5 mM (similar to modern seawater) close to the seafloor to 11.2 mM at 12 mbsf. Below 12 mbsf, K⁺ decreases with depth throughout the hole, with a minimum value of 3.4 mM at 605 mbsf. Concentrations higher than the modern seawater value occur in the uppermost 26 m of sediment. This phenomenon is also observed at Sites U1431 and U1432 and is attributed to ion exchange with clay minerals (see **Geochemistry** in the Site U1431 chapter and **Geochemistry** in the Site U1432 chapter [Li et al., 2015c, 2015d]).

Alkalinity, sulfate, ammonium, and phosphate

Alkalinity, sulfate, ammonium, and phosphate profiles are shown in Figure F42. Alkalinity increases from 9.7 mM close to the seafloor to a maximum of 25.8 mM at ~30 mbsf, where sulfate is completely consumed. Below 40 mbsf, alkalinity decreases with depth to 1.4 mM at 549 mbsf. The increase in alkalinity promotes carbonate precipitation in the uppermost 40 m, as suggested by the calcium and magnesium concentrations (Figure F43). The low alkalinity below 200 mbsf is probably caused by low amounts of organic matter diagenesis due to the relatively low sedimentation rates of 5–9 cm/ky estimated for this interval (Figure F22; see also **Biostratigraphy**).

Sulfate concentrations decrease with depth and sulfate is almost completely depleted at ~30 mbsf (Figure F42). This is consistent with the increase of methane concentration to 1100 ppmv at 30 mbsf, reaching a maximum of 93 × 10³ ppmv at ~200 mbsf (Figure F46). Based on sulfate and methane concentrations, the sulfate–methane transition zone (SMTZ) occurs at ~30 mbsf.

Ammonium concentrations increase from 0.6 mM near the seafloor to a maximum 3.6 mM at ~100 mbsf, 70 m below the SMTZ. This suggests organic matter fermentation producing ammonium continues below the sulfate reduction zone. From 200 to 570 mbsf,

Figure F41. Interstitial water chloride, bromide, sodium, and potassium, Holes U1433A (red) and U1433B (black).

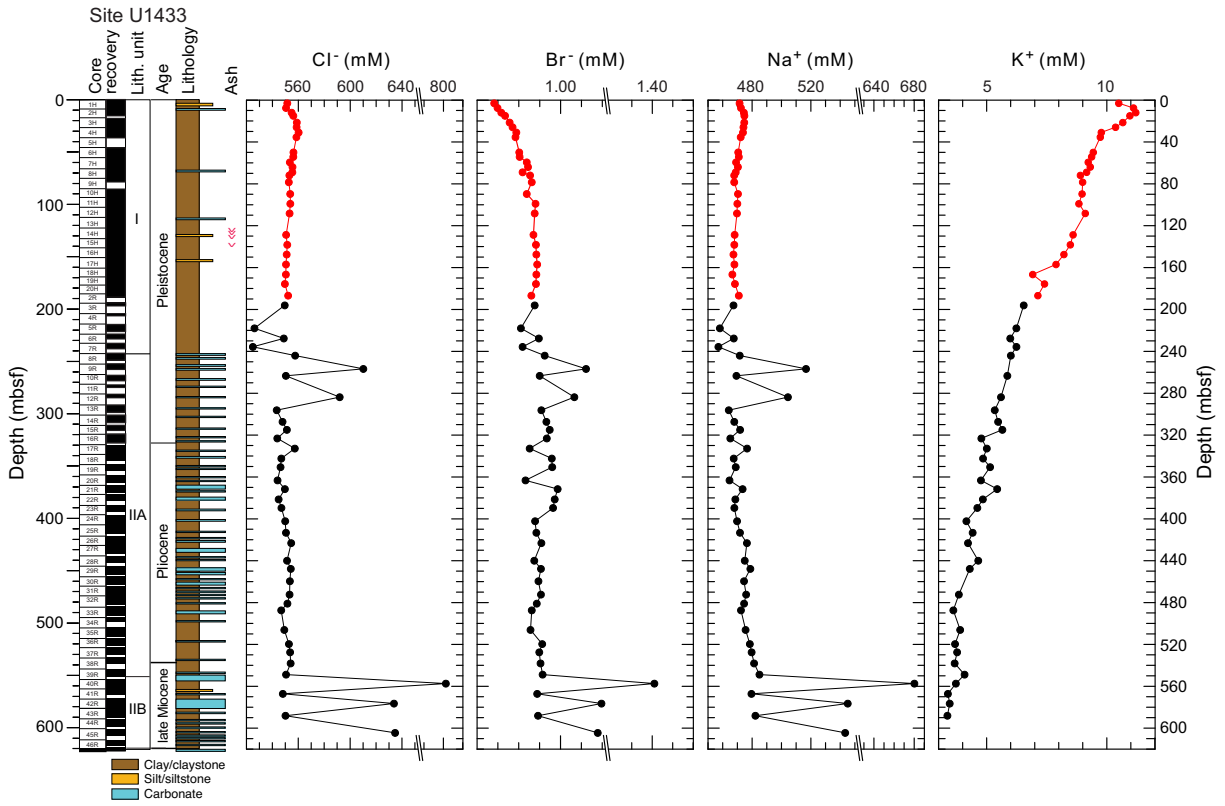


Figure F42. Interstitial water sulfate, alkalinity, ammonium, and phosphate, Holes U1433A (red) and U1433B (black).

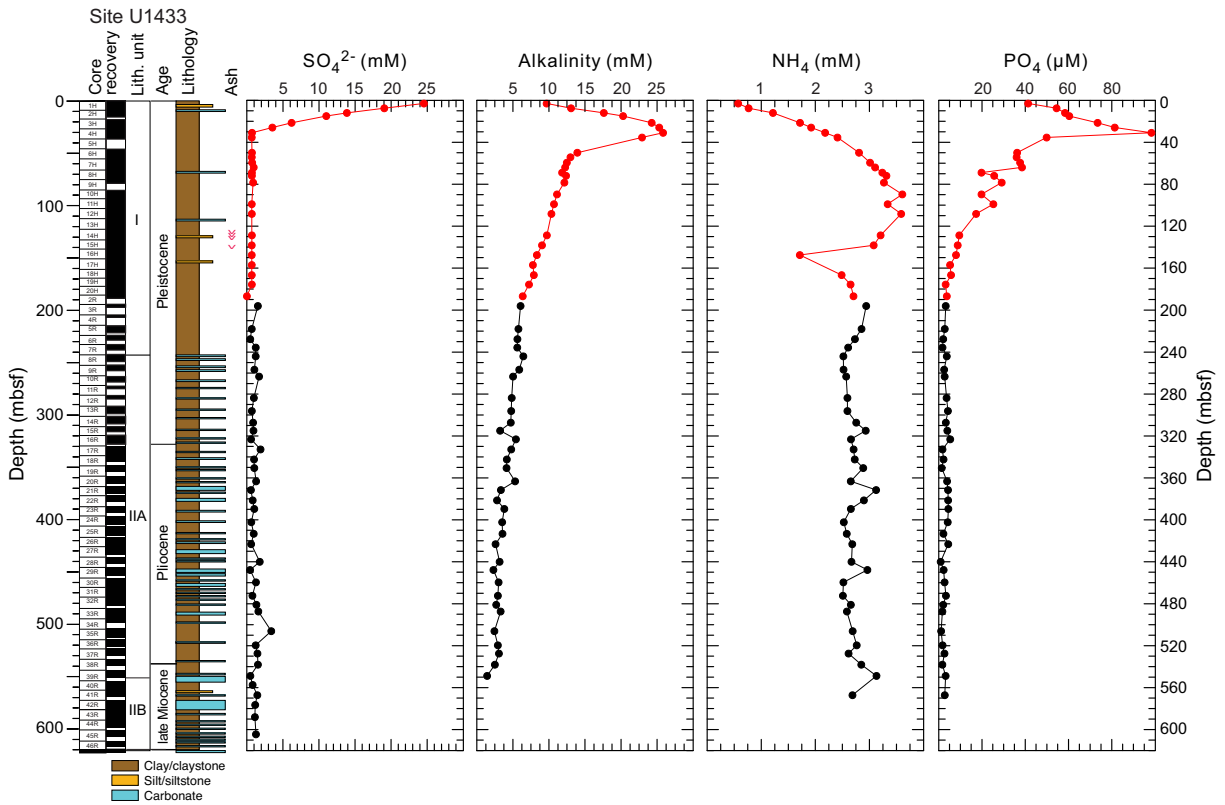


Figure F43. Interstitial water calcium, magnesium, and strontium, Holes U1433A (red) and U1433B (black).

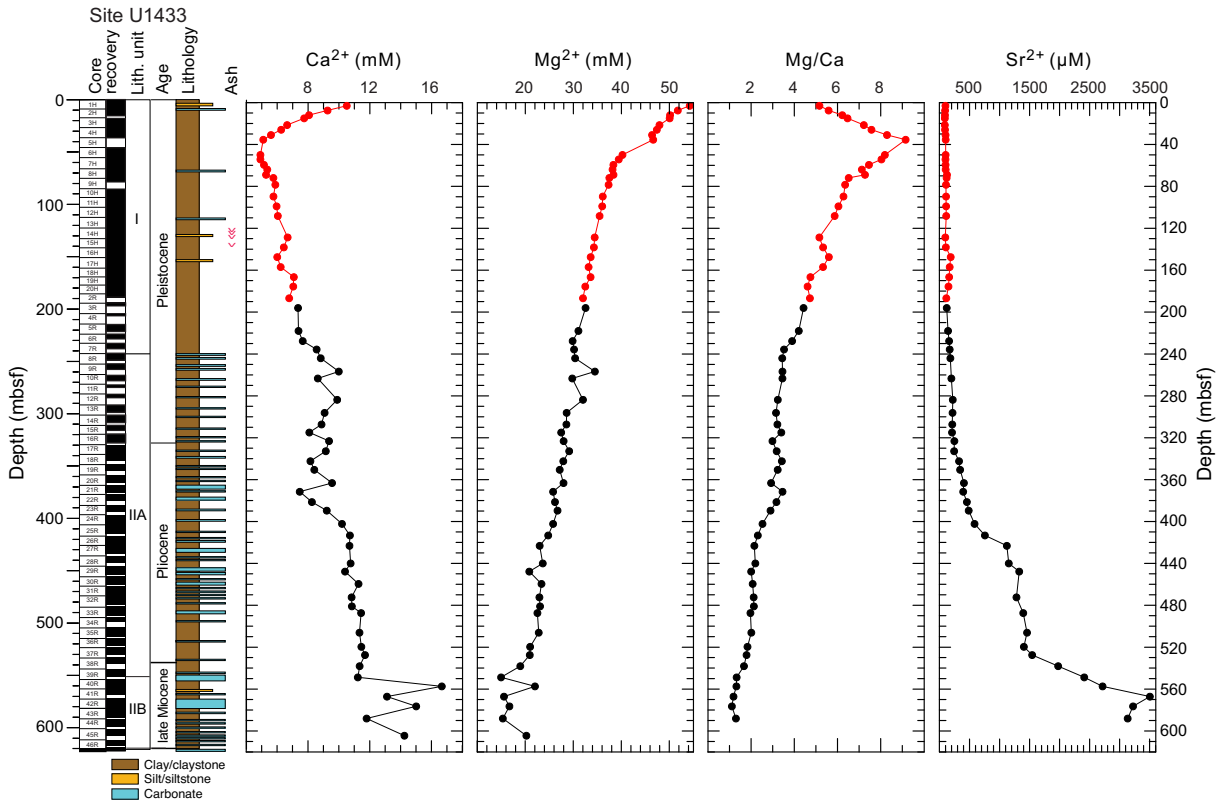


Figure F44. Interstitial water barium, boron, lithium, and silica, Holes U1433A (red) and U1433B (black).

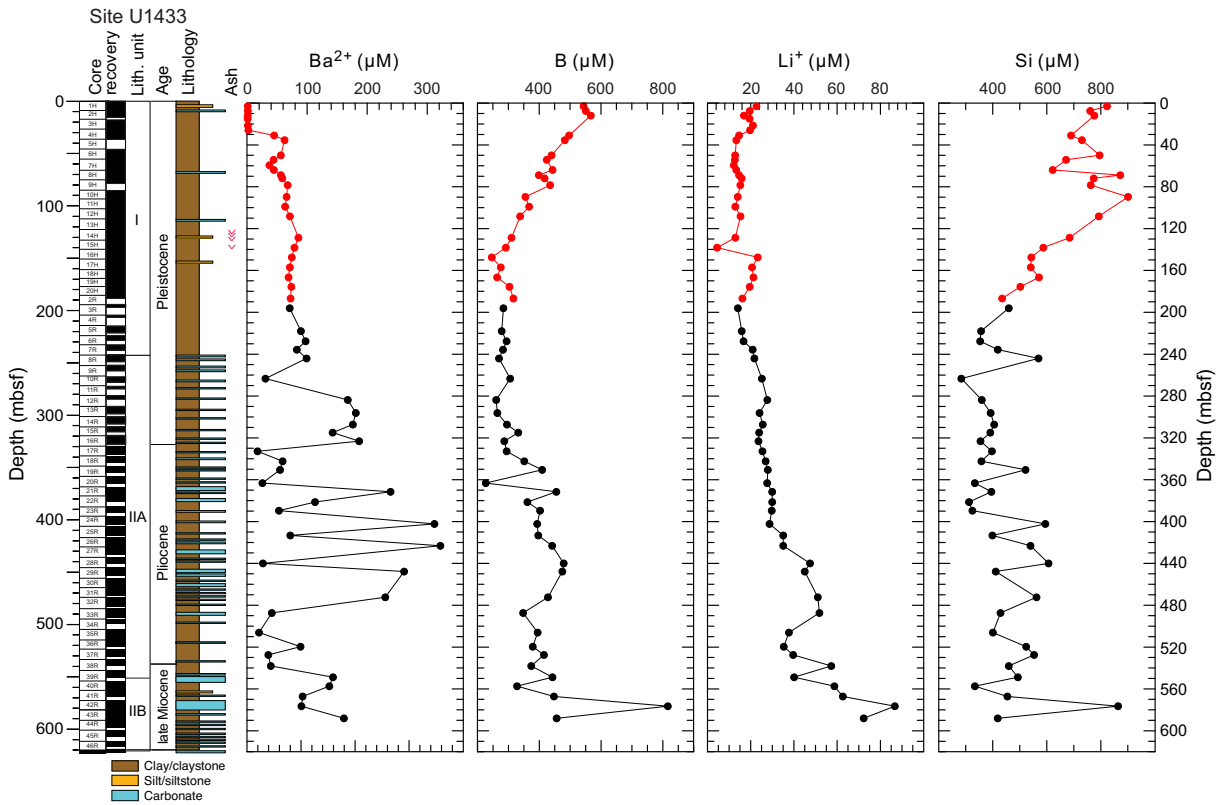


Figure F45. Interstitial water iron and manganese, Holes U1433A (red) and U1433B (black).

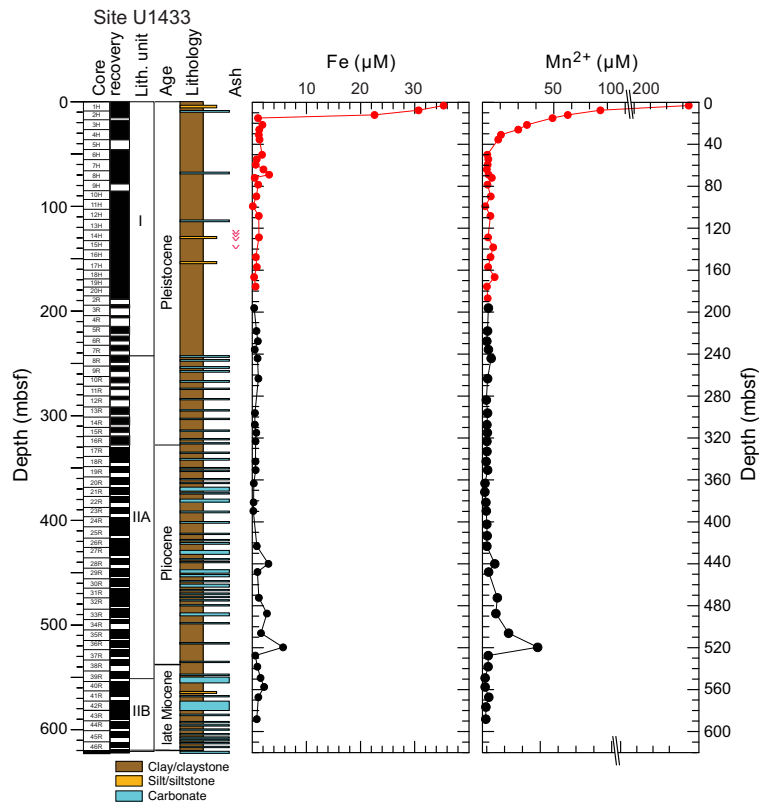
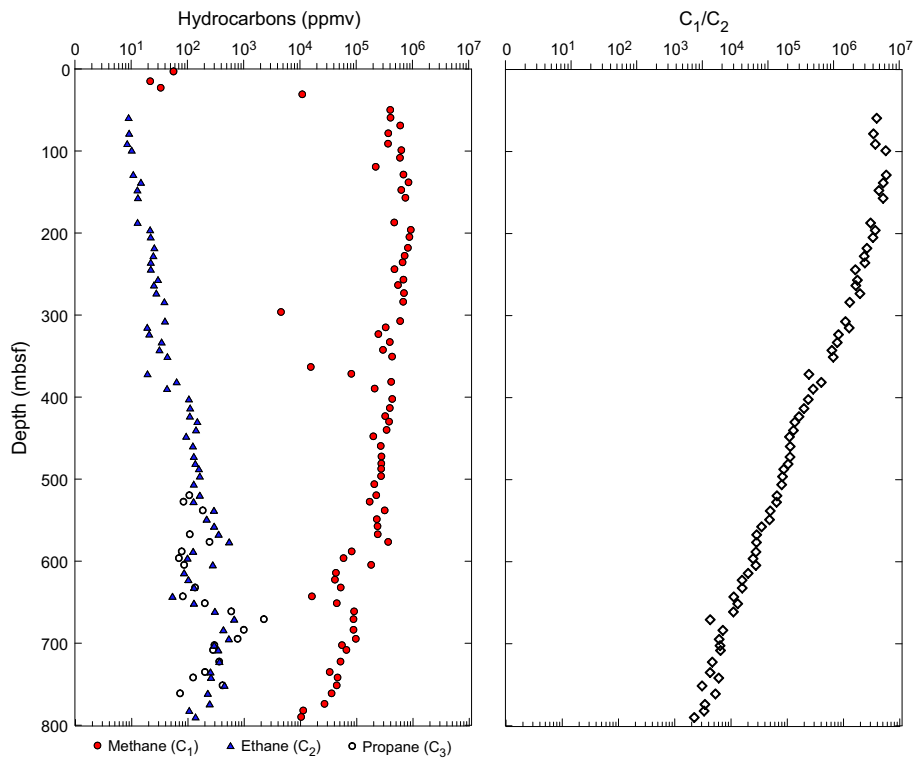


Figure F46. Hydrocarbon gases and methane/ethane ratios, Site U1433.



ammonium averages around 2.8 mM. Phosphate behaves differently from ammonium; phosphate concentrations increase from 40 μM at the top to a maximum 98 μM at the SMTZ and then decrease with depth to 1.7 μM at ~235 mbsf. Below that depth, phosphate concentrations remain approximately constant at ~2 μM down to 570 mbsf. The low phosphate concentrations below 200 mbsf are likely caused by less reactive organic matter due to the low sedimentation rates of 5–9 cm/ky (see [Biostratigraphy](#)).

Calcium, magnesium, and strontium

Downhole distributions of Ca^{2+} , Mg^{2+} , Mg/Ca ratio, and Sr^{2+} are shown in Figure [F43](#). Calcium concentrations decrease from 10.5 mM near the seafloor to a minimum of 5.1 mM at 35.4 mbsf, approximately at the SMTZ, where the alkalinity reaches a maximum and could trigger diagenetic carbonate precipitation, taking up Ca^{2+} and some of the other alkaline earth elements, particularly Mg^{2+} and Sr^{2+} . The Mg/Ca ratio increases from ~5 (modern seawater value) near the seafloor to a maximum of 9 (almost twice that of modern seawater) at ~35 mbsf, indicating that carbonate precipitation is dominated by preferential uptake of Ca^{2+} compared to Mg^{2+} in the uppermost part of the hole. Below 35 mbsf, calcium concentrations gradually increase to 11.5 mM, corresponding to a gradual Mg^{2+} decrease to a minimum 14.9 mM and a gradual Mg/Ca ratio decrease to ~2 at ~548 mbsf. These distributions could indicate dolomitization of calcite occurring in the sediment. Below 550 mbsf, calcium concentrations increase significantly to a maximum 16.7 mM at ~557 mbsf and then vary from 11.8 to 16.7 mM downhole to 605 mbsf. Magnesium concentrations also show more variability below 550 mbsf, varying from 15.3 to 22.0 mM.

Sr^{2+} behaves differently from Ca^{2+} and Mg^{2+} because carbonate precipitation and recrystallization does not affect Sr^{2+} concentrations at low temperatures. Sr^{2+} concentrations are low and relatively constant (<200 μM) in the uppermost 200 mbsf. Below that depth, Sr^{2+} concentrations increase slowly to 500 μM at 400 mbsf, before reaching a maximum of ~3500 μM at ~567 mbsf and then slightly decreasing to 3100 μM at 588 mbsf.

Higher Sr^{2+} and Ca^{2+} concentrations deeper than 550 mbsf may derive from a deep fluid source. This is supported by the high concentrations of boron, lithium, and silica in the same horizon (Figure [F44](#)). Shore-based isotopic analysis of interstitial water should provide better constraint for the fluid source.

Barium, boron, lithium, silica, iron, and manganese

Downhole distributions of barium, boron, lithium, silica, iron, and manganese are shown in Figures [F44](#) and [F45](#). Barium concentrations are elevated with respect to modern seawater (0.032–0.15 μM), ranging from 1.0 to 322 μM . Barium reaches a first peak of 62.4 μM at ~35 mbsf, corresponding to the SMTZ. Deeper than 35 mbsf, barium increases slightly to ~100 μM down to ~250 mbsf and then varies significantly between 10 and 300 μM , showing lower values in clay and higher values in carbonate turbidites. The Ba^{2+} profile is likely related to the stability of barite (BaSO_4) in sediment. The Ba^{2+} concentration increase may result from in situ barite dissolution due to sulfate reduction or the migration of Ba^{2+} in the low-sulfate fluid. Shore-based solid-phase barium analyses will be critical for determining the origin of the elevated barium and the history of the fluid flow.

In the uppermost 200 mbsf, boron concentrations decrease from ~550 μM close to the seafloor to a minimum ~246 μM at 147 mbsf. Deeper than 200 mbsf, boron concentrations show a very gradual increase to ~500 μM at 450 mbsf. Below this depth, boron

concentrations vary around 400 μM , with a single peak of 801 μM at 565 mbsf

Lithium concentrations decrease from 22.7 μM close to the seafloor, which is slightly lower than the modern seawater value (25 μM), to 4.5 μM at ~138 mbsf. Deeper than 140 mbsf, lithium concentrations gradually increase to a maximum of 86.7 μM at ~580 mbsf before decreasing to 72.3 μM at 590 mbsf.

In the uppermost 140 mbsf, silica concentrations are elevated compared to modern seawater (0–180 μM), ranging from 600 to 901 μM (Figure [F44](#)), possibly due to dissolution of siliceous microfossils, including diatoms, radiolarians, and sponge spicules, that occurs in the uppermost part of Hole U1433A (see [Lithostratigraphy](#) and [Biostratigraphy](#)). Deeper than 140 mbsf, silica concentrations are much lower, mostly fluctuating between 400 and 600 μM with a single peak of 864 μM at ~576 mbsf. This is consistent with the lithology change from predominantly clay in lithostratigraphic Unit I to interbedded clay and carbonate turbidite deposits in Unit II (see [Lithostratigraphy](#)).

Both dissolved iron and manganese concentrations decrease in the uppermost ~40 mbsf (Figure [F45](#)), corresponding to the zone of active sulfate reduction. Usually in this zone, iron and manganese concentrations increase with increasing sulfate reduction; oxidized iron and manganese are being reduced and released into the interstitial fluid as Fe^{2+} and Mn^{2+} , which are more soluble than the oxidized species. The decrease in iron and manganese concentrations likely suggests that Fe^{2+} and Mn^{2+} are taken up by diagenetic precipitation of sulfides and carbonates. From 40 to 423 mbsf, both Fe^{2+} and Mn^{2+} concentrations are very low, ranging from 0.2 to 3.1 μM and 2.7 to 4.1 μM , respectively. Below 430 mbsf, Fe^{2+} and Mn^{2+} concentrations increase to 5.7 and 38.7 μM , respectively, at ~520 mbsf before decreasing again to very low values from 520 to 580 mbsf.

Headspace gas geochemistry

Sediments recovered from Holes U1433A and U1433B were monitored for hydrocarbon gases as part of the shipboard safety and pollution prevention program (Figure [F46](#); Table [T14](#)). Headspace methane content increases from 2–5 ppmv close to the seafloor to 1101 ppmv at 30 mbsf corresponding to the SMTZ. Methane content reaches a maximum 93,595 ppmv at 196 mbsf before decreasing slowly with depth. Ethane is present at low concentrations below 59 mbsf, ranging from 0.9 to 681 ppmv. Propane is present between 519 and 774 mbsf, ranging from 7 to 287 ppmv. The C_1/C_2 ratio gradually decreases from >50,000 at ~150 mbsf to ~1000 at 800 mbsf at the base of the sediment section in Hole U1433B. These values are well within the normal range based on the relatively high thermal gradient of ~78°C/km at this site (see [Downhole measurements](#)) (Pimmel and Claypool, 2001). Shore-based carbon isotopic analysis of methane in the headspace gas samples will provide more insights on the origin of hydrocarbon gases.

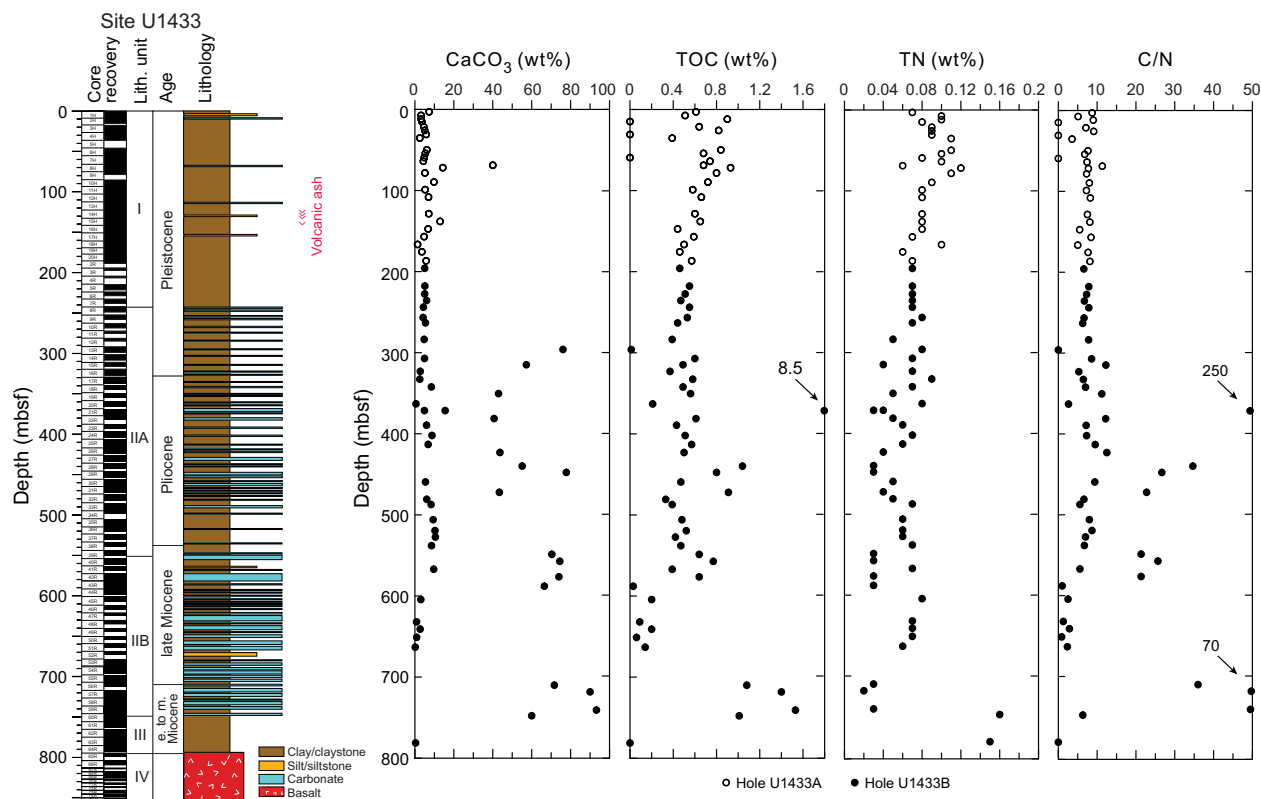
Bulk carbon and nitrogen analysis

Organic and inorganic carbon distributions for Site U1433 are illustrated in Figure [F47](#) and listed in Table [T15](#). In the uppermost

Table T14. Headspace sample hydrocarbon concentrations, methane, ethane, ethane, propene, and propane, Holes U1433A and U1433B. [Download table in .csv format.](#)

Table T15. Carbon and nitrogen content, Holes U1433A and U1433B. [Download table in .csv format.](#)

Figure F47. Calcium carbonate, TOC, TN, and C/N ratio, Site U1433.



300 mbsf, CaCO_3 content is <15 wt%, except for one peak of 40 wt% at ~70 mbsf that corresponds to a nannofossil ooze turbidite layer. Below 300 mbsf, CaCO_3 is more variable, with values >40 wt% corresponding to carbonate horizons, whereas clay intervals have CaCO_3 content of <15 wt%. Total organic carbon (TOC) content decreases slightly in the upper 200 mbsf, suggesting organic matter diagenesis. From 200 to 300 mbsf, TOC is relatively constant at ~0.5 wt%. Below 300 mbsf, TOC is more variable, with a peak of 8.5 wt% at 371 mbsf (measured twice to confirm the high value). The TOC to total nitrogen (C/N) ratio at this depth is also abnormally high (250). There are several other intervals of higher TOC and C/N ratios at 440–460, 550–570, and 700–750 mbsf. Samples from these intervals are from carbonate turbidite deposits thought to have been derived from shallow-water locations south of Site U1433 (see [Lithostratigraphy](#)). The C/N ratio also increases in these intervals with higher TOC, reaching >20, which suggests a terrestrial source for the organic carbon. This is consistent with organic carbon-rich sandstone in lithostratigraphic Unit IIB (Figure [F20](#); see also [Lithostratigraphy](#)).

Igneous rock geochemistry

Eighteen igneous rock samples from Cores 349-U1433B-65R through 75R were analyzed for concentrations of major and minor elements by inductively coupled plasma–atomic emission spectroscopy (ICP-AES) (Table [T16](#)).

Table T16. Major and minor element compositions of igneous rock samples, SiO_2 , TiO_2 , Al_2O_3 , $\text{Fe}_2\text{O}_3\text{T}$, MgO , MnO , CaO , Na_2O , K_2O , P_2O_5 , total element oxides, LOI, Ba, Co, Cr, Sc, Sr, V, Zn, and Zr, Hole U1433B. [Download table in .csv format.](#)

Total weight percentage for the major element oxides varies from 98.0 to 103.8 wt%. For comparison with data from other sites, measured major element total values were normalized to 100 wt%. The loss on ignition (LOI) values, which serve as a rough indicator of the overall level of alteration in the rocks, are low, ranging from 0.52 to 2.06 wt%. The samples have extremely low K_2O (0.11–0.29 wt%), moderate TiO_2 (1.32–1.63 wt%), MgO (5.01–8.22 wt%), Fe_2O_3 (9.20–11.39 wt%), Na_2O (2.63–3.02 wt%), and SiO_2 (48.5–51.1 wt%), and high Al_2O_3 (16.37–18.55 wt%) and CaO (10.89–12.13 wt%) compared to an average basalt. In general, concentrations of major elements vary within a narrow range (Figure [F48](#)).

When plotted on the alkali vs. silica diagram of volcanic rock types (Le Maitre et al., 1989) (Figure [F49](#)), the samples plot as tholeiitic basalt. As shown in Figure [F50](#), these rocks are similar to both Indian and Pacific MORB but are distinct from the Hainan Island ocean-island basalt (OIB) and the seamount basalts in the South China Sea. Thus, the basalt samples from Hole U1433B are tholeiitic basalt and are considered representative of South China Sea MORB.

Figure F48. LOI and major element composition of igneous rock samples, Hole U1433B. EOH = end of hole. Lithostratigraphy column includes lithology, igneous lithologic units (1–45), and lithostratigraphic units (III and IV).

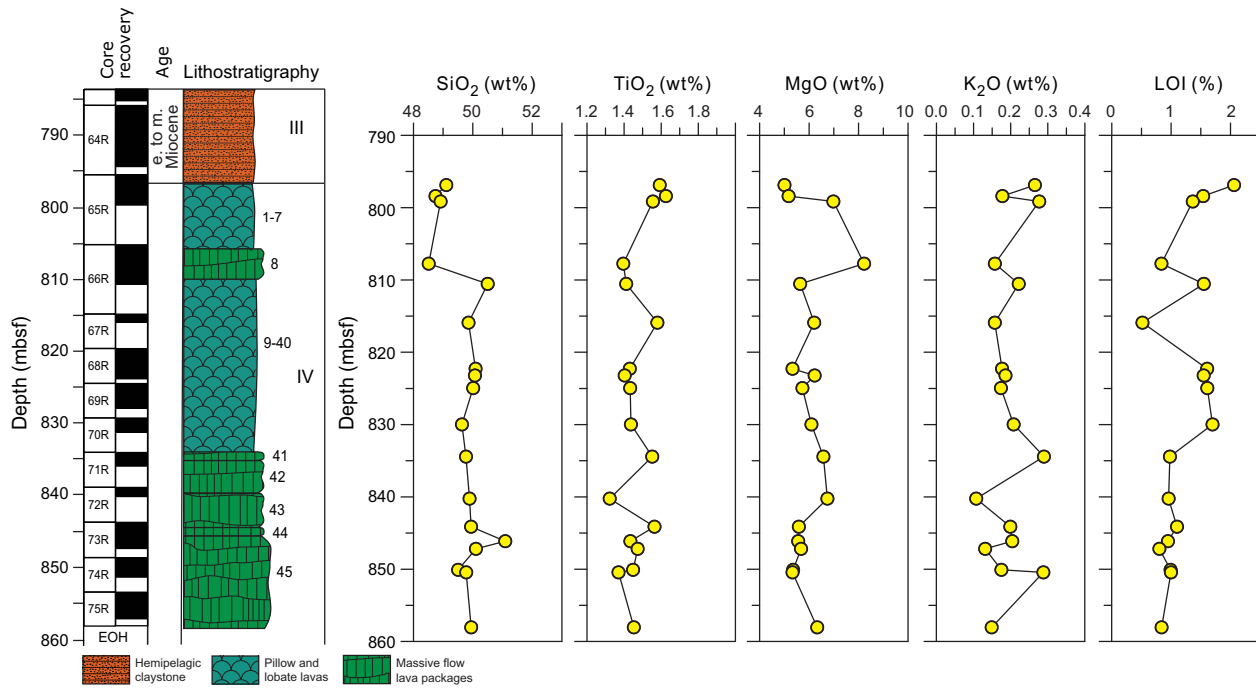


Figure F49. Total alkalis vs. silica for igneous rocks, Hole U1433B. Classification of volcanic rock types from Le Maitre et al. (1989). The dashed blue line divides data between tholeiitic and alkalic lavas of Hawaii (Macdonald and Katsura, 1964; Macdonald, 1968). Shown for comparison are data for Indian Ocean MORB from the Geochemical Rock Database (georoc.mpch-mainz.gwdg.de), seamounts in the SCS (Tu et al., 1992; Hékinian et al., 1989), OIB in the Hainan Island (Wang et al., 2012), and Pacific Ocean MORB (Zhang et al., 2009, 2012a, 2012b, 2013).

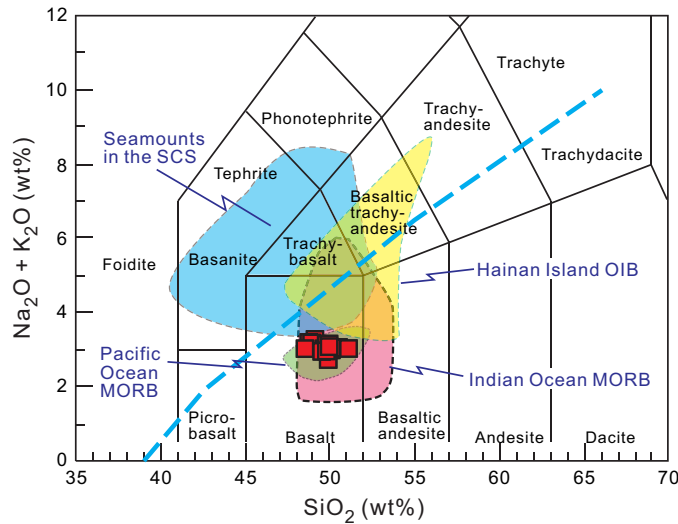
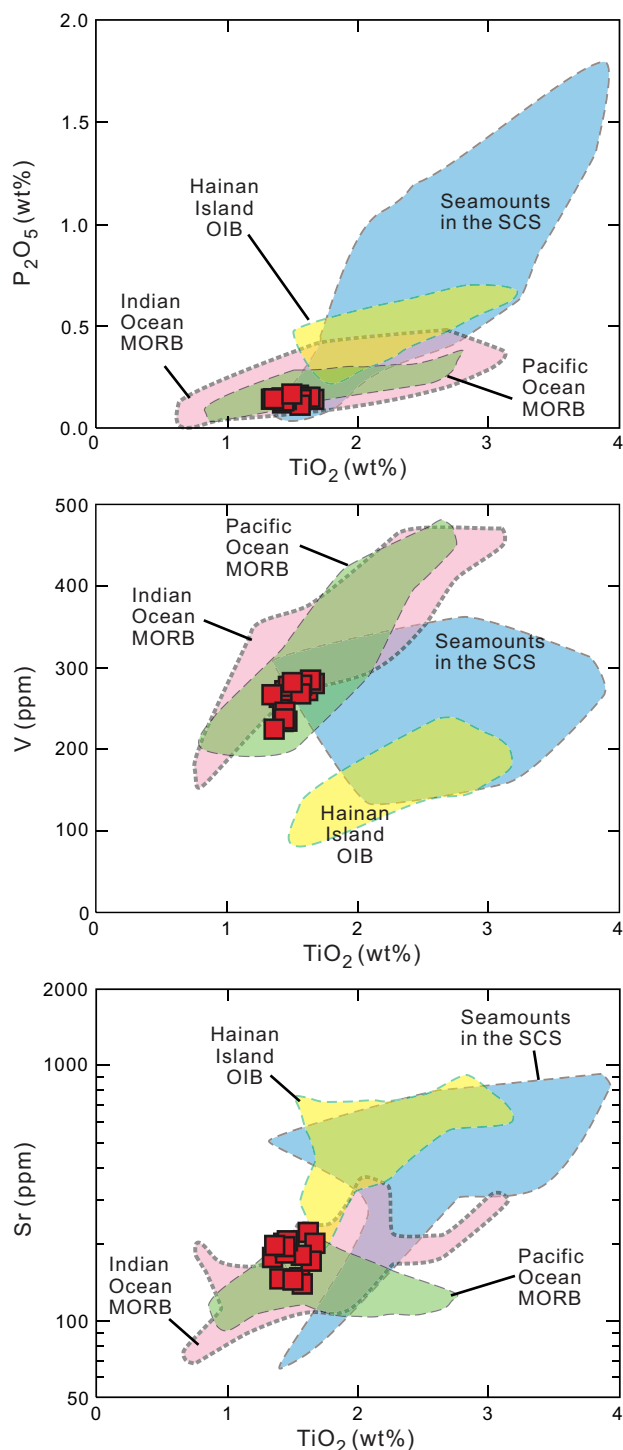


Figure F50. TiO_2 vs. P_2O_5 , V, and Sr, Hole U1433B. Shown for comparison are data for Indian Ocean MORB from the Geochemical Rock Database (geo-roc.mpch-mainz.gwdg.de), seamounts in the SCS (Tu et al., 1992; Hékinian et al., 1989), OIB in the Hainan Island (Wang et al., 2012), and Pacific Ocean MORB (Zhang et al., 2009, 2012a, 2012b, 2013).



Microbiology

Our goal for microbiological research conducted at Site U1433 was to collect and preserve samples for shore-based characterization of microbial communities. We collected samples on a routine

basis throughout the cored intervals and on a case-by-case basis according to features in the cores that suggested the presence of important geological interfaces. A number of samples were used to start microbial cultivations aboard the ship. In addition, we collected samples for measuring contamination, including perfluorocarbons, microspheres, and fluid community tracers (FCT).

Specific depths sampled for microbiology at Site U1433 are shown in Figure F51. Coring at Site U1433 yielded 50 routine, 5–10 cm whole-round samples to be used for microbiological analysis from the seafloor to 790 mbsf from Holes U1433A and U1433B. We collected whole-round samples for microbiology adjacent to samples for interstitial water measurements (see [Geochemistry](#)) in order to understand proximal interstitial water chemistry.

We collected and preserved 164 samples from the split cores for investigating the microbiology of interfaces or coring-induced disturbance using lipid and nucleic acid analyses. We obtained these samples between 4 and 154 mbsf in Hole U1433A and between 187 and 854 mbsf in Hole U1433B. Two sets of interface samples were obtained from volcanic ash/clay interfaces and four sets were obtained from turbidite/clay interfaces. From the split cores, we also sampled four horizons (2 from Hole U1433A and 2 from Hole U1433B) that were within 1 cm of the depth where a whole-round sample was taken on the catwalk several hours previously. We will measure lipids and DNA in these samples to estimate the effect of storage in the core laboratory during the period between when the core arrives at the surface and when the samples are obtained from the split cores on the sampling table. Samples from the split cores from Hole U1433B will be used to compare the microbial communities that are present within intact core biscuits and those that are present in the proximal sediment that has been severely altered during drilling. Twenty sample sets were collected to make this comparison. We selected all interface samples by recognition of key intervals and through consultation with sedimentologists or petrologists.

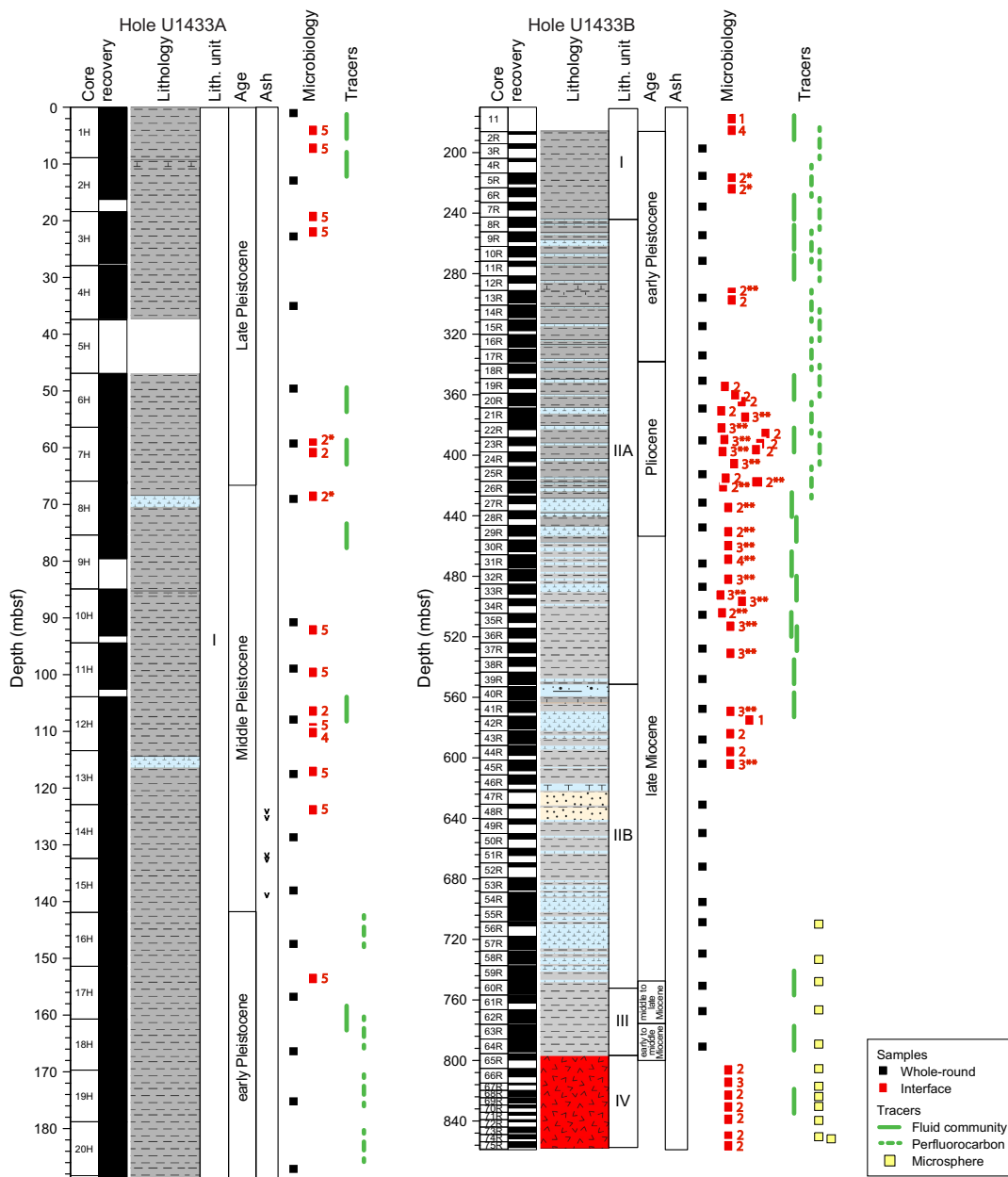
Microbiological analyses

Most of the samples collected at Site U1433 were preserved for shore-based analysis. Samples to be used for DNA and RNA extractions and sequencing were frozen at -80°C , and samples to be used for lipid extraction and analysis were frozen at -80°C or -20°C . Portions of the whole-round samples were selected for cultivation-based studies to enrich for anaerobic autotrophs and heterotrophs.

Contamination testing

We used three different methods of contamination testing during coring at Site U1433. The PFT perfluoromethylcyclohexane was introduced into the drilling fluid during coring of Holes U1433A and U1433B to trace potential drilling fluid contamination of the cores. PFT samples were acquired from the outside and inside of 16 cores during the coring of these holes (Figure F51). The concentration of PFTs measured on samples from the outside of Sections 349-U1433B-3R-2 (195.9 mbsf) and 13R-4 (296.1 mbsf) were higher than those measured on the inside of these same sections, which indicates no apparent drilling fluid contamination of the interiors of these cores. However, PFTs were not detected in most of the samples collected, regardless of whether the samples were taken from the outside or the inside of the core. The PFT pump was operating during these coring events. One possible explanation for the lack of detectable PFTs in most of the samples from Site U1433 is a leak in the system between the PFT pumps and where the PFT enters the drilling fluid.

Figure F51. Microbiology whole-round and interface samples and contamination testing samples, Site U1433. Numbers next to red squares indicate number of samples taken from those depths. * = sample collected within a centimeter of previously collected whole-round samples, ** = sample collected to determine how microbial communities change as a result of severe sample disturbance that can occur during coring.



Microsphere tracers were used with the RCB coring system in Hole U1433B by adding them to the core catcher sub in Cores 349-U1433B-56R through 75R (709–854 mbsf). Two microsphere samples were collected from each of these cores: one from scrapings of the core surface and one as a subsample from the interior of each whole-round sample. Microscopic counts of the microspheres in these samples will be performed in shore-based laboratories using the Procedure for Curation of DeepBIOS (www.kochi-core.jp/DeepBIOS).

Twenty-four FCT samples were collected either from the drilling fluids that drained from the core liners when cores arrived on the catwalk or from a sampling port near the mud pumps on the rig floor during active coring. The fluids collected for FCT samples correspond to cores obtained between 6 and 824 mbsf. Microbial community DNA and lipids from FCT samples will be compared to the same measurements made on the core samples to determine if the drilling fluids contain microbes that can be regularly tracked as recognizable contaminant taxa.

Paleomagnetism

Shipboard paleomagnetic study at Site U1433 consisted of pass-through magnetometer measurements on all archive-half cores and on representative discrete samples taken from the working halves. At Site U1433, Cores 349-U1433A-1H through 20H were cored with the APC using nonmagnetic core barrels equipped with the FlexIT orientation tool. Thus, both paleomagnetic inclinations and corrected declinations are available for Hole U1433A to construct magnetostratigraphy. Cores 349-U1433B-2R through 75R were cored using the RCB with nonmagnetic core barrels.

In order to isolate characteristic remanent magnetization (ChRM), sedimentary archive-half cores were demagnetized in an alternating field (AF) using steps of 5, 10, 15, and 20 mT and then were measured with the pass-through superconducting rock magnetometer (SRM) at a 2.5 cm interval. Selected discrete samples were AF demagnetized with an ASC Scientific D-2000 AF demagnetizer using 5, 10, 15, 20, 30, 40, 60, 80, and 100 mT steps. The results were analyzed using Zijderveld diagrams (Zijderveld, 1967), and ChRM directions were obtained using principal component analysis (Kirschvink, 1980).

Natural remanent magnetization of sedimentary cores

Downhole variation in natural remanent magnetization (NRM) properties is illustrated in Figures F52 and F53. In Hole U1433A, NRM inclinations are strongly biased toward vertical (mostly toward +90°). Upon 20 mT AF demagnetization, a significant decrease in intensity and a shift of inclination toward shallower or negative values were observed for intervals with normal or reversed polarity, respectively, suggesting the presence of drilling-induced remagnetization.

Although this drilling-induced remagnetization is not a welcome feature in isolating the characteristic component of magnetization, its steep positive inclinations do serve as a useful check for whether or not core sections and shipboard paleomagnetic samples were inverted by human error during either collection or measurement processes. Using this information, we successfully identified and corrected several such errors for core sections from Hole U1433A. An example is for Sections 349-U1433A-10H-1 through 10H-3, in which the correct orientation was not known after curation on the catwalk, but their steep negative NRM inclinations served as useful confirmation that the up/down directions of these sections were inverted.

Hole U1433B was drilled by RCB, which resulted in stronger drilling-induced remagnetization (Figure F53). Nevertheless, for most cores, 10–20 mT AF demagnetizations significantly removed the drilling-induced remagnetization. To the first order, the variation of NRM intensity is highly tied to lithology. For sediment shallower than 800 mbsf, NRM intensity is less than ~0.025 A/m but sharply increases by about 2 orders of magnitude in the underlying basalt units. This increase indicates that the basalt contains more strongly magnetic iron oxide than the sediment. Variations in magnetic susceptibility are consistent with variations in NRM intensity (see [Physical properties](#)).

As with Sections 349-U1433A-10H-1 through 10H-3 mentioned above, Section 349-U1433B-54R-CC was thought by shipboard sedimentologists to have been inverted based on the observed turbidite sequence in the core. We were able to use the polarity of magnetization of the overlying section to confirm that the core catcher section was indeed inverted.

Figure F52. Paleomagnetic measurements of NRM inclination and intensity on archive sections of sediment after 0 mT (red) and 20 mT (blue) AF demagnetization, Hole U1433A.

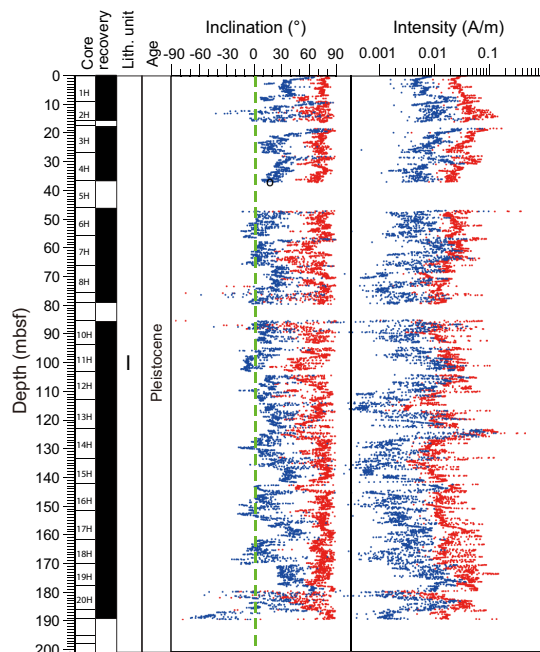
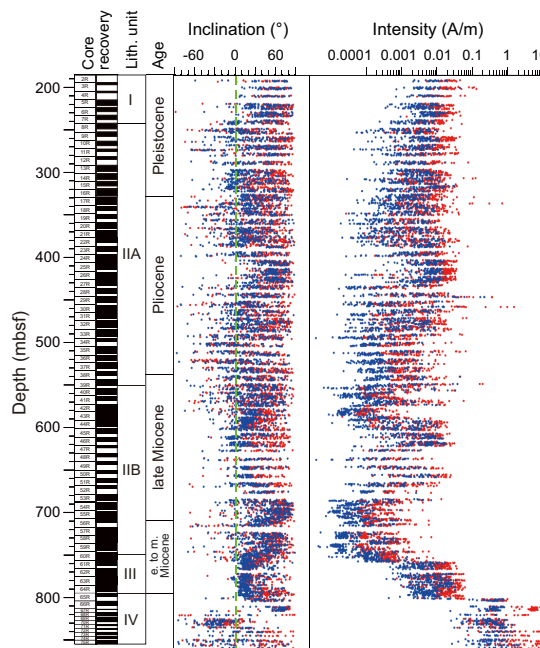


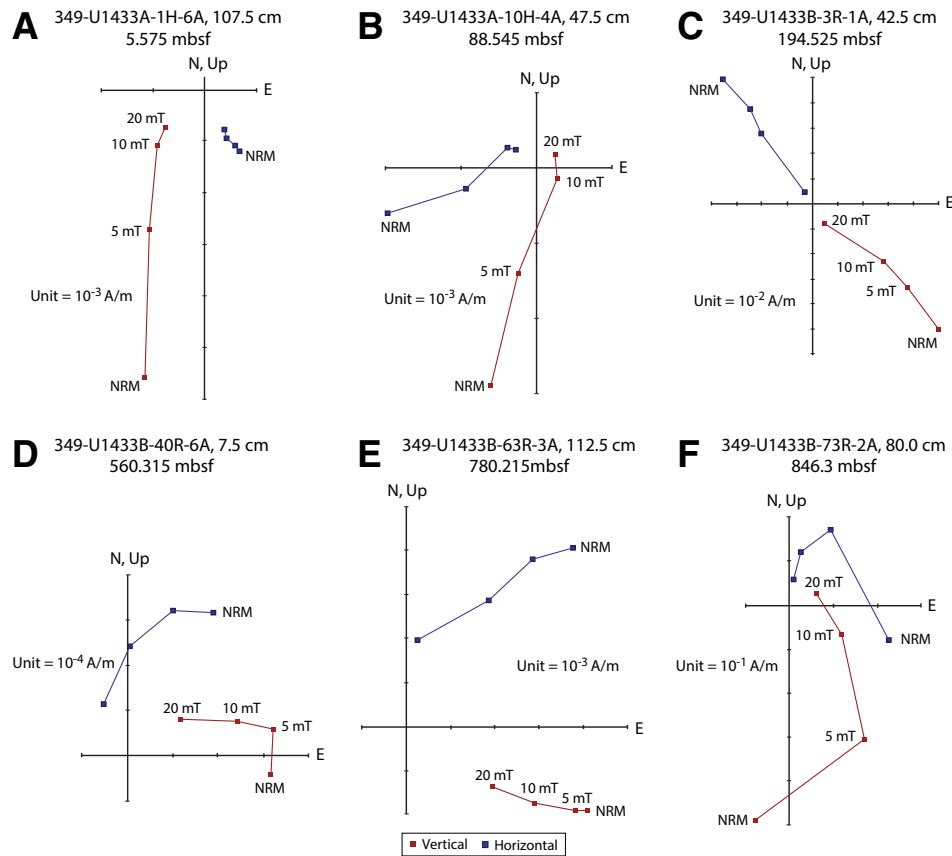
Figure F53. Paleomagnetic measurements of NRM inclination and intensity on archive sections of sediment and basalt after 0 mT (red) and 20 mT (blue) AF demagnetization, Hole U1433B.



Paleomagnetic demagnetization results

Representative vector plots (Zijderveld, 1967) showing magnetic behavior during AF demagnetization are given in Figure F54. The vertical overprint affects magnetic minerals with lower remanence coercivity ($B_{cr} < 10$ mT). Generally, B_{cr} is affected by the type and grain size of magnetic minerals. Therefore, downhole variations

Figure F54. A–F. Representative vector endpoint diagrams (Zijderveld, 1967) for sediment and basalt samples through stepwise AF demagnetizations. The characteristic remanent magnetization of most samples can be separated after 10 mT AF demagnetization.



in magnetic minerals result in changes in B_{cr} . Theoretically, the effects of vertical overprint are significant for samples containing more low-coercivity minerals (e.g., pseudosingle-domain and multiple-domain magnetite particles in sediment). In contrast, basalt usually contains much finer grained magnetite particles in pseudo-single- and single-domain grain size with higher B_{cr} values and in turn is less affected by the vertical overprint. Such a phenomenon can be seen in Figure F54. For example, Sample 349-U1433A-1H-6A, 107.5 cm, exhibits a strong vertical overprint that can be removed by 10 mT AF demagnetization. In contrast, for basalt samples such as Sample 349-U1433B-73R-2A, 80.0 cm, the overprint effects are insignificant.

The ChRM of Sample 349-U1433A-3R-1A, 42.5 cm, is well defined by a linear trend toward the origin of the vector plot. For other samples (Figure F54B, F54D, F54F), the inclination changes from positive to negative values. This change indicates that the overprint and viscous remanent magnetization effects have been largely removed. For such cases, the remanent magnetization after 20 mT AF demagnetization can be used to represent ChRM for constructing magnetostratigraphy.

At Site U1433, we also obtained representative paleomagnetism directions from several intervals for structural analysis and core orientation. Paleomagnetic core reorientation methods have been successfully used for both continental and oceanic rocks from outcrops or drill cores (e.g., Fuller, 1969; Kodama, 1984; Shibuya et al., 1991). Assuming that the direction of stable remanent magnetization (either viscous remanent magnetization or primary magnetization)

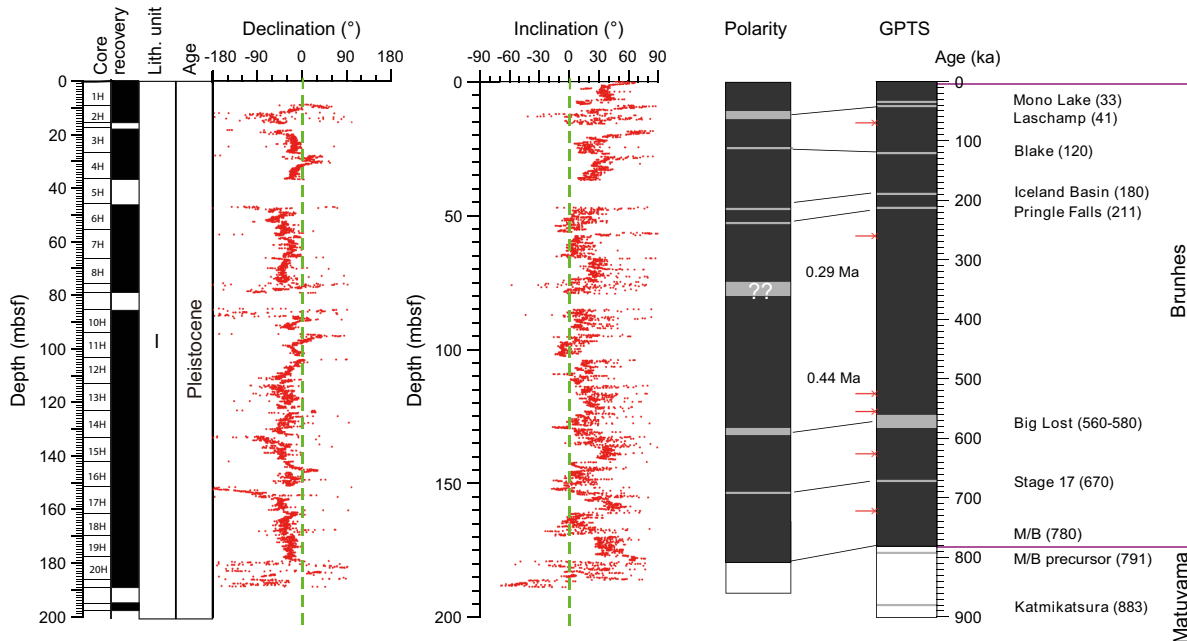
represents the expected magnetic direction at the site, the orientation of the paleomagnetic ChRM, which specifies the rotation of the core relative to the geographic coordinates, is then used to restore the azimuth of the core. For intervals of particular interest for structural geology at Site U1433, we either used the stable ChRM isolated from progressive demagnetization of small homogeneous segments (that contain structural features) or an average declination from 3–4 consecutive measurement intervals with the same inclination sign from the archive-half core data. The preliminary results suggest that, overall, paleomagnetic data are reasonably robust and can provide information to serve as the reference direction for structural studies.

Magnetostratigraphy

Constrained by biostratigraphic data, the basal age for Core 349-U1433A-20H (~188 mbsf) is <0.91 Ma, which indicates a rather high sedimentation rate compared to both Sites U1431 and U1432. The major shift in both declination and inclination at ~180 mbsf is therefore assigned to the Matuyama/Brunhes reversal boundary (0.781 Ma) (Figure F55). This correlates to a sedimentation rate of ~23.7 cm/ky. Such a high sedimentation rate facilitates preservation of short-lived paleomagnetic features (e.g., paleomagnetic excursions; Roberts, 2008).

Within the Brunhes Chron, 8 polarity shifts are observed. These short-lived events most likely represent geomagnetic excursions as evidenced by both declination and inclination changes. The polarity shifts at ~12, 18, 28, 48, 53, 132, and 152 mbsf match well with

Figure F55. Magnetostratigraphic results, Hole U1433A. Paleomagnetic declination and inclination after 20 mT AF demagnetization. For polarity and GPTS (Gradstein et al., 2012), black = normal polarity and white = reversed polarity. Red arrows indicate possible paleomagnetic excursions (Roberts, 2008). M/B = Matuyama/Brunhes boundary.



known excursion events: Mono Lake (33 ka), Laschamp (41 ka), Blake (120 ka), Iceland Basin (180 ka), Pringle Falls (211 ka), Big Lost (560–580 ka), and Stage 17 (670 ka), respectively. For the other 2 directional anomalies at ~78 and 88 mbsf, there are no counterparts from previous studies. In addition, these 2 anomalies bracket an interval without core recovery. Therefore, further studies are needed to confirm the origin of these 2 anomalies.

Only inclinations in Hole U1433B can be used to construct magnetostratigraphy. Because of the more severe overprint effects of the RCB than the APC, the overall paleomagnetic pattern of cores from Hole U1433B is less obvious (Figure F56). Therefore, we define the positive chrons on the basis of the first-order pattern as constrained by biostratigraphy. Altogether, 6 major positive chrons are recognized. The basal boundaries for the Matuyama (2.581 Ma), Gauss (3.596 Ma), and Gilbert (6.066 Ma) Chrons are therefore defined at ~350, 420, and 550 mbsf, respectively. The basal age for sediment

(Core 349-U1433B-60R) is ~11 Ma (see [Biostratigraphy](#)). On the basis of this age model, the sedimentation rate changes at ~660 mbsf (between ~9 and 10 Ma).

Paleomagnetic results for the basement show that the upper part of the unit (805–817 mbsf) is dominated by positive polarity (Figure F57). Between ~817 and 830 mbsf, a reversed polarity zone is observed. Below this depth range, paleomagnetic inclinations display both normal and reversed polarities. Overall, remanent magnetization of rock deeper than ~817 mbsf is dominated by reversed polarity. The variation of remanent magnetization intensity after 20 mT AF demagnetization shows a downhole increasing trend. Magnetization values of the upper units are less than ~1 A/m and increase to 2–2.5 A/m at the bottom. For comparison, the magnetic signature of the basalt units recovered at Site U1431 is also plotted in Figure F57.

Figure F56. Magnetostratigraphic results, Hole U1433B. Paleomagnetic inclination after 20 mT AF demagnetization. For polarity and GPTS (Gradstein et al., 2012), black = normal polarity and white = reversed polarity.

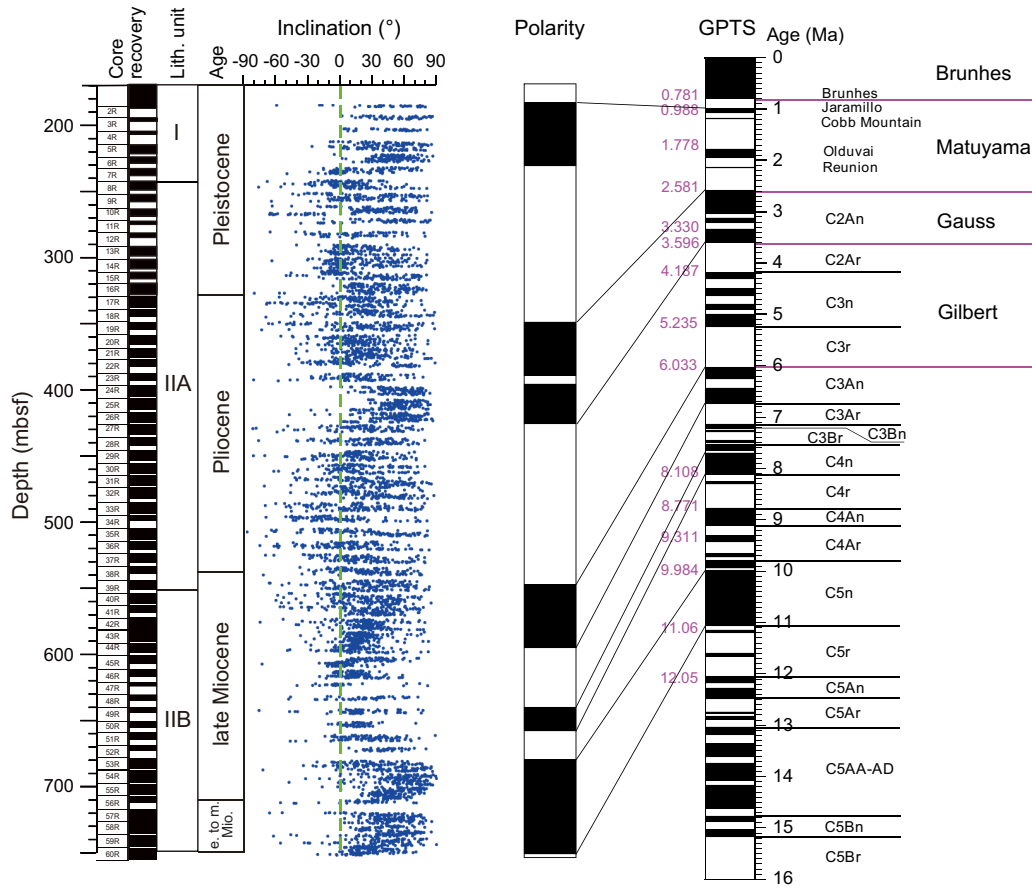
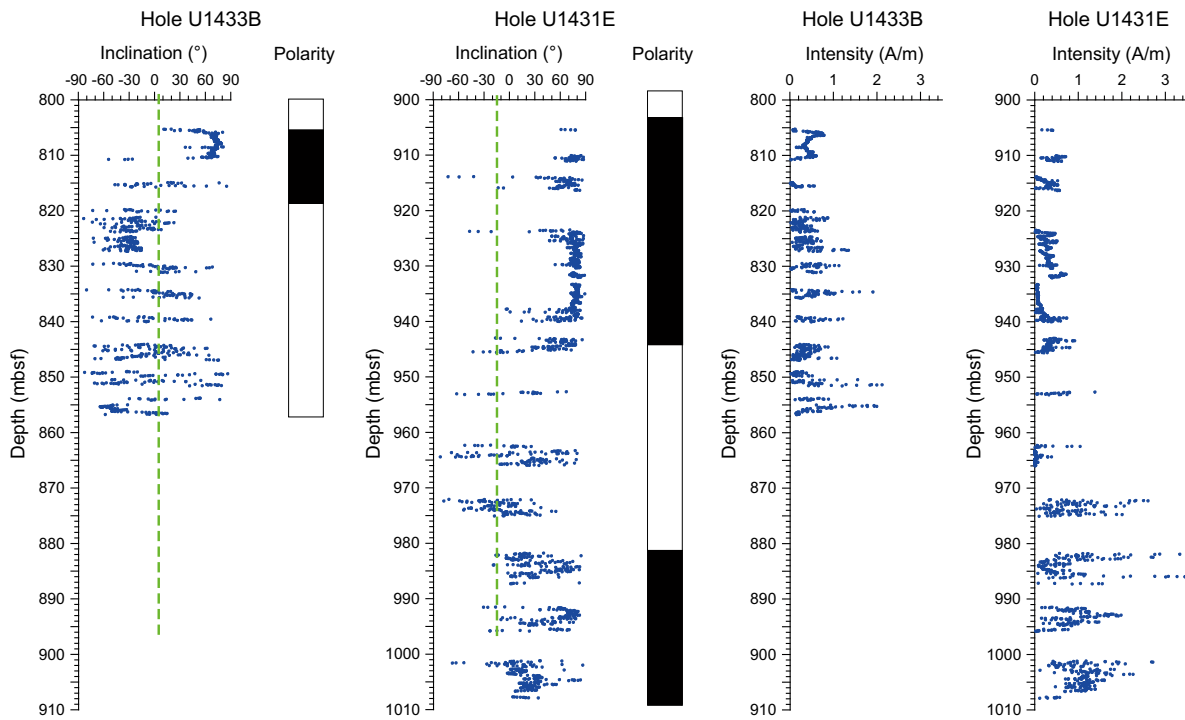


Figure F57. Comparison of paleomagnetic results from the basalt units in Holes U1433B and U1431E. For polarity, black = normal polarity and white = reversed polarity.



Physical properties

Cores from Holes U1433A and U1433B were measured for physical properties on whole-round cores (*P*-wave velocity, bulk density, magnetic susceptibility, and NGR), as well as on split cores (point magnetic susceptibility and *x*-caliper and *z*-bayonet *P*-wave velocity) and discrete samples (moisture and density). Thermal conductivity was measured with a needle probe in soft sediment and then with a contact probe in the lithified sediment and igneous rock. Most *P*-wave velocities measured on whole-round cores from Hole U1433A are orders of magnitude out of range and not shown in the figures, probably because of the relatively high gas content in the sediment. *P*-wave measurements were not made on the RCB whole-round cores from Hole U1433B because the space between the core and the liner prevented reliable measurements.

Whole-Round Multisensor Logger measurements

Measurement points that were orders of magnitude out of range were removed from the whole-round core data, which were then smoothed using a five-point average moving window for gamma ray attenuation (GRA) density and a ten-point average moving window for magnetic susceptibility and NGR. The measurements of physical properties in Holes U1433A and U1433B are compiled in Figure F58. Measurements in sediment and basalt are presented in Figures

F59 and F60, respectively, to enhance the observations in the corresponding lithostratigraphic units.

Gamma ray attenuation bulk density

Bulk density measured from GRA on the Whole-Round Multisensor Logger (WRMSL) increases with depth from 1.4 to nearly 2 g/cm³ in the uppermost 150 m and remains constant near 2 g/cm³ downhole to ~600 mbsf in the clay and carbonate of lithostratigraphic Units I and II. Density gradually decreases with depth from 2.0 to 1.8 g/cm³ in the clay of Unit III, whereas porosity increases with depth in this unit. Density shows large variations from 1.7 to 2.8 g/cm³ in the basalt of Unit IV.

Magnetic susceptibility

Large variations in Site U1433 magnetic susceptibility data with lithology are shown on the log-scale plot in Figure F58. Values increase with depth from 30 × 10⁻⁵ to 40 × 10⁻⁵ SI in the uppermost 150 m. A peak reaching 100 × 10⁻⁵ SI near 125 mbsf corresponds to an ash layer (red arrows in Figures F58, F59). Values are relatively constant at ~40 × 10⁻⁵ SI in the clays of Unit I. Magnetic susceptibility values generally decrease with depth in Unit II, from values of 30 × 10⁻⁵ to 50 × 10⁻⁵ near 240 mbsf to 0–30 × 10⁻⁵ SI near 750 mbsf, but the values also show large variability corresponding to changes in lithology in the interbedded clay and carbonate. Magnetic susceptibility values increase with depth in the clays of Unit III and show a large variability in the basalt of Unit IV, from 0 to 2000 × 10⁻⁵ SI.

Figure F58. Combined results of physical property measurements, Holes U1433A and U1433B. Note log scale for magnetic susceptibility plot. Red arrow denotes magnetic susceptibility peak associated with ash layer. Red lines delineate correlation between changes in physical properties and lithostratigraphic boundaries. MS = magnetic susceptibility. WRMSL = Whole Round Multisensor Logger, SHMSL = Section-Half Multisensor Logger.

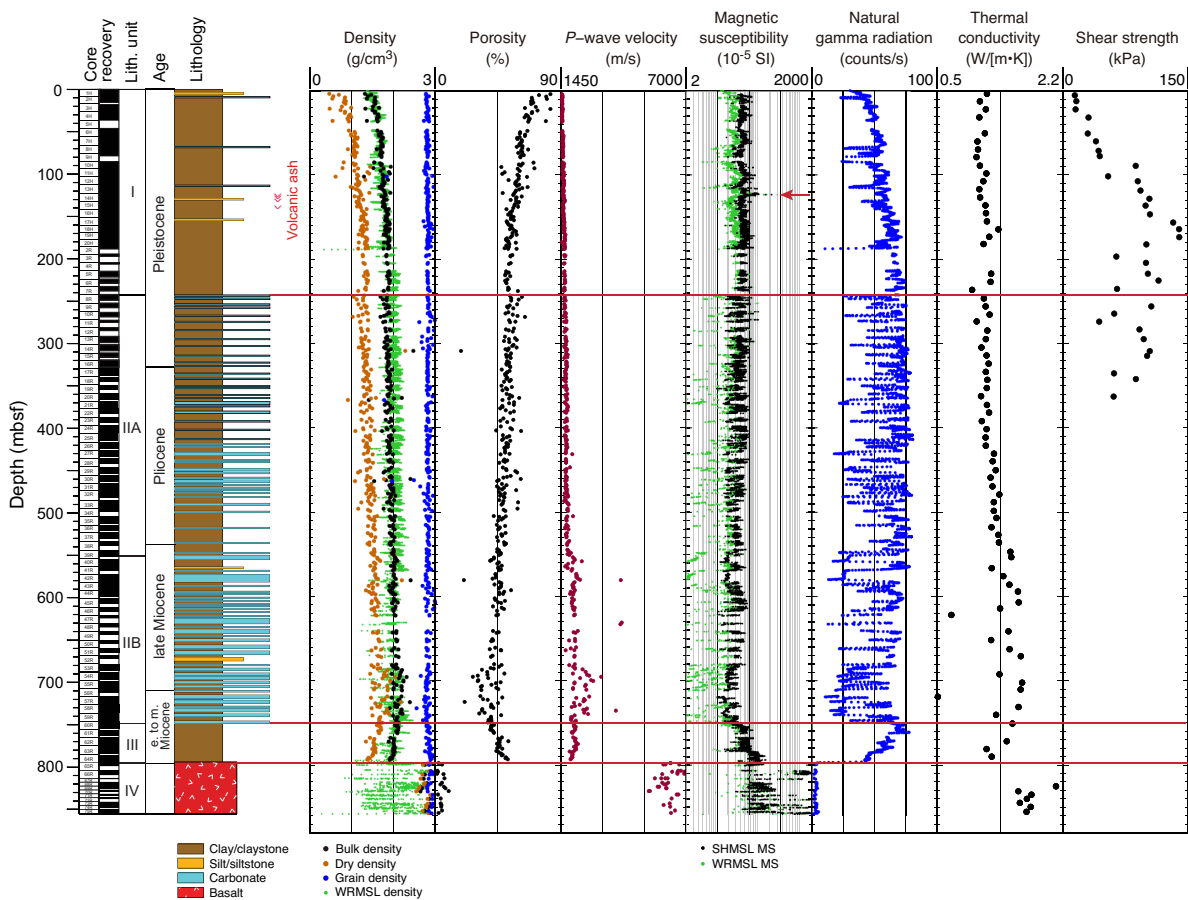
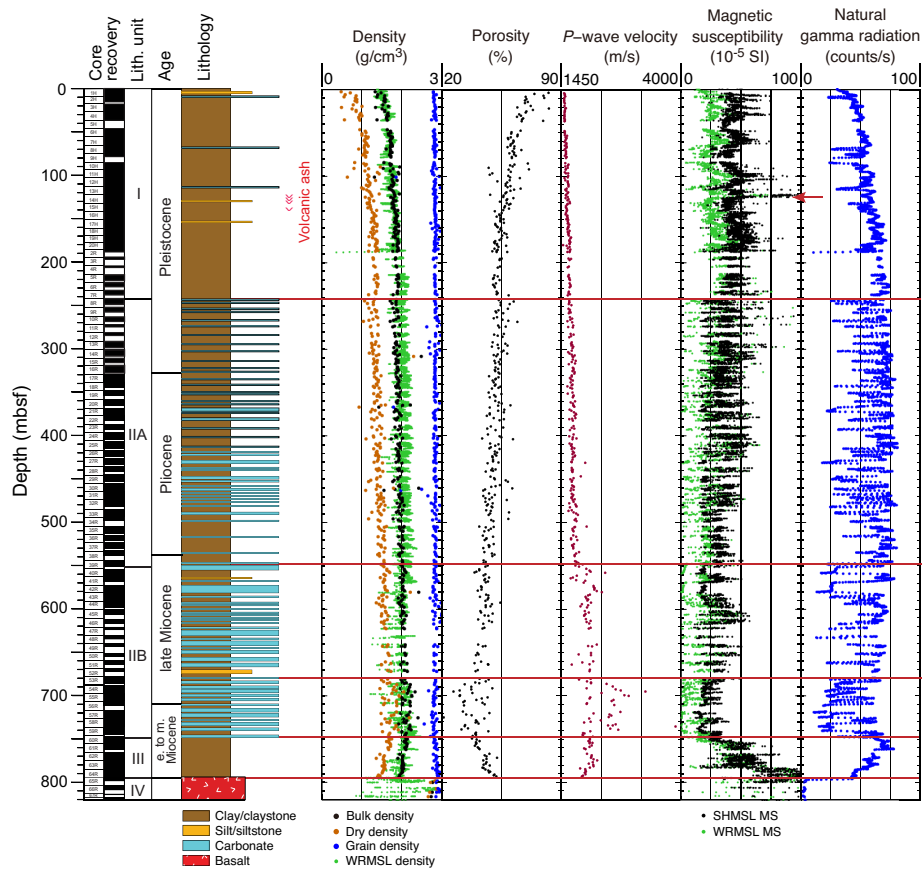


Figure F59. Combined results of physical property measurements of sediment, Holes U1433A and U1433B. Scales have been adjusted to the values in the sediment. Some values from basalt do not appear on the plots. Red arrow denotes magnetic susceptibility peak associated with ash layer. MS = magnetic susceptibility.



Natural gamma radiation

In Holes U1433A and U1433B, NGR values display trends and variability similar to the magnetic susceptibility values within the different lithostratigraphic units. NGR counts increase with depth from 30 to 70 counts/s over the uppermost 240 m. Below this depth, values alternate between 70 and 30–40 counts/s throughout Unit II downhole to 750 mbsf. NGR counts decrease with depth from 70 to 40 counts/s in Unit III, between ~750 and 800 mbsf, and then are very low in the basalt of Unit IV.

Thermal conductivity

Thermal conductivity increases from 1 to 1.2 W/(m·K) in the uppermost 150 m and then gradually increases to ~1.4 W/(m·K) downhole to ~540 mbsf (Subunit IIA/IIB boundary). Thermal conductivity shows large variations and relatively high values between 1.2 and 1.7 W/(m·K) in the interbedded clay and carbonate of Subunit IIB and the clay of Unit III and is very high in the basalt of Unit IV, from 1.8 to 2.2 W/(m·K). The contact probe requires that measurements in lithified sediment and basalt cores be made on large pieces with smooth splitting surfaces, so the measured values likely overestimate the average in situ thermal conductivity.

Point magnetic susceptibility

Point magnetic susceptibility measurements from the Section Half Multisensor Logger (SHMSL) agree well with WRMSL results. A small offset observed between the 2 types of measurements re-

sults from the difference in instrument resolution (see [Physical properties](#) in the Methods chapter [Li et al., 2015b]). On average, point magnetic susceptibility is 20×10^{-5} SI greater than WRMSL magnetic susceptibility. Point magnetic susceptibility peaks in lithostratigraphic Unit I reflect the presence of ash layers (red arrow in Figures F58, F59). Magnetic susceptibility values for the basalt of Unit IV range between 0 and 2000×10^{-5} SI, with the highest values in the thick lava flows (Figure F60).

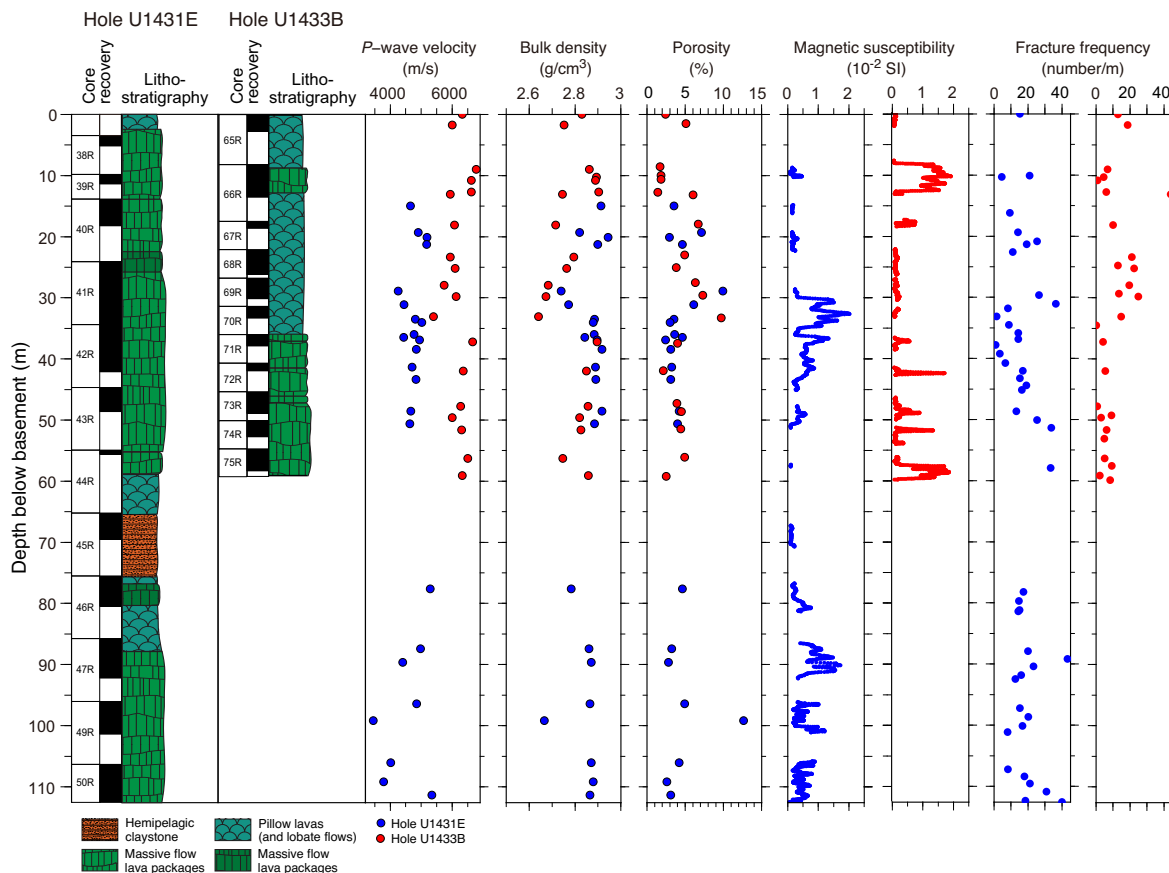
Compressional wave (*P*-wave) velocity

In Holes U1433A and U1433B, *P*-wave velocity gradually increases from near seawater velocity at the seafloor (1480 m/s) to ~1700 m/s at 540 mbsf in the soft sediment of lithostratigraphic Units I and II and increases again to ~2000 m/s in the more indurated sediment of Subunit IIB downhole to ~680 mbsf. Below this depth, *P*-wave velocity shows very variable values from 1800 to 4000 m/s at the bottom of Subunit IIB, with the highest values in the more indurated carbonate layers. *P*-wave velocity shows lower values near 1900–2000 m/s in the clay of Unit III, with slightly lower values near the sediment/basement interface. *P*-wave velocity increases to very high values between 5000 and 7000 m/s in the basalt of Unit IV.

Shear strength

Shear strength increases with depth from 20 to 150 kPa in the uppermost 150 m. Below 150 mbsf, shear strength decreases with

Figure F60. Comparison of physical property measurements of basalt, Holes U1431E and U1433B. Note that the highest *P*-wave velocities and magnetic susceptibility values correspond to the lowest rock fracture frequency, reflecting the role of alteration in basalt physical properties.



depth, with more variability in the measurements, between 150 and 60 kPa (Figure F58). Because of sediment compaction, vane shear strength was not measured below 370 mbsf, as many cracks started to develop during measurement.

Moisture and density

Bulk and dry density measured on individual samples show the same variations as bulk density measured on whole-round cores. Grain density is almost constant ($\sim 2.8 \text{ g/cm}^3$) in sediment (lithostratigraphic Units I–III). Basalt grain densities are close to 2.9 g/cm^3 . Porosity shows a large decrease with depth in the uppermost 150 m, from 90% to 50%, decreases more slowly with depth from 60% to 40% downhole to 750 mbsf, and increases again in the clay of Unit III, up to 60%. Porosity drops to 1%–10% in basalt.

Data interpretation and lithologic correlation

In Holes U1433A and U1433B, physical properties correlate both with lithology and observed lithification. The variations near the seafloor of some physical properties reflect compaction of sediment. Large variations are observed in the basalt layers that result from a combination of factors discussed below.

Surface sediment compaction

In Hole U1433A, bulk density, *P*-wave velocity, shear strength, NGR, and thermal conductivity increase gradually with depth over the uppermost 150 m, whereas porosity measured on discrete samples decreases from 90% to 50% over the same depth range. This indicates that sediment compaction dominates some of the physical

property variations above 150 mbsf. Below that depth, bulk and dry densities, *P*-wave velocity, and thermal conductivity continue to increase at a slower rate downhole to ~ 540 mbsf, showing that compaction is still significant in the soft sediment.

Interbedding of clays and carbonates and lithification

Between 240 and 750 mbsf (lithostratigraphic Unit II), variability in porosity, magnetic susceptibility, and NGR values reflects the interbedding of carbonate and clay layers. The carbonates have low magnetic susceptibility and NGR compared to the clays. An increase in *P*-wave velocity from ~ 1700 to ~ 2000 m/s near 540 mbsf coincides with stronger lithification of the more deeply buried sediment between Subunits IIA and IIB. From 680 to 750 mbsf, *P*-wave velocities measured in the lithified carbonates reach ~ 2600 m/s, showing a strong contrast with those measured in clay (~ 2000 m/s). The strong reflectors observed in the seismic profile (Figure F3) probably result from this contrast in velocity in Subunit IIB, which is also supported by downhole sonic velocities and conversion to two-way traveltimes, which indicate that the top of Subunit IIB appears to coincide with the strong reflector above basement (see [Downhole measurements](#)).

Basalt and basalt alteration

The basalt below 800 mbsf in Hole U1433B (Unit IV) displays very low NGR (< 6 counts/s) and highly variable magnetic susceptibility (0 to 2000×10^{-5} SI) and porosity (1%–10%) (Figures F58, F60). Some of the relatively unaltered, phenocryst-rich basalt has very high magnetic susceptibility and *P*-wave velocity (up to

Figure F61. Correlation between P -wave velocity and rock fracture frequency, Holes U1431E and U1433B (see [Igneous petrology and alteration](#)).

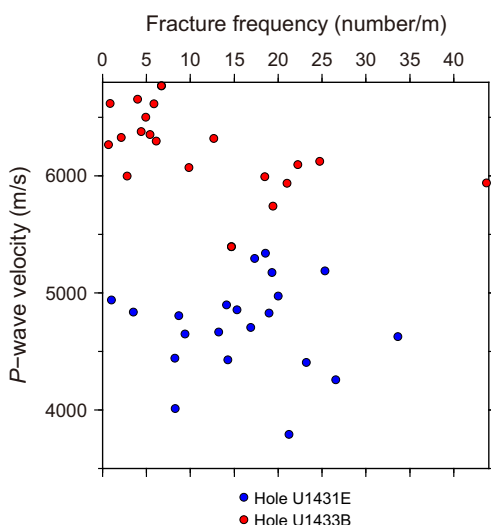
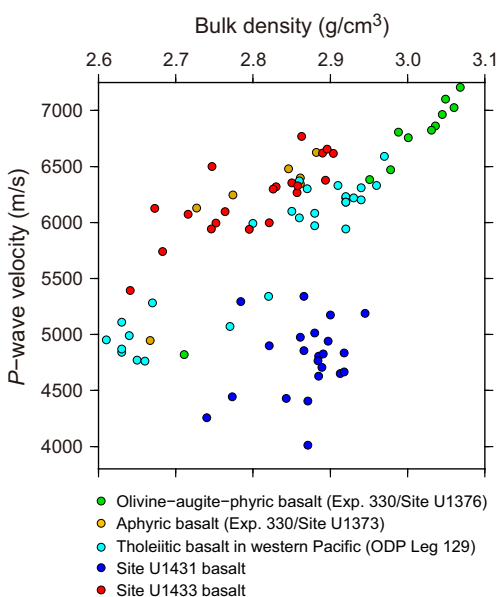


Figure F62. Correlation between P -wave velocity and bulk density in SCS basalt in Holes U1431E and U1433B and Pacific basalt from Integrated Ocean Drilling Program Expedition 330 Sites U1373 and U1376 and ODP Leg 129 Sites 801 and 802. Basalt in Hole U1433B follows the general correlation, whereas basalt in Hole U1431E does not; the difference probably results from basalt alteration (Bush et al., 1992; Expedition 330 Scientists, 2012a, 2012b).



7000 m/s). Variations in physical properties in the basalt may result from different factors, including degree of alteration and fracture, size of phenocrysts, and composition. To better analyze the physical properties of the basalt layers, we compare their variations between basalt units from Sites U1431 and U1433 and with other basalt collected during 2 previous drilling expeditions. We plot physical property data as a function of depth below the top of the basement instead of depth below seafloor for both holes. P -wave velocity in the basalt of Hole U1431E is on average 30% (~1500 m/s) lower than

in the basalt of Hole U1433B, but bulk densities do not show significant differences, with variations between 2.6 and 2.9 g/cm³ in both holes. In addition, basalt from Hole U1431E exhibits smaller P -wave velocity variations compared to that of Hole U1433B but relatively higher frequency of rock fractures and vein injection (Figure F61), reflecting higher alteration (see [Igneous petrology and alteration](#)). The relatively low P -wave velocity measured for the basalt of Holes U1431E and U1433B may be associated with higher porosity, from 1% to 14%, which may itself result from fractures and vein injection (Busch et al., 1992). Variations in P -wave velocity in Hole U1433B (5400–6770 m/s) compared to bulk density show the same linear trend observed on typical aphyric to olivine-plagioclase-phyric basalt recovered during previous drilling expeditions (ODP Sites 801 and 802 in the western Pacific and Integrated Ocean Drilling Program Sites U1373 and U1376 along the Louisville Seamount chain [Busch et al., 1992; Expedition 330 Scientists, 2012a, 20012b]) (Figure F62). In addition, magnetic susceptibility values display a good relationship to fracture frequency in both Holes U1431E and U1433B. These comparisons between parameters and basalt characteristics suggest that P -wave velocity variation may be dominated by rock fractures, vein injection, and alteration (Figure F61), rather than phenocryst size.

Downhole measurements

Logging operations

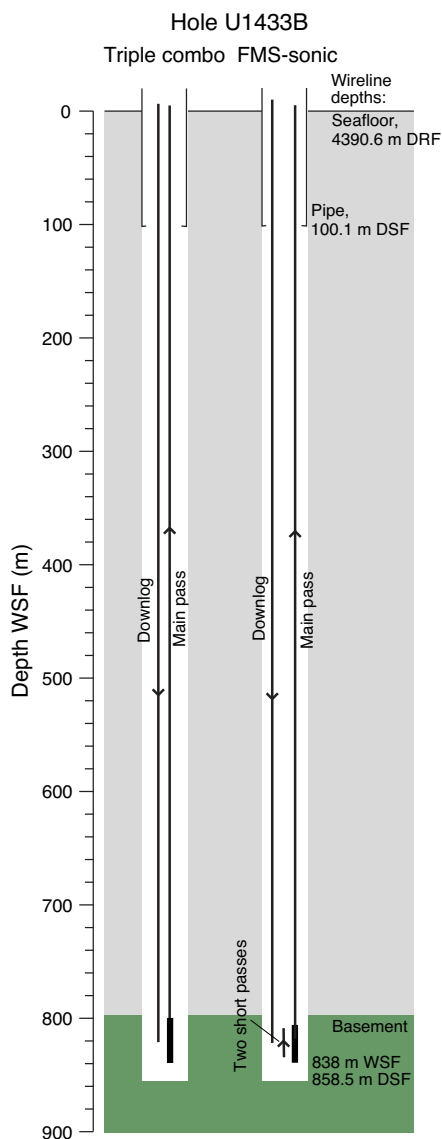
The last core from Hole U1433B arrived on deck at 2145 h on 17 March 2014. Hole preparation for the logging program included a 50 bbl sepiolite mud sweep, a wiper trip from 858.5 to 786.3 mbsf, a further 50 bbl sepiolite mud sweep, release of the RCB drill bit, and displacement with 225 bbl of heavy (10.5 lb/gal; barite weighted) mud from 689.1 mbsf. The pipe was raised to a logging depth of 100.4 m drilling depth below seafloor (DSF) (4491 m drilling depth below rig floor). The heavy mud aimed to prevent cave-ins in a potentially suspect interval of low core recovery. Rig-up for downhole logging started at 1100 h on 18 March. Seas were calm, with heave at ~30 cm peak-to-peak, so the wireline heave compensator was not used.

The modified triple combo tool string started downhole at 1345 h on 18 March and reached 830 m WSE, ~18 m short of the bottom of the hole (Figure F63). The tool string included the Hostile Environment Natural Gamma Ray Sonde, Hostile Environment Litho-Density Sonde, and High-Resolution Laterolog Array. The FMS-sonic tool string was run into the pipe at 0145 h on 19 March and, after passing an obstruction in the upper part of the basement section, reached the same depth as the triple combo tool string. Two short passes were taken in the basement below the obstruction. During the main upward log, the FMS caliper arms were closed while the obstruction was passed.

Log data quality

Between 100 and 550 m WSE, rapid variations in borehole diameter from 25 cm (9.84 inches) to wider than 43 cm (16.9 inches) caused density values to be underestimated (Figure F64). The NGR log was affected to a lesser extent. Deeper than 550 m WSE, the hole diameter tended to be in gauge with fewer washed out zones. In general, there were fewer bridged (narrow borehole) zones than at Site U1431. However, high cable tension had to be employed to pull the tool string up through an obstruction just above the basement on the FMS-sonic main pass, which caused some depth discrepancies in the FMS-sonic logs around the sediment/basement interface.

Figure F63. Logging operations summary diagram, Hole U1433B.



FMS resistivity images are generally of good quality, although washed-out zones are characterized by conductive (dark) images.

The barite-weighted mud that was pumped uphole from 689 m DSF appears not to have had a large effect on the photoelectric effect factor (PEF) log, perhaps only slightly raising the lower envelope of this log at ~570–700 m WSF. This pumping also appears to have caused a deviation to colder temperatures in the borehole fluid temperature log (not plotted).

The triple combo main upward pass was taken as the depth reference, and the other logging runs were depth matched to it by means of the NGR logs.

Logging units

Logging Unit 1: base of drill pipe (100 m WSF) to 245 m WSF

Logging Unit 1 is characterized by relative homogeneity in the sonic velocity log, without major excursions to higher velocity values (Figure F64). NGR values are relatively high, averaging ~65 gAPI, with a 10 m interval at the base of the unit with NGR values at

~85 gAPI. This logging unit corresponds to lithostratigraphic Unit I (see [Lithostratigraphy](#)).

Logging Unit 2: 245–550 m WSF

At the top of logging Unit 2, NGR values drop to levels averaging ~55 gAPI. This unit is characterized by the appearance of meter-scale beds with higher sonic velocity and PEF values (Figure F65). A steady downhole increase in background density and sonic velocity reflects compaction with depth. This logging unit corresponds to lithostratigraphic Subunit IIA (see [Lithostratigraphy](#)), which includes carbonate turbidites.

Logging Unit 3: 550–750 m WSF

The top of logging Unit 3 corresponds to the first appearance of sonic velocity values >2300 m/s and also to high velocity and low NGR layers >5 m thick. The downhole compaction and lithification trend continues in this unit. This logging unit corresponds to lithostratigraphic Subunit IIB (see [Lithostratigraphy](#)), which includes thick carbonate turbidites.

Logging Unit 4: 750–800 m WSF

The top of logging Unit 4 is marked by an increase in NGR values to ~85 gAPI and a drop in sonic velocity values. There is an absence of excursions to higher velocities and lower NGR values, and the downhole trend in this ~50 m thick unit is to lower densities and sonic velocities. This logging unit corresponds to lithostratigraphic Unit III, which is composed of reddish to yellowish brown clay (see [Lithostratigraphy](#)).

Logging Unit 5: 800–840 m WSF (base of logging data)

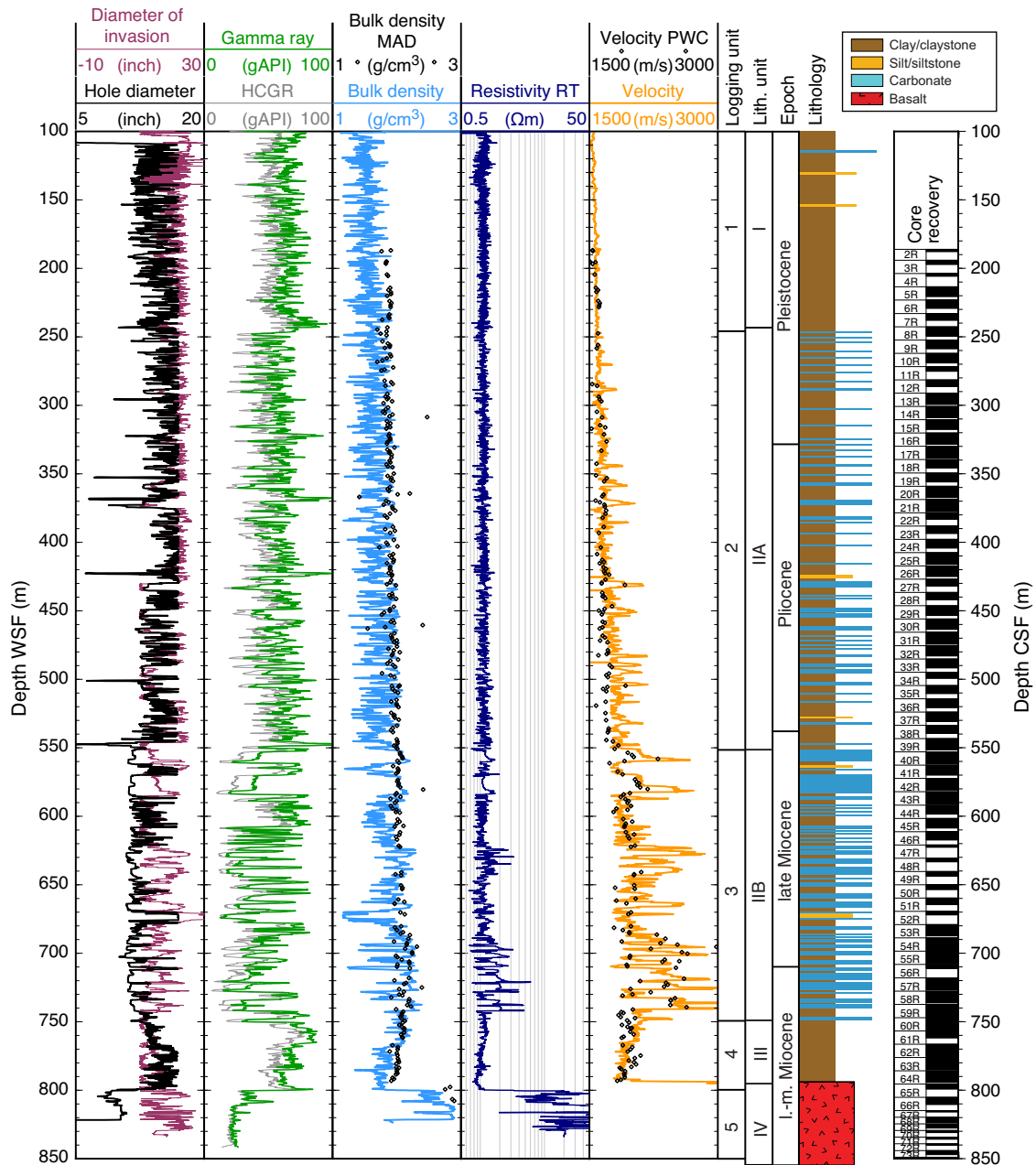
A step increase to higher sonic velocity, density, and resistivity values marks the top of basaltic basement. NGR drops to lower values (Figures F64, F66). Logging Unit 5 is not homogeneous; it contains resistivity changes varying over 2 orders of magnitude. Two thin intervals at 808 and 816 m WSF have higher NGR values and low sonic velocity and resistivity.

Downhole logs and lithology

Downhole logs and FMS images reflect lithology at Site U1433. The clay-dominated sediment of logging Unit 1 has high NGR because of K and Th in the clay minerals. Clay-rich lithologies form the background sediment in logging Units 2 and 3, but carbonate turbidites appear at the top of Unit 2 and become more common downhole, becoming the dominant lithology in Unit 3. The carbonates are apparent by their low NGR values, due to the lack of clay minerals, and high PEF, due to the relatively high concentration of calcium. The carbonates are also more cemented than the background sediment, as seen in the high velocity log values. Sharp bases in the FMS images support the interpretation of these beds as turbidites (Figures F67, F68A, F68B). The higher resistivity and higher velocity values in the lower part of these beds implies more cementation in the coarser part of the turbidites (Figure F67). The presence of thin, highly resistive laminations is observed in the lower part of some of the turbidites, particularly in Unit 3, perhaps indicating that the Unit 3 turbidites come from a more proximal source than the more distal turbidites of Unit 2.

Logging Unit 4 is composed of yellowish to reddish brown clay (see [Lithostratigraphy](#)) and accordingly has relatively high NGR, reaching 85 gAPI at the top of the unit. NGR values decrease and PEF increases with depth downhole in the unit. This potentially reflects an increasing abundance of hematite and other oxides in the

Figure F64. Downhole logs with lithostratigraphic and logging units, Hole U1433B. Note that the downhole logs are on the logging depth scale, whereas the moisture and density discrete sample (MAD), P-wave caliper (PWC), and core recovery data are on the core depth scale. There are small depth shifts between the 2 depth scales, usually <2 m in amplitude. Lithology was interpreted jointly from core and log data. HCGR = computed (U-free) gamma radiation, RT = "true" resistivity.



sediment, because a greater concentration of heavy elements would be required to produce the observed PEF values. The concentration of such oxides could result from hydrothermal processes and/or the removal of other sediment components in this interval overlying the basaltic basement. FMS images from this unit have distinct centimeter-scale resistive patches (Figure F68C) whose origin is uncertain at this time.

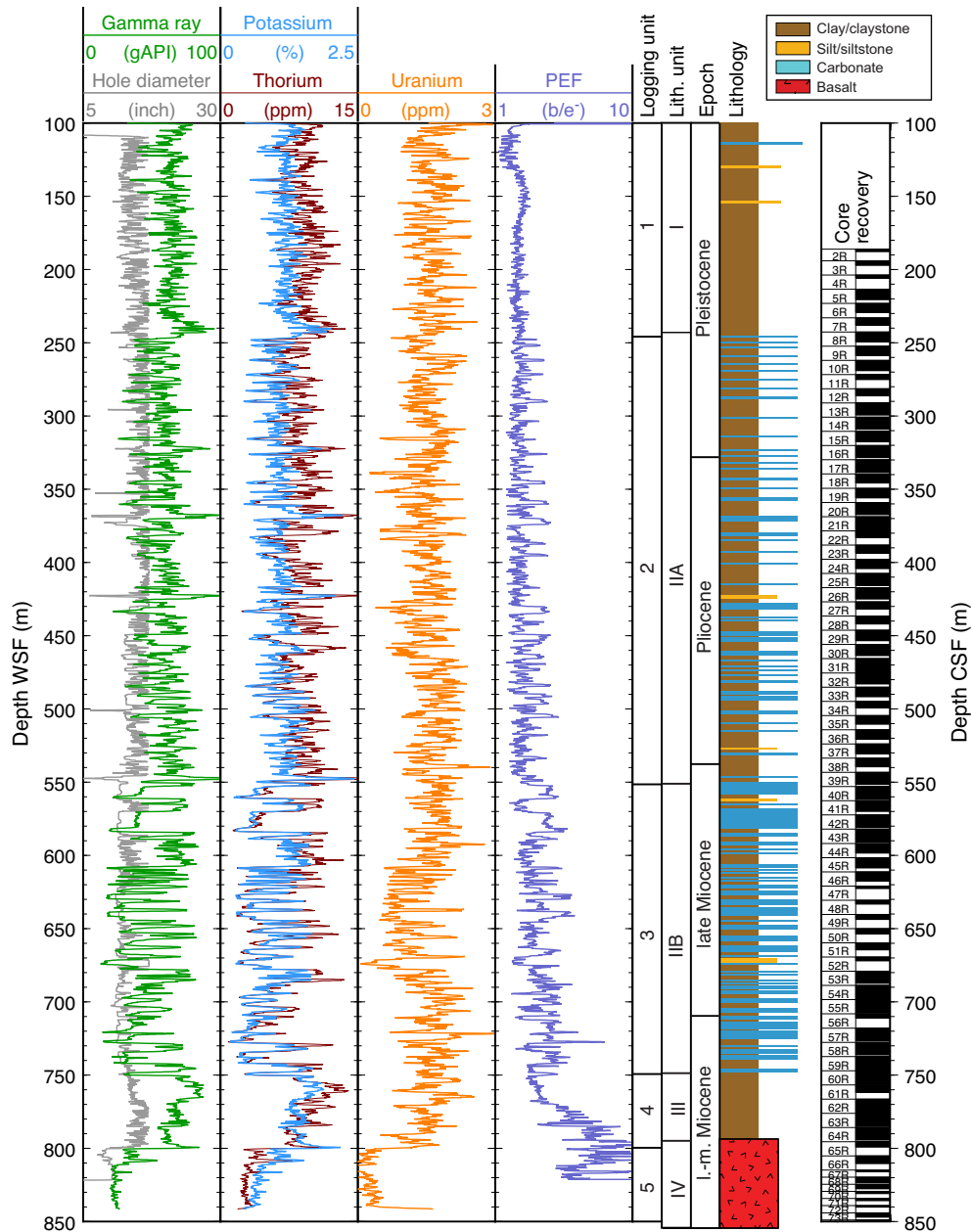
As expected, the step in physical and chemical properties at the basalt interface is clearly seen in nearly all of the downhole logs. However, NGR does not fall to values as low as those seen in the core measurements or as low as is expected of basalt, so the NGR

log measurements in the basalt unit should be regarded with caution. A massive flow and pillow basalt can be distinguished in the FMS images (Figure F68B), as well as veins and 2 possible sediment interlayers (Figures F66, F68D).

Sonic velocity and two-way traveltime

In general, the sonic velocity log repeated reasonably well between the upward and downward passes of the logging tool, so the data are considered to be robust, a conclusion that is supported by the general similarity to the P-wave velocities measured on core samples (Figures F64, F66, F69A). The laboratory measurement

Figure F65. Downhole logs from Hole U1433B that are dependent on the geochemistry and mineralogy of the formation. Note that the downhole logs are on the logging depth scale, whereas core recovery data are on the core depth scale. Lithology was interpreted jointly from core and log data.

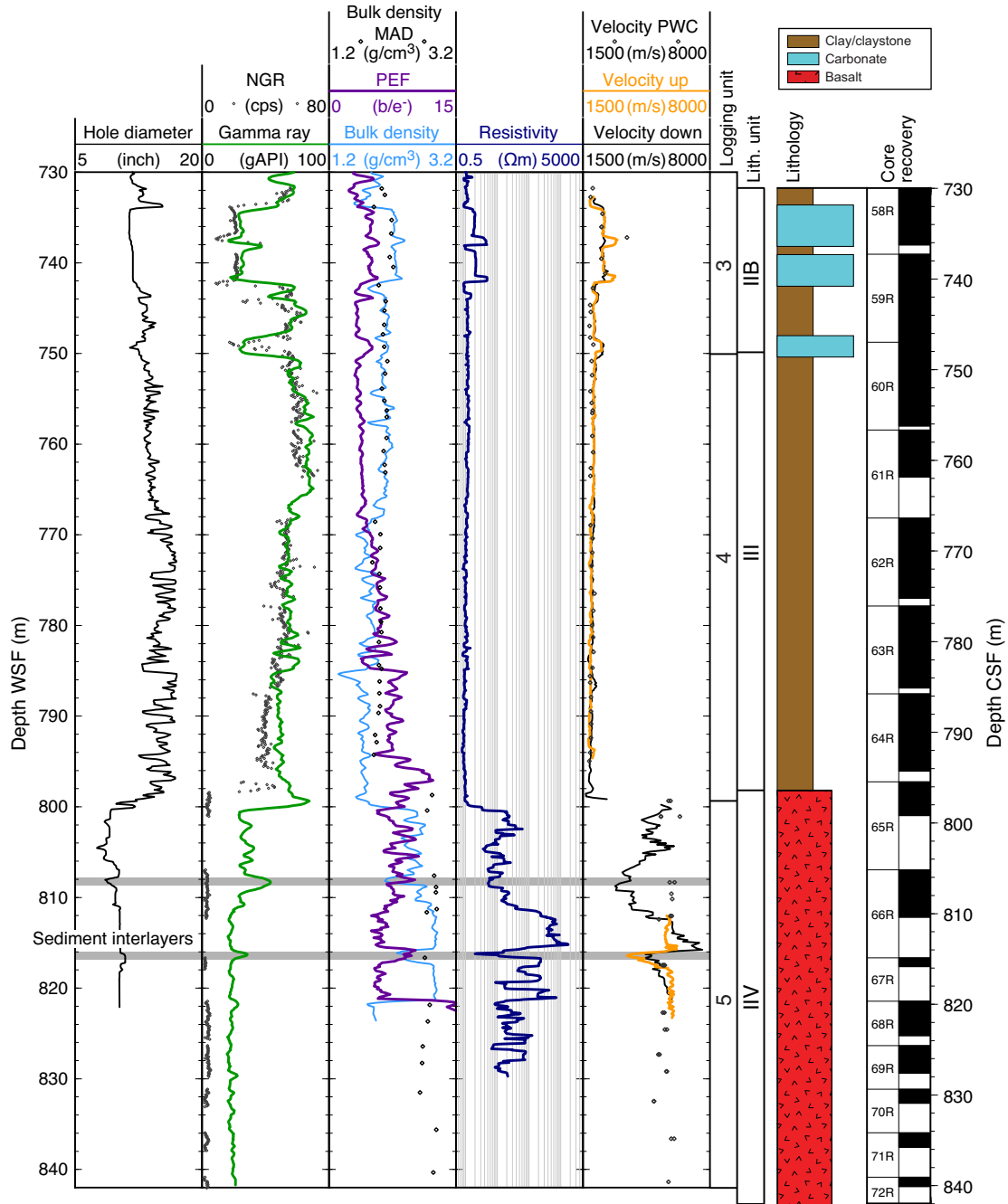


sometimes underestimates in situ velocity because of the removal of high-pressure conditions when the sediment is raised to the ship (e.g., from 470 to 550 m CSF in Figure F64). The upward sonic velocity log was recorded using a medium sonic source frequency, and the downward log was recorded using a high sonic source frequency. The high frequency is the standard Schlumberger setting, but in the mostly slow formations logged here (and in general during the Integrated Ocean Drilling Program), the medium sonic frequency source proved to be more reliable because of lower signal attenuation. An example is seen in the turbidites at 738 and 742 m WSF (Figure F66); the medium-frequency upward pass records the

higher velocities at the base of the turbidites, whereas the high-frequency downward pass does not.

Sonic velocities increase with depth to 750 m WSF, decrease to lower values in the reddish brown clay (750–800 m WSF), and exceed 6000 m/s in the basaltic basement. This data set was used to calculate interval velocities between measurement points, and then these interval velocities were summed and doubled to yield two-way traveltime for Site U1433 (Figure F69B). From these data, the boundary between logging Units 2 and 3 at 550 m WSF lies at the top of the set of high-amplitude reflectors in the seismic section at ~6.5 s two-way traveltime (Figure F3). The basement two-way traveltime is predicted to be at 6.74 s.

Figure F66. Detail of downhole logs and comparison to core physical properties and lithology between 730 and 842 m WSF, Hole U1433B. Gray rectangles indicate presumed sediment interlayers interpreted based on the downhole logs.



Downhole temperature and heat flow

Four downhole temperature measurements were made using the advanced piston corer temperature tool (APCT-3) in Hole U1433A, yielding values from 6.0°C at 37.4 m DSF to 12.2°C at 122.9 m DSF (Table T17; Figures F70, F71A) and giving a geothermal gradient of 78°C/km. These measurements, together with the seafloor temperature of 2.5°C, indicate that temperature increases approximately linearly with depth.

Thermal conductivity under in situ conditions was estimated from laboratory-determined thermal conductivity from Hole

U1433A using the method of Hyndman et al. (1974) (see **Physical properties** in the Methods chapter [Li et al., 2015b]). The calculated in situ values average 1.1% lower than the measured laboratory values. Thermal resistance was then calculated by integrating the inverse of the in situ thermal conductivity over depth (Figure F71B). A heat flow of 83 mW/m² was obtained from the linear fit between temperature and thermal resistance (Figure F71C) (Pribnow et al., 2000). This geothermal gradient and heat flow at Site U1433 are similar to the closest values for this part of the deep South China Sea Basin (Li et al., 2010).

Figure F67. Detail of downhole logs and FMS images between 605 and 632 m WSF, Hole U1433B. Inferred carbonate sediment layers (blue shaded areas) are characterized by low NGR, high PEF, and high velocity. In the FMS images, some layers appear massive and homogeneous, whereas others have thin resistive layers at their base.

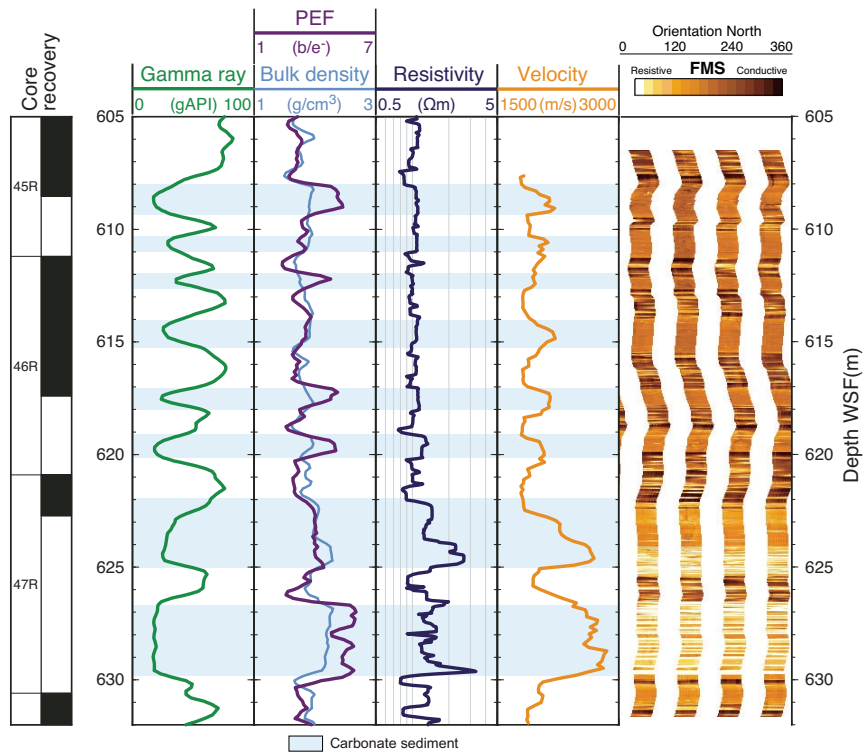


Figure F68. Examples of FMS images, Hole U1433B. A. Carbonate turbidites with sharp resistive bases and homogeneous appearance, with some mottling probably due to bioturbation (logging Unit 3, 588–593 m WSF). B. A 3 m thick carbonate turbidite, the lower half of which has few-centimeter thick high-resistivity bands (logging Unit 3, 619–623 m WSF). C. Centimeter-scale mottling in the reddish brown clay interval; origin unknown but likely due to alteration (logging Unit 4, 756–760 m WSF). D. Highly resistive basalt flow overlying slightly less resistive pillow basalts, with veins and fractures apparent as more conductive linear features (logging Unit 5, 817–822 m WSF).

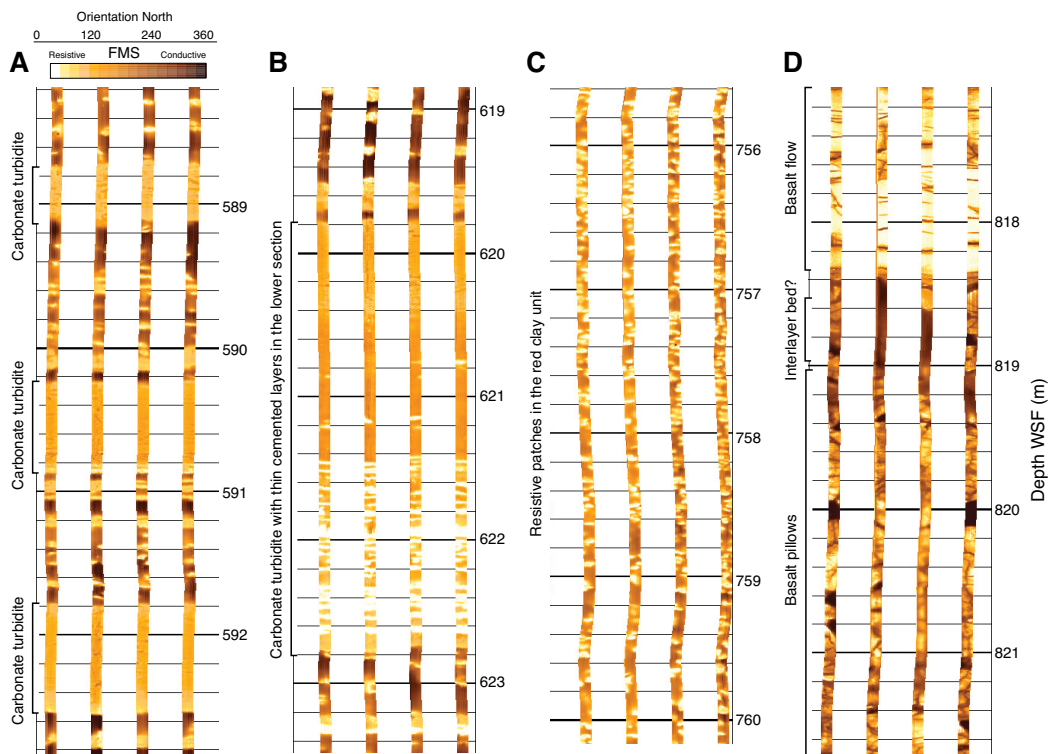


Figure F69. Plots of (A) sonic velocity and (B) two-way travelttime data. Two-way travelttime was calculated from the main pass of sonic velocity log data between 155 and 430 m WSF. The top part of the hole was estimated to be a linear increase of velocity from 1500 to 1535 m/s at 100 m WSF.

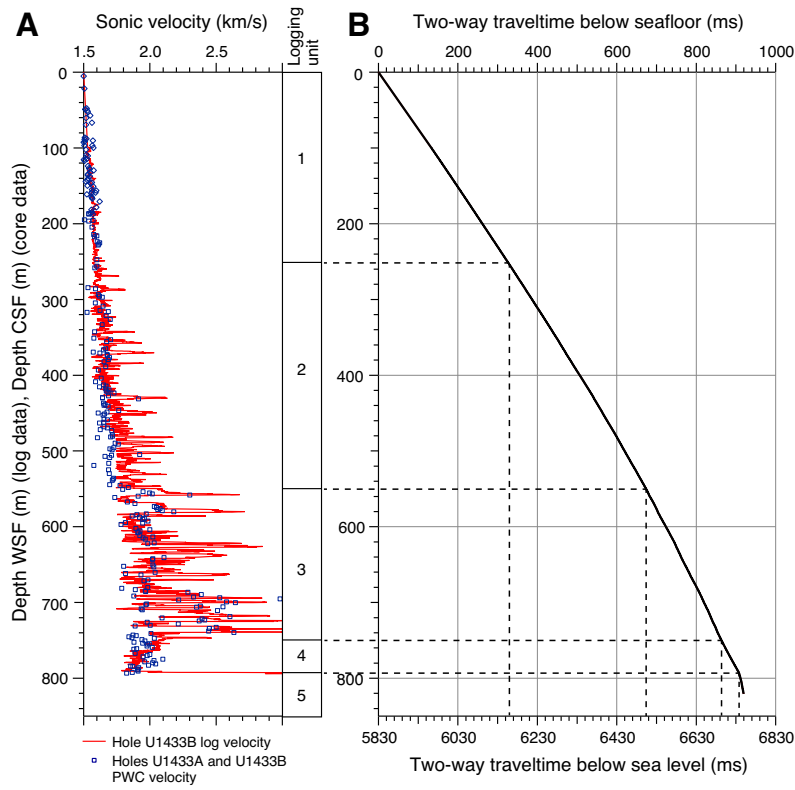


Table T17. APCT-3 temperature measurements, Hole U1433A. [Download table in .csv format.](#)

Core	Depth DSF (m)	Temperature (°C)
Seafloor	0.0	2.5
4H	37.4	6.0
7H	65.9	8.5
10H	94.4	10.1
13H	122.9	12.2

Figure F70. APCT-3 temperature-time series with extrapolated formation temperature estimates, Hole U1433A.

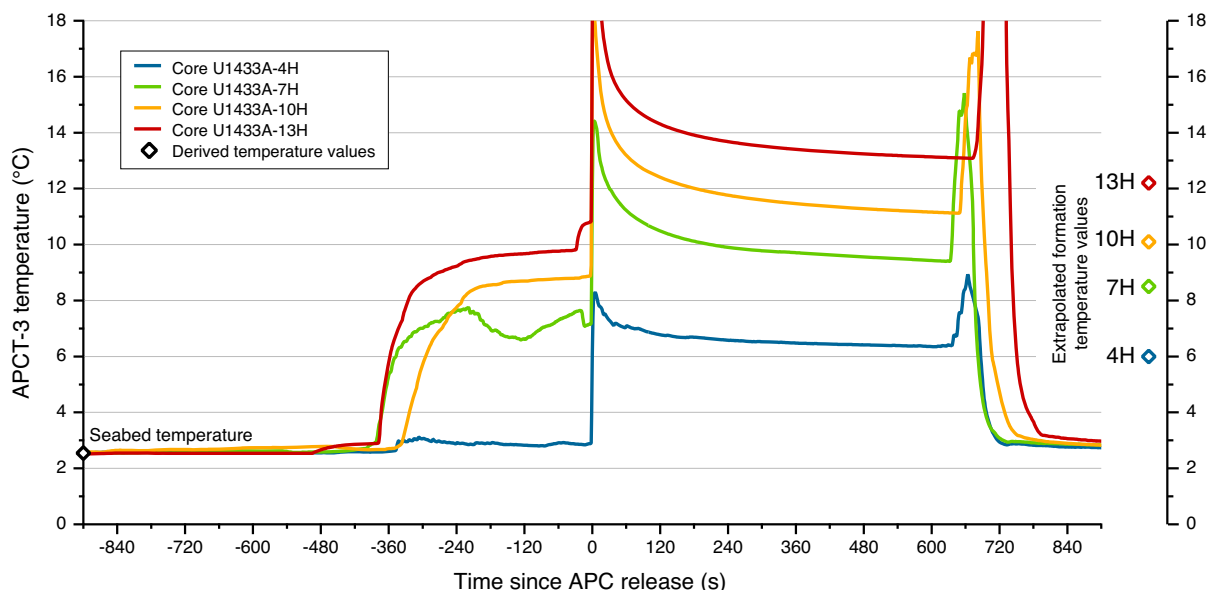
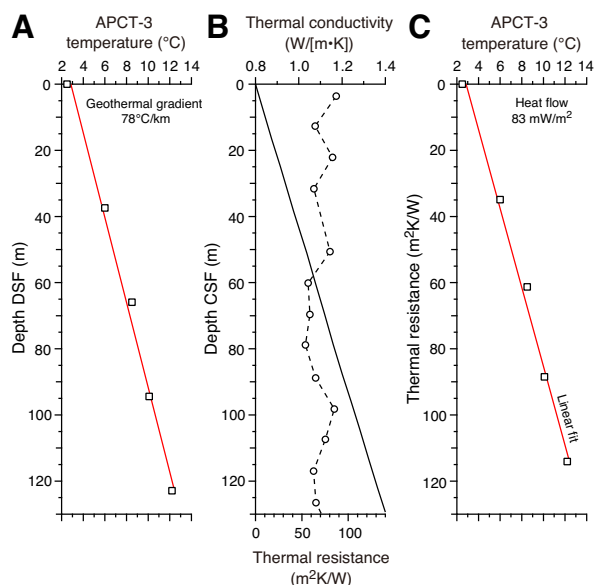


Figure F71. Plots of heat flow calculations, Hole U1433A. A. Sediment temperature. B. Thermal conductivity data from Hole U1433A (circles and dashed line) with calculated thermal resistance (solid line). C. Bullard plot of heat flow calculated from a linear fit of the temperature data.



References

- Alt, J.C., France-Lanord, C., Floyd, P.A., Castillo, P., and Galy, A., 1992. Low-temperature hydrothermal alteration of Jurassic ocean crust, Site 801. In Larson, R.L., Lancelot, Y., et al., *Proceedings of the Ocean Drilling Program, Scientific Results*, 129: College Station, TX (Ocean Drilling Program), 415–427. <http://dx.doi.org/10.2973/odp.proc.sr.129.132.1992>
- Berggren, W.A., Kent, D.V., Swisher, C.C., III, and Aubry, M.-P., 1995. A revised Cenozoic geochronology and chronostratigraphy. In Berggren, W.A., Kent, D.V., Aubry, M.-P., and Hardenbol, J. (Eds.), *Geochronology, Time Scales and Global Stratigraphic Correlation*. Special Publication - SEPM (Society for Sedimentary Geology), 54:129–212. <http://dx.doi.org/10.2110/pec.95.04.0129>
- Bolli, H.M., and Saunders, J.B., 1985. Oligocene to Holocene low latitude planktic foraminifera. In Bolli, H.M., Saunders, J.B., and Perch-Nielsen, K. (Eds.), *Plankton Stratigraphy* (Vol. 1): *Planktic Foraminifera, Calcareous Nannofossils and Calpionellids*: Cambridge, UK (Cambridge University Press), 155–262.
- Bouma, A.H., 1962. *Sedimentology of Some Flysch Deposits: A Graphic Approach to Facies Interpretation*: Amsterdam (Elsevier).
- Briais, A., Patriat, P., and Tapponnier, P., 1993. Updated interpretation of magnetic anomalies and seafloor spreading stages in the South China Sea: implications for the Tertiary tectonics of Southeast Asia. *Journal of Geophysical Research: Solid Earth*, 98(B4):6299–6328. <http://dx.doi.org/10.1029/92JB02280>
- Bryant, W.R., and Bennett, R.H., 1988. Origin, physical, and mineralogical nature of red clays: the Pacific Ocean Basin as a model. *Geo-Marine Letters*, 8(4):189–249. <http://dx.doi.org/10.1007/BF02281640>
- Busch, W.H., Castillo, P.R., Floyd, P.A., and Cameron, G., 1992. Effects of alteration on physical properties of basalts from the Pigafetta and East Mariana Basins. In Larson, R.L., Lancelot, Y., et al., *Proceedings of the Ocean Drilling Program, Scientific Results*, 129: College Station, TX (Ocean Drilling Program), 485–499. <http://dx.doi.org/10.2973/odp.proc.sr.129.139.1992>
- Carter, A., Roques, D., and Bristow, C.S., 2000. Denudation history of onshore central Vietnam: constraints on the Cenozoic evolution of the western margin of the South China Sea. *Tectonophysics*, 322(3–4):265–277. [http://dx.doi.org/10.1016/S0040-1951\(00\)00091-3](http://dx.doi.org/10.1016/S0040-1951(00)00091-3)
- Ekdale, A.A., Bromley, R.G., and Pemberton, S.G. (Eds.), 1984. *Ichnology: The Use of Trace Fossils in Sedimentology and Stratigraphy*. SEPM Short Course, 15.
- Expedition 329 Scientists, 2011. Site U1368. In D'Hondt, S., Inagaki, F., Alvarez Zarikian, C.A., and the Expedition 329 Scientists, *Proceedings of the Integrated Ocean Drilling Program, 329*: Tokyo (Integrated Ocean Drilling Program Management International, Inc.). <http://dx.doi.org/10.2204/iodp.proc.329.106.2011>
- Expedition 330 Scientists, 2012a. Site U1373. In Koppers, A.A.P., Yamazaki, T., Geldmacher, J., and the Expedition 330 Scientists, *Proceedings of the Integrated Ocean Drilling Program, 330*: Tokyo (Integrated Ocean Drilling Program Management International, Inc.). <http://dx.doi.org/10.2204/iodp.proc.330.104.2012>

- Expedition 330 Scientists, 2012b. Site U1376. In Koppers, A.A.P., Yamazaki, T., Geldmacher, J., and the Expedition 330 Scientists, *Proceedings of the Integrated Ocean Drilling Program*, 330: Tokyo (Integrated Ocean Drilling Program Management International, Inc.). <http://dx.doi.org/10.2204/iodp.proc.330.107.2012>
- Fuller, M., 1969. Magnetic orientation of borehole cores. *Geophysics*, 34(5):772–774. <http://dx.doi.org/10.1190/1.1440047>
- Gradstein, F.M., Ogg, J.G., Schmitz, M.D., and Ogg, G.M. (Eds.), 2012. *The Geological Time Scale 2012*: Oxford, UK (Elsevier).
- Hanebuth, T.J.J., and Statteger, K., 2004. Depositional sequences on a late Pleistocene–Holocene tropical siliciclastic shelf (Sunda Shelf, southeast Asia). *Journal of Asian Earth Sciences*, 23(1):113–126. [http://dx.doi.org/10.1016/S1367-9120\(03\)00100-7](http://dx.doi.org/10.1016/S1367-9120(03)00100-7)
- Haq, B.U., Hardenbol, J., and Vail, P.R., 1987. Chronology of fluctuating sea levels since the Triassic. *Science*, 235(4793):1156–1167. <http://dx.doi.org/10.1126/science.235.4793.1156>
- Hékinian, R., Bonté, P., Pautot, G., Jacques, D., Labeyrie, L.D., Mikkelsen, N., and Reys, J.-L., 1989. Volcanism from the South China Sea ridge system. *Oceanologica Acta*, 12(2):101–115.
- Hu, J., Kawamura, H., Hong, H., and Qi, Y., 2000. A review on the currents in the South China Sea: seasonal circulation, South China Sea Warm Current and Kuroshio Intrusion. *Journal of Oceanography*, 56(6):607–624. <http://dx.doi.org/10.1023/A:101117531252>
- Hutchison, C.S., 2004. Marginal basin evolution: the southern South China Sea. *Marine and Petroleum Geology*, 21(9):1129–1148. <http://dx.doi.org/10.1016/j.marpetgeo.2004.07.002>
- Hutchison, C.S., and Vijayan, V.R., 2010. What are the Spratly Islands? *Journal of Asian Earth Sciences*, 39(5):371–385. <http://dx.doi.org/10.1016/j.jseaes.2010.04.013>
- Hyndman, R.D., Erickson, A.J., and Von Herzen, R.P., 1974. Geothermal measurements on DSDP Leg 26. In Davies, T.A., Luyendyk, B.P., et al., *Initial Reports of the Deep Sea Drilling Project*, 26: Washington, DC (U.S. Government Printing Office), 451–463. <http://dx.doi.org/10.2973/dsdp.proc.26.113.1974>
- Ishihara, T., and Kisimoto, K., 1996. Magnetic anomaly map of East Asia, 1:4,000,000 (CD-ROM version). Geological Survey of Japan, Coordinating Committee for Coastal and Offshore Geoscience Programs in East and Southeast Asia (CCOP).
- Jin, Z., Xu, S., and Li, Z., 2002. Inversion of heterogeneous magnetism for seamounts in the South China Sea. *Journal of Ocean University of Qingdao* (English Edition), 32:926–934. (in Chinese)
- Kemp, A.E.S., 1995. Variation of trace fossils and ichnofacies in Neogene and Quaternary pelagic sediments from the eastern equatorial Pacific Ocean (Leg 138). In Piasias, N.G., Mayer, L.A., Janecek, T.R., Palmer-Julson, A., and van Andel, T.H. (Eds.), *Proceedings of the Ocean Drilling Program, Scientific Results*, 138: College Station, TX (Ocean Drilling Program), 177–190. <http://dx.doi.org/10.2973/odp.proc.sr.138.110.1995>
- Kennett, J.P., and Srinivasan, M.S., 1983. *Neogene Planktonic Foraminifera: A Phylogenetic Atlas*: Stroudsburg, PA (Hutchinson Ross).
- Kirschvink, J.L., 1980. The least-squares line and plane and the analysis of palaeomagnetic data. *Geophysical Journal of the Royal Astronomical Society*, 62(3):699–718. <http://dx.doi.org/10.1111/j.1365-246X.1980.tb02601.x>
- Kodama, K.P., 1984. Palaeomagnetism of granitic intrusives from the Precambrian basement under eastern Kansas: orienting drill cores using secondary magnetization components. *Geophysical Journal International*, 76(2):273–287. <http://dx.doi.org/10.1111/j.1365-246X.1984.tb05045.x>
- Le Maitre, R.W., Bateman, P., Dudek, A., Keller, J., Lameyre, J., Le Bas, M.J., Sabine, P.A., Schmid, R., Sorensen, H., Streckeisen, A., Woolley, A.R., and Zanettin, B., 1989. *A Classification of Igneous Rocks and Glossary of Terms*: Oxford, UK (Blackwell Science Publishing).
- Li, C.-F., Lin, J., Kulhanek, D.K., Williams, T., Bao, R., Briais, A., Brown, E.A., Chen, Y., Clift, P.D., Colwell, F.S., Dadd, K.A., Ding, W., Almeida, I.H., Huang, X.-L., Hyun, S., Jiang, T., Koppers, A.A.P., Li, Q., Liu, C., Liu, Q., Liu, Z., Nagai, R.H., Peleo-Alampay, A., Su, X., Sun, Z., Tejada, M.L.G., Trinh, H.S., Yeh, Y.-C., Zhang, C., Zhang, F., Zhang, G.-L., and Zhao, X., 2015a. Expedition 349 summary. In Li, C.-F., Lin, J., Kulhanek, D.K., and the Expedition 349 Scientists, *Proceedings of the Integrated Ocean Drilling Program, 349: South China Sea Tectonics*: College Station, TX (International Ocean Discovery Program). <http://dx.doi.org/10.14379/iodp.proc.349.101.2015>
- Li, C.-F., Lin, J., Kulhanek, D.K., Williams, T., Bao, R., Briais, A., Brown, E.A., Chen, Y., Clift, P.D., Colwell, F.S., Dadd, K.A., Ding, W., Almeida, I.H., Huang, X.-L., Hyun, S., Jiang, T., Koppers, A.A.P., Li, Q., Liu, C., Liu, Q., Liu, Z., Nagai, R.H., Peleo-Alampay, A., Su, X., Sun, Z., Tejada, M.L.G., Trinh, H.S., Yeh, Y.-C., Zhang, C., Zhang, F., Zhang, G.-L., and Zhao, X., 2015b. Methods. In Li, C.-F., Lin, J., Kulhanek, D.K., and the Expedition 349 Scientists, *Proceedings of the Integrated Ocean Drilling Program, 349: South China Sea Tectonics*: College Station, TX (International Ocean Discovery Program). <http://dx.doi.org/10.14379/iodp.proc.349.102.2015>
- Li, C.-F., Lin, J., Kulhanek, D.K., Williams, T., Bao, R., Briais, A., Brown, E.A., Chen, Y., Clift, P.D., Colwell, F.S., Dadd, K.A., Ding, W., Almeida, I.H., Huang, X.-L., Hyun, S., Jiang, T., Koppers, A.A.P., Li, Q., Liu, C., Liu, Q., Liu, Z., Nagai, R.H., Peleo-Alampay, A., Su, X., Sun, Z., Tejada, M.L.G., Trinh, H.S., Yeh, Y.-C., Zhang, C., Zhang, F., Zhang, G.-L., and Zhao, X., 2015c. Site U1431. In Li, C.-F., Lin, J., Kulhanek, D.K., and the Expedition 349 Scientists, *Proceedings of the Integrated Ocean Drilling Program, 349: South China Sea Tectonics*: College Station, TX (International Ocean Discovery Program). <http://dx.doi.org/10.14379/iodp.proc.349.103.2015>
- Li, C.-F., Lin, J., Kulhanek, D.K., Williams, T., Bao, R., Briais, A., Brown, E.A., Chen, Y., Clift, P.D., Colwell, F.S., Dadd, K.A., Ding, W., Almeida, I.H., Huang, X.-L., Hyun, S., Jiang, T., Koppers, A.A.P., Li, Q., Liu, C., Liu, Q., Liu, Z., Nagai, R.H., Peleo-Alampay, A., Su, X., Sun, Z., Tejada, M.L.G., Trinh, H.S., Yeh, Y.-C., Zhang, C., Zhang, F., Zhang, G.-L., and Zhao, X., 2015d. Site U1432. In Li, C.-F., Lin, J., Kulhanek, D.K., and the Expedition 349 Scientists, *Proceedings of the Integrated Ocean Drilling Program, 349: South China Sea Tectonics*: College Station, TX (International Ocean Discovery Program). <http://dx.doi.org/10.14379/iodp.proc.349.104.2015>
- Li, C.-F., Shi, X., Zhou, Z., Li, J., Geng, J., and Chen, B., 2010. Depths to the magnetic layer bottom in the South China Sea area and their tectonic implications. *Geophysical Journal International*, 182(3):1229–1247. <http://dx.doi.org/10.1111/j.1365-246X.2010.04702.x>
- Li, C.-F., Zhou, Z., Li, J., Chen, B., and Geng, J., 2008. Magnetic zoning and seismic structure of the South China Sea ocean basin. *Marine Geophysical Research*, 29(4):223–238. <http://dx.doi.org/10.1007/s11001-008-9059-4>
- Li, C.-F., Zhou, Z., Li, J., Hao, H., and Geng, J., 2007. Structures of the northeasternmost South China Sea continental margin and ocean basin: geophysical constraints and tectonic implications. *Marine Geophysical Research*, 28(1):59–79. <http://dx.doi.org/10.1007/s11001-007-9014-9>
- Li, L., Clift, P.D., and Nguyen, H.T., 2013. The sedimentary, magmatic and tectonic evolution of the southwestern South China Sea revealed by seismic stratigraphic analysis. *Marine Geophysical Research*, 34(3–4):341–365. <http://dx.doi.org/10.1007/s11001-013-9171-y>
- Macdonald, G.A., 1968. Composition and origin of Hawaiian lavas. In Coats, R.R., Hay, R.L., and Anderson, C.A. (Eds.), *Studies in Volcanology—A Memoir in Honor of Howel Williams*. Memoir - Geological Society of America, 116:477–522. <http://dx.doi.org/10.1130/MEM116-p477>
- Macdonald, G.A., and Katsura, T., 1964. Chemical composition of Hawaiian lavas. *Journal of Petrology*, 5(1):82–133. <http://petrology.oxfordjournals.org/content/5/1/82.abstract>
- Martini, E., 1971. Standard Tertiary and Quaternary calcareous nannoplankton zonation. In Farinacci, A. (Ed.), *Proceedings of the Second Planktonic Conference, Roma 1970*: Rome (Edizioni Tecnoscienza), 2:739–785.
- Pautot, G., Rangin, C., Briais, A., Tapponnier, P., Beuzart, P., Lericolais, G., Mathieu, X., Wu, J., Han, S., Li, H., Lu, Y., and Zhao, J., 1986. Spreading direction in the central South China Sea. *Nature*, 321(6066):150–154. <http://dx.doi.org/10.1038/321150a0>
- Pimmel, A., and Claypool, G., 2001. Introduction to shipboard organic geochemistry on the JOIDES Resolution. *ODP Technical Note*, 30. <http://dx.doi.org/10.2973/odp.tn.30.2001>

- Pribnow, D., Kinoshita, M., and Stein, C., 2000. *Thermal Data Collection and Heat Flow Recalculations for Ocean Drilling Program Legs 101–180*: Hanover, Germany (Institute for Joint Geoscientific Research, Institut für Geowissenschaftliche Gemeinschaftsaufgaben [GGA]). <http://www-odp.tamu.edu/publications/heatflow/ODPReprt.pdf>
- Roberts, A.P., 2008. Geomagnetic excursions: knowns and unknowns. *Geophysical Research Letters*, 35(17):L17307. <http://dx.doi.org/10.1029/2008GL034719>
- Sanfilippo, A., and Nigrini, C., 1998. Code numbers for Cenozoic low latitude radiolarian biostratigraphic zones and GPTS conversion tables. *Marine Micropaleontology*, 33(1–2):109–117, 121–156. [http://dx.doi.org/10.1016/S0377-8398\(97\)00030-3](http://dx.doi.org/10.1016/S0377-8398(97)00030-3)
- Shibuya, H., Merrill, D.L., Hsu, V., and Leg 124 Shipboard Scientific Party, 1991. Paleogene counterclockwise rotation of the Celebes Sea—orientation of ODP cores utilizing the secondary magnetization. In Silver, E.A., Rangin, C., von Breyman, M.T., et al., *Proceedings of the Ocean Drilling Program, Scientific Results*, 124: College Station, TX (Ocean Drilling Program), 519–523. <http://dx.doi.org/10.2973/odp.proc.sr.124.169.1991>
- Steuer, S., Franke, D., Meresse, F., Savva, D., Pubellier, M., and Auxietre, J.-L., in press. Oligocene–Miocene carbonates and their role for constraining the rifting and collision history of the Dangerous Grounds, South China Sea. *Marine and Petroleum Geology*. <http://dx.doi.org/10.1016/j.marpetgeo.2013.12.010>
- Theyer, F., Mato, C.Y., and Hammond, S.R., 1978. Paleomagnetic and geochronologic calibration of latest Oligocene to Pliocene radiolarian events, equatorial Pacific. *Marine Micropaleontology*, 3(4):377–395. [http://dx.doi.org/10.1016/0377-8398\(78\)90019-1](http://dx.doi.org/10.1016/0377-8398(78)90019-1)
- Tu, K., Flower, M.F.J., Carlson, R.W., Xie, G., Chen, C.-Y., and Zhang, M., 1992. Magmatism in the South China Basin: 1. Isotopic and trace-element evidence for an endogenous Dupal mantle component. *Chemical Geology*, 97(1–2):47–63. [http://dx.doi.org/10.1016/0009-2541\(92\)90135-R](http://dx.doi.org/10.1016/0009-2541(92)90135-R)
- Vail, P.R., Mitchum, R.M., Jr., Todd, R.G., Widmier, J.M., Thompson, S.I., Sangree, J.B., Bubb, J.N., and Hatlelid, W.G., 1977. Seismic stratigraphy and global changes of sea level, Parts 1–11. In Payton, C.E. (Ed.), *Seismic Stratigraphy: Applications to Hydrocarbon Exploration*. AAPG Memoir, 26:51–212.
- Wade, B.S., Pearson, P.N., Berggren, W.A., and Pälike, H., 2011. Review and revision of Cenozoic tropical planktonic foraminiferal biostratigraphy and calibration to the geomagnetic polarity and astronomical time scale. *Earth-Science Reviews*, 104(1–3):111–142. <http://dx.doi.org/10.1016/j.earscirev.2010.09.003>
- Wang, R., and Abelmann, A., 1999. Pleistocene radiolarian biostratigraphy in the South China Sea. *Science in China (Series D)*, 42(5):537–543.
- Wang, X.-C., Li, Z.-X., Li, X.-H., Li, J., Liu, Y., Long, W.-G., Zhou, J.-B., and Wang, F., 2012. Temperature, pressure, and composition of the mantle source region of late Cenozoic basalts in Hainan Island, SE Asia: a consequence of a young thermal mantle plume close to subduction zones? *Journal of Petrology*, 53(1):177–233. <http://dx.doi.org/10.1093/petrology/egr061>
- Wetzel, A., 2002. Modern *Nereites* in the South China Sea—ecological association with redox conditions in the sediment. *Palaiois*, 17(5):507–515. [http://dx.doi.org/10.1669/0883-1351\(2002\)017<0507:MNITSC>2.0.CO;2](http://dx.doi.org/10.1669/0883-1351(2002)017<0507:MNITSC>2.0.CO;2)
- Yao, B., 1995. Characteristics and tectonic significance of the Zhongnan-Lile fault. *Geological Research of South China Sea, Memoir*, 7:1–14. (in Chinese)
- Zhang, G., Smith-Duque, C., Tang, S., Li, H., Zarikian, C., D'Hondt, S., Inagaki, F., and IODP Expedition 329 Scientists, 2012. Geochemistry of basalts from IODP Site U1365: implications for magmatism and mantle source signatures of the mid-Cretaceous Osborn Trough. *Lithos*, 144–145:73–87. <http://dx.doi.org/10.1016/j.lithos.2012.04.014>
- Zhang, G., Zeng, Z., Yin, X., Wang, X., and Chen, D., 2009. Deep fractionation of clinopyroxene in the East Pacific Rise 13°N: evidence from high MgO MORB and melt inclusions. *Acta Geologica Sinica*, 83(2):266–277. <http://dx.doi.org/10.1111/j.1755-6724.2009.00030.x>
- Zhang, G.-L., Chen, L.-H., and Li, S.-Z., 2013. Mantle dynamics and generation of a geochemical mantle boundary along the East Pacific Rise—Pacific/Antarctic Ridge. *Earth and Planetary Science Letters*, 383:153–163. <http://dx.doi.org/10.1016/j.epsl.2013.09.045>
- Zhang, G.-L., Zong, C.-L., Yin, X.-B., and Li, H., 2012. Geochemical constraints on a mixed pyroxenite–peridotite source for East Pacific Rise basalts. *Chemical Geology*, 330–331:176–187. <http://dx.doi.org/10.1016/j.chemgeo.2012.08.033>
- Zijderveld, J.D.A., 1967. AC demagnetization of rocks: analysis of results. In Collinson, D.W., Creer, K.M., and Runcorn, S.K. (Eds.), *Methods in Palaeomagnetism*: Amsterdam (Elsevier), 254–286.

Site U1434¹



Contents

- 1 Background and objectives
- 1 Operations
- 3 Lithostratigraphy
- 8 Biostratigraphy
- 10 Igneous petrology and alteration
- 14 Structural geology
- 14 Geochemistry
- 18 Microbiology
- 19 Paleomagnetism
- 20 Physical properties
- 21 References

C.-F. Li, J. Lin, D.K. Kulhanek, T. Williams, R. Bao, A. Briais, E.A. Brown, Y. Chen, P.D. Clift, F.S. Colwell, K.A. Dadd, W.-W. Ding, I. Hernández-Almeida, X.-L. Huang, S. Hyun, T. Jiang, A.A.P. Koppers, Q. Li, C. Liu, Q. Liu, Z. Liu, R.H. Nagai, A. Peleo-Alampay, X. Su, Z. Sun, M.L.G. Tejada, H.S. Trinh, Y.-C. Yeh, C. Zhang, F. Zhang, G.-L. Zhang, and X. Zhao²

Keywords: International Ocean Discovery Program, IODP, *JOIDES Resolution*, Expedition 349, Site U1434, South China Sea, pelagic red clay, nannofossils, seamount volcanoclastics, Ar-Ar dating, mid-ocean-ridge basalt, calcite compensation depth, basalt alteration, seafloor spreading, cooling effect, gravity flow deposit

Background and objectives

Site U1434 (proposed Site SCS-4E) is located about 40 km northwest of Site U1433 and is directly on the uplifted shoulder of the relict spreading center in the Southwest Subbasin (Figures F1, F2, F3). This site is also located just south of a large seamount that formed near the relict spreading center after the termination of seafloor spreading. During coring at Site U1433, we decided to use some of our remaining time to core at a second site in the Southwest Subbasin to obtain basement samples more proximal to the extinct spreading center. Site U1434 also offered the opportunity to sample volcanoclastic material from the nearby seamount, which can be compared to the seamounts located near Site U1431 in the East Subbasin.

Sites U1434 and U1433 form a short sampling transect in the Southwest Subbasin (see Figure F7 in the Expedition 349 summary chapter [Li et al., 2015a]), and with age control from these two sites, the evolution of the Southwest Subbasin can be better understood. Coring at these sites should help to explain the sharp differences in magnetic amplitude between the East and Southwest Subbasins and test the existing opening models for the Southwest Subbasin (e.g., Pautot et al., 1986). Coring will help determine the age of this subbasin near the end of spreading and allow for correlation of ages from magnetic anomalies with biostratigraphic, magnetostratigraphic, and radiometric ages. The apparent weak magnetization in basement rocks (Li et al., 2008) will be examined through petrological analyses of chemical compositions and measurements of magnetic susceptibility. Rock samples cored here will place constraints on mantle evolution and oceanic crustal accretion, terminal processes of seafloor spreading, and the timing and episodes of postspreading seamount volcanism at the relict spreading center.

Operations

Site U1434 was an alternate site that was originally planned to core from the seafloor with the advanced piston corer/extended core barrel (APC/XCB) systems to refusal, drop a free-fall funnel, change to the rotary core barrel (RCB), and then core 100 m into basement. Because of time considerations, the plan was modified so that we drilled without coring to ~200 m below seafloor (mbsf) using the RCB and then cored into basement as deeply as time permitted. Logging would then be considered depending on hole depth and condition. Hole U1434A was drilled to 197.0 mbsf and then cored with the RCB (Table T1). Basement was encountered at ~280 mbsf, and the hole was advanced by rotary coring to a final depth of 312.5 mbsf. The hole was terminated because of poor hole conditions and poor recovery. In Hole U1434A, we drilled one interval of 197.0 m. The RCB was deployed 14 times, recovering 26.43 m of core over 115.5 m of penetration (22.9% recovery).

Transit to Site U1434

After an 18 nmi transit lasting 2 h, the vessel arrived at Site U1434 and switched into dynamic positioning mode at 0048 h (UTC + 8 h) on 20 March 2014. At 0110 h, an acoustic positioning beacon was deployed. The position reference was a combination of GPS signals and a single acoustic beacon.

Hole U1434A

An RCB bottom-hole assembly (BHA) was assembled with a new RCB C-7 bit. The core barrels were spaced out at the surface, and the 172.07 m BHA assembled. The BHA was lowered to 4000.9 m below rig floor (mbrf), and the top drive was picked up and spaced out to 4020.0 mbrf to spud Hole U1434A. A center bit

¹ Li, C.-F., Lin, J., Kulhanek, D.K., Williams, T., Bao, R., Briais, A., Brown, E.A., Chen, Y., Clift, P.D., Colwell, F.S., Dadd, K.A., Ding, W.-W., Hernández-Almeida, I., Huang, X.-L., Hyun, S., Jiang, T., Koppers, A.A.P., Li, Q., Liu, Q., Liu, Z., Nagai, R.H., Peleo-Alampay, A., Su, X., Sun, Z., Tejada, M.L.G., Trinh, H.S., Yeh, Y.-C., Zhang, C., Zhang, F., Zhang, G.-L., and Zhao, X., 2015. Site U1434. In Li, C.-F., Lin, J., Kulhanek, D.K., and the Expedition 349 Scientists, *Proceedings of the International Ocean Discovery Program, 349: South China Sea Tectonics*: College Station, TX (International Ocean Discovery Program). <http://dx.doi.org/10.14379/iodp.proc.349.106.2015>

² Expedition 349 Scientists' addresses.

Figure F1. A. Bathymetric map of South China Sea region. Solid yellow circles = Expedition 349 sites. Pink circles = ODP Leg 184 sites. Yellow dashed line = inferred continent/ocean boundary, blue lines = fossil South China Sea spreading center, white flagged line = Manila Trench. B. Detailed bathymetry around Sites U1433 and U1434 (red box in A) showing nearby seamounts, Dangerous Grounds, and Reed Bank.

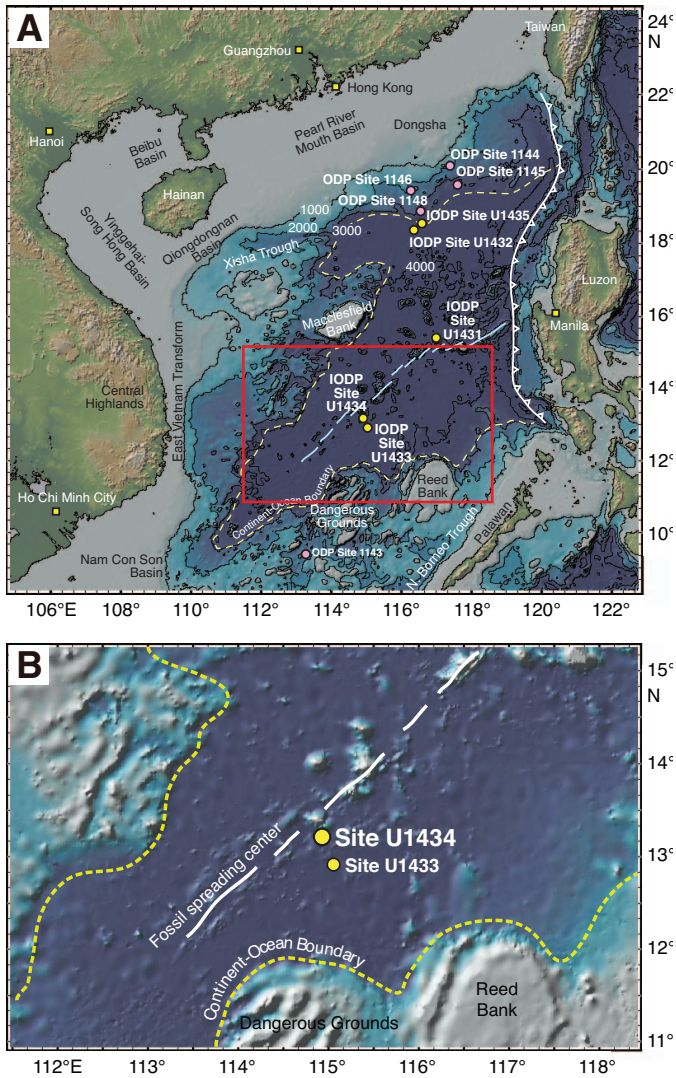


Figure F2. Magnetic anomalies near Sites U1433 and U1434 (data from Ishihara and Kisimoto, 1996). Bold black lines mark 3000 m isobaths outlining seamounts. Magnetic anomaly picks are from Briais et al. (1993).

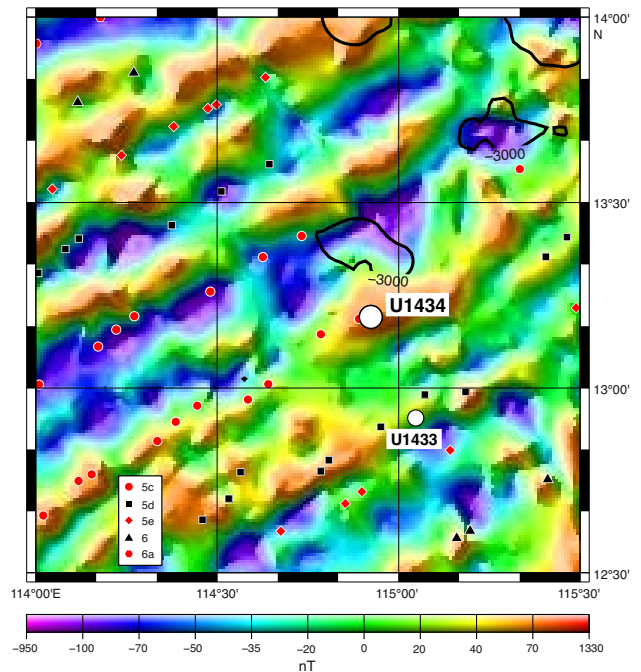
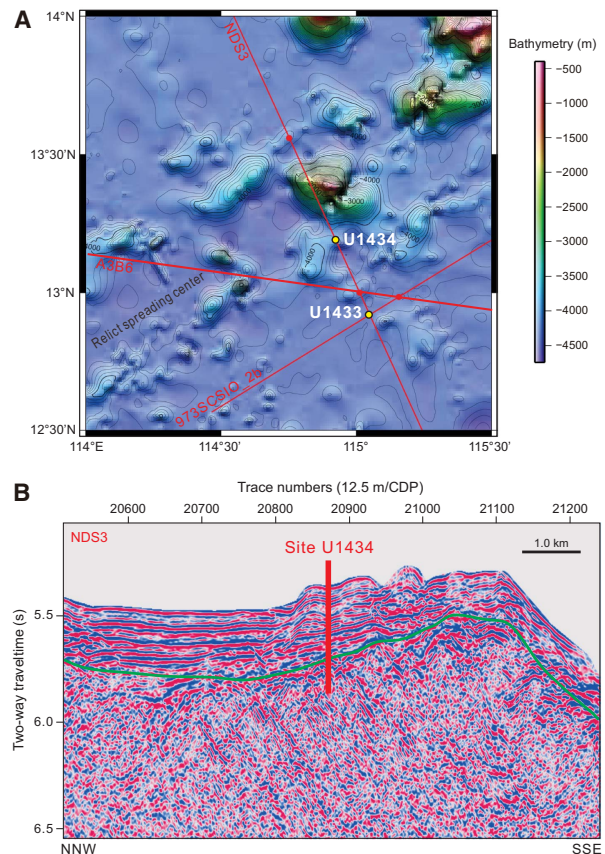


Figure F3. A. Regional bathymetric map showing seismic reflection profiles (red lines) and locations of Sites U1433 and U1434. Contour interval = 100 m. B. Seismic profile Line NDS3, with location of Site U1434. CPD = common depth point. Green line = interpreted top of basement.



was dropped and pumped down the drill string to land out in the bit. Hole U1434A was spudded at 1215 h on 20 March 2014. The estimated depth of the seafloor was determined to be 4020.4 mbrf using the precision depth recorder. The final seafloor depth for the hole was 4020.4 mbrf (4009.0 m below sea level [mbsl]), which was determined by tagging the seafloor with the drill bit. Hole U1434A was advanced by drilling without coring from the seafloor to 4217.4 mbrf (197.0 mbsf) over a 10 h period. The center bit was then pulled, and a core barrel dropped to start continuous RCB coring from Core 349-U1434A-2R. Coring continued through Core 15R to a total depth of 4332.9 mbrf (312.5 mbsf). Microspheres were deployed in each RCB core catcher sub for the duration of RCB coring. We encountered the sediment/basement interface in Core 10R, with the formation change at ~280 mbsf. Coring continued into acoustic basement from Core 10R through 15R to a total depth of 4332.9 mbrf (312.5 mbsf). Half-cores were started with Core 12R and continued to total depth. Penetration rates varied

Table T1. Coring summary, Site U1434. CSF = core depth below seafloor, DRF = drilling depth below rig floor, DSF = drilling depth below seafloor. R = rotary core barrel, numeric core type = drilled interval. RCB = rotary core barrel. [Download table in .csv format.](#)

Hole U1434A												
Latitude: 13°11.5080'N												
Longitude: 114°55.4005'E												
Water depth (m): 4009												
Date started (UTC): 19 March 2014, 1648 h												
Date finished (UTC): 22 March 2014, 1548 h												
Time on hole (days): 3.0												
Seafloor depth (m DRF): 4020.4												
Seafloor depth calculation method: seafloor tag with drill bit												
Rig floor to sea level (m): 11.40												
Drilling System: 9-7/8 inch RCB bit with 172.07 m BHA												
Penetration depth (mbsf): 312.50												
Cored interval (m): 115.50												
Recovered length (m): 26.43												
Recovery (%): 23												
Drilled interval (m): 197												
Drilled interval (no.): 1												
Total cores (no.): 14												
RCB cores (no.): 14												
Age of oldest sediment cored: middle Miocene												
Core	Date (2014)	Time UTC (h)	Depth DSF (m)		Interval advanced (m)	Depth CSF (m)		Length of core recovered (m)	Length of core cored (m)	Recovery (%)	Sections (no.)	Comments
			Top of interval	Bottom of interval		Top of cored interval	Bottom of cored interval					
349-U1434A-												
11	20 Mar	1525	0	197.00	197.0	***Drilled from 0 to 197.0 m DSF without coring***						
2R	20 Mar	1630	197.00	206.00	9.0	197.00	197.55	0.55	0.55	6	2	Microspheres
3R	20 Mar	1830	206.00	215.70	9.7	206.00	209.27	3.27	3.27	34	4	Microspheres
4R	20 Mar	2020	215.70	225.40	9.7	215.70	216.49	0.79	0.79	8	2	Microspheres
5R	20 Mar	2145	225.40	235.10	9.7	225.40	225.82	0.42	0.42	4	1	Microspheres
6R	20 Mar	2320	235.10	244.80	9.7	235.10	239.72	4.62	4.62	48	4	Microspheres
7R	21 Mar	0050	244.80	254.50	9.7	244.80	247.23	2.43	2.43	25	3	Microspheres
8R	21 Mar	0220	254.50	264.20	9.7	254.50	258.82	4.32	4.32	45	4	Microspheres
9R	21 Mar	0350	264.20	273.90	9.7	264.20	266.71	2.51	2.51	26	3	Microspheres
10R	21 Mar	0610	273.90	283.60	9.7	273.90	278.46	4.56	4.56	47	5	Microspheres
11R	21 Mar	1405	283.60	293.30	9.7	283.60	284.63	0.82	1.03	8	1	Microspheres
12R	21 Mar	1620	293.30	298.10	4.8	293.30	293.95	0.66	0.65	10	1	Microspheres
13R	21 Mar	1910	298.10	302.90	4.8	298.10	298.85	0.75	0.75	10	1	Microspheres
14R	21 Mar	2320	302.90	307.70	4.8	302.90	303.56	0.66	0.66	10	1	Microspheres
15R	22 Mar	0220	307.70	312.50	4.8	307.70	308.65	0.95	0.95	15	1	Microspheres
Total:					312.5			26.43	27.51	21	33	

from 1.57 to 5.76 m/h over the basement interval. Coring was finally halted because of poor core recovery coupled with high torque and poor coring conditions. The total depth of Hole U1434A was reached at 0925 h on 22 March. After reaching total depth, the final core was pulled to the surface and laid out. At the completion of coring Hole U1434A, 14 RCB cores had been cut over a 115.5 m interval, recovering 26.43 m of core (22.9% recovery).

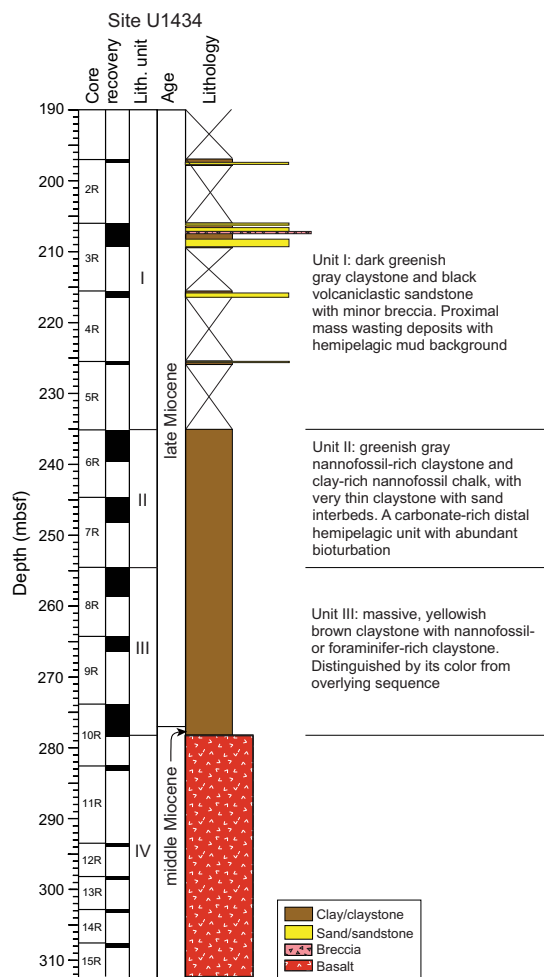
After retrieving the final core, we attempted to pull the drill string from the hole; however, the high torque and high overpull made this impossible. After 1.5 h of working the pipe with a combination of high torque (900 A), overpull, and constant pumping action, the drill string came free and was pulled out of the hole with the top drive to 4117.4 mbrf (97.0 mbsf). The top drive was then set back, and the drill string was tripped to the surface. The bit cleared the seafloor at 1500 h and cleared the rotary table at 2300 h. After securing the rig floor for transit and pulling the hydrophones and thrusters, the vessel switched to cruise mode and began the transit to Site U1435 at 2348 h on 22 March. Total time spent in Hole U1434A was 71.0 h (3.0 days).

Lithostratigraphy

Lithostratigraphic units

Four lithostratigraphic units are defined within the cored sequence at Site U1434 based on a combination of visual core description and smear slide and thin section inspection as well as scanning for an array of physical properties, including magnetic susceptibility and color spectra (see [Lithostratigraphy](#) and [Physical properties](#) in the Methods chapter [Li et al., 2015b] for details). Three sedimentary units overlie a single igneous unit in the basaltic basement (Figures F4, F5). Unit I is composed of interbedded dark greenish gray claystone and black sandstone with occasional volcanoclastic breccia intervals. Unit II contains thick greenish gray nannofossil-rich claystone with very thin sandstone interbeds. Unit III dominantly consists of massive yellowish brown claystone with nannofossil- or foraminifer-rich claystone. This unit lies directly on the basaltic basement. Unit IV is discussed in detail in [Igneous petrology and alteration](#).

Figure F4. Lithostratigraphy summary and interpretation of depositional processes, Site U1434.



Unit descriptions

Unit I (197.00–235.10 mbsf)

Interval: 349-U1434A-2R-1, 0 cm, through 6R-1, 0 cm
 Depth: 197.00–235.10 mbsf
 Age: late Miocene

Unit I has extremely poor recovery in each core. Based on the recovered lithologies, we conclude that the unit is composed of interbedded claystone and sandstone with occasional volcaniclastic breccia intervals. Sandstone forms the majority of the recovered material (Figure F6). The claystone is mottled greenish and light buff brown with browner sediment preferentially found in burrows. The unit is marked by strong bioturbation within the claystone intervals that form ~40% of the total recovered sediment. The trace fossil assemblage in the claystone intervals is indicative of sedimentation in deep water (i.e., lower bathyal or abyssal depths, >2000 m), with assemblages dominated by *Chondrites* and *Zoophycos*, although vertical burrows are also noted.

Sandstone beds are typically dark gray or black and volcaniclastic in composition. They are interpreted to be relatively proximal deposits based on their medium- to coarse-sand grain size, and the presence of minor granule-sized breccia intervals. The grains are relatively angular and often moderately or even poorly sorted, especially at the base of clastic intervals. Sediment appears to have been

Figure F5. Correlation of lithostratigraphic units with magnetic susceptibility and reflectance spectroscopy data (after 20-point running average), Site U1434. Note the sharp increase in reflectance a* and b* at the Unit II/III boundary, which defines the transition.

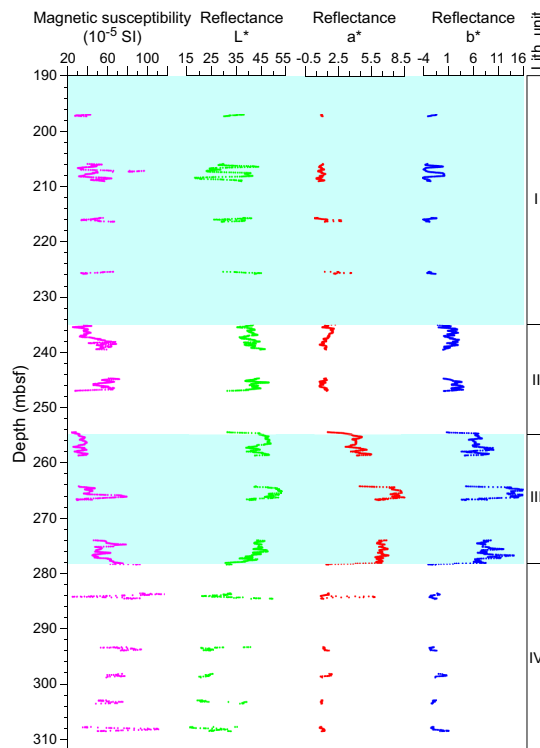
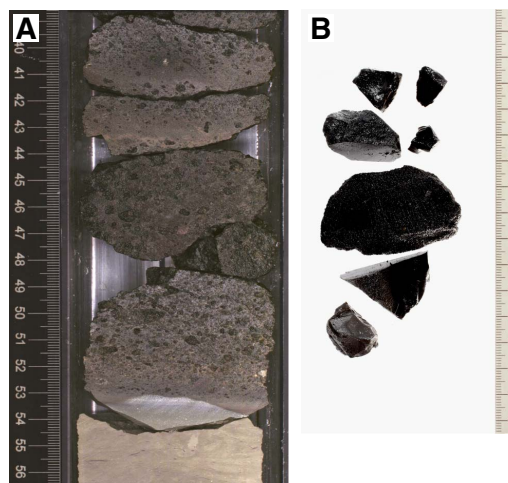


Figure F6. Volcaniclastic sandstone in Hole U1434A, Unit I. A. 3R-2A, 39–56 cm. B. 4R-1A, 17–32 cm.



transported by high-energy currents inferred from the observed parallel lamination within otherwise massive sandstone beds (Figure F7). More rarely, we observed ripple cross-lamination within coarse-grained, volcanic glass-rich sands that fine upward (Figure F8), indicative of a high-energy depositional environment. Some of the coarser intervals have a carbonate sand component, especially toward the base of the unit, although volcaniclastic material dominates the sand-sized fraction in the unit overall. Sandstone beds have sharp erosive bases and show poorly defined fining-upward se-

Figure F7. Gravity flow deposits in Hole U1434A, Unit I. A. Coarse-grained volcanoclastic sandstone and breccia (3R-1A, 5–22 cm). B. Graded sandstone with parallel and wavy laminations (3R-3A, 23–38 cm). C. Coarse-grained volcanoclastic sand grading upward into mottled greenish claystone with silt (4R-1A, 14–21 cm).

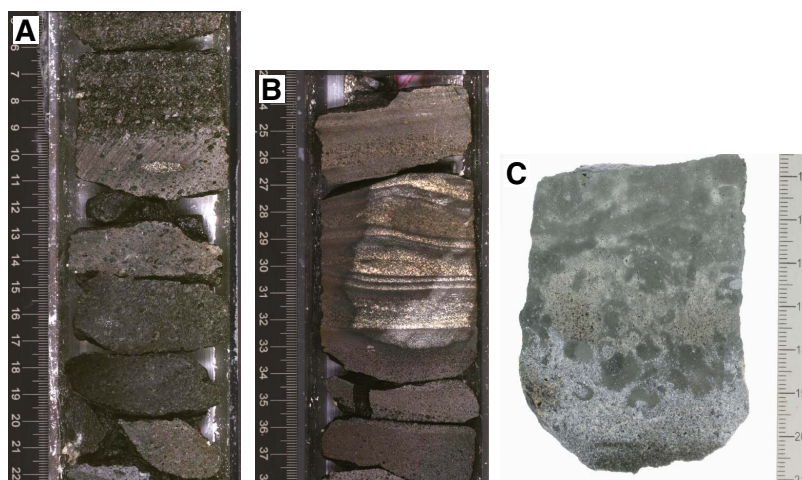
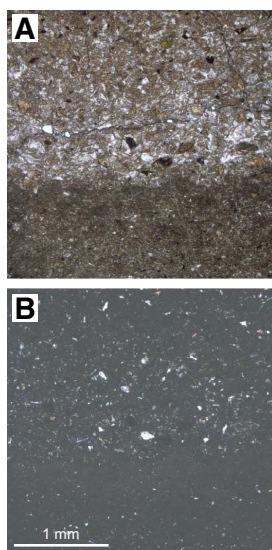


Figure F8. Laminated sandstone in Hole U1434A, Unit I, showing coarse-grained volcanic glass sands fining upward and with a sharp depositional base with the underlying fine-grained volcanic material (Sample 3R-3, 31 cm). A. Plane-polarized light (PPL). B. Cross-polarized light (XPL).



quences. Some of the beds have gradational upper contacts, passing uphole progressively into claystone intervals, although a minority of the sandstone intervals have sharp tops with a planar contact juxtaposing medium-grained sandstone directly with the overlying claystone.

We interpret the sandstone beds to be the product of gravity flow sedimentation during mass wasting. The claystone represents background hemipelagic sedimentation related to distal sediment flux. The lack of well-defined or expanded (>10 cm) graded tops indicates that there was little fine-grained material involved with these gravity flows. The common poor sorting of grains is suggestive of relatively rapid sedimentation close to the source, likely from a local volcanic edifice.

Unit II (235.10–254.59 mbsf)

Interval: 349-U1434A-6R-1, 0 cm, through 8R-1, 9 cm

Depth: 235.10–254.59 mbsf

Age: late Miocene

Unit II has better recovery and is finer grained than Unit I. The unit is dominated by nannofossil-rich claystone and nannofossil chalk with significant but variable quantities of clay. The color of the sediment varies at the decimeter scale as a result of the changing balance between carbonate and clay contents. The sediment is locally light greenish gray, reflecting higher biogenic carbonate content over those intervals. Bioturbation showing a typical deepwater assemblage is pervasive, and particularly visible in the interfaces between different sediment intervals. Compared to other ichnofacies seen in the Southwest Subbasin, we note fewer *Chondrites* and more large trace fossils, including *Planolites*, *Zoophycos*, and *Palaeophycus* (Figure F9), which are observed in present-day sediments in the South China Sea (Wetzel, 2009). The claystone is not purely composed of clay minerals and often contains fragments of volcanic glass, quartz silt, and large quantities of biogenic carbonate, largely in the form of nannofossils (Figure F10). Apart from bioturbation, the sediment is massive, suggesting no current influence during sedimentation. Although Unit II is distinguished from Unit I by its lack of significant sand content, we noted several very thin interbeds of graded claystone with sand that have erosive bases and gradational contacts with the overlying claystone. We interpret these intervals to be turbidites (Figure F11). These deposits are volumetrically insignificant. Overall, Unit II is more calcareous, more biogenic, and less siliciclastic than the overlying unit.

Unit III (254.59–278.27 mbsf)

Interval: 349-U1434A-8R-1, 9 cm, through 10R-CC, 13 cm

Depth: 254.59–278.27 mbsf

Age: latest middle to late Miocene

Unit III was recovered in three cores immediately overlying the basaltic basement. Like Unit II, this unit is dominated by fine-grained sediment, in particular claystone with variable amounts of

Figure F9. Nanfossil-rich claystone with heavy bioturbation in Hole U1434A, Unit II. Burrows are dominated by *Planolites*, *Palaeophycus*, and *Zoophycos*. A. Large vertical *Planolites* burrow (6R-1A, 4–22 cm). B. Inclined *Zoophycos* burrow (6R-1A, 44–59 cm). C. *Palaeophycus* burrows (7R-1A, 5–21 cm).

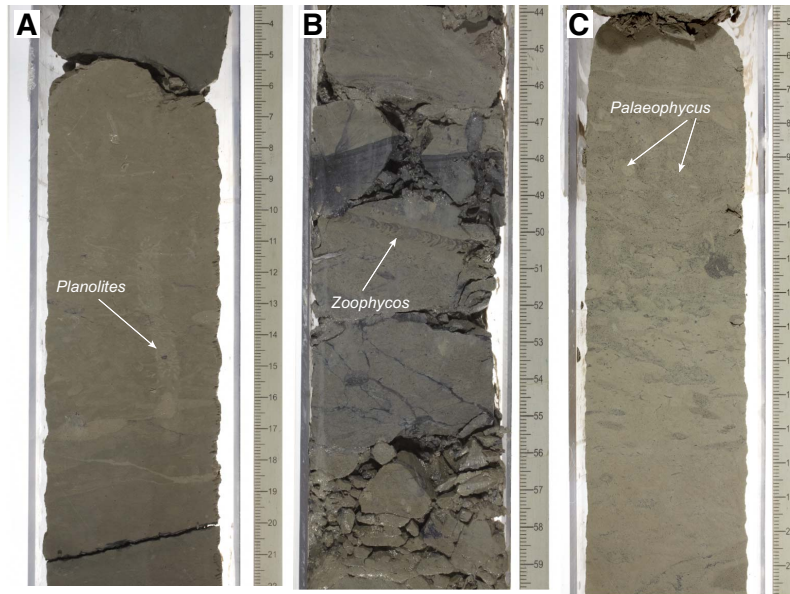
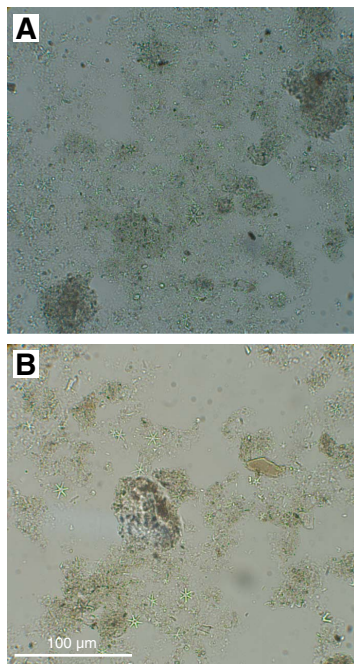
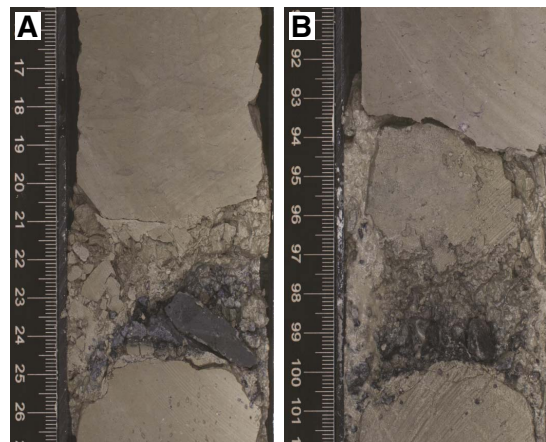


Figure F10. Typical nanofossil-rich claystone in Hole U1434A, Unit II (PPL). A. Nanofossil-rich claystone with minor quartz silt (6R-1A, 3 cm). B. Nanofossil-rich claystone with feldspar silt grain (7R-1A, 35 cm).



nanofossils that form the primary carbonate component in this sequence. This unit is primarily distinguished from Unit II by its color, which tends to be more yellowish or reddish brown compared to the greenish gray tones associated with the overlying unit (Figure F12). The claystone is especially saturated in dark yellowish brown tones in Core 349-U1434A-10R and becomes progressively lighter toward the unit top.

Figure F11. Very thin, dark sand layers with erosive bases, fining upward into carbonate-rich claystone in Hole U1434A, Unit II (6R-3A, (A) 16–26 cm, and (B) 91–102 cm).



The boundary between this unit and the overlying Unit II is best observed in the color reflectance data (Figure F5) rather than in the lithology. As with Unit II, the sediment tends to be rather massive and structureless and shows very little evidence for current influence during sedimentation. The most obvious sedimentary structures are bioturbation features, which are relatively large and favor *Planolites* and vertical burrows rather than the delicate, branching *Chondrites* forms (Figure F12). At interval 349-U1434A-9R-1A, 13–16 cm, we identified a particularly large *Thalassionoides*-type burrow measuring 2.5 cm across. There is minor synsedimentary deformation in the form of faulting. Because some faults are small and do not cross the entire core, we suggest that movement occurred in a steep slope environment soon after the sediments had been consolidated (Figure F13). Foraminifers are clearly visible in this unit, especially in Core 349-U1434A-10R, where they are apparent on the

Figure F12. Burrows in yellowish brown claystone in Hole U1434A, Unit III. A. *Planolites* burrows (8R-2A, 0–18 cm). B. *Thalassionoides* and *Planolites* burrows (9R-1A, 6–22 cm).

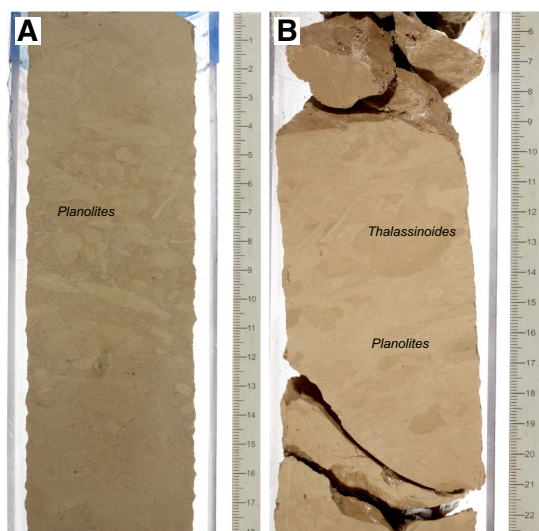
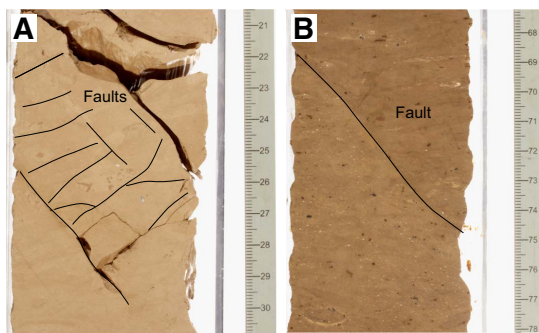


Figure F13. Small faults showing that tectonic activity affected Hole U1434A, Unit III. A. Small faults cutting burrows (9R-1A, 21–31 cm). B. Fault separating different colored claystone (10R-1A, 68–78 cm).



core surface as small white dots against the background of dark yellowish brown clay (Figure F14). In the lowermost 1 m of the unit are well-formed calcite crystals within an otherwise clay-rich sediment. These crystals do not show any evidence of having been redeposited or eroded and are assumed to have been recrystallized in situ. When these crystals are present, we see no other types of calcite of biogenic origin within the clay. Banding within the unit reflects variable amounts of carbonate versus pure clay material, which results in color variability. Typically, the different lithologies grade from one into the other with very little evidence of sharp or erosive boundaries within the unit; however, different-colored claystone intervals are juxtaposed across a fault at Section 349-U1434A-10R-1A, 71 cm (Figure F13B). The effects of diagenesis are visible in this unit, and are possibly caused by fluids derived from fluid-basalt interaction or by an increase in heat flow within the basin. The mottled yellowish brown and greenish claystone contains authigenic carbonate grains and abundant pyrite crystals (Figure F15).

We interpret Unit III to be largely the product of hemipelagic sedimentation with open-ocean biogenic carbonate mixing with distal clay derived from an adjacent continental margin, although exactly which landmass is the source of the clay is not apparent from

Figure F14. Yellowish brown claystone with planktonic foraminifers (10R-2A, 84 cm), showing well-preserved species of (a) *Dentoglobigerina altispira* and (b) *Globigerinoides sacculifer* (PPL).

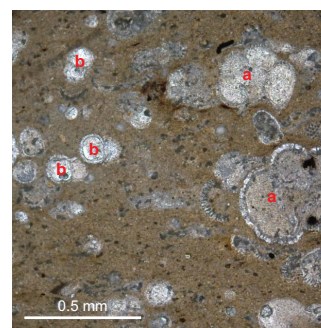
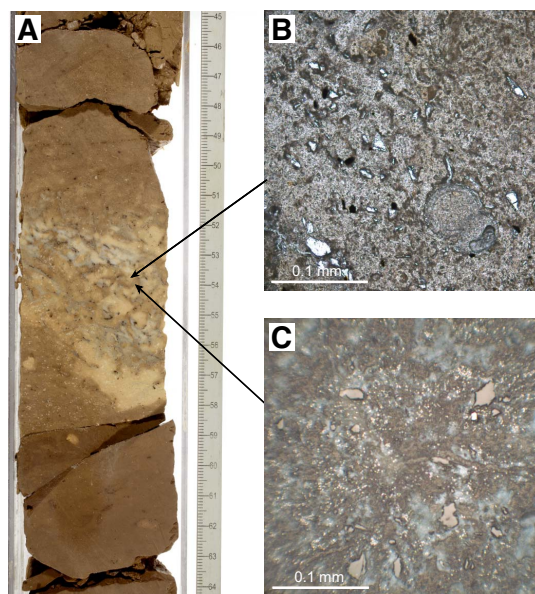


Figure F15. Yellowish brown and greenish mottled claystone, Hole U1434A (10R-3A, 45–64 cm). A. Mottled yellowish and greenish claystone with tiny pyrite microcrystals. B. Clay-sized grains with volcanic glass and plagioclase silt; authigenic carbonate occurs with the clay grains. Note the well-preserved planktonic foraminifer *Globigerinoides sacculifer* (PPL). C. Microcrystals of pyrite (10R-3, 53 cm) (reflected light).



shipboard measurements alone. Strong current activity does not appear to have been important during the deposition of this unit, nor is there evidence to indicate hydrothermal influences or alteration after sedimentation beyond normal and rather mild degrees of burial diagenesis.

Discussion

Breccia and sandstone

The small amounts of breccia and black volcanoclastic sandstone in Unit I are in strong contrast to the clay and carbonate turbidite sediments recovered at Site U1433, which is located just ~35 km to the south. The coarse grain size and poor sorting indicate a relatively local provenance, and the volcanic character of the grains suggests the source is a volcanic edifice, most likely the adjacent seamount ~20 km to the north (Figures F1, F3). Based on the parallel lamination and erosive bases that are often associated with these deposits, the sediment was probably transported by gravity flow

currents, although some more localized mass wasting may be responsible for the less well sorted and coarser grained material.

Yellowish brown claystone

Like the other deepwater sites in the South China Sea basin drilled during Expedition 349, the volcanic basement at Site U1434 is covered by a deposit, ~25 m thick, of fine-grained reddish to yellowish brown claystone. The sediment is well consolidated but not entirely lithified, which is consistent with the relatively moderate depths of burial. The clay could be transported by hypopycnal plumes released from river mouths during periods of enhanced discharge, for example during heavy monsoon floods in Southeast Asia. The forcing of muddy megaturbidites from the neighboring continents by distal turbidity currents could be a mechanism of transportation (Wetzel and Unverricht, 2013). Mixture of this clay with significant amounts of biogenic carbonate suggests deposition at or above the calcite compensation depth.

Unlike for the relatively thick and common carbonate beds at Site U1433, which were interpreted as turbidites, we do not have evidence that the carbonate at Site U1434 is redeposited. Indeed, the well-formed, unbroken foraminifers seen within the claystone toward the base of Unit III are more suggestive of direct pelagic sedimentation without significant reworking, in contrast to the clay-rich siliciclastic component, which must be transported a long distance from the continental margin.

The location of the site on an uplifted and tilted footwall block of the oceanic basement is likely responsible for raising the subs basin in which Site U1434 was drilled above the abyssal seafloor and out

of the path of many of the abyssal plain turbidites that we encountered at Site U1433. The relatively high elevation of the drill site area likely has resulted in a reduced flux of clastic turbidite muds to dilute the pelagic carbonate rain from the upper levels of the ocean. Pelagic carbonate microfossils preserved at this site indicate that it was located above the calcite compensation depth.

The reddish to yellowish brown color of much of Unit III is likely related to more enhanced oxidation of the clastic components of the sediment compared to the more rapidly deposited dark greenish gray claystone found at shallower levels at this site. Advanced oxidation of this type is typical in regions of slow sedimentation and oxygenated bottom water, and similar deposits are known throughout much of the Pacific away from the equatorial zone of enhanced biogenic production (Bryant and Bennet, 1988). The red clays at this site are thicker than might be expected from the Pacific analogs given their relative youth, but this may reflect the faster sediment supply linked to the relative proximity to continental sources.

Biostratigraphy

We analyzed all core catcher samples from Hole U1434A for calcareous nannofossils, planktonic foraminifers, and radiolarians. Calcareous nannofossils in selected split-core samples were also analyzed. Coring started at 197.0 mbsf at this site. Biostratigraphy based on calcareous nannofossils and planktonic foraminifers indicates that the sediment recovered at Site U1434 spans the uppermost middle to upper Miocene, with the base of the sequence younger than 11.9 Ma (Figure F16; Tables T2, T3). Calcareous nan-

Figure F16. Age-depth model, Site U1434. FAD = first appearance datum, FCA = first common appearance, LAD = last appearance datum.

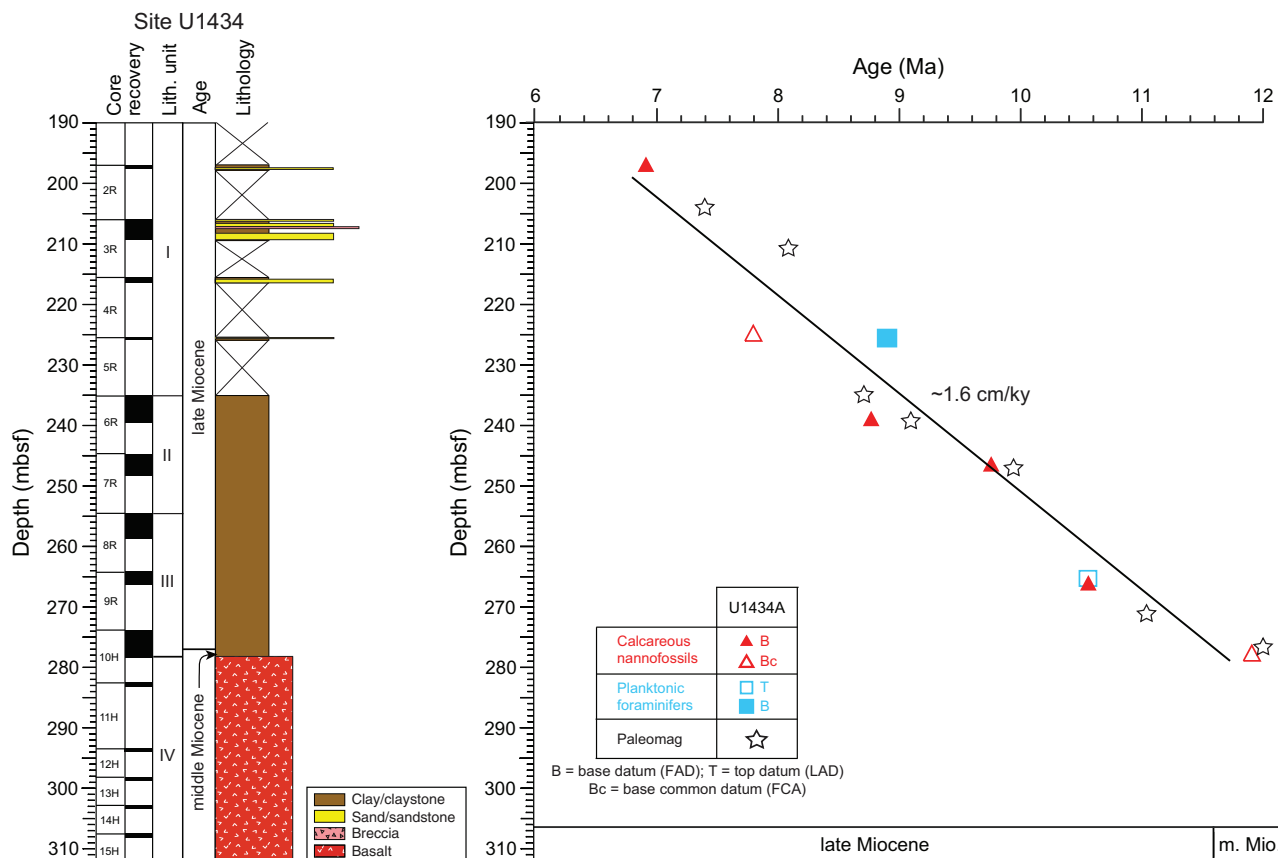


Table T2. Depths and ages of calcareous nannofossil events, Hole U1434A. T = top/last appearance datum, B = base/first appearance datum, Bc = base common/first common appearance. [Download table in .csv format.](#)

Epoch	Zone (Martini, 1971)	Calcareous nannofossil event	Hole U1434A		
			Core, section, interval (cm)	Top depth (mbsf)	Age (Ma)
late Miocene	NN11	B <i>Nicklithus amplificus</i>	2R-CC	197.47	6.91
		Bc <i>Discoaster surculus</i>	5R-CC	225.56	7.79
	NN10	B <i>Discoaster loeblichii</i>	6R-CC	239.62	8.77
		B <i>Minylitha convallis</i>	7R-CC	247.08	9.75
middle Miocene	NN9	B <i>Discoaster hamatus</i>	9R-CC	266.61	10.55
		Bc <i>Discoaster kugleri</i>	10R-CC, 14–16	278.28	<11.9

Table T3. Depths and ages of planktonic foraminifer events, Hole U1434A. T = top/last appearance datum, B = base/first appearance datum. [Download table in .csv format.](#)

Epoch	Zone (Berggren et al., 1995; Wade et al., 2011)	Planktonic foraminifer event	Hole U1434A		
			Core, section	Top depth (mbsf)	Age (Ma)
late Miocene	M13a	B <i>Globigerinoides extremus</i>	5R-CC	225.71	8.93
	M12/M11	T <i>Paragloborotalia mayeri</i>	9R-CC	266.61	10.46

Table T4. Distribution of calcareous nannofossils, Hole U1434A. [Download table in .csv format.](#)

Table T5. Distribution of planktonic foraminifers, Hole U1434A. [Download table in .csv format.](#)

Table T6. Distribution of radiolarians, Hole U1434A. [Download table in .csv format.](#)

nofossil age control is based on six bioevents; planktonic foraminifer age control is based on two bioevents and the overall assemblage.

Calcareous nannofossils are generally common to abundant with poor to moderate preservation, although the abundance decreases downhole (Table T4). Planktonic foraminifer abundance varies from common to barren, and preservation varies from good to poor with frequent observance of test fragmentation (Table T5). Radiolarians are absent in most samples, except for Sample 349-U1434A-8H-CC (258.56 mbsf), where a few well-preserved specimens are present (Table T6).

Correlation of microfossil biohorizons with paleomagnetic data suggests a sedimentation rate of ~1.6 cm/ky during the late middle to late Miocene at Site U1434 (Figure F16).

Calcareous nannofossils

Calcareous nannofossil biostratigraphy in Hole U1434A was established through analysis of core catcher and additional split core samples. Nannofossils are abundant to common in most samples but rare to absent in Samples 8R-CC (258.56 mbsf), 10R-CC (278.14 mbsf), and 10R-CC, 14–16 cm (278.28 mbsf). Preservation of nannofossils is poor to moderate (Table T4). Five late Miocene and one middle Miocene nannofossil bioevents indicate that the age of the sedimentary sequence is ~6.9 to <11.9 Ma (Table T2; Figure F16).

The presence of the first appearance datum (FAD) of *Nicklithus amplificus* (6.91 Ma) in Sample 349-U1434A-2R-CC (197.47 mbsf) and the first common appearance (FCA) of *Discoaster surculus* in Sample 5R-CC (225.56 mbsf) indicate Zone NN11. The FAD of *Discoaster berggrenii*, which marks the Zone NN11/NN10 boundary, is

found in Sample 5R-1, 16–20 cm (225.56 mbsf). The FAD of *Discoaster loeblichii* (8.77 Ma) in Sample 6R-CC (239.62 mbsf) falls within Zone NN10, whereas the FAD of *Minylitha convallis* (9.75 Ma) in Sample 7R-CC (247.08 mbsf) occurs within Zone NN9, indicating that the Zone NN10/NN9 boundary occurs in Core 7R. The Zone NN9/NN8 boundary is assigned to Sample 9R-CC (266.61 mbsf) based on the FAD of *Discoaster hamatus* (10.55 Ma). The presence of *Cyclicargolithus floridanus* (LAD at 11.85 Ma) and *Discoaster kugleri* (FCA at 11.9 Ma) in Sample 10R-CC, 14–16 cm (278.28 mbsf) from the base of the brown claystone (lithostratigraphic Unit III) immediately overlying basalt, indicates an age <11.9 Ma for the base of the sediment section recovered at this site. The middle/late Miocene boundary is placed between Samples 9R-CC and 10R-CC (266.61 and 278.14 mbsf, respectively).

Planktonic foraminifers

Planktonic foraminifers were analyzed in core catcher samples from Hole U1434A. Foraminifer abundance varies from common to barren with good to poor preservation (Table T5). Recrystallization, partial dissolution, and fragmentation also occur, with fragments accounting for as much as 50% of the assemblage in Sample 9R-CC (266.61 mbsf), and heavy dissolution is evident in Samples 9R-CC (266.61 mbsf) and 10R-CC (278.14 mbsf). In these samples, the planktonic foraminifer assemblage is dominated by dissolution-resistant species such as *Sphaeroidinellopsis seminulina*.

The planktonic foraminifer assemblage includes species typical of the late Miocene, such as *Dentoglobigerina altispira*, *S. seminulina*, *Sphaeroidinellopsis kochi*, *Globoturborotalita nepenthes*, *Neogloboquadrina acostaensis*, and *Globorotalia limbata*. The planktonic foraminifer biostratigraphy for Hole U1434A is based on two bioevents, as well as the species composition of the planktonic foraminifer assemblage, which indicate late Miocene Zones M13–M11 (Table T3; Figure F16).

The absence of the dissolution-resistant species *Pulleniatina primalis* from the assemblage indicates an age >6.60 Ma (Subzone M13b) for the upper sedimentary sequence recovered in the hole. The FAD of *Globigerinoides extremus* (8.93 Ma) is observed in Sample 5R-CC (225.71 mbsf), indicating Subzone M13a. The Subzone M13a/Zone M12 boundary could not be identified because plank-

tonic foraminifers are either scarce or absent in Samples 6R-CC through 8R-CC (239.62–258.56 mbsf). The last appearance datum (LAD) of *Paragloborotalia mayeri* (10.46 Ma) in Sample 9R-CC (266.61 mbsf) indicates the Zone M12/M11 boundary. From the base of the sedimentary sequence, Sample 10R-CC (278.14 mbsf) also contains *P. mayeri* and other middle to late Miocene species, indicating Zone M11 (older than 10.46 Ma).

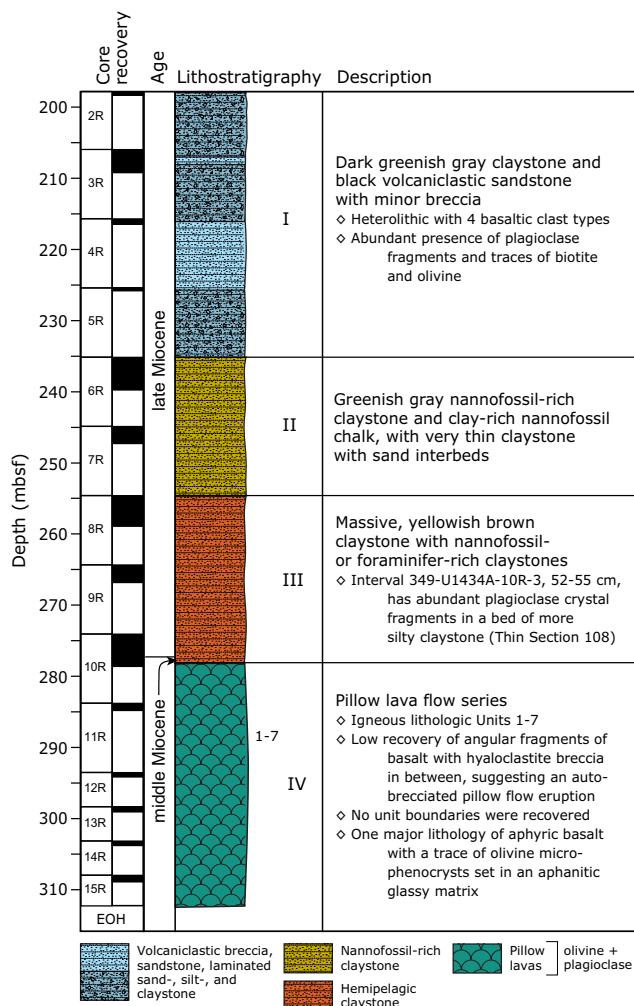
Radiolarians

In Hole U1434A, all core catchers are barren of radiolarians, except Sample 8H-CC (258.56 mbsf), which contains a few well-preserved specimens. However, this sample does not contain any marker species, although the presence of *Astrophacus* sp. indicates a biostratigraphic range between the middle Miocene and early Pliocene (Wang and Yang, 1992) (Table T6).

Igneous petrology and alteration

We cored 30.38 m into igneous basement below 278.27 mbsf in Hole U1434A and recovered 3.05 m of basalt (10.0% recovery). This short basement succession is divided into 7 igneous lithologic units, which are grouped into lithostratigraphic Unit IV (Figure F17). The

Figure F17. Lithostratigraphic summary of igneous rocks and lithologic features, Hole U1434A. Lithostratigraphy column includes lithology, igneous lithologic units (1–7), and lithostratigraphic units (I–IV). EOH = end of hole.



basement at Site U1434 comprises a succession of small pillow basalt flows, or a single thicker autobrecciated pillow lava flow, with three occurrences of hyaloclastite breccia. The igneous basement is overlain by hemipelagic yellowish brown claystone (Unit III) that grades upward into nannofossil-rich claystone and chalk (Unit II) and a volcanoclastic series containing black volcanoclastic sandstone and minor breccia (Unit I). The latter volcanoclastic sandstone and breccia are interpreted to be part of the sedimentary apron of a nearby seamount, as they contain abundant volcanic glass fragments, scoria, and basalt clasts, as well as crystal fragments of plagioclase, olivine, and sparse biotite.

The igneous basement comprises angular to subangular basalt fragments that are aphyric and have glassy to microcrystalline groundmasses. The only phenocryst observed is olivine, which occurs as a sparse euhedral to subhedral equant mineral phase throughout the recovered igneous unit basement. The groundmass texture ranges from hypocrySTALLINE to hypohyaline, mostly consisting of variably altered glass and mesostasis, but with abundant plagioclase microlites that grow in spherulitic and variolitic patterns. Clinopyroxene is only observed in a few thin sections in Cores 349-U1434A-13R through 15R, where it crystallized in small (<0.5–1 mm) patches, filling the interstitial spaces between plagioclase microlites in the groundmass. Most basalts are nonvesicular to sparsely vesicular. Chilled margins are mostly absent, although hyaloclastite breccia with abundant fresh volcanic glass shards set in a light brown carbonate and clay matrix is encountered in three intervals. Despite their cryptocrystalline and aphyric nature, all basalts have phase assemblages of olivine + plagioclase, with clinopyroxene as a sparse interstitial groundmass phase. These minerals are typical of mid-ocean-ridge basalt (MORB) crystallization assemblages and, in conjunction with geochemical evidence, we conclude that the basement basalt at Site U1434 is MORB (see [Geochemistry](#)).

Basalt alteration at Site U1434 is typical of that of MORB and ranges in intensity from slight to moderate. The majority of the pillow basalt pieces exhibit alteration halos with colors ranging from dark gray in their fresh interiors to light yellow-brown along the altered outer rims. More altered pieces are light gray with brown alteration tinges. Secondary minerals include a low-temperature alteration assemblage of clay, Fe oxide, carbonate, and celadonite. Fresh basaltic glass occurs in some of the pillow basalt margins and as clasts in the hyaloclastite breccia. Those basaltic glasses are partly altered to palagonite, ranging in color from orange to brown. Most vesicles are not filled or are partly filled with Fe oxide, saponite, celadonite, and carbonate. Alteration veins are uncommon in the recovered basement cores, with only two thin carbonate-filled veins recorded.

Lithostratigraphic Unit IV is devoid of seamount-derived volcanic products, but the cored sequence of volcanoclastic rocks in Unit I (and a single ~10 cm interbed in Unit III) probably originated from intraplate volcanism, as evidenced by plagioclase and biotite crystal fragments and high abundances of highly vesicular scoria, plagioclase-phyric and trachytic basalt clasts, and finer grained (fresh) volcanic glass shards in these intervals. As was the case for Site U1431, it is likely that we penetrated (partly) through the volcanic apron of the nearby seamount to the north (Figure F1), which must have been active during the late Miocene (see [Lithostratigraphy](#)).

Basaltic clasts in volcanoclastic Unit I

Lithostratigraphic Unit I contains a sequence of black volcanoclastic sandstone and minor breccia alternating with greenish gray

claystone. This late Miocene unit contains volcanoclastic sandy turbidites and may represent part of a seamount apron series (see [Lithostratigraphy](#)). All cored volcanoclastic breccias and sandstones are heterolithic and contain up to three basaltic clast types, as well as many broken pieces of primary volcanic crystal phases, including mainly plagioclase and olivine but also sparse biotite. Although Unit III comprises a yellowish brown claystone rich in nanofossils and foraminifers, it also contains a single bed with abundant plagioclase fragments. Each major basalt clast type and crystal fragment type (Figure [F18](#)) is described below from highest to lowest abundance in the section.

Type 1: nonvesicular basaltic glass shards

As one of the two major clast types, these Type 1 glass shards are angular to subangular, show minor feldspar laths, and are typically nonvesicular (Figures [F18A](#), [F18B](#), [F18D](#)). In many of the volcanoclastic breccias and sandstones, this clast type appears to be most common in the finer grain size fraction (Figure [F18D](#)).

Type 2: vesicular devitrified basaltic glass shards

As the other major clast type, these Type 2 glass shards or clasts are often scoriaceous with well-developed rounded vesicles clearly visible (Figure [F18A](#)). These clasts are angular to subangular, dark gray, and brown-gray when oxidized. Some clasts contain plagioclase microlites. All clasts are cryptocrystalline and seem to consist of completely devitrified volcanic glass.

Type 3: plagioclase and olivine crystal fragments

Throughout lithostratigraphic Unit I, plagioclase fragments (1%–2%) are up to 10 mm in size with generally sharp outlines (Figure [F18C](#)). These Type 3 plagioclase fragments are overall unal-

tered. Although plagioclase dominates the crystal fragments in the volcanoclastic sandstone and breccia, flakes of well-preserved biotite and crystal fragments of relatively unaltered olivine occur in many thin sections. The combined presence of plagioclase, olivine, biotite, and trachytic basalt points to an intraplate volcanic source, potentially the neighboring seamount near Site U1434 (Figures [F1](#), [F3](#)).

Type 4: trachytic basalt

This minor clast type is not easily observed macroscopically in the archive-half sections; however, it occurs in thin sections (Figure [F18A](#)). The clasts are subangular, small (up to 5 mm) and have a fine-grained groundmass with many flow-aligned plagioclase laths. These clasts are typically nonvesicular and slightly to moderately altered.

Lithostratigraphic and igneous lithologic units Unit IV

Interval: 349-U1434A-10R-CC, 13 cm, to 15R-1, 95 cm

Depth: 278.27–308.65 mbsf

Thickness: 30.38 m (3.05 m at 10.0% recovery)

Lithology: pillow basalt flows with interspersed hyaloclastite breccia

Igneous lithologic units: 1–7

The base of the yellowish brown hemipelagic claystone (lithostratigraphic Unit III) and the first appearance of aphyric pillow basalt fragments in the lowermost 8 cm of the core catcher of Core 349-U1434A-10R mark the upper boundary of lithostratigraphic Unit IV at 278.27 mbsf (curated depth). Unit IV comprises blocky (small) pillow basalt fragments with three occurrences of hyaloclastite breccia in between (Figures [F19](#), [F20](#), [F21](#), [F22](#)). All basalt samples are aphyric and have glassy to aphanitic groundmasses, with olivine being the singular phenocryst phase present (Figure [F22C](#)). The groundmass contains a high proportion of variably altered and devitrified glass and mesostasis, with plagioclase microlites forming typical spherulitic and variolitic textures (Figure [F22A](#), [F22B](#), [F22D](#)) indicative of relatively high cooling rates upon eruption. Clinopyroxene is only observed in a few thin sections, where it crystallized in patches (<0.5–1 mm) and fills interstitial spaces between plagioclase microlites (Figure [F22D](#)). Most basalts are nonvesicular to sparsely vesicular. Chilled margins are mostly absent, although in three intervals hyaloclastite breccias were encountered with shards of fresh volcanic glass (Figures [F21C](#), [F21D](#)) or blocky aphyric basalt with chilled margins (Figure [F21A](#), [F21B](#)) appearing in a carbonate and/or clayey matrix.

Igneous lithologic Units 1, 3, 5, and 7 are poorly recovered, and unit boundaries are inferred from the occurrence of chilled margins on separate angular basalt pieces and hyaloclastite breccias that make up igneous lithologic Units 2, 4, and 6. The aphyric basalt has rare olivine phenocrysts that form the center of radially arranged plagioclase microlites. The olivine crystals are typically subhedral (and sometimes euhedral) in shape and up to 1.6 mm in size. The groundmass is glassy and cryptocrystalline to microcrystalline with up to 1% vesicles smaller than 1.5 mm in some of the pieces. Clinopyroxene is rare and was only observed in the groundmass for Units 5 and 7 (based on thin sections TS116 through TS118; Figure [F21D](#)).

Igneous lithologic Units 2, 4, and 6 are recorded as hyaloclastite breccia with clasts of volcanic glass (up to 10 mm) in Units 2 and 4 and larger, angular aphyric basalt clasts (up to 7 cm) in Unit 6 (Figure [F19B](#)). The volcanic glass in both the glass shards and the

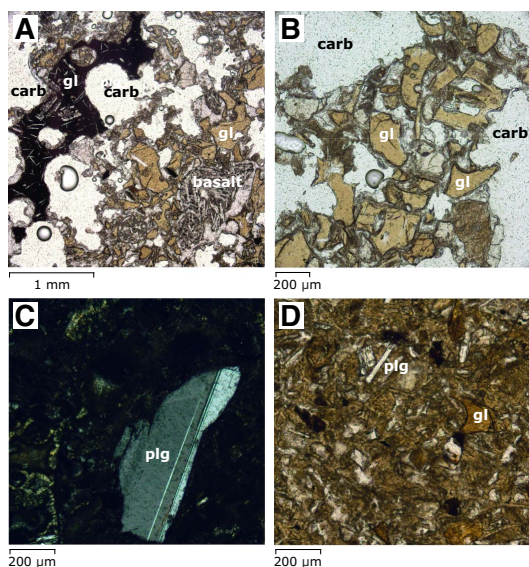
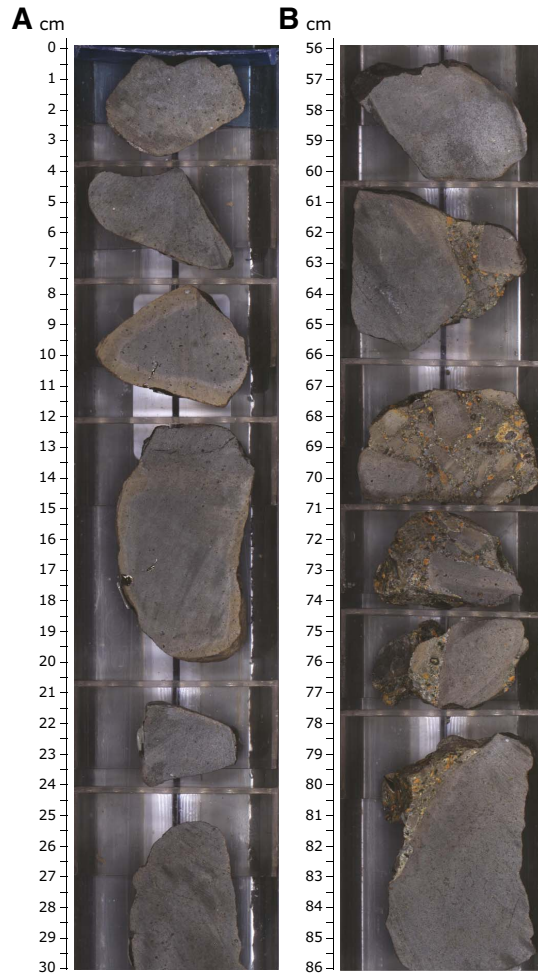


Figure F19. Basement basalt features, Hole U1434A, Unit IV. A. Aphyric basalt with alteration halos (light yellowish brown) along margins of subangular basalt pieces (14R-1A, 0–30 cm; Unit 5). B. Hyaloclastite breccia with larger blocky fragments of aphyric basalt (15R-1A, 56–86 cm; Unit 6).



chilled margins of the larger aphyric basalt clasts is generally unaltered, except for a narrow rim that is replaced by palagonite (Figures F20, F21). Based on microscope observation, sparse well-preserved microphenocrysts of olivine (Figure F21D) as well as plagioclase are found in the volcanic glass, confirming the general phenocryst phase assemblage of olivine + plagioclase. Drilling at Site U1434 terminated at 308.65 mbsf, after encountering sustained hole instabilities.

Interpretation of the igneous succession at Site U1434

Site U1434 is located ~40 km away from Site U1433 and is closer to the fossil spreading axis of the Southwest Subbasin. This site is also close to a nearby seamount (Figures F1, F3). We recovered only 3.05 m of basalt after penetrating 30.38 m into igneous basement. Seven igneous lithologic units were recorded and include pillow basalt alternating with hyaloclastite breccia. Because no characteristic curved chilled margins, vesicle banding, or pillow basalt fractures were observed, this succession could be interpreted as the remnants of a thicker autobrecciated pillow lava flow. The phase assemblage consisting of olivine phenocrysts with plagioclase, and clinopyroxene in the groundmass, is typical of that of MORB and, in conjunc-

Figure F20. Interpillow hyaloclastite breccia, Hole U1434A, Unit IV. A, B. 11R-1, 17–23 cm (wet surface). C, D. 13R-1, 24–31 cm (wet surface; enhanced in Adobe Photoshop).

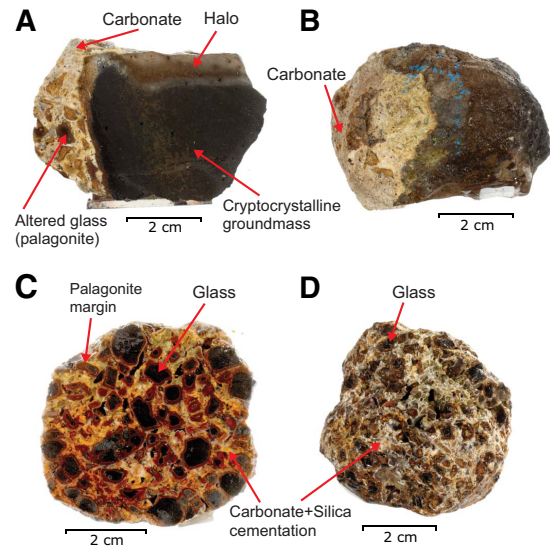
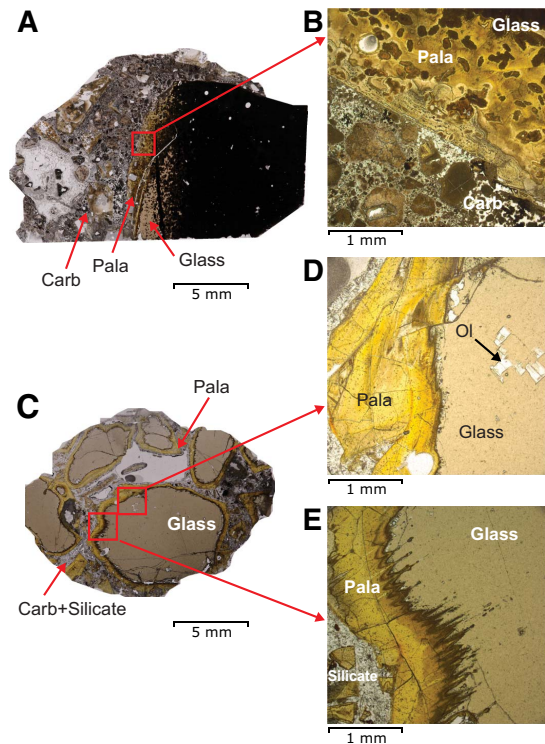


Figure F21. Hyaloclastite breccia, Hole U1434A, Unit IV (PPL). Pala = palagonite, Carb = carbonate. A, B. 11R-1, 17–19 cm; TS110. C, D, E. 13R-1, 13–18 cm; TS114.

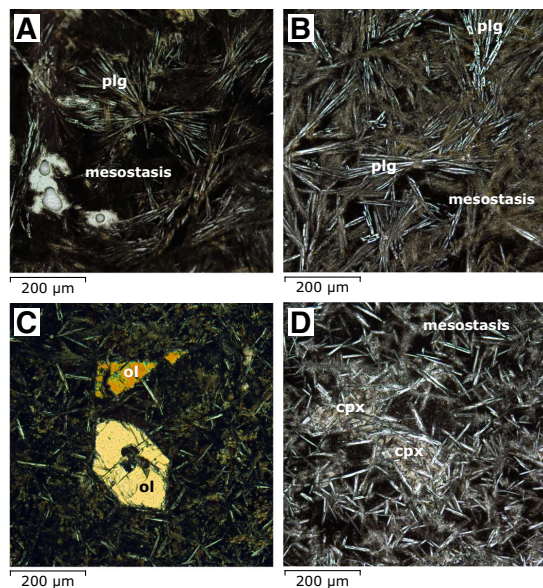


tion with geochemical evidence, we conclude that the basement basalt at Site U1434 is MORB (see [Geochemistry](#)).

Alteration

Similar to Site U1433, igneous basement basalt recovered at Site U1434 shows a low-temperature alteration assemblage that includes clay, Fe oxide, carbonate, and celadonite. Some fresh basaltic glass is preserved near the pillow basalt margins and in clasts making up the hyaloclastite breccia, but some are partly altered to palagonite,

Figure F22. Basalt, Hole U1434A, Unit IV. A. Aphanitic basalt with plagioclase (plg) microlites showing variolitic textures, leaving a large part of (devitrified) mesostasis (12R-1, 63–66 cm; TS113; PPL). B. Similar to A, but with a higher proportion of plagioclase microlites (14R-1, 4–8 cm; TS116; PPL). C. Small olivine (ol) microphenocrysts with euhedral crystal shape (11R-1, 44–46 cm; TS111; XPL). D. Patch with clinopyroxene (cpx) growing interstitially between plagioclase, whereas the rest of the mesostasis remains free of clinopyroxene (15R-1, 57–59 cm; TS117; PPL).



ranging in color from orange to brown. The few vesicles are not filled or are partly filled with Fe oxide, saponite/clay, celadonite, and carbonate. Alteration veins are uncommon, with only two thin carbonate-filled veins recorded. Based on macroscopic and thin section observations, the overall alteration style is characterized by the following categories:

- Patchy background alteration evenly distributed throughout the groundmass and mesostasis of the basalt;
- Alteration halos at the margins of basalt fragments;
- Partial palagonitization of glass fragments in hyaloclastite breccia; and
- Partial vesicle fillings (Figure F23) by secondary minerals, typically Fe oxide, clay, celadonite, and carbonate, in decreasing order.

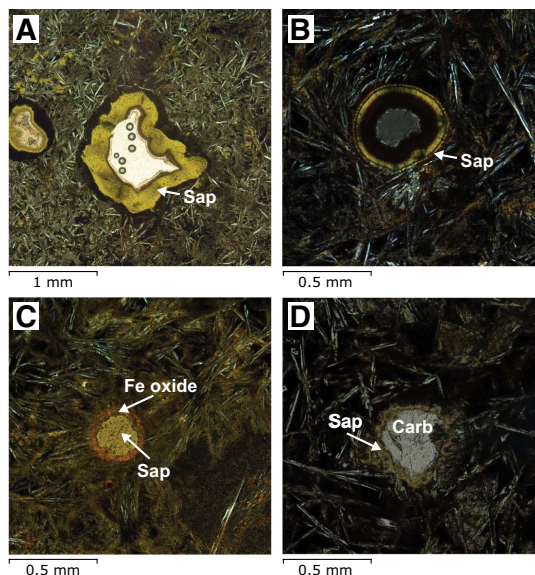
Alteration phases

Alteration in the basement of Site U1434 is characterized by formation of celadonite, saponite/clay, carbonate, brown palagonite, and Fe oxide, consistent with interaction of basalt with oxidative seawater at low temperatures. Most of the crypto- to microcrystalline basalt fragments have patches with light brown to brown alteration colors in their groundmass. Mostly unaltered plagioclase microlites exist in the groundmass.

Alteration of primary minerals

Larger olivine microphenocrysts are partially altered to secondary minerals along cracks and margins but are mostly fresh in the volcanic glass. Plagioclase microlites in the groundmass are fresh or only slightly altered. Clinopyroxene is rare and microcrystalline in this basalt but appears relatively unaltered in thin section.

Figure F23. Vesicle fillings, Hole U1434A (PPL). A. Saponite (Sap) partially filling vesicle (11R-1, 44–46 cm; TS111). B. Saponite partially filling vesicle (14R-1, 4–8 cm; TS116). C. Fe oxide and saponite completely filling vesicle (15R-1, 57–59 cm; TS117). D. Saponite and carbonate (Carb) completely filling vesicle (15R-1, 79–81 cm; TS118).



Background alteration and halos

Background alteration at Site U1434 accounts for the majority of the alteration and is pervasive throughout the units. No downhole trend of alteration extent can be observed. The background alteration is most evident in the crypto- to microcrystalline basalt, with formation of secondary minerals such as Fe oxide, saponite/clay, celadonite, and carbonate, particularly in patches in the mesostasis. Alteration halos exist in the margin of many basalt pieces, with colors ranging from yellowish brown to brown (Figure F19A).

Vesicles

Vesicles make up <1% of the recovered basement basalt in Hole U1434A. Based on thin section observations, vesicles are only partly filled with Fe oxide, palagonite, celadonite, and carbonate (Figure F23).

Hyaloclastite breccia

Igneous lithologic Units 2, 4, and 6 are composed of cryptocrystalline to microcrystalline pillow basalt pieces and glass as clasts that are cemented by carbonate, clay minerals, and likely also some silica. This basaltic glass is mostly well preserved with minor alteration to greenish palagonite, usually along rims (Figures F19B, F20, F21).

Interpretation of alteration

Alteration of basalts recovered at Site U1434 occurred under oxidative conditions with seawater/fluids, as shown by the secondary mineral assemblages of carbonate, Fe oxide, celadonite, and brown palagonite, which is a typical alteration style for MORBs and is recognized at previous sites, such as Integrated Ocean Drilling Program Site U1367 (Expedition 329 Scientists, 2011). Most vesicles are not filled or are partly filled with Fe oxide, saponite, celadonite, and carbonate, indicating limited fluid flow and alteration extent at this site. Uncommon occurrence of alteration veins is consistent with the limited fracturing in those basalt pieces.

Structural geology

Site U1434 lies on the southern shoulder of the relict spreading ridge of the Southwest Subbasin, South China Sea (Figure F1). A northwest–southeast oriented seismic profile across this site shows a local depression with one volcanic seamount located immediately to the north (Figure F3). Seismic reflections above the basement are generally continuous without obvious evidence of faults or unconformities, although the reflectors are slightly curved on the upper part.

The core recovery in Hole U1434A is relatively poor. We observed traces of deformation in consolidated sediment and basement rock and measured the dip orientation and angle of fractures and veins. Compared with Holes U1431E and U1433B, fractures and veins at this site are rare. However, it is unclear if this is because of poor recovery or if the basement has fewer fractures and veins at this site. Only 2 fractures and 4 veins were measured. Most of the fractures observed in the sedimentary rocks are drilling induced, except one with a slight offset in the claystone (Figure F24). The hanging and foot walls are now fused, with no gap along

Figure F24. A closed fault observed in the claystone, Interval 349-U1434A-10R-1A, 65–74 cm. (A) Line-scan image; (B) Geological interpretation. White line traces the fault with arrow indicating direction of offset. White brush strokes are drawn tracing the claystone laminations, whose orientation change slightly between hanging and foot walls.

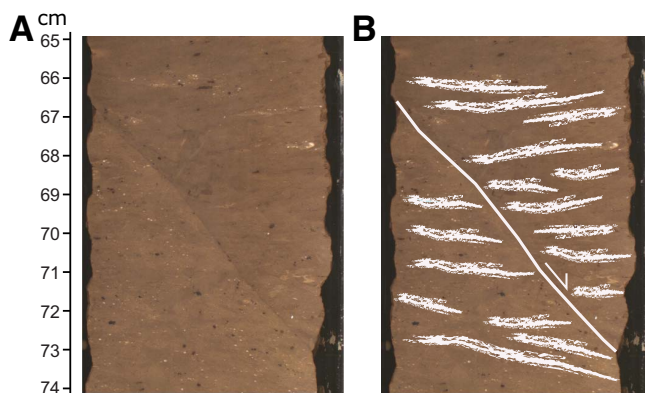
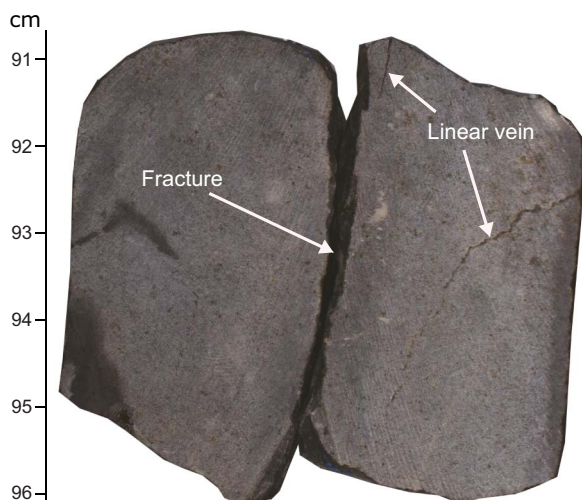


Figure F25. Typical fracture and veins observed in the basalt, Interval 349-U1434A-11R-1A, 91–96 cm. Veins are linear with small thickness, infilled with Fe-oxide. The fracture is drilling induced along an existing vein.



the fracture plane. We interpret that this fracture might have been formed before consolidation of the clay. As a result of the very poor recovery of the basement, most of the basalts are broken pieces with lengths between 3 and 8 cm. Only 4 veins are identified in separate basalt pieces. These veins are straight with no more than 0.2 cm thickness (Figure F25) and are filled with white carbonate and brown Fe oxide.

Geochemistry

Interstitial water chemistry

We collected 5 whole-round samples (10–15 cm long) for interstitial water measurements from 207.9–275.0 mbsf in Hole U1434A at a frequency of one sample per core. No interstitial water samples were taken when core recovery was <10%. Interstitial water chemistry data are given in Table T7 and shown in Figures F26 and F27.

Chloride, bromide, and sodium

Downhole profiles of chloride, bromide, and sodium in Hole U1434A are shown in Figure F26. Chloride, bromide, and sodium concentrations vary with depth, with values close to modern seawater in lithostratigraphic Unit I, reaching minima in the greenish nannofossil-rich claystone of Unit II, and increasing to near modern seawater values in the yellowish brown claystone of Unit III.

Alkalinity, sulfate, calcium, and magnesium

Alkalinity, sulfate, calcium, and magnesium profiles are shown in Figure F27. Alkalinity increases from 0.5 mM at ~210 mbsf to a maximum 3.5 mM at the boundary between lithostratigraphic Units II and III, before decreasing to 2.4 mM at 275 mbsf in Unit III. Sulfate concentrations decrease from 27.2 mM in Unit I to 26.5 mM in Unit II and then increase to ~27.6 mM in Unit III. Calcium concentrations are much higher than the modern seawater value (10.5 mM) throughout the cored section, decreasing from 26.5 mM to 17.9 mM at the bottom of the hole. Magnesium concentrations are much lower than the modern seawater value (54 mM), increasing from 33 to 44 mM downhole, probably due to clay ion exchange.

Headspace gas geochemistry

Headspace gas was monitored in cores from Hole U1434A as part of the shipboard safety and pollution prevention program. Methane concentrations in all samples from Hole U1434A are very low (<5 ppmv). Ethane and propane were not detected (Figure F28; Table T8).

Bulk carbon and nitrogen analysis

Total organic carbon (TOC), CaCO₃, total nitrogen, and TOC to nitrogen (C/N) ratio distributions for Hole U1434A are listed in Table T9 and illustrated in Figure F29. Because of the low core recovery, only six samples were collected for carbon and nitrogen content analysis. The CaCO₃ content is <10 wt% in the four samples taken above 260 mbsf, but is higher (15–30 wt%) in the two samples from the lower part of lithostratigraphic Unit III. TOC is low (<0.5 wt%) throughout the hole. Total nitrogen is low, except for one higher value (1.53 wt%) from a sample near the top of Unit II. The C/N ratio is also generally low (<5), which indicates a dominant marine

Table T7. Interstitial water major element concentrations, salinity, pH, alkalinity, sulfate, chloride, bromide, calcium, magnesium, sodium, and potassium Hole U1434A. [Download table in .csv format.](#)

Figure F26. Interstitial water bromide, chloride, and sodium, Hole U1434A.

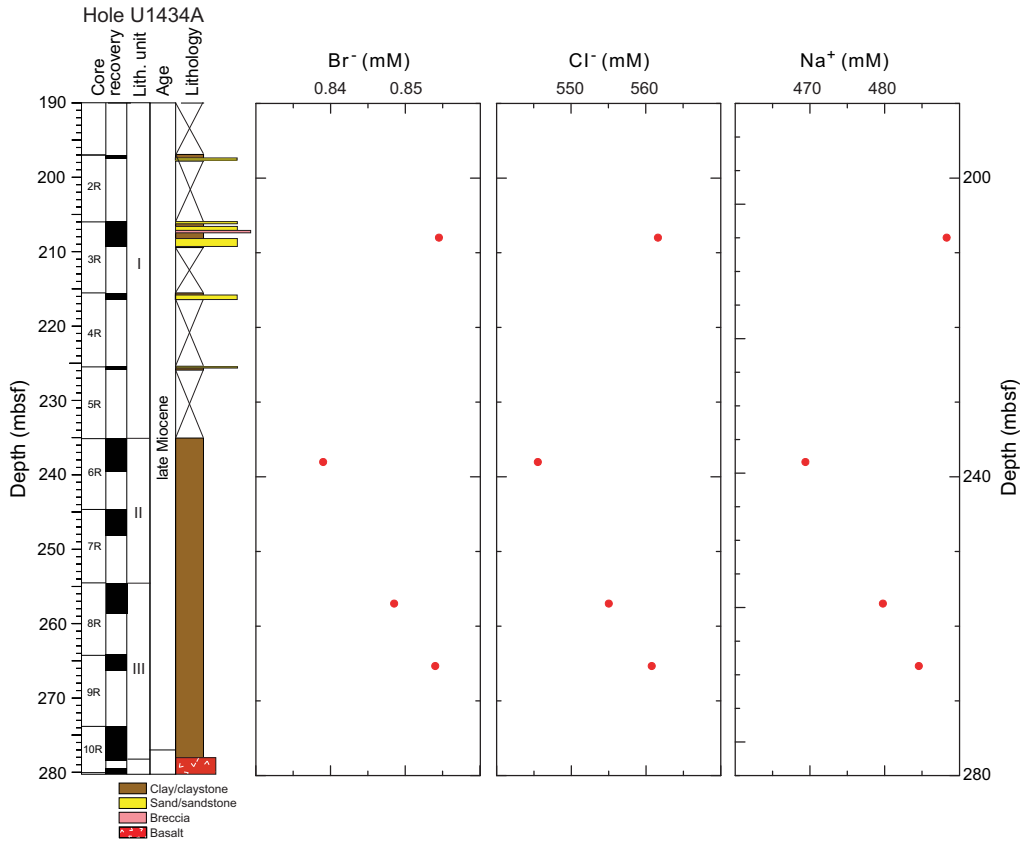


Figure F27. Interstitial water alkalinity, sulfate, calcium, and magnesium, Hole U1434A.

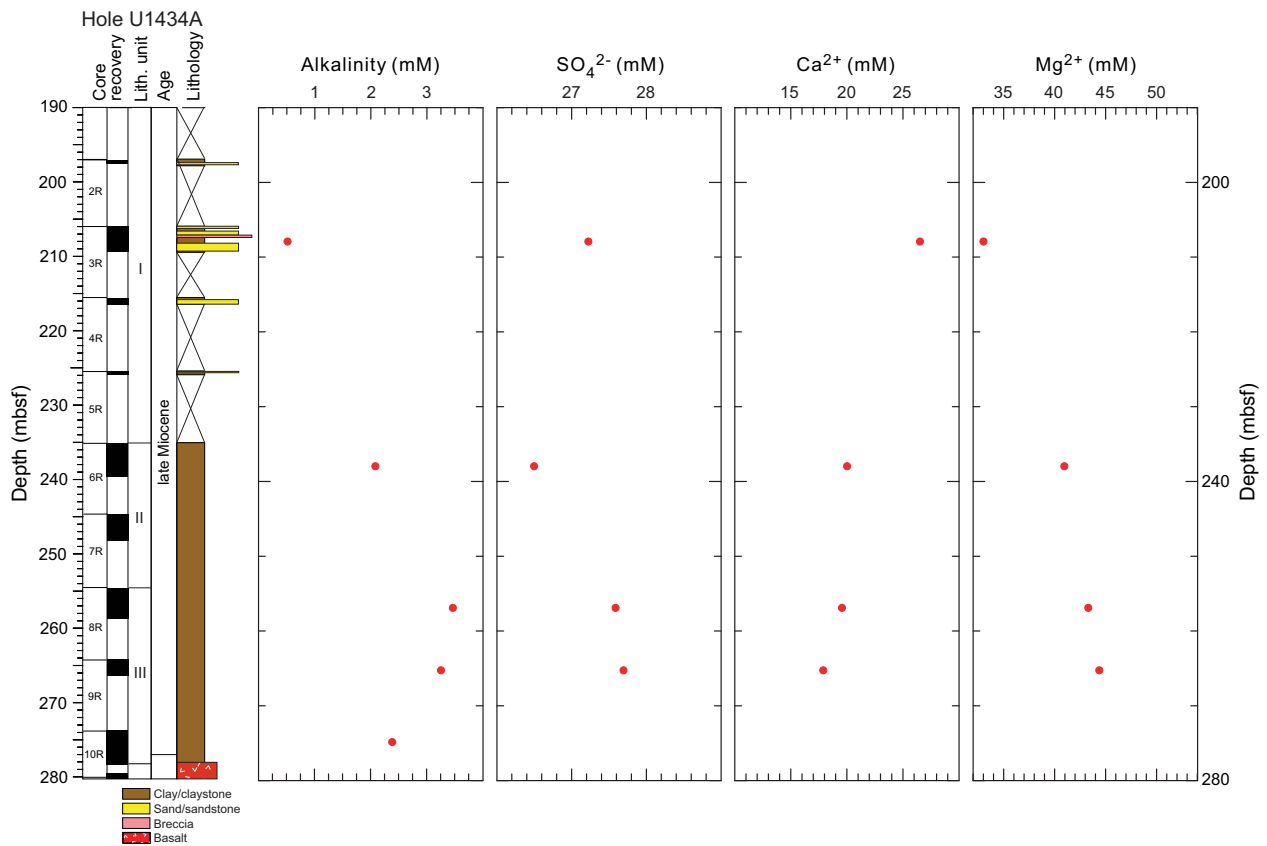


Figure F28. Methane in headspace gas, Hole U1434A.

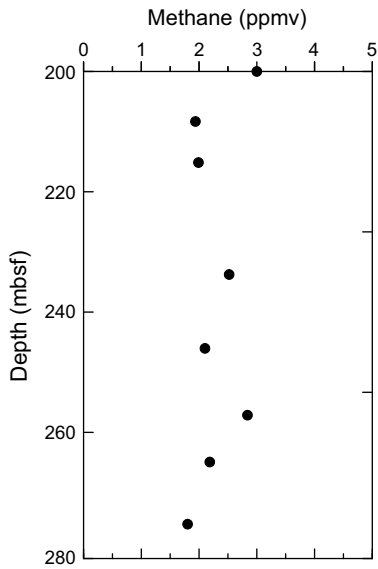
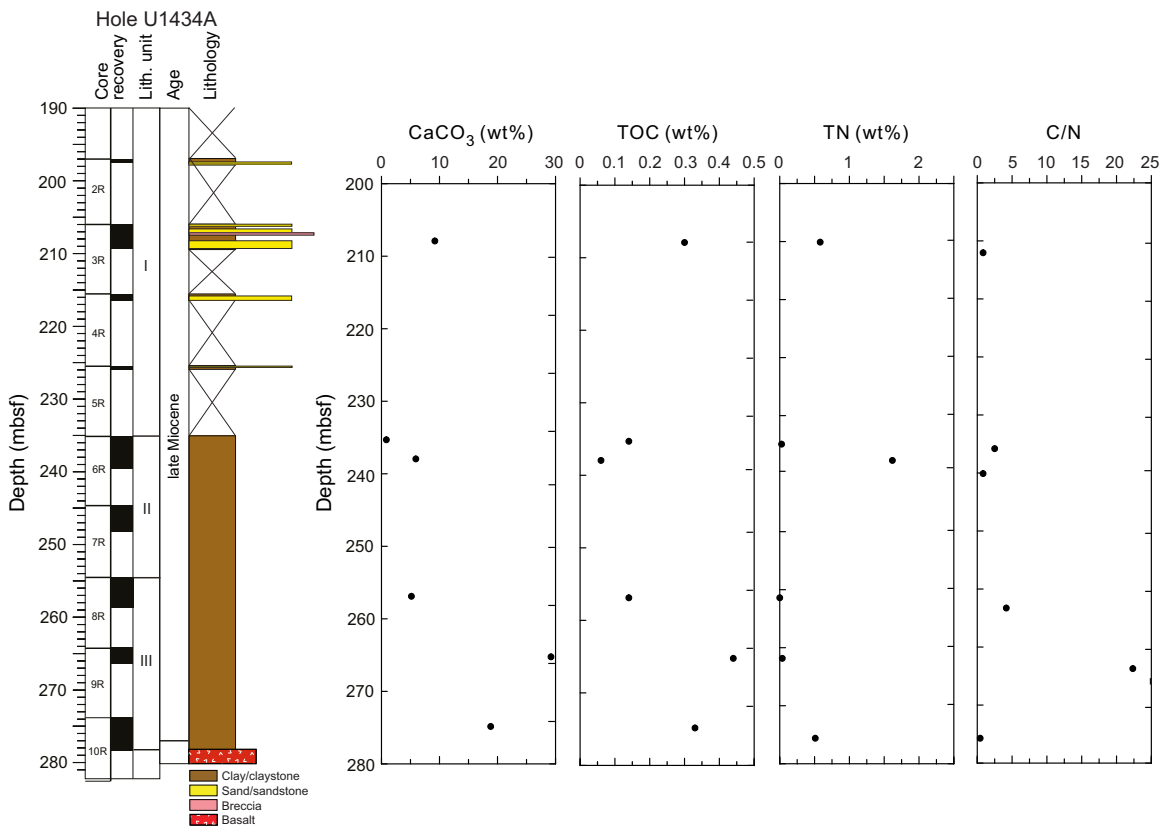


Table T8. Headspace sample hydrocarbon concentrations, methane, Hole U1434A. [Download table in .csv format.](#)

Table T9. Carbon and nitrogen contents, CaCO₃, TOC, TC and C/N ratios, Hole U1434A. [Download table in .csv format.](#)

Figure F29. Calcium carbonate, TOC, total nitrogen (TN), and C/N ratio, Hole U1434A.



source for the organic matter. One sample in Unit III has a higher C/N ratio (~23), which could indicate an influx of terrestrial organic matter.

Igneous rock geochemistry

Six igneous rock samples from Cores 349-U1434A-10R through 15R were analyzed for concentrations of major and trace elements by inductively coupled plasma–atomic emission spectroscopy (Figure F30; Table T10).

Loss on ignition values, which serve as a rough indicator of the overall level of alteration in the rocks, are generally low, ranging from 1.05 to 1.93 wt%. One sample has a total weight percentage for the major element oxides of 120.9 wt%, and the other five samples vary from 101.8 to 105.4 wt%. The monitored standards BCR-2 and HBVO-2 measurements were consistent and within recommended values; the high total weight percentage for these samples is most likely due to large weighing errors resulting from ship motion during the transit from Site U1434 to U1435. For comparison with data from other sites, measured major element total values were normalized to 100 wt%. The samples have moderate K₂O (0.11–0.29 wt%), TiO₂ (1.51–1.69 wt%), MgO (5.50–7.22 wt%), Fe₂O₃ (9.89–11.54 wt%), and Na₂O (2.77–3.65 wt%) and high SiO₂ (50.6–55.5 wt%), Al₂O₃ (13.83–15.27 wt%), and CaO (9.46–11.00 wt%) concentrations, compared with average basalt. Concentrations of major elements vary within narrow ranges for all measured samples.

When plotted on the alkali versus silica diagram of volcanic rock types (Le Maitre et al., 1989) (Figure F31), five samples are tholeiitic

Figure F30. Loss on ignition (LOI) and major element composition of igneous rock samples, Hole U1434A. Lithostratigraphy column includes lithology, igneous lithologic units (1–7), and lithostratigraphic units (III and IV). EOH = end of hole.

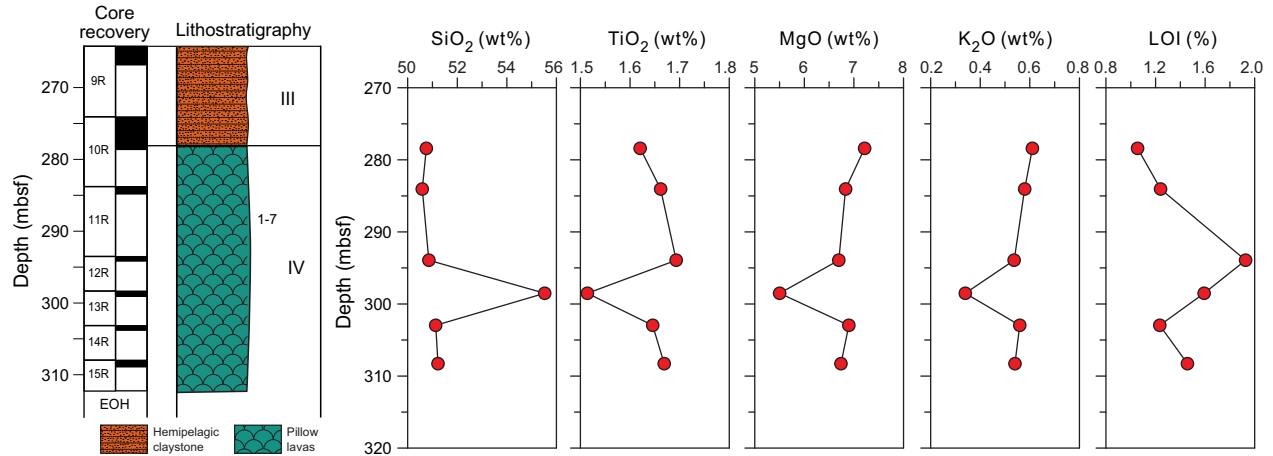
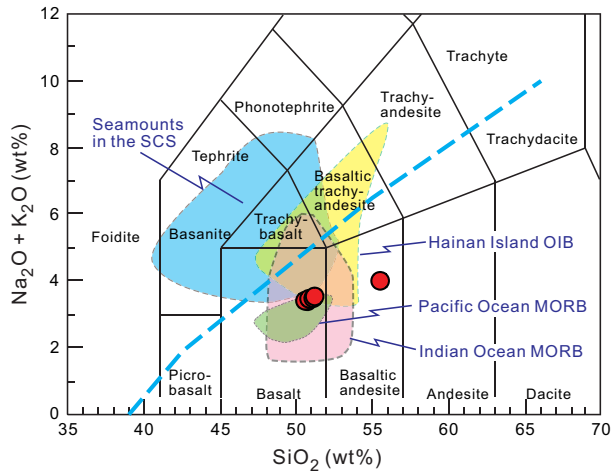


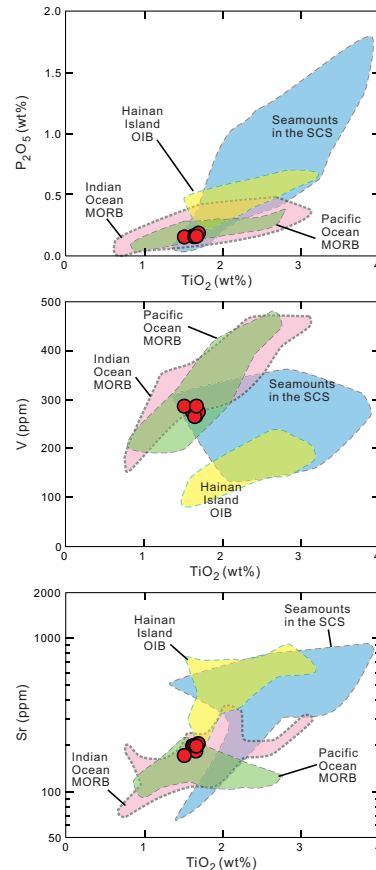
Table T10. Major and minor element compositions of igneous samples, SiO₂, TiO₂, Al₂O₃, Fe₂O₃^T, MnO, MgO, CaO, Na₂O, K₂O, P₂O₅, LOI, Ba, Co, Cr, Sc, Sr, V, and Zn, Hole U1434A. [Download table in .csv format.](#)

Figure F31. Total alkalis vs. silica, Hole U1434A. Classification of volcanic rock types from Le Maitre et al. (1989). The dashed blue line divides data between tholeiitic and alkalic lavas of Hawaii (Macdonald and Katsura, 1964; Macdonald, 1968). Shown for comparison are data for Indian Ocean MORB from the Geochemical Rock Database ([georoc.mpch-mainz.gwdg.de](#)), seamounts in the SCS (Tu et al., 1992; Hékinian et al., 1989), OIB in the Hainan Island (Wang et al., 2012), and Pacific Ocean MORB (Zhang et al., 2009, 2012a, 2012b, 2013).



basalt and one plots in the basaltic andesite field. As shown in Figure F32, these rocks are similar to Pacific and Indian Ocean MORB and are distinct from the Hainan Island ocean-island basalt (OIB) and the basalt from seamounts in the South China Sea. Thus, the basalt samples from Cores 349-U14344A-10R through 15R are tholeiitic basalt, representative of South China Sea MORB.

Figure F32. TiO₂ vs. P₂O₅, V, and Sr, Hole U1434A. Shown for comparison are data for Indian Ocean MORB from the Geochemical Rock Database ([georoc.mpch-mainz.gwdg.de](#)), seamounts in the SCS (Tu et al., 1992; Hékinian et al., 1989), OIB in the Hainan Island (Wang et al., 2012), and Pacific Ocean MORB (Zhang et al., 2009, 2012a, 2012b, 2013).



Microbiology

Our goal for microbiological research at Site U1434 was to collect and preserve samples for shore-based characterization of microbial communities. We collected samples on a routine basis throughout the cored intervals and on a case-by-case basis according to features in the cores that suggested the presence of important geological interfaces. In addition, we collected samples for measuring contamination, using microspheres and fluid community tracers.

Specific depths sampled for microbiology at Site U1434 are shown in Figure F33. Coring in Hole U1434A yielded 6 routine, 5–10 cm whole-round samples to be used for microbiological analysis from 208 to 275 mbsf. We collected whole-round samples for microbiology adjacent to samples for interstitial water measurements in order to understand proximal interstitial water chemistry (see [Geochemistry](#)).

We collected and preserved 13 samples either from the split cores on the sampling table or from basement samples shortly after the samples were retrieved from the catwalk for investigating the microbiology of interfaces using lipid and nucleic acid analyses. We obtained these samples between 207 and 303 mbsf in Hole U1434A. We selected these samples by depending on recognition of key intervals and through consultation with sedimentologists or petrologists.

Microbiological analyses

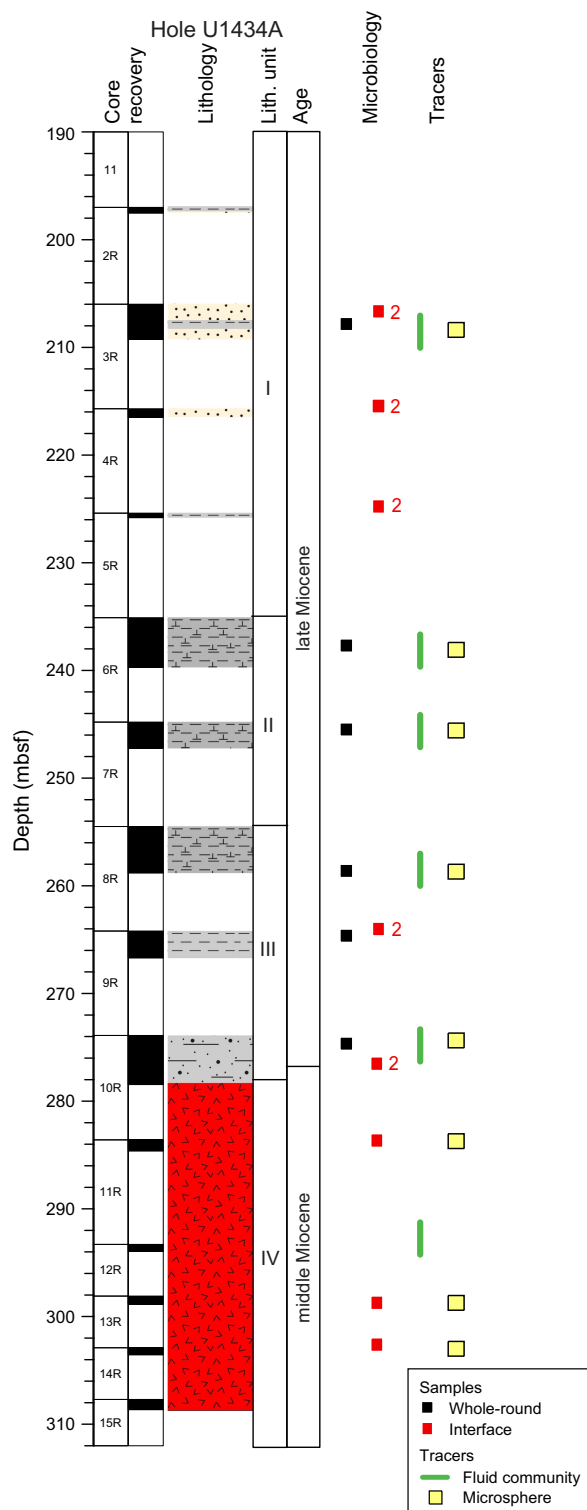
Most of the samples collected at Site U1434 were preserved for shore-based analysis. Samples to be used for DNA and RNA extractions and sequencing were frozen at -80°C , and samples to be used for lipid extraction and analysis were frozen at -80° or -20°C . Portions of the whole-round samples were selected for cultivation-based studies to enrich for anaerobic heterotrophs and autotrophs.

Contamination testing

We used two different methods of contamination testing during coring at Site U1434. Microsphere tracers were used with the RCB coring system in Hole U1434A by adding them to the core catcher sub in Cores 349-U1434A-3R through 14R (208–303 mbsf; Figure F33). Two microsphere samples were collected from each of those cores: one from scrapings of the core surface and one as a subsample from the interior of each sample. Microscopic counts of the microspheres in these samples will be performed in shore-based laboratories using the Procedure for Curation of DeepBIOS (www.kochi-core.jp/DeepBIOS).

Six fluid community tracer (FCT) samples were collected either from the drilling fluids that drained from the core liners when cores arrived on the catwalk or from a sampling port near the mud pumps on the drill rig floor during active coring. The fluids collected for FCT samples correspond to cores obtained between 208 and 293 mbsf (Figure F33). Microbial community DNA and lipids from FCT samples will be compared to the same measurements made on the microbiology samples to determine if the drilling fluids contain microbes that can be regularly tracked as recognizable contaminant taxa.

Figure F33. Collection depths of microbiology whole-round and interface samples and contamination testing samples, Hole U1434A. Number "2" means two samples were collected at the specified depth.



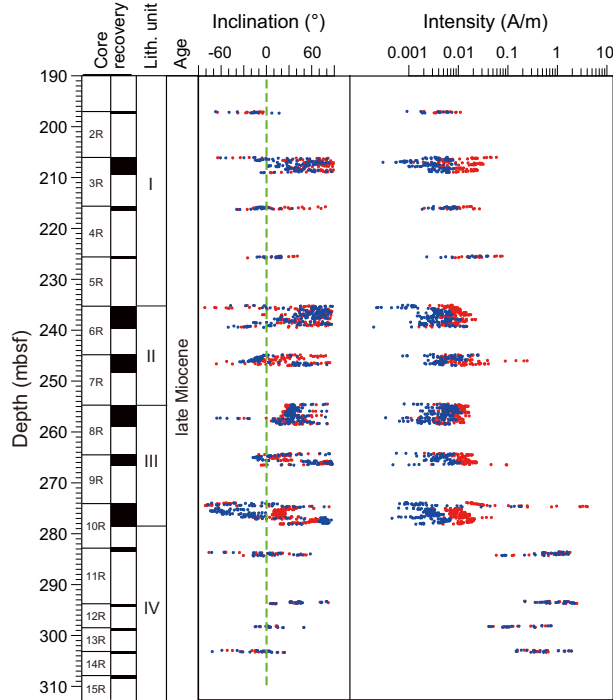
Paleomagnetism

At Site U1434, the pass-through magnetometer measurements on all archive-half cores were conducted using the 2G superconducting rock magnetometer, with demagnetization steps of 0, 5, 10, and 20 mT. The results were analyzed using Zijderveld diagrams (Zijderveld, 1967), and the characteristic remanent magnetization direction was obtained using principal component analysis (Kirschvink, 1980).

Natural remanent magnetization of sedimentary cores

Downhole variation in paleomagnetic data obtained from Hole U1434A is illustrated in Figure F34. The generally low recovery rate limits magnetic characterization of sediment and basement rock at this site. Natural remanent magnetization (NRM) intensity ranges between 0.001 and 0.1 A/m for sediment units and increases to several amperes per meter (A/m) for basalt units (Figure F34), suggesting that the basalt units contain more iron oxide than the overlying sediment. Most cores exhibit positive inclinations, with the maximum values close to $\sim 90^\circ$. Similar to all previous sites, after 20 mT alternating field (AF) demagnetization, the near-vertical inclinations caused by drilling-induced remagnetization shift to lower values for sediment; NRM intensity of sediment significantly decreases but only slightly for basalt. This indicates that basalt contains more high-coercivity minerals, mostly in single domain state. In contrast, sediment contains more pseudo-single domain or multiple domain magnetic particles.

Figure F34. Paleomagnetic measurements of NRM inclination and intensity on archive core sections of sediment after 0 mT (red) and 20 mT (blue) AF demagnetization for Hole U1434A.



Paleomagnetic demagnetization results and magnetostratigraphy

Representative vector plots (Zijderveld, 1967) showing magnetic behavior of detailed AF demagnetization are given in Figure F35. Generally, behavior can be classified into two groups. The first group (sediment) exhibits relatively larger vertical overprints (Figures F35A, F35B), which can be removed by 10 mT AF demagnetization. In contrast, the second group (basalt) is more resistant to AF demagnetization (Figure F35C, F35D).

Because of the poor recovery in Hole U1434A, only fragmentary patterns of magnetic polarity can be observed, rendering it difficult to construct a reliable magnetostratigraphy for the hole (Figure F36). Nevertheless, available calcareous nannofossil ages allow us to tentatively correlate certain parts of the magnetic polarity interval recorded in the sediment with the geomagnetic polarity timescale (GPTS; Gradstein et al., 2012). Biostratigraphic samples at ~ 278 mbsf have been assigned an age < 11.9 Ma (see **Biostratigraphy**); therefore, we interpret that sediment with observed negative inclinations at this depth were likely deposited within Chron C5r (11.056–12.049 Ma). The dominant long positive inclinations between ~ 250 and 270 mbsf may represent the Subchron C5n (9.984–11.06 Ma). The short positive polarity zone between ~ 235 and 240 mbsf appears to have recorded Chron C4An (8.771–9.015 Ma), and the positive polarity zone between 205 and 210 mbsf can be tentatively assigned to Chron C4n at ~ 7.15 Ma. Such a pattern also indicates a low sedimentation rate for sediment recovered at this site.

Figure F35. Representative vector end-point diagrams (Zijderveld, 1967) of magnetization directions for (A, B) sediment and (C, D) basalt samples through stepwise alternating field demagnetization.

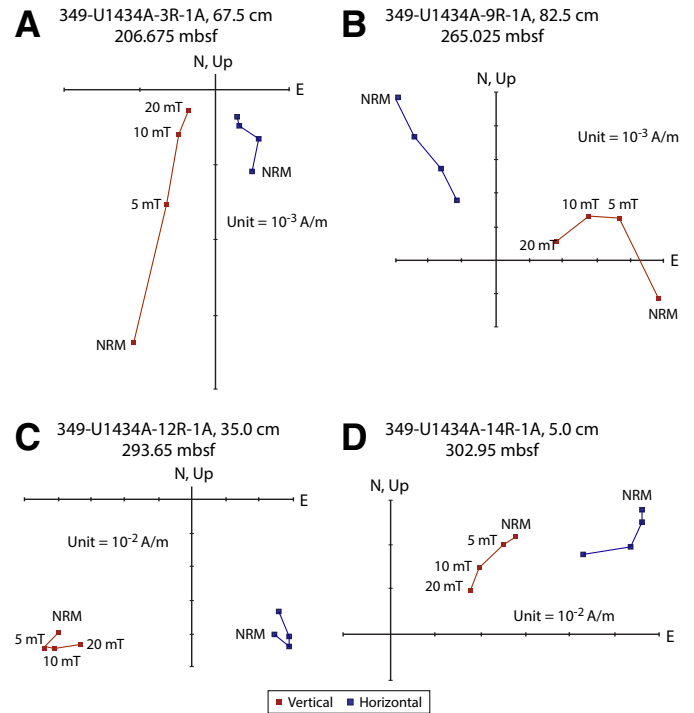
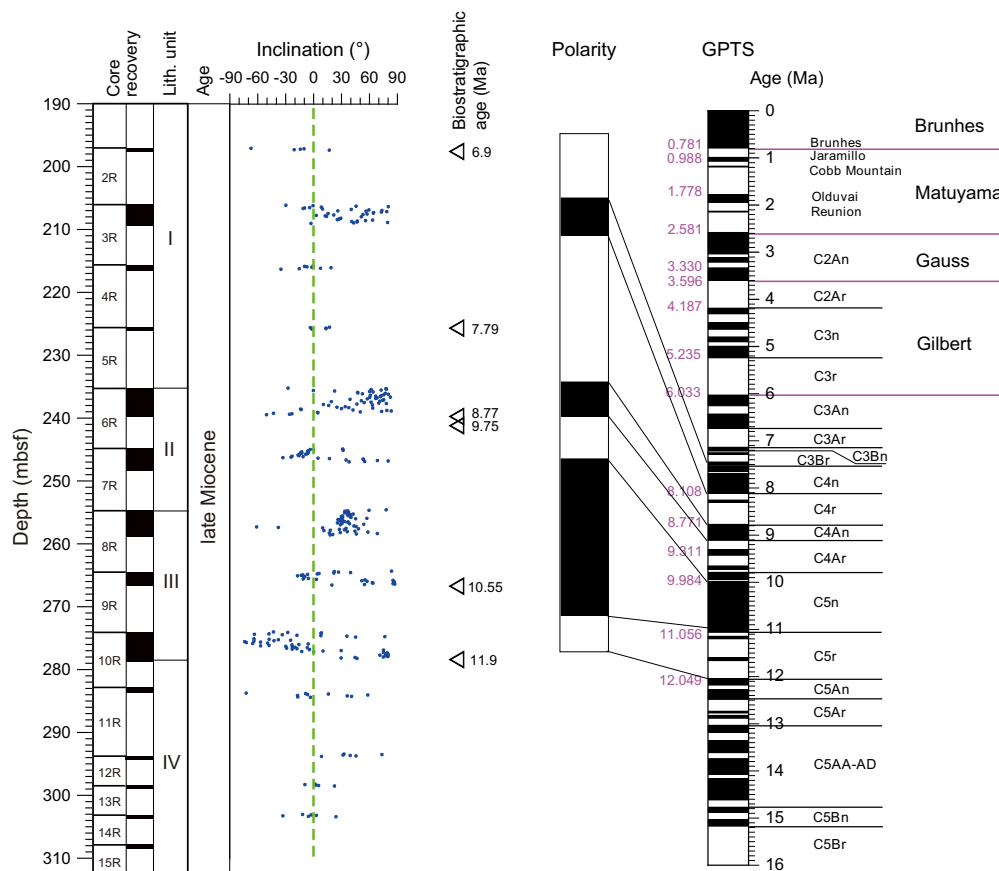


Figure F36. Magnetostratigraphic results with biostratigraphic age correlation for Hole U1434A using paleomagnetic inclination after 20 mT alternating field demagnetization. For GPTS (Gradstein et al., 2012), black = normal polarity and white = reversed polarity.



The basalt unit below 280 mbsf appears to have recorded positive polarity. This coincides with Sites U1431 and U1433, at which positive polarities are observed for the upper part of the basalt units. These preliminary magnetostratigraphic signatures at Site U1434 await verification by shore-based studies.

Physical properties

At Site U1434, we measured physical properties on whole-round cores (bulk density from gamma ray attenuation [GRA], magnetic susceptibility, and natural gamma radiation [NGR]), on split cores (thermal conductivity and α -caliper P -wave velocity), and on discrete samples (porosity, moisture, and density) (Figure F37). Because of the low recovery rate, measurements of physical properties show significant gaps between measured intervals. No discrete samples were taken for physical property measurements in the basalt sections because of poor recovery (lithostratigraphic Unit IV; 278.27–312.50 mbsf).

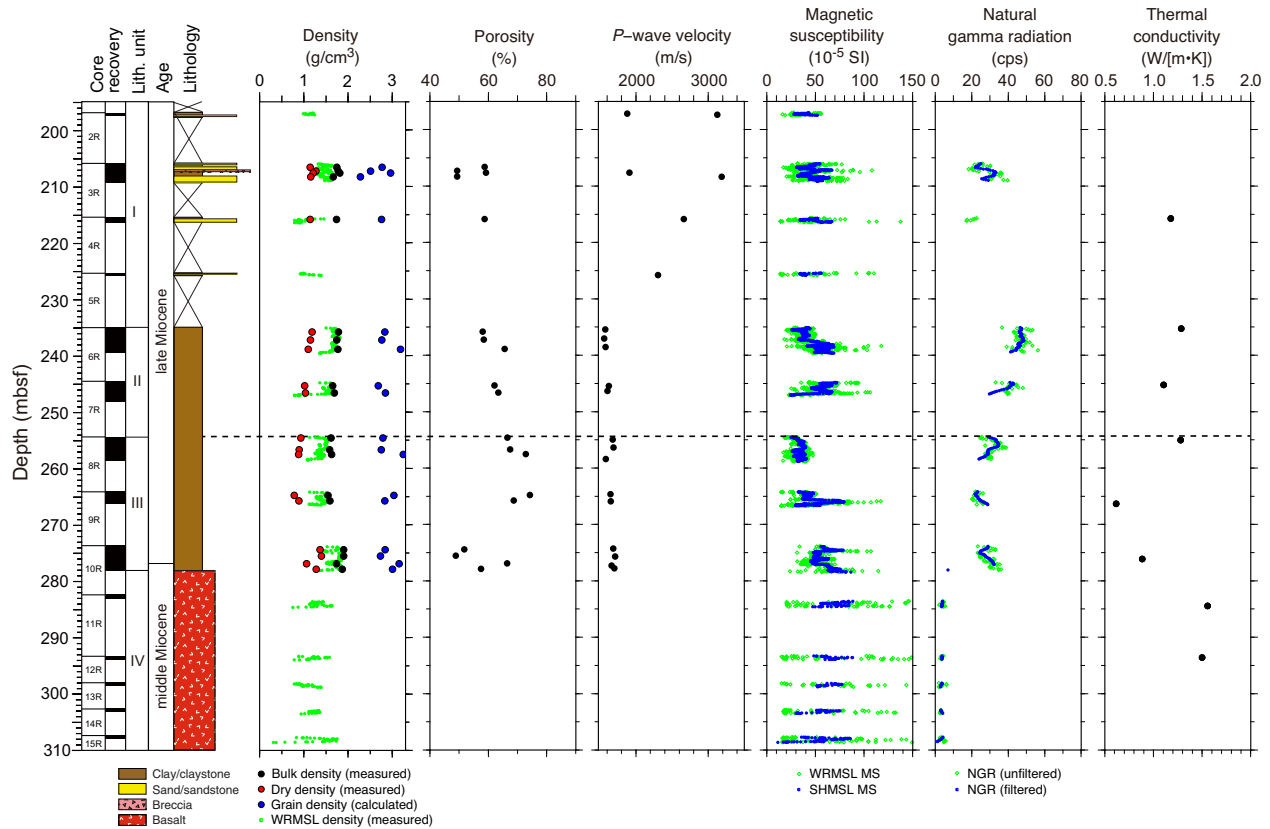
Physical property measurements

After whole-round core measurements were made, data points out of range were removed. The whole-round core data were then smoothed using a 10-point average moving window (Figure F37). Magnetic susceptibility values in Hole U1434A are relatively uniform (30×10^{-5} to 70×10^{-5} SI; average = 50×10^{-5} SI) in lithostratigraphic Unit I (197.00–235.10 mbsf), which consists of interbedded claystone and volcanoclastic sandstone. In Unit II (nannofossil clay-

stone; 215.10–254.59 mbsf), magnetic susceptibility increases slightly to a range of 30×10^{-5} to 80×10^{-5} SI, with an average of 60×10^{-5} SI. In Unit III (yellowish brown claystone; 254.59–278.27 mbsf), magnetic susceptibility reaches a minimum (20×10^{-5} SI) at the Unit II/III boundary and then increases to a range of 60×10^{-5} to 90×10^{-5} SI at the Unit III/IV boundary. The range of magnetic susceptibility values in the basalt section (Unit IV; 278.27–308.65 mbsf) is 10×10^{-5} to 90×10^{-5} SI.

Because of the low recovery rate, NGR data are only available for 205–212 mbsf in Unit I, with values ranging from 20 to 30 counts/s. NGR decreases from ~ 45 to ~ 30 counts/s in Unit II, stays relatively uniform at ~ 25 counts/s in Unit III, and then drops to low values < 5 counts/s in the basalt of Unit IV. P -wave velocity ranges from 1950 to 3100 m/s in Unit I, drops to ~ 1850 m/s in the claystone of Units II and III, and was not measured on the basalt pieces of Unit IV. Bulk density remains relatively constant (~ 1.8 g/cm³) in Unit II and the top half of Unit III and then increases slightly to 1.8–2.0 g/cm³ in the sediment layer (275–278 mbsf) immediately above the basaltic section. Dry bulk density remains constant (1.2 g/cm³) in Unit I, decreases gradually through Unit II and top half of Unit III, reaches a minimum (~ 0.7 g/cm³) at 265 mbsf, and then increases to 1.3 g/cm³ in the sediment layer (275–278 mbsf) immediately above the basalt. Grain density is quite variable through Units I and II and reaches 3.25 g/cm³ in the yellowish brown clays of Unit III. Porosity increases with depth from $\sim 50\%$ to $\sim 75\%$ in Units I and II and the top half of Unit III and then drops to 50% in the sediment layer immediately above the basalt.

Figure F37. Physical property measurements, Hole U1434A. Dashed line marks the lithostratigraphic boundary between Units II and III. WRMSL = Whole Round Multisensor Logger, SHMSL = Section-Half Multisensor Logger.



Thermal conductivity remains constant (~ 1.1 – 1.3 W/[m·K]) in Units I and II, drops to 0.7 – 0.9 W/[m·K] in Unit III, and then increases to ~ 1.5 W/[m·K] in Unit IV.

Data interpretation and lithology correlation

In general, physical properties correlate with lithology, composition, and lithification. In Hole U1434A, the observed range of values for magnetic susceptibility (30×10^{-5} to 80×10^{-5} SI) and NGR (25–45 counts/s) in lithostratigraphic Units I–III are typical for clay material, which dominates the sediment layers. The low NGR values in Unit IV correspond to the basalt layer. Magnetic susceptibility values in the basalt range from 10×10^{-5} to 90×10^{-5} SI, which is much lower than typical basalt. This is probably at least partly due to the poor recovery and the relatively low volume of basalt pieces in the core liner.

High grain densities in the claystone of Units II and III suggest the presence of heavy minerals, such as hematite. Porosity measured on discrete samples increases from 40% to 60% with depth, which might be correlated to lithification and composition of the claystone.

References

- Briaes, A., Patriat, P., and Tapponnier, P., 1993. Updated interpretation of magnetic anomalies and seafloor spreading stages in the South China Sea: implications for the Tertiary tectonics of Southeast Asia. *Journal of Geophysical Research: Solid Earth*, 98(B4):6299–6328. <http://dx.doi.org/10.1029/92JB02280>
- Bryant, W.R., and Bennett, R.H., 1988. Origin, physical, and mineralogical nature of red clays: the Pacific Ocean Basin as a model. *Geo-Marine Letters*, 8(4):189–249. <http://dx.doi.org/10.1007/BF02281640>
- Expedition 329 Scientists, 2011. Site U1367. In D'Hondt, S., Inagaki, F., Alvarez Zarikian, C.A., and the Expedition 329 Scientists, *Proc. IODP*, 329: Tokyo (Integrated Ocean Drilling Program Management International, Inc.). doi:10.2204/iodp.proc.329.105.2011.
- Gradstein, F.M., Ogg, J.G., Schmitz, M.D., and Ogg, G.M. (Eds.), 2012. *The Geological Time Scale 2012*: Oxford, UK (Elsevier).
- Hékinian, R., Bonté, P., Pautot, G., Jacques, D., Labeyrie, L.D., Mikkelsen, N., and Reyss, J.-L., 1989. Volcanics from the South China Sea ridge system. *Oceanologica Acta*, 12(2):101–115.
- Ishihara, T., and Kisimoto, K., 1996. Magnetic anomaly map of East Asia, 1:4,000,000 (CD-ROM version). Geological Survey of Japan, Coordinating Committee for Coastal and Offshore Geoscience Programs in East and Southeast Asia (CCOP).
- Kirschvink, J.L., 1980. The least-squares line and plane and the analysis of palaeomagnetic data. *Geophysical Journal of the Royal Astronomical Society*, 62(3):699–718. <http://dx.doi.org/10.1111/j.1365-246X.1980.tb02601.x>
- Le Maitre, R.W., Bateman, P., Dudek, A., Keller, J., Lameyre, J., Le Bas, M.J., Sabine, P.A., Schmid, R., Sorensen, H., Streckeisen, A., Woolley, A.R., and Zanettin, B., 1989. *A Classification of Igneous Rocks and Glossary of Terms*: Oxford, UK (Blackwell Science Publishing).
- Li, C.-F., Lin, J., Kulhanek, D.K., Williams, T., Bao, R., Briaes, A., Brown, E.A., Chen, Y., Clift, P.D., Colwell, F.S., Dadd, K.A., Ding, W., Almeida, I.H., Huang, X.-L., Hyun, S., Jiang, T., Koppers, A.A.P., Li, Q., Liu, C., Liu, Q., Liu, Z., Nagai, R.H., Peleo-Alampay, A., Su, X., Sun, Z., Tejada, M.L.G., Trinh, H.S., Yeh, Y.-C., Zhang, C., Zhang, F., Zhang, G.-L., and Zhao, X., 2015a. Expedition 349 summary. In Li, C.-F., Lin, J., Kulhanek, D.K., and the Expedition 349 Scientists, *Proceedings of the Integrated Ocean Drilling*

- Program, 349: *South China Sea Tectonics*: College Station, TX (International Ocean Discovery Program). <http://dx.doi.org/10.14379/iodp.proc.349.101.2015>
- Li, C.-F., Lin, J., Kulhanek, D.K., Williams, T., Bao, R., Briais, A., Brown, E.A., Chen, Y., Clift, P.D., Colwell, F.S., Dadd, K.A., Ding, W., Almeida, I.H., Huang, X.-L., Hyun, S., Jiang, T., Koppers, A.A.P., Li, Q., Liu, C., Liu, Q., Liu, Z., Nagai, R.H., Peleo-Alampay, A., Su, X., Sun, Z., Tejada, M.L.G., Trinh, H.S., Yeh, Y.-C., Zhang, C., Zhang, F., Zhang, G.-L., and Zhao, X., 2015b. Methods. In Li, C.-F., Lin, J., Kulhanek, D.K., and the Expedition 349 Scientists, *Proceedings of the Integrated Ocean Drilling Program, 349: South China Sea Tectonics*: College Station, TX (International Ocean Discovery Program). <http://dx.doi.org/10.14379/iodp.proc.349.102.2015>
- Li, C.-F., Lin, J., Kulhanek, D.K., Williams, T., Bao, R., Briais, A., Brown, E.A., Chen, Y., Clift, P.D., Colwell, F.S., Dadd, K.A., Ding, W., Almeida, I.H., Huang, X.-L., Hyun, S., Jiang, T., Koppers, A.A.P., Li, Q., Liu, C., Liu, Q., Liu, Z., Nagai, R.H., Peleo-Alampay, A., Su, X., Sun, Z., Tejada, M.L.G., Trinh, H.S., Yeh, Y.-C., Zhang, C., Zhang, F., Zhang, G.-L., and Zhao, X., 2015c. Site U1433. In Li, C.-F., Lin, J., Kulhanek, D.K., and the Expedition 349 Scientists, *Proceedings of the Integrated Ocean Drilling Program, 349: South China Sea Tectonics*: College Station, TX (International Ocean Discovery Program). <http://dx.doi.org/10.14379/iodp.proc.349.105.2015>
- Li, C.-F., Zhou, Z., Li, J., Chen, B., and Geng, J., 2008. Magnetic zoning and seismic structure of the South China Sea ocean basin. *Marine Geophysical Researches*, 29(4):223–238. <http://dx.doi.org/10.1007/s11001-008-9059-4>
- Macdonald, G.A., 1968. Composition and origin of Hawaiian lavas. In Coats, R.R., Hay, R.L., and Anderson, C.A. (Eds.), *Studies in Volcanology—A Memoir in Honor of Howel Williams*. Memoir - Geological Society of America, 116:477–522. <http://dx.doi.org/10.1130/MEM116-p477>
- Macdonald, G.A., and Katsura, T., 1964. Chemical composition of Hawaiian lavas. *Journal of Petrology*, 5(1):82–133. <http://petrology.oxfordjournals.org/content/5/1/82.abstract>
- Pautot, G., Rangin, C., Briais, A., Taponnier, P., Beuzart, P., Lericolais, G., Mathieu, X., Wu, J., Han, S., Li, H., Lu, Y., and Zhao, J., 1986. Spreading direction in the central South China Sea. *Nature*, 321(6066):150–154. <http://dx.doi.org/10.1038/321150a0>
- Tu, K., Flower, M.F.J., Carlson, R.W., Xie, G., Chen, C.-Y., and Zhang, M., 1992. Magmatism in the South China Basin: 1. Isotopic and trace-element evidence for an endogenous Dupal mantle component. *Chemical Geology*, 97(1–2):47–63. [http://dx.doi.org/10.1016/0009-2541\(92\)90135-R](http://dx.doi.org/10.1016/0009-2541(92)90135-R)
- Wang, X.-C., Li, Z.-X., Li, X.-H., Li, J., Liu, Y., Long, W.-G., Zhou, J.-B., and Wang, F., 2012. Temperature, pressure, and composition of the mantle source region of late Cenozoic basalts in Hainan Island, SE Asia: a consequence of a young thermal mantle plume close to subduction zones? *Journal of Petrology*, 53(1):177–233. <http://dx.doi.org/10.1093/petrology/egr061>
- Wang, Y., and Yang, Q., 1992. Neogene and Quaternary radiolarians from Leg 125. In Fryer, P., Pearce, J.A., Stokking, L.B., et al., *Proceedings of the Ocean Drilling Program, Scientific Results*, 125: College Station, TX (Ocean Drilling Program), 95–112. <http://dx.doi.org/10.2973/odp.proc.sr.125.174.1992>
- Wetzel, A., 2009. The preservation potential of ash layers in the deep-sea: the example of the 1991-Pinatubo ash in the South China Sea. *Sedimentology*, 56(7):1992–2009. <http://dx.doi.org/10.1111/j.1365-3091.2009.01066.x>
- Wetzel, A., and Unverricht, D., 2013. A muddy megaturbidite in the deep central South China Sea deposited ~350 yrs BP. *Marine Geology*, 346:91–100. <http://dx.doi.org/10.1016/j.margeo.2013.08.010>
- Zhang, G., Smith-Duque, C., Tang, S., Li, H., Zarikian, C., D'Hondt, S., Inagaki, F., and IODP Expedition 329 Scientists, 2012a. Geochemistry of basalts from IODP Site U1365: implications for magmatism and mantle source signatures of the mid-Cretaceous Osborn Trough. *Lithos*, 144–145:73–87. <http://dx.doi.org/10.1016/j.lithos.2012.04.014>
- Zhang, G., Zeng, Z., Yin, X., Wang, X., and Chen, D., 2009. Deep fractionation of clinopyroxene in the East Pacific Rise 13°N: evidence from high MgO MORB and melt inclusions. *Acta Geologica Sinica*, 83(2):266–277. <http://dx.doi.org/10.1111/j.1755-6724.2009.00030.x>
- Zhang, G.-L., Chen, L.-H., and Li, S.-Z., 2013. Mantle dynamics and generation of a geochemical mantle boundary along the East Pacific Rise—Pacific/Antarctic Ridge. *Earth and Planetary Science Letters*, 383:153–163. <http://dx.doi.org/10.1016/j.epsl.2013.09.045>
- Zhang, G.-L., Zong, C.-L., Yin, X.-B., and Li, H., 2012b. Geochemical constraints on a mixed pyroxenite–peridotite source for East Pacific Rise basalts. *Chemical Geology*, 330–331:176–187. <http://dx.doi.org/10.1016/j.chemgeo.2012.08.033>
- Zijderveld, J.D.A., 1967. AC demagnetization of rocks: analysis of results. In Collinson, D.W., Creer, K.M., and Runcorn, S.K. (Eds.), *Methods in Palaeomagnetism*: Amsterdam (Elsevier), 254–286.

doi:10.14379/iodp.proc.349.107.2015

Site U1435¹



Contents

- 1 Background and objectives
- 1 Operations
- 3 Lithostratigraphy
- 10 Biostratigraphy
- 12 Geochemistry
- 15 Microbiology
- 16 Paleomagnetism
- 18 Physical properties
- 20 References

C.-F. Li, J. Lin, D.K. Kulhanek, T. Williams, R. Bao, A. Briais, E.A. Brown, Y. Chen, P.D. Clift, F.S. Colwell, K.A. Dadd, W.-W. Ding, I. Hernández-Almeida, X.-L. Huang, S. Hyun, T. Jiang, A.A.P. Koppers, Q. Li, C. Liu, Q. Liu, Z. Liu, R.H. Nagai, A. Peleo-Alampay, X. Su, Z. Sun, M.L.G. Tejada, H.S. Trinh, Y.-C. Yeh, C. Zhang, F. Zhang, G.-L. Zhang, and X. Zhao²

Keywords: International Ocean Discovery Program, IODP, *JOIDES Resolution*, Expedition 349, Site U1435, South China Sea, continent/ocean boundary, continental breakup, synrift sediment, microbiological community, seafloor spreading, unconformity, benthic foraminifers, shallow-marine deposits, manganese nodule

Background and objectives

Coring at Site U1435 became a high priority after failing to achieve our basement objectives at Site U1432 because the final cementing operation compromised the reentry system. This site was originally added as an alternate because of the high risk of being unable to reach basement at Site U1432, which required ~1900 m of penetration to reach the target depth.

Site U1435 is located on a structural high at the transition between the extended continental crust and the oceanic crust (Figures F1, F2). Similar conspicuous structural-high features can be found on the continent/ocean boundary in many other seismic profiles crossing the South China Sea northern margin and therefore appear to represent tectonic structures typical of the area. The true lithology and formation mechanism of this structural high were speculative; it could be a volcanic extrusion associated with continental extension at the onset of seafloor spreading, lower crust material emplaced from preferential lower crust extension, exhumed mantle material, or a structural high composed of older (Mesozoic) sedimentary rocks. Coring at this location was designed to help pinpoint the exact nature of this structure and improve our understanding of early continental breakup, the rift-to-drift transition, and seafloor spreading processes.

Operations

Site U1435 (proposed Site SCS-6C) was an alternate site selected when we were unable to reach our basement objectives at Site U1432. Because we anticipated shallow Cenozoic sediment cover (~10 m) above the acoustic basement, we conducted a 3.5 kHz sonar survey to select a location with maximum sediment thickness to help stabilize the drill string when trying to penetrate basement

with thin sediment cover in rough weather. After reaching basement, the plan was to core as deeply into basement as time permitted. Cenozoic sediment thickness was greater than expected based on the seismic interpretation. Hole U1435A was cored with the rotary core barrel (RCB) to a final depth of 300.0 m below seafloor (mbsf) when time allocated to the expedition expired (Table T1). The RCB was deployed 32 times, recovering 171.37 m of core over 300.0 m of penetration (57.1% recovery).

Transit to Site U1435

After a 336 nmi transit lasting 39.65 h, the vessel arrived at Site U1435 and switched into dynamic positioning mode at 1524 h (UTC + 8 h) on 24 March 2014. At 2045 h, an acoustic positioning beacon was deployed. The position reference was a combination of GPS signals and a single acoustic beacon.

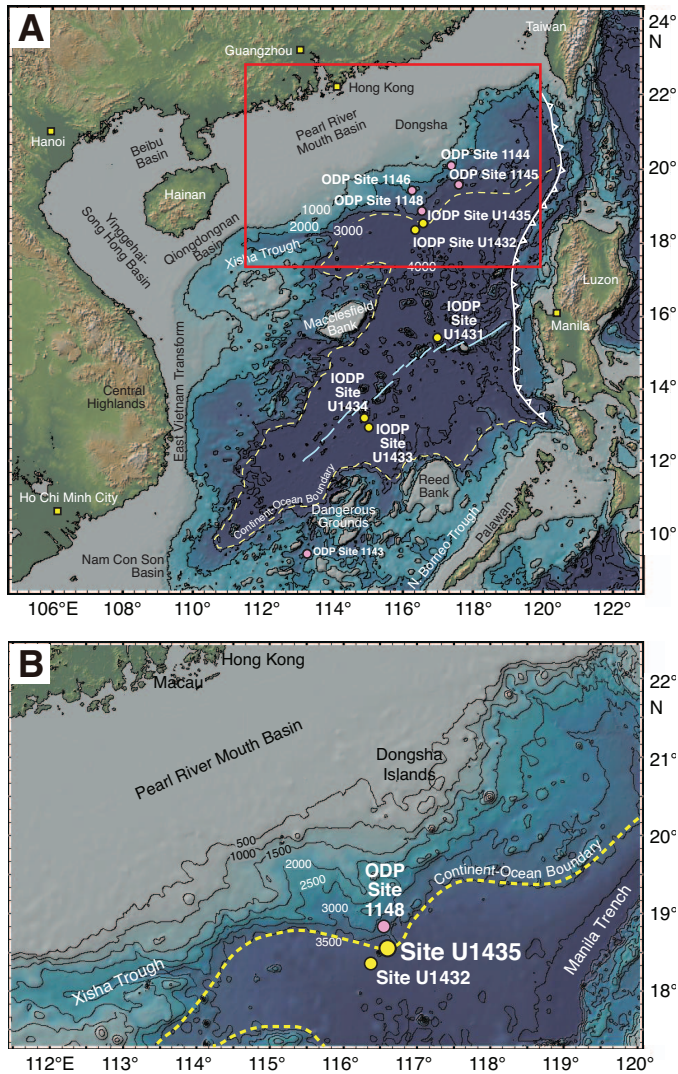
Hole U1435A

After arriving on site and deploying the acoustic positioning beacon, an RCB bottom-hole assembly (BHA) was assembled with a new RCB C-7 bit. The core barrels were spaced out at the surface, and the 172.07 m BHA was assembled. The BHA was then run in the hole to 3214.9 m below rig floor (mbrf), and the top drive was picked up and spaced out to 3261.6 mbrf to spud Hole U1435A. While lowering the drill pipe, we conducted a sonar survey with the 3.5 kHz array sonar to select a hole location to maximize sediment thickness. Hole U1435A was spudded at 0035 h on 25 March 2014. The estimated depth of the seafloor was 3261.6 mbrf using the precision depth recorder. Final seafloor depth for the hole was 3264.0 mbrf (3252.5 m below sea level [mbsl]), which was determined by tagging the seafloor with the drill bit. We advanced Hole U1435A by coring from the seafloor to 3564.0 mbrf (300.0 mbsf). Microspheres were deployed in each RCB core catcher sub from

¹ Li, C.-F., Lin, J., Kulhanek, D.K., Williams, T., Bao, R., Briais, A., Brown, E.A., Chen, Y., Clift, P.D., Colwell, F.S., Dadd, K.A., Ding, W.-W., Hernández-Almeida, I., Huang, X.-L., Hyun, S., Jiang, T., Koppers, A.A.P., Li, Q., Liu, C., Liu, Q., Liu, Z., Nagai, R.H., Peleo-Alampay, A., Su, X., Sun, Z., Tejada, M.L.G., Trinh, H.S., Yeh, Y.-C., Zhang, C., Zhang, F., Zhang, G.-L., and Zhao, X., 2015. Site U1435. In Li, C.-F., Lin, J., Kulhanek, D.K., and the Expedition 349 Scientists, *Proceedings of the International Ocean Discovery Program, 349: South China Sea Tectonics*: College Station, TX (International Ocean Discovery Program). <http://dx.doi.org/10.14379/iodp.proc.349.107.2015>

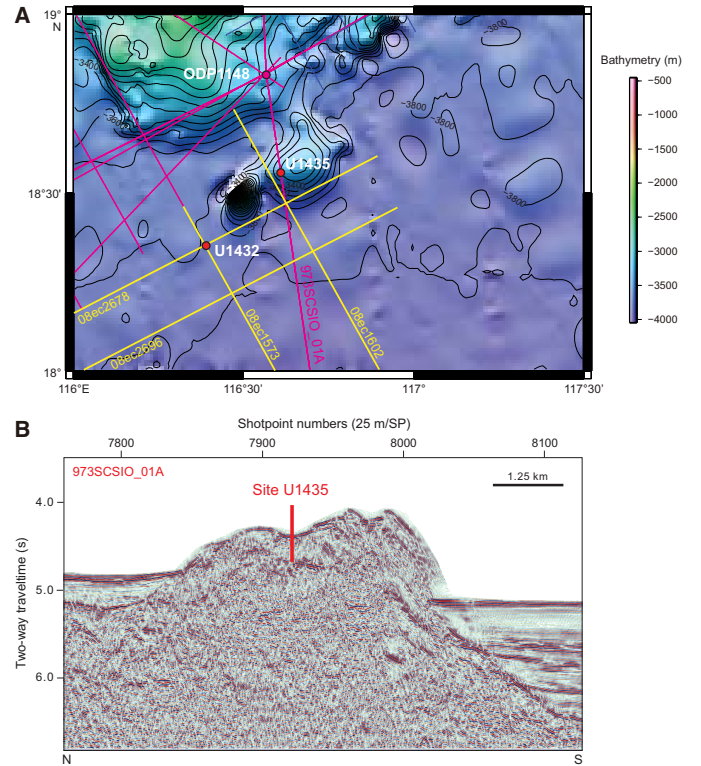
² Expedition 349 Scientists' addresses.

Figure F1. A. Bathymetric map of the South China Sea region. Solid yellow circles = Expedition 349 sites. Solid pink circles = ODP Leg 184 sites. Yellow dashed line = inferred continent/ocean boundary, blue lines = fossil South China Sea spreading center, white-flagged line = Manila Trench. B. Detailed bathymetry around Site U1432 (red box in A) showing nearby continental shelf, the Manila Trench, and inferred continent/ocean boundary.



Core 349-U1435A-5R to total depth. Coring continued to Core 32R (300 mbsf), when operational time for the expedition expired. Penetration rates varied from 2.8 to 58.2 m/h over the cored interval.

Figure F2. A. Regional contoured bathymetric map showing seismic reflection profiles (yellow, pink, and blue lines) and the location of Sites U1432 and U1435 and Ocean Drilling Program (ODP) Site 1148. Contour interval = 100 m. B. Seismic profile Line 973SCSIO_01A with location of Site U1435. SP = shotpoint.



Total depth of Hole U1435A was reached at 0730 h on 27 March. After reaching total depth, the final core was pulled to the surface and laid out. At the completion of coring Hole U1435A, 32 RCB cores had been cut over a 300.0 m interval, recovering 171.37 m of core (57.1% recovery).

After reaching total depth and laying out the last core, the drill string was pulled out of the hole with the top drive to 3535.1 mbrf (271.1 mbsf). The drilling knobbies were laid out, the top drive set back, and the drill string tripped to the surface. The bit cleared the seafloor at 1020 h and then cleared the rotary table at 1835 h. After securing the rig floor for transit and pulling the hydrophones and thrusters, the vessel switched to cruise mode and began the transit to Keelung, Taiwan, at 1900 h on 27 March. Total time spent in Hole U1435A was 75.5 h (3.2 days). Expedition 349 officially ended with the first line ashore in Keelung at 0710 h on 30 March.

Table T1. Coring summary, Site U1435. CSF = core depth below seafloor, DRF = drilling depth below rig floor, DSF = drilling depth below seafloor. R core type = rotary core barrel. RCB = rotary core barrel. [Download table in .csv format.](#)

Hole U1435A

Latitude: 18°33.3466'N
 Longitude: 116°36.6174'E
 Water depth (m): 3252.46
 Date started (UTC): 24 March 2014, 0724 h
 Date finished (UTC): 27 March 2014, 1100 h
 Time on hole (days): 3.2
 Seafloor depth (m DRF): 3264
 Seafloor depth calculation method: Seafloor tag with drill bit
 Rig floor to sea level (m): 11.54
 Drilling System: 9-7/8 inch RCB bit with 172.07 m BHA
 Penetration depth (mbsf): 300
 Cored interval (m): 300
 Recovered length (m): 171.37
 Recovery (%): 57
 Total cores (no.): 32
 RCB cores (no.): 32
 Age of oldest sediment cored: pre-Oligocene

Core	Date (2014)	Time UTC (h)	Depth DSF (m)		Interval advanced (m)	Depth CSF (m)		Length of core recovered (m)	Recovery (%)	Sections (no.)	Comments
			Top of interval	Bottom of interval		Top of cored interval	Bottom of cored interval				
349-U1435A-											
1R	24 Mar	1715	0.00	9.70	9.7	0.00	0.00	0.00	0	0	No rotation or pumping
2R	24 Mar	1800	9.70	19.40	9.7	9.70	9.71	0.01	0	1	No rotation or pumping
3R	24 Mar	1905	19.40	26.30	6.9	19.40	19.45	0.03	0	1	
4R	24 Mar	2045	26.30	36.00	9.7	26.30	26.77	0.47	5	2	
5R	24 Mar	2225	36.00	45.70	9.7	36.00	39.68	3.68	38	4	Microspheres
6R	24 Mar	2340	45.70	55.40	9.7	45.70	49.30	3.60	37	4	Microspheres
7R	25 Mar	0055	55.40	65.10	9.7	55.40	59.60	4.20	43	4	Microspheres
8R	25 Mar	0220	65.10	74.80	9.7	65.10	71.61	6.51	67	6	Microspheres
9R	25 Mar	0340	74.80	84.50	9.7	74.80	79.84	5.04	52	5	Microspheres
10R	25 Mar	0510	84.50	94.20	9.7	84.50	87.75	3.25	34	3	Microspheres
11R	25 Mar	0630	94.20	103.90	9.7	94.20	95.05	0.85	9	2	Microspheres
12R	25 Mar	0755	103.90	113.60	9.7	103.90	110.10	6.20	64	5	Microspheres
13R	25 Mar	0945	113.60	123.30	9.7	113.60	121.86	8.26	85	7	Microspheres
14R	25 Mar	1115	123.30	133.00	9.7	123.30	125.57	2.27	23	3	Microspheres
15R	25 Mar	1250	133.00	142.70	9.7	133.00	138.47	5.47	56	5	Microspheres
16R	25 Mar	1435	142.70	152.40	9.7	142.70	151.86	9.16	94	7	Microspheres
17R	25 Mar	1625	152.40	162.10	9.7	152.40	160.58	8.18	84	7	Microspheres
18R	25 Mar	1810	162.10	171.80	9.7	162.10	172.04	9.94	102	8	Microspheres
19R	25 Mar	1930	171.80	181.50	9.7	171.80	181.33	9.53	98	8	Microspheres
20R	25 Mar	2005	181.50	191.20	9.7	181.50	191.12	9.62	99	8	Microspheres
21R	25 Mar	2230	191.20	200.90	9.7	191.20	200.03	8.83	91	7	Microspheres
22R	26 Mar	0020	200.90	210.60	9.7	200.90	201.09	0.19	2	1	Microspheres
23R	26 Mar	0200	210.60	220.30	9.7	210.60	218.23	7.63	79	6	Microspheres
24R	26 Mar	0350	220.30	230.00	9.7	220.30	229.92	9.62	99	8	Microspheres
25R	26 Mar	0545	230.00	239.70	9.7	230.00	237.16	7.16	74	6	Microspheres
26R	26 Mar	0755	239.70	249.40	9.7	239.70	249.23	9.53	98	8	Microspheres
27R	26 Mar	1055	249.40	259.10	9.7	249.40	258.36	8.96	92	7	Microspheres
28R	26 Mar	1420	259.10	268.80	9.7	259.10	268.73	9.63	99	8	Microspheres
29R	26 Mar	1635	268.80	278.50	9.7	268.80	276.41	7.61	78	6	Microspheres
30R	26 Mar	1825	278.50	288.20	9.7	278.50	282.16	3.66	38	4	Microspheres
31R	26 Mar	2230	288.20	297.90	9.7	288.20	289.22	1.02	11	2	Microspheres
32R	27 Mar	0030	297.90	300.00	2.1	297.90	299.16	1.26	60	2	Microspheres
Total:					300.0			171.37	57	155	

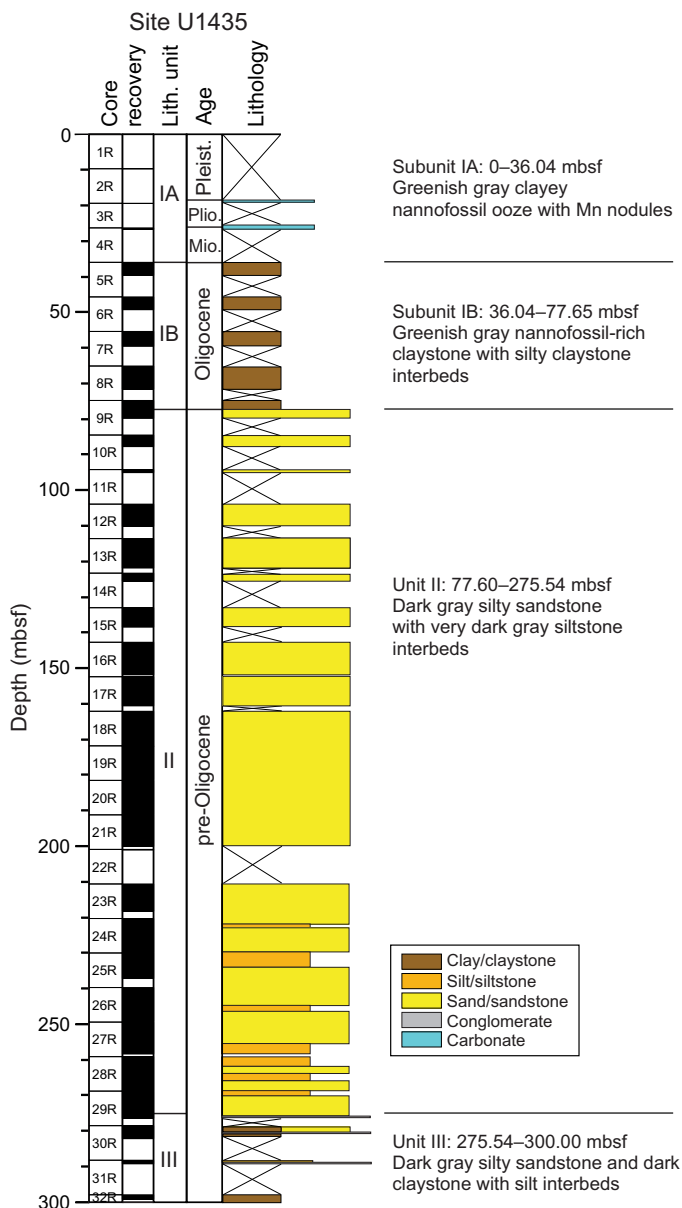
Lithostratigraphy

Lithostratigraphic units

Three lithostratigraphic units are defined within the cored sequence at Site U1435 based on a combination of visual core description and smear slide and thin section inspection, as well as scanning for an array of physical properties, including magnetic susceptibility and color spectra (see [Lithostratigraphy](#) and [Physical properties](#) in the Methods chapter [Li et al., 2015], for details). All three units

are sedimentary (Figures [F3](#), [F4](#)). The site is located on a structural high where sedimentation rates might be expected to be lower than normal. Subunit IA is composed of greenish gray clayey nannofossil ooze and manganese nodules. Subunit IB is composed of nannofossil-rich claystone, clay with nannofossils, and claystone with nannofossils. Unit II is a sequence of dark gray silty sandstone with minor interbeds of very dark gray siltstone. Unit III is composed of dark gray silty sandstone and significant thicknesses of dark gray claystone with silt.

Figure F3. Lithostratigraphy summary, Site U1435.



Unit descriptions

Unit I (0–77.65 mbsf)

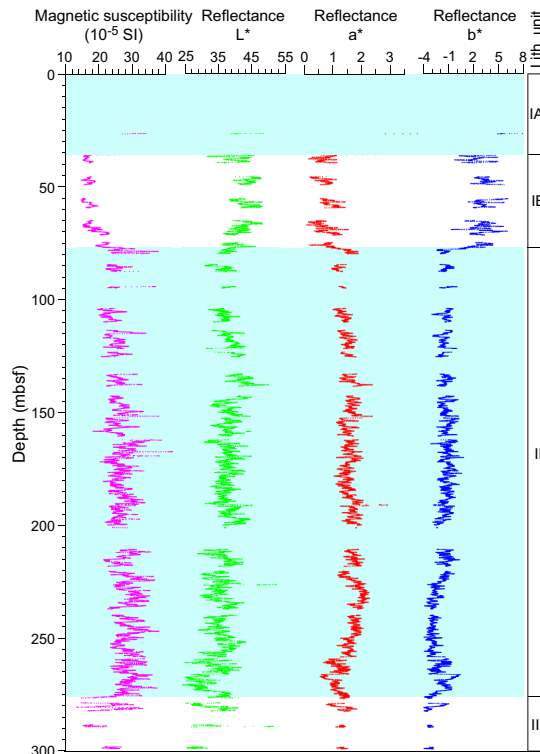
Interval: seafloor to 349-U1435A-9R-2, 135 cm

Depth: 0–77.65 mbsf

Age: Pleistocene–Oligocene

Unit I is a hemipelagic sedimentary deposit with a mixture of continentally derived clays and biogenic microfossils, especially nannofossils. Sedimentation was in deep water, not fundamentally different from the modern setting. However, because sediment did accumulate, the site must not have been continually swept by bottom currents as it is now by westward-moving flow related to the influx from the Pacific through the Luzon Strait (Wang et al., 2011). This period of accumulation was one with sediment starvation and manganese nodule formation, possibly linked to a change in current regime keeping the site free of clastic sediment. Very little sediment

Figure F4. Correlation of lithostratigraphic units with magnetic susceptibility and reflectance spectroscopy (after 20-point running average), Site U1435.



of Oligocene–Pleistocene age was recovered. Therefore, it is not apparent if sedimentation was actually slow during this entire period or whether more hemipelagic sediment had accumulated but was subsequently removed by current activity after the Miocene.

Subunit IA (0–36.04 mbsf)

Interval: seafloor to Sample 349-U1435A-5R-1, 4 cm

Depth: 0–36.04 mbsf

Age: Pleistocene–Miocene

The youngest sediment at this site was likely not recovered either because of poor recovery by RCB coring in soft sediment or because of Mn nodules blocking the core catchers. Core 349-U1435A-1R recovered a tiny amount of clay, whereas Section 3R-1 contained very hard manganese nodules with a typical lobate appearance (Figure F5). These deposits are typically associated with very low sedimentation rates, as the manganese is precipitated directly from seawater and is unable to form except in sediment-starved settings (Cronan, 1980). Manganese crusts normally grow at rates of 0.5–4.0 mm/million years (Cronan, 1980), so the amount of time represented by these nodules could be significant. Recovery of these nodules indicates that sedimentation rates at Site U1435 were very low in the most recent past, further evidence that the position of the drill site on a structural high allowed currents to remove hemipelagic sediment from the area (Hu et al., 2000). Manganese nodules are also found in Cores 4R and 5R, but these are likely fragments that have fallen into the hole from shallower depths.

Below the manganese nodules in Core 3R, the character of Subunit IA is based on only a single core with a recovery of 47 cm. The lithology is dominated by massive clayey nannofossil ooze with a few *Planolites* trace fossils visible on the cut surface.

Subunit IB (36.04–77.65 mbsf)

Interval: Sample 349-U1435A-5R-1, 4 cm, to 9R-2, 135 cm

Depth: 36.04–77.65 mbsf

Age: Oligocene

Subunit IB spans five cores with poor recovery and is composed of mostly greenish gray nannofossil-rich clay and lesser quantities of greenish gray claystone, silty claystone, and claystone with silt. Core 349-U1435A-5R contains interbedded silty claystone and claystone with silt intervals, but deeper in the section the sediment becomes more calcareous, with an increase in the proportion of nannofossils. The nannofossil-rich claystone, clay with nannofossils, and claystone with nannofossils are largely massive and homogeneous, but strong biscuiting over this interval may obscure some features. In more coherent sections, the sediment is heavily bioturbated with trace fossils of the *Nereites* ichnofacies. Figure F6 shows examples of the three burrow types most commonly observed in Subunit IB, *Chondrites*, *Planolites*, and less commonly *Thalassinoides*. The first two in particular are typical of sedimentation below 2500 m water depth (Ekdale et al., 1984).

Subunit IB sediment often shows decimeter-scale color banding caused by changing proportions of clay versus nannofossils. In Core 349-U1435A-7R, two thin intervals of very light colored sediment are noted (Figure F7). The larger of these is ~4 cm thick and has both a sharp top and base and is almost pure white. The interior of this interval is faintly laminated, but no internal grading is observed. Smear slide analysis indicates that this layer is composed of clay, but without X-ray diffraction (XRD) analysis we were unable to tell what specific minerals may be present. Nonetheless, such a pure deposit without significant contamination from other sources represents a depositional anomaly of unknown origin at that time.

Figure F5. Manganese nodule, suggestive of very slow sedimentation at this site in the recent geological past during deposition of Subunit IA, Hole U1435A (3R-CCA, 1–5 cm).



Figure F6. Burrows in Subunit IB, Hole U1435A. A. *Planolites*, *Chondrites*, and *Thalassinoides* (5R-1A, 106–114 cm). B. *Zoophycos* and *Planolites* (7R-2A, 137–144 cm).

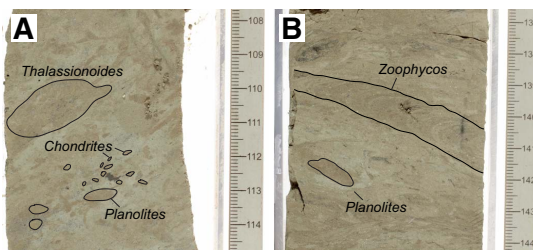


Figure F8 shows a typical example of a smear slide from Subunit IB. The bulk of the sediment is clay and nannofossils, but smaller amounts of volcanic glass (both felsic and darker mafic compositions), opaque materials, broken fragments of foraminifer tests, rare silt-sized grains of quartz, and rock fragments (usually quartz bearing) are also seen. The sediment is all fine grained but not well sorted. Subunit IA is essentially similar but with more nannofossils and slightly less clay.

The composition of Subunit IB changes a few meters above the basal contact with an underlying carbonate that forms the top of underlying Unit II. Nannofossils are generally abundant throughout Subunit IB but become rare toward the base of the subunit, whereas clay over this interval contains larger amounts of euhedral crystalline calcite, with grains typically 3–8 μm across (Figure F9). Calcite makes up a significant proportion of the total sediment volume. Both calcite crystals and nannofossils are found in some samples (Figure F9B). We suggest that the disappearance of calcareous

Figure F7. White clay layer in Subunit IB nannofossil-rich clay, Hole U1435A (7R-1A, 138–145 cm).



Figure F8. Clay with nannofossil ooze in Subunit IB, Hole U1435A (6R-1A, 95 cm; plane-polarized light [PPL]).

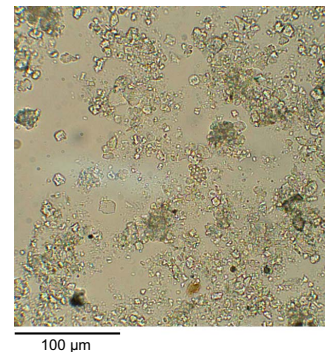
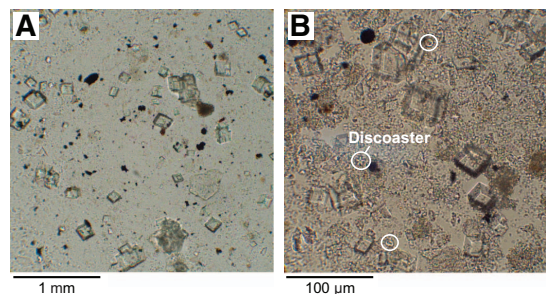


Figure F9. Clay with calcite crystals in Subunit IB, Hole U1435A (PPL). Calcite is a diagenetic product. A. 9R-2A, 91 cm. B. 7R-2A, 138 cm. Sparse nannofossils are circled.



microfossils and the presence of pristine crystalline calcite are linked, representing dissolution of the fossils toward the unit base and the precipitation of calcite during early diagenesis.

Unit II (77.65–275.54 mbsf)

Interval: 349-U1435A-9R-2, 135 cm, through 29R-5, 74 cm

Depth: 77.65–275.54 mbsf

Age: pre-Oligocene

Most of the drilled section at Site U1435 is represented by the dominantly sandy sediment of Unit II. The division between Units I and II is marked by a carbonate cap rock spanning interval 349-U1435A-9R-2A, 135–141 cm (Figure F10A), with a few disrupted pieces of this material floating in the underlying sands likely caused by drilling. We recognize that the Unit I/II boundary may be more complex because there is a sharp but contorted interface at Section 9R-2A, 70 cm, where muddy and more calcareous material changes downsection to clayey sandy sediment just above the carbonate. We place the boundary at the top of the carbonate because it is easy to identify and likely represents a hiatus in the sedimentation history, whereas the overlying sand may represent sediment reworking or gradual environmental changes. In thin section, the carbonate is fine grained and dominated by microcrystalline calcite with small, rounded pods of crystalline calcite floating in the medium-gray background sediment (Figure F10B). There are also minor amounts of brown and opaque materials of unknown composition.

Given the location of the carbonate at the boundary between two contrasting facies and the distinctly different lithology, we consider this carbonate to be a hardground-type deposit, representing a lengthy period of no or very slow accumulation. The carbonate must have accumulated at a time of minimal clastic sedimentation, and its highly cemented character is unusual compared to the sediment above and below. The major change in composition between Units I and II can be explained by a switch in depositional environment. Although the magnetostratigraphy does not require a significant hiatus, the sedimentary evidence would be supportive of a break of up to millions of years.

The bulk of Unit II is composed of dark gray silty sandstone, mostly medium sand sized and thick bedded with very little carbonate. The sandstone is better cemented than the Unit I nannofossil-rich clay and increases in lithification downhole. Although coarse sandstone is seen, it is minor, and pebble conglomerate is only recovered in Section 29R-CC (Figure F11). The sediment is thus more proximal than in Unit I but is still moderately distal from the source because the grain size of the vast majority of the sediment is not very coarse. This is indicative of current sorting over moderate transport distances, possibly only on the order of tens of kilometers. Larger clasts are very rare, with the exception of a subrounded, 2.5 cm wide clast of limestone (interval 15R-1A, 29–32 cm; Figure F12B), which is very similar to that seen at the top of the unit. This clast was found significantly below the top contact, so we do not think that it represents downhole contamination, although that remains a possibility. Alternatively, the carbonate clast could be the product of reworking laterally across the basin during sedimentation or erosion from an outcrop of limestone not far from the basin edge.

A more typical feature of Unit II is the common observation of dispersed black carbon fragments within the massive gray sandstone (Figure F12A). These dispersed fragments do not represent a large proportion of the total lithology but are common throughout

Figure F10. (A) Core image and (B, C) photomicrographs (PPL) of the carbonate rock separating Units I and II, immediately overlying sandstone, Hole U1435A (9R-2, 137–140 cm; TS119). In photomicrographs, note pods of recrystallized calcite spar within a background of micritic carbonate mudstone.

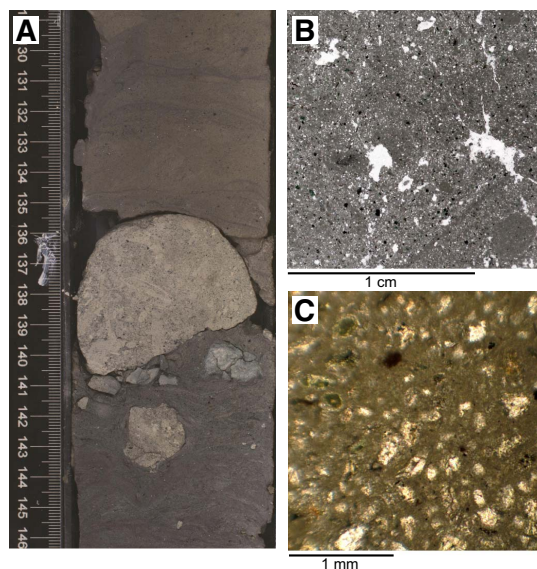


Figure F11. Conglomerate bed in Unit III, Hole U1435A (29R-CC, 23–29 cm).

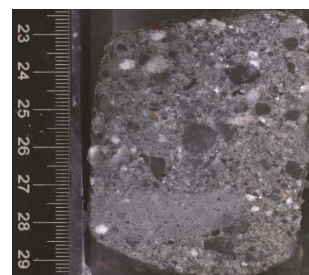
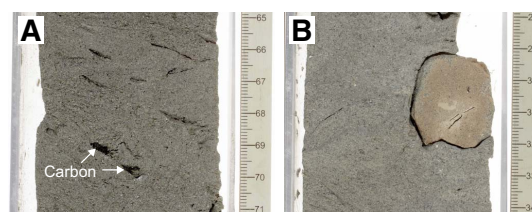


Figure F12. Unit II, Hole U1435A. (A) Carbon fragments in sandstone (10R-2A, 65–71 cm) and (B) limestone pebble in sand (15R-1A, 28–34 cm).



the coarser sediment of the unit, with fragments often >5 mm across and sometimes as much as 15 mm across. The fragments appear to be generally dispersed and not preferentially concentrated into layers or burrows.

Sandstone is by far the most abundant lithology in this unit, particularly at the top of the unit, but there are also fine-grained rocks. Figure F13A shows an example of a relatively continuous sequence of clayey siltstone overlain sharply by fine sandstone. The clayey siltstone shows faint laminations and is marked by minor *Planolites*-type burrows. These are most visible toward the top of the sec-

Figure F13. Finer grained facies, Hole U1435A. A. Clayey siltstone with *Planolites* burrows (27R-6A, 55–65 cm; Unit II). B. Very thin sand lenses interbedded with mudstone (29R-5A, 99–107 cm; Unit III). C. Massive black silty claystone (32R-1A, 29–37 cm; Unit III).

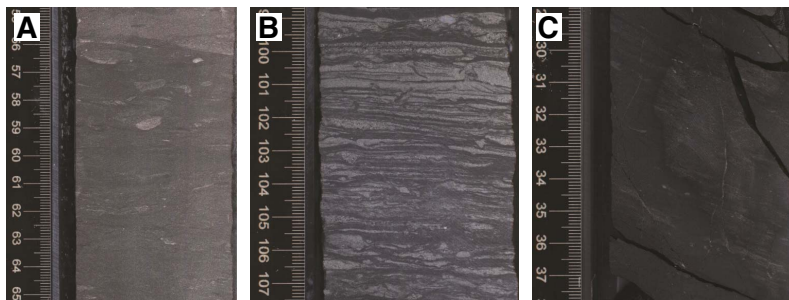
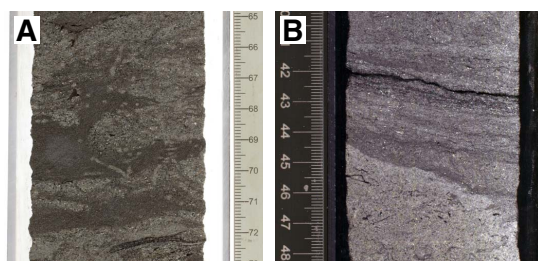


Figure F14. Sandstone in Unit II, Hole U1435A. A. Medium sandstone and interbedded claystone with *Chondrites* trace fossils (19R-6, 65–73 cm). B. Laminated silty sandstone overlying a gently inclined erosion surface (19R-2A, 40–48 cm).



tion where burrowing has placed sand of contrasting color into these structures so that they stand out against the darker background.

Alternation of fine and coarser grain sizes can be found intermittently through the unit. Figure F14A shows an example where silty claystone is interbedded with laminated sandstone. In this example, the general sedimentary layering has been further disrupted by bioturbation, which results in an interfingering geometry between the two lithologies, with claystone being in the minority. Current activity is implied throughout Unit II because of the common grain orientation lamination, even in the massive sandstone, and in some cases erosion and reactivation surfaces are visible in the core. Figure F14B shows where darker colored, parallel-laminated silty sandstone is lying with an erosional contact on top of lighter colored, coarser grained, more massive sandstone. Although these surfaces are not common, they do indicate that depositional environments associated with Unit II were high energy and included erosion as well as deposition. The sandstone shows cycles of both fining upward into silty sandstone or claystone and coarsening upward. These grain size-related cycles span several meters of section and could represent a response to varying sea level, with coarser grained sediment associated with higher energy after a sea level fall in a shallow-marine setting. Alternatively, the cycles may reflect a simple switching of sediment supply.

The thickest section of fine-grained sediment can be found right at the base of Unit II where >1 m of very dark gray, massive, poorly laminated claystone was recovered. This sediment appears to be relatively organic rich and less bioturbated than other units, as there is little color contrast to pick out the burrows. This lithology suggests sedimentation in a lower energy setting compared to the high-energy sandstone that dominates the rest of the section, but this could

simply represent the effects of local sediment bypassing or abandonment of a channel.

Almost all the sediment recovered in Unit II shows some form of mostly shallow marine bioturbation, with common *Planolites* (Figure F15A) and abundant *Thalassinoides* (Figure F15B), as well as some vertical or subvertical burrows ~5–10 mm across. We interpret this assemblage to indicate sedimentation in an environment with a soft seafloor and probably one in relatively shallow water (<100 m) and high-energy conditions, such as the *Cruziana* ichnofacies (Ekdale et al., 1984). In contrast to overlying Unit I, we note that there are almost no *Chondrites*, and we see a dominance of the larger *Thalassinoides*. Much of the sand is quite intensively burrowed, suggesting a relatively productive environment with an active and flourishing fauna. These trace fossils can be seen throughout the unit and underline the marine character of the sedimentation.

There is a significant amount of evidence to show that sedimentation likely occurred in near-shore, shallow-marine conditions. As well as the organic carbon mentioned above, there are examples of broken shelly material throughout much of the sandstone, albeit much of it broken into small pieces (<2 mm) and disseminated throughout the sediment; however, some larger and more coherent fragments are observed. Figure F16A shows an example of a large bivalve shell surrounded by the background sandstone. This is in contrast to the example seen in Figure F16B, where the bivalve shell is surrounded by orangeish pink sandstone and forms a clast that has been eroded from an earlier sedimentary deposit. This is not so dissimilar to the limestone clast seen in Figure F12B, providing evidence for significant reworking into the basin. Nonetheless, there is plenty of evidence for a bivalve community living either at or near the site because several of the shells are not broken and have both valves in place. We presume that the fragmented shell material represents the breakdown of more distally derived material that is abraded during transport.

At the microscopic scale, the sandstone is not very well sorted and has grains that are mostly subangular (Figure F17A). The mineralogy is dominated by quartz, although there are grains of feldspar and quartz-bearing lithic fragments, as well as opaque minerals and a minority of heavy minerals. There are small amounts of clay that act as a matrix to the sandstone. This rather immature textural character suggests that sediment transport distances may not have been very far from the original source and that some of the deposition could have been rapid and not very heavily worked by currents. Some intervals of the core show well-developed current structures, so there is some variability in the flow regime within the unit. Figure F17B shows a close-up of some of the mineral grains, largely quartz

Figure F15. Bioturbated silty sandstone in (A, B) Unit II and (C) Unit III showing large *Thalassinoides* burrows (circled in A and B), Hole U1435A. A. 20R-5A, 129–138 cm. B. 18R-5A, 58–70 cm. C. Vertical burrows in 30R-1A, 28–38 cm.

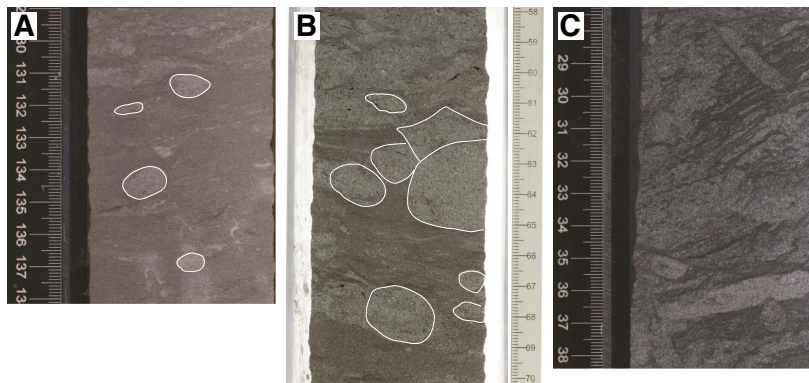
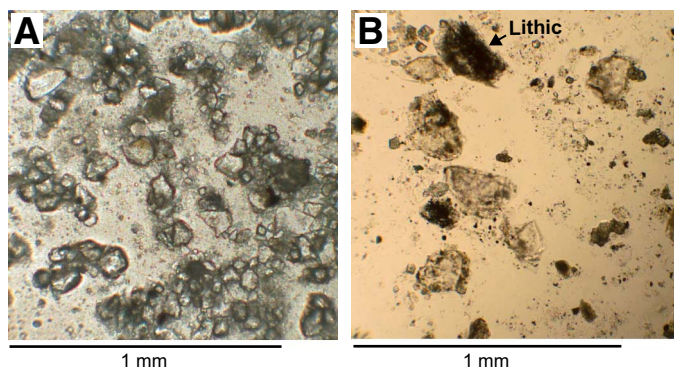


Figure F16. Bivalves in sandstone of Unit II, Hole U1435A. A. 20R-CC, 10–16 cm. B. 16R-7A, 23–29 cm.



Figure F17. Sand in Unit II showing poor sorting, subangular grains, and quartz-dominated mineralogy, Hole U1435A (PPL). A. 9R-3A, 60 cm. B. 18R-4A, 113 cm.



fragments, as well as one darker lithic grain. It is noteworthy that some of the smaller fragments are less dominated by quartz than the sand grains and highlight the significance of mafic minerals to the overall composition.

Simply considering the degree of lithification, we infer that diagenesis is more advanced in Unit II compared to Unit I. We see little alteration or growth of nodules or concretions. Pyrite is, however, visible in some smear slides and is visible on the cores in the lower part of Unit II as sparse, relatively small nodules (<5 mm) within sandstone. Compared to other sites cored during this expedition, the degree of pyrite growth is relatively moderate.

Overall, the sandstone characteristics indicate deposition of Unit II in a relatively high-energy shallow-marine environment. There was significant supply of coarse clastic material to the basin,

and the sources may not have been very far from the depocenter based on the textural evidence from the sandstone, as well as the occasional observation of minor conglomerate, which bears quartzite and rare carbonate pebbles. Trace fossil assemblages also point to a shallow-marine, high-energy environment with a soft seafloor. The proportion of sand in Unit II suggests that Site U1435 was close to a major sediment delivery pathway, and the most likely setting is a river mouth or deltaic environment. This conjecture is favored because such settings would provide the required sediment supply and also the relatively high energies related to both river discharge and tidal currents. Such environments are also relatively nutrient rich and would sustain the strong burrowing fauna observed and provide organic carbon through terrestrial run-off. This interpretation is consistent with the absence of typical marine microfossils, as well as with the occurrence of shallow- to brackish-water benthic foraminifers that require marine conditions but not normal salinities (see [Biostratigraphy](#)). The coarsening and fining upward cycles seen in the unit are explained by the progradation of delta lobes that would generate a coarsening-upward cycle. When each lobe is abandoned, it would then be covered by more distal hemipelagic sediment, generating a fining-upward cycle.

Unit III (275.54–300.00 mbsf)

Interval: 349-U1435A-29R-5, 74 cm, through 32R-CC, 10 cm

Depth: 275.54–300.00 mbsf (total depth)

Age: pre-Oligocene

Unit III is distinguished from Unit II largely on the basis of being finer grained. The top boundary is placed at the top of a mixed claystone–sandstone interval and at the base of a major sandstone layer. We note that fine-grained intervals also occur in Unit II but are more dominant in Unit III, even though sand and conglomerate are also recognized. Fine-grained sedimentary rocks are often interpreted to indicate low-energy depositional settings, but that may only be the case part of the time in Unit III. Some fine-grained intervals show alternation of thin-bedded fine sandstone together with mudstone, mixed in relatively equal proportions and interbedded on the scale of a few millimeters. These structures are indicative of continued high-energy current activity and relatively modest amounts of bioturbation (Figure F13B). These sandstone structures are reminiscent of flaser bedding and are suggestive of high current velocities across an unconsolidated seafloor. The most coherent section of muddy sediment occurs in the final core (349-U1435A-32R), where there is >1 m of silty mudstone marked by poorly de-

finned lamination (Figure F13C). Even here there are common thin, fine sandstone intervals and occasional burrows filled with fine sandstone. The lamination that we do see is defined by slightly coarser layers and does not imply stagnant conditions or slow sedimentation. This deposit is similar to ones seen in Unit II but is thicker. The presence of conglomerate in Section 349-U1435A-31R-1 indicates that Unit III is not exclusively a fine-grained or low-energy sequence. Clasts in the conglomerate are >8 mm across and moderately sorted. Clast compositions are similar to those seen in Unit II and require high-energy flow and erosion to have affected the site between periods of slower flow and faster accumulation.

Trace fossils in Unit III are similar to those seen in Unit II and mostly show vertical and subvertical burrows (Figure F15C) consistent with a shallow-marine, soft-bottomed seafloor setting.

Diagenesis has lithified the sandstone of Unit III, and pyrite is visible as small nodules (<5 mm), as was the case in the lower parts of Unit II. The better-preserved laminations in Unit III sandstone illuminate the timing of pyrite growth (Figure F18), which must have been relatively late stage because the laminations do not drape around and are not compacted across nodules, suggesting that they formed after initial lithification.

Unit III is interpreted as a shallow-water marine deposit and could represent a more sheltered setting within the river mouth/delta interpretation favored for Unit II. Finer grained intervals represent accumulation of mud, either because of switching sediment delivery pathways, potentially on relatively small spatial scales, or in response to moderate changes in sea level. Abandonment of a channel system within a delta would result in a clay-rich drape, but more distal suspended sediment delivery would continue. Unit III also shows evidence for strong current activity and even gravel/conglomerate sedimentation, so this is not an especially sheltered or intrinsically different depositional setting. A possible depositional environment for the more claystone-rich intervals would be within some type of coastal lagoon system, which could then alternate with periods of more active deltaic sedimentation driven by the autocyclic migration and avulsion of the river mouth.

Discussion

The stratigraphy at Site U1435 divides neatly into three units, which can be formed into two groups. Unit I is clearly of much deeper water origin than the lower units and was likely deposited on the Chinese continental margin in the present location under something comparable to modern conditions (i.e., water depths deeper than 2500 m). The fact that significant material is no longer accumulating is unlikely to be related to significant subsidence generating accommodation space since the Miocene because we would anticipate that postrift thermal subsidence had largely occurred before that time. Tectonic activity was largely stable during the time of low sedimentation because this is in the postrift stage of basin de-

velopment. The lack of accumulation, as evidenced by manganese nodules and extremely thin sediment cover, probably reflects both the elevated position of the drill site on a structural high after 33 Ma, as well as changing oceanographic conditions, particularly the start of strong bottom currents along the base of the continental slope that are related to overflow of Pacific water into the South China Sea through the Luzon Strait (Wang et al., 2011).

Reduced sediment flux to the outer part of the continental margin is a little unusual in the context of generally lower sea levels since the Miocene, which should reduce accommodation space on the shelf and force sediment into deeper water. Increased flux to deeper water settings would also be expected given the more erosive environmental conditions onshore linked to glacial–interglacial climatic cycles that are generally associated with enhanced sediment delivery to passive continental margins worldwide (Zhang et al., 2001). Because most sediment budgets for East Asia also show this increased sediment flux (Métivier et al., 1999), the lack of accumulation at Site U1435 reflects the fact that either the sediment is not being transported to this location in the first place, or more likely, it is deposited then eroded and not preserved because of the location on top of a structural high.

The sediment of Unit I most likely came from southern China; however, since ~6 Ma, Taiwan has probably dominated as a sediment source for the northeastern South China Sea since uplift began in the latter part of the late Miocene (Huang et al., 2006). Earlier work has established that Taiwan is the primary source of sediment to nearby Ocean Drilling Program Site 1148 (Prell, Wang, Blum, Rea, and Clemens, 2006), at least in post-Oligocene periods (Li et al., 2003; Clift et al., 2014), and a similar source is inferred for Site U1435.

The two older units cored at Site U1435 both represent relatively shallow marine conditions. The pre-Oligocene age, together with observed extensional structures in the core (see **Lithostratigraphy**), indicate that this unit is syntectonic and deposited at a time of rapid extension in the adjacent continental shelf (Ru and Pigott, 1986; Clift and Lin, 2001). Unit II in particular shows evidence of high-energy conditions and the types of facies associated with rapid sediment delivery. Unit III is generally finer grained but probably part of a single shallow-marine–deltaic depositional environment. The finer-grained material would represent sedimentation in a slightly more sheltered setting than the more massive sandstone, but this is explained by the variety of different environments found in a deltaic system, such as abandoned channels or lagoons that are close to the main distributary channels.

The source of sediment to Units II and III is not entirely obvious, as there has been some debate about whether Oligocene and presumably older materials at Site 1148 are coming from the north (i.e., from southern China) or from the southwest from Indochina (e.g., Li et al., 2003). Given the coarse grain size and the textural immaturity, a more proximal source seems likely. The source must have been dominated by quartzose bedrock, and the granite and volcanic rock that dominate the geology of Southeast China are therefore suitable. During the early stages of extension, structural highs in the basement of the Chinese continental margin would have been exposed to erosion, providing a very local source of sediment from what are now the horst structures that underlie the outer part of the continent shelf, separating the Pearl River Mouth Basin and the continental slope. The fact that the bedrock geology of both onshore and offshore areas is formed from the Mesozoic arc complexes of southeast China, indicates that the structural highs within the margin are probably magmatic-arc related. We envisage a del-

Figure F18. Pyrite concretion in thinly laminated sandstone and claystone in Unit III, Hole U1435A (30R-3A, 61–64 cm).



taic system building out into the initiating rift basin at a time when it had already been connected to the open ocean as a result of extension within the rift axis. Because of the location of Site U1435 directly next to the continent/ocean boundary, we would anticipate the highest degrees of extension and synrift subsidence to have taken place in this region. This would result in Site U1435 having a more distal, marine sedimentary assemblage compared to more continental-type facies developed in subbasins closer to the South China block.

Biostratigraphy

All core catcher samples from Hole U1435A were analyzed for calcareous nannofossils, planktonic foraminifers, and radiolarians. In addition, split-core samples were analyzed to refine the ages of core sections. Based on nine nannofossil and four planktonic foraminifer bioevents (Figure F19; Tables T2, T3), the sedimentary sequence shallower than 77.62 mbsf is assigned an age spanning the early Oligocene (<33.43 Ma) to the Pleistocene (>0.12 Ma), with possible unconformities or condensed sections existing between the upper Oligocene and middle Miocene, the upper Miocene and lower Pliocene, and the upper Pliocene and Middle Pleistocene.

No nannofossils, planktonic foraminifers, or radiolarians were found from 79.78 mbsf to the bottom of the hole at 299.16 mbsf. A few benthic foraminifers occur in samples from Core 349-U1435A-21R through 26R, which indicate a shallow-water marine to brackish water depositional environment for lithostratigraphic Unit II (see Lithostratigraphy). Pollen specimens from gymnosperms (conifer) and angiosperms (S. Warny, pers. comm., 2014) also occur in some samples from Unit II intervals and are presumed to be derived from source areas in southern China. Shore-based studies of palynomorph assemblages are needed to determine if Units II and III can be dated biostratigraphically.

Because the upper part of the sedimentary sequence is truncated by hiatuses or condensed sections, it is difficult to calculate sedimentation rates; however, the Oligocene section is fairly continuous and we calculate sedimentation rates to have been ~0.5 cm/ky during that time, based on a limited number of bioevents (Figure F19).

Calcareous nannofossils

Calcareous nannofossil biostratigraphy for Hole U1435A was established by analyzing all core catcher samples and additional split-core samples. Nannofossils are found only in the upper part of the hole, from Core 349-U1435A-2R (9.7 mbsf) to the upper part of Core 9R (77.62 mbsf). All of these samples have abundant nannofossils, except for Sample 9R-2, 132–136 cm, which has few. The rest of the hole, from the lower part of Core 9R to 32R (77.66–299.06 mbsf) corresponding to lithostratigraphic Units II and III, is barren of nannofossils (Table T4). Preservation of nannofossils is good to moderate with heavy overgrowth on discoasters (e.g., Samples 4R-CC and 5R-CC; 26.65 and 39.62 mbsf, respectively).

The nannofossil bioevents identified show that the sedimentary sequence at this site consists of a discontinuous record dated to the early Oligocene (Zone NP21; <33.43 Ma) to the Pleistocene (Zone NN21; <0.29 Ma) (Table T2; Figure F19). The presence of *Emiliania huxleyi* in Sample 2R-CC (9.7 mbsf) indicates a Pleistocene age (<0.29 Ma). Two subsamples were taken from Sample 3R-CC (19.43 mbsf): one from the upper greenish gray clay and another from the lower brown clay forming the contact with a manganese nodule. The greenish gray clay yielded a Pliocene nannofossil Zone

NN15 assemblage characterized by the presence of *Reticulofenestra pseudoumbilicus* (LAD at 3.7 Ma). However, the brown clay is late Miocene in age based on the presence of *Cyclicargolithus floridanus* (LAD at 11.85 Ma within Zone NN7). These two events suggest a hiatus or very low sedimentation rate during deposition of the gray and brown clay and the formation of the manganese nodules. The age of the next sample (4R-CC; 26.65 mbsf), which is also brown clay, is middle Miocene based on the presence of common *Discoaster kugleri*. This taxon has a short range within Zone NN7 (11.58–11.90 Ma).

A significant hiatus (~12 million years) occurs between Cores 4R and 5R. Samples 5R-CC (39.62 mbsf) and 6R-CC (49.25 mbsf) contain nannofossils that indicate a late Oligocene age representing Zones NP25 and NP24 (last common appearance [LCA] of *Cyclicargolithus abisectus* at 24.67 Ma and LAD of *Sphenolithus predistentus* at 26.93 Ma, respectively). Three early Oligocene nannofossil datums spanning Zones NP23–NP21 occur from 59 to 77.62 mbsf:

1. The FAD of *Sphenolithus distentus* (26.93 Ma) in Sample 7R-CC (59.54 mbsf),
2. The LAD of *Reticulofenestra umbilicus* (32.02 Ma) in Sample 8R-CC (71.55 mbsf), and
3. The LAD of *Coccolithus formosus* (32.92 Ma) in Sample 9R-1, 69–73 cm (75.19 mbsf).

The deepest sample examined that contains nannofossils, Sample 9R-2, 132–136 cm (77.62 mbsf), does not contain *Clauasicoccus subdistichus*, suggesting this sample is younger than 33.43 Ma (the last appearance of the acme of *C. subdistichus*). Based on these findings, the oldest sediment that contains calcareous nannofossils at this site is <33.43 Ma (early Oligocene). The presence of the LAD of *C. formosus* at this site allows correlation to the base of the sequence at Site 1148 in the South China Sea, located north of Site U1435 (Su et al., 2004).

Planktonic foraminifers

Planktonic foraminifers were analyzed in all core catcher and additional split-core samples from Hole U1435A. In general, planktonic foraminifers are common to abundant with moderate to good preservation in the upper section shallower than 70 mbsf but become rare in samples from Cores 349-U1435A-8R and 9R and barren from Sample 9R-CC (79.78 mbsf) to the base of the hole (Table T5). Our results indicate that the sedimentary sequence recovered in Hole U1435A spans three discontinuous intervals: the lower Oligocene (Zone O2/O1; ~32 Ma), the upper Miocene (Zones M9–M10; ~12 Ma), and the Pleistocene (Subzone Pt1b; <0.4 Ma) (Table T3; Figure F19). In Sample 2R-CC (9.70 mbsf), the planktonic foraminifer assemblage is dominated by species characteristic of the late Quaternary tropical Indo-Pacific, such as *Globigerinoides ruber*, *Globigerinoides sacculifer*, *Globorotalia menardii*, *Pulleniatina obliquiloculata*, *Neogloboquadrina dutertrei*, *Sphaeroidinella dehiscentis*, and *Orbulina universa*. The LAD (0.12 Ma) and FAD (0.4 Ma) of *G. ruber* (pink) in Samples 2R-CC (9.70 mbsf) and 3R-CC (19.43 mbsf), respectively, indicate Pleistocene Subzone Pt1b. The occurrence of many typical Pliocene species such as *Dentoglobigerina altispira*, *Globorotalia multicamerata*, and *Sphaeroidinellopsis seminulina* in the latter sample is attributed to mixing due to drilling disturbance in an interval with manganese nodules (see Lithostratigraphy). Postcruise studies may help clarify whether any Pliocene sediments were recovered in Cores 3R and 4R. Sample 4R-CC (26.65 mbsf) contains abundant late Miocene species, mainly *D. altispira*, *Dentoglobigerina globosa*, *Globoquadrina dehiscentis*, and

Figure F19. Age-depth model. FAD = first appearance datum, LAD = last appearance datum, FCA = first common appearance, LCA = last common appearance, wavy line = possible hiatus.

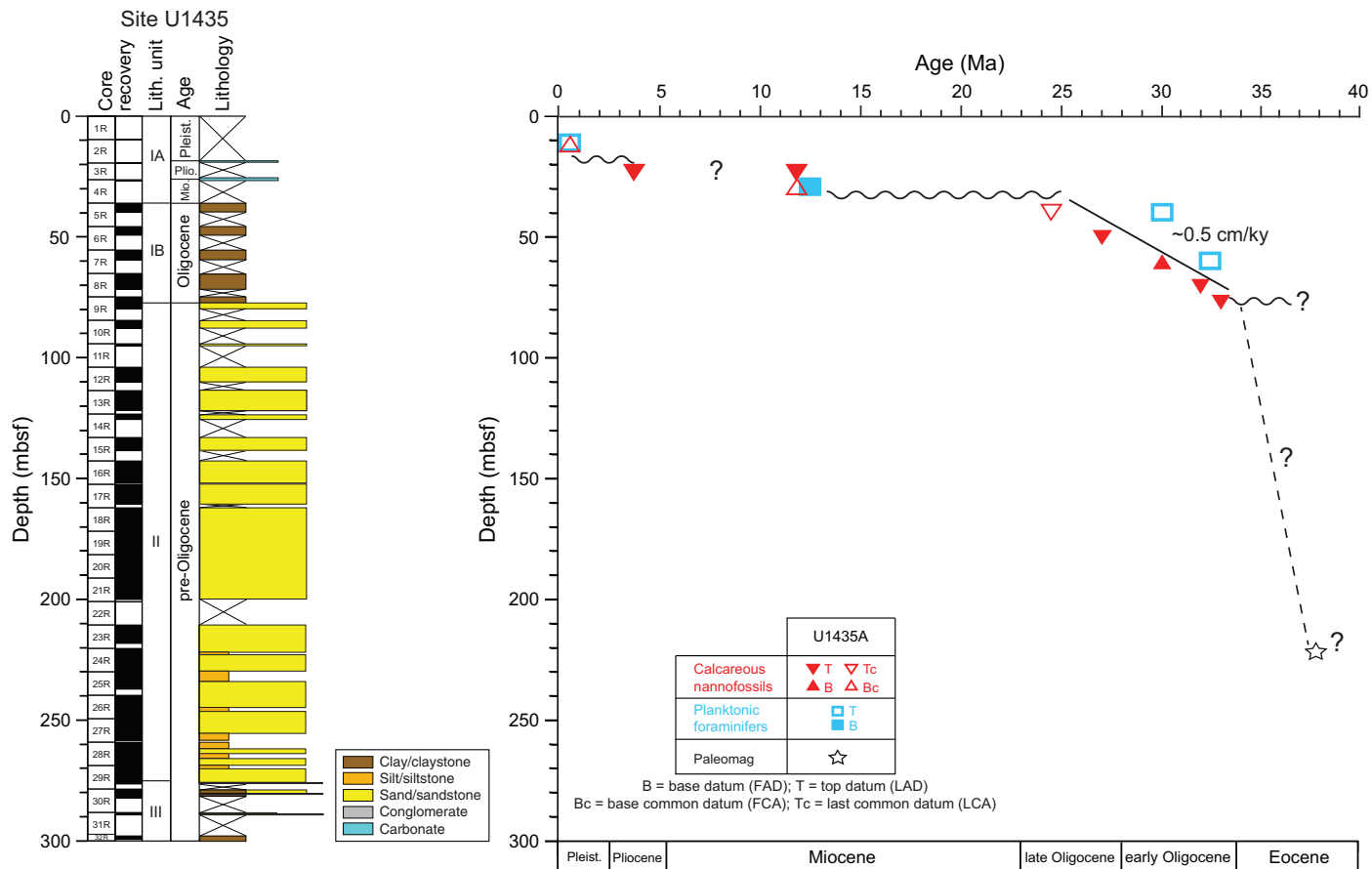


Table T2. Depths and ages of calcareous nannofossil events, Hole U1435A. T = top/last appearance datum, Tc = top common, B = base/first appearance datum, Bc = base common. [Download table in .csv format.](#)

Epoch	Zone (Martini, 1971)	Calcareous nannofossil event	Hole U1435A		
			Core, section, interval (cm)	Top depth (mbsf)	Age (Ma)
Pleistocene	NN21	B <i>Emiliania huxleyi</i>	2R-CC	9.70	<0.29
Pliocene	NN15	T <i>Reticulofenestra pseudoumbilicus</i>	3R-CC (gray)	19.43	>3.7
late Miocene	NN7	T <i>Cyclicargolithus floridanus</i>	3R-CC (brown)	19.43	<11.85
middle Miocene	NN6	Bc <i>Discoaster kugleri</i>	4R-CC	26.65	<11.9
late Oligocene	NP25	Tc <i>Cyclicargolithus abisectus</i>	5R-CC	39.62	24.67
	NP24	T <i>Sphenolithus predistentus</i>	6R-CC	49.25	26.93
early Oligocene	NP23	B <i>Sphenolithus distentus</i>	7R-CC	59.54	30.00
	NP22	T <i>Reticulofenestra umbilicus</i>	8R-CC	71.55	32.02
	NP21	T <i>Coccolithus formosus</i>	9R-1, 69-73	75.19	32.92

Table T3. Depths and ages of planktonic foraminifer events, Hole U1435A. T = top/last appearance datum, B = base/first appearance datum. [Download table in .csv format.](#)

Epoch	Zone (Berggren et al., 1995; Wade et al., 2011)	Planktonic foraminifer event	Hole U1435A		
			Core, section	Top depth (mbsf)	Age (Ma)
Pleistocene	PT1b	T <i>Globigerinoides ruber rosa</i>	2R-CC	9.70	0.12
late Miocene	M9b	B <i>Globorotalia linguaensis</i>	4R-CC	26.65	12.84
early Oligocene	O3/O2	T <i>Turborotalia ampliapertura</i>	5R-CC	39.62	30.28
	O2/O1	T <i>Pseudohastigerina nagewichiensis</i>	7R-CC	59.64	32.10

Table T4. Distribution of calcareous nannofossils, Hole U1435A. [Download table in .csv format.](#)

Table T5. Distribution of planktonic foraminifers, Hole U1435A. [Download table in .csv format.](#)

Table T6. Distribution of radiolarians, Hole U1435A. [Download table in .csv format.](#)

Globoquadrina venezuelana, although the assemblage has been altered by dissolution, as indicated by a high proportion (30%–40%) of broken tests. This sample likely represents deposition at ~12 Ma (Zones M9–M10) based on the occurrence of *Globorotalia linguaensis* (FAD at 12.84 Ma), *G. dehiscens* (local LAD at ~10 Ma; Li et al., 2006), and *Paragloborotalia mayeri* (LAD at 10.46 Ma), as well as the absence of *Globoturborotalita nepenthes* (FAD at 11.63 Ma). The sporadic occurrence of younger, mainly Quaternary species such as *S. dehiscens* and *Globigerinoides obliquus*, is considered to be contamination caused by drilling disturbance.

Further downhole, abundant moderately preserved Oligocene planktonic foraminifers, including *Turborotalia ampliapertura* (LAD at 30.28 Ma), *Dentoglobigerina galavisi*, *Cassigerinella chipolensis*, *Chiloguembelina cubensis* (LCA at 28.5 Ma), and *G. venezuelana*, occur in Samples 349-U1435A-5R-CC through 7R (39.62–59.64 mbsf), indicating lower Oligocene Zones O2 and O1. The LAD of *Pseudohastigerina naguwichiensis* (32.10 Ma) in Sample 7R-CC (59.54 mbsf) marks the Zone O2/O1 boundary. Rare, poorly preserved specimens and the occurrence of *C. chipolensis* (FAD at 33.89 Ma) in Samples 8R-CC through 9R-2, 132–136 cm (71.55–77.62 mbsf) indicate an earliest Oligocene age for this interval. Samples 9R-CC through 32R-CC (79.78–299.16 mbsf) are barren of planktonic foraminifers, thus hampering age determination for lithostratigraphic Units II and III in Hole U1435A. Sporadic benthic foraminifers (mainly *Ammonia beccarii* var. and *Florilus* sp.) in Samples 21R-CC (199.95 mbsf), 24R-CC (229.86 mbsf), and 26R-CC (249.14 mbsf) may indicate a brackish water or coastal marine environment.

Radiolarians

All core catcher samples from Hole U1435A were analyzed for radiolarians, which are abundant and well preserved only in Samples 349-U1435A-2R-CC and 3R-CC (9.7–19.43 mbsf). The presence of Late Pleistocene radiolarian species *Buccinosphaera invaginata* in Sample 2H-CC (9.7 mbsf) indicates an estimated age younger than 0.21 Ma (Table T6). Radiolarians are rare and poorly preserved in Sample 3R-CC (19.43 mbsf). No biostratigraphic markers were found in this sample. Downhole, samples are barren of radiolarians but sponge spicules are abundant in Sample 4R-CC (26.65 mbsf) and between Samples 6R-CC and 7R-CC (49.05–59.54 mbsf).

Geochemistry

Interstitial water chemistry

No interstitial water samples were collected shallower than 50 mbsf due to extremely poor core recovery. We collected 20

Table T7. Interstitial water major element concentrations, salinity, pH, alkalinity, sulfate, chloride, bromide, calcium, magnesium, sodium, potassium, and Na/Cl ratios, Hole U1435A. [Download table in .csv format.](#)

whole-round samples (5–15 cm long) for interstitial water measurements from 58 to 244 mbsf in Hole U1435A at a frequency of one sample per core, unless core recovery was <10%. Interstitial water chemistry data are given in Table T7 and shown in Figures F20 and F21.

Chloride, bromide, and sodium

Downhole profiles of chloride, bromide, sodium, and Na/Cl ratio at Site U1435 are shown in Figure F20. Chloride, bromide, and sodium concentrations show similar profiles with depth. The concentrations are similar to the values of modern seawater in lithostratigraphic Subunit IB but increase slightly at the transition from the nannofossil-rich clay of Subunit IB to the sandstone of Unit II. Concentrations are then constant and similar to modern seawater values shallower than 150 mbsf in Unit II but become more variable below that depth. As the Na/Cl ratio is ~0.85 (similar to modern seawater) throughout the hole, the anomalies could be caused by simple evaporation.

Alkalinity, sulfate, calcium, and magnesium

Alkalinity, sulfate, calcium, and magnesium profiles are shown in Figure F21. As the volume of interstitial water was limited (mostly <10 mL), only 5 interstitial water samples from the uppermost part of Unit II were analyzed for alkalinity; values for which range from 3.8 to 4.1 mM. Sulfate concentrations gradually decrease from 25.5 mM at 58 mbsf to 23.1 mM at 170 mbsf. Below 175 mbsf, sulfate concentrations are variable, ranging from 25.0 to 21.6 mM. Calcium concentrations increase from 15.9 to 38.2 mM at 244 mbsf, which is likely caused by dissolution of calcareous microfossils (see [Lithostratigraphy](#)). Magnesium concentrations decrease from 49 mM at 58 mbsf to 32 mM at 244 mbsf.

Headspace gas geochemistry

Headspace gas was monitored in cores from Hole U1435A as part of the shipboard safety and pollution prevention program. Methane and ethane were detected in very low concentrations of <10 ppmv (Figure F22; Table T8).

Bulk carbon and nitrogen analysis

Thirteen samples from lithostratigraphic Units I and II, between ~50 and 180 mbsf, were analyzed for total carbon, total inorganic carbon, and total nitrogen (TN). Distributions of CaCO₃, total organic carbon (TOC), TN, and total organic carbon to nitrogen ratio (C/N) for Hole U1435A are illustrated in Figure F23 and listed in Table T9. The CaCO₃ content decreases from 40.9 to 16.0 wt% from 58–90 mbsf and then generally remains below 10 wt% to 180 mbsf. The low values correspond to the lithologic change from nannofossil-rich clay in Subunit IB to sandstone in Unit II (see [Lithostratigraphy](#)). TOC ranges from 0.5 to 1.3 wt%, except for one sample at ~58 mbsf that contains no measurable TOC. Total nitrogen is very low (<0.05 wt%). C/N is generally high, ranging from 10 to 31, especially in the upper part of Unit II (Figure F23), indicating a dominantly terrestrial source for the organic matter.

Figure F20. Interstitial water bromide, chloride, and sodium contents and Na/Cl ratios.

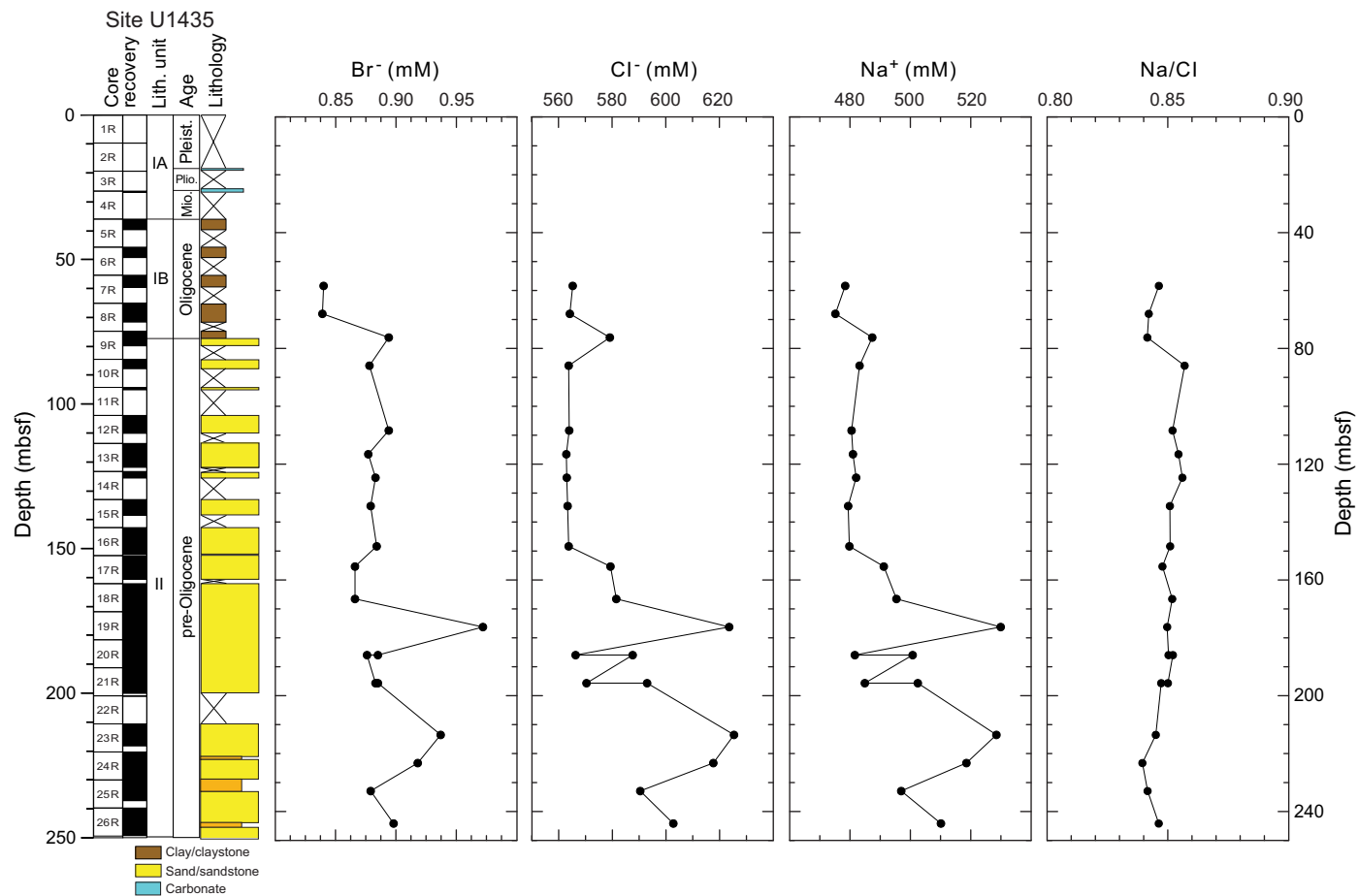


Figure F21. Interstitial water alkalinity, sulfate, calcium, and magnesium, Hole U1435A.

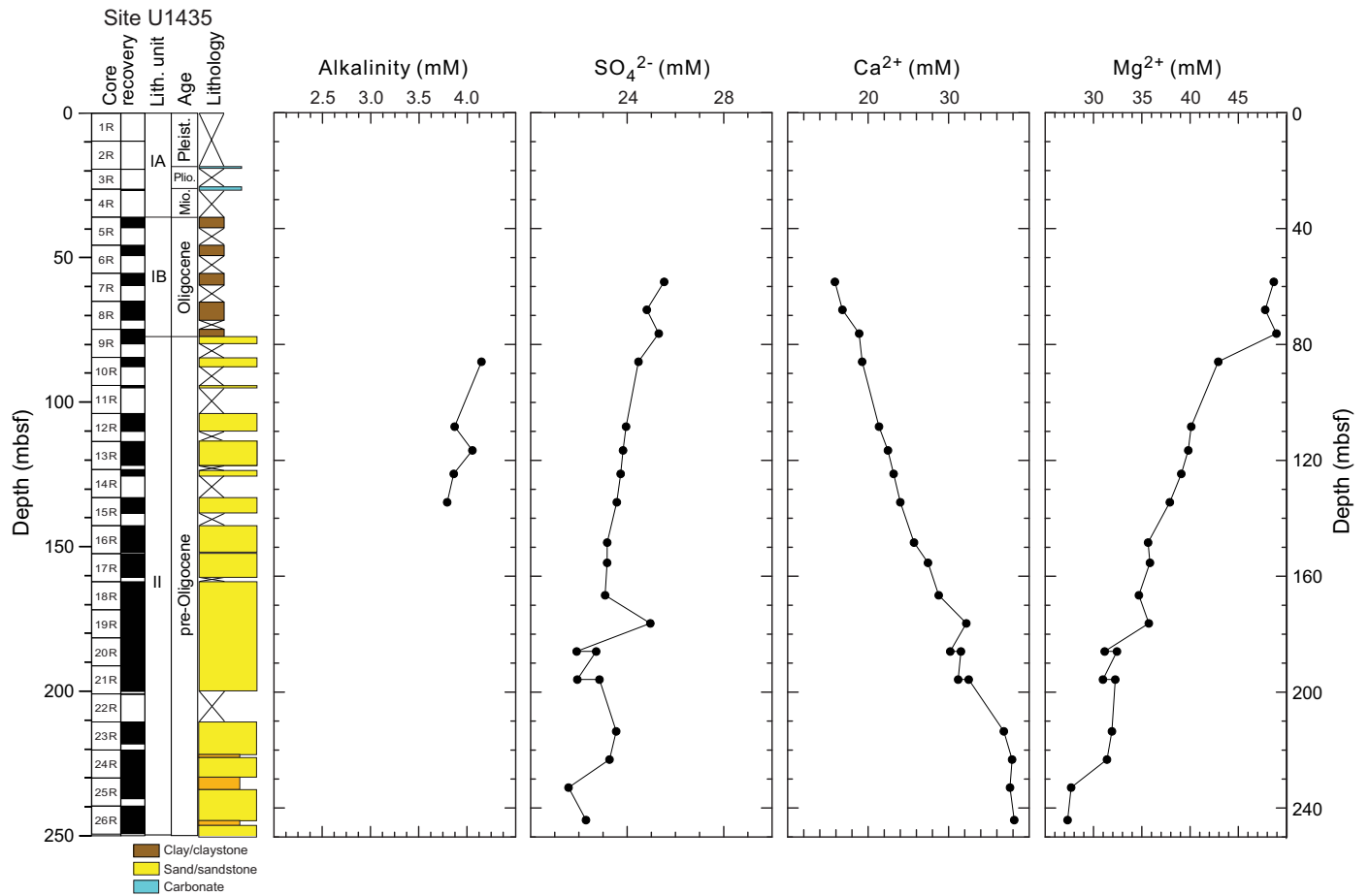


Figure F22. Hydrocarbon gases, Hole U1435A.

Table T8. Hydrocarbon headspace gas concentrations, methane and ethane, Hole U1435A. [Download table in .csv format.](#)

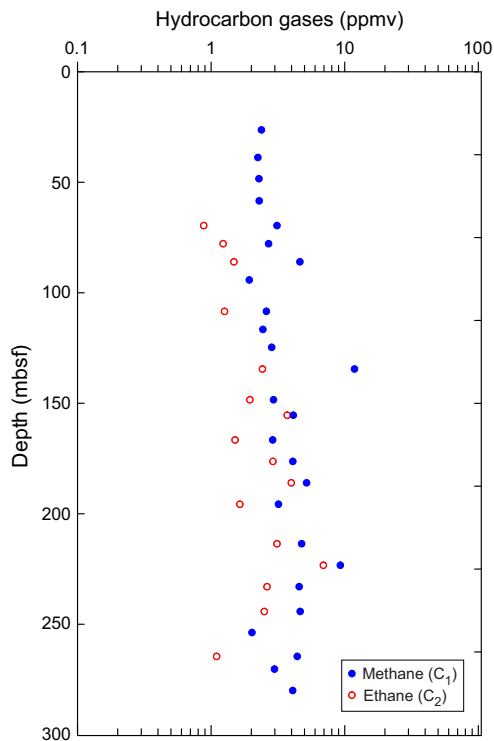


Figure F23. Calcium carbonate, TOC, total nitrogen, and C/N ratios.

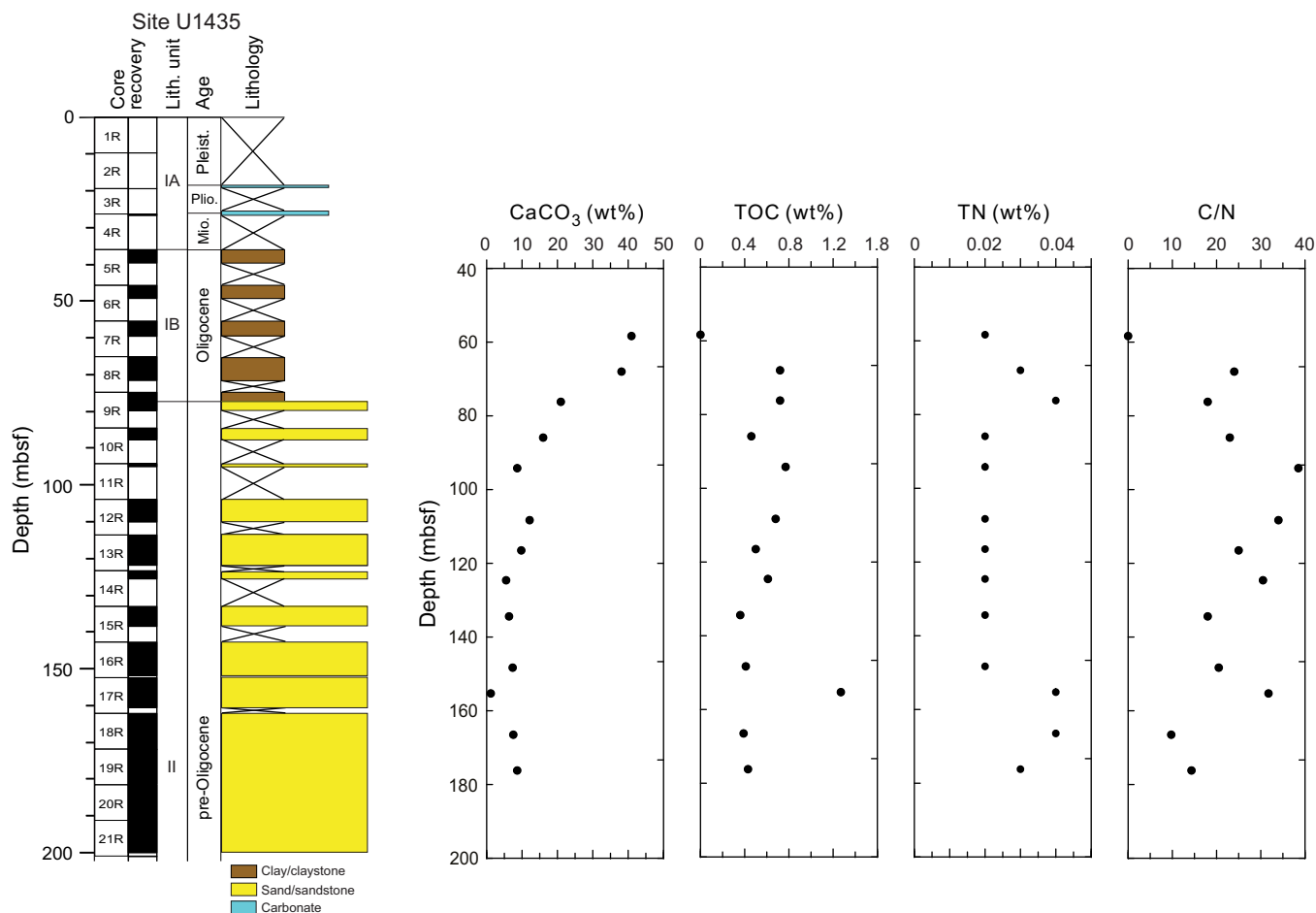


Table T9. Carbonate, total nitrogen, and TOC contents and C/N ratios, Hole U1435A. [Download table in .csv format.](#)

rich for anaerobic heterotrophs, autotrophs, and predatory bacteria were preserved at 4°C.

Microbiology

Our goal for microbiological research conducted at Site U1435 was to collect and preserve samples for shore-based characterization of the microbial communities. We collected 25 routine, 5 cm whole-round samples to be used for microbiological analysis from 37 to 299 mbsf in Hole U1435A (Figure F24). The whole-round samples for microbiology were taken adjacent to samples for interstitial water measurements in order to understand proximal interstitial water chemistry. In addition, we collected samples for measuring contamination testing tracers, including microspheres and fluid community tracers.

Microbiological analyses

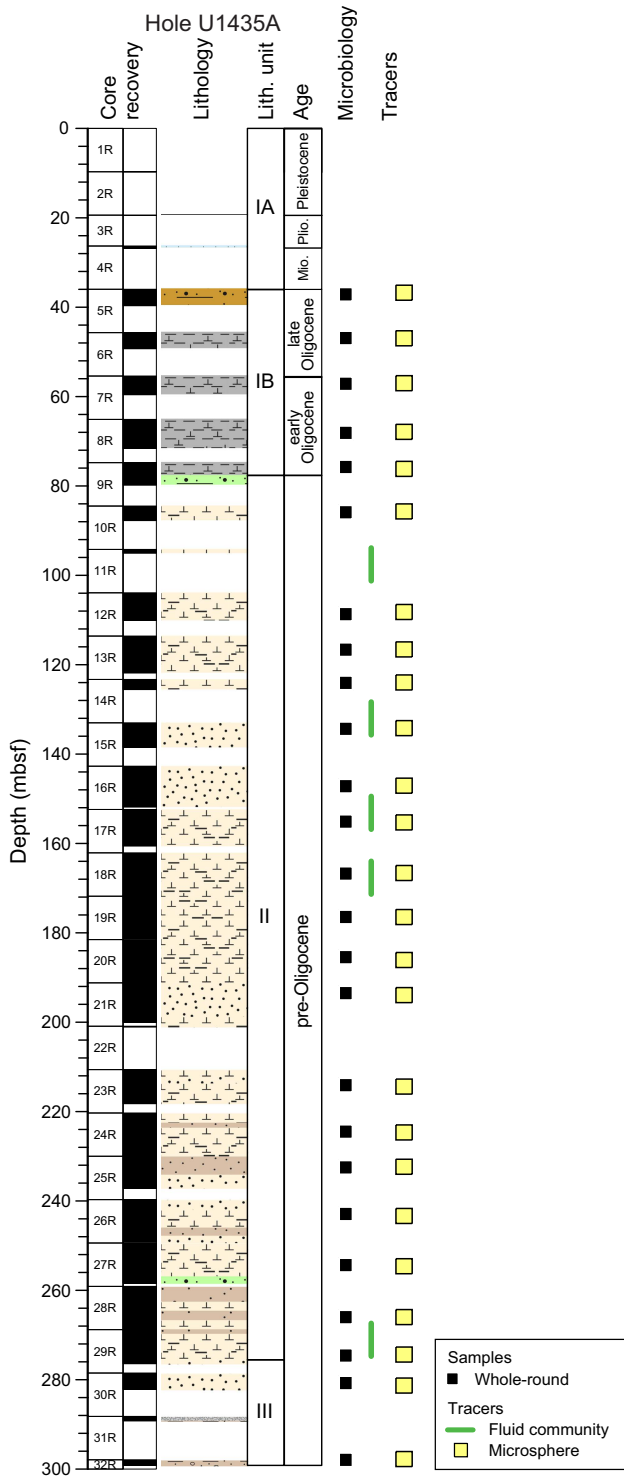
Most of the samples collected at Site U1435 were preserved for shore-based analysis. Samples to be used for DNA extractions and sequencing were frozen at 80°C, and samples to be used for lipid extraction and analysis were frozen at -80° or -20°C. Portions of the whole-round samples selected for cultivation-based studies to en-

Contamination testing

We used two different methods of contamination testing during coring at Site U1435. Microsphere tracers were used with the RCB coring system in Hole U1435A by adding them to the core catcher sub for Cores 349-U1435-5R through 32R (37–299 mbsf; Figure F24). Two microsphere samples were collected from each of the cores collected between those depth intervals: one from scrapings of the core surface and one as a subsample from the interior of each sample. Microscopic counts of the microspheres in these samples will be performed in shore-based laboratories using the Procedure for Curation of DeepBIOS (www.kochi-core.jp/DeepBIOS).

Five fluid community tracer (FCT) samples were collected either from the drilling fluids that drained from the core liners when cores arrived on the catwalk or from a sampling port near the mud pumps on the rig floor during active coring. The fluids collected for FCT samples correspond to cores obtained between ~90 and 273 mbsf. Microbial community DNA and lipids from FCT samples will be compared to the same measurements made on the core samples to determine if the drilling fluids contain microbes that can be regularly tracked as recognizable contaminant taxa.

Figure F24. Microbiology whole-round and contamination testing sample collection depths.



Paleomagnetism

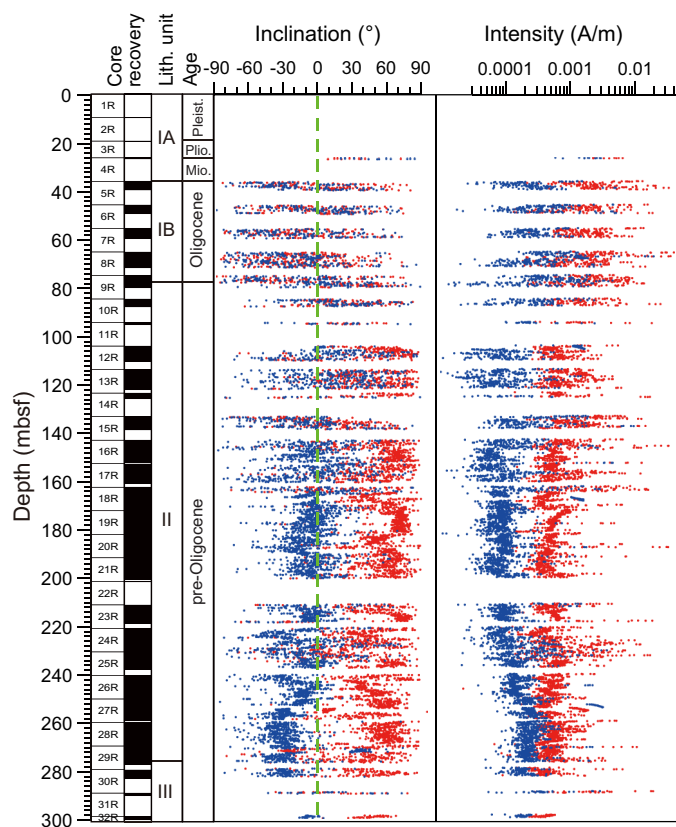
Because of time constraints at the end of Expedition 349, regular discrete sample measurements and demagnetization could not be carried out for Site U1435. Therefore, only pass-through magnetometer measurements on all archive-half Cores 349-U1435A-4R through 32R were conducted using the 2G superconducting rock magnetometer (SRM) with demagnetization steps of 5, 10, and 20 mT. We analyzed the results in Zijderveld diagrams (Zijderveld, 1967) and calculated the characteristic remanent magnetization (ChRM) direction by using principal component analysis (Kirschvink, 1980).

Natural remanent magnetization of sedimentary cores

Paleomagnetic data obtained at Site U1435 exhibit significant variations in magnetic property among the various lithologies recovered. As shown in Figure F25, the natural remanent magnetization (NRM) intensity for the recovered sediment in Hole U1435A ranges between 0.0001 and 0.01 A/m. Shallower than ~100 mbsf, paleomagnetic measurements indicate that the average NRM intensity for the greenish gray clayey nannofossil ooze and claystone in lithostratigraphic Unit I and upper part of Unit II averages ~0.002 A/m and then decreases to ~0.0005 A/m between ~80 and 200 mbsf. After 20 mT AF demagnetization, the remanent magnetization significantly decreases by almost 80% for the dark gray silty sandstone in Unit II below 80 mbsf, which indicates that the NRM carrier for this interval is magnetically soft. Generally, in sand layers, coarser grained (pseudosingle domain [PSD] and multiple domain) magnetite is abundant. These pseudosingle-domain/multiple-domain magnetite particles have lower remanence coercivity ($B_{cr} < 10\text{--}15\text{ mT}$) compared to their single-domain counterparts ($B_{cr} > 20\text{ mT}$); therefore, they can be easily AF demagnetized. In contrast, the upper part of the section has relatively higher remanent magnetization and is also magnetically harder than the underlying Units II and III. This indicates that sediments above 100 mbsf contain relatively finer grained (PSD) magnetic particles than Units II and III. From ~210 mbsf to near the bottom of Unit II (~280 mbsf), NRM intensities consistently exhibit higher values (Figure F25).

For the units deeper than 80 mbsf, initial NRM exhibits steep downward inclinations up to ~80°, which indicates strong drilling-induced remagnetization. For the sediment shallower than 80 mbsf, NRM inclinations alternate between positive and negative values, indicating that either strong disturbance effects or the presence of magnetically hard minerals (e.g., hematite, which may be more resistant to drilling-induced overprint) may have played a role. The appearance of upward (negative) inclinations before any AF demagnetization is puzzling but could indicate inversion of core sections either during the coring process or measurement on the magnetometer. Further shore-based experiments on the corresponding discrete samples are required to understand the origin of these NRMs with negative inclinations.

Figure F25. Paleomagnetic measurements of NRM inclination and intensity on archive core sections after 0 mT (red) and 20 mT (blue) AF demagnetization, Hole U1435A.

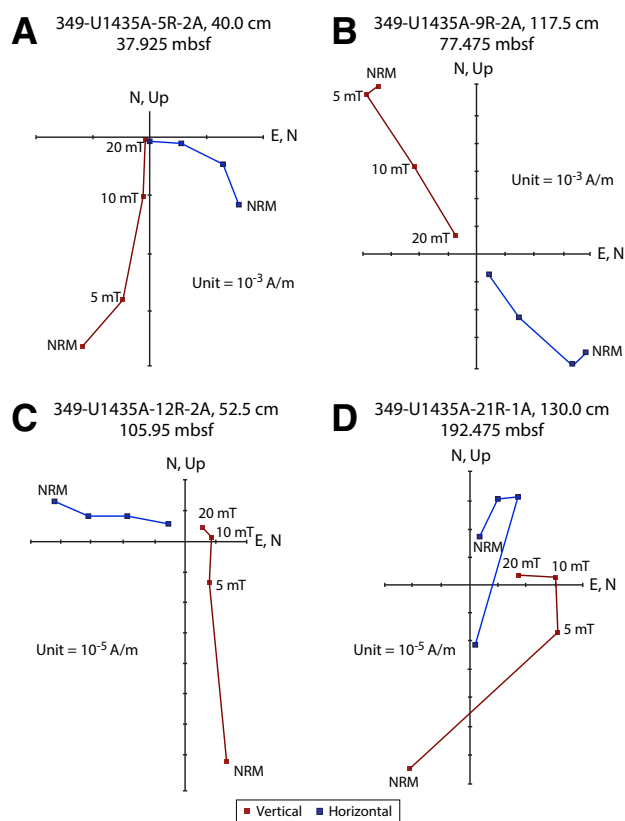


Paleomagnetic demagnetization results and magnetostratigraphy

Representative vector plots (Zijderveld, 1967) showing magnetic behavior of detailed AF demagnetization are given in Figure F26. Overall, the plots exhibit very soft magnetic behavior. For example, Samples 349-U1435A-5R-2A, 40.0 cm (Figure F26A), and 9R-2A, 117.5 cm (Figure F26B), were fully demagnetized by 20 mT AF demagnetization. For samples from greater depths (Figures F26C, F26D), initial NRM intensities are only on the order of 10^{-5} A/m, indicating that the samples contain either only minor amounts of magnetic minerals or more antiferromagnetic minerals (e.g., hematite and goethite) with weak magnetic properties.

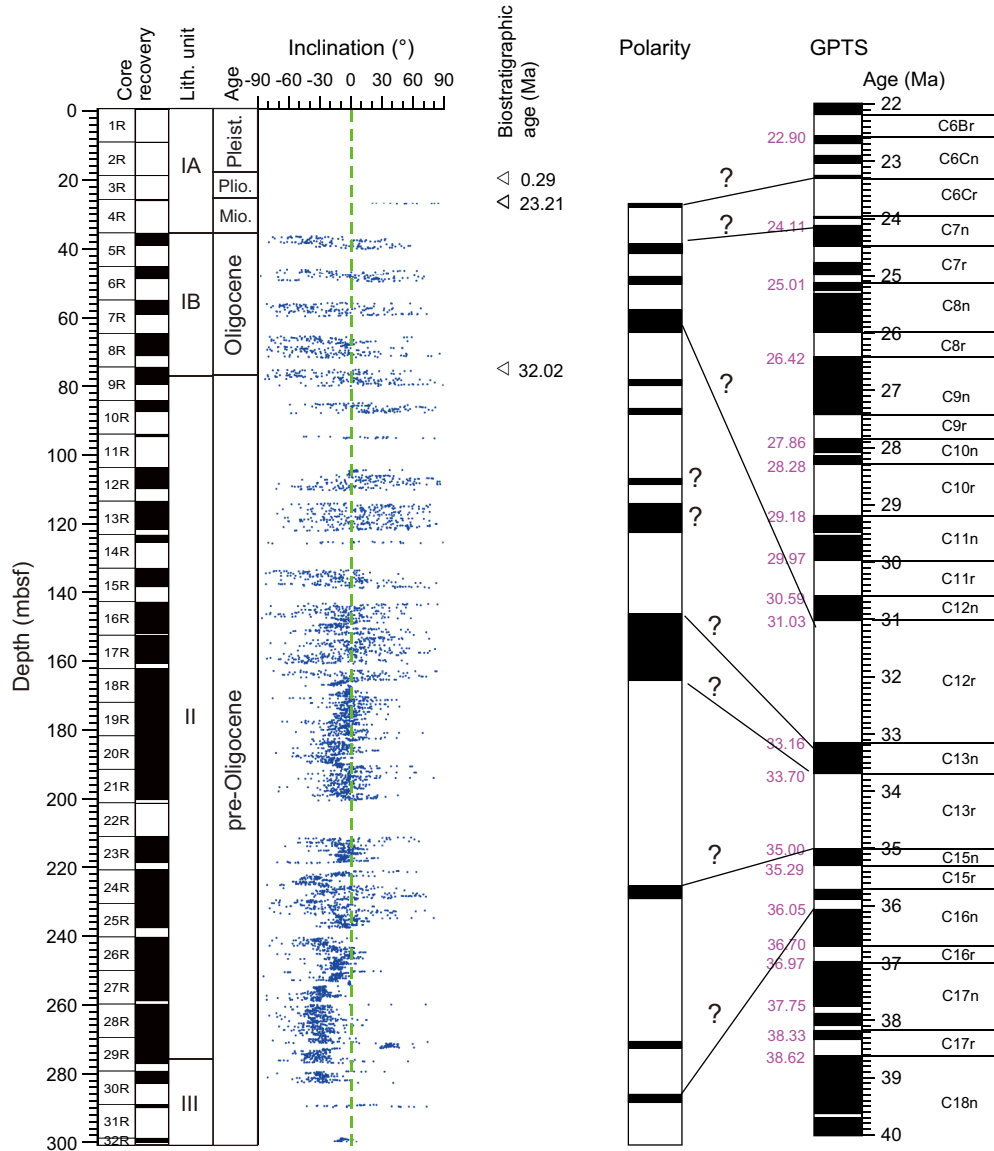
Because of the rotary technique used for drilling, relative rotation frequently occurs between different segments of sediment

Figure F26. A–D. Representative vector endpoint diagrams (Zijderveld, 1967) of magnetization directions for sediment samples through stepwise AF demagnetization.



within the core. Consequently, we used ChRM inclinations to define polarity sequences for Hole U1435A (Figure F27). Overall, the polarity pattern can be roughly divided into two parts. Shallower than ~165 mbsf, the inclinations alternate more frequently between positive and negative polarities. In contrast, core sections between 165 and 280 mbsf show dominantly reversed polarity. Biostratigraphic samples at ~77.6 mbsf have been assigned an age of ~33.0 Ma (see Biostratigraphy), suggesting that the reversed polarity zone between ~77 and 146 mbsf could be of Chron C12r age (31.03–33.16 Ma) if there is not a significant hiatus between lithostratigraphic Units I and II. This match is reasonable because Chron C12r is the only reversed chron of this particular age with relatively longer duration. Furthermore, this information also suggests that the relatively well defined polarity record at ~165–290 mbsf might span Chrons C13r (33.70–35.00 Ma) to C16n (36.05–36.70 Ma).

Figure F27. Magnetostratigraphic results with biostratigraphic age correlation, Hole U1435A. Paleomagnetic inclination after 20 mT AF demagnetization. For polarity and GPTS (Gradstein et al., 2012), black = normal polarity and white = reversed polarity. ? = uncertain correlation or questionable chron identification.



Physical properties

Cores from Hole U1435A were measured for physical properties on whole-round cores (*P*-wave velocity, gamma ray attenuation [GRA] bulk density, magnetic susceptibility, and natural gamma radiation [NGR]), as well as on split cores (point magnetic susceptibility and *x*-caliper *P*-wave velocity) and discrete samples (moisture and density). Because of the poor recovery at the top of the hole, measurements start from ~30 mbsf. Thermal conductivity was measured with a needle probe in soft sediment and then with a contact probe in lithified sediment.

Whole-Round Multisensor Logger measurements

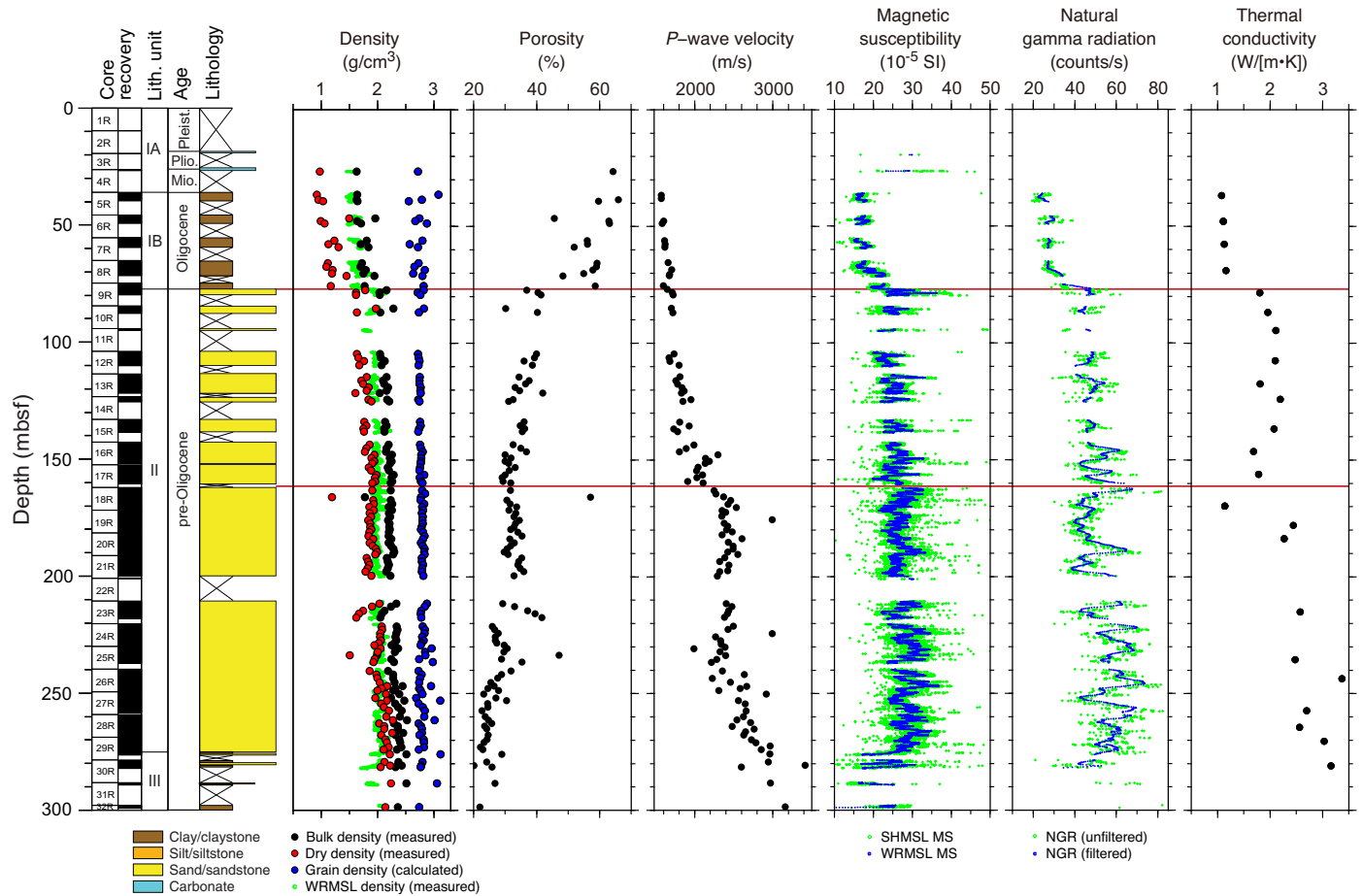
Measurement points that are orders of magnitude out of range were removed from the whole-round core data, which were then

smoothed using a five-point average moving window for GRA density and a 10-point average moving window for magnetic susceptibility and NGR. Plots of the physical property data in Hole U1435A are compiled in Figure F28.

GRA bulk density

Bulk density, measured from GRA on the Whole-Round Multisensor Logger (WRMSL) as well as on discrete samples, increases with depth from 1.5 to ~1.8 g/cm³ in the uppermost 78 mbsf. Dry density measured on discrete samples follows a similar trend, with values from 1 to 1.5 g/cm³ over the same depth interval. Bulk and dry densities increase by ~0.5 g/cm³ near 78 mbsf at the boundary between the claystone of lithostratigraphic Unit I and the sandstone of Unit II. Grain density varies between 2.5 and 3.2 g/cm³ in the uppermost 78 mbsf and then remains nearly constant around 2.8 g/cm³ deeper. Porosity decreases with depth in the uppermost

Figure F28. Physical property measurements, Hole U1435A. Red lines = correlation between physical property changes associated with lithostratigraphic boundaries and lithification changes.



78 mbsf, from 65% to 50% in the claystone, drops to 40% in the sandstone of Unit II, and then continues to decrease to 30% near 150 mbsf. Porosity then varies between 20% and 40% to the bottom of the hole.

Magnetic susceptibility

Magnetic susceptibility values are relatively constant, near 15×10^{-5} to 20×10^{-5} SI, downhole to 70 mbsf in the claystone of lithostratigraphic Subunit IB and increase with depth from 70 to 78 mbsf, reaching values of $\sim 20 \times 10^{-5}$ to 30×10^{-5} SI in the sandstone of Unit II. Magnetic susceptibility values then remain relatively constant to ~ 165 mbsf, where they slightly increase to 25×10^{-5} to 35×10^{-5} SI, remain relatively constant to 275 mbsf, and then decrease with depth to $\sim 20 \times 10^{-5}$ SI in the silty sandstone and shale of Unit III.

Natural gamma radiation

In Hole U1435A, NGR values display trends and variations similar to magnetic susceptibility values across the different lithologic boundaries. NGR counts are close to 20–30 counts/s in the claystone of Subunit IB, increase to ~ 50 counts/s in the sandstone of Unit II, and show a slight increase to ~ 60 counts/s near 220 mbsf. The values decrease with depth to 40 counts/s in Unit III.

Thermal conductivity

Thermal conductivity is constant in the claystone of lithostratigraphic Subunit IB at 1 W/(m·K). Values increase to ~ 2 W/(m·K) in the sandstone, where they remain relatively constant downhole to ~ 165 mbsf. Below this depth, thermal conductivity increases to 2.2–3.2 W/(m·K) in the rest of the hole, with higher variability than in the uppermost 165 m.

Compressional wave (P-wave) velocity

In Hole U1435A, P-wave velocity gradually increases from near seawater velocity at the seafloor (1480 m/s) to ~ 2200 m/s at 165 mbsf. Values do not change significantly at the lithostratigraphic Subunit IB/Unit II boundary near 78 mbsf, whereas most other properties show large changes across the boundary. P-wave velocity remains constant near 2400 m/s from 165 to 220 mbsf and then increases with depth to the bottom of the hole to values near 3000 m/s.

Data interpretation and lithology correlation

In Hole U1435A, variations of some of the physical properties near the seafloor reflect compaction of sediment, but most variations appear to be related to lithology and lithification. P-wave ve-

locity increases gradually with depth over the uppermost 150 m, whereas porosity measured on discrete samples decreases from 65% to 30% over the same depth range, reflecting sediment compaction. Bulk density, NGR, magnetic susceptibility, and thermal conductivity show a sharp increase near 78 mbsf at the boundary between the claystone of lithostratigraphic Subunit IB and the sandstone of Unit II. A significant increase in *P*-wave velocity and thermal conductivity is observed near 165 mbsf, which is associated with an increase in sandstone lithification. Magnetic susceptibility and NGR values tend to decrease with depth below 270 mbsf. This corresponds to the increase in silt and mud content in the rocks of Unit III compared to Unit II, which is dominated by sandstone.

References

- Berggren, W.A., Kent, D.V., Swisher, C.C., III, and Aubry, M.-P., 1995. A revised Cenozoic geochronology and chronostratigraphy. In Berggren, W.A., Kent, D.V., Aubry, M.-P., and Hardenbol, J. (Eds.), *Geochronology, Time Scales and Global Stratigraphic Correlation*. Special Publication - SEPM (Society for Sedimentary Geology), 54:129–212. <http://dx.doi.org/10.2110/pec.95.04.0129>
- Clift, P., and Lin, J., 2001. Preferential mantle lithospheric extension under the South China margin, *Marine and Petroleum Geology*, 18(8):929–945. [http://dx.doi.org/10.1016/S0264-8172\(01\)00037-X](http://dx.doi.org/10.1016/S0264-8172(01)00037-X)
- Clift, P.D., Wan, S., and Blusztajn, J., 2014. Reconstructing chemical weathering, physical erosion and monsoon intensity since 25 Ma in the northern South China Sea: a review of competing proxies. *Earth-Science Reviews*, 130:86–102. <http://dx.doi.org/10.1016/j.earscirev.2014.01.002>
- Cronan, D.S., 1980. *Underwater Minerals*: London (Academic Press).
- Ekdale, A.A., Bromley, R.G., and Pemberton, S.G. (Eds.), 1984. *Ichnology: The Use of Trace Fossils in Sedimentology and Stratigraphy*. SEPM Short Course, 15.
- Hu, J., Kawamura, H., Hong, H., and Qi, Y., 2000. A review on the currents in the South China Sea: seasonal circulation, South China Sea Warm Current and Kuroshio Intrusion. *Journal of Oceanography*, 56(6):607–624. <http://dx.doi.org/10.1023/A:1011117531252>
- Huang, C.-Y., Yuan, P.B., and Tsao, S.-J., 2006. Temporal and spatial records of active arc-continent collision in Taiwan: a synthesis. *Geological Society of America Bulletin*, 118((3–4):274–288. <http://dx.doi.org/10.1130/B25527.1>
- Kirschvink, J.L., 1980. The least-squares line and plane and the analysis of palaeomagnetic data. *Geophysical Journal of the Royal Astronomical Society*, 62(3):699–718. <http://dx.doi.org/10.1111/j.1365-246X.1980.tb02601.x>
- Li, C.-F., Lin, J., Kulhanek, D.K., Williams, T., Bao, R., Briaes, A., Brown, E.A., Chen, Y., Clift, P.D., Colwell, F.S., Dadd, K.A., Ding, W., Almeida, I.H., Huang, X.-L., Hyun, S., Jiang, T., Koppers, A.A.P., Li, Q., Liu, C., Liu, Q., Liu, Z., Nagai, R.H., Peleo-Alampay, A., Su, X., Sun, Z., Tejada, M.L.G., Trinh, H.S., Yeh, Y.-C., Zhang, C., Zhang, F., Zhang, G.-L., and Zhao, X., 2015. Methods. In Li, C.-F., Lin, J., Kulhanek, D.K., and the Expedition 349 Scientists, *Proceedings of the Integrated Ocean Drilling Program, 349: South China Sea Tectonics*: College Station, TX (International Ocean Discovery Program). <http://dx.doi.org/10.14379/iodp.proc.349.102.2015> [This volume]
- Li, Q., Li, B., Zhong, G., McGowran, B., Zhou, Z., Wang, J., and Wang, P., 2006. Late Miocene development of the western Pacific warm pool: planktonic foraminifer and oxygen isotopic evidence. *Palaeogeography, Palaeoclimatology, Palaeoecology*, 237(2–4):465–482. <http://dx.doi.org/10.1016/j.palaeo.2005.12.019>
- Li, X., Wei, G., Shao, L., Liu, Y., Liang, X., Jian, Z., Sun, M., and Wang, P., 2003. Geochemical and Nd isotopic variations in sediments of the South China Sea: a response to Cenozoic tectonism in SE Asia. *Earth and Planetary Science Letters*, 211(3–4):207–220. [http://dx.doi.org/10.1016/S0012-821X\(03\)00229-2](http://dx.doi.org/10.1016/S0012-821X(03)00229-2)
- Martini, E., 1971. Standard Tertiary and Quaternary calcareous nannoplankton zonation. In Farinacci, A. (Ed.), *Proceedings of the Second Planktonic Conference, Roma 1970*: Rome (Edizioni Tecnoscienza), 2:739–785.
- Métivier, F., Gaudemer, Y., Tapponnier, P., and Klein, M., 1999. Mass accumulation rates in Asia during the Cenozoic. *Geophysical Journal International*, 137(2):280–318. <http://dx.doi.org/10.1046/j.1365-246X.1999.00802.x>
- Prell, W.L., Wang, P., Blum, P., Rea, D.K., and Clemens, S.C. (Eds.), 2006. *Proceedings of the Ocean Drilling Program, Scientific Results*, 184: College Station, TX (Ocean Drilling Program). <http://dx.doi.org/10.2973/odp.proc.sr.184.2006>
- Ru, K., and Pigott, J.D., 1986. Episodic rifting and subsidence in the South China Sea. *AAPG Bulletin*, 70(9):1136–1155. <http://aapgbull.geoscienceworld.org/content/70/9/1136.short>
- Su, X., Xu, Y., and Tu, Q., 2004. Early Oligocene–Pleistocene calcareous nanofossil biostratigraphy of the northern South China Sea (Leg 184, Sites 1146–1148). In Prell, W.L., Wang, P., Blum, P., Rea, D.K., and Clemens, S.C. (Eds.), *Proceedings of the Ocean Drilling Program, Scientific Results*, 184: College Station, TX (Ocean Drilling Program), 1–24. <http://dx.doi.org/10.2973/odp.proc.sr.184.224.2004>
- Wade, B.S., Pearson, P.N., Berggren, W.A., and Pälike, H., 2011. Review and revision of Cenozoic tropical planktonic foraminiferal biostratigraphy and calibration to the geomagnetic polarity and astronomical time scale. *Earth-Science Reviews*, 104(1–3):111–142. <http://dx.doi.org/10.1016/j.earscirev.2010.09.003>
- Wang, G., Xie, S.-P., Qu, T., and Huang, R.X., 2011. Deep South China Sea circulation. *Geophysical Research Letters*, 38(5):L05601. <http://dx.doi.org/10.1029/2010GL046626>
- Zhang, P., Molnar, P., and Downs, W.R., 2001. Increased sedimentation rates and grain sizes 2–4 Myr ago due to the influence of climate change on erosion rates. *Nature*, 410(6831):891–897. <http://dx.doi.org/10.1038/35073504>
- Zijderveld, J.D.A., 1967. AC demagnetization of rocks: analysis of results. In Collinson, D.W., Creer, K.M., and Runcorn, S.K. (Eds.), *Methods in Palaeomagnetism*: Amsterdam (Elsevier), 254–286.